AD-A268 535

|||||||||||||||||||| (barcode)

DOCUMENTATION PAGE

	2. REPORT DATE March 1993	**3. REPORT TYPE AND DATES COVERED** Final Report 9/1/91-8/31/92

4. TITLE AND SUBTITLE Japan-U.S. Conference on Composite Materials	**5. FUNDING NUMBERS**
6. AUTHOR(S) K. L. Reifsnider	61102F 2306 A2

7. PERFORMING ORGANIZATION NAME(S) AND ADDRESS(ES) Virginia Polytechnic Inst & State Univ 301 Burruss Hall Blacksburg, VA 24061	**8. PERFORMING ORGANIZATION REPORT NUMBER** AFOSR-TR- 93 0620

9. SPONSORING / MONITORING AGENCY NAME(S) AND ADDRESS(ES) AFOSR/ NC Building 410, Bolling AFB DC 20332-6448	**10. SPONSORING / MONITORING AGENCY REPORT NUMBER** AFOSR-91-0330

11. SUPPLEMENTARY NOTES

12a. DISTRIBUTION / AVAILABILITY STATEMENT APPROVED FOR PUBLIC RELEASE; DISTRIBUTION IS UNLIMITED.	**12b. DISTRIBUTION CODE**

13. ABSTRACT *(Maximum 200 words)*

See Attached

DTIC
ELECTE
AUG 20 1993
S B D

93-19371
|||||||||||||||||||| (barcode)

93 8 19 081

14. SUBJECT TERMS			**15. NUMBER OF PAGES** 866
			16. PRICE CODE

17. SECURITY CLASSIFICATION OF REPORT UNCLASSIFIED	**18. SECURITY CLASSIFICATION OF THIS PAGE** UNCLASSIFIED	**19. SECURITY CLASSIFICATION OF ABSTRACT** UNCLASSIFIED	**20. LIMITATION OF ABSTRACT**

NSN 7540-01-280-5500

Standard Form 298 (Rev 2-89)
Prescribed by ANSI Std. 239-18
298-102

DISCLAIMER NOTICE
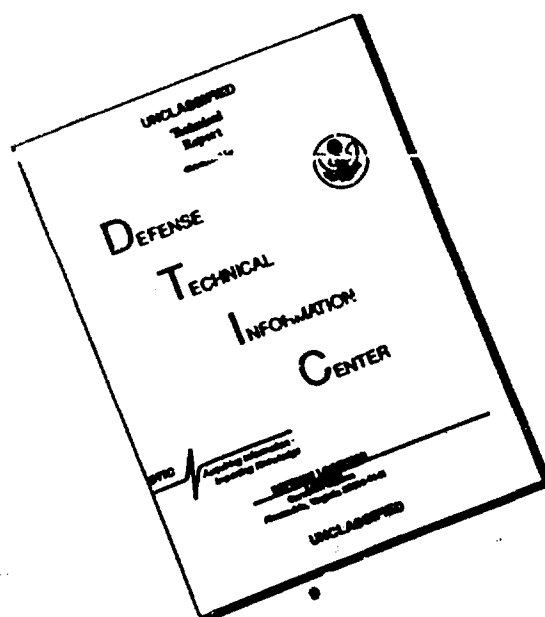
THIS DOCUMENT IS BEST
QUALITY AVAILABLE. THE COPY
FURNISHED TO DTIC CONTAINED
A SIGNIFICANT NUMBER OF
PAGES WHICH DO NOT
REPRODUCE LEGIBLY.

13. This conference has achieved its goal of updating the research and development community about recent advances in the area of modern composite materials, and about interactions and opportunities associated with US-Japan Cooperation.

The conference was organized and administered by the US-Japan Council for Composite Materials, with financial backing from the Virginia Institute for Materials Systems, which is part of Virginia Tech. Cooperating organizations include the American Society for Composites, American Society of Mechanical Engineers, Ohio Aeronautics Institute, and the Society of Engineering Mechanics. The scope of the Conference included all types of high performance composite systems, interfaces and interphases, high temperature materials, smart materials and structures, fracture, fatigue, and damage analysis Specific topic areas include: Materials System Design, Manufacturing and Processing. Fabrication of Components, Interfaces and Interphases, Woven and n-Dimensional Materials, High Temperature Materials, Stress Analysis and Micromechanics. The conference lasted for three days with 120 papers presented (40 from Japan and 80 from the US).

The papers presented at the conference were relevant for the current Air Force technology thrusts such as the Integrated High Performance Turbine Engine Program and the National Aerospace Plane.

Proceedings of the
Sixth Japan–U.S. Conference on Composite Materials

PROCEEDINGS OF THE
SIXTH JAPAN-U.S. CONFERENCE ON COMPOSITE MATERIALS

SPONSORED BY:

Air Force Office of Scientific Research
Army Research Office
Office of Naval Research
3M Corporation
Virginia Institute for Material Systems
Center for Adhesive and Sealant Science
VIRGINIA POLYTECHNIC INSTITUTE AND STATE UNIVERSITY

JUNE 22-24, 1992   **GROSVENOR RESORT**   **ORLANDO, FLORIDA**

TECHNOMIC
PUBLISHING CO., INC.
LANCASTER · BASEL

Proceedings of the Sixth Japan-U.S. Conference on Composite Materials

a TECHNOMIC publication

Accession For

NTIS GRA&I	☑
DTIC TAB	☐
Unannounced	☐
Justification	

By
Distribution/
Availability Codes

| Dist | Avail and/or Special |
| A-1 | |

DTIC QUALITY INSPECTED 3

Table of Contents

Preface

The Sixth Japan-U.S. Conference on Composite Materials was held in Orlando on 22–24 June, 1992. The meeting was an unqualified success and marked several firsts in the eleven-year history of the joint conference.

Attendance at the conference exceeded the 120 attendees anticipated. Papers were contributed by 32 industries (19 American, 13 Japanese), 15 government agencies (8 American, 7 Japanese), and 38 universities (26 American, 12 Japanese). Industry participation was a major objective of this conference; record levels were achieved, with remarkable balance between industry/university/government participation and American/Japanese contributions. The technical focus on high temperature composites was also highly successful, with four sessions and substantial discussion. In addition, there were sessions on stress analysis, interfaces and material systems, durability, micromechanics, structural analysis, design and optimization, test methods, strength analysis, and data bases. Finally, the five poster papers and six displays (especially the computerized data base displays) were very well received.

The post-conference tour was also a great success. The participants were lucky enough to get V.I.P. passes to see the Columbia launch from Cape Kennedy. (Columbia flew her maiden flight the year of the First Japan-U.S. Conference!) Our Japanese colleagues were thrilled with seeing the launch, as were the attending U.S. hosts.

The Sixth Japan-U.S. Conference on Composite Materials upheld the tradition of excellence established over the years, and added new dimensions to the event. The Japanese Organizing Committee has invited the U.S. to the seventh such conference in Japan, to be held in 1994.

K. L. REIFSNIDER
General Chairman

M. W. HYER
Program Chairman
Blacksburg, VA
September, 1992

JAPAN ORGANIZING COMMITTEE

Akira Kobayashi (Chair)

K. Kawata

T. Akasaka

Shigeo Kobayashi

S. Momoshima

M. Morita

I. Kimpara

N. Takeda

Tsuyoshi Hayashi

M. Uemura

S. Umekawa

H. Hojo

S. Kimura

Ryuichi Hayashi

I. Shiota

H. Miyairi

U.S. COUNCIL

K. Reifsnider (Chair)

R. Sierakowski (V. Chair)

D. Adams

T. K. O'Brien

K. Prewo

J. Quinliven

R. Christensen

M. Salkind

K. Kedward

M. Hyer

P. Beardmore

M. Taya

J. Vinson

S. S. Wang

Y. D. S. Rajapakse

C. Zweben

C. T. Sun

T. Mura

C. Bert

C. Chamis

J. Whitney

A. Dhingra

R. Schapery

G. Sendeckyj

CONFERENCE ORGANIZING COMMITTEE

K. Reifsnider (General Chair)

M. Hyer (Program Chair)

K. Prewo (Vice Chair for Industry)

K. Gramoll (Tours)

D. Adams (Reviews)

J. Lilly (Arrangements)
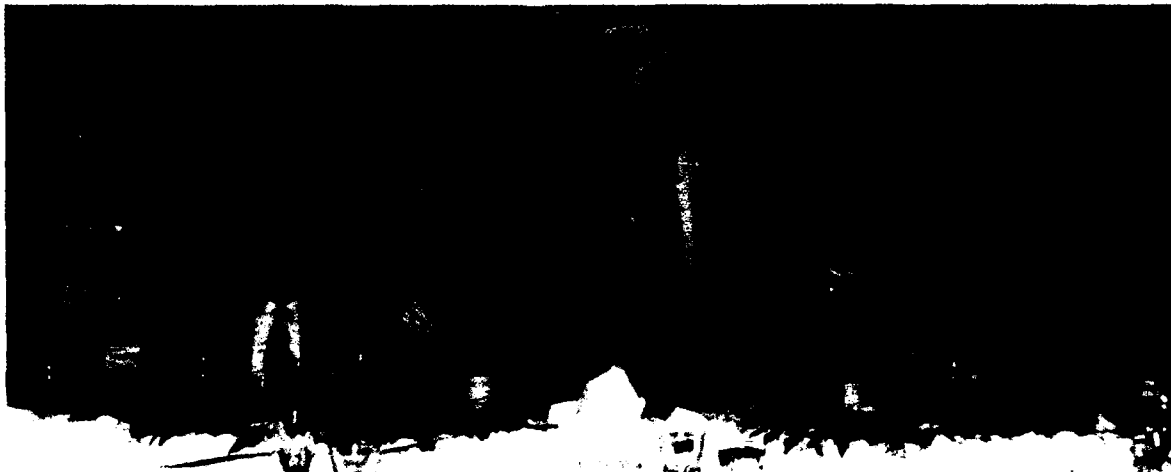
Japan–U.S. Council Dinner, June 24, 1992—*seated left to right,* S. Kimura, J. Whitney, A. Kobayashi, M. Hyer, K. Reifsnider, R. Sierakowski, *standing left to right,* A. Dhingra, M. Salkind, M. Shiao, I. Shiota, T. Akasaka, E. Lenoe, S. Umekawa, C. Bert C. Gramoll, N. Takeda

Keynote Address

Advances in Structural Mechanics of Rubber Composites

T. AKASAKA

ABSTRACT

The pneumatic tire is one of the typical goods of rubber composite, being known historically as the most aged in all composites. The rubber composites are characterized by the extremely low stiffness of rubber matrices compared with that of reinforcing cords. This characteristic feature yielded so far various unique theories for rubber composite materials and laminates, resulting in the existence of a characteristic cord angle, together with the derivation of explicit formulae for anisotropic elastic constants, some coupled deformations and interply shear deformations. In this paper, the basic concepts of these composite theories are described briefly, with stressing their significant rolles in the application for tire structures.

INTRODUCTION

Structural theories for rubber composites of tire, air-spring, flexible diaphragms, rubber bearing etc, have been developed since approximately 1950. These fiber reinforced rubber(FRR) composites are characterized by the extremely low stiffness of rubber matrices to that of reinforcing fibers(cords) and the considerable amount of interply shear deformation in the interply rubber layer, which are not observed in other composites. These characteristic features of rubber composites yielded various unique theories as (1)Netting Theory, (2)Cord-Inextensibility Theory, (3)Classical Lamination Theory, (4)Modified Lamination Theory and (5)Three Dimensional Theory.

Netting Theory was used not only for determining the tire cross section shape but also for estimating non-linear spring constants of tire sidewall under inflation pressure.

Cord-Inextensibility Theory could provide simple representations of two dimensional elastic constants with hyperbolic orthotropy for a laminated-biased FRR sheet and then showed the existence of characteristic cords together with the characteristic cord angle

Takashi Akasaka, Department of Precision Mechanics, Faculty of Science and Engineering, Chuo University, Kasuga 1-13-27, Bunkyo-ku, Tokyo 112, Japan

of 54.7°.

Classical Lamination Theory was developed originally for FRP composites with extensible fibers. This theory has been used extensively to FRR composites, since approximately 1964. From this theory, several coupled deformations of FRR laminates were clearly predicted by means of the coupling matrix elements.

Modified Lamination Theory, which is a modified theory of the classical lamination theory by considering the shearing deformation of thin rubber layers, has been used for analyzing the tire belt structure under various loadings, resulting in interply shearing stress concentration, structural stiffnesses and coupled deformations.

Three Dimensional Theory has been developed lately for FEM analysis for enabling large deformation analysis of the tire under inflation pressure and in contacting with the roadway.

The author intends here to explain the basic concepts of these theories and some useful results in their application for tire structures.

NETTING THEORY

Netting theory is based on the assumptions for cord-rubber composites that the cord is inextensible and the rubber matrix is so soft that is approximately ignored. Consequently, this could not be a structural theory, because such a composite sheet as above can not carry the general system of in-plane stresses. However, this theory has been used as a design theory, for providing the cross sectional shape of tire under inflation pressure. In a bias net structure, shown in Fig.1, which could be seen as a constituent element of the filament wound pipe or the tire carcass, the ratio of two membrane forces, N_y and N_x, in the directions of symmetric axes y and x respectively, is related uniquely to the bias angle, θ, as follows.

$$\frac{N_y}{N_x} = \tan^2\theta \qquad (1)$$
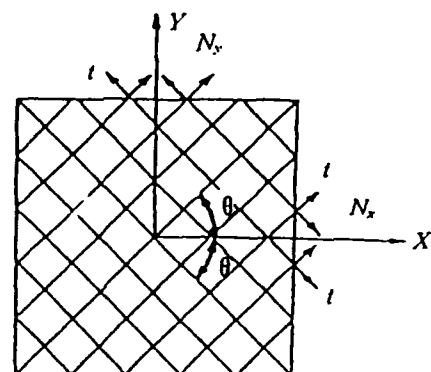
Fig.1 Bias net structure

Since the ratio of N_y/N_x is 2 for the filament wound pipe under the inflation pressure, the equilibrated bias angle θ^* becomes $\tan^{-1}\sqrt{2} = 54.7°$, as well known. The cross section shape of a radial tire sidewall, shown in Fig.2, is given by using the netting theory[1] as

$$z = \int_r^{r_D} \frac{A}{\sqrt{A_0^2 - A^2}} dr \qquad (2)$$

where

$$A = (r^2 - r_C^2)\sin\phi_D$$
$$A_0 = r_D^2 - r_C^2 \qquad (3)$$

Fig.2 Cross section of a radial tire sidewall

and B, C and D denote the bead, the turning point and the tread end, respectively.

It is noted that this tire cross section shape given by Eq.(2) can be written also by the use of elliptic integrals[2]. The cord length of sidewall, L, and the cord tension, t, are

given as follows.

$$L = \int_{r_B}^{r_D} \frac{A_0}{\sqrt{A_0^2 - A^2}} dr \qquad (4)$$

$$t = \frac{\pi p}{N} \frac{A_0}{\sin \phi_D} \qquad (5)$$

where N is the total number of radial carcass cords.

Since Eqs.(2),(4) and (5) contain three parameters of r_C, r_D and ϕ_D, the relationship between the deformation and the applied load, can be obtained by considering parameter variations of $\delta r_C, \delta r_D$ and $\delta \phi_D$.

For an example, the radial spring constant, K_r[3], is defined by the ratio of δH to δr_D, where δH denotes the radial tension distributed uniformly along the periphery of the tread end D, as shown in Fig.2.

Then, we have

$$H = t \cos \phi_D = \frac{\pi p}{N}(r_D^2 - r_C^2) \cot \phi_D \qquad (6)$$

and thus

$$\delta H = \frac{\partial H}{\partial r_C} \delta r_C + \frac{\partial H}{\partial \phi_D} \delta \phi_D + \frac{\partial H}{\partial r_D} \delta r_D \qquad (7)$$

The cord inextensibility condition, $\delta L = 0$, and the fixed condition of the bead, $\delta z_B = 0$, are represented by

$$\delta L = \frac{\partial L}{\partial r_C} \delta r_C + \frac{\partial L}{\partial \phi_D} \delta \phi_D + \frac{\partial L}{\partial r_D} \delta r_D = 0$$

$$\delta z_B = \frac{\partial z_B}{\partial r_C} \delta r_C + \frac{\partial z_B}{\partial \phi_D} \delta \phi_D + \frac{\partial z_B}{\partial r_D} \delta r_D = 0 \qquad (8)$$

Fig.3 Variation of radial spring constant K_r due to inflation pressure p

where z_B is provided by putting r_B in the lower limit of integral given by Eq.(2), in place of r. Elimination of δr_C and $\delta \phi_D$ from Eq.(7) and (8), yields the radial spring constant, $K_r(C)$, per unit length of the bead periphery with the consideration for both sides of the sidewall as

$$K_r(C) = \frac{\delta H}{\delta r_D} \frac{2N}{2\pi r_B} \qquad (9)$$

where the notation(C) denotes the contribution of cord tension and thus $K_r(C)$ is proportional to the inflation pressure p. The additional contribution of the rubber matrix to K_r, which is denoted by $K_r(R)$, can be evaluated approximately by considering the strain energy due to the stretching

Fig.4 Nonlinear characteristic curve for $K_C(C)$ vs η

in the circumferentical direction together with the
bending deformation in the meridian section, con-
sidering the change of curvature κ as

$$\kappa = \frac{dA/dr}{A_0} = \frac{2r\sin\phi_D}{r_D^2 - r_C^2} \qquad (10)$$

Evidently, $K_r(R)$ is independent of the inflation
pressure p. The predicted result for $K_r = K_r(C) + K_r(R)$ is shown in Fig.3, compared with the ex-
perimental results. The above mentioned linear
analysis is available for deriving a nonlinear rela-
tionship between K_r and the radial displacement
δr_D, by using the successive integration method.
The calculated result for $K_r(C)$ vs $\delta r_D (= -\eta)$ is
shown in Fig.4[4], indicating that $K_r(C)$ increases
sharply with the increase of outward displacement
δr_D, while it decreases markedly with the increase
of inward displacement of η. Additional spring
constants of lateral and rotational stiffnesses of
tire sidewall, denoted by K_s[5] and K_t[6] respec-
tively, are also analyzed by the same procedure as
above. These results are shown in Figs.5 and 6.

CORD INEXTENSIBILITY THEORY [7]

The assumption of cord inextensibility was intro-
duced first by Adkins and Rivlin[8] in their model
of rubber composite, made of incompressible rub-
ber and stiff cords with zero cross sectional area.
This assumptions are effectively used for estab-
lishing the two dimensional orthotropy of a lami-
nated biased sheet model shown in Fig.7. Elastic-
ity laws for this sheet are given by

$$\sigma_x = E\left(\epsilon_x + \frac{1}{2}\epsilon_y\right) + (\sigma_1 + \sigma_2)\cos^2\theta$$

$$\sigma_y = E\left(\epsilon_y + \frac{1}{2}\epsilon_x\right) + (\sigma_1 + \sigma_2)\sin^2\theta \qquad (11)$$

$$\tau_{xy} = (\sigma_1 - \sigma_2)\sin 2\theta$$

Fig.5 Variation of lateral spring
constant K_s due to inflation pressure p
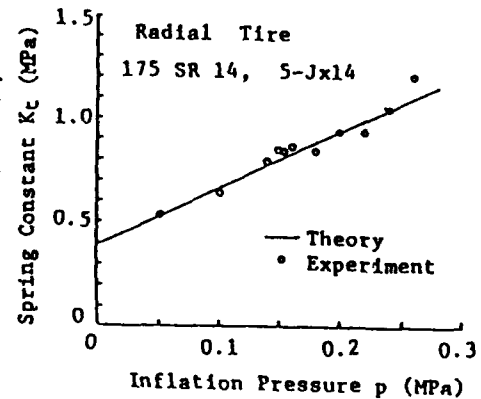
Fig.6 Variation of rotational spring
constant K_t due to inflation pressure p
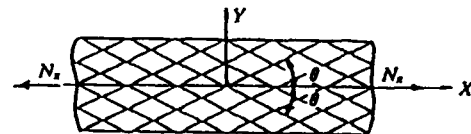
Fig.7 A laminated biased sheet of
inextensible cord reinforced rubber

where σ_x, σ_y and τ_{xy} are the plane stress system with respect to the coordinate axes x
and y bisecting the cord angle 2θ, σ_1 and σ_2 denote cord tensions and E is the modified
elastic modulus of rubber, which is represented approximately by $(4/3)E_R$ with the use
of rubber modulus E_R and Poisson's ratio of rubber $\nu_R = 0.5$. Considering the cord
inextensibility condition of

$$\epsilon_x \cos^2\theta + \epsilon_y \sin^2\theta = 0 \qquad (12)$$

and the inherent condition of $\gamma_{xy} = 0$ as far as both σ_1 and σ_2 are positive, lead to the following representations for elastic moduli:

$$E_x = E(1 - \cot^2\theta + \cot^4\theta), \qquad \nu_x = -\frac{\varepsilon_y}{\varepsilon_x} = \cot^2\theta$$

$$E_y = E(1 - \tan^2\theta + \tan^4\theta), \qquad \nu_y = -\frac{\varepsilon_x}{\varepsilon_y} = \tan^2\theta \qquad (13)$$

$$G_{xy} = \infty$$

where the Maxwell-Betti's reciprocal relation of $E_x/E_y = \nu_x/\nu_y$ is automatically satisfied.

An experimental verification for the inverse value of elastic modulus $1/E_x(\theta)$ was made through simple extension tests, as shown in Fig.8. The minimum value of $E_x(\theta)$ becomes equal to E_R for the characteristic bias angle of $\theta^* = \tan^{-1}\sqrt{2} = 54.7°$. It is noted here that the black circles located in the bias angle range of $\theta^* < \theta < 90°$, correspond to the case when the cord tension of σ_1 or σ_2 attains a negative value. The compatibility equation for the stress function $F(x,y)$ of an orthotropic plate is provided by

$$\frac{\partial^4 F}{\partial x^4} + E_y\left(\frac{1}{G_{xy}} - \frac{2\nu_x}{E_x}\right)\frac{\partial^4 F}{\partial x^2 \partial y^2} + \frac{E_y}{E_x}\frac{\partial^4 F}{\partial y^4} = 0 \qquad (14)$$

which is reduced to

$$\left(\frac{\partial^2}{\partial x^2} - \tan^2\theta\frac{\partial^2}{\partial y^2}\right)^2 F = 0 \qquad (15)$$

by using the elastic moduli given in Eq.(13). Equation(15) is a differential equation of bi-hyperbolic type. Denoting the displacement functions in the x and y directions by u and v respectively, we have

$$\left(\frac{\partial^2}{\partial x^2} - \tan^2\theta\frac{\partial^2}{\partial y^2}\right)(u,v) = 0 \qquad (16)$$

which is the wave equation.

General solution of $F(x,y)$ is given by

Fig.8 Variation of $E_x(45)/E_x(\theta)$ due to bias angle θ

$$F = \xi f_1(\eta) + \eta f_2(\xi) + g_1(\eta) + g_2(\xi) \qquad (17)$$

which leads to the following representations for stresses and displacements:

$$\sigma_x = \lambda^2[\xi f_1''(\eta) + \eta f_2''(\xi) - 2f_1'(\eta) - 2f_2'(\xi) + g_1''(\eta) + g_2''(\xi)]$$
$$\sigma_y = \xi f_1''(\eta) + \eta f_2''(\xi) + 2f_1'(\eta) + 2f_2'(\xi) + g_1''(\eta) + g_2''(\xi) \qquad (18)$$
$$\tau_{xy} = \lambda[\xi f_1''(\eta) - \eta f_2''(\xi) + g_1''(\eta) - g_2''(\xi)]$$

$$u = -\frac{4\lambda^4}{E_x}[f_2(\xi) + f_1(\eta)]$$
$$v = \frac{4\lambda^3}{E_x}[f_2(\xi) - f_1(\eta)] \qquad (19)$$

where

$$x + \lambda y = \xi, \quad x - \lambda y = \eta, \quad \lambda = \cot\theta \qquad (20)$$

f_1, f_2, g_1, g_2 are arbitrary functions and the prime
denotes the differentiation with respect to each
reference argument. As an example, we analyzed
the deformation and stress distributions of a long
rubber composite strip having the width a, sub-
jected to a wavy extension in the width direction
along the edge, $x = \pm a/2$ shown in Fig.9, as

Fig.9 Long rubber composite strip
under a wavy lateral extension along
both sides

$$u = \pm u_0\left(1 + \beta\cos\frac{2\pi}{b}y\right) \qquad (21)$$

The result on the distribution of
displacement function u is depicted
in Fig.10, which shows an alternate
change of sign of u in the width
direction with a wavy pattern, as
predicted by the wave equation of
Eq.(16). The distribution of stress
in the x direction σ_x is illustrated in
Fig.11, which exhibits a pattern of
damped oscillation as predicted by
the bi-hyperbolic equation Eq.(15)
for the stress function F. These dis-
tributions are apparently so pecu-
liar properties that we can not ob-
serve in other composites. It should
be noted further that the character-
istic curves could happen to appear
in these composite sheets of hyper-
bolic type orthotropy under the spe-
cial boundary conditions[9].

Fig.10 Distribution of u of a long strip
under a periodic extension along the
edge,when $a/\lambda b = 1.5$,
$\lambda = \sqrt{3}$, $\beta = 0.5, 1$
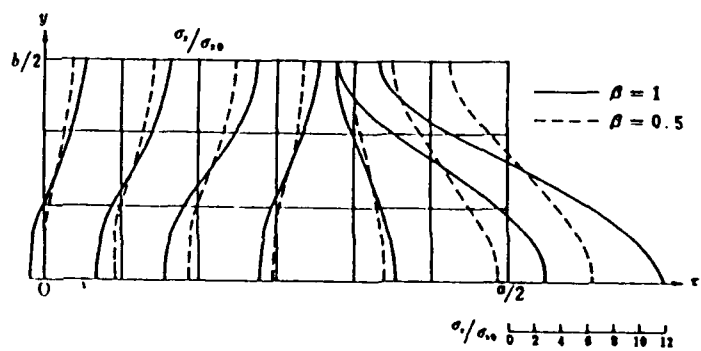
Fig.11 Distribution of σ_x of a long
strip under a periodic extension along
the edge,when $a/\lambda b = 1.5$,
$\lambda = \sqrt{3}$, $\beta = 0.5$ and 1

UDCRR SHEET

UDCRR(Uni-Directional Cord Reinforced Rubber) sheet is the fundamental structural
element of rubber composites.

We consider here the orthotropic elasticity law of UDCRR sheet, shown in Fig.12, with
consideration of cord extensibility.

Denoting the cord direction by L and the transverse direction by T, elastic constants,
E_L, E_T, ν_L, ν_T and G_{LT}, are given by several authors as,

(a)Halpin-Tsai's formulae:

$$E_L = E_f V_f + E_m V_m$$
$$E_T = E_m(1 + 2V_f)/(1 - V_f)$$
$$G_{LT} = \frac{G_m[G_f + G_m + (G_f - G_m)V_f]}{G_f + G_m - (G_f - G_m)V_f} \quad (22)$$
$$\nu_L = \nu_f V_f + \nu_m V_m, \quad \nu_T = \nu_L E_T/E_L$$
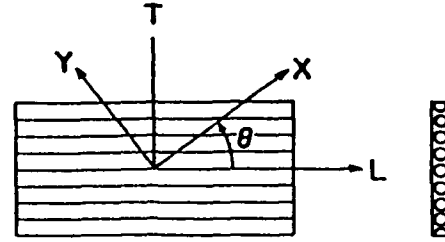
(b)Gough-Tangorra's formulae:

$$E_L = E_f V_f + E_m V_m$$
$$E_T = \frac{4E_m(1 - V_f)(E_f V_f + E_m V_m)}{3E_f V_f + 4E_m V_m}$$
$$G_{LT} = \frac{G_m}{V_m} \quad (23)$$
$$\nu_L = 0.5, \quad \nu_T = \nu_L E_T/E_L$$

(c)Akasaka-Hirano's formulae:

$$E_L = E_f V_f \qquad E_T = \frac{4}{3}\frac{E_m}{V_m}$$
$$G_{LT} = \frac{G_m}{V_m}, \quad \nu_L = 0.5, \quad \nu_T = \nu_L E_T/E_L \quad (24)$$
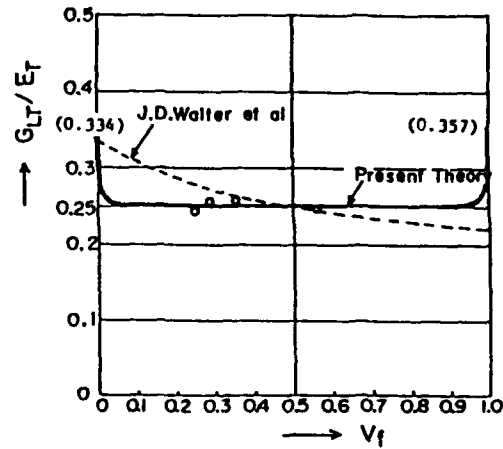
Fig.12 UDCRR sheet

Fig.13 Effect of Vf on the ratio of G_{LT}/E_T in a UDCRR sheet

where letters of f and m denote cord fiber and rubber matrix respectively, E, G and ν are elastic moduli and V is the volume fraction.

In these mixture rules, the assumptions of $E_f \gg E_m$, and $\nu_m \simeq 0.5$ are preferably used for rubber composites. An investigation on the accuracy of these mixture rules for a UDCRR sheet of the practical use was conducted by Walter et al[10], who concluded that the differences among these formulae might remain within the experimental errors.

According to the simplest formulae (c), we obtain an important relationship between G_{LT} and E_T as

$$G_{LT} = \frac{E_T}{4} \quad (25)$$

by taking the approximation of $G_m = E_m/3$.

Another formula for E_T and G_{LT} were obtained by the present author[11] for a UDCRR model with a rectangular cord cross section, as

$$\frac{1}{E_T} = \frac{V_f}{E_f} + \frac{V_m}{E_m} - V_f V_m \frac{(\nu_m/E_m - \nu_f/E_f)^2}{V_f/E_m + V_m/E_f}$$
$$\frac{1}{G_{LT}} = \frac{V_f}{G_f} + \frac{V_m}{G_m} \quad (26)$$

By using the approximations that $E_f \gg E_m, G_f \gg G_m$ and $\nu_m = 1/2$, we arrive at the same result as Eq.(25).

Figure 13 shows the relationship between the ratio of G_{LT}/E_T and the volume fraction of V_f compared with the experimental results for specimens of Rayon-Rubber composite,

where the broken curve comes from the modified Halpin-Tsai's formula[12] given by

$$\frac{G_{LT}}{E_T} = \frac{1+V_f}{3(1+2V_f)} \tag{27}$$

The elasticity laws for the UDCRR sheet with respect to the x and y coordinates, illustrated in Fig.12, are written by means of Eq.(25) as follows[13]:

$$\left\{ \begin{array}{c} \sigma_x \\ \sigma_y \\ \tau_{xy} \end{array} \right\} = \left[\begin{array}{ccc} E_{xx} & E_{xy} & E_{xs} \\ E_{xy} & E_{yy} & E_{ys} \\ E_{xs} & E_{ys} & E_{ss} \end{array} \right] \left\{ \begin{array}{c} \epsilon_x \\ \epsilon_y \\ \gamma_{xy} \end{array} \right\}, \text{or} \left\{ \begin{array}{c} \epsilon_x \\ \epsilon_y \\ \gamma_{xy} \end{array} \right\} = \left[\begin{array}{ccc} C_{xx} & C_{xy} & C_{xs} \\ C_{xy} & C_{yy} & C_{ys} \\ C_{xs} & C_{ys} & C_{ss} \end{array} \right] \left\{ \begin{array}{c} \sigma_x \\ \sigma_y \\ \tau_{xy} \end{array} \right\} \tag{28}$$

where elements of stiffness matrix $[E]$ are given by

$$\begin{aligned} E_{xx} &= E_L \cos^4 \theta + E_T, & E_{yy} &= E_L \sin^4 \theta + E_T \\ E_{xy} &= E_L \sin^2 \theta \cos^2 \theta + \frac{1}{2}E_T, & E_{xs} &= -E_L \sin \theta \cos^3 \theta \\ E_{ys} &= -E_L \sin^3 \theta \cos \theta, & E_{ss} &= E_L \sin^2 \theta \cos^2 \theta + \frac{1}{4}E_T \end{aligned} \tag{29}$$

Elements of compliance matrix $[C] = [E]^{-1}$ are provided by

$$\begin{aligned} C_{xx} &= \frac{1}{E_T} \sin^2 \theta (1 + 3\cos^2 \theta) + \frac{1}{E_L} \cos^2 \theta \cos 2\theta \\ C_{yy} &= \frac{1}{E_T} \cos^2 \theta (1 + 3\sin^2 \theta) - \frac{1}{E_L} \sin^2 \theta \cos 2\theta \\ C_{xy} &= -\frac{3}{E_T} \sin^2 \theta \cos^2 \theta - \frac{1}{2E_L} \cos^2 2\theta \\ C_{xs} &= \frac{1}{E_T} \sin 2\theta (2\cos^2 \theta - \sin^2 \theta) - \frac{1}{2E_L} \sin 2\theta (3\cos^2 \theta - \sin^2 \theta) \\ C_{ys} &= \frac{1}{E_T} \sin 2\theta (2\sin^2 \theta - \cos^2 \theta) - \frac{1}{2E_L} \sin 2\theta (3\sin^2 \theta - \cos^2 \theta) \\ C_{ss} &= \frac{1}{E_T}(1 + 3\cos^2 2\theta) + \frac{2}{E_L} \sin^2 2\theta \end{aligned} \tag{30}$$

For the uniaxial extension in the x direction, denoted by $\{\sigma_x, 0, 0\}^t$, Eq.(28) leads to

$$\gamma_{xy} = C_{xs}\sigma_x \approx \frac{2\sigma_x}{E_T} \sin \theta \cos^3 \theta (2 - \tan^2 \theta) \tag{31}$$

which reveals that the coupled shear strain vanishes at $\theta^* = \tan^{-1} \sqrt{2} = 54.7°$, that is the characteristic angle defined previously.

CLASSICAL LAMINATION THEORY

Classical lamination theory, which were extended for composite laminates with rather hard matrices of plastics and metals, has been useful also for rubber composites in estimating their stiffnesses and the coupling deformations.

Elasticity law involved in the in-plane and the out-of-plane deformations is given by

$$
\left\{
\begin{array}{c}
N_x \\
N_y \\
N_{xy} \\
M_x \\
M_y \\
M_{xy}
\end{array}
\right\}
=
\left[
\begin{array}{cccccc}
A_{xx} & A_{xy} & A_{xs} & B_{xx} & B_{xy} & B_{xs} \\
A_{xy} & A_{yy} & A_{ys} & B_{xy} & B_{yy} & B_{ys} \\
A_{xs} & A_{ys} & A_{ss} & B_{xs} & B_{ys} & B_{ss} \\
B_{xx} & B_{xy} & B_{xs} & D_{xx} & D_{xy} & D_{xs} \\
B_{xy} & B_{yy} & B_{ys} & D_{xy} & D_{yy} & D_{ys} \\
B_{xs} & B_{ys} & B_{ss} & D_{xs} & D_{ys} & D_{ss}
\end{array}
\right]
\left\{
\begin{array}{c}
\epsilon_x^o \\
\epsilon_y^o \\
\gamma_{xy}^o \\
\kappa_x \\
\kappa_y \\
\kappa_{xy}
\end{array}
\right\}
\tag{32}
$$

Elements of stiffness matrix are provided by

$$
(A_{ij}, B_{ij}, D_{ij}) = \sum_{m=1}^{N} \int_{h_{m-1}}^{h_m} \left(1, -z, z^2\right) E_{ij}^{(m)} dz \qquad (i, j = x, y, s) \tag{33}
$$

where the standard plane can be arbitrarily chosen and $E_{ij}^{(m)}$ denotes the stiffness matrix element of m-th layer illustrated in Fig.14.

Orthotropic elastic constants for the two-ply laminated biased UDCRR sheet, shown in Fig.7, can be determined from Eq.(32) as follows.

$$
\begin{array}{ll}
E_x = E_{xx}^* - (E_{xy}^*)^2/E_{yy}^*, & E_y = E_{yy}^* - (E_{xy}^*)^2/E_{xx}^* \\
\nu_x = E_{xy}^*/E_{yy}^*, & \nu_y = E_{xy}^*/E_{xx}^*, \qquad G_{xy} = E_{ss}^*
\end{array}
\tag{34}
$$

where

$$
A_{ij} = \frac{h}{2}\{E_{ij}(\theta) + E_{ij}(-\theta)\} \equiv h E_{ij}^*(\theta) \tag{35}
$$

and

$$
[E^*(\theta)] =
\left[
\begin{array}{ccc}
E_{xx}^* & E_{xy}^* & 0 \\
E_{xy}^* & E_{yy}^* & 0 \\
0 & 0 & E_{ss}^*
\end{array}
\right]
\tag{36}
$$

Fig.14 Composite laminates and standard plane($z = 0$)

These equations were obtained by Clark[14], who verified them experimentally. Equation(34) can be further simplified by applying Eq.(29) as the following explicit formulae[13]:

$$
E_x = [E_L E_T(\sin^4\theta - \sin^2\theta \cos^2\theta + \cos^4\theta) + \frac{3}{4}E_T^2]/(E_L \sin^4\theta + E_L)
$$

$$
E_y = [E_L E_T(\sin^4\theta - \sin^2\theta \cos^2\theta + \cos^4\theta) + \frac{3}{4}E_T^2]/(E_L \cos^4\theta + E_L)
$$

$$
\nu_x = (E_L \sin^2\theta \cos^2\theta + \frac{1}{2}E_T)/(E_L \sin^4\theta + E_T) \tag{37}
$$

$$
\nu_y = (E_L \sin^2\theta \cos^2\theta + \frac{1}{2}E_T)/(E_L \cos^4\theta + E_T)
$$

$$
G_{xy} = E_L \sin^2\theta \cos^2\theta + \frac{1}{4}E_T \cos^2 2\theta
$$

where the Maxwell-Betti's relation $E_x/E_y = \nu_x/\nu_y$ holds true. Figures.15,16 and 17 show the relationships of E_x, G_{xy} and ν_x respectively to the bias angle θ for an example, in which $E_L = 1440\,MPa$ and $E_T = 6.9\,MPa$. The broken lines in these figures denote the theoretical results and the small circles denote experimental results, both obtained by

Clark. The solid lines are obtained from Eq.(37), which are shown to be very close to the curves obtained from Eq.(36). It is found in Fig.15 that the curve of cord inextensibility theory is not valid in a narrow interval of bias angle ranging from $0°$ to $15°$ for this example. The laminated biased rubber composite with low bias angle of approximately $20°$ well corresponding to the belt structure of radial tire, embodies B_{xs} being largest in the coupling matrix of $[B]$. Then, the marked coupled correlations occur between N_x and κ_{xy} and also between M_x and γ_{xy}^o as easily seen from Eq.(32). The former is the coupled extensional-torsional deformation, while the latter is the coupled bending-shear deformation which is deeply related to the "Ply Steer" phenomenon of radial tire.

The cylindrical bending stiffness of the tire belt structure, D_x, is obtained from Eq.(32)[15] as

$$D_x = \frac{M_x}{\kappa_x} = D_{xx} - \frac{B_{xs}^2}{A_{ss}} \qquad (38)$$

Figure 18 shows the variation of D_x of the tire belt structure due to the bias angle θ, compared with the experimental results. It should be noted that the bending stiffness D_x varies considerably due to the boundary conditions other than the cylindrical bending.
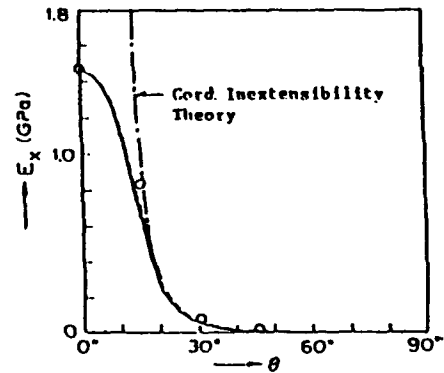
Fig.15 Variation of E_x due to bias angle θ
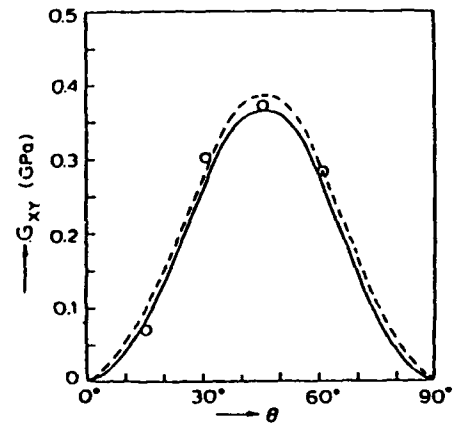
Fig.16 Variation of G_{xy} due to bias angle θ
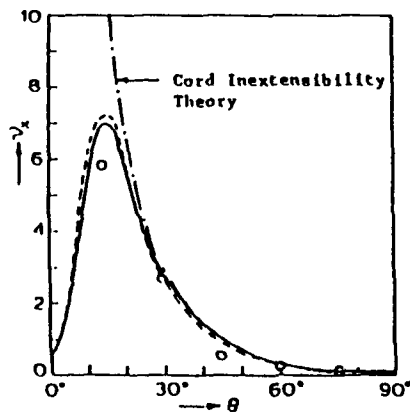
Fig.17 Variation of Poisson's ratio ν_x due to bias angle θ
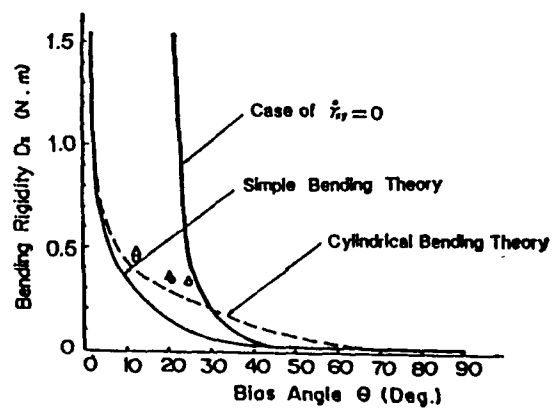
Fig.18 Variation of cylindrical bending stiffness D_x of tire belt structure due to bias angle θ

MODIFIED LAMINATION THEORY

A characteristic feature of rubber composite laminates is the interply shear deformation which is not considered in the classical lamination theory. Then, we should built up the equilibrium equation for each constituent ply which is subjected to shearing stresses transmitted from the interply rubber layer. The rubber layer is considered to be so thin that its contribution to the tensile stiffness of the composite is negligible. Following the notations of Fig.19, the equilibrium conditions for each constituent ply ($i = 1, 2$)[16] are

ORTHOTROPIC LAYER 2

INTERPLY RUBBER LAYER

ORTHOTROPIC LAYER 1

Fig.19 Free body diagram of a laminate having two biased plies and interply rubber layer

$$\frac{\partial N_x^{(i)}}{\partial x} + \frac{\partial N_{xy}^{(i)}}{\partial y} = (-1)^i p_x$$

$$\frac{\partial N_{xy}^{(i)}}{\partial x} + \frac{\partial N_y^{(i)}}{\partial y} = (-1)^i p_x$$

$$\frac{\partial}{\partial x}\left(Q_x^{(1)} + Q_x^{(2)} + \bar{Q}_x\right)$$

$$+ \frac{\partial}{\partial y}\left(Q_y^{(1)} + Q_y^{(2)} + \bar{Q}_y\right) = q \qquad (39)$$

$$\frac{\partial M_x^{(i)}}{\partial x} + \frac{\partial M_{xy}^{(i)}}{\partial y} = Q_x^{(i)} + p_x\frac{h}{2}$$

$$\frac{\partial M_{xy}^{(i)}}{\partial x} + \frac{\partial M_y^{(i)}}{\partial y} = Q_y^{(i)} + p_y\frac{h}{2}$$

$$\bar{Q}_x = -p_x\bar{h}, \quad \bar{Q}_y = -p_y\bar{h}$$

where p_x and p_y denote the interply shearing stresses in the x and y directions respectively, h is the thickness of each ply and $\bar{h}$ is the thickness of the interply rubber layer.

Three membrane forces and moments, denoted by N and M respectively, are defined by

$$\left(N_x^{(i)}, N_y^{(i)}, N_{xy}^{(i)}\right) = \int_{-h/2}^{h/2}(\sigma_x^{(i)}, \sigma_y^{(i)}, \tau_{xy}^{(i)})dz^{(i)}$$

$$\left(M_x^{(i)}, M_y^{(i)}, M_{xy}^{(i)}\right) = -\int_{-h/2}^{h/2}(\sigma_x^{(i)}, \sigma_y^{(i)}, \tau_{xy}^{(i)})z^{(i)}dz^{(i)} \qquad (40)$$

Elasticity law for each ply expressed in terms of displacement components $u^{(i)}, v^{(i)}$ and w in the x, y and z directions respectively, is given by

$$\left\{\begin{array}{c} \sigma_x^{(i)} \\ \sigma_y^{(i)} \\ \tau_{xy}^{(i)} \end{array}\right\} = \left[\begin{array}{ccc} E_{xx}^{(i)} & E_{xy}^{(i)} & E_{xs}^{(i)} \\ E_{xy}^{(i)} & E_{yy}^{(i)} & E_{ys}^{(i)} \\ E_{xs}^{(i)} & E_{ys}^{(i)} & E_{ss}^{(i)} \end{array}\right]\left\{\begin{array}{c} u_{,x}^{(i)} - z^{(i)}w_{,xx} \\ v_{,y}^{(i)} - z^{(i)}w_{,yy} \\ u_{,y}^{(i)} + v_{,x}^{(i)} - 2z^{(i)}w_{,xy} \end{array}\right\} \qquad (41)$$

The interply shearing stresses are related to the displacements and the shear modulus G_m of the rubber layer as

$$p_x = G_m\psi_x = (G_m/\bar{h})(v^{(2)} - u^{(1)} + Hw_{,x})$$

$$p_y = G_m\psi_y = (G_m/\bar{h})(v^{(2)} - v^{(1)} + Hw_{,y}) \qquad (42)$$

where $H = h + \bar{h}$, and ψ_x and ψ_y denote the interply shear strains.

The following differential equations are obtained in terms of displacement components:

$$\{A_{xx}^{(i)}u_{,xx}^{(i)}+2A_{xs}^{(i)}u_{,xy}^{(i)}+A_{ss}^{(i)}u_{,yy}^{(i)}\}+\{A_{xs}^{(i)}v_{,xx}^{(i)}+(A_{xy}^{(i)}+A_{ss}^{(i)})v_{,xy}^{(i)}+A_{ys}^{(i)}v_{,yy}^{(i)}\} = (-1)^{i}\kappa(u^{(2)}-u^{(1)}+Hw_{,x})$$

$$\{A_{xs}^{(i)}u_{,xx}^{(i)}+(A_{xy}^{(i)}+A_{ss}^{(i)})u_{,xy}^{(i)}+A_{ys}^{(i)}u_{,yy}^{(i)}\}+\{A_{ss}^{(i)}v_{,xx}^{(i)}+2A_{xs}^{(i)}v_{,xy}^{(i)}+A_{yy}^{(i)}v_{,yy}^{(i)}\} = (-1)^{i}\kappa(v^{(2)}-v^{(1)}+Hw_{,y})$$

$$\bar{D}_{xx}w_{,xxxx} + 4\bar{D}_{xs}w_{,xxxy} + 2(\bar{D}_{xy} + 2\bar{D}_{ss})w_{,xxyy} + 4\bar{D}_{ys}w_{,xyyy} + \bar{D}_{yy}w_{,yyyy}$$
$$-\kappa H\{u_{,x}^{(2)} - u_{,x}^{(1)} + v_{,y}^{(2)} - v_{,y}^{(1)} + H(w_{,xx} + w_{,yy})\} = q \tag{43}$$

where

$$\kappa = G_m/h, \qquad A_{\alpha\beta}^{(i)} = hE_{\alpha\beta}^{(i)}, \qquad \bar{D}_{\alpha\beta} = \frac{h^3}{12}\sum_{i=1}^{2}E_{\alpha\beta}^{(i)} \tag{44}$$
$$(\alpha, \beta = x, y, s)$$

A Laminated Biased Strip of Two-Ply UDCRR Sheets under Extension[16]

We consider a laminated biased strip of two identical UDCRR sheets with the bias angle θ under the axial extension with a uniform strain ϵ_0 shown in Fig.20. The identity condition of two UDCRR sheets yields

$$A_{xx}^{(2)} = A_{xx}^{(1)} \equiv A_{xx}, \qquad A_{yy}^{(2)} = A_{yy}^{(1)} \equiv A_{yy}$$
$$A_{xy}^{(2)} = A_{xy}^{(1)} \equiv A_{xy}, \qquad -A_{xs}^{(2)} = A_{xs}^{(1)} \equiv A_{xs}$$
$$-A_{ys}^{(2)} = A_{ys}^{(1)} \equiv A_{ys}, \qquad A_{ss}^{(2)} = A_{ss}^{(1)} \equiv A_{ss} \tag{45}$$

Assuming the dislpacement components as

$$u^{(1)} = U(y) + u(y)x \quad , \quad v^{(1)} = V(y) + v(y)x$$
$$u^{(2)} = -U(y) + u(y)x \quad , \quad v^{(2)} = V(y) + v(y)x$$
$$w = \Omega xy \tag{46}$$
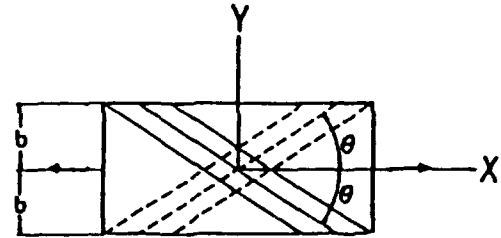
Fig.20 Laminated biased strip of ι ply UDCRR sheets under extension

and substituting these into Eq.(43) with considering Eq.(45), we obtain

$$A_{ss}u'' + A_{ys}v'' = 0, \qquad v' = 0$$
$$2A_{xs}u' + (A_{xy} + A_{ss})v' + A_{ss}U'' + A_{ys}V'' = \kappa(2U - \Omega Hy)$$
$$(A_{xy} + A_{xs})u' + 2A_{ys}v' + A_{ys}U'' + A_{yy}V'' = 0 \tag{47}$$
$$A_{ys}u'' + A_{yy}v'' = \kappa(2v - \Omega h)$$

Solutions of these equations under the loading condition of a constant mean strain across the width, the boundary conditions of zero stress along the edges and the zero torsional moment at any cross section, are obtained as:

$$\frac{N_x^{(2)}}{\epsilon_0} = \frac{N_x^{(1)}}{\epsilon_0} = \frac{\bar{A}_{ss}}{A_{yy}} - \frac{\bar{A}_{xs}^2}{A_{yy}\bar{A}_{xx}}\left[\frac{\cosh(\alpha y)}{\cosh(\alpha b)} + \frac{\Omega H}{\epsilon_0}\left\{1 - \frac{\cosh(\alpha y)}{\cosh(\alpha b)}\right\}\right] \tag{48}$$
$$N_y^{(2)} = N_y^{(1)} = 0 \tag{49}$$

$$-\frac{N_{xy}^{(1)}}{\varepsilon_0} = \frac{N_{xy}^{(2)}}{\varepsilon_0} = \frac{2D_{ss}\bar{A}_{xs}\{1 - \cosh(\alpha y)/\cosh(\alpha b)\}}{2D_{ss}A_{yy} + H^2\bar{A}_{xx}\{1 - \tanh(\alpha b)/\alpha b\}} \qquad (50)$$

$$\frac{\Omega}{\varepsilon_0} = \frac{H\bar{A}_{xs}\{1 - \tanh(\alpha b)/\alpha b\}}{2D_{ss}A_{yy} + H^2\bar{A}_{xx}\{1 - \tanh(\alpha b)/\alpha b\}} \qquad (51)$$

$$\frac{p_x}{\varepsilon_0} = -\frac{2\kappa}{\alpha}\frac{\bar{A}_{xs}2D_{ss}A_{yy}\sinh(\alpha y)/\cosh(\alpha b)}{\bar{A}_{xx}[2D_{ss}A_{yy} + H^2\bar{A}_{xx}\{1 - \tanh(\alpha b)/\alpha b\}]} \qquad (52)$$

$$p_y = 0 \qquad (53)$$

where $\bar{A}_{\alpha\beta}$ is the cofactor of $A_{\alpha\beta}$ in the matrix $[A]$ and

$$\alpha^2 = 2\kappa A_{yy}/\bar{A}_{xx} \qquad (54)$$

Both Ω and p_x vanish for the bias angle θ being equalized to the characteristic cord angle $\theta^* = \tan^{-1}\sqrt{2} = 54.7°$, because $\bar{A}_{xs} = A_{ys}A_{xy} - A_{yy}A_{xs}$ can be approximated by using Eq.(29), as follows.

$$\bar{A}_{xs} \approx -h^2(E_{ys}E_{xy} - E_{yy}E_{xs}) \approx -\frac{h^2}{2}E_L E_T \sin\theta\cos^3\theta\,(2 - \tan^2\theta) \qquad (55)$$

The notation $\bar{A}_{xx} = A_{ss}A_{yy} - A_{ys}^2$ is proved to be always positive as seen in the following approximation.

$$\bar{A}_{xx} \approx \frac{h^2}{4}E_T\{E_L\sin^2\theta\,(1 + 3\cos^2\theta) + E_T\} > 0 \qquad (56)$$

Figure 21 shows the distribution of axial stress $\sigma_x = N_x/h$ across the width for an example, in which $E_L = 1.960\,GPa, E_T = 39\,MPa, G_m = 4.9\,MPa, b = 50\,mm, h = 5\,mm$, and $\bar{h} = 1\,mm$. The stress decays rapidly as approaching the free edges.

Figure 22 shows the maximum interply shearing stress, $p_x(max)$, at the free edges as a function of the bias angle θ for the same laminate as shown in Fig.21. The peak value of $p_x(max)$ appears at $\theta \approx 10°$ and $p_x(max)$ vanishes at $\theta = \theta^* = 54.7°$.

Figure 23 shows the coupled rate of twist, Ω, as a function of the bias angle θ for an example, in which $E_L = 58.8\,GPa, E_T = 118\,MPa, G_m = 4.9\,MPa, h = 1.5\,mm, \bar{h} = 7\,mm$ and $b = 50\,mm$. Note that Ω vanishes also at $\theta = \theta^*$.
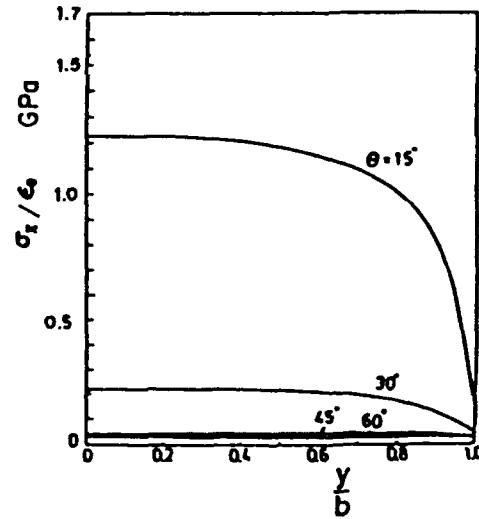
Fig.21 Distribution of axial stress σ_x across the half width for each of four bias angle

A Laminated Biased Strip of Two-Ply UDCRR Sheets under In-Plane Bending Moment[17]

For the next example, in which a laminated biased strip of two-ply UDCRR sheets is subjected to an in-plane bending moment M_0 shown in Fig.24, the displacement
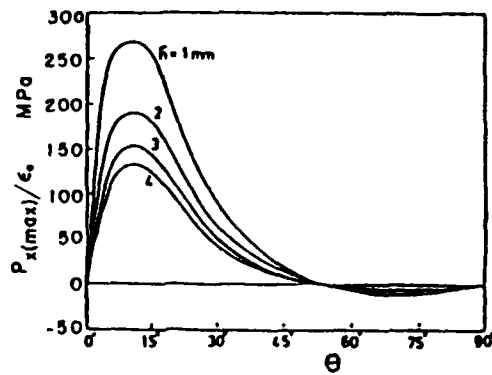
Fig.22 Variation of the maximum
interply shearing stress $p_x(max)$
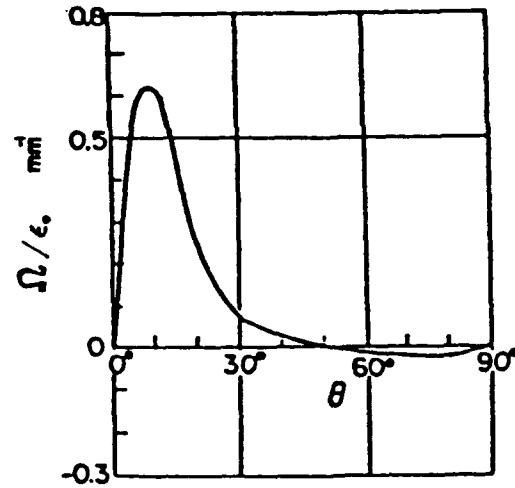
Fig.23 Variation of the angle of twist
Ω due to bias angle θ

components are assumed as

$$u^{(1)} = U(y) + u(y)x \quad , \quad v^{(1)} = V(y) + v(y)x^2$$
$$u^{(2)} = -U(y) + u(y)x \quad , \quad v^{(2)} = V(y) + v(y)x^2 \tag{57}$$
$$w = 0$$

The following system of differential equations is derived by substituting Eq.(57) into Eq.(43):

$$2A_{xs}u' + 2A_{xs}v + A_{ss}U'' + A_{ys}V'' = 2\kappa U$$
$$(A_{xy} + A_{ss})u' + 2A_{ss}v + A_{ys}U'' + A_{yy}V'' = 0$$
$$A_{ss}u'' + 2(A_{xy} + A_{ss})v' = 0$$
$$A_{ys}u'' + 4A_{xs}v' = 0, \qquad v'' = 0 \tag{58}$$

These equations are solved under the following boundary conditions:

Fig.24 Laminated biased strip of
two-ply UDCRR sheets under in-plane
bending moment

$$\int_{-b}^{b} (N_x^{(1)} + N_x^{(2)})dy = 0$$
$$\int_{-b}^{b} (N_x^{(1)} + N_y^{(2)})ydy = M_0 \tag{59}$$
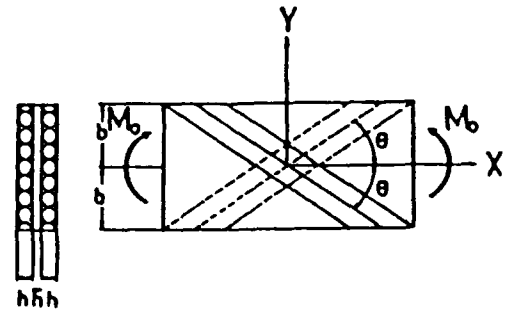
together with the stress free condition along the edges of the laminate. The membrane force N_x and the interply shearing stress p_x are obtained as follows.

$$N_x^{(2)} = Nx^{(1)} = -\frac{6\kappa M_0}{B}A_{yy}\left\{\frac{\bar{A}_{xs}^2}{\bar{A}_{xx}}b\sinh(\alpha y) - \bar{A}_{ss}\sinh(\alpha b)y\right\} \tag{60}$$

$$p_x = -\frac{6\kappa M_0}{B}A_{yy}\bar{A}_{xs}\{\alpha b\cosh(\alpha y) - \sinh(\alpha b)\} \tag{61}$$

where

$$B = 12b\bar{A}_{xs}^2\{\alpha b\cosh(\alpha b) - \sinh(\alpha b)\} - 8\kappa b^3 A_{yy}\bar{A}_{ss}\sinh(\alpha b) \tag{62}$$

The in-plane bending stiffness, D, is obtained from the ratio of M_0 to the curvature $d^2 v^{(1)}/dx^2$ as

$$D = \frac{-B}{6\kappa A_{yy} \sinh(\alpha b)} \tag{63}$$

Figure 25 shows the distribution of N_x across the width of the laminate, which have $E_L = 58.8\,GPa$, $E_T = 118\,MPa$, $G_m = 4.9\,MPa$, $h = 1.5\,mm$, $\bar{h} = 7\,mm$ and $b = 50\,mm$. The sigmoidal shape of N_x distribution, shown in Fig.25, is caused by the interply shear deformation. However, this distribution turns to be linear when the bias angle θ is equalized to $\theta^* = 54.7°$, for which $\bar{A}_{xs}$ vanishes in Eq.(60).

Figure 26 shows the maximum interply shearing stress $p_x(max)$, which always appears at the free edge of the laminate, as a function of the bias angle θ, compared with the experimental points that were obtained by the transparent grid method. It should be noted that $p_x(max)$ vanishes for the bias angle $\theta = \theta^*$ due to $\bar{A}_{xs}$ involved in Eq.(61).
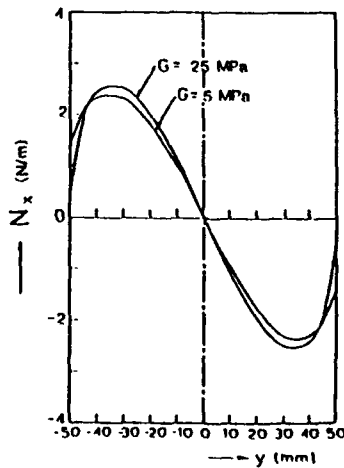
Fig.25 Distribution of N_x across the width of the laminate in Fig.24
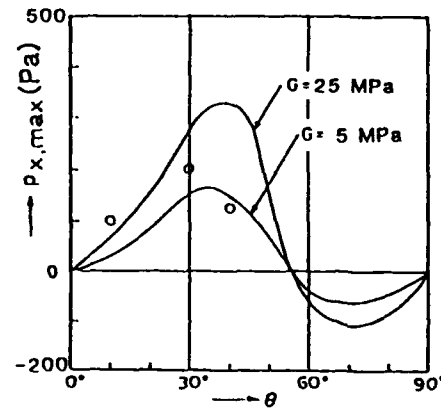
Fig.26 Variation of the max. interply shearing stress $p_x(max)$,due to bias angle θ
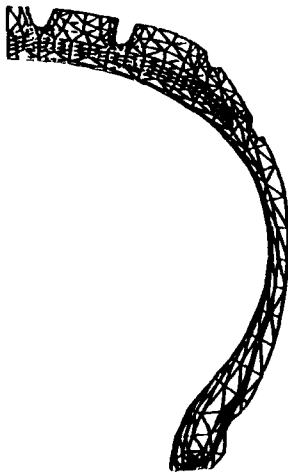
Fig.27 Three dimensional finite elements of tire structure
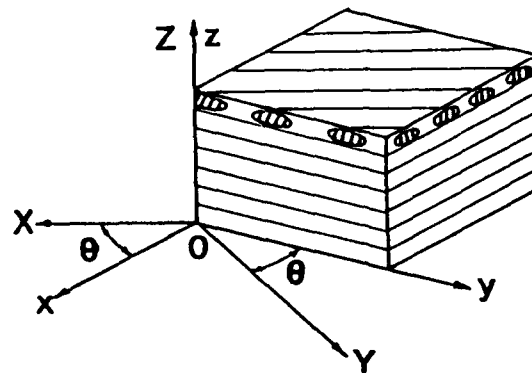
Fig.28 A composite laminate of multi UDCRR sheets

THREE DIMENSIONAL THEORY

The three dimensional finite element method has been widely used for tire structure

analysis on its stress distribution and deformation under static and dynamic loadings in contacting with the roadway. Figure 27[18] exhibits an example of divided elements in a tire cross section.

Some evaluation methods for the three dimensional elasticity of laminated composites have been developed by several authors[19][20], stressing interply shear deformations and the stiffness in the thickness direction. These results could be useful also for tire structural analyses. Three dimensional elasticity law for a UDCRR sheet, that is the i-th constituent layer of a composite laminate, is written with referencing the orthogonal coordinate axes of X, Y and Z, shown in Fig.28, as follows,

$$
\begin{Bmatrix} \varepsilon_X^{(i)} \\ \varepsilon_Y^{(i)} \\ \varepsilon_Z^{(i)} \\ \gamma_{XY}^{(i)} \\ \gamma_{YZ}^{(i)} \\ \gamma_{ZX}^{(i)} \end{Bmatrix} = \begin{bmatrix} \dfrac{1}{E_X^{(i)}} & -\dfrac{\nu_{XY}^{(i)}}{E_X^{(i)}} & -\dfrac{\nu_{XZ}^{(i)}}{E_X^{(i)}} & 0 & 0 & 0 \\[2mm] -\dfrac{\nu_{XY}^{(i)}}{E_X^{(i)}} & \dfrac{1}{E_Y^{(i)}} & -\dfrac{\nu_{YZ}^{(i)}}{E_Y^{(i)}} & 0 & 0 & 0 \\[2mm] -\dfrac{\nu_{XZ}^{(i)}}{E_X^{(i)}} & -\dfrac{\nu_{YZ}^{(i)}}{E_Y^{(i)}} & \dfrac{1}{E_Z^{(i)}} & 0 & 0 & 0 \\[2mm] 0 & 0 & 0 & \dfrac{1}{G_{XY}^{(i)}} & 0 & 0 \\[2mm] 0 & 0 & 0 & 0 & \dfrac{1}{G_{YZ}^{(i)}} & 0 \\[2mm] 0 & 0 & 0 & 0 & 0 & \dfrac{1}{G_{ZX}^{(i)}} \end{bmatrix} \begin{Bmatrix} \sigma_X^{(i)} \\ \sigma_Y^{(i)} \\ \sigma_Z^{(i)} \\ \tau_{XY}^{(i)} \\ \tau_{YZ}^{(i)} \\ \tau_{ZX}^{(i)} \end{Bmatrix} \tag{64}
$$

where X and Y denote the cord and the transverse directions respectively and $E_X^{(i)}, E_Y^{(i)}$, $E_Z^{(i)}$ are Young's moduli, $\nu_{XY}^{(i)}, \nu_{YZ}^{(i)}$ and $\nu_{ZX}^{(i)}$ are Poisson's ratios and $G_{XY}^{(i)}, G_{YZ}^{(i)}$ and $G_{ZX}^{(i)}$ are shear moduli of the i-th layer.

Transformation from the coordinates of X, Y, Z to the coordinates of x, y, z with the rotation angle θ_i in the counterclockwise direction around Z axis, yields,

$$
\begin{Bmatrix} \sigma_x^{(i)} \\ \sigma_y^{(i)} \\ \sigma_z^{(i)} \\ \tau_{xy}^{(i)} \\ \tau_{yz}^{(i)} \\ \tau_{zx}^{(i)} \end{Bmatrix} = \begin{bmatrix} A_{11}^{(i)} & A_{12}^{(i)} & A_{13}^{(i)} & A_{14}^{(i)} & 0 & 0 \\ A_{12}^{(i)} & A_{22}^{(i)} & A_{23}^{(i)} & A_{24}^{(i)} & 0 & 0 \\ A_{13}^{(i)} & A_{23}^{(i)} & A_{33}^{(i)} & A_{34}^{(i)} & 0 & 0 \\ A_{14}^{(i)} & A_{24}^{(i)} & A_{34}^{(i)} & A_{44}^{(i)} & 0 & 0 \\ 0 & 0 & 0 & 0 & A_{55}^{(i)} & A_{56}^{(i)} \\ 0 & 0 & 0 & 0 & A_{56}^{(i)} & A_{66}^{(i)} \end{bmatrix} \begin{Bmatrix} \varepsilon_x^{(i)} \\ \varepsilon_y^{(i)} \\ \varepsilon_z^{(i)} \\ \gamma_{xy}^{(i)} \\ \gamma_{yz}^{(i)} \\ \gamma_{zx}^{(i)} \end{Bmatrix} \tag{65}
$$

where

$$A_{11}^{(i)} = l^4 E_{XX}^{(i)} + 2l^2 m^2 E_{XY}^{(i)} + m^4 E_{YY}^{(i)} + 4l^2 m^2 G_{XY}^{(i)}$$

$$A_{12}^{(i)} = (l^4 + m^4) E_{XY}^{(i)} + l^2 m^2 (E_{XX}^{(i)} + E_{YY}^{(i)}) - 4l^2 m^2 G_{XY}^{(i)}$$

$$A_{13}^{(i)} = l^2 E_{XZ}^{(i)} + m^2 E_{YZ}^{(i)}$$

$$A_{14}^{(i)} = -l^3 m E_{XX}^{(i)} + lm(l^2 - m^2) E_{XY}^{(i)} + lm^3 E_{YY}^{(i)} + 2lm(l^2 - m^2) G_{XY}^{(i)}$$

$$A_{22}^{(i)} = l^4 E_{YY}^{(i)} + 2l^2 m^2 E_{XY}^{(i)} + m^4 E_{XX}^{(i)} + 4l^2 m^2 G_{XY}^{(i)}$$

$$A_{23}^{(i)} = i^2 E_{YZ}^{(i)} + m^2 E_{XZ}^{(i)}$$

$$A_{24}^{(i)} = -lm^3 E_{XX}^{(i)} - lm(l^2 - m^2)E_{XY}^{(i)} + l^3 m E_{YY}^{(i)} - 2lm(l^2 - m^2)G_{XY}^{(i)}$$

$$A_{33}^{(i)} = E_{ZZ}^{(i)}$$

$$A_{34}^{(i)} = -lm E_{XZ}^{(i)} + lm E_{YZ}^{(i)}$$

$$A_{44}^{(i)} = l^2 m^2 E_{XX}^{(i)} - 2l^2 m^2 E_{XY}^{(i)} + l^2 m^2 E_{YY}^{(i)} + (l^2 - m^2)^2 G_{XY}^{(i)}$$

$$A_{55}^{(i)} = l^2 G_{YZ}^{(i)} + m^2 G_{ZX}^{(i)}$$

$$A_{56}^{(i)} = lm(G_{YZ}^{(i)} - G_{ZX}^{(i)})$$

$$A_{66}^{(i)} = m^2 G_{YZ}^{(i)} + l^2 G_{ZX}^{(i)}$$

and

$$
\begin{bmatrix}
E_{XX}^{(i)} & E_{XY}^{(i)} & E_{XZ}^{(i)} \\
\\
E_{XY}^{(i)} & E_{YY}^{(i)} & E_{YZ}^{(i)} \\
\\
E_{XZ}^{(i)} & E_{YZ}^{(i)} & E_{ZZ}^{(i)}
\end{bmatrix}
=
\begin{bmatrix}
\dfrac{1}{E_X^{(i)}} & -\dfrac{\nu_{XY}^{(i)}}{E_X^{(i)}} & -\dfrac{\nu_{XZ}^{(i)}}{E_X^{(i)}} \\
\\
-\dfrac{\nu_{XY}^{(i)}}{E_X^{(i)}} & \dfrac{1}{E_Y^{(i)}} & -\dfrac{\nu_{YZ}^{(i)}}{E_Y^{(i)}} \\
\\
-\dfrac{\nu_{XZ}^{(i)}}{E_X^{(i)}} & -\dfrac{\nu_{YZ}^{(i)}}{E_Y^{(i)}} & \dfrac{1}{E_Z^{(i)}}
\end{bmatrix}^{-1}
\tag{66}
$$

and further $l = \cos\theta_i$, $m = \sin\theta_i$.

Taking the mean stresses and strains of the whole laminate as

$$
\bar{\sigma}_x = \frac{\sum t_i \sigma_x^{(i)}}{\sum t_i} \quad , \quad \bar{\sigma}_y = \frac{\sum t_i \sigma_y^{(i)}}{\sum t_i} \quad , \quad \bar{\sigma}_z = \sigma_z^{(i)}
$$

$$
\bar{\tau}_{xy} = \frac{\sum t_i \tau_{xy}^{(i)}}{\sum t_i} \quad , \quad \bar{\tau}_{yz} = \tau_{yz}^{(i)} \quad , \quad \bar{\tau}_{zx} = \tau_{zx}^{(i)}
\tag{67}
$$

$$
\bar{\varepsilon}_x = \varepsilon_x^{(i)} \quad , \quad \bar{\varepsilon}_y = \varepsilon_y^{(i)} \quad , \quad \bar{\varepsilon}_z = \frac{\sum t_i \varepsilon_z^{(i)}}{\sum t_i}
$$

$$
\bar{\gamma}_{xy} = \gamma_{xy}^{(i)} \quad , \quad \bar{\gamma}_{yz} = \frac{\sum t_i \gamma_{yz}^{(i)}}{\sum t_i} \quad , \quad \bar{\gamma}_{zx} = \frac{\sum t_i \gamma_{zx}^{(i)}}{\sum t_i}
\tag{68}
$$

We obtain finally

$$
\begin{Bmatrix}
\bar{\varepsilon}_x \\
\bar{\varepsilon}_y \\
\bar{\varepsilon}_z \\
\bar{\gamma}_{xy} \\
\bar{\gamma}_{yz} \\
\bar{\gamma}_{zx}
\end{Bmatrix}
=
\begin{bmatrix}
H_{11} & H_{12} & H_{13} & H_{14} & 0 & 0 \\
H_{12} & H_{22} & H_{23} & H_{24} & 0 & 0 \\
H_{13} & H_{23} & H_{33} & H_{34} & 0 & 0 \\
H_{14} & H_{24} & H_{34} & H_{44} & 0 & 0 \\
0 & 0 & 0 & 0 & H_{55} & H_{56} \\
0 & 0 & 0 & 0 & H_{56} & H_{66}
\end{bmatrix}
\begin{Bmatrix}
\bar{\sigma}_x \\
\bar{\sigma}_y \\
\bar{\sigma}_z \\
\bar{\tau}_{xy} \\
\bar{\tau}_{yz} \\
\bar{\tau}_{zx}
\end{Bmatrix}
\tag{69}
$$

Then, adopting the appropriate values of $E_X^{(i)}, E_Y^{(i)}, E_Z^{(i)}, \nu_{XY}^{(i)}, \nu_{YZ}^{(i)}, \nu_{ZX}^{(i)}, G_{XY}^{(i)}, G_{YZ}^{(i)}$, and $G_{ZX}^{(i)}$, we have the following mean elastic constants for the laminate as

$$\bar{E}_x = \frac{1}{H_{11}} \quad , \quad \bar{E}_y = \frac{1}{H_{22}} \quad , \quad \bar{E}_z = \frac{1}{H_{33}}$$

$$\bar{\nu}_{xy} = -\frac{H_{12}}{H_{11}} \quad , \quad \bar{\nu}_{yz} = -\frac{H_{23}}{H_{22}} \quad , \quad \bar{\nu}_{zx} = -\frac{H_{13}}{H_{33}} \qquad (70)$$

$$\bar{G}_{xy} = \frac{1}{H_{44}} \quad , \quad \bar{G}_{yz} = \frac{1}{H_{55}} \quad , \quad \bar{G}_{zx} = \frac{1}{H_{66}}$$

For a laminated biased strip of two identical UDCRR sheets, the Poisson's ratio $\bar{\nu}_{zx}$ becomes as

$$\bar{\nu}_{zx} = -\frac{H_{13}}{H_{11}} \approx \nu_{yz}(1 - \cot^2\theta) \qquad (71)$$

Then, $\bar{\nu}_{zx}$ takes a negative value for the bias range of $0 < \theta < \pi/4$, which implies that the thickness of the laminate increases by the axial extension. This phenomenon is verified by the experiments, as shown in Fig.29, where the full curve shows the following formula[21] as

$$\bar{\nu}_{zx} = -\frac{\bar{\epsilon}_z}{\bar{\epsilon}_x} = 1 + \frac{\bar{\epsilon}_y}{\bar{\epsilon}_x} = 1 - \bar{\nu}_{xy} \qquad (72)$$

Fig.29 Variation of Poisson's ratio ν_{zx} due to bias angle θ

which is given from the incompressibility assumption that $\bar{\epsilon}_x + \bar{\epsilon}_y + \bar{\epsilon}_z = 0$. The Poisson's ratio $\bar{\nu}_{xy}$ is given from Eq.(29) as

$$\bar{\nu}_{xy} = \frac{E_{xy}}{E_{yy}} = \frac{E_L \sin^2\theta \, \cos^2\theta + E_T/2}{E_L \sin^4\theta + E_T} \approx \cot^2\theta \qquad (73)$$
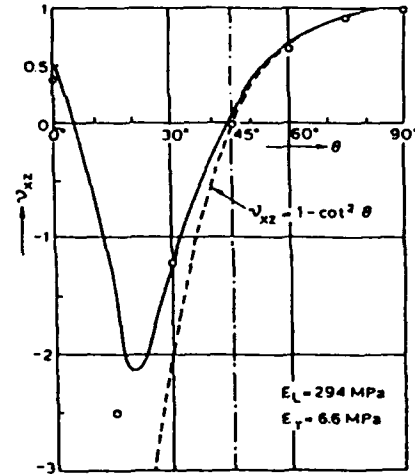
APPLICATION FOR TIRE STRUCTURE

Buckling Due To In-plane Bending Moment[22]
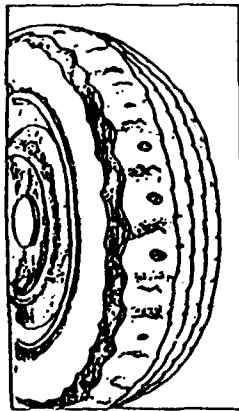
Fig.30 Exposed steel cords of a radial tire due to repeated cornering turns
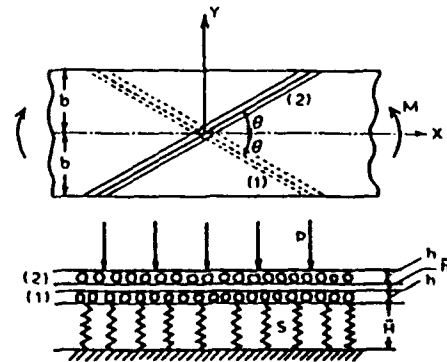
Fig.31 Laminated biased belt structure model on the elastic foundation of tread rubber having spring constants

Sharp cornering turns of radial tire on the roadway often induce the fatigue damage of

exposing steel cords at the periphery of the belt edge, as shown in Fig.30. The interval of neighbouring exposed steel cords is nearly 40mm. This phenomenon is due to buckling of the belt on the elastic foundation of the tread rubber having the spring constant, s, shown in Fig.31 under the in-plane bending moment transmitted from the roadway during cornering turns.

The practical distribution of the contact shear acting between the tread surface and the roadway is so complicated that the in-plane bending moment dose not always distribute uniformly. However, the contact patch is so short relative to the belt width and the in-plane shear stiffness of the laminated biased belt is so large that we could assume approximately a uniform bending deformation for the belt structure in the quasi-static cornering turn.

Then, we have the following basic equation for the deflection function, w,

$$
\begin{aligned}
&\bar{D}_{xx}w_{,xxxx} + 2\left(\bar{D}_{xy} + 2\bar{D}_{ss}\right)w_{,xxyy} + \bar{D}_{yy}w_{,yyyy} \\
&-\kappa H\left[u_{,x}^{(2)} - u_{,x}^{(1)} + v_{,y}^{(2)} - v_{,y}^{(1)} + H(w_{,xx} + w_{,yy})\right] = q + 2N_{xo}w_{,xx} - sw
\end{aligned}
\tag{74}
$$

together with the equations for $u^{(i)}$ and $v^{(i)}(i = 1, 2)$ given in Eq.(43), where N_{xo} is the bending membrane force given previously by Eq.(60).

Employing the Galerkin's method for an assumed function of $w(x, y)$, that satisfies the clamped condition along the belt edges, we obtain an approximate formula for the characteristic wave length λ_{cr} as

$$
\lambda_{cr} = 2\pi\left\{\frac{2D_L}{s + \frac{(2\pi)^2}{3}\kappa\left(\frac{H}{b}\right)^2}\right\}^{\frac{1}{4}}\cos\theta
\tag{75}
$$

where $H = h + \bar{h}$, D_L is the out-of-plane bending stiffness of a UDCRR layer in the cord direction, and κ is the shear spring constant previously given by Eq.(44). The numerical calculation for a 165 SR 13 radial tire yields $\lambda_{cr} = 43.5\,mm$, which is very close to the measured mean value of $40\,mm$.

Load-Deflection Property and Contact Pressure Distribution[23][24]

Tire structure has been modelled by a spring bedded ring, in which the ring is the laminated biased belt supported by various springs having spring constants, K_r, K_t and K_s, of the sidewall in the radial, tangential and lateral directions respectively, together with K_m of the tread rubber in the thickness direction, playing the roll of elastic foundation.

Figure32 shows the deformation of a radial tire compressed to the roadway by the vertical load W, where the contact patch is assumed to be a rectangular shape.

After the deformation of the belt is geometrically determined under the contact deflection of δ, the additional deflection of the belt in the contact patch w, shown in Fig.33, can be determined from the following equation:

$$
\begin{aligned}
&\bar{D}_{xx}w_{,xxxx} + 2\left(\bar{D}_{xy} + 2\bar{D}_{ss}\right)w_{,xxyy} + \bar{D}_{yy}w_{,yyyy} \\
&= -p + K_m\left(\delta - \eta_0 - w\right) + N_x w_{,xx} + N_y w_{,yy}
\end{aligned}
\tag{76}
$$
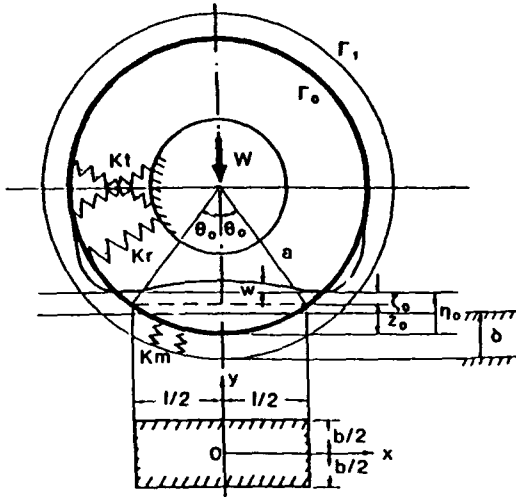
Fig.32 Contact deformation of a radial tire to the flat roadway
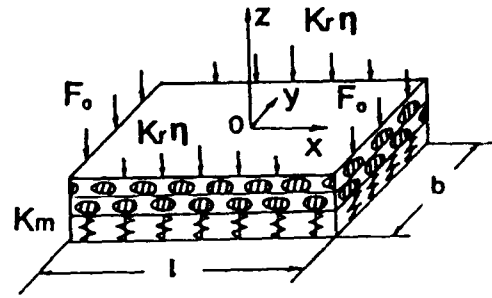
Fig.33 Rectangular contact patch under the distributed load and transverse shearing forces along the edges
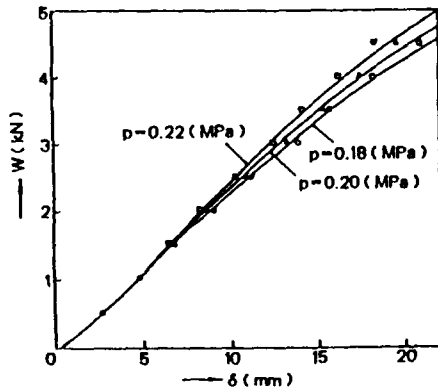
Fig.34 Load-deflection curve under different inflation pressure
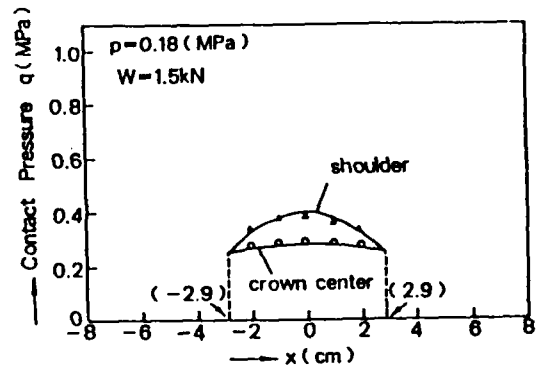
Fig.35 Contact pressure distribution when $W = 1.5kN$
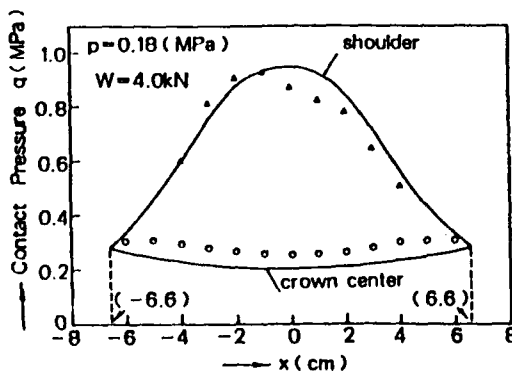
Fig.36 Contact pressure distribution when $W = 4.0kN$
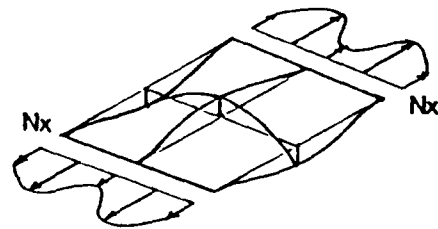
Fig.37 Deflection pattern of the contact path

together with the boundary condition along the edges of the contact patch , y= ± b/2

$$\left(\bar{D}_{xy} + 2\bar{D}_{ss}\right) w_{,xxy} + \bar{D}_{yy} w_{,yyy} = K_r \eta \tag{77}$$

where p is the inflation pressure, η_0 is the geometrical deflection of the contact patch, N_x and N_y are the membrace forces in the x and y directions respectively, involved in the inflation pressure and the geometrical deformation of the contact patch, and η denotes the deflection of the belt edge correlated to both geometrical and additional deflections. It should be noted here that the spring constant K_r is not constant but decreases with the increase of deflection η, as shown in Fig.4. Then, this analysis is conducted by using the successive integration method for each incremental loadings, $\Delta W^j, (j = 1, 2, \cdots N)$. Solution for each ΔW^j can be obtaind by applying the Galerkin's method to both equations given by Eqs.(76) and (77) with the use of a constant value of K_r^j corresponding to the deflection η^{j-1}. Then, the contact pressure q^j is obtained from:

$$q^j = K_m \left(\delta^j - \eta_0^j - w^j \right) \tag{78}$$

Figure 34 shows the load-deflection curve of a radial tire under different inflation pressures, compared with the measured points.

Figures 35 and 36 show the contact pressure distributions along the crown center and the shoulder, in the loading cases of $W = 1.5\,KN$ and $4.0\,KN$ respectively, compared with measured results with pressure sensors.

Figure 37 illustrates the deflection pattern of the additional deflection w, which corresponds well with the contact pressure distribution that is high along the belt edge, but low along the crown center.

CONCLUSION

Basic concepts of various structural theories developed up to date are described with emphasizing the usefulness for tire structure analysis. These fundamental properties of cord-rubber compoites are believed to play the significant roles in tire design, tire manufacturing and even in FEM analysis. However, we have a lot of problems for evaluating material and structural properties of not only tire structures but also the other rubber goods, diaphragm, air spring, rubber bearing and so on, under the static and dynamic loadings accompanied with large deformations. Then, the concluding remarks on future advancements of cord-rubber composites are summarized as follows.

(1) The contribution of the twisted cord on the coupling deformation, stiffness and strength of cord-rubber composites should be studied, by microscopic analyses.

(2) The test method for evaluating various kinds of stiffness of FRR composite laminates should be established, because they are influenced considerably by the end effects.

(3)The static and dynamic behaviors of the rotating tire belt in the contact region have been considered as mysterious problems, which should be clarified analytically and experimentally in near future.

REFERENCES

1.Day R.B.and S.D.Gehman, 1963." Theory for Meridian Section of Inflated Cord Tires." Rubber Chemistry and Technology, 36(1):11-27.

2.Akasaka T., K.Kabe and H.Togawa, 1977." Cross Section Shape of Radial Tire." Journal of Japan Society for Composite Materials, 3(4):149-154.

3.Akasaka T. and S.Yamazaki, 1986." Analytical Study on Radial Stiffness of Radial Tire." Journal of Society of Rubber Industry, Japan, 59(7):24-31.

4.Akasaka T. and S.Yamazaki, 1987." Radial Stiffness of Radial Tire." Bulletin of the Faculty of Science and Engineering, Chuo University, 30:141-153.

5.Akasaka T., K.Asano and J.Miyamoto, 1982." Lateral Stiffness of Tire Structure." Bulletin of the Faculty of Science and Engineering, Chuo University, 25:185-199.

6.Akasaka T., S.Yamazaki and K.Asano, 1984." An Approximate Evaluation of Rotational Stiffness of Radial Tire." Transaction of Japan Society for Composite Materials, 10(1):24-31.

7.Akasaka T., 1959."Fundamental Elastic Properties and Two Dimensional Problem." Bulletin of the Faculty of Science and Engineering, Chuo University, B4(9):1-14.

8.Adkins J.E. and R.S.Rivlin, 1955." Large Elastic Deformations of Isotropic Materials (x) Reinforcement by Inextensible Cords." Philosophical Transaction A., 248:201-223.

9.Akasaka T. and T.Takagishi,1959."Experiment on Nonuniform Stress Distribution of Hyperbolic-Orthotropic Rectangular Plate under Extension." Bulletin of the Faculty of Engineering, Chuo University, B6(12):1-18.

10.Walter J.D., and H.P.Patel, 1979." Approximate Expressions for the Elastic Constants of Cord-Rubber Laminates." Rubber Chemistry and Technology, 52(4):710-724.

11.Akasaka T., K.Asano and K.Kabe, 1987." A Relation between Elastic Constants of Unidirectional Cord Reinforced Rubber Sheet." Transaction of Japan Society for Composite Materials, 4(1):12-16.

12.Walter J.D., G.N.Argeropoulus, M.L.Janssen and G.R.Potts, 1973." Advances in Tire Composite Theory." Tire Science and Technology, 1(2):210-250.

13.Akasaka T. and M.Hirano, 1972."Approximate Elastic Constants of Fiber Reinforced Rubber Sheet and Its Composite Laminate." Fukugo Zairyo(Composite Materials and Structures), 1(2):70-76.

14.Clark S.K., 1963." The Plane Elastic Characteristics of Cord-Rubber Laminates." Textile Research Journal, 33(4):295-313.

15.Akasaka T., K.Kabe and K.Sako, 1985." Bending Stiffness and Coupled Bending-Shear Deformation of Laminated Biased Steel Cords Reinforced Rubber Strip." Composite Science and Technology, 24:1-16.

16. Hirano M. and T.Akasaka, 1973." Coupled Deformation of an Asymmetrically Laminated Plate." Fukugo Zairyo(Composite Materials and Structures), 2(3):6-11.

17. Akasaka T., M.Hirano and K.Motomura, 1974." In-Plane Bending Rigidity of Biasly Laminated Composite Strip." Fukugo Zairyo(Composite Materials and Structures), 3(4):12-16.

18. Ridha R.A.,1980."Computation of Stresses, Strains and Deformations of Tires." Rubber Chemistry and Technology, 53(4):849-902.

19. Sun C.T. and Sijian Li, 1988." Three-Dimensional Effective Elastic Constants for Thick Laminates," Journal of Composite Materials, 22(7):629-639.

20. Yamada Y., 1990." Calculation Method for Stiffness of Anisotropic Laminate in the Thickness Direction."(Not Published)

21. Akasaka T. and K.Kabe, 1977." Thickness Variation of Laminated Biased Fiber Reinforced Rubber Sheet." Journal of Japan Society for Composite Materials, 3(2):76-78.

22. Akasaka T., S.Yamazaki and K.Asano, 1984." Buckling Behavior of Tire Breaker Structure." Tire Science and Technology, 11(1-4):3-19.

23. Akasaka T., M.Katoh, S.Nihei and M.Hiraiwa, 1990." Two-Dimensional Contact Pressure Distribution of a Radial Tire." Tire Science and Technology, 18(2):80-105.

24. Kagami S., T.Akasaka and A.Hasegawa, 1992." Load-Deflection Property and Contact Pressure Distribution of Radial Tire." Journal of Society of Rubber Industry, Japan, 65(4):241-249.

SESSION 1A

Stress Analysis I

The Effect of Bending-Twisting Coupling on the Critical Speed of a Driveshaft

CHARLES W. BERT

ABSTRACT

A simplified theory for calculating the first-order critical speed of a flexible driveshaft constructed of composite material is developed. Numerical results are presented for a slender thin-walled driveshaft typical of a helicopter drive application. The results are compared with those measured experimentally and predictions of other analyses.

INTRODUCTION

In the past twenty years, there has been considerable helicopter-industry interest in the development of lightweight driveshafts constructed of fiber-reinforced composite materials [1-5]. Since the primary emphasis has been on reducing the weight, the geometric configuration of importance is thin-walled circular. Another application is in automotive driveshafts.

One of the most important design characteristics of a shaft is its first critical speed. Although the gyroscopic action of a massive disk mounted on shafting was analyzed in the early years of this century by Stodola, it was not until 1961 that the distributed gyroscopic action of a rotating shaft alone was analyzed by Dimentberg [6]. This action causes the natural frequencies of the shaft to bifurcate into a higher one which is associated with forward precession and a lower one which is associated with backward precession. An important representation of these phenomena is called the Campbell diagram, which is a plot of natural frequency versus rotational speed. The forward precession natural frequencies increase with increasing rotational speed, while the backward-precession ones decrease. The speed at which the rotational speed coincides with the first backward-precession natural frequency is known as the first critical speed.

The effect of anisotropic shear-normal coupling in producing bending-twisting coupling in rectangular cross-section bars was analyzed by Lekhnitskii [7]. This same concept was extended to free vibration by Ritchie et al. [8]. To the best of the present investigator's knowledge, no analogous analysis applicable to bars of solid or hollow circular cross section exists. A simple analysis for this case is presented in the Appendix of the present paper.

Charles W. Bert, School of Aerospace and Mechanical Engineering, The University of Oklahoma, 865 Asp Avenue, Rm. 212, Norman, OK, 73019-0601

The results of the present analysis are compared with those of another one which is based on the Sanders shell theory and, thus, is much more complicated [9].

ANALYSIS

HYPOTHESES

In the interest of simplicity, the following hypotheses are selected as the basis for the analysis:

1. Transverse shear deformation is neglected.

2. The shaft rotates at constant speed and has a uniform, circular cross section (either solid or hollow), i.e., no imperfections.

3. The shaft is perfectly balanced, i.e., the mass center coincides with the geometric center.

4. There is no axial force and no axial torque.

5. All damping and nonlinear effects are omitted.

The analysis includes bending, twisting, and bending-twisting coupling as well as distributed lateral, torsional, and rotatory inertia and gyroscopic action.

THEORY

A Cartesian coordinate system fixed in space is used; x is measured along the axis of the shaft. Let v and w represent the displacements in the y and z directions and ϕ be the angle of twist. Then, the equations of motion for bending in the xy and xz planes and twisting about the x axis can be written as

$$E_1 I_1 v_{,xxxx} + C_{1T}\phi_{,xx} + \rho A v_{,tt} - \rho J\left(v_{,xxtt} + 2\Omega w_{,xxt}\right) = 0 \tag{1}$$

$$E_1 I_2 w_{,xxxx} + C_{2T}\phi_{,xx} + \rho A w_{,tt} - \rho J\left(w_{,xxtt} - 2\Omega v_{,xxt}\right) = 0 \tag{2}$$

$$C_{1T} v_{,xxxx} + C_{2T} w_{,xxxx} + C_T \phi_{,xx} - \rho J\phi_{,tt} = 0 \tag{3}$$

Here, A is the cross-sectional area, C_{1T} and C_{2T} are bending-twisting coupling coefficients, C_T is the torsional stiffness, $E_1 I_1$ and $E_1 I_2$ are flexural stiffnesses, J is the area polar moment of inertia, t is time, ρ is the material density, Ω is the rotational speed, and $(\ )_{,xxtt}$ denotes $\partial^4(\ )/\partial x^2 \partial t^2$, etc.

The absence of imperfections implies that $E_1 I_1 = E_1 I_2 = C_B$ and $C_{1T} = C_{2T} = C_{BT}$. Now multiplying Eq. (2) by $i\left(= \sqrt{-1}\right)$ and adding it to Eq. (1) yields

$$C_B r_{,xxxx} + C_{BT} \phi_{,xx} + \rho A r_{,tt} - \rho J \left(r_{,xxtt} - 2i\Omega r_{,xxt} \right) = 0 \qquad (4)$$

and Eq. (3) becomes

$$C_{BT} r_{,xxxx} + C_T \phi_{,xx} - \rho J \phi_{,tt} = 0 \qquad (5)$$

where $r = v + iw$ and ϕ replaces $\phi + i\phi$. Equations (4) and (5) are the partial differential equations (PDE's) governing the problem.

SOLUTION

Assuming normal modes, one can write

$$r(x,t) = R(x) e^{i\omega t} \quad , \quad \phi(x,t) = Q(x) e^{i\omega t} \qquad (6)$$

where ω is the circular natural frequency. Thus, PDE's (4) and (5) are reduced to the following ODE's:

$$C_B R^{IV} + C_{BT} Q' - \rho A \omega^2 R + \rho J (\omega^2 - 2\Omega\omega) R' = 0 \qquad (7)$$

$$C_{BT} R^{IV} + C_T Q' + \rho J \omega^2 Q = 0 \qquad (8)$$

where $(\ )^{IV}$ denotes $d^4(\ )/dx^4$, etc.

Equations (7) and (8) can be uncoupled as follows. First, solve Eq. (8) for Q:

$$Q = \frac{-C_{BT} d_x^4}{C_T d_x^2 + \rho J \omega^2} R \qquad (9)$$

where d_x denotes d/dx.

Next, substitute this expression for Q into Eq. (7) with the following result:

$$\left[C_B d_x^4 - \frac{C_{BT}^2 d_x^6}{C_T d_x^2 + \rho J \omega^2} - \rho A \omega^2 + \rho J (\omega^2 - 2\Omega\omega) d_x^2 \right] (R) = 0 \qquad (10)$$

Considering the boundary conditions to be pinned at each end, one can take the mode shape to be

$$R(x) = R_o \sin \lambda x \quad ; \quad \lambda = \pi/L \qquad (11)$$

where L is the length of the shaft.

Substitution of Eq. (11) into ODE (10) reduces it to the following algebraic equation:

$$\left(C_{B}/\rho A\right)\lambda^{4} - \frac{\left(C_{BT}^{2}/\rho A \rho J\right)\lambda^{6}}{\left(C_{T}/\rho J\right)\lambda^{2} - \omega^{2}} - \omega^{2} - \left(J/A\right)\left(\omega^{2} - 2\Omega\omega\right)\lambda^{2} = 0 \qquad (12)$$

Equation (12) is quartic in the frequency ω. However, it can be converted to the form of a quadratic in ω_{cr}, since at the first critical speed, $\omega = \Omega = \omega_{cr}$ for forward precession and $\omega = -\Omega = \omega_{cr}$ for backward precession.

REDUCTION TO SPECIAL CASES

Case 1: No coupling and no gyroscopic action

Thus, $C_{BT} = 0$ and $J = 0$. then,

$$\omega_{cr}^{2} = \left(C_{B}/\rho A\right)\lambda^{4}$$

This is the frequency of a Bernoulli-Euler beam.

Case 2: No coupling

Now, $C_{BT} = 0$

For forward precession, $\omega = \Omega = \omega_{cr}$

$$\omega_{cr}^{2}{}_{fwd.} = \frac{\left(C_{B}/\rho A\right)\lambda^{4}}{1 - \left(J/A\right)\lambda^{2}} \qquad (13)$$

For backward precession, $\omega = -\Omega = \omega_{cr}$

$$\omega_{cr}^{2}{}_{bwd.} = \frac{\left(C_{B}/\rho A\right)\lambda^{4}}{1 + 3\left(J/A\right)\lambda^{2}} \qquad (14)$$

Both Eq. (13) and Eq. (14) are in agreement with the work of Dimentberg [6] and Yu [10].

NUMERICAL RESULTS

Numerical results are presented for a shaft having the same length and mean diameter and constructed

of the same material (boron-epoxy) as the shaft used in the experiments of Ref. [1] and analyzed by a finite-element approach by dos Reis [11]. The data are as follows:

$$L = 97.25 \, in \, , \qquad 2R_m = 4.998 \, in \, ; \quad ply \ thickness = 0.0052 \, in$$

$$E_1 = 30.6 \times 10^6 psi \, , \quad E_2 = 3.5 \times 10^6 psi$$

$$G_{12} = 1.0 \times 10^6 psi \, , \quad v_{12} = 0.36 \, ; \quad specific \ gravity = 1.967$$

The simplest laminate having the greatest bending-twisting coupling would be an off-axis parallel-ply laminate having all of the layers oriented at an acute angle θ. For a shaft with such a laminate having ten layers, the critical speed was calculated for various values of θ. The results are listed in Table 1, along with those calculated in Ref. [9] by use of the Sanders shell theory.

TABLE I - FIRST BACKWARD - PRECESSION CRITICAL SPEED (RPM)
FOR A THIN-WALLED, OFF-AXIS, BORON-EPOXY DRIVESHAFT

Investigators	Lamination Angle θ, deg.						
	0	15	30	45	60	75	90
Present	7141	4966	3722	3011	2569	2433	2415
Ref. [9]	5714	4432	3048	2529	2425	2512	2582

From the table, it is clear that an off-axis parallel-ply laminate is less desirable than one having all of the fibers oriented axially $(0 \ deg.)$. For $0 < \theta < 90 \ deg.$, this is due to the combination of shear-normal coupling and low transverse extensional stiffness, while for $\theta = 90 \ deg.$, it is due to the latter effect only. Also, it can be seen that the simple, approximate theory presented here gives results that are in reasonably good agreement with the more accurate results obtained by the much more complicated theory of Ref. [9]. The present solution involves solution of a simple quadratic equation, while the theory of Ref. [9] involves the iterative solution of a 10×10 eigenvalue problem for shear deformable shell theory or a 6×6 eigenvalue problem for thin shell theory (adequate for the present thin-walled shaft).

As a further demonstration of the validity of the present theory, the same shaft tested by Zinberg and Symonds [1] is considered. The layup consists of ten layers with the following orientations, from the inner surface of the shaft to the outer surface: $90°$, $45°$, $-45°$, $0_6°$, and $90°$. The results of the experiment reported in [1] as well as those obtained by various analyses, are summarized in Table II.

TABLE II - FIRST BACKWARD - PRECESSION CRITICAL SPEED (RPM)
FOR THE THIN-WALLED, LAMINATED, BORON-EPOXY DRIVESHAFT OF [1]

Investigators	Method of Determination	Critical Speed
Zinberg & Symonds [1]	Measured experimentally	~ 6000
dos Reis et al. [11]	Shaft theory in conjunction with FE shell determined stiffnesses	4942
Kim & Bert [9]	Sanders shell theory	5872
Kim & Bert [9]	Donnell shell theory	6399
Present	Simplified shaft theory	5724

It can be seen that there is quite good agreement among the present analysis, Sanders shell theory [9], and the experiment. Donnell shallow shell theory is known to give inaccurately high frequencies for long shells, such as the present shaft. It is not known why the Ref. [11] prediction is so low.

CONCLUSIONS

The simplified theory presented here has been shown to be practical for predicting the first-order critical speed of a typical helicopter driveshaft of laminated composite material.

REFERENCES

1. Zinberg, H. and M. F. Symonds, June 1970. "The Development of an Advanced Composite Tail Rotor Driveshaft," presented at the 26th Annual Forum of the American Helicopter Society, Washington, DC.

2. Wright, C. C., D. J. Baker, N. Corvelli, L. Thurston, and R. Clary, Oct. 1971. "Progress Report of Cooperative Program for Design, Fabrication, and Testing of Graphite/Epoxy Composite Helicopter Shafting," Report PA-TR-4240, Picatinny Arsenal, Dover, NJ.

3. Figge, I.E., J. Henshaw, R. A. Roy, and E. F. Olster, 1974. "Low-Weight, Impact-Resistant Helicopter Drive Shafts," in Composite Materials: Testing and Design (Third Conference), ASTM STP 546, pp. 651-662.

4. Faust, H., J. Mack, and B. Spencer, 1984. "A Composite Rotor Shaft for the Chinook." Journal of the American Helicopter Society, 29(3):54-58.

5. Hetherington, P. L., R. F. Kraus, and M. S. Darlow, 1990. "Demonstration of a Supercritical Composite Helicopter Power Transmission Shaft." Journal of the American Helicopter Society, 35(1):23-28.

6. Dimentberg, F. M., 1961. Flexural Vibrations of Rotating Shafts, English translation, London: Butterworths, Ch. 5.

7. Lekhnitskii, S. G., 1963. Theory of Elasticity of an Anisotropic Body, English translation, San Francisco, CA: Holden Day.

8. Ritchie, I. G., H. E. Rosinger, and W. H. Fleury, 1975. "The Dynamic Behavior of a Fibre-Reinforced Composite Sheet: II. The Transfer Matrix Calculation of the Resonant Frequencies and Vibration Shapes." Journal of Physics D: Applied Physics, 8:1750-1768.

9. Kim, C. D. and C. W. Bert, Sept. 1992. "Critical Speed Analysis of Laminated Composite Driveshafts," to be presented at the 29th Annual Technical Meeting of the Society of Engineering Science, La Jolla, CA.

10. Yu, H., 1987. "The Stability of Rotating Shafts When Distributed Gyroscopic Effects Are Taken into Account," in Rotating Machinery Dynamics, Vol. 1, A. Muszynska and J. C. Simonis, ed. New York, NY: ASME DE Vol. 1, pp. 35-39.

11. dos Reis, H. L. M., R. B. Goldman, and P. H. Verstrate, 1987. "Thin-Walled Laminated Composite Cylindrical Tubes: Part III - Critical Speed Analysis." Journal of Composites Technology and Research, 9(2):58-62.

12. Jones, R. M., 1975. Mechanics of Composite Materials, New York, NY: Hemisphere Publishing Corp., Ch. 2.

APPENDIX: DERIVATION OF STIFFNESSES FOR A CIRCULAR-CROSS-SECTION SHAFT WITH BENDING-TWISTING COUPLING

For a case of a material which is thin and orthotropic, the generalized Hooke's law can be written as

$$\begin{Bmatrix} \sigma_1 \\ \sigma_2 \\ \tau_6 \end{Bmatrix} = \begin{bmatrix} Q_{11} & Q_{12} & 0 \\ Q_{12} & Q_{22} & 0 \\ 0 & 0 & Q_{66} \end{bmatrix} \begin{Bmatrix} \epsilon_1 \\ \epsilon_2 \\ \gamma_6 \end{Bmatrix} \tag{A-1}$$

where σ_1 and σ_2 are in-plane normal stresses, τ_6 is the in-plane shear stress, ϵ_1 and ϵ_2 are in-plane normal strains, and γ_6 is the in-plane engineering shear strain $\left(\gamma_6 = 2\epsilon_6 \right)$. The $Q's$ are known as the planar reduced stiffnesses, and they can be expressed in terms of the engineering properties [12].

For an orthotropic layer in which the major material symmetry direction is oriented at an acute angle to the reference direction, the material behaves as if it is anisotropic in its plane, i.e.,

$$\begin{Bmatrix} \sigma_1 \\ \sigma_2 \\ \tau_6 \end{Bmatrix} = \begin{bmatrix} \bar{Q}_{11} & \bar{Q}_{12} & \bar{Q}_{16} \\ \bar{Q}_{12} & \bar{Q}_{22} & \bar{Q}_{26} \\ \bar{Q}_{16} & \bar{Q}_{26} & \bar{Q}_{66} \end{bmatrix} \begin{Bmatrix} \epsilon_1 \\ \epsilon_2 \\ \gamma_6 \end{Bmatrix} \tag{A-2}$$

The transformed $\bar{Q}'s$ can be expressed in terms of the $Q's$ [12].

It is now assumed that a section of shaft material is subjected to bending and torsional strains as follows:

$$\epsilon_1 = \kappa_1 z = \kappa_1 \bar{r} \sin \beta$$
$$\gamma_6 = (\bar{r}/L) \phi = \bar{r} \phi' \tag{A-3}$$

where $\bar{r}, \beta$ are polar coordinates in the plane of the cross section and κ_1 is bending curvature.

The internal bending moment M_1 associated with an axial bending stress σ_1 is

$$M_1 = \sum_{k=1}^{N} 4 \int_0^{\pi/2} \int_{R_{i(k)}}^{R_{o(k)}} \sigma_1^{(k)} z \ \bar{r} \, d\bar{r} \, d\beta \tag{A-4}$$

where N is the total number of layers.

Substituting σ_1 from Eq. (A-2) and using strain distributions (A-3), one can express Eq. (A-4) as

$$M_1 = \kappa_1 \left(4 \int_0^{\pi/2} \sin^2 \beta \, d\beta \right) \left(\sum_{k=1}^{N} \int_{R_{i(k)}}^{R_{o(k)}} \bar{Q}_{11}^{(k)} \bar{r}^3 \, d\bar{r} \right)$$
$$+ \phi' \left(4 \int_0^{\pi/2} \sin \beta \, d\beta \right) \left(\sum_{k=1}^{N} \int_{R_{i(k)}}^{R_{o(k)}} \bar{Q}_{16}^{(k)} \bar{r}^3 \, d\bar{r} \right) \tag{A-5}$$

The stiffnesses are defined as

$$C_B = M_1 \bigg|_{\substack{/\kappa_1 \\ \phi'=0}} = \sum_{k=1}^{N} \bar{Q}_{11}^{(k)} \left[(\pi/4) \left(R_{o(k)}^4 - R_{i(k)}^4 \right) \right] = \sum_{k=1}^{N} \bar{Q}_{11} I^{(k)} \qquad (A-6)$$

$$C_{BT} = M_1 \bigg|_{\substack{/\phi' \\ \kappa_1=0}} = \sum_{k=1}^{N} \bar{Q}_{16}^{(k)} \left(R_{o(k)}^4 - R_{i(k)}^4 \right) \qquad (A-7)$$

Similarly,

$$T = 4 \sum_{k=1}^{N} \int_0^{\pi/2} \int_{R_{i(k)}}^{R_{o(k)}} \bar{r} \tau_6^{(k)} \; \bar{r} \, d\bar{r} \; d\beta \qquad (A-8)$$

Using Eqs. (A-2) and (A-3) in Eq. (A-8), one finds

$$C_T = T \bigg|_{\substack{/\phi' \\ \kappa_1=0}} = \sum_{k=1}^{N} 2 \, \bar{Q}_{66}^{(k)} I^{(k)} \qquad (A-9)$$

$$C_{BT} = T \bigg|_{\substack{/\kappa_1 \\ \phi'=0}} = \sum_{k=1}^{N} \bar{Q}_{16}^{(k)} \left(R_{o(k)}^4 - R_{i(k)}^4 \right) \qquad (A-10)$$

The last equation is an independent check of Eq. (A-7).

The above equations are exact within the theory used, regardless of whether the shaft is solid, thick-walled hollow, or thin-walled hollow. However, for a thin-walled shaft, they can be simplified further by assuming that all of the layers are located at the mean radius of the laminate, R_m. Then

$$C_B = \pi R_m^3 A_{11} \quad , \quad C_{BT} = 4 R^3 A_{16} \quad , \quad C_T = 2 \pi R^3 A_{66} \qquad (A-11)$$

where the A_{ij} are the usual extensional stiffnesses given by

$$A_{ij} = \sum_{k=1}^{N} \bar{Q}_{ij}^{(k)} h_k \qquad (A-12)$$

Nonlinear Analysis of Composite Structures Based on a Modern Continuum Mixture Theory

ANDREW C. HANSEN

ABSTRACT

An advanced finite element formulation for composite structures based on a modern continuum mixture theory is presented. The development is unique in that each node of the finite element mesh is assumed to have double the number of degrees of freedom over that of a single continuum. In particular, the degrees of freedom represent the displacements of the individual constituents, thereby allowing for independent constituent motions. The behavior of the composite is then determined by the governing rules for summing constituent variables of the mixture.

The primary advantage of developing a multiphase theory for structural analysis is that detailed information regarding the state of the constituents is retained while at the same time performing structural analysis. For instance, in addition to capturing the mechanical behavior at the structural level, the stress and strain fields of each constituent are available at every continuum point in the structure. Hence, the mixture theory represents a marriage of micromechanics to structural analysis.

The mixture formulation is shown to capture the mechanical behavior of a unidirectional composite under both uniaxial and multiaxial loadings. Finally, an example of structural analysis is presented for a composite plate with a hole in it. Unique nonlinear modeling capabilities which are not possible with a single continuum theory are also discussed.[1]

INTRODUCTION

This paper is concerned with improving the ability to characterize and quantify the performance of advanced multiphase composite systems used in structural applications. Candidate materials for high performance structural systems are almost all multiphase in nature. The multiphase characteristics of these materials present analysis problems which transcend those of the more traditional single continuum. In particular, knowledge of the constituent behavior is critical to understanding the behavior of the system. However, the geometric scale of the structural problem generally precludes modeling at the constituent level. Hence, the material properties are based on some "average" properties of the continuum thereby sacrificing valuable constituent information.

---

[1]Andrew C. Hansen, Assistant Professor, Department of Mechanical Engineering, University of Wyoming, Laramie, Wyoming 82071.

One means of retaining constituent information while analyzing a composite structural system is to develop a multiphase theory based on a continuum theory of mixtures. Consistent with a single continuum theory, each constituent is assumed present at every point in the continuum. The fundamental difference here is that the constituents retain their identity rather than being homogenized in some sense. Furthermore, each constituent is allowed to undergo individual deformations even though the material is assumed to be perfectly bonded. Balance equations are then postulated for each constituent which resemble those of a single continuum. However, an additional supply term is present in each equation which goverms the interactions between constituents which occur at a continuum point.

In what follows, a modern continuum mixture theory is specifically developed for application to the analysis of composite structures. The constituent balance equations are solved in a unique finite element analysis which uses constituent displacements as nodal variables. Hence, at each node, independent constituent motions are allowed even though the composite is assumed to be perfectly bonded. The behavior of the mixture is then governed by specific rules for summing of the constituent field variables.

Formulating the problem at the constituent level poses some unique difficulties when implementing boundary conditions. In particular, boundary conditions are known at the structural (mixture) level whereas boundary conditions on each constituent are required. This problem is dealt with by introducing constraints on the boundary with Lagrange multipliers. The net effect is at each node, either a mixture (structural) force or a mixture displacement must be specified, thereby giving the code an appearance of a *traditional* structural finite element analysis.

FIELD EQUATIONS

In what follows, the basic field equations for a volume fraction based mixture theory are presented. The reader is referred to the work of Hansen *et al.* [1,2] for a detailed development of the theory.

Let u_α represent the *deformation displacement* of constituent α. The term *deformation displacement* refers to the deformation of constituent α neglecting the influence of the deformation of constituent β. In reality, there may be additional carrier displacements involving constituent α caused by the motion of constituent β.

The constituent strain has the usual definition and is given by

$$\epsilon_\alpha = \frac{1}{2}\left[(u_\alpha \vec{\nabla}) + (\vec{\nabla} u_\alpha)\right] \quad . \tag{1}$$

Here, ϵ_α represents the true strain in constituent α as the strains are unaffected by the carrier motions discussed previously.

The constituent equilibrium equations are given by

$$\vec{\nabla} \cdot t_\alpha + \rho_\alpha b_\alpha + \hat{p}_\alpha = 0 \quad . \tag{2}$$

In the above, t_α is the partial stress tensor, b_α is the body force, and $\hat{p}_\alpha$ is the linear momentum supply. The momentum supply term arises as the result of interactions between constituents at a point in the mixture and is not present in a single continuum theory.

Summing over all constituents leads to the following mixture definitions [1,2]:

$$u - \sum_\alpha \nu_\alpha u_\alpha \quad , \tag{3}$$

$$\epsilon - \sum_\alpha \nu_\alpha \epsilon_\alpha \quad , \tag{4}$$

$$t - \sum_\alpha t_\alpha \quad , \tag{5}$$

where ν_α represents the volume fraction of constituent α. It should be noted that the partial stress, t_α, of equation (5) is implicitly scaled by the volume fraction [2].

CONSTITUTIVE ASSUMPTIONS

In order to complete the development of a mechanical theory, constitutive relations must be postulated for the partial stresses, t_α, and the momentum supplies, $\hat{p}_\alpha$. The constituents are assumed to be ideal in the sense that the mechanical behavior of each constituent depends only on its own kinematic variables. This assumption is consistent with the concept of immiscibility in that the constituents remain physically separate on a local scale. The exception to this is the interaction terms (momentum supplies) which are allowed to depend on both constituents.

For the present discussion, both constituents are assumed to be isotropic elastic solids governed by Hooke's law. The remaining problem essentially reduces to developing an accurate constitutive law for the momentum supplies, $\hat{p}_\alpha$. The momentum supplies are assumed to depend on both materials. Furthermore, for a two-phase mixture, the momentum supplies satisfy [3]

$$\hat{p}_\alpha - -\hat{p}_\beta \quad . \tag{6}$$

In developing a specific constitutive relation for the momentum supply, we regard the momentum interaction at a continuum point as a diffusional problem dependent on the relative constituent deformations. Therefore, the momentum supply is chosen to be represented by

$$\hat{p}_\alpha - C \left[u_\alpha - A u_\beta \right] \quad . \tag{7}$$

The functional form of the tensors **A** and **C** in the above may be restricted by invoking invariance requirements based on material symmetry. In what follows, the material is taken to be a unidirectional, continuous fiber composite with the fibers running parallel to the X_1 direction. Therefore, assuming transverse isotropy one can write

$$A_{ij} - \begin{bmatrix} A_1 & 0 & 0 \\ 0 & A_2 & 0 \\ 0 & 0 & A_2 \end{bmatrix} \quad \text{and} \quad C_{ij} - \begin{bmatrix} C_1 & 0 & 0 \\ 0 & C_2 & 0 \\ 0 & 0 & C_2 \end{bmatrix} \quad . \tag{8}$$

The degree of coupling between constituents is directly related to the

coefficients A_1 and A_2 which are in turn a function of the microstructure of the material. For instance, for coupling in the longitudinal direction we can write by inspection, $A_1 = 1$. In effect, the momentum supply is forcing the constituent displacements to be equal in the longitudinal direction.

The remaining coefficient, A_2, is determined with the aid of a micromechanical analysis of an assumed unit cell. In particular, the coefficient is chosen such that the mixture theory solution for a transverse tension test yields the same constituent stresses as those determined by averaging the constituent stresses of the micromechanics solution [3]. The specific choice of A_2 determined in this matter is further justified by comparing the results of micromechanics with the mixture theory analysis for multiaxial states of stress. The value of A_2 was found to be $A_2 = 0.329$. The difference in the values of A_i may be solely attributed to the composite microstructure.

Finally, the coefficients C_i must be specified to close the theory. Physically, these coefficients scale the momentum supply to the local stress gradient. Given that the geometric scale of the fibers is on the order of microns, the coefficients, C_i, are chosen such that boundary effects are diminished within a single element. This is physically reasonable considering there are perhaps hundreds of fibers within an element. The specific values of C_1 and C_2 were both taken as 250 MPa/m^2.

FINITE ELEMENT IMPLEMENTATION

The field equations presented previously have been implemented in a displacement based finite element formulation for a two-phase mixture. The analysis was formulated using a constant stress, triangular finite element. The degrees of freedom represent the constituent deformations described earlier, thereby allowing for independent constituent motions. Therefore, since each element in the structure contains both fibers and matrix material, the three nodes each have four degrees of freedom for a total of twelve degrees of freedom per element. These are shown in the schematic of a representative element shown in Figure 1. The reader is referred to Hansen et al. [3] for a detailed development of the finite element implementation.

RESULTS

In this section, results of the displacement based finite element formulation for a two-phase mixture are presented. The material was taken to be a continuous fiber unidirectional boron/aluminum composite with a 60 percent fiber volume. A square packing arrangement for the fibers was assumed.

MICROMECHANICS CORRELATIONS

Consider a uniaxial transverse tension test modeled with two elements using the mixture theory code. In particular, a structural tensile stress, t_{22}, of 10,000 kPa was applied to the model. Table I compares the partial stresses predicted by the two-element model with those obtained by volume averaging the stress fields in the quarter-fiber micromechanics model.
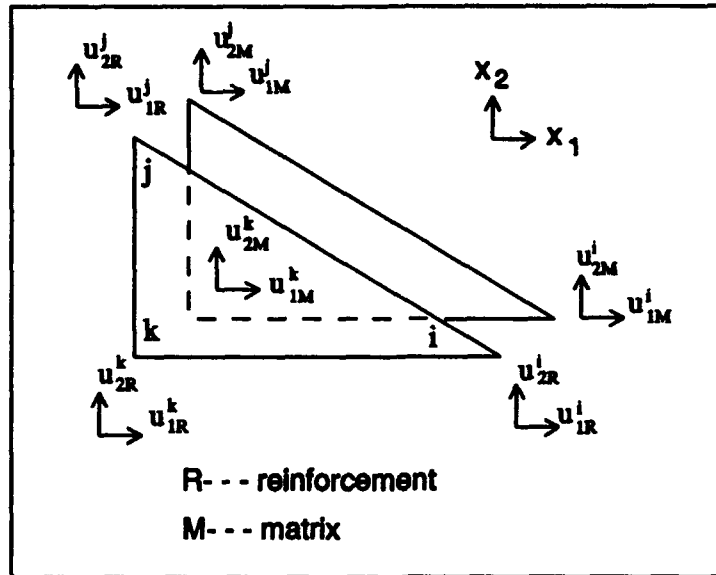
Figure 1.   Two-dimensional constant stress finite element for a mixture
consisting of two constituents.

The partial stresses, t_α, are identical for the two approaches in the loading direction. The constituent stress fields, $t_{\alpha 22}$, were properly matched by adjusting the coefficient, A_2, to its value given previously. Therefore, this result does not represent a predictive capability of the mixture theory.

Now consider the off-axis partial stresses, $t_{\alpha 11}$, as predicted by the two approaches. Clearly, the mixture stress, t_{11}, must be zero as no loads are applied in the X_1 direction. This result is in fact predicted by both the mixture theory and the volume averaged micromechanics stress fields. However, the individual constituent stresses are nonzero with the fiber being in compression while the matrix is in tension.   The presence of off-axis constituent stresses is caused by the strong coupling between the fiber and the matrix in the longitudinal (X_1) direction.

A possible explanation for the difference in the constituent stress fields, $t_{\alpha 11}$, predicted by the mixture theory when compared to the micromechanics results may be attributed to the mixture analysis being plane stress.   As a result, the mixture theory is incapable of modeling the interaction between constituents in the out-of-plane direction. In contrast, the micromechanics model is based on a generalized plane strain formulation which accounts for coupling in all three coordinate directions.   It is believed the difference in the predicted stress fields will diminish by extending the mixture theory formulation to three-dimensions.   Furthermore, this difference may be reduced by sacrificing some accuracy in the matching of the partial stresses in the loading direction.

The results of Table I show that even for the simplest case of uniaxial tension, the constituents of the composite are subjected to multiaxial stress states.   Furthermore,   the magnitudes of the off-axis stresses are significant. For instance, the off-axis matrix stress (t_{M11}) represents 25-30 percent of the stress carried by the matrix in the direction of loading (t_{M22}).   This may have a significant effect on accurately predicting failure and/or yielding of the matrix material within the composite.

In contrast to the mixture theory analysis presented above, a

Table I. Mixture theory and micromechanics stresses for a transverse tension
test of t_{22}=10,000 kPa.

stress	t_{11}		t_{22}		t_{12}	
	mixture	micro.	mixture	micro.	mixture	micro.
mixture	0	0	10,000	10,000	0	0
fiber	-718	-935	7190	7190	0	0
matrix	718	935	2810	2810	0	0

conventional finite element analysis will simply yield "mixture" stresses of
0 and 10,000 kPa for t_{11} and t_{22} respectively. Hence, all information
regarding the true stress states of the constituents is lost. Although
simple, this example illustrates the tremendous advantages associated with
using the mixture theory analysis. Finally, as stated previously, the
mixture theory results were generated using a two-element model. In
contrast, the finite element micromechanics solution was generated on a mesh
consisting of 192 constant stress elements.

Now consider the two-element mixture theory model subjected to a
biaxial stress of 10,000 kPa and 5000 kPa for t_{11} and t_{22} respectively. Table
II shows the mixture theory analysis compares very favorably with the results
predicted by volume averaging the micromechanics stress fields. The
differences between the predicted constituent stress fields of the mixture
theory and the micromechanics analysis are substantially less than that of
the uniaxial case. The *maximum* deviation between the two theories is
approximately seven percent. Finally, it must be noted that constituent
strain correlations showed similar agreement.

The close correlation of the two approaches for multiaxial stress
states lends credibility to applying the mixture theory to complex structures
which may exhibit significantly varying stress fields. It is precisely this
situation in which the mixture theory formulation dramatically extends the
current state-of-the-art in structural analysis. For instance,
micromechanics is no longer a viable option as one cannot model each fiber
individually. At the same time, conventional structural analysis codes fall
down in that no information on the state of the individual constituents is
available. In contrast, the mixture theory formulation allows one to perform
structural analysis while retaining information at the constituent level.

Table II. Mixture theory and micromechanics stresses for a biaxial loading
of t_{11}/t_{22}=2 (t_{11}=10,000 kPa).

stress	t_{11}		t_{22}		t_{12}	
	mixture	micro.	mixture	micro.	mixture	micro.
mixture	10,000	10,000	5000	5000	0	0
fiber	8560	8480	3620	3510	0	0
matrix	1440	1520	1380	1490	0	0

PLATE WITH A HOLE

In order to demonstrate the structural analysis capabilities of the mixture theory, consider a unidirectional composite plate with a hole subjected to a far field uniaxial stress, t_{11}, of 10,000 kPa. Two orientations of the fibers with respect to the loading are considered. The first assumes the fibers are oriented in the direction of loading (X_1) while the second assumes the fibers are oriented transverse to the loading.

Figures 2a and 2b show the mixture (structural) stresses, t_{11}, for the two plates as predicted by the mixture theory finite element analysis. The results are interesting in that the stress fields are nearly identical for both plates. The close correlation of the stress fields has been verified using a traditional anisotropic linear elastic finite element analysis for a boron/aluminum composite. Greater differences in the two stress fields are observed in composites with higher degrees of anisotropy.

The results of Figure 2 again dramatically reveal the shortcomings of a conventional structural analysis as this is the only stress information available. However, clearly the stress fields of the individual constituents will be significantly different. The question is: "What do the specific constituent stress fields look like?"

Figure 3 shows the partial stresses, t_{R11}, of the fiber for the two load cases. Figure 3b shows the stress in the fibers drops for the transverse load case as compared to the longitudinal fiber orientation of Figure 3a. This stress reduction is to be expected as the fibers are certainly carrying less of the structural load for the transverse load case.

The differing constituent stress fields are best seen in the matrix stresses of Figure 4. Figure 4a shows a very small "hot" zone for the longitudinally loaded plate. In contrast, the highly stressed region virtually explodes in an outward fan from around the hole of the transversely loaded plate, Figure 4b. The peak stress near the hole has increased by a factor of three. These results graphically depict the lost information in a conventional structural analysis.

DISCUSSION

The multiphase continuum mixture theory presented here-in represents a premier analysis in that it allows one to perform structural analysis while retaining detailed information regarding the constituent stress and strain fields. This capability offers unique possibilities when studying the behavior of a structural system. For instance, a particularly important nonlinear problem is improving the ability to quantify microstructural damage in a structure. The mixture formulation allows one to fail a constituent in some localized region of a structure while redistributing the load to the other constituent. The theory is also capable of quantifying the effects of bond weakening and/or bond failure during structural analysis.

A second major advantage of the mixture formulation lies in the nonlinear modeling of constituent material behavior. Many structural systems are composed of isotropic constituents whereas the composite may be highly anisotropic. By formulating the problem at the constituent level, advanced isotropic constitutive models and continuum damage theories may be utilized. The development of unique nonlinear isotropic constitutive theories is far more advanced than their anisotropic counterparts.

The success of the theory developed in this work relies on an accurate representation of the momentum supply. The results presented indicate the

relatively simple form chosen here works well for a mixture consisting of two linear elastic constituents. Elastic-plastic behavior has also been successfully modeled using the diffusional representation of the momentum supply discussed previously. However, the introduction of advanced constitutive models at the constituent level will require more complex representations of the momentum supply. Hence, a fundamental research effort must be directed towards developing analytical techniques for modeling the momentum supply.

REFERENCES

1. Hansen, A.C., 1989. "Reexamining Some Basic Definitions of Modern Mixture Theory." International Journal Engineering Science, 27(12):1531-1544 (1989).

2. Hansen, A.C., R.L. Crane, M.H. Damson, R.P. Donovan, D.T. Horning, and J.L. Walker, 1991. "Some Notes on A Volume Fraction Mixture Theory and A Comparison with the Kinetic Theory of Gases." International Journal of Engineering Science, 29(5):561-573.

3. Hansen, A.C., J.L. Walker, and R.P Donovan. "A Finite Element Formulation for Composite Structures Based on a Volume Fraction Mixture Theory." International Journal of Engineering Science, (Submitted May 1991).

27000= A

23500= B

20000= C

16500= D

13000= E

9500 = F

6000 = G

2500 = H

-1000= I

X_2

X_1
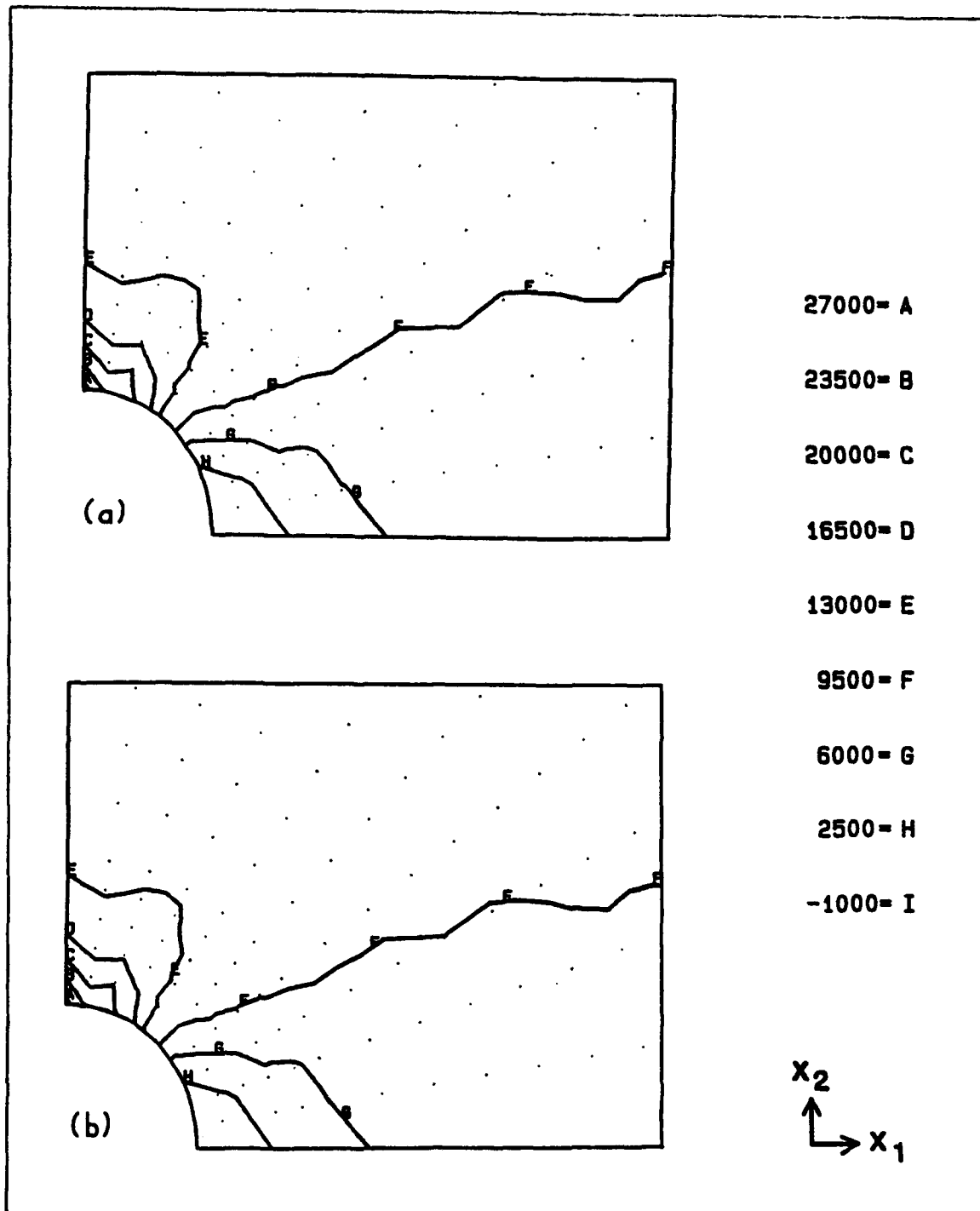
Figure 2. Mixture stresses, t_{11}, for a composite plate with fiber orientations: (a) longitudinal, (b) transverse.
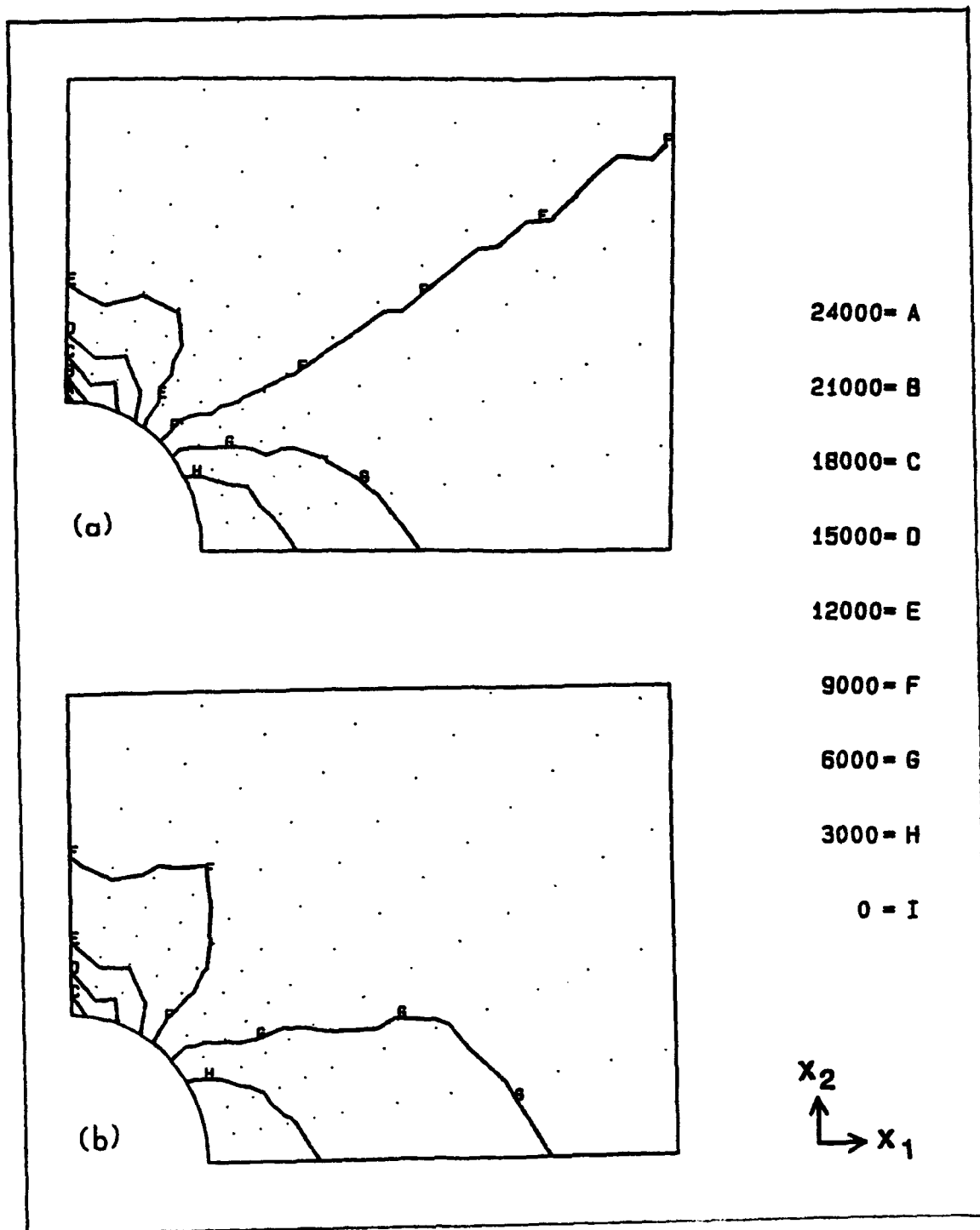
Figure 3. Fiber partial stresses, t_{R11}, for a composite plate with fiber orientations: (a) longitudinal, (b) transverse.
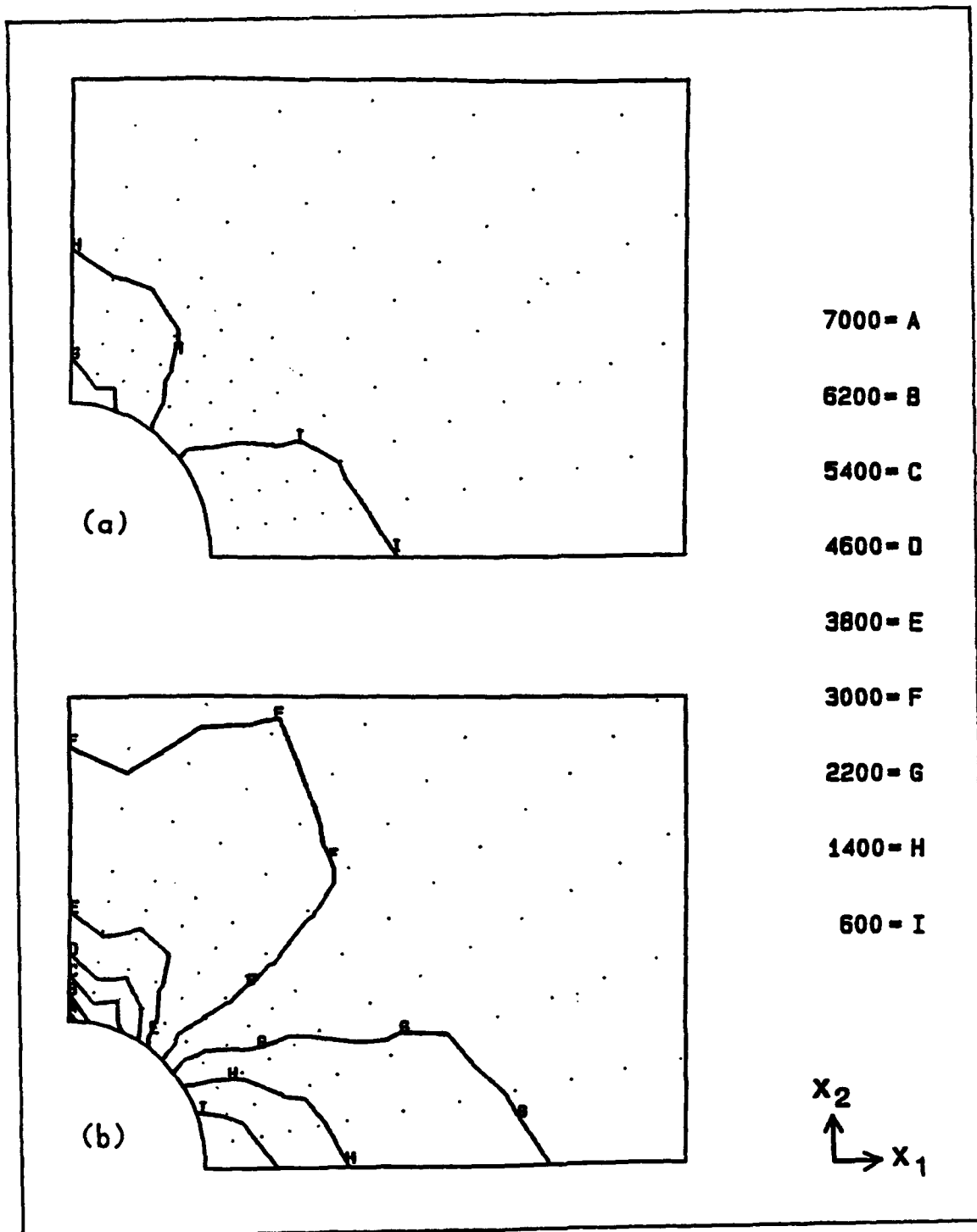
Figure 4. Matrix partial stresses, t_{M11}, for a composite plate with fiber orientations: (a) longitudinal, (b) transverse.

47

Comparison of Two-Dimensional Continuum and Layered Beam Finite Element Models of a Composite Notched Tensile Bar

STUART J. HARBERT AND HARRY A. HOGAN

ABSTRACT

The notched tensile bar (NTB) can be considered to be a one-dimensional analog of a composite material pressure vessel containing an external part-through hole. This simpler model provides a useful framework for studying the basic behavior of these kinds of problems and also for developing modeling approaches that can subsequently be extended to the three-dimensional cylindrical configuration. In the present work, a layered beam finite element approach is compared to two-dimensional continuum element modeling of the NTB. With the layered beam approach each ply is modeled explicitly by a separate layer of elements, which are constrained together kinematically to form a laminate. This accommodates delaminations at any ply interface as well as the possibility of multiple delaminations. Beam element results are compared with continuum element solutions for different layups, notch depths, and delamination locations for the NTB. Stress distributions and strain energy release rates agree quite well between the two approaches. Strain energy release rates are least accurate for ply angles of 30-60° for the angle-ply layup studied but nevertheless remain within 15% of continuum element results.

INTRODUCTION

The failure of fiber reinforced composite structures is a complex multi-mode process in most cases, particularly when damage, cracks, or holes are present. The current work has been motivated by the need to model the progressive failure of an internally pressurized composite cylinder with an external part-through hole. The original problem of interest is a composite pressure vessel subjected to high-power laser ablation which gives rise to a steadily deepening external hole. Similar flaws are also associated with impact damage in composite panels. Failure processes for these problems can generally be grouped into two broad categories: (1) in-plane failure within plies (e.g. matrix cracking, fiber fracture, ply failure); and (2) out-of-plane failure between plies (primarily delamination fracture).

Stuart J. Harbert, Research Assistant, and Harry A. Hogan, Assistant Professor
Department of Mechanical Engineering, Texas A&M University, College Station, TX 77843-3123.

A simplified, lower-order model is currently being studied as modeling procedures are being developed. The notched tensile bar (NTB) is considered to be a one-dimensional analog of the cylinder problem as shown in Figure 1. Only half of the NTB is modeled since the left end can be taken as a plane of symmetry. A tensile force P is applied along the main axis of the NTB. A delamination crack initiates and grows from the notch region and is assumed to extend completely through the width of the specimen. This simpler configuration is much more amenable to studying the effects of variations in model parameters as is necessary in this developmental phase. The current work is also focussing exclusively on delamination failure with in-plane damage effects to be incorporated later. The main objective at this point is to develop a relatively general method for modeling delaminations explicitly using conventional structural finite elements. This approach can then be extended to the 3-D cylindrical structure with reasonable prospects for computational tractability.
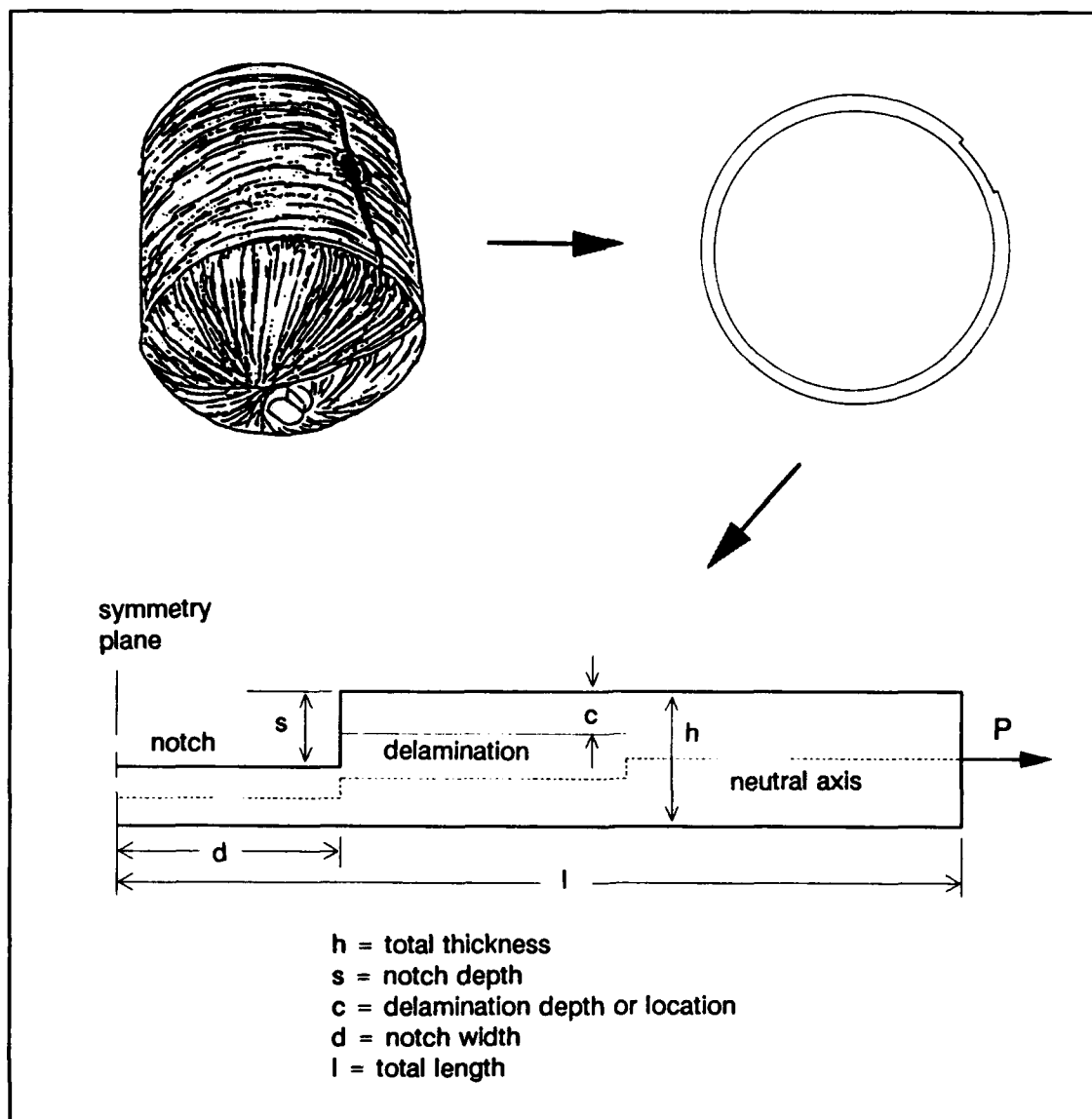
Figure 1. Notched tensile bar configuration and parameters.

MODELING

Two-dimensional plane strain finite element models of the notched tensile bar have been studied extensively in previous work [1,2]. Factors such as notch depth, delamination location, composite layup, and curvature have been examined. Eight-noded plane strain isoparametric elements were employed. Geometrically non-linear solutions are required since the model displaces transverse to the axis of loading in the notch region. A typical mesh for the region near the notch and delamination is shown in Figure 2 for a notch depth of two plies.The un-notched portion is eight plies thick. Two layups have been considered: a uni-directional $[0°]_8$ model, and an unsymmetric $[0°,0°,+77°,-77°]_2$ model (shown in Fig. 2). The latter represents a cylinder with alternating hoop and helical plies. Each of the eight plies is 0.02794cm thick giving a height (h) of 0.2235cm. The notch width (d) is 0.50cm and the total length (l) is 9.9746cm. Two notch depths have been studied: two plies deep (s/h= ¼), and four plies deep (s/h = ½). The material is a baseline S-glass/epoxy with the following lamina properties: $E_1 = 53.7$GPa, $E_2 = E_3 = 15.3$GPa, $G_{12} = 4.6$GPa, $v_{12} = 0.272$, $v_{23} = 0.535$, and $v_{31} = 0.078$. The axial load is 13.46kN/cm which is the net section force created by a pressure of 10.04MPa in an undamaged 25.4cm (10") diameter cylinder. Strain energy release rates were calculated using the virtual crack closure technique [3].

The same cases have also been modeled using constrained layered beam finite elements with each layer of elements representing an individual ply. Elements in adjacent plies are connected by kinematic constraints. These constraints relate mid-plane displacements and rotations such that displacements are continuous at ply interfaces but rotations can be different in adjacent plies. Delaminations are modeled by releasing the constraints. Shear deformation is included within each layer of elements. Further details of this approach are presented elsewhere [4]. The virtual crack closure concept is again used to calculate strain energy release rates for delamination. Modifications to the procedures are required, however, to properly estimate crack tip forces and displacements [4]. A sample mesh for the region near the notch and delamination is given in Figure 3. A potential advantage offered by this method is that standard elements can be used rather than specialized delamination elements [5]. Wilt et al. [6] used an approach similar to the present work but lumped each sublaminate above and below delaminations into a single layer of plate elements. The ply-by-ply representation adopted here can treat multiple delaminations and also provides a mechanism for explicitly modeling progressive failure in individual plies.
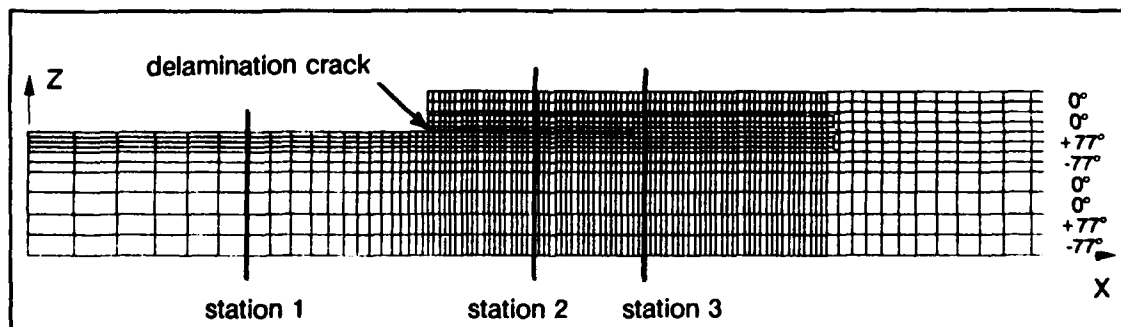
Figure 2. Plane strain finite element mesh of NTB.
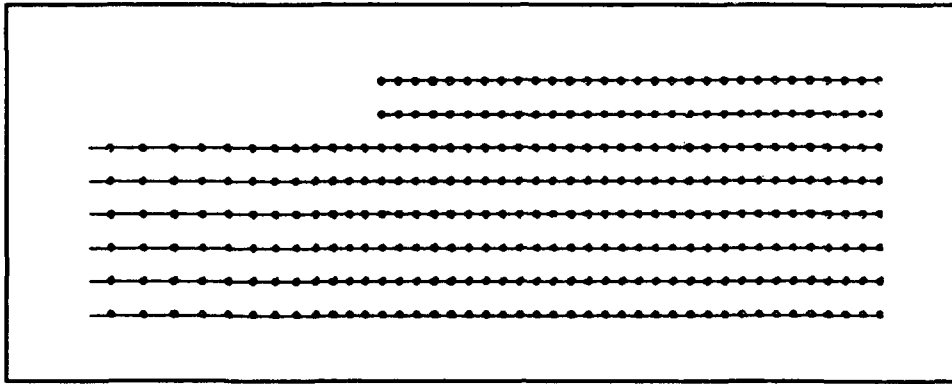
Figure 3. Beam element mesh of NTB.

RESULTS AND DISCUSSION

STRESS DISTRIBUTIONS

Solutions for the continuum and beam finite element approaches are first compared in terms of stress distributions. The variations in stresses through the thickness of the specimen are compared at three locations in Figure 4. These solutions are for a delamination crack 0.75cm long and located at the bottom of the notch (c=s). The locations are denoted stations 1, 2, and 3 in Figure 2 and correspond to positions X=0.250cm, 0.624cm, and 0.784cm, respectively. Station 3 is thus 0.034cm to the right of the delamination crack tip. Recall that the left end of the model is a plane of symmetry. The stress component plotted is σ_{xx}, which is analogous to the hoop stress of the cylinder configuration. The stress distributions for the layered beam element model agree well with the continuum results but are generally slightly lower. The loading at station 1, the notch bottom, is predominantly tensile with only slight bending. More significant bending is evident in the region of the delamination as reflected in the plots for station 2. Note that these plots are only for the six plies below the delamination. Stress gradients are larger but the agreement remains good. The stress distributions are much more irregular at station 3 which is near the crack tip. The extremely high gradient region is at the same depth as the delamination crack (Z=0.16764cm). Stresses for all eight plies are included. The plies bounding the crack plane are a 0° hoop ply above and a +77° ply below. The stresses for the layered beam mode' 'e again slightly lower but the trends are captured extremely well.

STRAIN ENERGY RELEASE RATES

The continuum and beam finite element approaches are also compared in terms of strain energy release rates. Total strain energy release rates (SERR) for a two ply deep notch are presented in Figure 5(a) as a function of crack length. The beam solutions agree quite well with the plane strain results for both layups studied (denoted "Uni" and
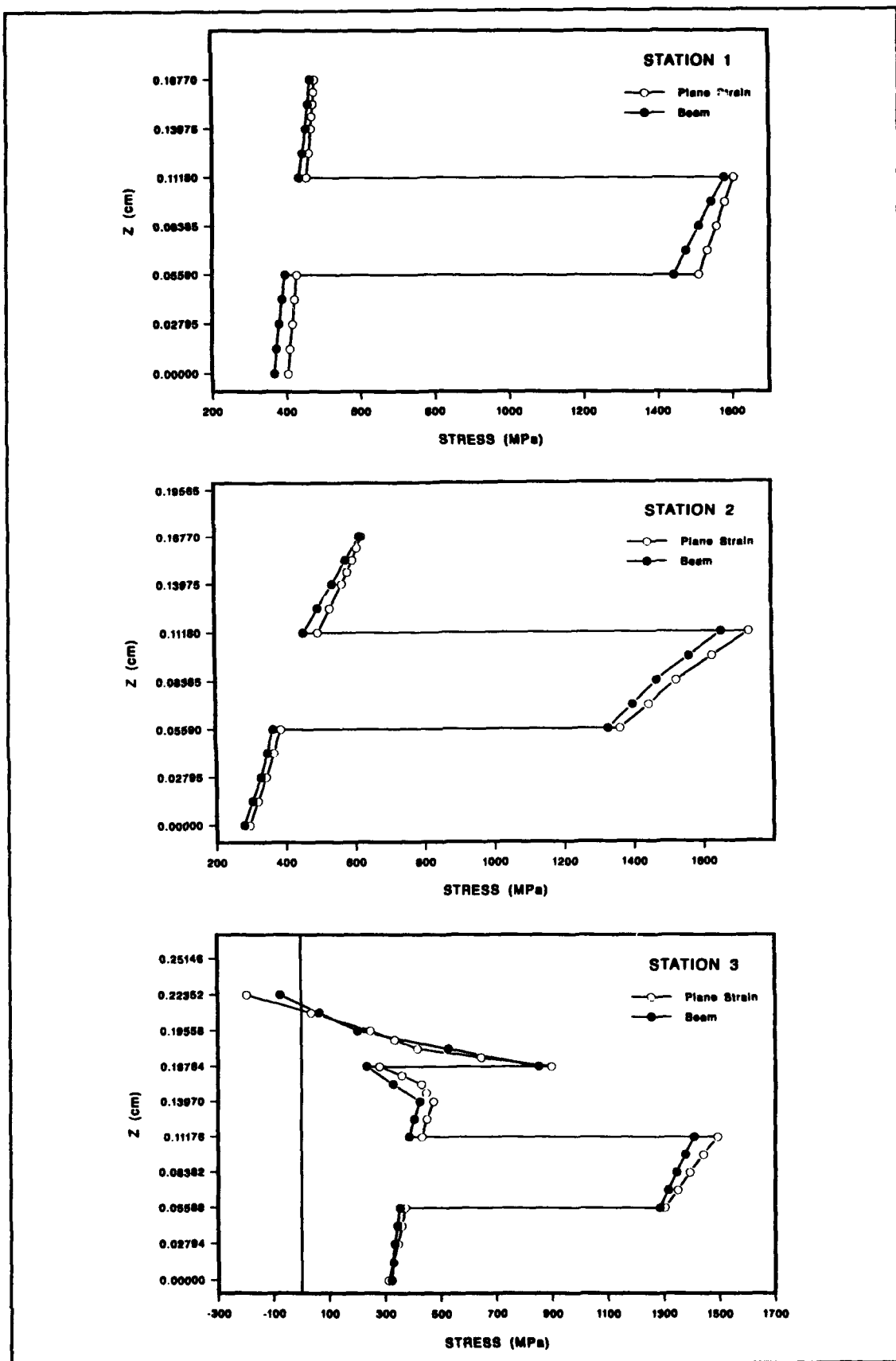
Figure 4. Stress comparison for plane strain and beam models.

"Angle"). The total SERR remains essentially constant with delamination length in this case and roughly triples for the angle-ply layup as compared to the uni-directional layup. The beam results are consistently lower by about 3-3½%. Results for the angle-ply case only are re-plotted in Figure 5(b) to show the mode I and mode II components of the SERR in addition to the total. This clearly reveals the source of the discrepancy to be the underestimation of the mode I component of the SERR by the beam approach. The same is true for the uni-directional case.
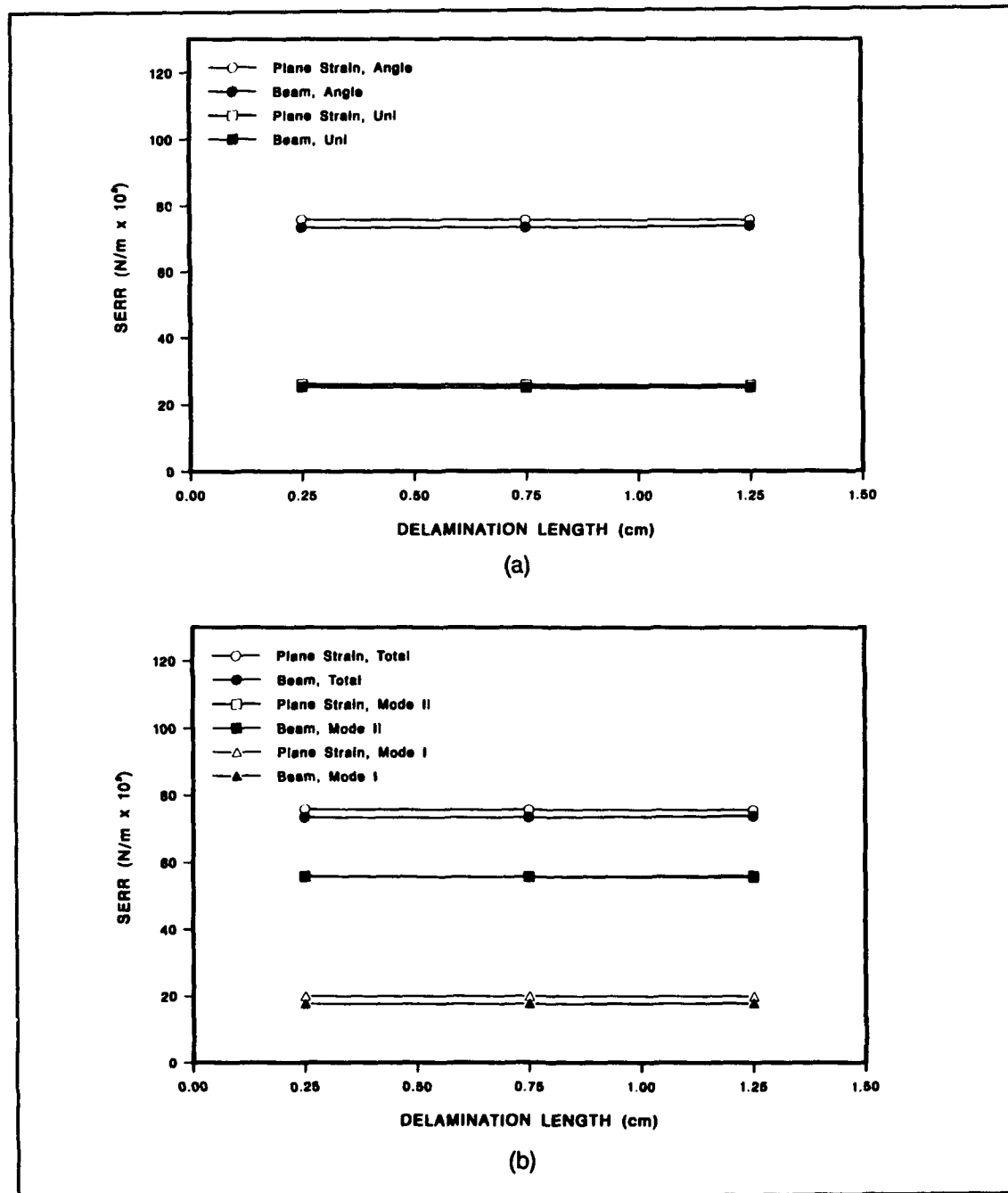
Figure 5. Strain energy release rate comparisons for the two ply deep notch.
(a) Total SERR. (b) SERR components for angle-ply layup.

Similar results are presented in Figure 6 for the case of a four ply deep notch. The beam results are again slightly lower than the continuum element solutions. The total SERR's in Figure 6(a) are generally higher than for the two ply deep notch. Results for the angle-ply layup are less than double those of the uni-directional layup in the four ply case, whereas they were triple in the two ply case. Figure 6(b) also shows that increasing the notch depth from two to four plies for the angle-ply layup causes the mode I component to increase substantially more than mode II. In fact, the two
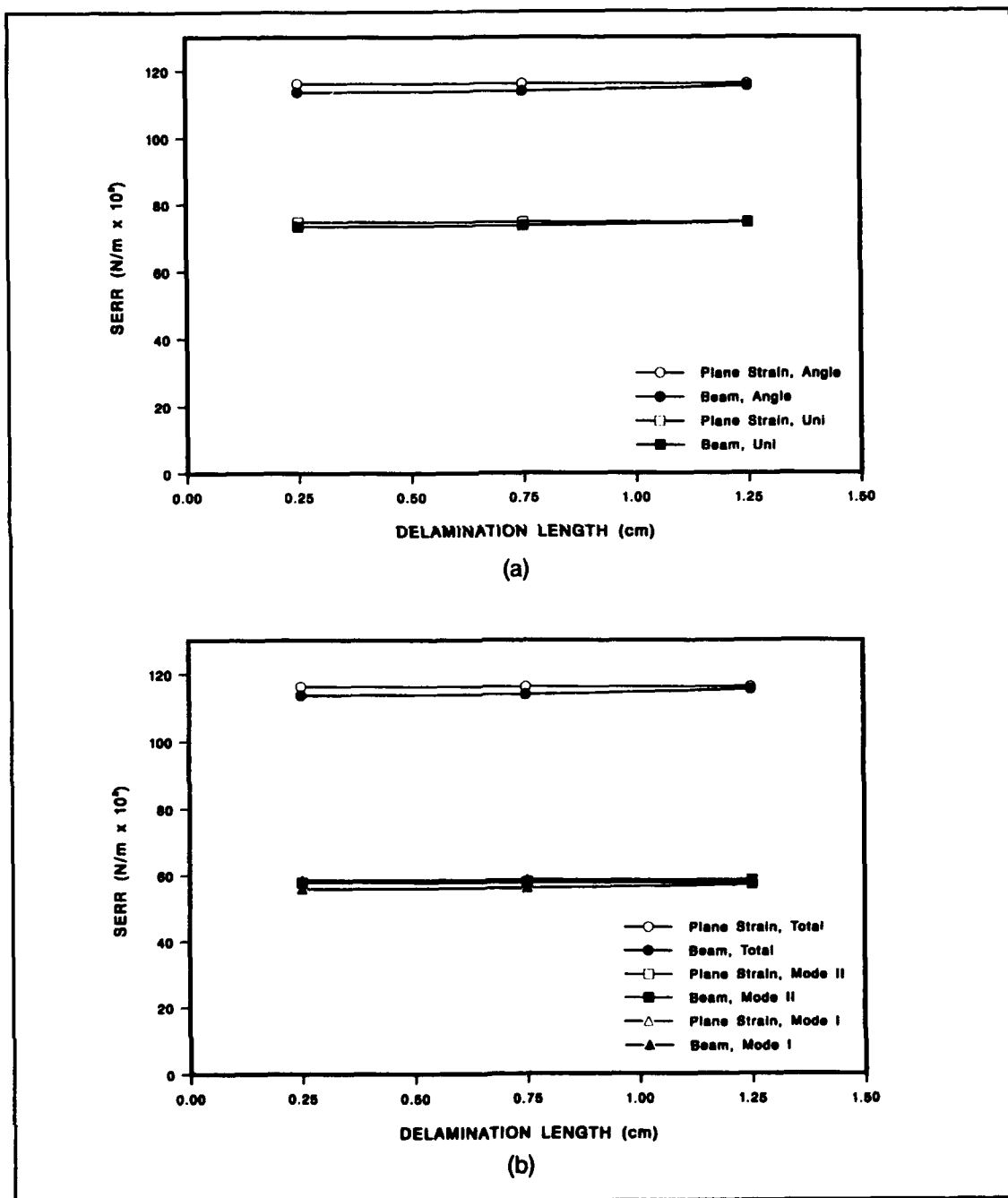
Figure 6. Strain energy release rate comparisons for the four ply deep notch.
(a) Total SERR. (b) SERR components for angle-ply layup.

components are basically the same for the four ply notch. When the delamination is not at the notch bottom the SERR's tend to increase with crack length as shown in Figure 7. These results are for a four ply deep notch with the crack located at the interface between the 0° ply and the +77° ply at c=s/2 (i.e. at the second ply interface from the top). The beam elements are again able to capture the characteristic trends.
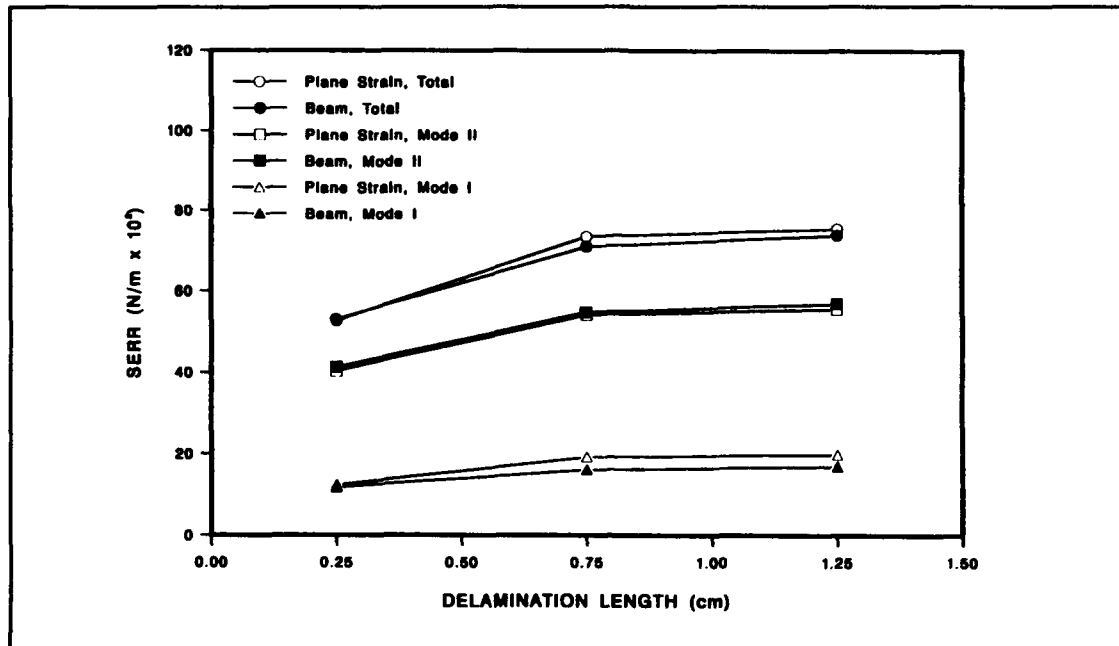
Figure 7. SERR results for delamination at second ply interface for four ply notch.
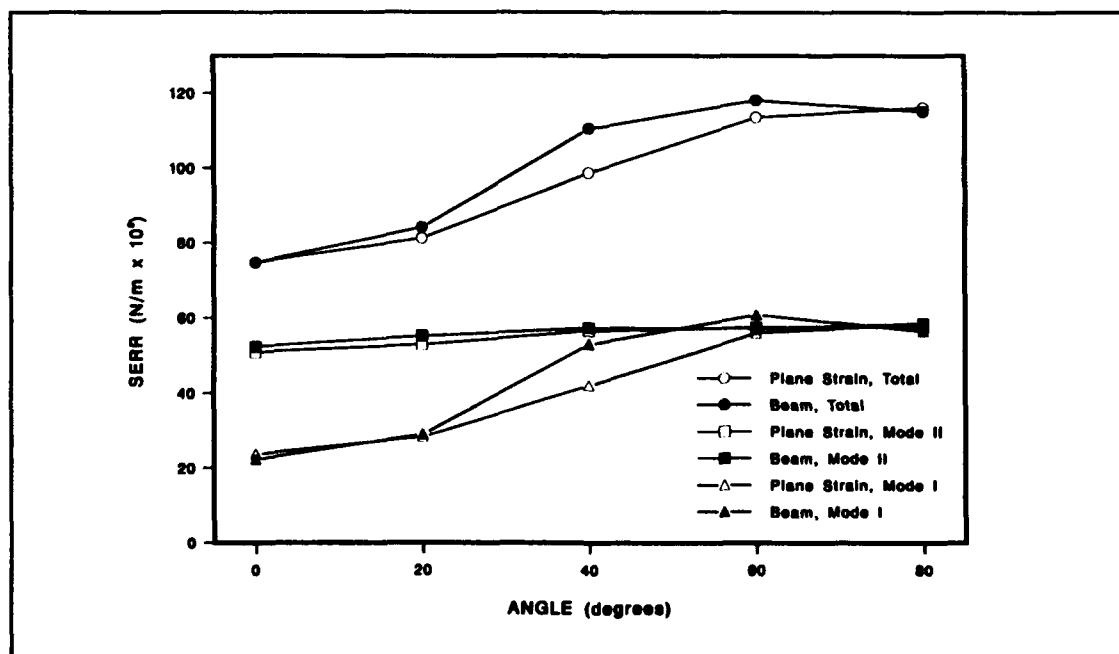
Figure 8. Effect of layup angle on SERR components.

As a final comparison, the angle of the off-axis plies has been varied. The results for the four ply deep notch with the delamination at the notch bottom are presented in Figure 8. In the range of 30-60° the beam element results show a larger deviation from the continuum results and reach a maximum of about 12% at 40°. The differences are almost solely due to an overprediction in mode I by the beam elements. The mode II SERR's remain fairly constant with ply angle. These results suggest that the present beam element approach is not as accurate for intermediate ply angles. The maximum difference only reaches 10-15%, however. Overall, the present work indicates that the layered beam element approach is able to accurately model the stress distributions and strain energy release rates in the NTB when compared with continuum finite element solutions. The approach has also been successively extended to plate and shell elements and is currently being used to study the cylindrical pressure vessel configuration.

ACKNOWLEDGEMENT

REFERENCES

1. Harbert, S. J. and H. A. Hogan, 1992. "An Analysis of Curvature and Layup Effects on Delamination in Notched Composite Beams." Journal of Reinforced Plastics and Composites, 11(4):443-457.

2. Harbert, S. J. and H. A. Hogan, 1991. "An Analysis of Delamination in a Fiber Reinforced Composite Material Notched Tensile Bar," Composite Material Technology - 1991, PD-Vol. 37, D. Hui and T. J. Kozik, eds., New York: ASME, pp. 153-160.

3. Rybicki, E. F. and M. F. Kanninen, 1977. "A Finite Element Calculation of Stress Intensity Factors by Modified Crack Closure Integral." Engr. Fracture Mech., 9:931-938.

4. Harbert, S. J. and H. A. Hogan, 1992. "Modeling Delamination Growth in Composite Notched Tensile Bars Using Constrained Plate Finite Elements," Composite Material Technology - 1992, PD-Vol. 45, D. Hui, T. J. Kozik, and O. Ochoa, eds., New York: ASME, pp. 107-112.

5. Sankar, B. V., and M. A. Pinheiro, 1990. "An Offset Beam Finite Element for Fracture Analysis of Delaminations," AIAA 31st Structures, Structural Dynamics and Materials (SDM) Conference, paper no. AIAA-90-1024-CP, pp. 1227-1233.

6. Wilt, T. E., P. L. N. Murthy, and C. C. Chamis, 1988. "Fracture Toughness Computational Simulation of General Delaminations in Fiber Composites," AIAA 29th Structures, Structural Dynamics and Materials (SDM) Conference, paper no. 88-2261, pp. 391-401.

Modeling and Analysis of Torsion in Shafts Made of Composite Materials

ENAYAT MAHAJERIN

I- ABSTRACT

In this paper the Fundamental Collocation Method (FCM) is applied to torsion of bars made of anisotropic and nonhomogeneous materials. The idea consists of transformation of the region into a hypothetical isotropic region for which the fundamental solution is available. The method is illustrated by means of some examples.

II- NOTATION

$C_{ij} = C_{ij}(x,y)$	Elastic compliances
$\sigma_{ij}, \epsilon_{ij}$	Stresses and strains respectively
$\varepsilon_i = C_{ij}\sigma_j$	(Hooke's law, $i,j = 1,2,...,6$)
u,v,w	Displacements in x,y,z respectively
W(x,y)	Warping function
θ	Angle of twist per unit length of the bar
$J = T/\theta$	Torsional rigidity of the bar (T = torque)
n_j	Unit normal on the boundary

III- FORMULATION

Torsion of bars may be formulated in two ways, the "stress function" and the "warping function" concepts. In the stress function method the governing differential equation for relatively difficult but the corresponding boundary condition is simple. This method is suitable for the finite element method [1]. The differential equation for the warping function case is of Laplace's type, but the corresponding boundary condition is relatively difficult. The warping function is suitable for the boundary element method [2]. It is assumed that the axis of the bar coincides with z-axis and its cross section, R, with boundary ∂R represented by $b(x,y) = 0$ lie in the x-y plane (Figure 1).

Enayat Mahajerin, Professor of Mechanical Engineering, Saginaw Valley State University, University Center, MI 48710 USA

Since the only non-zero strains in torsion are γ_{zy} and γ_{zx}, the equilibrium equations $(\sigma_{ij,j} = 0$ in R and $\sigma_{ij} n_j = 0$ on $\partial R)$ become:

$$\sigma_{zx},x + \sigma_{zy},y = 0 \quad \text{in R} \tag{1}$$

$$\sigma_{zx}n_x + \sigma_{zy}n_y = 0 \quad \text{on } \partial R \tag{2}$$

Consequently, Hooke's law becomes:

$$\gamma_{zy} = C_{44}\sigma_{zy} + C_{45}\sigma_{zx} \tag{3}$$
$$\gamma_{zx} = C_{45}\sigma_{zy} + C_{55}\sigma_{zx} \tag{4}$$

$$\sigma_{zy} = (C_{55}\gamma_{zy} - C_{45}\gamma_{zx})/\det \tag{5}$$
$$\sigma_{zx} = (-C_{45}\gamma_{zy} + C_{44}\gamma_{zx})/\det \tag{6}$$

where $\det = C_{44}C_{55} - C_{45}^2$

Displacements, strains, and stresses are related to the warping function $W = W(x,y)$,

$$u = -\theta yz, \quad v = \theta xz, \quad \text{and} \quad w = \theta W \tag{7}$$

$$\gamma_{zx} = w,x + u,z = \theta(W,x-y) \tag{8}$$
$$\gamma_{zy} = w,y + v,z = \theta(W,y+x) \tag{9}$$

$$\sigma_{zx} = \theta[-C_{45}(W,y+x) + C_{44}(W,x-y)]/\det \tag{10}$$
$$\sigma_{zy} = \theta[C_{55}(W,y+x) - C_{45}(W,x-y)]/\det \tag{11}$$

The governing equation of torsion is obtained by substituting (10) and (11) in (1),

$$AW,xx + BW,xy + CW,yy + DW,x + EW,y + FW = G \quad \text{in R} \tag{12}$$

This equation is of a general form $L[W] = f$ where L is an operator consists of the partial derivatives. The corresponding boundary condition (2) will be:

$$(AW,x + .5BW,y)n_x + (CW,y + .5BW,x)n_y = (Ay-.5Bx)n_x - (Cx-.5By)n_y \quad \text{on } \partial R \tag{13}$$

where

$A = C_{44}$; $B = -2C_{45}$; $C = C_{55}$; $D = C_{44},x - C_{45},y$; $E = C_{55},y - C_{45},x$; and
$G = C_{44},x - C_{55},y + C_{45},x - C_{45},y$

VI- NUMERICAL SOLUTION OF (12) and (13)- THE FUNDAMENTAL CONCEPTS OF FCM

The FCM approach is similar to the Boundary Element Method except that the

sources are distributed outside the boundary of the region at a distance DS away from the boundary of the region (Figure 2). Consequently, there will be no singularities in the formulation [2]. For illustration, suppose we require the solution of Laplace equation $W,xx + W,yy = 0$ subjected to known W on the boundary. The region is imagined to be embedded inside an infinite plane of the same material. If a series of sources of unknown strength s_j are applied at source points (X_j, Y_j), $j = 1, 2, .., N$, outside ∂R, then W can be expressed as a weighted summation of the fundamental solution of the Laplace equation,

$$W(x,y) = \sum_{j=1}^{N} s_j \ln[(x-X_j)^2 + (y-Y_j)^2] \tag{14}$$

The weights s_j are then adjusted by matching boundary conditions at N boundary points (x_i, y_i), i.e.,

$$c_i = \sum_{j=1}^{N} s_j \ln[(x_i - X_j)^2 + (y_i - Y_j)^2] \tag{15}$$

where $c_i = W_i$ are prescribed boundary conditions at the boundary points $i = 1, 2, .., N$. Equation (15) is of the form $HS = C$ where H is an NxN matrix known as the "influence matrix," S is a vector containing source weights, and C contains the prescribed boundary conditions. Once $HS = C$ is solved for S, we can compute W (and its derivatives) at any point inside R from (14). The process can be applied to the general boundary condition $aW + bW,n = c$ in a similar fashion [2]. However, if a fundamental solution for (12) is not available the method requires some modifications. Equation (12) is rewritten as

$$AW,xx + BW,xy + CW,yy = F^*(x;y;W,x;W,y) \tag{16}$$

where $F^* = G - DW,x - EW,y - FW$ \hfill (17)

It is possible to find a pair of coordinate systems $p = p(x,y)$ and $q = q(x,y)$ and use canonical transformation [3] to convert (16) to

$$W,pp + W,qq = F^*(p;q;W;W,p;W,q) \tag{18}$$

When this transformation is done, R transforms to a new region R^* with its boundary represented by $b^*(p,q) = 0$. Region R^* may be regarded as an isotropic equivalent of region R (Figure 3).

One possible method to find p and q is to find the roots of $Ar^2 - Br + C = 0$ where $r = dy/dx$ and then determine solutions y_1 and y_2 of the characteristic equations $dy/dx = .5(B \pm (B^2 - 4AC)^{.5})/A$. From y_1 and y_2 we may find p and q via $p = .5(y_1 + y_2)$ and $q = .5(y_1 - y_2)/i$ where $i = \sqrt{-1}$.
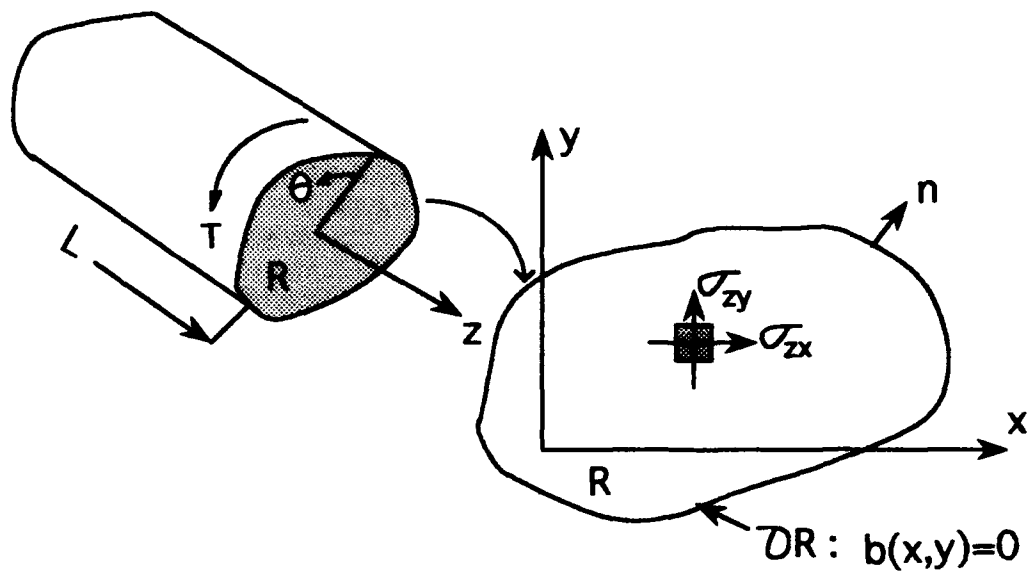
FIGURE 1- Geometry
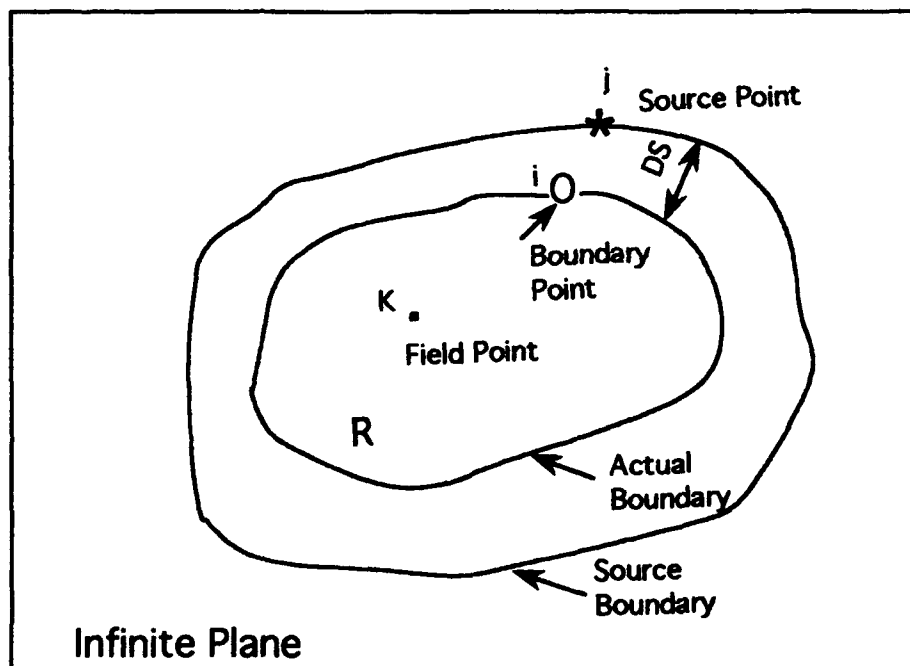
FIGURE 2- The Set Up for FCM

The FCM process for (18) and its appropriate boundary condition requires representation of the boundary ∂R^* by N points and representation of the interior R^* by M cells each of area ΔA_k, $k = 1, 2, .., M$ (Figure 4). The homogeneous part of the solution we is obtained via (14) and the nonhomogeneous part similarly but instead of the outside source strengths, s_j, we use values of F^* at the center of each cell. Combining both parts,

$$W(p,q) = \sum_{j=1}^{N} s_j \ln[(p-P_j)^2 + (q-Q_j)^2] + \sum_{k=1}^{M} F^*_k \Delta A_k \ln[(p-p_k)^2 + (q-q_k)^2]/4\pi \qquad (19)$$

From this the derivatives of W may be expressed in a similar fashion. Using the prescribed boundary conditions, c_i, at boundary points $i = 1, 2, .., N$ gives (19) in a matrix form,

$$HS + H^* F^* = c \qquad (20)$$

where

H is the NxN "boundary" influence matrix
S is the Nx1 vector containing the strengths of the sources
H^* is the NxM "cell" influence matrix
F^* is Mx1 vector evaluated at the center of each cell

Since F^* contains W and its derivatives, it must be solved iteratively by isolating S in one side of the equation, i.e.,

$$S = c^* - H^{-1} H^* F^* \, , \quad c^* = H^{-1} c \qquad (21)$$

The iterative solution of (21) require the following steps:

Step 1. Choose an initial guess for W (and therefore its derivatives $W_{,x}$ and $W_{,y}$)
Step 2. Compute the corresponding F^* from (17)
Step 3. Compute the vector S from (21)
Step 4. Compute W and its derivatives at interior points via (19)
Step 5. Update F^*
Step 6. Update W and its derivatives (step 4).
Step 7. STOP if converges, repeat (step 2) otherwise

The steps are easily performed on personal or mainframe computers.
Once W's are determined we can compute stresses from (10) and (11).
The torsional rigidity is computed from $J = T/\theta$ where

$$T = \int \int (x\sigma_{zy} - y\sigma_{zx})dA \qquad (22)$$

The area integral over R^* may simply be approximated by dividing R^* into small cells, i.e., $T = \sum (...)_k \Delta A_k$ where $k =$ center of the cell.
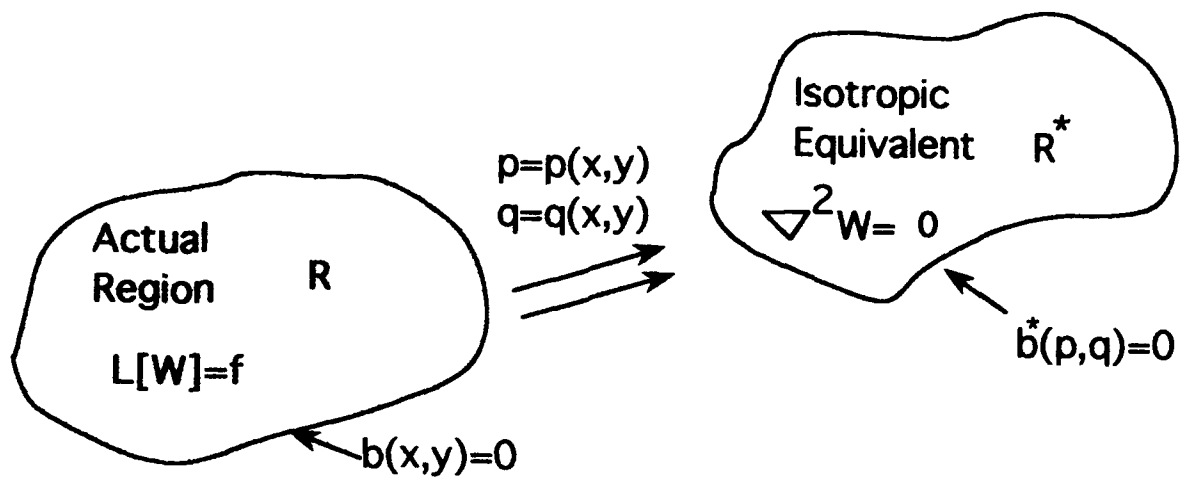
FIGURE 3- Transformation
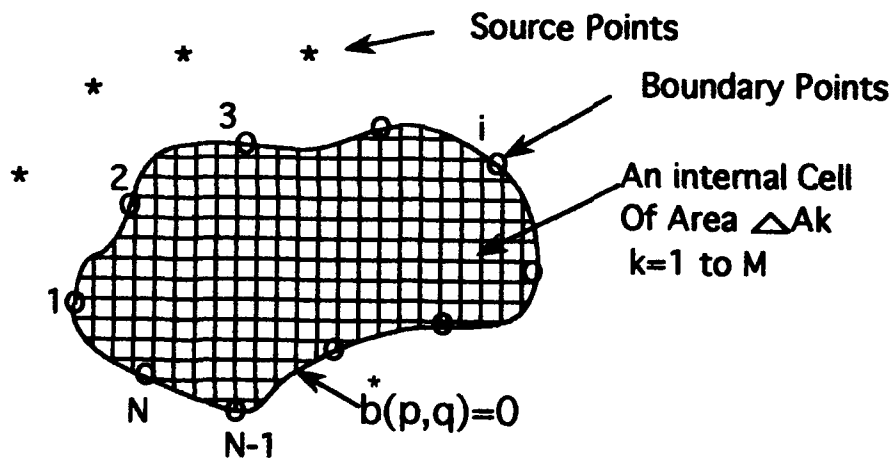
FIGURE 4- Discretization

Table 1. COMPLIANCES FOR VARIOUS STRUCTURES

Material	Example	Symm. Planes	C_{ij}/indep-endent C_{ij}	Remark
General	–	None	36/36 (9/9)	$C_{ij} \neq C_{ji}$
Materials with strain energy	Triclinic systems	None	36/21 (9/6)	$C_{ij} = C_{ji}$
Nonhomogeneous Anisotropic	Monoclinic systems	1	20/13 (9/6)	$C_{ij} = C_{ij}(x,y)$
Homogeneous Anisotropic	Alkali metals	1	20/13 (9/6)	C_{44}, C_{45}, C_{55} nonzero
Orthotropic	Laminated Composites	3 ♣	12/9 (5/4)	$C_{45}=0$ $C_{44}=1/G_1$ $C_{55}=1/G_2$
Transversely Isotropic	HCP metals Sheets of fibers	1 6-fold	12/5 (5/4)	$C_{45}=0$ $C_{44}=1/G_1$ $C_{55}=1/G_2$
Cubic	BCC & FCC metals	4 3-fold	12/3 (5/4)	$C_{45}=0$ $C_{44}=C_{55}=1/G$
Isotropic	Tungsten	∞	12/2 (5/2)	$C_{44}=C_{55}=1/G$

* Values in parenthesis are for two dimensional cases
♣ mutually orthogonal planes

Table 2. VARIOUS DIFFERENTIAL EQUATIONS FOR TORSION

Material	Governing Differential Equation	
Anisotropic, Nonhomogeneous	Equations (12) Equation (13)	in R on B
Anisotropic, Homogeneous	AW,xx+BW,xy+CW,yy=0 Equation (13)	in R on B
Orthotropic, Nonhomogeneous	AW,xx+BW,xy+CW,yy+A,xW,x+C,yW,y=0 AW,xn$_x$+CW,yn$_y$=C(yn$_x$-xn$_y$)	in R on B
Orthotropic, Homogeneous	AW,xx+BW,xy+CW,yy=0 AW,xn$_x$+CW,yn$_y$=yAn$_x$-xCn$_y$	in R on B
Transversely Isotropic	AW,xx+CW,yy=0 AW,xn$_x$+CW,yn$_y$=yAn$_x$-xCn$_y$	in R on B
Cubic	W,xx+W,yy=0 W,n=yn$_x$-xn$_y$	in R on B
Isotropic	W,xx+W,yy=0 W,n=yn$_x$-xn$_y$	in R on B

V- EXAMPLES

Example 1. Consider an elliptical cross-section (2a=2, 2b=1), made of an isotropic material. The governing equation is $\nabla^2 W=0$ (i.e., $F^*=0$) and the corresponding boundary condition is W,n= yn$_x$-xn$_y$. Stresses and the torsional rigidity are $\sigma_{zx}=$ $G\theta$(W,x-y), $\sigma_{zy}=G\theta$(W,y+x) and $J=\iint$ (x^2y^2+xW,y-yW,x)dA. Using N=9 and DS=1 the result for J=.31315 agrees well with the $J_{Exact}=\pi/10$ [4].
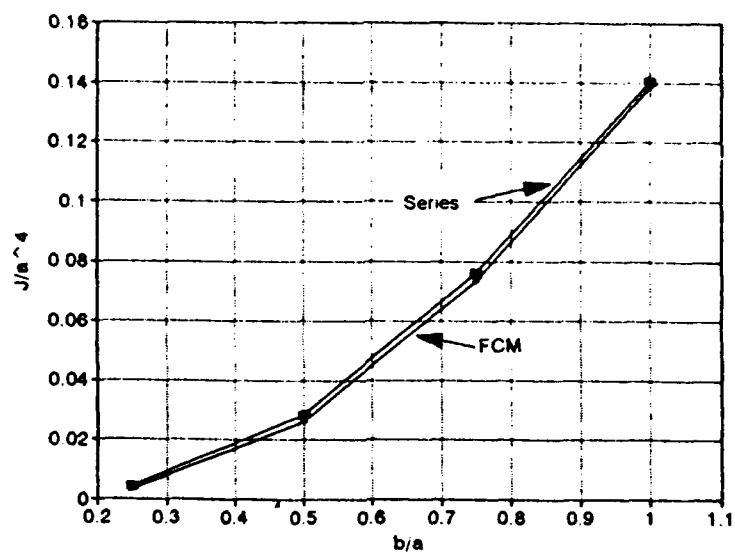
FIGURE 5- Example 2, CASE 1.
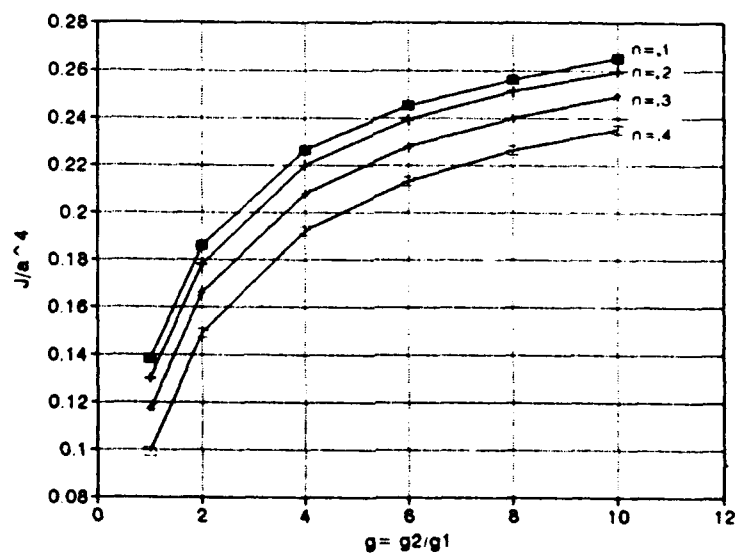
FIGURE 6- Example 2, CASE 2.

64

Example 2. A rectangular region axb made of an orthotropic $(C_{44}=1/G_1, C45=0, C_{55}=1/G_2)$ and nonhomogeneous of the form

$$G_1 = g_1 \, e^{n\pi(b/2 - y)/b} \quad , \quad G_2 = g_2 \, e^{n\pi(b/2 - y)/b}$$

where G_1 and G_2 are shear moduli along the axes of symmetry and g_1, g_2 are constants and n is a parameter representing the degree of nonhomogeniety. Consequently, (12) and (13) become

$$W,xx + g \, W,yy = (n\pi/b)g(x+W,y) \qquad \text{in R}$$

$$W,x \, n_x + g \, W,y \, n_y = y \, n_x - xg \, n_y \qquad \text{on B}$$

Using $p = g^{.5} x$ and $q = y$ we can transform R to R^* in which

$$W,pp + W,qq = (n\pi/b)(g^{-.5} p + W,q)$$

Two cases were investigated using N=24, M=100 and DS=1.

case 1. Variation of J versus the aspect ratio b/a for constant n=.1. The results are given in **Figure 4**.
case 2. Variation of J versus n at constant aspect ratio b/a=1. The results are shown in **Figure 5**.

Both results seem to be consistent and agree closely with the series approximation [4].

VI- CONCLUSIONS

The method seems to be suitable for torsion problems involving anisotropic and nonhomogeneous materials. The iterative procedure is straightforward and may be performed on personal or mainframe computers. Examples show that the method can handle various assumptions including geometry, anisotropy and nonhomogeneiety.

VII- REFERENCES

1. Segerlind, L. J., 1984. <u>Applied Finite Element Analysis</u>, Wiley, New York.

2. Burgess, G. and Mahajerin, E., 1985. "On the Numerical Solution of Laplace's Equation Using personal Computers," <u>International Journal of Mechanical Engineering Education</u>, 2(1):45-54.

3. Tyn Mynt-U and Debnath, L., 1987. <u>Partial Differential Equations for Scientists and Engineers</u>, 3rd. ed., North Holland.

4. Lekhnitskii, S. G., 1981. <u>Theory of Elasticity of an Anisotropic Body</u>, Mir Publisher, Moscow.

SESSION 1B

Test Methods I

Combined Shear- and End-Loaded Compression Strength Testing of Advanced Composite Materials

STEVEN E. HAHN AND KEN L. REIFSNIDER

ABSTRACT

In this study, the Wyoming End-Loaded Side-Supported (ELSS) compression test method was investigated experimentally in a combined shear- and end-loaded mode, with the goal of developing the method as a reasonable alternative to IITRI testing. Combined loading was accomplished by applying a controlled amount of clamping force to the fixture stabilizing blocks, allowing them to transmit shear force to the coupon faces through friction.

Experimental results include strengths and failure modes for both tabbed and untabbed unidirectional graphite/bismaleimide specimens tested by the combined loading ELSS method, and these data are compared to the results given by the IITRI method. For a particular range of clamping, both the strength and failure mode achieved with the combined loading ELSS method using tabbed specimens are similar to those seen in the IITRI tests. Based on this result, the modified ELSS technique can be considered equivalent to the IITRI method. Preliminary data from tests using novel nonbonded tabs were also similar to those given by the IITRI method. The finite element method was used to analyze the physical phenomena responsible for the observed performance of the ELSS system.

INTRODUCTION

The determination of compressive properties of advanced composite materials has long been a formidable challenge. The short, thick specimens used in the compressive testing of metals are neither appropriate nor economically feasible for anisotropic composite laminates built up from thin, expensive layers. The challenge, then, has been to develop test specimens and test techniques to accurately, repeatably and conveniently characterize the compressive properties of composites. Several alternate methods have been developed over the years, with varying degrees of acceptance. In general, those methods which produce accurate, repeatable results are expensive and difficult to perform, and those methods which have attempted to reduce cost and complexity have proven incapable of producing consistently good results.

Steven E. Hahn, currently with Boeing Defense & Space Group, MS 82-97, P.O. Box 3999, Seattle, WA, 98124-2499; formerly Graduate Research Assistant, Engineering Science and Mechanics Department, Virginia Polytechnic Institute and State University
Ken L. Reifsnider, Alexander Giacco Professor, Engineering Science and Mechanics Department, Virginia Polytechnic Institute and State University, Blacksburg, VA, 24061
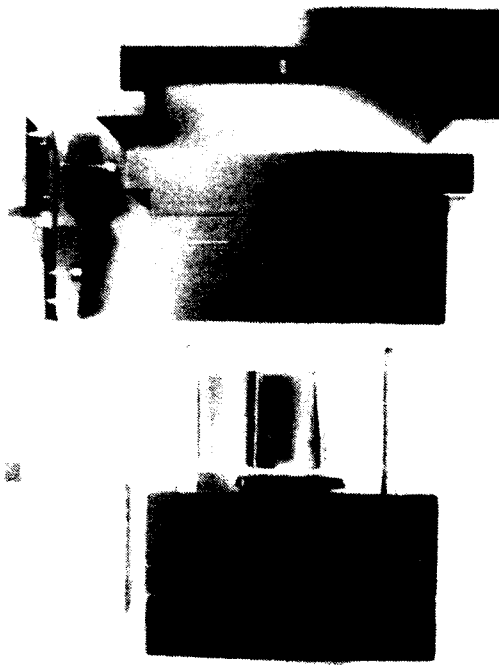
Figure 1. IITRI Compression Test Fixture
(Photo Courtesy of Wyoming Test Fixtures, Inc.)
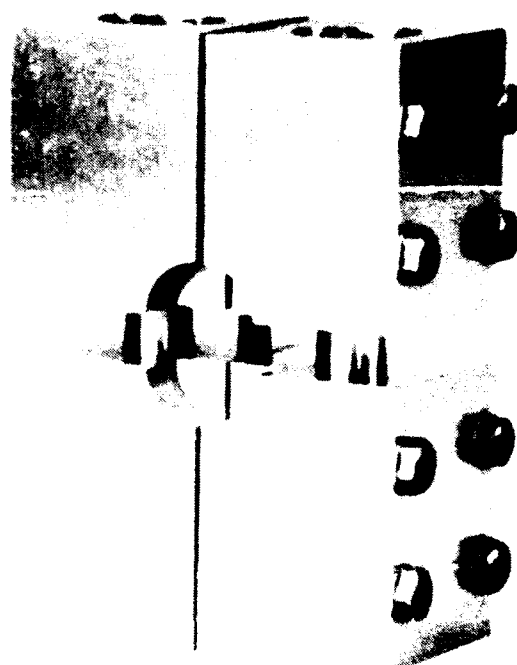
Figure 2. ELSS Compression Test Fixture
(Photo Courtesy of Wyoming Test Fixtures, Inc.)

It is possible to divide the bulk of the available composite compression test methods into two groups based on the load introduction scheme. The shear loaded group is characterized by the Illinois Institute of Technology Research Institute (IITRI) method. Probably the most widely used and extensively accepted compression test method, the IITRI method [1] was developed to address the perceived deficiencies of the then-industry-standard Celanese method. The IITRI fixture, Figure 1, utilizes serrated steel flat wedge grips to apply a shear load to the specimen faces. The colinearity of the fixture halves is maintained by linear bearings and hardened shafts.

This method has been shown to provide results similar to the Celanese test [2], and has been incorporated into the current revision of ASTM D 3410 [3]. However, difficulties associated with the application of this method, typical of shear loaded methods, have fueled continued research into compression test methodology. It has been shown [2], for example, that it is necessary to guarantee that the gripped surfaces are flat and parallel. The serrated grip surfaces require the use of tabs to protect the specimen faces. The IITRI fixture is also quite massive (greater than 40 kg or 90 lbs), which is of concern both for ease of testing and testing at elevated temperatures, where the large mass would require long soak times to reach equilibrium. It has also been determined [4] that the nonuniform stress field associated with the transition from the applied shear load to the desired uniform compressive stress can extend well into the gage section, a potential problem for accurate strain measurement.

The Wyoming End-loaded Side-supported (ELSS) method, Figure 2, is representative of end loaded test methods. The ends of the untabbed coupon are borne upon directly, theoretically providing a uniform compressive stress throughout the specimen. The coupon is supported between two stabilizing blocks on either end to prevent buckling. Hardened shafts on linear

bearings are used to provide support against bending. The light weight of the fixture makes it easy to use and ideal for environmental testing.

It is necessary, however, to control the flatness and parallelism of the coupon ends closely, and the fit in the stabilizing block slot cannot be too close, or problems develop with restraint against Poisson expansion [5]. Another significant difficulty noted for this method is the tendency for end crushing failures with unidirectional specimens [5-8]. Exploring techniques for overcoming this tendency was a major component of the present study.

Adams [7,8] has hypothesized that the transfer of a portion of the load by shear through the specimen faces would reduce the stresses at the end of the specimen and eliminate the end crushing failures. The use of tabbed specimens with this method (to increase the bearing area) has also been suggested as a means to relieve end crushing failures. To accomplish combined shear/end loading with this fixture, a controlled amount of clamping force can be applied to the stabilizing blocks, allowing them to transmit shear force to the coupon faces through friction.

In this study, the effect of varying the clamping force on the ELSS specimen was examined. Experiments were performed on both tabbed and untabbed ELSS coupons, and those data were compared to the results by the IITRI method. Preliminary experiments with novel nonbonded tabs are also presented, showing promise for this technique to provide a bridge between the simplicity of untabbed specimens and the accuracy of tabbed specimens.

EXPERIMENTAL PROCEDURE

Unidirectional test specimens for this study were fabricated from a BASF Celion G40-600 graphite fiber/5245C bismaleimide (BMI) matrix material system. Coupons were cut from three panels manufactured in the Virginia Tech fabrication laboratory. Nominal panel thickness was approximately 3.5 mm (0.14 in). Ultrasonic C-scan examination of the panels was used to insure consistent quality of the specimens. Fiberglass cloth/epoxy tabs were bonded to selected specimens using a room temperature cure epoxy adhesive.

Strain gages were installed to the front and back center of a representative set of specimens in order to characterize the stress-strain response of the material. The required torque was applied to the bolts on the ELSS fixture using a torque wrench. Testing was performed using a screw-type testing machine, at a platen displacement rate of 1.27 mm/min (0.05 in/min). Strain and load data were collected using a computer acquisition system.

EXPERIMENTAL RESULTS

The average strength measured in the IITRI tests was 1246 MPa (181 ksi). Figure 3 shows an IITRI failure typical of those observed. This failure can be classified as "split transverse," described by Odom and Adams [9] as characterized by shear failure across the specimen width accompanied by multiple longitudinal splits emanating from the failure surface. Odom and Adams determined that this particular failure mode was indicative of a "good" test, lending confidence to the use of these data as a baseline.

The plot of the average strengths measured with untabbed ELSS coupons is presented in Figure 4. This plot shows that the measured strength increases with increasing torque (clamping force) up to about 4.5 N-m (40 in-lbs), and then declines over the range of torques examined. The maximum strength achieved was about 900 MPa (130 ksi), which is 28% lower than the IITRI strength, a significant difference. End crushing failures were typically observed at low clamping

Figure 3. "Split Transverse" Failure Typical in IITRI Testing
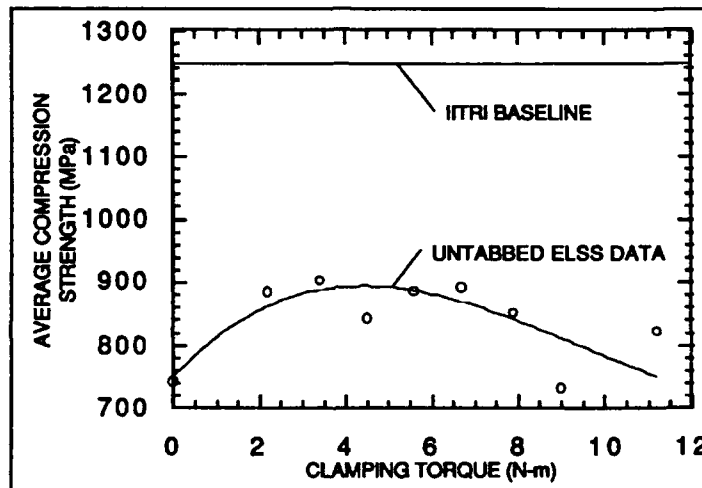
Figure 4. Compression Strength Measured by the
ELSS Method with Untabbed Specimens

Figure 5. "Brooming" Failure Typical in ELSS Testing with Untabbed Specimens
and High Clamping Torque

torques. Figure 5 illustrates what has been classified as a "brooming" failure. The gage section appears to have delaminated "explosively," accompanied by shear failure across the specimen width. This failure was typical at torques near and above the maximum in measured strength. The third failure type observed was labeled "mixed mode," as there was evidence of both end crushing and brooming failures. Noise events which occurred prior to the final specimen failure indicated that the crushing failure occurred first.

Figure 6 shows the plot of the average strengths measured with tabbed ELSS specimens, compared with the IITRI baseline and the untabbed ELSS data. The overall trend is similar to that exhibited in the untabbed testing, but the maximum is much higher (comparable to the IITRI data), and occurs at a much higher torque, around 9.0 to 11.2 N-m (80 to 100 in-lbs). At low torques, the predominant mode of failure was end crushing, similar to that exhibited by the untabbed specimens, but more catastrophic. As the torque was increased, the failures were a mixture of the end crushing and split transverse modes. Further increase lead to split transverse failures similar to those observed in the IITRI testing, as shown in Figure 7.

Figure 8 shows the strength data obtained with nonbonded, tabbed ELSS coupons in relation to the bonded tab ELSS data and the IITRI data. It is clear that the highest of these data are also comparable to the IITRI values. At the lowest clamping torque the failure was by end crushing. At the intermediate value, where the strength was comparable to the IITRI value, there was evidence of both end
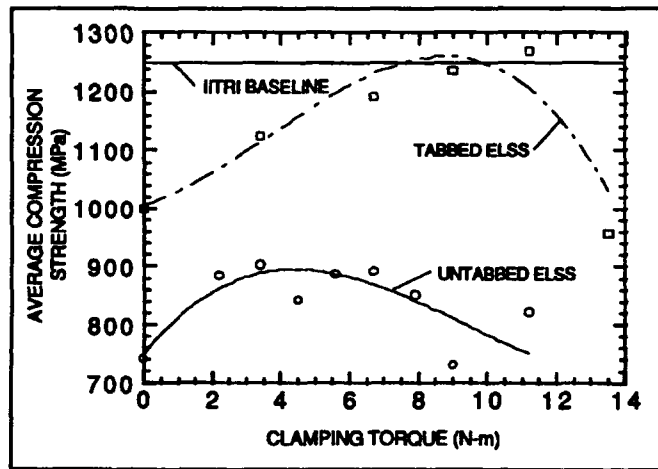
Figure 6. Compression Strength Measured by the ELSS Method with Bonded, Tabbed Specimens

Figure 7. "Split Transverse" Failure Observed in ELSS Testing with Bonded, Tabbed Specimens and High Clamping Torque

crushing and split transverse fail-
ures (Figure 9), while the failure at
the highest level was split trans-
verse.

DISCUSSION

The crushing of the specimen
ends at low torque corresponds to
the results reported by other re-
searchers [5-8]. Figure 10 illustrates
a hypothesis which can qualitatively
explain the observed behavior of the
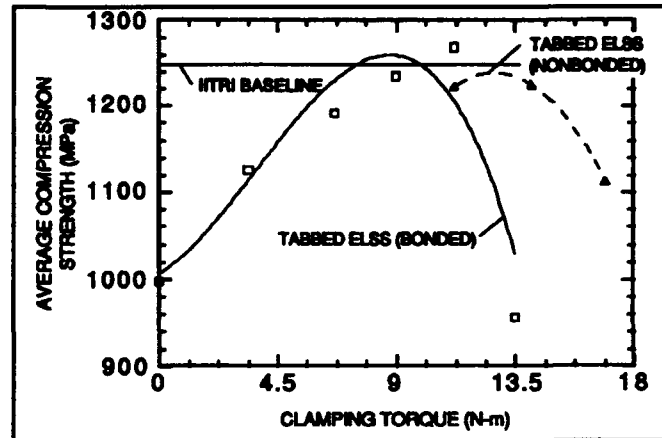
Figure 8. Compression Strength Measured by the ELSS
Method with Nonbonded, Tabbed Specimens
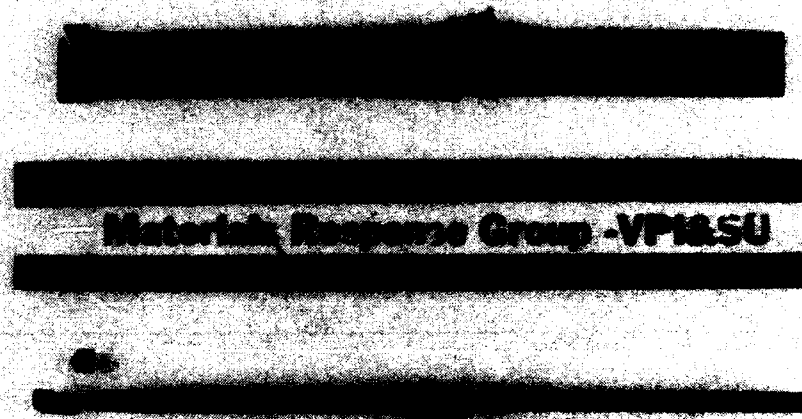
Figure 9. "Split Transverse" Failure Observed in ELSS Testing with
Nonbonded, Tabbed Specimen and High Clamping Torque

ELSS system under combined loading. The "End Constraint Effect" curve describes an increase
in measured strength as the clamping torque is increased. This is due to increased frictional shear
loading of the specimen faces, which reduces the local stresses which cause crushing failure.
Simultaneously, however, increased shear loading increases the effect of the stress concentration
at the edge of the block, leading to a decline in the measured strength, as represented by the "Stress
Concentration Effect" curve. As shown by the "Observed Behavior" curve, the specimen will fail
in the mode which requires the least stress, hence the observed maximum and transition of failure
mode.

In order to verify this hypothesis, a finite element method (FEM) analysis was performed.
A two dimensional, quarter symmetric model of the ELSS fixture and specimen was constructed.
The applied clamping torque was varied from no clamping to 11.2 N-m (100 in-lbs). For each
torque value, the compressive loading was increased until the maximum stress at the specimen
end indicated failure, then again for failure in the gage section. The lower of the two failure
stresses as determined by the average stress at the center of the specimen gave the measured
strength for that level of clamping torque.
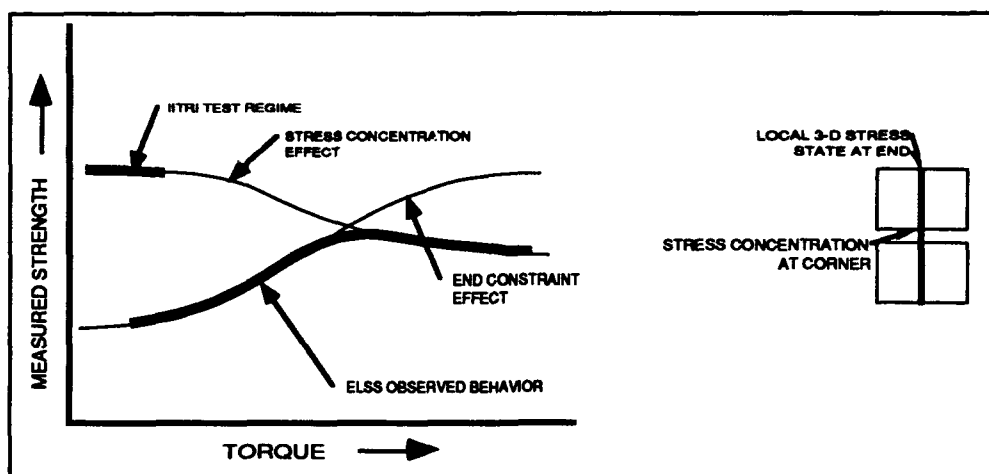
Figure 10. Qualitative Hypothesis Explaining Observed ELSS Behavior

Figure 11 compares the resultant composite strength versus clamping torque curves for four values of the coefficient of friction, which was not known a priori, and the data from the untabbed ELSS experiments. While none of the curves correlates precisely with the experimental data, the general trend in measured strength as torque increases is similar. Due to the maximum stress failure criterion used, the analysis was optimistic; reducing the strengths would improve the correlation with the experimental data. In any event, the similarity is sufficient to reasonably corroborate the previously

Figure 11. FEM Analysis Results Compared to Experimental Results for Untabbed ELSS Tests

advanced hypothesis for the observed changes in measured strength with increased clamping torque.

In light of the previously presented hypothesis for untabbed specimens, the effect of the tabs can be described as shown in Figure 12. The compliant tab between the block and the specimen mitigates the effect of the stress concentration, and simultaneously reduces the stress level at the specimen ends by increasing the bearing area, thus allowing the strength of the material to be measured.

Although these results show that by using the proper testing parameters, either the ELSS or IITRI methods will yield useful results, the adhesive bonding process is costly and time consuming, and should be avoided if possible. The investigation of nonbonded tabs in this study was an attempt to relieve the necessity for adhesive bonding. Insufficient data were taken to provide conclusive results, but the correlation of the nonbonded data with the bonded results is unmistakable, both in measured strength and failure mode.
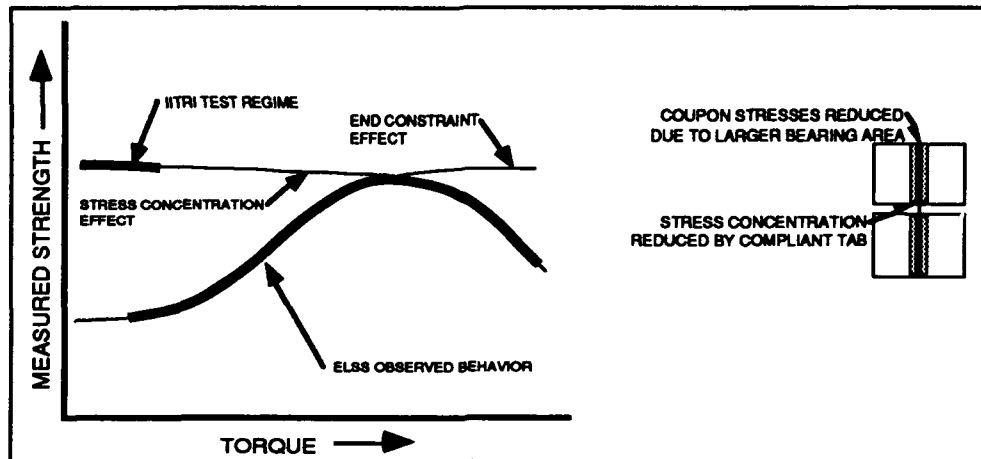
Figure 12. Qualitative Effect of Tabbed Specimens in ELSS Testing

CONCLUSIONS

The experimental results clearly indicate that for a particular range of clamping torques, when tabbed specimens are used, the combined loading ELSS compression test method provides the same value of compressive strength as the IITRI method, with similar failure modes. Further work is necessary, however, to verify these results for a wide range of material systems, and to further define appropriate test parameters.

It seems that strength results similar to those generated by the IITRI method can be obtained from the ELSS method using either bonded or nonbonded tabs. Nonbonded tabs appear to require greater torque to achieve similar results. It also seems that there is less difference between failure stresses in the end crushing and the split transverse modes with the nonbonded tabs, leading to greater overlap of these failures. Initial damage in the end crushing mode can be tolerated, provided final failure is in the split transverse or other acceptable mode.

This conclusion regarding the use of nonbonded rather than bonded tabs is consistent with the long-standing recommendations of researchers at Virginia Tech with regards to tensile and fatigue test specimens [10,11]. The use of bonded tabs for these tests has been discouraged to avoid the positive interlaminar stresses associated with the termination of the tab. Hart-Smith [12] has recently made similar recommendations for all types of testing, including static compression. The use of nonbonded tabs in combined loading compression testing is a promising development which merits further investigation to determine the appropriate testing parameters (including tab geometry, material, and clamping torque), as well as any limitations to the application of this technique.

ACKOWLEDGEMENT

REFERENCES

1. Hofer, K. E., and P. N. Rao, July 1977, "A New Static Compression Fixture for Advanced Composite Materials," Journal of Testing and Evaluation, 5(4):278-283.

2. Adsit, N. R., 1983, "Compression Testing of Graphite/Epoxy," in Compression Testing of Homogeneous Materials and Composites, ASTM STP 808, Richard Chait and Ralph Papirno, ed., Philadelphia, PA: American Society for Testing and Materials, pp. 175-186.

3. 1991, "Standard Test Method for Compressive Properties of Unidirectional or Crossply Fiber Resin Composites," ASTM D 3410, 1991 Annual Book of Standards, Vol. 15.03, Philadelphia, PA: American Society for Testing and Materials.

4. Bogetti, T. A., J. W. Gillespie, and R. B. Pipes, 1988, "Evaluation of the IITRI Compression Test Method for Stiffness and Strength Determination," Composites Science and Technology, 32(1):57-76.

5. Berg, J. S., and D. F. Adams, Summer 1989, "An Evaluation of Composite Material Compression Test Methods," Journal of Composites Technology and Research, 11(2):41-46.

6. Adams, D. F., 1989, "A Comparison of Composite Material Compression Test Methods in Current Use," Proceedings of the 34th International SAMPE Symposium, Covina, CA: Society for the Advancement of Material and Process Engineering, pp. 1422-1433.

7. Adams, D. F., 1989, "Influence of Specimen Configuration and Test Fixture on Compressive Strength," Proceedings of the Third Annual Thick Composites in Compression Workshop, Covina, CA: Society for the Advancement of Material and Process Engineering.

8. 1989, "Wyoming End-Loaded, Side-Supported Compression Test Fixture (Model No. CU-EL)," Sales Brochure, Laramie, WY: Wyoming Test Fixtures

9. Odom, E. M., and D. F. Adams, July 1990, "Failure Modes of Unidirectional Carbon/Epoxy Composite Compression Specimens," Composites, 21(4):289-296.

10. Williams, R. S., and K. L. Reifsnider, October, 1974, "Investigation of Acoustic Emission During Fatigue Loading of Composite Specimens," Journal of Composite Materials, 8:340-355.

11. Reifsnider, K. L., E. G. Henneke II, and W. W. Stinchcomb, 1977, "Delamination in Quasi-Isotropic Graphite-Epoxy Laminates," in Composite Materials: Testing and Design (Fourth Conference), ASTM STP 617, Philadelphia, PA: American Society for Testing and Materials, pp. 93-105.

12. Hart-Smith, L. J., 1991, "Generation of Higher Composite Material Allowables Using Improved Test Coupons," Proceedings of the 36th International SAMPE Symposium, Covina, CA: Society for the Advancement of Material and Process Engineering, pp. 1029-1044.

The Dependence of Composite Lamina Compression Strength on Matrix Modulus

DOUGLAS P. GOETZ, GENE B. PORTELLI AND ANDREW M. HINE

ABSTRACT

The objective of this study is to experimentally investigate the relationship of composite compression strength to matrix modulus in the context of SACMA test method SRM-1. A single material system (IM7/SP500-2) was used; matrix modulus was varied by changing the test temperature. Unidirectional, cross-ply, and quasi-isotropic laminates were tested to check the effect of stacking sequence on the apparent compression strength.

OBJECTIVE AND MOTIVATION

The purpose of the present work is to revisit the problem of determining the relationship of the compression strength of carbon fiber-reinforced polymeric composites to the modulus of the matrix material. The thrust of the study is to find out how sensitive a typical industry testing method is to variations in modulus. The sensitivity impacts the utility of the method for materials development and screening.

The matrix stiffness is a primary variable controlling composite compression strength because fiber buckling depends on the lateral support offered by the matrix. For extensive reviews on this subject, see [1,2]. The references cited in these reviews contain several analytical models for fiber microbuckling, all of which depend in some way on matrix constitutive behavior. Experimental investigations have established fiber microbuckling as a primary failure mechanism, confirming the importance of matrix support for the fibers. In addition, fiber waviness, matrix non-linearity, and (in some cases) fiber/matrix interface strength have been identified as important parameters for commercial composite systems. The roles and interactions of these material variables are of interest in the development, processing, and selection of composites for particular applications.

Douglas Goetz, Andrew Hine, 3M, Building 201-1W-28, 3M Center, St. Paul, MN 55144
Gene Portelli, 3M, Building 201-BS-07 , 3M Center, St. Paul, MN 55144

Compression testing is known to be very sensitive to details of specimen design, fixturing, and load introduction, complicating the study of the variables controlling compression strength. Several recent articles have surveyed the numerous types of specimens and fixtures which have been reported in the literature [2-4]. These test methods give somewhat different results depending on the extent to which global buckling, eccentric loading, etc. are avoided as well as the details of the stress state in the test section associated with the method of load introduction into the test section. Clearly, if different methods give different results, then the apparent relationships between matrix properties and composite compressive strength will also be different for the various methods.

The present work is concerned with the practical problem of how one widely-used test method reflects the dependence of composite compression strength on matrix stiffness. The specimen and fixture used in this study is that of SACMA recommended test method SRM-1 [5] (a modification of ASTM D695-89). The specimen is tabbed with an unguided, short test section. It is end-loaded in a fixture which aligns the specimen with the load line and supports the tabs. See Figure 1. Advantages of the method are the modest size of the specimen (minimizing material requirements) and the small mass of the fixture and ease of specimen insertion into the fixture which facilitate elevated temperature testing. Although this method has been found to give strengths lower than some other methods [2], it is one of the most commonly employed in industry [3].

Currently there is interest by the composites community in using cross-ply laminates to determine the lamina compression strength [6]. Lamination theory is used to infer the stresses in the plies oriented in the loading direction. Some investigators have found higher strengths, lower variability, and less sensitivity to details of specimen preparation than for unidirectional laminates [7]. Because of the possibility that the sensitivity of the strength to matrix modulus might be masked by experimental artifacts in the unidirectional data, the effect of stacking
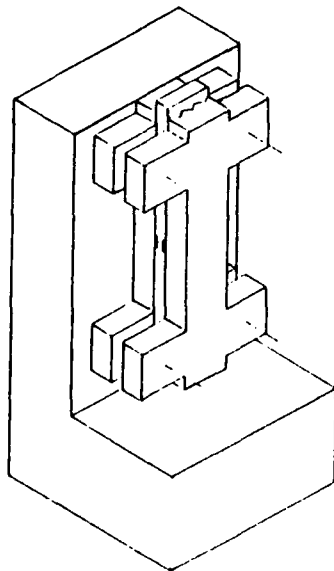
Figure 1. Test Specimen and Fixture for SRM-1

sequence was also examined, including a quasi-isotropic sequence.

As noted above, initial curvature of the fibers is a significant variable. As an extreme case, the behavior of material with fabric reinforcement was considered. Fabric-reinforced composites are widely used in structures, but most work to date on the effect of modulus has dealt with laminates fabricated from unidirectional prepreg.

The primary material variable, modulus, was varied by changing the test temperature. Other variables such as fiber/interface strength may change with temperature besides the matrix constitutive behavior. The motivation for this approach rather than testing various materials was to minimize the number of material variables such as fiber volume fraction. It allowed the use of one lot of material, minimizing processing variations.

EXPERIMENTS

Three main types of tests were done: 1) testing to determine the matrix modulus as a function of temperature in order to attempt correlations with the compression strength data, 2) tensile testing to determine lamina moduli as a function of temperature for use with lamination theory to reduce the compression test results, and 3) compression testing of unidirectional, cross-ply, and quasi-isotropic, and fabric-reinforced laminates. The test plan is shown in Table I.

The material used for this study was SP500-2 from 3M. It is a high performance carbon fiber prepreg system with an excellent combination of hot/wet performance (155 C) and toughness. The fiber used in the SP500-2 is IM7, a 276 GPa modulus fiber made by Hercules. The matrix resin, referred to as PR500-2, is a single-phase epoxy. As can be seen by the dynamic mechanical profile in Figure 2, the resin modulus varies widely below the T_g of 220 C.

Resin from the batch used to make the prepreg was used to make neat resin castings and to fabricate a fabric-reinforced panel by the Resin Transfer Molding (RTM) process. The fabric was an IM7 plain weave. The fiber volume fraction of both the prepreg and RTM panels was 0.55.

TABLE I - TEST PLAN

TEST	LAY-UP	PROPERTIES
Tension	Neat Resin	E_m, ν_m
"	$[0]_{16}$	E_{11}, ν_{12}
"	$[90]_{16}$	E_2
"	$[+45/-45]_{2s}$	G_{12}
Compression	$[0]_8$	σ_c
"	$[0/90]_{4s}$	"
"	$[0_2/90_2]_{2s}$	"
"	$[90_2/0_2]_{2s}$	"
"	$[+45/0/-45/90]_{2s}$	"
"	$[\{0/90\}_{12}]$ (fabric)	"

Note: All tests were performed at 23, 46, 82, 121, and 177 C.

Figure 2. Dynamic Mechanical Spectrum for PR500-2
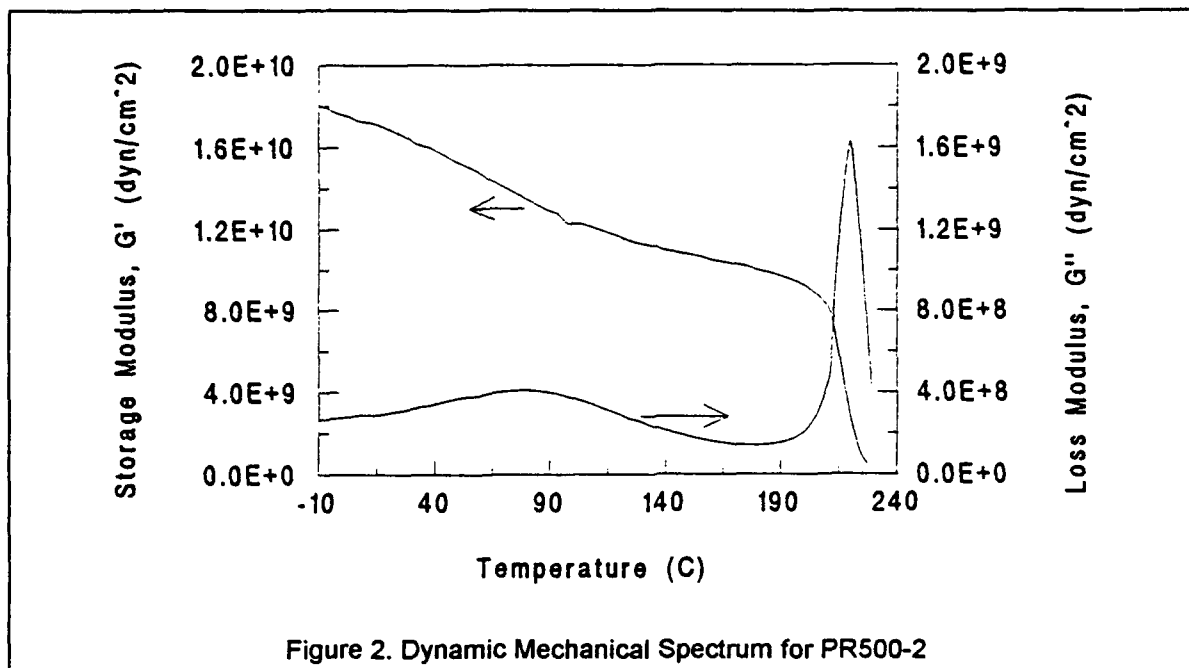
Specimen dimensions, preparation, and conditioning are reported in [8]. Additional details of the test procedures can also be found there. Two details are included here for later reference. First, the displacement rate for both tensile and compression testing was 1.27 mm/min. Therefore, strain rates in the test sections of tensile and compression specimens were not matched, since they have different gage lengths. Second, tabs for the cross-ply and quasi-isotropic compression specimens tested at 23, 46, and 82 C were glass fabric reinforced epoxy; the remainder of the compression specimens were tabbed with material cut from each respective panel. All tabs were untapered.

RESULTS AND DISCUSSION

Typical tensile stress-strain curves for PR500-2 are shown in Figure 3. As expected, the curves become increasingly non-linear as the temperature increases. When seeking to relate the matrix stiffness to composite compression strength, the non-linearity has been found to be an important feature. The non-linearity has been shown computationally to interact with any fiber waviness to influence the local strains in the matrix and the failure loads even for nominally linear global stress-strain behavior [1]. Local matrix strains can be significantly higher than global strains, suggesting that correlation of compression strength with initial (small-strain) modulus alone may not be possible. Considering the data in Figure 3, the curves can be seen to be of the same character, with the exception of the 177 C curve, which is more non-linear at small strains. The initial modulus values were obtained by linear regression of the data up to 0.5% strain. Values of Poisson's ratio came from the same range of axial strain. Table II lists the shear modulus values calculated using

Figure 3. PR500-2 Neat Resin Tensile Stress-Strain Curves
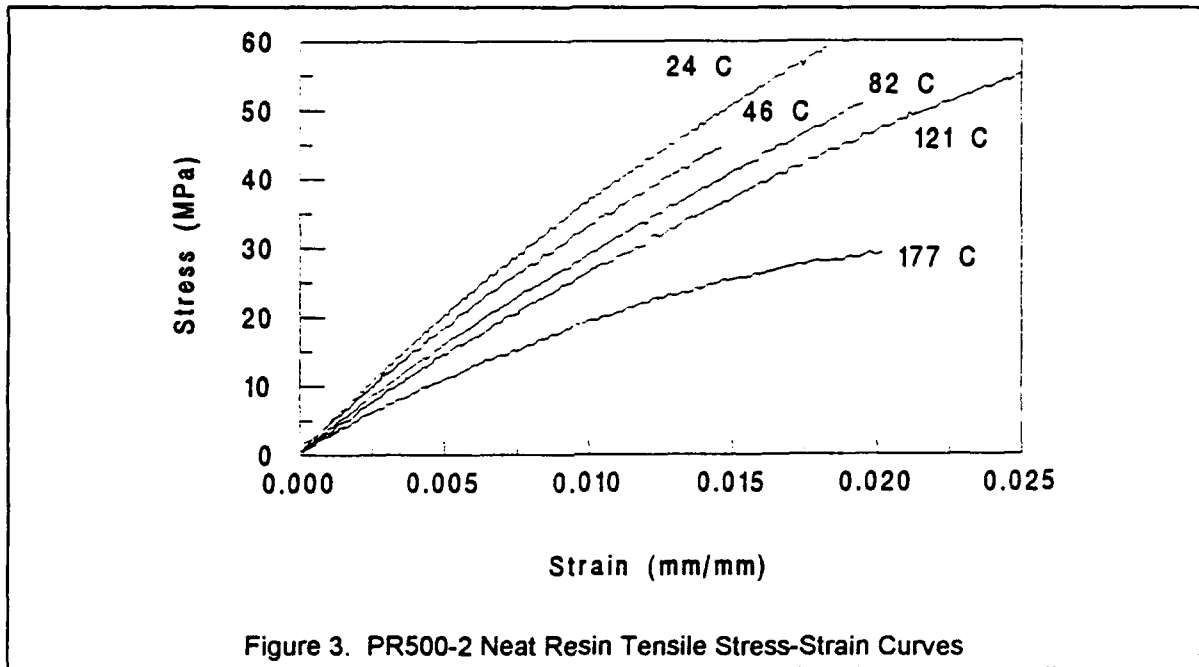
$$G = E/[2(1+\nu)] \tag{1}$$

Data in Figure 3 and Table II are all from one loading rate. Rate effects were not considered in this study. (Also, it should be noted that the failure stresses and strains do not form a consistent trend because imperfections in the specimens caused premature failure. This does not bear on this study.)

The lamina modulus values and equations used to calculate multiplying factors for the laminate compression strengths to determine the 0 degree ply stresses at failure are listed in [8]. These multiplying factors have been shown to be relatively insensitive to variations in laminate moduli used [7].

The appropriateness of the lamina moduli was checked by measuring the compression modulus of one cross-ply laminate and the quasi-isotropic laminate at the various test temperatures by means of strain-gaged, untabbed specimens. The laminate moduli calculated from laminate theory were in fair agreement with experiment, but tended to be 3 to 6% high. This illustrates how the use of tensile

TABLE II - MODULUS AND COMPRESSION STRENGTH

Temp. (C) >>	24	46	82	121	177
G_m (GPa)	1.445	1.272	1.127	1.041	0.773
Multiplier					
F (cross-ply)	1.892	1.896	1.902	1.907	1.915
F (quasi)	2.652	2.676	2.705	2.707	2.768
σ_c (MPa)					
$[0]_8$	1519.0 (9.6)	1428.6 (7.3)	1234.9 (7.6)	1142.5 (7.6)	688.1 (1.6)
$[0/90]_{4s}$	1670.9 (7.9)	1611.9 (7.0)	1575.2 (6.0)	1390.8 (7.2)	845.0 (4.0)
$[0_2/90_2]_{2s}$	1463.5 (4.8)	1430.2 (5.0)	1424.4 (8.0)	1380.3 (1.5)	677.3 (8.9)
$[90_2/0_2]_{2s}$	1659.1 (5.7)	1618.4 (7.1)	1463.7 (5.1)	1653.8 (6.0)	694.5 (9.2)
$[+45/0/-45/90]_{2s}$	1837.9 (6.5)	1736.2 (8.4)	1624.6 (5.6)	1538.1 (5.4)	935.1 (6.9)
$[\{0/90\}_{12}]$	653.6 (12.3)	655.7 (8.0)	639.9 (7.3)	613.0 (4.8)	522.0 (6.7)

rather than compressive moduli is less desirable. Factors used for calculating the 0 degree ply strengths are listed in Table II.

Reduced data from the compression testing are given in Table II. (The compression strengths for the RTM panel cannot be used to determine the 0 degree ply strength because of the fabric reinforcement.) It was noted earlier that there is interest in using cross-ply laminates to determine the lamina compression strength in order to achieve lower variability of results relative to data from unidirectional specimens. The standard deviations reported in Table II do not show consistently lower variability than for the other laminates.

The compression strengths for the prepreg specimens are plotted against matrix shear modulus in Figure 4. First consider the unidirectional data. The unidirectional strengths are the lowest, in agreement with the results of other investigators [e.g., 7].

The quasi-isotropic laminates gave consistently high strengths (20-35% higher than the unidirectional laminates). Sohi et al. used the IITRI compression test method for unidirectional and quasi-isotropic laminates of a variety of systems, observing higher failure strains for the latter lay-up in all cases [9]. They observed that the off-axis plies not only gave better support to 0 degree plies, but also suppressed fiber kinking both in-plane and out-of-plane even after initiation. The trend for the present data is similar to that of the unidirectional data, but of slightly shallower slope.

The cross-ply strengths are generally between the unidirectional and quasi-isotropic data. Of the cross-ply laminates, the $[0_2/90_2]_{2s}$ laminate gave a consistently lower strength than the others. This laminate gives less support to the outer plies against buckling. The effect of unsupported outer plies has also been seen in notched multidirectional laminates [10]. However, Hansen and coworkers measured higher strength for a $[0_2/90_2]_s$ laminate than a $[90_2/0_2]_s$ laminate [7]. It is interesting to note here that the $[(0/90)_4]_s$ laminate displayed

Figure 4. Compression Strength vs. Matrix Shear Modulus
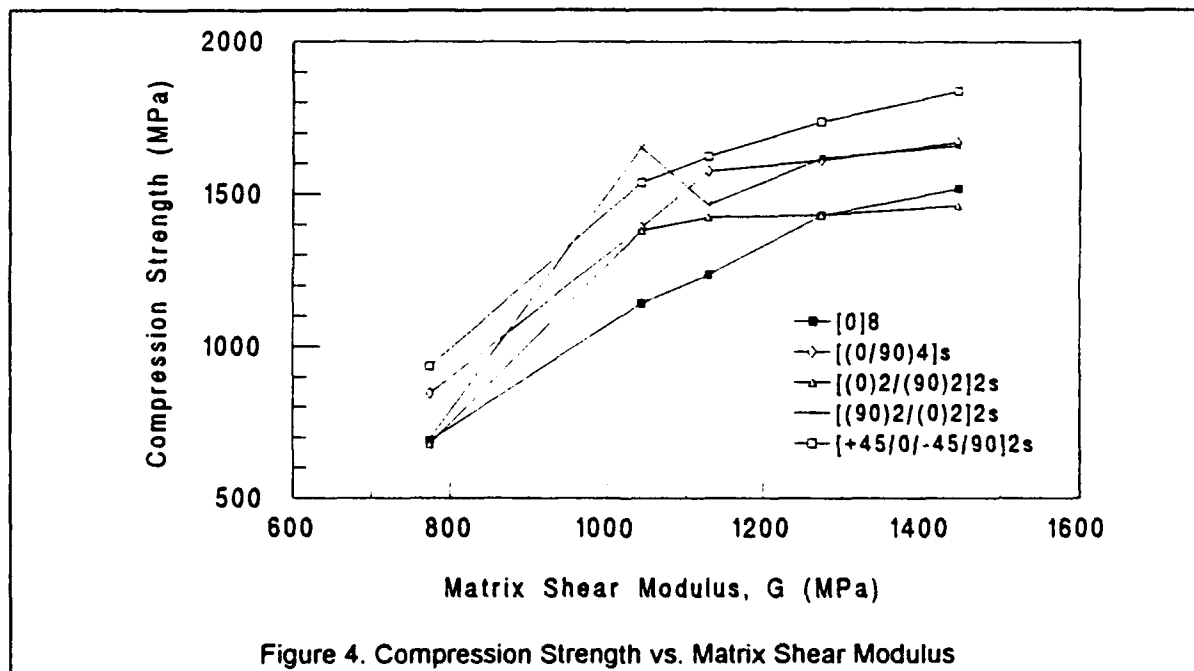
higher strengths than the $_{[0_2/90_2]_s}$ laminate, suggesting that a single outer 0 degree ply may behave differently than two together or that 0 degree ply pairs in the interior more easily fail for the latter lay-up. Observation of the failure initiation would be necessary to identify the controlling mechanism. It has been suggested that grouped 0 degree plies lead to lower strength because the amount of load redistribution and reduction in load-carrying capacity are greater upon initiation of fiber microbuckling [10].

Note that on the basis of this data no effect of changing tabbing material for the cross-ply and quasi-isotropic laminates (as described earlier) can be discerned, since the trends are generally continued for the 121 C (1.041 GPa) data.

One of the main concerns of this study is the sensitivity of compression strength to variations in matrix modulus. This is shown graphically in Figure 5. The compression data of Table II have been normalized by the 24 C data. The RTM compression data are also included. The sensitivity of the unidirectional data to decreased resin modulus is greatest, being nearly one-to-one. The quasi-isotropic data is somewhat less sensitive, and the cross-ply data are much less sensitive except at the lowest modulus. The RTM (fabric) data follow a similar trend to the cross-ply data with the exception of the data point at the lowest modulus, which is remarkably higher than all the other data at that modulus.

The trends seem to exhibit a break at the lowest modulus. In a similar study by Wilson [6] no such break was seen. It seems likely that the non-linear matrix behavior at low strains for 177 C (Figure 3) is a prime cause of the behavior for this study. At the elevated temperature, strain-rate effects may be important. However, the nominal strain rate in the compression specimen with its short gage length was higher than the strain rate for the long neat resin tensile specimens, since they were loaded at the same displacement rate. Local strain rates in the multidirectional compression specimens would be higher than the nominal rate in

Figure 5. Compression Strength vs. Matrix Shear Modulus Normalized by 24 C Values
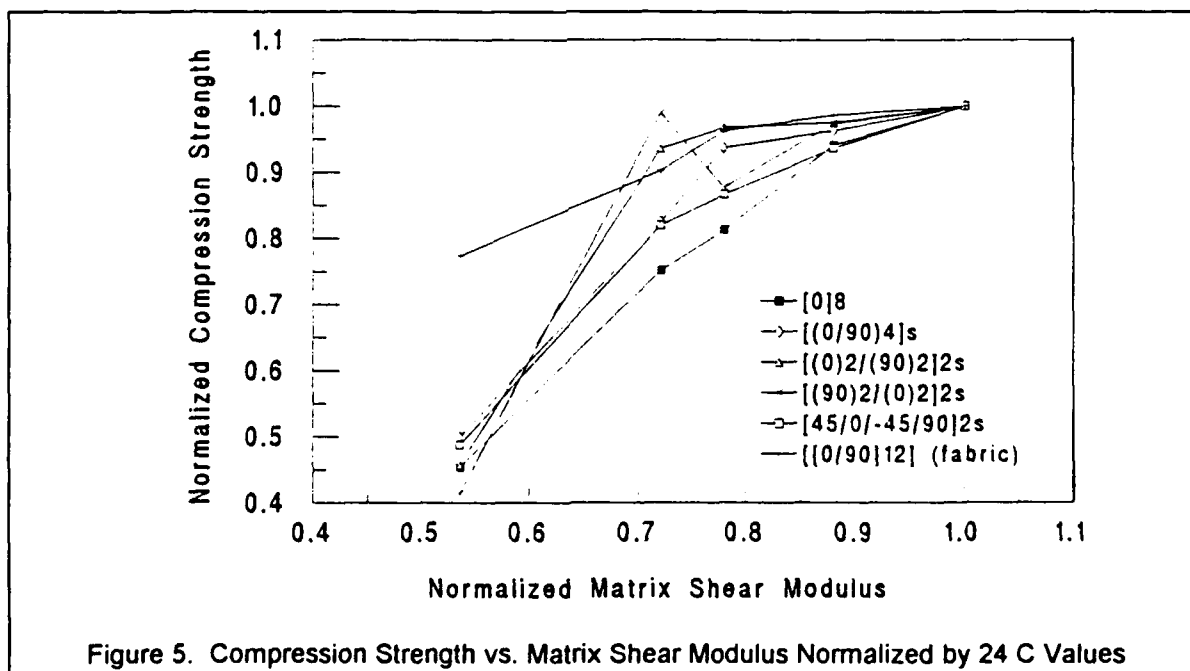
areas where the strains exceed the nominal strain. Therefore the actual matrix stiffness would be expected to be higher, not lower, than the neat resin tensile tests indicate, so that the data cannot be easily rationalized in terms of strain rate effects giving a lower matrix stiffness than neat resin tensile tests would indicate. Aside from matrix non-linearity, there is the possibility that the fiber/matrix interface strength was reduced at that temperature so that an intervening micro-mechanism operated. It is significant that the unidirectional and fabric laminates did not exhibit breaks as dramatic as the other laminates. In light of this, it is likely that explanation of the breaks must involve more than matrix behavior.

The patterns of sensitivity described above should be kept in mind when comparing materials with different moduli (or strengths at different temperatures, as here). Cross-ply tests and fabric tests will not be nearly so discriminating as unidirectional tests.

SUMMARY AND CONCLUSIONS

The dependence of composite compression strength on to matrix shear modulus was examined experimentally for several stacking sequences in the context of the specimen and fixture of SACMA SRM-1. The modulus was varied by testing a single material system, SP500-2, with unidirectional and fabric reinforcement at several temperatures. The 0 degree ply strengths were inferred from classical lamination theory. The major findings of the study were:

1) The sensitivity of strength to modulus varied widely depending on the stacking sequence. The unidirectional compression strengths were most sensitive to variations in matrix shear modulus, the cross-ply and fabric-reinforced laminate strengths were the least sensitive, and the quasi-isotropic laminate strengths had an intermediate sensitivity. These trends bear on the utility of this test methodology for studying modulus effects, as well as its use for ranking materials with respect to compression strength.

2) In general, the unidirectional strengths were lowest, while the inferred 0 degree ply strengths in the quasi-isotropic laminates were the highest. Of the cross-ply data, the $[0_2/90_2]_{2s}$ strengths tended to be lower than the $[0/90]_{4s}$ and $[90_2/0_2]_{2s}$ values.

3) A distinct break in some of the plots of strength vs. matrix modulus was seen for the temperature within 50 C of the matrix glass transition temperature. The break is pronounced for the cross-ply and quasi-isotropic laminates and small for the unidirectional and fabric-reinforced laminates. Thus, explanation on the basis of matrix behavior alone is unlikely.

This study highlights the wide variations in results possible using different implementations of one compression test method. It is hoped that these findings will motivate more detailed examination of the mechanisms and variables controlling compression failure in this context.

REFERENCES

1. Guynn, E. G., O. O. Ochoa, and W. L. Bradley. "A Parametric Study of Variables That Affect Fiber Microbuckling Initiation in Composite Laminates, Part I: Analyses." submitted to Journal of Composite Materials.

2. Camponeschi, Jr., E. T.. 1991. "Compression of Composite Materials: A Review," in Composite Materials: Fatigue and Fracture (Third Volume), ASTM STP 1110, T. K. O'Brien, ed. American Society for Testing and Materials, pp. 550-578.

3. Schoeppner, G. A., and R. L. Sierakowski. 1990. "A Review of Compression Test Methods for Organic Matrix Composites." Journal of Composites Technology and Research, 12(1):3-12.

4. Adams, D. F., and E. M. Odom. 1991. "Influence of Test Fixture Configuration of the Measured Compressive Strength of a Composite Material." Journal of Composites Technology and Research, 13(1):36-40.

5. "SACMA Recommended Test Method for Compressive Properties of Oriented Fiber-Resin Composites SRM-1." 1988. Suppliers of Advanced Composite Materials Association.

6. Wilson, D. W., V. Altstadt, and J. Prandy. 1992. "On the Use of Laminate Test Methods to Characterize Lamina Compression Strength," presented at the 37th International SAMPE Symposium, Anaheim, CA.

7. Hansen, G. E., B. J. Rutkoski, and S. T. Wareham. 1991. "Compression Testing of 0/90 Laminates." minutes of ASTM subcommittee D30.04 meeting, Indianapolis, IN.

8. Portelli, G. B., D. P. Goetz, J. A. Graske, and A. M. Hine. 1992. "The Effect of Matrix Modulus on Lamina Compression Strength," presented at the 37th International SAMPE Symposium, Anaheim, CA.

9. Sohi, M. M., H. T. Hahn, and J. G. Williams. 1987. "The Effect of Resin Toughness and Modulus on Compressive Failure Modes of Quasi-Isotropic Graphite/Epoxy Laminates." in Toughened Composites, ASTM STP 937, N. J. Johnston, ed. American Society for Testing and Materials, pp. 37-60.

10. Guynn, E. G., W. L. Bradley, and O. O. Ochoa. "A Parametric Study of Variables That Affect Fiber Microbuckling Initiation in Composite Laminates, Part II: Experiments." submitted to Journal of Composite Materials.

Biaxial Compression Testing of G-10 Woven Fabric Composite Laminates

JERRY ZHIQI WANG AND DARRELL F. SOCIE

ABSTRACT

Glass fiber-reinforced ASTM G-10 grade woven composite laminates were tested under quasi-static uniaxial and biaxial compression loadings to failure. Small (12.5mm) IITRI and larger (125mm) square specimens in uniaxial compression failed in an out-of-plane kink band mode in both the warp and fill directions of the laminate. Compressive failure stress, strain and failure mode were independent of the specimen type. Test results show that an out-of-plane kink band was also the failure mode for square specimens in biaxial compression and the formation of out-of-plane kink bands was not affected by the in-plane transverse stress and strain. The biaxial compression failure envelope for G-10 woven fabric composite laminates can be adequately described by a maximum stress or a maximum strain criteria based on the data of small IITRI specimens because the failure mode is not affected on specimen size or transverse loading.

INTRODUCTION

Woven fabrics are considered an important form of reinforcements for composite laminates. Studies on woven fabric composites are limited compared to unidirectional-ply tape laminates which have been extensively investigated through both theoretical and experimental approaches [1-3]. Woven fabric composites have fiber reinforcements in two or more directions within a single ply. They have several distinct advantages over unidirectional-ply tape laminates which include high impact resistance, better in-plane and interlaminar shear strengths, dimensional stability, and economical fabrication.

In spite of these attractive properties of woven fabric composites, the mechanical and failure behavior of these composites are not well understood. Ishikawa et al. [4-5]

Jerry Zhiqi Wang: Research Assistant. Department of Mechanical Engineering, UIUC, IL 61801, U.S.A.

Darrell F. Socie: Professor, Department of Mechanical Engineering, UIUC, IL 61801, U.S.A.

developed different models to describe the elastic and non-linear elastic behavior of woven fabric composites under a in-plane uniaxial load along the warp and fill directions. According to the authors, the predictions of basic tensile elastic stress-strain response of woven fabric composites based on analytical models proposed coincided very well with experimental stress-strain response. Moghe [6] set up a mathematical model based on the fabric deformation to predict elastic response of woven fabric composites under a biaxial tensile load, and the analytical results were found to agree with the experimental data obtained from biaxial tensile tests of tubular specimens.

Woven fabric composite laminates are mostly used in structures and the loading conditions of these structures require a comprehensive understanding of the behavior of woven fabric composite laminates under an in-plane biaxial stress state. However, experimental studies on the mechanical behavior of woven fabric composite laminates under an in-plane biaxial compressive stress state are not available in the literature, impeding the study of failure mechanisms and evaluation of available failure theories for woven fabric composites.

In the present work, test results of ASTM G-10 grade glass fiber-reinforced woven composite laminates under an in-plane biaxial compressive stress state are presented and the failure mechanism of these laminates is discussed.

EXPERIMENTS

Test specimens were made from ASTM G-10 grade woven composite laminates which are epoxy resin reinforced with E-glass plain woven fabrics. The E-glass plain woven fabric consists of warp and fill yarns crossing alternately above and below the adjacent yarns along the entire length and width. The fiber volume fractions in the two perpendicular directions are slightly different such that the nominal fiber volume in the fill direction is about 75% of that in the warp direction. The laminates are stacked by plies with the warp fibers in the same direction. Crimp angles of both warp and fill yarns are smaller than 10°.

Two types of specimens were prepared from G-10 woven fabric composite laminates. Standard IITRI specimens were made in accordance with ASTM standard test method D3410-87 [7] with a gage section of 12.5mm and thickness of 3.0mm. Specimens were prepared with either warp or fill fibers running parallel to the loading axis, (for convenience, denoted as W or F laminates). Tensile and compressive tests of the IITRI specimens were conducted in a closed-loop, servo-hydraulic MTS test system.

Square specimens with a gage section of 125mm by 125mm and a thickness of 3.0mm with flexible end reinforcements to prevent the edge failure were employed for the biaxial tests. Flexible end reinforcements were achieved by slotted aluminum plates which were

attached to the edge of specimen with a flexible epoxy adhesive. The experiments showed that edge failure was successfully prevented by the flexible end reinforcements and almost all the square specimens were broken at the gage section. The biaxial compressive tests of square specimens were conducted in an INSTRON multiaxial test machine that has four linear actuators located on the center of each side of the square frame of the test machine. Alignment of the loading axes is a critical issue for successful multiaxial material testing with compression loadings. A specially designed fixture was used which had 4 guide bars in the two perpendicular directions to guarantee the loading alignment In order to determine the material strength, lateral supports were employed to reduce structural buckling of square specimens before they reached the material failure strength. A relatively homogeneous stress distribution in the gage section of square specimens can be achieved under uniaxial and biaxial compressive stress states with this fixture. Testing details are given in reference [8].

All tests were conducted in displacement control with a microcomputer to control the test machine and obtain the test data. Results from uniaxial tests are given in Table 1. Test results show that the tensile and compressive failure stress and strain in both warp and fill directions are almost the same and the failure stress and strain in fill direction is about 95% of these in the warp direction. Results for square specimens are presented in terms of failure stress in Fig.1a and in terms of failure strain in Fig.1b. Failure strains were determined from the average of 4 or 8 strain gages located on the specimens. Failure envelopes in terms of stress or strain are rectangular which indicates the failure stress and strain in one direction are almost independent of the stress and strain in the perpendicular direction. Comparisons of test results for IITRI and square specimens are also given in Fig.1a and Fig.1b. The failure stress and strain for square specimens under uniaxial compression are almost the same as those for IITRI specimens in the same direction. From discussion below, this is expected since the same failure modes for IITRI and square specimens were observed in uniaxial compression in both warp and fill directions.

FAILURE MECHANISM AND DISCUSSION

Failure modes are very important in the study of composite materials, as failure modes control the behavior and determine the strength of composite materials. Failure of composite materials are determined not only by their internal properties such as properties of constituents (fiber, matrix and interface) and microstructural parameters but also by external conditions such as geometric variables, type of loading and boundary conditions, [9]. Whether experimental data from small specimens can be used for larger structural

design depends whether the large structures have the same failure mode as the small specimens.

In order to identify predominant failure modes of G-10 woven fabric composite laminates, failure surfaces of both specimen types were studied with a scanning electron microscope. Fracture surfaces of IITRI specimens under a tensile load in both warp and fill directions show a typical tensile fracture characteristic. The fracture surface is rather smooth and is perpendicular to the loading direction. SEM observation shows that the fibers fracture in a brittle manner without any indication of yield or flow and the fracture surface of the fibers is perpendicular to the fiber axis. Fracture surfaces for both IITRI and square specimens under uniaxial compression in the warp and fill directions show a compressive failure characteristic. The failure surface is oriented about 45° through the thickness. Out-of-plane kink bands are formed on the fracture surface for both specimen types and fibers are fractured at the kink boundary, Fig.2. Bending fracture of the fibers can be observed on the fracture surface with both tensile and compressive fractures in a single fiber, Fig.3. Bending induces tensile and compressive stresses across the fiber and the brittle glass fibers are fractured in the tensile region of each fiber in a brittle manner followed by shear failure in the compressive region. For the square specimens under biaxial compression, the fracture surface is also oriented about 45° through the thickness and out-of-plane kink bands are also found on the fracture surface in both warp and fill directions. All of these observations indicate that the failure mode of square specimens under biaxial compression is the same as that of square specimens under uniaxial compression.

Kink banding as a compressive failure mode has been investigated [10-11]. Although different models have been used to describe the kink behavior, a common feature of the models is that formation of kink band is associated with shear stress, strain or energy. The test results of G-10 woven fabric composite laminates under biaxial compression show that the out-of-plane kink band failure is not affected by the transverse in-plane stress.

In order to modify the failure surfaces for anisotropic materials, various anisotropic strength theories have been developed in the literature [12]. Anisotropic strength theories can be classified into two categories [13]. In the first category, the anisotropic strength theories are failure mode dependent, which means failure will occur if any one or all of longitudinal, transverse, and shear stresses or strains exceed the limits determined by tests. Typical failure mode dependent strength theories are maximum stress and maximum strain criteria. In the second category of anisotropic strength theories, gradual transition from one failure mode to another is assumed. Failure envelopes predicted by these theories have smooth failure surfaces. Almost all the second category of anisotropic strength theories are

different expressions of a quadratic form $F_i\sigma_i + (F_{ij}\sigma_i\sigma_j)^\alpha = 1$, with or without non linear terms. In plane stress problems, this category of criteria becomes:

$$F_1\sigma_1 + F_2\sigma_2 + F_6\sigma_6 + \left(F_{11}\sigma_1^2 + F_{22}\sigma_2^2 + 2F_{12}\sigma_1\sigma_2 + F_{66}\sigma_2^2\right)^\alpha = 1$$

The term $F_{12}\sigma_1\sigma_2$ represents the interaction among the stress components. In most secondary category of anisotropic strength theories, such as Hoffman theory, Fischer theory, Hill theory, Norris Theory and Tsai-Hill theory [12], F_{12} is considered to be negative. If σ_6 equals zero as in our case, these criteria predict that the composite laminates are stronger under the same sign biaxial loadings and are weaker under different sign biaxial loadings. The theoretical justification of these criteria is that the in-plane shear stress caused by tension compression in-plane biaxial loadings is larger than that caused by biaxial tension or biaxial compression loading. For the G-10 woven fabric composite laminates in a biaxial compression loading, the external loads were carried by the fibers parallel to the loading direction. Although each fiber was in an in-plane biaxial compression stress state, the two in-plane compression stresses are unequal on the scale of a single fiber. Longitudinal compression stress and strain cause the fibers to fail in a shear or bending mode. Transverse compression stress on a fiber or fiber bundle is smaller than the applied stress because the transverse strain is accommodated by the low modulus matrix. Consider the unit cell illustrated in figure 4. The longitudinal strain ε_y, is transferred directly to the fiber resulting in a fiber stress, $\sigma_{fy} = \varepsilon_y E_f$. Transverse stresses in the matrix σ_{mx}, and fiber σ_{fx} can be approximated as $\sigma_{fx} = \varepsilon_x (V_m/E_m + V_f/E_f)$. Computed transverse stresses are no more than 15% of the longitudinal stresses. Finally the fiber fails in out-of-plane bending because of weak support in the out-of-plane direction. Increased material strength under biaxial compression loadings which is predicted by most of failure mode independent anisotropic strength theories is not found in the test results of G-10 woven fabric composite laminates.

Since the out-of-plane kinking is the failure mode under both uniaxial and biaxial compression loadings and out-of-plane kink formation is not affected by the in-plane transverse stress, the failure stress and strain are almost the same for different loading conditions. The failure envelope of G-10 square specimens under biaxial compression loadings can be reasonable predicted by failure mode dependent anisotropic strength criteria (maximum stress and maximum strain criteria) based on the data of small IITRI specimens, Fig.1a and Fig.1b. It seems that maximum strain criterion gives a little better estimations than maximum stress criteria, which may indicate that the formation of out-of-plane kink

bands associated with fiber bending is controlled by the in-plane longitudinal strain instead of stress.

A note of caution is needed here. This data indicates that small specimens may be used to estimate the strength of larger specimens or structures. This is only possible when the failure mode remains the same. Recent work by the authors [9] has shown a change in failure mode and reduction in strength in a cross ply laminate with a similar set of experiments report here.

CONCLUSIONS

Based on the test results of G-10 woven fabric composite laminates under biaxial compression loadings and discussion above, the following conclusions may be reached:

1. The failure mode is very important in study of composite failure behavior. Although the gage sections of small IITRI and large square specimens are different, similar failure modes result in similar failure stress and strain under uniaxial compression in both warp and fill directions.

2. The formation of out-of-plane kink bands under a biaxial compression loading is not affected by the in-plane transverse stress and is controlled by the in-plane longitudinal stress or strain.

3. The failure envelope under biaxial compression can be adequately estimated from the test data of small IITRI specimens because the failure mode is specimen independent.

REFERENCES

1. Guess, T. R., " Biaxial Testing of Composite Cylinders: Experimental-Theoretical Comparison, " Composites, 1980, pp. 139-148

2. Swanson, S. R. and Christoforou, A. P., " Progressive Failure in Carbon/Epoxy Laminates under Biaxial Stress, " Transactions of ASME, Vol. 109, 1987, pp. 12-16

3. Odom, E. M. and Adams, D. F., " Failure Modes of Unidirectional Carbon/Epoxy Composite Compression Specimens, " Composites, Vol. 21, 1990, pp. 289-296

4. Ishikawa, T. and Chou, T. W., " Elastic Behavior of Woven Hybrid Composites, " Journal of Composite Materials, Vol. 16, 1982, pp. 2-19

5. Ishikawa, T. and Chou, T. W., " Nonlinear Behavior of Woven Fabric Composites, " Journal of Composite Materials, Vol. 17, 1983, pp. 399-413

6. Moghe, S. R., " Elastic Response of Fabric Reinforced Composites to Biaxial Load Conditions, " Advances in Composite Materials and Structures, Proceedings of the Winter Annual Meeting of ASME, 1986, pp. 147-152

7. Standard Test Method for Compressive Properties of Unidirectional or Crossply Fiber-Resin Composites," ASTM Designation: D3410-87, 1987

8. Doong, S. H., Faoro, J. E. and Socie, D. F., " Development of a Test System and Experimental Method for In-Plane Biaxial Compressive Deformation and Failure of Fiber Composite Materials, " ASTM STP1120, American Society for Testing and Materials, pp. 87-102, 1992

9. Wang, Z. J. and Socie, D. F., " Failure Strength and Damage Mechanisms of E-Glass/Epoxy Laminates under In-Plane Biaxial Compressive Deformation, " Accepted by Journal of Composite Materials, 1993

10. Argon, A. S., " Fracture of Composites, " Treatise on Materials Science and Technology, Vol. 1, Academic Press, New York, 1972, pp. 79-114

11. Chaplin, C. R., " Compressive Fracture in Unidirectional Glass-Reinforced Plastics, " Journal of Materials Science, Vol. 12, 1977, pp. 347-352

12. Rowlands, R. E., " Strength (Failure) Theories and Their Experimental Correlation, " Handbook of Composites, Vol. 3, Edited by Sih, G. C. and Skudra, A. M., 1985, pp. 71-125

13. Sandhu, R. S., " A Survey of Failure Theories of Isotropic and Anisotropic Materials, " Technical Report, AFFDL-TR-72-71, 1972

Table 1 Results from IITRI Specimen Tests

	WARP	FILL
Elastic Modulus (10^4MPa)	2.28	2.17
Poisson's Ratio	0.175	0.168
Tensile Strength (MPa)	331	322
Tensile Failure Strain	0.017	0.016
Compressive Strength (MPa)	-332	-312
Compressive Failure Strain	-0.016	-0.015
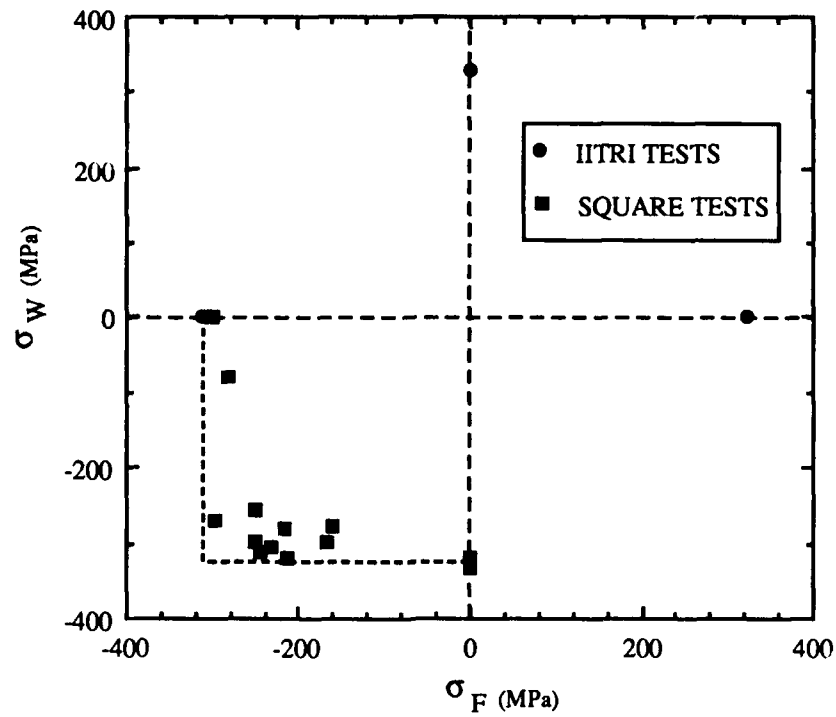
Fig.1a Failure Stress of G-10 Laminates
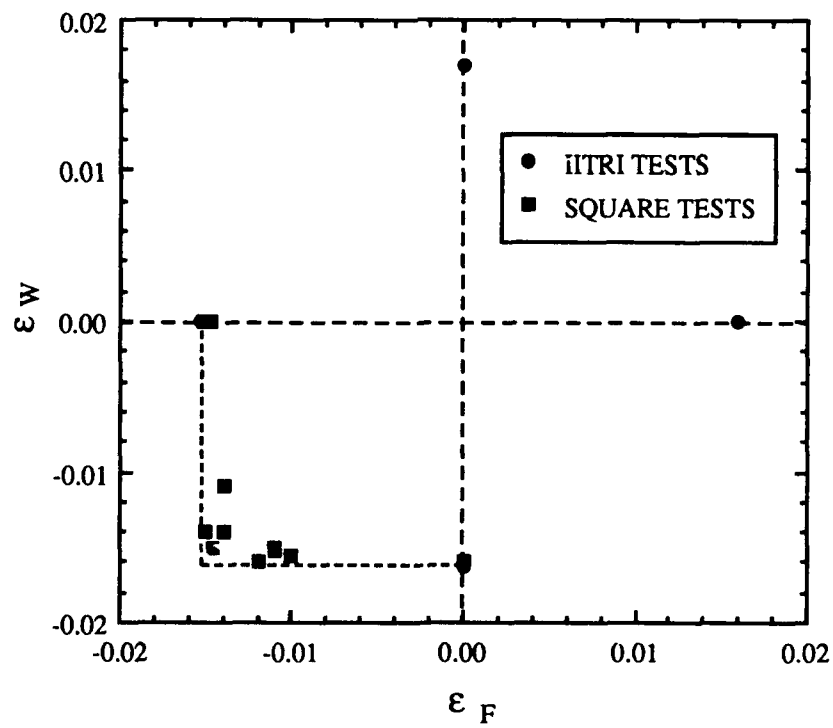
Fig.1b Failure Strain of G-10 Laminates

Fig.2 SEM Fractograph Showing a Out-of-Plane
Kink Band on the Fracture Surface of G-10
Woven Fabric Composite Laminates under
Uniaxial or Biaxial Compression
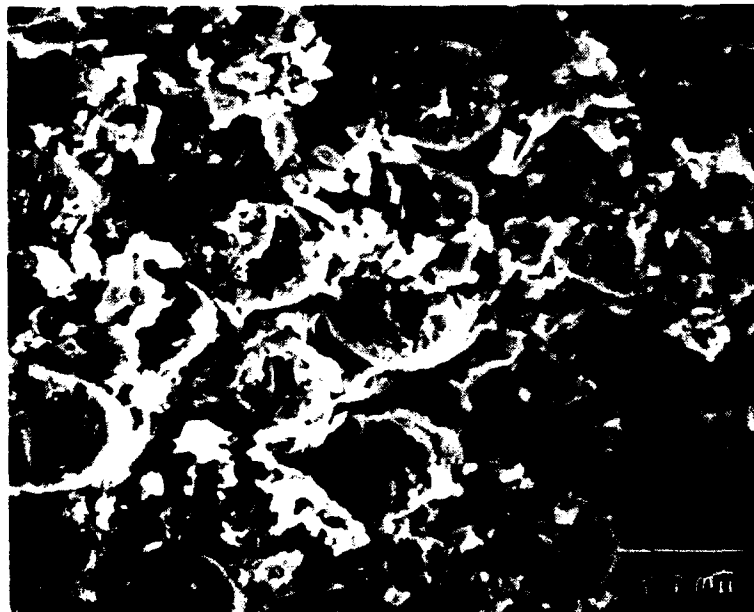
Fig.3 SEM Fractograph Showing Tensile and
Compressive Fractures in a Single Fiber of
G-10 Woven Fabric Composite Laminates
under Uniaxial or Biaxial Compression
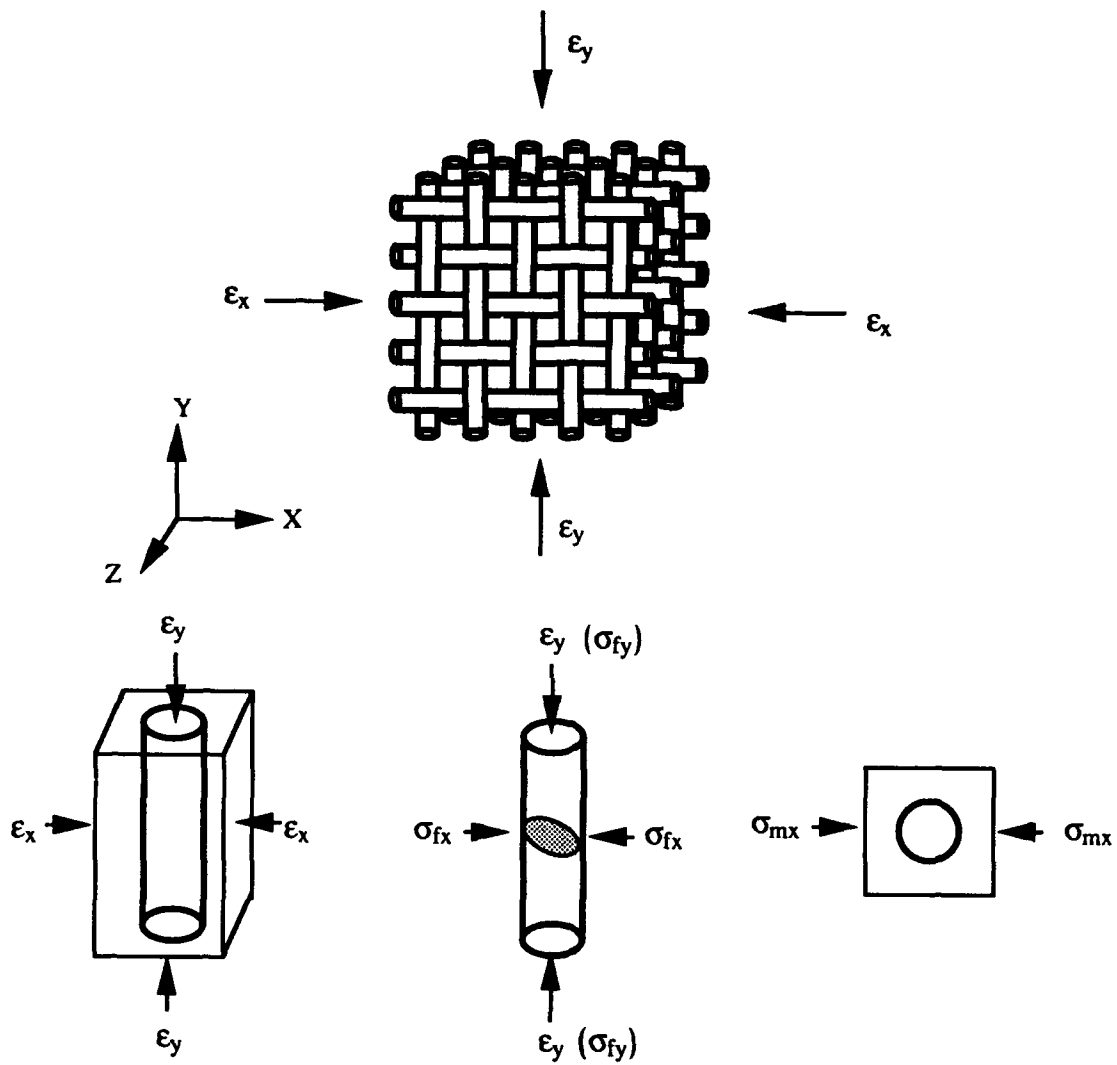
Fig.4 A Schematic Indicating the Failure of Fibers in a Biaxial CompressiveStress State

Damping Properties of Plastic for Composites

K. NISHIYAMA, Y. SHIRAI, N. EGUCHI AND S. UMEKAWA

Abstract

Damping capacities of various kinds of plastics for composites were determined by a torsional vibration methods. The damping capacity and modulus were measured as a function of strain amplitude and temperature. The results were compared with those of metals and ceramics. The damping and Young's modulus of two kinds of PET- and PBT-based composites containing glass fibers were also examined. The relation between elastic and nonelastic behavior of such composites is discussed.

Introduction

In general, plastic materials exhibit a viscoelastic behavior compared with other materials such as metals and ceramics at ambient temperature. A few results had been presented on damping capacity of plastic, even the previous study dealt with the physical view point[1].
Plastic materials are widely used for transportation vehicles and other advanced apparatus to utilize their characteristics such as low density, productivity, and high cost performance. Unlike metallic or ceramic materials, plastics have a possibility to posses both high rigidity and damping capacity simultaneously. Damping capacity is strongly required with the concept of noise suppression and vibration control.

The present study was conducted not physical interest but actual engineering applications. Then the measuring of damping indexes of plastics as a data base for machine designing is primarily focused. Damping capacities for up to sixteen kinds of plastic materials that would be used for FRP have been studied using a bulky specimen were measured and compared with other engineering materials.

Katsuhiro Nishiyama, Noboru Eguchi and Sokichi Umekawa, Science University of Tokyo, 2641 Yamazaki, Noda, 278, Japan.
Yasunori Shirai, Mitsubishi Rayon Co. Ltd., 4-1-2 Ushikawatori, Toyahashi, 440, Japan

Experimental procedure

Materials

Fourteen kinds of materials such as acrylonitrile/butadiene/ styrene(ABS), polyethylene terephthalate(PBT), polyamide(PA), 6-Nylon(6N), 6,6-Nylon(66N), polypropylene(PP), polyethylene(PE), polycarbonate(PC), polyvinyl chloride(PVC), polytetrafluoroethylene (PTFE), polymethyl methacrylate(PMMA), High density polyethylene (HDPE), and phenolic resin(FE), polyethylene terephthalate(PET) were studied as listed in Table 1. Among various plastics, PET and PBT were selected, then six kinds of PET- and PBT-based composites containing glass were prepared as shown in Table 2.

Damping Measurements

Two types of the damping measuring apparatus based on the torsional and the lateral vibration were used, as shown in Fig. 1 and Fig. 2. The specific damping capacity and shear modulus were measured by using the torsional vibration technique previously described by Hatfield et al.[2]. The dimension of the torsion specimen is 66mm long of a test portion and a grip at each end 77mm long, a total length of 220mm. The grip cross section is a 14mm square and the test portion has a circular cross section, 8mm in diameter, as shown in Fig. 3(a). The top of specimen was clamped and the lower end was attached to the inertia bar by which the torsional strain was applied. The free decay curves of the vibration were recorded. The damping capacity is given by the ratio $\Delta W/W$, where ΔW is the energy loss per one cycle of variation and W is the elastic energy of the specimen. The amplitude-dependent damping was measured at the maximum surface shear strain range between 10^{-5} and 10^{-3} under the static tensile stress of 2MPa. The damping capacity and Young's modulus were measured by cantilever-type apparatus. The dimensions of the specimen are 10mm x 100mm x 2mm, as shown in Fig. 3(b).

Results and Discussion

Amplitude-dependent damping

Fig. 4 shows the damping capacity of fourteen kinds of plastics as a function of the maximum surface shear strain by means of the torsional vibration at room temperature. The 6N and PTFE had high damping capacities compared to other plastics. The damping capacities of PTFE, 6N, PE, HDPE, PET and PBT depended on the shear strain amplitude. Particularly, the damping of PTFE strongly depended on the shear strain amplitude, and reached a maximum damping value of

Table 1 Samples of plastics

Symbol	Name		
ABS	Acrylonitrile/butadiene/styrene	PC	Polycarbonate
FE	Phenol resin	PE	Polyethylene
PET	Poly(ethylene terephthalate)	PEEK	Poly(etheretherketon)
PA	Polyamide	PP	Polypropylene
6N	6-Nylon	PTFE	Poly(tetrafluoroethylene) : Teflon
66N	6,6-Nylon	PVC	Poly(vinyl chloride)
PBT	Poly(butylene terephthalate)	HDPE	High density polyethylene
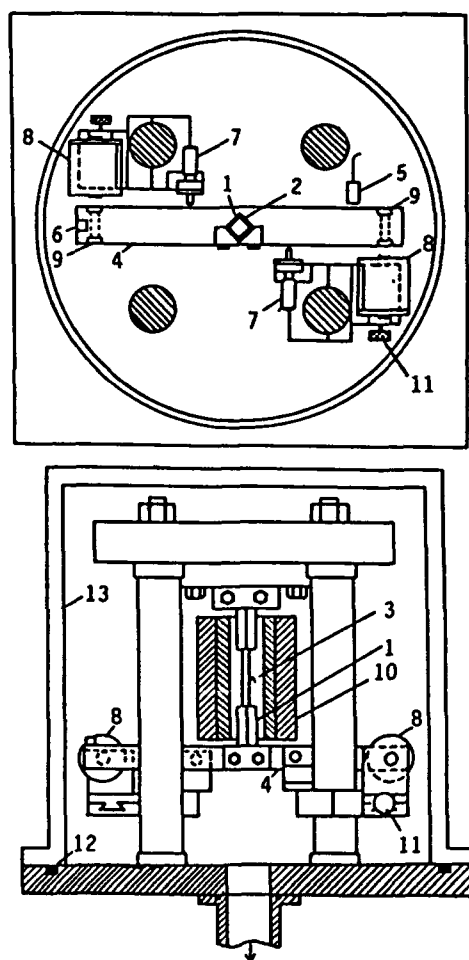
Fig.1 Schematic drawing of torsion pendulum apparatus: 1, test-piece; 2, ceramics spacer; 3, thermocouples; 4, inertia bar; 5, displacement pick-up; 6, accelerometer; 7, micrometer head; 8, magnetic coil; 9, permalloy rod;10, furnance; 11, adjustable screw; 12, O-ring; and13,bell jar.

Table 2 Samples of FRP

PET/glass fiber(0~50vol%)
PBT/glass fiber(0~50vol%)
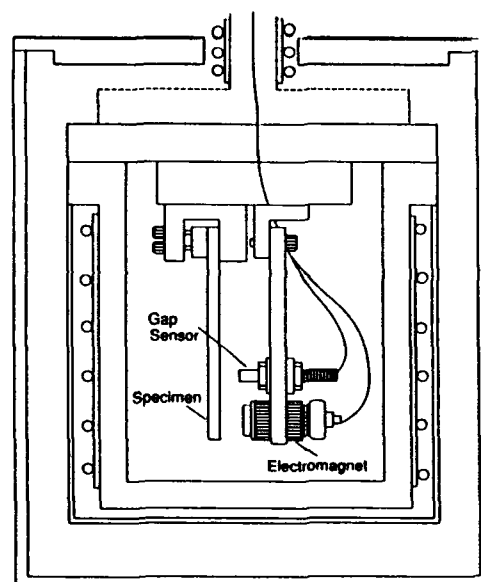
Fig.2 Schematic drawing of cantilever apparatus.
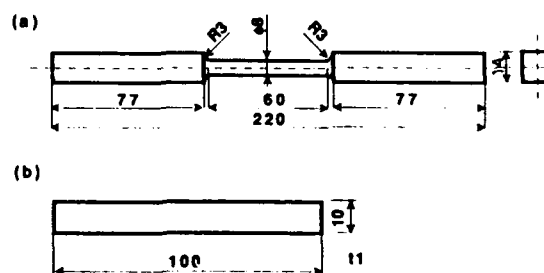
Fig.3 Dimensions of specimen:
(a) Torsion pendulum method,
(b) Cantilever-type method.
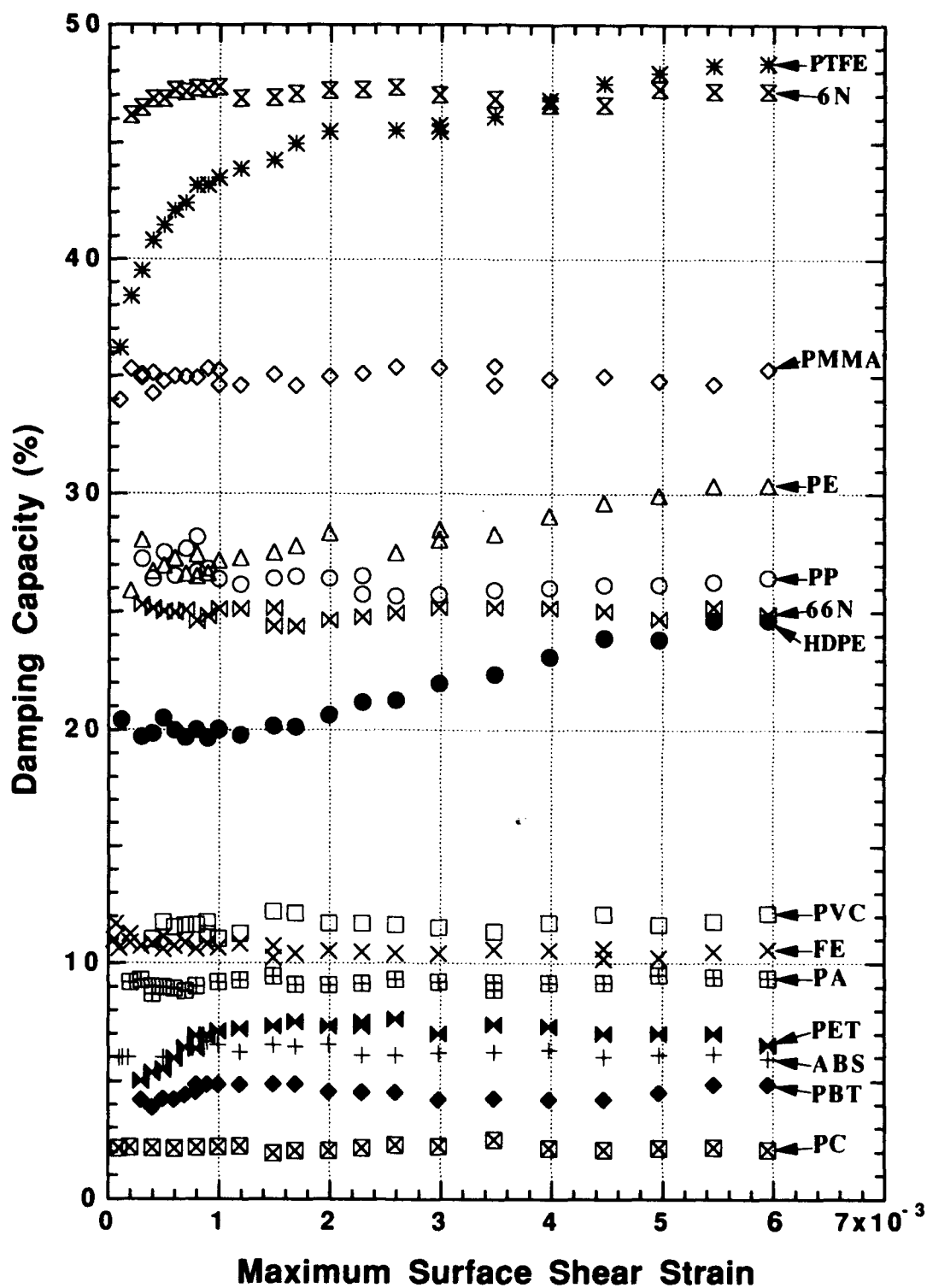
Fig.4 Amplitude dependent damping of plastics.

48% at the strain of 6 x 10^{-3}. The PMMA, PP, 66N, PVC, FE, PA, ABS, and PC showed almost strain-independent damping. The HDPE and PE showed almost constant damping capacity up to the strain value of 1 x 10^{-3}, and showed by a steady rise with increasing the shear strain.

Temperature dependence of damping

Fig. 5 shows the damping capacity and shear modulus of 6N at the temperature range from 15°C to 120°C. The heating plot of damping capacity and shear modulus of first cycle did not agree with that of the fist cooling. The disagreements are explain by a phase lag of the structure change because of the glass transition of 6N. The damping peak was observed at about 45°C. It can be seen that the damping peak is caused by the polymer chain motion.

Fig. 6 shows the damping capacity and the shear modulus of PTFE between 15°C and 120°C. The plots in Fig. 6 for PTFE were the result of a first cycle of heating and cooling. For the first cooling, the damping and modulus slightly shifted downward from those for the first heating. The damping peak was observed at about 30°C.

Fig. 7 shows the damping capacity and the shear modulus of PE between 15°C and 120°C. The damping capacity of PE increased with increasing temperature. The damping peak of PE disappeared because of the glass-transition temperature to be much lower(-125°C).

Relationships of damping capacity and modulus of FRP

Fig. 8 shows the relation between the damping capacities and the Young's moduli of PET- and PBT-based composites containing glass fiber as a function of glass fiber content. The damping capacity and Young's modulus were determined by the lateral vibration. at room temperature. The Young's modulus in both composites increased remarkably with increasing glass fiber content. The damping capacity of glass fiber/PBT composites gradually decreases with increasing glass fiber content. On the other hand, the damping of glass fiber/PET composites was almost independent of the glass fiber content.

Comparison of plastics with metals and ceramics.

The damping index-tensile strength relationships for plastics, metals, MMC and ceramics are given in Fig. 9. The damping index has been defined by James[3]. The damping index is the specific damping capacity(S.D.C.) measured at the maximum surface shear stress-amplitude of $\sigma_y/10$ by means of a torsion pendulum, where σ_y is the 0.2%-proof stress in the tensile testing of the material. The damping index is, therefore, more convenient for design engineers than
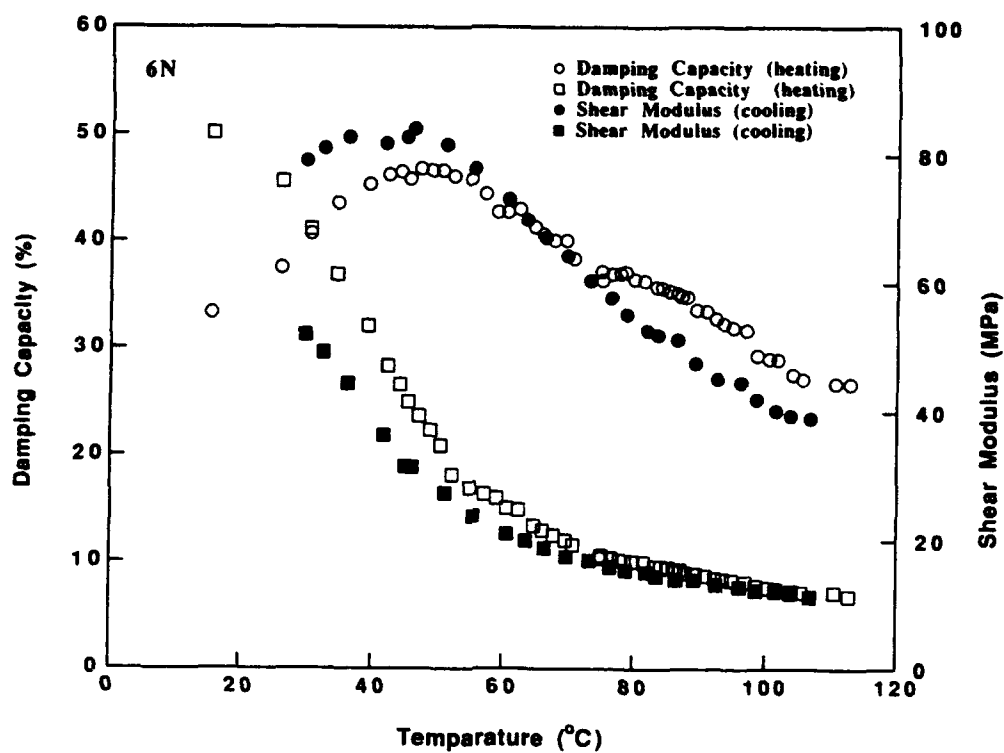
Fig.5 Effect of temperature on damping capacity and shear modulus of 6N.
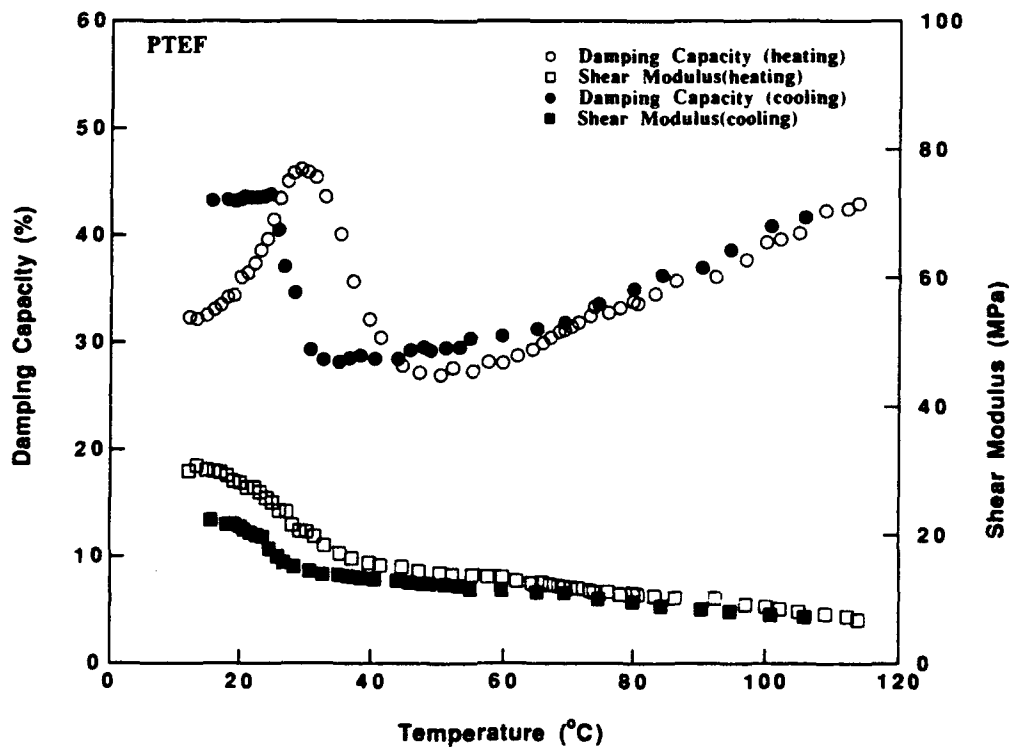
Fig.6 Effect of temperature on damping capacity and shear modulus of PTFE.
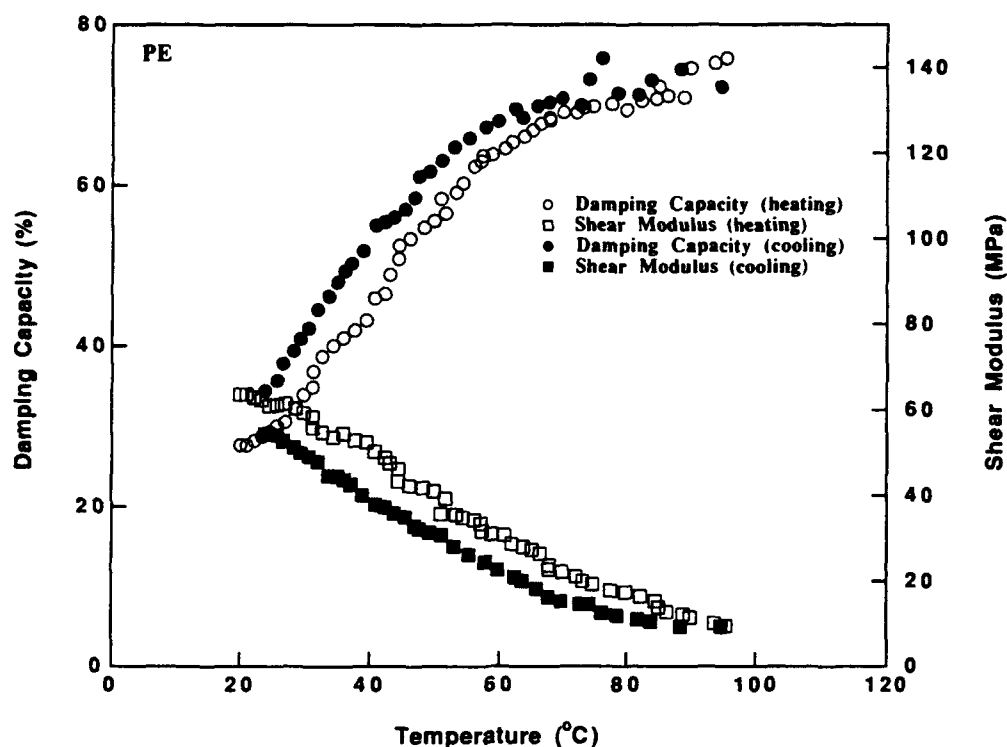
Fig.7 Effect of temperature on damping capacity and shear modulus of PE.
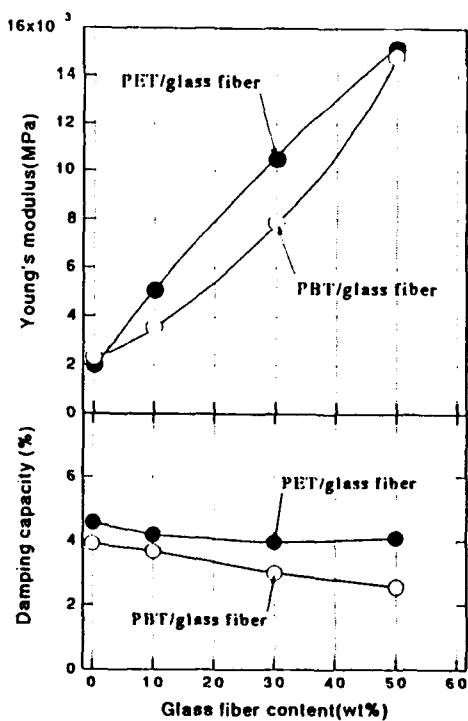
Fig.8 Effect of reinforcement content on damping capacity and Young's modulus of PET /glass fiber and PBT/glass fiber composites.
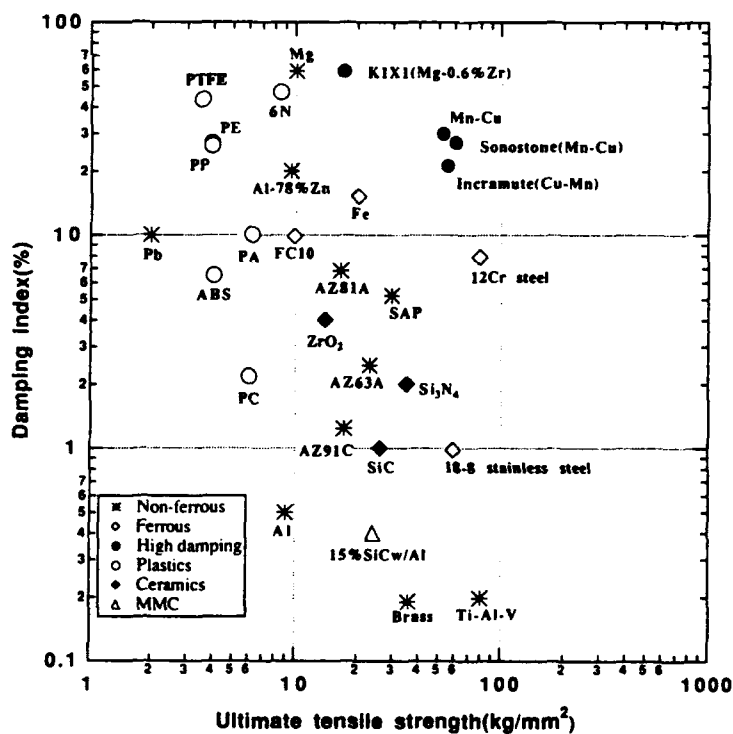
Fig.9 Damping index of plastics, metals, ceramics and metal matrix composite.

the specific damping capacity, for selection of the materials with different yield or tensile strength[4].

In Fig. 9, the damping indices are scattered in a wide range from 0.2% to 60%. Among the metallic materials pure Mg and Mg-0.6%Zr alloy(K1K1)[5] show a maximum value of 60%. In the case of the metallic materials there is a tendency of decreasing damping index with increase in the tensile strength. On the other hand, the damping indices of the plastic materials have no relation to the tensile strength.

Conclusion

The damping capacities of fourteen kinds of pure plastics, and of six kinds of PET- and PBT-based composites containing glass fiber have been determined by a torsional and a lateral vibration methods. Results are summarized as follows:

(1) The 6N and PTFE have extremely high damping capacity at room temperature, compared to other plastics, because of the glass transition. The damping value of 48% is measured for 6N and PTFE.

(2) The PMMA, PE, PP, PP, 66N, and HDPE have the medium values of damping capacity.

(3) The PC, PBT, ABS, PET, PA, FE, and PVC give the lowest values of damping capacity.

(4) The rigidity of plastics increase drastically with increasing the reinforcement content, but the damping is almost independent of the glass fiber content.

Acknowledgment

The authors thank Mr. Shouzo Ito, Chief Director of Machining Center, Science University of Tokyo, for his skillful machining of test specimens.

References

1. J. D. Ferry, "Viscoelastic Properties of Polymers," John Wily & Sons, Inc., New York, 1980.

2. W. H. Hatfield, G. Stanfield and L. Rotherham, Trans. NE Coast Instn Engrs Shipbuilders 58(1942) 273.

3. D. W. James, Mat., Sci. Eng., 4, 1969, 1.

4. K. Sugimoto, "Basic and Applied Research on high-Damping Alloys for Application to Noise Control", Mem. Inst. Sci. Ind. Res., Osaka Univ., 35, 1978, 31-44.

5. G. F.Weissman and W. Babington, "A High Damping Magnesium Alloy for Missile Applications", Proc. ASTM, 58, 1958, 869-892.

Evaluation of Impact Damage in Composites by Wave Propagation Analysis

**TSUYOSHI OZAKI, ISAO KIMPARA, TOSHIO SUZUKI
AND SHIGENORI KABASHIMA**

ABSTRACT

We have been proposing a new system to evaluate defects in composites by analyzing elastic wave propagation in the material. In this system, longitudinal wave is introduced into the composites by a ultrasonic testing probe which is specially made for FRP. The measured through-transmitted wave signals are Fourier transformed into frequency spectrum data and evaluation parameters are calculated. In this study, we applied this system to the evaluation of impact damage in composites. The specimens were impacted by an instrumented drop weight impact test system with a steel hemispherical-end impactor. Evaluation parameters in different frequency ranges were calculated, and the parameter obtained in higher frequency range were found to be more effective to detect impact damage, which suggested the possibility of the short-time evaluation of defects in composites. Dynamic simulations on elastic wave propagation in composites are also carried out, in which the reflection, refraction and mode transition of elastic wave were visualized in detail. The evaluations of impact damage in composites are successfully simulated.

INTRODUCTION

Ultrasonic inspection is said to be the most effective way for the detection of defects in composites, and delaminations, voids, porosity, and lack of bonding are detected by various ultrasonic techniques, such as through-transmission scanning, pulse-echo, thickness gaging and resonance impedance. However, it is generally more difficult than that of metal because of their heterogeneity and anisotropy. Some types of defects parallel to a lamina, such as fiber break and crack perpendicular to a lamina have been very difficult to detect. Recently, several new techniques to examine frequency spectrum of received ultrasonic wave have been devised, and defects such as micro-cracks, voids in fine ceramics [1,2] and σ embrittlement of stainless steel [3] have been successfully evaluated. As for composites, some reports have described possibility of detection in similar ways [4], but there have been few experimental results. Therefore, we have been establishing a new system to evaluate defects in composites effectively by analyzing through-transmission waveform and calculating evaluation parameters, and model defects in unidirectional CFRP have already detected, in which the size and type of these defects were successfully evaluated by the parameter [5]. In this paper, we aim at applying this system to evaluation of defects in composite which have not been fully examined by conventional method. Impact damages caused on composite structures in service

Tsuyoshi Ozaki, Materials & Electronic Device Laboratory, Mitsubishi Electric Corporation, 1-1-57, Miyashimo, Sagamihara 229, Japan
Isao Kimpara, Toshio Suzuki and Shigenori Kabashima, Faculty of Engineering, The University of Tokyo, 7-3-1, Hongo, Bunkyo-ku 113, Japan

(for example by dropping object) is one of the most important defects. When the damage includes delamination between laminates, it can be detected by high resolution C-scan or X-ray investigation. In case of unidirectionally reinforced composites, however, no pulse echo can be detected. So we tried to detect them by examining the evaluation parameters. Dynamic simulation of wave propagation in unidirectional composites are also carried out in order to examine how waves are affected by the impact damage.

EVALUATION OF IMPACT DAMAGE

SETUP OF NONDESTRUCTIVE EVALUATION SYSTEM

Figure 1 shows the schematic diagram of NDE system. The elastic wave is introduced into the specimen by a high damping type probe which is acoustically in conformity with plastic matrix composites. The center frequency of the probe is 5MHz. The through-transmitted wave is picked up by an AE transducer through the acryl triangular column (width = 3mm) mounted on the specimen at certain distance (usually 20 to 100mm) from the introduced point and routed to the pre-amplifier. The time-dependent wave signal is recorded by the transient memory temporary and Fourier transformed by the FFT analyzer. A frequency spectrum is obtained by averaging the 16 measured spectra. Finally, The obtained frequency spectrum data are transmitted to the computer and evaluation parameters are calculated.

The procedures of calculation is as follows: (1) Correlation between waveform at the head of testing area and behind the area are examined with coherence coefficient and further calculation is carried out in the frequency range where the value is above 0.8. (2) Each frequency spectrum is divided by the spectrum received at the wave-introduced edge, which makes the parameter independent of the effect of coupling, attachment, transducer, and so on. (3) Acquired value, which is a kind of transmission function of the material, is integrated in several frequency ranges respectively and evaluation parameters are obtained.

SPECIMEN

Specimens examined here are unidirectional carbon/epoxy composite plates. The size of the plate were 300mm in the fiber direction x 50mm perpendicular to the fiber with thickness of
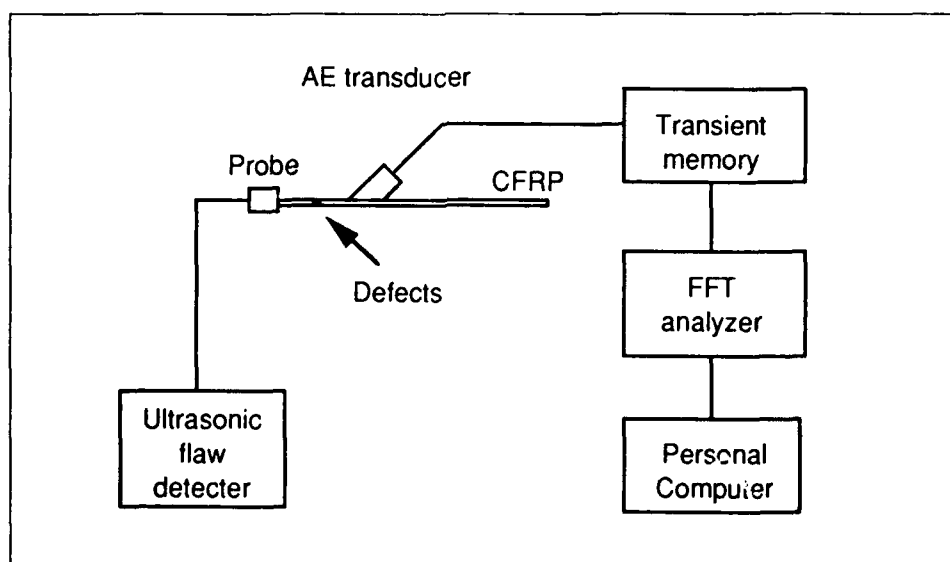
Figure1. Schematic diagram of NDE system

3mm. Impact damage was conducted with an instrumented drop weight impact test system (IITM-18, Yonekura), in which the applied load is sensored by an accelerometer attached on the impactor. The plates were set on the aluminum plate and fixed at the four corners. They were impacted by a vertically falling 10mm diameter steel hemispherical-end impactor, at the center of the width and 15mm from one edge. The weight of the impactor was 1.14kg, and the drop height were 100 to 150 mm.

DAMAGES CHARACTERIZATION

Figure 2 illustrates typical impact damages caused at the contact point. When the applied energy was low (1.0J), only a small dent was observed. As the energy became large (1.25 to 1.5J), transverse cracking from the edge of the dent, small cracks in the dent, and fiber breaks at the edge of the dent were observed. Figure 3 shows the X-ray computer tomography of the cross section including the damaged point. In the damaged area, CT values are a little lower than the normal area, which suggest that microcrack or micropore should exist in this region.
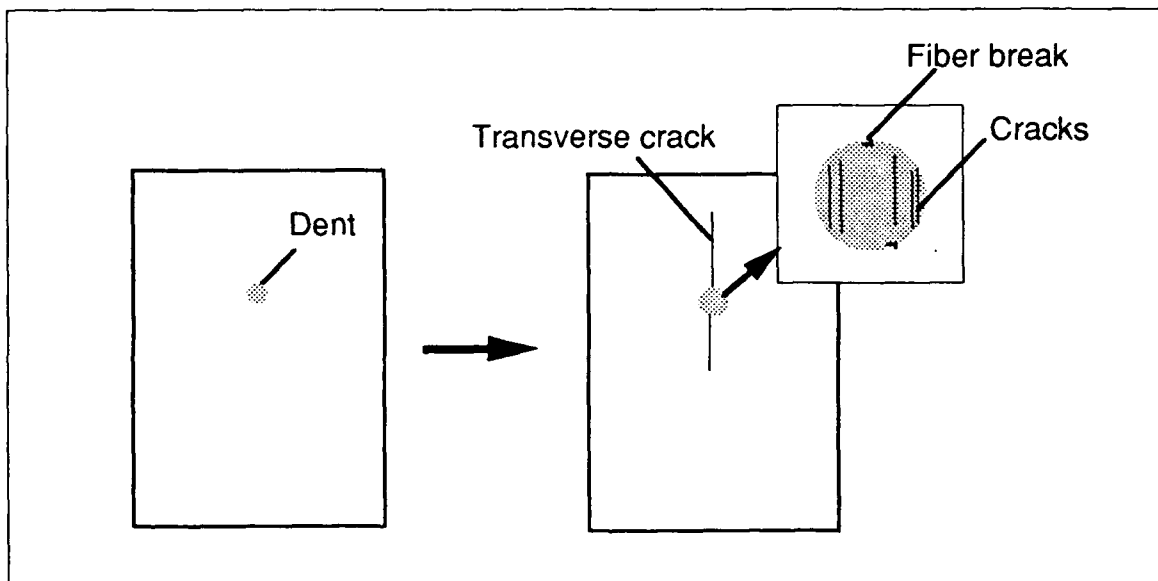
Figure 2. Typical aspects of the impact damage.
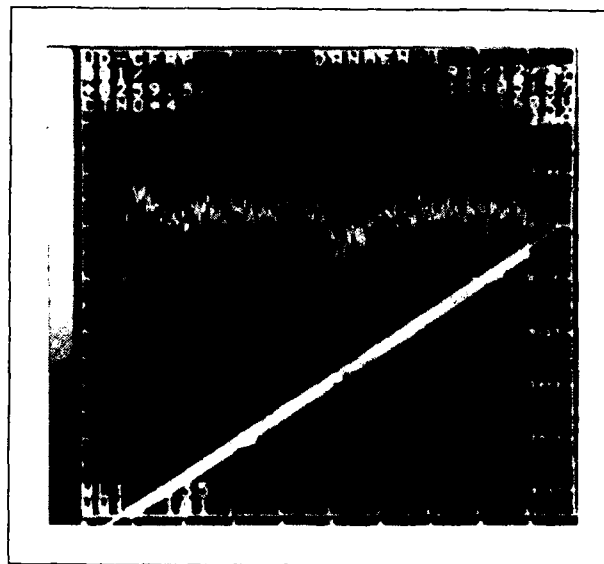
Figure 3. X-ray CT image of impact damaged specimen.

WAVE PROPAGATION ANALYSIS

The through-transmitted wave are picked up at 30mm from the wave-introduced edge. When the applied impact energy was large, the amplitude of time-dependent waveforms propagating through the damaged specimen were clarified to be smaller than that of undamaged. However, it is difficult to detect defects by time-dependent waves alone, especially in the specimens with small damage. Figure 4 shows a series of frequency spectra. The most behind data in the figure is the spectrum received at the introducing edge. In case of undamaged specimen, there is little difference between the spectrum at the edge and at the picked-up point. Though amplitude of less damaged specimen (Energy =1.0J) is a little lower than that of undamaged in all frequency range, amplitude of more damaged specimen becomes clearly small especially in higher frequency range. These aspects are quantified by the evaluation parameters shown in Fig.5. Detection of the impact damage is more effectively performed with the parameter obtained in the higher frequency range. When the probe sets are scanned perpendicular to the reinforcing fibers, all the regions of the specimen is to be evaluated. Since the span of the probe sets corresponds the size of the scanning mesh in the fiber direction, the short-time evaluation is expected.

Ultrasonic C-scan testing were also performed by submerging the specimens into the water tank. In this method, the defects are usually imaged by detecting the presence of the pulse echo from the defects, and the delamination in the laminate composites are often evaluated. In case of the unidirectional composites as sre evaluated here, however, little echo from the damage was received and it was so difficult to image as shown in the left-hand side of Fig.6. Therefore we make an image by evaluating the amplitude of wave propagating through the cross section of the plate and reflected at the bottom. Because the amplitude in damaged area was smaller than that of the undamaged area, we can make an image as shown in the right-hand side of Fig.6, when the proper time-gate is set and the scanning mesh is fine enough.
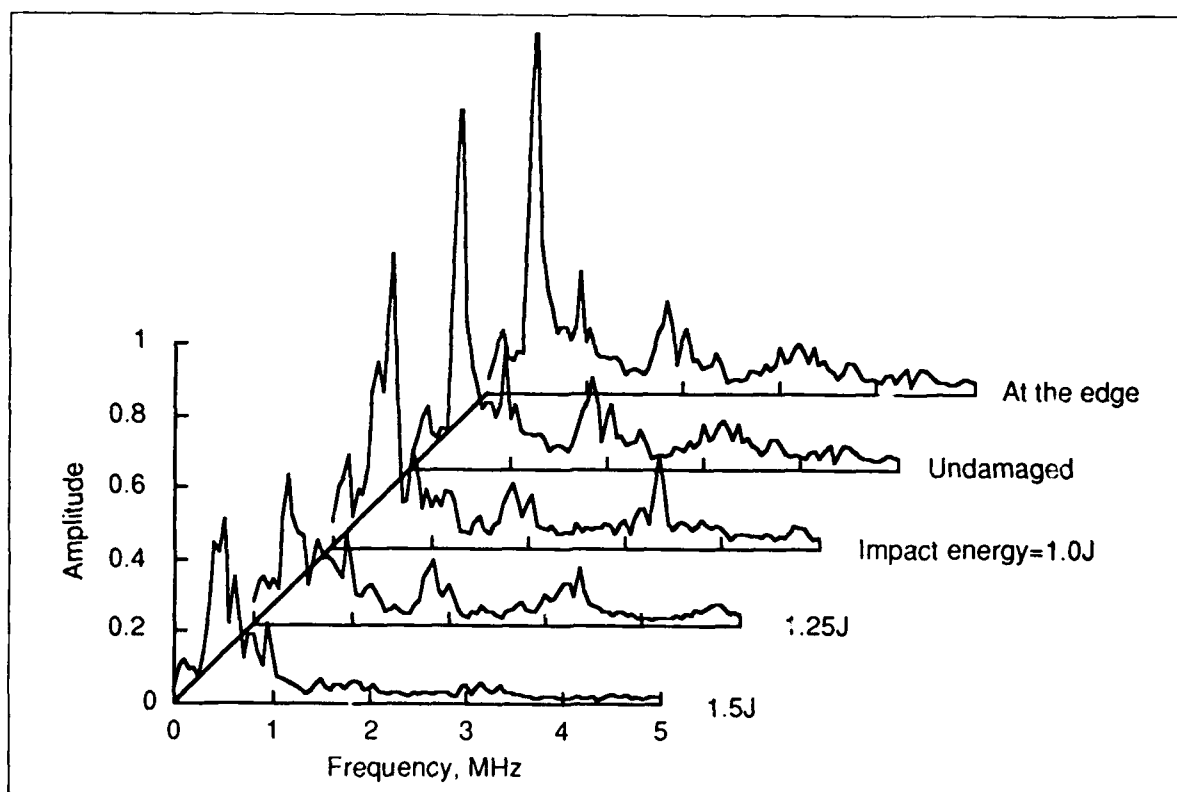
Figure 4. Frequency spectra of received wave.
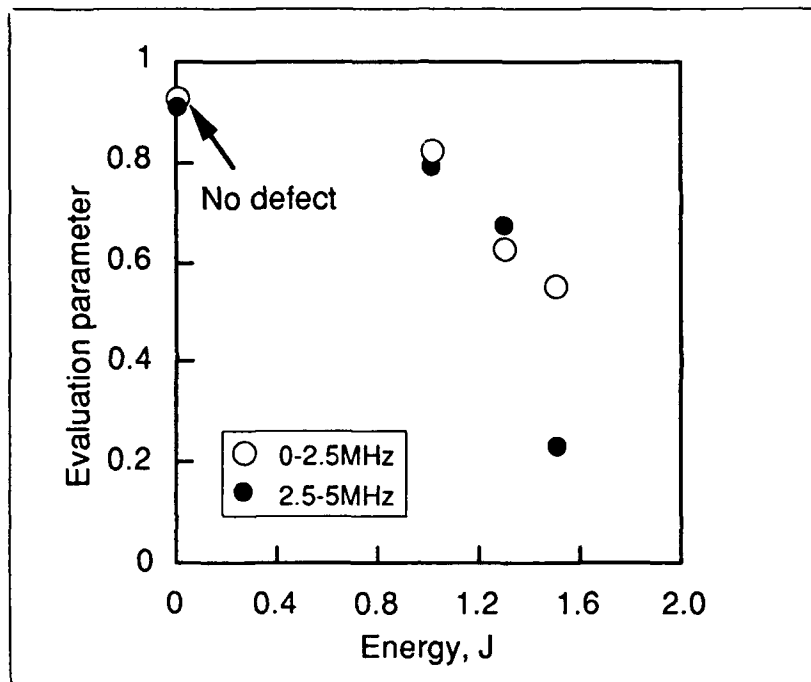
Figure 5. Evaluation parameters versus applied energy.
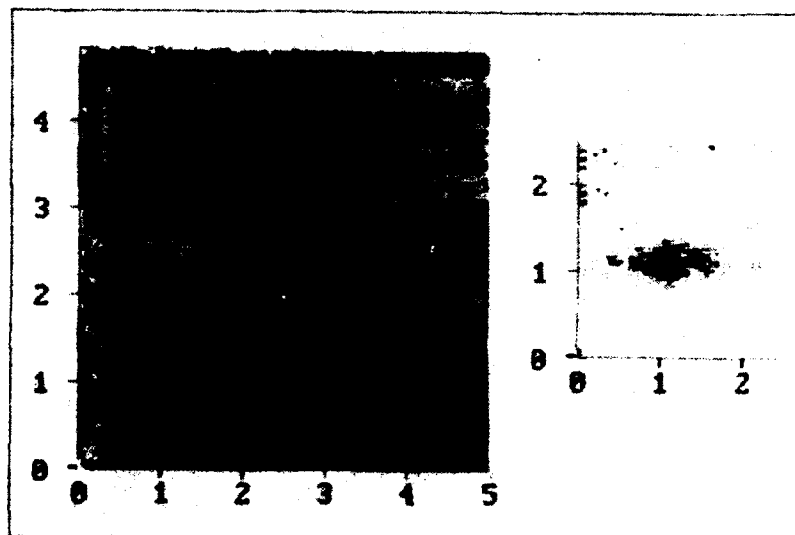
Figure 6. Ultrasonic C-scan image of the impact damaged specimen.

SIMULATIONS ON ELASTIC WAVE PROPAGATION

SIMULATION MODEL

In examining defects in composites by means of elastic wave propagation analysis, it is important to know how the waves propagate in the material and how they are affected by the defects. Though some theoretical analyses have been made on the wave propagation in composites [6,7], there are so many types of inherent defects in composites that the general aspects have not been fully clarified. Therefore, we propose a new two-dimensional wave propagation model of a unidirectional fiber reinforced composites, in which many types of defects are easily simulated, and dynamic simulations based on this model are carried out.

Figure 7 shows the simulation model. Nodal points are placed on fibers, which requires a small number of nodal points for the number of elements. The defects of fiber and matrix are assumed to be between two nodal points, which is convenient because the displacement array is not cognizant of the defect and mass of the element remains unchanged when fibers and matrices are disconnected at the location. A section enclosed with dotted lines is defined as "Composite element", including fiber and matrix. Assuming the stiffness of fiber is much larger than that of matrix, equation of motion of composite element in the x-direction, is:

$$\rho d\delta \frac{\partial^2 u}{\partial t^2} = \left(\lambda_f + 2\mu_f\right)\delta d_f \frac{\partial^2 u}{\partial x^2} + \left(\lambda_m + \mu_m\right)\delta d_m \frac{\partial^2 w}{\partial x \partial z} + \mu_m \delta d_m \frac{\partial^2 u}{\partial z^2} \tag{1}$$

where, u: displacement in the x-direction, w: displacement in the z-direction, r: density, d: distance between nodes in the z-direction, d: distance between nodes in the x-direction, l:, m: Lame's constants. Subscriptions f, m denote fiber, matrix, respectively. The second order partial differentials in the right side of Eq. (1) are approximated by the difference forms,

$$\frac{\partial^2 u_i^j}{\partial x^2} = \frac{1}{\delta^2}\left(u_i^{j-1} - 2u_i^j + u_i^{j+1}\right) \tag{2}$$

(a) Nodes and composite elements   (b) Defect models and the affected nodes
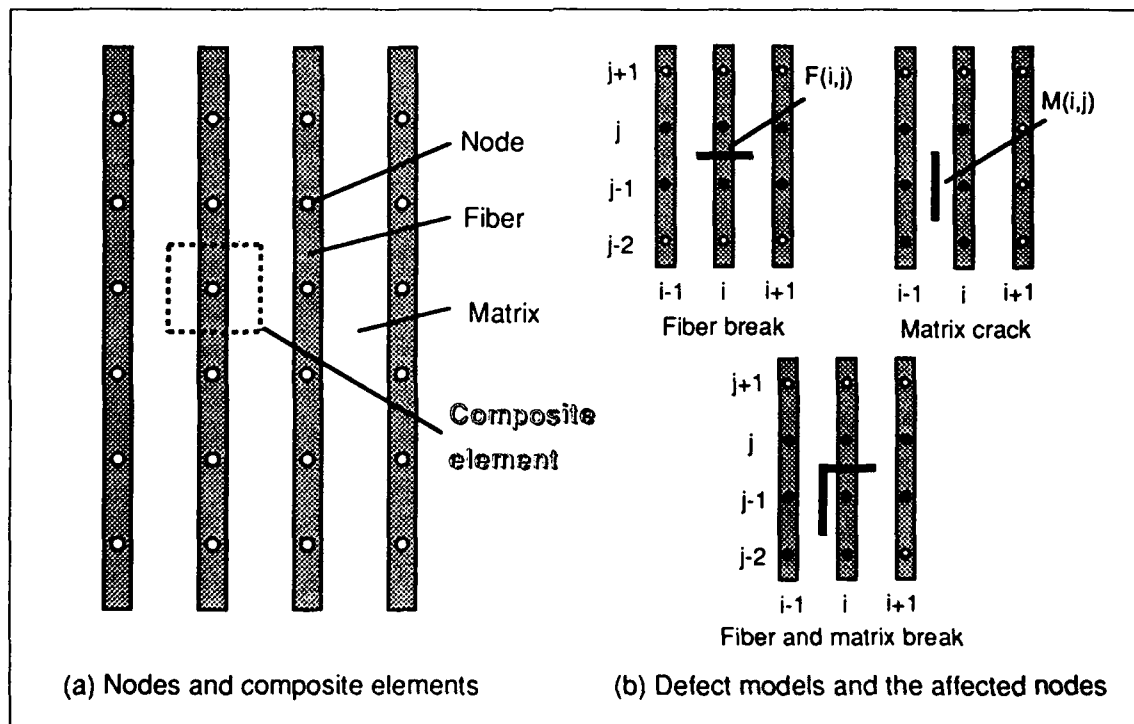
Figure 7. Simulation model.

$$\frac{\partial^2 u_i^j}{\partial z^2} = \frac{1}{d_m^2}\left(u_{i-1}^j - 2u_i^j + u_{i+1}^j\right)$$

$$\tag{3}$$

$$\frac{\partial^2 w_i^j}{\partial x \partial z} = \frac{1}{4\delta d_m}\left(w_{i+1}^{j+1} - w_{i+1}^{j-1} - w_{i-1}^{j+1} + w_{i-1}^{j-1}\right)$$

$$\tag{4}$$

where, the superscript j denotes node number in the x-direction and the subscript i denotes node number in the z-direction. Time-dependent nodal displacements are calculated by means of the Newmark's β method ($\beta = 1/4$) with the initial conditions, $u(o) = w(o) = o$.

Defects of composite are formulated by replacing some difference forms of equations for the nodal points around the broken elements as illustrated in Fig.7(b). If the fiber is broken between nodal points, N_i^j and N_i^{j-1}, Eq. (2) and Eq. (4) are replaced by the following equations:

$$\frac{\partial^2 u_i^j}{\partial x^2} = \frac{4}{3\delta^2}\left(u_i^{j+1} - u_i^j\right)$$

$$\tag{5}$$

$$\frac{\partial^2 w_i^j}{\partial x \partial z} = \frac{1}{4\delta d_m}\left(w_{i+1}^{j+1} - w_{i-1}^{j+1}\right)$$

$$\tag{6}$$

Similarly, the difference forms for N_i^{j-1} are replaced. In addition, difference forms for N_{i-1}^j, N_{i-1}^{j-1}, N_{i+1}^j and N_{i+1}^{j-1} are also replaced.

As for the matrix break, the matrix between two nodal points is assumed to have no stiffness. If the matrix between N_i^j and N_{i+1}^j is broken, Eq. (3) is replaced with,

$$\frac{\partial^2 u_i^j}{\partial z^2} = \frac{1}{d_m^2}\left(u_{i-1}^j - u_i^j\right)$$

$$\tag{7}$$

The other replacements about 6 nodes shown in Fig.7(b) applies correspondingly to the case of fiber break. In case of complex defects of fiber and matrix, equations for marked 8 nodes will be replaced.

ELASTIC WAVE PROPAGATION IN THE IMPACT DAMAGED COMPOSITE

Dynamic simulations are carried out under the condition that one edge of a unidirectional CFRP (in the fiber direction) is fixed and time-dependent force is loaded on the other edge. Influences of fiber defects on the elastic wave propagation are examined. Figure 8 shows the vector charts after a single sine wave is loaded on the edge of unidirectional CFRP which has a impact damage. Impact damage was simulated by the combination of fiber breaks and matrix cracks as shown in the left-hand side of the figure.

First, longitudinal wave, propagates in a row. When the wave gets to the fiber break, small reflected wave is observed. The diffraction wave is also observed, but amplitude is rather small because of anisotropy. The frequency of detected wave behind the damage is lower than that of through transmitted wave, which is in good accordance to experimental result. In addition, the wave-screened zone is observed to last rather long from the damaged area, which suggests that the length of evaluated region can be set long and faster detection by the larger scanning mesh is possible.

CONCLUSION

The objective of this study was to detect more kinds of defects in composites by analyzing the elastic wave propagation. Impact damages in unidirectionally reinforced composite in which no apparent delaminations exists, were examined. The existence and magnitude of the
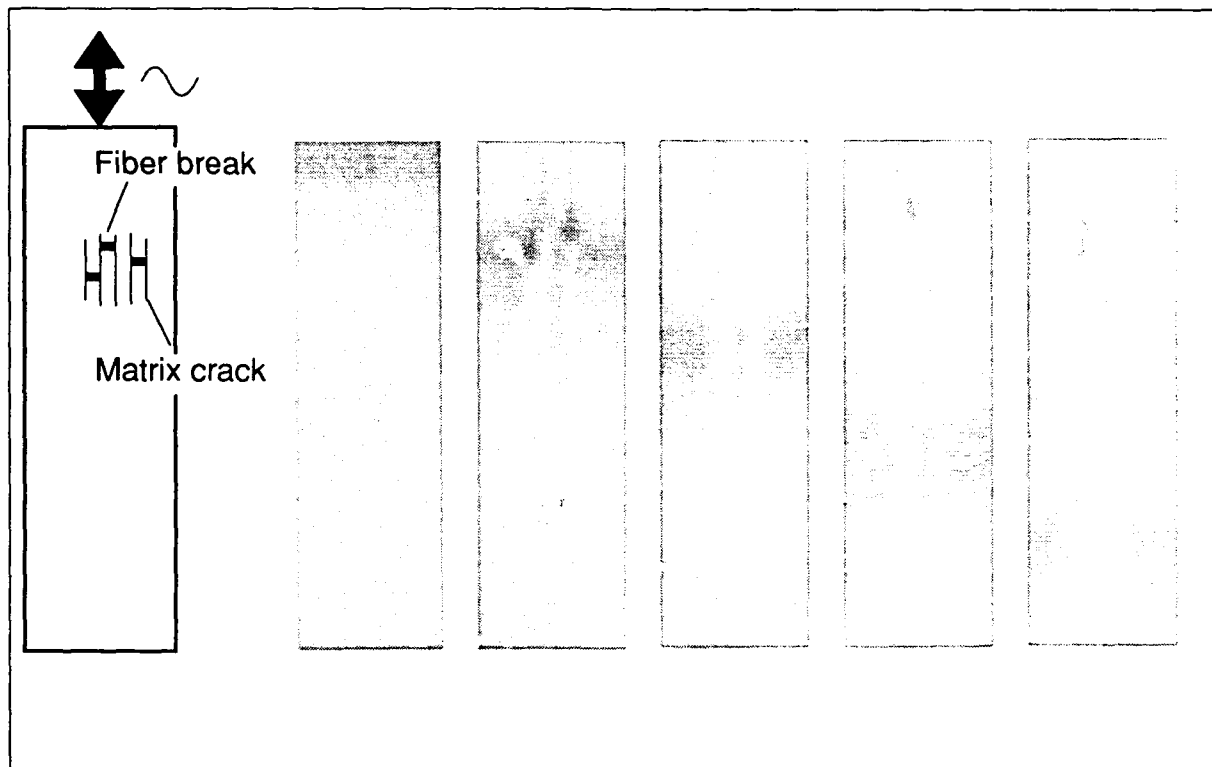
Figure 8. Vector charts of simulated elastic wave propagation.

damage were successfully evaluated by calculating the parameters, especially in higher frequency range, which suggests the possibility of a new fast nondestructive evaluation system. Dynamic simulations based on 2-D wave propagation model of unidirectional composites were also carried out, and the influences of defects on the wave propagation were examined.

REFERENCES

1. A. G. Evans, et. al.,1978, Jour. Appl. Phys., 49 (5): 2669.
2. Y. Tomikawa, et. al., 1987, Japanese Journal of Applied Physics, 26-2: 162.
3. T. Mihara, et. al., 1987, Jour. Japan Soc. Non-Destructive Inspection, 36, 10.
4. H. E. Gundtoft, 1985, Riso M-2509, 5.
5. T. Ozaki, et. al., 1991, Proc. ICCM-8, 39-D.
6. J. C. Peck and G. A. Gurtman, 1969, Jour. Appl. Mech., 36, 479.
7. M. Stern, et. al., 1971, Jour. Appl. Mech., 38, 448.

Stress Analysis II

Geometrically Nonlinear Cylindrical Bending of Laminates

H. H. LEE AND M. W. HYER

ABSTRACT

This paper outlines the details that lead to closed-form solutions for two approaches for studying the nonlinear cylindrical bending response of symmetric laminates: classical lamination theory and first-order shear deformation theory. For each theory two cases are studied: transverse pressure loading and compressive inplane edge loading. With the availability of the solutions it is possible to compare predictions based on the two theories. Closed-form expressions for interlaminar stresses are derived by using the stresses from the bending analysis and integrating the equilibrium equations of elasticity in the thickness direction. The paper shows that even for what would be considered thick plates, there is little difference between the deflections and stresses predicted by the two theories for the pressure loaded case. For the case of inplane loading, however, there are substantial differences in the predictions of the two theories. Thus whether or not shear deformations are important depends on loading as well as a laminate geometry.

BACKGROUND

There is a continuing interest in calculations of structural response using so-called shear deformable theories. There are a variety of theories available, and a large number of these theories have been applied to problems wherein the deflections are so small that geometrically linear kinematics can be used. The purpose of the present paper is to examine the importance of shear deformations for a class of laminated plate problems that must be modeled using geometrically nonlinear kinematics. For geometrically nonlinear problems there are few closed-form solutions available and the finite-element approach must generally be used. For the cylindrical bending problem studied here, however, closed-form solutions are obtained, providing a convenient and accurate framework for studying the effects of shear deformations in the context of geometric nonlinearities. Solutions for cylindrical bending within the framework of the linear elasticity were obtained by Pagano[1]. In the current study deflections are studied, but more importantly, the stresses within the laminate are computed, including the interlaminar stresses. The stresses and deflections of the laminates

H.H. Lee and M.W. Hyer, Department of Engineering Science and Mechanics,
Virginia Polytechnic Institute and State University, Blacksburg, VA 24061-0219

are also computed using a geometrically nonlinear but nonshear deformable classical lamination theory, and the results compared. With the comparisons, the importance of using a shear deformable theory can then be evaluated.

APPROACH

The problem considered is that of cylindrical bending of a symmetrically laminated plate of thickness H due to either a transverse pressure or a compressive inplane edge loading. The plate is of length L in the x direction and infinitely long in the y direction. The edges at $x = \pm L/2$ are simply supported. For the pressure loading the edges are restrained against any movement in the x direction. For the inplane edge loading the edges are free to move in the x direction. The problem is symmetric about $x = 0$ and is treated as such. For the classical lamination theory approach, the governing equations are

$$\frac{dN_x}{dx} = 0$$

$$\frac{d^2 M_x}{dx^2} + N_x \frac{d^2 w}{dx^2} + q = 0 ,$$

(1)

where

$$N_x = A_{11}\varepsilon_x^0 = A_{11}\left\{ \frac{du}{dx} + \frac{1}{2}\left(\frac{dw}{dx}\right)^2 - \frac{1}{2}\left(\frac{dw^p}{dx}\right)^2 \right\}$$

$$M_x = D_{11}\kappa_x^0 = -D_{11}\left(\frac{d^2 w}{dx^2} - \frac{d^2 w^p}{dx^2} \right)$$

(2)

The nomenclature used above includes midsurface displacements and stress resultants, and they have their usual meaning[2]. The quantity w^p is the initial deflection due to imperfections that are inevitable with composite plates. For the first-order shear deformable theory, the governing equations are

$$\frac{dN_x}{dx} = 0$$

$$\frac{dQ_x}{dx} + N_x \frac{d^2 w}{dx^2} + q = 0$$

(3)

$$\frac{dM_x}{dx} - Q_x = 0 ,$$

where

$$N_x = A_{11}\varepsilon_x^0 = A_{11}\left\{ \frac{du}{dx} + \frac{1}{2}\left(\frac{dw}{dx}\right)^2 - \frac{1}{2}\left(\frac{dw^p}{dx}\right)^2 \right\}$$

$$M_x = D_{11}\kappa_x^0 = D_{11}\frac{d\psi}{dx}$$

(4)

$$Q_x = A_{55}\left(\psi + \frac{dw}{dx} - \frac{dw^p}{dx} \right).$$

Here ψ is cross-section rotation in the $x - z$ plane and A_{55} is a transverse shear stiffness. Both theories make use of the fact that for cylindrical bending it is assumed the response is independent of y and the displacement in the y direction, v, is zero.

It's not difficult to obtain the closed-form solutions from above governing equations. For the pressure loading case, as initial deflections are not important, zero initial deflection is assumed. The boundary conditions $u = 0$, $w = 0$, $M_x = 0$ are enforced at the supported edge, and the closed-form solutions are obtained. For the inplane loading case, with a sinusoidal initial imperfection of 5% plate thickness, closed-form solutions are obtained for boundary conditions $w = 0$, $M_x = 0$, and $N_x =$ known at the supported edge.

INTERLAMINAR STRESSES

Equations of elasticity for cylindrical bending are expressed as

$$\frac{\partial \sigma_x}{\partial x} + \frac{\partial \tau_{xz}}{\partial z} = 0$$

$$\frac{\partial \tau_{xy}}{\partial x} + \frac{\partial \tau_{yz}}{\partial z} = 0. \tag{5}$$

The stresses σ_x and τ_{xy} which appear in the equilibrium equations can be calculated in closed-form from the exact solutions. By substituting these stresses in terms of the constitutive equations into equilibrium equations and performing integration in z-direction, explicit expressions for the interlaminar stresses can be found[3]. The interlaminar stresses should be continuous at the interfaces of the layers. By applying this continuity condition at the interfaces, and boundary conditions on the bottom surface of the plate, the following expressions for interlaminar stress within the k-th layer are obtained.

$$\tau_{xz} = -\left\{ \overline{Q}^k_{11}(z - z_k) + \sum_{i=1}^{k-1} \overline{Q}^i_{11}(z_{i+1} - z_i) \right\} \frac{\partial \varepsilon^0_x}{\partial x}$$

$$-\frac{1}{2} \left\{ \overline{Q}^k_{11}(z^2 - z_k^2) + \sum_{i=1}^{k-1} \overline{Q}^i_{11}(z_{i+1}^2 - z_i^2) \right\} \frac{\partial \kappa^0_x}{\partial x} \tag{6}$$

$$\tau_{yz} = -\left\{ \overline{Q}^k_{16}(z - z_k) + \sum_{i=1}^{k-1} \overline{Q}^i_{16}(z_{i+1} - z_i) \right\} \frac{\partial \varepsilon^0_x}{\partial x}$$

$$-\frac{1}{2} \left\{ \overline{Q}^k_{16}(z^2 - z_k^2) + \sum_{i=1}^{k-1} \overline{Q}^i_{16}(z_{i+1}^2 - z_i^2) \right\} \frac{\partial \kappa^0_x}{\partial x}, \tag{7}$$

where $\overline{Q}^k_{11}$, $\overline{Q}^k_{12}$, $\overline{Q}^k_{16}$ are the reduced stiffness components for the k-th layer. The expressions also satisfy the redundant boundary conditions on the top surface,

namely, $\tau_{xz} = 0$ and $\tau_{yz} = 0$ at $z = z_{N+1}$. As an example, the argument for τ_{xz} can be shown as follows. At $z = z_{N+1}$,

$$\tau_{xz} = -A_{11}\frac{d\varepsilon_x^0}{dx} = -\frac{dN_x}{dx} \tag{8}$$

where the A_{ij} came from the summations in eq. (6). From the equilibrium equations, eqs. (1) or (3), it is not difficult to deduce $\tau_{xz} = 0$ on the top of the surface.

RESULTS

Figures 1, 2, and 3 are the results for the pressure loading, and figs. 4, 5 and 6 are the results for inplane loading for $[0/90]_s$ laminate. The nondimensional parameters appearing in the figures are

$$\bar{x} = \frac{x}{L}, \quad \bar{z} = \frac{z}{H}, \quad \bar{w} = \frac{w}{H}, \quad \bar{q} = \frac{q}{(\frac{D_{11}H}{L^4})}, \quad \bar{\sigma}_x = \frac{\sigma_x}{q},$$

$$\bar{\tau}_{xz} = \frac{\tau_{xz}}{q}, \quad \bar{\sigma}_x^\star = \frac{\sigma_x}{(\frac{N_x}{H})}, \quad \bar{\tau}_{xz}^\star = \frac{\tau_{xz}}{(\frac{N_x}{H})}, \quad \bar{N}_x = \frac{N_x}{A_{11}(\frac{H}{L})^2}. \tag{9}$$

Figure 1 illustrates the deflections for both the classical and the shear deformable theories for a 4-layer cross-ply graphite epoxy laminate loaded with a uniform pressure. The normalized deflection at the center of the plate, $x = 0$, vs. the normalized applied load is shown. The plate deflection has been normalized by the plate thickness so moderate nonlinearities are being considered in the figure. The results of a linear analysis are included for comparison, and two laminate length to thickness ratios, $L/H = 10$ and $L/H = 4$, are considered, the value $L/H = 4$ being classified as a thick laminate. The conclusion that can be drawn from the figure is that for the case of nonlinearities, there is not much difference in the predictions of the deflections between the two theories. The linearized theories, however, show considerable difference between the two theories for the thick laminate. Hence conclusions made in the context of a linear theory may not transfer to the context of a nonlinear theory.

The normalized bending stresses $\bar{\sigma}_x$ at the center of the laminate($x = 0$) as a function of the normalized distance through the thickness for the pressure-loaded laminate are shown in fig. 2. Two normalized load levels are considered, $\bar{q} = 100$ and $\bar{q} = 200$, $\bar{q} = 200$ causing the plate to deflect one plate thickness. Again the linearized theory is included and in fact, the linearized classical lamination theory and the linearized shear deformable theory are indentical. The linearized theories are independent of load level. There is little difference between the two nonlinear theories for the thin laminate and some difference for the thick laminate.

For both theories the interlaminar stresses are computed by integrating the differential equations of elasticity through the thickness of the plate. This is somewhat contradictory, as the first-order shear deformation theory gives the shear stresses directly. However, the first-order theory predicts shear stresses that are constant through the thickness and do not satisfy the traction-free boundary conditions at the top and bottom surface of the laminate. Figure 3 illustrates the

normalized interlaminar shear stress $\bar{\tau}_{xz}$ at the right support, the location where the shear stresses are the greatest, as a function of distance through the thickness of the laminate. The two linearized theories are again identical but there is a difference between the two nonlinear theories, particularly for the thick case, the shear stresses being different by a factor of 2 for the thick laminates. At both load levels, the shear deformable theory predicts lower interlaminar shear stress.

Fig. 4 shows the out-of-plane deflection response for inplane loading. For an inplane compressive loading the semi-infinite plate responds like an Euler beam and can buckle. For L/H = 10, the buckling loads are: $(\bar{N}^{cr})_C = 1.364$ for the classical theory, and $(\bar{N}^{cr})_S = 1.154$ for the shear deformable theory. For L/H = 4, the buckling loads are: $(\bar{N}^{cr})_C = 1.364$ for the classical theory, and $(\bar{N}^{cr})_S = 0.638$ for the shear deformable theory. For L/H = 4, there is a larger difference in the buckling loads for the two theories. As the load level approaches the buckling loads for each theory, the out-of-plane deflection increases rapidly. The important point to realize is that for a given inplane load level, $\bar{N}$, a shear deformable theory predicts larger out-of-plane deflections, particularly as the shear deformable theory buckling load is approached.

Figures 5 and 6 show the distribution of the bending stresses $\bar{\sigma}_x^*$ at the center of the plate and the shear stresses $\bar{\tau}_{xz}^*$ at the supported edge, respectively, for the inplane loading case. The selected load level for figs. 5 and 6 produces 0.5H out-of-plane deflection for the shear deformation theory. At this load level the out-of-plane deflection for classical theory is 0.22H for L/H = 10, and 0.08H for L/H = 4. Figures 5 and 6 indicate that there is a difference in the stresses for the two theories, the difference being quite significant for the shear stresses. These differences are attributable to the greater deflections of the shear deformable theory.

CONCLUSION

The exact solution for nonlinear cylindrical bending was derived for classical lamination theory and shear deformation theory. Explicit expressions for interlaminar stresses were obtained. It was shown that for transverse loading the classical theory and the shear deformation theory predict similar deflections and stresses in the geometrically nonlinear range. However, the two theories diverge for the case of inplane compressive edge loading.

REFERENCES

1. Pagano, N. J. ; "Exact Solutions for Composite Laminates in Cylindrical Bending " , *J. Composite Materials,* Vol. 3, 1969, pp 398-411.
2. Whitney, J. M. ; *Structural Analysis of Laminated Composite Plates,* Technomic Publishing Co., 1987
3. Sims, D. F. and Wilson, H. E. ; "Distribution of Shearing Stresses in a Composite Beam under Transverse Loading," *Composites* , July, 1978, pp 185-191.

nonlinear classical	nonlinear shear def.	linear classical	linear shear def.
——	···	—	- - -
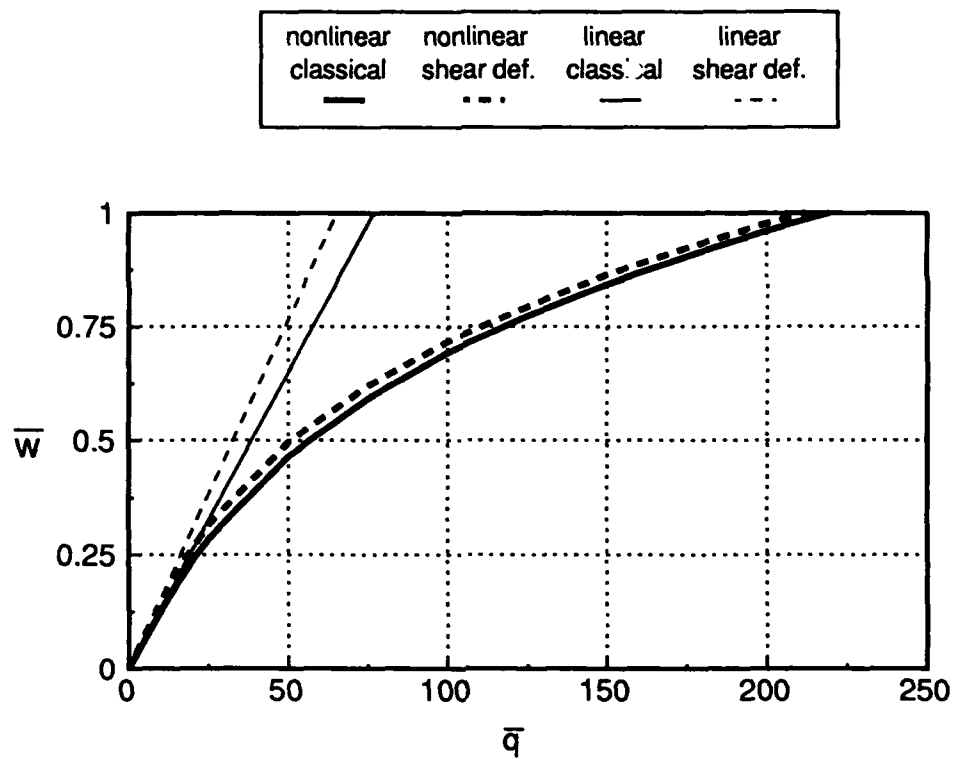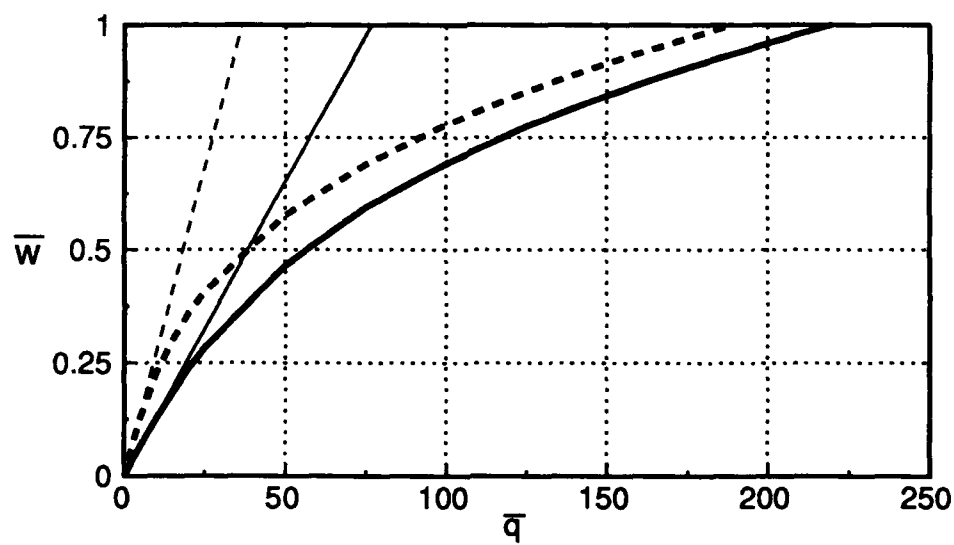
(a) L/H = 10

(b) L/H = 4

Fig. 1   Load vs. out-of-plane deflection relation.
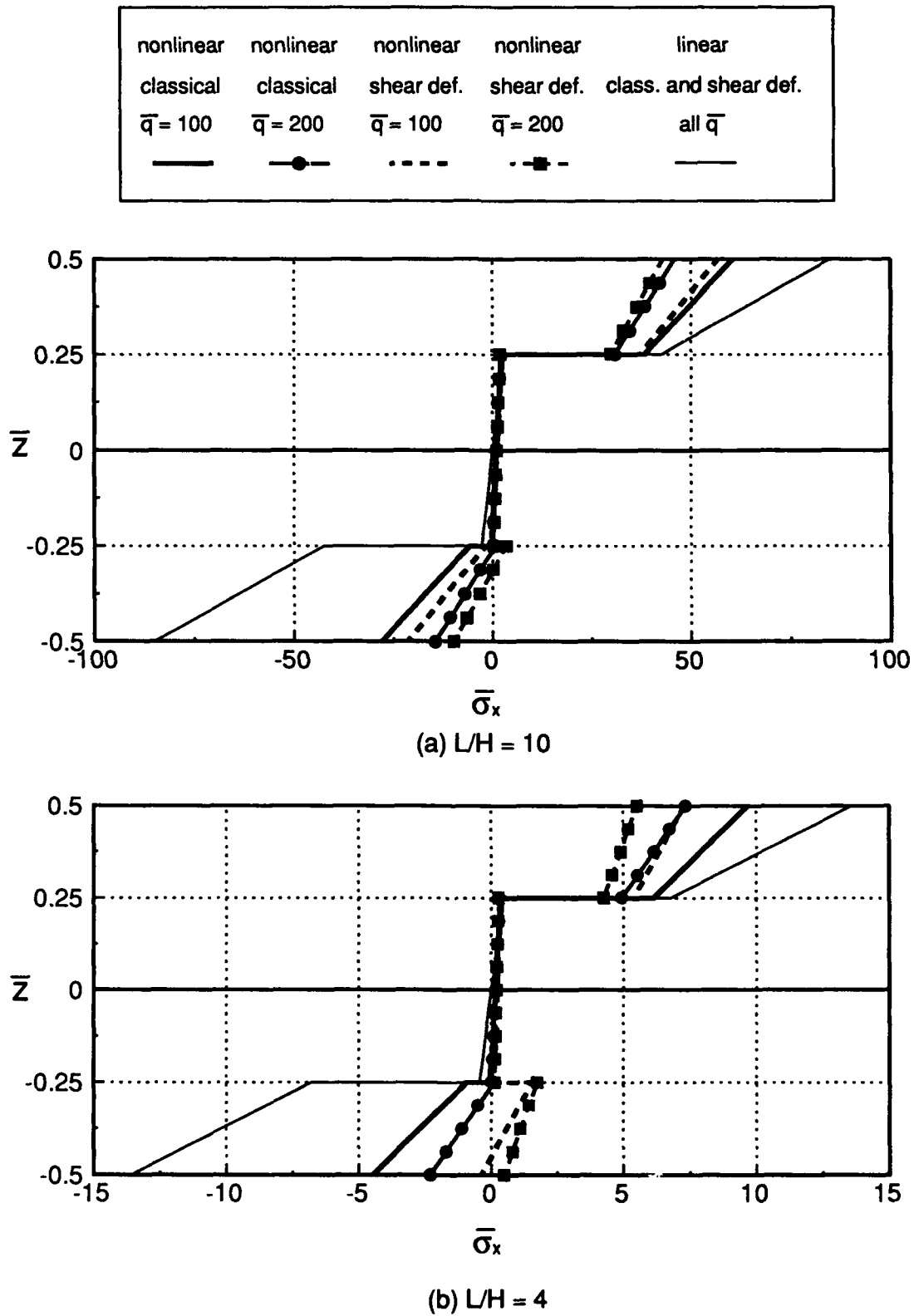
Fig. 2   Through the thickness distribution of $\bar{\sigma}_x$ at $\bar{x} = 0$ for transverse loading.
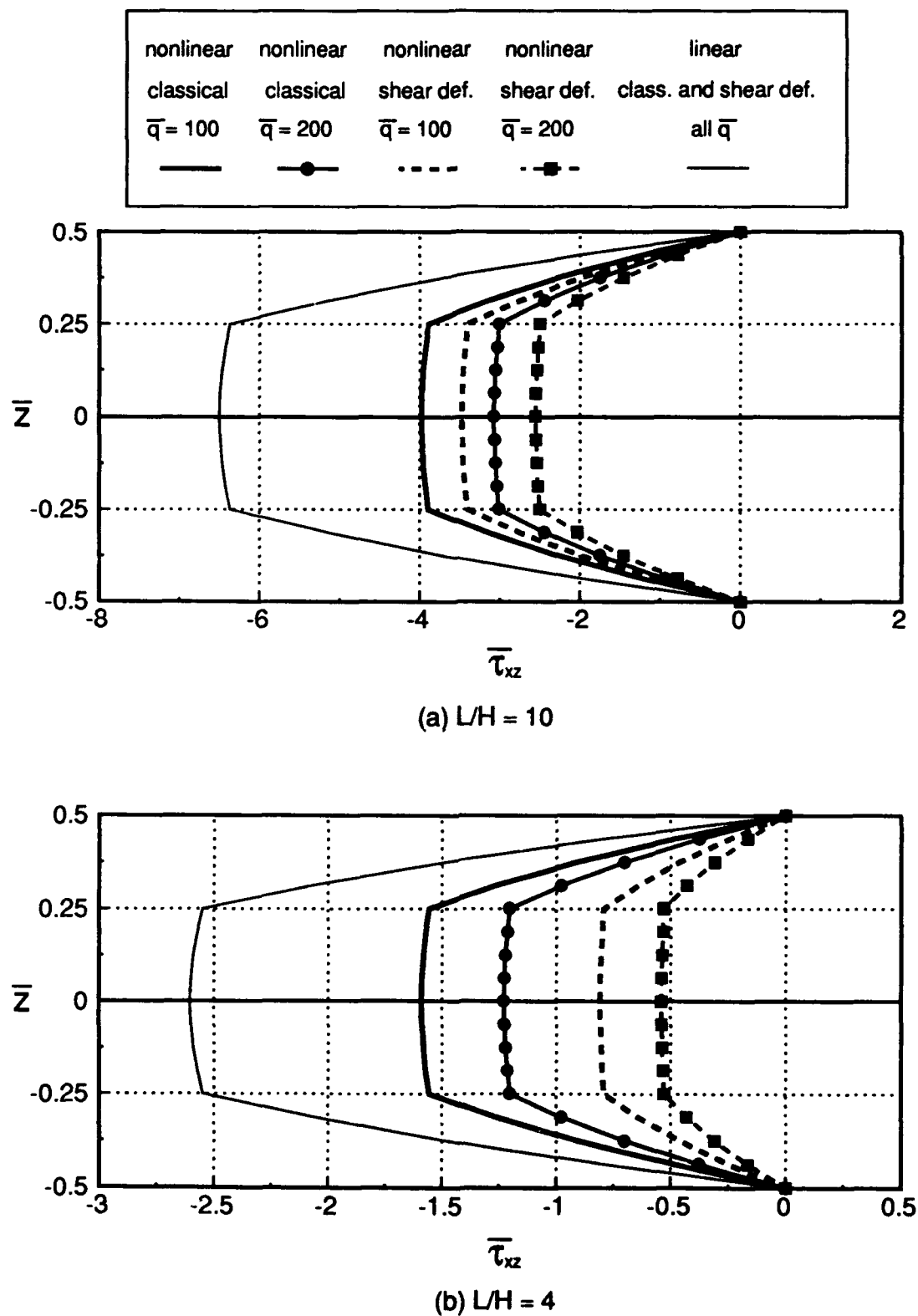
Fig. 3 Through the thickness distribution of $\overline{\tau}_{xz}$ at $\overline{x} = 0.5$ for transverse loading.
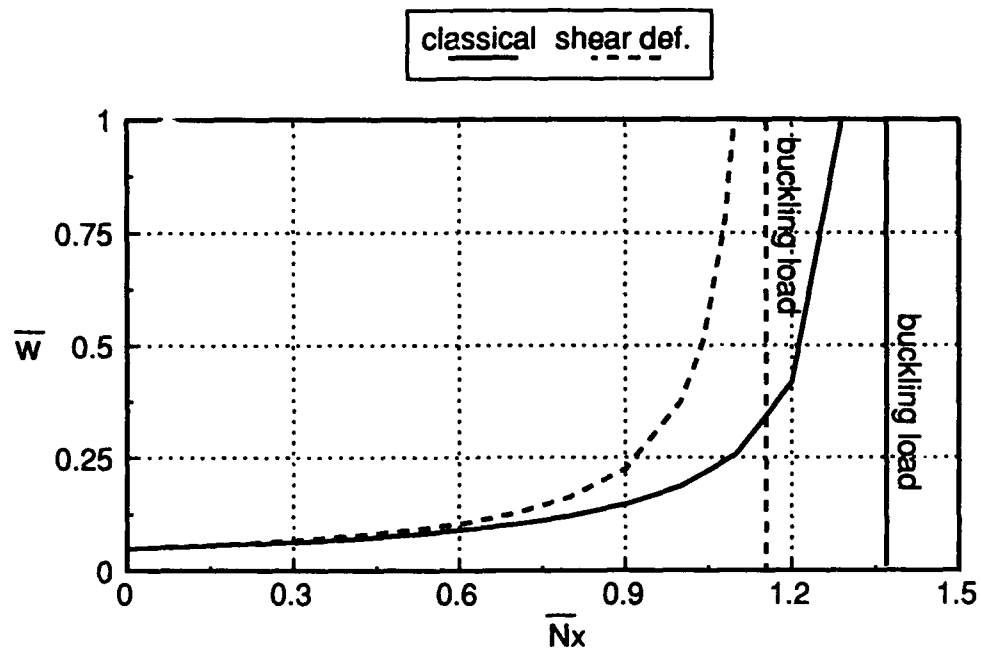
(a) L/H=10
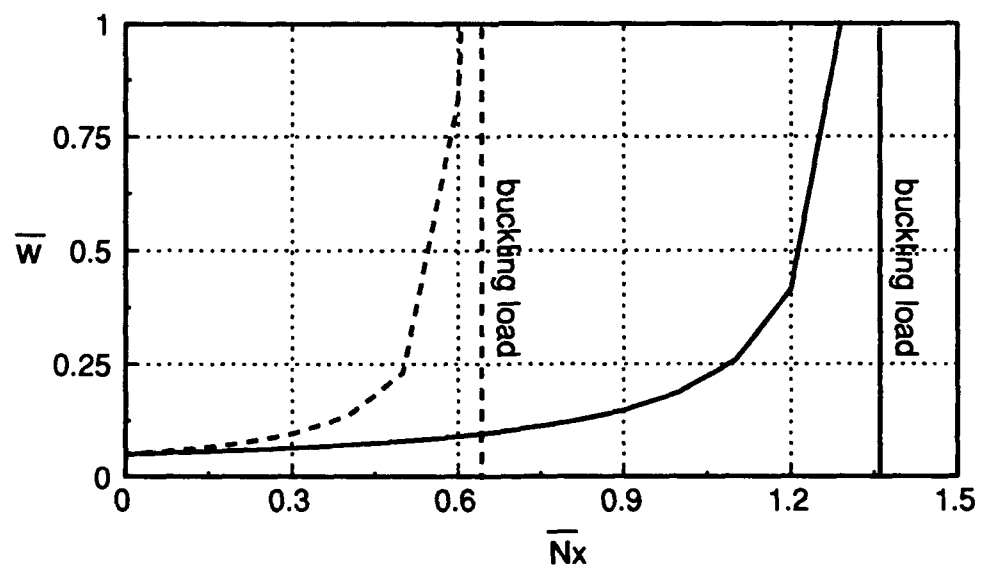
(b) L/H=4

Fig. 4 Load vs. out-of-plane deflection relation for inplane loading.

(a) L/H = 10, $\overline{N}x$ = 1.04

(b) L/H = 4 , $\overline{N}x$ = 0.575
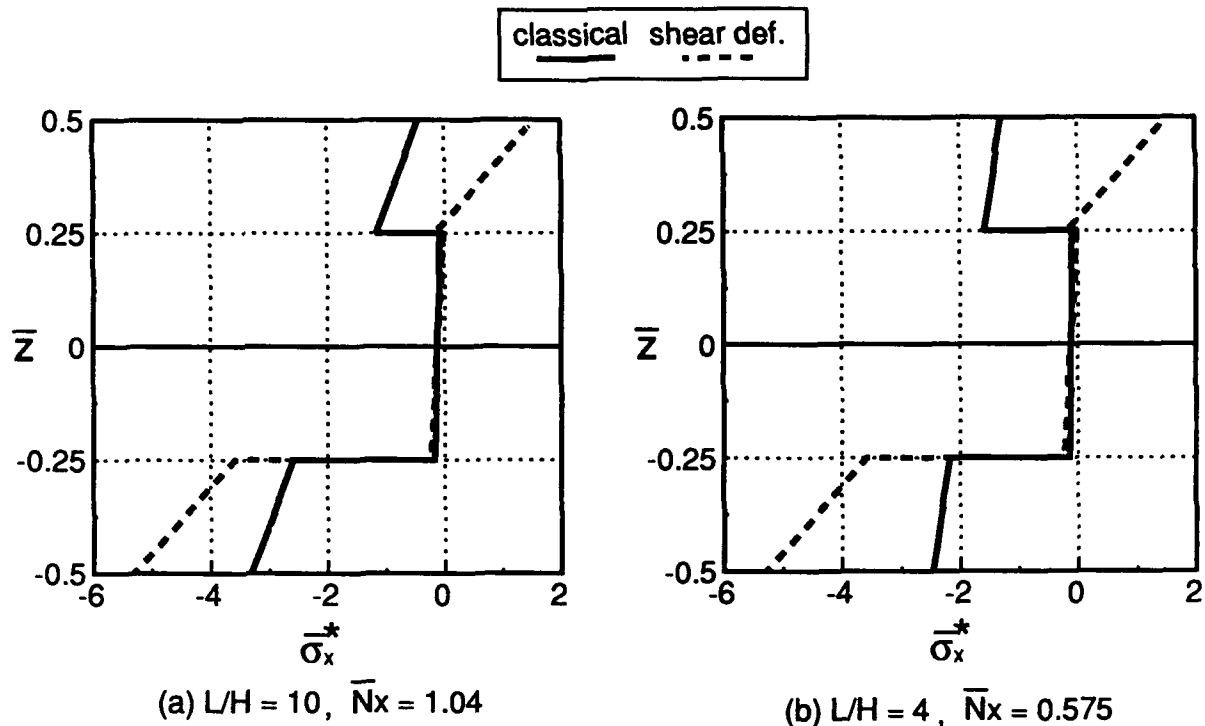
Fig. 5   Through the thickness distribution of $\overrightarrow{\sigma}_x^*$ at $\overline{x}$ = 0 for inplane loading.

classical   shear def.

(a) L/H = 10, $\overline{N}x$ = 1.04

(b) L/H = 4 , $\overline{N}x$ = 0.575
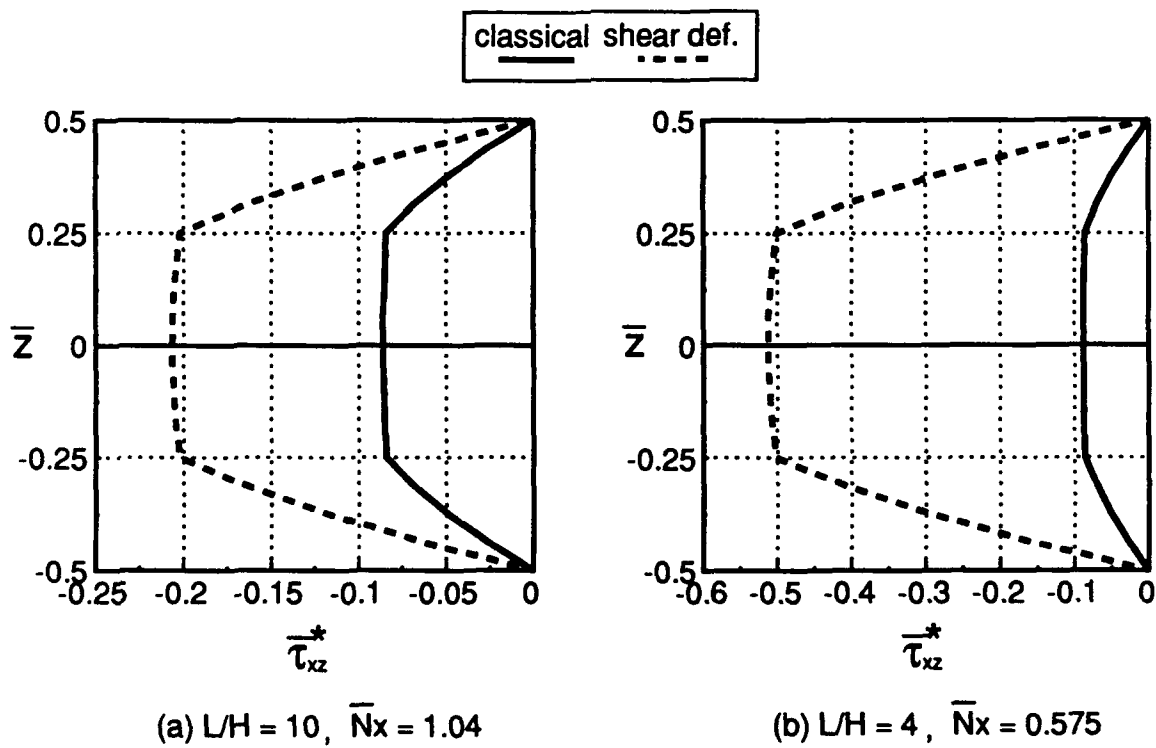
Fig. 6   Through the thickness distribution of $\overrightarrow{\tau}_{xz}^*$ at $\overline{x}$ = 0.5 for inplane loading.

Stress Analysis for Twisted Cord and Rubber of FRR

KAZUYUKI KABE, MASATAKA KOISHI AND TAKASHI AKASAKA

ABSTRACT

In the cord-reinforced materials, the cord modulus is much larger than that of the matrix. In the case of FRP(Fiber Reinforced Plastics), the modulus ratio of the cord to the matrix is approximately 10 - 100, while in the case of FRR(Fiber Reinforced Rubber), it increases up to 100 - 10000. Since FRR undergoes larger deformation than FRP, the twisted cords have been used in FRR structures to improve the fatigue properties.

In this paper, the tensile modulus of FRR column with a twisted cord is analyzed first by neglecting the effect of rubber and then by Finite Element Analysis(FEA) with the consideration of stresses and strains of both cord and rubber. In particular, the effects of the pitch length of the twisted cord and the rubber modulus on the tensile stiffness of the FRR column is studied theoretically and experimentally.

Good correlations are obtained among the analytical, the FEA and the experimental results for the tensile modulus of a FRR column.

INTRODUCTION

There are many FRR goods, for example, tire, belt-conveyer, hoses, oil-fence, diaphragm, air-spring and so on. Above them all, the tire, which plays an important role on a transportation, is forced to provide various kinds of functions simultaneously of load carrying capacity, functions of transmitting driving and braking torques, cushioning ability and road-holding performance.

The tire structure has been made of FRR materials consecutively since 1880, as well fitting to these multiple requirements under the inflation pressure.

Figure 1 shows a radial tire construction, having a laminated-biased-FRR strip(the belt) and a radial ply casing of FRR(the carcass).

Kazuyuki Kabe, Masataka Koishi, Yokohama Rubber Co., LTD. 2-1 Oiwake, Hiratsuka-shi, Kanagawa-ken, 254, Japan.
Takashi Akasaka, Department of Precision Mechanics, Faculty of Science and Engineering, Chuo University, 1-13-27 Kasuga, Bunkyo-ku, 112, Japan.
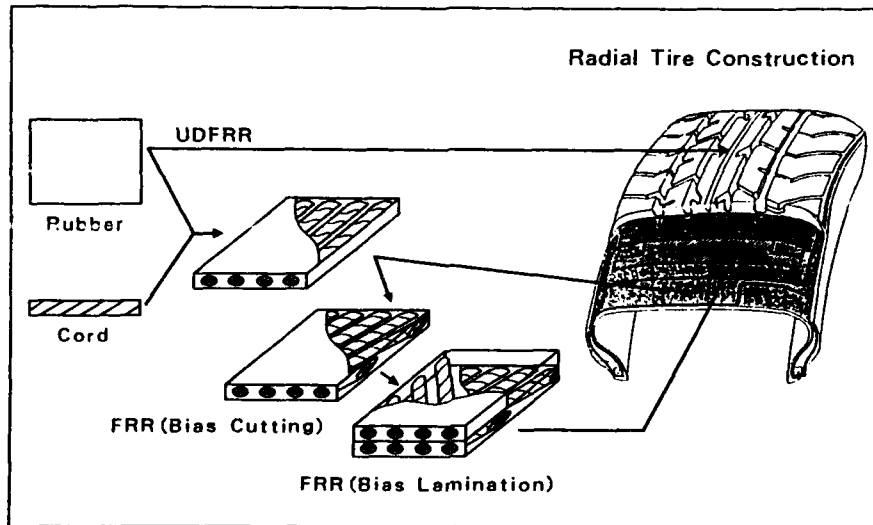
Fig. 1 FRR ; Component of tire construction

Figure 2 shows the relationship between the elastic modulus(E) and the tensile strength(σ_b) of some constituent materials for composites. It should be noted that in the case of FRR, the modulus of rubber matrix is extremely smaller than that of plastics and the modulus ratio of the cord to the rubber matrix becomes approximately up to 100 - 10000. The cord materials of nylon, polyester and steel wire, conventionally used in FRR, are originally twisted. The reason of this cord-twisting is as follows. As the cord modulus is too high, while FRR structures undertake usually large deformations, it is required to reduce the tensile and the bending stiffnesses of the cord to some extent by the cord-twisting process for arriving at high endurance property through improving the fatigue strength of the FRR structure.

Some analytical studies were given previously on the deformation of twisted wire ropes and cables [1] and continuous filament yarns [2] and so on. Recently, one of the present authors analyzed the torsional stiffness of a twisted cord having single or
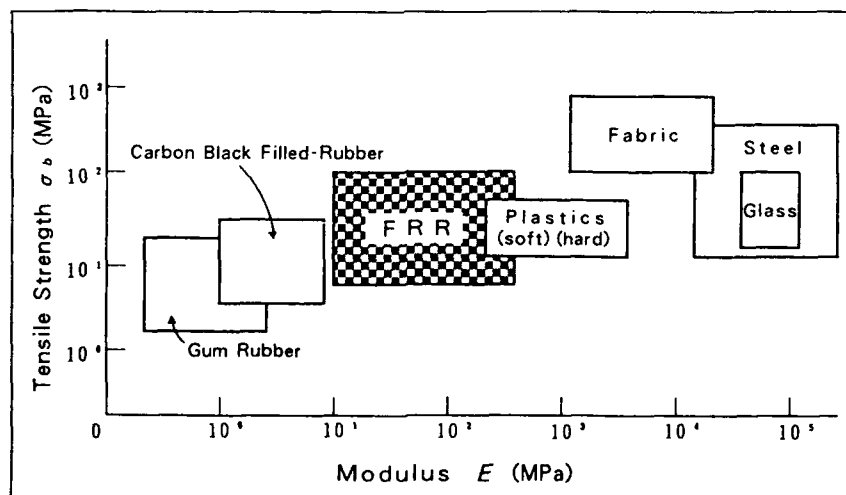
Fig. 2   Relationship between tensile strength and tensile modulus

double layers [3], predicting good agreement between the analytical and the experimental results. However, the extensional stiffness of the FRR column having a twisted cord has not yet been studied, although a lot of papers for the stress analysis of composite materials without considering the twisted cord effects [4]-[6] have been presented.

In this paper, the tensile modulus of a FRR column having a twisted cord is analyzed first by neglecting the rubber stiffness. Then, Finite Element Analysis(FEA) is conducted to estimate the tensile modulus by considering stresses and strains of both cord and rubber. Finally, the effects of pitch of a twisted cord and the rubber stiffness on the tensile modulus of FRR column are predicted.

ANALYSIS ON TENSILE MODULUS OF TWISTED CORD.

The contribution of a twisted cord on the tensile modulus of FRR column might be much larger than that of the rubber matrix. Simplifying the analysis, the FRR model is assumed to be made of only a twisted cord as shown in fig. 3. In this cord with the diameter, D, and the pitch length, p, each constituent filament has a helix angle θ to the axial direction, y.

The elastic modulus E_y of each constituent filament in the y direction can be given by

$$E_y = E_f \cos^4 \theta \tag{1}$$

where E_f is the Young's modulus of the filament. When we assume that a lot of filaments aggregate densely in a cord with a constant pitch length and the cross sectional area of each filament is infinitesimally small, the helix angle θ of the filament wound with radius r is given by

$$\tan \theta = \frac{2 \pi r}{p} \tag{2}$$
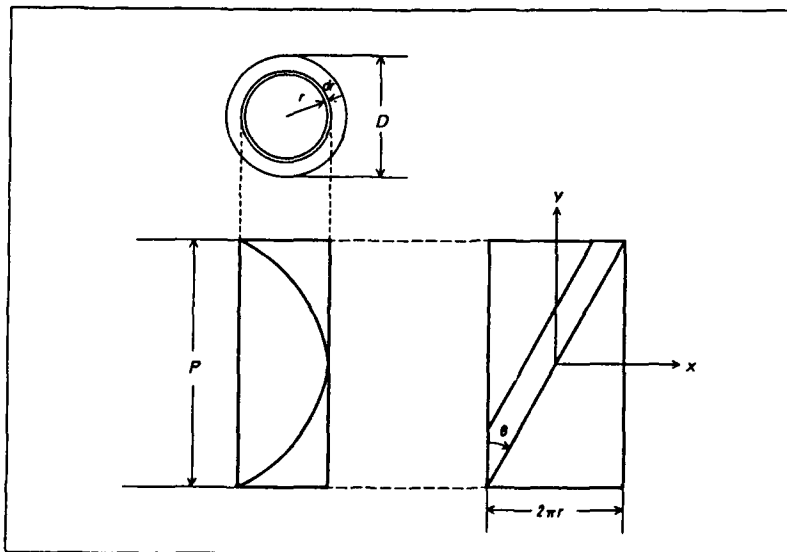
Fig. 3 Analytical model of twisted cord.

Since the total cross sectional area A is $\pi D^2/4$, the tensile modulus of twisted cord, E, is provided by

$$E = \frac{1}{A} \int_A E_r \, dA \tag{3}$$

Substituting Eq. (1) into Eq. (3), we have

$$E = \frac{1}{A} \int_A E_f \cos^4\theta \, dA \tag{4}$$

Then, considering the following relations

$$\begin{cases} \cos^2\theta = \dfrac{1}{1 + \tan^2\theta} = \dfrac{p^2}{p^2 + 4\pi^2 r^2} \\[2mm] dA = 2\pi r \, dr \end{cases} \tag{5}$$

we obtain

$$E = E_f \cos^2\bar{\theta} = \frac{E_f}{1 + \tan^2\bar{\theta}} = \frac{E_f}{1 + \dfrac{\pi^2 D^2}{p^2}} \tag{6}$$

where $\bar{\theta}$ denotes the helix angle of the outermost filament.   This equation indicates that the modulus of E relates not only to the filament modulus of E_f, but also to the diameter D and the pitch length p.   Then, we find that the modulus of the twisted cord increases with the increase of pitch length and decreases with the increase of the diameter.   These qualitative tendency coincides well with our experimental results. It should be mentioned here that Eq. (6) is the same as that given in references of [2] and [7].

FINITE ELEMENT ANALYSIS FOR FRR COLUMN WITH TWISTED CORD

Finite element analysis is conducted for a FRR column with a twisted cord under the axial tension as shown in Fig. 4.   This cord has the dimension of $(1\times5\times0.25)$,
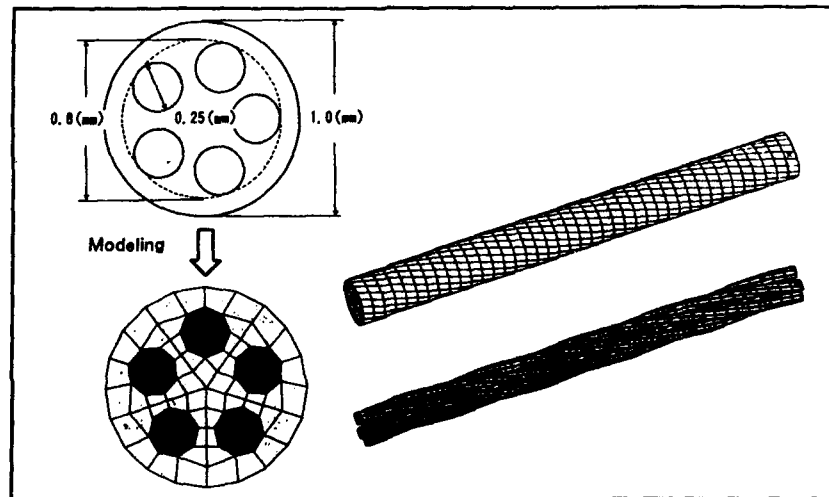
Fig. 4   FE Model of FRR column

which is made of one strand of five steel filaments of diameter 0.25 ㎜. The finite element model is divided into so many small elements for each filament and rubber matrix as shown in Fig. 4.

The details of the finite element model are as follows;

(1) Number of elements : 3000, Number of nodes : 3526

(2) Material properties : For the steel filament; $E_f = 180$ GPa and Poisson's ratio $\nu_f = 0.33$, and for rubber matrix; $C_1 = E_R / 6$, $C_2 = 0$ (Mooney - Rivlin material)

(3) Boundary conditions : For the face of one edge; the center node is fixed perfectly while the other each node is set free in the face plane.
For the other edge face; all nodes have displacements in the longitudinal direction where the center node is fixed only in the face plane and the other each node is set free in all direction.

(4) Solver : ABAQUS

(5) Element : For the twisted cord; an element of C3D8 (8 node, linear displacement brick) is used, while for the rubber; an element of C3D8H (8 node, liner displacement, constant pressure brick) is used.

Parametric studies are conducted by using this model, resulting in the stress and strain curves for the following parameters.

Pitch length : 5, 7.5, 10(control) and 15 ㎜
Rubber modulus : 1, 5, 10(control), 15, 50 and 100 MPa

CALCULATED RESULTS

Effect of Pitch Length on Tensile Modulus of FRR Column

Figure 5 shows the stress-strain curves for each pitch length obtained from FEA, where the stress is defined by dividing the total tensile force with the cross sectional
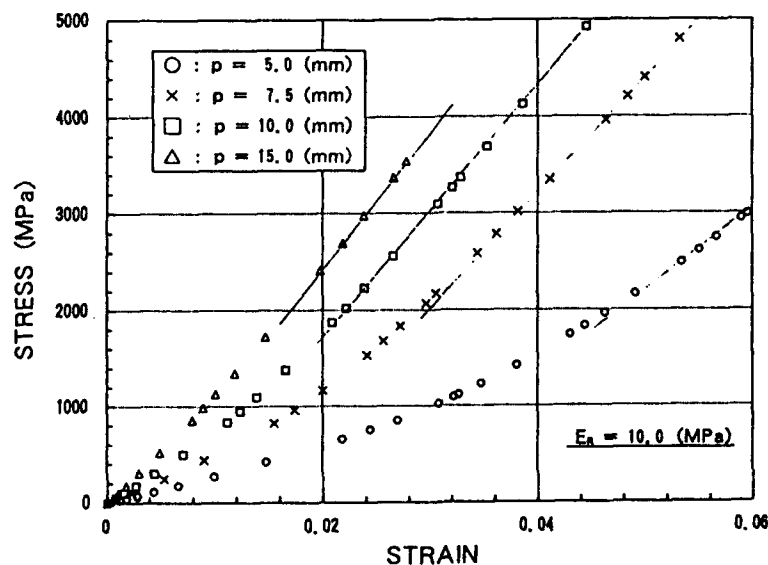
Fig. 5　Stress ~ Strain curves with variation of pitch length
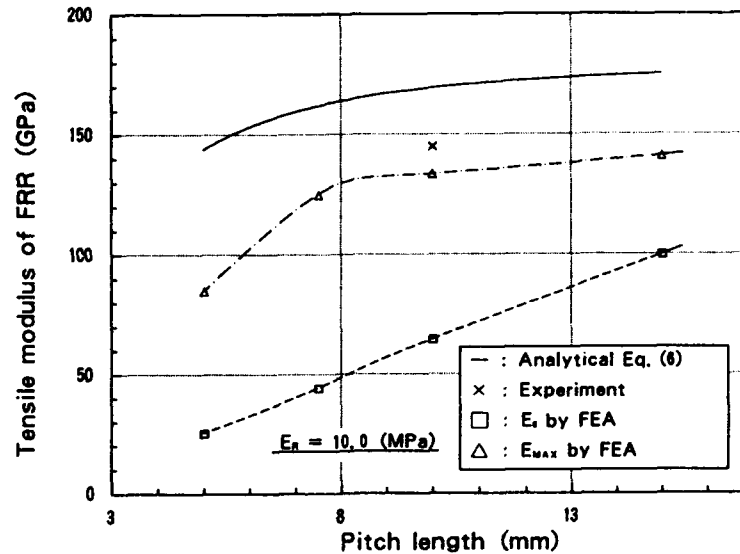
Fig. 6   Relationship between tensile modulus of FRR column and pitch length of twisted cord (analytial, FEA, and experimental Results)

area of a twisted cord.   It is seen from this figure that the slope of these stress-strain curves increases as the pitch length increases, and is lower in the vicinity of zero strain but becomes higher linearly in the large strain range over 0.02.   For convenience, E_0 is defined as the slope at zero strain and E_{MAX} is defined as the maximum slope in large strain range over 0.02.

Figure 6 shows the relationship between the tensile modulus of FRR column and the pitch length.   It is evident that E_0 increases linearly with the increases of the pitch length, while E_{MAX} increases linearly also up to the pitch length of 7.5 ■■ but turns to be flat over there.   The analytical result of Eq. (6) has a similar tendency to
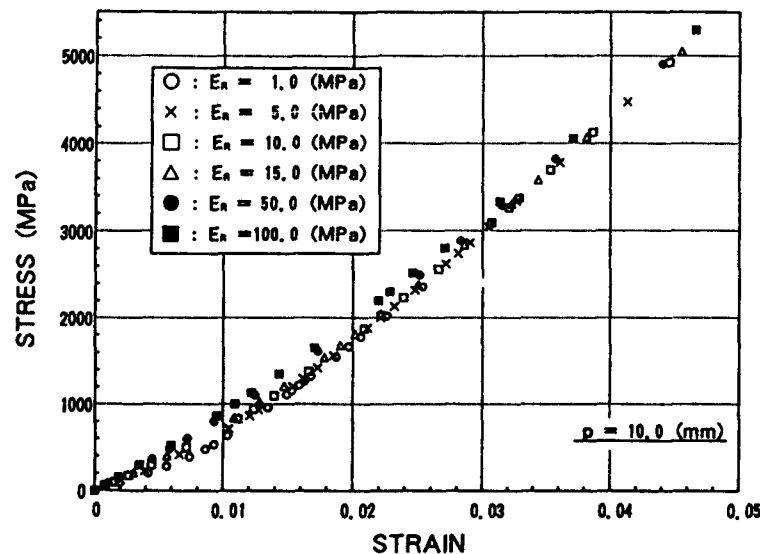
Fig. 7   Stress ~ strain curves with variation of rubber modulus
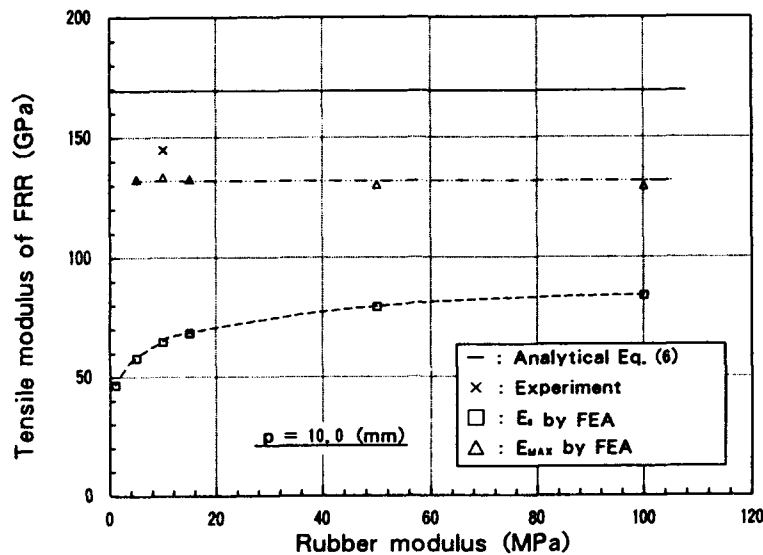
Fig. 8 Relationship between tensile modulus of FRR column and rubber modulus (analytial, FEA, and experimental results)

the FEA result for E_{MAX} but is somewhat larger than that presumably because the analytical result is based on the assumption of rubber matrix being ignored. The symbol (x) shows an experimental result, which is located inbetween the analytical and FEA curves.

Effect of Rubber on Tensile Modulus of FRR Column

Figure 7 shows the stress-strain curves of the FRR column obtained by FEA for various rubber moduli. In this figure, the differences among these curves are so small that the effect of rubber modulus on the modulus of FRR column might be ignored. However, inspecting in details of this figure, the rubber effects on the FRR modulus are slightly larger in the small strain range up to 0.02 than in the large strain range over 0.02.

Figure 8 shows a relationship between the FRR modulus and the rubber modulus, predicting that E_0 increases with the increase of rubber modulus approaching a constant value, while E_{MAX} remains constant independently of the rubber modulus as seen in Fig. 8.

Stress Contours for Twisted Cord and Rubber

Figures 9 and 10 illustrate the stress contours for the twisted cord and the rubber matrix of a FRR column under the longitudinal strain of 0.02 respectively, where the stress intensity is taken as the so-called Mises'es stress.

Figure 9 shows the stress concentration at the inside part of each filament, which exhibits a similar stress behavior to that of a coil spring under axial tension.
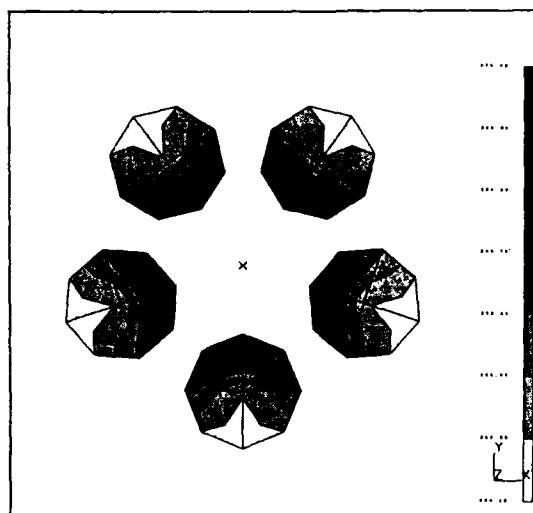
Fig. 9   Stress contour for twiested cord
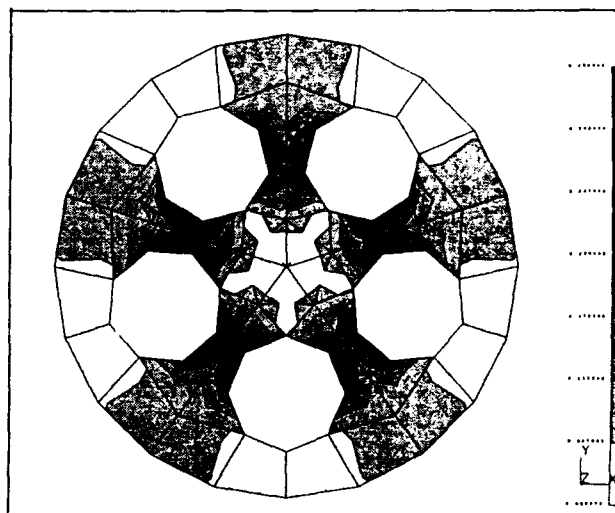
Fig. 10   Stress contour for rubber

Figure 10 also shows the stress concentration occuring in the rubber matrix along the boundary contacting with each filament in the narrowest band area, where the largest compressive stress could be expected due to the squeezing action of filaments under axial tension.

CONCLUSIONS

Some concluding remarks are listed below.
(1) A good correlation is obtained among the analytical, the FEA and the experimental results on the tensile modulus of a FRR column with a twisted cord.
(2) The tensile modulus of the FRR column increases with the increase of the pitch length.
(3) The effect of rubber matrix on the tensile modulus of the FRR column is very small as predicted by FEA.
(4) The stress concentration occurs at the inside part of each filament in the twisted cord.
(5) The stress concentration also occurs in the rubber matrix along the boundary contacting with each filaments in the narrowest band area.

REFERENCE

1. Ohwada, S., 1955. "Reseach on the Mechanical Properties of Twisted Wire Ropes or Cables" Report of the Institute of Industrial Science Univesrity of Tokyo, 4 (6): 238—282.

2. Hearle, J. W. S., P. Grosberg, and S. Backer, 1969. Structual Mechanics of Fibers, Yarns, and Fabrics, Wiley-Interscience, 175—212.

3. Akasaka, T., M. Katoh and A. Noda, 1988. "Torsional Stiffness of Steel Cords" Journal of the Japan Society for Composite Materials, 14(6):228-232.

4. Ishikawa, T. and S. Kobayashi, 1976. "Stress Analysis of Unidirectional Fiber-Reinforced Composites, Part I. Langitudinal Shear Loads" Journal of the Japan Society for Compsite Materials, 2(3):126-132.

5. Ishikawa, T. and S. Kobayashi, 1977. "Stress Analysis of Unidirectional Fiber-Reinforced Composites, Part II. Transverse Loads" Journal of the Japan Society for Composite Materials, 3(4):141-148.

6. Takahashi, K and T. Hisayama, 1989. "Analysis of the Interfacial Slippage and Transverse Stress Distriction of Unidirectional Fiber Composite" Journal of the Japan Society for Composite Materials. 15(2):78-84.

7. Clark, S. K., 1971, Mechanics of Pneumatic Tires, National Bureau of Standards Monograph 122, 117-120.

Finite Element Analysis of Rayleigh/Lamb-Type Channel Waves in Sandwich Plates

HIDEHITO OKUMURA

ABSTRACT

A finite element analysis of channel waves(guided waves) for sandwich plates is presented. The Rayleigh/Lamb type channel waves propagating along layers with lower velocity in laminate construction are higher order waves in general and have dispersive characteristic.

It is shown that a characteristic matrix equation obtained using finite element formulation based on the principle of virtual work can be solved for the complex eigenvalue problem of Rayleigh/Lamb type waves.

Verifications of this formulation and the computer code are shown through the problem of a multiple laminated medium. The results of the computational analysis for the Rayleigh type wave were good agreement with the analytical values by the Haskel's method presented in the literature. From the results of the finite element analysis of the Lamb type waves for sandwich plates, it was clear that the channel wave propagating along sandwich core existed even at a fundamental frequency owing to low rigidity of core and its large volume fraction in sandwich plate.

And also for the time harmonic problem of sandwich plate with adhesive layers, existence of Stonley wave travelling along the interface of two dissimilar materials was confirmed for the first time in the finite element eigenvalue problem. Amplitudes of this wave decrease with distance from the interface.

Since the channel wave motions are generally higher order modes of propagation, analyses of the channel wave using the computational simulation are expected to estimate the dynamic strength of sandwich plates.

Hidehito Okumura, National Aerospace Laboratory,
7 - 44 - 1 Jindaiji - Higashi Machi, Chofu-Shi, Tokyo
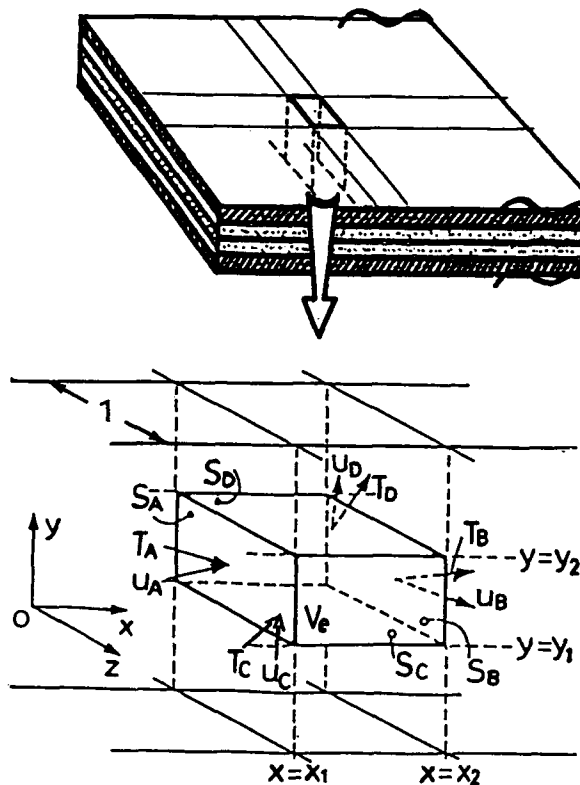
Figure 1. A laminated plate.
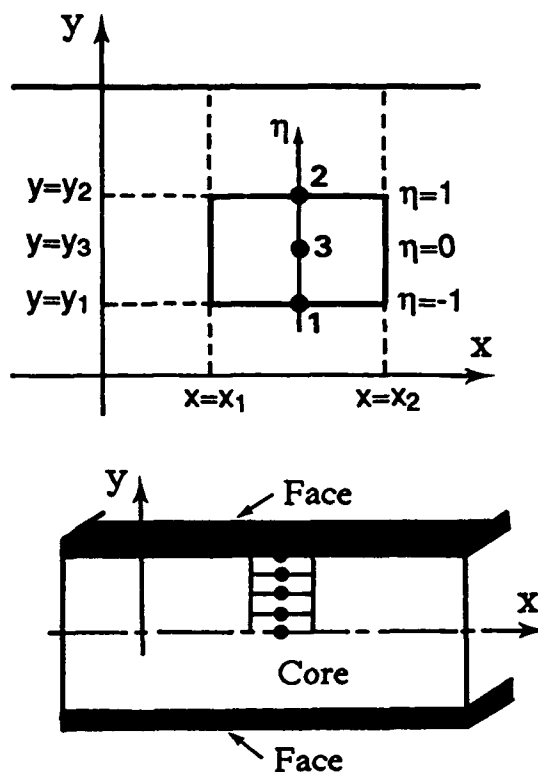
Figure 2. A finite element and
a sandwich plate.

INTRODUCTION

Dynamic analysis is one of the most important problems in composite structure designs.

The subjects of elastic wave propagation in layered media has been treated in geophysics and the Lg and Rg waves,called guided wave, are described by Ewing and Jardetzky [1]. Finite element analysis for Rayleigh waves has been given by Lysmer [2]. In this literature lumped mass method and an asymptotical approach in the horizontal direction were used.

On the other hand,the characteristic matrix equation for Saint-Venant end effects has been obtained using finite element formulation based on the principle of virtual work by Okumura et. al. [3]. Furthermore, this formulation has been extended to treat the time harmonic motion of the Rayleigh - Lamb type channel wave (guided wave), which is higher order wave and propagates in laminate media by Okumura and Ohtake [4].

In this paper the analysis of the Rayleigh/Lamb type channel wave is applied

for sandwich plates.   Firstly the verification of the finite element analysis program is carried out through computational studies of a multiple laminated media.   Secondly this paper treats the channel wave propagating along a sandwich core.   Finally the channel wave travelling along the interface between two different materials are considered.

Analysis of the channel wave is important in relation to the estimation of the dynamic strength of laminated composite materials; therefore, computer simulation is very efficient to study the motion for the channel waves.

FINITE ELEMENT APPROACH

Fig. 1 shows a rectangular region Ve whose range is x1 to x2 and y1 to y2 in a infinite elastic plate. For plane problems the virtual work principle [5] to the region Ve is expressed as

$$\int_{x_1}^{x_2} \int_{y_1}^{y_2} \sigma_{ij}\delta\epsilon_{ij} dxdy = \int_{x_1}^{x_2} \int_{y_1}^{y_2} F_i\delta u_i dxdy + \int_S T_i\delta u_i ds \qquad (1)$$

In this analysis a rectangular element with two to three variable nodes as shown in Fig.2 is used. The displacement field inside the element is assumed to be as

$$u(x,y) = \exp i(\omega t - kx)\, \overline{u}(y) = \exp(i\omega t - \lambda x)[H]\{\overline{u}_{node}\} \qquad (2)$$

where

$$u^T(x,y) = [u(x,y),v(x,y)]\quad,\overline{u}^T(y) = [\overline{u}(y),\overline{v}(y)]\quad,$$

$$[H] = \begin{bmatrix} H_1 & 0 & H_2 & 0 & H_3 & 0 \\ 0 & H_1 & 0 & H_2 & 0 & H_3 \end{bmatrix},$$

$$H_1 = \frac{1}{2}\eta(-1 + \eta),\ H_2 = \frac{1}{2}\eta(1 + \eta),\ H_3 = (1 - \eta)(1 + \eta)$$

$$\{\overline{u}_{node}\}^T = [\overline{u}_1\overline{v}_1\overline{u}_2\overline{v}_2\overline{u}_3\overline{v}_3],\ \lambda = ik \qquad (3)$$

and i is the imaginary unit, $\sqrt{-1}$, ω and k are an angular frequency and a wave number, respectively.

Following the ordinary manner in the finite element method using the strain-displacement relation   and the stress-strain relationship, the overall structural equation is given as follows

$$\{\lambda^2 [A] + \lambda [B] + [C] - \omega^2 [M]\}\{\overline{U}\} = 0 \qquad (4)$$
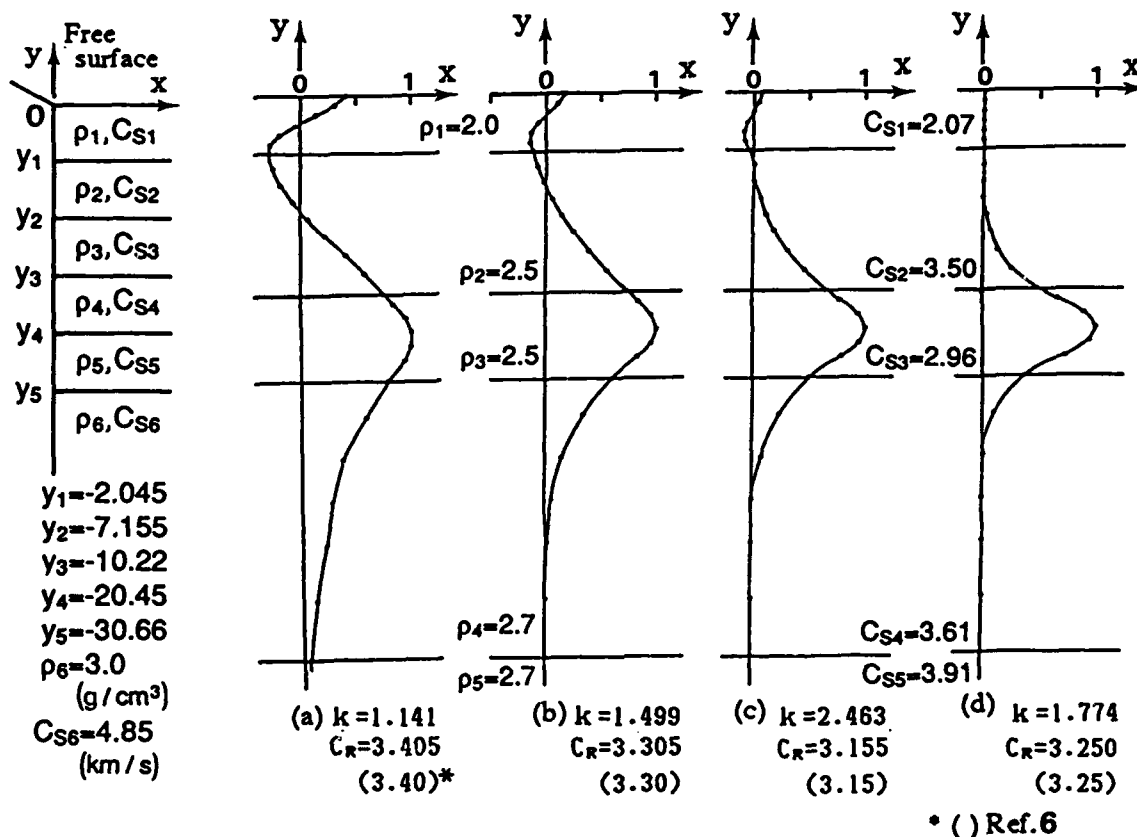
Figure 3. The third mode of vertical displacement.

This matrix equation indicates the relation of k and ω , and can be solved using either of two method. One is a transformation method into the standard eigenvalue problem yields solutions for any value of the angular frequency. Another is the complex standard eigenvalue problem yields solutions for any value of the wave number.

NUMERICAL EXAMPLES

A computer program was developed to evaluate dispersion relations of harmonic motions for the Rayleigh/Lamb type waves propagating in laminated plates. For verification of the finite element formulation and computer code, the problem of channel wave propagating in multilayered media with low velocity layers is considered.

Construction of layers and material properties are shown in Fig.3. All layers have the same poisson's ratio of 0.25. There are two layers, the first and the third one, which shear wave speed are lower than other layers.
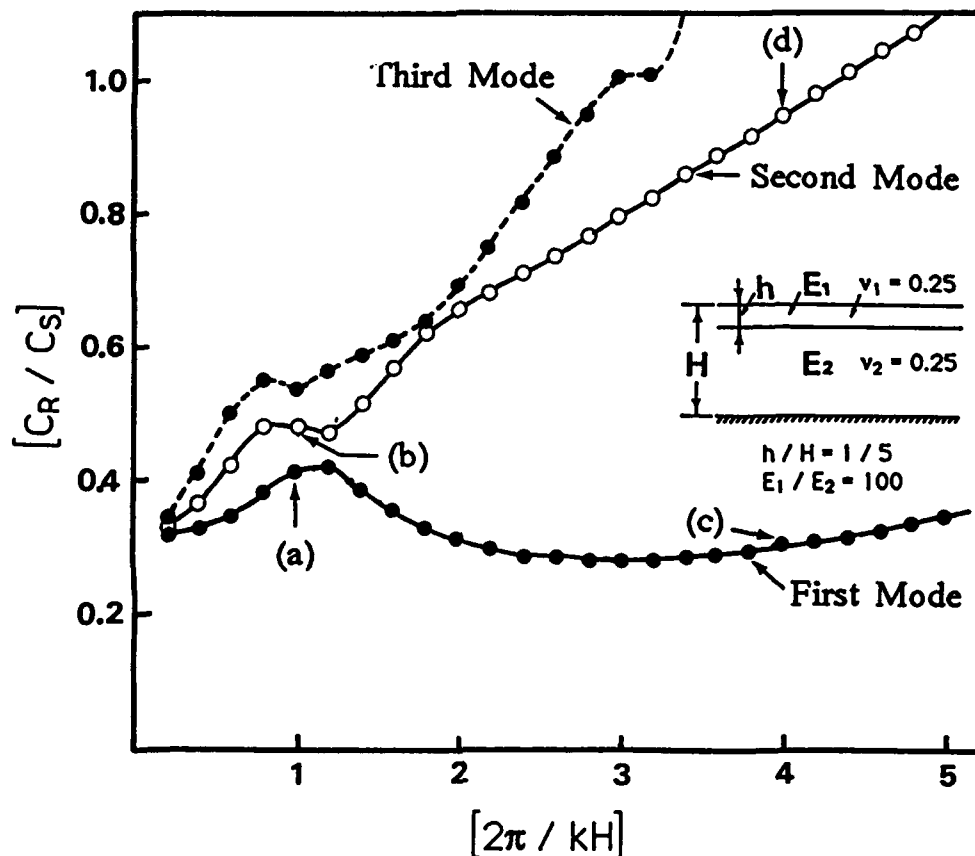
Figure 4. Variation of phase velocity with wave number.

Fig.3 shows the third eigenvalues and the corresponded vertical displacement modes.   The values in parentheses are obtained by Sato [6] using the method of Haskel.   From Fig.3 (c) and (d) It is found that the vertical displacements are concentrated in the third layer and these mode are equivalent to channel wave behaviour.

Secondly the case of two layered media on a rigid base (a half upper part of sandwich plate) is studied.   The analytical region is divided into 40 linear elements (include 8 elements in the surface layer) using the fixed displacement condition at the bottom node.   Material properties and dispersion curves of the three lowest modes are shown in Fig.4.

Fig.5 shows the displacement mode of propagation.   Fig.5 (a),(b),(c),and (d) correspond to the point (a),(b),(c) and (d) indicated in Fig.4, respectively. From Fig.5   it is understood that there will be a tendency for displacements to concentrate in the zone of the sandwich core with lower velocity.

Finally the problem of Lamb wave propagating on a sandwich plate (Fig.6) composed of three dissimilar isotropic materials is considered.   Material properties and construction of layer are shown in Fig.6.   A half upper region

(a) First Mode   (b) Second Mode   (c) First Mode   (d) Second Mode

$[2\pi / kH = 1]$ $[2\pi / kH = 1]$ $[2\pi / kH = 4]$ $[2\pi / kH = 4]$

Figure 5. Displacement modes.   —— u , ---- v
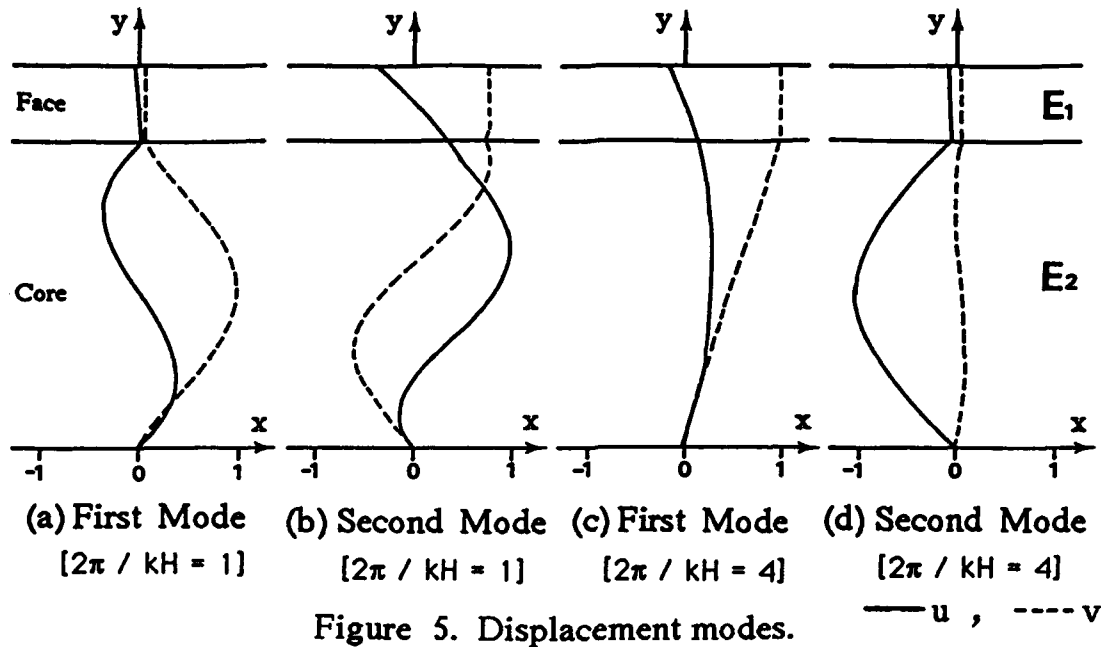
is divided into 38 linear elements (include 13 elements in face layer and 4 elements in adhesive layer). The displacement condition on the neutral axis of sandwich plate is u=0. This condition is equivalent to the antisymmetric mode (SV wave).

Fig.7 shows the vertical displacement modes for the fundamental frequency. From Fig.7 (d) it is found that existence of Stonley wave propagating along the interface of two dissimilar materials is confirmed.

Fig.8 shows the strain and the stress modes for Fig.7 (d).   Interlaminar stress and strain for the antisymmetric mode are concentrated in the vicinity of the interface between adhesive layer and sandwich core. These stresses are related with delamination induced by dynamic loadings.

CONCLUSION

The results of the computational analysis for Rayleigh/Lamb type channel waves (guided waves) propagating in sandwich plates are summarized :

(1) The computational results for the Rayleigh type waves propagating in a multilayered media with two low velocity layers were good agreement with the analytical values by the Haskel's method in the literature. It was found that the vertical displacement for third mode was concentrated in the one layer of lower velocity in laminate construction and this mode was equivalent to a channel wave behaviour.   And also it was clear that the Rayleigh type channel waves have dispersive characteristic and exist at higher order mode in general.
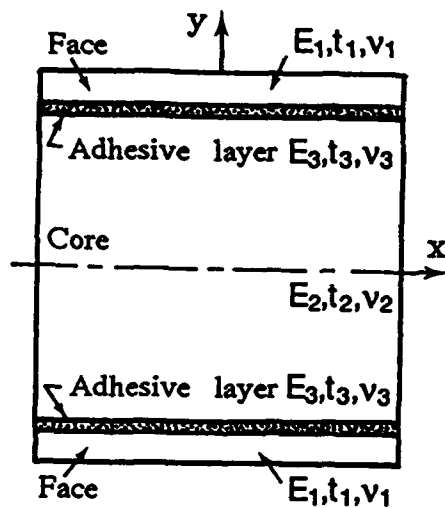
$E_1 / E_2 = 100$, $E_1 / E_3 = 200$
$t_1 / t_2 = 1 / 5$, $t_1 / t_3 = 4$
$v_1 = v_2 = 0.25$, $v_3 = 0.35$

Figure 6. A sandwich plate
with adhesive layers.
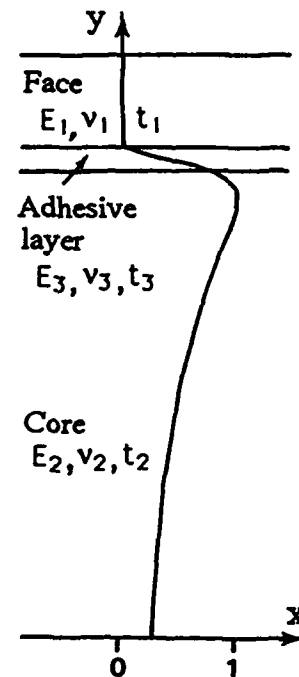
(a) k~4.19
C/Cs~0.389
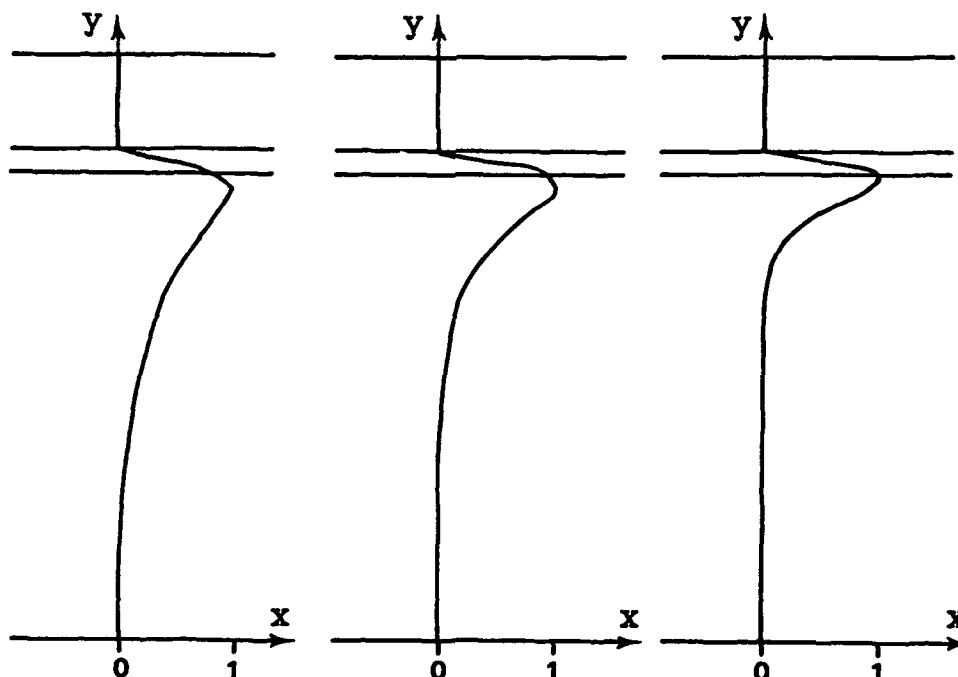
(b) k~5.03
C/Cs~0.315

(c) k~6.28
C/Cs~0.314

(d) k~8.38
C/Cs~0.311

Figure 7. Vertical displacement modes $Cs = \sqrt{G_1 / \rho_1}$
for the fundamental frequency.

140

Figure 8. Strain and stress modes.

(2) It was clear that the displacement modes of the channel waves propagating in sandwich plate were concentrated in the region of lower velocity, i.e. sandwich core. Although the channel wave motions are generally higher order modes of propagation, it was found that the channel wave travelling along sandwich core existed even at a fundamental frequency owing to low rigidity of core and its large volume fraction in sandwich plate. It is necessary to analyze these guided waves for the accurate estimation of dynamic strength of sandwich plates.

(3) It was found that Stonley waves propagating along the interface of two different materials existed in the region between adhesive layer and sandwich core. Amplitudes of this wave decrease with distance from the interface. It was understood that the interlaminar shearing stress and strain for the Stonley wave were concentrated in the vicinity of the interface. The delamination of laminated composite plates are related to the Stonley wave in

dynamic problems. It is expected to estimate the stacking sequences position of delamination in laminated composite materials subjected to the transient dynamic loading using the computational results of the channel waves.

REFERENCES

1. Ewing, W.M., W. Jardetzky and F. Press. 1957. Elastic Waves in Layered Media : McGraw - Hill, New York, pp. 219 - 222.
2. Lysmer, J.. 1970. "Lumped Mass Method for Rayleigh Waves. " Bulletin of the Seismological Society of America, 60 (1), 89.
3. Okumura, H., K. Watanabe and Y. Yamada. 1985. "Finite - Element Analyses of Saint - Venant End Effects for Composite Materials," in Recent Advances in COMPOSITES United States and Japan, ASTM STP 864, J.R. Vinson and M.Taya, ed., pp. 225 - 235.
4. Okumura, H. and K. Ohtake. 1991. "Finite Element Analysis of Channel Waves in Laminated Materials, " in COMPOSITES Design, Manufacture, and Application , Proceedings of the Eighth International Conference on Composite Materials (ICCM/8), S. W. Tsai and G. S. Springer, ed., pp. 1-O-1 - 1-O-8.
5. Washizu, K.. 1968. Variational Method in Elasticity and Plasticity : Pergamon Press, Oxford, pp. 13 - 17.
6. Sato, Y.. 1978. Dansei Hadou Ron (in Japanes) : Iwanami Shoten, pp. 125 - 128.
7. Achenbach, J. D.. 1973. Wave Propagation in Elastic Solids : NORTH - HOLLAND, pp. 194 - 195.

Singular Stress Distribution of Fiber Reinforced Elastomer Strip under Axial Tension

NARUHISA MONDEN AND TAKASHI AKASAKA

ABSTRACT

Discontinuous and concentrated stress distribution in a laminated-biased, steel-cord-reinforced rubber plate of rectangular shape subjected to axial tension, was found previously by one of the present authors through an analysis by the use of the cord-inextensibility theory.

In order to examine the validity of the assumption of cord inextensibility made for cord-rubber composites and to study how the stress distribution mode would change from singular to regular due to the variance of matrix stiffness, we analyzed the same problem by using two dimensional finite element method for some cases with different matrices of soft rubber, hard rubber and plastics, considering the steel cord being extensible. The calculated results for stress and strain distributions agreed well with that of the cord-inextensibility theory for the case of soft rubber matrix. However, for the other cases these distributions transffered to continuous behavior and at last arrived at a completely uniform mode without stress concentration. These drastic changes in stress distribution would be deeply related to the variance of governing equation from the hyperbolic to the elliptic type.

INTRODUCTION

A laminated-biased-cord-reinforced rubber strip is a representative of the tire belt structure which is always subjected to tensile force due to inflation pressure. One of the present authors analyzed previously the stress distribution of a rectangular belt structure, having a special length/width ratio characterized by the cord angle, under an axial tension which is applied directly to the both rigid end plates of the belt structure. He found that the stress distribution in each subdomain divided by a pair of characteristic cords started from the corners of rigid end plates becomes uniform but different with each other. The discontinuous stress distribution was elucidated by the existence of strongly concentrated tensile forces carried by characteristic cords which were assumed to be in-extensible.

Naruhisa Monden, Yokohama Rubber Co., 2-1 Oiwake, Hiratsuka-shi, Kanagawa-ken 254, Japan.

Takashi Akasaka, Department of Precision Mechanics, Faculty of Science and Engineering, Chuo University, 1-13-27 Kasuga, Bunkyo-ku, Tokyo 112, Japan.

However, the stress distribution of a laminated biased composite strip consisted of extensible cords and various high-polymer matrices could be expected to transfer gradually from discontinuous to continuous by changing the matrix stiffness larger than that of rubber and at last to arrive at a uniform distribution as seen in FRP strip.

In this paper, we analyzed the stress and strain distributions of a laminated-biased composite strip under axial tension via rigid end plates, by using the two dimensional finite element method.   In this analysis, the length/width ratios of the composite strip were adopted as 2cotα, 2.5cotα and 4cotα, where α is the bias angle, and the tensile stiffness of matrices were varied systematically covering FRR (Fiber Reinforced Rubber) and FRP (Fiber Reinforced Plastics).

ANALYSIS ON FRR COMPOSITES

FUNDAMENTAL EQUATION

Figure 1 shows a laminated-biased composite strip having a length/width ratio of 2cotα, where x and y denote the orthogonal coordinate axes established in the directions bisecting the cord crossing angle, 2α.
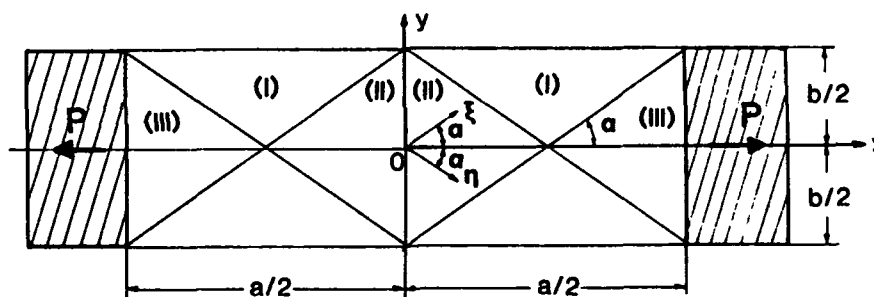
Fig. 1.   A laminated-biased composite strip with length/width ratio of
2cot α, under tensile force, P, via rigid end plates

The compatibility equation for the stress function, $F(x, y)$, of the orthotropic plate is given by

$$\left(\frac{\partial^4}{\partial x^4} + 2A \frac{\partial^4}{\partial x^2 \partial y^2} + B^2 \frac{\partial^4}{\partial y^4} \right) F = 0$$

(1)

where

$$A = \frac{E_y}{2G_{xy}} - v_y$$

$$B = \sqrt{E_y / E_x}$$

(2)

E_x, E_y denote Young's moduli, v_x, v_y are Poisson's ratios and G_{xy} is shear modulus of the

orthotropic plate. It should be noticed here that Maxwell-Betti's reciprocal theorem, $E_x/E_y = v_x/v_y$, is given.

The differential equation (1) can be converted to a factorized form as

$$\left(\frac{\partial^2}{\partial x^2} - \kappa_1 \frac{\partial^2}{\partial y^2}\right)\left(\frac{\partial^2}{\partial x^2} - \kappa_2 \frac{\partial^2}{\partial y^2}\right)F = 0 \tag{3}$$

where

$$\kappa_1, \kappa_2 = -A \pm \sqrt{A^2 - B^2} \tag{4}$$

Coefficients of κ_1 and κ_2 could be real when $A^2 > B^2$, and they are both negative if A is positive, but both positive if A is negative. Then Eq. (1) becomes an elliptic type and a hyperbolic type, in the respective cases. The other case where $A^2 < B^2$, leads to κ_1 and κ_2 being not real, therefore Eq. (1) could be called as mixed type. These types of Eq. (1) are classified by values of A and B as depicted in Fig. 2, where three regions of elliptic, hyperbolic and mixed types are divided by two lines of $A = B$ and $A = -B$. In Fig. 2, the line of $B = 1$ signifies the tetragonal orthotropy, because of $E_x = E_y$, and the point, P, corresponds to isotropy, because its coordinates of $A = B = 1$ are obtained from

$$E_x = E_y \equiv E , \quad v_x = v_y \equiv v$$

$$G_{xy} = E/2(1 + v) \tag{5}$$

Furthermore, taking the elastic constants of a laminated-biased composite with in-extensible cords as given by

Fig. 2. Three domains of elliptic, hyperbolic and mixed type of orthotropy in A – B plane

$$E_x = E_T (1 - \cot^2\alpha + \cot^4\alpha) , \quad v_x = \cot^2\alpha$$

$$E_y = E_T (1 - \tan^2\alpha + \tan^4\alpha) , \quad v_y = \tan^2\alpha \tag{6}$$

$$G_{xy} = \infty$$

We obtain $A = -\tan^2\alpha$ and $B = \tan^2\alpha$ from Eq. (2), then we have $A + B = 0$, which coincides with a border line of OQ, where points of O and Q correspond to cases of $\alpha = 0$ and 45 degrees respectively. Then, we acquire the following differential equation as

$$\left(\frac{\partial^2}{\partial x^2} - \tan^2\alpha \frac{\partial^2}{\partial y^2}\right)^2 F = 0 \tag{7}$$

for the stress function, $F(x,y)$, as a particular case of Eq. (1) which could be denoted by

bi-hyperbolic type. Almost all wooden plates (oak, beech, birch, pine and spruce etc.) have elliptic type orthotropy as depicted in Fig. 2, while conventional FRP laminates have elliptic and, or mixed types of orthotropy according to the combination of fiber orientations.

Considering the extensibility of cord fibers, shear modulus of G_{xy} is represented by

$$G_{xy} = \frac{1}{4} (E_L \sin^2 2\alpha + E_T \cos^2 2\alpha) \tag{8}$$

and thus we obtain

$$A = \frac{2E_T (1 - \tan^2\alpha + \tan^4\alpha)}{E_L \sin^2 2\alpha + E_T \cos^2 2\alpha} - \tan^2\alpha \tag{9}$$

where E_L and E_T denote Young's moduli of the constituent layer in the cord fiber and its perpendicular directions respectively. An example of correlated curve for a definite value of stiffness ratio, $E_T/E_L = 0.08$, is illustrated by a broken curve in Fig. 2 by taking α as a parameter. This curve predicts that the orthotropy of FRR strip could be changeable from bi-hyperbolic, type to elliptic type via mixed type by adopting appropriate values of bias angle and the stiffness ratio of E_T/E_L. Since the analysis on stress and deformation of such a composite strip covering various types of orthotropy is difficult, the finite element method is preferable to use.

CORD INEXTENSIBILITY THEORY AND CHARACTERISTIC CORD

The general solution of Eq. (7) can be obtained as

$$F = \xi f_1(\eta) + \eta f_2(\xi) + g_1(\eta) + g_2(\xi) \tag{10}$$

where

$$x + \lambda y = \xi, \quad x - \lambda y = \eta$$

$$\lambda = \cot \alpha \tag{11}$$

and f_1, f_2, g_1, g_2 are arbitrary functions.

Then, we have following representations for stress components.

$$\sigma_x = \frac{\partial^2 F}{\partial y^2} = \lambda^2 \left[\xi f_1''(\eta) + \eta f_2''(\xi) - 2 f_1'(\eta) - 2 f_2'(\xi) + g_1''(\eta) + g_2''(\xi) \right]$$

$$\sigma_y = \frac{\partial^2 F}{\partial x^2} = \xi f_1''(\eta) + \eta f_2''(\xi) + 2 f_1'(\eta) + 2 f_2'(\xi) + g_1''(\eta) + g_2''(\xi) \tag{12}$$

$$\tau_{xy} = -\frac{\partial^2 F}{\partial x \partial y} = \lambda \left[\xi f_1''(\eta) - \eta f_2''(\xi) + g_1''(\eta) - g_2''(\xi) \right]$$

The displacement functions of u and v are solved as

$$u = -\frac{4\lambda^2}{E_x}\left[f_2(\xi) + f_1(\eta) \right]$$

$$v = \frac{4\lambda^3}{E_x}\left[f_2(\xi) - f_1(\eta) \right]$$

(13)

The basic equation of bi-hyperbolic type yields a pair of characteristic cords starting from the corners of rigid end plates as shown in Fig. 1 and partitioning the whole rectangular region into three kinds of subdomain, I, II and III. The equilibrium conditions among the characteristic cord tension N and the normal and shearing stresses σ_N, τ_N of the neighboring subdomains, I and II, are given by

$$\sigma_{NI} = \sigma_{NII}$$

$$(\tau_{NI} - \tau_{NII}) + \frac{dN}{ds} = 0$$

(14)

where s denotes the coordinate axis along the characteristic cord depicted in Fig. 3.

Stresses of σ_N and τ_N in these sub-domains partitioned by the characteristic cord, which is denoted by $\xi = \xi_0 = a/4$, are represented by
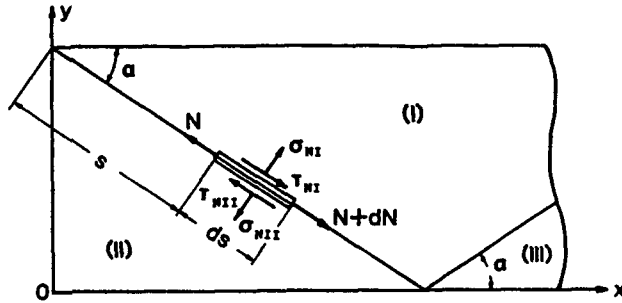
Fig. 3.   Tensile force N of a characteristic cord equilibrating with the shearing stresses in subdomains of I and II

$$\sigma_N = \sin^2 \alpha \left[\sigma_x + \lambda^2 \sigma_y + \lambda \tau_{xy} \right]$$

$$\tau_N = \sin^2 \alpha \left[\lambda (\sigma_x - \sigma_y) + (\lambda^2 - 1)\tau_{xy} \right]$$

(15)

Considering the following boundary conditions:

$$u = u_0, \quad v = 0 \qquad (\text{along } x = \pm a/2)$$

$$\sigma_y = \tau_{xy} = 0 \qquad (\text{along } y = \pm b/2)$$

(16)

We obtain expressions for displacement and stress components of each subdomain, as

$$\frac{u_I}{u_0} = \frac{1}{2} + \frac{2}{a}(x - \lambda y), \qquad \frac{v_I}{u_0} = \lambda\left[-\frac{1}{2} + \frac{2}{a}(x - \lambda y)\right]$$

$$\frac{u_{II}}{u_0} = \frac{4}{a}x, \qquad \frac{v_{II}}{u_0} = -\lambda^2\frac{4}{a}y$$

$$\frac{u_{III}}{u_0} \doteq 1, \qquad \frac{v_{III}}{u_0} = 0$$

(17)

$$\frac{\sigma_{xI}}{\sigma_0} = 1, \qquad \frac{\sigma_{yI}}{\sigma_0} = 0, \qquad \frac{\tau_{xyI}}{\sigma_0} = 0$$

$$\frac{\sigma_{xII}}{\sigma_0} = \frac{3}{2}, \qquad \frac{\sigma_{yII}}{\sigma_0} = -\frac{1}{2\lambda^2}, \qquad \frac{\tau_{xyII}}{\sigma_0} = 0 \tag{18}$$

$$\frac{\sigma_{xIII}}{\sigma_0} = \frac{1}{2}, \qquad \frac{\sigma_{yIII}}{\sigma_0} = \frac{1}{2\lambda^2}, \qquad \frac{\tau_{xyIII}}{\sigma_0} = 0$$

where $\pm u_0$ is the extensional displacement of the rigid end plates in x direction, and σ_0 is the tensile stress defined by

$$\sigma_0 = E_x \frac{2u_0}{a} = \frac{P}{1.5b} \tag{19}$$

The characteristic cord tension N is obtained from Eq. (14) as

$$N = \frac{\sigma_0}{2\lambda} s \tag{20}$$

FEM ANALYSIS

We conducted a FEM analysis for nine cases combined with three different dimensions listed in Table 1 and three different material constants listed in Table 2, by the use of MSC/NASTRAN. Numerical examples denoted by A, B and C having markedly different stiffnesses of matrices, represent FRR, soft FRP and FRP respectively.

TABLE 1   DIMENSIONS OF NUMERICAL EXAMPLE

	l(m)	b(m)	h(m)	α(deg.)	u_0(m)	$\varepsilon_0 = 2u_0/l$
(i)	$a = 0.3464$	0.1	4.0×10^{-3}	30.0	1.732×10^{-3}	0.01
(ii)	$1.25a$	0.1	4.0×10^{-3}	30.0	2.165×10^{-3}	0.01
(iii)	$2a$	0.1	4.0×10^{-3}	30.0	3.464×10^{-3}	0.01

TABLE 2   MATERIAL CONSTANTS OF NUMERICAL EXAMPLE

	E_f(GPa)	V_f	v_f	E_m(MPa)	v_m
(A)	2.0×10^2	0.5	0.3	5.0	0.5
(B)	2.0×10^2	0.5	0.3	2.5×10^2	0.4
(C)	2.0×10^2	0.5	0.3	3.0×10^3	0.3

Cases (i), (ii) and (iii) are only different in strip length. Considering the symmetry of the

problem with respect to x and y axes, we confined the analysis only to the first quadrant of the strip. Nodal points are taken as 861, 4141 and 3751 for (i), (ii) and (iii) cases respectively.

Figure 4 shows a divided element diagram for the case (i), where the figures attached to x axis denote the section number. Deformed behaviors of A type specimen under extension are illustrated in Figs. 5, 6 and 7 cases respectively. These figures exhibit the characteristic deformations having uniform but discontinuous strains in every divided regions, as predicted by the cord-inextensibility theory.
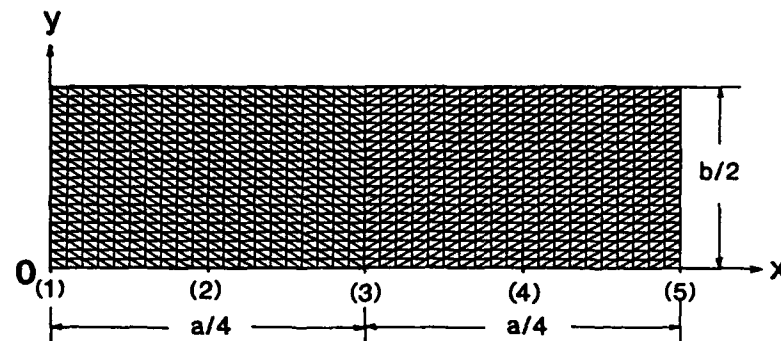
Fig. 4. Divided element diagram for the case (i)
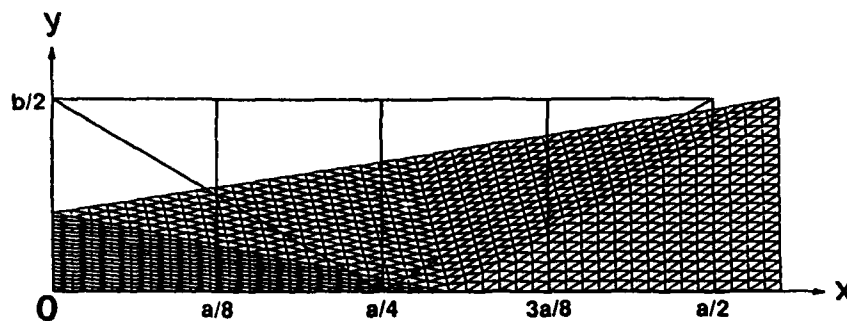
Fig. 5. Deformation of the specimen, A – (i), under extension
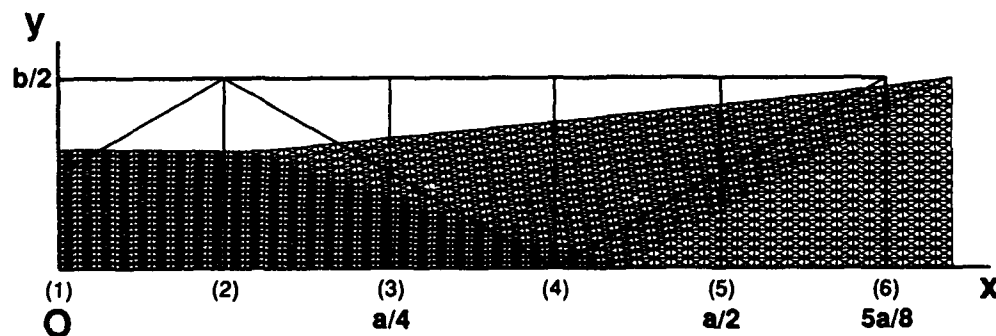
Fig. 6. Deformation of the specimen, A – (ii), under extension
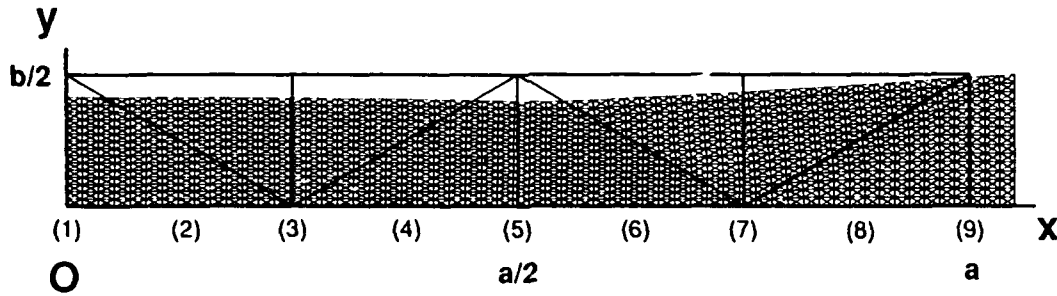
Fig. 7.   Deformation of the specimen, A - (iii), under extension

Figure 8 shows the distribution of the strain ε_x at the section 2 ($x = a/8$) depicted in Fig. 4, for the case of (i) with varying types of A, B and C, where the stepped curve exhibits $\varepsilon_{II}/\varepsilon_0$ = 2 and $\varepsilon_I/\varepsilon_0$ = 1, as given by Eq. (17).   The curve A follows well the stepped curve, while the curve C behaves like wholly uniform and the curve B takes an intermediate behavior between the two curves A and C.
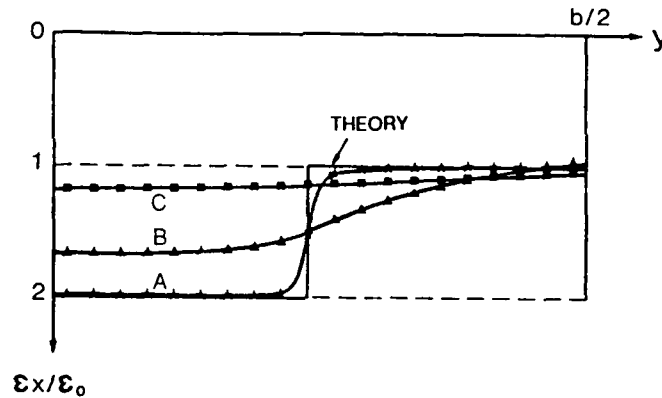
Fig. 8.   Distribution of ε_x at the cross section $x = a/8$, of the specimen (i), under extension with varying types of A, B and C, compared with the cord inextensibility theory

Figure 9 shows the distribution of tensile stress, σ_x, across the half width, at the cross section, $x = a/8$ of the specimen (i) with varying types of A, B and C, where the stepped curve exhibits σ_0 = 1.5, and σ_I/σ_0 = 1 as predicted by Eq. (18).   The curve A follows approximately the stepped curve, however has a peak value at the crossing point with the characteristic cords which is evidently due to dispersion of the concentrated cord tension.

The curve B becomes moderately smooth with attenuation of the peak value, while the curve C has a so uniform distribution as observed usually in FRP specimen.

The same tendencies in ε_x and σ_x distributions as above mentioned are confirmed by FEM results obtained for the other cases of (ii) and (iii).
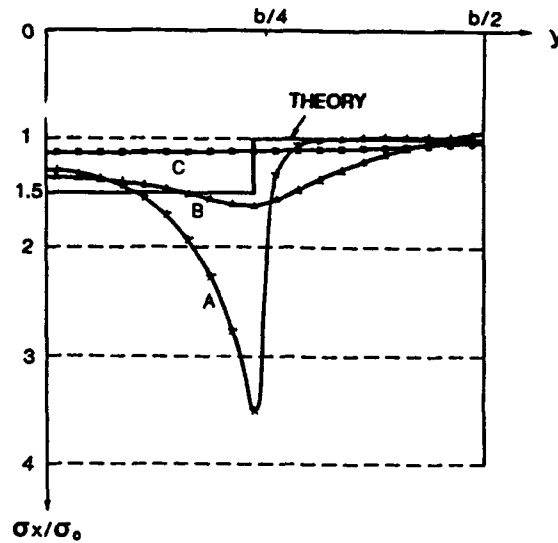
Fig. 9.   Distribution of σ_x at the cross section, $x = a/8$, of the specimen (i),
with varying types compared with the cord inextensibility theory

CONCLUSION

(1) The existence of characteristic cords and the discontinuous stress distribution in a laminated-biased FRR composite strip predicted by the cord inextensibility theory are confirmed by this FEM analysis.

(2) The transfer process that the effect of characteristic cords on the stress and strain distributions attenuates gradually by increasing matrix stiffness from rubber to plastics, is made clearly by the FEM analysis.   This process could be understood also as the type of orthotropy being transferred from bi-hyperbolic to elliptic.

(3) We could recognize through this analysis that the mechanical properties of FRR and FRP differ considerably.

REFERENCES

1. Akasaka, T. and Takagishi, T., 1959. "Experiment on Non-Uniform Stress Distribution of A Hyperbolic-Orthotropic Rectangular Plate under Extension".   Bull., Faculty of Engineering, Chuo University, B-6(12):1-18

Stress Analysis of Transverse Cracking in Cross-Ply Composite Laminates

F. G. YUAN* AND M. C. SELEK*

ABSTRACT

The paper studies the stress redistribution resulting from the multiple transverse cracks in cross-ply composite laminates under uniaxial extension. A singular finite element is developed to further investigate the detailed stress gradients near the crack tip. An elasticity basis for the singular element is established by employing Lekhnitskii's complex variable potentials and the method of eigenfunction expansion. The strength of the stress singularity and associated nonsingular eigenvalue terms in the vicinity of the transverse crack are conveniently determined by traction-free and continuity boundary conditions in conjunction with the symmetrical condition.

For the numerical analysis, the singular element, which is formulated on the basis of the variational principle of a modified hybrid functional, in conjunction with nonsingular isoparametric finite elements, are used to cover a representative volume element. The stress distributions attained from the singular element model are compared with those from the non-singular finite element model. Singular hybrid element modelling provides very good prediction of the stress field, especially in the singular domain near the transverse crack tip where the nonsingular finite element model fails to capture the stress field consistently. Finally, the stress distributions along the width and through the thickness of the cross-ply laminates are examined and their implications of associated microdamage are discussed.

INTRODUCTION

The well-known excellent mechanical properties of composite materials are often accompanied by many failure or damage mechanisms. Although composite materials can be tailored efficiently to match the specific design requirements, the failure mechanisms may degrade the structural functionality. In particular, these failure mechanisms cause internal stress redistribution, affect structural integrity, and precipitate premature laminate failure. Therefore the optimal design of composites generally demands consideration of how the stresses are perturbed due to these damage mechanisms.

The transverse cracking(intralaminar crack) presents one of the damage modes. Such cracks occur parallel to the fibers in planes perpendicular to the interface of the laminate. Garrett and Bailey[1] have conducted experiments with cross-ply glass-reinforced polyester composites. The results showed that the transverse crack spacing is decreasing with increasing applied stress and increasing with increasing ply thickness. Reifsnider[2] was the first to report the existence of the Characteristic Damage State(CDS) in which the transverse cracks

* Department of Mechanical and Aerospace Engineering, North Carolina State University, Raleigh, North Carolina, 27695-7910

form periodic saturation patterns. The CDS is reached after certain high static loads or fatigue cycles at lower stress levels and remains constant. Highsmith and Reifsnider[3] also found that the degree of delamination damage increases and microdamage of fiber breakage and longitudinal splitting occur in the primary load-carrying plies prior to the ultimate failure. Continuing experimental investigations have been reported(Flaggs and Kural[4], Crossman and Wang[5], Kim[6], Daniel et al.[7]).

Analytical studies on the transverse crack problems have also attracted much attention. For instance, the strength of singularity of transverse cracks in anisotropic composite laminates has been examined by Ting and Hoang[8] using Stroh's approach. Hashin[9] investigated the stress field and stiffness reduction in cross-ply composites using a variational approach. Lee and Daniel[10] introduced a simplified shear lag analysis using a progressive damage scheme. Lim and Hong[11] presented a modified shear lag analysis, taking into account the interlaminar shear with an energy concept. Recently, Im[12] used a boundary collocation method for the transverse cracks in cross-ply composite laminates.

FORMULATION AND METHOD OF SOLUTION

In this paper a symmetric cross-ply $[0/90]_s$ composite laminate under in-plane tensile loading is considered, where the $0°$ layers are designated as the fibers parallel to the direction of the load. It is assumed that the laminate is perfectly bonded along the interfaces and uniformly distributed transverse cracks in the inner $90°$ layers have developed. The cracks terminate at interfaces between the adjacent layers. For convenience, a Cartesian coordinate system originating from a crack tip is constructed with the x axis running parallel to the interface, the y axis directing upward along the crack and the z axis being normal to the x-y plane. The laminate is assumed to be sufficiently long in the z-direction so that the plane strain condition holds. Following the theory of anisotropic elasticity [13], a stress function $F(x,y)$ which satisfies the partial differential equation is shown as follows:

$$L_4F(x,y) = \left(\tilde{S}_{22}\frac{\partial^4}{\partial x^4} + (2\tilde{S}_{12} + \tilde{S}_{66})\frac{\partial^4}{\partial x^2\partial y^2} + \tilde{S}_{11}\frac{\partial^4}{\partial y^4}\right)F(x,y) = 0 \qquad (1)$$

where $\tilde{S}_{ij}$ is the reduced compliance matrix defined by

$$\tilde{S}_{ij} = S_{ij} - S_{i3}S_{j3}/S_{33}, \qquad (i,j = 1,2,6). \qquad (2)$$

The stress components that relate the stress function are expressed by

$$\sigma_x = \frac{\partial^2F}{\partial y^2}, \quad \sigma_y = \frac{\partial^2F}{\partial x^2}, \quad \tau_{xy} = -\frac{\partial^2F}{\partial x\partial y}, \quad \sigma_z = -\sigma_{3i}\sigma_i/S_{33}, \qquad (i = 1,2,6) \qquad (3)$$

The solutions for the stress function $F(x,y)$ take the form

$$F(x,y) \equiv F(z_k) = \sum_{k=1}^{4} F_k(x + \mu_k y) . \qquad (4)$$

where μ_k are the roots of the following characteristic algebraic equation:

$$\tilde{S}_{11}\mu^4 + (2\tilde{S}_{12} + \tilde{S}_{66})\mu^2 + \tilde{S}_{22} = 0 . \qquad (5)$$

Further, the form for $F_k(z_k)$ is chosen as [14]:

$$F(z_k) = \sum_{n=1}^{N} \sum_{k=1}^{4} C_{kn}z_k^{\delta_n+2}/(\delta_n + 1)(\delta_n + 2) . \qquad (6)$$

where C_{kn} and δ_n are arbitrary constants to be determined and N is the number of δ_n's included in the solutions. Complete solutions for the stress and displacement field can be obtained:

$$\sigma_i = \sum_{n=1}^{N} \sum_{k=1}^{2} [C_{kn}\Lambda_{ik}z_k^{\delta_n} + C_{(k+3)n}\bar{\Lambda}_{ik}\bar{z}_k^{\delta_n}] , \quad \sigma_z = -S_{3i}\sigma_i/S_{33} , \quad (i = 1,2,6) \quad (7)$$

$$u_i = \sum_{n=1}^{N} \sum_{k=1}^{2} [C_{kn}\Gamma_{ik}z_k^{\delta_n} + C_{(k+3)n}\bar{\Gamma}_{ik}\bar{z}_k^{\delta_n}] , \quad (i = 1,2) , \quad (8)$$

where $\Lambda_{1k} = \mu_k^2$, $\Lambda_{2k} = 1$, $\Lambda_{6k} = -\mu_k$, $\Gamma_{1k} = \tilde{S}_{11}\mu_k^2 + \tilde{S}_{12}$, $\Gamma_{2k} = \tilde{S}_{12}\mu_k + \tilde{S}_{22}/\mu_k$

Under the uniaxial in-plane loading, the laminate experiences the symmetric conditions of deformation: u(x,y) = -u(-x,y), v(x,y) = v(-x,y) or in equivalent forms

$$\frac{\partial u^{(1)}(0,y)}{\partial y} = 0 , \qquad \frac{\partial v^{(1)}(0,y)}{\partial x} = 0 \quad (9)$$

where the superscript 1 refers to the 0° layer, subsequently the superscript 2 for 90° layer. The eigenvalues δ_n can be determined by using the above equations, traction-free boundary conditions along the crack surface and continuity conditions along the interface in the domain x > 0. Since strain energy density is positively definite, the eigenvalues, δ_n, bounded by -1<Re[δ_n]<0 characterize the order of stress singularity. Once the eigenvalues are determined, the relationships among the eigenvectors C_{kn}'s are obtained. The stresses and the displacements can be written in more desirable form:

$$\sigma_i = \sum_{n=1}^{N_1} \beta_n \left(\sum_{k=1}^{2} \left\{ Re\left[b_{kn}\Lambda_{ik}z_k^{\delta_n} \right] + Im\left[b_{(k+3)n}\bar{\Lambda}_{ik}\bar{z}_k^{\delta_n} \right] \right\} \right) , \quad (10)$$

$$u_i = \sum_{n=1}^{N_1} \beta_n \left(\sum_{k=1}^{2} \left\{ Re\left[b_{kn}\Gamma_{ik}z_k^{\delta_n+1} \right] + Im\left[b_{(k+3)n}\bar{\Gamma}_{ik}\bar{z}_k^{\delta_n+1} \right] \right\} \middle/ (\delta_n + 1) \right) , \quad (11)$$

if δ_n are real. and

$$\sigma_i = \sum_{n=N_1+1}^{N-1} \left\{ \beta_n Re\left[\sum_{k=1}^{4} b_{kn}\Lambda_{ik}z_k^{\delta_n} \right] + \beta_{n+1}Im\left[\sum_{k=1}^{4} b_{kn}\Lambda_{ik} z_k^{\delta_n} \right] \right\} , \quad (12)$$

$$u_i = \sum_{n=N_1+1}^{N-1} \left\{ \beta_n Re\left[\sum_{k=1}^{4} b_{kn}\Gamma_{ik}z_k^{\delta_n+1} \middle/ (\delta_n+1) \right] + \beta_{n+1}Im\left[\sum_{k=1}^{4} b_{kn}\Gamma_{ik}z_k^{\delta_n+1} \middle/ (\delta_n+1) \right] \right\} , \quad (13)$$

if δ_n are complex conjugates. In the above formulas, N_1 is the number of distinct real δ_n selected, b_{kn} are the known constants related to the eigenvectors C_{kn}. The β_i are the undetermined real stress coefficients to be obtained in the singular hybrid finite element analysis.

A singular hybrid finite element is then formulated for the transverse crack problem, based on the eigenfunction solution just described and the variational principle of a modified hybrid functional. The variational functional can be rewritten by following the procedure given in[15]:

$$\pi_{mH} = -\frac{1}{2}\beta^T H\beta + \beta^T Gq , \quad (14)$$

where

$$H = \frac{1}{2}\int_{\partial A_m} (R^T U + U^T R)ds , \qquad G = \int_{\partial A_m} R^T L\, ds. \qquad (15)$$

Taking variation of functional π_{mH} with respect to $\underline{\beta}$ leads to

$$\underline{\beta} = H^{-1} Gq. \qquad (16)$$

Substituting equation (16) into equation (14) yields

$$\pi_{mH} = \frac{1}{2}q^T\, k_s\, q , \qquad (17)$$

where k_s is the stiffness matrix for the singular hybrid element and expressed as

$$k_s = G^T H^{-1} G. \qquad (18)$$

Note that, in the present analysis, a 9-node singular hybrid finite element with 18 degrees of freedom (2 d.o.f.'s per node) is formulated in conjunction with nonsingular isoparametric finite elements each possessing 8 nodes with 16 d.o.f's.

The use of quadratic interpolation functions for displacements along the boundaries of the singular hybrid element enables the crack element to match conveniently with neighboring regular elements. The global stiffness matrix, K, can be assembled by using the procedure of the matrix-displacement method, utilizing the singular hybrid element and regular finite element stiffness matrices, k_s and k_r, respectively. The solution procedure can be expressed in symbolic form by

$$K = \sum_m k_r^{(m)} + k_s \qquad (19)$$

where m is the total number of regular elements. Once the nodal displacements are determined from the finite element procedure, the stresses in the whole region are obtained. In particular, stress coefficients β_i in the singular element are determined through the equation(16).

NUMERICAL RESULTS AND DISCUSSIONS

A graphite/epoxy composite material with properties (E_L = 137.9 GPa, E_T = E_Z = 14.48 GPa, G_{LT} = G_{LZ} = 5.86 GPa, G_{TZ} = 3.52 GPa, ν_{LT} = ν_{LZ} = 0.21, ν_{TZ} = 0.32.) is selected for calculating internal stress distribution due to transverse cracks in the $[0/90]_s$ laminate. Owing to geometric symmetry, one quadrant of the representative volume element shown in Fig. 1 is modelled. The representative volume element is assumed to be subjected to a uniform extension $\varepsilon_x = \hat{\varepsilon}_x$ at x=b.The layers are of equal thicknesses, i.e. h=0.25 mm., and half the laminate width is selected as b=8h. A typical mesh configuration of total 77 elements with 269 nodes and 3 elements per ply through the laminate thickness direction is also shown in the figure. The singular element with a square configuration covering one third of the laminate thickness has been shown to give the best solution accuracy[16]. In addition, the first 10 noninteger eigenvalues to be used in the singular hybrid finite element formulation are tabulated in Table 1. The results have also shown that the stress intensity factors which characterize the steep stress gradients are in excellent agreement with a previous theoretical study[12].

Fig. 2 shows the distribution of interlaminar normal and shear stresses, σ_y and τ_{xy} along the interface. Both stress components are responsible for the onset of delamination cracks along the interface. It is observed that both σ_y and τ_{xy} are highly singular near the crack tip and vanish in the far field. The figure also provides the stress distribution obtained from the regular finite element model. The mesh configuration of the regular element model consists of 234 elements with 793 nodes and 3 elements per ply through the thickness direction. The

mesh is constructed such that the lengths of the regular elements in the x-direction decrease as the crack is approached. The regular finite element solution for τ_{xy} obtained from the 0° ply exhibits strong deviation, not only in magnitude but also in sign of the computed stress value, both from those of regular finite element modeling obtained from the 90° ply and singular hybrid finite element modeling. Even by increasing the number of elements through the laminate thickness direction, i.e. up to 10 elements per ply, the results improves very slowly and sign disparity between the two methods in the neighborhood of the transverse crack remains. This discrepancy apparently results from the singular nature of the stress field in the crack-tip region which the nonsingular finite element solution fails to account for. It is worth noting that the in-pane stresses obtained from these two models give the same trend throughout the region.

The in-plane stress components $\sigma_x^{(2)}$ and $\sigma_z^{(2)}$ along the interface($y = 0^-$) is displayed in Fig. 3 It is observed that both $\sigma_x^{(2)}$ and $\sigma_z^{(2)}$ are in tension throughout the interface and the stresses converge to the classical lamination theory (CLT) in the far field. From the numerical solution, the value of $\sigma_x^{(2)}$ at x/b=1.0 is 14.23 GPa per unit ε_x^0, whereas the CLT which corresponds to the undamaged laminate, predicts 14.5 GPa. Similarly, the numerical solution predicts the far field numerical value of $\sigma_z^{(2)}$ being 3.01 GPa per unit ε_x^0 which is very close to the CLT solution of 3.05 GPa. Severe stress gradients of $\sigma_x^{(2)}$ and $\sigma_z^{(2)}$, are observed near the crack-tip. This has significant importance since $\sigma_x^{(2)}$ makes the major contribution to the further transverse crack formation, whereas high tensile $\sigma_z^{(2)}$ near the crack-tip could reach the tensile strength of the fiber.

The next two figures give the in-plane stress components $\sigma_x^{(1)}$ and $\sigma_z^{(1)}$ along the interface($y = 0^+$). The tensile $\sigma_x^{(1)}$ displayed in Fig. 4 may cause fiber breakage in the 0° layer due to extreme stress gradient at the close vicinity of the intralaminar crack. Experiments have confirmed that fiber breakage indeed occurs in the region[3]. The stress converges to the CLT solution in the far field. The numerical solution for $\sigma_x^{(1)}$ yields 136.50 GPa per unit ε_x^0 while the CLT predicts 138.54 GPa. Fig. 5 shows the distribution of in-plane stress $\sigma_z^{(1)}$ near the interface. The tensile $\sigma_z^{(1)}$ is of significant importance in promoting longitudinal splitting in the 0° layer. The basic mechanisms in the 0° ply splitting are much the same as in the 90° ply transverse cracking. However, it can be inferred that matrix cracking is less likely to occur in the 0° ply than in the 90° ply, since, although the singular nature of $\sigma_z^{(1)}$ near the crack tip, it is observed to be much smaller than the tensile $\sigma_x^{(2)}$ which may cause transverse crack formation in the 90° ply.

Distribution of stresses along the width of the laminate with various y/h values are given in Figures 6 to 9. The variation of σ_x through the thickness shown in Figs. 4 and 6 is in contradiction with the assumption made by Hashin[9]. It is observed that the stress-free crack surface boundary conditions are satisfied as can be seen in Figs. 7-9, whereas symmetry boundary conditions in the 0° ply at x/b=0.0 are satisfied as shown in Fig. 7 verifying the validity of the formulation of the present method. Of particular interest is the stresses along the midplane since the location may also provide subsequent failure site[6]. The distribution of the stress components, $\sigma_x^{(2)}$, $\sigma_y^{(2)}$, and $\sigma_z^{(2)}$ on the laminate midplane is illustrated in Fig. 10. In the neighborhood of the center of crack, $\sigma_y^{(2)}$ is shown to be compressive which reveals that formation of delamination cracks along the midplane is unlikely.

Fig. 11 indicates the through thickness distribution of the axial stress σ_x both at x/b=0.0 and 0.85. Note that the σ_x varies dramatically throughout the thickness of the 0° ply at x/b=0.0. It is observed the σ_x is tensile and highly concentrated when the interface is approached, while the σ_x being identical to zero throughout the thickness of the 90° ply, thus, satisfying the stress-free crack surface conditions. The large magnitudes of $\sigma_x^{(1)}$ near the crack tip may result in possible 0° ply fiber breakage as mentioned previously. However, a constant σ_x distribution is observed through the thickness direction of each ply in the far field (x/b=0.85). The results are in very good agreement with CLT solutions which have been presented earlier in this section. To this end, Fig. 12 displays the through thickness distribution of σ_z at x/b=0.0 and 0.85. In the 0° ply, the σ_z is fully tensile and extreme stress gradient occurs near the interface at x/b=0.0. However, in the 90° ply, the σ_z is compressive

through most of the thickness at x/b=0.0 and becomes tensile reaching high values close to the interface. Once again, it is emphasized that high tensile value of σ_z near the interface may cause fiber breakage in the 90^{0} ply and longitudinal splitting in the 0^{0} ply. Evaluation of the far field solution (x/b=0.85) reveals that σ_z is tensile and constant in both plies as given by the CLT solution.

REFERENCES

1. Garrett, K. W., and Bailey, J. E., "Multiple Transverse Fracture in 90° Cross-Ply Laminates of a Glass Fiber-Reinforced Polyester", Journal of Materials Science, Vol.12, 1977, pp. 157-168.

2. Reifsnider, K. L., "Some Fundamental Aspects of the Fatigue and Fracture Response of Composite Materials", Proc. 14th Annual Meeting, Soc. of Engng. Sci., Bethlehem, PA., 1977, 343-384.

3. Highsmith, A. L., and Reifsnider, K. L., "Stiffness-Reduction Mechanisms in Composite Laminates", Damage in Composite Materials, ASTM 775, K. L. Reifsnider, Ed., American Society for Testing and Materials, pp.103-117, 1982.

4. Flaggs, D. L., Kural,M. H., "Experimental Determination of the In Situ Transverse Lamina Strength in Graphite/Epoxy Laminates", Journal of Composite Materials, Vol.16, pp.103-116, 1982.

5. Crossman, F. W., and Wang, A. S. D., "The Dependence of Transverse Cracking and Delamination on Ply Thickness in Graphite/Epoxy Laminates", Damage in Composite Materials, ASTM STP 775, K. L. Reifsnider, Ed., American Society for Testing and Materials, pp.118-139, 1982.

6. Kim, R. Y., Interlaminar Response of Composite Materials, N. J. Pagano, Ed., Elsevier Science Publishing Company Inc., Chapter 3, pp. 111-160, 1989.

7. Daniel, I. M., Lee, J. W., and Yaniv, G., "Damage Development and Property Degradation in Composite Materials", Mechanics of Composite Materials - 1988, G. J. Dvorak, and N. Laws, Eds., pp. 149-160, 1988.

8. Ting, T. C. T. and Hoang, P. H., "Singularities at the Tip of a Crack Normal to the Interface of an Anisotropic Layered Composites", International Journal of Solids and Structures, Vol. 20, 1984, 430-454.

9. Hashin, Z., "Analysis of Cracked Laminates: A Variational Approach", Mechanics of Materials, Vol.4, pp.121-136, 1985.

10. Lee, J. W. and Daniel, I. M., "Progressive Transverse Cracking of Crossply Composite Laminates", Journal of Composite Materials, Vol. 24, 1990, 1225-1243.

11. Lim, S. G. and Hong, C. S., "Prediction of Transverse Cracking and Stiffness Reduction in Cross-Ply Laminated Composites", Journal of Composite Materials, Vol. 23, 1989, 695-713.

12. Im, S., "Asymptotic Stress Field Around a Crack Normal to the Ply-Interface of an Anisotropic Composite Laminate", International Journal of Solids and Structures, Vol. 26, No. 2, 1989, 111-127.

13. Lekhnitskii, S. G., Theory of Elasticity in an Anisotropic Body, Holden-Day, San Francisco, 1963.

14. Wang, S. S. and Choi, I., "Boundary-Layer Effects in Composite Laminates - I. Free-Edge Stress Singularities", Journal of Applied Mechanics, ASME, Vol. 49, 1983, 541-549.

15. Wang, S. S., and Yuan, F. G., "A Hybrid Finite Element Approach to Composite Laminate Elasticity Problems with Singularities", Journal of Applied Mechanics, ASME, Vol. 50, pp. 835-844, 1983.

16. Selek, M. C., and Yuan, F. G., "Singular Hybrid Finite Element Analysis of Transverse Cracking in Composite Laminates", The Second International Symposium on Composite Materials and Structures, August 3-7, 1992, Beijing, China.

Table 1.   First 10 noninteger eigenvalues[†] associated with [0/90]$_s$ Graphite/Epoxy Composite to be used in singular hybrid finite element analysis.

δ_n
-0.3488950260
0.7471878555 ± i 0.2591510950
2.5608778232 ± i 1.1381117763
4.3379706000 ± i 1.7965985957
6.1027692935 ± i 2.4435258783
7.8654235482 ± i 3.0903654088
9.6278628064 ± i 3.7373859677
11.3902975277 ± i 4.3844427806
13.1527420477 ± i 5.0314919258
14.9158630784 ± i 5.6800794177

[†] Integers (n=0,1,2,...) are also eigenvalues
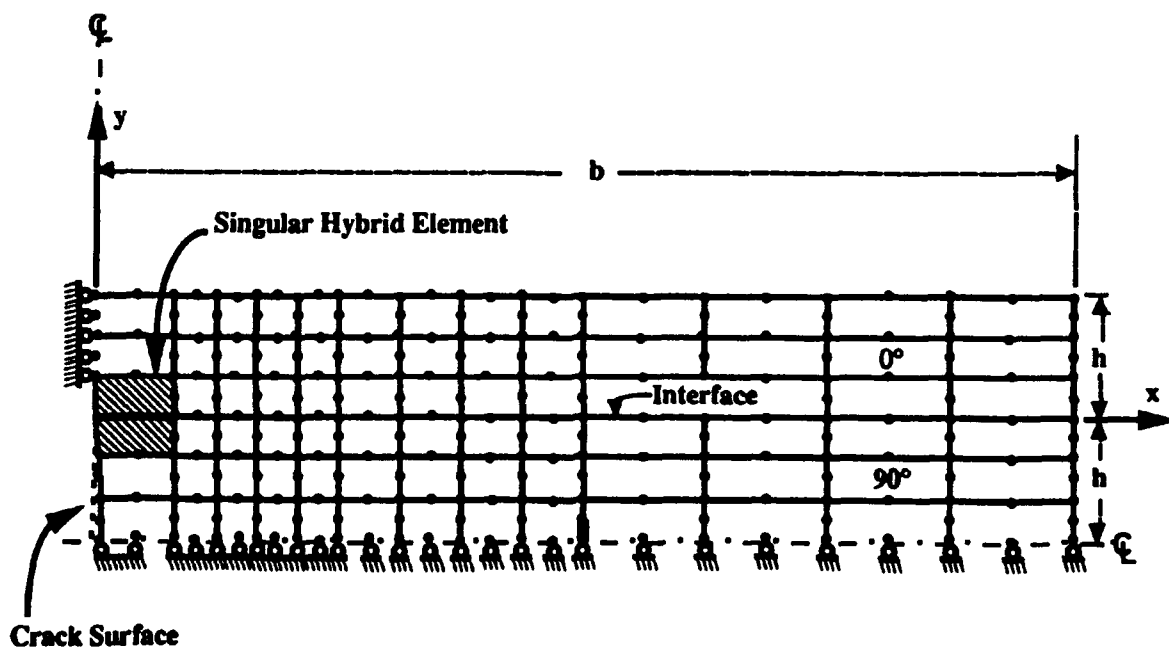
Fig. 1. Finite element modeling of one quadrant of a representative element of a [0/90]$_s$ composite laminate
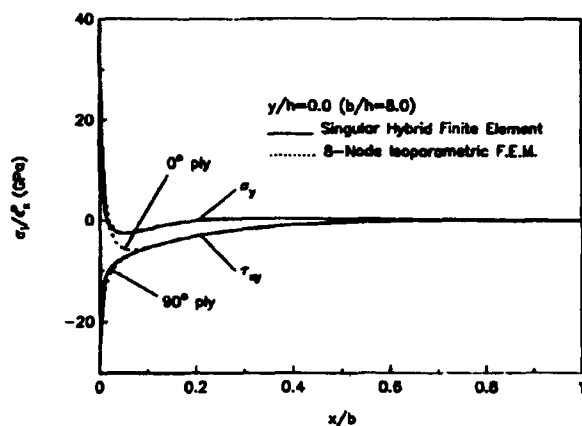
Fig. 2. Distribution of interlaminar stresses, σ_y and τ_{xy}, along the interface in $[0/90]_s$ composite laminate
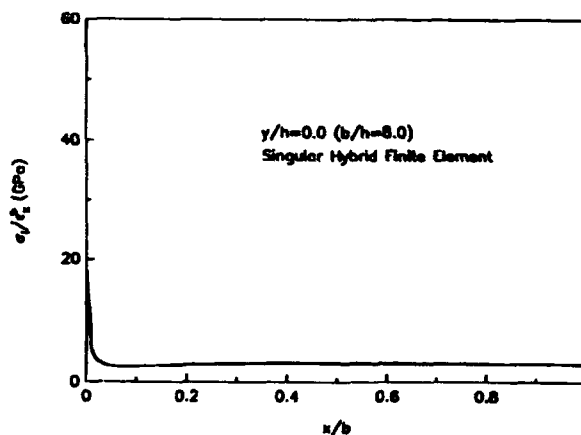
Fig. 5. Distribution of in-plane stress, σ_z, along $0°$ ply in $[0/90]_s$ composite laminate (y/h=0.0)
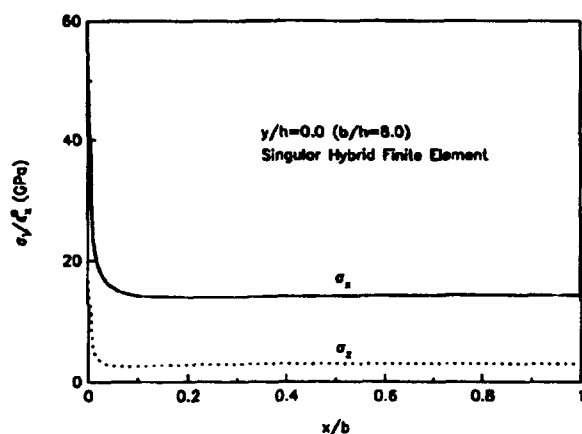
Fig. 3. Distribution of in-plane stresses, σ_x and σ_z, along $90°$ ply in $[0/90]_s$ composite laminate (y/h=0.0)
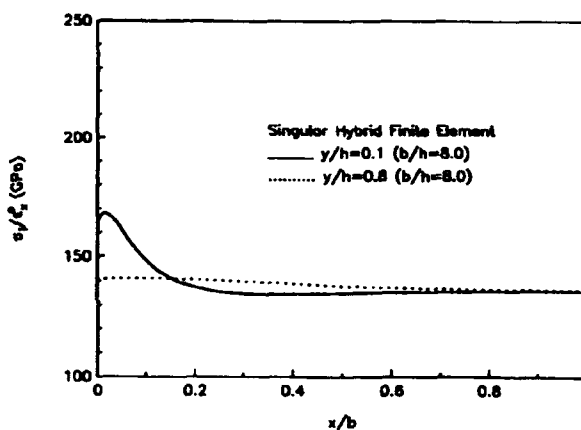
Fig. 6. Distribution of σ_x at y/h=0.1 and y/h=0.8 in $[0/90]_s$ composite laminate
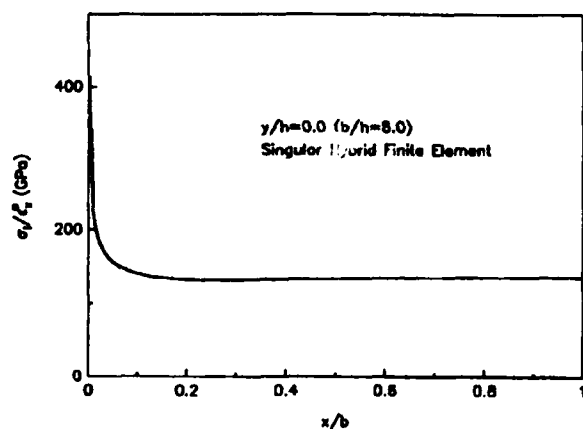
Fig. 4. Distribution of in-plane stress, σ_x, along $0°$ ply in $[0/90]_s$ composite laminate (y/h=0.0)
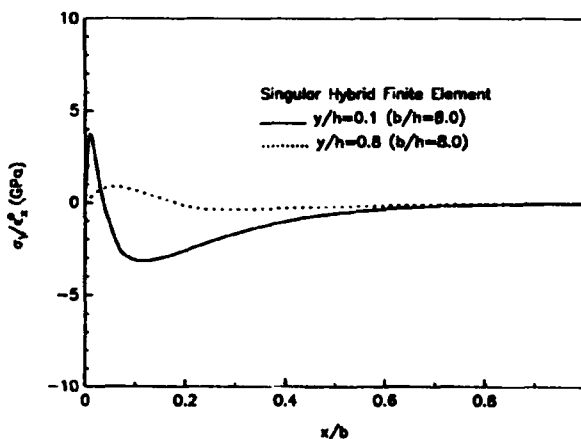
Fig. 7. Distribution of τ_{xy} at y/h=0.1 and y/h=0.8 in $[0/90]_s$ composite laminate.

159
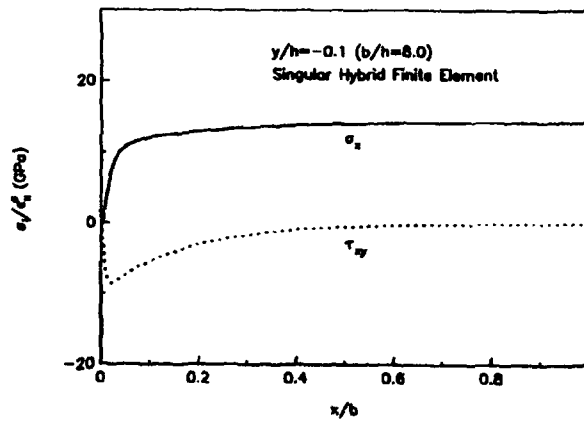
Fig. 8. Distribution of σ_x and τ_{xy} at y/h=−0.1 in [0/90]$_s$ composite laminate
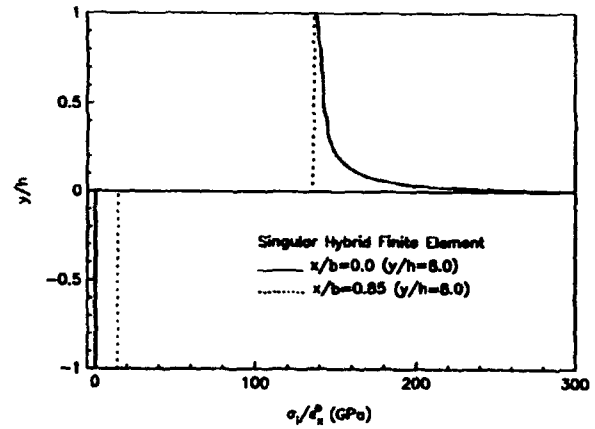
Fig. 11. Through-thickness distribution of σ_x in [0/90]$_s$ composite laminate
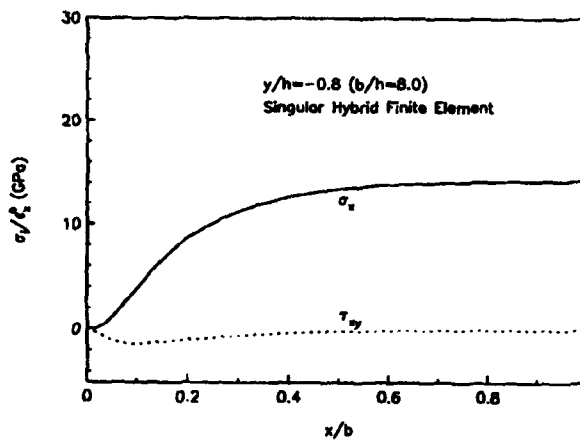
Fig. 9. Distribution of σ_x and τ_{xy} at y/h=−0.8 in [0/90]$_s$ composite laminate
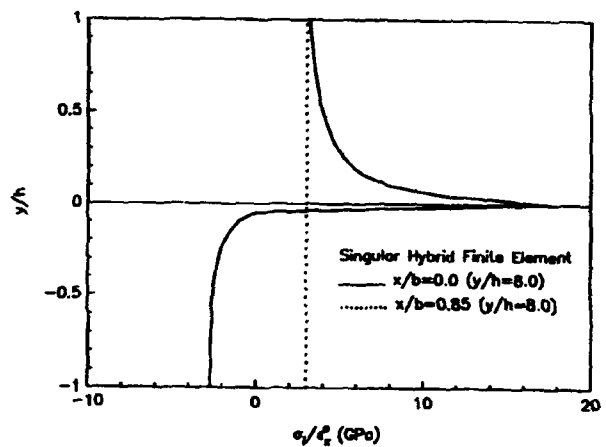
Fig. 12. Through-thickness distribution of σ_z in [0/90]$_s$ composite laminate
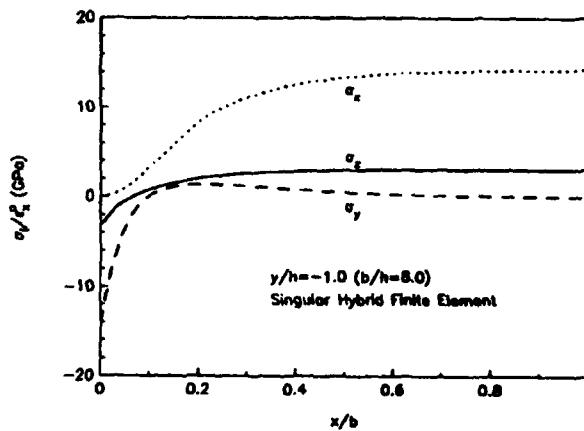
Fig. 10. Distribution of σ_x, σ_y, and σ_z at the midplane in [0/90]$_s$ composite laminate

SESSION 2B

Interfaces and Material Systems I

Reaction Processing: Route for Controlling Composite Interfacial Behavior

S. G. FISHMAN

ABSTRACT
Recent mechanical analyses and experimental corroboration have indicated that greater strength and improved toughness can be achieved in both composites with ductile and with brittle matrices in which controlled debonding is obtained than for those with high interfacial strengths and little debonding. The application of artificial debond-coatings, the standard method to achieve controlled debonding, is expensive. A different strategy, in which inexpensive in-situ techniques, using kinetic biasing to achieve desired reaction phases is presented.

INTRODUCTION
Metal matrix, intermetallic matrix, and ceramic matrix composites are being considered as potential candidate materials for a variety of structural applications for which high temperature operation is necessary. The mechanical properties of these materials, in terms of important parameters such as strength, stiffness and density are very impressive. However, other parameters such as ductility, impact resistance and fracture toughness, especially for composites reinforced with discontinuous fibers or particles are often poor, and in may cases precludes use of these composites for specific applications. The importance of the matrix-reinforcement bond in promoting desirable mechanical behavior has long been appreciated. It is well recognized that weak interfaces are necessary in composites with brittle matrices, in order to obtain high toughness. In the case of metallic matrix composites, the conventional wisdom has been that strong bonding is necessary for efficient stress transfer between matrix and fibers[1]. Unfortunately, such materials are frequently very brittle.

MICROMECHANICS CONSIDERATIONS
There has been considerable effort expended to understand fiber-matrix debonding, primarily in brittle/brittle systems, in which matrix cracking occurs prior to fiber-failure. More recently, such efforts have been extended to ductile/brittle systems, in which fiber failure precedes matrix failure[2,3,4]. For ductile matrix systems with "strong" interfaces, failure subject to longitudinal loading invariably occurs when the ultimate

S. G. Fishman, Office of Naval Research, Arlington, VA 22217

163

values of the normalized strength (ultimate strength/fiber bundle strength) and strain (ultimate strain/matrix cracking strain) are both less than unity. However, for ductile matrix systems in which some interfacial debonding is allowed, rule-of-mixtures strengths are achieved, and as shown in Figure 1, normalized strengths of greater than unity are achieved[5]. In the former case, that of strongly bonded interfaces in a ductile matrix, although cracks that form in the fiber are blunted by the matrix, some concentration of stress still occurs and is transmitted to adjacent fibers. This leads to a progressive fiber overload situation, and results in a relatively planar crack and a somewhat weaker than rule-of-mixtures strength. In the latter case, that of a ductile matrix exhibiting interfacial debonding, the debonding and interfacial sliding relieves stress concentrations, and fiber fractures are non-interactive. The consequence is a composite with greater strength and toughness than that for composites with strongly-bonded interfaces. In Figure 2, is presented a schematic of the two cases illustrating the possible modes of crack propagation into or along the fiber, depending upon whether fiber-matrix decoupling occurs.

The problem of defining the preconditions for interfacial debonding has been addressed in terms of both fracture energy and cohesive strength considerations correlated with fiber-matrix elastic parameters[6,7]. In the former case, debonding initiates, only if the magnitude of the interfacial fracture energy is small with respect to that of the fiber. For brittle matrix systems, in which matrix cracking typically precedes fiber cracking, debond occurs preferentially to fiber failure provided that the fracture energy ratio is less than or equal to 1/4[6]. Such a criterion has yet to formulated for ductile matrix systems. In the latter approach, the ratio of interfacial cohesive strength to fiber fracture strength is correlated with the Dunders parameter, alpha, a measure of fiber-matrix (or coating-fiber) stiffness mismatch. Micromechanical formulations, using the interfacial strength approach, have been summarized in terms of interface delamination charts, an example of which is shown in Figure 3[7]. Using these charts, along with a knowledge of compliances of interface coatings, fibers and matrices, and of the tensile strengths of reinforcing fibers, one can determine the maximum cohesive interfacial strength which is consistent with debonding.

STRATEGY FOR ACHIEVING DESIRABLE INTERFACE COATINGS

Most composite systems consist of matrices and reinforcements which are rarely, if ever, at thermodynamic equilibrium. Consequently, a reaction layer usually forms between the fiber and matrix during processing. Such layers are frequently deleterious either because the fiber is weakened or a thick, embrittling crack-initiation zone is formed. As a result, artificial fiber-coatings are applied as diffusion barriers or to promote controlled interfacial debonding. The cost of such fiber-coatings, which are applied by a variety of techniques (chemical vapor deposition, magnetron sputtering, etc.) are high and raise the price of materials which are already to expensive for non-aerospace applications. In order to develop materials for commercial
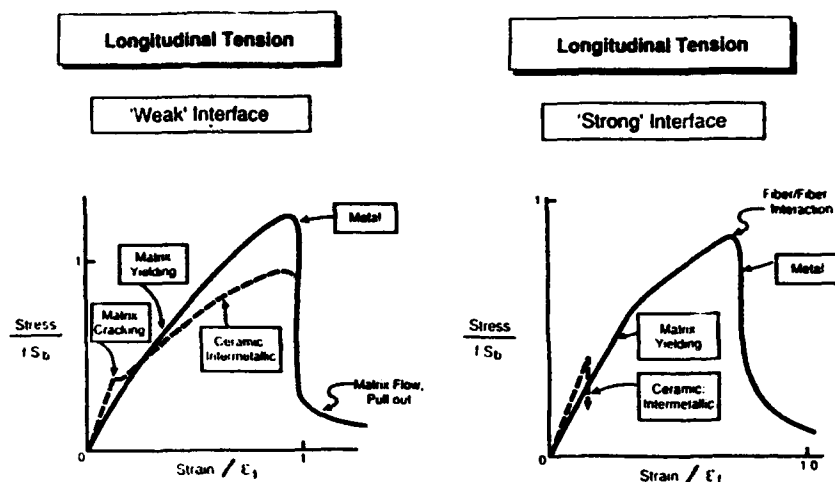
Figure 1. Effect of Interfacial Strength on Fiber Composite Tensile Behavior[5]
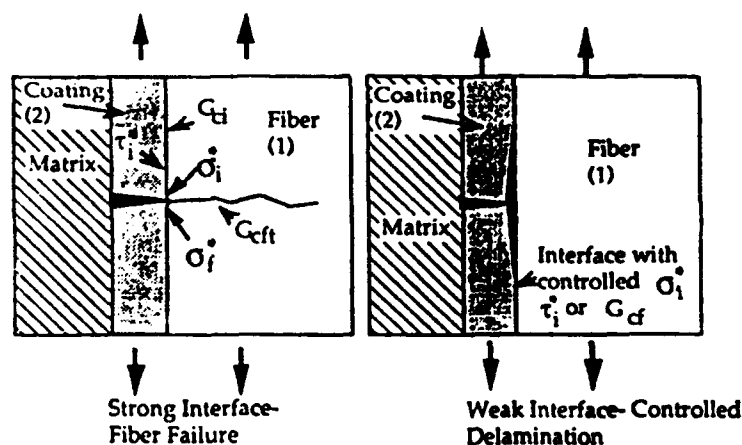
Figure 2. Interface Delamination Preconditions for Crack Bridging/Frictional Pull-Out[7]
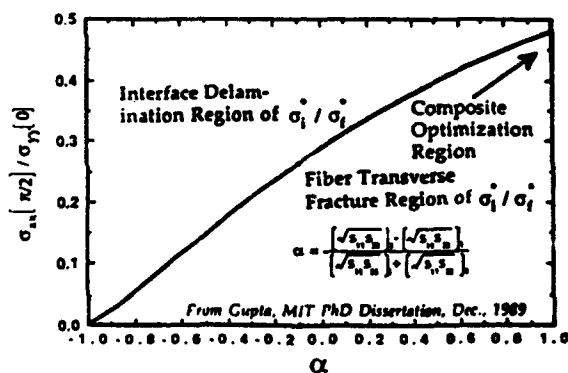
Figure 3. Interface Delamination Chart[7]

applications new inexpensive processing routes must be identified.

A strategy, to achieve such inexpensive fabrication of reinforcement-coatings and barrier layers, is based on the application of information from phase diagrams and kinetic investigations of interdiffusion pathways to control reactions at fiber-matrix interfaces[8]. It involves the selection of combinations of phases, which possess desirable thermal stability and phase interaction properties, and the pre-selection of reaction pathways to generate reaction layers which will promote desirable composite mechanical behavior. As an example, consider a hypothetical composite consisting of a reinforcement, gamma, embedded in a matrix of B, the ternary phase diagram of which is displayed in Figure 4. The two phases are not in thermodynamic equilibrium, and there are four possible pairings of reaction products, all of which represent stable two-phase mixtures, but evolve through different phase sequencing pathways. It is not possible to determine, from theory, which of these pathways is selected, Instead, such information must be generated experimentally. However, the multiplicity of such pathways offers a potential strategy for altering the sequences of phases in order to select the one providing optimum composite behavior. Figure 5 provides a schematic free energy diagram for the hypothetical composite described above. The decrease in free energy for the nucleation of alpha and beta phases is the distance given by the arrows M-alpha and L-beta on the diagram, respectively. If the initial nucleation is the alpha phase, the residual driving free energy to form the beta compound is considerably reduced (to the quantity designated by the arrow L'-beta on the diagram). This reduction in driving force may well preclude the formation of the beta phase during the composite service lifetime. The conclusion from this analysis is that there are strategies for pre-treating either fibers or matrices to bias the reaction pathway to generate desired reaction coatings.

APPLICATION OF REACTION PATHWAY BIASING STRATEGIES

In a recent investigation, a reinforcement pre-treatment was used to achieve desirable interfacial debonding performance in a system of practical engineering importance[9]. The process included coupling reinforcement pre-treatment with reactive hot compaction to synthesize a niobium aluminide composite reinforced with ductile niobium filaments as a toughening phase, is shown schematically in Figure 6. Pre-oxidized niobium filaments, niobium powder and aluminum powder were blended and compacted in the presence of a low melting point transient liquid phase, which accelerated diffusional mixing of the constituents. It had been previously determined that alumina coating of the niobium filament was necessary as a diffusion barrier to prevent the formation of strongly-bonded, embrittling reaction layers. Pre-oxidation of the niobium filaments encourages the formation of alumina, in-situ, during the reactive sintering of the niobium aluminide matrix, as shown in Figure 7, since alumina is considerably more stable than the oxides of niobium. Not only is alumina a desirable diffusion barrier between niobium and $NbAl_3$, but it also promotes interfacial
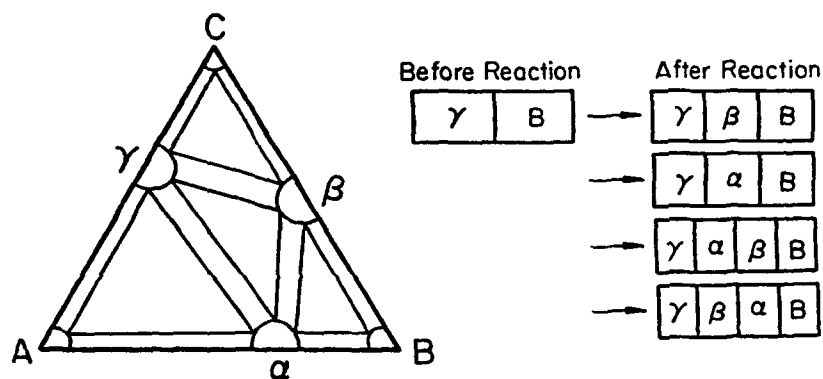
Figure 4.   Hypothetical Phase Diagram for Three
             Component System[8]
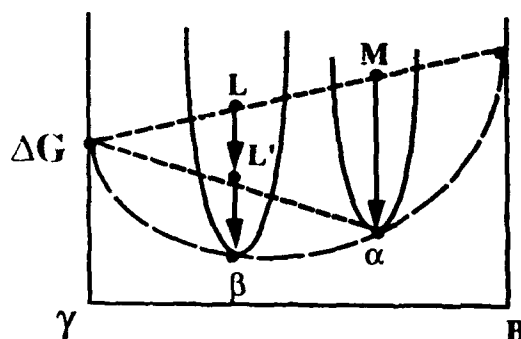
Figure 5.   Free Energy-Composition Diagram for
             Hypothetical Three Component System[8]
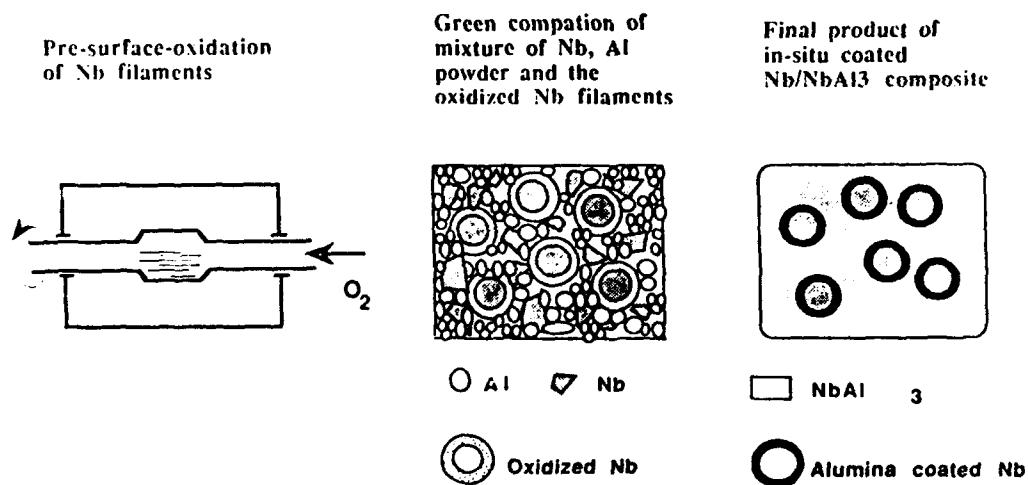
Figure 6.   Simultaneous In-Situ Formation of Nb/NbAl₃
             Composite and Al₂O₃ Diffusion Barrier[9]

debonding which enhances composite toughness by fiber bridging and fiber plastic work mechanisms. Mechanical evaluation of such composites reveal a factor of six enhancement in fracture toughness (9.6 MPa(m)$^{1/2}$ as compared with 1.6 MPa(m)$^{1/2}$) compared with the matrix[9].

An example of how minor changes in matrix composition can be used to pre-select a reaction pathway can be demonstrated by consideration of the nickel-alumina system. An isotherm from the nickel-aluminum-oxygen ternary phase diagram is presented in Figure 8[10]. As shown, at 1400 °C, nickel is in equilibrium with alumina, spinel, and NiO. There has not been a great deal of understanding concerning the reaction pathway or reaction mechanisms for this system, with previous investigators proposing that the reaction between nickel and alumina must proceed through a NiO intermediate before being converted to the spinel[11].

An enlargement of the Ni-rich corner of the ternary provides a clue as to how minor matrix compositional variations can be used to determine the presence or absence of reaction layers between the nickel and alumina. The diffusion path is determined by the composition of the constituents of the diffusion couple. In order to conserve mass, the average composition along the diffusion path must lie along a straight line connecting the two end constituents, and the diffusion path must cross this straight line at least once[12]. As shown in Figure 8, the diffusion path fixes which tie-lines will connect the nickel to the alumina, and other tie-lines can be selected by slight (on the orders of a few hundreds of part-per-million change in oxygen content) variation in composition of the nickel alloy. Figure 9 compares the structure of nickel-alumina interfaces hot pressed at 1390 °C[13]. The upper photograph shows an interface which was determined to be atomically clean (in terms of absence of reaction layer) fabricated from oxygen-free nickel. The lower photograph shows the presence of a spinel interphase layer fabricated from nickel containing 670 ppm oxygen. Although the authors did not quantify interfacial mechanical properties, one assumes that thick spinel layers would be weak and brittle.

By suitable choice of processing parameters, composition, partial pressure of oxygen, processing time and temperature, etc., it is possible to control nucleation and growth of metal phases both at reinforcement interfaces and within grains of mixed oxide constituents to produce a wide range of microstructures[14]. In principal, it is possible to produce, at one extreme, metal-ceramic composites, and at the other, ceramic grains containing fine distributions of metal particles. As above, a knowledge of phase equilibria, in particular, the effect of oxygen partial pressure, is mandatory. Such information, presented in an activity-composition diagram, which is topologically equivalent to a composition-temperature binary phase diagram, is presented in Figure 10, for the manganese-iron-oxygen system at 1000 °C[15]. At an Fe/(Fe+Mn) ratio of 0.6 (x=0.4) and an oxygen partial pressure slightly below log a_{oxygen} = -15.1, reduction of the most nobel metal occurs and a metallic alloy of almost pure iron is formed which coexists with the rock salt mixed oxide phase. Also
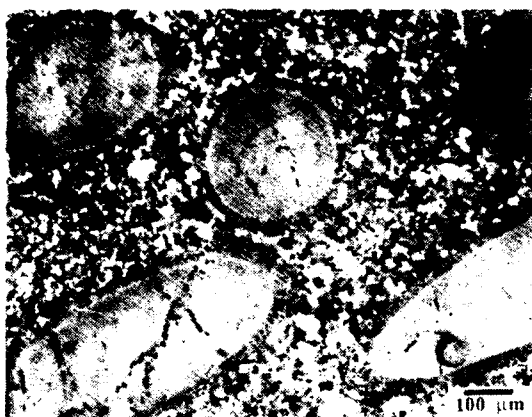
Nb FILAMENTS WITHOUT DIFFUSION BARRIER
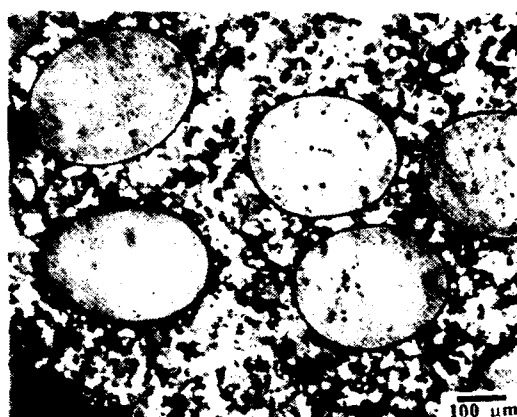
Nb FILAMENTS WITH DIFFUSION BARRIER

Figure 7. Microstructures of Nb/NbAl₃ Composites[9]
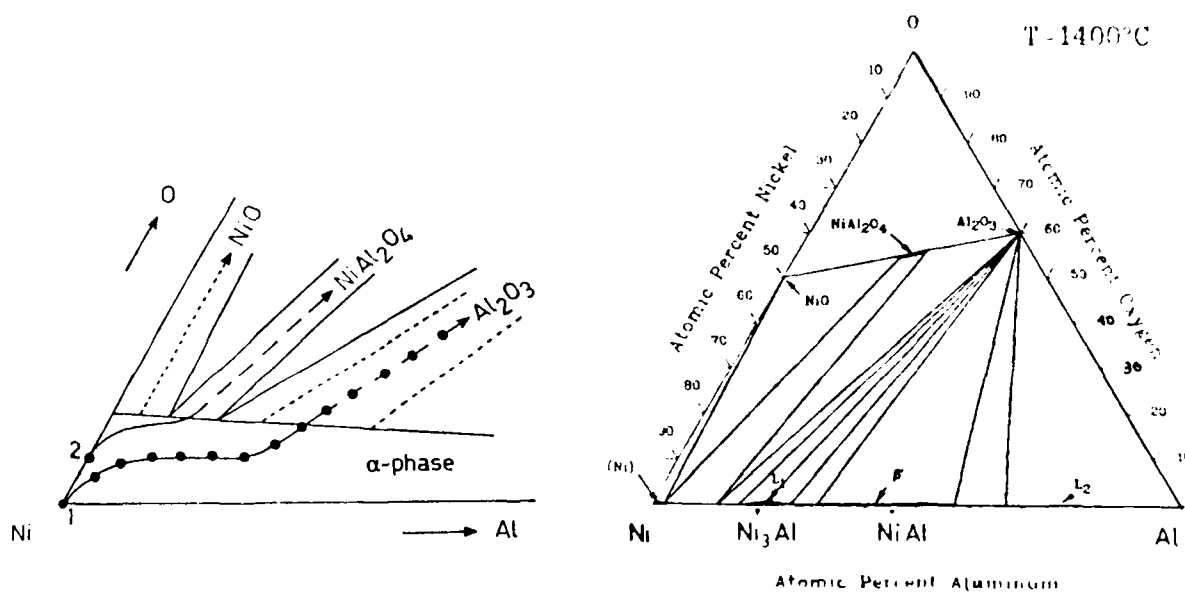
Figure 8. Ni-Al-O Ternary Phase Diagram[10]

Figure 9. Effect of Matrix Oxygen Content on Modifying
Reaction Pathway in Ni/Al$_2$O$_3$ Couples[14]
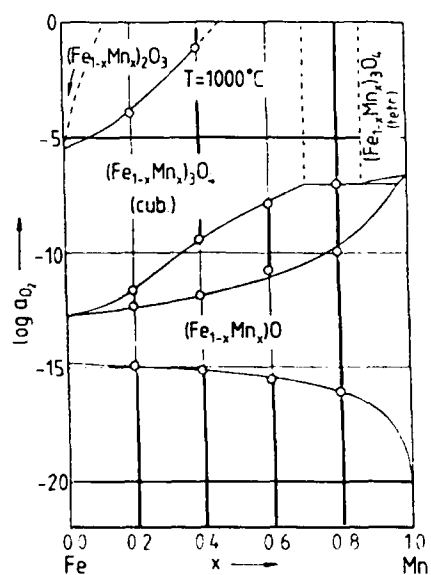
Figure 10. Oxygen Activity-Composition Diagram for Fe-Mn-O
System and Metal-Ceramic Microstructure Produced
by Internal Reduction of (Fe$_{0.7}$Mn$_{0.3}$)O[16]

shown in Figure 10, is a photomicrograph of mixed oxide particles the on surface of which have been nucleated a coating of iron. In another example, aspects of the aluminum-chromium-oxygen system equilibria were exploited to produce alumina fiber-reinforced alumina-chromia solid solutions containing chromium metal (with some aluminum in solution) both within the oxide grains and at the interfaces of the alumina fibers[16].   In the optical photomicrograph, shown in Figure 11, the light-colored phase, at the fiber interfaces and within the dark ceramic grains, is the metal.   The small light-colored particles within the fibers are zirconia particles which are added as grain growth inhibitors. As in the above Fe-Mn-O example, the compositions and volume fractions of the equilibrium solid solutions depends on the original composition of the mixed oxide, the oxygen partial pressure and the reduction kinetics.   The authors demonstrated how the interfacial frictional sliding stress could be varied by over an order of magnitude (32 MPa as compared with 750 MPa) as a function of initial composition of the Al_2O_3-Cr_2O_3 solid solution.

Figure 11. Al_2O_3-Cr_2O_3 Solid Solution Matrix Containing Al_2O_3
            Fibers and Cr(Al) Particles[17]

SUMMARY
    The application of micromechanical understanding of phenomena occurring at composite interfaces to the design of composite systems has resulted in the ability to predict desirable mechanical properties for these interfaces. Since matrices and reinforcements in composites are usually not in thermodynamic equilibrium, it is necessary to coat reinforcements with expensive diffusion barrier or debond coatings.   This paper described a strategy for using knowledge of phase equilibria and diffusion phenomena to bias reaction pathways and form in-situ desirable interfacial coatings.

REFERENCES

1. Hull, D., _An Introduction to Composite Materials_, Cambridge Solid State Science Series, Cambridge, UK (1981), p. 37.

2. Deve, H.E., Evans, A.G., Odette, G.R., Mehrabian, R., Emiliani, M.L., and Hecht, R.J., "Ductile Reinforcement Toughening of gamma-TiAl: Effects of Debonding and Ductility", _Acta Metall Mater_, _38 No 8_, (1990), p. 1491.

3. Fishman, S.G., "Interfacial Science of Structural Composites: Debonding Aspects", _Fabrication of Particulate Reinforced Metal Composites_, Eds. J. Masounave and F.G. Hamel, ASM Int (1990), p 1.

4. Zok, F., Jannson, S., Evans, A.G., and Nardone, V., "The Mechanical Behavior of a Hybrid Metal Matrix Composite", _Met Trans A_, _22A_, (1991), p. 2107.

5. Evans, A.G., "The Mechanical Properties of Fiber-Reinforced Ceramic, Metal and Intermetallic Composites", University of California at Santa Barbara Annual Report, University Research Initiative "The Processing and Mechanical Properties of High Temperature/High Performance Composites", ONR Contract N0001486K0753, Sept. 15 1989 - Sept. 14 1990.

6. Hutchinson, J.W., "Mixed Mode Fracture Mechanics of Interfaces", _Metal-Ceramic Interfaces_, Ed. by M. Ruhle, A.G. Evans, M. Ashby, and J. Hirth, Pergamon Press (1990), p. 307.

7. Cornie, J., Argon, A.S., and Gupta, V., "Designing Interfaces in Inorganic Matrix Composites", _MRS Bulletin_, _XVI No 4_, (1991), p.32.

8. Perepezko, J.H., "Interfacial Reactions and Microstructure Control in Composite Processing", _Comp. Interfaces_, (to be published).

9. Lu, L., Gokhale, A.B., and Abbaschian, R., "Reactive Hot Compaction and 'In Situ' Reinforcement Coating for $NbAl_3$ Matrix Composites", _Matls Sci and Eng_, _A144_, (1991) p. 11.

10. Backhaus-Ricoult, M., "Diffusion Processes and Interphase Boundary Morphology in Ternary Metal-Ceramic Systems", _Ber. Bunsenges. Phys. Chem._, _90_, (1986), p. 684.

11. Bailey, F., and Borbidge, W., _Mat Sci Res_, _14_, (1981), p. 525.

12. Kirkaldy, J.S., and Young, D.J., _Diffusion in the Condensed State_, Inst. of Metals, London, UK, (1987), p. 371.

13. Trumble, K.P., and Ruhle, M., "The Oxygen Activity Dependence of Spinel Interphase Formation During Ni/Al^2O^3 Diffusion Bonding", _Metal-Ceramic Interfaces_, Ed. by M. Ruhle, A.G. Evans, M. Ashby, and J.P. Hirth, Pergamon Press (1990), p. 144.

14. Ustundag, E., Subramanian, R., Vaia, R., Dieckmann, R., and Sass, S.L., "In Situ Formation of Metal-Ceramic Microstructures, Including Metal-Ceramic Composites, Using Reduction Reactions", Cornell University Materials Science Center Report #7390, ONR Contract N00014-92-J-1526, May 1992.

15. Franke, P., and Dieckmann, R., "Thermodynamics of Iron Manganese Mixed Oxides at High Temperatures", _J Phys Chem Solids_, _51 (1)_, (1990), p. 49.

16. Handwerker, C.A., Deshmukh, U.V., and Cranmer, D.C., "Fabrication and Interface Debonding of $Al^2O^3-Cr^2O^3-Cr$ Composites", _Metal & Ceramic Matrix Composites: Processing, Modelling and Mechanical Behavior_, Ed. by R.B. Bhagat, A.H. Clauer, P. Kumar, and A.M. Ritter, _TMS_, (1990), p. 457.

Interfacial Fracture Toughness of Continuous Fiber Reinforced Metal Matrix Composites under Mixed Mode Loading

KAZUMI HIRANO, SHINJI SETO, MASAHIKO OZAKI AND MASANORI KIKUCHI

ABSTRACT

The objective of this study is to develop and standardize the fracture toughness testing for continuous fiber reinforced metal matrix composites. The interfacial fracture toughness tests under the mixed mode loading (Modes I and II) were conducted on continuous silicon carbide (SiC$_{\text{CVD}}$), Nicalon (SiC$_{\text{PCS}}$) and carbon (M40J) fibers unidirectionally reinforced aluminum alloys matrix composites. The J-integral for mixed-mode crack was also calculated by finite element method. The mixed-mode interfacial fracture characteristics were determined on the basis of fracture mechanics and electron microfractography.

INTRODUCTION

As R&D on metal matrix composites (MMC) technology is serious and mature for practical use, the significance of understanding fracture mechanics characterization is recognized for ensuring the composite structural integrity. In particular, it has recently been the most important and urgent problems to characterize the damage tolerance behavior for a wide use of advanced MMCs for primary structural applications. We have already done the fracture mechanics characterizations of advanced MMCs in order to establish the material design concepts for high strength, high toughness and high durability [1~13].

The objective of this study is to develop and standardize the fracture toughness testing for continuous fiber reinforced metal matrix composites. The interfacial fracture toughness tests under the mixed mode (Modes I and II) loading were conducted on continuous fiber unidirectionally reinforced aluminum alloy matrix composites. The J-integral were analyzed for mixed-mode cracks by finite element method (FEM). The mixed-mode interfacial fracture characteristics were investigated on the basis of fracture mechanics and electron microfractography.

Kazumi HIRANO, Mechanical Engineering Laboratory, Agency of Industrial Science and Technology, Ministry of International Trade and Industry(MITI). Namiki 1-2, Tsukuba-shi, Ibaraki-ken 305, JAPAN.
Shinji SETO and Masahiko OZAKI, Graduate Student, Science University of Tokyo.
Masanori KIKUCHI, Faculty of Engineering, Science University of Tokyo.

EXPERIMENTAL PROCEDURE

MATERIALS

The materials investigated in this study are continuous silicon carbide, Nicalon and carbon fibers unidirectionally reinforced aluminum alloys matrix composites, $SiC_{CVD}/6061Al$, $SiCpcs$ /1050Al and M40J/1080Al. They were fabricated by hot press diffusion bonding process in a solid state with approximately 40-45% fiber volume fraction (Vf). The mechanical properties are also listed in TABLE I. It is highly anistropic properties, with tensile strength and elastic modulus values being much greater parallel to the fiber direction (L) than in the transvese direction (T).

TABLE I - MECHANICAL PROPERTIES

Materials	Ori.	E (GPa)	σ_{UTS} (MPa)	ε_f (%)
$SiC_{CVD}/6061Al$	L	208	1620	0.93
Vf = 40 %	T	129	91	0.15
SiCpcs/1050Al	L	105	562	0.87
Vf = 40 %	T	99	90	---
M40J/1080Al	L	167	1070	---
Vf = 44 %	T	42	27	---

TEST PROCEDURE

The laminates, approximately 200 x 100 x (1.4~2.0) mm, were machined by electron discharge machining into 25 x 30 mm single edge notched (SEN) specimens. Initial notch of approximately 12.5 mm long and 0.4 mm wide were parallel to the reinforcement fiber direction. Some specimens for $SiC_{CVD}/6061$ Al were introduced the fatigue precracking of approximately 2.5 mm length at the initial notch tip at a constant stress intensity factor level below fracture toughness value. All specimens were tested in the as-fabricated condition.

The fracture toughness tests under the mixed-mode loading condition were conducted in a room temperature environment using a MTS closed loop electrohydraulic material testing system, in a displacement controlled mode with a constant displacement rate (1 mm/min.) according to ARCAN method [14]
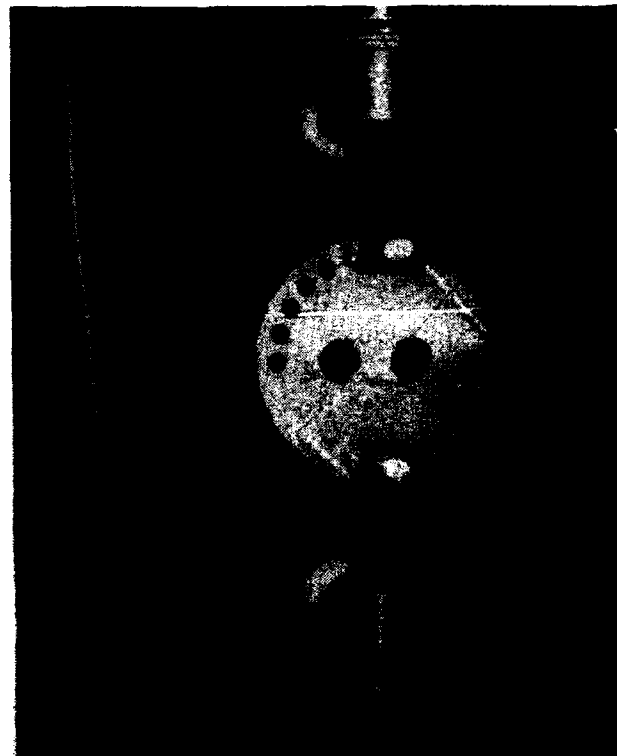
Figure 1. General view of mixed-mode fracture toughness testing.

schematically illustrated in Fig. 1. Mixed-mode interfacial fracture toughness was determined at a maximum load Pmax on the basis of the analytical results by FEM. After the fracture toughness tests, fractographic examinations on the fracture surface were carried out using a scanning electron microscope (SEM) in order to investigate the fracture micromechanism.

FEM ANALYSIS FOR MIXED MODE CRACK

J-INTEGRAL ANALYSIS

J-integral for both notched and cracked specimens under the mixed-mode loading were calculated based on 2-dimensional anisotropic FEM analysis code using 8-nodes isoparametric elements.

Relationships between J-integral, J_I, J_{II} and stress intensity factor, K_I, K_{II} can be expressed as follows.

$$J_I = A K_I^2 \tag{1}$$

$$J_{II} = B K_{II}^2 \tag{2}$$

$$J_{tot} = J_I + J_{II} \tag{3}$$

where A and B are the orthotropic material constants of the composite.

Now, introduce the following equation.

$$K_{II} / K_I = \tau / \sigma = C \tag{4}$$

The C-value can be determined by the outerploation method from the analytical results of stress field at a crack tip.

Substitution of Eq. 4 into Eqs. 1, 2 and 3 yields

$$K_I = (J_{tot} / (A+BC^2)) \tag{5}$$

Therefore, we can convert separately the J-integral into K_I and K_{II} values.

ANALYTICAL RESULTS

A example of the analytical results is shown in Fig. 2 for the fatigue precracked specimen of SiC$_{CVD}$/6061Al. J-integral values are per unit load and unit specimen thickness. It can be seen from this figure that the total J-integral increase monotonously with the loading angle θ.
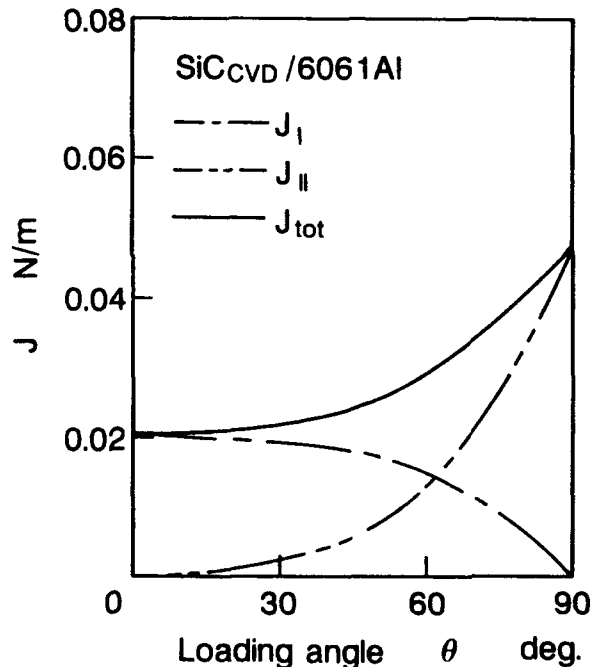
Figure 2. Variations of J-integral with loading angle for the fatigue precracked specimen of SiC$_{CVD}$/ 6061Al.

EXPERIMENTAL RESULTS AND DISCUSSION

K_I VERSUS K_{II} RELATIONSHIPS

In order to investigate the mixed-mode fracture characteristics, plots of K_I against K_{II} are made for SiC$_{CVD}$/6061Al in Fig. 3. K_I values on the longitudinal axis are critical stress intensity factor K_{IC} under pure mode I loading and K_{II} values are K_{IIC} under pure mode II loading condition. The average values of K_{IC} and K_{IIC} are approximately 1.5 and 8.0 MPam$^{1/2}$, respectively. Therefore, for the unidirectional SiC$_{CVD}$/6061Al, K_{IIC}/K_{IC} is approximately 5.3. This means that there is 5.3 times more resistance to fracture in the shearing mode than that in the opening mode for interfacial fracture.

Figure 3 shows that there is little influence of specimen thickness on mixed-mode interfacial fracture toughness, although there is remarkable variation in the K_I versus K_{II} relationships. There is also no meaningful difference in the K_I versus K_{II} relationships between the notched and precracked specimens.
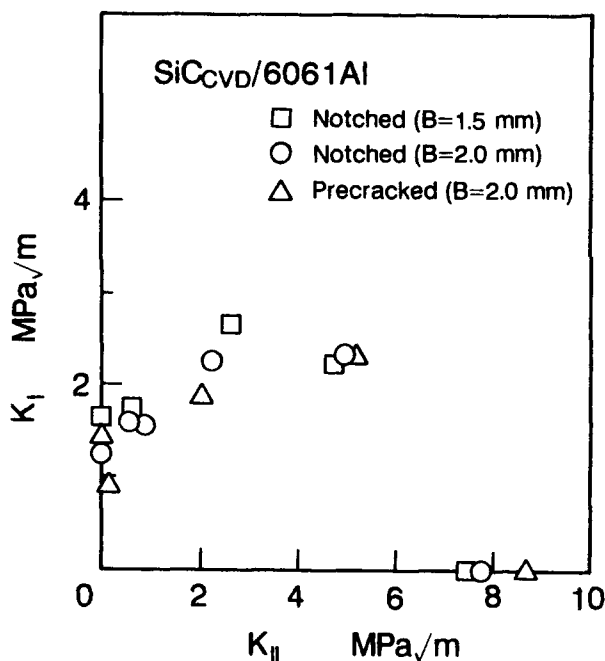
Figure 3. K_I versus K_{II} relationships for SiC$_{CVD}$/6061Al.
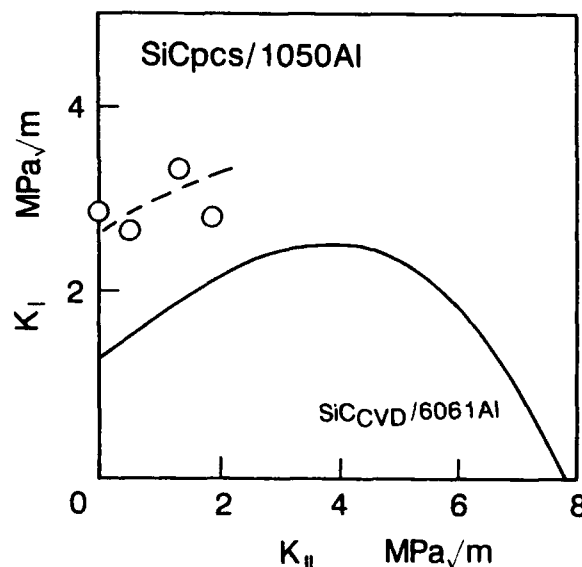
Figure 4. Comparisons of SiC$_{PCS}$/1050Al with SiC$_{CVD}$/6061Al.

Comparisons of SiC$_{CVD}$/6061Al with SiC$_{PCS}$/1050Al

Results for SiC$_{PCS}$/1050Al are compared with that for SiC$_{CVD}$/6061Al in Fig. 4. It can be seen from this figure that interfacial fracture resistance for SiC$_{PCS}$/1050Al is superior to SiC$_{CVD}$/6061Al. It results from the difference of fracture micromechanism as discussed later. It is therefore concluded that the interfacial fracture characteristics strongly depends on the reinforcement fiber/matrix interface.

MIXED-MODE FRACTURE CRITERIA

Empirical Formulations

A general formulation has been proposed in the following form [15]

$$(K_I / K_{IC})^m + (K_{II} / K_{IIC})^n = 1 \tag{6}$$

for the I-II tension/shear quadrant. The coefficients m and n are determined by curve-fitting and the K's are the appropriate stress intensity factors. The present data shown in Figs. 3 and 4 are not always consistent with the above quadratic relation.

Constant $J_{tot,c}$

A more fundamental fracture criterion, which is often assumed when there is insufficient data to support any other, is that of constant fracture energy release rate

$$J_{tot,c} (\sim G_C) = J_I + J_{II} + J_{III} = \text{constant} \tag{7}$$

The Mode III antiplane shear strain energy release rate J_{III} is equal to zero in present study.

Mixed-mode interfacial fracture toughness in terms of J-integral, $J_{tot,c}$ defined at maximum load are plotted against the loading angle in Fig. 5 for both $SiC_{CVD}/6061Al$ and $SiCpcs/1050Al$ and Fig. 6 for M40J/1080Al. It can be seen from these figures that M40J/1080Al shows the lowest fracture resistance in this investigated materials, and that mixed-mode interfacial fracture toughness for $SiCpcs/1050Al$ are superior to that for $SiC_{CVD}/6061Al$. It is found that the mixed mode interfacial fracture toughness is strongly dependent on both the kinds of reinforcement fiber and the fiber/matrix interface characteristics.
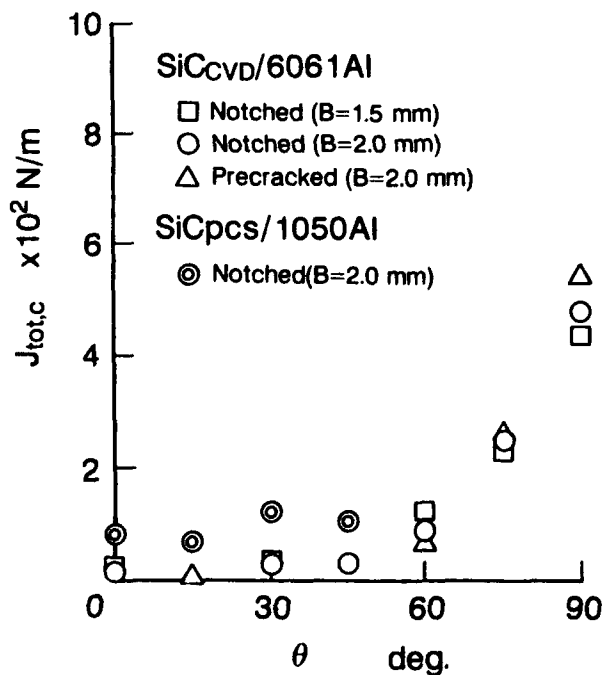
Figure 5. Mixed-mode fracture toughness $J_{tot,c}$ for $SiC_{CVD}/6061Al$ and $SiCpcs/1050Al$.
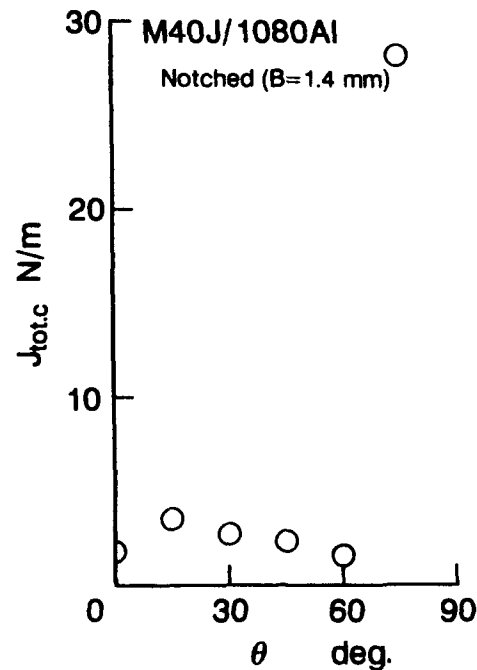
Figure 6. Mixed-mode fracture toughness $J_{tot,c}$ for M40J/1080Al.
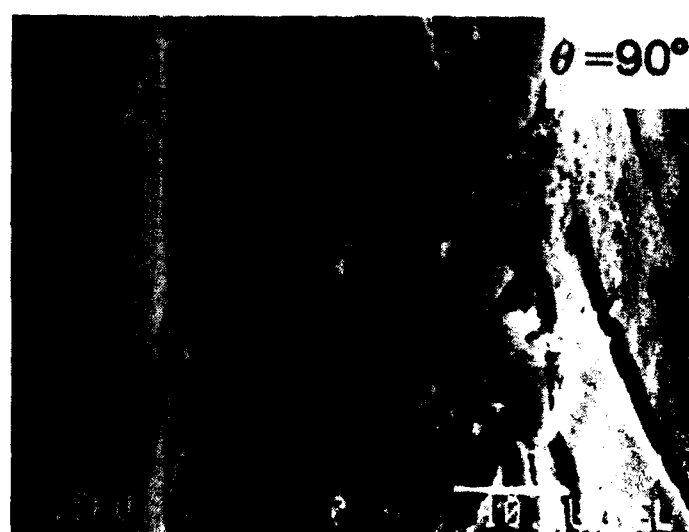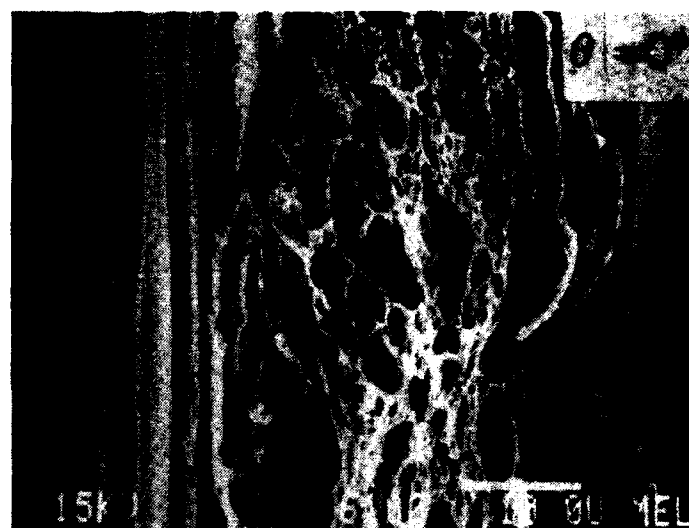
Figure 7. Fractographs showing microscopic fracture mechanism for SiC$_{CVD}$/6061Al.

Figures 5 and 6 also shows that $J_{tot,c}$ are nearly constant until the loading angle is approximately 60° where mode I component is larger than mode II, and then rapidly increases with increasing the loading angle. The present data do not always support Eq. 7. There is also little influence of specimen thickness and fatigue precraking in $J_{tot,c}$.

FRACTOGRAPHIC EXAMINATIONS

Fractographs of fracture surfaces are shown in Fig. 7 for SiC_{CVD}/6061Al. The pure mode I fracture surface ($\theta = 0^\circ$) shows the equiaxed dimple pattern of the matrix metal, while the pure mode II surface ($\theta = 90^\circ$) shows the shear dimple pattern. Clearly the fracture surfaces are quite dissimilar. The equiaxed dimple pattern are also predominantly observed under the mixed mode loading until θ is approximately 60°, although the shear dimple pattern partially observed with the proportion of Mode II in-plane shear. These fractographic examinations are consistent with the analytical results described earlier.

It is also found from the fractographic examinations that SiC_{pcs}/1050Al are fractured with the reinforcement fiber bridging and breakage, on the other hand the fiber breaking is not occurred for SiC_{CVD}/6061Al. It is considered to be a reason that the mixed-mode fracture resistance for SiC_{pcs}/1050Al is superior to that for SiC_{CVD}/6061Al.

SUMMARY AND CONCLUSIONS

The mixed-mode interfacial fracture characteristics for continuous fiber reinforced metal matrix composites have been experimentally determined using the FEM analysis. The conclusions may be summarized as follows.
(1) There is a great difference in the mixed-mode fracture behavior between SiC_{CVD}/6061Al and SiC_{pcs}/1050Al.
(2) Critical stress intensity factor under pure mode I loading is lower than that under pure mode II loading.
(3) Interfacial fracture resistance for SiC_{pcs}/1050Al is superior to SiC_{CVD}/6061Al. It is due to the difference of fracture micromechanism.
(4) K_I versus K_{II} relationships are not always consistent with the empirical quadratic formulation.
(5) Mixed-mode interfacial fracture toughness, $J_{tot,c}$ are nearly constant until the loading angle is approximately 60 degrees where Mode I component is larger than Mode II, and then rapidly increases with the proportion of Mode II in-plane shear. $J_{tot,c}$ are not always constant, and the mixed-mode interfacial fracture criterion can not be described uniquely in terms of J-integral concept.

ACKNOWLEDGEMENTS

REFERENCES

1. Hirano, K., F. Tamae and K. Nonaka, 1988. "Fracture mechanics of transverse fatigue crack growth characteristics of advanced continuous fiber reinforced metal." *Trans.JSME., 54-501*, pp.910-916 (in Japanese).

2. Hirano, K. 1988. "Near-threshold transverse fatigue crack growth characteristics of unidirectional continuous fiber reinforced metals." *Proc. of 4th Japan-U.S. Conference on Composite Materials,* pp.633-642.

3. Hirano, K. and H. Takizawa, 1989. "Evaluation of fatigue crack growth characteristics of whisker reinforced metals." *Trans. JSME., Ser.A, 55-511,* pp.373-379(in Japanese).

4. Hirano, K. and H. Nakazawa, 1989. "Fracture toughness of whisker reinforced aluminum alloys." *Trans. JSME., Ser.A, 55-520,* pp.2427-2433(in Japanese).

5. Hirano, K. and T. Sasaki, 1990. "Fracture toughness of advanced whisker reinforced metal matrix composites." *Advanced Composite Materials (edited by C. Bathias and M. Uemura)* , pp.115-120.

6. Hirano, K., 1990. "Fatigue crack growth characteristics of whisker reinforced aluminum alloys." *Proc. of the 5th Conf. of Fatigue and Fatigue Threshold,* pp.863-868.

7 Hirano, K., 1990. "Mixed mode(I,II) fatigue crack growth characteristics of contin .ous ⁻⌐⌐ⁿ fiber reinforced aluminium and titanium alloys matrix composites." *Proc. of 5th Japan-ʋ.. (ɔnf. on Composite Materials,* pp.311-319.

8. Hirano, K., 1990. "Evaluation of high temperature tensile strength characteristics for advanced continuous fiber reinforced metal matrix composites." *Proc. of Symp. on Materials and Mechanics. No.900-86,* pp.174-176 (in Japanese).

9. Hirano, K., Seto, S., Ozaki, M. and Kikuchi, M., 1990. "Interfacial fracture toughness of continuous fiber reinforced metal matrix composites under mixed mode loading." *Proc. of Symp. on Materials and Mechanics. No.900-50,* pp.251-256(in Japanese).

10. Geni, M., Kikuchi, M. and Hirano, K. 1991. "Fracture analysis of whisker reinforced aluminum alloys." *Proc. of 4th Conf. on Asian-Pacific Congress on Strength Evaluation.* to be published.

11. Hirano, K., Kashiwagi, M. and Kikuchi, M., 1991. "Fatigue crack growth characteristics of SiC_{CVD}/Ti alloy under mixed mode loading." *Preprint of Annual Meeting of Japan Society of Mechanical Engineers. No.910-71(Vol.B),* pp.97-99(in Japanese).

12. Hirano, K., 1991. "Determination of fracture toughness for whisker-reinforced aluminium alloy matrix composite using chevron-notched specimen. *JSME Int. J.,* 34-310, pp.234-239.

13. Hirano K., 1991. "Fatigue crack growth characteristics of metal matrix composites." *Proc. of the 6th Int. Conf. on Mechanical Behavior of Materials. Vol. 3,* pp.93-100.

14. Arcan, M., Hashin, Z. and Voloshin, A., 1978. "A Method to Produce Uniform Plane-stress States with Applications to Fiber-Reinforced Materials." *Experimental Mechanics,* pp.141-146.

15. Spencer, B. and Barnby, J. T., 1976. *Journal of Material Science, 11,* pp.83-85.

Effect of Annealing the Polymer on the Adhesion between Carbon Fibers and a Thermoplastic Matrix

PASCAL COMMERÇON AND JAMES P. WIGHTMAN

ABSTRACT

The surface chemistry and surface energetics of IM7 carbon fibers are characterized prior to and after plasma treatment of the fibers. The adhesion between the fibers and a thermoplastic matrix, polyethersulfone, is evaluated from the microbond pull-out test. The strength and the durability of the adhesive bond is studied as a function of the fiber surface treatments and the polymer annealing conditions.

INTRODUCTION

The development of tough thermoplastic polymers opened the way for a new family of high-performance composites. These polymers are attractive in part because of their processing advantages such as short cycles, scrap recovery and indefinite shelf life [1]. The optimum mechanical properties of a carbon fiber-thermoplastic matrix composite cannot be achieved if the fiber-matrix interface, or more appropriately the fiber-matrix interphase [2,3], is the limiting factor. A common approach, in the case of epoxy-carbon fiber composites, has been to modify the surface of the fibers through sizing, thermal or other chemical treatments, the purpose of which is to improve the epoxy-carbon fiber adhesion.

The question arises as to whether the fiber surface treatments, which have been optimized for fiber-epoxy interphases, are also appropriate in the case of fiber-thermoplastic interphases. The objective of this work was to study the effect of both the plasma treatment of the carbon fibers and the thermal treatment of the polymer on the adhesion between carbon fibers and a thermoplastic polymer.

EXPERIMENTAL

The carbon fibers used in this study were manufacturer-treated, unsized intermediate modulus IM7 fibers obtained from Hercules. The average fiber diameter, which was determined by scanning electron microscopy (SEM) as well as by a contact angle method, is about 5.5 μm. Various plasma treatments were utilized. The fibers were treated either

Pascal Commerçon and James P. Wightman, Chemistry Department, Virginia Tech, Blacksburg, VA, 24061

for 15 sec. in an inorganic gas plasma, such as air and ammonia (NH_3), or for 2 min. in an organic gas plasma, such as methane (CH_4), ethylene (C_2H_4), fluoromethane (CF_4) and fluoroform (CHF_3). The surface chemistry of the fibers was determined by x-ray photoelectron spectroscopy (XPS). The effect of the plasma treatments on the fiber surface energy parameters was measured by a two-liquid tensiometric technique [4-6]. The adhesion between the amorphous polyethersulfone (PES), Tg = 220°C, and the treated fibers was measured from the microbond pull-out test [7,8]. In this test a droplet of polymer is deposited on a single filament by melting a small strip of polymer film [9,10]. The test consists in pulling the fiber through the droplet that is maintained in a fixed position between the jaws of a microvise. In some instances the resin droplets were annealed at Tg for about 30 min. (A240SFC) or between 220°C and 260°C for 45 min. (A280Q) or 100 min. (A280SFC) [10]. Samples that were not annealed after the droplet formation are referred to as quenched samples (Q). The fiber-matrix bond durability was tested by aging samples for a week at 50°C and 0% relative humidity (RH) or 80-90% RH prior to testing. All tests were performed at room temperature.

RESULTS AND DISCUSSION

FIBER SURFACE CHARACTERIZATION

The air plasma treatment resulted in a significant oxidation of the carbon fiber surface, as indicated by XPS analysis (see Table I.); there was a 100% increase in oxygen concentration. A 50% increase in nitrogen surface atomic concentration was observed after NH_3 plasma treatment. An XPS detailed analysis of the N1s region of the spectrum indicates that the nitrogen increase is due to a cleaning effect of the NH_3 plasma rather

TABLE I. ATOMIC CONCENTRATIONS (%)

Element → Surface Treatment ↓	Carbon	Oxygen	Nitrogen	Fluorine
as-received	85.0 ± 1.3	9.9 ± 0.8	5.1 ± 0.6	/
air plasma (15 sec.)	76.0 ± 2.2	19.8 ± 1.2	4.1 ± 1.3	/
NH_3 plasma (15 sec.)	84.8 ± 0.7	8.0 ± 0.3	7.2 ± 0.7	/
CH_4 plasma (2 min.)	90.9 ± 0.8	5.8 ± 0.4	3.3 ± 0.4	/
C_2H_4 plasma (2 min.)	96.2 ± 0.9	3.2 ± 0.3	0.9 ± 0.5	/
CHF_3 plasma (2 min.)	36.5 ± 0.5	1.6 ± 0.1	0.7 ± 0.1	61.2 ± 0.5
CF_4 plasma (2 min.)	56.7 ± 0.6	3.3 ± 0.7	1.7 ± 0.2	38.4 ± 0.0

than to a direct functionalization of the surface. The other ablative treatment was the CF_4 plasma. CF_4 plasma treatments are used in the electronic industry to etch silicone-containing materials. In our study this plasma did not produce any significant polymeric deposit on the fibers, as did the other organic gas plasmas, but resulted in the fluorination of the fibers, as indicated by the fluorine atomic concentration. The fluoroform plasma deposited a layer of fluorocarbon akin to, but structurally different than, a "Teflon" coating. Both methane and ethylene plasmas deposited layers of hydrocarbon material on the fiber surface.

The fiber surface chemistry has a direct influence on the fiber surface free energy which, in turn, affects the wetting of the polymer and the capability of establishing strong bonds between the polymer and the fibers. The values of the dispersion component of the fiber surface free energy, γ_s^d, and the non-dispersion term, I_{sf}^p, are used to characterize the fiber energetics and are summarized in Table II. The air plasma decreases γ_s^d by an order of magnitude while increasing the I_{sf}^p term, which can be related to the oxidation of the air plasma treated fibers. The NH_3 plasma treatment does not change I_{sf}^p, when compared to as-received fibers, but increases the value of γ_s^d. This is consistent with the cleaning effect of this plasma. All organic gas plasmas give lower surface energy parameters, in accord with what could be expected from the surface chemistry.

SEM observation of the fibers before and after plasma treatments does not reveal any significant change in surface morphology. In particular there is no evidence, at a 5000X magnification. of surface roughening after air, NH_3 or CF_4 plasma treatments.

TABLE II. SURFACE ENERGY PARAMETERS (mJ/m^2)(advancing contact angle)

Surface Energy → Surface Treatment ↓	γ_s^d	I_{sf}^p
as-received	27	42
air plasma (15 sec.)	3	55
NH_3 plasma (15 sec.)	48	39
CH_4 plasma (2 min.)	11	10
C_2H_4 plasma (2 min.)	25	5
CHF_3 plasma (2 min.)	7	12
CF_4 plasma (2 min.)	14	14
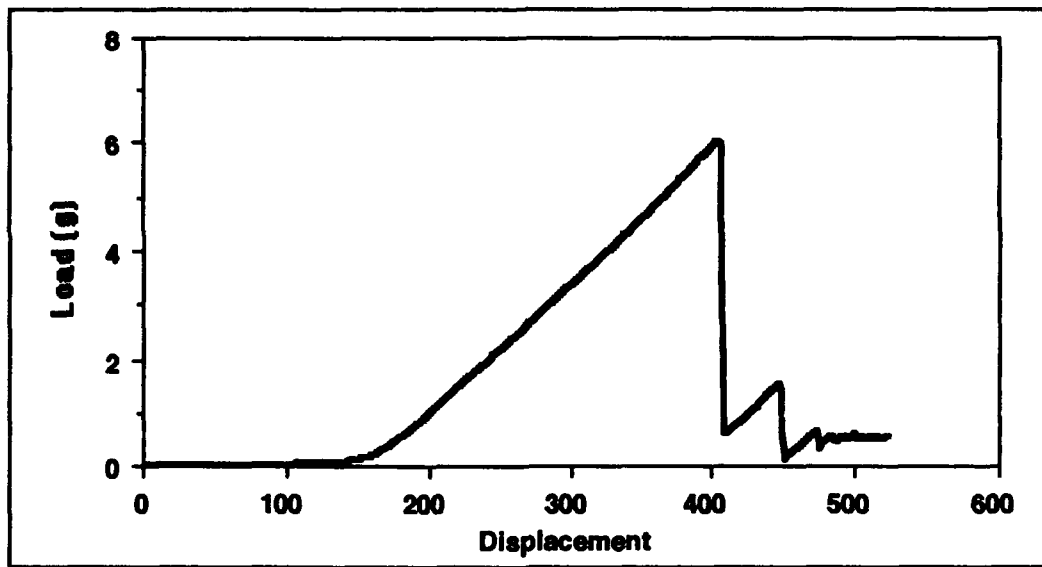
Figure 1. Load vs Displacement curve obtained during a microbond pull-out test.

FIBER-MATRIX ADHESION

Figure 1 shows an example of a load vs displacement curve obtained during a microbond pull-out test. The load increases linearly until debonding occurs. The sharp drop in load at debonding indicates a catastrophic type of failure. A plot of debonding
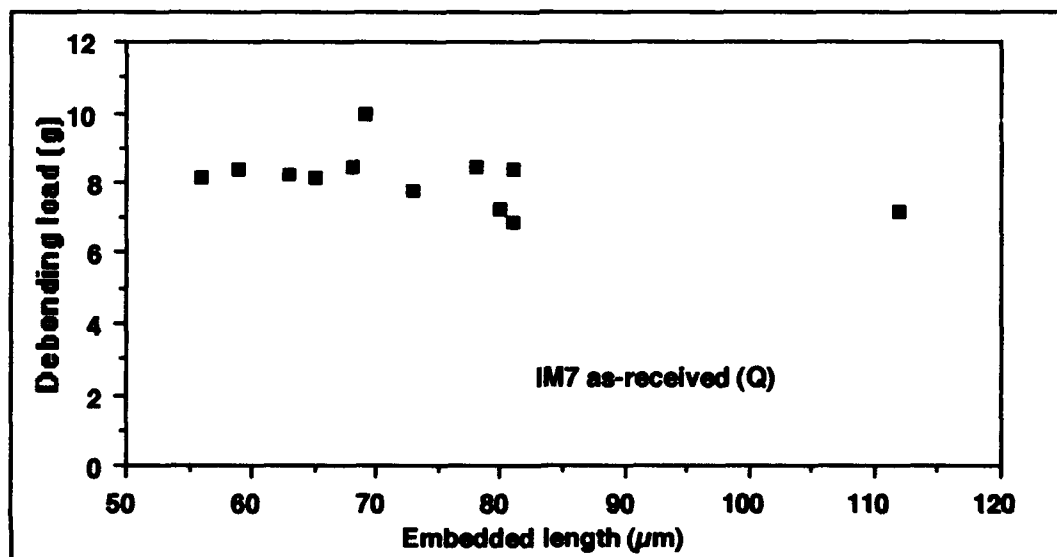
Figure 2. Debonding Load (in grams) vs droplet embedded length (in μm) for as-received fibers and quenched PES.
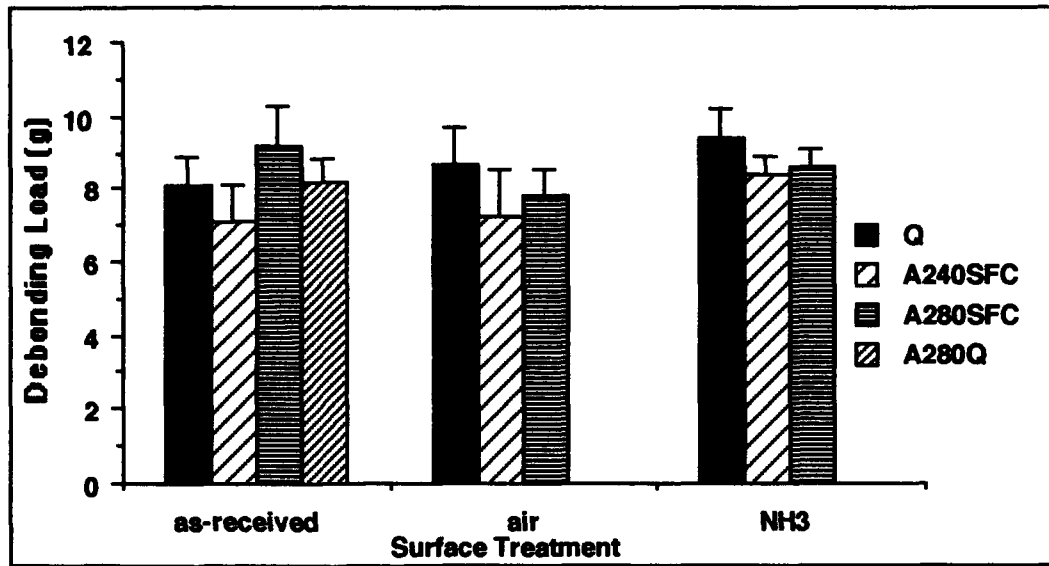
Figure 3. Debonding load (in grams) as a function of the fiber surface treatment and the annealing conditions.(inorganic gas plasmas)

load as a function of droplet embedded length is shown in Figure 2 for as-received fibers and quenched PES. This indicates that the debonding load is independent of the embedded area, thus the debonding mechanism proceeds by crack propagation rather than by yielding. The average debonding load (in grams) is used as an indicator of the goodness of the fiber-matrix bond.
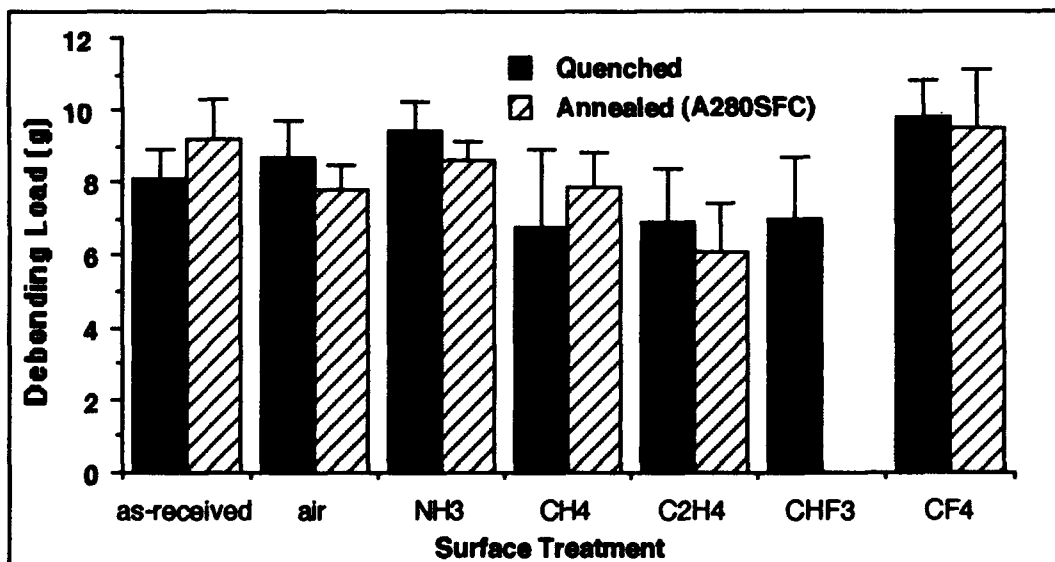
Figure 4. Debonding load (in grams) as a function of the fiber surface treatment for quenched and annealed (A280SFC) samples.

The effect of annealing time and temperature is illustrated in Figure 3 for as-received, air and NH_3 plasma treated fibers. In all cases the lower temperature annealing (A240SFC) gave lower debonding loads than for quenched samples. The A280SFC annealing increased significantly the adhesion for as-received fibers. This was determined by an analysis of variance at the 95% confidence level. However, annealing (A280SFC) of samples prepared with plasma treated fibers showed either no improvement or no significant effect on adhesion when compared to quenched samples (Figure 4). Finally, the comparison of A280SFC and A280Q annealings on the adhesion of PES to as-received fibers indicates that the longer the polymer is annealed above its Tg the more time the molecules have to "flow" and the better is the adhesion. The molecules at the interphase may adopt "preferred low-energy adsorbed conformations". The following is proposed as a tentative explanation for the stronger bond observed for as-received fibers when the PES is annealed (A280SFC). The complementary heat treatment (annealing) facilitates the wetting of the polymer by "dissolving" or penetrating the thin, weak boundary layer that surrounds the fibers. All plasma treatments tend to ablate the surface to some extent. It is assumed that the weak initial layer is thus removed before the polymer is melted to form the droplet. Optimum wetting is therefore achieved during the droplet formation step and annealing does not result in further improvement.

The influence of annealing on the bond durability after thermal aging in dry (0% RH) and humid (80-90% RH) conditions is summarized in Table III for as-received fibers and in Table IV for air plasma treated fibers. For as-received fibers no significant difference is observed between aging at 0% RH or 80-90% RH, regardless of the annealing conditions, but annealed samples give more durable bonds than quenched samples. In the case of air plasma treated fibers, samples aged in humid conditions give systematically lower debonding loads than samples aged in dry conditions, regardless of the annealing. The difference between dry and humid results for air plasma treated fibers can be explained by the greater hydrophilicity (higher I^p_{sf} and lower γ^d_s) of these fibers compared to as-received fibers. As a result, there is a greater driving force for moisture absorbed by the PES to diffuse through the polymer to the fiber-matrix interphase and weaken the bond.

TABLE III. DEBONDING LOAD (g) AS A FUNCTION OF ANNEALING AND AGING CONDITIONS.(as-received fibers)

	Q	A240SFC	A280SFC
0% RH	7.4 ± 1.1	8.0 ± 1.4	nd
80-90% RH	7.5 ± 0.6	8.7 ± 1.1	8.1 ± 1.8

nd: not determined

TABLE IV. DEBONDING LOAD (g) AS A FUNCTION OF ANNEALING AND AGING CONDITIONS.(air plasma treated fibers)

	Q	A240SFC	A280SFC
0% RH	8.6 ± 0.9	8.5 ± 1.2	nd
80-90% RH	7.3 ± 1.7	7.3 ± 1.3	7.4 ± 1.3

nd: not determined

CONCLUSION

Plasma treatments are very effective in altering the surface chemistry and surface energetics of carbon fibers. The wetting of the polyethersulfone on IM7 car'Jon fibers is affected by both the fiber surface treatments and the polymer annealing. The annealing process plays a significant role only for as-received fibers where it is thought to overcome the negative effect of the initial "weak boundary layer". Annealed PES on as-received fibers leads to strong and durable fiber-matrix adhesion.

REFERENCES

1. Committee on thermoplastic composite and structural components, "The Place for Thermoplastic Composites in Structural Components", final report, NMAB-434, National Academy Press 1987.

2. L. Sharpe, 1972. "The Interphase in Adhesion." Journal of Adhesion,4, 51-64.

3. R.E. Swain, K.L. Reifsnider, K. Jayaraman and M. El-Zein, 1990. "Interface/Interphase Concepts in Composite Materials Systems." Journal of Thermoplastic Composite Materials,3, 13-23

4. Y. Tamai, K.Makuuchi and M. Suzuki, 1967. "Experimental Analysis of Interfacial Forces at the Plane Surface of Solids." Journal of Physical Chemistry, 71(13), 4176-4179.

5. J. Schultz, C. Cazeneuve, M.E.R. Shanahan and J.-B. Donnet, 1981. "Fibre Surface Characterization." Journal of Adhesion, 12, 221-231.

6. K. Tsutsumi, S. Ishida and K. Shibata, 1990. "Determination of the Surface Free Energy of Modified Carbon Fibers and its Relation to the Work of Adhesion." Colloid and Polymer Science, 268, 31-37.

7. B. Miller P. Muri and L. Rebenfeld, 1987. ""A Microbond Method for the Determination of the Shear Strength of a Fiber/Resin Interface." Composites Science and Technology, 28, 17-32

8. U. Gaur and B. Miller, 1989. "Microbond Method for Determination of Shear Strength of a Fiber/Resin Interface: Evaluation of Experimental Parameters." Composites Science and Technology, 34, 35-51

9. G.P. Desio, B. Miller and L. Rebenfeld. November 1988. " The Microbond Method for the Evaluation of Interfacial Shear Strengths of Composites." Paper presented at. AIChE Annual Meeting, Washington, D.C.

10.P. Commerçon and J.P. Wightman, 1992. "Surface Characterization of Plasma Treated Fibers and Adhesion to a Thermoplastic Polymer." J. Adhesion (in press.).

A Homogenization Theory for Fiber Composites with Imperfect Interface at Elevated Temperatures

YOTSUGI SHIBUYA* AND SU-SU WANG**

ABSTRACT

A homogenization theory with multi-scale asymptotic expansion is used to determine thermomechanical properties of fiber composite materials at elevated temperatures. To solve the perturbed displacement field in the composite, a boundary integral equation method is introduced with an eigenstrain concept for thermal and applied strain fields. The method is applied to a SCS-6/Ti-6Al-4V metal matrix composite with an imperfect interface between the fiber and the matrix. Effective nonlinear constitutive behavior of the composite is predicted due to complex deformations of the interface. The fiber-matrix interface is modeled as a spring layer of infinitesimal thickness initially, where discontinuity of displacements, under loading, between the fiber and the matrix is assumed to be proportional to the associated tractions on the interface. A generalized plane-strain analysis is employed for analyzing the unidirectional fiber composite. Residual thermal stresses due to high processing and operating temperatures are included in the analysis. Effective thermoelastic properties and thermal expansion coefficients of the composite material at several temperatures are determined by the present method. Microscopic stresses and deformations around the fiber-matrix interface are also studied. Finally, the numerical solutions are compared with experimental results obtained at room temperature and at 320°C(600°F).

INTRODUCTION

Deformation and failure behavior of advanced fiber composite materials at elevated temperatures are very complex owing to a number of microstructural and environmental factors, including residual stresses caused by high processing temperatures and interfacial mismatch and property degradation. To understand thermomechanical behavior of the composites, a detailed thermomicromechanics study is needed to determine both microscopic deformations and stresses and macroscopic effective properties of the material with various interfacial conditions.

Early work, for example, in Refs.[1,2,3], has employed homogenization theory to study elastic properties of heterogeneous media. A homogenization theory with multi-scale asymptotic expansion is introduced to obtain effective elastic properties of composites by Bensoussan, et al.[4]. The homogenization theory has high compatibility to modern numerical analyses, such as finite element methods, because final formulation for effective homogenized constitutive equations leads to the solution for perturbed displacements in a composite material. Lene and Leguillon[5] and Devries, et al.[6] apply homogenization theory

---

* Yotsugi Shibuya, Dept. of Mechanical Engineering, University of Houston, 4800 Calhoun Road, Houston, TX 77204, U.S.A.; Now, with Dept. of Mechanical Engineering, Akita University, Akita 010, Japan.
** Su-Su Wang, Dept. of Mechanical Engineering, University of Houston, 4800 Calhoun Road, Houston, TX 77204, U.S.A.

to determine effective properties of fiber composite materials with a slip fiber-matrix interface and broken fibers, respectively.

In order to study mechanical behavior of composites with an imperfect interface or interphase, a spring-layer interface model has been proposed[5], where discontinuity of displacements at the interface between fibers and the matrix are assumed to be proportional to the associated tractions on the interface. For example, Lene and Leguillon[5] and Benveniste[7] analyze properties of composites with a spring interface model. Achenbach and Zhu[8] also use an interface model to analyze mechanical behavior of a fiber composite with hexagonal unit cells by a boundary integral equation(BIE) method. Hashin[9] analyzes thermoelastic properties of a fiber composite with an imperfect interface using the well-known cylinder assembly model.

In this study, a homogenization theory is developed to study thermomechanical properties of composite materials at elevated temperatures. To solve the perturbed displacement field in the composite, a boundary integral equation method is introduced along with the well-known eigenstrain concept for thermal and applied strains. The perturbed displacements in the composite material can be obtained by an analytic formulation which is derived with the aid of known Green's functions. The method is applied to examine thermomechanical behavior of a unidirectional SCS-6/Ti-6Al-4V composite with the interface modeled as a spring-layer interface. The effect of interface conditions on effective thermomechanical properties of the composite with the presence of thermal residual stresses is examined. Effective nonlinear constitutive equations of the composite are obtained due to complex deformation of the interface.

GOVERNING EQUATIONS FOR HOMOGENIZATION THEORY

A homogenization theory is derived here for a unidirectional fiber composite. The microstructure of the composite is assumed to be periodical, and an associated hexagonal unit cell in the composite is shown in Fig. 1. Two coordinate systems are placed in the composite material. A large-scale coordinate system $x=(x_1, x_2, x_3)$, which indicates overall structural and homogenized fields, is shown in the figure. A small-scale coordinate system $y=(y_1, y_2, y_3)$, which is associated with microscopic structural details, is located in each unit cell region Y of the composite. From the condition of periodicity, each unit cell has the same microstructure. The periodicity conditions for stress and strain in a unit cell are given as

$$\sigma_{ij}^{k}(y) = \sigma_{ij}^{l}(y) = \cdots\cdots = \sigma_{ij}(y) \quad , \quad \varepsilon_{ij}^{k}(y) = \varepsilon_{ij}^{l}(y) = \cdots\cdots = \varepsilon_{ij}(y) \tag{1}$$

where σ_{ij} and ε_{ij} are stresses and strains, respectively. The superscript (k) indicates quantities associated with the k-th unit cell of a period Y.
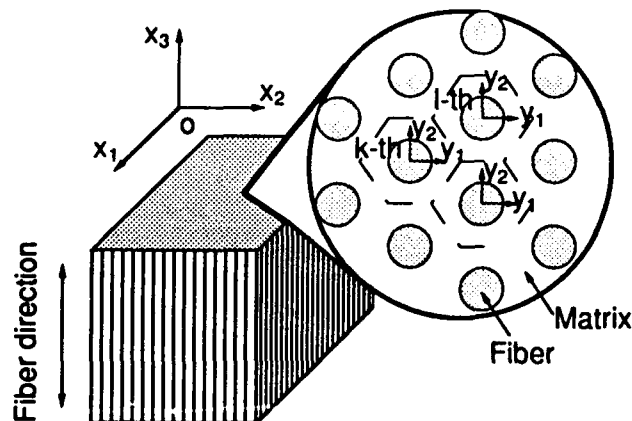
Fig.1 Fiber composite material and two coordinate systems.

Consider a composite material at the microscopic level as an inhomogeneous medium with a periodic structure. The governing equations for the composite are

$$\frac{\partial}{\partial x_j}\sigma_{ij}(x,y) + F_i(x) = 0 \tag{2}$$

$$\sigma_{ij}(x,y) = C_{ijkl}(y,T)[\varepsilon_{kl}(x,y) - \varepsilon_{kl}^T(y,T)] \tag{3}$$

$$\varepsilon_{ij}(x,y) = \frac{1}{2}[\frac{\partial u_i(x,y)}{\partial x_j} + \frac{\partial u_j(x,y)}{\partial x_i}] \tag{4}$$

$$\varepsilon_{ij}^T(y,T) = \int_{T_r}^{T} \alpha_{ij}(y,\tau)\, d\tau \tag{5}$$

where F_i are body forces; u_i, displacements; and $C_{ijkl}(y,T)$ and $\alpha_{ij}(y,T)$ are elastic stiffnesses and thermal expansion coefficients of the inhomogeneous medium. The T_r is a reference temperature, i.e., thermal residual stress free temperature.

In order to derive homogenization equations for the composite, a two-scale asymptotic expansion of the displacements is made. The displacement in the inhomogeneous medium with a periodical structure is replaced by asymptotic expansion with a scaling parameter λ as

$$u_i(x,y) = u_i^{(0)}(x,y) + \lambda u_i^{(1)}(x,y) + \lambda^2 u_i^{(2)}(x,y) + \cdots \tag{6}$$

where λ characterizes the microstructure or unit cell of the composite. Relationships between large-scale and small-scale coordinate systems, and the differential operator are

$$y \rightarrow x/\lambda, \qquad \frac{\partial}{\partial x_j} \rightarrow \frac{\partial}{\partial x_j} + \frac{1}{\lambda}\frac{\partial}{\partial y_j} \tag{7}$$

By substituting Eq.(7) into the governing equations(2)-(5), equilibrium equations of the composite yield the following equations of different orders in λ:

$$\lambda^{-2}: \quad \frac{\partial}{\partial y_j}[C_{ijkl}\varepsilon_{kl}^{(0)}] = 0 \tag{8}$$

$$\lambda^{-1}: \quad \frac{\partial}{\partial y_j}\{C_{ijkl}[\varepsilon_{kl}^{(1)} - \varepsilon_{kl}^T + e_{kl}^{(0)}]\} + \frac{\partial}{\partial x_j}[C_{ijkl}\varepsilon_{kl}^{(0)}] = 0 \tag{9}$$

$$\lambda^{0}: \quad \frac{\partial}{\partial y_j}\{C_{ijkl}[\varepsilon_{kl}^{(2)} + e_{kl}^{(1)}]\} + \frac{\partial}{\partial x_j}\{C_{ijkl}[\varepsilon_{kl}^{(1)} + e_{kl}^{(0)} - \varepsilon_{kl}^T]\} = -F_i \tag{10}$$

$$\lambda^{1}: \quad \cdots\cdots$$

where

$$e_{ij}^{(k)} = \frac{1}{2}[\frac{\partial u_i^{(k)}}{\partial x_j} + \frac{\partial u_j^{(k)}}{\partial x_i}] \qquad \varepsilon_{ij}^{(k)} = \frac{1}{2}[\frac{\partial u_i^{(k)}}{\partial y_j} + \frac{\partial u_j^{(k)}}{\partial y_i}] \tag{11}$$

As the zeroth-order terms $u_i^{(0)}$ do not depend on the microscopic field, i.e., $u_i^{(0)}(x,y) = u_i^{(0)}(x)$, Eq.(8) is always satisfied. The λ^{-1} order terms in Eq.(9) can be reduced to the following:

$$\frac{\partial}{\partial y_j} \{C_{ijkl}[\varepsilon_{kl}^{(1)} - \varepsilon_{kl}^T(y,T) + \varepsilon_{kl}^*]\} = 0 \tag{12}$$

where ε_{ij}^* are defined by $\varepsilon_{ij}^* = e_{ij}^{(0)}$, which are constants in the unit cell Y. As the zeroth-order displacements, $u_i^{(0)}$, are macroscopic displacements in the composite which depends on the x coordinates only, the solution for Eq.(12) may be expressed by the sum of the applied strains ε_{ij}^* and the thermal strains ε_{ij}^T as

$$u_i^{(1)}(y) = \Phi_{ikl}\varepsilon_{kl}^* + \Psi_i(\varepsilon_{kl}^T) \tag{13}$$

The Φ_{ikl} and Ψ_i will be determined later as solutions in the unit cell for Eq.(12). In conjunction with the compatibility conditions, $u_i^{(1)}$ can be obtained through the principle of superposition of the applied strains and the thermal strains.

By substituting Eq.(12) into Eq.(10) and integrating over the unit cell region Y, we can determine homogenized thermoelastic constitutive equations of the composite as

$$\sigma_{ij}^*(x) = \{\frac{1}{V}\int_Y [C_{ijkl} + \frac{1}{2} C_{ijmn}(\frac{\partial\Phi_{mkl}}{\partial y_n} + \frac{\partial\Phi_{nkl}}{\partial y_m})] \, dY(y)\}\varepsilon_{kl}^*$$

$$-\frac{1}{V}\int_Y C_{ijkl}[\varepsilon_{kl}^T - \frac{1}{2}(\frac{\partial\Psi_k}{\partial y_l} + \frac{\partial\Psi_l}{\partial y_k})] \, dY(y) \tag{14}$$

where the symbol (*) indicates quantities in the homogenized field, and V is the volume of the unit cell region Y. The effective elastic moduli of the composite can be expressed as

$$C_{ijkl}^* = \frac{1}{V}\int_Y [C_{ijkl} + \frac{1}{2} C_{ijmn}(\frac{\partial\Phi_{mkl}}{\partial y_n} + \frac{\partial\Phi_{nkl}}{\partial y_m})] \, dY(y) \tag{15}$$

Thermal strains and effective thermal expansion coefficients of the composite can also be determined as follows:

$$C_{ijkl}^*\varepsilon_{kl}^{T*} = \frac{1}{V}\int_Y C_{ijkl}[\varepsilon_{kl}^T - \frac{1}{2}(\frac{\partial\Psi_k}{\partial y_l} + \frac{\partial\Psi_l}{\partial y_k})] \, dY(y) \tag{16}$$

Fig. 2   Unit cell with hexagonal fiber array.

$$\alpha_{ij}^* = \frac{d\,\varepsilon_{ij}^{T*}}{dT} \tag{17}$$

Thus, complete effective thermoelastic properties of a composite can be obtained from the above equations. We note that the formulation requires the solution for Eq.(12) in a unit cell. These equations will be solved on the basis of the eigenstrain concept[10] with the applied strains ε_{ij}^* and thermal strains ε_{ij}^T. Higher-order contributions from $u_i^{(2)}$, $u_i^{(3)}$,..... are small in general and neglected.

BOUNDARY VALUE PROBLEM FOR Φ_{ijk} AND Ψ_i

In the boundary value problem for solving Φ_{ijk} and Ψ_i, the unit cell in the composite is taken as a regular hexagonal array as shown in Fig. 2. The microstructure-scale coordinate systems, (y_1,y_2) and (r,θ), are located in the unit cell with the origin at the center of the fiber with a radius a. The w and h are distances between fibers along x_1 and x_2 directions, respectively.

Along the outside boundary, the displacements $u_i^{(1)}(y)$ and tractions $t_i(y)$ are continuous through the neighboring cells. As the perturbed displacements are periodical, the $u_i^{(1)}(y)$ are the same in each unit cell. In view of these, the conditions on the outside boundaries of the unit cell, AB, BC,CD, DE, EF and FA, are written as follows:

$$u_i^{m(1)}(\xi_j) = -u_i^{m(1)}(-\xi_j), \quad t_i^m(\xi_j) = t_i^m(-\xi_j) \quad (i=1,2,3;\ j = 1,2,\cdots,6) \tag{18}$$

where the superscript (m) indicates the matrix region, and ξ_j are local coordinates along AB, BC, CD, DE, EF and FA with the origin at the center of each line segment.

The interface between the fiber and the matrix is modeled as a layer with spring constants. It may be assumed that discontinuity of displacements between the fiber and the matrix is proportional to the associated tractions along the interface. Thus, the interface conditions can be written as

(a) along the interface (I_s) separated with spring constants k_r and k_θ:

$$\sigma_{rr}^m = \sigma_{rr}^f = k_r[u_r^{m(1)} - u_r^{f(1)}] \quad , \quad u_r^{m(1)} > u_r^{f(1)} \tag{19}$$

$$\sigma_{r\theta}^m = \sigma_{r\theta}^f = k_\theta[u_\theta^{m(1)} - u_\theta^{f(1)}] \tag{20}$$

$$u_3^{m(1)} = u_3^{f(1)} \tag{21}$$

(b) along interface (I_c) with a spring constant k_θ:

$$\sigma_{rr}^m = \sigma_{rr}^f < 0 \tag{22}$$

$$\sigma_{r\theta}^m = \sigma_{r\theta}^f = k_\theta[u_\theta^{m(1)} - u_\theta^{f(1)}] \tag{23}$$

$$u_r^{m(1)} = u_r^{f(1)} \tag{24}$$

$$u_3^{m(1)} = u_3^{f(1)} \tag{25}$$

where $\sigma_{ij}^{(1)}$ are replaced by σ_{ij} for convenience. The superscript (f) indicates the quantities associated with the fiber region, and k_r and k_θ are spring constants of the interface along radial and circumferential directions. The case of $k_r=k_\theta=\infty$ indicates a perfectly bonded interface; and $k_r=0$ and $k_\theta=0$ correspond to a stress-free, separated interface with frictionless contact.

NUMERICAL METHOD

Equations(11) and (12) for the perturbed displacements and strains in the unit cell with the aforementioned boundary and interface conditions are solved by a boundary-integral-equation(BIE) method. The integral equation expression of the problem with an eigenstrain distribution in an arbitrary body is written, with the aid of the Green's functions G_{ij} reported by Swedlow and Cruse[10], as follows:

$$u_i^{(1)}(y) = \int_\Gamma [G_{ij}(y,y')t_j(y') - H_{ij}(y,y')u_j^{(1)}(y')]\, d\Gamma(y')$$

$$+ \int_\Omega F_{ik\iota}(y,y')\varepsilon_{k\iota}^a(y')\, d\Omega(y') \tag{26}$$

where t_j are traction components on the boundary Γ, and $\varepsilon^a_{ij} = (\varepsilon^T_{ij} - \varepsilon^*_{ij})$ are eigenstrains in the region Ω. The kernels F_{ijk} and H_{ij} can be determined from the fundamental solutions G_{ij} [10].

The perturbed displacements and tractions on the surface of the cell are determined by the boundary integral equations(26) numerically. Solutions for the inhomogeneous medium, i.e., the unit cell, may be obtained by dividing the cell into homogeneous subregions, i.e., subregions in matrix and fiber domains.

NUMERICAL EXAMPLES AND DISCUSSION

The homogenization theory developed in this study is applied to determine thermoelastic properties of metal matrix composites with various interface conditions. The metal matrix composite treated in this study is a SCS-6/Ti-6Al-4V material system which has SCS-6 silicon carbide fibers embedded in a Ti-6Al-4V alloy. The fiber diameter is about 140 μm and the fiber volume fraction is 0.4. The processing temperature T_r is 925°C [11]. The composite is assumed to be stress free at the temperature T_r. The thermoelastic properties of the constituent materials used in this study are summarized in TABLE 1[12]. Shear modulus and thermal expansion coefficient of the matrix are considered as linear and bilinear functions in temperature, respectively. The composite has large residual stresses due to the high processing temperature. The effect of thermal residual stress on thermomechanical properties of the composite will be addressed in this section.

TABLE 1 THERMOELASTIC PROPERTIES OF SCS-6 FIBERS
AND Ti-6Al-4V ALLOY.

Properties Material	Shear modulus G(GPa)	Poisson's ratio ν	Thermal Expansion Coefficient $\alpha(\times 10^{-6}\ 1/°C)$
Ti-6Al-4V	linear in T 41.4 at 20°C 12.4 at 1122°C	Constant in T 0.33	bilinear in T 8.6 at 22°C 10.0 at 399°C 11.7 at 1093°C
SCS-6 Fiber	175.	0.17	3.8
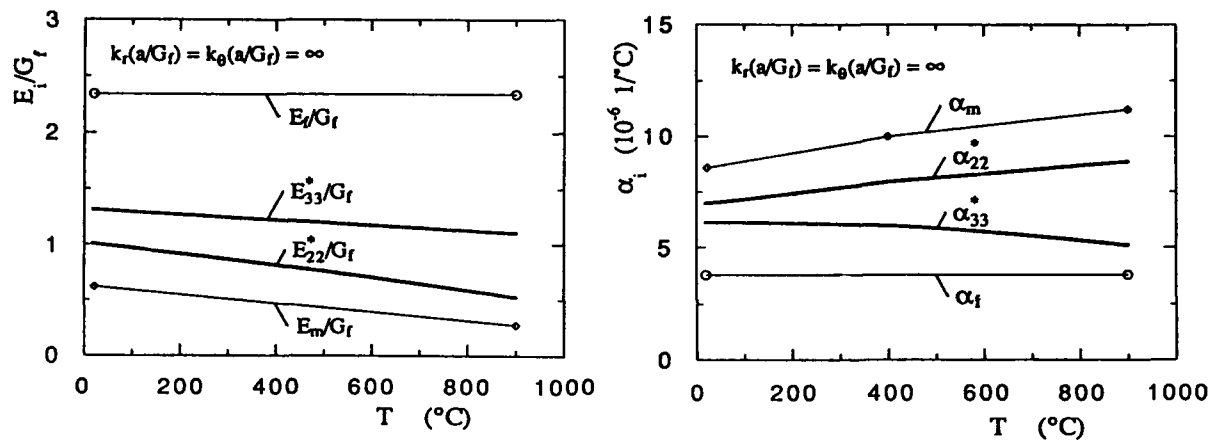
Figure 3   Thermoelastic moduli of SCS-6/Ti-6Al-4V MMC
with perfect fiber/matrix interface.

In Fig. 3, thermoelastic properties of the composite with a perfect interface are shown. The transverse Young's modulus E^*_{22} of the composite decreases with increase in temperature. But the decrease in composite modulus along the fiber direction is small owing to temperature-insensitive E_f of the fiber. The thermoelastic properties of the composite with a perfect interface condition are not related to thermal residual stress, because the principle of superposition for a thermoelastic problem is valid in the case of the perfectly bonded interface. Therefore, the composite thermoelastic properties are independent of the thermal strain terms Ψ_i as expressed in Eq.(15). The longitudinal thermal expansion coefficient of the composite is observed to get close to the thermal expansion coefficient of the fiber with increase in temperature due to reduction of Young's modulus of the matrix. The transverse thermal expansion coefficient α^*_{22} of the composite is found to increase with temperature appreciably as shown in the figure.

To understand microscopic thermomechanical behavior of the composite, thermal residual stresses distributions induced by cooling from the processing temperature T_r are presented in Fig. 4 for the composite with a perfect interface. The thermal residual stresses are calculated at $20°C(70°F)$ and $320°C(600°F)$. The residual stresses, which are internal
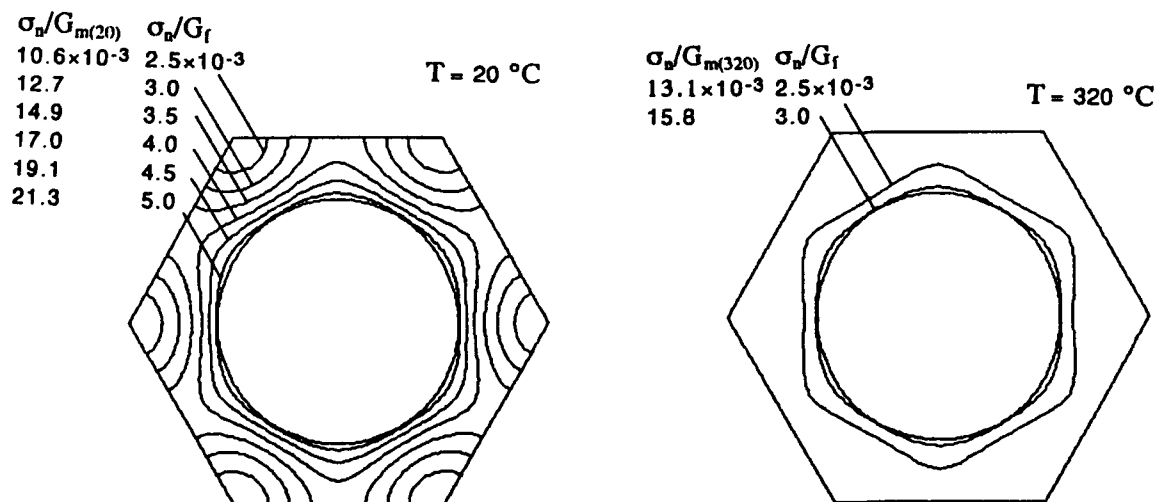
Fig. 4   Residual thermal stress distributions (in von Mises stress σ_n form)in the matrix at T=20°C and 320°C.
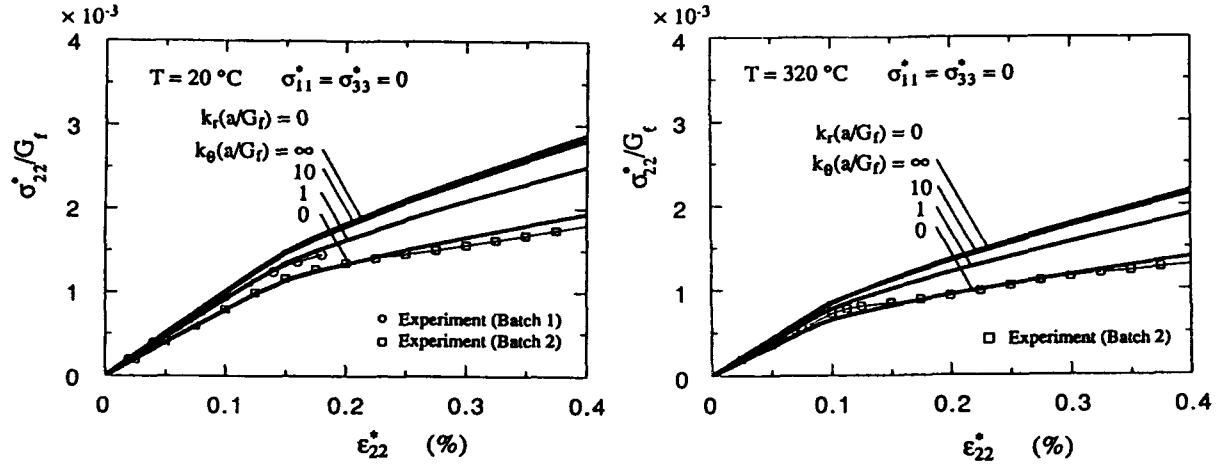
Fig. 5 Effect of the interface elastic conditions on thermoelastic properties
of SCS6/Ti-6Al-4V composite.

microscopic stresses, are determined by setting the effective stress σ^*_{ij} to zero in the homogenized field. The residual stresses, expressed in the von Mises form σ_n, are normalized by fiber and matrix shear moduli at 20°C and 320°C, respectively. At T=20°C, high residual stress gradients are observed, and the largest residual stress occurs near the fiber, but the stress is greatly relaxed at 320°C.

The transverse stress-strain relationship for the composite, including thermal residual stress, is evaluated using Eq.(14) for the composite with several interface conditions. A nonlinear σ^*_{22}-ε^*_{22} relationship is obtained due to the imperfect interface conditions. The results are shown in Fig.5 and compared with experimental data. The experimental results[12] are obtained from tests of two SCS6/Ti-6Al-4V composite specimens from panels named as Batch 1 and Batch 2. [The fiber array is observed to be almost hexagonal in the Batch 1 specimen, and is slightly deviated from the hexagonal pattern for the Batch 2 specimen.] In the
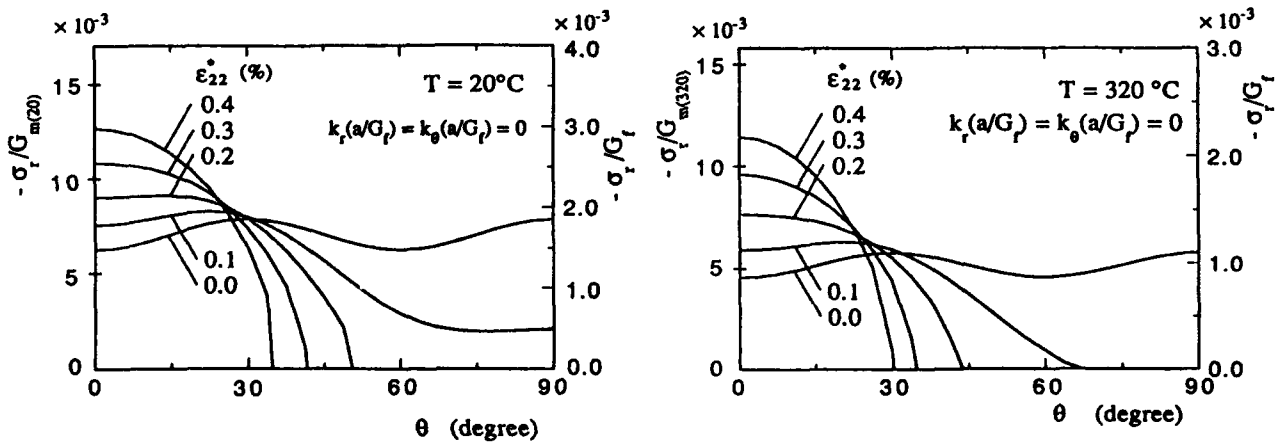
Fig. 6 Angular distributions of Interfacial radial stress σ_r at fiber-matrix interface.

figures, the normalized interfacial elastic constants, $k_r(a/G_f)=0$ and $k_\theta(a/G_f)=0,1,10$ and ∞, are used. Square symbols show experimental data of the Batch 1 specimen and circular symbols, experimental data of Batch 2. The parameters $k_r(a/G_f)=k_\theta(a/G_f)=0$ correspond to the composite containing a stress-free, separated interface with frictionless contact. At T=20°C, the fiber-matrix interface begins to separate at an applied strain $\varepsilon^*_{22}=0.15\%$. The stress-strain curves change their slopes near that point. At 320°C, the interface separation occurs, due to the lower thermal residual stress, at the applied strain $\varepsilon^*_{22}=0.1\%$. The results with $k_r(a/G_f)=0$, $k_\theta(a/G_f)=1$ agree well with the experimental data from the Batch 1 specimen. Although the fiber array in the Batch 2 specimen is slightly different from the regular hexagonal array used in this numerical calculation, the results with interface conditions $k_r(a/G_f)=k_\theta(a/G_f)=0$ are very close to the experimental data obtained from the Batch 2 specimen.

In Fig. 6, angular distributions of the radial stress σ_r at the interface r=a, are reported for T=20°C and 320°C. Thermal residual stresses and the interface elastic constants $k_r(a/G_f)=k_\theta(a/G_f)=0$, which give good agreement with the experimental results from the Batch 2 specimen as shown in Fig.5, are included in the analysis. It can be clearly seen when the applied strain ε^*_{22} increases, interfacial separation starts to become appreciable along θ, and the radial stress is reduced to zero in this part of the interface. The results with $\varepsilon^*_{22}=0$ correspond to the case of pure thermal residual stress. Obviously, the thermal residual stress decreases at T=320°C. Separation of the interface occurs easily at this temperature owing to reduction of the radial residual stress.

CONCLUSIONS

A homogenization theory with multi-scale asymptotic expansion is successfully developed to study thermoelastic properties of composite materials. The perturbed displacement field in a periodical unit cell is obtained with the aid of a BIE method and the well known eigenstrain approach. The theory and the numerical method are applied to a SCS6/Ti-6Al-4V metal matrix composite. Thermomechanical properties of the composite are obtained. Based on the results obtained, the following conclusions can be reached:

1. Nonlinear effective thermoelastic constitutive properties at both room and elevated temperatures are obtained for composites with various imperfect fiber-matrix interfaces.
2. The effect of elevated temperatures on nonlinear effective thermoelastic properties of the composite is related to imperfect interface elastic constants and interface separation.
3. Microscopic deformations and stresses at the imperfect interface can have appreciable effects on effective composite thermoelastic constitutive properties at both room and elevated temperatures.
4. Microscopic residual thermal stresses are found to be very high. They have significant effects on effective thermoelastic properties of the composite with the imperfect interface, but have no effect on thermoelastic properties of the composite with a perfectly bonded interface.
5. With proper selection of interfacial elastic constants k_r and k_θ, effective thermoelastic constitutive properties of a composite can be predicted and compared well with experimental data.

REFERENCES

1. Sanchez-Palencia, E., 1974, "Comportement Local et Macroscopique D'un Type de Milieux Physiques Heterogenes," International Journal of Engineering Science, 12: 331-351.

2. Duvaut, G., 1976, "Materiaux Elastiques Composites a Structure Periodique, Homogeneisation," Proc. Congres IUTAM, Delft.

3. Sanchez-Palencia, E., 1980, Non Homogeneous Media and Vibration Theory, Lecture Notes in Physics No. 127, Springer-Verlag, Berlin.

4. Bensoussan, A., Lions, J.L. and Papanicolaou, G., 1978, Asymptotic Analysis for Periodical Structure, North-Holland.

5. Lene, F. and Leguillon, D. 1982, "Homogenized Constitutive Law for a Partially Cohesive Composite Material," International Journal of Solids and Structures, 18: 443-458.

6. Devries, F., Dumontet, H., Duvaut, G. and Lene, F., 1989, "Homogenization and Damage for Composite Structures," International Journal for Numerical Methods in Engineering, 27: 285-298.

7. Benveniste, Y., 1985, "The Effective Mechanical Behavior of Composite Materials with Imperfect Contact between the Constituents," Mechanics of Materials, 4: 197-208.

8. Achenbach, J.D. and Zhu, H., 1990, "Effect of Interphases on Micro and Macromechanical Behavior of Hexagonal-Array Fiber Composites," Journal of Applied Mechanics, 57: 956-963.

9. Hashin, Z., 1990, "Thermoelastic Properties of Fiber Composites with Imperfect Interface," Mechanics of Materials, 8: 333-348.

10. Swedlow, J.L. and Cruse, T.A., 1971, "Formulation of Boundary Integral Equations for Three-Dimensional Elasto-Plastic Flow," International Journal of Solids and Structures, 7:1637-1683.

11. Smith, P.R. and Froes, F.H., 1984, "Developments in Titanium Metal Matrix Composites," Journal of Metals, 36: 19-26.

12. Wang, S.S., 1992, "Unit Cell Investigation of the Nonlinear Transverse Behavior of SCS-6/Ti-6Al-4V Metal Matrix Composite," unpublished data, Mechanical Engineering Department, University of Houston.

Smart Structures

Impact Monitoring in Smart Composite Structures Using Piezoelectric Sensors

I. KIM* AND H. T. HAHN**
The Pennsylvania State University
University Park, PA

D. WEEMS†
Boeing Defense & Space Group
Helicopters Division
Philadelphia, PA

ABSTRACT

One promising method of monitoring structural integrity of composite structures is based on the use of piezoelectric sensors to detect potentially damage-inducing impact events. The present paper describes the results of a research effort to characterize the performance of piezopolymer sensors in a smart composite structure subjected to low-velocity impact. In order to predict the sensor output signal due to impact, equations describing the piezoelectric behavior of the sensor were developed and combined with a Rayleigh-Ritz analysis of the impact event. In the experimental portion of this work, piezopolymer sensors were epoxy-bonded to the surface of a laminate and impact testing was conducted to establish the relationship between the sensor response and impact location and energy. As impact energy was increased for a given impact location, it was found that the shape of the sensor output waveform remained consistent but the amplitude of the signal increased. The analytical solution showed good agreement with experimental data for the initial sensor response due to impact.

INTRODUCTION

In recent years, advanced technology from such diverse fields as structures, materials, electronics, instrumentation, and control have been brought together to realize the concept of smart structures, i.e., structures which incorporate integral sensing, actuation, and control capability to allow them to react intelligently to outside stimuli. One of the first applications foreseen for this new technology is the use of permanently incorporated sensors to continuously monitor the health of aircraft structures [1]. For the advanced composite structures employed on current aircraft and rotorcraft, a key feature of a health monitoring system would be the ability to detect impact events and the damage they cause. An impact detection system could record the location and severity of impact events for post-flight retrieval by maintenance crews and, for severe impacts, could provide a real-time warning to the flight crew. Eventually, such a system may even employ actuators capable of reacting to an impact event in order to mitigate damage or divert load away from the damaged structure.

The overall objective of our effort was to develop smart composite structure technology for detecting low-velocity impact events. Piezoelectric sensors were chosen because they offer a simple and cost-effective means of detecting impact. Previous work includes an evaluation of sensors made from lead zirconate titanate (PZT), and polyvinylidene fluoride (PVDF)[2].

---

* Graduate Research Assistant, Engineering Science and Mechanics.
** Currently Professor, Mechanical, Aerospace, and Nuclear Engineering, University of California, Los Angeles.
† Technical Specialist.

Several techniques of incorporating the sensors into composite laminates and sandwich panels were investigated and the structural integrity of the host structure and attached sensors evaluated. Piezopolymer sensors were found to be capable of monitoring low-velocity impact without affecting the integrity of the host structure. Both types of sensors were also found to function well until laminate failure in static tests and after one million cycles in fatigue conducted at 50% of the static strength.

The specific objective of the present paper is to develop an analytical model for predicting piezoelectric sensor response to impact and to conduct impact testing to characterize the response of attached piezopolymer sensors.

EXPERIMENTAL PROCEDURE

The composite specimens used in this study were $[0/90]_{2S}$ laminates of T650/ERL-1902 graphite/epoxy fabric. Overall specimen dimensions were 406 x 83 mm with a nominal thickness of 1.88 mm. Two piezopolymer sensors were attached to the bottom surface of each specimen using a two-part epoxy, as shown in Figure 1.
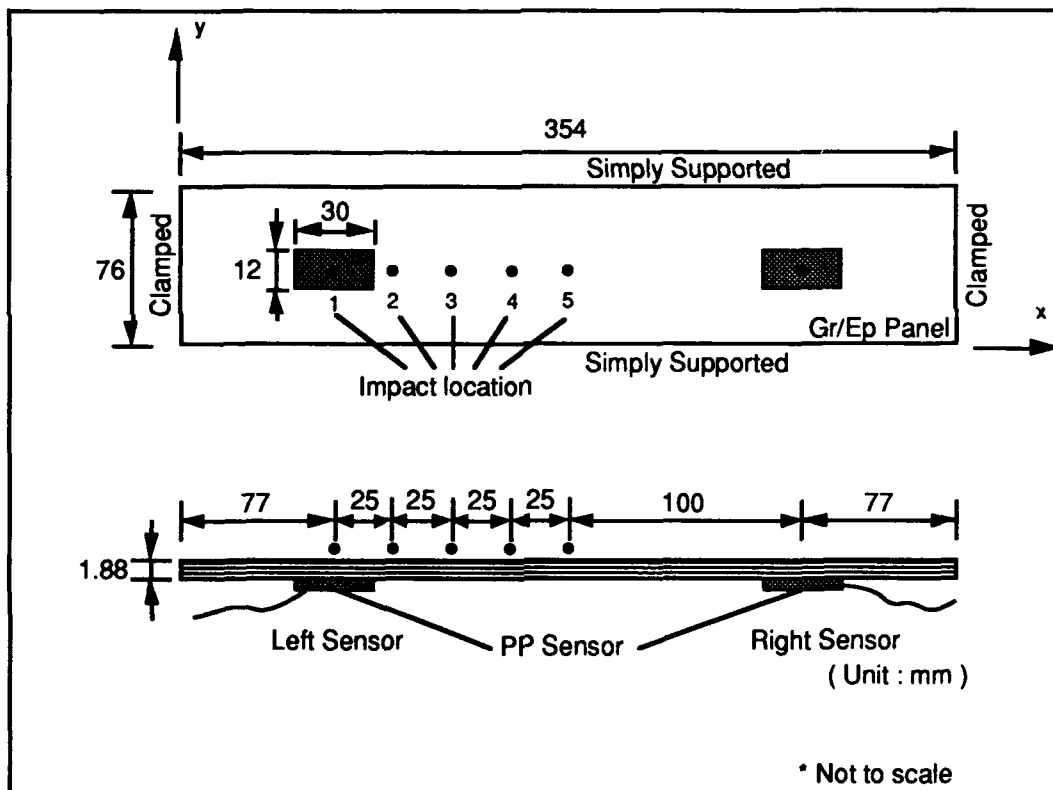
Figure 1. Graphite/Epoxy Specimen with Piezopolymer Sensors.

The sensors consisted of 52 μm-thick PVDF film with conductive and protective coatings, and had an active area of 30 x 12 mm. For impacting, the panel was clamped on its ends and simply-supported on its sides in order to simulate aircraft skin panels with stringers and stiffeners. The actual test section inside the supports was 354 x 76 mm. The panel was impacted normal to the surface by dropping a 5.59 gram, 11 mm diameter steel ball at several different locations along the center line. Several drop heights were used to establish the relationship between sensor response and impact energy. Sensor signals were recorded by a Data 6000 wave analyzer and transferred to a computer for further analysis. Each impact test

was repeated three times to verify the consistency of sensor responses. In addition, selected tests were duplicated on different specimens to assess repeatability.

ANALYSIS

BEHAVIOR OF PIEZOPOLYMER FILM

Piezopolymer film has several advantages as a sensor [3]: it is compliant, lightweight, tough, and available in a wide variety of thicknesses and surface areas. When operating as a sensor, applied strains cause a change in the surface charge density, resulting in a voltage between the surface electrodes. However, because of the rapid decay of the induced charge, piezopolymer sensors are insensitive to static loading, and should therefore be used under dynamic loadings.

A set of equations describing the behavior of piezopolymer devices has been developed. The low-frequency flexural and extensional plate equations of a single-layer piezoelectric plate were derived by Lee [4]. This theory, which incorporates the piezoelectric effects into the classical laminate theory, was combined with an impact model of the test panel in order to predict the response of the sensor to low velocity impact .

Constitutive equations of a linear piezoelectric material can be written in the form [5].

$$\varepsilon_p = S_{pq}\,\sigma_q + d_{pi}\,E_i\,, \qquad p, q = 1, 2, 3, 4, 5, 6 \qquad (1)$$
$$D_i = d_{iq}\,\sigma_q + \varepsilon_{ik}\,E_k\,, \qquad i, k = 1, 2, 3 \qquad (2)$$

where the contracted notation has been used and

σ_p = stresses; ε_p = strains; S_{pq} = elastic compliances; E_i = electric fields;

D_i = electric displacements; d_{ip} = piezoelectric strain constants; ε_{ik} = permittivities

For PVDF film, there are only five non-zero piezoelectric strain constants. Thus, an electric field applied in the out-of-plane direction (E_3) will induce only the normal strains ε_1, ε_2, ε_3. Under plane stress conditions with $\sigma_3=0$ and no applied electrical fields, the electric displacement D_3 is related to in-plane strains ε_1 and ε_2 by

$$D_3 = e_{31}\,\varepsilon_1 + e_{32}\,\varepsilon_2 \qquad (3)$$

where the permittivities ε_{31} and ε_{32} are defined as

$$\left\{ \begin{matrix} e_{31} \\ e_{32} \end{matrix} \right\} = (\frac{E_p}{1-v_p^2})\begin{bmatrix} 1 & v_p \\ v_p & 1 \end{bmatrix}\left\{ \begin{matrix} d_{31} \\ d_{32} \end{matrix} \right\} \qquad (4)$$

Here the PVDF film has been assumed elastically isotropic with Young's modulus E_p and Poisson's Ratio v_p. Typical properties of the Kynar PVDF film used in the present work are listed in Table I [6].

Table I. Typical Properties of PVDF Piezoelectric Polymer Sensors

Property	Symbols	Units	Value	Conditions
Density	ρ_p	10^3 x (kg/m^3)	1.78	
Young's Modulus	E_p	10^9 x (N/m^2)	2.0	
Poisson's Ratio	v_p		0.33	
Piezo Strain Constants	d_{31}	10^{-12} x (m/m)/(V/m)	23.0	laterally
	d_{32}	or (C/m^2)/(N/m^2)	3.0	clamped
	d_{33}		-33.0	
Permittivity	ε_{33}	10^{-12} x (F/m)	106	@10 KHz
Speed of	V_s	10^3 x (m/sec)	1.5	1 direction
Sound			2.2	3 direction

When a PVDF film of area A_p and thickness t_p is subjected to in-plane strains ε_1 and ε_2, the charge developed in the film is given by Q and the corresponding open circuit voltage V is then

$$V = \frac{Q}{C_p} = \frac{1}{A_p} \int_{A_p} (C_x \varepsilon_1 + C_y \varepsilon_2) \, dA \tag{5}$$

where $C_x = \dfrac{t_p}{\varepsilon_{33}} e_{31}$ and $C_y = \dfrac{t_p}{\varepsilon_{33}} e_{32}$ $\qquad$ (6)

and ε_{33} is the permittivity in the thickness direction.

FORMULATION OF THE IMPACT PROBLEM

Response of laminated composite plates to impact has been studied by several investigators [7,8,9]. Sun [7] and Dobyns [8] used the plate equations developed by Whitney and Pagano [10] to analyze a simply-supported orthotropic plate subject to center impact. Dobyns assumed that the impact force history was known while Sun and Chattopadhyay [8] noted that in impact by a foreign body, the impact force should be computed as part of the problem. Sun solved the nonlinear integral equation numerically for the contact force . Birman and Bert [9] obtained a closed-form solution for a simply-supported angle-ply laminated plate subject to blast loading, again assuming that the force history is known.

Closed-form solutions of impact problems such as these can be obtained only in a very few limited cases. Therefore, approximate methods such as Rayleigh-Ritz or finite elements may have to be utilized for laminated composite plates with arbitrary boundary conditions. In the present study, a Rayleigh-Ritz solution is obtained because it requires less computation and provides more insight into the physics of impact response. Once its accuracy is proven, the approximate closed-form solution can be used not only to simulate the sensor response to impact but also to develop a model to solve the inverse problem of estimating the impact location and force history from measured sensor responses.

Consider an a x b rectangular plate subjected to a transverse load q(x,y,t). The kinetic energy of the plate, T where the in-plane and rotary inertia terms have been neglected and the potential energy, V including the bending strain energy and work done by the lateral load can be expressed in terms of displacement w. The following series approximation is used for the transverse displacement w:

$$w(x,y,t) = \sum_{m=1}^{M} \sum_{n=1}^{N} A_{mn}(t) \, X_m(x) \, Y_n(y) \tag{7}$$

The Hamilton's principle is then used to derive the following M x N simultaneous second order differential equation for A_{ij} :

$$\sum_{m=1}^{M} \sum_{n=1}^{N} (M_{ijmn} \ddot{A}_{mn} + K_{ijmn} A_{mn}) = Q_{ij} \tag{8}$$

Here, components of the coefficient matrices and Q_{ij} are given by

$$M_{ijmn} = \rho < X_i \, Y_j \, X_m \, Y_n > \tag{9.a}$$

$$K_{ijmn} = D_{11} < X_i'' \, Y_j \, X_m'' \, Y_n > + 2 D_{12}[< X_i'' \, Y_j \, X_m \, Y_n'' >$$
$$+ < X_i \, Y_j'' \, X_m'' \, Y_n >] + D_{22} < X_i \, Y_j'' \, X_m \, Y_n'' > \tag{9.b}$$
$$+ 4 D_{66} < X_i' \, Y_j' \, X_m' \, Y_n' >$$

$$Q_{ij} = < q \, X_i \, Y_j > \tag{9.c}$$

where a prime indicates differentiation and the symbol < > indicates an integral over the plate.

For clamped boundary conditions at x = 0, a, and simply supported boundary conditions at y = 0, b , Hearman [11] suggested the following shape functions :

$$X_m(x) = \gamma_m \cos\frac{\lambda_m x}{a} - \gamma_m \cosh\frac{\lambda_m x}{a} + \sin\frac{\lambda_m x}{a} - \sinh\frac{\lambda_m x}{a} \tag{10}$$

$$Y_n(y) = \sqrt{2} \sin\frac{n\pi}{b}y \tag{11}$$

where λ_m and γ_m are determined from the clamped boundary conditions.

When these shape functions are used, the effect of coupling between different vibration modes is not significant, and Eq. (8) reduces to a set of M x N uncoupled second-order differential equations:

$$M_{mn\ mn}\ddot{A}_{mn}(t) + K_{mn\ mn}A_{mn}(t) = Q_{mn}(t) \tag{12}$$

Natural frequencies ω_{mn} are then determined as $\omega_{mn} = (K_{mn\ mn}/M_{mn\ mn})^{1/2}$ [12].

If the plate is initially at rest and the impact is assumed to induce a concentrated load at point (x_0, y_0) so that

$$q(x,y,t) = \delta(x-x_0)\ \delta(y-y_0)\ F(t) \tag{13}$$

the final solution for w becomes

$$w(x,y,t) = \sum_{m=1}^{M} \sum_{n=1}^{N} \frac{W_{mn}(x,y;x_0,y_0)}{\omega_{mn}} \int_0^t F(\tau)\ \sin(\omega_{mn}(t-\tau))\ d\tau \tag{14}$$

where

$$W_{mn}(x,y;x_0,y_0) = \frac{X_m(x_0)\ Y_n(y_0)\ X_m(x)\ Y_n(y)}{M_{mn\ mn}} \tag{15}$$

The resulting bottom surface strains at (x,y) are

$$\varepsilon_x(x,y,t;\ x_0,y_0) = \frac{-h}{2} \sum_{m=1}^{M} \sum_{n=1}^{N} \frac{1}{\omega_{mn}} \frac{\partial^2 W_{mn}(x,y;\ x_0,y_0)}{\partial x^2} \int_0^t F(\tau)\ \sin(\omega_{mn}(t-\tau))\ d\tau \tag{16}$$

and

$$\varepsilon_y(x,y,t;\ x_0,y_0) = \frac{-h}{2} \sum_{m=1}^{M} \sum_{n=1}^{N} \frac{1}{\omega_{mn}} \frac{\partial^2 W_{mn}(x,y;\ x_0,y_0)}{\partial y^2} \int_0^t F(\tau)\ \sin(\omega_{mn}(t-\tau))\ d\tau \tag{17}$$

Substituting Eqs. (16) and (17) into Eq. (5) finally yields the output voltage for the left sensor:

$$V_L(x_0,y_0,t) = \frac{1}{A_p} \int_{A_p} [C_x\ \varepsilon_x(x_L,y_L,t;\ x_0,y_0) + C_y\ \varepsilon_y(x_L,y_L,t;\ x_0,y_0)]\ dxdy \tag{18}$$

A similar equation can be derived for right sensor.

CALCULATION OF CONTACT FORCE

In order to complete the analytical model, a satisfactory expression for the contact force F(t) must be developed. One of the conditions which the contact force must satisfy is that its time integral for the duration of impact must equal the change in momentum of the striking body. From the equivalence of impulse and momentum, for the impact of a mass on a plate, the sum of the kinetic and potential energies may be expressed in terms of the unknown contact force. If e denotes the coefficient of restitution, the impulse integral J in terms of the contact force may be expressed as

$$J = \int_0^t F(t)\, dt = mv_i\, (1 - \frac{v_f}{v_i}) = mv_i\, (1+e) \tag{19}$$

where m is impactor mass and v_i and v_f are the impactor velocities just before and after the impact, respectively. A satisfactory approximation to F(t) is defined in terms of a normalized force $\overline{F}(t)$:

$$F(t) = mv_i\, (1+e)\, \overline{F}(t) \tag{20}$$

To perform the necessary integrations, a suitable function F(t) which closely approximates the actual normalized contact force is chosen as follows [13]:

$$\overline{F}(t) = \frac{\pi}{2\tau_c} \sin \frac{\pi}{\tau_c} t \qquad \text{for} \ \ 0 \le t \le \tau_c$$

$$\overline{F}(t) = 0 \qquad \text{for} \ \ \tau_c < t \tag{21}$$

RESULTS AND DISCUSSION

Measured response of the left-hand sensor due to impacts at the center of the specimen (location 5 in Figure 1) are shown in Figures 2, 3, and 4. Figure 2 compares the measured responses from six impacts, three at each of two drop heights, on the same specimen. These results illustrate not only the similarity in signals for different drop heights but also the excellent consistency between trials, with hardly any scatter visible in each set of three signals. In another test of repeatability, similar impact tests were performed on different specimens cut from the same laminate. The measured responses, shown in Figure 3, are initially identical but show some divergence after about 1 ms. The principal cause of the differences between specimens is thought to be variation in the thickness of the epoxy bondline under the sensors.
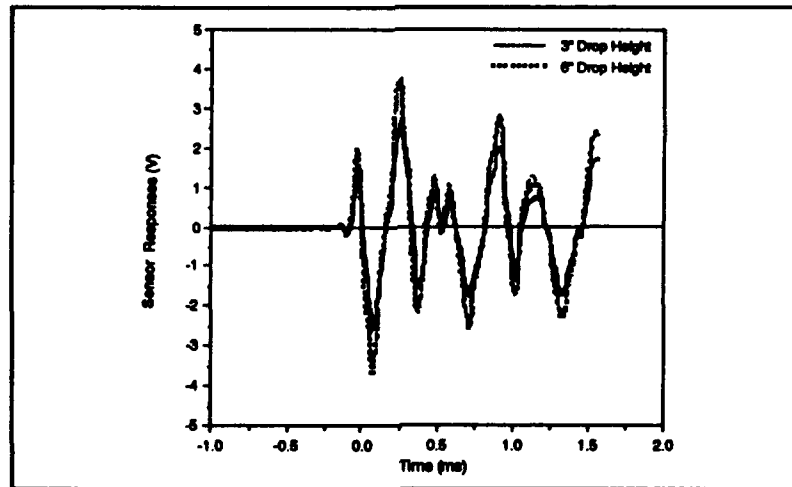
Figure 2. Consistency of Sensor Response (Center Impact).

The effect of impact energy on sensor response is shown in Figure 4, which compares responses for three different drop heights at the same location. As the drop height was increased, the shape of the sensor output waveform remained consistent with only wave form amplitudes increasing. The peak voltages for each drop height are approximately proportional to square root of drop height. The peak voltages are thus proportional to the initial impact velocity for the single impact mass evaluated.
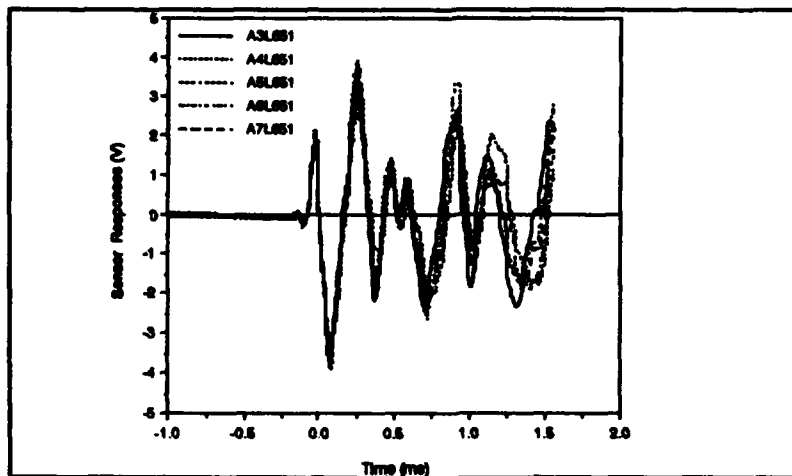
Figure 3. Sensor Output Voltage for 5 Different Specimens
(center impact, 150 mm drop height).
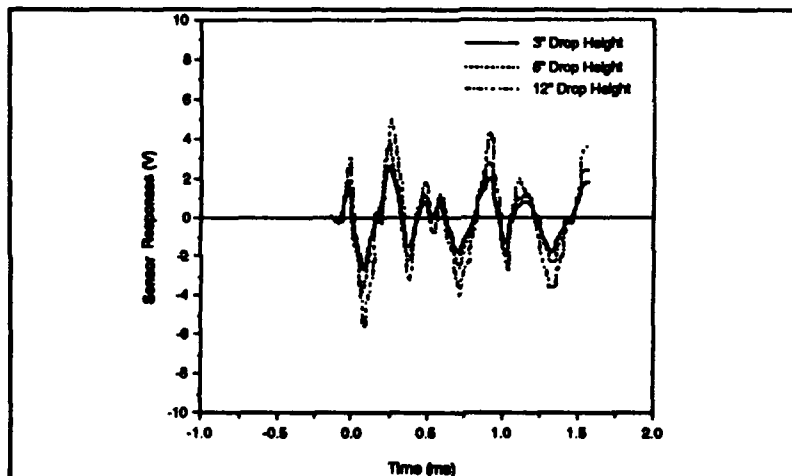
Figure 4. Effect of Drop Height on Sensor Responses (Center Impact).

As noted above, evaluation of the Rayleigh-Ritz analysis requires assuming a contact time. Increasing the contact time from 0.1 to 0.4 ms while maintaining a constant impulse decreased the amplitude and frequency of the predicted responses. A contact time of 0.15 ms was chosen as best matching the experimental results. Other input parameters for the analysis are summarized in Table II.

Figure 5 compares predicted and measured sensor responses for a center impact, for which the same response is predicted from the left and right sensors. The two predicted responses correspond to the measured impactor rebound (coefficient of restitution e = 0.49) and no impactor rebound (e = 0). The predictions match the initial measured values well but overpredict the portion of the measured response after about 1 ms. Figure 6 compares predicted and measured response for each sensor for location 3, an off-center impact. Once again, the predictions match the shape of the measurements but overpredict the amplitude, especially as time after impact increases.

Table II. Summary of Input Data for Rayleight-Ritz Analysis

Plate	T650/5HS/ERL-1902 (Amoco)	graphite/epoxy fabric
- Ply orientation		$[0/90]_{2S}$
- Bending stiffnesses	D_{11}	42.1 N-m
	D_{22}	42.1 N-m
	D_{66}	3.05 N-m
	D_{12}	2.10 N-m
- Density	ρ_o	1,570 kg/m^3
- Boundary Conditions	Clamped , simply supported	C-SS-C-SS
Sensor	piezopolymer film	PVDF
- Geometry	length, a_p	30 mm
	width, b_p	12 mm
	thickness, t_p	52 mm)
- Sensor Location	left sensor, (x_L, y_L)	(77, 38)
	right sensor, (x_R, y_R)	(277,38)
No. of modes	M x N	19 x 5
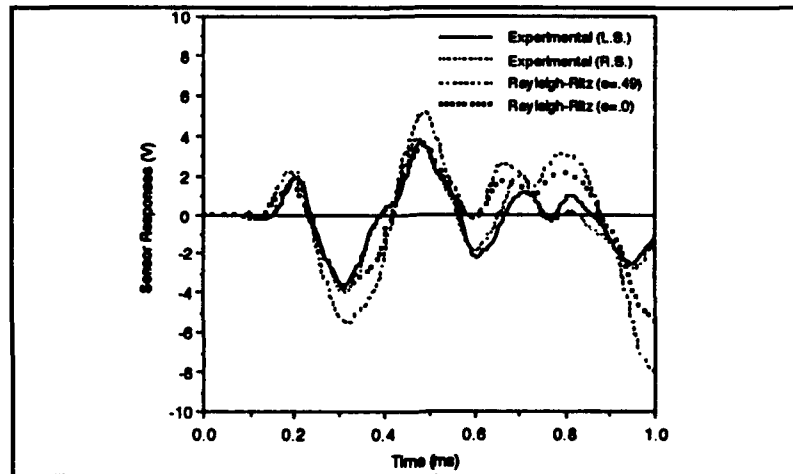
Figure 5. Comparison of Predicted and Measured Sensor Responses (Center Impact).

(a) Left sensor response   (b) Right sensor response
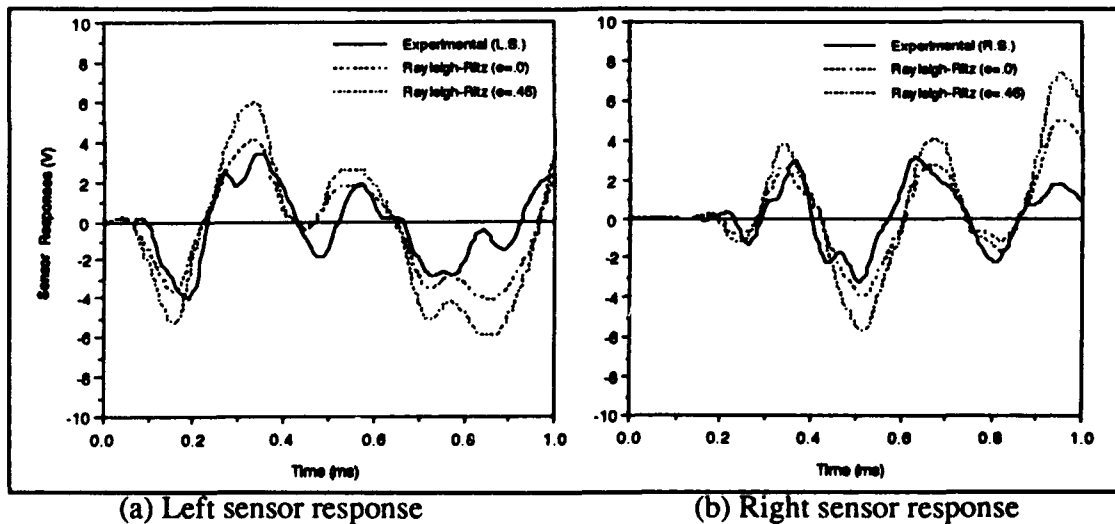
Figure 6. Comparison of Predicted and Measured Sensor Responses (Off-Center Impact).

CONCLUSIONS

The performance of piezopolymer sensors attached to solid laminates subjected to low-velocity impact have been examined experimentally, and an analytical model of response of the laminate and sensor to impact has been developed. Experimentally, the repetition of sensor response is very good for multiple impacts on one specimen and for similar impacts on different specimens. As impact energy was increased for a given impact location, the shape of the sensor output waveform remained consistent with only wave amplitude increasing. The analytical solution, which utilizes a Rayleigh-Ritz approximation of the impact problem, shows good agreement with experimental data for the initial sensor response due to impact. This suggests that an approximate closed-form solution of the impact problem can be employed to determine the contact force history from measured sensor output.

ACKNOWLEDGEMENTS

REFERENCES

1. C. J. Mazur, G. P. Serdeckyj, and D. M. Stevens,"Air Force Smart Structures/Skin Program Overview", SPIE Fiber Optic Smart Structures and Skins Vol.986 (1988), pp.19-29.
2. D. Weems, H. T. Hahn, E. Granlund, and I. Kim, "Impact detection in Composite Skin Panels Using Piezoelectric Sensors", 47th Annual Forum of the American Helicopter Society, Washington, D.C., May 1991.
3. J. V. Chatigny and L. E. Robb, "Piezo Film Sensor," Sensors, (1986), pp. 6-18.
4. C.-K. Lee and F. C. Moon, "Laminated Piezopolymer Plates for Torsion and Bending Sensors and Actuators", Journal of the Acoustic Society of America, Vol.85, No.6 (1989), pp. 2432-2439.
5. G. S. Kino, Acoustic Waves: Devices, Imaging, and Analog Signal Processing, Eaglewood Cliffs: Prentice-Hall, 1987.
6. Atochem Sensors, Technical Manual, 1991.
7. C. T. Sun and S. Chattopadhyay, "Dynamic Response of Anisotropic Plates under Initial Stress due to Impact Mass", Journal of Applied Mechanics Vol. 42 (1975), pp. 693-698.
8. A. L. Dobyns, "Analysis of Simply-Supported Orthotropic Plate Subject to Static and Dynamic Loads", AIAA Journal Vol. 19 (1981), pp. 642-650.
9. V. Birman, and C. W. Bert, "Response of Composite Plates to Blasting Loading", Proceedings of 5th ICCM and ECCM Conference, July 1987, pp. 192-201.
10. J. M. Whitney and N. J. Pagano, "Shear Deformation in Heterogeneous Anisotropic Plates", J. Applied Mechanics Vol. 37 (1970), pp. 1031-1036.
11. R. F. S. Hearmon, "The Frequency of Flexural Vibration of Rectangular Orthotropic Plates with Clamped or Supported Edges", J. Applied Mechanics, (1959), pp. 537-549.
12. J. M. Whitney, Structural Analysis of Laminated Anisotropic Plate, Lancaster: Technomic, 1987.
13. C. M. Harris and C. E. Crede, Shock and Vibration Handbook, Third Edition, New York: McGraw-Hill , 1987.

Interfaces and Material Systems II

Molecular Design of Processable High T$_g$ Thermoplastic Matrix Resins and Structural Adhesives

J. E. McGRATH,* H. GRUBBS,* M. E. ROGERS,* T. M. MOY,* W. A. JOSEPH,* R. MERCIER,* H. MARAND,* A. PRASAD* AND A. BRENNAN**

ABSTRACT

Utilizing solution cyclization, molecular weight and end group control techniques, soluble, fully cyclized polyimides and polybenzoxazoles with very high glass transition temperatures have been developed to meet high temperature applications. Aspects of solution imidization by both the polyamic acid route and by the ester-acid route are investigated. Polyimides based on pyromellitic dianhydride and a 3F diamine exhibit glass transition temperatures of 420°C. These polyimides are soluble in polar aprotic solvents and form tough, transparent films which demonstrate excellent mechanical integrity and thermooxidative stability. Fully cyclodehydrated, fluorinated polybenzoxazoles have been prepared by a low temperature solution cyclization method. The resulting polybenzoxazoles exhibit high glass transition temperatures, excellent thermooxidative stability and solubility in NMP. These materials are candidates for 700°F matrix resin and structural adhesive applications. An overview of the synthesis and characterization of these materials will be provided.

1. INTRODUCTION

Over the past 2 decades, polyimides have become an important class of polymers which have found a wide range of applications as high performance materials in the aerospace and electronics industries. Several polyimides with good thermooxidative stability and mechanical properties have been developed which are suitable as adhesives, coatings and in fiber reinforced composites [1-3]. However, further development of polyimides is required to meet the increasing demands placed on high performance materials and to reduce production costs. One major limitation which has hampered the widespread use of these materials is their intractability in the fully cyclized state. In the past, we have shown that incorporation of the "6F" dianhydride along with the utilization of molecular weight control and a "one pot", two step solution imidization method results in processable, thermally stable polymers [4-6]. Using these methods, we have recently explored the incorporation of "3F" monomers based on trifluoroacetophenone in polyimides [7,8]. Fully cyclized polyimides made from pyromellitic dianhydride and 3F diamine are soluble in polar aprotic solvents and have glass transition temperatures exceeding 400°C. The 3F diamine containing polyimides have demonstrated exceptional thermal and mechanical properties and thus are candidates for high performance applications.

Polyimides may also be synthesized from the diester-diacid derivatives of aromatic tetracarboxylic dianhydrides and aliphatic diamines in bulk [9] or aromatic diamines in solution [10]. This method has several advantages over the more conventional "two step" synthesis. As the product of alcoholysis is used rather than the dianhydride itself, the presence of small amounts of moisture in glassware and polymerization solvents does not present a problem, and ester-acids are generally more soluble in the polymerization solvents than the corresponding dianhydrides or tetraacids. In addition, the polymerization

* To whom all correspondence should be addressed. Departments of Chemistry and The NSF Science and Technology Center: High Performance Polymeric Adhesives and Composites, Virginia Polytechnic Institute and State University, Blacksburg, VA 24061
** University of Florida, Department of Material Science and Engineering, 317 MAE, Gainesville, FL 32611

can be conducted using a "one pot" solution imidization process [11]. Unlike the conventional synthesis, the ester-acid route does not yield high molecular weight polymer at low temperatures; the lower initial solution viscosity in these systems is expected to provide for better fiber wetting in composite applications. An additional anticipated benefit is that ester-acids are expected to be less irritating than the analogous anhydrides. This has been found to be a convenient method for the reproducible synthesis of fully imidized soluble polyimides; it is possible to prepare high (uncontrolled) molecular weight polyimides, controlled molecular weight polyimides with non-functional end groups, and controlled molecular weight ethynyl functionalized imide oligomers.

Another polymer system closely related to the polyimides in structure and properties is the polybenzoxazoles (PBO's). Like the polyimides, PBO's possess excellent thermo-oxidative stability, good mechanical properties and chemical resistance [12-14]. In addition, polybenzoxazoles exhibit superior hydrolytic stability relative to the imides. Unfortunately the aromatic PBO's have enjoyed much less success in the market place due to difficulties in synthesis and processing. Synthesis of soluble or thermoplastic polybenzoxazoles has been a major part of our research efforts and has been accomplished at least in part via the incorporation of fluorinated monomers and utilization of solution cyclization processes. Cyclodehydration of poly(hydroxy amides) in solution decreases the potential of crosslinking side reactions and thus enhances solubility and processability. Early work in this area resulted in a series of high molecular weight, bis-A based PBO's, which showed solubility in m-cresol [15].

The research presented here revolves around fluorinated monomer linkages. Published work on poly(arylene ethers) [16], polyimides [17] and polybenzoxazoles [7, 18] has demonstrated the ability of fluorinated monomers to impart solubility to polymers in common processing solvents. Reinhardt's research [19] has demonstrated that fluorinated PBO's consisting of various aromatic acids and 2,2-bis(3-amino-4-hydroxyphenyl)-1,1,1,3,3,3-hexafluoropropane can be synthesized in o-dichlorobenzene with the aid of a silyl catalyst. Results of work performed in our laboratories have further demonstrated the enhanced solubility of polymers synthesized with fluorine containing monomers, more specifically the trifluoroethylidene linked systems. PBO's generated from either the trifluoroethylidene linked bisaminophenol or diacid chloride monomer display improved solubility while retaining excellent thermal properties. Solubility in NMP, o-dichlorobenzene, chlorobenzene and m-cresol was achieved for various monomer combinations.

2. EXPERIMENTAL

2.1 Synthesis

2.1.1 Materials: N-methyl pyrrolidinone, N-cyclohexyl pyrrolidinone and 1,2-dichlorobenzene were obtained from Fisher and were vacuum distilled after stirring 12 hours over P_2O_5 prior to use. N,N-dimethyl acetamide, also obtained from Fisher, was used as received. Figure 1 illustrates the anhydrides used in polyimide synthesis; PMDA and BTDA were donated by ALLCO, ODPA from OxyChem, and 6FDA was kindly provided by Hoechst-Celanese. BPDA was obtained from Chriskev. These were monomer grade materials and were not further purified. 3-aminophenyl acetylene was donated by Eastman Kodak and was vacuum distilled before use. 3,3'DDS and 4,4'DDS were obtained from Chriskev and recrystallized twice from deoxygenated ethanol before use; 4,4'ODA, also obtained from Chriskev, was vacuum sublimed twice prior to use. 1,4-phenylene diamine (pPD) was obtained from Aldrich and was vacuum sublimed three times before use. 1,4 bis (4-aminophenoxy) benzene ("TPE-Q"), 4,4' bis (4-aminophenoxy) biphenyl ("BAP-B") and 9,9 bis (4-aminophenyl) fluorene were obtained from Kennedy & Klim and 3,3' dimethyl benzidene was obtained from TCI America; all were recrystallized from toluene prior to use. Bis aniline P was donated by Shell and was recrystallized from ethanol before use. The synthesis and purification of bis(3-aminophenoxy-4'-phenyl) phenylphosphine oxide (BAPPO) [20] and 1,1-bis(4-aminophenyl)-1-phenyl-2,2,2-trifluoroethane (3F diamine) [21] has been reported. Ester-acids were prepared by dissolving purified phthalic anhydride or monomer grade dianhydrides in excess refluxing ethanol (7-10 ml ethanol per gram anhydride) under nitrogen and distilling off the alcohol after a clear solution was obtained.

The monomers used in the PBO synthesis are shown in Figure 2. The diacid chloride of 1,1-bis(4-carboxyphenyl)-1-phenyl-2,2,2-trifluoroethane (3FAC) was generated using the low temperature $SOCl_2/DMF$ chlorination reaction. The diacid was generated from the corresponding bistolyl compound via $KMnO_4$ oxidation in a pyridine/water mixture. Simple vacuum distillation afforded good yields of 3FAC. 1,1-bis(3-amino-4-hydroxyphenyl)-1-phenyl-2,2,2-trifluoroethane was synthesized via the method of Joseph et. al. Silylation of diaminoresorcinol·2HCl was accomplished using a slight excess of $(CH_3)_3SiCl$ in THF with an excess of TEA [18a]. Following standard workup techniques and vacuum

Figure 1: Monomers used in polyimide synthesis
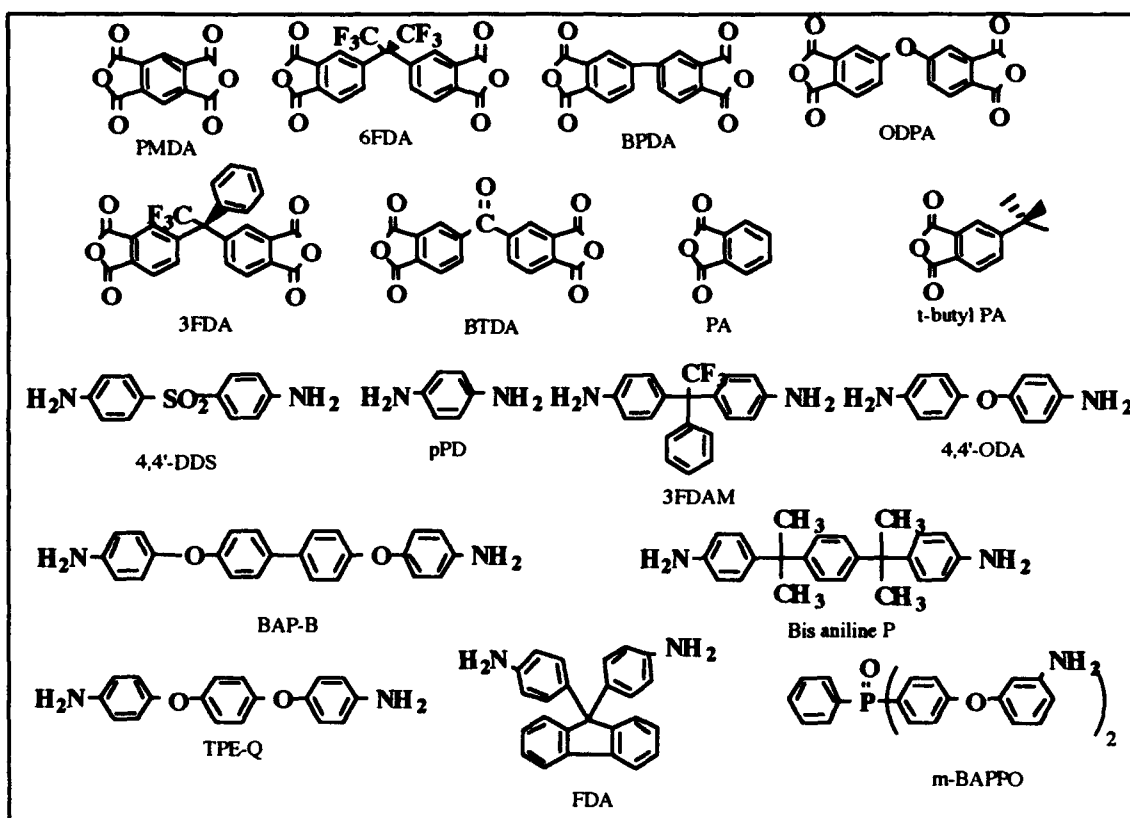
distillation (115-120°C, 0.5 torr), a 60% yield of an off-white crystalline product was achieved.
The synthesis of polyimides by the ester-acid route has been reported elsewhere [22]. An example of an
ODPA-3,3' DDS polyimide synthesized by the ester route is shown in Figure 3. The 3F diamine
containing polyimides were synthesized by the solution imidization route shown in Figure 4. Details of
the solution imidization method are given elsewhere [8]. The polymerization methodology employed in
the generation of PBO's utilizes a low temperature polycondensation reaction driven by efficient removal
of the condensate. All polymers except 3FAC-DAR were generated following the procedure of McGrath
et. al [7]. Polybenzoxazoles generated from diaminoresorcinol were synthesized according to the
procedure of Imai [18a] . (Figure 5).

Figure 2: Polybenzoxazole Monomers
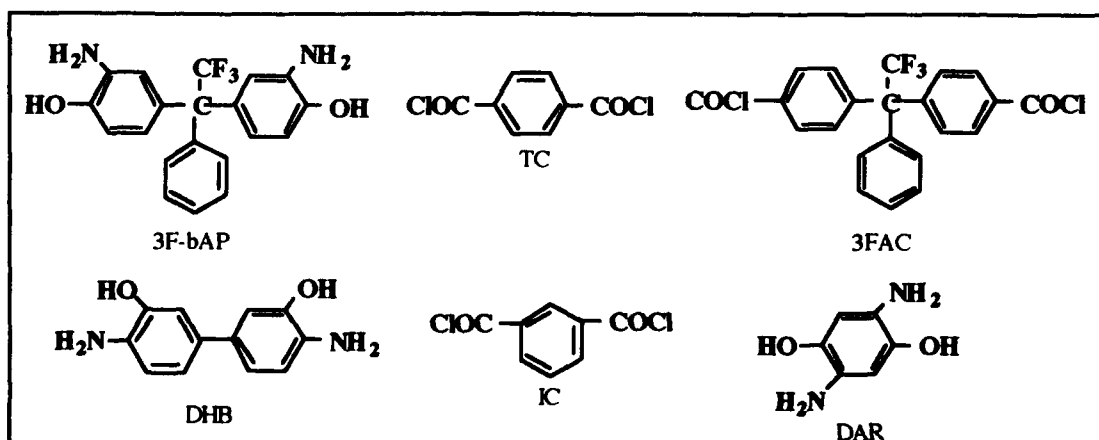
Figure 3. Polyimide Synthesis by the Ester-acid Route
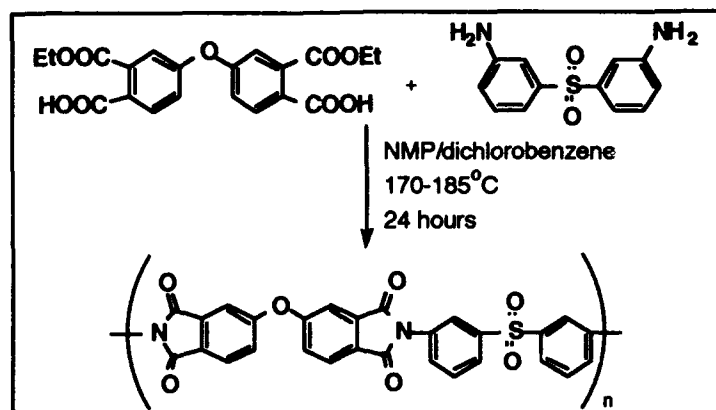
2.2 Characterization

2.2.1 Fourier Transform Infrared Spectroscopy (FTIR): FTIR was used to determine the presence of imide groups in the polymers; spectra were obtained with a Nicolet MX-1 FTIR spectrometer.

2.2.2 Intrinsic viscosity: Intrinsic viscosity measurements gave an indication of the molecular weights attained. The intrinsic viscosities were performed in NMP or 0.1 M NMP/LiBr solution for the polyimides and in m-cresol for the PBO's at 25°C using a Canon-Ubbelohde viscometer.

2.2.3 Thermal Analysis: Glass transition temperatures were determined by differential scanning calorimetry (DSC) using a Perkin Elmer DSC 7. Scans were run at a heating rate of 10°C/minute; reported values were obtained from a second heat after quick cooling. Dynamic mechanical thermal analysis (DMTA) was also carried out on the 3F polyimide films using a Seiko Model 200 DMS at 1Hz. Thermogravimetric analyses were performed on a Perkin Elmer TGA 7 Thermogravimetric Analyzer at 10°C/minute in air. Isothermal TGA's were also carried out in an atmosphere of air.

Figure 4: Synthesis of PMDA-3F diamine Polyimides
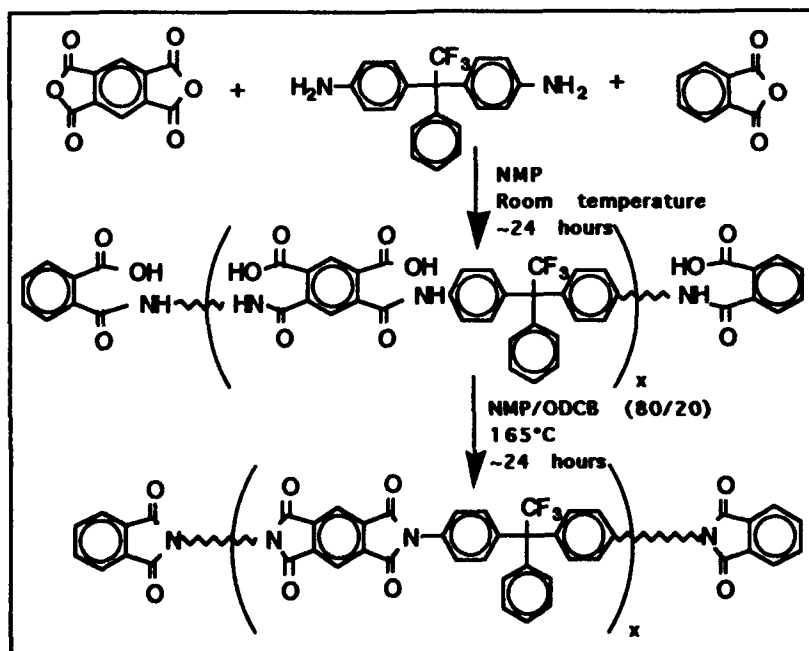
Figure 5: Polybenzoxazole Synthesis
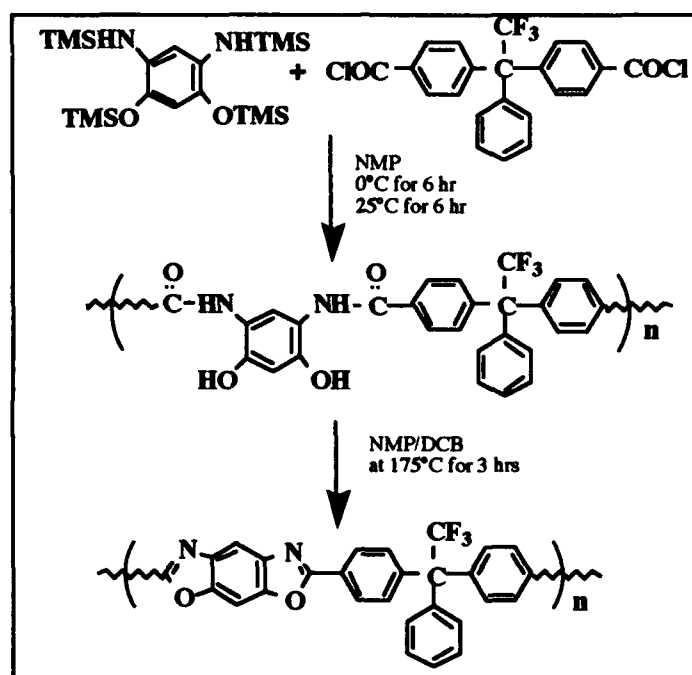
3. RESULTS AND DISCUSSION

3.1. Solution Imidization by the Ester-Acid Route

3.1.1. Polymers by the ester-acid route: The ester-acid route is generally applicable to a wide variety of soluble polyimide systems. A partial list of soluble polyimides prepared by the ester-acid route and their respective intrinsic viscosities is given in Table I; with few exceptions, moderate to high molecular weights may be achieved in 8-24 hours. All are soluble in NMP, DMAc and DMSO. Polyimides based on m-BAPPO are soluble in chloroform, as are the BTDA/bis P and BTDA/FDA polyimides. In addition,

TABLE I. Reaction times and intrinsic viscosities of uncontrolled molecular weight polyimides

System	Time (hours)	$[\eta]^{25^\circ C}_{NMP}$ (dl/g)
BTDA/3,3'DDS	24	0.37
BTDA/m-BAPPO	24	0.24
BTDA/bis P	24	1.19
BTDA/FDA	18	0.70
PMDA/m-BAPPO	08	0.63
ODPA/3,3'DDS	24	0.57
6FDA/3,3'DDS	24	0.43
6FDA/m-BAPPO	24	0.56
6FDA/FDA	18	0.55
6FDA3,3'DMB	18	0.86
6FDA/pPD	08	0.78
6FDA/4,4'ODA	18	1.06
6FDA/TPE-Q	08	1.05
6FDA/ BAP-B	08	0.77

TABLE II. Acetylene Functionalized ODPA/3,3'DDS Oligomers

Conventional Synthesis			Ester-Acid Route		
Target MW	$[\eta]^{25^\circ C}_{NMP}$ (dl/g)	$T_g(^\circ C)$	Target MW	$[\eta]^{25^\circ C}_{NMP}$ (dl/g)	$T_g(^\circ C)$
5000	0.22	244	5000	0.20	244
10000	0.26	241	10000	0.22	239
15000	0.32	246	15000	0.28	242

several of the 6FDA polyimides are chloroform soluble, including 6FDA/FDA, 6FDA/3,3' DMB, 6FDA/ TPE-Q and 6FDA/BAP-B.

3.1.2. Acetylene functionalized imide oligomers: Acetylene terminated ODPA/ 3,3'DDS imide oligomers were chosen as a model system for this study. No solid precipitated and no turbidity was observed during the polymerization, indicating that no crosslinking occurred. In addition, the isolated oligomers completely redissolve in NMP. Although the ethynyl endgroups could not be detected spectroscopically, these materials became insoluble after heating to 350°C, swelling but not dissolving in NMP. Table II lists data for the ODPA/DDS oligomers; the ethynyl terminated materials prepared by both the conventional synthesis and the ester-acid route show glass transition temperatures in the range of 240-246°C after crosslinking, slightly less than the value of 248°C measured for a high molecular weight linear ODPA/DDS polyimide. The intrinsic viscosities of both series of oligomers indicate that molecular weights were indeed limited, although the desired degree of molecular weight control might not have been achieved. The difficulty in achieving the target molecular weights for this system may be a consequence of the low mutual reactivity of ODPA and 3,3'DDS. Nevertheless, the intrinsic viscosities show the correct trend, and for a given molecular weight the intrinsic viscosities of these oligomers before crosslinking are similar regardless of the synthetic method. These results indicated that the ester-acid route should indeed be a suitable method for the preparation of controlled molecular weight functionalized imide oligomers. Table III lists some properties for additional acetylene terminated imide oligomers prepared by the ester-acid route. It was expected that more reactive monomer combinations would result in a greater degree of molecular weight control and this was indeed the case, as evidenced by the intrinsic viscosities of the BTDA/3,3'DDS, 6F/4,4'ODA, 6F/pPD and BPDA/6F/4,4'DDS imides. Molecular weight control was difficult for the 6FDA/FDA system however, and this was also attributed to low mutual reactivity of the monomers as in the ODPA/3,3'DDS system. Again, there was no evidence of crosslinking during oligomer synthesis and heating to 400°C resulted in materials which swell but do not dissolve in NMP. The ethynyl carbon-carbon bond could not be detected by FTIR spectroscopy but all samples displayed imide absorbances at ~1780, ~1730, ~1370 and 710-720 cm^{-1} and an absence of

TABLE III. Acetylene functionalized imide oligomers

System	Target MW	$[\eta]^{25^\circ C}_{NMP}$ (dl/g)	$T_g(^\circ C)$	5% wt loss, air ($^\circ C$)
BTDA/3,3'DDS	5.0 K	0.14	257	
	10 K	0.20	255	500
	15 K	0.28	255	
6FDA/4,4'ODA	5.0 K	0.26	305	
	10 K	0.34	303	525
	15 K	0.45	303	
6FDA/pPDA	10 K	0.32	360	
	15 K	0.40	360	525
	20 K	0.46	364	
6FDA/FDA	5.0 K	0.17	370	
	10 K	0.19	361	530
	15 K	0.27	367	
6FDA/BPDA/	11 K	0.25	366	
4,4'DDS	16 K	0.35	361	535
	21 K	0.43	364	

TABLE IV- 3F Diamine Containing Polyimides

Polyimide	Theoretical <Mn>	[η] (dl/g) 25°C, NMP	Tg °C	TGA 5% wt. loss (°C)
PMDA-3F diamine-PA	30,000	0.65	432	540
BPDA-3F diamine-PA	30,000	0.47	350	536
6FDA-3F diamine-PA	30,000	0.36	313	525
PMDA(80%)6FDA(20%)- 3F diamine-PA	30,000	0.50	392	554
PMDA(70%)6FDA(30%)- 3F diamine-PA	30,000	0.46	379	547
BPDA-3F diamine(90%)- pPD(10%)-PA	30,000	0.51	357	562

absorbances attributable to amide-acid. Measured T_g's (DSC) and 5% weight losses (dynamic TGA) are consistent with the respective values for the linear high molecular weight polyimides.

3.2. High Glass Transition Temperature, Fluorinated Polyimides

The preparation of the PMDA-3F diamine polyimides was conducted by the solution imidization method shown in Figure 4. The monomers used in the polyimide synthesis are shown in Figure 1. Solution imidization of the amic acid was performed in a cosolvent system of NMP with DCB at 165°C for 24 hours. Addition of the cosolvent into the polyamic acid solution as an azeotroping solvent at an 8:2 mixture was sufficient for the efficient removal of water which is formed upon the conversion of the amic acid to the imide. Complete imidization was confirmed by the appearance of characteristic imide related infrared absorption bands in the range 1770-1780 cm^{-1} (symmetrical imide I), 1710-1735 cm^{-1} (asymmetrical imide I) and disappearance of an amic acid band at 1535 cm^{-1}. The intrinsic viscosities of the polyimides are given in Table IV.

All of the 3F diamine containing polyimides are soluble in polar aprotic solvents such as NMP and DMSO. The 3F diamine polyimides using BPDA and 6FDA were even soluble in chloroform and THF. The PMDA-3F diamine polyimides exhibit glass transition temperatures exceeding 420°C. The dynamic mechanical analysis in Figure 6 compares the dynamic storage modulus of a PMDA-3F diamine-PA polyimide with the state of the art high temperature polyimide based on 6F-pPD-PA. For the 6F-pPD-

Figure 6: Dynamic Mechanical Spectrum of PMDA-3F diamine-PA and 6F-pPD-PA
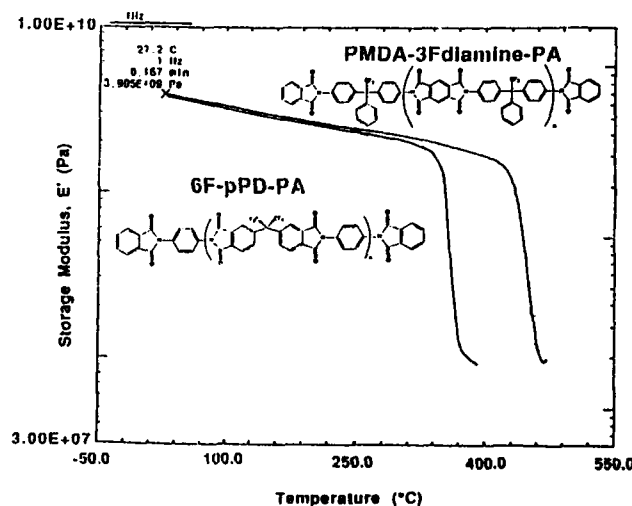
Table V
Solution and Thermal Properties of Various Fluorine Containing Polybenzoxazoles

Polymer	[η] (dL/g)	Tg (°C)	5% Wt. Loss (°C)
6F-bAP-TC	0.48	363	536
6F-bAP-IC	0.26	296	536
3F-bAP-TC	0.23	369	512
3FAC-DHB	0.37	355	509
3FAC-10%IC-DHB	0.47	357	535
3FAC-DAC	0.74	>450	527

PA polyimide, a sharp decline in the storage modulus, corresponding to the glass transition temperature, occurs in the range of 350°C. The PMDA-3F diamine polyimide maintains mechanical integrity over the temperature range of 350 to 400°C and does not show a drop in storage modulus until 430°C. Incorporating more flexible linkages into the "3F" polyimides results in remarkably lower glass transition temperatures than the PMDA-3F diamine polyimides. The BPDA-3F diamine polyimide has a Tg of 350°C, and the 6FDA-3F diamine polyimide has a Tg of 313°C. The Tg of the "3F" polyimides can be readily tailored by the incorporation of various comonomers. Copolymers incorporating 6FDA intothe PMDA-3F diamine polyimide shows a reduced glass transition temperature. The 3F diamine copolyimide containing 20 mole% 6FDA has a Tg of 392°C and 30 mole% 6FDA gives a Tg of 379°C. The Tg of the BPDA-3F diamine can be improved through the incorporation of 10% pPD which raises the Tg to 357°C.

Dynamic thermogravimetric analysis (TGA) of the 3F diamine containing polyimides given in Table IV demonstrate thermal stability above 450°C in air with 5% weight loss values of 525°C to 540°C. Since dynamic TGA is not a realistic measure of a materials long term stability, isothermal TGA was performed. An isothermal TGA of the 25,000 g/mole PMDA-3F diamine-PA polyimide shows that relatively little weight loss occurs after 48 hours at 371°C (700°F) in air.

3.3. Fluorinated Polybenzoxazoles

Synthesis of the various polybenzoxazoles was carried out by first forming the precursor poly(hydroxy amide) followed by subsequent cyclodehydration via acid catalyzed azeotropic distillation. Under these conditions, quantitative cyclization is completed in as little as 3 hours as determined by infrared spectroscopy. Disappearance of the OH and NH stretches (2500-3450 cm^{-1}) and carbonyl stretch (1647 cm^{-1}) along with the appearance of a prominent oxazole vibration around 1060 cm^{-1} and C=N stretch at 1620 cm^{-1}, verified the transformation. In addition, ^{1}H NMR and TGA-MS were used to confirm quantitative cyclization.

A summary of the thermal and solution properties of these polymers is given in Table V. In general, polybenzoxazoles containing the fluorinated acid chloride polymerized to higher molecular weights and exhibited higher intrinsic viscosities. It is worth pointing out at this time that the lower degrees of polymerization found in the fluorine containing polymers is a result of the initial polycondensation and not degradation during the cyclization step. All fluorinated systems exhibited high glass transition temperatures and excellent thermo-oxidative stabilities as demonstrated by 5% weight losses. It is also interesting to note that the 6F and 3F polybenzoxazoles of analogous structure have nearly identical Tg's.

Glass transition temperatures increased in the expected order, that is as the polymer backbone becomes more rigid, the Tg increases. The glass transition temperatures of these polymers matched well with the thermally cyclized polybenzoxazoles mentioned in the literature [7,8].

Enhancing the solubility of the polybenzoxazoles was partially achieved with respect to the fluorinated polymers. All polymers, except the 3FAC-DAR PBO, showed solubility in NMP at 100°C (15% w/v). The 3F polymers appeared to exhibit enhanced solubility. However, it is realized that molecular weight plays an enormous role in solubility and that these polymers do exhibit relatively low intrinsic viscosities. All the polybenzoxazoles did however show solubility in warm m-cresol,

Thermal analysis of the fluorinated polymers indicated no crystallinity, but optical microscopy did detect spherulites in the 6F-bAP-TC PBO when cast from chloroform.

Mentioned in Table V is the 5% weight losses of the polybenzoxazoles, and as expected the fluorinated polymers exhibit excellent thermo-oxidative stability. However, dynamic weight loss over estimates long-term thermo-oxidative stability; therefore the 3F-bAP-TC PBO and 3FAC-DAR PBO were

exposed to isothermal analysis. Results revealed, after initial weight loss due to solvent, the 3F-bAP-TC PBO displays excellent thermal stability at 371°C (700°F) in air for 24 hours (3% weight loss). Mechanical properties are also maintained in this system up to 350°C, with a tan δ maximum near 375°C. The 3FAC-DAR system on the other hand showed much less stability and lost approximately 25% of its initial weight under the same conditions.

4. CONCLUSIONS

Solution imidization techniques were used to prepare fully cyclized polyimides and PBO's of controlled molecular weight having non reactive end groups or ethynyl functionalized end groups. In addition, the synthesis of soluble, high Tg polyimides and PBO's based on the "3F" monomers has been demonstrated. These polymers exhibit excellent long term thermooxidative stability making them excellent candidates for 700°F applications.

5. ACKNOWLEDGMENTS

6. REFERENCES

1. C. Mittal, Editor, Polyimides, Vol. 1 and 2, Plenum Press, 1984.
2. D. Wilson, P. Hergenrother, and H. Stenzenberger, Editors, Polyimides, Chapman and Hall, 1990.
3. J. E.McGrath, M. M. Khojasteh and C. Feger, Editors, Polyimides: Materials, Chemistry and Characterization, Elsevier, 1989.
4. R. O. Waldbauer, et. al., Polymer Preprints, 31 (2), 430 (1990).
5. C. Arnold, J. D. Summers, Y. P. Chen, and J. E. McGrath, Polymer(London), 30 (6), 986 (1989).
6. J. E. McGrath, M. E. Rogers, C. A. Arnold, Y. J. Kim and J. C. Hedrick, Makromol. Chem., Macromol. Symp. 51, 103-125 (1991).
7. J. E. McGrath, H. Grubbs, M. E. Rogers, A. Gungor, W. A. Joseph, R. Mercier, D. Rodrigues, G. L. Wilkes and A. Brennan, 23rd International   SAMPE Tech. Conf., 23, 119 (1991).
8. M. E. Rogers, H. Grubbs, A. Brennen, D. Rodrigues, T. Lin, H. Marand, G. L. Wilkes, J. E. McGrath, 37th International SAMPE Symposium, 37, 717 (1992).
9. W. M. Edwards and I. M. Robinson, US Patent 3,867,609 (1955)
10. M. E. Quenneson, J. Garapon, M. Bartholin and B. Sillion, Proceedings from the Second International Conference on Polyimides, Ellenville, NY, 74 (1985).
11. C. A. Arnold, J. D. Summers, Y. P. Chen, T. H. Yoon, B. E. McGrath, d. Chen and J. E. McGrath, Proceedings from the Third International Conference on Polyimides, NY, 69 (1989).
12. C. Arnold, Jr., Polym. Sci., Macromol. Rev., 14 265 (1979).
13. J. F. Wolfe in "Encyclopedia of Polymer Science and Technology", Vol. 11, Mark, Bikales, Overberger and Menges, Eds., Wiley, 1988, p. 601.
14. P. E. Cassidy "Thermally Stable Polymers", Marcel Dekker, New York, 1980.
15. W. D. Joseph, R. Mercier, A. Prasad, H. Marand and J. E. McGrath, Polym. Preprints, 33(1), 501 (1992).
16. G. L. Tullos, P. E. Cassidy, A. K. St. Clair, Macromol., 24, 6059-6064 (1991).
17. M. E. Rogers, M. H. Woodard, A. Brennan, P. M. Cham, H. Marand and J. E. McGrath, Polym. Preprints, 33 (1), 461 (1992); Polymer, in press, (1992).
18. a) Y. Maruyama, Y. Oishi, M. Kakimoto and Y. Imai, Macromol., 21 2305 (1988). b) J. G. Hilborn, J. W. Labadie and J. L. Hedrick, Macromol. 23, 2854 (1990).
19. B. A. Reinhardt, Polymer Communications, 31(12), 453 (1990).
20. A. Gungor, C. D. Smith, J. Wescott, S. Srinivasan, J. E. McGrath, Polym. Prep., 32 (1), 172 (1991).
21. J. E. McGrath, H. Grubbs, M. E. Rogers, R. Mercier, W. A. Joseph, W. Alston, D. Rodrigues and G. L. Wilkes, Polym. Prepr., 32(2), 103 (1991).
22. T. M. Moy, C. D. De Porter and J. E. McGrath, Polym. Preprints, 33(1), 489 (1992).

Peculiar Chemical Reactions of NCO-Modified Epoxy Acrylate Resin System with Fiber Surface Treatment Agents within CF/GF Hybrid Laminates and Their Mechanical Properties

YOSHIKUNI YOSHIMITSU, KIMITAKA TAHIRA, TOSHIHIKO OHASHI, ICHIRO SHIMOHARA AND JUNICHI SAKATA

ABSTRACT

The resin modification technique is one of the most useful methods which improve toughness of thermoset composites. In this work, some peculiar chemical reactions of diphenyl methane diisocyanate(MDI) as modifier of epoxy acrylate resin with fiber surface treatment agents were studied and some mechanical properties of CF/GF hybrid composites used these resin systems were mainly investigated.

The experimental results indicated that mechanical properties of the laminates were strongly affected by the interlaminar adhesion force, therefore, interlaminar shear and flexural bending strength were remarkedly improved by means of the strong interface chemically bonded between fiber surface and resin matrix in which a urethane bond or urea bond might be formed by the reaction of isocyanate and hydroxyl or amino group. Damage resistance of these laminates in the penetrating impact behaviors was also improved by a good delamination resistance.

INTRODUCTION

It has been well known diphenyl methane diisocyanate(MDI) is the raw material of polyurethane or one of the thickners of unsaturated polyester resin for SMC and BMC. However, its own reactivity was available to improve the characteristics of the resin[1-2]. In this work, we applied MDI to improve the interfacial bonding force between fiber surface and resin matrix by means of chemical bonds among functional groups in epoxy acrylate(EPA) prepolymer and the surface treatment agents on fiber surfaces, such as hydroxyl(-OH), epoxy and amino(-NH$_2$) group.

In composites, we used CF(T300) roving plain cloth treated with a digrycidil ether and GF(E glass) yarn plain cloth treated with vinyl, epoxy, or amino silane coupling agent, respectively. GF, CF/GF and CF laminates were fabricated with EPA resin system

Yoshikuni Yoshimitsu, Kimitaka Tahira, Toshihiko Ohashi and Ichiro Shimohara, Western Industrial Research Institute of Hiroshima, 6-21 Nishichuo 3 Chome Kure, Hiroshima 737 Japan
Junichi Sakata, MANAC Inc. 92 Minookicho Fukuyama, Hiroshima 721 Japan

and its MDI modified system,respectively,by a hot press method after wet lay up.
As regard EPA resin,2 kinds of EPA resins were synthesized from 2 epoxy oligomers
(n=0,2),and methyl methacrylic acid under the catalyst,and dissolved them into the
styrene monomer,respectively.Then they were mixed in various ratio to study the
effect of oligomer n value in EPA resin to the mechanical properties,such as heat
distorsion temperature(HDT) and bending flexural properties of neat resin.

MDI modification to improve the characteristics of composites was as follows.

The amount of MDI which was mainly equivalent weight to hydroxyl group of the EPA
resin was added into EPA resin system before moulding.The isocyanate group in MDI
could react with hydroxyl group in EPA to create a macro molecular linkage of EPA.
It could also react with hydroxyl group or amino group in the fiber surface treat-
ment agents.High quality composites with strong interface chemically bonded might
be made by these chemical process.The mechanical properties to be evaluated were
tensile,flexural,impact properties and interlaminar shear strength.

The results showed that large improvement of interlaminar bonding strength led to
large improvement of static mechanical properties of these composites,specially,in
CF and CF/GF hybrid laminates.And it was certificated that these phenomena were
dew to increase of delamination resistance and adhesion force of interface between
fiber surface and resin matrix by optical and SEM observations.

EXPERIMENTAL PROCEDURE

RESIN MODIFICATION

The purpose of this experiment was to investigate the effects of molecular weight
(oligomer n value) and isocyanate modification of EPA resin to the characteristics
of neat resin.We synthesized a couple of fundamental EPAs from bisphenol A typed
epoxy oligomer and methyl methacrylic acid by usual method.The oligomer n value
were selected approximately 0 and 2.Consequently,they were dissolved into 4 times
mole weight of styrene to be an EPA resin. And 2 kinds of EPA resins were mixed at
various ratio to make various molecular weight of EPA resin.

Modified diphenyl methan diisocyanate(MDI) was applied to resin modification for
the reason of safety and stabiliity.Various amount of MDI was added into these EPA
resin systems and mixed.After degases under vacuum,they were pored into the mould
to make the plaque of neat resin.The existence of free organic acid or water brou-
ght about foaming and it should change bulk matrix into foamed matrix.It should be
necessary that acid value of EPA was less than 2 or 3.

FIBEROUS MATERIALS

We used cabon fiber(abbr.:CF,eq.T300) 3K roving plain cloth(abbr.:CFCL,MITSUBISHI
RAYON,PYROFIL TR3110) which was a popular grade treated with diglycidil ether and
glass fiber(abbr.:GF,E glass) yarn plain cloth(abbr.:GFCL,FUJI FIBER GLASS;FECR 25
21) with the same thickness to CFCL,which was specially treated epoxy silane or
amino silane in addition to conventional vinyl silane in order to form a stronger
interfacial bond between fiber and matrix.It was estimated that MDI and hydroxyl
or amino group might form a urethane or urea bond,and fiber surface,MDI,and EPA
might be strongly linked.

MOULDING

The laminate constitution was able to describe equation(1) and (2).Detail of the laminate constitution was shown in table 1.

$$(CFCL/GFCL_m)_n + CFCL \qquad (1)$$
$$(CFCL_2/GFCL)_5 + CFCL_2 \qquad (2)$$

where, m, n and number are the number of repetition; $m=0$ to $14, n=1$ to 8

In hybrid laminates,both top and bottom layers were CFCL layers and the middle of the laminates was consisted of GFCL and CFCL layers,and the number of CFCL layers were changed to investigate the effect of CFCL volume fraction(Vf) to the mechanical properties.The resin were selected EPA resin whose n value was 1.3 on the view point of mouldability and adhesive compatibility[3].These laminates were moulded by hand lay up method and cured by hot press method with 3.0 mm spacer under 0.98 MPa pressure and 120℃ for 30 minutes.

TESTING

In this work,the laminates fabricated with plain cloth were supplied to testing and their mechanical properties were measured,such as tensile and bending flexural properties,interlaminar shear strength,and impact behaviors.As concern impact behaviors,both charpy impact and penetrating impact behaviors were investigated and damaged area were measured by ultrasonic c-scan.The fractured surfaces after impact were observed by optical microscope and scanning electron microscope(SEM).

Table 1 The composition of the laminates to be moulded

Resin	Laminate constitution	Surface treatment agent of GF	Vf %	
			C F	G F
Epoxy acrylate resin	$GFCL_{16}$	Vinyl silane	0	35.3
	$CFCL/GFCL_{14}/CFCL$		7.8	35.0
	$(CFCL/GFCL_3)_4 + CFCL$		17.8	27.5
	$(CFCL/GFCL_2)_5 + CFCL$		22.1	23.7
	$(CFCL/GFCL)_8 + CFCL$		30.6	17.5
	$CFCL_{16}$		53.3	0
MDI modified epoxy acrylate resin	$GFCL_{16}$	Vinyl silane	0	30~32
	$CFCL/GFCL_{14}/CFCL$		6~8	27~35
	$(CFCL/GFCL_3)_4 + CFCL$		15~18	23~28
	$(CFCL/GFCL_2)_5 + CFCL$	Amino silane	18~22	20~24
	$(CFCL/GFCL)_8 + CFCL$		31~32	17~27
	$(CFCL_2/GFCL)_5 + CFCL_2$	Epoxy silane	35.7	9.
	$CFCL_{16}$		53~59	0

RESULTS AND DISCUSSIONS

NEAT RESIN

The effects of molecular weight and MDI modification of EPA resin to the mechanical properties of neat resins were shown in Fig.1.These plots were typical data to show each average bihaviors since the effects were changeable under the reacting conditions. H.R.Edwards reported about coiling phenomena in unsaturated polyester urethane hybrids[3].Generating phenomena of polymerized block was very sensitive.

However, it might be certain that MDI modification considerably improved HDT of neat resin.The length of molecular linkage might be in proportion to HDT,but other mechanical properties were not changed.It showed that mechanical properties at RT were mainly affected by cross-linking of styrene monomer with EPA.
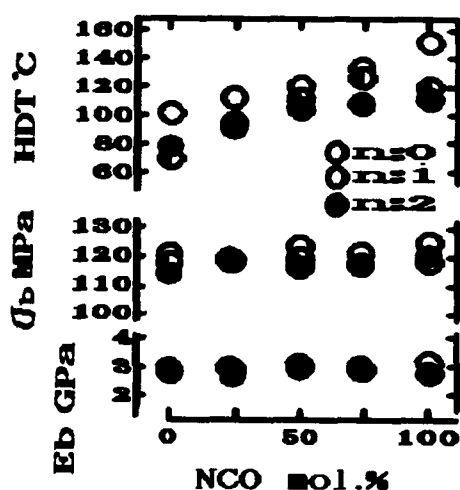
Fig.1 The mechanical properties of
        EPA neat resin
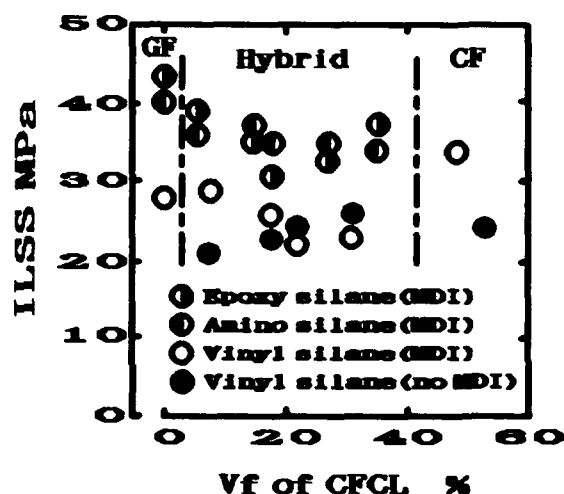
Fig.2 ILSS versus Vf of CFCL in each
        laminates

INTERLAMINAR SHEAR STRENGTH OF THE LAMINATES

Interlaminar shear strength(ILSS) should mainly depend on the interlaminar and interfacial bonding force.Y.Suzuki et al reported the interesting results about improvement of interfacial adhesion bond in epoxy-GF laminates by epoxy or amino silane coupling agent[4]. However,the problems in the improvement of interfacial and interlaminar adhesion bond in the hybrid composites were very complicated because of existence of different
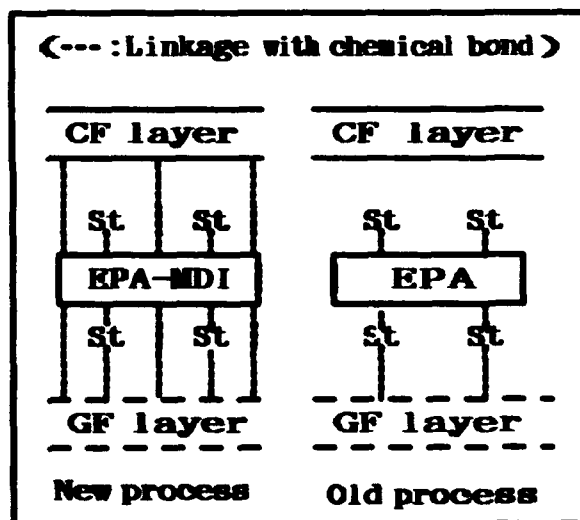
Fig.3 The illlustration of estimated
        bonding process between layers

fiberous layers. So it should be very important to improve the interlaminar adhesi-
on bond between neighbored layers as well as interfacial adhesion bond between the
fiber surface and matrix. In this work, we applied MDI to improve both adhesion bond.
The average ILSS value of each laminates were plotted in Fig. 2. The laminates used
the reactable materials with MDI showed high value of ILSS, and it presumed to occ-
ur the reaction between fiber surface and resin matrix. The GF surface with epoxy
or amino group and the CF surface with hydroxyl group might be more effective to
mprove ILSS of the laminates and superior to conventional process. Moreover, the
interlaminar adhesion between CF and GF layers might be improved since MDI might
strongly connect to the both layers by the reactions of their functional groups,
respectively. The estimated reaction process between layers was illustrated in Fig.
3. The reactivity of styrene monomer has been mainly applied into the conventional
FRP. So, GF surface treatment agent has been mostly used acryl or vinyl silane.

That was different from this new process which was applied the reactivity of MDI
with both EPA resin matrix and fiber surface treatment agents.

TENSILE AND FLEXURAL PROPERTIES

It seemed tensile property was depended on the properties of reinforcement fiber
as shown in Fig. 4 and 5. Tensile modulus and strength of each laminates increased
in proportion to only the CFCL volume fraction and chemical process were seemed
quite unrelated. But each pattern of stress-strain curve was quite different and
fracture mode was also quite different. The laminates with modified matrix showed a
brittle fracture mode like epoxy-CF laminates and the other showed non linear mode
like flexible thermo plastics pattern whose limit of elasticity was very low range
as describing in Fig. 6. Elongation at fracture of all laminates were plotted in
Fig. 7. The laminates used new chemical process(Blank mark) showed low elongation
value, specially, in high volume fraction of CFCL, which suggest a brittle materials,
but the laminates used vinyl silane treated GF and MDI modified EPA resin showed a
large variance. The laminates used conventional process showed only a bit decrease
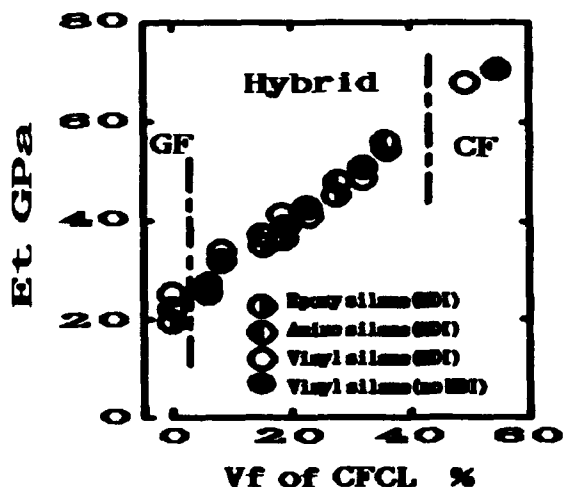
Fig. 4 Tensile modulus versus Vf of
CFCL in each laminates
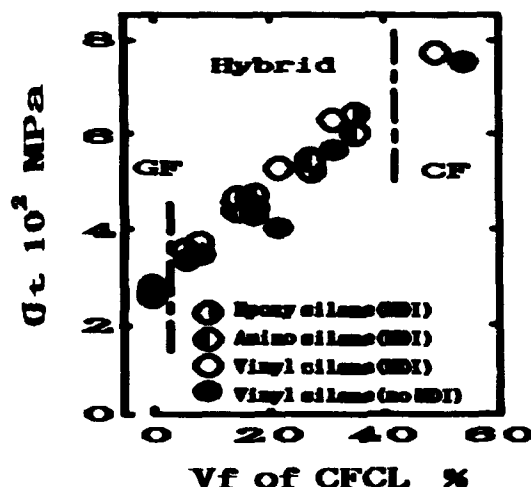
Fig. 5 Tensile strength versus Vf of
CFCL in each laminates
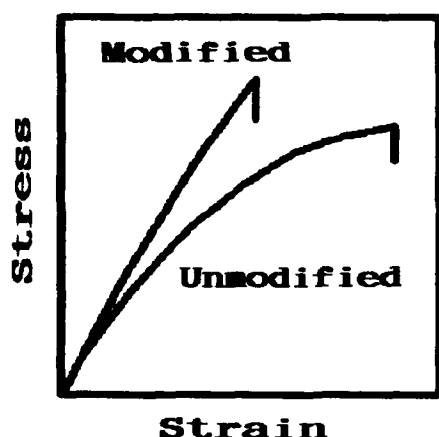
Fig. 6 The pattern of stress-strain curvature line
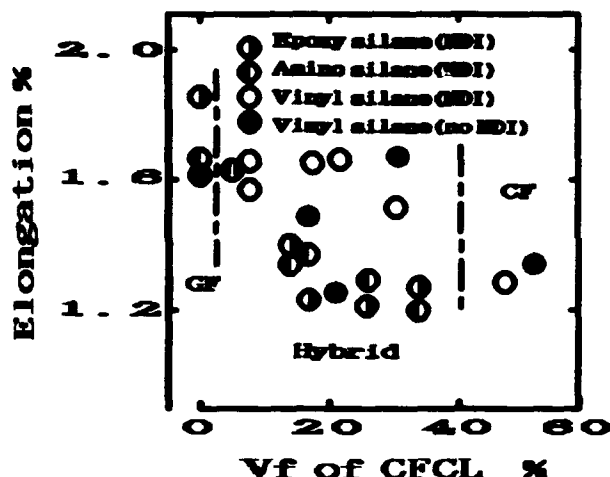
Fig. 7 Tensile elongation at break versus Vf of CFCL in each laminates

though CFCL volume fraction was increasing. It seemed the bonding force between CF and GF layers was very low and binding force within CF layer was also very low. The flexural property of the hybrid laminates typically showed the behavior of sandwich laminates with top and bottom layers of CFCL. For example, Fig. 8 showed flexural bending modulus was increased to be about 2 times of GFRP's modulus at a stroke by laying CFCL to both top and bottom layer, and it was not increased in the range of CFCL volume fraction up to 25%. Fig. 9 showed flexural bending strength of these laminates were also deeply altered by these chemical process, specially in the hybrid laminates. And stress-displacement curve of each laminates was similar
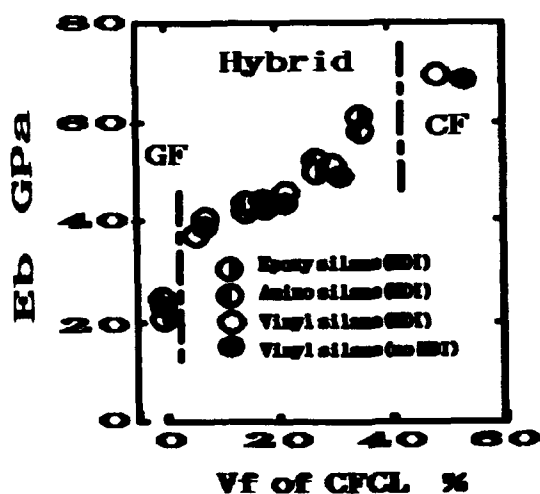
Fig. 8 Flexural bending modulus versus Vf of CFCL in each laminates
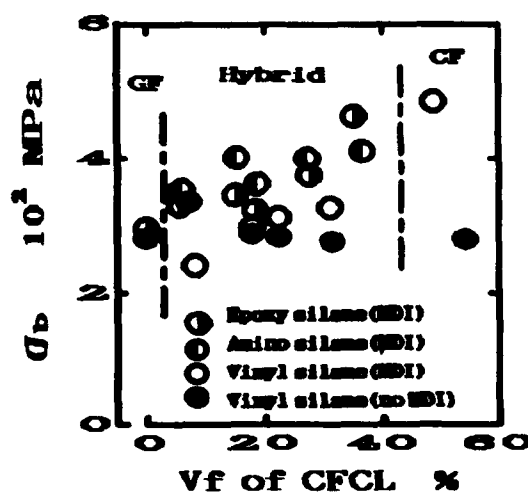
Fig. 9 Flexural bending strength versus Vf of CFCL in each laminates

to tensile behavior. As already mentioned, these results showed a good adhesion to which interfaces of fiber-resin matrix, layer-layer(adjoining), and fiber-fiber in each layer were included might be deeply influenced the properties of the resulting composites. We did not mentioned the state of oxidative surface treatment of CF in this discussion. So these results might indicate one of the methods to improve the properties of composites in processing

IMPACT PROPERTIES

Many methods to increase toughness and impact resistance of thermoset composites have been reported in ACM field. Many of them were apllication of useful additives to improve the toughness and impact resistance of composites[5-6]. B. Z. Jang et al reported that impact energy of thin laminates was mainly affected by the toughness of reinforcement fiber and the major factors were the interlaminar and interfacial fracture energies[7]. In this work, we discussed total energy, fracture mode and damaged area in impact test. The penetrating impact value plotted in Fig. 10 were total absorbed energy devided by the thickness of test specimen(Et/h) versus CFCL volume fraction in each laminates in order to minimize the thickness effect[8]. And the test specimen supporting diameter adopted in this work was more than 40 times to its thickness, which might be in-plane flexural bending mode and showed little variance. The result indicated this property were more sensitive to the constitution of each laminates than the charpy impact property which was shown in Fig. 11. In the CFCL laminates, MDI modified EPA resin matrix was inferior to unmodified resin matrix in the energy absorption. Fig. 12 showed damaged area measured by the ultrasonic c-scan(average of 4 samples). The damaged area of composites from modified resin was considerably smaller than the composites from unmodified resin. The photomicrographs of [(CFCL/GFCL)a+CFCL] hybrid laminates after charpy impact were shown in Fig. 13. Those clearly showed to be changed the failure mode and good delamination resistance by chemical process. As concerning interfacial adhesion on each fiber surface, the scanning electron micrograghs of the same hybrid laminates were also
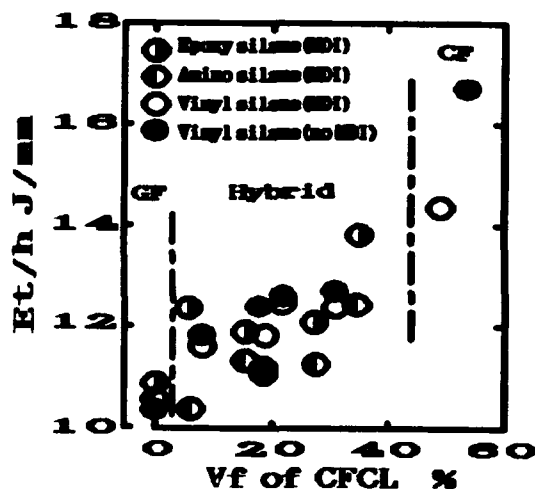
Fig. 10 Penetrating impact energy versus
         Vf of CFCL in each lamiuates
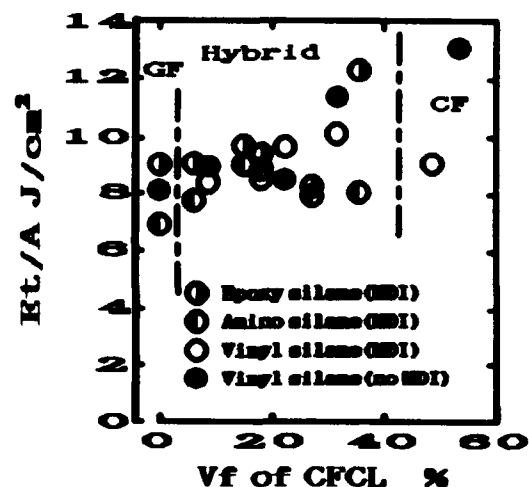
Fig. 11 Charpy impact strength versus
         Vf of CFCL in each laminates
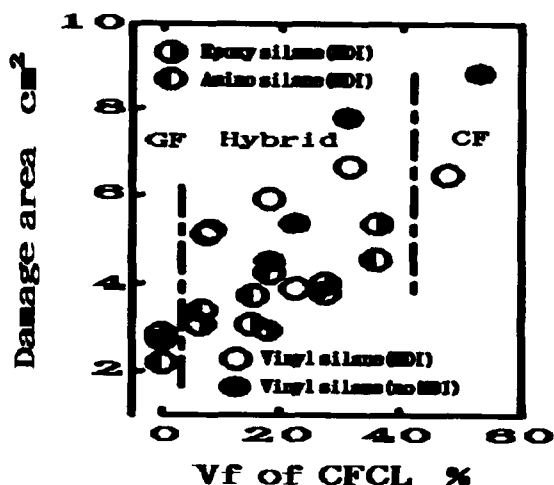
Fig. 12 Impact damage area in penetrating
versus Vf of CFCL in each laminate
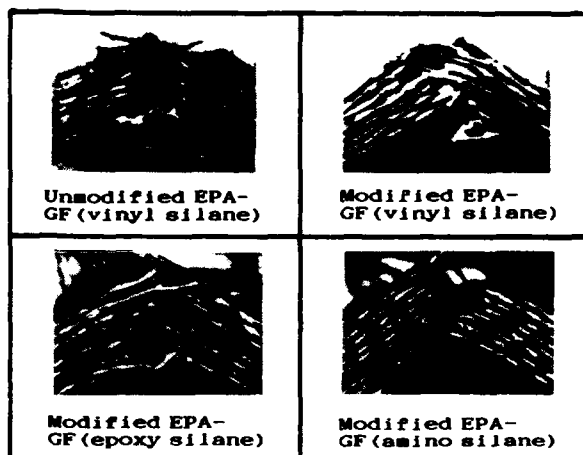
Fig. 13 Micrograpfs of fracture cross
section after charpy impacts
in (CFCL/GFCL)ₐ+CFCL laminates
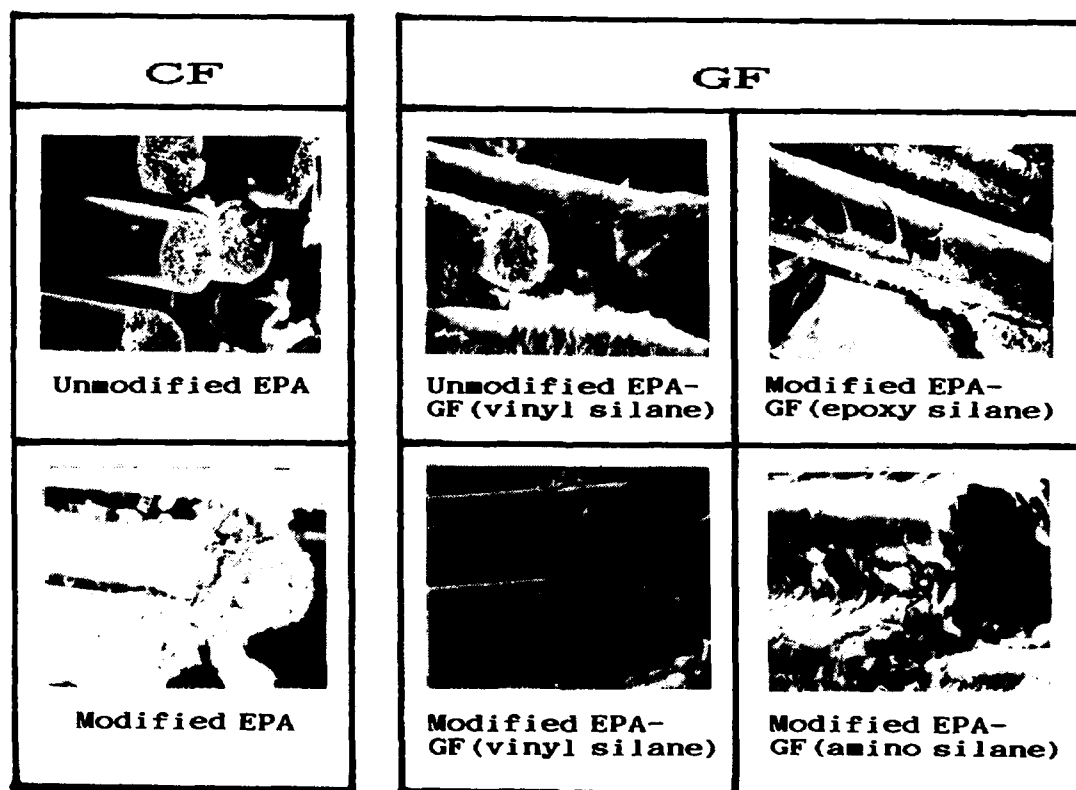
Fig. 14 SEM of fiber surface in (CFCL/GFCL)ₐ+CFCL laminates after charpy impact

shown in Fig. 14. As considering these results, it was clear that this chemical proc-
ess had an advantage in the optimization of the interfacial bond. Further more, it
was mentioned that the adequate interfacial bonding force raised the mechanical

properties of the resulting composites[10].

Thus the selection of surface treatment agent and confirmation of its reactivity was very important to create high performance composites.

CONCLUSIONS

Some peculiar chemical reaction of MDI with EPA resin and fiber surface functional group were applied mainly to CF/GF hybrid composites in order to improve their mechanical properties. The results showed considerable increase of those properties as we had presumed, and, specially, ILSS, flexural bending strength, and impact damage resistance were remarkedly improved. And these chemical process might change the characteristics of the laminates into more brittle material. Therefore, it should be important to use the reactive agents showed adequate interfacial bonding force. The combination of EPA, MDI, and epoxy silane treated GF showed adequate interfacial and interlaminar bonding force. The optical micrographs and SEM observations indicated that above mentioned phenomena might be occurred with repeatability.

REFFERENCES

1. Weldon N. Reed and Michael Kallaur, 1987. 'Interpenetrating Polymer Networks-versatile tool for solving Tough Problem.' Proc. of 42nd Ann. Tech. Conf. Reinforced Plastics. Conf. Inst. Ses. 8-B.

2. T. Jeffrey Hsu and L. James Lee, 1987. 'Processing of Polyurethane-Polyester Interpenetrating Polymer Network.' Proc. of 42nd Ann. Tech. Conf. Reinforced Plastics. Conf. Inst. Ses. 18-C.

3. H. R. Edwards, 'The Application of Isophthalic Unsaturated Polyester Urethane Hybrids in Conventional Molding Techniques.' Proc. of 42nd Ann. Tech. Conf. Reinforce Plastics. Conf. Inst. Ses. 8-C.

4. Yoshiharu Suzuki, Motoharu Murakoshi and Junichi Saitoh, 1990. 'Interfacial Adhesion Between Glass Fiber and Epoxy Matrix.' Proc. of 45th Ann. Tech. Conf. Reinforced Plastics. Conf. Inst. Ses. 10-A

5. Gail L. Dolan, 1988. 'Characterization of Carbon/Bismaleimid interleafed for Improved Resistance to Delamination and impact.' Proc. of 20th SAMPE Tech. Conf. Inst. 20:34 -35

6. Russel L. Turpin and Anthony L. Green, 1990. 'Improved Damage Tolerance by Controlling Thermoplastic Solubility in Thermoset Composites.' Proc. of 35th Int. SAMPE Symp.: 1079-1088

7. B. Z. Jang, C. Z. Wang, B. P. Jang and R. H. Zee, 1989. 'Low Velocity Failure Mechanics of Advanced Fablic Reinforced Composites,' Proc. of 21tst Int. SAMPE Tech. Conf.: 825-839

8. Yukio Kawazu and Kenichi Nogami, 1991. 'The Penetrating Impact Properties of CFRP Laminates,' Proc. of 20th FRP Symp. (Japan):31(Japanese)

9. Yoshikuni Yoshimitsu, Ichiro Shimohara, Akira Yorihashi and Tomoyuki Nakamoto, 1992. 'Optimization of Penetrating Impact Condition and Improvement of Impact Resistance of Hybrid Composites by Chemical Process,' Reinforced Plastics 38(1):12-14 (Japanese)

10. P. Ehrburger and J. B. Donnet, 1985. HAND BOOK OF COMPOSITES 1, IV:579

The Role of Partial Miscibility on the Properties of Blends of Polyetherimide and Two Liquid Crystalline Polymers

S. S. BAFNA, J. P. DE SOUZA, T. SUN AND D. G. BAIRD

ABSTRACT

This paper is concerned with the existence of partial miscibility of a polyetherimide (PEI) with both amorphous as well as semi-crystalline liquid crystalline polymers (LCP's) and its effect on the morphology of blends based on these polymers. Partial miscibility was determined by measuring the shift in the glass transition temperatures as determined by dynamic mechanical thermal analysis (DMTA) and differential scanning calorimetry (DSC). With increasing concentration of the LCP in the PEI/LCP blends, the glass transition temperature of the PEI phase shifted to lower temperatures. A similar shift in the glass transition temperature was also determined by means of DSC. Annealing and mixing history were also observed to affect the degree of shift in the glass transition temperature. Morphologies of the partially miscible systems were found to be quite different from those of an immiscible system. In particular, in the case of the immiscible system, numerous microfibrils of LCP pull out from the other side on fracturing, revealing poor matrix/fibril interfacial adhesion. In contrast, for the partially miscible blends no pull out of the microfibrils was observed. Furthermore the matrix itself shows a distinct tendency to form fibrils itself. It is likely that due to partial miscibility in these blends, a PEI-LCP solid solution coexists with the neat LCP phase.[1]

INTRODUCTION

Interest in in situ composites based on blending liquid crystalline polymers (LCP's) with engineering thermoplastics has grown in recent years primarily due to the possibility of their having a variety of processing options and relatively high mechanical performance (1-9). It has been well known that the maximum enhancement in mechanical properties of short fiber composites can be achieved by using very fine fibers with a large aspect ratio and by promoting strong interfacial adhesion between the fibers and the polymeric matrix (10). As pointed out by Baird et al., the morphology and properties of in situ composites should

be affected by the interaction between the LCP and the matrix (11). Factors such as miscibility or compatability could contribute significantly to the interaction between the matrix and the LCP and hence to the physical properties of in situ composites.

Studies dealing with the miscibility of blends of a thermotropic liquid crystalline copolymer consisting of p-hydroxybenzoic acid and ethylene terephthalate (PET/PHB) with various thermoplastics can be found in literature (12-15). The effects of miscibility of the matrix and reinforcing phase on the development of in situ composites have been studied by Zhuang et al. (14). Polystyrene (PS), poly(ethylene terephthalate) (PET) and polycarbonate (PC) were used as the matrices and PET/60PHB (60 denotes the mole percent of PHB in the copolyester) as the reinforcing phase. Blends were prepared by both solution and melt blending. On the basis of the results from differential scanning calorimetry (DSC), scanning electron microscopy (SEM), and dielectric thermal analysis (DETA), the authors concluded that PS was immisicible, whereas both PC and PET were partially miscible with PET/60PHB; PET being miscible to a higher degree than PC. The glass transition corresponding to the thermoplastic phase did not shift for PS upon blending with the LCP. There was a small but significant decrease in the glass transition temperature upon blending with PC and the shift was detectable across the entire composition range for PET blends. The presence of ellipsoidal LCP particles and microfibrils was observed. However, little attempt was made to explain the reason for the observed morphology or correlate it with miscibility. Recently, it has been found that a single phase can be prepared with PET/60PHB and PC through solvent casting (15). The blends of PET/60PHB with PC were originally reported to be only partially miscible (14). However, they phase separate upon heating.

Polyethermide (PEI), an amorphous polymer commercially known as Ultem, has been blended with LCP's to prepare high modulus in situ composites (4, 16, 20, 21). It has been reported that Ultem is miscible with polybenzimidazole (PBI) (17) and polyetheretherketone (PEEK) (18, 19). Recently the miscibility between Ultem and LCP's and its effect on the morphology and mechanical properties of Ultem/LCP in situ composites were studied in our laboratory (20). It has been found that Ultem is immiscible with Vectra A900 (a liquid crystalline aromatic copolyester consisting of 73% hydroxybenzoic acid and 27% 2-hydroxy 6-naphthoic acid moities), but partially miscible with Granlar (a liquid crystalline aromatic copolyester consisting of terephthalic acid, phenyl-hydroquinone and phenyl-ethyl hydroquinone) (21). As revealed by dynamic mechanical thermal analysis (DMTA), the mixing of the latter can be improved by increasing the number of passes through an extruder. The flexural and tensile moduli of the in situ composites based on these two blend systems have also been determined as a function of the blend composition. The modulus deviations from the rule of mixtures was interpreted in terms of differences in miscibility and hence, differences in the interfacial adhesion between components for these two blend systems.

In this paper, the existence of partial miscibility of Ultem with both an amorphous as well as a semi-crystalline LCP and its effect on the morphology of the in situ composites based on these blends are studied. The effect of the annealing and mixing history on partial miscibility and phase dispersion are also discussed.

EXPERIMEMTAL

MATERIALS AND SAMPLE PREPARATION

The amorphous matrix polymer used was a polytherimide (Ultem 1000) made by General Electric. Two liquid crystalline polymers (HX1000 and HX4000) made by DuPont were used in this study. HX4000 is a semi-crystalline copolyester while HX1000 is an amorphous copolyester.

Pellets of Ultem were dried at 170°C. Pellets of the liquid crystalline polymers, HX1000 and HX4000, were dried at 150°C. All drying processes were carried out in a vacuum oven for at least 24 hours. The dried pellets were then tumbled in predetermined weight ratios. A laboratory single screw extruder (Killion KL100) connected to a 102 mm wide sheet die was used to generate the sheets. Rectangular plaques measuring approximately 75 mm x 85mm x 1.75 mm were molded using an Arburg (221-55-250 Allrounder) injection molding unit. Temperatures were set at 300, 355, 360°C in zones 1, 2, and 3 of the barrel, respectively, and at 360°C in the nozzle. The mold temperature was set at 150°C.

To study the effect of mixing history, pellets of Ultem and the LCP were mixed together and extruded in a single or a twin screw extruder connected to a pelletizing die. The extrudate was quenched in ice water and continously pelletized. In order to impart additional mixing history, the pellets were re-extruded in the single screw extruder and then pelletized again. The blended pellets were then used to make molded plaques.

DYNAMIC MECHANICAL TESTS

Dynamic mechanical tests on the injection molded plaques were carried out in the torsional mode using a Rheometrics Mechanical Spectrometer (RMS 800). Rectangular samples with dimensions of 45 x 12.5 mm were cut from the injection molded plaques. The loss tangent (tan δ) of the samples was monitored and recorded as a function of temperature. The frequency of oscillation was 10 rad/s and the strain was 0.05%. The experimental temperature was raised stepwise at a rate of 5°C per minute until the modulus of a given sample dropped appreciably.

THERMAL ANALYSIS

A Sieko 1 DSC (Model 210) was utilized for the thermal analysis of these blends. The heating rate was fixed at 10°C per minute for all the samples and pre-purified nitrogen was used as the purge gas.

MORPHOLOGY

The morphology of the blends was determined by scanning electron microscopy (SEM) using a Cambridge Stereoscan S200 with an accelerating voltage of 25 kV. The samples were fractured perpendicular or parallel to the main flow direction after the

immersing them in liquid nitrogen. The fractured surfaces were sputter coated with gold to provide enhanced conductivity.

RESULTS AND DISCUSSION

To study the miscibility of the Ultem/HX4000 and Ultem/HX1000 blends, their glass transition temperature was measured as a function of the blend composition using DMTA and DSC. The dynamic torsion test results for the Ultem/HX4000 system are shown in Fig. 1. The glass transition temperatures of Ultem and HX4000 were found to be 228°C and 183°C, respectively. With increasing concentration levels of HX4000 in the injection molded Ultem/HX4000 composites, the glass transition temperature of the Ultem phase shifts to a lower temperature and the peak height of the loss tangent (tan δ) versus temperature curve decreases. Meanwhile, a shoulder which characterizes the segmental motion of HX4000, can be observed for all the blend compositions studied. The shift in Tg suggests that HX4000 is partially miscible with Ultem. It seems there are two phases existing in the composite: a pure HX4000 phase and a phase rich in Ultem with some HX4000 dissolved in it. The latter phase presents a lower Tg than that of neat Ultem and may give a higher matrix/fibril interaction in the (Ultem-HX4000)/HX4000 system.

To confirm the results obtained from dynamic mechanical analysis, DSC thermograms of the Ultem/HX4000 composites at various blend compositions have also been studied (Fig. 2). With increasing content of HX4000 in the blends, the Tg of the Ultem-rich phase also shifts to a lower temperature. This again suggests that Ultem and HX4000 are partially miscible. The observed endothermic peak is caused by the melting of HX4000 crystallites in the blends. In the case of the Ultem/HX1000 blends, two glass transitions can also be observed (Fig. 3). The lower one (at 185°C), characterizing the glass transition of HX1000, remains almost unchanged as the blend composition is varied. But the higher one (i.e. the glass transition temperature of the Ultem-rich phase) decreases as the concentration level of HX1000 is increased. The DSC thermograms of the Ultem/HX1000 blends show similar trends (Fig. 4). The Tg, as determined by DSC, of the Ultem phase in the blends dropped to 212°C as compared with 218°C for neat Ultem. The fact that no endothermic melting peak can be detected in Ultem/HX1000 DSC thermograms implies that the HX1000 phase in the blend is amorphous.

In an effort to provide more support of partial miscibility the morphologies of Ultem/HX4000 and Ultem/HX1000 blend systems were studied and compared with those of the immiscible Ultem/Vectra blend system. The SEM micrographs of their fractured surfaces are shown in Fig. 5 - 7. For the immiscible Ultem/Vectra composites, numerous microfibrils can be observed to be pulled out from the surface (Fig. 5a and Fig. 6b). Large matrix voids generated by the pullout of microfibrils reveal the poor matrix / fibril interfacial adhesion for this system. In the case of the Ultem/HX4000 (Fig. 5c and 6c) and the Ultem/HX1000 (Fig. 5b and 7) in situ composites, no pulled out microfibrils can be observed. Furthermore, the matrix shows a distinct tendency to form fibrils itself (Fig. 5 - 7). It is most likely that due to the partial miscibility of the Ultem/HX4000 and the Ultem/HX1000 systems in these blends, an Ultem-LCP solid solution phase coexists with the LCP phase. Also the interfacial adhesion appears to be good which is suggestive of an interaction between LCP and the matrix. For this reason, no matrix voids and pulled-out fibrils can be observed.

It was reported in the literature that Ultem is miscible with PBI when solvent cast or co-precipitated, but phase seperation takes place as the blend is heated to a temperature above or close to the glass transition temperature (17). To understand the possible influence of annealing on the phase separation of the Ultem/HX4000 and the Ultem/HX1000 blends, injection molded plaques were annealed at a temperature higher than the Tg of the Ultem and the LCP's (i.e. annealed at 250°C for 24 hours) and then their glass transition behavior before and after annealing were compared. As seen from Figs. 8 and 9, in both blend systems no increase in Tg of the Ultem-rich phase can be observed. For the Ultem/HX1000 70/30 blend (Fig. 9), the Ultem-rich phase remains at 223°C before and after annealing. For the Ultem/HX4000 70/30 blend (Fig. 8), the Tg of the Ultem-rich phase decreases from 223°C (before annealing) to 215°C (after annealing). The above facts imply that no phase seperation occurs for these two blend systems during heat treatment. The extent of the partial miscibility between the non-crystalline LCP HX1000 and Ultem remains almost unchanged. In the case of the Ultem/HX4000 70/30 blend, it appears that a part of the free HX4000 further "dissolves" into the Ultem phase leading to a decrease in the Tg of the Ultem-rich phase.

CONCLUSIONS

Partial miscibility between a polyetherimide (PEI) and an amorphous as well as a semi-crystalline LCP was determined by measuring the shift in the glass transition temperature as determined by DMTA and DSC. With increasing concentration of the LCP in the PEI/LCP blends, the glass transition temperature of the PEI phase shi.'ed to a lower temperature. A similar shift in the glass transition temperature was also determined by means of DSC. It was found that the extent of mixing between the PEI and the LCP can be improved (upto a certain extent) by increasing the number of passes through a single screw or passing the material through a twin screw extruder. Irrespective of the composition of the composites, the diameter of the LCP microfibrils decreased upon increasing the number of passes through the extruder. This morphological feature implies that the extent of the dispersion of the LCP phase, and thus the fineness of the reinforcing fibrils in the in situ composites, can be improved by a suitable mixing process. Morphologies of the partially miscible systems were found to be quite different from that of an immiscible system (which showed pull out of LCP microfibrils and large voids where the microfibrils were pulled out of the matrix revealing poor matrix/fibril interfacial adhesion). In contrast, partially miscible blends do not show the pulled out microfibrils and futhermore the matrix itself shows a distinct tendency to form fibrils. It can be concluded that due to partial miscibility in these blends, a PEI-LCP solid solution coexits with the neat LCP phase.

ACKNOWLEDGEMENT

REFERENCES

1. Siegmann, A., Dagan, A. and Kenig, S., Polymer 1985, 26, 1325.

2. Blizard, K. G., and Baird, D. G., Polym. Engr. Sci. 1988, 28, 17.

3. Isayev, A. I. and Modic, M., Polymer Composites 1987, 8, 3, 158. 4. Weiss, R. A., Huh, W. and Nicolais, L., Polym. Engr. Sci. 1987, 27, 684.

5. Kiss, G., Polym. Engr. Sci. 1987, 27, 410.

6. Ramanathan, R. and Baird, D. G., Poly. Engr. Sci. 1988, 28,17.

7. Baird, D. G., Sun, T., Done, D. S. and Ramanathan, R., ACS Polymer Preprints 1989, 30, 546.

8. Kohli, A., Chung, N. and Weiss, R. A., Polym. Engr. Sci. 1989, 29 573.

9. Swaminathan, S. and Isayev, A. I., Polym. Mat. Sci. Eng. 1987, 27, 684.

10. Mascia L., "Thermoplastics - Materials Engineering", Second Edition, Elsevier Applied Science, London and New York, p. 98, 1989.

11. Baird, D. G. and Ramanathan, R. in "Contemporary Topics in Polymer Science. Volume 6: Multiphase Macromolecular Systems" (Ed. B. M. Culberston), Plenum Press, New York, 1989.

12. Nakai, A., Shiwaku, T., Hasegawa, H. and Hashimoto, T. Macromolecules 1986, 19, 3010.

13. Paci, M., Barone, C. and Magagnini, P.J., Polym. Sci. Poly. Phys. Ed. 1987, 25, 1595.

14. Zhuang, P., Kyu, T. and White, J. L., Polym. Eng. Sci. 1988, 28, 17.

15. Kyu, T. and Zuang, P., Polym. Communications, 1988, 29, 99.

16. Baird, D. G. and Sun. T., ACS Symposium Series 435 (Eds. R. A. Weiss and C. K. Ober), Chapter 29, 1990.

17. Choe, S., Karasz, F. E. and Macknight, W. J., in "Contemporary Topics in Polymer Science. Volume 6: Multiphase Macromolecular Systems" (Ed. B. M. Culbertson), Plenum Press, New York, 493, 1989.

18. Harris, J. E. and Robeson, L. M., J. Appl. Polym. Sci. 1988, 35, 1877.

19. Marand, H. and Prasad, A., submitted to Macromolecules.

20. Bafna, S. S., De Souza, J. P., Sun T. and Baird D. G., submitted to Polymer Composites.

21. Bafna, S. S., De Souza, J. P., T. Sun and Baird D. G., submitted to Polymer.
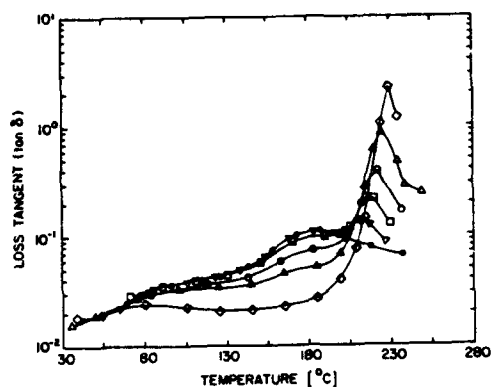
Figure 1.   Loss tangent (tan δ) versus temperature for Ultem/HX4000 blends with various composition ratios: (a) diamonds=100/0; (b) triangles=70/30; (c) unfilled circles=50/50; (d) squares=30/70; (e) inverted triangles=10/90; (f) filled circles=0/100.
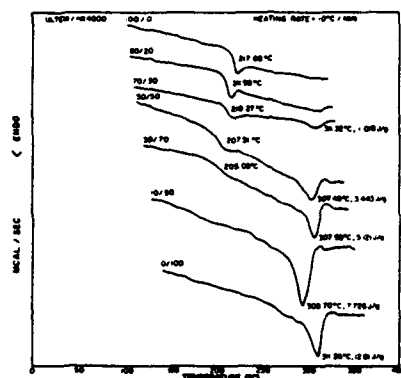
Figure 2.   DSC thermograms of Ultem/HX4000 blends with various composition ratios.
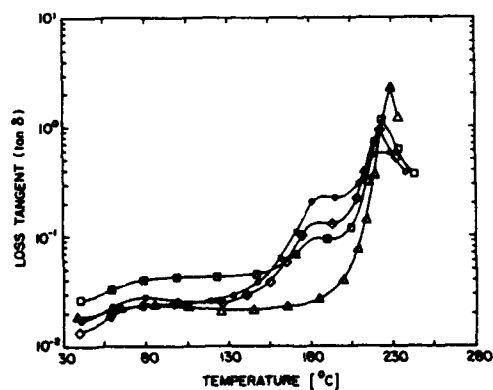
Figure 3.   Loss tangent (tan δ) versus temperature for Ultem/HX1000 blends with various composition ratios: (a) triangles=100/0; (b) squares=70/30; (c) diamonds=50/50; (d) circles=30/70.

237
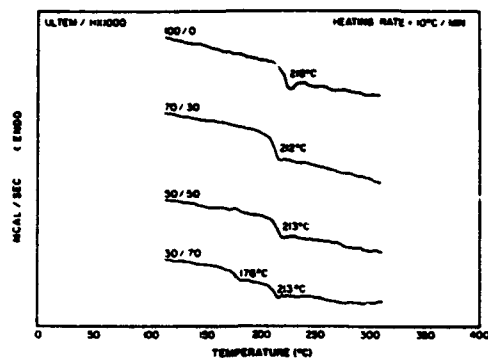
Figure 4.   DSC thermograms of Ultem/HX1000 blends with various composition ratios.
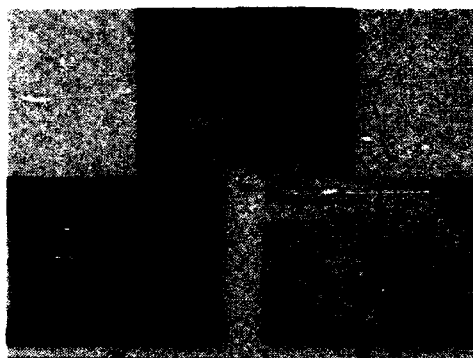
Figure 5.   SEM micrographs of the fractured surfaces of injection molded Ultem/LCP blend plaques: (a) Ultem/Vectra 70/30; (b) Ultem/HX1000 70/30; (c) Ultem/HX4000 70/30.
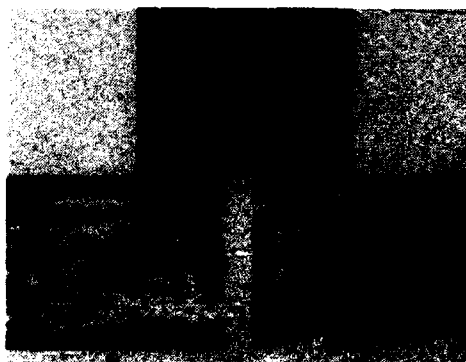
Figure 6.   SEM micrographs of the fractured surfaces of extruded sheets: (a) Ultem; (b) Ultem/Vectra 90/10; (c) Ultem/HX4000 70/30.
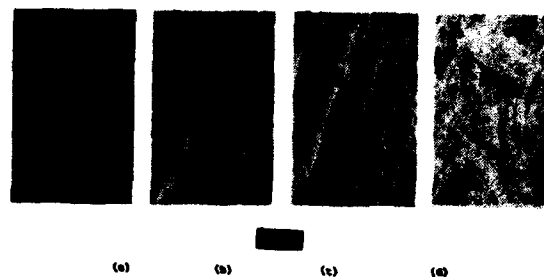
Figure 7.   SEM micrographs of the fractured surfaces of injection molded Ultem/HX1000 plaques: (a) Ultem/HX1000 70/30; (b) Ultem/HX1000 50/50; (c) Ultem/HX1000 30/70; (d) HX1000.
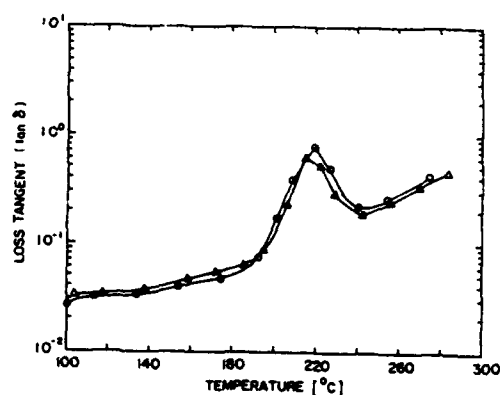
Figure 8.   Loss tangent (tan δ) versus temperature for Ultem/HX4000 70/30 blend: (a) circles=as injection molded; (b) triangles=annealed at 250°C for 24 hours.
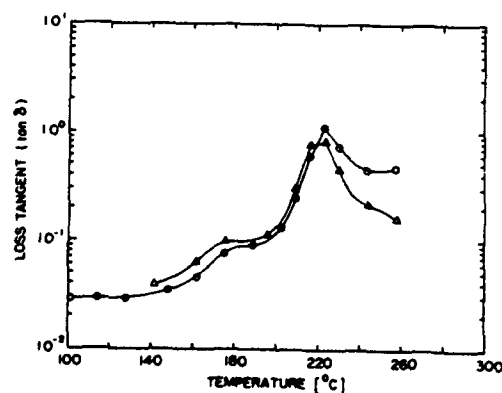
Figure 9.   Loss tangent (tan δ) versus temperature for Ultem/HX1000 70/30 blend: (a) circles=as injection molded; (b) triangles=annealed at 250°C for 24 hours.

Toughened Bismaleimides and Their Carbon Fiber Composites for Fiber-Matrix Interphase Studies

S. P. WILKINSON, S. C. LIPTAK, J. J. LESKO, D. A. DILLARD, J. MORTON, J. E. McGRATH AND T. C. WARD

ABSTRACT

Through employing engineering thermoplastics to serve as toughness modifiers for a BMI network the fracture toughness was improved by several orders of magnitude. Improvements were monitored by varying molecular weight, weight percent incorporation and end group chemistry of the polysulfone modifiers, while still maintaining high temperature performance and good processing characteristics for hot-melt techniques. To study how the fracture toughness transfers into the composite material mode I and mode II fracture toughness tests were performed. The results illustrated how substantial improvements could be made using the polysulfone modifiers. Mode I strain energy release rate G_{Ic} values increased from 359 ± 17 J/M^2 to 734 ± 12 J/M^2 for 20% by weight loadings of maleimide terminated polysulfone (Mn=12800 g/mole).

Toughened BMI matrix resins were prepregged onto carbon fibers that formed laminates containing contrasting changes at the fiber matrix interphase. These materials were then employed within an interdisciplinary research programme to study indentation techniques as possible methods to measure the interfacial response. The techniques of Micro and Meso-indentations into polished cross-sections of unidirectional laminates were performed. As were the more common 90° tension, flexure and Iosipecsu tests. All techniques showed a dramatic improvement in strength measurements when toughened BMI laminates containing AU4 and AS4 fibers were tested. However, certain anomalies were observed with the results from micro-indentations. These anomalies were not found using the meso-indentation test method. The improvement in interfacial measurement by using AS4 fibers compared with the AU4 fibers was described as a ratio. Comparable values for these ratios were obtained giving further evidence to suggest that the meso-indentation technique has potential for providing useful information concerning the fiber/matrix interface.

INTRODUCTION

Thermoset resins based on Bismaleimide (BMI) chemistry have been marketed to compete with epoxy resins as they too possess many desirable properties that are associated with thermoset networks. These include high tensile strength and modulus, excellent chemical and corrosion resistance and good dimensional stability. A major reason for the substantial interest in Bismaleimide resins at present, is that they process in a similar manner to epoxies, and cure without the evolution of volatiles, and exhibit higher glass transition temperatures than epoxies (approximately 250°C and above). Bismaleimide resins can be processed together with carbon fibers. Major applications for these BMI structural composites are in military aircraft and aero-engines. One major disadvantage associated with many thermosetting networks is their inherent brittle character. For BMI's to be used as matrix resins for high performance structural composite materials, their fracture toughness must be

Virginia Polytechnic Institute and State University, Chemistry Department and Department of Engineering Science and Mechanics, Blacksburg, Virginia, 24061

improved without sacrificing other important mechanical properties, such as high temperature flexure strength and storage modulus. One approach that can be taken, and has been the focus of several research efforts (1,2,3,4,5), is to employ engineering thermoplastics to serve as toughness modifiers for the thermoset network. Through controlling the molecular weight, weight percent incorporation, backbone structure and end group chemistry of these modifiers, the BMI fracture toughness has been studied while maintaining high temperature performance and good characteristics for hot-melt processing techniques.

As the modified resin system is still capable of being processed using existing hot-melt technology, attempts were made to prepare unidirectional carbon fiber prepreg to be consolidated into laminates for mechanical testing. A laboratory scale drum-winding prepregger was utilized to prepare unidirectional prepreg. Laminates were consolidated from the prepreg, and to study how the fracture toughness transfers into the composite material, mode I and mode II fracture toughness tests were performed, their results are presented.

Toughened BMI matrix resins were prepregged onto certain carbon fibers that would introduce both contrasting and subtle changes at the fiber matrix interphase. This was done using the fibers AU4, AS4, and IM7. Utilizing a variety of test methods such as 90°flexure,90°tension, and 90° Iosipescu the mechanical property evaluation for these laminates were obtained. These materials were then integrated within an interdisciplinary research program to study indentation techniques as possible methods to measure the interfacial response in fiber composites. Such information, concerning interfacial response, is needed by the mechanics community to learn how to develop mechanical tests that probe the engineering properties of the fiber-matrix interface. The ultimate goal is to use these measurements in models predicting life/strength of important structural materials such as toughened thermoset carbon fiber composites.

EXPERIMENTAL

MATERIALS

A commercial BMI based formulation termed Matrimid 5292 A/B was used as the base hot-melt resin. This two part system was comprised of 4,4'-bismaleimido-diphenyl methane and o,o' diallyl of bisphenol A (Figure 1). In all formulations containing the thermoplastic modifiers, the BMI/diallyl ratio was kept to 57:43 parts by weight (1:0.85 mole ratio).
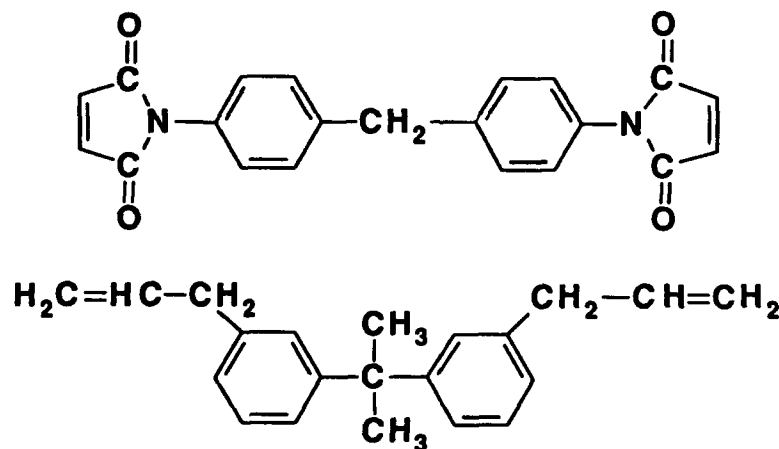
Figure 1
4,4' bismaleimido-diphenyl methane and the diallyl of bisphenol A
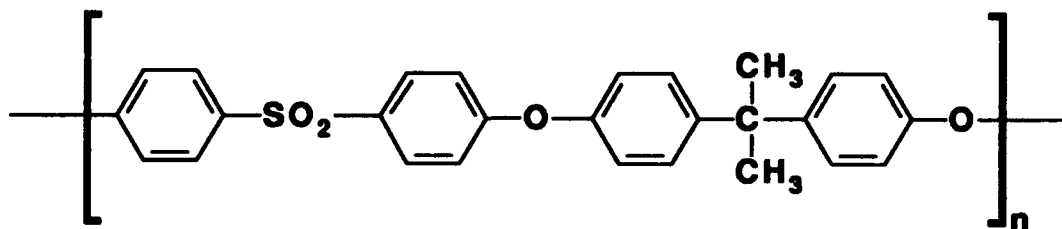
Figure 2
Backbone structure of the polysulfone toughness modifier

The polysulfone toughness modifiers were all specifically synthesized in our research laboratories. The backbone structure is illustrated in Figure 2. The well known nucleophilic aromatic substitution reaction common to the synthesis of numerous high molecular weight polyarylene ethers was employed (6,7,). Thermoplastic weight control was achieved by varying the stoichiometry of monomers involved in the synthetic reaction and for functionalized poly(arylene ether sulfone)s has been reported elsewhere in the literature (8). End group functionality was controlled by performing post-reactions on amine terminated polysulfones using phthalic and maleic anhydride monomers. Experimental conditions necessary for end capping these amine terminated polymers to maleimide groups have been reported by McGrath et al. (9,10)

The carbon fibers were purchased from Hercules Corporation. The 'A' type fiber was obtained both with and without surface treatments to provide composite laminates with contrasting interphases. IM7 carbon fiber was utilized in other studies regarding translation of fracture toughness, but was also used in the interfacial evaluation to compare it's performance with the AS4 carbon fiber.

NEAT RESIN PROCESSING

The amorphous polysulfone modifiers were dissolved in the diallyl of bisphenol A compound and degassed under vacuum with constant stirring at 135°C. Once a bubble free homogeneous melt had been obtained, the temperature was raised to 140°C and the BMI was added. After reaching temperature and continually being degassed for a further 20-30 minutes, the hot-melt resin was poured into preheated (150°C) R.T.V. silicone molds specifically prepared for fracture toughness specimens. To cure the samples, the temperature was raised to 200°C at 5°C/min, and held for one hour, then raised to 250°C at 5°C/min and held for a further 2 hours. This cure cycle would be sufficient to raise the glass transition temperature of the cured network to 250°C well above the service temperature of bismaleimide resins. The samples were slow cooled to room temperature at 2-3 °C per minute.

NEAT RESIN TEST METHODS

Fracture toughness measurements were performed in accordance with the ASTM E399 test method. Specimen dimensions were 3.2mm x 6.5mm x 38mm. A sharp crack was initiated in each specimen using a razor blade (cooled in liquid nitrogen) at the base of a notch (~0.5mm deep) and tapping the blade with an aluminum bar. Specimens were placed in a three point bend apparatus fixed to an Instron test machine (Model 1123). The load to brittle failure was recorded and the initial crack length was measured from the resulting fracture surface using a digital caliper. The stress intensity factor K_{Ic} was calculated in accordance with the ASTM E399 test method. Number average molecular weights of the amine terminated polysulfone modifiers were determined using an automatic potentiometric titration. Differential scanning calorimetry at 10°C/minute heating rates were used to determine the

modifiers glass transition temperatures. A Cannon Ubbelhode viscometer with four concentrations was required to determine the modifiers intrinsic viscosities.

COMPOSITE PROCESSING

Homogeneous hot-melt resin systems were prepared as described in the previous section and poured into the resin pot (heated to 120°C) of a Research Tool hot-melt drum-winding prepregger. IM7 fiber was passed into the resin pot, over impregnation pins and exited a die (3.429mm x 0.1651mm) used to meter the desired resin content on the prepreg. The fiber aerial weights and resin content for each tape run were obtained by dissolving 50.8mm x 50.8mm pieces of prepreg in chloroform and ratioing the weight of fiber remaining to the original weight of prepreg.

The prepreg tape containing the toughness modifiers had little drape and no tack. To improve the prepreg handling characteristics, heating lamps were used to soften the resin while rolling, cutting and laying up the prepreg plies. All laminates were vacuum bagged and consolidated in a Tetrahedron press using the following temperature and pressure cycle.

Heat at 5°C per minute to 130°C under contact pressure.
Isothermal hold at 130°C for 30 minutes.
Temperature raised to 200°C at 3°C per minute.
During the above temperature ramp, raise pressure to 200psi at five minute intervals
Hold laminates at 200°C at 200psi for one hour
Slow cool to room temperature maintaining pressure.

The laminates were C-scanned and post cured for two hours at 250°C in a computer controlled convection oven.

MECHANICAL PERFORMANCE OF LAMINATED COMPOSITES

Mode I (G_{Ic}) and mode II (G_{IIc}) strain energy release rate specimens were prepared from 152.4mm x 152.4mm (6" x 6") laminates. Each panel consisted of 18 plies of prepreg providing a laminate thickness of approximately 2.5mm. A Kapton film 152mm x 50.8mm (6" x 2") was inserted at the mid-plane to act as the crack initiator. Typical specimen dimensions were 152.4mm in length and 12.7mm wide. G_{Ic} values were obtained using double cantilever beam specimen geometry. The Berry data reduction method was used to calculate the strain energy release rates (11). G_{IIc} values were obtained using the same coupon specifications, the end notch flexure test was used to perform the mode II crack opening.

A number of mechanical properties were performed that may be considered to yield matrix dominated failure processes. For the 90° flexure tests, specimen dimensions were 76.2mm x 20.3mm x 2.54mm in thickness. A span to thickness ratio of 16:1 was maintained with the span length being kept to 63mm in accordance with the ASTM test method D790 M. The 90° tension experiments utilized specimens with dimensions 152.4mm x 15.5mm x 3.6mm. Strain gages (350±0.5% ohms, gage factor 2.095%) were used to monitor the stress-strain response within the gage section. The load was increased at a rate of 20lbs per second until failure occurred. The 90° Iosipescu V-notched beam specimen, in the modified Wyoming test fixture, was used to obtain the in-plane shear modulus (G_{12}). Specimen dimensions were 76.2mm x 19.1mm x 2.6mm. 'V' notches were precisely machined into the specimen and strain gages carefully attached to both front and back surfaces. Two strain gages were arranged at ±45° to the longitudinal axis. The load and individual gage readings were logged using an Apple Macintosh SE computer equipped with a Strawberry tree data acquisition system. Shear stress-strain data were obtained from average shear stresses plotted against shear strain determined from the strain gages. The in-plane shear modulus values

were obtained using correction factors and a data reduction procedure described by Morton and co-workers (12).

INTERFACE EVALUATION

The Dow Interfacial testing system was utilized for the micro-indentation analysis. Specimen preparation and testing were kindly performed by S. Mudrich from the Dow Chemical company. The single fiber micro-indentation technique employs a compressive force upon a single fiber. The force required to debond the fiber from the surrounding matrix is measured and substituted with other material properties of the fiber composite constituents into the Finite Element Model developed by Grande (13). Such properties include modulus values for the fiber and matrix resin, the indented fiber diameter and it's distance from the nearest neighboring fiber and also, the axial stress on the fiber at debond.

Sample preparation for the meso-indentation test was identical to the method described for micro-indentation. Typically, samples were greater than 2.5mm (1/10 ") thick and mounted in room cure epoxy, the fibers were oriented perpendicular to the polished cross-section. The method and instrumentation for the meso-indentations were first described by Lesko and co-workers (14,15,16) and are currently being modified and updated.

Indentations were performed using the continuous ball indentor developed by J.J. Lesko at the University of Maryland as a student of Dr. R.W. Armstrong in the Mechanical Engineering department. The indentor head is 1.58mm in diameter thus requiring relatively thick laminates for indentation specimens. The indentor head, a hardened steel ball bearing, was driven into the polished composite surface using displacements attained from the thermal expansion of an aluminum rod. Typical indentation rates were 0.4 microns per second which produced residual indentations of approximately 0.6mm in diameter depending on the maximum load reached. A calibrated load cell monitored the applied load and real time penetration measurements were obtained using a direct current Linear Variable Differential Transformer (DCDT). A more complete description on the indentation apparatus is given in elsewhere (14,15,16).

A measured output can be transformed into a load displacement plot. The load increased until a sudden drop occurs. At present this decrease in the load carrying capability of the fiber composite is assumed to be the point at which interfacial failure is occurring. More work is being undertaken to verify that differences observed in this type of failure are indeed due to variations in interphase properties, the reader is directed towards reference (14,15) for more details regarding these correlations. Indenting past the initial drop in load is performed followed by unloading back to a zero applied force, the indentation depth, h, can now be measured.

The load displacement plot can be transformed into a representative stress versus strain response by utilizing the load P, and penetration depth h, to calculate values termed the Mean Hardness Pressure (MHP), and a representative strain d/D. Here, d, is the contact diameter and and D represents the indenter diameter. Expression 1 describes the necessary calculation to obtain the contact diameter.

$$d = 2\sqrt{(Dh-h^2)} \tag{1}$$

The mean hardness pressure is calculated using expression 2. It can be taken as a measure of the applied indentor pressure and considered as an applied stress.

$$MHP = 4P/\pi d^2 \tag{2}$$

The results for analyzing the interfacial response can be represented as a Maximum Mean Hardness Pressure (MMHP) at the point where the load drops.The representative strain to failure appears to provide a strain to failure measurement of the interphase (14,15). The composite laminate panel lends itself to many indentations on one sample. This provides an

excellent opportunity for a statistical analysis to be performed on the indentation results. It would be beneficial to report an interfacial bond strength from these meso-indentations, however, to date the technique has only provided an interfacial bond strength when an elasticity solution and the application of a micromechanical analysis were utilized.

An elasticity solution exists in the literature (17) for an elastic contact between a transversely isotropic half space and an isotropic sphere. The solution naturally requires only elasticity constants and was utilized by Lesko to describe the stress state beneath the ball contact for the indentations on material provided by the Composite Materials and Structures Center of Michigan State University (15,16), which possessed a contrasting interphase.

The micromechanics analysis developed by Carman (18) was based on a "cellular element" approach. Any fiber-interphase-matrix element could be extracted from anywhere beneath the indentation response subject to the boundary conditions that are dictated by the elasticity solution, and consistent with the applied pressure at the composite surface. In subjecting this element to the pertinent stresses (the desired element was taken from the position at which the elasticity solution indicated that a maximum in shear stress occurred) the micromechanical analysis was able to describe, on a point wise basis, the stresses in the element moving from the fiber center through the interphase and into the matrix. The maximum stress was noted to occur at the interface boundary furthest away from the indentation center and was taken to calculate a maximum interfacial shear strength value.

This elaborate and detailed interpretation of the indentation response was only possible for composite materials that failed in the linear elastic region. Work is continuing in the Materials Response Group at Virginia Tech to investigate if the materials failing in the non-linear region can be analyzed. A finite element model could be used to ease such an interpretation; however, only average point stresses can be obtained.

Composite specimens prepared by the author all exhibited failure in the meso-indentation tests within the non-linear region of the representative stress-strain plot. Thus, no interfacial shear strength values can be reported. However, the Maximum Mean Hardness Pressures (MMHP) and representative strain values (d/D) can be described for the location where interfacial failure is believed to occur. Weibull statistics have been applied to the data for the Meso-indentation results.

RESULTS AND DISCUSSION

NEAT RESIN SPECIMENS

Table I describes how the neat resin fracture toughness increases with a systematic increase in the molecular weight (Mn) of the toughness modifiers. In this case the modifier's weight percent loading was maintained at 20% by weight. Table I provides evidence that the stress intensities reach a limiting level at the higher Mn values . The polymeric blend appears to follow a typical "knee" shaped curve for properties against polymer molecular weight plots.

The BMI/diallyl of bisphenol A network becomes difficult to process at much higher weight percent loadings. Also, at higher molecular weight values of the toughness modifiers, difficulty was encountered in attempting to modify the hot-melt thermoset resin at 20 weight percent loadings.

TABLE I-FRACTURE TOUGHNESS VALUES FOR AMINE TERMINATED POLYSULFONE MODIFIERS THAT VARY IN MOLECULAR WEIGHT

Mn (g/mole) Theory	Mn (g/mole) Titration	$[\eta]_{CHCl_3}^{25°C}$ (dL/g)	Tg(°C)	$K_{Ic}(MPa.m^{1/2})$
5000	6000	0.13	166	1.0 ± 0.2
10000	10900	0.18	178	1.1 ± 0.2
10000	12800	0.22	182	1.4 ± 0.2
15000	15760	0.27	181	1.5 ± 0.1

The effect on fracture toughness properties by simply increasing the weight percent loading is illustrated in Table II. Here, with the same polysulfone backbone structure and a constant molecular weight modifier (Mn= 12800 g/mole), all being maleimide terminated, the stress intensities increase and level off at loadings around 20-25% by weight.

TABLE II - FRACTURE TOUGHNESS VALUES FOR VARIOUS WEIGHT PERCENT LOADINGS OF POLYSULFONE MODIFIERS

Weight % Incorporation	Fracture Toughness $K_{Ic}(MPa.m^{1/2})$ MI-PES Mn=12800 g/mole
0%	0.5±0.2
10%	1.0±0.2
15%	1.2±0.2
20%	1.4±0.2
25%	1.5±0.2

Utilizing results from Tables I and II, to improve the fracture properties of the BMI/diallyl of bisphenol A network without sacrificing the desirable hot-melt processing characteristics, modifiers with molecular weights ca. 11-13 000 g/mole may be used at loadings of approximately 20% by weight.

Thermoplastic modifiers that contain reactive end groups to chemically bond with the thermoset as it cures, should provide the composite matrix with a certain degree of solvent resistance, as by themselves the polysulfone toughness modifiers are amorphous and soluble. Also, this *good* interfacial adhesion between the phase separated thermoplastic phase and the thermoset network should provide an increase in fracture toughness. This was observed when comparing modifiers of the same backbone structure, molecular weight, and weight percent loading that varied only in their end group functionality (Table III).

TABLE III - FRACTURE TOUGHNESS VARIATIONS BY CHANGING ONLY THE END GROUP FUNCTIONALITY ON POLYSULFONE MODIFIERS

End Group	$K_{IC}(MPa.m^{1/2})$	$Tg(°C)$	$[\eta]_{CHCl_3}^{25°C}$ (dL/g)
Phthalimide	0.9 ± 0.2	182	0.25
Amine	1.4 ± 0.2	182	0.22
Maleimide	1.4 ± 0.3	186	0.25

COMPOSITE PROPERTIES AND INTERFACE EVALUATION

Table IV details the mode I and mode II strain energy release rate values for all composite specimens. A respectable increase in mode I strain energy release rate values was measured for the composites containing 15 and 20 weight percent loadings of polysulfone, $489\pm25J/M^2$ and $734\pm10J/M^2$ respectively. The mode II values appeared rather high. One possible explanation could be related to a resin rich layer being formed on one side of the prepreg, thereby creating an in-situ interlaminar toughening effect. Table IV also details the mode I and mode II strain energy release rate values for composites possessing untreated and surface treated carbon fibers. In comparing the composites with 15% maleimide polysulfone as the

toughness modifier but prepregged on AU4, AS4, and IM7 fibers, no effect was observed on the mode I toughness values. However, the mode II test, which propagates the crack in a shear mode, gave significantly higher values for the surface treated fibers ($1194\pm56J/M^2$ and $2255\pm399J/M^2$) over the untreated fiber ($429\pm59J/M^2$). Thereby, indicating how the interphase appears to be more sensitive to the mode II strain energy release rate test.

The importance of a good interphase/interface is illustrated when analyzing Table V. All the 90° tests performed are believed to possess matrix dominated failures. Each test method indicates a substantial improvement in strength when composites possessing surface teated fibers are used. Specimens possessing these same interphases were tested using the micro and meso indentation test methods, their results are given in Table VI.

TABLE IV - MODE I AND MODE II STRAIN ENERGY RELEASE RATE VALUES FOR TOUGHENED BMI MATRICES ON DIFFERENT CARBON FIBERS AND DIFFERENT WEIGHT PERCENT LOADINGS

	IM7/ 0% MI-PES (12.8K) BMI/DABA		IM7/15% MI-PES (12.8K) BMI/DABA		IM7/20% MI-PES (12.8K) BMI/DABA		AU4/15% MI-PES (12.8K) BMI/DABA		AS4/15% MI-PES (12.8K) BMI/DABA	
	G_{Ic} J/M^2	G_{IIc} J/M^2	G_{Ic} J/M^2	G_{IIc} J/M^2	G_{Ic} J/M^2	G_{IIc} J/M^2	G_{Ic} J/M^2	G_{IIc} J/M^2	G_{Ic} J/M^2	G_{IIc} J/M^2
1	---	586	471	2589	739	2556	484	394	410	1299
2	361	466	468	2576	719	2553	405	457	407	1061
3	378	454	485	2564	733	2063	431	417	429	1180
4	360	475	490	1673	746	2539	404	529	480	1355
5	337	578	530	1875	---	2357	---	351	487	1075
mean	359	512	489	2255	734	2411	431	429	433	1194
s.d	17	65	25	399	10	189	37	59	38	56

TABLE V-90° FLEXURE,TENSION,AND IOSIPESCU TEST RESULTS FOR COMPOSITES POSSESSING A CONTRASTING INTERPHASE

	AU4/ 15% MI-PES (12.8K) BMI/DABA	AS4/15% MI-PES (12.8K) BMI/DABA	IM7/ 15% MI-PES (12.8K) BMI/DABA	Ratio of AS4/AU4 Strength Increase
90° Flexure Strength MPa	51.3±4.7	104±6.6	112.2±5.7	2.02
90° Tension Strength MPa	31.0±3.2	70.0±3.7	67.8±2.3	2.25
90° Iosipescu Strength MPa	28.2±1.8	48.0±4.0	------------	1.7

TABLE VI - MICRO-INDENTATION VALUES COMPARED WITH THE MESO-INDENTATION RESULTS

	AU4 15% PES (12.8K-MI) BMI/DABA	AS4 15% PES (12.8K-MI) BMI/DABA	IM7 15% PES (12.8K-MI) BMI/DABA	AS4/AU4 Indentation ratio's
Micro-indentation (MPa)	102.7	123.4	82.7	1.20
Meso-indentation MMHP (MPa)	652.9	757	703.2	1.16

As described in the experimental section detailing the meso-indentation test, the technique is still in it's infancy and the methodology for providing interface strength values is still being pursued. Thus it is not possible to compare at present the exact numbers produced from the indentation tests. However, it is interesting to compare the ratio of improvement from untreated to surface treated fiber, for both the micro and meso indentation tests on the AU4 and AS4 fiber composites. The improvements are small, approximately 1.2:1.0. This small increase in response is interesting, bearing in mind the large increase in strength values obtained from the macromechanical tests. What is more surprising, is the anomaly found with the micro-indentation test result using the IM7 surface treated fiber. The result (82.7 MPa) was lower than that found for the AU4 fiber composite (102.7 MPa) which possesses a much weaker interphase. Although the micro-indentation technique has numerous advantages their are still disadvantages found within the test method itself, and may provide possible explanations for the observed discrepancy. The major assumptions in the technique are that the test method does not consider compressive fiber failure during the indentation, and damage to the fiber surface by the probe tip is ignored. These may be the cause for some form of premature failure that created the low interfacial strength in the IM7 fiber composites. The fibers are of slightly different type, and, due to their differences in properties, will no doubt possess a certain degree of heterogeneity both in their internal structure and on their surfaces. These differences may create different failure processes during the indentation techniques, these differing failure processes being possibly ignored in the micro-indentation method and averaged-out in the meso-indentation technique.

CONCLUSIONS

The most significant improvement in neat resin fracture toughness values, found by changing the various parameters of the polysulfone toughness modifiers, was an increase from 0.8 $MPa.M^{1.5}$ to 1.4 $MPa.M^{1.5}$ by changing only the end group functionality. Composite mode I strain energy release rate tests produced respectable values for the polysulfone modified BMI networks. This same test was found to be insensitive to the contrasting interphase created by using untreated and surface treated fibers. The mode II strain energy release rate test was found to be sensitive to such changes, as were three 90° test methods. Each showed significant improvements in strength values for the composites with contrasting interphases. Similar laminates were used for both the micro and meso-indentation test methods. Anomalies found for the IM7 fiber composite in the micro-indentation test method were attributed to possible differences in failure modes, between the two fiber types, during the indentation procedure. No such anomalies were observed in the results using the meso-indentation test. Both indentation methods on composites prepared from AU4 and AS4 fibers gave similar ratios of improvements, being an approximate 20% increase in value. Such an increase was considered surprising when composites of the same material provided a strength increase in bulk mechanical properties on the order of 100%.

REFERENCES

1.) M. S. Sefton, P. T. McGrail, S. P. Wilkinson, J. A. Peacock, M. Davies, P. Crick and G. Almen, Int. SAMPE Tech. Conf., 19, 700 (1987).

2.) H. G. Recker, T. Allspach, V. Altstadt, T. Folda, W. Heckmann, P. Itteman, H. Tesch and T. Weber, Int. SAMPE Tech. Conf., 21, 25 (1989).

3.) S. G. Chu, H. Jabloner and B. J. Swetlin, European Patent (to Hercules Incorporated) (1986).

4) H. D. Stenzenberger, W. Romer, P. M. Hergenrother, and B . J. Jensen, Int. SAMPE Symp., 34, 1877 (1989).

5.) H. D. Stenzenberger, W. Romer, P. M. Hergenrother, B. J. Jensen and W. Breitigam, Int. SAMPE Symp., 35, 2175 (1990).

6.) R. N. Johnson, A. G. Farnham, R. A. Clenndening, W. F. Hale and C. N. Merriam, J. Polym. Sci., 5, 2375 (1967).

7.) S.Maiti and B.K. Mandal, Prog. Polym. Sci., 12, 111 (1986).

8.) M. J. Jurek and J. E. McGrath, Polymer, 30, 1552 (1989).

9.) S. P. Wilkinson, S. C. Liptak, P. A. Wood, J. E. McGrath and T. C. Ward, Int. SAMPE Symp., 36, 482 (1991).

10.) G.T. Kwiatakowski, L.M. Robeson, G.L. Brode and A.W. Bedwin, J. Polym. Sci. Polym. Chem. Ed., 13, 961 (1975).

11.) J.P. Berry, J.Appl.Phys., 34, 62 (1963).

12.) J. Morton, H. Ho, and M.Y. Tsai, J. Comp.Mat. in press (1991).

13.) D.H. Grande, J.F. Mandell and K.C.C Hong, J. Mat. Sci., 12, 311 (1988).

14.) J.J. Lesko,G.P. Carman, D.A. Dillard and K.L. Reifsnider in Composite Materials: Fatigue and Fracture (4th Symposium ASTM), 1156, (1991).

15.) J.J. Lesko, Masters Thesis, Virginia Polytechnic Institute and State University, Blacksburg, VA 24061, March (1991).

16.) J.J. Lesko, G.P. Carman, D.A. Dillard, K.L. Reifsnider and W.W. Stinchcomb in CCMS report # 91-12, Virginia Polytechnic Institute and State University, Blacksburg, Va 24061 (1991).

17.) M. Dahan and J. Zarka, Int. J. Solids and Structures, 16, 409 (1980).

18.) G.P. Carman, J.J. Lesko and K.L. Reifsnider, J. Comp. Mat., Submitted for publication

ACKNOWLEDGEMENTS

SESSION 4A

Ceramic Matrix Composites

Fracture and Sliding in the Fiber-Matrix Interface in Ceramic Composites

R. J. KERANS, P. D. JERO, T. A. PARTHASARATHY AND A. CHATTERJEE

ABSTRACT

It is evident that fiber debonding and sliding are important factors in determining the mechanical behavior of ceramic composites. They are also complicated processes dependant upon several variables. Numerous issues exist regarding measurement and interpretation of interface properties and elucidation of the roles of these variables. An analytical model of pull/push-out tests which allows separation of many of these factors is used for detailed evaluation of experimental load-deflection curves. Interfacial tensile strength is measured using transverse tensile properties. Recent efforts to identify the role and implications of interfacial topography (roughness) are discussed in detail.

INTRODUCTION

It has become evident that the mechanical properties of the fiber/matrix interface are important in determining the mechanical behavior of brittle-matrix composites (for reviews see [1,2]). Modulus and strength increases are principally a direct consequence of having fiber reinforcements of higher modulus and strength than the matrix, provided the interface is able to transfer load from the matrix to the fiber. However, strain-to-failure and toughness depend on more complex mechanisms. It has been observed that composites which exhibit long pull-out of fibers are tougher; and composites with low apparent interfacial shear strength are presumed to exhibit longer pull-out lengths. It seems evident that interfaces must have sufficient apparent shear strength for load transfer, but be weak enough to debond or slip when close to a propagating crack. Hence, the control of interface behavior has become a key factor in the development of brittle matrix composites.

THE FRACTURE PROCESS AND INTERFACE PARAMETERS

The fracture process of a uni-directional composite is imagined to occur in the following sequence. The composite is loaded elastically until the formation of the first matrix crack. The crack then propagates until it encounters a fiber. Either the crack provides sufficient stress concentration to fracture the fiber, or the fiber debonds with the initiation of secondary cracks in the fiber-matrix interface which propagate in either direction away from the plane of the primary matrix crack.

It is not known if the initial debonding of a fiber which is normal to the plane of an approaching crack occurs as a predominantly mode I failure of the interface in the tensile stress

Ronald Kerans and Paul Jero, Wright Laboratory, WL/MLLM, Wright-Patterson AFB, OH, 45433
Triplicane Parthasarathy, Universal Energy Systems Inc., 4401 Dayton-Xenia Rd., Dayton, OH, 45432
Amit Chatterjee, Allison Gas Turbine Co., PO Box 420, Indianapolis, IN 46206

field ahead of the crack or as a predominantly mode II failure when the crack tip arrives at the interface. It is generally assumed to be a mode II failure, but this is an issue which merits further investigation. In either case the initiation of the debonding crack in such a configuration is probably significantly different than in a pull or push-out specimen. However, as soon as the crack has passed the fiber, the configuration is very similar.

In the case where fibers are debonding rather than breaking, the crack continues to bypass fibers until it completely traverses the specimen leaving only the fibers bridging the crack to carry the load. As the matrix crack widens, the debonding cracks propagate along the fibers and the fibers slide out of the matrix against frictional resistance. Once the matrix is traversed by multiple cracks (spaced at a distance determined by the interface properties), the configuration does not change significantly until fibers begin to break and pull out.

If the toughness of the interface is too high, or if the frictional resistance to sliding of an unbonded interface is too high, the fibers will fracture rather than debond and slide. Therefore, we expect both the interfacial toughness and friction to be important in determining the extent of crack bridging which occurs. The magnitude of the frictional resistance to the sliding of the fiber determines both how far the debond crack propagates and the energy required for pull-out after the fiber breaks. Since the friction will depend upon residual stresses, coefficient of friction, interface topography, and interface degradation mechanisms (abrasion, plastic deformation); these are all important parameters. Furthermore, they are not all constants. Abrasion and, as will be shown, roughness effects are functions of sliding distance. The effective coefficient of friction might also be expected to change with the accumulation of abrasion debris in the interface.

INTERFACIAL SHEAR PROPERTIES FROM PUSH-OUT TESTS

Single fiber push-out tests were used in conjunction with the analysis of Kerans and Parthasarathy [3] to measure interfacial properties in a series of SiC* fiber/potassium borosilicate glass# matrix composites [4,5]. The series of six glasses and corresponding composites were designated simply as "B" through "G". The Glasses were formulated so as to provide a range of coefficient of thermal expansion (CTE), increasing from approximately 3.0 (B) to 4.7 x 10^{-6}/°C (G). The CTE of glass E matched that of the fiber quite closely.

The details of the test have been reported elsewhere [6]. Briefly, thin slices of composite were prepared and mounted over a narrow slot. A flat bottomed tungsten carbide probe 100 μm in diameter was used to push individual fibers partially out of the sample. The system employs a constant displacement rate test machine and computer data acquisition to generate the load-displacement curve.

The analysis of Kerans & Parthasarathy [3] was used to calculate interface parameters from the push-out data. The model assumes that a debond crack initiates at some critical fiber stress then propagates in a stable fashion down the interface as the applied load increases. The stability of the crack is due to the frictional force acting on the debonded portion of the interface and the increased compliance of the debonded portion of the fiber. At some point when the debond crack is near the end of the specimen, it becomes unstable and grows catastrophically through the rest of the specimen. Within this region of progressive debonding, the model relates the applied load, P_a, to the external displacement, δ, in terms of the friction coefficient, μ, the residual clamping stress at the interface, σ_N, the residual axial stress in the fiber, $P_r/\pi r^2$, and the interfacial toughness, G_i. The analysis includes the effects of Poisson expansion, residual axial strain in the fiber, and has provision for including a frictional term to account for the effects of interfacial roughness.

Although recent work has shown conclusively that interfacial roughness is present in these composites and significantly effects the level of friction observed [5-8], there is some evidence to indicate that it does not make a major contribution to the push-out behavior until substantial

---

*   SCS-6, Textron Specialty Materials, Lowell, MA
#   Corning Glass Works, Corning, NY

sliding (approximately one half the period of the roughness) has taken place [4]. In these composites the displacements during progressive debonding are around 1 to 2 μm while the period of the roughness is around 10 μm. Consequently interfacial roughness has been neglected in the reduction of data from the progressive debonding portion of the curve. The experimental load-displacement data were fit to the model using a non-linear least squares fitting routine that uses the downhill Simplex method.

In order to fit the data to the model, the system compliance must be known or measured experimentally. It was found that the compliance varies enough from sample to sample and from fiber to fiber within a given sample that a compliance must be calculated for each push-out test and removed from the raw data before analysis.

In a typical push-out load-displacement curve, the load rises, peaks, and eventually falls off to a lower level as the fiber begins to push out. Due to the system compliance, it is not apparent from the rising portion of the curve whether the debonding is catastrophic or progressive; that is, whether the curve is truly straight or slightly curved due to increasing compliance as the interface debonds and an increasing length of the embedded fiber begins to slide. As a result, the compliance must be calculated and removed from the data. This was accomplished by calculating the slope of the rising portion of the curve using the best linear fit over small increments of load and displacement (a numerical derivative).

Figure 1 shows the push-out load-displacement data for composites D, E, and F with the system compliance removed (CE or corrected effective displacement). Several items are worthy of note. In all of the fibers in composite E and a few in composite F, the first deviation from linearity is an abrupt jump in displacement with virtually no change in load. The abrupt displacement is believed to occur upon debond initiation because the stress required to initiate the crack is greater than that necessary to propagate it, once a sharp crack exists. Since it seems reasonable that crack initiation is typically more difficult than crack propagation, the question arises as to why this effect is absent in the other specimens. The most likely explanation would seem to be that during the cutting and polishing procedure the interface is typically damaged slightly, producing a small precrack. In this case no distinct, initiation would be observed.

Another common feature is a transition from smooth to stick-slip behavior with increasing load. This is believed to be associated with the transition from crack propagation to total frictional sliding of the fiber. The continued rise in load is believed to be due to interfacial roughness. This behavior is different from that seen previously (ref 4, Figure 3), and may be associated with interfacial chemistry differences due to the sizing on the fibers of the earlier samples. In those specimens there was no stick-slip behavior observed with rising load. In Figure 1a it can be seen that the measured peak load varies substantially from fiber to fiber in composite D. Large scatter in measured peak loads (the commonly measured parameter) has often been reported as a problem with push-out and pull-out tests. By simply subtracting the system compliance, however, it is seen that the behavior is not all that different. In fact, all of the fibers begin to debond at approximately the same load and follow nearly the same curve until the point at which failure of the final bonded ligament occurs. The exact reason for the variation between fibers in this sample when the others show highly consistent sliding loads is not known, but again, interfacial damage during sample preparation may be the culprit, particularly since composite D has a slightly tensile interfacial radial stress.

It is also notable that the load at which the first nonlinearity occurs increases in the series from composite D to E to F. This load should be related to the sum of the load required for crack propagation, P_d, and the load required to overcome the axial residual tension, P_r. Since there is little reason to expect large differences in P_d within this series of composites, the combined load should rise with the level of the residual stress, as observed.

Finally, it is observed that the slope of the curve within the debond propagation region increases in the series from D to E to F. Again, since there is no reason to expect substantial physical differences between interfaces in the different composites, an increase in slope is reasonable due to the increasing normal stress on the fiber and the release of axial strain in the fiber as debonding proceeds.
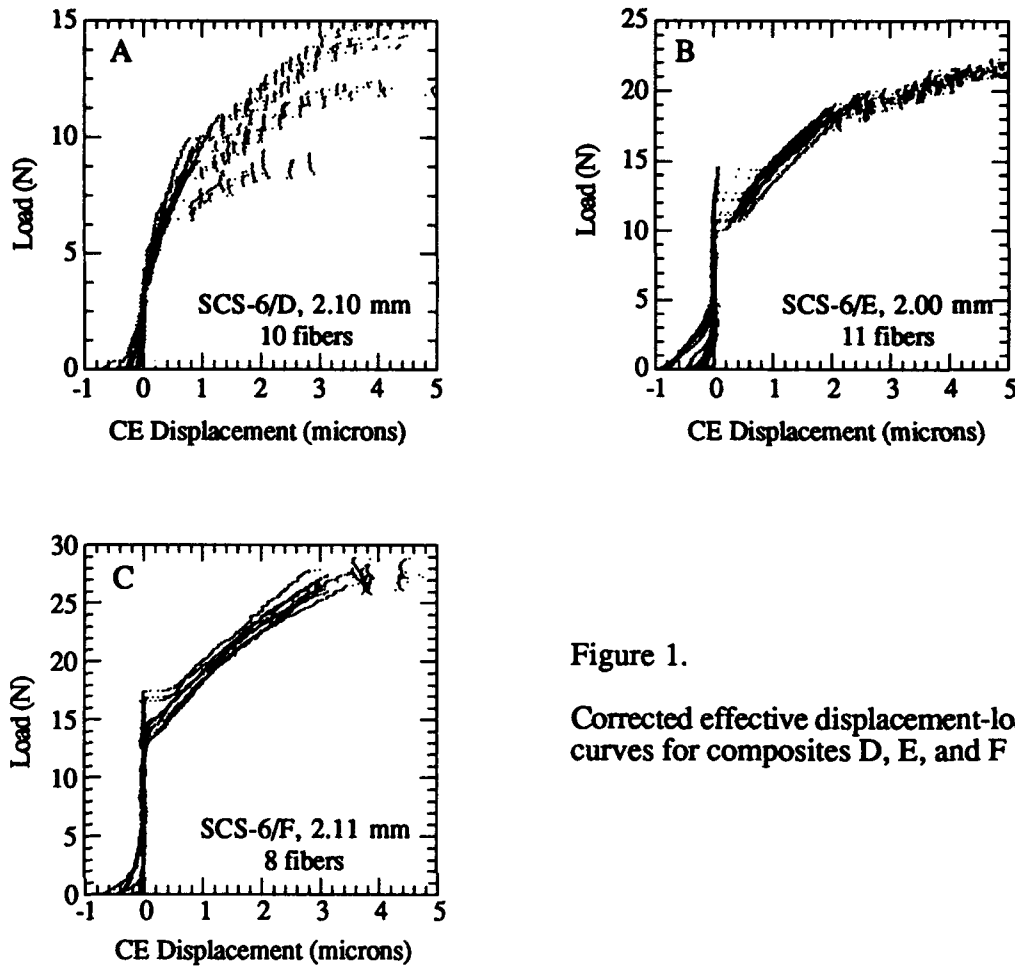
Figure 1.

Corrected effective displacement-load curves for composites D, E, and F

Figure 2 shows the fit of the model to the curves of Figure 1b. Table I records the calculated interfacial parameters for each of the composites. The peak load indicated in Figure 2 was calculated assuming a final ligament debond length of twice the fiber diameter. The interfacial parameters were calculated for each specimen using the combined data from several fibers. Although there is little to compare them to, the calculated interfacial parameters seem reasonable. Parthasarathy et. al. [4] noted previously that the calculated residual stress, σ_N,
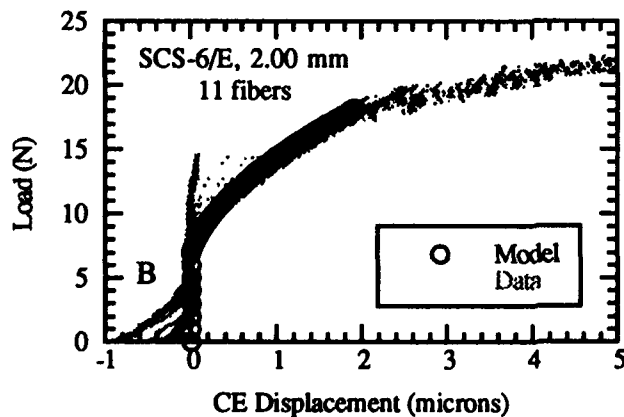
Figure 2.

Fit of the model to the curves of Figure 2b

TABLE I. CALCULATED INTERFACIAL PROPERTIES

Composite	μ	σ_N (MPa)	$P_r/\pi r^2$ (MPa)	G_c (J/m^2)
D	0.54	13.3	1.99	~0
E	0.31	33.6	5.05	0.63
F	0.25	53.7	8.06	1.78

is high compared to the value one calculates from the measured CTE's and an assumed stress-free temperature. This may be associated with interfacial roughness causing an increase in the residual stress as the fiber is displaced slightly. The inconsistency of this suggestion with the decision to ignore interfacial roughness in the present analysis is apparent.

SURFACE ROUGHNESS EFFECTS: EXPERIMENTAL EVIDENCE

Single fiber push-out tests in conjunction with interfacial topography characterization of both fibers and troughs were used to examine the effect of sliding distance on the interface [8]. A series of fibers in composite E was pushed and pushed back repeatedly, increasing the push distance each time in order to examine the effect of extended fiber sliding on the interface. The total sliding distance approached 5 mm for two of the fibers. The magnitude of each seating drop was measured and compared with the sliding distance. After push-out testing, the sample was sectioned by polishing. Some of the fibers were lost during the sectioning procedure, but others remained intact and were subsequently removed using a tweezer. A laser interferometric microscope* was used to examine the roughness of the fibers which were extracted after push-out testing and the corresponding troughs in the matrix. The fibers were typically examined using a 40 x objective which yielded a maximum scan length of approximately 270 μm, and a point-to-point (spatial) resolution of 0.85 μm. Figure 3 shows several typical line traces of the roughness of as-received SCS-6 fibers. Figure 4 shows the effect of extended sliding on the fiber and trough. The RMS roughness is a measure of the average roughness amplitude. Although the scatter is high, it is seen that the roughness of the trough is decreased while that of the fiber remains practically unchanged. Finally, Figure 5 compares the decrease in the magnitude of the seating drop with sliding distance, to the decrease seen in the roughness of the fiber troughs. Although the exact nature of the correlation is not known, it is interesting to note the similarity.
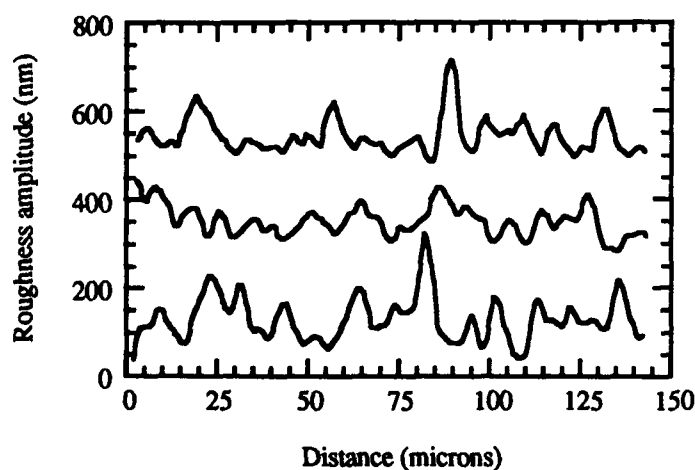
Figure 3.

Surface traces showing the roughness of as-received SCS-6 fibers

---

* Model 5610, Zygo Corp., Middlefield, CT
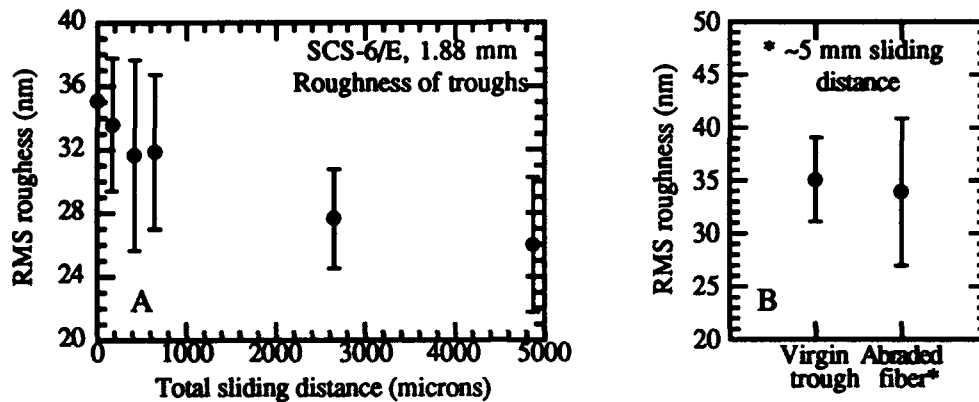
Figure 4.

(A) Measured roughness of the troughs as a function of sliding distance and (B) comparison of virgin (unabraded) trough with an abraded fiber. Error bars are ± one standard deviation.

There are at least three debonding scenarios which would result in a significantly rough interface: 1) debonding of a rough fiber along a relatively weak interface, such that the debonded interface mirrors the surface roughness of the fiber, 2) debonding of a (smooth or rough) fiber along a relatively strong interface, such that the crack runs at least partially through the matrix leaving portions of the matrix bonded to the fiber, 3) debonding within a weak or porous coating on a (smooth or rough) fiber such that the crack kinks back and forth within the coating.

Actual interfacial debonding may well be some combination of these. In practice, the second case is unlikely to provide the interfacial properties necessary for a successful composite and so is of little relevance. The realization that interfacial roughness can substantially affect the sliding friction of debonded fibers, combined with the ability to quantify the effect, has implications regarding the manufacture of fibers, design of fiber coating schemes and the design, use, and testing of composites. It is apparent that in a composite the interfacial roughness can influence the debond length, the fiber pull-out distance, and the fracture energy. Composites with extremely rough interfaces may exhibit such small debond/pull-out lengths, irrespective of the actual fiber/matrix bond strength, that they fail like monolithic materials. Alternately, without adequate interfacial roughness,
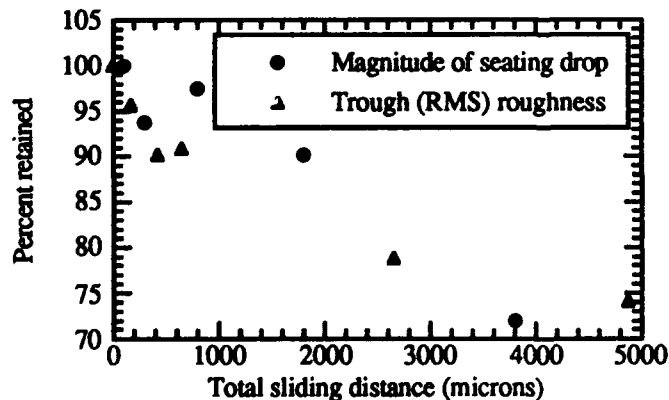
Figure 5.

Comparison of the magnitude of the decrease in the seating drop with the decrease in the roughness of the fiber troughs as a function of sliding distance

composites (particularly those in which $\alpha_f > \alpha_m$) which have sufficiently weak bond strength for fibers to debond in the stress field of a propagating crack may obtain little benefit (toughness contribution) from fiber pull-out, even though the pull-out length is very large. Furthermore, appreciation of the role of surface topography is not only recognition of another important variable but recognition of the opportunity provided by an interfacial parameter which is adjustable independently of processing temperature, chemistry, and thermal expansion.

Another effect which will almost certainly be important is the effect of abrasion upon cyclic properties of composites. With each succeeding loading cycle of a microcracked composite, abrasion along the debonded and sliding lengths of the fibers will decrease the interfacial friction leading to additional propagation of the debonding cracks. This will cause some relaxation of the bridging tractions leading to additional propagation of the matrix cracks, and the associated debonding of additional fibers. It is proposed that this effect will play a dominant role in the fatigue of brittle fiber/brittle matrix composites.

INTERFACIAL TENSILE PROPERTIES

The weak interface which is desirable for toughness can also be expected to have a deleterious effect on the transverse properties of the composite. However, transverse properties of either the interface or the composite have received little attention. This has been primarily due to the unavailability of specimens, test techniques, and analytical models to explain the complex failure behavior under transverse loading.

The approach taken in this work [9] was to measure the tensile strength of uniaxial SiC/glass composites loaded normal to the fiber axes (transverse tension). The objective was to carefully examine the stress-strain behavior under transverse loading, determine the effect of thermal residual stresses on the mechanical behavior, and calculate the interfacial tensile strength. The magnitude and sign of residual stresses at the interface were varied by utilizing a series of glass matrix composites with varying matrix CTE (composites B through G, discussed above).

A schematic of a generalized stress-strain curve which includes all observed behavior is shown in Figure 6. In Region I the plot is linear. The stress, σ_i, indicates the onset of non-linearity and the beginning of Region II. In Region III the response is again linear. The stress-strain behavior of particular combinations of glass and fiber may not include all portions of this curve. The evidence supports the following rationalization of the stress-strain curves: Region I is elastic loading of the undamaged composite, the increasing compliance of Region II is the result of increasing debonding and unloading of fibers, and Region III is the elastic response of the fully debonded composite.

When $\alpha_f > \alpha_m$, there is residual radial tensile stress at the interface. In these composites the load to first non-linearity (the beginning of Region II) was small. The load to non-linearity increased as the CTE mismatch decreased. Specimens made with glasses E, F and G had radial compressive stresses at the interface. The stress-strain plots for these composites were linear nearly to failure. In these specimens Region II was very small and region III was not observed at all, presumably because the stresses in the matrix were sufficiently high to cause fracture before substantial numbers of fibers debonded.

The applied stress at non-linearity consists of two components: the stress needed to overcome the thermal residual stresses and the stress required to break the interfacial bond. The interface bond can be expected to fail when the total tensile stress at the interface exceeds the interfacial tensile strength. Since the matrices in all the composites are potassium borosilicate glasses with similar compositions it is expected that the nature and strength of any chemical bond would be the same. The calculated stress in the matrix at the fiber-matrix interface is a function of the elastic properties of the constituents and the applied loads and can be calculated using the NDSANDS computer model [10].
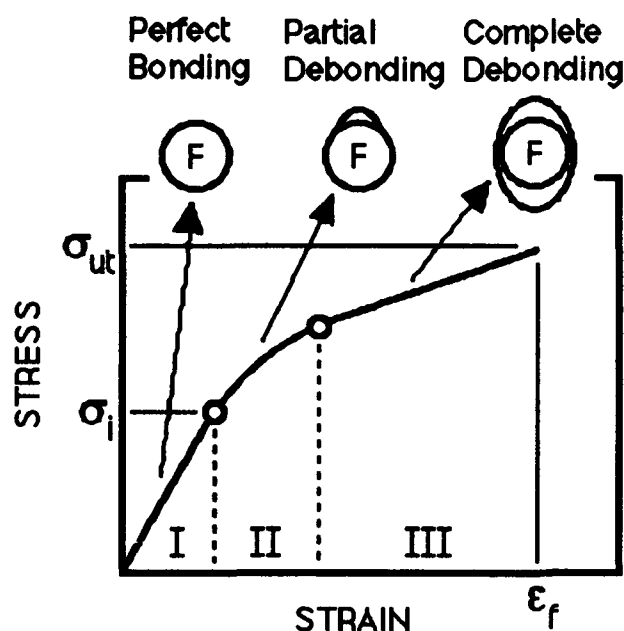
Figure 6.

Generalized stress-strain curve for transverse loading

The total stresses, σ_{rr}^T and $\sigma_{\theta\theta}^T$, at the interface in the loading direction are plotted in Figure 7. $\sigma_{\theta\theta}^T$ increases with the CTE mismatch whereas σ_{rr}^T becomes constant. This indicates that σ_{rr}^T is the stress component responsible for the deviation from linearity in these specimens and is indicative of the mode of failure. It has already been argued that the radial stresses can cause debonding. It is this constant value of σ_{rr}^T which is an estimate of the interfacial tensile strength of the composite. Using a maximum stress criterion for failure as a first approximation, this yields an estimated interface normal strength, σ_b, of 10 MPa.

Much of the work in ceramic composites indicates that for tough composites a weak interface and $\alpha_f > \alpha_m$ are desirable. These analyses and predictions have considered a unidirectional composite with a crack at 90° to the fiber direction. This study shows that for $\alpha_f > \alpha_m$ and weak bonding, the transverse modulus of the composite is significantly lower than the idealized case. From the structural standpoint this is also undesirable as the onset of damage due to transverse loading can occur at very low stresses. When $\alpha_f < \alpha_m$ the effective modulus is higher and can be predicted by the model for perfect bonding. The gain in transverse modulus and failure stress may, however, be at the cost of lower axial strains to
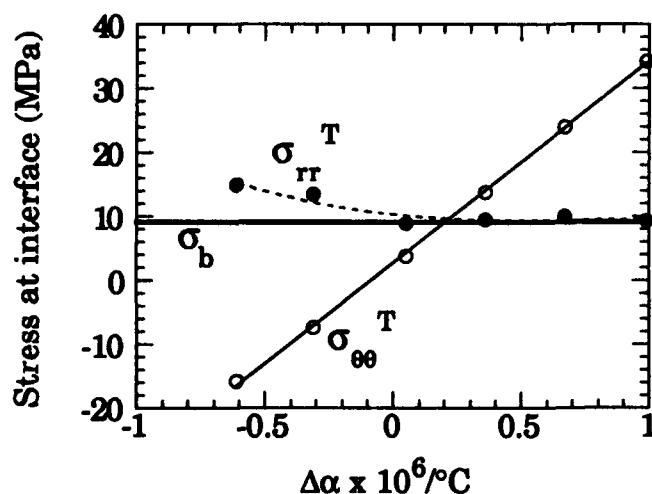
Figure 7.

Plot of the total stress at the interface as a function of the CTE mismatch

failure and possibly lower toughness as now a growing crack may lead to fiber cracking at the matrix crack tip. Good laminate properties, will involve a compromise of these factors, perhaps by having the interface in slight residual compression coupled with a very weak chemical bond at the interface. This combination would provide an initial linear region of the transverse stress-strain curve with high modulus yet still allow for debonding and enhanced toughness.

SUMMARY

Evidence has been provided to illustrate that fracture and sliding in the fiber-matrix interface is not a simple process that can be described by a single parameter. Moreover, while progress has been made in identifying and measuring some of the governing parameters, it is evident that there remain some, such as abrasion, which have only been superficially examined. While it is not necessary to understand all the nuances of a material system in order to use it in practice (in fact, that has never occured), the probability of success and of avoiding spectacular disasters increases strongly with fundamental understanding. In systems such as ceramic composites in which a component is as much a structure made up of laminae, or arrangements of fiber bundles and matrix blocks, as it is a monolithic part as we normally think of it, this will be especially important.

REFERENCES

1. R. J. Kerans, R. S. Hay, N. J. Pagano, and T. A. Parthasarathy, 1989. "The Role of the Fiber-Matrix Interface in Ceramic Composites," Am. Ceram. Soc. Bull., 68(2):429-442.

2. A. G. Evans and D. B. Marshall, 1989. "The Mechanical Behavior of Ceramic Matrix Composites," Acta Metall., 37(10):2567-2583.

3. R. J. Kerans and T. A. Parthasarathy, 1991. "Theoretical Analysis of the Fiber Pull-Out and Push-Out Tests," J. Am. Ceram. Soc., 74(7):1585-1596.

4. T. A. Parthasarathy, P. D. Jero, and R. J. Kerans, 1990. "Extraction of Interface Properties from a Fiber Push-out Test," Scripta Metall. & Mater., 25:2457-2462.

5. P. D. Jero, T. A. Parthasarathy, and R. J. Kerans, 1992. "Measurement of Interface Properties from Fiber Push-out Tests," Ceram. Eng. & Sci. Proc., 13(7-8):54-63.

6. P. D. Jero, R. J. Kerans, and T. A. Parthasarathy, 1991. "Effect of Interfacial Roughness on the Frictional Stress Measured Using Push-Out Tests," J. Am. Ceram. Soc., 74(11):2793-2801.

7. P. D. Jero and R. J. Kerans, 1990. "The Contribution of Interfacial Roughness to Sliding Friction of Ceramic Fibers in a Glass Matrix," Scripta Metall. & Mater., 24:2315-2318.

8. P. D. Jero, T. A. Parthasarathy, and R. J. Kerans, 1992. "Interfacial Roughness in Ceramic Matrix Composites," Ceram. Eng. & Sci. Proc., 13(7-8):64-69.

9. A. Chatterjee, R. J. Kerans, and T. Mah, "Residual Stresses and Their Effects on Transverse Properties and Interfacial Debonding in SiC Fiber Reinforced Borosilicate Glasses," submitted to J. Am. Ceram. Soc.

10. N. J. Pagano and G. P. Tandon, 1990. "Thermo-elastic Model for Multidirectional Coated-Fiber Composites: Traction Formulation," Compos. Sci. Tech., 38:247-269.

Transverse Cracking in a Fiber Reinforced Ceramic Matrix Composite

S. MALL AND S. E. BACHMANN

ABSTRACT

The transverse matrix cracking behavior in the cross-ply lay-up of a ceramic matrix composite was investigated. For this purpose, three cross-ply lay-ups, [0$_3$/90$_n$/0$_3$] with n = 1, 2 and 3 of silicon carbide fiber reinforced aluminosilicate glass ceramic composite were tested. The crack spacing increased with the increase of transverse ply thickness at a given strain level and the saturation crack spacing decreased with the decrease of transverse ply thickness.

INTRODUCTION

Continuous fiber reinforced ceramic matrix composites possess high strength and toughness along with low density. They are projected to be employed at high temperatures. Ceramic composites consists of brittle matrix reinforced with strong fibers. Transverse matrix cracks often generate in these composites at very low loads. There is, therefore, a need to characterize the effect of matrix cracking on the mechanical behavior of these composites before their practical applications. A number of studies, involving the matrix cracking behavior of unidirectional fiber reinforced ceramic composites, are available in the literature [1-5]. However, studies involving matrix cracking in off-axis plies of these composites has been very limited [6-7]. The focus of the present study is in this direction. For this purpose, three cross-ply lay-ups, [0$_3$/90$_n$/0$_3$] with n = 1, 2 and 3 were investigated. The objective of this study was to investigate the effect of transverse ply thickness on the crack initiation stress and crack spacing in a model ceramic matrix composite, SiC/1723. This composite consisted of aluminosilicate glass ceramic (1723) reinforced with silicon carbide fibers (SiC). The present study was conducted at the room temperature.

EXPERIMENTAL PROCEDURE

The ceramic composite used in this study was manufactured at the U.S. Air Force Materials Laboratory, Wright-Patterson Air Force Base, as follows. The SiC fibers, with

S. Mall, Department of Aeronautics and Astronautics, Air Force Institute of Technology, Wright-Patterson Air Force Base, OH 45433
S.E. Bachmann, Former Graduate Student, Air Force Institute of Technology

trade name Nicalon (Nippon Carbon Co., Yokohama, Japan), were ceramic grade fibers which came with a protective type M sizing. The fibers have an average diameter of 12.5 microns and came as a tow of 500 fibers wound on a spool. As received fibers were cleaned of their sizing by passing the fiber tow through a burn-off furnace. The fiber tow was then pulled through a glass slurry mixture of glass frit, distilled water, and an organic binder. The glass frit is an alkaline earth aluminosilicate, code 1723, from Corning Glass Works. The infiltrated fiber tows were wound onto an eight sided mandrel, lamp dried, and cut into 10 cm x 10 cm laminae. These laminae were stacked into a laminate in a graphite die. The whole assembly was then densified in a vacuum hot press at elevated temperature and pressure. The fabricated plates were 10 cm x 10 cm with a nominal thickness of 0.25 cm for each ply. They had an average fiber volume fraction of 40 percent.

Four different cross-ply lay-ups were studied: $[0_3/90/0_3]$, $[0_3/90_2/0_3]$, $[0_3/90_3/0_3]$, and $[0/90/0_4/90/0]$. The first three lay-ups were chosen to study the effect of the transverse ply thickness, while the fourth one was used to examine the impact of the location of the 90° plies. One plate of each lay-up was fabricated. From these plates, 100 mm long and 6.4 mm wide specimens were cut. Beveled end tabs made of glass/epoxy (1.5 mm thick and 19 mm long) were bonded to the ends of the specimens for gripping during testing. After tabbing, each specimen was polished on one edge to enhance microscopic imaging and replication for crack detection. The specimens were first wet sanded on a polishing wheel with 600 and 800 grit aluminum oxide sand paper. Then specimens were polished on the wheel using 3.0, 1.0, and 0.3 micron alumina. Next, a strain gage along the axial direction was attached on each specimen. All specimens were tested in tension in a testing machine at a cross-head speed of 0.25 mm/minute.

The first specimen of each lay-up was tested with an acoustic emission system only to pick up the instant of the initiation of transverse cracking. In subsequent tests, replications were concentrated near the stress levels where the acoustic emission indicated that cracking had occurred. In this manner it was possible to verify the stress level for crack initiation, with reasonable accuracy in subsequent testing with other specimens. To determine the stress level for crack initiation, a replication was made at a stress level 6.9 MPa below the level indicated by the acoustic emission in the first test. Then replications were made at every interval of 1.4 MPa until crack initiation was detected. The replications were made while the specimen was loaded. This kept cracks open and hence easy to detect. Further, the stress level for transverse crack initiation was same from both acoustic emission and replication techniques. To monitor crack progression and crack density, replications were taken at intervals of approximately 6.9 MPa up to failure. The crack density was measured from the replication which was typically 25 mm long.

RESULTS AND DISCUSSION

For all the laminate tested, the failure initiated as the transverse crack in matrix usually formed at the 0°/90° ply interface and progressed straight through the 90° ply, perpendicular to the applied load. Figure 1 shows this feature. As the applied load was increased more transverse cracks formed, evenly spaced along the length of the 90° ply. Increasing the load more resulted in an increase in the number of transverse cracks up to a certain point. As the applied load was further increased longitudinal cracks began to form,

joining the transverse cracks together. This phenomenon can be seen in Fig. 2. However, there was no delamination observed in any of the tests. Reifsnider et al observed this same longitudinal cracking behavior generated from transverse cracks in graphite/epoxy [8]. These longitudinal cracks were probably caused by the Poisson's effect. In the region near the transverse cracks, 90° plies became stress free. This caused the contraction of the 90° plies in the thickness direction in the region near the transverse cracks. However, this was not the situation in the region away from the transverse cracks. This resulted in a compressive stress near the transverse cracks and a tensile stress in the portion between the cracks. This tensile stress in the thickness (transverse) direction probably caused the longitudinal cracks as observed in these tests. On further increase of load, several transverse and longitudinal cracks penetrated in the 0° plies. Finally the 0° plies had enough cracks or damage with increase of load which caused eventually the failure of specimen.

As mentioned above, after a certain stress level was achieved, the transverse plies became saturated and no new transverse cracks developed. This phenomenon was similar as in the case of polymeric matrix composites. Figure 3 shows the crack spacing as a function of the percent strain for the three lay-ups with the transverse plies in the center of the laminate. As it can be seen that the spacing of transverse cracks decreased sharply as the applied strain increased, and then appears to be approaching to a limiting value, i.e. a saturation crack spacing. Further, for a given strain, the crack spacing increased as the transverse ply thickness was increased, and the saturation crack spacing decreased as the transverse ply thickness decreased. For polymeric matrix composites, it has been observed that the saturation matrix cracking corresponds to an average crack spacing of the order of the ply thickness, e.g. see Ref. 9. The present study appears to show the same trend. The saturation crack spacings for three different laminates tested in the present study are summarized in Table I, and these are about equal to the total thickness of 90° plies in each case.

Figure 4 shows the strain for crack initiation as the function of number of transverse plies. The strain for crack initiation increased with the increase of the transverse ply thickness suggesting the constraining effect of the 0° plies as seen in the polymeric composites. As the number of 90° plies was increased, the strain for crack initiation in the cross-ply laminates is approaching to a value equal to the strength of 90° lamina. This is expected as the thickness of the transverse ply overcomes the constraining effects of the longitudinal plies. Similar observations were found by Wang and Parvizi-Majidi in a similar fiber reinforced ceramic matrix composite, SiC/CAS (silicon fiber in calcium aluminosilicate glass-ceramic matrix) [6].

As previously mentioned, a laminate with lay-up of [0/90/0$_4$/90/0] was used to study the effect of the placement of the 90° plies. It was expected that this lay-up would yield results similar to the [0$_3$/90/0$_3$] lay-up because of the constraining 0° plies on both sides of the 90° plies. Figure 5 provides a comparison of the crack spacing in the [0/90/0$_4$/90/0] lay-up to that in the [0$_3$/90/0$_3$] lay-up which are in reasonable agreement of each other. However, there was a difference in the strain for crack initiation (289 $\mu\varepsilon$ for the [0/90/0$_4$/90/0] and 331 $\mu\varepsilon$ for the [0$_3$/90/0$_3$]). These observations were somewhat expected. Cracks initiated in the [0/90/0$_4$/90/0] laminate at lower stress and strain levels because the transverse ply in that lay-up has less constraint from the adjacent 0° plies than does the

$[0_3/90/0_3]$. Further studies with other distributed 90° ply lay-ups are needed to fully characterize the effect of the location of the 90° plies.

All specimens failed in the gage length. No delamination was observed in any of the tested specimens. The stress-strain relations were relatively linear up to failure for all lay-ups except for $[0/90/0_4/90/0]$ lay-up. Figure 6 shows the typical relations from each lay-up. The stress-strain curves for the $[0/90/0_4/90/0]$ specimens showed a considerable nonlinearity at higher stress values that was not seen with the other lay-ups. Using the classical lamination theory, the first ply failure stress (i.e. crack initiation stress in the cross-ply) was computed, and these are compared with the corresponding experimental value in Table I. As can be seen in the table, the experimentally observed stress levels are all higher than the predicted values. Mall and Kim investigated several lay-ups of silicon fiber reinforced calcium aluminosilicate glass-ceramic matrix composite, SiC/CAS [10]. They found that the crack initiation stress in 90° ply was considerably higher than predicted from the classical lamination theory. There are several possible explanations for this disagreement. One of these is obvious i.e. these predictions are based on the transverse strength of composite. As discussed earlier and shown in Fig. 4, the constraining effects of the adjacent plies are not accounted in these predictions.

SUMMARY

Three cross-ply lay-ups, $[0_3/90_n/0_3]$ with n = 1, 2 and 3 of a fiber reinforced ceramic matrix composite were investigated to understand their transverse cracking behavior under uniaxial tension. Transverse cracking developed in the 90° plies at relatively low stress levels. The cracks generally formed at the 0°/90° ply interface and progressed straight through the 90° ply, perpendicular to the applied load. As the applied load was increased more cracks formed, evenly spaced along the length of the 90° ply. The transverse cracks were totally constrained by the 0° plies in all of lay-ups. For a given strain, the crack spacing increased as the transverse ply thickness was increased. The saturation crack spacing decreased (i.e., the cracks were closer together) as the transverse ply thickness was decreased. The strain for the onset of transverse cracking increased as the transverse ply thickness was decreased.

ACKNOWLEDGEMENTS

REFERENCES

1.   Aveston, J. and A. Kelly, 1980. "Theory of Multiple Fracture of Fibrous Composite." Journal of Materials Science, 8(3): 352-362.

2.   Brennan, J.J. and K.M Prewo, 1982. "Silicon Carbide Fiber Reinforced Glass-Ceramic Matrix Composites Exhibiting High Strengh and Toughness." Journal of Materials Science, 17: 2371-2383.

3.   Marshall, D.B. and A.G Evans, 1985. "Failure Mechanisms In Ceramic-Fiber/-Matrix Composites." Journal of American Ceramic Society, 68: 225-231.

4.   Marshall, D.B., Cox, B.N. and A.G. Evans, 1985. "The Mechanics of Matrix Cracking in Brittle-Matrix Fiber Composites." Acta Metall., 33 (11): 2013-2021.

5.   Budiansky, B., J.W. Hutchinson and A.G. Evans, 1986. "Matrix Fracture in Fiber-reinforced Ceramics." Journal of Mechanics and Physics of Solids, 34 (2): 167-189.

6.   Wang, S.W. and A. Parvizi-Majidi, January 1990. "Mechanical Behavior of Nicalon Fiber Reinforced Calcium Aluminosilicate Matrix Composites." presented at The 14th Annual Conference on Composites and Advanced Ceramic Materials, Cocoa Beach, FL.

7.   Pryce, A.W. and P.A. Smith, July 1991. "Matrix Cracking in Ceramic Matrix Composites under Quasi-Static Tensile Loading." in Proc. of International Conference on Composite Materials, S.W. Tsai and G.S. Springer, ed. pp. 24-I-1 to 24-I-10.

8.   Reifsnider, K.L., E.G. Henneke and W.W. Stinchcomb, June 1979. "Defect-Property Relationships in Composite Materials." AFML-TR-76-81, Part IV. Air Force Materials Laboratory.

9.   Highsmith, A.L. and K.L. Reifsnider, 1982. "Stiffness-Reductions Mechanisms in Composite Laminates." in Damage in Composite Materials, ASTM STP 775, pp. 103-117.

10.   Mall, S. and R.Y. Kim, 1992. "Failure Mechanisms in Laminates of Silicon Carbide/Calcium-Aluminosilicate Ceramic Composites." Composites (in press).

TABLE I - EXPERIMENTAL AND CALCULATED DATA

Lay-up	Total Thickness of 90° Plies (mm)	Saturation Crack Spacing (mm)	Average Measured Matrix Cracking Initiation Stress (MPa)	Predicted First Ply Failure Stress (MPa)
$[0_3/90/0_3]$	0.25	0.32	40.93	34.11
$[0_3/90_2/0_3]$	0.50	0.56	30.18	25.15
$[0_3/90_3/0_3]$	0.75	0.86	25.77	24.46
$[0/90/0_4/90/0]$	0.25	0.28	30.45	25.15
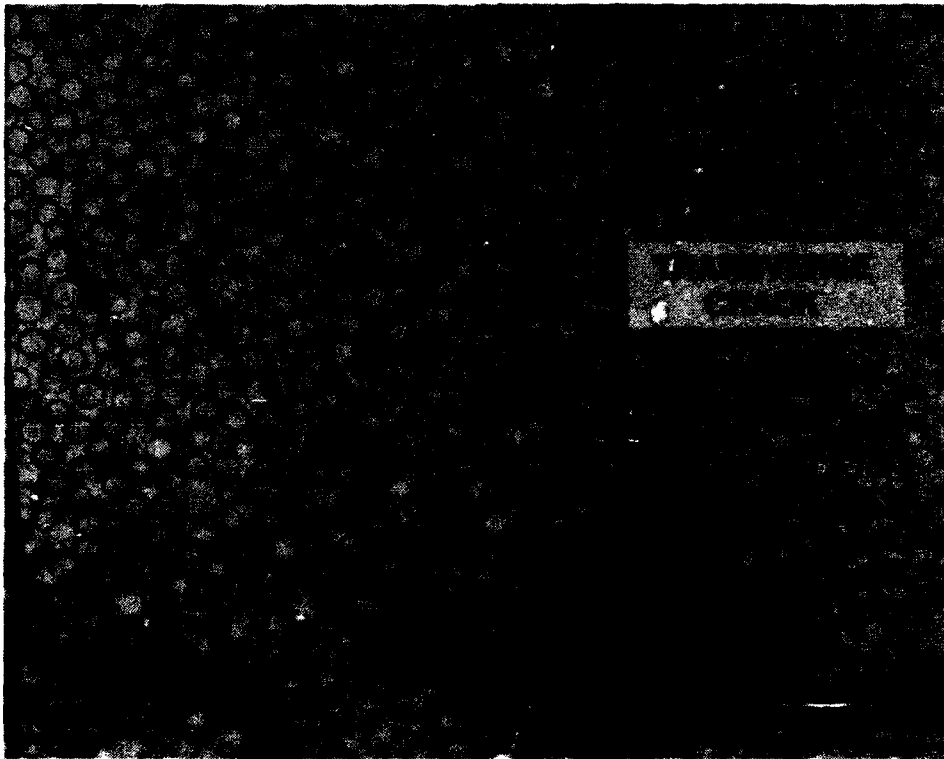
FIG. 1.   Initiation of Transverse Crack (X200).
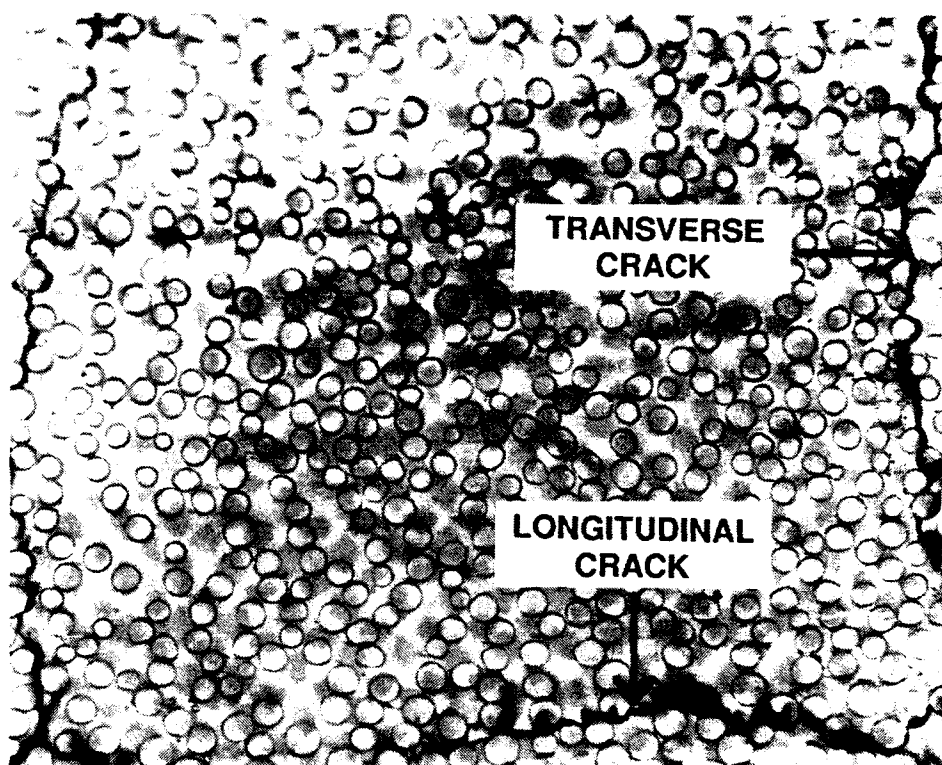
FIG. 2.   Longitudinal Crack (X200).
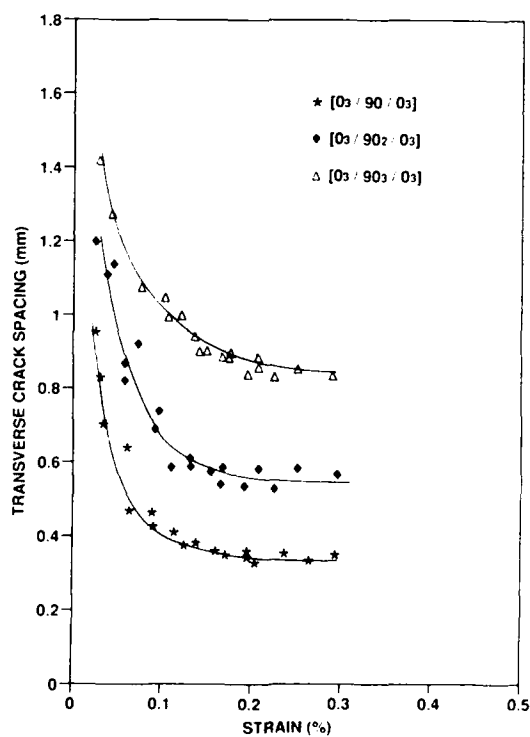
FIG. 3.   Crack Spacing as a Function of Strain and Transverse Ply Thickness.

268
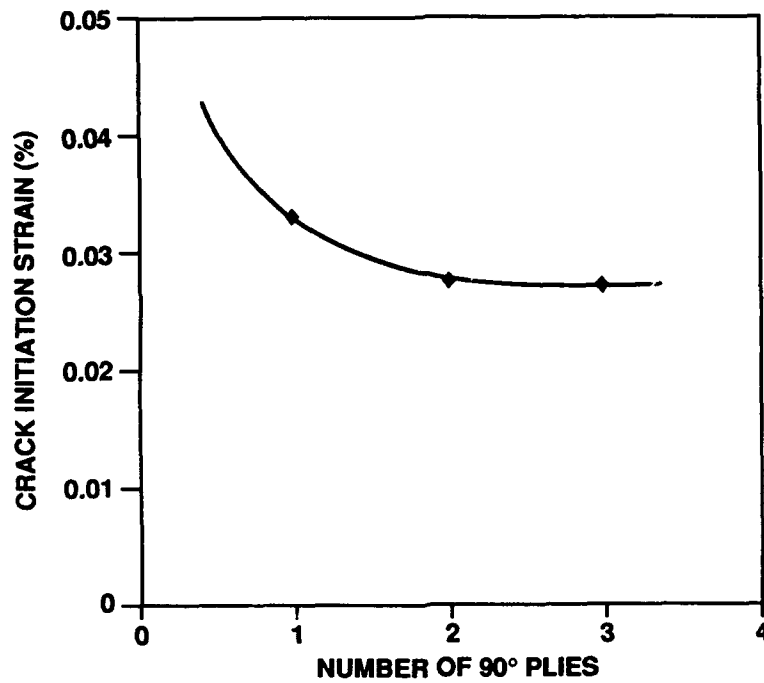
FIG. 4.   Crack Initiation Strain versus Thickness of Transverse Ply.
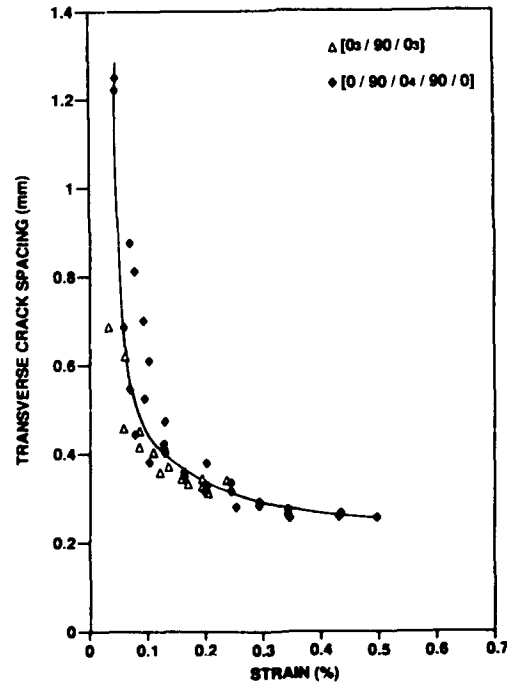
FIG. 5.   Comparison of Crack Spacing in $[0_3/90/0_3]$ to $[0/90/0_4/90/0]$.
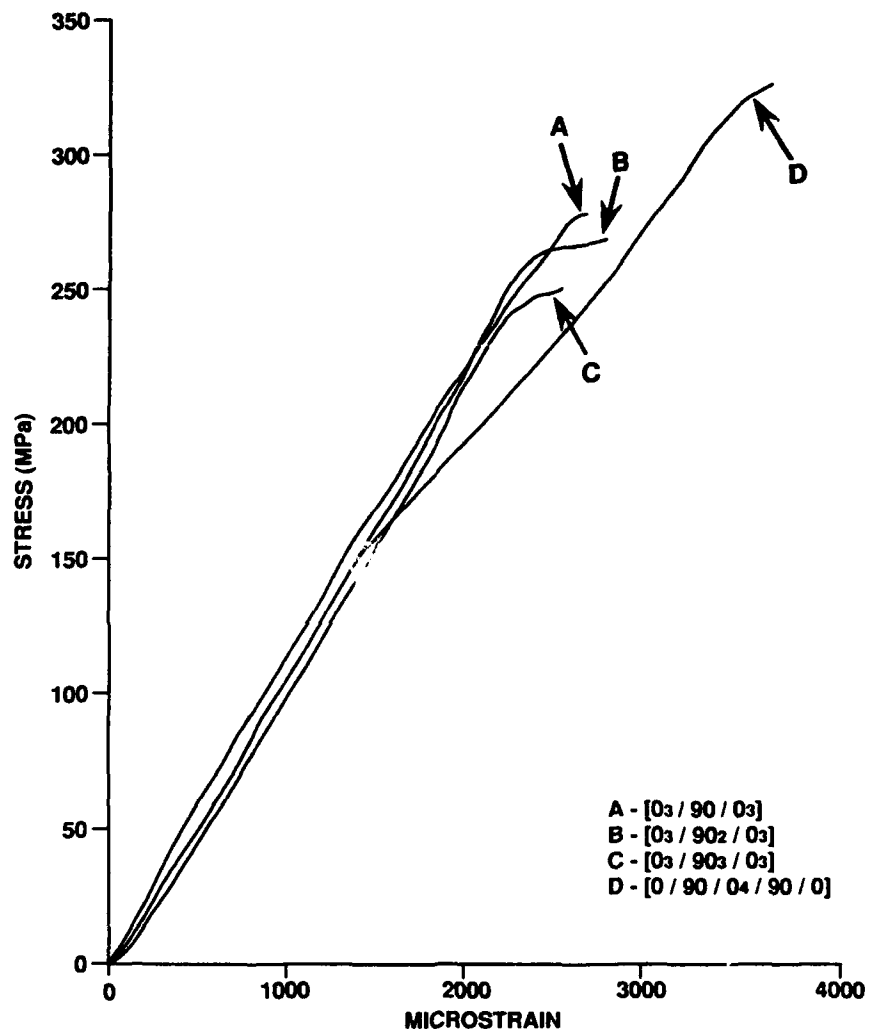
FIG. 6.   Typical Stress-Strain Relationships.

Status of R&D Project on High-Performance Materials for Severe Environments

AKIRA SAKAMOTO

ABSTRACT

The purpose of this project is to develop the basic technologies for advanced materials which can withstand the extremely severe environmental condition inherent to hypersonic aircrafts and space planes. The project within the framework of R&D project of basic technologies for future industries, has been undertaken with close cooperation among industrial, academic, and govermental institutes since 1989 as an 8-year project. The material systems under research are titanium-aluminides and titanium-aluminide matrix composites for the target of 1100℃ temperature capability, niobium-aluminides for 1800℃ capability, and high performance C/C composites for use at peak temperature of 2000℃.

INTRODUCTION

Various significant R&D projects are underway today in our advance into the 21st century, such as aerospace projects for developing space planes, supersonic transports and hypersonic transports, and energy resource development of coal gasification power generation systems and nuclear fusion reacters.

These project objectives all require the development of structural materials with properties which cannot be achieved by conventional materials such as superlative specific strength, stiffness, and resistance to thermal

Akira Sakamoto, R&D Institute of Metals and Composites for Future Industries, Tranomon Hirai Bldg., 17-7 Tranomon 3 Chome Minatoku, Tokyo 105 JAPAN
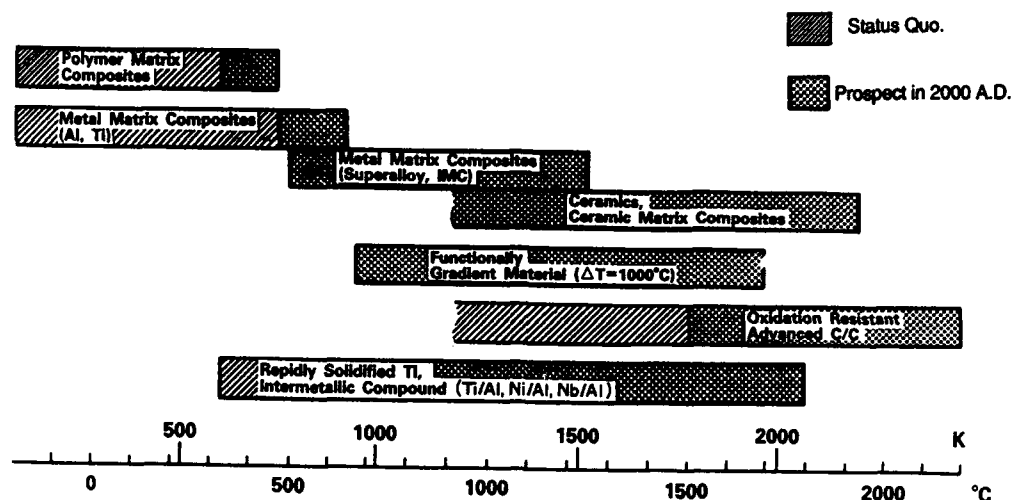
Figure 1 Expected temperature capability of advanced materials

shocks, thermal fatigue and oxidation. In particular, the development of lightweight structural materials capable of withstanding temperatures as high as 1000∼2000°C for use in space plane airframe and engine components, gas turbine parts and nuclear reactor walls are required. Figure 1 the temperature capability of promising materials, in temperature ranges conceivable with space planes. The hatched areas show currently available ranges and dotted areas are those expected to be obtained in the beginning of 21st century.

The figure shows that few lightweight heat resistant materials available in the ranges of 500∼1000°C and above 1500 °C. The former temperature range is currently covered by superalloys. New materials to cover this range is expected to have superior specific strength and specific creep strength to those of superalloys. Ceramics, CMCs (ceramic matrix composites) and C/C composites are candidates for the range above 1200 °C.

The improvement of heat resistance of composite materials is possible also through level-up of material designs and fabrication technologies, and much effort is being made to that direction. However, further development of novel materials for reinforcement and matrix is needed for remarkable improvements in heat resistance, and goals rely on remarkable innovations in future.

In this R&D project on high-performance materials, the material systems selected and being under research are titanium-aluminides and their matrix composites, niobium-aluminides, and high performance C/C composites.

BASIC R&D PLAN AND TARGETS

An 8-year project starting in FY 1989 will establish the basic technologies for advanced materials capable of withstanding severe environments superlative heat resistance, specific strength and stiffness, and oxidation resistance for use in various fields such as aerospace vehicles, and energy-related systems and equipment.

The project objective is to establish for the development of intermetallic compounds with excellent strength, toughness and oxidation resistance in high-temperature environments, and advanced high-temperature composite materials with excellent heat resistance and specific strength at high temperatures. Specifically, the project will develop the following material systems:

(1) Intermetallic Compounds

- High Specific Intemetallic Compounds
  Specific strength (strength/specific gravity) of over 100 MPa
  at 1100°C,and elongation of over 3 % at room temperature.

- High Temperature Intermetallic Compounds
  Tensile strength of over 75 MPa at 1800°C, and elongation of over 3 %
  at room temperature.

(2) Advanced Composite Materials

- Carbon/Carbon Composites (Fiber Lay up 2 D)
  retain the fllowing mechanical properties after heating for 20 hrs in
  air at 2000°C:
  Tensile strength of over 700 Mpa
  Tensile elasticity of over 200 GPa,
  and retain such mechanical properties after heating for 200 hrs in air
  at 1800°C.

- Fiber-Reinforced Intermetallic Compound Composites (Fiber Lay up UD)
  Tensile strength of over 1200 PMa and tensile elasticity of over 180 GPa
  at 1100°C,and retain these mechanical properties after heating for 200
  hrs in air at 1000 °C.

Agency of Industrial Science and Technology, MITI		

Program Evaluation Committee	Program Steering Committee

New Energy and Industrial Technology Development Organization

National Research Laboratory of Metrology			Q	R&D Institute of Metals & Composites for Future Industries		
Mechanical Engineering Laboratory	I		Q	Ishikawajima-Harima Heavy Industries Co.,Ltd.	I	
Government Industrial Research Institute, Nagoya	I			Ube Industries Ltd.		C
Industrial Products Research Institute		C	Q	Kobe Steel Ltd.	I	C
Government Industrial Research Institute, Kyushu		C		Nippon Steel Corporation	I	C
National Research Institute for Metals, STA	I			Nippon Carbon Co.,Ltd.		C
				Fuji Heavy Industries, Ltd.		C
University of Tokyo, Fac. of Engineering			S	Mitsui Engineering & Shipbuilding Co.,Ltd.	I	
Kyoto University, Dep. of Science & Technology			S	Mitsubishi Materials Corporation	I	
Tohoku University, Fac. of Engineering			S	Mitsubishi Heavy Industries, Ltd.	I	C
University of Osaka Prefecture, Coll. of Eng.			S	Petroleum Energy Center		C

I : Intermetallic Compounds,   C : Advanced Composite Materials,   Q : Quality Evaluation Technology,   S : Fundamental Science & Technology

Figure 2 Functional organization of the project

(3) Evaluation Technologies

Evaluation technologies will be developed for use in the development of these materials.

PRESENT R&D [1], [2]

Figure 2 shows the functional organization of the project, in which research activities are being conducted with close cooperation among industrial, academic and govermental institutes. This research project extends over a period of 8 years, consisting of the first period (FY 1989-1992) and the second period (FY 1993-1996).

Typical results of research conducted up to the middle of FY 1991 are described here.

High Specific Strength Intermetallic Compounds

In this sector, the target of development is a TiAl-based alloy and most of the effort has been placed on materials and process development for the alloy

to improve the ductility at ambient temperature ductility and the hot workability. These efforts fall into four categories: alloy design, melting and solidification technologies, thermo-mechanical treatment, and manufacturing process.

By using a high-temperature X-ray diffraction system equipped with an atmosphere control system, structure analysis was performed of the Ti-Al-X systems at high temperatures, and the effect of additional elements X (X = V, Cr, Mn, Nb, Mo and Ta) on TiAl-based alloys has been investigated. The addition of elements X caused a change in phase equilibria among the gamma (TiAl), alpha-2 (Ti_3Al) and beta (b.c.c.-Ti) phases; the beta phase is stabilized by the addition, except X = Ta, resulting in a drastic change in microstructures. The preliminary study for mechanical properties of Ti-Al-X systems suggests that Ta and Nb addition would increase the high temperature strength of TiAl.

The manufacturing process adapted is a TiAl thin plate manufacturing technology called "sheet casting and isothermal rolling processing", which consists of manufacturing the parent materials for rolling by using a sheet caster in an inert gaseous atmosphere.

The development of a process based on powder metallurgy uses near net shape forming using the powder injection molding technique. The binding agents for the granular injection molding materials and dewaxing are now being studied.

High Temperature Intermetallic Compounds

The Nb-Al system was selected as the target for the high temperature intermetallic compound. In this program, determination of phase diagram, alloy design and processing technologies are being investigated. Activities first concentrated on determination of the phase diagram. Using a newly developed high temperature X-ray diffraction system and levitation melting method, phase stabilities of Nb-Al binary system have been studied.

Melting and casting for a precision casting technology, and process development of rapidly solidification for powder metallurgical approach are presently in progress. A unique Plasma Melt Gas Atomization process (PMGA) has been developed for making rapidly-solidified powder of high temperature intermetallic compounds such as Nb_3Al. Crystal structure of PMGA'ed Nb_3Al powder consists of almost Al-saturated solid solution of niobium.

Carbon/Carbon Composites

The goals of the C/C composites program are to develop high performance C/C comjposites for use at peak temperature of 2000°C. Research activities are being performed on several material systems of C/C composites using various carbon fibers as reinforcement, such as a PAN-based, a coal tar pitch-based and three kinds of petroleum pitch-based fibers.

The program is divided into the following four categories. Basic studies will elucidate the oxidation behaivors of carbon fibers and C/C composites as well as improve the performance of the composites by identifying an oxidation inhibitor for making the matrix oxidation-resistant.

a. Improvement of tensile and compressive properties for petroleum pitch-based fibers.

b. Improvement of matrix precursors for inhibiting oxidation and yielding higher carbonization.

c. Development of new composite-fabrication processes such as the pressurized resin char method, high-pressure impregnation carbonization method, chemical vapor infiltration method (CVI), and fabrication of composite rods by CVI which can be utilized as elements for multi-axial structure.

d. Coating systems for oxidation protection.

Three types of petroleum pitch-based carbon fibers with different cross-sections, that is, random, onion and skin-core structures were proposed to improve the fiber properties. By optimizing spinning conditions of a single-hole spinning apparatus, all these types of fibers were prepared respectively and the process development of multi-hole spinning is presently in progress.

The carbonization yields and the oxidation resistance of matrix were improved by adding pitch to pehnolic resin, and elevated pressure gave higher yield in the carbonization. The densification of matrix by high pressure impregnation increased the tensile properties of C/C composites. The high tensile properties of 700 MPa levels were obtained in the 2D composites made by a resin char method using the petroleum pitch-based fiber,Granoc XN-70 and a phenolic resin. However the flexural and compressive strength remained still on low levels.

Three kinds of CVI methods, that is, thermal-gradient CVI, pulse CVI and fabrication of composite rods by impregnating carbon fiber yarn with CVD carbon have been studied. In the pulse CVI, the process development for infiltration of SiC into the preformed porous C/C was conducted to obtain oxidation resistant high strength.

In regard to the coating systems for oxidation protection, oxidation tests were carried out in air at 1700 ℃ to find that the coating sytem of a combination of coversion SiC, CVD-SiC and seal coat was considered to be the most preferable as far as the state-of-the-art coating systems are concerned.

Fiber-Reinforced Intermetallic Compound Composites

In parallel with the development of TiAl, the SiC fiber/TiAl was selected as the target for fiber-reinforced intermetallic compound composites. While the heat resistance of this composite material is similar to that of a matrix intermetallic compound, the specific strength and stiffness of the material are to be improved by the fiber-reinforcement.

The research is divided into the following three categories, but since these categories are interrelated, category b is regarded a common theme with categories a and c.

a. Development of high-performance (heat-resistant, high-strength) silicon cabide-based fibers (polymer precursor type).

b. Improvement of compatibility between fibers and matrices.

c. Process development of composite-fabrication.

Advance in thermal stability has been achieved in the two types of silicon carbide-based fibers with reduced oxygen contents by means of the radiation curing process of electron beam. Concerning the compatiblity study and the process development of fabrication, basic and preliminary studies are being carried out.

Evaluation Technology

At present, there is little data accumulated on the evaluation on material characteristics in ultrahigh-temperature environments, so the development of evaluation technology is quite important. Therefore, research will firstly develop technology for measuring the thermal properties at high temperatures, and in parallel develop technology for evaluating the mechanical properties and corrosion- and oxidation-resistances in high-temperature environments.

CONCLUSION

The current status of the national project on High-Performance Materials for Severe Environments was outlined, in onder to introduce some aspects of activities on advanced materials in Japan.

The realization of advanced aerospace systems and power generation systems will be decisively influenced by the availability of various advanced high-temperature materials. To meet these demands, an accelerated R&D and scall-up program for challenging matrial technologkies is needed.

REFERENCES

1. Symposium proceedings, Basic Technologies for Future Industries, High-performance Materials for Severe Environments-First Meeting, Tokyo, Oct. 24-25, 1990 (in Japanese)

2. Symposium proceedings, Basic Technologies for Future Industries, High-performance Materials for Severe Environments-Second Meeting, Tokyo, Nov. 28-29, 1991 (in Japanese)

Development of Carbon-Carbon Composites for Primary Structure and Thermal Protection System of Space Vehicles

TSUNEO KINJO, SHOJI MAEKAWA AND TOMOYUKI KOBAYASHI

ABSTRACT

A highly durable and oxidation-resistant advanced carbon-carbon composite material which has high mechanical strength and stiffness has been developed for structural and thermal protection use in the space vehicle called "HOPE" which is currently on the drawing board of the National Space Development Agency of Japan (NASDA).

The carbon-carbon composite developed for HOPE is reinforced with two dimensional carbon fiber fabrics and coated with multiple SiC layers by chemical vapor deposition.

Preliminary data acquisition tests were conducted, and some trial products such as an integral skin-stringer panel, a leading edge of wing and other shapes of components were fabricated for development of the forming process and for demonstrating the feasibility of the material system.

Anti-oxidation properties of the carbon-carbon composite were evaluated by accelerated heating and cooling test after acoustic vibration test and mechanical vibration test, since the space vehicle will meet the similar operating condition through launching and reentry.

INTRODUCTION

Carbon-carbon is a high-strength refractory composite material which has excellent specific strength at very high temperatures. Therefore, it is a prime candidate material for a Japanese spaceplane, "HOPE" which is currently under study by National Space Development

Tsuneo Kinjo, Kawasaki Steel Corporation, 1, Kawasaki-cho, Chiba 260, Japan
Shoji Maekawa, Kawasaki Heavy Industries, Ltd., 1, Kawasaki-cho, Kakamigahara, Gifu 504, Japan
Tomoyuki Kobayashi, National Space Development Agency of Japan, 2-4-1, Hamamatsu-cho,Minato-ku, Tokyo 105, Japan

Agency of Japan (NASDA) (Figure 1)[1,2]. During its atmospheric reentry,HOPE will encounter severe aerodynamic heating and the surface temperature may reach up to 1700℃ at the stagnation point. The hot structures of its nose cone, wing leading edges, tip fins, elevons, rudders and body flap will be constructed with the carbon-carbon material.

A carbon-carbon thermal protection system (C/C TPS) is also under development to apply on the surface below 1300℃.

Figure 1   HOPE Proposed by Kawasaki Heavy Industries

MATERIAL CHARACTERISTICS

To achieve high performance and good formability, prepregs made of high modulus carbon cloths and phenol resin are preformed by an autoclave. The preform is then carbonized in an inert gas. The carbonized composite is impregnated with pitch and carbonized again. This process is repeated several times and it is graphitized finally.
The carbon-carbon material requires anti-oxidation coating to be used at high temperatures. The coating is basically Silicon-Carbide (SiC) by chemical vapor deposition (CVD). To avoid thermal expansion mismatch between the CVD-SiC layer and the C/C substratum, a SiC layer by diffusion-conversion process is inserted [3,4]. Typical material properties from the preliminary data acquisition test are shown in Figure 2. NASA RCC design allowables [5] are also shown in the grapns for comparison. Flexural tests were also performed to evaluate the effect of temperature and coating. The results show no degradation due to high temperature (Table 1).
The coating property was examined by plasma flame tests. Coated specimens were exposed to high speed plasma flame with the

temperature of 1300, 1500, and 1700℃. Six minute exposure was repeated ten times for each temperature. The weight loss of the specimens was less than 30 mg which is about 0.6% of their original weight.
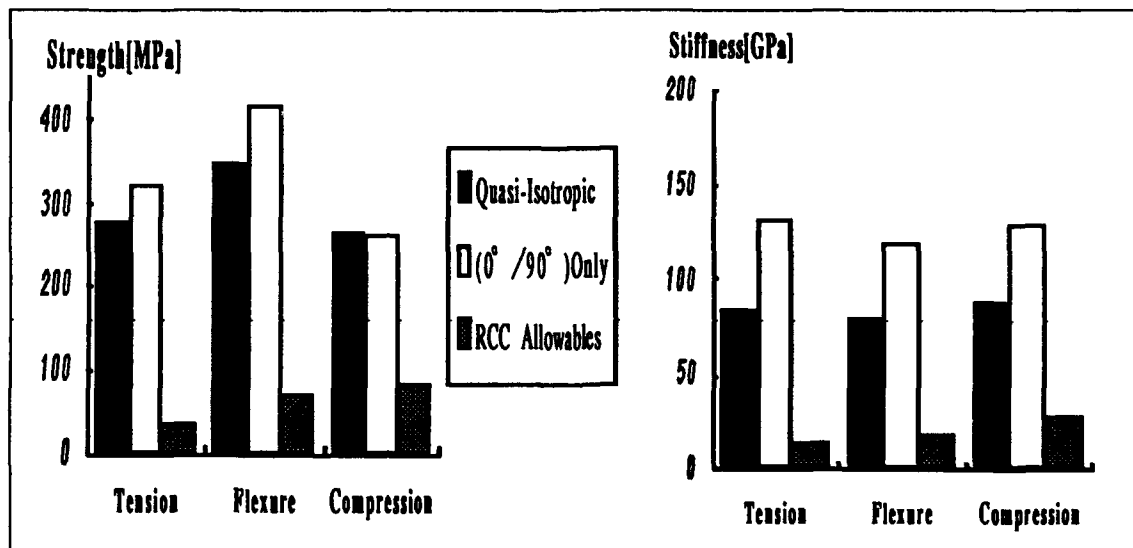
Figure 2 Preliminary Data Acquisition Test Results

TABLE 1 EFFECT OF TEMPERATURE AND COATING ON FLEXURAL PROPERTIES

Test Temperature	Coating	Testing	Strength [MPa]	Stiffness [GPa]
-50℃	No	4 points	371	74
Room Temp	No	4 points	347	79
Room Temp	Coated	4 points	360	75
Room Temp	Coated	3 points	439	68
1700℃	No	3 points	448	64
1700℃	Coated	3 points	551	90

STRUCTURAL ELEMENT TESTS FOR C/C HOT STRUCTURES

The fastener joint test, tension clip test and compression test of stiffened panels were performed to acquire the design data for the C/C hot structures.

The fastener joint test (shown in Figure 3) was carried out with two values of the edge distance, e/D. The specimens with e/D=2.5 showed tensile rupture whereas those with e/D=3.0 showed bearing mode destruction. Therefore, the net strength is shown for e/D=2.5

and the bearing strength is calculated for e/D=3.0 in Table 2. The tension clip test (Figure 4) was performed to evaluate the feasibility of the C/C material because its interlaminar shear strength is rather low. The results are shown in Table 3 and the rupture mechanism,i.e. interaction between interlaminar shear and interlaminar tension is to be elucidated. The compression test of the stiffened panel was also performed to examine the strength retention when the C/C is molded to a complex shape structure. The maximum measured rupture stress is about 90% of the coupon test result.
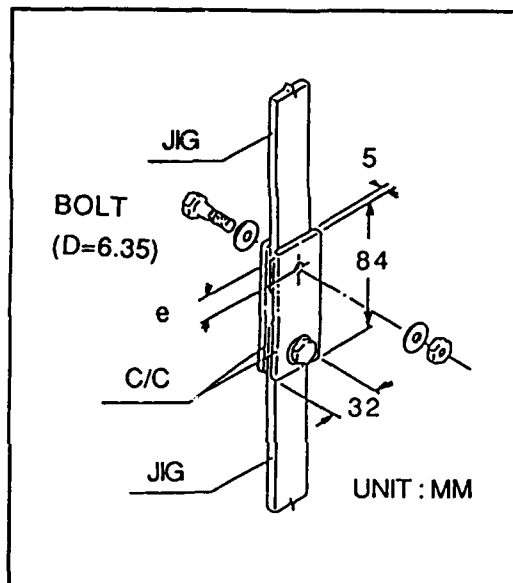
Figure 3 Fastener Joint Test
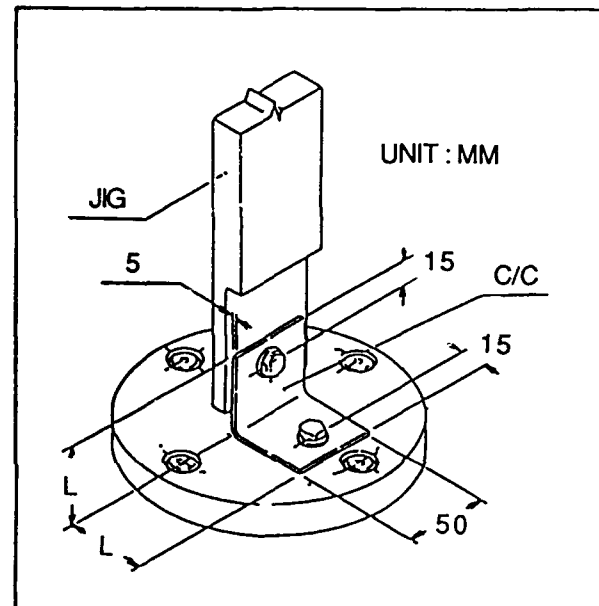
Figure 4 Tension Clip Test

TABLE 2 FASTENER JOINT TEST RESULTS

Specimen e/D	No. of Specimens	Average Rupture Load (kN)	Average Strength (MPa)	Rupture Mode
2.5	3	23.7	102.4 (Net Strength)	Tension
3.0	4	29.4	513(Bearing Strength)	Bearing

TABLE 3 TENSION CLIP TEST RESULTS

Specimen L (mm)	No. of Specimens	Average Rupture Load (kN)
35	4	1.643
50	4	1.454

ENVIRONMENT TEST FOR C/C TPS

The carbon - carbon TPS, which is planned to be installed on C/Pi warm structure to protect it from heating up to 1300℃, consists of a fibrous insulator package, a C/C panel and four sets of posts and fasteners to support the C/C panel. A test specimen which consists of two units of the C/C TPS was exposed to HOPE operational environments such as acoustic vibration, mechanical vibration, and impact load. The levels of these environmental conditions are listed in Tables 4-6. These are tentatively fixed values for the HOPE TPS. The specimen survived these environmental conditions and then the C/C panel was heat-cycled to 1000℃ . The ambient air was depressurized to 10^{-3} atms to simulate the reentry condition. The TPS units including the C/C panels showed no damage. The mass loss of the C/C panel after ten times of the heat cycles was 0.25% of the original weight.

TABLE 4 ACOUSTIC VIBRATION TEST

1/1 Oct. Center Frequency (H_z)	Sound Pressure Level (dB)
31.5	145.5
63	148.0
125	149.0
250	148.0
500	146.0
1000	144.0
2000	140.0
4000	137.5
8000	136.0
O.A.	155.0
Duration	120sec × 10 times

TABLE 6 IMPACT TEST

Direction	Amplitude	No.of Loading
In-plane	Half-Sine	10 times
Out-of-plane	40G(9ms)	10 times

TABLE 5 MECHANICAL VIBRATION TEST

Direction	Frequency (H_z)	Acceleration (Go-p)	Sweep Rate
In-plane	5~15	2.5	20 oct/min
	15~30	5.0	×
	30~100	2.5	10 times
Out-of-plane	5~100	2.5	

FABRICATION OF COMPONENTS

Several components have been fabricated to demonstrate the formability of the C/C composite. An integral skin-stringer panel, which simulates a prime structural member of the hot structure was successfully fabricated (Figure 5). The panel is 1000mm long, 500mm wide and has blade type stringers. A nosecone-like component is 380mm in diameter and 200mm in height (Figure 6). Figure 7 shows a component which simulates the wing leading edge. A C/C panel for the C/C TPS is also fabricated and the size is 300mm times 300mm (Figure 8). All of these trial products were successfully fabricated and the formability of the C/C has been confirmed.
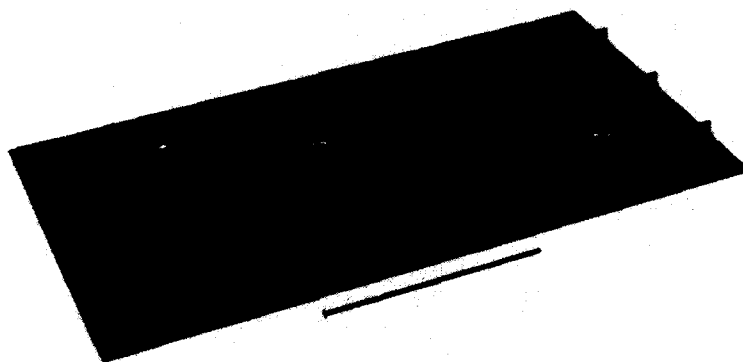
Figure 5   Integral Skin-Stringer Panel
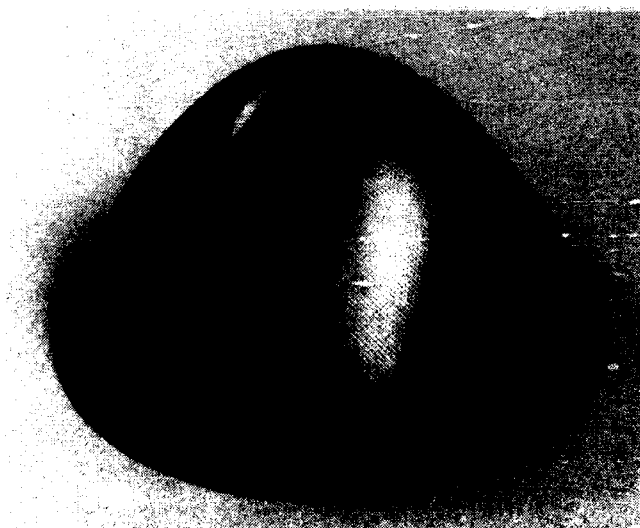
Figure 6 Nosecone-Like Component
          Component

Figure 7   Leading Edge-like
           Component
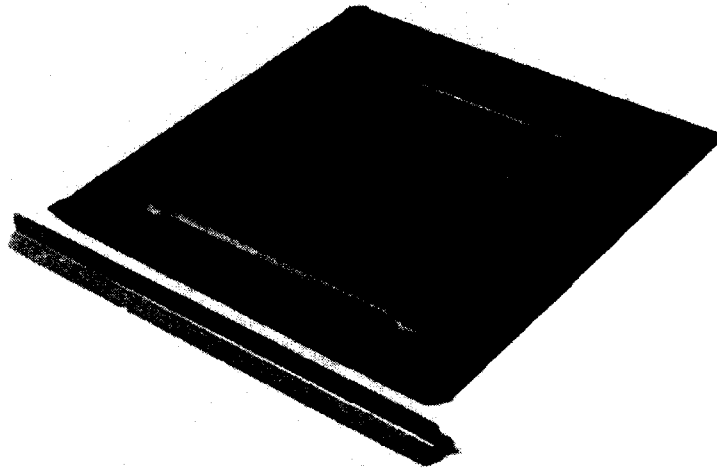
Figure 8   C/C TPS Panel

CONCLUSIONS

High performance C/C material development has been performed successfully.   We have obtained a high   strength and high stiffness C/C material   and   fabrication   technologies   to   complex   shaped components.   Anti-oxidation coating system up to 1700℃ has been developed.   Basic structural element tests were conducted for HOPE's hot structures and the C/C TPS has shown the feasibility to the HOPE environmental   conditions.   We   plan   to   continue   the   structural element tests and component tests   to   obtain   more   detailed   design data.

REFERENCES

1. T.Ito, S.Matsubara, H.Katsuta, T.Akimoto, Y.Takizawa,"Development Scenario of H-II Orbiting Plane, HOPE, " 38th IAF, Oct.10-17,1987.

2. T.Kobayashi, T.Matsushita, H. Mitsuma, H.Tamura, H.Atsumi, "Research and Development of the Primary Structural Members and Thermal Protection System for HOPE", Proc.of 27th Aircraft Symposium, 1989.

3. T.Matsushita, H.Mitsuma, T.Kobayashi, S.Maekawa, K.Kosugi, N.Tsuchiya, and T.Kinjo, "Development of High Performance Carbon - Carbon Composites for Space Applications", Proc. of 17th International Symposium on Space Technology and Science, 1990.

4. K.Hasegawa, S.Takano, T.Kinjo, A.Sakai, M.Noda, and K.Itoh,
   "Oxidation Resistant Coating on Advanced Carbon - Carbon
   Composite for Space Craft", Proc. of 1st Japan International SAMPE
   Symposium,1989.

5. D.W.Johnson, D.M.Curry, and R.E.Kelly, "Space Shuttle Orbiter :
   Leading Edge Structural Design/Analysis and Material Allowables",
   AIAA paper 86-0949, 1984.

Tensile Strength of Chemical Vapor Deposited Silicon Carbide Fibers

E. M. LENOE AND J. N. BEYERS

ABSTRACT

Cvd silicon carbide fiber is a high performance fiber manufactured in the United States by Textron Corporation. In this study several types of this SiC fiber were evaluated via tensile tests. Experiments were completed on commercially produced fibers (.0056 inches in diameter) and on an experimental batch of larger diameter(.011 in. dia.) fibers. Motivation to produce the large diameter fibers was both economic and technical. On the one hand larger diameter fibers would require fewer fibers to be aligned in a composite to achieve a particular volume fraction of reinforcement. Composite fabrication costs could thereby be reduced. The larger diameter fibers were anticipated to be less costly due to reduced handling of core materials as well as varying deposition conditions. From the performance viewpoint the larger fibers would have less interface surface possibly improving elevated temperature resistance. Large diameters were expected to resist microbuckling resulting in higher composite compressive strength. Average room temperature tensile strengths of 920ksi were for the small diameter and 420ksi for the experimental large diameter fibers. Both fiber types were observed to be severely degraded by elevated temperature exposure in an oxidizing atmosphere.

Professor, USMA,West Point, NY 10996
Cadet, USMA,West Point,NY

INTRODUCTION

The large diameter proprietary ceramic wire monofilaments
tested were produced by a proprietary chemical vapor
deposition process. Silicon carbide is precipitated from a
gaseous mixture, swirling through a rather long
reactor(several meters length), and settles on a heated
carbon core. This continuous core is coated with pyrolytic
graphite and is heated as it is drawn through mercury seals
at either end of the reactor.

Scanning electron microscopy reveals that immediately
adjacent to the carbon core is a region of carbon rich beta
silicon carbide. Towards the fiber periphery there is
stociometric beta silicon carbide. At the outside surface s
carbon rich surface occurs. Overall a "corn-cob' type
structure with residual stresses results from the Cvd
process. Several researchers have observed trace elemnt
impurities in the outer zone of the fiber. These occur at
the level of thousands of parts per million and consist
largely of silicides of Ni along with Fe,Cr, and Ti. The
basic features of the silicon carbide monofilament are shown
in the accompanying schematic.

Chemical Vapor Deposited Silicon Carbide
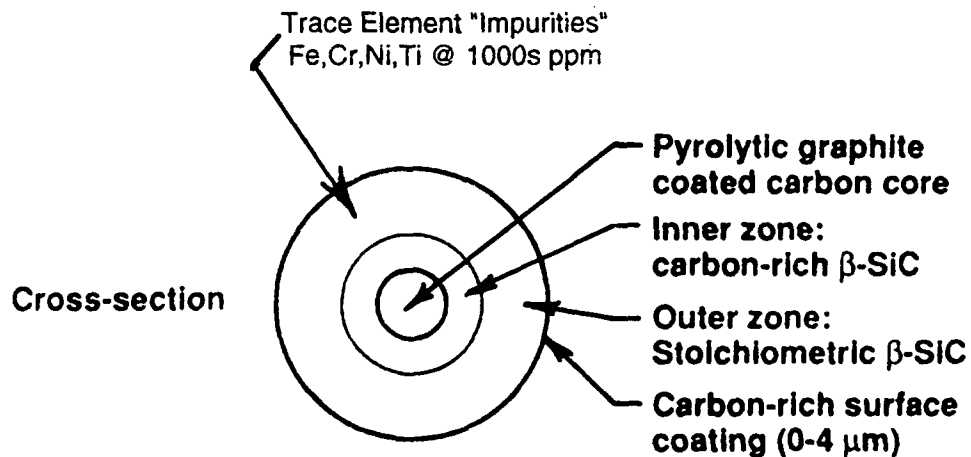
FIGURE 1. SCHEMATIC OF 5.6 MIL FIBER

TENSILE TESTS OF FIBERS

Our uniaxial tension tests were conducted using a large capacity Materials Testing System (MTS) load frame. A piezoelectric load cell, calibrated electrically and mechanically to within 0.1 pound, measured the load. Wedge action grips, as shown schematically in Figure 2, were used to apply monotonically increasing loads. The test durations were typically fifteen to twenty seconds. All tests were carefully observed while attempting to discover initial failure locations and sequence of events.

Quality control(QC) of boron and silicon carbide fibers is based on periodic sampling and tension tests of these Cvd fibers. Small load capacity Instron testers are used. The QC test specimens ordinarily are four inches overall length, with a two inch "Gage Lenth". Pneumatically actuated pressure clamping grips are used to transfer load to the fiber. Aluminum foil cushions the fiber ends in the clamps. A skilled operator conducts these tests rapidly and achieves excellent fiber alignment sighting along carefully inscribed guide lines. Fiber breaking loads are recorded automatically and monitored for statistical significance in production control.

DETAILS OF GRIPPING MTS MACHINE

LOAD CELL

WEDGE INSERT

FIBER

TABS

WEDGES

EPOXY

ACTUATOR PISTON
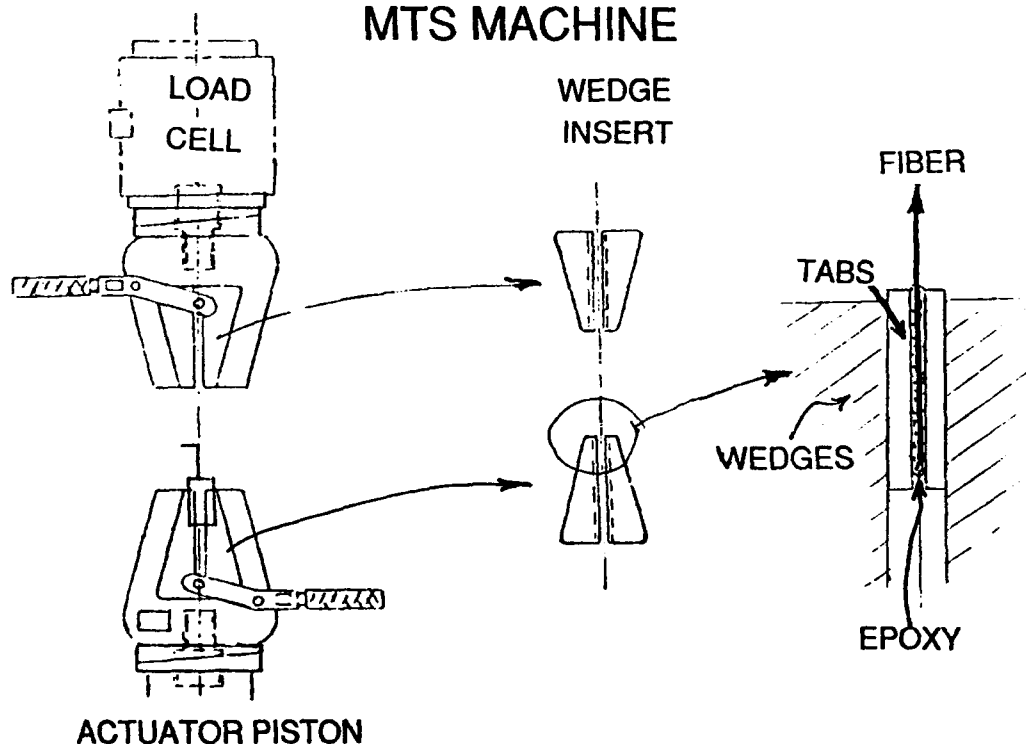
FIGURE 2: TENSION TEST DETAILS

In contrast to QC tests our specimens were fourteen inches overall length with three and a half inches grip tabs at each end. The fiber ends were sandwiched between a pair of aluminum plates, nominally one eighth inch thick, one inch wide and three and a half inches long. The inner adherend surfaces of the aluminum tabs were roughened using a high speed grinding wheel.The fiber was centered in the tabs during the bonding process. This configuration was the result of investigation of a variety of end attachment proceedures. The first attempts included simple tabs of aluminum foil, wood and sandpaper. All these resulted in fiber slippage or breaks within the grips. The objective was to induce failure within the gage lentgh at some distance removed from the grips.The next end grips used bonded tabs of wood , metal or fiberglass. Experiments were completed with various polymer and ceramic adhesives. The most satifactory results were obtained with a room temperature curing epoxy. This one type of epoxy adhesive gave the majority of gage length breaks. Note that our data reports only failure loads associated with fractures occuring in the gage length, and observably distant from the grips. There were several motivations for using a large gage length. It was desireable to attempt to determine failure initiation sites in hopes of seeking correlations of microstructure at the fracture site with observed strength. Long gage lengths might make this an easier task. We had planned on completing high temperature tensile tests but did not succeed in developing a successfull elevated temperature grip. The long gage length fibers would permit gripping outside the hot zone of the furnace and allow high temperature tensile testing. Room temperature results obtained are presented in Figure 3. Note the substantial differences in strength of the commercial grade of 5.6 mil fiber and the lower strength of the developmental 11 mil fiber. Particularly in the 5.6 mil fibers there were mutiple breaks and in only several instances was it possible to observe initial failure location. The high level of stored energy released on fracture produces dynamic stress waves which induce multiple fractures. Considerable ingenuity would be required to devise a scheme to automatically photograph failure sequence , to capture fractured parts and maintain identity of the fragments! On the otherhand witnessing the location of breaks, coupled with analysis of stress wave propagation, would yield data to describe spatial vaiation of strength in these fibers.

Results presented in Figure 3, as mentioned previously are only those fractures which occured within the seven inch gage length. Breaks which happen in the grip regions are subject to a complex stress state and are not representative of uniaxial tensile strength. It would be interesting to learn the percentage of non-gage length fractures during routine quality control testing of production fibers!

WEIBULL PLOTS

SMALL FIBERS
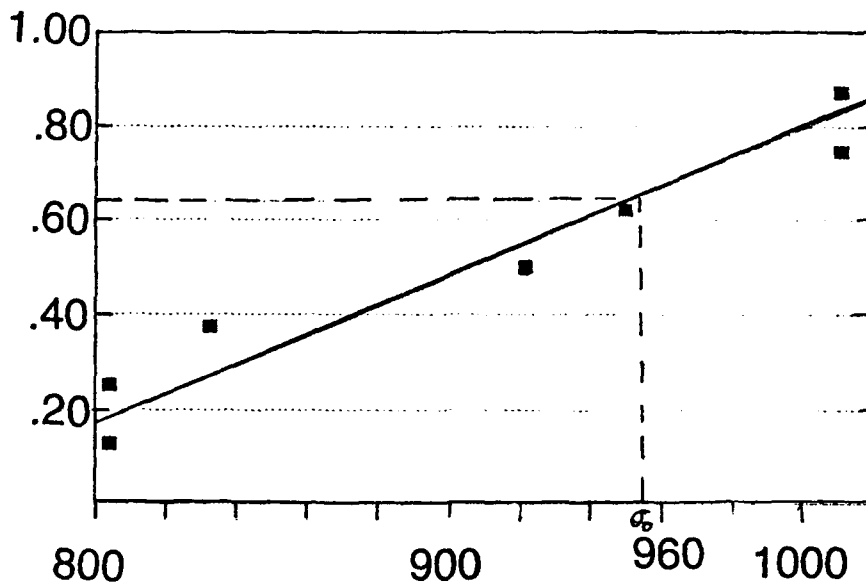
LARGE FIBERS
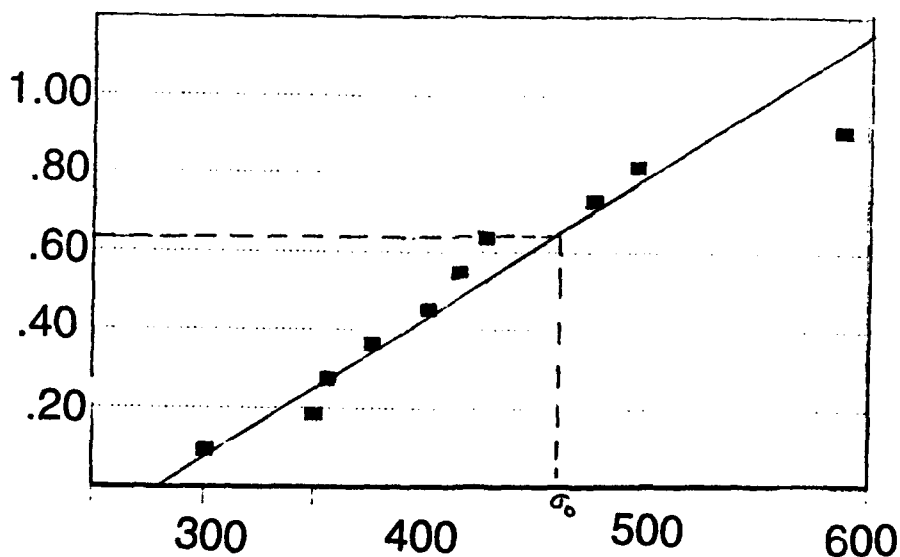
FIGURE 3: TENSILE STRENGTHS, 5.6 & 11 MIL FIBERS

ELEVATED TEMPERATURE EXPOSURE

The two types of fibers were also subjected to
environmental exposures, using a conventional refractory
lined heat treat furnace. Treatments investigated were
twenty four hours of exposure in oxidizing environments at
temperatures of 1200 ,1100 and 1000 degrees farenheit.
During exposure the fiber specimens were set to rest on the
rim of a whiteware crucible. At the 1200 temperature the
fibers were extensively reacted and embrittled so that they
broke on handling. At the lower temperature the fibers were
also degraded so that they could not be tested. The "dirty"
oxidizing environment resulted in disasterous phase changes
and strength loss.

A number of researchers have reported intrinsic strength
loss of Cvd silicon carbide fibers at elevated temperatures.
The fibers suffered strength loss above 2500 F. In
particular recrystallization and grain growth in the outer
regions of the fibers resulted in strength loss. On the
otherhand the inner reions of beta silicon carbide appear to
be stable and resistant to phase changes up to 3000F.

SUMMARY

Reaction kinetics of Cvd SiC fibers need further
investigation in a variety of environments, particularly in
oxidizing exposures. It is important to understand the role
or relevance of trace "impurities" such as Fe,Cr,Ni and Ti.
If they are determining factors in strength and elevated
temperature performance, understanding their source and
elimination becomes important. As for fiber improvements, it
is known that carbon rich beta silicon carbide resists
intrinsic flaws. Possible approaches to improve high
temperature resistance include appropriate coatings and
capitalizing on in-situ reactions.

As for fiber tensile strengths reported herein, and
refering to a three parameter Weibull strength
representation, we found Weibull moduli of m = 6.2 and 3.5
for the 5.6 and 11 mil fibers respectively. This is based on
using a very low threshold stress level of 50 ksi and the
"characterisitic values at Pf = .632 , based on the Weibull
plots of Figure 3. The Weibull moduli of the small diameter
fibers compares favorably to values of 6 to 8 reported for
silicon carbide yarns!

ACKNOWLEDGEMTS

REFERENCES

1. Bhatt,R.T. and D.R.Hull,"Microstructural and Strength Stability of CVD SiC Fibers in Argon Environment" NASA Technical Memorandum 103772, AVSCOM TR 91-C-014 and Presented at 15 Annual Conference on Composites and Advanced Ceramics 13-16 January 1991.
2. L. M. Sheppard, "Progress in Composites Processing", Ceramics Bulletin,Vol.69,N).4,1990666-673.

Durability: Prediction and Observation I

Life Prediction and Cumulative Damage Analysis in Random Fiber Composites

MOHAMAD S. EL-ZEIN AND HENRY D. BERNS

ABSTRACT

A fatigue life prediction scheme for random fiber composites using energy as a parameter is presented. Moreover, a linear damage model was used to study cumulative damage. A good correlation is shown between the theory and the experimental results.

INTRODUCTION

The response of structural components to fatigue loading has been a major concern since engineers became familiar with strength of materials. For metals, models for predicting the life of a component and modes of failures are well developed for uniaxial fatigue loading. There is both a crack initiation and a crack propagation model for the prediction of the nucleation and growth of a single crack. As a result, for metals, the fatigue process has a distinct crack initiation period followed by crack growth until final fracture occurs. Development of biaxial loading is currently being studied, but for many applications with uniaxial loading, predictions are quite satisfactory. The ability to do something similar for uniaxial loading of composite s would greatly assist in their use in structural components.

In fiber reinforced composites (FRC), cracks can be expected during the manufacturing process and several types of damage modes interact and contribute to the final failure. Damage can be due to matrix cracking, fiber/matrix debonding, fiber breakage, etc. Various modeling schemes have been developed to predict the life of structural FRC. Currently, the essential parameter monitored and used for predicting life is stiffness. Although the stiffness of a component is fundamental for structural integrity, and in some component design a criterion for failure (helicopter rotor blades), it is uncertain if it can be used to predict life where stress raisers exist. Moreover, the majority of degradation occurs toward the end of life.

In the following, the authors would like to contrast the damage development between FRC and metals. When small metal coupons are subjected to long life fatigue testing, the majority of the life is spent in initiating a crack and the propagation is a small percentage of the total fatigue life. Therefore, if we measure the change in stiffness of the specimen during crack initiation, very little change will be observed. However, during the propagation of the crack, there is a definite stiffness degradation. During low cycle fatigue, however, both the initiation and propagation may contribute significantly to the total life before fracture. Figure 1 shows a typical rate of crack propagation for metal components. For a metal component with this type of crack growth, the stiffness reduction could certainly be used as a measure of damage. This concept of stiffness reduction and damage was first used by Kachanov[1]. A stiffness degradation curve for a composite structure would look similar to the curves in Figure 1.

Mohamad S. El-Zein and Henry D. Berns, Deere & Company Technical Center, 3300 River Drive, Moline, IL, 61265

Rate of Crack Growth

Figure 1.

Stress-Strain Curve
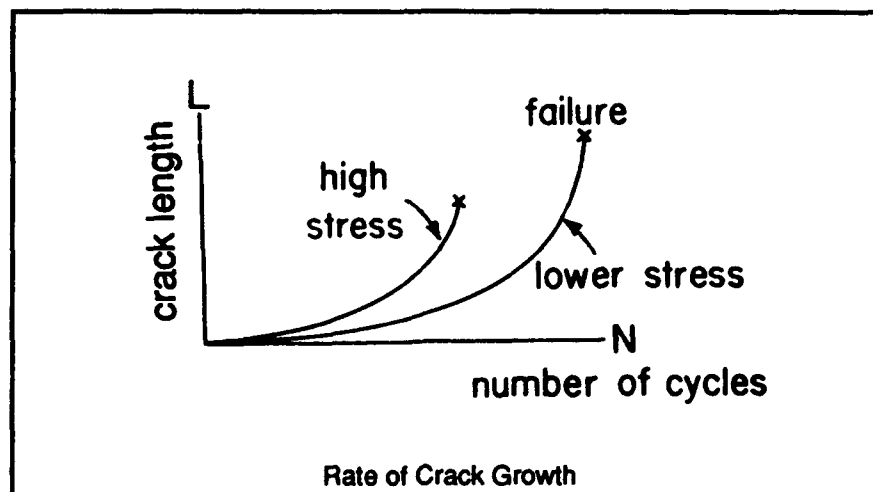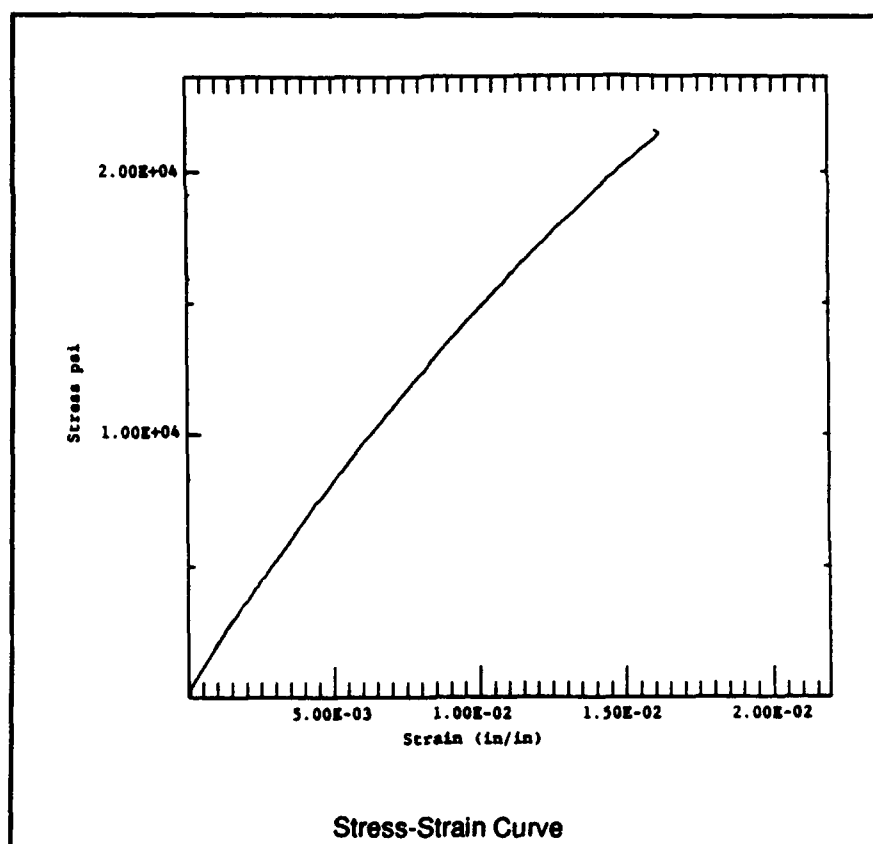
Figure 2.

Grey cast iron is a metal that is in reality a composite material. It has a low carbon steel matrix with various size and shape of graphite flakes distributed throughout the material. Downing[2], modeled this material and noted that the strength and stiffness of the steel matrix was reduced due to the size, shape and number of the graphite flakes. It is important to note that for this metal composite, the steel matrix and graphite flakes are reversed in strength and stiffness from a fiber reinforced plastic composite material. In the metal composite, the steel matrix is the stronger material, while in the plastic composite, the plastic matrix material is the weaker material. Downing made use of Kachanov's model in his development of a fatigue damage model that includes a reduction in stiffness as fatigue damage is accumulated.

This paper will introduce a local stress analysis approach for predicting the fatigue life of random fiber composites and a simple linear model for damage. For this material, the dominant modes of failure are matrix cracking, fiber matrix debonding, and fiber breakage. These failure modes are repeatable which makes the use of a simple linear model practical to use for fatigue.

EXPERIMENTAL PROGRAM

The material used was thermoset polyurethane with 40% continuous strand mat. The specimens tested were cut using a diamond plated wheel and machined on a tensile cut machine. The specimens were dog bone shaped with dimensions of (216/15.24/3.2) mm.

The tensile properties of the material were determined and a typical stress-strain curve shown in Figure 2. Fatigue testing was performed on a closed loop servo controlled machine at a frequency of 5 Hz. The S-N curves for this material are shown in Figure 3.

In order to introduce a stress raiser, a 3.2 mm hole was drilled in the middle of the specimen. The strain close to the hole and a nominal strain away from the discontinuity were measured by laying strain gages. From the data acquired, a strain concentration factor was obtained. The stress equivalent to the strain measured at the hole was determined from the stress-strain curve and a stress concentration factor was also determined.

THEORETICAL ANALYSIS

It is well known that the stress concentration in an infinite plate containing a circular hole is 3, provided the stress applied is in the elastic region. In the linear elastic region, there is no difference between the stress and the strain concentration factors. As the linear elastic region is exceeded, the stress concentration decreases while the strain concentration increases. This relationship was first developed by Neuber[3] for prismatic bodies loaded beyond the linear stress-strain point. It states that the theoretical stress concentration is the geometric mean of the stress and strain concentrations or the square root of the product of the stress and strain concentrations. Neuber's rule has also been used to relate nominal and notch root stress and strain relationships for fatigue analysis as noted by Professor Morrow and others at the University of Illinois, see reference [4]. Neuber's rule used in this manner can be written in the following form:

$$K_f^2 S_N e_N = Se \qquad (1)$$

where S_N and e_N are the nominal stress and strain and S and e are the notched stress and strain values, respectively.

Realizing if both sides of Equation 1 are divided by a factor n, that the terms will become energy terms. For linear elastic materials, n is equal to 2. In this model for random fiber composite, a relation similar to Neuber's equation is written in terms of energy, i.e.,

$$K_f W_N = W_f \qquad (2)$$

S-RIM REVERSED LOADING
TENSION-COMPRESSION   R=-1

(a)

TENSION-TENSION FATIGUE OF S-RIM (R=0.1)
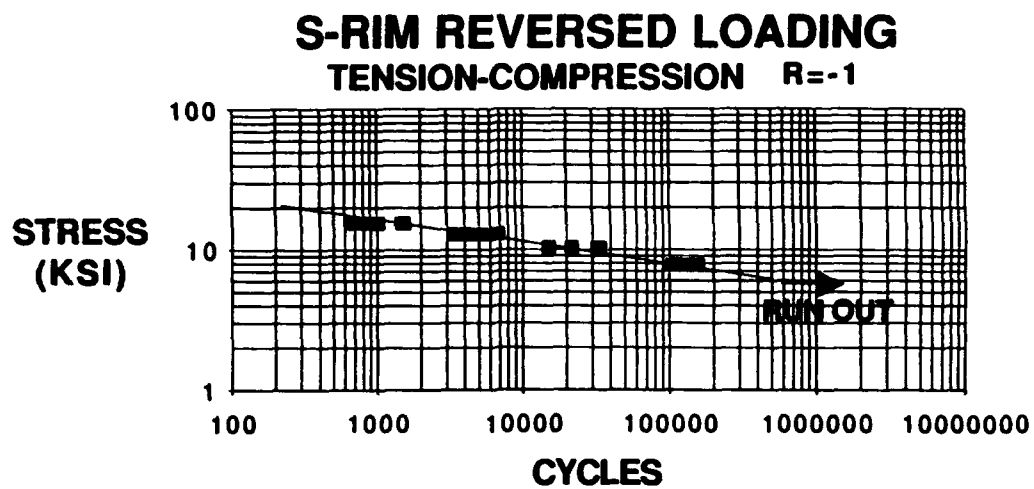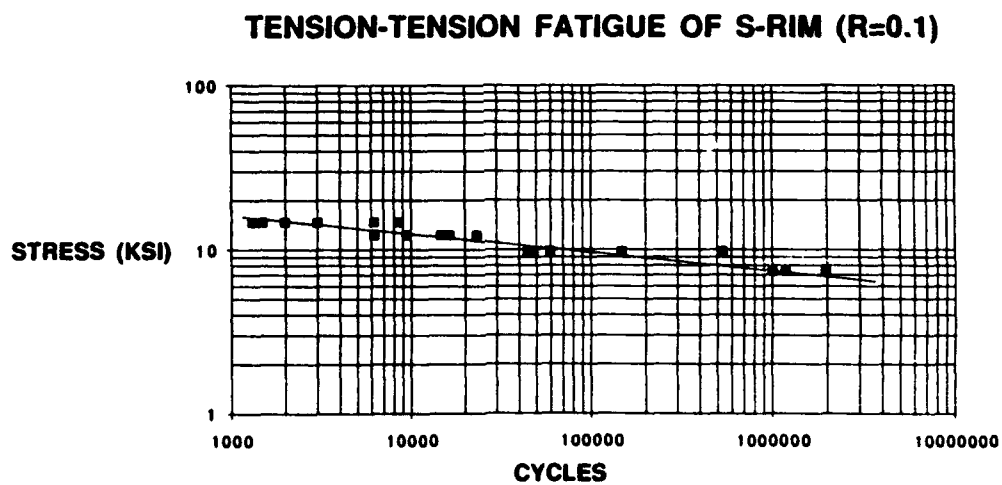
(b)

S-N Curves for Polyurethane 40% Glass

Figure 3.

where W_N and W_f are the areas under the stress-strain curve (energies) corresponding to the stresses S_N and S_F, and S_F is the fatigue stress of an unnotched specimen required to produce an equivalent life for the notched specimen.

K_f has the same definition as K_f in Neuber's approach

$$K_f = (K_s K_e)^{1/2} \tag{3}$$

where K_s and K_e are the stress and strain concentration factors.
The process of predicting life using this approach is as follows:

1. Measure e_N and e experimentally or analytically.

2. Get S_N and S from S-e curve.

3. Determine $K_s = \dfrac{S}{S_N}$ and $K_e = \dfrac{e}{e_N}$.

4. Find $W_N \equiv$ area under curve.

5. $W_F = K_f W_N = \sqrt{K_s K_e} \; W_N$

6. Find S_F from S-e curve.

7. Find N_F from S-N curve.

It should be noted that the concept of energy has been used before by several researchers. An example would be the work of Halford[5] in fatigue of metals.

The question of damage accumulation in composite materials has not been addressed thoroughly. Boller[6], Hofer and Olsen[7], and Broutman and Sahu[6] attempted to use Miner's linear damage theory to study damage accumulation. Broutman and Sahu concluded that Miner's rule was not adequate for composites. However, a review of the results presented in [6] revealed that Miner's rule is within reasonable accuracy except for two loading levels.

In this paper, Miner's[9] linear theory is used to study damage accumulation in random fiber composite materials. In mathematical form, Miner's rule is written as

$$\frac{n_1}{N_1} + \frac{n_2}{N_2} + \cdots = 1$$

Based on the constant amplitude stress life curve for the material, half the cycles needed for failure were run for the first load level. The second load level was then run until the specimen failed.

RESULTS AND DISCUSSION

To verify the proposed methodology, a central circular hole was introduced as a stress raiser. A small strain gage was placed at the edge of the hole to measure the notch strain "e". A second gage was placed away from the hole to measure the nominal strain "e_N". Using the measured strains, a value for the strain concentration was obtained and the procedure outlined above was followed to determine S_f and hence N_f for reversed loading. The results of a typical prediction of fatigue life is shown in Figure 4. The data in Figure 4 are the results of five specimens tested at each load level. It is apparent, keeping in mind the scatter characteristic in fatigue, that the current methodology yields good agreement with the experimental data.

```
Applied Stress                      =   7,350 psi
N (predicted)                       =   8,000 cycles
N (actual) →    minimum             =   7,874 cycles
                mean                =   11,302 cycles
                maximum             =   14,225 cycles


Applied Stress                      =   4,891 psi
N (predicted)                       =   300,000 cycles
N (actual) →    minimum             =   59,666 cycles
                mean                =   220,141 cycles
                maximum             =   405,678 cycles
```

Typical Prediction of Fatigue Life

Figure 4.

Tension-Tension Cumulative Damage

Figure 5.

Tension-Compression Cumulative Damage
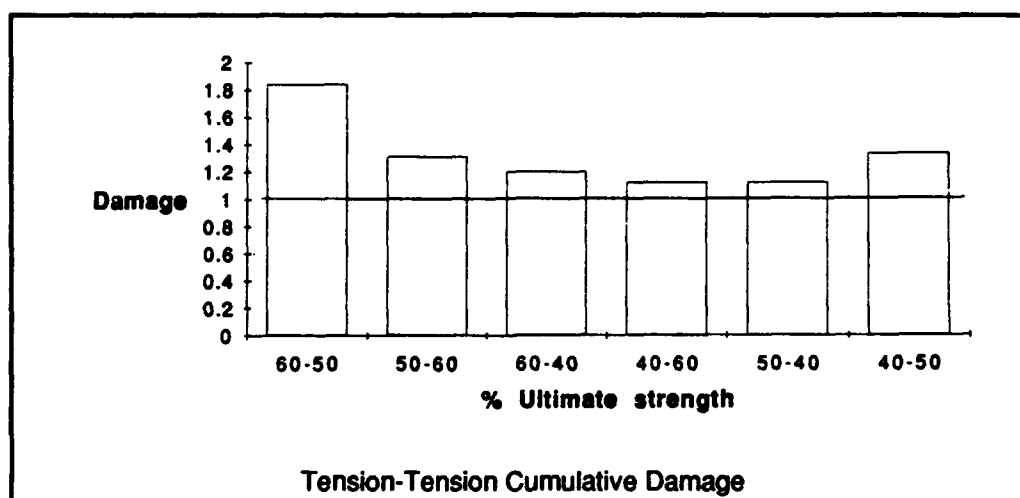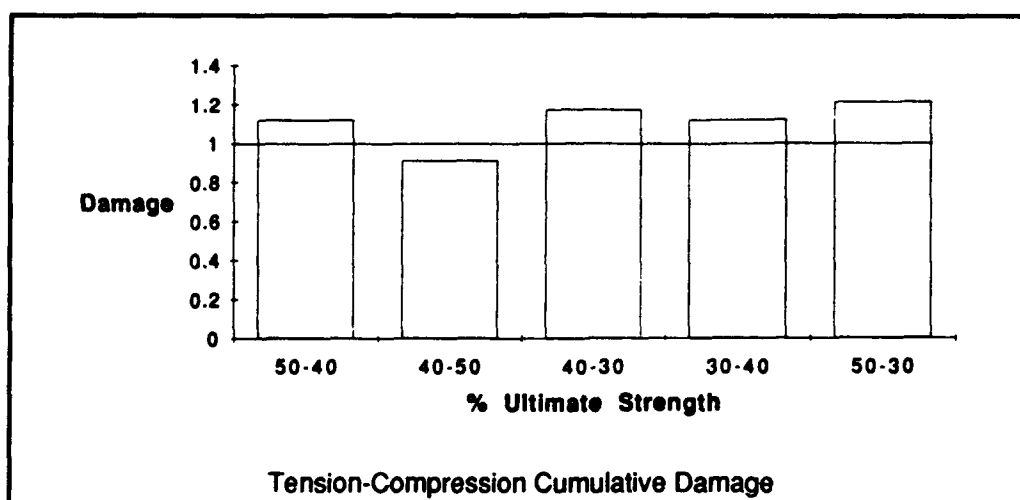
Figure 6.

Damage accumulation was performed under tension-tension and tension-compression. The average of five specimens for each load level are shown in Figures 5 and 6. Figures 5 and 6 show load levels as percent of ultimate strength. The plots then show the summation of damage for the two levels. It should be noted that as one goes from high to low and then low to high, Miner's rule does hold.

CONCLUSION

A methodology for predicting the life of composite materials containing a discontinuity was proposed. The result seems to be very encouraging and agree with experimental data. The theory will be tested for other forms of discontinuities. Moreover, damage accumulation prediction in random fiber composites using Miner's rule yielded good agreement with experimental data.

The theory used to predict life is novel and based on an important concept, i.e., energy.

ACKNOWLEDGEMENT

REFERENCES

1. Kachanov, L.M., "Introduction to Continuum Damage Mechanics," Martinus Nijhoff Publishers, 1986.

2. Downing, S.D., "Modeling Cyclic Deformation and Fatigue Behavior of Cast Iron Under Uniaxial Loading," FCP Report No. 101, A report of the Fracture Control Program, University of Illinois at Urbana-Champaign, January 1984.

3. Neuber, H., "Theory of Stress Concentration for Shear Strained Prismatical Bodies with Arbitrary Non-Linear Stress-Strain Law," Journal of Applied Mechanics, ASME, 1961, p. 544-550.

4. Topper, T.H., Wetzel, R.M., and Morrow, JoDean, "Neuber's Rule Applied to Fatigue of Notched Specimens." Journal of Materials, JMLSA, Vol. 4, No. 1, March 1969, p. 200-209.

5. Halford, G.R., "The Energy Required for Fatigue," Journal of Materials, Vol. 1, No. 1, March 1966, p. 3-18.

6. Boller, K.H., "Effect of Single Stress Change in Stress on Fatigue Life of Plastic Laminates Reinforced with Unwoven E Glass Fibers," Technical Report AFML-TR-66-220, December 1966.

7. Hofer, K.E., Jr., and Olsen, E.M., "An Investigation of the Fatigue and Creep Properties of Glass Reinforced Plastics for Primary Aircraft Structures," AD-652415, IIT Research Institute, Chicago, IL, April 1967.

8. Broutman, L.J., and Sahu, S., "A New Theory to Predict Cumulative Fatigue Damage in Fiberglass Reinforced Plastics," ASTM STP 497, 1972, p. 170-188.

9. Miner, M.A., "Cumulative Damage in Fatigue," Journal of Applied Mechanics, Vol. 12, 1945.

Probabilistic Simulation of Multi-Scale Composite Behavior

D. G. LIAW, M. C. SHIAO, C. C. CHAMIS AND S. N. SINGHAL

ABSTRACT

A methodology is developed to computationally simulate the scatter in composite material properties at all composite scales due to the scatter in the constituent (fiber and matrix) properties and in the fabrication process variables. The methodology is computationally efficient for simulating the probability distributions of material properties. Sensitivity of the probabilistic composite material property to each uncertain variable is determined. This information can be used to reduce undesirable scatter in material properties at macro composite scale by reducing the scatter in the most influential uncertain variables at micro composite scale. This methodology has been implemented into the computer code PICAN (Probabilistic Integrated Composite ANalyzer). The code is demonstrated via simulation of the scatter in material properties for a typical laminate. The sensitivity information is also computed.

INTRODUCTION

Composites are an important class of engineering materials in structural design. Their outstanding mechanical properties, particularly the high strength to density ratio, are very attractive to the aerospace industry. They also possess excellent durability and corrosion-resistance. The mechanical properties of composite materials are derived from those of the fiber and matrix constituents, which depend on a wide variety of variables. These variables include, for example, the fiber and matrix material properties (constituent scale) and fabrication variables at all stages of fabrication process such as fiber volume ratio, void volume ratio, ply misalignment and ply thickness. These variables are statistical in nature, therefore, the mechanical properties of a composite material should be quantified probabilistically. As a consequence, the behavior of composite structures shows a scatter from its average value. Traditionally, a "safety

D. G. Liaw, Sverdrup Technology, Inc., 2001 Aerospace Parkway, Brookpark, Ohio, 44142

M. C. Shiao, Sverdrup Technology, Inc., 2001 Aerospace Parkway, Brookpark, Ohio, 44142

C. C. Chamis, NASA Lewis Research Center, 20001 Brookpark Rd., M.S. 49-8, Cleveland, Ohio, 44135

S. N. Singhal, Sverdrup Technology, Inc., 2001 Aerospace Parkway, Brookpark, Ohio, 44142

factor" is used in the design to account for this unpredictable behavior. However, this approach results in either an overconservative or an unsafe design. In order to probabilistically assess the behavior of composite structures, a methodology was developed at the NASA Lewis Research Center for simulating the probabilistic material properties in all composite scales. The methodology requires the identification of uncertainties at constituents and ply scales including material properties and fabrication variables. The uncertain variables are then filtered through an analyzer which combines the composite mechanics and probability theory to computationally simulate the probabilistic material properties. Although the scatter in material properties can be computed by the Monte Carlo simulation method, it is inefficient and expensive. In order to save the computational time, the newly developed methodology uses special structural reliability algorithms, instead of the Monte Carlo simulation, to provide an efficient and affordable way for computationally simulating the scatter in composite material properties. The methodology is implemented in the computer code PICAN (Probabilistic Integrated Composite ANalyzer) (Ref. [1]) and is described in the present paper. Composite material properties at ply and laminate scales were simulated via PICAN. The scatter in the material properties was computed. The sensitivity of a given material property to each uncertain variable was also quantified.

PROBABILISTIC SIMULATION OF THE COMPOSITE MATERIAL

Composite materials are made of fiber and matrix through an appropriate fabrication process. Since the mechanical properties of the constituent material vary statistically, the uncertainties in composite material properties are not only inherent from the scatter in the constituent material properties, but also result from the scatter in the fabrication process variables. Probabilistic simulation of composite material properties requires identification of uncertainties at all composite scales as described below.

The laminated fiber-reinforced composite materials are manufactured by two basic steps: layup and curing. The uncertainties incurred during the layup process are due to the misalignment of ply orientation. Typical uncertainties incurred from the curing process are interlaminate voids, incomplete curing of resin, excess resin between plies, excess matrix voids and porosity, and ply variable thickness. Uncertainties incurred in the constituent material properties include all the fiber and matrix material properties. The uncertainties incurred during the manufacturing process include the fiber volume ratio, void volume ratio, ply misalignment and ply thickness. These uncertainties are referred to as the uncertain variables (as shown in Figure 1) which will be processed computationally through composite mechanics and probability methods as depicted in Figure 2. The details of the computer code PICAN for the computational simulation of uncertainties is described next.

PROBABILISTIC INTEGRATED COMPOSITE ANALYZER : PICAN

PICAN (Probabilistic Integrated Composite ANalyzer) is a computer code for the probabilistic simulation of composite material properties. It integrates two NASA

in-house computer programs, ICAN (Integrated Composite ANalyzer) (Ref. [2]) and FPI (Fast Probability Integrator) (Ref. [3]) developed recently. ICAN was developed based upon composite mechanics to simulate the composite material behavior at all composite scales including the effect of environments and fabrication. FPI, developed using structural reliability algorithms, probabilistically processes the material property information generated by ICAN and efficiently computes the cumulative distribution functions (cdf) of composite material properties at all composite scales. Further details of ICAN and FPI are explained in the following.

ICAN MODULE

ICAN performs a comprehensive multi-scale perturbation analysis of composite material properties by selectively perturbing the uncertain variables at the constituent scale (fiber and matrix material properties, fiber volume ratio and void volume ratio), and at the ply scale (ply misalignment and ply thickness). Perturbed material properties at all composite scales corresponding to all the perturbed uncertain variables are computed and stored in a database. With this information, mathematical functions to represent the relationships between the material properties and the uncertain variables can be determined numerically. The functional relationship is expressed by Equation 1.

$$M_p = a_0 + \sum_{i=1}^{N} a_i V_i + \sum_{i=1}^{N} b_i V_i^2 \tag{1}$$

where M_p is any material property; N is the number of uncertain variables considered; V_i are uncertain variables; a_0, a_i, b_i are constants.

FPI MODULE

The FPI module first extracts the desired perturbed material properties from the database generated via ICAN. It then determines the constants in Eq.(1) to develop the relationship between the composite material property and the uncertain variables. Finally, FPI takes this relationship and the probability distributions of the uncertain variables to compute the probability distribution of that material property.

PICAN SIMULATION

The uncertain variables at the constituents and the ply scales are first identified and their respective distribution types and corresponding parameters are determined. These variables are then selectively perturbed several times in order to create a database for the determination of the relationship (as shown in Equation 1) between the composite material property and the uncertain variables. For a set of perturbed values of uncertain variables, composite micro-mechanics is used to determine the corresponding perturbed mechanical properties at the ply scale. Laminate theory is then used to determine the perturbed mechanical properties at the laminate scale. This process is repeated until enough data are generated and appropriate relationships

between material properties and uncertain variables are established through a numerical procedure. With the known probabilistic distributions of the uncertain variables and the numerically determined relationship between the material properties response and the primitive variables, fast probability integration is applied. For every discrete response value, a corresponding cumulative probability is computed by FPI. This process is repeated until the cumulative distribution function can be appropriately represented. The output information from FPI for a given material property includes its discretized cdf values, the coefficients for a special type of probability distribution function, and the sensitivities of the material property to the uncertain variables.

NUMERICAL RESULTS AND DISCUSSIONS

The methodology described previously was applied to a 16-ply $(0_2/\pm45/0_2/90/0)_s$ graphite/epoxy composite with 1.8% moisture at room temperature. The experimental data for the longitudinal modulus, transverse modulus, in-plane shear modulus, major Poisson's ratio, longitudinal and transverse tensile strengths, longitudinal and transverse compressive strengths, and in-plane shear strength of the graphite/epoxy unidirectional single ply and 16-ply composite laminate were found in Ref. [4]. Based upon these experimental results (mean values) for the ply and laminate properties, the mean values of constituent material properties (fiber and matrix) were estimated. The statistical properties (mean value, scatter, and distribution type) of the uncertain variables are listed in TABLE I. Typical probabilistic material properties for ply and laminate moduli and strengths were simulated. The sensitivities of the ply and laminate properties to the most sensitive uncertain variables were also computed at two cumulative probability levels, 0.001 and 0.999. All the cumulative distribution functions of the material properties at ply and laminate scales were compared with the results predicted by a Monte Carlo simulation with 1000 samples. Good agreement was observed.

The cumulative distribution functions (cdf) of the ply moduli and the sensitivity information are shown in Figures 3 to 5. In each figure, the experimental datum (mean value) is indicated by an arrow. In Figure 3, it was found that the ply modulus in the fiber direction is most sensitive to the fiber modulus and fiber volume ratio. This means that the reduction of the scatter in the ply modulus can be achieved mostly by the reduction of the scatter in the fiber modulus and fiber volume ratio. In Figure 4, it was found that the shear modulus of matrix and fiber volume ratio have the most contribution in the scatter of the ply in-plane shear modulus. The scatter in the ply major Poisson's ratio resulted mainly from the scatters in the fiber and matrix Poisson's ratios and the fiber volume ratio as shown in Figure 5. The probabilistic tensile strength in the fiber direction is simulated and shown in Figure 6. From the simulation, the probabilistic tensile strength is most sensitive to the uncertain fiber tensile strength and fiber volume ratio.

The cumulative distribution functions (cdf) of the laminate moduli and their sensitivities to the uncertain variables are shown in Figures 7 to 9. It is found that both the modulus in the X direction and the in-plane shear modulus are sensitive to the uncertain fiber modulus and fiber volume ratio as shown in Figures 7 and 8. In Figure 9, the scatter in the major Poisson's ratio is from the scatters in fiber modulus, fiber

volume ratio, fiber and matrix Poisson ratio, matrix shear modulus and ply misalignment. The laminate tensile strength in the X direction is predicted by both first ply failure mode and fiber fracture mode as shown in Figure 10, using the ply strengths predicted previously. It is shown that neither scatter predicted by these two criteria covers the experimental scatter. However, the experimental scatter falls between the scatter domain predicted by both failure criteria. It indicates that the actual failure mode is a combination of the two analytical failure modes. From the sensitivity analysis, the tensile strength predicted by first ply failure mode is most sensitive to the fiber modulus and matrix tensile strength. On the other hand, the tensile strength predicted by fiber fracture mode is most sensitive to fiber tensile strength and fiber volume ratio.

CONCLUDING REMARKS

A methodology has been developed to accurately and efficiently simulate the scatter in composite material properties at all composite scales considering the uncertainties in all variables describing the composite material behavior (constituent material properties and fabrication variables). This methodology, integrating the probabilistic concepts in conjunction with composite mechanics, has been implemented into the computer code PICAN. The accuracy and efficiency of the present methodology was demonstrated by comparison with the Monte Carlo simulation method. The scatter in ply and laminate properties was quantified. The sensitivity of the material property to each uncertain variable at the constituent and ply scales was computed. This information can be used as a guide to increase the structural reliability or to reduce the cost. Furthermore, the probabilistic structural analysis and risk assessment can be performed once the uncertain ply and laminate properties are computationally simulated.

REFERENCES

1. Shiao, M.C. and C.C. Chamis, 1991. "Probabilistic Evaluation of Fuselage-Type Composite Structures", in Proceedings of 9th DoD/NASA/FAA Conference on Fibrous Composite.

2. Murthy, P.L.N. and C.C. Chamis, 1986. "Integrated Composite Analyzer (ICAN), Users and Programmers Manual." NASA TP 2515.

3. Wu, Y.T., 1985. "Demonstration of a New, Fast Probability Integration Method for Reliability Analysis," in Advances in Aerospace Structural Analysis, O.H. Burnside and C.H. Parr, ed., ASME, New York, pp. 63-73.

4. Chamis, C.C., R.F. Lark, and J.H. Sinclair, 1978. "Integrated Theory for Predicting the Hygrothermomechanical Response of Advanced Composite Structural Components," ASTM STP-658, pp. 160-192.

TABLE I- STATISTICAL PROPERTIES OF PRIMITIVE VARIABLES

Uncertain Variables	Mean Value	Scatter	Distribution Type
Fiber:			
Normal modulus E_{f11}	32 mpsi	8%	Normal
Normal modulus E_{f22}	3 mpsi	8%	Normal
Poisson's ratio v_{12}	0.23	8%	Normal
Poisson's ratio v_{23}	0.25	8%	Normal
Shear modulus G_{f12}	2.5 mpsi	8%	Normal
Shear modulus G_{f23}	2.5 mpsi	8%	Normal
Tensile strength S_{fT}	400 ksi	8%	Weibull
Compressive strength S_{fC}	400 ksi	8%	Weibull
Matrix:			
Normal modulus E_m	0.45 mpsi	8%	Normal
Poisson's ratio v_m	0.41	8%	Normal
Tensile strength S_{mT}	6.7 ksi	8%	Weibull
Compressive strength S_{mC}	39 ksi	8%	Weibull
Shear strength S_{mS}	8.9 ksi	8%	Weibull
Fabrication Variables:			
Fiber volume ratio:	60%	8%	Normal
Void volume ratio:	0.01%	8%	Normal
Ply thickness:	0.0055 in.	5%	Normal
Ply misalignment:	0	$0.9°$	Normal
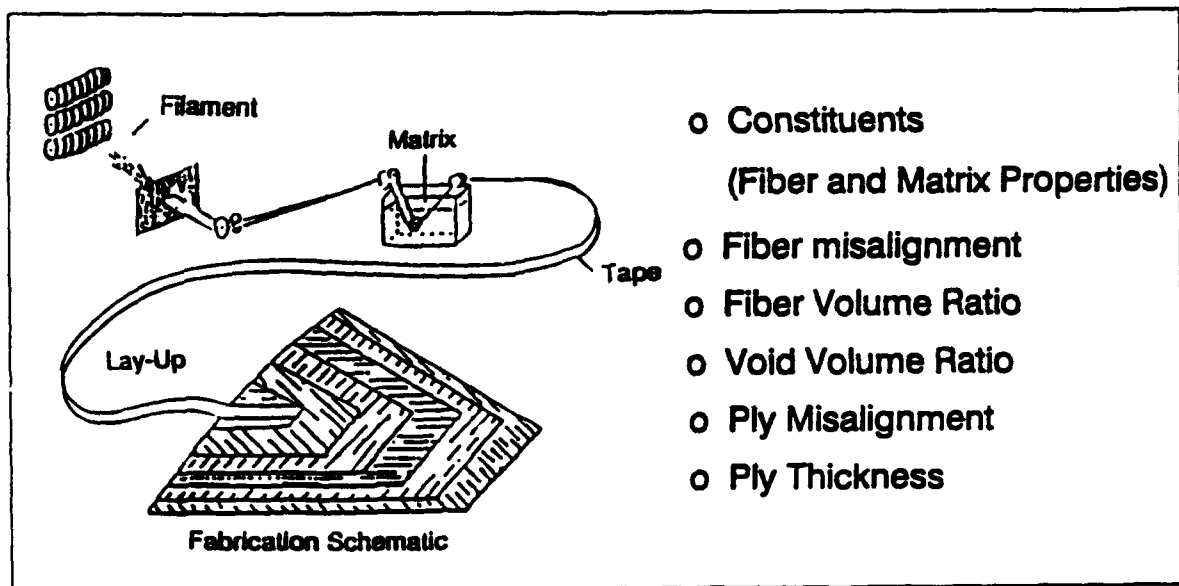
Figure 1. Source of Scatter - Uncertain variables
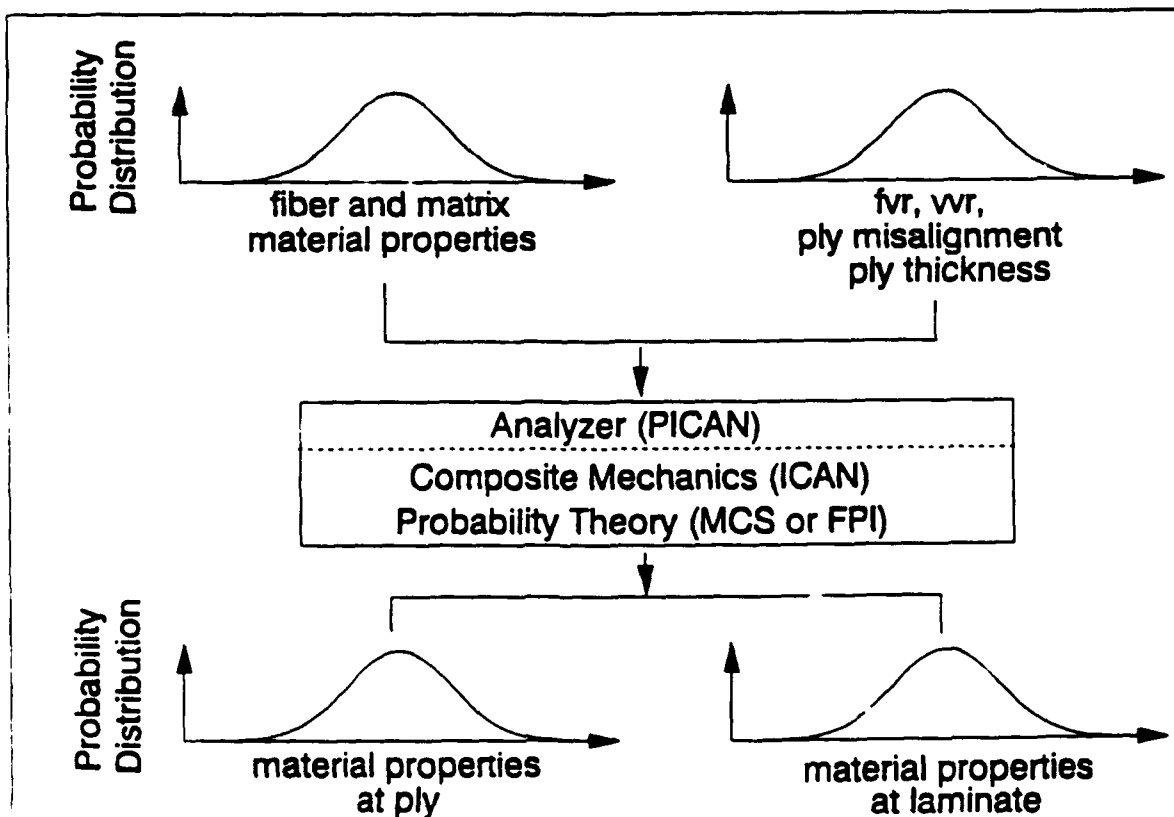
Figure 2. Probabilistic Simulation of Composite Materials
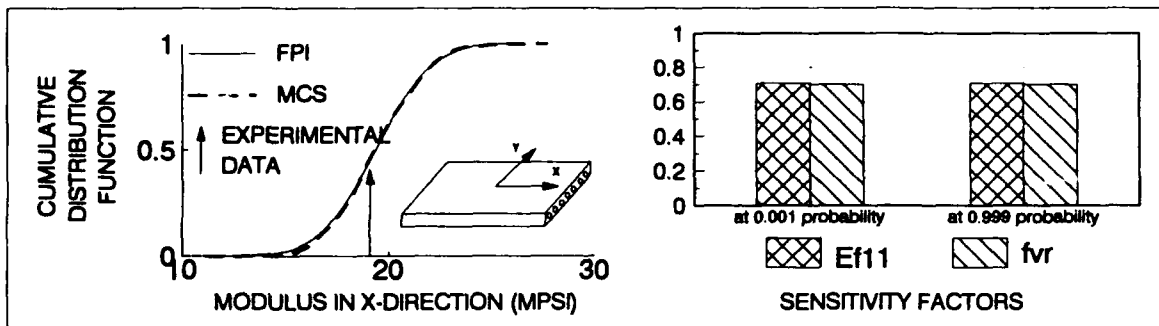
Figure 3. CDF's and Sensitivity Factors of Ply Modulus in X-Direction
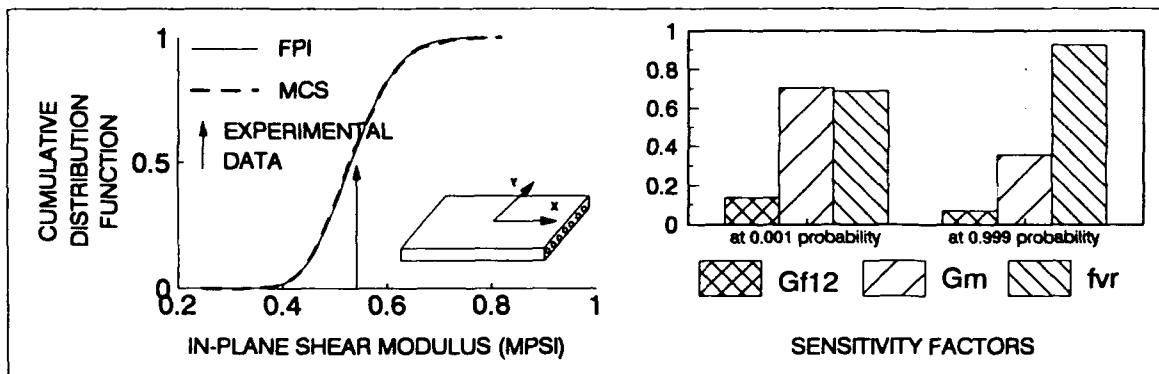
Figure 4. CDF's and Sensitivity Factors of Ply In-Plane Shear Modulus
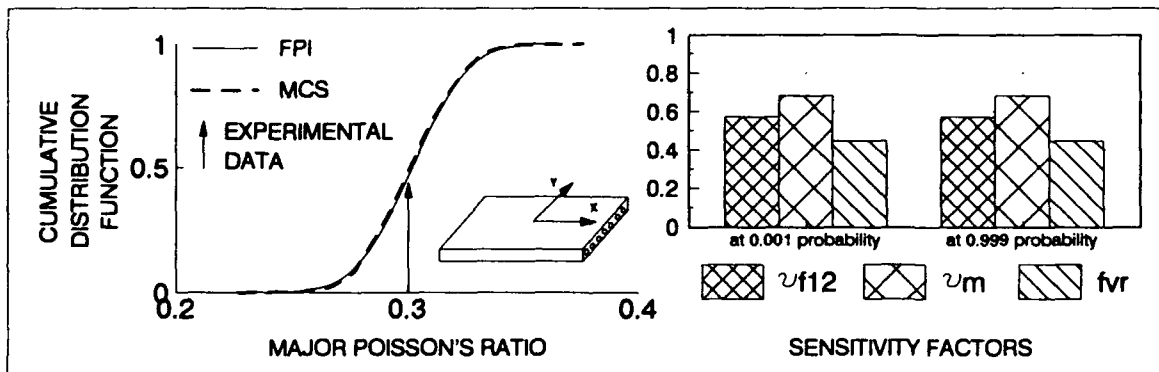
Figure 5. CDF's and Sensitivity Factors of Ply Major Poisson's Ratio
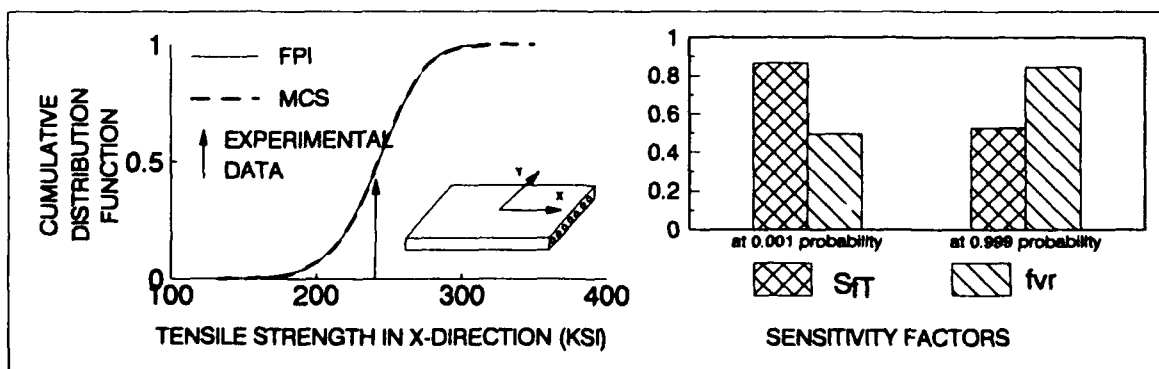
Figure 6. CDF's and Sensitivity Factors of Ply Tensile Strength in X-Direction

311
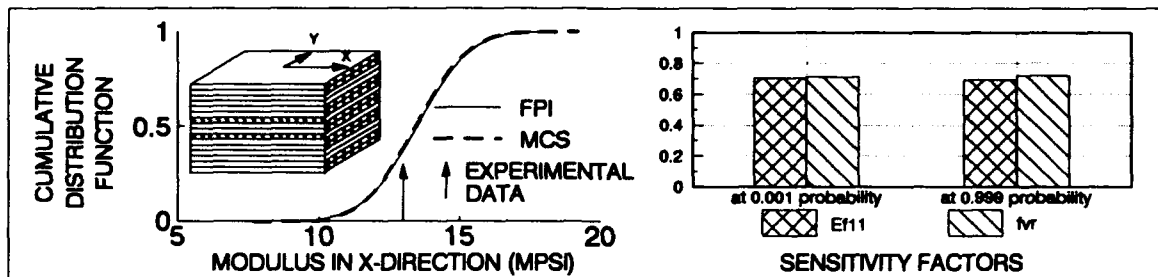
Figure 7. CDF's and Sensitivity Factors of Laminate Modulus in X-Direction
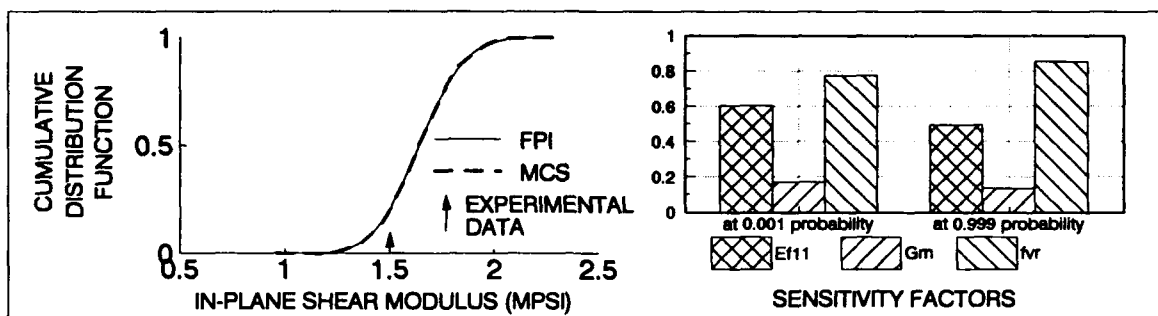
Figure 8. CDF's and Sensitivity Factors of Laminate In-Plane Shear Modulus
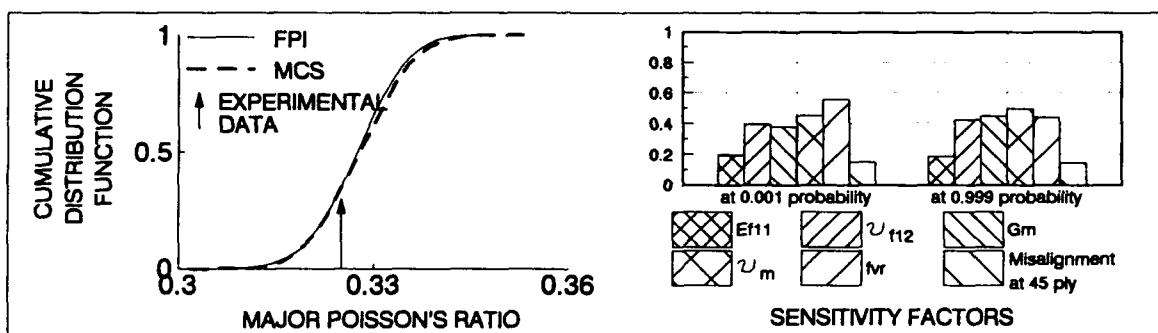
Figure 9. CDF's and Sensitivity Factors of Laminate Major Poisson's Ratio
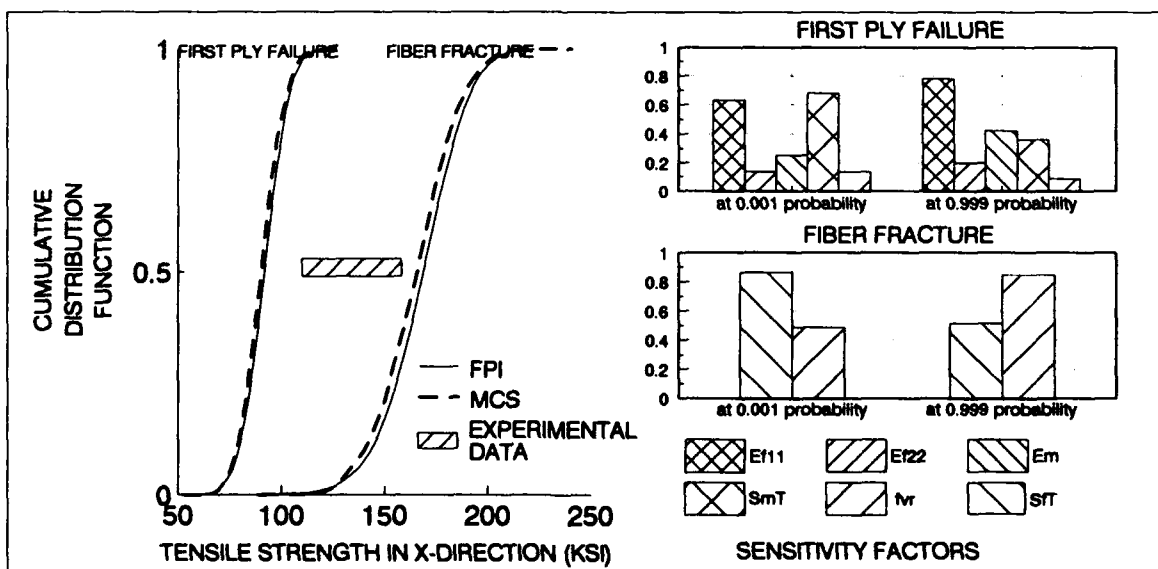
Figure 10. CDF's and Sensitivity Factors of Laminate Tensile Strength in X-Direction

312

Modeling Creep in Thermoplastic Composites

ILSUP CHUNG, C. T. SUN AND I. Y. CHANG

Abstract

A creep model for unidirectionally reinforced fiber composites was developed based on a one-parameter potential function. The same potential function was used to describe plastic flow and time-dependent creep deformation. The material constants in the model were determined by using the uniaxial tension test of off-axis coupon specimens. In terms of effective stress and effective creep strain, the anisotropic creep behavior can be given by a stress-dependent master creep curve irrespective of loading direction relative to fiber orientation. Du Pont's AS4/PEKK thermoplastic composites were used in the creep experiment.

Introduction

Creep is a phenomenon in materials that deform continuously under a constant stress. This material behavior is often more pronounced at high stresses and temperatures. In advanced fiber composites, the fiber is usually regarded as linearly elastic and does not creep. Thus, the observed creep behavior in composites originates from the matrix. In contrast to isotropic materials, composites, which are anisotropic, require characterizing creep behaviors in different directions relative to the fibers. There have been attempts to extend creep laws for isotropic materials to composite materials. Some of these works employed creep laws for the constituents to model the creep of the composite. Min and Crossman [1] employed the generalized Bailey-Norton law for aluminum matrix graphite fiber composite by micromechanical models. Lilholt [2] suggested modeling constant creep strain rates for various fiber orientations or loading directions. The authors as Brinson [3] and Schapery [4], used theory of viscoelasticity to describe creep of composites.

* Ilsup Chung and C. T. Sun, School of Aeronautics and Astronautics, Purdue University, West Lafayette, IN 47907-1282.

* I.Y. Chang, E.I.du Pont de Nemours & Co., Inc. Composite Division Wilmington, DE 19880-0702

It has been found that creep deformation shows similarities to plastic deformation. Consequently, the classical creep theory has closely followed the development of plasticity theories. By the same token, in this study, a creep theory based on a one-parameter potential function proposed by Sun et al [5,6] to model plastic behaviors in fiber composites is utilized to characterize the primary and steady creep of AS4/PEKK thermoplastic composites.

Experiment

The material system tested was Du Pont's PEKK-based thermoplastic composite reinforced with continuous AS4 graphite fibers. Off-axis creep specimens were cut from unidirectional composite panels by using a water cooled diamond saw. The fiber orientations of the specimens were $15°$, $30°$, $45°$, and $90°$. The nominal size of each specimen was 254 mm long, 20.3 mm wide, and 1.14 mm thick. A Micromeasurement EA-13-125AC-350 strain gage was mounted on the center of each specimen along the loading direction by using AE-610 adhesive.

Creep tests were conducted at $120°C$ using the lever arm tester made by Applied Test Systems. This load frame has a dual lever ratio of 3:1 and 20:1, with a maximum load of 53 MN (12000 lb). Several levels of load below failure strength were applied, and the variation of strain was recorded versus time. The time taken to lift the dead weights up to the designated position was about 20 seconds, which is quite short compared with the whole creep testing period of 24 hours.

Figures 1 show the experimental creep curves for the off-axis specimens. It was found that the amount of creep strain is appreciable compared with the initial deformation. After a transitional period, during which the creep strain rate decreases, the creep curves seem to reach a steady state with an almost constant creep strain rate. The steady creep strain rate in the following sections means the gradient of creep curves during the last 10 hours of the 24 hour testing period. The time-varying values of initial "instantaneous" strains are not discernible with the time scale shown in these figures, because the deformation progressed very fast in the beginning stage. However, a closer view of the initial portion of the creep curve in an expanded time scale would show distinct changes in creep strain rate before and after the complete application of the desired load. Henceforth, the strain which occurred during load application is referred to as the initial strain and is not included as part of the creep strain.

Creep Model

The strains resulting from application of a constant stress consist of time-independent initial strains and time-dependent creep strains. In the incremental formulation, we have

$$d\varepsilon_{ij} = d\varepsilon_{ij}^e + d\varepsilon_{ij}^p + d\varepsilon_{ij}^c \tag{1}$$

where the elastic strains ε_{ij}^e and plastic strains ε_{ij}^p are assumed to occur instantaneously as the load is applied, and ε_{ij}^c are creep strains.

In the present study, attention is focussed on the modeling of creep strains. To model the creep deformation, a potential function is proposed as

$$2f = \sigma_{22}^2 + 2a_{66}\sigma_{12}^2 \tag{2}$$

where 1 and 2 represent fiber and transverse directions, respectively. This function has been successfully employed to describe plastic behaviors of fibrous composites [5,6]. The parameter a_{66} is the only unknown orthotropy parameter to be determined experimentally.

The associated flow rule gives the creep constitutive equations

$$\dot{\varepsilon}_{ij}^c = \frac{\partial f}{\partial \sigma_{ij}} \dot{\lambda} \quad \text{or} \quad \begin{Bmatrix} \dot{\varepsilon}_{11}^c \\ \dot{\varepsilon}_{22}^c \\ \dot{\gamma}_{12}^c \end{Bmatrix} = \begin{Bmatrix} 0 \\ \sigma_{22} \\ 2a_{66}\sigma_{12} \end{Bmatrix} \dot{\lambda} \tag{3}$$

where $\dot{\lambda}$ is a proportionality factor. It is evident that according to this potential function, the creep strain rate in the fiber direction vanishes. This assumption agrees with the experimental result [7].

In order to model the multiaxial state of stresses using uniaxial experimental data, it is essential to employ the concept of effective stress and effective creep strain rate. In a similar way to the development in plasticity, the effective stress is defined as

$$\bar{\sigma} = \sqrt{3f} = \left[\frac{3}{2}(\sigma_{22}^2 + 2a_{66}\sigma_{12}^2) \right]^{1/2} \tag{4}$$

The corresponding effective creep strain rate can be defined by introducing the rate of work done, i.e., $\dot{W} = \bar{\sigma}\bar{\varepsilon}^c$. By using the creep law in equation (3) and the definition of effective stress, the effective creep strain rate can be expressed as

$$\bar{\dot{\varepsilon}}^c = \frac{\dot{W}}{\bar{\sigma}} = \frac{\sigma_{ij}\dot{\varepsilon}_{ij}^c}{\bar{\sigma}} = \frac{2f\dot{\lambda}}{\bar{\sigma}} = \frac{2}{3}\bar{\sigma}\dot{\lambda} \tag{5}$$

From equation (3) we have

$$\dot{\lambda} = \frac{\dot{\varepsilon}_{22}^c}{\sigma_{22}} = \frac{\dot{\gamma}_{12}^c}{2a_{66}\sigma_{12}} \tag{6}$$

When equation (6) is substituted in equation (5) in conjunction with the definition of effective stress, the effective creep strain rate becomes

$$\bar{\dot{\varepsilon}}^c = \left[\frac{2}{3}(\dot{\varepsilon}_{22}^c{}^2 + \frac{\dot{\gamma}_{12}^c{}^2}{2a_{66}}) \right]^{1/2} \tag{7}$$

Parameter a_{66} represents the orthotropic characteristics of the material system. The proper selection of a_{66} and the corresponding transformation of stress and creep strain rate into effective stress and strain domain should yield a unique creep law irrespective of fiber orientation. This condition will be imposed on the off-axis test data to determine a_{66} later.

A number of creep laws have been proposed for isotropic materials in various forms. These laws were generalized into the multiaxial case by replacing the uniaxial stress and strain with their effective multiaxial counterparts [8]. The same procedure is adopted here for the composite material by using the effective quantities defined in equations (4) and (7).

The creep law proposed in this study is

$$\bar{\varepsilon}^c = f_1(\bar{\sigma}) (1 - \exp[-f_2(\bar{\sigma})t^s]) + f_3(\bar{\sigma}) t \tag{8}$$

In the above equation, the first term represents the primary creep deformation. The value of this term varies from zero to a stress dependent value $f_1(\bar{\sigma})$ with vanishing strain rate in relatively short period. Generally, the shape of the primary creep curve depends on applied

stress as well as the functional form in time. The function $f_2(\bar{\sigma})$ takes the influence of stress on the decreasing strain rate into account. The second term is for steady state creep where the creep strain rate is constant, which is described by function $f_3(\bar{\sigma})$.

After all the functions and parameters in equation (8) are determined, the proportionality factor λ can be determined by using equation (5). This completes the creep constitutive equations in equation (3).

The initial strain must be characterized to complete the creep model. It is assumed that the period for applying the load is short enough to neglect time dependent deformation, and that the corresponding strain is elastic-plastic. The one-parameter plasticity in [5] is employed for this purpose.

Evaluation of Parameters

The unknown functions and parameters are found by using off-axis uniaxial creep data. Let the x-axis be parallel to the uniaxial loading direction, which makes an angle θ with the fiber direction, or x_1-axis. The transformed stress components referring to the material principal directions (x_1, x_2) are substituted into equations (4) and (5) to obtain

$$\bar{\sigma} = h(\theta)\, \sigma_x, \qquad \bar{\dot{\epsilon}}^c = \frac{2}{3} h(\theta) \sigma_x \dot{\lambda} \tag{9}$$

where

$$h(\theta) = \sqrt{\frac{3}{2}} \left[\sin^4\theta + 2a_{66}\sin^2\theta\cos^2\theta \right]^{\frac{1}{2}} \tag{10}$$

From the coordinate transformation of creep strain rate components, we have

$$\dot{\epsilon}_x^c = \cos^2\theta\, \dot{\epsilon}_{11}^c + \sin^2\theta\, \dot{\epsilon}_{22}^c - \sin\theta\cos\theta\, \dot{\gamma}_{12}^c \tag{11}$$

where $\dot{\epsilon}_x^c$ is the creep strain rate measured in the loading direction. Substitution of equations (3) into equation (11) yields

$$\dot{\epsilon}_x^c = \frac{2}{3} h^2(\theta)\, \sigma_x\, \dot{\lambda} \tag{12}$$

Equations (11) and (14) give

$$\bar{\dot{\epsilon}}^c = \dot{\epsilon}_x^c / h(\theta) \tag{13}$$

Since the loading in the off-axis specimen is proportional, equation (13) can be integrated to give

$$\bar{\epsilon}^c = \epsilon_x^c / h(\theta) \tag{14}$$

Using the first equation of (9) and equation (14), the off-axis creep data can be transformed into effective domain, where the unknown functions $f_i(\bar{\sigma})$ (i = 1,2,3) in equation (8) are determined as follows.

The initial plastic strain is computed by subtracting the elastic strain from the measured initial strain. The elastic properties of AS4/PEKK reported in [6] are used in the required computation. Figure 2 (a) shows the initial strain versus applied stress for various off-axis specimens. According to the one- parameter plasticity [5], these data can be plotted in terms of effective stress versus effective plastic strain. Figure 2 (b) shows the result indicating that with $a_{66} = 1.6$ the data from different off-axis specimens collapse into a single $\bar{\sigma}$ versus $\bar{\epsilon}^p$ curve as expected from the plasticity model. This master curve is fitted into a power law as

$$\bar{\epsilon}^p = A\bar{\sigma}^n \tag{15}$$

The next step is to characterize the steady creep strain rate. The data of the off-axis specimens are shown in figure 2 (c), which were measured by linear regression on the last 10 hour period of creep curves. Again, these curves, when plotted in terms of effective stress and effective creep strain rate, all collapse more or less into a single curve with $a_{66} = 1.6$. As shown in figure 2 (d), a power law is used to fit the stress-dependent creep strain rate as

$$f_3(\overline{\sigma}) = \overline{\dot{\epsilon}}_{ss}^c = B\overline{\sigma}^{-m} \tag{16}$$

In a similar manner, the magnitude of primary creep, $f_1(\overline{\sigma})$, can be found. The magnitude of primary creep is estimated by subtracting the initial strain and the steady creep strain at the 24th hour from the total strain at that moment. The results are plotted in physical and effective domains in figures 2 (e), and 2 (f), respectively. It is evident that in the effective domain, a single curve for $f_1(\overline{\sigma})$ results and is fitted by the power law,

$$f_1(\overline{\sigma}) = \Delta\overline{\epsilon}_{pri}^c = C\overline{\sigma}^{-n} \tag{17}$$

In equation (17), it is found that the same exponent "n" as in equation (15) is suitable for fitting the data.

The time dependency of primary creep can be investigated by normalization with respect to the magnitude of primary creep $f_1(\overline{\sigma})$. The proposed functional form is

$$\frac{\overline{\epsilon}_{pri}^c}{f_1(\overline{\sigma})} = 1 - \exp\left[-f_2(\overline{\sigma})t^s\right] \tag{18}$$

As implied in this expression, the effective stress participates in determining the shape of the primary creep curve. If the function $f_2(\overline{\sigma})$ is assumed as

$$f_2(\overline{\sigma}) = D\overline{\sigma}^{-r} \tag{19}$$

the argument of the exponential function in equation (18) becomes $(\sigma^{-r/s}t)^s$. Thus, the primary creep data for all off-axis specimens would collapse into a single curve if $\overline{\epsilon}_{pri}$ is plotted versus the combined variable $\sigma^{-r/s}t$ with a proper choice of r/s. Figure 3 shows the normalized primary creep curves with r/s = 1.2 . The collapsed curve is then fitted into the functional form of equation (18) with the result s = 0.5 .

All the material parameters in the initial plasticity and creep models are listed in table 1. Now that all the functions $f_i(\overline{\sigma})$ (i = 1,2,3) and the related parameters in equation (8) are known, λ can be computed by equation (5), and then the creep constitutive equations (3) are also determined.

Comparison of Model with Experiments

By using the evaluated parameters, the creep strain of any off-axis specimen can be predicted. From equation (7) and equation (14), the longitudinal creep strain is given by

$$\epsilon_x^c = h(\theta)[f_1(\overline{\sigma})\,(1 - \exp[-f_2(\overline{\sigma})t^s]) + f_3(\overline{\sigma})\,t] \tag{20}$$

The total strain is the sum of the elastic-plastic strain, which can be described by one-parameter plasticity theory [5], and the creep strain, i.e.,

$$\epsilon_x = \frac{\sigma_x}{E_x} + h(\theta)A\overline{\sigma}^{-n} + h(\theta)[C\overline{\sigma}^{-n}(1 - \exp(-D\overline{\sigma}^{-r}t^s)) + B\overline{\sigma}^{-m}t] \tag{21}$$

in which the explicit forms for f_i's are used. It is interesting to note that the same value of the orthotropy parameter a_{66} is used in both plastic and creep potential functions. From the comparisons presented in figures 1, it is evident that the present creep model is quite adequate.

The transverse strain in the off-axis specimen under uniaxial loading can also be derived. From equations (3), (12), and appropriate coordinate transformation of stress and

strain rate components, the transverse creep strain rate can be obtained. The proportionality of loading permits the integration of this rate relation to compute transverse creep strain as

$$\varepsilon_y^c = \frac{(1-2a_{66})\cos^2\theta}{\sin^2\theta + 2a_{66}\cos^2\theta} \, \varepsilon_x^c \tag{22}$$

This equation shows that the lateral creep contraction in composites is a function of a_{66} and fiber orientation. The total transverse strain is then obtained by adding the initial elastic-plastic transverse strain on this.

The creep model whose parameters are evaluated based on constant load tests is then employed to predict the step-loading cases. In this study, so-called strain hardening formulation [9], in which the creep strain rate is the function of current creep strain and applied stress, is adopted. The model predictions for longitudinal and transverse strains are computed by using equations (21) and (22), respectively. Figures 4 (a) and (b) show the predictions and experimental data for 15° and 45° off-axis specimens subjected to a multi-step loading history.

Conclusion

A creep model for anisotropic fiber composites was developed based on a one-parameter potential function. The same potential function was used to describe the plastic flow and time-dependent creep deformation. The material constants associated with the model were determined by using the results of uniaxial testing of off-axis coupon specimens.

Du Pont's AS4/PEKK thermoplastic composites were used to experimentally verify the creep model. The results showed that the present creep model can be used to predict creep strains for general loading conditions as well as creep in laminates.

References

1. Min, B.K. and Crossman, F.W., 1982. "Analysis of Creep for Metal Matrix Composites." Journal of Composite Materials 16 : 188-203.

2. Lilholt, H., 1988. "Models for Creep of Fibrous Composite Materials." Materials Forum 11 : 133-139.

3. Brinson, H.F. and Dillard, D.A., 1982. "The Prediction of Long-Term Viscoelastic Properties of Fiber Reinforced Plastics," in Progress in Science and Engineering of Composites ICCM-IV Tokyo : Japan Society of Composite Materials, 795-801.

4. Lou, Y.C. and Schapery, R.A., 1971. "Viscoelastic Characterization of a Nonlinear Fiber-Reinforced Plastic." Journal of Composite Materials 5 : 208-234.

5. Sun, C.T. and Chen, J.L., 1989. "A Simple Flow Rule for Characterizing Nonlinear Behavior of Fiber Composites." Journal of Composite Materials 23 : 1009-1020.

6. Sun, C.T., Chung, I. and Chang, I.Y., 1992. "Modeling of Elastic-Plastic Behavior of LDF^{TM} and Continuous Fiber Reinforced AS4/PEKK Composites." Composite Science and Technology, 43 : 339-345.

7. Chung, I. and Sun, C.T., 1990. "Creep of PEKK-Based Composites with Long Discontinuous Fibers," CML Report 90-1, Purdue University.

8. Kraus, H., 1980. <u>Creep Analysis,</u> New York, NY: John Wiley & Sons, 18-45.

9. Pugh, C.E., 1975. "Constitutive Equations for Creep Analysis of LMFBR Components," in <u>Advances in Design for Elevated Temperature Environment ASME National Congress on Pressure Vessels and Piping,</u> San Francisco : ASME, 1-15.

TABLE 1. VALUES OF PARAMETERS (ϵ IN %, σ IN MPa)

a_{66}	A	B	C	D	m	n	r	s
1.6	1.03×10^{-9}	2.55×10^{-8}	3.38×10^{-9}	0.08	2.61	4.19	0.6	0.5
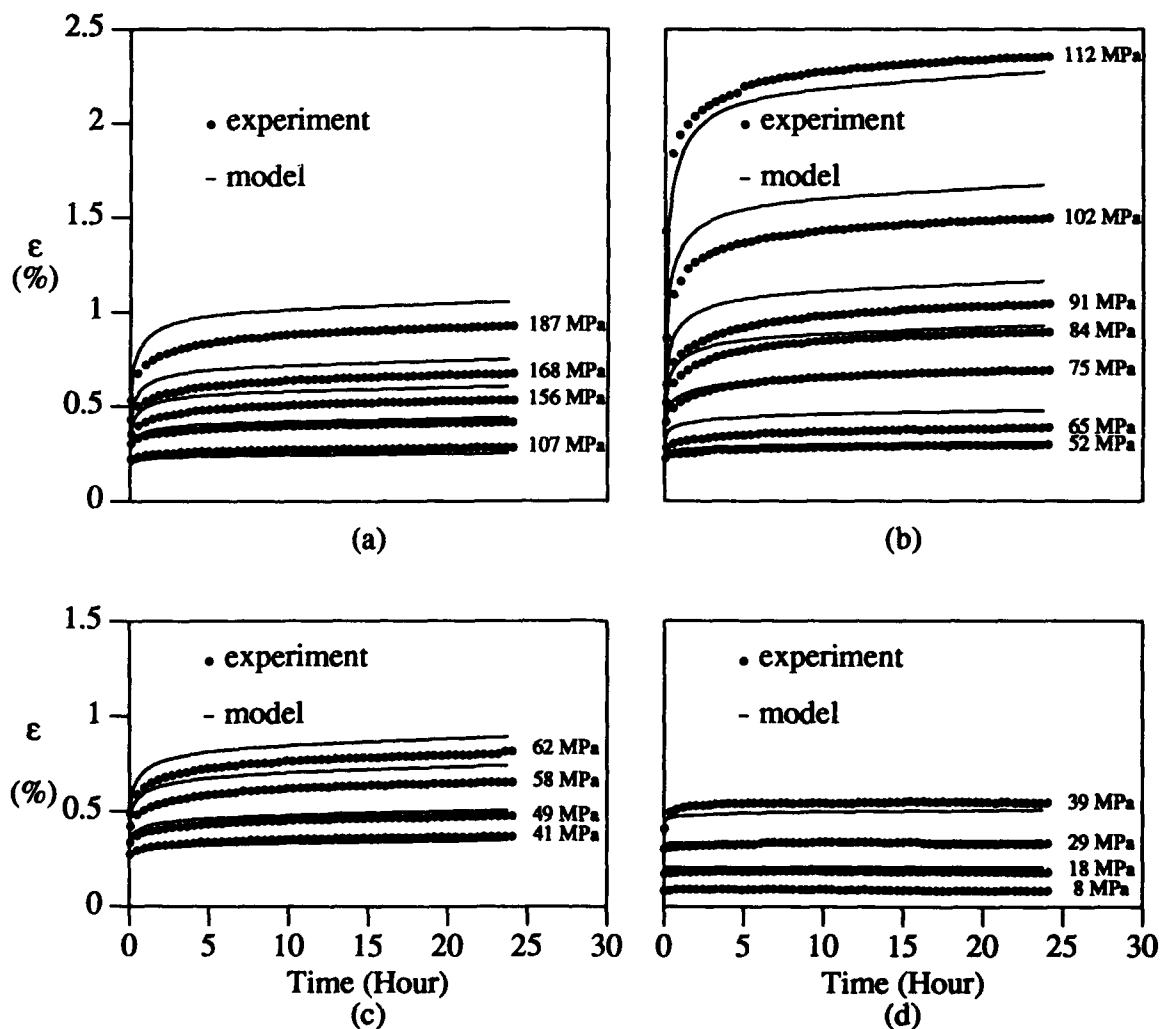
Figure 1. Creep curves at 120°C for off-axis continuous fiber specimens. (a) 15°, (b) 30°, (c) 45°, (d) 90°.
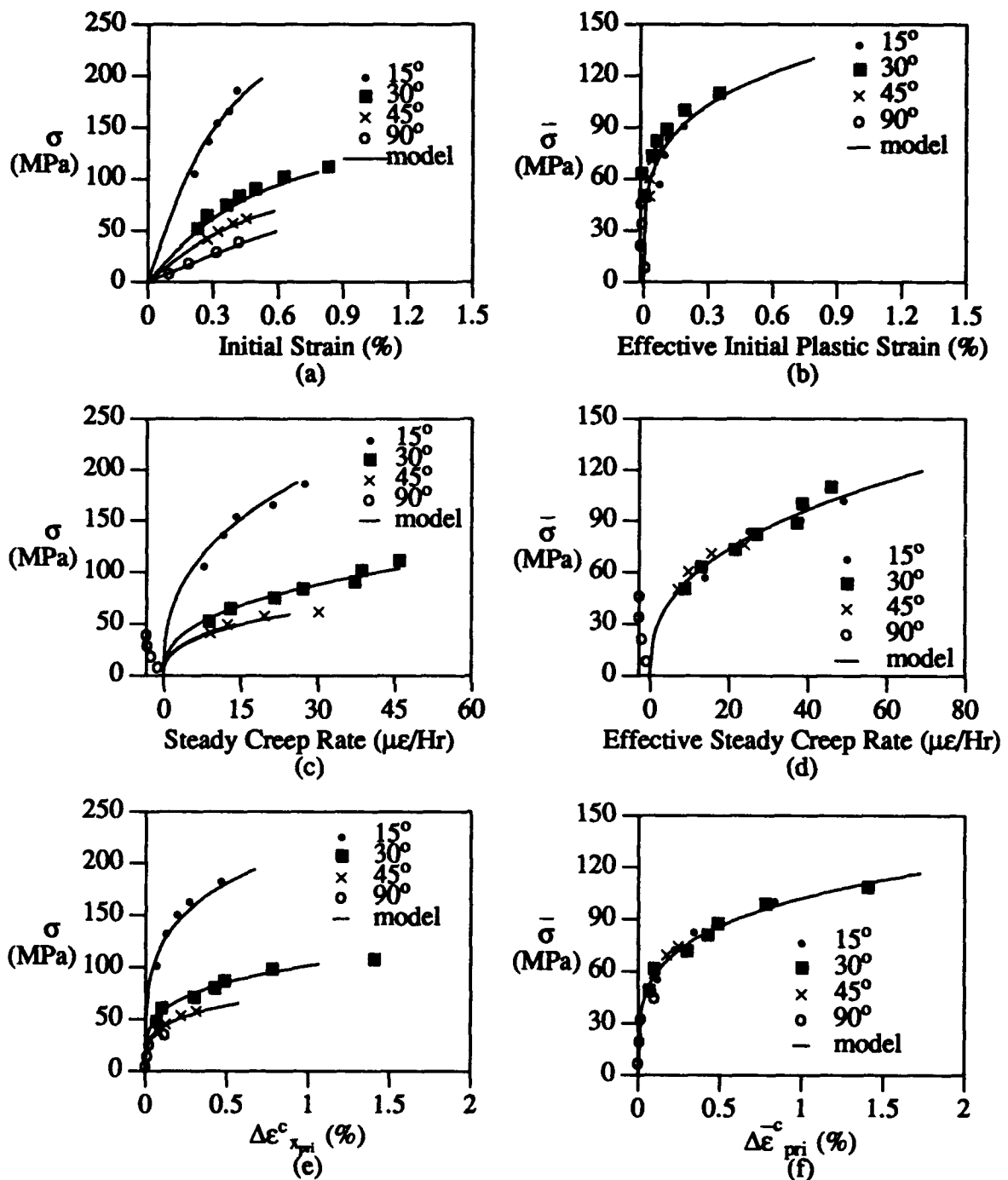
Figure 2. Determination of parameters: (a) initial strain of creep testing, (b) evaluating A and n, (c) steady creep strain rate, (d) evaluating B and m, (e) magnitude of primary creep strain, (f) evaluating C.
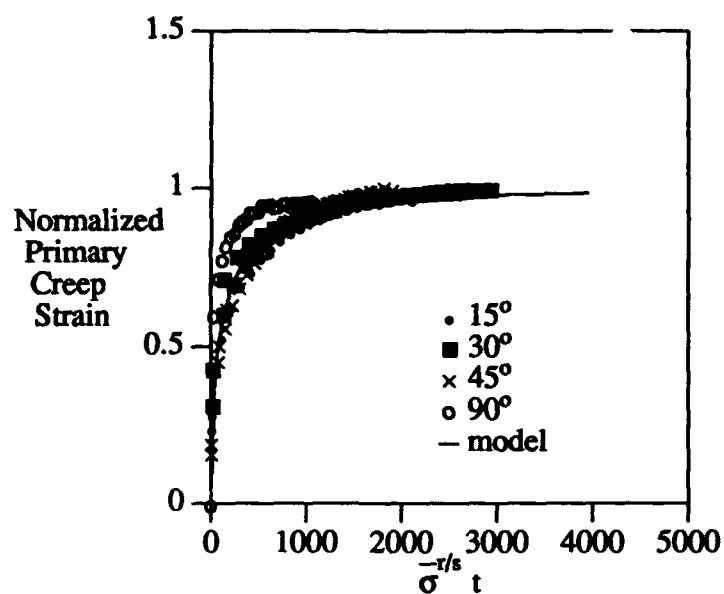
Figure 3. Normalized primary creep strain in effective time domain of continuous fiber specimens.
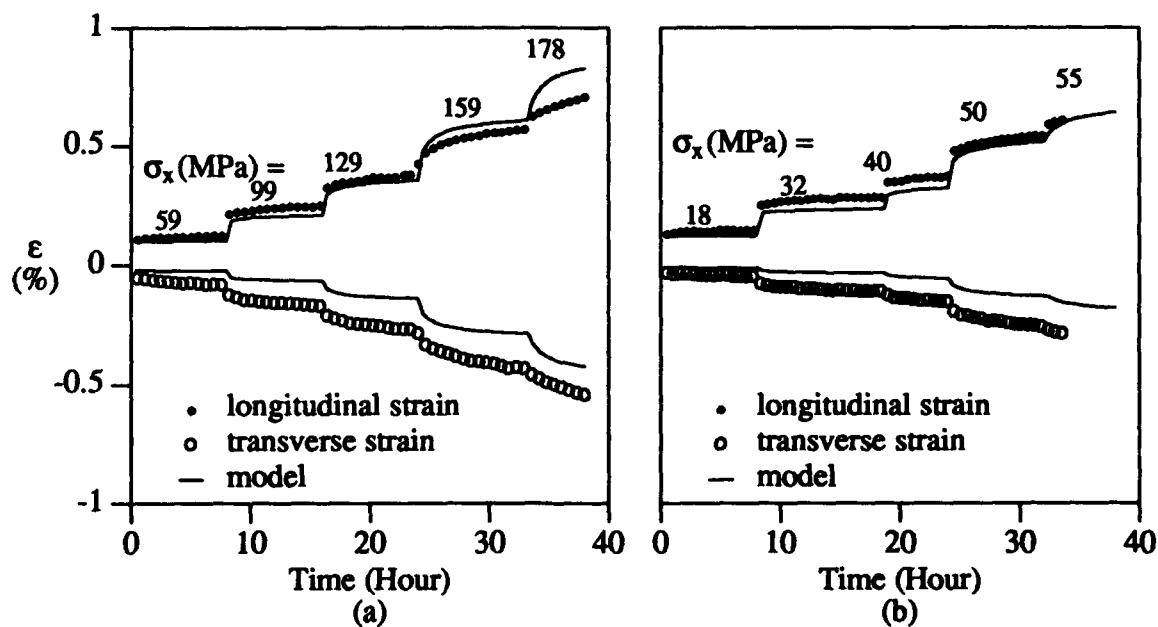
Figure 4. Comparison of model prediction with step loading experimental data. (a) 15°, (b) 45°.

Micromechanical Foundations
for Performance Simulations

K. L. REIFSNIDER AND YONGLI XU

ABSTRACT

Many applications involve long-term behavior such as creep and fatigue, especially for high performance composite components such as aerospace, energy, and power system elements. Since the understanding of such behavior is incomplete, we are ususlly faced with the need for extensive experimental characterization, at considerable cost. It would be desireable to have a rigorous method and methodology for bringing all of the pertinent data, understandings, and models together to predict the remaining strength and life of composite components (not just laboratory coupons) in the as-manufactured condition, and to extend this understanding to situations for which data are not available. Such a model must be constructed so that the engineer can use it to design engineering structures, and the designer of composite material systems must be able to use it to determine the influence of the synthesis, processing, and manufacturing parameters which can be altered to achieve the desired properties and performance. "Performance simulation" methods are one plausible answer to this problem, and the subject of this paper.

BACKGROUND

The construction of such a simulation must begin with the identification of the damage and failure modes which control long term behavior of composites under the service conditions expected. These damage and failure modes depend on the material system, and operating conditions, including the geometry of the component, and the nature of the applied stress, temperature, and environmental conditions.

A second requirement is the micro-analysis needed to properly determine the local stress state in the elements of material which control the remaining strength and life in the presence of degradation and damage (we will call these "critical elements"). This question must be asked for each distinct (generic) failure mode. Closely related to this part of the problem is the question of how to estimate strength if the micro-stress state is known. Phenomenological criteria such as the Tsai-Hill or generalized Mises conditions are not generally sufficiently

---

[1] Professor and Research Associate, respectively, Department of Engineering Science and Mechanics, Virginia Polytechnic Institute and State University, Blacksburg, VA 24061

sensitive to the details of the damage and failure process to make them useable for predictions; they may, of course, help to correlate data. Micromechanical strength models are preferred, since they can be constructed in a mechanistic way, and can be used to predict behavior for which data are not available.

A third part of the problem is the understanding the mechanisms and rates of degradation that are driven by environmental effects such as oxidation, corrosion, and erosion of ceramic composite components. Significant progress has been made in this area at the fundamental level, especially in the identification of mechanisms under carefully controlled conditions. However, establishing rates of action of these mechanisms for components exposed to elevated temperatures in combined aggressive environments has not been done, in many cases. As it happens, one of the greatest needs associated with this general problem is the determination of degradation rates for the material systems and conditions of interest.

Finally, it is critical to have a rigorous and systematic method of bringing together the knowledge of damage and failure modes (and their representations), the knowledge of degradation rates, and the information about how the CFCC materials were manufactured to predict remaining strength and life in terms of the history of applied mechanical, thermal, and chemical environments. This is the greatest current need, and an area that is quite inadequately addressed in existing literature. The present paper will address the use of micromechanics as foundation for the construction of performance simulation methods, and discuss an example of such a construction.

The Physical Problem

Figure 1 illustrates the physical problem to be considered. In Fig. 1(a), the relationship of global composite properties to the properties, geometry, and arrangement of the constituents, interfaces, and interphases is emphasized. Specifically, the stiffness and strength of a composite material is determined by the manner in which the composite is constructed.[1]

However, **performance** is concerned with the **behavior** of a material or material system during the application of long-term service conditions such as cyclic loading and thermal or chemical environments, i.e., with the **retention or change** in properties over that period. As Fig. 1(b) suggests, changes in properties can be traced to processes which alter the fundamental makeup of the composite, e.g., the properties, geometry, or arrangement of the constitutents, interfaces, or interphases. Microdefect initiation and growth changes geometry, chemical processes may cause constituent strength reduction, thermodynamic processes such as diffusion may cause stiffness or strength changes (aging, etc.), and unconservative deformation may cause geometry changes and stress concentrations (or relaxations) at the local level.

Generally, descriptions of the influence of these events are interpreted in terms of laminate behavior. For the "simple" case of matrix cracking in a multi-ply laminate, let us say that we can develop experimental information from which the changes in the stiffness of plies which crack during "service life"[2,3]. The experimental information (including the rate of cracking) can be used directly to define the channges in E_{ij} at the ply level. These

Properties of Constituents, Interfaces, Interphases

Global

Geometry and Arrangement

Composite

Properties

(a)

Time & repetition dependent Evolutional Processes

Microdefects Chemical Thermodynamic Unconservative deformation

Properties of Constituents, Interfaces, Interphases

Geometry and Arrangement

Remaining

Global

Composite

Properties

(b)
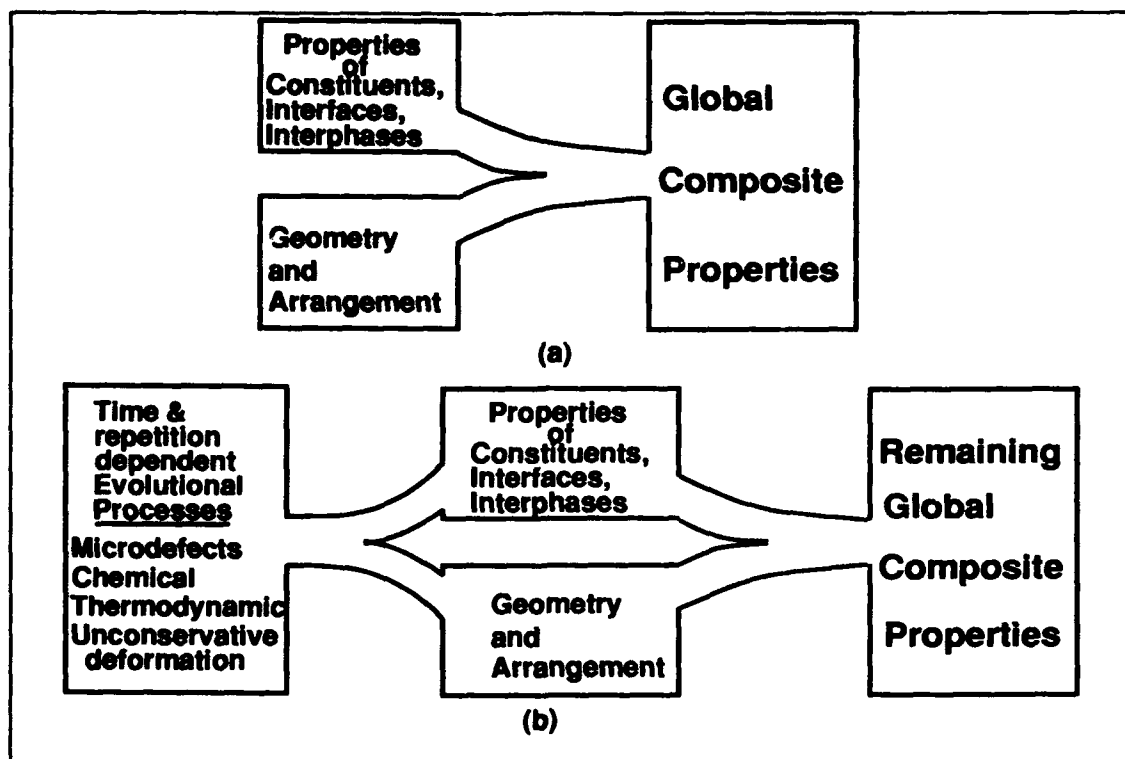
Figure 1 Physical processes to be represented with models.

quantities can, in turn, be used (in a laminate analysis or finite element analysis) to determine changes in the state of stress in the laminate, and the rate of those changes. However, the inherent strength (of the material) is not changed, since these cracks are not a failure mode if fibers are still bearing the applied load.

One class of evolutional processes may be the degradation of fibers, for example, by oxidation at elevated temperatures or other causes. This type of degradation may be characterized by such things as creep rupture data for unidirectional material (i.e., at the ply level). Recently, a representation of that type of degradation has been suggested by Reifsnider and Stinchcomb.[9] The form of the equation follows.

$$\sigma_r = (\sigma_{ult} - \sigma_{max}) \, [1 - (\frac{T(\log(t) + C)}{T_a(B - n\log(\sigma_{max}))})^y]^{1/x} + \sigma_{max} \tag{1}$$

in which σ_{ult} is the ultimate strength of the material, σ_{max} is the applied stress, T is temperature in degrees absolute, and B, C, n, y, and x are material constants.

Another type of evolution which influences remaining strength is viscoelastic stress redistribution. If the modulus of the matrix material changes due to viscoelastic creep, the internal stresses in a composite system change accordingly. In some cases, this type of change can be represented by correcting the matrix-dominated ply properties (E_2, G_{12}, v_{12}) in a manner defined by the relaxation rate of the matrix material involved[4].

Micromechanical Foundations
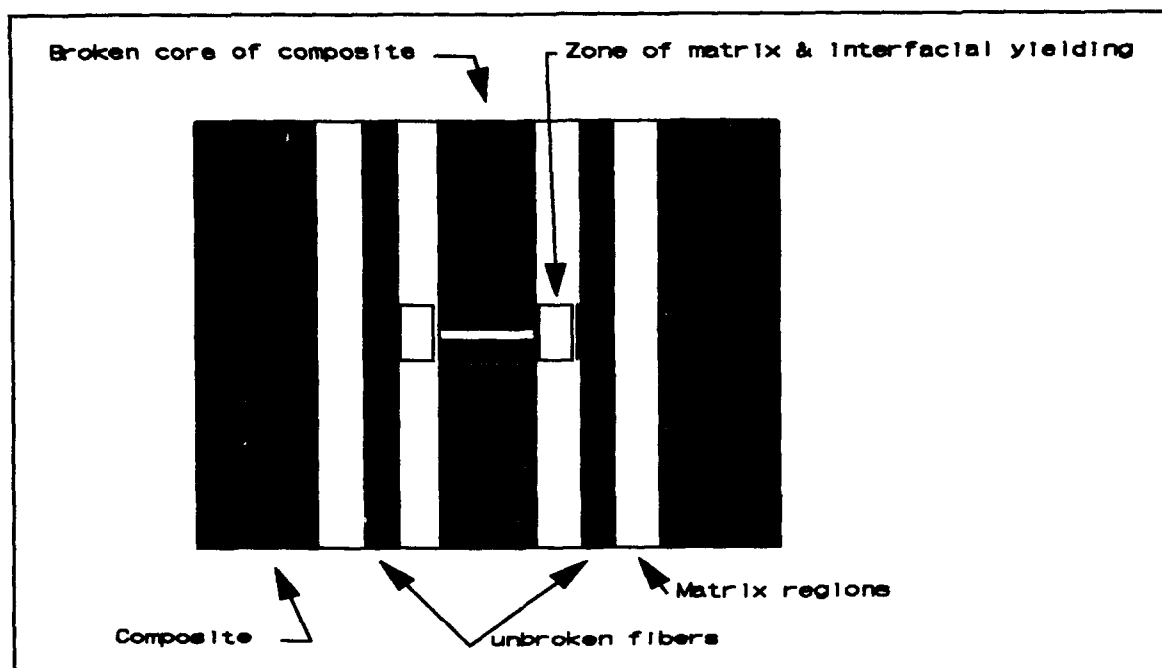
Figure 2 Schematic diagram of the micromechanical tensile strength model.

Ply level representations of the evolution of properties are not sufficient, and certainly not optimum for the discussion of the evolution of strength. The authors have shown that it is possible to represent ply-level strength strength in terms of fiber/interphase/matrix level micromechanics[5]. For example, the tensile strength in the direction of the fibers has been represented by a nonlinear boundary value problem, based on a elastic-plastic shear lag formulation in which the number of broken fibers is calculated as the local failure process progresses. The model includes a region of broken fibers, a region of matrix plasticity (or fiber/matrix slipping), and an outer region of elastic behavior. Fig. 2 is an indication of the manner in which the boundary value problem is set. This type of micormechanical representation has several distinct advantages. Since the properties of the fibers, matrix, and interphase regions enter the analysis directly, damage and material state changes can be directly entered into a calculation of the strength to estimate the strength evolution as a function of the behavior of the constituents and the interphases between them. Hence, this presents the opportunity to represent the manner in which material systems come apart in terms of the parameters which define how they are put together. This opens an entirely new vista of opportunity to design materials for specific behavior on the basis of such formulations.

Composite compressive strength has also been predicted, based on fiber microbuckling analysis using a beam-on-elastic-foundation model. The fiber buckling wavelength can be determined by applying the minimum buckling load condition, and the stiffness of the foundation is determined through an elasticity solution of a foundation model problem. An expression for the prediction is obtained as follows:

$$\sigma_{comp} = G_m[V_f + \frac{E_m}{E_f}(1-V_f)][2(1+v_m)\sqrt{\frac{\pi\sqrt{\pi}\eta r_f}{3\frac{E_m}{E_f}(V_f\frac{E_m}{E_f}+1-V_f)(1+V_f\eta r_f+v_m(1-V_f))}} + B(1-\xi-\frac{\sin\pi\xi}{2\pi})] \quad (2)$$

where $\xi = 2s/L$ (percentage of matrix slippage)[6]. From the expression, it is seen that for a given composite system, the possible factors affecting the composite compressive strength are fiber radius r_f, fiber volume fraction V_f, Young's moduli of constituents E_m and E_f, Poisson's ratios of constituents v_m and v_f, fiber debonding η(open mode debonding) and matrix slippage ξ(slide mode debonding). The last two factors are directly related to the interfacial strength of the composite.

Figure 3 illustrates the dependence of the compressive strength on the amount of slippage between the fiber and the matrix. This is clearly a very significant effect. In fact, the micromechanical formulation shows evidence that fiber matrix slippage has the largest single effect of any parameter that appears in the formulation, a key finding from the standpoint of composite material design.
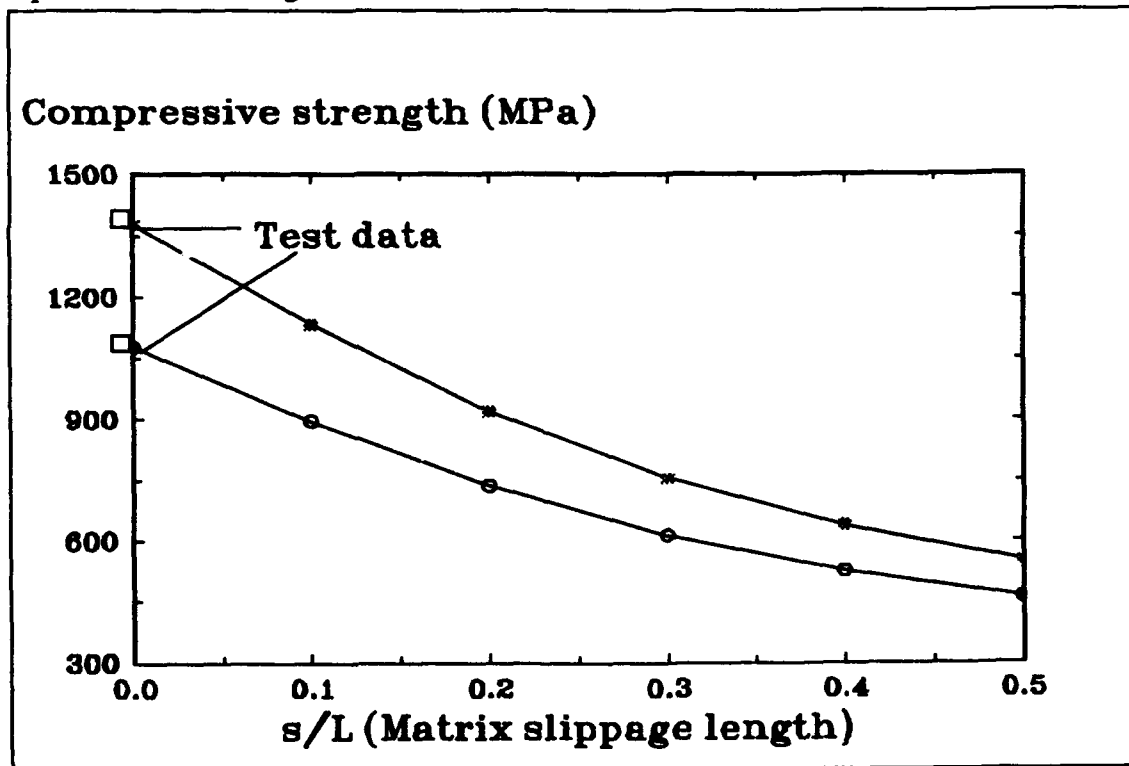
Figure 3   Effect of fiber-matrix slippage on the compressive strength of continuous fiber reinforced polymer matrix composite.

Simulation of Global Strength Evolution

The Materials Response Group has developed a performance simulation model and code series called MRLife which predicts remaining strength of laminates under combinations of cyclic and sustained loading, including such effects as viscoelastic creep, chemical attack,

creep rupture, and fatigue loading[7,8,9]. The code is based on interpretations of the parameters which appear in the micromechanics formulations discussed above. We introduce micromechanical representations of the primary (or principal) strengths (such as the two outlined above) into the model, so that performance can be "simulated" on a more mechanistic and basic level, in terms of the properties and performance of the constituents and their interfaces/interphases[5,6].

The authors have developed a simulation code series which uses the "critical element method" to combine these micromechanical representations of the state of stress and state of material, as well as the rate equations for environmental degradation and time dependent behavior to predict the remaining strength and life of composite materials. This code has shown considerable promise in the representation of combined fatigue - creep behavior[7,8,9].

In the present context, it has been found that the failure modes for many composite systems are defined by representative volumes that are quite small, often of the order of the dimensions of a single ply of a laminate, or comparable to the fiber diameters. If that is so, then, we must appeal to "micromechanics" to describe the state of stress and state of material in the representative volume[8], as we have discussed above.

Our problem, then, becomes the description of

$$F_a = F_a(\frac{\sigma_{ij}(n)}{X_{ij}(n)}) \; ; \; N = N(n) \; ; \; E_{ij} = E_{ij}(n) \tag{3}$$

which are the local normalized level of applied loading, the life (determined by the rate equation for the controlling degradation process) of the local element in the representative volume (at the ply level or at the constituent level, according to how our mechanics problem is set), and the inherent stiffness of the material (also defined at the appropriate level). It should be duely noted that all of these quantities are dependent on the processes discussed in Fig. 1. It should also be noted that in order to correctly represent the degradation of the quantities in equation 3, we must have considerable information about the rate of the processes that are damaging the material or material system.

In order to use the simulation scheme, we begin by identifying damage and failure modes of interest, as determined from careful laboratory investigations. Then, micromechanical modeling of strength, as described above, provides a representation of the observed failure modes. Micromechanical analysis is also used to establish the state of stress associated with local stress redistribution, such as the "shedding" of stress from plies which undergo matrix cracking. Since the micromechanical equations which represent global or ply-level strength in equation (1) are written in terms of the constituent properties (such as the stiffness and strength of the fiber, matrix, and interface or interphase region) and the local geometry (which controls the local stress state), the changes in these basic properties (which can be determined from independent experiments or from observations of the damage development process) or in the local geometry (due to cracking, debonding, etc. as determined from NDE measurements) can be used to calculate, directly, the changes in the global strength with history of loading. This is a true predictive capability, and can be used, not only to anticipate the performance of composites which have not actually been tested under conditions which

have not been applied to such materials in the laboratory, but the simulation can also be used to "design" composite material systems by determining the sensitivity of performance to the details of the constituents and their arrangements. Of course, since the micromechanical models are presently not complete or precise under many conditions, such predictions must be regarded as approximate, but the utility of the predictions is substantial.
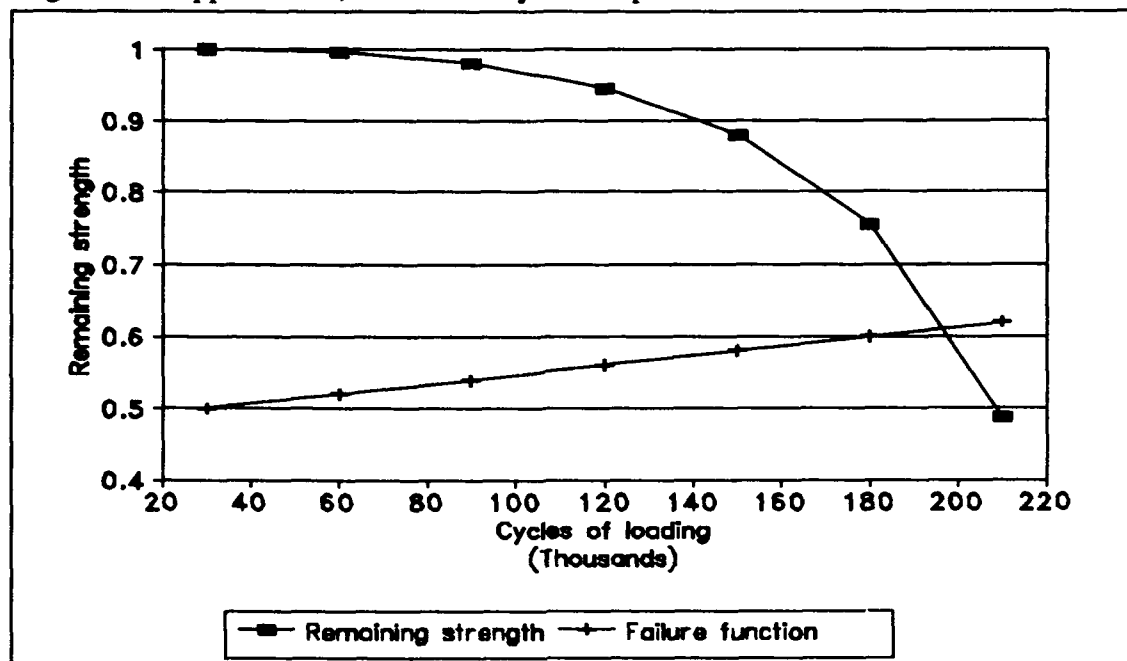
Figure 4   Simulation of the remaining strength of a graphite epoxy specimen subjected to tensile fatigue.

Fig. 4 shows an example of such a prediction. The figure shows the results of the calculation of the normalized failure function, F_a, for a loading that is (initially) about 50 percent of the strength of the laminate in tension (R=0.1). The laminate is symmetric with a stacking sequence of [0,45,0,-45,0]s. In the simulation shown, a representative volume of one ply thickness of the 0 degree ply is used for the analysis, and for this demonstration, only the fiber strength is degraded (as it might be by oxidation or chemical attack) to a very small value over one million cycles. The failure function increases by about 26 percent over the life of the specimen, which is reduced from 1.5 million to about 210 thousand cycles - about 14 percent of the baseline life. Also, the basic nature of the damage tolerance is altered by the fiber degradation; the remaining strength curve is relatively unchanged at the beginning of life, and drops off sharply near the end. For this example, the fiber degradation was taken to be linear with time, but the remaining strength is quite nonlinear. This is a good example of the type of information that can be gotten from a mechanistic simulation based on micromechanics (at the ply level in this case). Micromechanics at the fiber / matrix level adds additional dimensions to the simulation capabilities. Numerous other simulations can be made; some have been discussed in the literature[7-10].

Closure

The present paper suggests that micromechanics can be used to represent the changes in global composite properties and performance in terms of the changes in the constituents, the

interfaces and interphases between constituents, and the local geometry (as influenced by defect development). Moreover, micromechanical modeling can be used to represent progressive degradation processes, by allowing the properties of the constituents to change, or by changing the geometry at the local level. Since these constituent changes or local geometry changes can be measured directly and independently, the approach provides a sound and systematic method of representing, and in some cases predicting, the evolution of strength and life at the global level.

Acknowledgements

References

[1] Christensen, R.M., 1979. Mechanics of Composite Materials, New York: John Wiley & Sons.

[2] Reifsnider, K.L., Editor, 1991. Fatigue of Composite Materials, London: Elsevier Science Publishers.

[3] Reifsnider, K.L., Editor, 1982. Damage in Composite Materials, Philadelphia: ASTM STP 775, American Society for Testing and Materials.

[4] Dillard, D.A., 1991. "Viscoelastic Behavior of Laminated Composite Materials." in Fatigue of Composite Materials, K.L. Reifsnider, Ed., New York: Elsevier Science Pub., pp. 339-384.

[5] Gao, Z. and Reifsnider, K.L., 1991. "Micromechanics of Tensile Strength in Composite Systems," in Proc. Fourth Symp. on Composite Materials: Fatigue and Fracture, Indianapolis, IN: ASTM, (in press).

[6] Xu, Y. and Reifsnider, K.L., 1992. "Micromechanical Modeling of Composite Compressive Strength," submitted to J. Composite Materials.

[7] Reifsnider K.L. and Stinchcomb, W.W., 1986. "A Critical Element Model of the Residual Strength and Life of Fatigue-loaded Composite Coupons, in Composite Materials:Fatigue and Fracture, ASTM STP 907, H.T. Hahn, Ed., Philadelphia: Am. Soc. for Testing & Materials, pp.298-313.

[8] Reifsnider, K.L., 1991. "Performance Simulation of Polymer-based Composite Systems, in Durability of Polymer-Based Composite Systems for Structural Applications, A.H. Cardon & G. Verchery, Eds., New York: Elsevier Applied Science, pp.3-26.

[9] Reifsnider, K.L., 1992. "Use of Mechanistic Life Prediction Methods for the Design of Damage Tolerant Composite Material Systems," in ASTM STP 1157, M.R. Mitchell & O. Buck Eds., Philadelphia: American Society for Testing and Materials, pp.205-223.

[10] Reifsnider K.L. and Gao, Z., 1991. "Micromechanical Concepts for the Estimation of Property Evolution and Remaining Life," in Proc. Intl. Conf. on Spacecraft Structures and Mechanical Testing, Noordwijk, the Netherlands, 24-26 April 1991: (ESA SP-321, Oct. 1991) pp.653-657.

Postbuckling Behavior of AS4/J1 Thermoplastic-Matrix Composite Panel in Viscoelastic Creep Range

YUICHI NAKAJO

ABSTRACT

Above-critical behavior of AS4/J1 unidirectional thermoplastic-matrix composite panel at elevated temperature is analyzed taking time-dependency into consideration. The previously proposed curve-fitting technology is improved to double the fitting time span and accuracy. Constitutive equations obtained at present can express the properties of the composite in exponential series forms for the same length of time range obtained by the experiment[1] i.e., fifteen decades in log scale. The constitutive equations are used in the viscoelastic creep postbuckling analysis to derive explicit solutions adopting the correspondence principle and analytical inverse Laplace transformation.

1. INTRODUCTION.

The advanced structural applications of high-performance thermoplastic-matrix composites such as AS4/J1 requires accurate analyses and clear understanding of the above-critical behavior as well as critical behavior as structural elements.

In the previous study[2] fundamental creep buckling behaviors of the composite laminates are investigated as time-dependent bifurcation buckling adopting the correspondence principle. In another publication, viscoelastic creep postbuckling behavior of the same composite is studied by numerically integrating an indicial response (Duhamel integration)[3]. Both analyses are based on the numerical calculations to overcome the difficulty of inverse Laplace transformation of the complex expressions.

The major improvements in the present paper are; (1) modified curve-fitting which surpasses the previous fitting both in length of time range and in accuracy, and (2) creep postbuckling analysis adopting the analytical Laplace transformation and inverse Laplace transformation. To transform the equations efficiently and to verify the results definitely, a formula manipulation language is used throughoutthe calculations. From the results, validity to use the dedicated formula manipulation language as assistance deriving viscoelastic solutions is shown.

2. ANALYSIS.

2.1 Viscoelastic Constitutive Equation.

Firstly, experimental data of creep compliances are fit into the generalized Voigt model using the sequential unconstrained minimization technique (SUMT) similarly to the previous study. The difference which brought the present improvement are (1) intelligent selection of initial values, and (2) imposition of logarithmic contribution on the correction vectors for the

Yuichi Nakajo, Ashikaga Institute of Technology, 268 Omae-cho,Ashikaga City, Tochigi Pref. 326 JAPAN

coefficients of time. The previous study unveiled the difficulty in choosing the initial values of the design valuables. Because the time range to be fit is uniquely governed by the number of terms in exponential series (Prony series), the more number of terms are used, the longer and better curve-fitting is attained. During the iterative calculation, however, overflow and underflow prevent the precise evaluation of correction vectors and in the worst case, several design valuables head for single value and therefore the advantage to use many terms is lost as a result. To overcome this problem, design valuables in the exponential functions are modified in exponential form as follows.

$$J = C_0 + \sum_{i=1}^{N} C_i \, Exp\left(-\frac{10^\tau}{10^{\gamma_i}}\right) \tag{1}$$

The second problem is appropriate selections of the initial values. Starting from ill-natured initial values cause not only delay in reaching to proper curve but also a poor curve-fitting trapped in a local minimum. By starting the iteration from good-natured initial values, this problem can be avoided. Each term in the generalized Voigt model has an exponential form. By expressing each term in log scale, and by shifting the terms carefully, an almost straight line can be composed and this makes an ideal initial configuration of the design valuables. Figure 1 shows the experimental data and fitted exponential series.

2.2 Elastic Postbuckling Analysis.

Elastic postbuckling solution for simply supported orthotropic rectangular plates is obtained by reducing Von Karman type equation to infinite set of linear differential equations expanding the displacements in a power series of a perturbation parameter

Von Karman equation for large-displacement of orthotropic rectangular plates are shown below. The in-plane balance equations are

$$\partial N_x/\partial x + \partial N_{xy}/\partial y = 0$$

$$\partial N_{xy}/\partial x + \partial N_y/\partial y = 0 \tag{2}$$

The compatibility equation is

$$D_x\frac{\partial^4 w}{\partial x^4} + 2(D_{xy} + 2D_s)\frac{\partial^4 w}{\partial x^2 \partial y^2} + D_y\frac{\partial^4 w}{\partial y^4} + N_x\frac{\partial^2 w}{\partial x^2} + N_y\frac{\partial^2 w}{\partial y^2} + 2N_{xy}\frac{\partial^2 w}{\partial x \partial y} = 0 \tag{3}$$

The strain-membrane force relations are

$$N_x = \frac{E_x h}{1 - (E_x/E_y)\mu_y^2} (\varepsilon_x + \mu_y\varepsilon_y)$$

$$N_y = \frac{E_y h}{1 - (E_x/E_y)\mu_y^2} \left(\varepsilon_y + \mu_y \frac{E_x}{E_y} \varepsilon_x\right) \tag{4}$$

$$N_{xy} = Gh\gamma_{xy}$$

And the strain-displacement relations are

$$\varepsilon_x = \frac{\partial u}{\partial x} + \frac{1}{2}\left(\frac{\partial w}{\partial x}\right)^2$$

$$\varepsilon_y = \frac{\partial v}{\partial y} + \frac{1}{2}\left(\frac{\partial w}{\partial y}\right)^2 \tag{5}$$

$$\gamma_{xy} = \frac{\partial u}{\partial y} + \frac{\partial v}{\partial x} + \left(\frac{\partial w}{\partial x}\right)\left(\frac{\partial w}{\partial y}\right)$$

By assuming that the displacements u, v, and w can be expanded in a power series of perturbation parameter b as follows.

$$u = u_0 + \beta^2 u_2 + \beta^4 u_4 + \cdots,$$

$$v = v_0 + \beta^2 v_2 + \beta^4 v_4 + \cdots, \tag{6}$$

$$w = \beta w_1 + \beta^3 w_3 + \beta^5 w_5 + \cdots,$$

where

$$\beta^2 = (P - P_0)/P_0. \tag{7}$$

By substituting equations (6) and (4) into equations (5), following expansions for the forces are obtained.

$$N_x = \sum_{n=0,2,4,\cdots}^{\infty} N_{xn}\beta^n + \sum_{n=1,3,\cdots}^{\infty}\sum_{m=1,3,\cdots}^{\infty} N_{xnm}\beta^{m+n},$$

$$N_y = \sum_{n=0,2,4,\cdots}^{\infty} N_{yn}\beta^n + \sum_{n=1,3,\cdots}^{\infty}\sum_{m=1,3,\cdots}^{\infty} N_{ynm}\beta^{m+n}, \tag{8}$$

$$N_{xy} = \sum_{n=0,2,4,\cdots}^{\infty} N_{xyn}\beta^n + \sum_{n=1,3,\cdots}^{\infty}\sum_{m=1,3,\cdots}^{\infty} N_{xynm}\beta^{m+n},$$

where

$$N_{xn} = \frac{E_x h}{1 - (E_x/E_y)\mu_y^2}\left(\frac{\partial u_n}{\partial x} + \mu_y\frac{\partial v_n}{\partial y}\right)$$

$$N_{yn} = \frac{E_y h}{1 - (E_x/E_y)\mu_y^2}\left(\frac{\partial u_n}{\partial x} + \mu_y\frac{E_x}{E_y}\frac{\partial v_n}{\partial y}\right)$$

$$N_{xnm} = \frac{E_x h}{1 - (E_x/E_y)\mu_y^2}\left(\frac{1}{2}\right)\left(\frac{\partial w_m}{\partial x}\frac{\partial w_n}{\partial x} + \mu_y\frac{\partial w_m}{\partial y}\frac{\partial w_n}{\partial y}\right), \tag{9}$$

$$N_{ynm} = \frac{E_y h}{1 - (E_x/E_y)\mu_y^2}\left(\frac{1}{2}\right)\left(\frac{\partial w_m}{\partial x}\frac{\partial w_n}{\partial x} + \mu_y\frac{E_x}{E_y}\frac{\partial w_m}{\partial y}\frac{\partial w_n}{\partial y}\right),$$

$$N_{xyn} = Gh\left(\frac{\partial u_n}{\partial y} + \frac{\partial v_n}{\partial x}\right),$$

$$N_{xymn} = Gh\left(\frac{\partial w_m}{\partial x} \frac{\partial w_n}{\partial y}\right).$$

By substituting the above forces and displacement into equations (1), infinite set of equations are obtained as follows.

$$\partial N_{x0}/\partial x + \partial N_{xy0}/\partial y = 0$$

$$\partial N_{xy0}/\partial x + \partial N_{y0}/\partial y = 0$$

$$D_x\frac{\partial^4 w_1}{\partial x^4} + 2(D_{xy} + 2D_s)\frac{\partial^4 w_1}{\partial x^2 \partial y^2} + D_y\frac{\partial^4 w_1}{\partial y^4}$$

$$-\left(N_{x0}\frac{\partial^2 w_1}{\partial x^2} + N_{y0}\frac{\partial^2 w_1}{\partial y^2} + 2N_{xy0}\frac{\partial^2 w_1}{\partial x \partial y}\right) = 0$$

$$\partial N_{x2}/\partial x + \partial N_{xy2}/\partial y = -(\partial N_{x11}/\partial x + \partial N_{xy11}/\partial y),$$

$$\partial N_{xy2}/\partial x + \partial N_{y2}/\partial y = -(\partial N_{xy11}/\partial x + \partial N_{y11}/\partial y), \qquad (10)$$

$$D_x\frac{\partial^4 w_3}{\partial x^4} + 2(D_{xy} + 2D_s)\frac{\partial^4 w_3}{\partial x^2 \partial y^2} + D_y\frac{\partial^4 w_3}{\partial y^4}$$

$$-\left(N_{x0}\frac{\partial^2 w_3}{\partial x^2} + N_{y0}\frac{\partial^2 w_3}{\partial y^2} + 2N_{xy0}\frac{\partial^2 w_3}{\partial x \partial y}\right) = (N_{x2} + N_{x11})\frac{\partial^2 w_1}{\partial x^2}$$

$$+ (N_{y2} + N_{y11})\frac{\partial^2 w_1}{\partial y^2} + 2(N_{xy2} + N_{xy11})\frac{\partial^2 w_1}{\partial x \partial y}, \cdots.$$

The boundary conditions on the edges of the simply supported plates for zero deflection, zero bending moment, constant in-plane displacement, and zero shear stress are respectively

$$w(0,y) = w(a,y) = w(x,0) = w(x,b) = 0.$$

$$\frac{\partial^2 w}{\partial x^2}(0,y) = \frac{\partial^2 w}{\partial x^2}(a,y) = \frac{\partial^2 w}{\partial y^2}(x,0) = \frac{\partial^2 w}{\partial y^2}(x,b) = 0.$$

$$\frac{\partial u}{\partial y}(0,y) = \frac{\partial u}{\partial y}(a,y) = \frac{\partial v}{\partial x}(x,0) = \frac{\partial v}{\partial x}(x,b) = 0. \qquad (11)$$

and $\quad \frac{\partial u}{\partial y}(x,0) = \frac{\partial u}{\partial y}(x,b) = \frac{\partial v}{\partial x}(0,y) = \frac{\partial v}{\partial x}(a,y) = 0.$

The plate is subjected to uniform compressive force P in x direction. The boundary conditions for the forces are

$$\int_0^b (N_x)_{x=0,a} dy = -P.$$

$$\int_0^a (N_y)_{y=0,b} dx = 0.$$

(12)

Substituting the series form of the forces, we obtain the following set of boundary conditions.

$$\int_0^b (N_{x0})_{x=0,a} dy + P_0 = 0.$$

$$\int_0^b (N_{x2} + N_{x11})_{x=0,a} dy + P_0 = 0.$$

(13)

$$\int_0^a (N_{y0})_{y=0,b} dx = 0.$$

$$\int_0^a (N_{y2} + N_{y11})_{y=0,b} dx = 0.$$

From equations (10) and (9), next equations for displacements are obtained.

$$\frac{E_x h}{1 - (E_x/E_y)\mu_y^2} \frac{\partial^2 u_0}{\partial x^2} + Gh\frac{\partial^2 u_0}{\partial y^2} + \left(\frac{E_x h\mu_y}{1 - (E_x/E_y)\mu_y^2} + Gh\right)\frac{\partial^2 v_0}{\partial x \partial y} = 0,$$

$$\frac{E_y h}{1 - (E_x/E_y)\mu_y^2} \frac{\partial^2 v_0}{\partial x^2} + Gh\frac{\partial^2 v_0}{\partial y^2} + \left(\frac{E_x h\mu_y}{1 - (E_x/E_y)\mu_y^2} + Gh\right)\frac{\partial^2 u_0}{\partial x \partial y} = 0.$$

(14)

Solutions which satisfies the boundary conditions (10), (11), and (12) are

$$u_0 = -\frac{P_0}{hbE_x}\left(x - \frac{a}{2}\right),$$

$$v_0 = -\frac{P_0}{hbE_y}\mu_y\left(y - \frac{b}{2}\right),$$

(15)

$$P_0 = bN_{x0}, \quad N_{y0} = N_{xy0} = 0.$$

The compatibility equation (3) is now rewritten as follows.

$$D_x\frac{\partial^4 w_1}{\partial x^4} + 2(D_{xy} + 2D_s)\frac{\partial^4 w_1}{\partial x^2 \partial y^2} + D_y\frac{\partial^4 w_1}{\partial y^4} + (P_0/b)\frac{\partial^2 w_1}{\partial x^2} = 0$$

(16)

The following sinusoidal expression are assumed for the deflection to satisfy the boundary conditions.

$$w_1 = A_1 \sin\frac{m\pi x}{a} \sin\frac{n\pi y}{b} \ . \tag{17}$$

Substituting the above expression into the equation (15), the following buckling load is determined.

$$P_0 = \frac{b}{(m\pi/a)^2}\left[D_x \left(\frac{m\pi}{a}\right)^4 + 2(D_{xy} + 2D_s)\left(\frac{m\pi}{a}\right)^2\left(\frac{n\pi}{b}\right)^2 + D_y\left(\frac{n\pi}{b}\right)^4 \right]. \tag{18}$$

Similarly, from the equations (3) we obtain the following equations for u_2 and v_2.

$$\frac{E_x h}{1 - (E_x/E_y)\mu_y^2}\frac{\partial^2 u_2}{\partial x^2} + Gh\frac{\partial^2 u_2}{\partial y^2} + \left(\frac{E_x h\mu_y}{1 - (E_x/E_y)\mu_y^2} + Gh\right)\frac{\partial^2 v_2}{\partial x\partial y}$$

$$= \left(\frac{m\pi}{a}\right)\frac{A_1^2}{4}\frac{E_x h}{1 - (E_x/E_y)\mu_y^2}\left[-\left(\frac{m\pi}{a}\right)^2 + \mu_y\left(\frac{n\pi}{b}\right)^2\right]\sin\frac{2m\pi x}{a} -$$

$$\left(\frac{m\pi}{a}\right)\frac{A_1^2}{4}\left[\frac{E_x h}{1 - (E_x/E_y)\mu_y^2}\left(\frac{m\pi}{a}\right)^2 + \left(\frac{E_x h\mu_y}{1 - (E_x/E_y)\mu_y^2} + 2Gh\right)\left(\frac{n\pi}{b}\right)^2\right]\sin\frac{2m\pi x}{a}\cos\frac{2n\pi y}{b}$$

$$\tag{19}$$

$$\frac{E_y h}{1 - (E_x/E_y)\mu_y^2}\frac{\partial^2 v_2}{\partial x^2} + Gh\frac{\partial^2 v_2}{\partial y^2} + \left(\frac{E_x h\mu_y}{1 - (E_x/E_y)\mu_y^2} + Gh\right)\frac{\partial^2 u_2}{\partial x\partial y}$$

$$= \left(\frac{n\pi}{b}\right)\frac{A_1^2}{4}\frac{E_x h}{1 - (E_x/E_y)\mu_y^2}\left[\mu_y\left(\frac{m\pi}{a}\right)^2 - \frac{E_y}{E_x}\left(\frac{n\pi}{b}\right)^2\right]\sin\frac{2n\pi y}{b} -$$

$$\left(\frac{n\pi}{b}\right)\frac{A_1^2}{4}\left[\frac{E_y h}{1 - (E_x/E_y)\mu_y^2}\left(\frac{n\pi}{b}\right)^2 + \left(\frac{E_x h\mu_y}{1 - (E_x/E_y)\mu_y^2} + 2Gh\right)\left(\frac{m\pi}{a}\right)^2\right]\cos\frac{2m\pi x}{a}\sin\frac{2n\pi y}{b}$$

Solutions of the above equation which satisfy the boundary conditions are

$$u_2 = -\left[\frac{P_0}{E_x hb} + \frac{A_1^2}{8}\left(\frac{m\pi}{a}\right)^2\right]\left(x - \frac{a}{2}\right)$$

$$-\frac{A_1^2}{16}\left[\frac{(m\pi/a)^2 - \mu_y(n\pi/b)^2}{(m\pi/a)}\sin\frac{2m\pi x}{a} - \frac{m\pi}{a}\sin\frac{2m\pi x}{a}\cos\frac{2n\pi y}{b}\right] \tag{20}$$

$$v_2 = \left[\frac{P_0}{E_x hb} \frac{E_x \mu_y}{E_y} - \frac{A_1^2}{8} \left(\frac{n\pi}{b} \right)^2 \right] \left(y - \frac{b}{2} \right)$$

$$- \frac{A_1^2}{16} \left[\frac{(n\pi/b)^2 - (E_x/E_y)\mu_y(m\pi/a)^2}{(n\pi/b)} \sin\frac{2n\pi y}{b} - \frac{n\pi}{b}\cos\frac{2m\pi x}{a}\sin\frac{2n\pi y}{b} \right].$$

The coefficient A_1 is determined from the second compatibility equations in equations (10) as follows.

$$A_1^2 = \frac{16P_0}{E_x hb} \left(\frac{m\pi}{a} \right)^2 \left[\left(\frac{m\pi}{a} \right)^4 + \frac{E_y}{E_x} \left(\frac{n\pi}{b} \right)^4 \right]^{-1} \tag{21}$$

The expression for the total end shortening is then given as follows using the terms including β up to second order.

$$\Delta = \frac{Pa}{E_x bh} + 2(P - P_0)\frac{a\lambda^4}{(E_x\lambda^4 - E_y n^4)bh} u(P - P_0)$$

where $\lambda = \frac{ma}{b}$ \hfill (22)

2.3 Correspondence Principle and Inverse Laplace Trans-formation.

Viscoelastic solution is obtained by adopting the correspondence principle. At first, the elastic modulus in the elastic solutions are replaced as follows. The bar on the notations represents the Laplace transformation. In the present analysis, the fiber direction is parallel to y axis. The modulus in the fiber direction (y direction) is set to 1.75×10^7 (psi) and assumed to be time-independent. The other creep compliances are expressed in exponential series of 4 terms. The experimental data and the fitted series are compared in Figure 3. The time range which 4 term series can express is about 5 to 6 decades, hence, the time range in the example is not sufficient for the practical application. Although, to demonstrate the validity of analytical inverse Laplace transformation of the creep postbuckling solution which contains the constitutive equation of exponential series, the number of the terms or the range of the time is not essential. The Laplace transformed creep buckling load and the end shortening Δ are as follows.

$$\bar{P}_0 = \frac{\pi^2 h^3}{12\mu_y^2\lambda^2 b}\left[(\mu_y^2\lambda^4 + 2\mu_y^3\lambda^2 n^2)\frac{\frac{1}{s}}{s\bar{C}_x - \frac{\mu_y^2}{E_y}} + 4\lambda^2 n^2\mu_y^2 \frac{1}{s}\frac{1}{s\bar{J}_{66}} + \mu_y^2 E_y \frac{\bar{J}_{22}}{s\bar{J}_{22}-1} \right].$$

\hfill (23)

$$\bar{\Delta} = \frac{Pa\bar{J}_{22}}{bh} + \frac{2a\lambda^4}{bhE_y n^4}\frac{s\bar{J}_{22}}{s\bar{J}_{22} + \frac{\lambda^4}{E_y n^4}}\left(\frac{1}{s}P - \bar{P}_0 \right)u(P - P_0).$$

Provided the constitutive equation is expressed in an exponential series form, the each term in the equations (23) can be reduced to the next expression.

$$\frac{a_{n-1}s^{n-1} + a_{n-2}s^{n-2} + \cdots + a_1 s + a_0}{s^n + b_{n-1}s^{n-1} + b_{n-2}s^{n-2} + \cdots + b_1 s + b_0} \tag{24}$$

By factoring the denominator of the expression (24), we obtain

$$\frac{a_{n-1}s^{n-1} + a_{n-2}s^{n-2} + \cdots + a_1s + a_0}{s(s - \beta_1)(s - \beta_2)\cdots(s - \beta_{n-2})(s - \beta_{n-1})} \tag{25}$$

where b_1 to b_{n-1} are the poles. The above expression can be easily separated as follows.

$$\frac{\alpha_0}{s} + \frac{\alpha_1}{s - \beta_1} + \cdots + \frac{\alpha_{n-2}}{s - \beta_{n-2}} + \frac{\alpha_{n-1}}{s - \beta_{n-1}} \tag{26}$$

Then the inverse Laplace transformation can be carried out to obtain the following result.

$$\alpha_0 + \alpha_1 \text{Exp}(\beta_1 t) + \cdots + \alpha_{n-2}\text{Exp}(\beta_{n-2}t) + \alpha_{n-1}\text{Exp}(\beta_{n-1}t) \tag{27}$$

The analytically inverse Laplace transformed end shortening is plot versus time for different applied loads in Figure 4.

3.CONCLUSION.

(1) The curve fitting technology to express the constitutive equation in exponential series form is refined to double the previous limit of the fitting range.
(2) The validity to employ the formula manipulation language for creep postbuckling analysis is demonstrated successfully.

4.REFERENCES

[1] Miyase, a>, Chen, A., W.-L., Geil, P., H., and Wang, S.,S., 1986, "Anelastic Deformation and Fracture of Thermoplastic-Matrix Fiber Composite at Elevated Temperature., Part II Unidirectional Composite Laminate," American Chemical Society 20th. Great Lake Regional Meeting, Milwaukee , June.
[2] Nakajo, Y., and Wang, S., S., 1988, "Elevated-Temperature Creep Buckling of Thermoplastic-Matrix Fiber Composites under Biaxial Loading," Proc. of 4th. Japan-US Conference on Composite Materials, Technomic Publishing Company, Inc., New Holland, PA, p.696.
[3] Nakajo, Y., 1990, "Viscoelastic Creep PostBukling Behavior of AS4/J1 Thermoplastic-Matrix Composite Laminates," IUTAM Symposium, Troy, New York, May 29-June 1, "Inelastic Deformation of Composite Materials," Springer-Verlag New York Inc., p.727.
[4] Chandra, R., and Raju, B., B., "Postbuckling Analysis of Rectangular Orthotropic Plates," Int. J. mech. Sci. Pergamon Press. 1973, vol. 15, p.81.
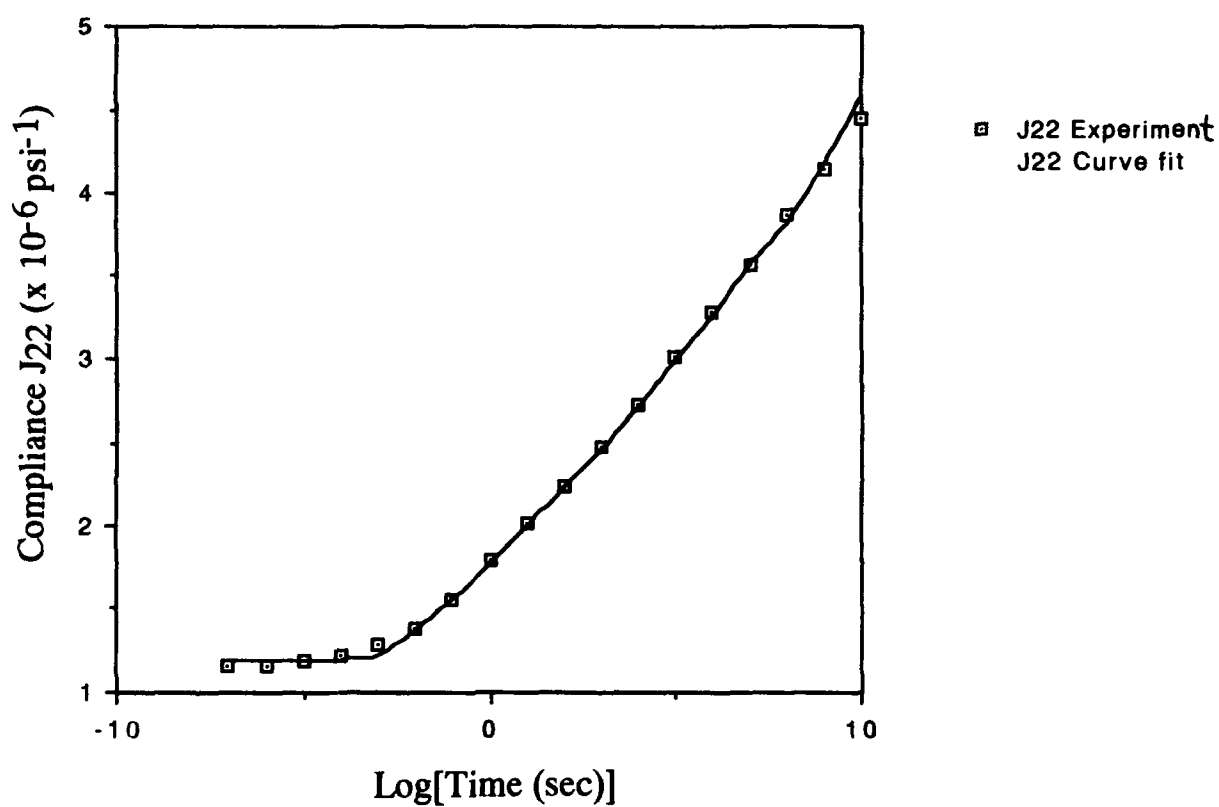
Fig.1 Modified curve fitting for creep compliance J_{22}.
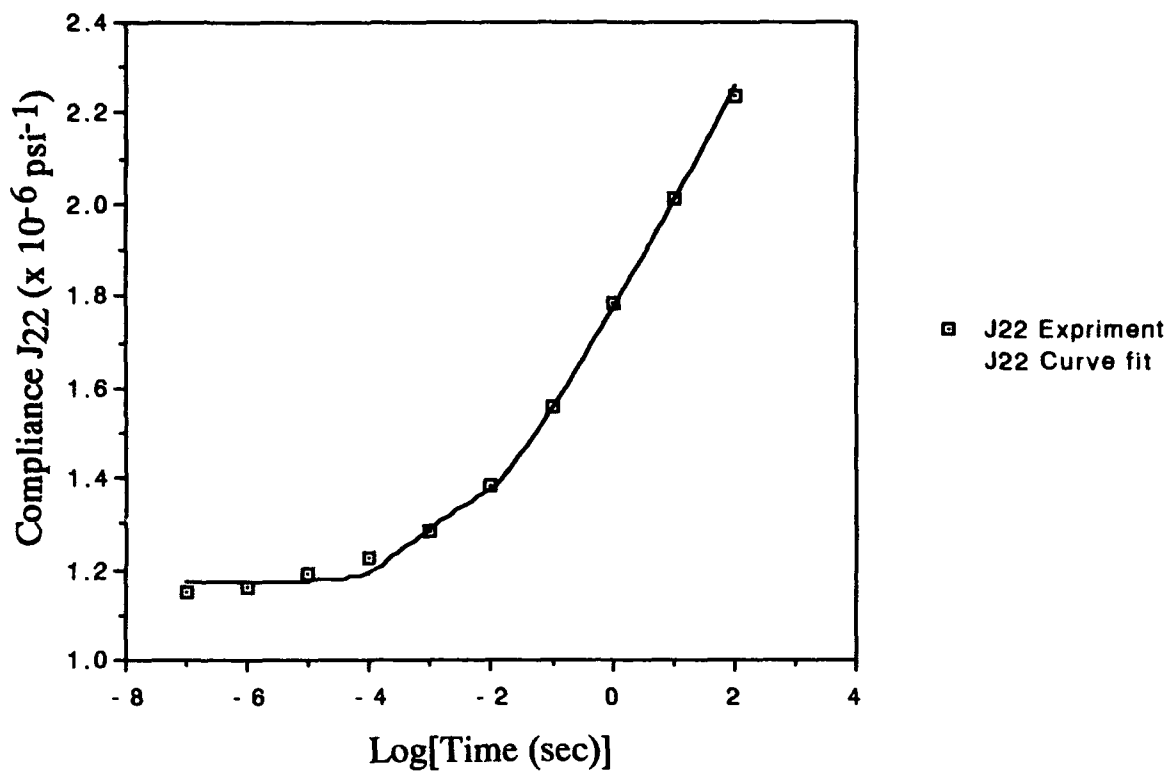
Fig.2 4 term curve fitting for creep compliance J_{22}.
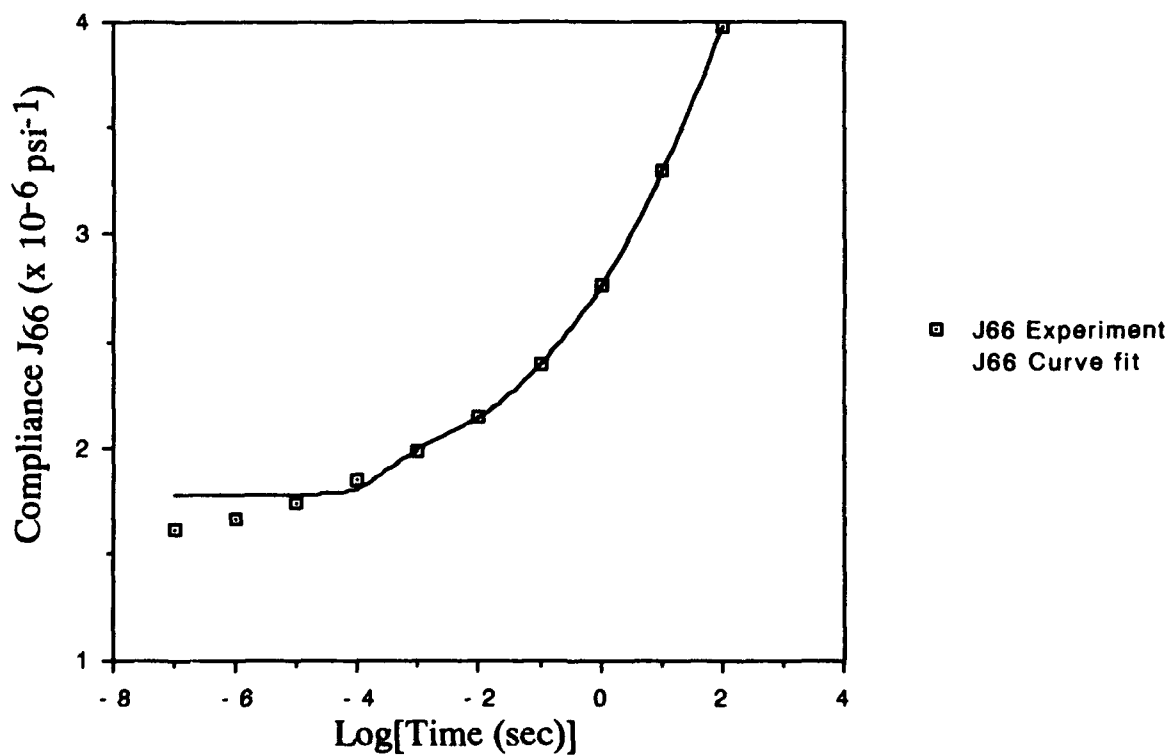
Fig.3 4 term curve fitting for creep compliance J_{66}.
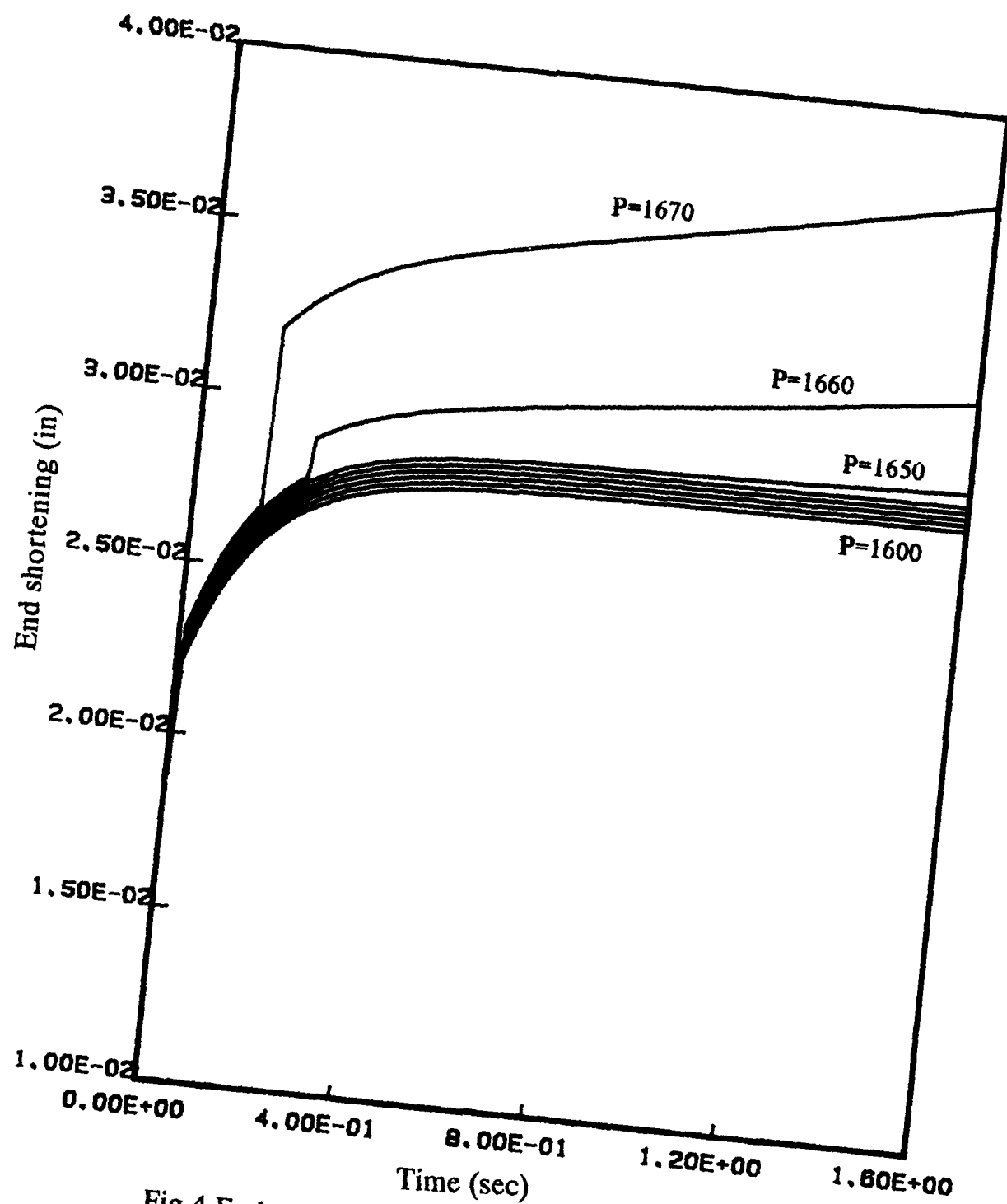
Fig.4 End shortening of the unidirectional composite panel after buckling.

Ceramic and Metal Matrix Composites

Pressureless Densification of Ceramic Matrix Composites: Analytical Model

W. HONG AND L. R. DHARANI

ABSTRACT

The presence of inert and rigid inclusions such as whiskers reduces the sinterability of a ceramic matrix. A finite element viscoelastic formulation is presented for predicting the densification behavior of particulate reinforced ceramic matrix composite undergoing pressureless sintering. The reduction in densification solely due to the constraint offered by the inert and rigid inclusion cannot account for the drastic reduction in densification rates observed in sintering experiments. The model also predicts that the quality of initial green compact and grain growth during sintering have a predominant effect on densification behavior.

INTRODUCTION

Fiber and whisker reinforced ceramic matrix composites (CMC) are of special interest in energy related and aerospace structural applications because of their unique potential for providing high temperature refractory materials which have high strength and strain tolerance. These advantages are contingent upon fabricating high density and flawless composites. The processing of ceramics containing stiff and non densifying phase, whisker and fibers has been traditionally very difficult. By hot pressing (pressure sintering), CMC of low to moderate volume fractions and simple geometries can be fabricated without too much difficulty. However, the microstructure and, therefore, the associated mechanical performance is very much dependant on the processing conditions such as temperature, pressure and length of hot pressing time. This problem is accentuated while fabricating complex geometries such as continuous fiber cross ply and angle ply laminates and whisker reinforced CMC with reentrant corners. The pressureless processing, on the other hand, is less expensive and requires smaller capital investment and is amenable for fabrication of complex geometries. These advantages are, however, offset by the increased difficulties in obtaining high density composites.

Many experiments on pressureless sintering have shown that the sintering rate of a polycrystalline matrix decreases significantly with increasing volume fraction of the reinforcing phase [1-3], starting from quite low inclusion contents. This significant decrease is independent of whether the green compact (composites) were formed by die-pressing of mixed powders [1,3] or by slip casting [2]. The reduction in the sintering rate of a glass (amorphous) matrix composites is much less drastic [4]. The effect of reinforcing particle size appears to depend on the method used for forming the green body [5]. The studies on the effects of matrix green density and sintering temperature [6] have shown that the sintering rate of a composite matrix relative to that for the unreinforced are drastically different.

W. Hong and L. R. Dharani, Department of Mechanical and Aerospace Engineering and Engineering Mechanics, University of Missouri-Rolla, Rolla, MO 65401-0249, USA

Several theories have been put forward to explain the reduced densification rates [7,8]. Some of these theories treat the sintering potential as a hydrostatic stress, so called sintering stress, under which ceramic powder shrinks [9,10]. The stresses induced by the constraints of non-sintered inclusions in the matrix can cancel part of the sintering stress, in other words produce opposite volumetric creep, in such a way that the densification rate is retarded. Another approach is similar to the analysis of thermal stress problems [11]. A sintering shrinkage coefficient for the constrained sintering problem similar to the thermal expansion coefficient for a thermal stress problem is fundamental for the analysis to be conducted. However, the shrinkage coefficient depends on many factors, such as density, grain size, diffusion rate and temperature in the crystalline matrix [12].

There have been some analyses for the constrained sintering problem, in which the free sintering strain rate, which is equivalent to shrinkage coefficient, of the constrained matrix was implicitly assumed to be the same as that of the unconstrained matrix under the same sintering condition [11]. However, the free sintering strain rate in the constrained matrix is not the same as that of the unconstrained matrix because they experience different histories. For example, they would have different densities after experiencing the same length of sintering time under an identical sintering condition, even if they had the same initial densities. The other limitation of these analyses is their snapshot approach that can not show how the density of the ceramic matrix changes over a meaningful length of sintering time. In this paper, an analytical model is developed to model the pressureless sintering of a particulate reinforced ceramic matrix composite. Unlike the snapshot approach of the earlier model our formulation presents the state variables such as stress, strain, and density as continuous functions of sintering time.

VISCOELASTIC FORMATION

From the continuum mechanics point of view, the matrix in a ceramic matrix composite undergoing sintering at temperatures that are very high but lower than the melting point of the ceramic as well as the reinforcement, the matrix phase is generally assumed to be viscoelastic. In general, viscoelastic behavior can be represented by a combination of elastic springs and viscous dashpots in parallel and series [13] in which the total strain rate vector $\{\dot{\varepsilon}\}$ can be written as

$$\{\dot{\varepsilon}\} = \{\dot{\varepsilon}^e\} + \{\dot{\varepsilon}^v\} + \{\dot{\varepsilon}^s\} \tag{1}$$

where the elastic strain rate $\{\dot{\varepsilon}^e\}$, the viscous strain rate $\{\dot{\varepsilon}^v\}$ and the sintering strain rate $\{\dot{\varepsilon}^s\}$ are given by

$$\{\dot{\varepsilon}^e\} = [D]^{-1} \{\dot{\sigma}\} \tag{2}$$

$$\{\dot{\varepsilon}^v\} = [\eta]^{-1} \{\sigma\} \tag{3}$$

$$\{\dot{\varepsilon}^s\} = \{\alpha \ \alpha \ \alpha \ 0 \ 0 \ 0\}^T \tag{4}$$

in which [D] and [η] are the elastic stiffness matrix and viscosity matrix, respectively, and α is referred to as the free sintering shrinkage coefficient.

The finite element formulation for viscoelastic analysis used in this paper is a special case of the inelastic finite element formulations developed by Yamada[14]. For sufficiently small time intervals, the material properties and sintering strain rate can be assumed constant within each time interval and that the quantities change instantaneously at the beginning of the subsequent time interval [15]. The stress increment can be expressed as

$$\{\Delta\sigma\} = [D]\{\Delta\varepsilon\} - [D][\eta]^{-1}\{\overline{\sigma}\}\Delta t - [D]\{\dot{\varepsilon}^s\}\Delta t \tag{5}$$

where $\{\overline{\sigma}\}$ are the average stresses in the current time interval given by Yamada [16]

$$\{\overline{\sigma}\} = \{\sigma\} + \frac{1}{2}\{\Delta\sigma\} \tag{6}$$

After considerable manipulation of equation (5), the stress increment can be written as

$$\{\Delta\sigma\} = [D^*]\{\Delta\varepsilon\} - [D^*][\eta]^{-1}\{\sigma\}\Delta t - [D^*]\{\dot{\varepsilon}^s\}\Delta t \tag{7}$$

where [D^*] is the modified elastic stiffness matrix given by

$$[D^*] = \left([I] + \frac{1}{2}[D][\eta]^{-1}\right)^{-1}[D] \tag{8}$$

In order to simulate the rheological behavior of sintering bodies, use of large deformation theory is essential and a special attention being given to the fact that the configuration of the body is changing continuously. The updated Lagrangian formulation will be used for its computational efficiency.

SHRINKAGE COEFFECIENT

In general, the matrix in a composite is constrained by the reinforcements and does not follow the same densification behavior as the unconstrained matrix. In most of the conventional analyses, the shrinkage term α is referred to as the free strain rate of the matrix, which is sometimes set equal to the linear contraction rate of the unconstrained sintering material. For homogeneous, neat matrix materials, the measured relative density ρ versus time relationship can be represented as $\rho = f(t)$. The shrinkage coefficient α of the unconstrained matrix can then be expressed as

$$\alpha = -\frac{\dot{\rho}}{3\rho} = -\frac{f'(t)}{3f(t)} \tag{9}$$

where $f'(t)$ is the derivative of $f(t)$ with respect to time. The shrinkage coefficient for the constrained matrix (α_c) in the composite is derived based on the following three different definitions:

$$\alpha_c = \alpha = -\frac{f'(t)}{3f(t)} \tag{10}$$

for the time dependent shrinkage

$$\alpha_c = -\frac{f'\left(f^{-1}(\rho_c)\right)}{3\rho_c} \tag{11}$$

for the density dependent shrinkage, where ρ_c is the relative density of a given material point in the constrained matrix

$$\dot{\rho} = A \left(1 - \frac{\rho}{\rho_f}\right)^{\beta} \left(1 - \frac{\sigma_m}{\Sigma}\right) G^{-a} \tag{16}$$

for the microstructure and density dependent shrinkage coefficient, where A is a temperature dependent parameter, ρ is the relative density, ρ_f is the final relative density, G the grain facet length, σ_m is the actual bulk stress, Σ is the sintering potential, a is a coefficient dependent on the nature of diffusion process during sintering [10], usually between 3 and 4 , and β is a material parameter.

RESULTS AND DISCUSSIONS

The material properties, such as Elastic modulus, viscosity and Poisson's ratio of the matrix materials are assumed to be density (ρ_c) dependent. The following well observed material property relations are used in this paper for computational purposes:

$$E = E_f \exp[-b_1(1 - \rho_c)] \tag{17}$$

$$\eta = \eta_f \exp[-b_2(1 - \rho_c)] \tag{18}$$

$$v = \frac{1}{2} \sqrt{\frac{\rho_c}{(3 - 2\rho_c)}} \tag{19}$$

where E, η and v are the current Elastic modulus, viscosity and Poisson's ratio, respectively, E_f and η_f are the elastic modulus and viscosity at fully dense state, and b_1 and b_2 are constants. For the numerical computation, we have used $E_f = 125$ GPa, $\eta_f = 5.8333$ GPa min., $b_1 = 1.6$, and $b_2 = 2.5$.

A composite cylinder in which the core is a non-sintering rigid inclusion and the clad is the matrix phase of appropriate outer radius to give a inclusion volume fraction of 10% is considered for the analysis. The schematic of the composite cylinder and the finite element mesh for the sector considered in the analysis is shown in Fig. 1. Due to the axisymmetric nature of the problem only a sector of the region need to be considered. After considerable study of convergence behavior of the results, a time step of $\Delta t = 0.01$ minute has been determined to be satisfactory for all the cases to be presented below.

EFFECT OF CONSTRAINT

First, we present numerical results for the case of a composite cylinder consisting of a rigid and non-sintering inclusion without taking into account the grain growth that takes place during sintering. Further, we assume that the initial density of the matrix is uniform, that is, the matrix particles are dispersed uniformly over the entire region. The predicted densification behavior of ZnO matrix containing 10% ZrO_2 particles, as a function of time, is shown in Fig. 2 along with the experimental results for a neat matrix and a composite with 10% ZrO_2 inclusions. The predicted densification plot shows a small reduction in densification rate as compared to that of the neat matrix. However, experimentally observed reduction in densification for a matrix reinforced with 10% inclusions is significantly lower than that predicted by viscoelastic finite element formulation. This shows that the constraint provided by the rigid inclusions alone cannot account for the observed densification reductions.
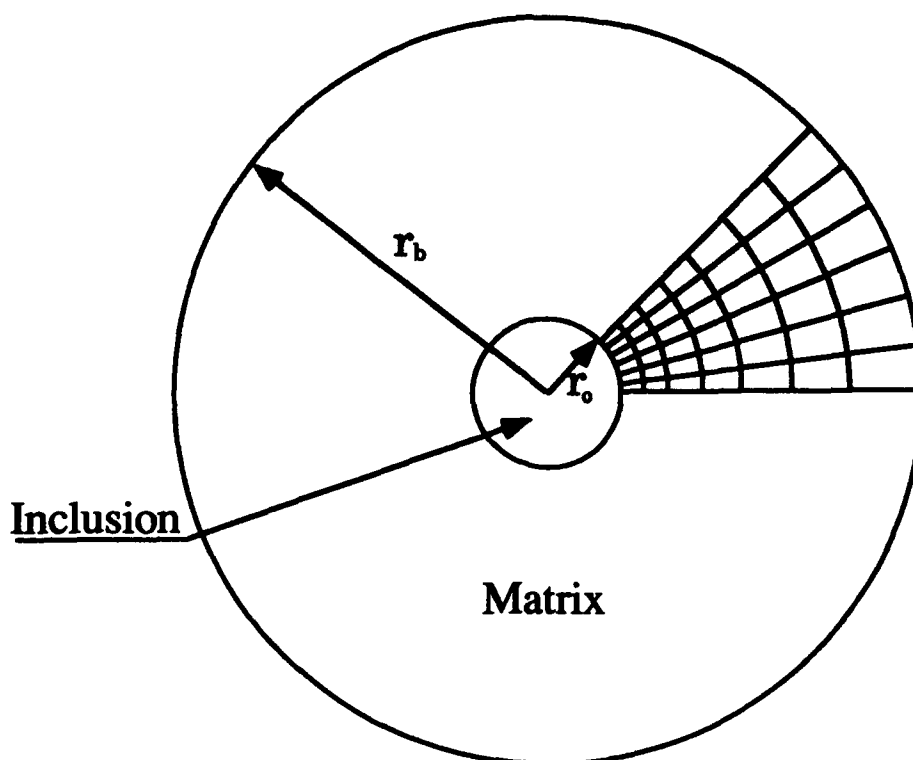
Fig. 1 Schematic of Composite Cylinder Model and FEM Mesh
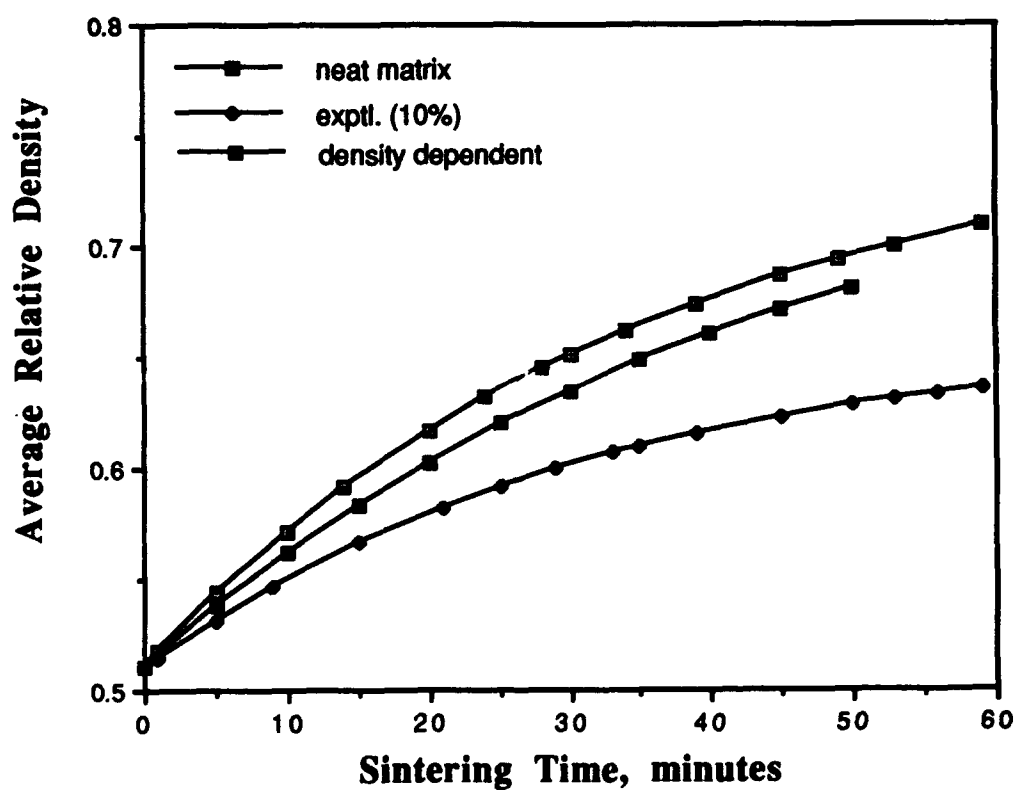
Fig. 2 Effect of Constraint due to inclusions

EFFECT ON NON-HOMOGENEOUS COMPACTION

While the pure matrix samples are always compacted fairly homogeneously, during formation of green samples, it is often observed that the density distributions in the matrix is quite heterogeneous when the dispersed inert and rigid inclusions are present in the matrix. Experimental microscopic observations of sintered composite samples have shown that the inclusions are generally surrounded by a region in which the matrix is loosely compacted. We approximate this scenario by a three phase composite cylinder model consisting of the outer matrix region with higher density than the initial average density of the green compact and an annular matrix region surrounding the inclusion having a density lower than the initial average density. The two densities of the matrix regions are so selected as to arrive at an overall density equal to that of the green compact. The densification behavior of such a non-uniform matrix with rigid inclusions is shown in Fig. 3 along with neat matrix and composite experimental results. A comparison of results of the two models, homogeneous and nonhomogeneous models, shows that the distribution of initial density has a significant effect on the overall densification of a composite. Elimination of such inhomogeneities and improving the quality of initial green compacts would definitely aid in obtaining fully dense composites.

EFFECT OF GRAIN GROWTH

It is known that the size of the grains increases as material undergoes heat treatment for extended length of time. The grain growth, generally, results in reduced densification rates. The shrinkage coefficient, accordingly, must account for this change in microstructure with sintering time, as shown in eqn (16). The constant a represents the nature of mass transport during the sintering process with $a = 0$ corresponding to the case in which there is no grain growth and the only factor effecting the densification retardation is the constraint provided by the inclusions. Figure 4 shows the finite element predictions for the three cases, $a = 0$, 3 and 4, along with the experimental results for the neat matrix and a composite with 10% inclusions. The grain growth, indeed, has the most dominant effect when compared to the other two factors considered earlier.

CONCLUSIONS

A finite element viscoelastic formulation is presented for predicting the densification behavior of a particulate reinforced ceramic matrix composite undergoing pressureless sintering. The reduction in densification solely due to the constraint offered by inert and rigid inclusion cannot account for the drastic reduction in densification rates observed in sintering experiments. The model also predicts that the quality of the initial green compact and grain growth during sintering have predominant effects on densification behavior.

ACKNOWLEDGEMENTS
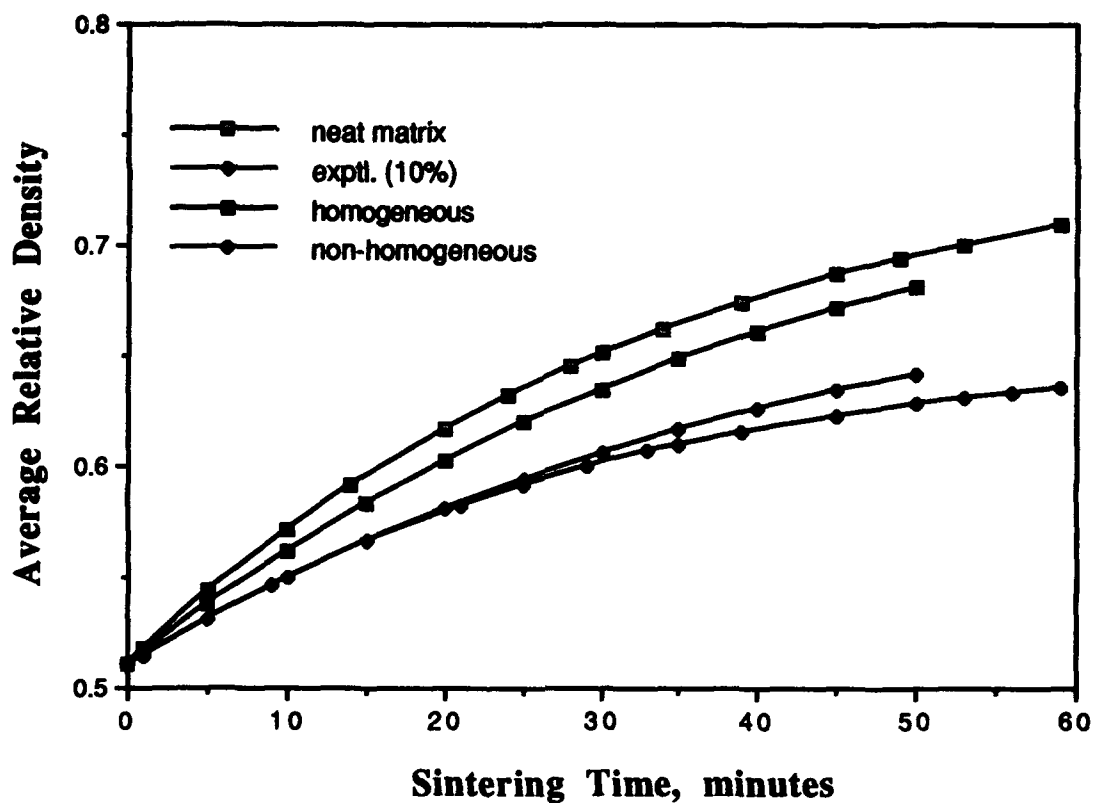
Fig. 3 Effect of Non-homogeneous Compaction
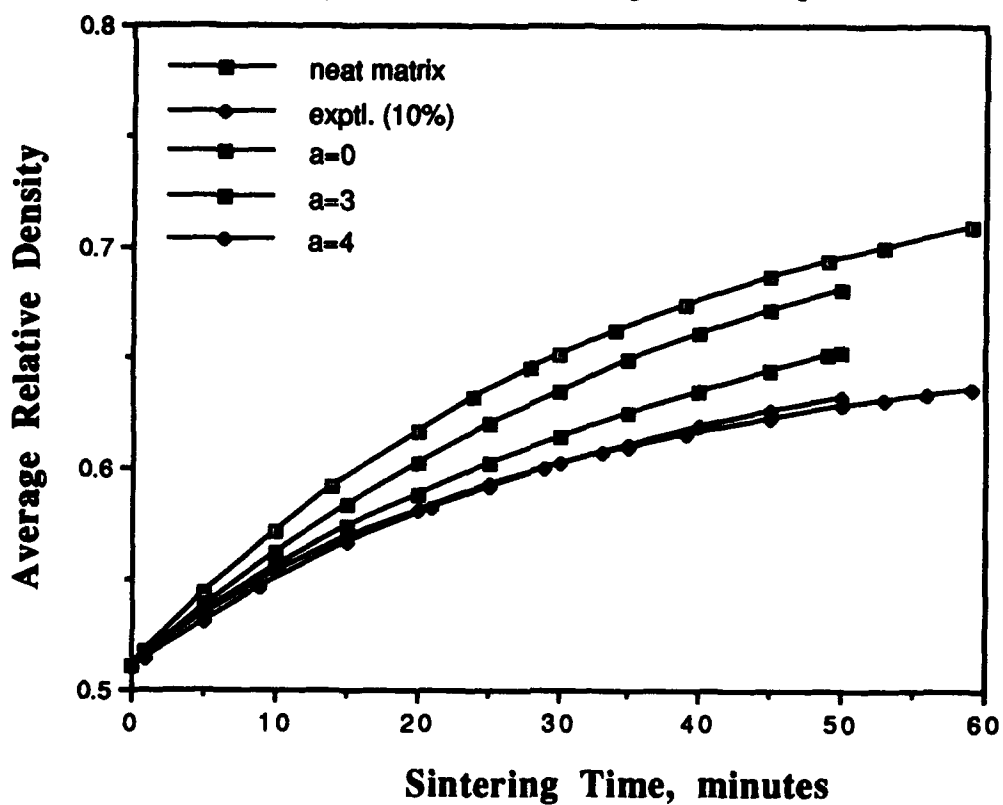
Fig. 4 Effect of Grain Growth and Microstructure

REFERENCES

1. De Jonghe, L. C., M. N. Rahaman, and C. H. Hsueh, 1986. "Transient stresses in bimodal compacts during sintering", Acta Metall., 34[7]: 1467.

2. Bordia, R. K. and R. Raj, 1988. "Sintering of TiO2-Al2O3 composites: A model experimental investigation", J Am. Ceram. Soc., 71[4]: 302.

3. Tuan, W. H., E. Gilbert, and R. J. Brook, 1989. "Sintering of heterogeneous ceramic compacts, Part I: Al2O3-Al2O3", J Mater. Sci., 24: 1062.

4. Rahaman, M. N. and L. C. De Jonghe, 1987. "Effect of rigid inclusions on the sintering of glass powder compacts", J Am. Ceram. Soc., 70[12]: C-348.

5. Weiser, M. N. and L. C. De Jonghe, 1988. "Inclusion size and sintering of composite powders", J Am. Ceram. Soc., 71[3]: C-125.

6. Rahaman, M. N. and L. C. De Jonghe, 1991. " Sintering of ceramic particulate composites: effects of matrix density", J Am. Ceram. Soc., 74[2]: 433.

7. Bordia, R. K. and G. W. Scherer, 1988. "On constrained sintering - I. constitutive model for a sintering body", Acta metall., 36[10]: 2393.

8. Bordia, R. K. and G. W. Scherer, 1988. "On constrained sintering - II. Comparison of constitutive models", Acta metall., 36[10]: 2399.

9. Raj, R. and R. K. Bordia, 1984. "Sintering of bimodal powder compacts", Acta Metall, 32[7]: 1003.

10. Hsueh, C. H., et al, 1986. "Viscoelastic stresses and sintering damage in heterogeneous powder compacts", Acta Metall., 34[5]: 927.

11. Scherer, G. W., 1987. "Sintering inhomogeneous glasses: application to optical waveguides", J. Non-Cryst. Solids 34: 239.

12. Scherer, G. W., 1991. "Viscous sintering of particle-filled composites", Ceramic Bulletin, 6: 384.

13. Findley,W. N., J.S. Lai and K. Onaran, 1976. Creep and Relaxation of Nonlinear Viscoelastic Materials, North-Holland Publishing Co.

14. Zienkiewicz, O. C., M. Watson and I. P. King, 1968. "A numerical method of viscoelastic stress analysis", Int. J. Mech. Sci., 10 807.

15. Yamada, Y., 1978. "Constitutive modelling of inelastic behavior and numerical solution of nonlinear problems by the finite element method", Comput. & structure, 8: 535.

16. Yamada, Y., 1982. "Nonlinear matrices, their implications and applications in inelastic large deformation analysis", Comput. Meth. Appl. Mech. Engng. 33: 417.

Performance of a Carbon Fiber Reinforced Mullite Matrix Composite

WILLIAM K. TREDWAY, KARL M. PREWO, TAKESHI ISODA AND MISAO IWATA

ABSTRACT

A carbon fiber reinforced mullite (C/Mullite) composite was fabricated in Japan in a joint project between Noritake Co. and Tonen Corporation. The composite was supplied to United Technologies Research Center (UTRC) in the USA for evaluation of mechanical and physical characteristics. Results of the evaluation showed that the material exhibited excellent mechanical properties at both room and elevated temperature (up to 1200°C). Oxidation behavior and thermal expansion characteristics were also assessed and agreed well with expected performance.

INTRODUCTION

Fiber reinforced ceramic matrix composites are being developed worldwide for a variety of intermediate and high temperature structural applications. Depending on the particular combination of fiber and matrix, service temperatures ranging from 500°C to 1400°C can be achieved. For applications where long-term oxidative stability is required, ceramic fibers such as SiC-based NICALON® and Tyranno or Al_2O_3-based Altex can be employed. Carbon fibers, which are unique in that they are available with a wide range of properties in terms of strength and elastic modulus, are most often considered for applications where oxidation is not a concern. However, for special applications or with adequate protection of the fiber, carbon fibers can also provide effective composite reinforcement at elevated temperature under oxidizing conditions. Indeed, considerable technology and production capability have been developed for carbon fiber reinforced SiC (C/SiC) and carbon fiber reinforced carbon (C-C) composites.

William K. Tredway and Karl M. Prewo, United Technologies Research Center, Silver Lane, East Hartford, CT, 06108, USA

Takeshi Isoda, Tonen Corporate Research and Development Laboratory, 1-3-1, Nishi-tsurugaoka Ohi-machi, Iruma-gun, Saitama 354, JAPAN

Misao Iwata, Noritake Co., Limited, R&D Department, Miyoshi, Aichi Prefecture 470-02, JAPAN

One ceramic oxide composition which exhibits temperature capability and creep resistance is mullite ($3Al_2O_3 \cdot 2SiO_2$). Dense polycrystalline mullite can be used at temperatures in excess of 1500°C and is very resistant to creep due to the interlocking nature of the elongated needle-shaped crystals that constitute the microstructure [1]. In past work, mullite has been investigated primarily as a matrix for whisker reinforced composites [2-4], with not much consideration being given to its use as a matrix for continuously reinforced composites. This is mainly due to the difficulties in matrix densification that would be encountered due to the constraining effect of either continuous fibers or long discontinuous fibers when using a traditional consolidation technique such as sintering or uniaxial hot-pressing [5]. More novel approaches must be used to enable the utilization of mullite as a matrix for composites containing these types of fiber reinforcements.

In this investigation, researchers from Noritake Company and Tonen Corporation took an approach whereby fine mullite powder was combined with an organosilicon resin that converted to mullite when pyrolyzed. This procedure resulted in composite preforms that could be consolidated to nearly full density, with the pyrolyzed resin acting as a filler material between the mullite particles. Continuous carbon fibers were used as the reinforcement in the work reported here. Carbon fiber reinforced mullite (C/Mullite) is viewed as a potential material for high temperature applications similar to those being considered for C/SiC or C-C. This paper describes the evaluation by United Technologies Research Center (UTRC) of a C/Mullite composite that was fabricated in Japan by Noritake and Tonen.

EXPERIMENTAL PROCEDURE

COMPOSITE FABRICATION

Carbon fiber tows were impregnated with fine stoichiometric mullite powder (0.7 μm diameter) by drawing the fiber through a slurry consisting of the mullite powder, an organosilicon resin (polymethylsilazane), and toluene. The prepreg was then cut into plies of the desired size and stacked to form a unidirectionally reinforced composite preform. The preform was isostatically pressed and then pyrolyzed in argon at a temperature of 700°C. Final composite consolidation was achieved by hot-pressing at a temperature of 1600-1700°C in argon using a pressure of 32 MPa.

TESTING AND ANALYSIS

The original C/Mullite composite was machined into a panel with dimensions of 152 mm x 44.5 mm x 9 mm and supplied to UTRC. The panel was then machined into test specimens of the appropriate geometry using an automated cutting/grinding machine with diamond tooling. All sample surfaces were completely machined.

Composite density and apparent porosity were determined using Archimedes' liquid displacement density technique with isopropanol as the reference fluid. Samples were

immersed in isopropanol and placed in an evacuation chamber to allow all surface-connected cracks and pores to fill with the fluid prior to density measurement.

Tensile behavior was determined using straight-sided specimens with dimensions of approximately 152 mm x 9.6 mm x 2.2 mm. Fiberglas tabs were bonded to both sides of the sample ends to provide a gripping surface for the test fixture grips. Strain gauges were adhesively bonded to both sides of the specimens in the center of the 51 mm gauge length. Samples were loaded at a crosshead speed of 1.3 mm/min.

Flexural performance was evaluated using specimens with dimensions of approximately 76.2 mm x 9.6 mm x 2.2 mm in a four-point testing configuration with an upper span of 1.9 cm and a lower span of 6.4 cm. Deflection was monitored using a deflectometer. Samples were again loaded at a crosshead speed of 1.3 mm/min.

Oxidation behavior was assessed by monitoring the weight loss of composite samples following exposure in a flowing air atmosphere (flow rate = 300 cc/min) at various temperatures. Heating of the samples was conducted in an Al_2O_3 tube furnace fitted with stainless steel end caps.

Thermal expansion behavior of the composite was evaluated against a SiO_2 standard using a horizontal dilatometer at a heating/cooling rate of 2°C/min. Dimensions of the sample were approximately 25.3 mm x 5.1 mm x 2.2 mm.

RESULTS AND DISCUSSION

COMPOSITE MICROSTRUCTURE AND DENSITY

Inspection of the composite microstructure in an optical microscope indicated that the fibers were well distributed throughout the composite, with some isolated regions of porosity evident in the matrix. Overall, the composite appeared to be well consolidated. The average fiber content as determined by electronic image analysis was 58.7 volume %, with an average void content of 1.4 volume %. This low void content confirms that the combination of fine mullite powder and the organosilicon resin produced a composite with very little porosity. The pyrolyzed resin appears to have acted as a very effective filler for any matrix porosity that would normally appear in a mullite matrix composite. The average density of the C/Mullite composite in the as-fabricated condition as determined via liquid displacement was 2.53 g/cc, with an apparent porosity (surface connected porosity) ranging from 2-3 volume % . The apparent porosity is a measure of any inherent matrix porosity that is connected to the surface as well as any matrix microcracks. Matrix cracks could have been introduced either during machining of the composite or during cooling from the consolidation temperature due to thermal expansion mismatch between the matrix and the fiber. It appears that limited matrix cracking did occur since the apparent porosity value is somewhat larger than the void content measured via image analysis.

ROOM TEMPERATURE TENSILE STRESS-STRAIN BEHAVIOR

The tensile behavior of the C/Mullite composites is summarized in Table I, with a tensile stress-strain curve from one of the samples being shown in Figure 1. The performance exhibited by the composite was quite good, with an average ultimate tensile strength of 64 ksi, an average elastic modulus of 30 Msi, and an average failure strain of 0.24%. The values for ultimate tensile strength and failure strain were nearly equal for the two samples tested, while the values for elastic modulus varied from 26 to 34 Msi. The reason for this large variation in stiffness was not completely understood, although it may suggest that the fiber volume varied somewhat in the two samples. The tensile stress-strain curve in Figure 1 indicates that linear elastic behavior was observed up to ~0.06% strain, after which the curve deviates from linearity and exhibits reduced stiffness. This non-linear stress-strain behavior is similar to that exhibited by pitch-based carbon fiber reinforced glass matrix composites as determined in previous work performed at UTRC [6].

Tensile fracture of the C/Mullite samples was observed to occur within the gauge section, with a splintered or "woody" mode of fracture. A typical fracture surface is shown in more detail in the SEM micrograph in Figure 2. Substantial fiber pullout is apparent in many regions of the fracture surface, while in other regions (not shown in Figure 2) it is evident that very little pullout exists. Small, isolated matrix-rich regions (i.e., no fiber reinforcement) were also observed in some areas of the composite fracture surface. These regions may act as sites for crack initiation and/or rapid crack propagation in the composite.

HIGH TEMPERATURE FLEXURAL PERFORMANCE

Four-point flexural testing was performed at room temperature and at temperatures of 500°C, 900°C, and 1200°C in both argon and air atmospheres. For the elevated temperature

TABLE I - TENSILE PERFORMANCE OF C/MULLITE COMPOSITES

ULTIMATE TENSILE STRENGTH (ksi)	ELASTIC MODULUS (Msi)	FAILURE STRAIN (%)
63	26	0.26
65	34	0.22
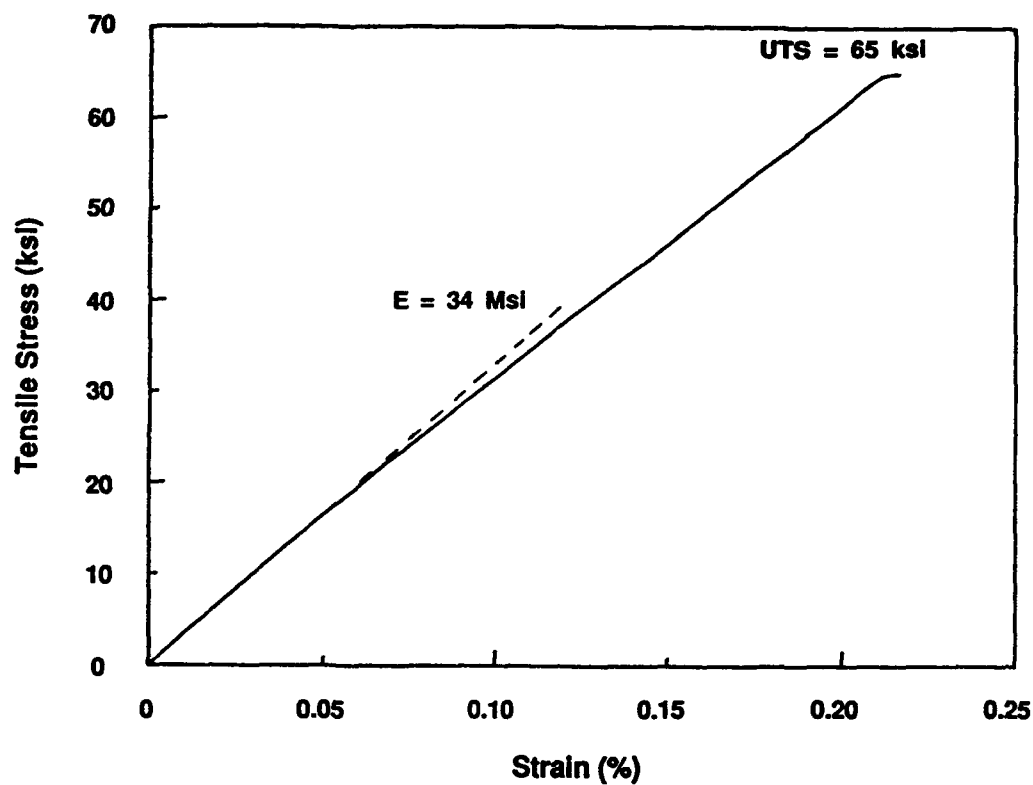
Figure 1.   A representative tensile stress-strain curve for the C/Mullite composite.

Figure 2.   SEM micrograph showing a region of the C/Mullite composite fracture surface exhibiting fiber pullout.

testing, samples were held at temperature for 15-20 minutes to allow equilibrium to be established. Figure 3 summarizes the flexural strength of the samples tested in argon. The samples gained in strength from room temperature to 500°C, and then maintained their strength up to the maximum temperature of 1200°C. The samples also exhibited a fairly constant elastic modulus up to 1200°C, with values ranging from 28 to 36 Msi. These results are impressive, suggesting that the mullite matrix maintains its structural integrity to at least 1200°C. Figure 4 shows a representative load-deflection curve at a test temperature of 1200°C in argon. The ability of the material to maintain load after reaching its maximum strength provides the material with the characteristic of "graceful failure" and indicates significant toughness.

Results of flexural strength for the samples tested in air are also summarized in Figure 3. The samples tested at 500°C exhibited a modest increase in strength over the room temperature value, but experienced a slight decrease in modulus. Higher test temperatures resulted in significant decreases in strength and stiffness, as would be expected in an oxidizing environment. Despite this decrease in performance, the degree of strength and stiffness maintained at 1200°C in air was still quite impressive. Load-deflection behavior for these samples was similar to that shown in Figure 4, with the material demonstrating the ability to carry load well past the point of maximum strength.

It should be noted that the samples tested in air at elevated temperature were observed to "burn" or flame for a short period of time during the test. Associated with this burning was an odor characteristic of the thermal decomposition of an organic resin or binder.
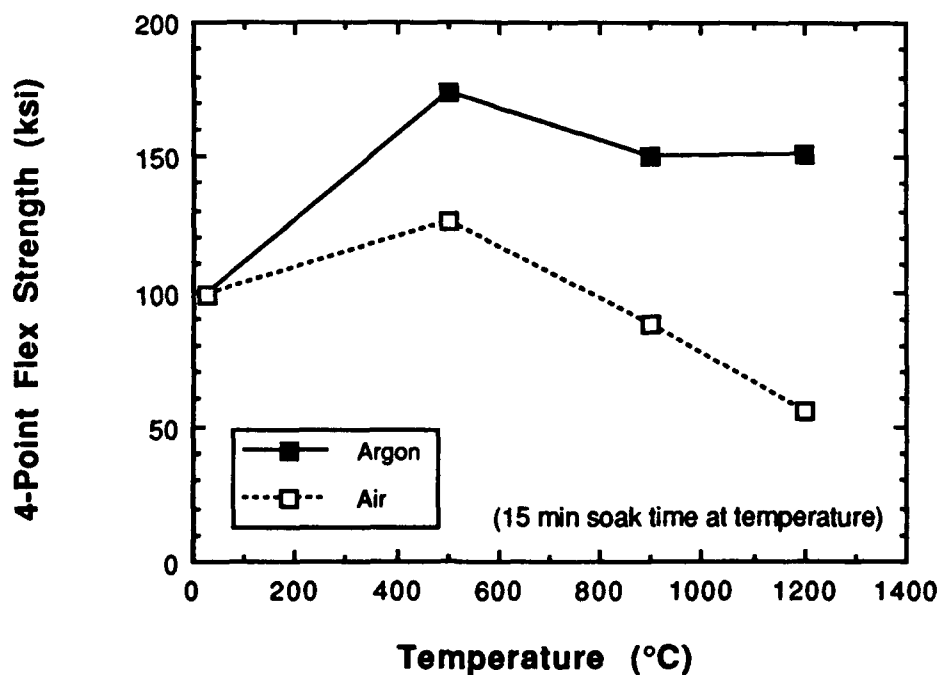
Figure 3.   Four-point flexural strength as a function of temperature in argon and in air for the C/Mullite composite.
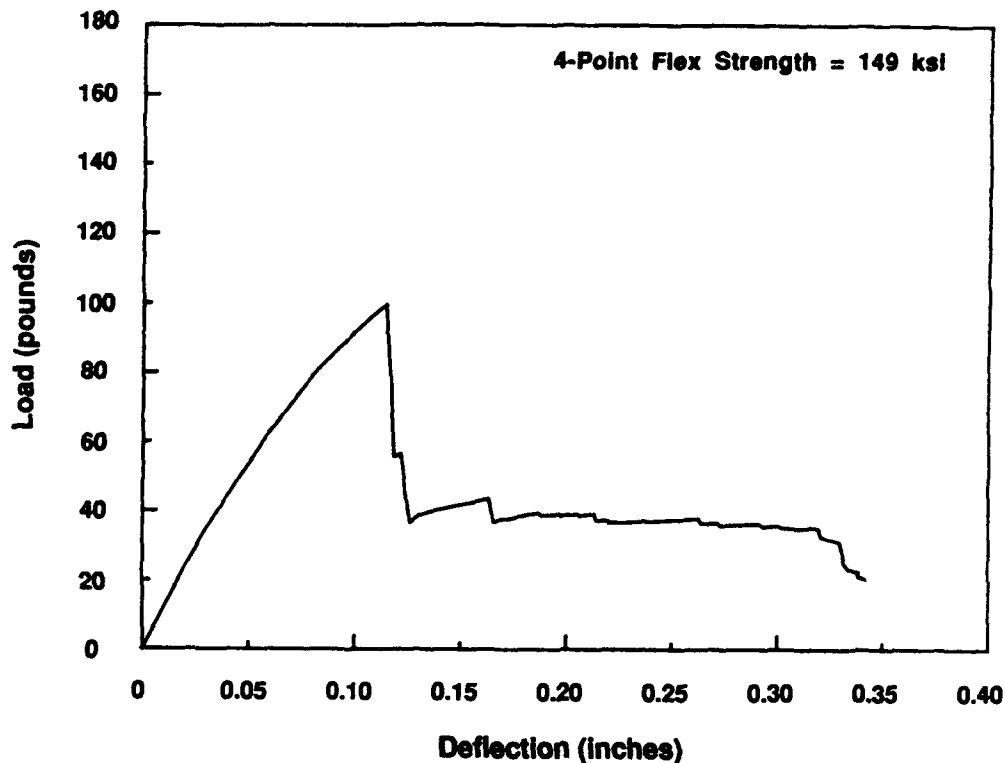
Figure 4. Flexural load-deflection curve for the C/Mullite composite at 1200°C in argon.

OXIDATION BEHAVIOR

Oxidation behavior of the C/Mullite material in air was assessed at temperatures of 500°C and 900°C. Mass loss as a function of oxidation time at those temperatures is shown in Figure 5. At 900°C, all of the fiber in the material oxidized during the initial 100 hour time interval as evidenced by the achievement of a constant mass. At 500°C, oxidation of the fiber occurred at a slower rate, with approximately half of the fiber being oxidized after 400 hours. Plotting the data at 500°C as a function of (oxidation time)$^{1/2}$ gives a near linear fit , suggesting that oxidation at this temperature is controlled by the diffusion of oxygen to the carbon fibers.

THERMAL EXPANSION BEHAVIOR

Composite thermal expansion behavior was measured from room temperature (RT) to 1000°C and back to RT in argon over five thermal cycles. Composite thermal strain for the fifth thermal cycle is shown in Figure 6. The hysteresis displayed is commonly observed in carbon fiber reinforced glass and glass-ceramic matrix composites investigated at UTRC and is believed to result from thermal strain mismatch between the fiber and matrix during heating/cooling. The average coefficient of thermal expansion (CTE) as a function of
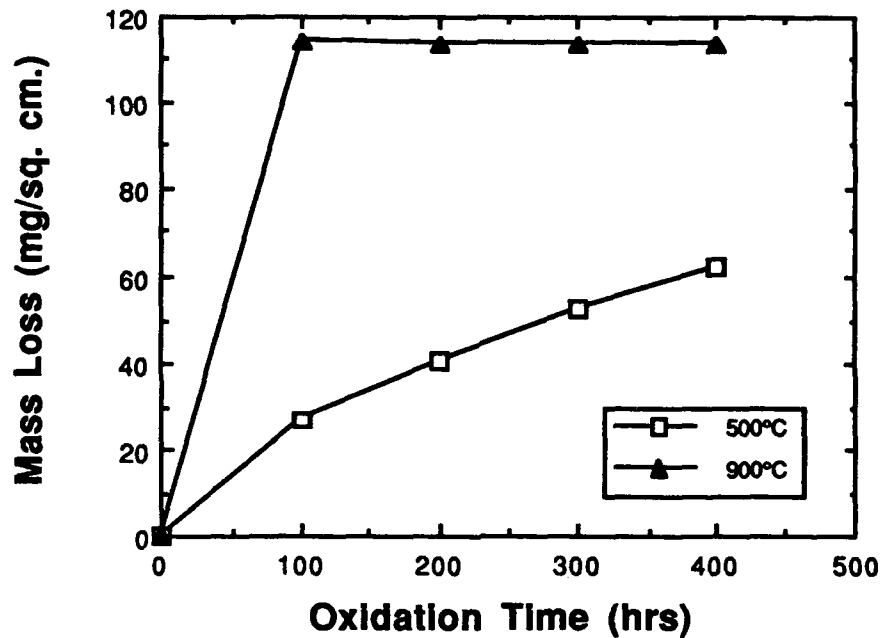
Figure 5.   Oxidation behavior of the C/Mullite composite at temperatures of 500°C and
900°C in flowing air.
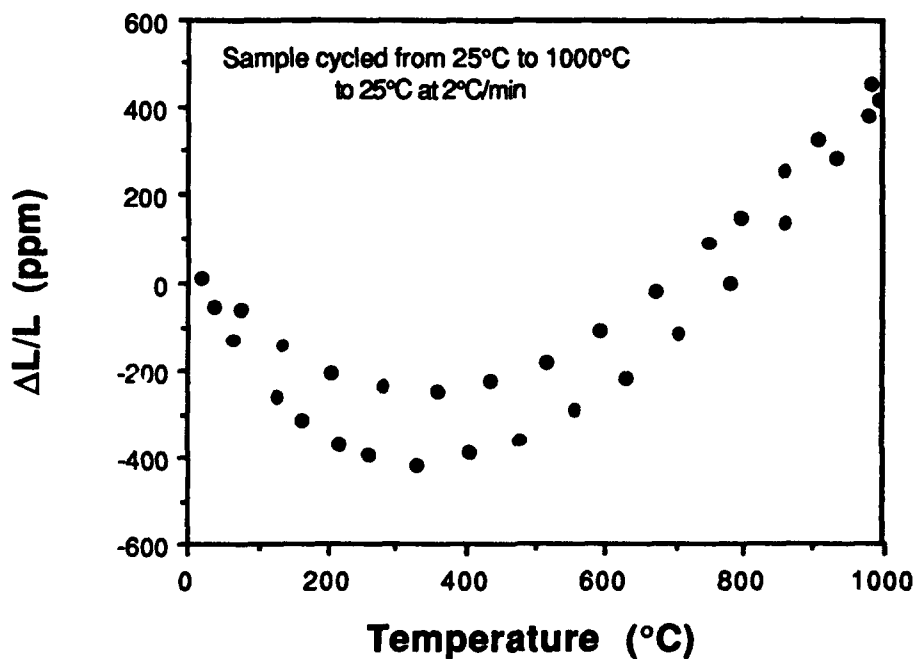
Figure 6.   Thermal strain as a function of temperature for the C/Mullite composite.

temperature was obtained by fitting a second order polynomial curve to the thermal strain data and taking the derivative. The average CTE varied from approximately -1.3 x $10^{-6}/^{\circ}C$ at room temperature to approximately 2.5 x $10^{-6}/^{\circ}C$ at 1000°C. The magnitude of the CTE as well as the dependence of CTE on temperature are typical of carbon fiber reinforced glass and glass-ceramic matrix composites studied at UTRC [7].

SUMMARY

A unidirectionally reinforced C/Mullite composite fabricated by Noritake Company and Tonen Corporation in Japan exhibited good tensile and flexural performance at room temperature. Flexural strength was retained to 1200°C in argon. Testing in air resulted in progressively lower flexural strength resulting from oxidation of the carbon fiber. However, the degree of strength retention at 1200°C in air (~50%) was thought to be impressive. Oxidation characteristics and thermal expansion behavior were found to be similar to carbon fiber reinforced glass and glass-ceramic matrix composites.

REFERENCES

1. Davis, R. F. and J. A. Pask. 1971. "Mullite," in High Temperature Oxides, Part IV, Refractory Glasses, Glass-Ceramics, and Ceramics, A. M. Alper, ed. New York: Academic Press, pp. 37-76.

2. Claussen, N. and G. Petzow. 1986. "Whisker-Reinforced Zirconia-Toughened Ceramics," in Tailoring Multiphase and Composite Ceramics, R. E. Tressler, et al., eds. New York: Plenum Press, pp. 649-662.

3. Becher, P. F. and T. N. Tiegs, 1987. "Toughening Behavior Involving Multiple Mechanisms: Whisker Reinforcement and Zirconia Toughening." Journal of the American Ceramic Society, 70 (9): 651-654.

4. Ruh, R., K. S. Mazdiyasni, and A. Zangvil. 1990. "Mullite-SiC-Whisker-Reinforced Ceramic Composites: Characterization and Properties," in Fiber Reinforced Ceramic Composites: Materials, Processing and Technology, K. S. Mazdiyasni, ed. Park Ridge, NJ: Noyes Publications, pp. 328-341.

5. Lange, F. F., et al., 1991. "Powder Processing of Ceramic Matrix Composites." Materials Science and Engineering, A144 (Oct): 143-152.

6. Tredway, W. K., K. M. Prewo, and C. G. Pantano, 1989. "Fiber-Matrix Interfacial Effects in Carbon Fiber Reinforced Glass Matrix Composites." Carbon, 27 (5): 717-727.

7. Tredway, W. K. and K. M. Prewo. July 31, 1989. "Carbon Fiber Reinforced Glass Matrix Composites for Structural Space Based Applications," UTRC Report R89-917704-1, Office of Naval Research Final Report, Contract N00014-85-C-0332.

Thermomechanical Response of a Cross-Ply Titanium Matrix Composite Subjected to a Generic Hypersonic Flight Profile

M. MIRDAMADI AND W. S. JOHNSON

ABSTRACT

Cross-ply laminate behavior of Ti-15V-3Cr-3Al-3Sn (Ti-15-3) matrix reinforced with continuous silicon-carbide fibers (SCS-6) subjected to a generic hypersonic flight profile was evaluated experimentally and analytically. Thermomechanical fatigue test techniques were developed to conduct a simulation of a generic hypersonic flight profile. A micromechanical analysis was used. The analysis predicts the stress-strain response of the laminate and of the constituents in each ply during thermal and mechanical cycling by using only constituent properties as input. The fiber was modeled as elastic with transverse orthotropic and temperature-dependent properties. The matrix was modeled using a thermo-viscoplastic constitutive relation. The fiber transverse modulus was reduced in the analysis to simulate the fiber-matrix interface failure. Excellent correlation was found between measured and predicted laminate stress-strain response due to generic hypersonic flight profile when fiber debonding was modeled.

INTRODUCTION

Titanium metal matrix composites, such as Ti-15V-3Cr-3Al-3Sn (Ti-15-3) reinforced with continuous silicon-carbide fibers (SCS-6), are being evaluated for use in hypersonic vehicle structure where high strength-to-weight and high stiffness-to-weight ratios are critical. This material system has the potential for applications up to 650°C. However, at temperatures above 400°C, titanium exhibits significant viscoplastic behavior. Since the operating temperatures of hypersonic vehicles airframe structure surface are well above 400°C, the viscoplastic behavior of the titanium must be accounted for in an analytical evaluation of titanium metal matrix composites (TiMMC).

The objectives of this research are to (1) experimentally determine the stress-strain response of a $[0/90]_{2s}$ SCS-6/Ti-15-3 laminate due to the thermomechanical fatigue (TMF) that will occur during hypersonic flight profile testing and (2) verify an analytical method to predict the measured laminate stress-strain response, including fiber-matrix interface failure.

Recently, Mirdamadi, et al. [1], used an analysis to predict the stress-strain response of unidirectional SCS-6/Ti-15-3 laminates subjected to simple in-phase and out-of-phase TMF loadings. Good agreement between experiment and prediction was found. This paper summarizes results for a more complex laminate, $[0/90]_{2s}$, with a more complicated TMF loading history [2].

M. Mirdamadi, National Research Council Research Associate, NASA Langley Research Center, Mail Stop 188E, Hampon, VA 23665-5225

W.S. Johnson, Senior Research Scientist, NASA Langley Research Center, Mail Stop 188E, Hampton, VA 23665-5225

MATERIAL AND TESTING PROCEDURE

A $[0/90]_{2s}$ SCS-6/Ti-15-3 laminate with a fiber volume fraction of 0.385 and a thickness of 1.68-mm was used in the present study. The SCS-6 fibers are continuous silicon-carbide fibers having a 0.140-mm diameter. The composite laminates were made by hot-pressing Ti-15-3 foil between tapes of unidirectional SCS-6 silicon-carbide fibers held in place with molybdenum wires. The Ti-15-3 matrix material is a metastable beta titanium alloy. Long exposures at elevated temperatures can lead to the precipitation of an α-phase which may alter the macroscopic mechanical behavior of the Ti-15-3 [3]. Therefore, the matrix and the composite in the present study was heat treated at 650°C for one hour in air followed by an air quench to stabilize the matrix material. This heat treatment was the same heat treatment used by Pollock and Johnson [4]. After the heat treatment, the viscoplastic material properties of the Ti-15-3 matrix at room temperature, 316°C, 482°C, 566°C, and 650°C were determined previously [1]; additional properties were also determined at 427°C [2]. It was assumed that the matrix properties remained the same from room temperature to 150°C and that the fibers remained elasic with temperature-dependent properties [2].

TMF spectrum testing was conducted on straight-sided rectangular specimens, 152-mm x 12.7-mm x 1.68-mm, cut using a diamond wheel saw. Brass tabs (10-mm x 30-mm x 1-mm) were placed between the end of the specimen and the grips to avoid specimen failure in the serrated grips. The brass tabs were not bonded to the specimens but were held in place by the grips.

A TMF test capability was developed to conduct hypersonic flight profiles. The temperature and the load spectrum of a generic hypersonic mission flight profile are shown in Figure 1. The letters shown in Figure 1 will be used later for comparison with stress-strain results. As shown in the figure, the flight profile consists of both isothermal and non-isothermal load cycling at 1 Hz with hold times at different temperatures. The thermal loading rates during heating and cooling were 2.8°C/sec and 1.4°C/sec, respectively.
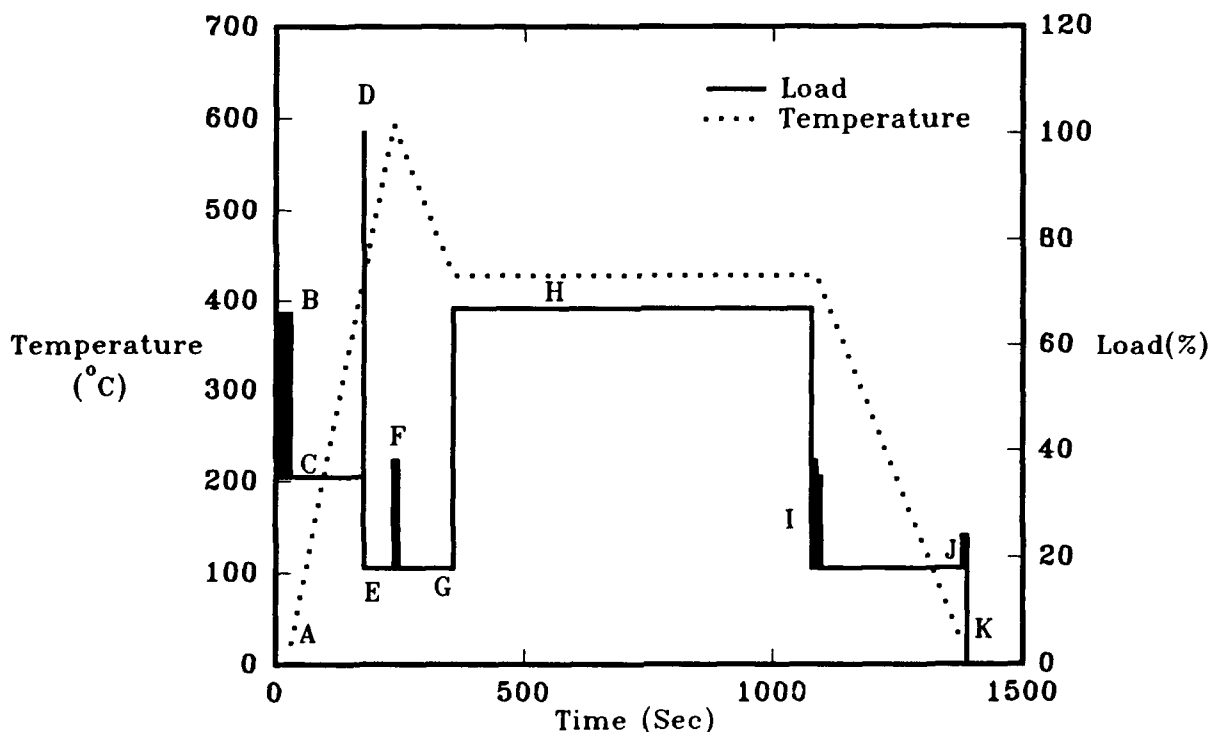
Figure 1. Generic hypersonic flight profile.

The TMF test setup consisted of a 100-kN servo-hydraulic test frame with water-cooled grips, a load profiler, a 5-kW induction generator controlled by a temperature profiler, and a nitrogen supply tank. The load and temperature spectra are independently controlled by load and a temperature profilers. The temperature profiler was modified to accept a command signal from the load profiler to initiate temperature spectrum at any desired point in the load profile. More details on the TMF test setup are given in [2]. Axial strains were measured on the edge of the specimen using a high temperature water-cooled quartz rod extensometer with a 25-mm gage length. An eight channel analog/digital PC based data acquisition system was used to record and store the test data. Prior to the flight profile test, the specimen was subjected to the temperature profile alone to ensure thermal stability and synchronization with the load profiler command.

ANALYTICAL METHOD

The stress-strain response of the $[0/90]_{2s}$ laminate was predicted using a micromechanics analysis. The VISCOPLY code, developed by Bahei-El-Din, is based on constituent properties. The program uses the vanishing fiber diameter (VFD) model [5] to calculate the orthotropic properties of a ply. The ply properties are then used in a laminated plate analysis [6] to predict the overall laminate stress-strain response. Both the fiber and the matrix can be described as thermo-viscoplastic materials. The viscoplastic theory used in the VISCOPLY program was developed by Bahei-El-Din [7] for high temperature, nonisothermal applications and is based on the viscoplasticity theory of Eisenberg and Yen [8]. The theory used in the VISCOPLY program assumes the existence of an equilibrium stress-strain curve which corresponds to the theoretical lower bound of the dynamic response. The theory further assumes that the elastic response is rate-independent and that inelastic rate-dependent deformation takes place if the current stress state is greater than the equilibrium stress.

Combinations of thermal and mechanical loads can be modeled. Sequential jobs can be run for varying order and rate of load and temperature. Fiber and matrix average stresses and strains and the overall composite response under thermomechanical loading conditions are calculated. Although not used in the current work, the program has the capability to model the fiber as a viscoplastic material with transverse orthotropic properties.

A simple procedure was used to analytically simulate the fiber-matrix interface failure known to occur in the SCS-6/Ti-15-3 material. In room temperature fatigue tests [9], a distinct knee was observed in the stress-strain response at stress levels well below the yield stress of the matrix material. In the first cycle, this knee was found to correspond to the stress required to overcome the thermal residual stresses and fail the fiber-matrix interface in the off-axis plies. In subsequent fatigue cycles, the knee was observed at a lower stress level, the stress required to overcome the thermal residual stresses in the matrix. To simulate the fiber-matrix interfacial failure, the transverse modulus of the fibers in the 90° plies was reduced for stress levels above the stress level corresponding to the observed knee in the stress-strain response of the $[0/90]_{2s}$ laminate at room temperature. In elevated temperature fatigue tests, however, no knee was apparent in the stress-strain response [4] and it was assumed that fiber-matrix interfacial failure occurred upon loading. Thus, the fiber transverse modulus in the 90° plies was reduced at the start of loading for temperatures above 400°C.

RESULTS AND DISCUSSION

In this section, the experimental and analytical results are presented. The isothermal stress-strain response of the $[0/90]_{2s}$ laminates is analyzed to assess the effects of fiber-matrix separation and loading rates. The experimental results and the theoretical predictions for the flight profile are presented.

ISOTHERMAL LAMINATE BEHAVIOR

First, the appropriate reduction of the transverse modulus of the fibers in the 90° plies to simulate the fiber-matrix interface failure was determined. At room temperature the fiber-matrix interface failure occurred at a stress level of 70 MPa determined from the knee in the experimental stress-strain curve [2]. At 427°C, it was assumed that the fiber-matrix interface failed instantly upon loading. The experimental and predicted stress-strain response of the SCS-6/Ti-15-3 $[0/90]_{2s}$ laminate at 427°C (stress rate of $\dot{S}=1250$ MPa/s) is shown in Figure 2. The VISCOPLY correlations are shown for various ratios of the fiber transverse modulus to the fiber axial modulus (E_t^f / E_a^f) in the 90° ply ranging from 1.0 to 0.001. Multiplying the 90° fiber transverse modulus by a factor of 0.1 produced very good correlations at 427°C. The room temperature correlations for $E_t^f / E_a^f = 0.1$ were also fairly good [2]. Therefore, a multiplication factor of 0.1 was used to model fiber-matrix interface failure at all temperatures. This reduction factor may be dependent on, fiber volume fraction, processing parameters, fiber-matrix interface strength, and fiber and matrix properties.
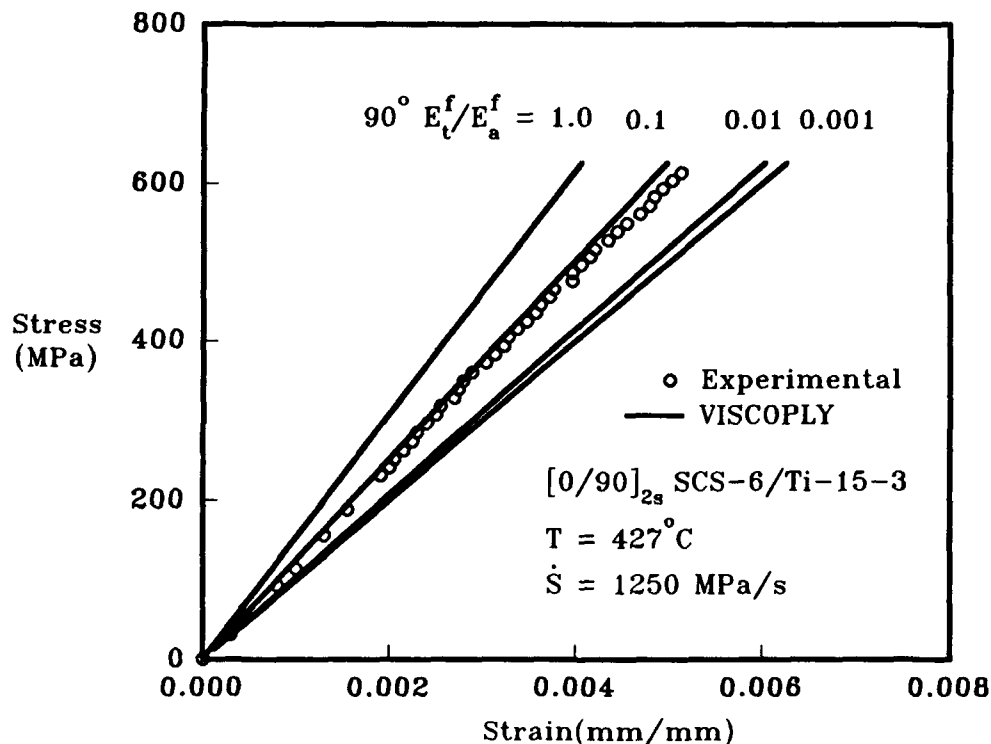
Figure 2. Effect of reducing 90° fiber transverse modulus on
VISCOPLY predictions at 427°C.

Next, the effect of loading rate on the predictions was examined. Figure 3 shows the composite experimental stress-strain response during the second cycle (i.e., subsequent to the fiber-matrix interface failure of the 90° plies) at a stress rate of 10 MPa/sec at 650°C [4]. Included in the figure are the VISCOPLY predictions with fiber-matrix interface failure of the 90° plies (E_t^f / E_a^f=0.1). The VISCOPLY prediction at a rate of 900 MPa/sec is also shown. The 900 MPa/sec rate corresponds to the loading rate used in the hypersonic flight profile. As seen in the figure VISCOPLY accurately predicted the initial elastic modulus but was somewhat less accurate at higher stress levels. The predicted maximum strain was 7% smaller than observed experimentally. The VISCOPLY prediction at the rate of 900 MPa/sec resulted in a nearly linear stress-strain response. These comparisons demonstrate the effect of the matrix rate-dependent behavior on composite stress-strain response.

FLIGHT PROFILE BEHAVIOR

In this section, the stress-strain response of the laminate subjected to the flight profile shown in Figure 1 will be analyzed and compared to experimental results. Predictions will be made assuming perfect bonding of the fiber-matrix interface in the 90° plies and assuming failure of the 90° fiber-matrix interfaces. For clarity, during the rapid cycling segments of the flight profile (e.g., segments B, F, I and J in Figure 1), only the first loading and last unloading cycle will be shown in the figures.
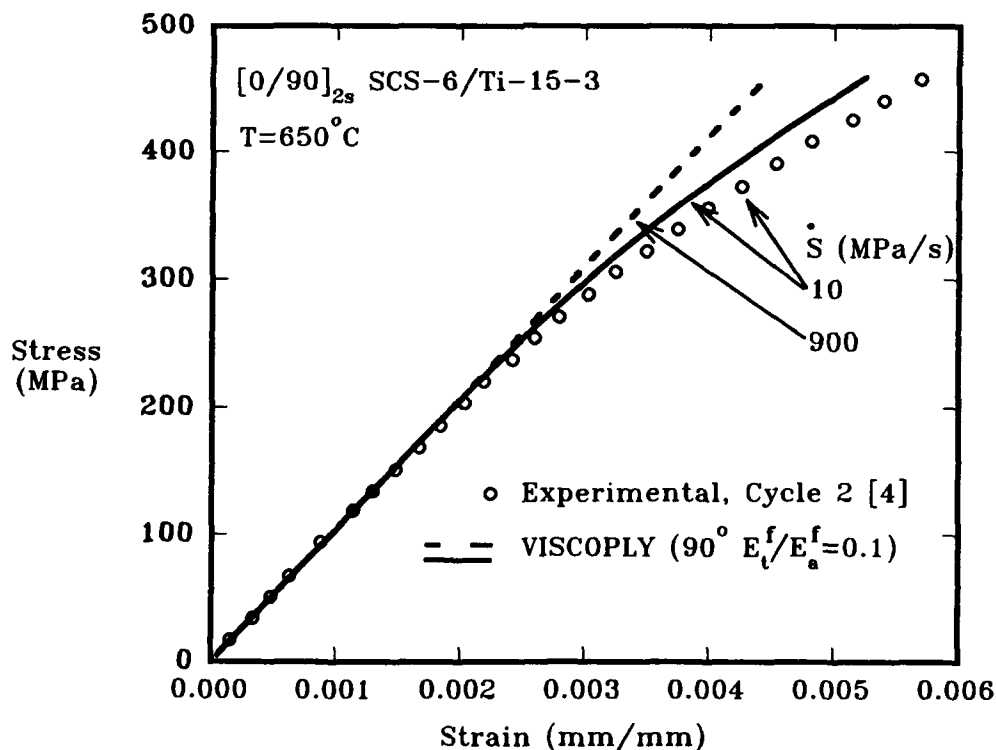
Figure 3. Prediction of stress–strain response of $[0/90]_{2s}$ scs–6/Ti–15–3 composite at 650°C.

One test was conducted applying only the thermal history of the flight profile shown in Figure 1. The measured thermal strains and the VISCOPLY predictions are shown in Figure 4. The measured thermal strains match the applied temperature profile previously shown in Figure 1 indicating excellent control of the heating and cooling rates. The thermal strain of the laminate was accurately predicted by VISCOPLY.

The specimen was then subjected to the full thermal and mechanical flight profile shown in Figure 1 at 100% stress equal to 420 MPa. The stress-strain response of the fifth repetition of the flight profile is shown in Figure 5. The letters placed at various locations on the stress-strain response can be referenced back to Figure 1 to find the associated point in the flight profile. The horizontal portions of the predictions and the experimental data indicate an increase in strain due solely to temperature changes while the mechanical loads were held constant. The VISCOPLY predictions assumed perfect fiber-matrix interface bonding. As seen in Figure 5, VISCOPLY predicted a stiffer response than was observed experimentally. The predictions of the cyclic loads shown at locations F and I appear broad because the temperature was changing. The experimental and predicted creep strain during hold period at H was very small. Predictions of the composite response under the flight profile made with simulated interface failure of the 90° plies are shown in Figure 6. The prediction agreed well with the experimental behavior when the interface failure was modeled as previously discussed.
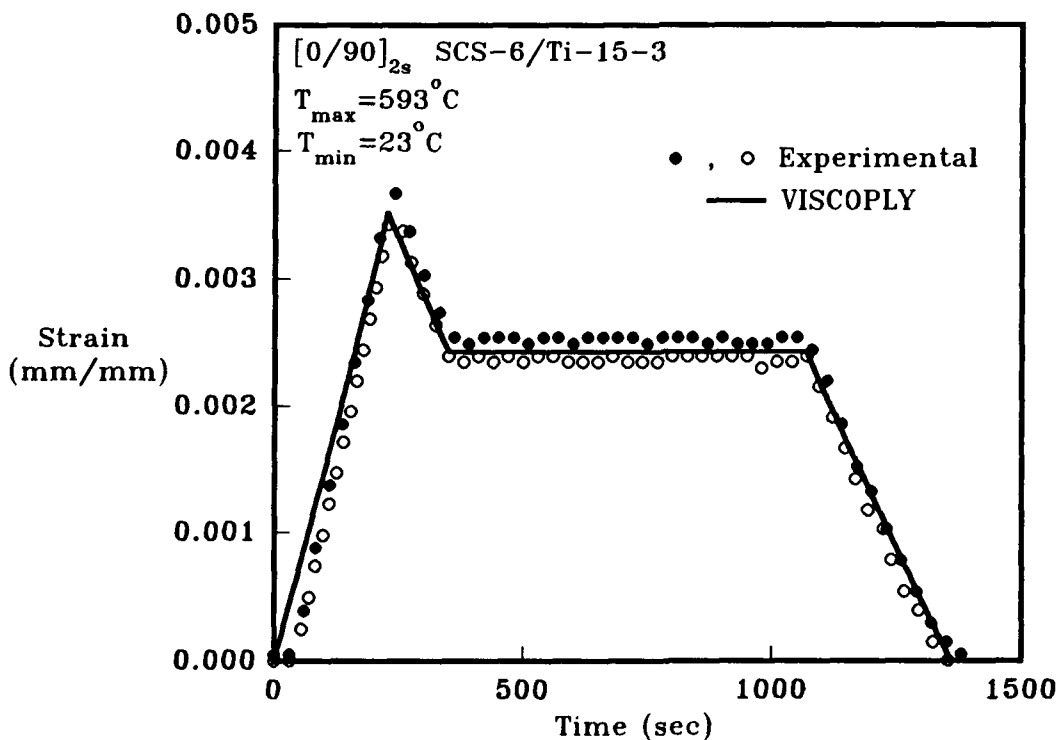
Figure 4. Predicted and experimental thermal strains as a function of time.
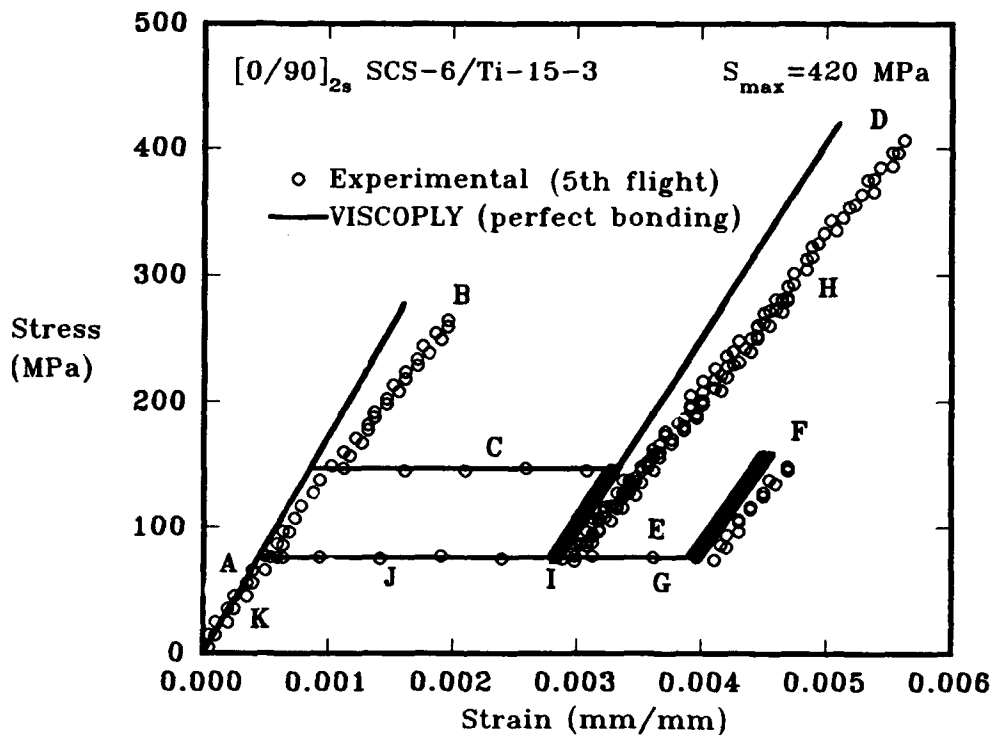
Figure 5. VISCOPLY prediction of composite response to the flight profile assuming perfect bonding.
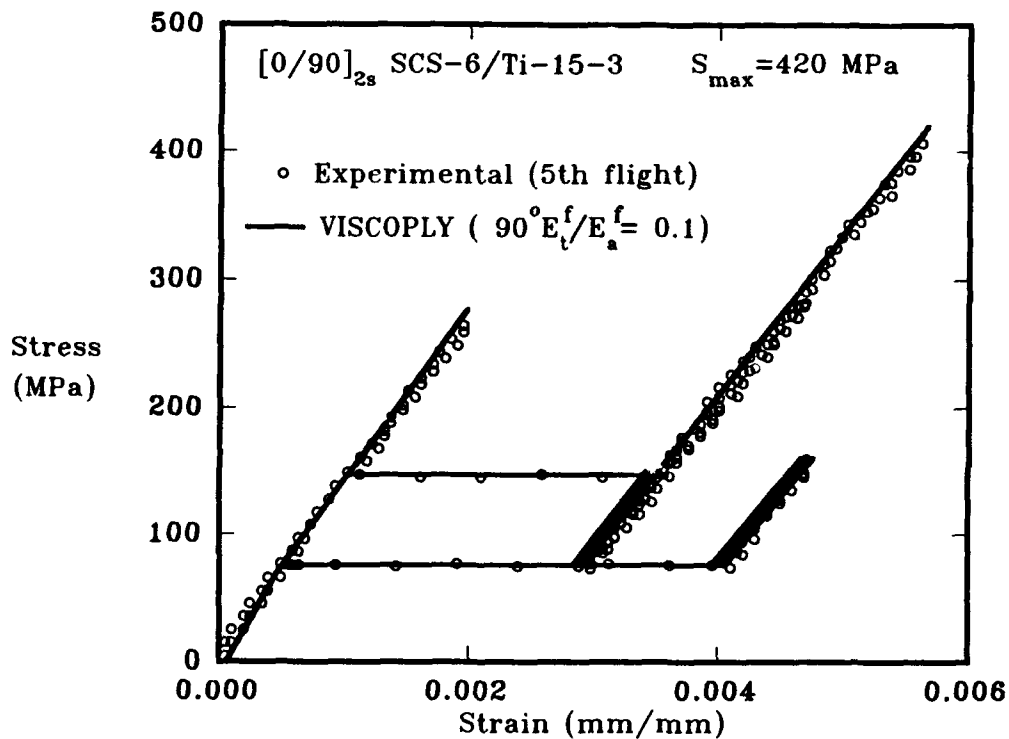
Figure 6. VISCOPLY prediction of composite response to the flight profile with fiber-matrix interface failure of $90°$ plies.

If the fatigue behavior of the laminate is to be well understood and prediction methodology developed, the behavior of the composite constituents must be understood. Previous work by Johnson, et al. [9] showed good correlation between the stress range in the 0° fiber and the number of cycles to failure of the laminate at room temperature. More recently, Mirdamadi, et al. [1] used the 0° fiber stress range calculated from a micromechanics analysis to compare the TMF data of Castelli, et al. [10], Gabb, et al. [11], and the isothermal fatigue data of Pollock and Johnson [4]. They determined that for a given condition, the fatigue strength of the 0° fiber was controlled by a combination of temperature, loading frequency, and time at temperature. Furthermore, for a given temperature, loading frequency, and time at temperature, the stress range in the 0° fiber controlled the fatigue life. Bigelow and Johnson [12] and Bakuckas, Johnson, and Bigelow [13] accurately predicted the static strength of virgin specimens and fatigued specimens by monitoring the 0° fiber stress. Therefore, the 0° fiber stress (or strain) plays a major role in the static and fatigue strength of TiMMC. Under isothermal loading conditions, the 0° fiber strain is equivalent to the overall composite axial strain. However, under non-isothermal loading conditions, where the load and the temperature are cycled, determination of the 0° fiber stress is not straight forward and micromechanics-based models are required to predict the 0° fiber stress. Figure 7 shows the VISCOPLY predictions of the 0° fiber stress as a function of time during the flight profile. This prediction was made assuming fiber-matrix interface failure in the 90° plies. Such predictions are important when analyzing the fatigue behavior of the composite and could be used in a failure criteria.
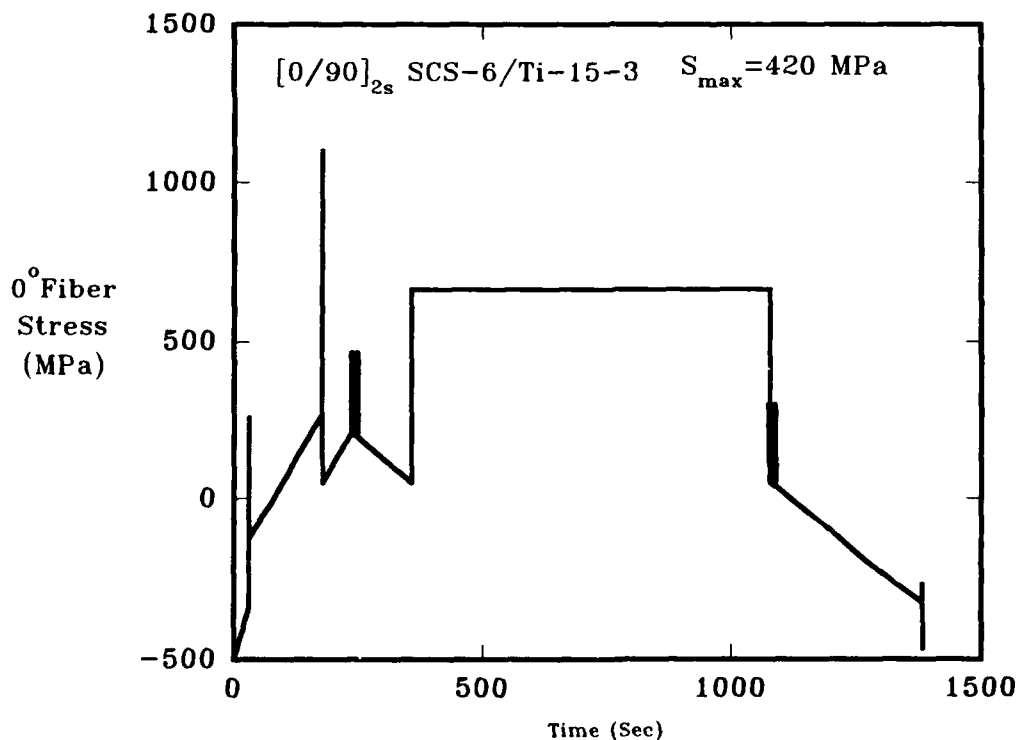
Figure 7. VISCOPLY prediction of 0° fiber stress under flight profile with fiber-matrix interface failure of 90° plies.

CONCLUSIONS

A TMF test capability was developed to simulate a generic hypersonic flight profile. The VISCOPLY analysis was used to analyze the stress-strain response of the $[0/90]_{2s}$ SCS-6/Ti-15-3 laminate subjected to the flight profile loading. The following conclusions were made:

o   In this material system, fiber-matrix interface failure must be modeled for accurate predictions. Fiber-matrix interface failure was modeled in VISCOPLY program by dividing the transverse modulus of the fibers in the 90° plies by a factor of 10.

o   The mechanical response of these composites is rate-dependent at elevated temperatures. The VISCOPLY analysis can predict such dependence.

o   VISCOPLY accurately predicted the composite stress-strain response for a generic hypersonic flight profile.

REFERENCES

1. M. Mirdamadi, W.S. Johnson, Y.A. Bahei-El-Din, and M.G. Castelli., "Analysis of Thermomechanical Fatigue of Unidirectional Titanium Metal Matrix Composites," NASA TM-104105, NASA Langley Research Center, July (1991).

2. M. Mirdamadi and W.S. Johnson, "Stress-Strain Analysis of a $[0/90]_{2s}$ Titanium Matrix Laminate Subjected to a Generic Hypersonic Flight Profile," NASA TM-107584, NASA Langley Research Center, March (1992).

3. H.W. Rosenberg, "Ti-15-3: A New Cold-Formable Sheet Titanium Alloy," Journal of Metals, 35(11)(1986), 30-34.

4. W.D. Pollock and W.S. Johnson, "Characterization of Unnotched SCS-6/Ti-15-3 Metal Matrix Composites at 650°C," Composite Materials: Testing and Design (Tenth Volume), ASTM STP 1120, Glen C. Grimes, Ed., American Society for Testing and Materials, Philadelphia, (1992), 175-191.

5. G.J. Dvorak and Y.A. Bahei-El-Din, "Plasticity Analysis of Fibrous Composites," Journal of Applied Mechanics, 49 (1982), 327-335.

6. Y.A. Bahei-El-Din, "Plasticity Analysis of Fibrous Composite Laminates Under Thermomechanical Loads," Thermal and Mechanical Behavior of Ceramic and Metal Matrix Composites, ASTM STP 1080, J.M. Kennedy, N.H. Moeller, and W.S. Johnson, eds., American Society for Testing and Materials, Philadelphia (1990), 20-39.

7. Y.A. Bahei-El-Din, R.S. Shah, and G.J. Dvorak, "Numerical Analysis of the Rate-Dependent Behavior of High Temperature Fibrous Composites," Symposium on Mechanics of Composites at Elevated and Cryogenic Temperatures, ASME Applied Mechanics Division Meeting, Columbus, Ohio, June 16-19 (1991), 67-78.

8. M.A. F'senberg and C.F. Yen, "A Theory of Multiaxial Anisotropic Viscoplasticity," ASME Journal of Applied Mechanics, 48 (1981), 276-284.

9. W.S. Johnson, S.L. Lubowinski, and A.L. Highsmith, "Mechanical Characterization of Unnotched SCS-6/Ti-15-3 Metal Matrix Composites at Room Temperature," Thermal and Mechanical Behavior of Metal Matrix and Ceramic Matrix Composites, ASTM STP 1080, J.M. Kennedy, H.H. Moeller, and W.S. Johnson, eds., American Society for Testing and Materials, Philadelphia (1990), 193-218.

10. M.G. Castelli, P. A. Bartolotta, and J.R. Ellis, "Thermomechanical Fatigue Testing of High Temperature Composites: Thermomechanical Fatigue Behavior of SiC (SCS-6)/ Ti-15-3," Composite Materials: Testing and Design (Tenth Volume), ASTM STP 1120, Glen C. Grimes, ed., American Society for Testing and Materials, Philadelphia, (1991), 70-86.

11. T.P. Gabb, J.Gayda, and R.A. MacKay "Isothermal and Nonisothermal Fatigue Behavior of a Metal Matrix Composite," Journal of Composite Materials, 24 (1990), 667-686.

12. C. A. Bigelow and W. S. Johnson, "Effect of Fiber-Matrix Debonding on Notched Strength of Titanium Metal Matrix Composites," NASA TM-104131, NASA Langley Research Center, August (1991).

13. J. G. Bakuckas, W. S. Johnson, and C. A. Bigelow, "Fatigue Damage in Cross Plied Titanium Metal Matrix Composites Containing Center Holes," NASA TM-104197, NASA Langley Research Center, February (1992).

Theoretical Analysis for Fiber Orientation Observed in One Visual Field

ICHIRO SHIOTA, YOSHIO IMAI, YOSHIKAZU SHINOHARA AND SUSUMU IKENO

ABSTRACT

Mechanical properties of an FRM depend not only on the properties of component materials, fiber volume fraction and aspect ratio, but also on fiber orientation. Y.Imai et al. advocated a new simple experimental method to describe the fiber orientation which was observed in one tilted visual field. But the distribution in one tilted visual field is only a projection from a certain angle. In this report, the probability of finding a fiber in a certain angle range was theoretically described to support the advocate.

INTRODUCTION

Properties of a fiber reinforced composite material are mainly described by properties of the reinforcement and the matrix, fiber volume fraction, aspect ratio and fiber orientation (hereafter, simply as "orientation"). We can describe the mechanical properties of component materials quantitatively. Fiber volume fraction and aspect ratio of a fiber can be measured experimentally. It is easy to determine fiber orientation in the case of continuous reinforcement.

On the other hand, there is no simple way to quantitatively describe the orientation in an FRM with short fiber reinforcement, even though it is equally important to the other factors. As is known, mechanical properties such as modulus and tensile strength of an FRM are rather high along the fiber direction. Therefore the orientation in

National Research Institute for Metals, STA
3-12, 2-chome, Nakameguro, Meguro-ku, Tokyo 153, JAPAN

short fiber reinforced materials is often extruded to obtain unidirectional orientation along the stress axis. However, the orientation varies widely, as every fiber has its own orientation. Then the orientation should be described statistically. In the case of an extruded FRM by short fibers, the orientation is usually described by visual approximation at the cross section of the FRM, say "90% unidirectional" and so on. This is quite unclear.

Y.Imai et al.[1] advocated an experimental method to describe the orientation. In this report, we attempt to give a theoretical support to their advocate.

EXPERIMENTAL METHOD TO DETERMINE THE FIBER ORIENTATION

Let us start with the experimental methods. There are several methods to determine the orientation[1]-[3]. They are classified into two groups.

One is based on the observation of projecting fibers from an etched surface, which is normal to the extrusion direction as shown in Fig.1 a. If we have only one visual field, we cannot measure the deviation angle from the extrusion axis, but only the deviation direction as schematically shown in the figure. Then we have to carry out very elaborate work to take two photographs from different angles and adopt a stereology technique.

The other is based on observation of fibers at a polished surface, which is parallel to the extrusion direction as shown Fig.1 b'. In this case, the parallel fibers, which are most important, may fall down more easily

whiskers on etched surface

see Photo 1

a

φ

c

b

b'

Extrusion
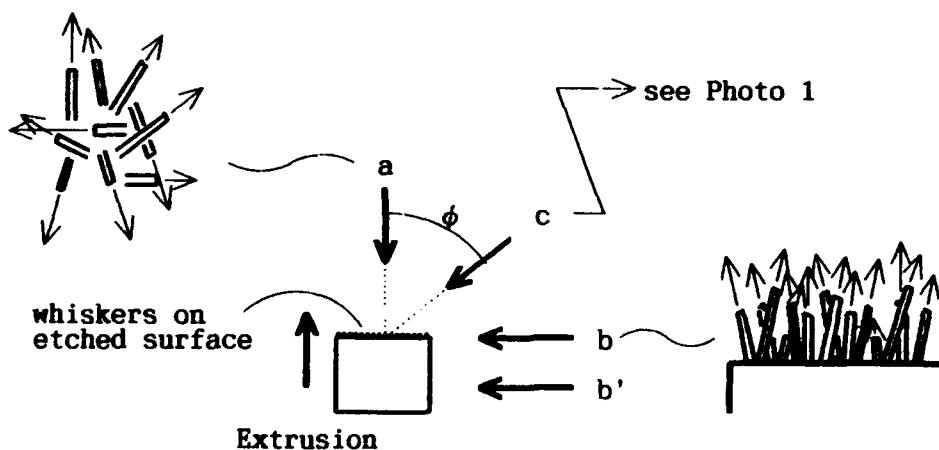
Fig.1 Observation direction for fiber orientation

than the others during polishing. If we observe the fibers at the etched surface as shown in Fig.1 b, we can observe only a limited number of fibers from this direction.

Besides these methods, slantwise observation of the etched surface, as shown in Fig.1 c, may be useful, because we can observe many fibers and also their directions in one visual field. From this point of view, Imai et al. recommend an angle in the range of 40° to 50° to observe as many fibers as possible and to measure their deviation angles easily in one visual field. An example is shown in Photo 1 which was taken from 40° by using SEM. Deviation angles of the fibers were measured on the photograph. Deviations of positive and negative angles result in identical properties. Therefore only absolute values of angles are considered. The distribution was expressed by a simple form as follows;

$$Y=100/(1+X^m)$$
1)

where m is a function of orientation.

The final result by this method is described with solid crosses in Fig.8. The distribution of the orientation in the photograph is naturally different from the real distribution, because the distribution in the photograph is only a projection from a certain angle. Here, we shall confirm whether this curve can be obtained theoretically.

5μm
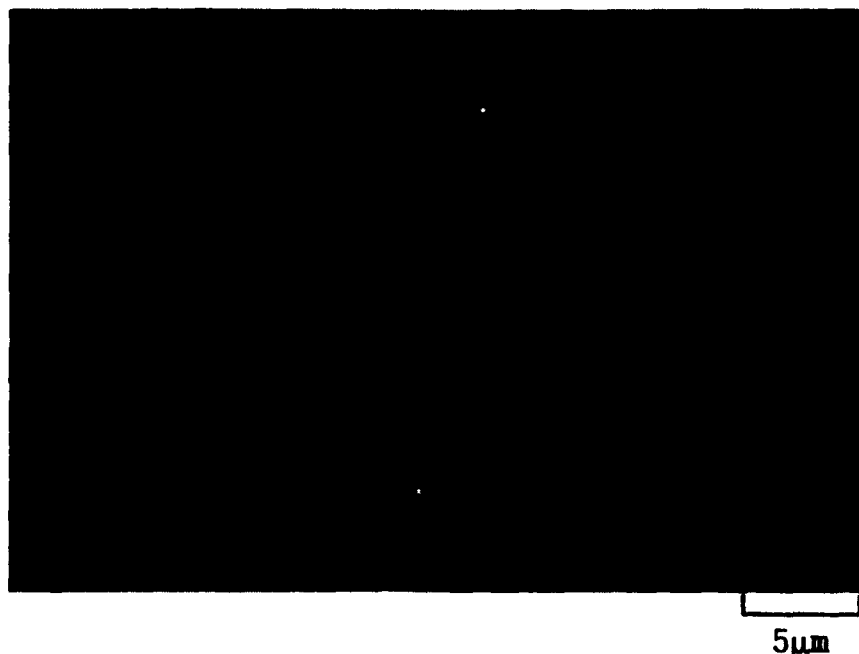
Photo 1 SEM micrograph by 40° tilting of the sample.

THEORETICAL DESCRIPTION OF FIBER ORIENTATION

We assume the extrusion direction coincides with x-axis, and a fiber with unit length deviates θ-degrees from the x-axis, as shown in Fig.2. The top of the fiber is found on the circle at an angle ψ from the y-direction, and the probability of finding the top is equal at any point of the circle around the x-axis. The coordinates of the top of the fiber (A) can be described as follows;

$$(A) = (x,y,z) = (\cos\theta, \sin\theta\cdot\cos\psi, \sin\theta\cdot\sin\psi) \qquad 2)$$

Now we turn the extrusion direction(x') by ϕ around the y-axis as shown in Fig.3. In this case, only the coordinate of x and z may change, while y does not change. Then we can describe the coordinates of the top of the fiber(A') as follows;

$$\left.\begin{array}{c} \left(\begin{array}{c} x' \\ z' \end{array} \right) = \left(\begin{array}{cc} \cos\phi & -\sin\phi \\ \sin\phi & \cos\phi \end{array} \right) \left(\begin{array}{c} x \\ z \end{array} \right) \\[12pt] y' = y \end{array}\right\} \qquad 3)$$

Observation

Observation
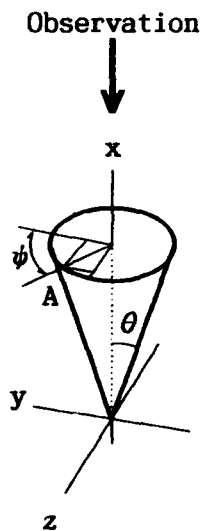
Fig.2
Position of the
fiber top around
the x-axis.
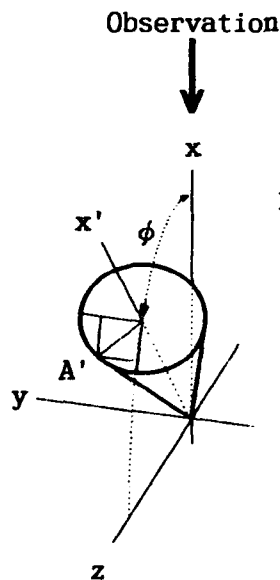
Fig.3
Position of the
fiber top around
slant axis(x').
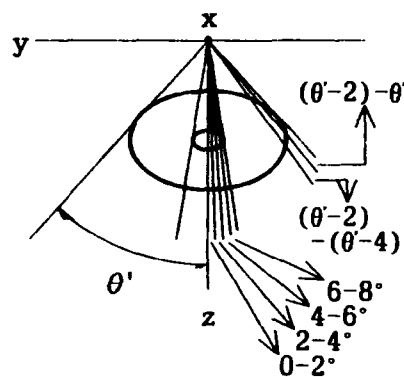
Fig.4
Projected position of
the fiber top on y-z
plane, and periphery
length in an angle
range for θ=5° and 20°.

Let us assume that we observe the fiber from the x-axis. This is the same as observing the projection of a fiber on the y-z plane, and the direction of the extrusion axis coincides with the z-axis. The deviation(θ') from the z-axis of a fiber is expressed as follows by substituting x and z of eq.2) into z' of eq.3);

$$\theta' = \tan^{-1}\left(\frac{y'}{z'}\right) = \tan^{-1}\left(\frac{\sin\theta\cdot\cos\psi}{\cos\theta\cdot\sin\phi + \sin\theta\cdot\sin\psi\cdot\cos\phi}\right) \quad 4)$$

The projection of the top of the fiber is on the small and large ellipses for θ=5° and 20°, respectively as shown in Fig.4. In the case of ϕ=40°, θ' is shown as the function of ψ for θ=5°,10°,20° and 30° in Fig.5. We can understand from Fig.4 that θ'max is larger than θ, and the angle ψ at which θ'max occurs approaches 270° as θ increases as seen in Fig.5.

The probability of finding a fiber in the angle range of θ'=0 to 2° is the ratio of the total length of near site and far site peripheries to the total length of the periphery of the ellipse. This technique can be applied to any angle range. As we can see in Fig.4, the length of the periphery at the tangent direction is longer than one for the smaller angles. So the probability of finding a fiber in the direction of θ'max is larger than one around θ=0°. Calculated results of the probability vs. angle range are shown in Fig.6.

Here, we assume the deviation angle of the fiber obeys the following normal distribution.

$$P = \frac{h}{\sqrt{\pi}} \exp\left\{-h^2\left(\frac{\theta}{10}\right)^2\right\} \quad 5)$$
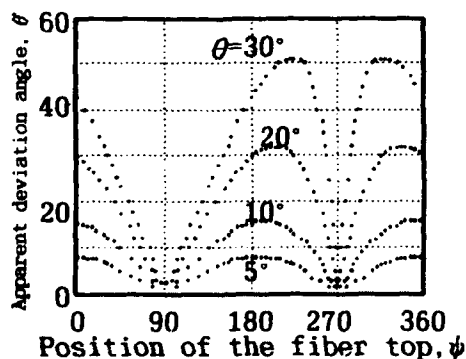
Fig.5 The apparently observed angle(θ') vs the position of the fiber top as the function(ψ) in case θ=40°.
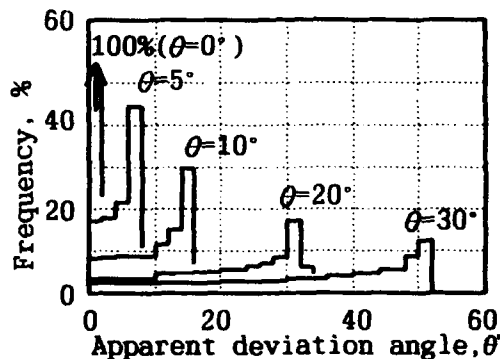
Fig.6 Probability of finding a fiber in θ' range for θ=5°,10°,20° and 30°, in case ϕ=40°.

Integration of this equation from $\theta=-\infty$ to $\theta=\infty$ yields 1. Naturally, $\theta=0°$ is the center of the distribution and it coincides with the extrusion direction, and it is enough to consider the absolute value of deviation as described above. Fig.7 a is an example in which the fibers are highly oriented, while c is rather random. Here, the longitudinal scale is doubled to take the absolute value of θ. In Imai's data, we can see a rather large frequency of orientation angle up to 15–20°. Then let us adopt the curve of Fig.7 b in which the half height width is approximately 17°. In this figure, we can calculate the ratio of fibers in each deviation angle range.

For example, the ratio of hatched area at $\theta=0$ to 2° to total area under the curve of b (i.e. =1) is 11.2%, similarly 10.6% for $\theta=4-6(=5°)$, 8.8% for $\theta=10°$, 4.2% for 20°, 1.2% for 30°, and so on.

Then the probability of finding a fiber in the range of θ' to $(\theta'+d\theta')$ is as follows; the distribution for each θ from $\theta'=0$ to θ'max, which is shown as examples in Fig.6, is multiplied by the ratio of the corresponding angle in Fig.7.

This means that 11.2% of the fibers are parallel to the extrusion direction, i.e. $\theta=0°$. In this case, all the fibers (11.2% x 100%) are observed along the z-axis. In the case of $\theta=5°$, there are about 10.6% of the fibers as shown in Fig.7, and approximately 17% of these fibers are observed along the z-axis as shown in Fig.6, then 1.8% (=10.6% x 17%) of the total fibers should be observed in the range of $\theta'=0$ to 2°. Similarly, 3.3% for $\theta=3°$, 0.7% for $\theta=10°$, 0.16% for
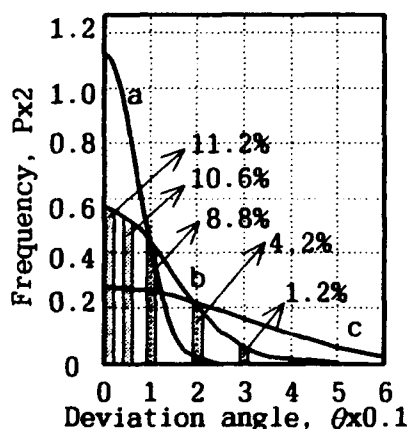
Fig.7 Normal distribution
curves and ratio in
an angle range.
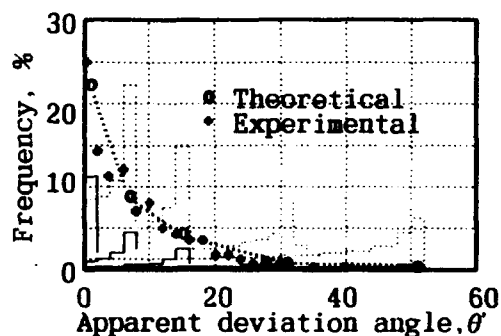
Fig.8 The apparent observation
angle(θ') vs. frequency of
experimental(•) and theo-
retical(◦)values.
··· :Original frequency x 0.5
— :Weighted frequency for
each deviation angle(θ)
····· :Theoretical frequency

θ=20°, 0.004% for θ=30°, and so on, are observed in the range of θ'=0 to 2°. All these are summed up, and 22% was obtained as the probability of finding a fiber in the range of θ'=0 to 2°. Then the probability is described by summing each weighted distribution in every θ' range. The final result is shown in Fig.8, which agrees well with Imai's experimental results with m=1.2.

CONCLUDING REMARKS

The probability of finding a fiber in a certain angle range in one tilted visual field was theoretically described. This result agrees well with the distribution of the fiber orientation by Y.Imai et al. By this theoretical support, it is confirmed that the simple experimental method advocated by Imai et al. is practically useful.

ACKNOWLEDGEMENT

REFERENCES

1.Imai,Y.,Shiota,I.,Shinohara,Y. and Ikeno,S.,1992."Evaluation of Fiber Orientation in Short Fiber Reinforced Metals", Journal of Japan Society of Composite Materials,in printing. (in Japanese)

2.Osawa,T.,1975."Composite Materials," in General Chemistry vol.8, ed.Japan Chem. Soc.,Tokyo Univ. Press,pp74-88, (in Japanese)

3.Hull,D., Trans. Miyairi,H. et al.,1984.Introduction of Composite Materials, Baihukan, pp.54-73,(in Japanese)

SESSION 5B

Durability: Prediction and Observation II

Investigating Near Tip Damage Mechanics and Crack Growth Behavior in a Particulate Composite Material

C. T. LIU[1] AND C. W. SMITH[2]

ABSTRACT

In this study, the local behavior and the strain fields near the crack tip in centrally cracked sheet specimens of a particulate composite were investigated. The specimens were subjected to a constant crosshead speed of 2.54 cm/min. at room temperature. The grid method was used to determine the strain fields near the crack tip at two different applied strain levels. The effects of the applied strain level on the strain fields and the local damage and fracture processes near the crack tip were investigated and the results are discussed.

INTRODUCTION

In recent years, a considerable amount of work has been done in studying crack growth behavior in highly filled polymeric materials.[1-5] These materials consist of hard particles contained in a soft elastomeric binder. It is well known that, on the microscopic scale, these materials can be considered nonhomogeneous materials. When these materials are stretched, the different sizes and distribution of filler particles, the different crosslink density of polymeric chains, and the variation of the bond strength between the particles and the binder can produce highly nonhomogeneous local stress and deformation fields. Depending upon the magnitude of the local stress and deformation, damage can be developed in the material, especially near the crack tip region. The damage developed in the material may be in the form of microvoids or microcracks in the binder or in the form of dewetting between the binder and the filler particle. The growth of the damage in the material may take place by material tearing or by successive nucleation and coalescence of the microcracks. These damage processes are time–dependent and are the main factor responsible for the time–sensitivity of the strength degradation as well as the fracture behavior of the material. Therefore, in order to obtain a fundamental understanding of crack growth behavior in the highly filled polymeric material, a detailed knowledge of the characteristics of damage evolution and local fracture behavior near the crack tip is required.

[1]Program Manager, Phillips Laboratory (AFSC), PL/RKPB, Edwards AFB, CA 93523–5000, Phone (805) 275–5642.
[2]Alumni Professor, Department of Engineering Science and Mechanics, Virginia Polytechnic Institute and State University, Blacksburg, VA 24061–0219, Phone (703) 231–6159.
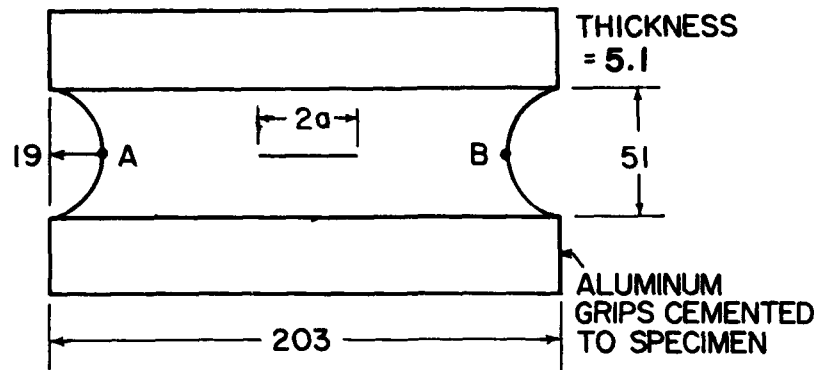
INITIAL CRACK LENGTH (2a) 3.81 CM: DIMENSIONS IN MILLIMETERS

FIGURE 1.   Biaxial Test Specimen Dimensions

In this study, the local strain fields and damage accumulation process near the tip of a crack in a composite solid propellant subjected to a constant crosshead speed were investigated using pre-cracked sheet specimens. The specimens were 20.32 cm. wide, 5.08 cm. long and 0.51 cm. thick (Fig. 1). A 3.81 cm. crack, which was parallel to the longest side of the specimen and perpendicular to the loading direction was cut at the edge of each specimen. A coarse grid with 0.2 mm. spacing between the vertical and the horizontal grid lines was deposited on the surface of the specimens. During the test, a camera was used to photograph the deformed grid near the crack tip at selected time intervals. The experimental data were processed to determine the strain fields near the crack tip. The local strain fields and fracture behavior prior to and after crack growth were investigated and the results are discussed.

In addition to investigating the local strain fields and damage accumulation process, the crack growth behavior in the specimen was also investigated. In this study, the experimental data (crack length, load, time) were used to calculate the instantaneous crack growth rates as a function of time. The results of the crack growth rate analysis and the local damage analysis were used to explain the crack growth behavior in the material.

THE EXPERIMENTS

The displacement and strain fields near the crack tip in the biaxial specimens were determined by the grid method. Prior to testing, a coarse cross grating consisting of squares of 0.2 mm. on each side and which had a thickness of less than 2.5×10^{-2} mm. was deposited in the neighborhood of the crack tip. The procedure to print the grid on the surface of the specimen was to cover an area of about 5.08 by 5.08 cm. with a very thin layer of mixed silicone grease and titanium dioxide. Then a mesh of 5 lines per millimeter was placed on that area. The grid was pressed gently onto the specimen and the excess grease mixture removed. The specimen was then placed in a vacuum machine and aluminum was evaporated on it. After the evaporation process, the mesh was removed. A detailed description of the method of grid transfer is given in Appendix E of Reference 6.

The determination of the displacements and the strain fields requires digitizing the data from the photographs. When digitizing the data, points located at the

intersection of the grating lines are selected close together in regions of expected high gradients and further apart away from these regions. These points in groups of four form quadrilaterals (initially rectangular) and values are read at each of four points and averaged before and after loading. The value of the four points average is located at the central of each quadrilateral and the difference between the no–load and loaded values becomes the digitized displacement at that point. This four–point smoothing method used to calculate the displacement at a given point will reduce the experimental error of reading the grid and it also reduces the local anomalies that exist in the real deformation of the heterogeneous specimen. The calculated displacement data were stored in a computer and processed to calculate the strains (ϵ_y, ϵ_x, and ϵ_{xy}) and to plot the iso–strain contours. In calculating the strains, small strain definitions were used. Therefore, strain contours for strain level greater than 20% should be ignored.

RESULTS AND DISCUSSION

A typical set of photographs showing the crack surface profile and local damage during the opening and growth of a crack in the specimen is shown in Fig. 2. According to Fig. 2, crack tip blunting takes place both before and after the crack growth. Due to the heterogeneous nature of the highly filled polymeric material, the degree of blunting varies with the position of the advancing crack tip. This suggests that the local microstructure, or local material damage, near the crack tip plays a significant role in the blunting phenomena. Fig. 2 also reveals that local damage can be developed in a small region near the crack tip. This damaged region may be defined as the failure process zone[7–8] in which the material has disintegrated into ligament form or becomes porous. In other words, a large number of small voids are generated in the failure process zone. Because of the random nature of the material, the local stress and the strength ahead of the crack tip vary in a random fashion. Thus, first the failure site in the material does not necessarily coincide with the maximum stress location. As the applied load is increased with time, additional voids are generated; both on the surface and in the interior of the specimen. Consequently, there are a large number of strands, which separate the voids and are essentially made of the binder material, formed inside the failure process zone. The growth of the damage in the failure process zone may take place by tearing the material or by successive

(a) Crack opening.
$\overline{\epsilon}y= 1.7\%$.

(b) Tip blunting at onset of crack growth.
$\overline{\epsilon}y= 3.3\%$.

(c) Resharpened tip and increased blunting during growth
$\overline{\epsilon}_y= 5.8\%$.
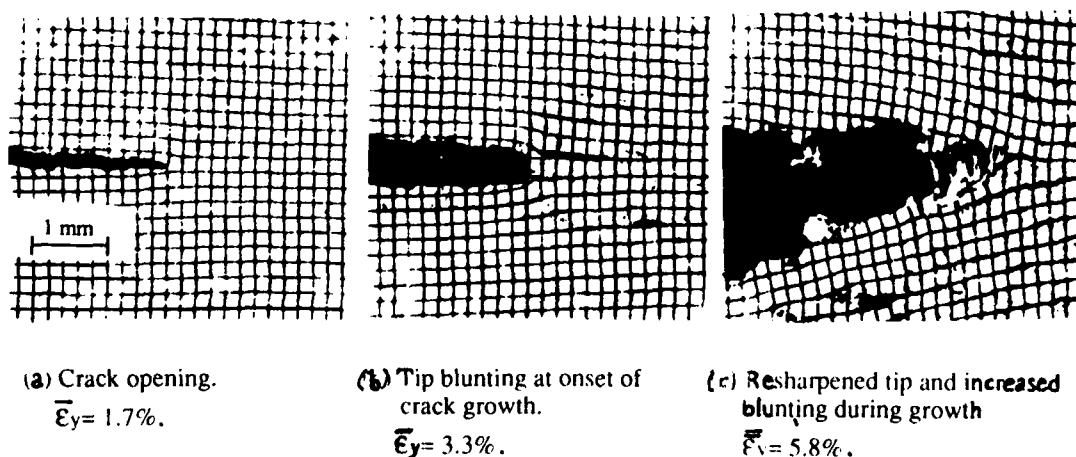
FIGURE 2.   Crack Tip Opening and Growth Process

nucleation and coalescence of the small voids. The successive coalescence of the main
crack tip with the void near the crack tip leads to crack growth to a distance which is
approximately equal to the length of the failure process zone. It is interesting to point
out that the size of the failure process zone and the intensity of damage in the failure
process zone vary with time. This phenomenon is similar to the crack tip blunting
phenomenon mentioned earlier.

As discussed in the above paragraphs, the local microstructure has a significant
effect on the near tip damage state which, in turn, has a significant effect on the degree
of crack tip blunting. The blunting of the crack tip will relax the local stresses,
resulting in a high resistance to propagation of the main crack. This resistance to
crack growth decreases as the magnitude of the applied load and the degree of damage
are increased. It is believed that the time—dependence of the damage and fracture
mechanisms are contributing factors to the time—sensitivity and discontinuous crack
growth behavior in highly filled polymeric materials.

The above discussion is centered on local damage and fracture mechanisms near
the crack tip. In the following paragraphs we shall discuss the crack growth behavior
observed experimentally and use the results of a "first cut" three dimensional elastic
finite element model to describe some of the features of crack—damage interaction as
well as crack opening and growth in the material.

Typical plots of crack length versus time and crack growth rate versus time are
shown in Figs. 3 and 4. The data shown in Fig. 3 reveal that the crack does not grow
in a continuous and smooth manner. It appears that crack growth rate undergoes
irregular fluctuations (Fig. 4). In other words, the crack growth process consists of a
slow—fast—slow phenomenon. The magnitude of fluctuation seems to be relatively high
during the early stage of crack growth. A possible explanation for this type of behavior
is that the crack tip and the failure process zone do not propagate in the same manner.
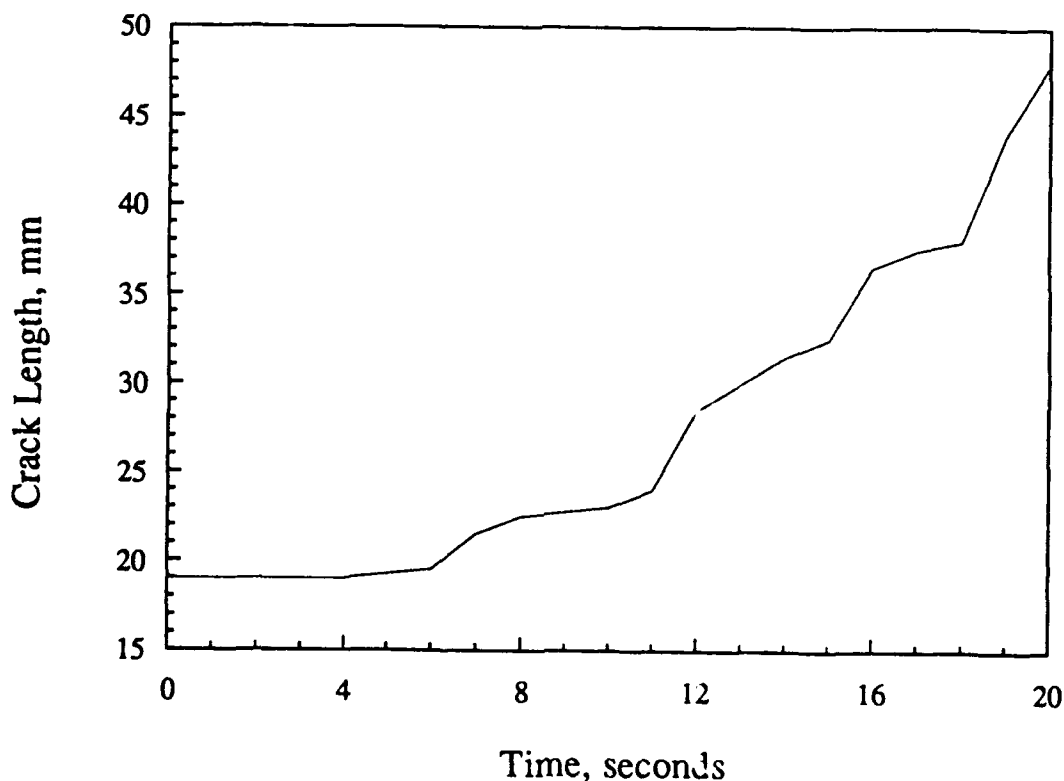
FIGURE 3.   Crack Length vs. Time
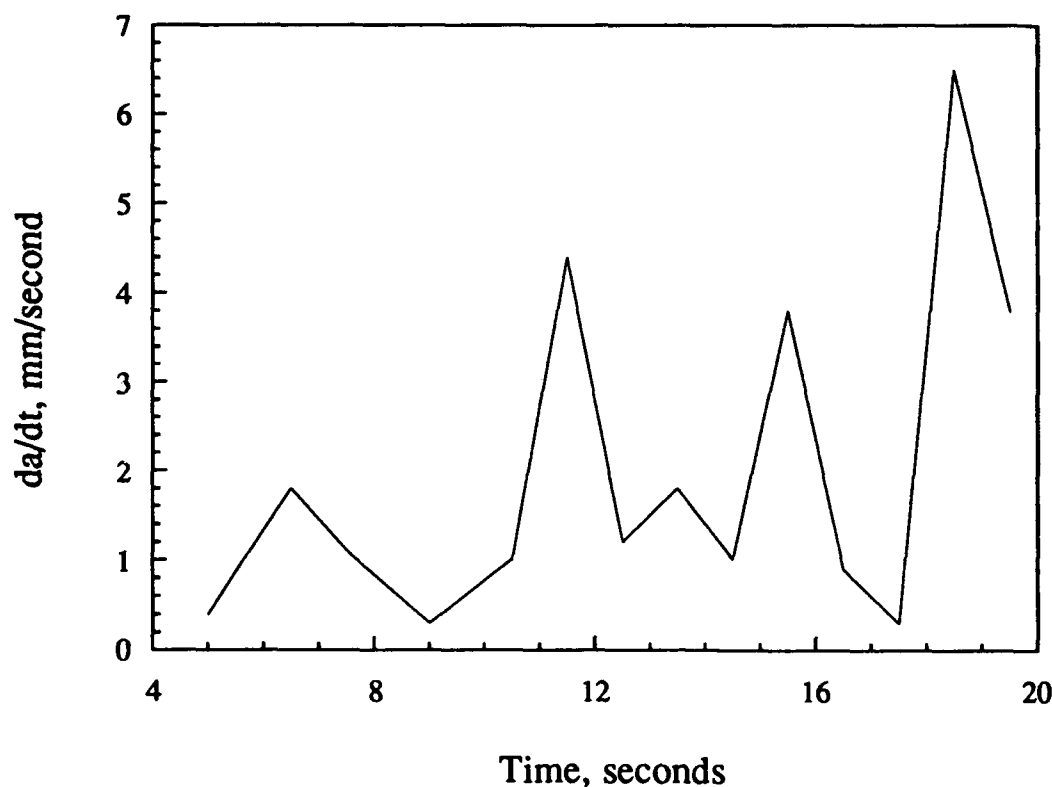
FIGURE 4.   Crack Growth Rate vs. Time

As mentioned earlier, the damage process is a time—dependent process and it requires some time to develop the failure process zone ahead the crack tip. The crack advanced by coalescence of large voids with the main crack tip. As the crack advanced into the failure process zone, a complicated stress redistribution takes place near the crack tip region and the local stresses are transferred in the direction of the tip of the failure process zone. When the tip of the main crack and the tip of the failure process zone coincide, the main crack tip resharpens temporarily. Thus, the crack growth process consists of blunt—growth—blunt and slow—fast—slow phenomena as shown in Figs. 3 and 4.

Secondary cracks were developed ahead of the main crack tip on planes which are different from the main crack plane. (Fig. 2b)   Depending upon the relative distance between the main crack and the secondary crack an interaction zone, due to the interaction of the stress fields at the crack tips, can develop. The intensity of the interaction and the size of interaction zone depend on the relative distance between the tips of the main crack and the secondary crack as well as the lengths of the two cracks, as pointed out by Liu and Smith[5] in their study of crack—defect interaction. Based on the results of a three dimensional elastic finite element analysis, it was found that, depending on the relative distance between the main and the secondary cracks, the value of the Mode I stress intensity factor K_I can be increased or decreased, as shown in Fig. 5.   Fig. 5 shows the percentage change of K_I at the main crack tip, $(K_1-K_{10}/K_{10})\%$ as a function of the vertical distance, h, and the horizontal distance, d, between the tips of the main crack and the defect when the defect length is equal to 3 mm.   Fig. 5 clearly indicates the effect of defect location on K_I at the main crack tip.

For example, when $h=1$ mm., $(K_I-K_{10}/K_{10})\%$ decreases from 20 to 5.98 as d increases from 0 to 3 mm. This indicates that when the defect tip is aligned with the main crack tip, i.e., when $d=0$, the value of K_I increases by 20%. The percentage increase in K_I decreases as the horizontal distance d is increased. This trend will continue until d reaches a limit value beyond which no change in K_I will occur. Referring back to Fig. 5, we note that when $h=3$ mm. and $d=0$ mm., the value of $(K_1-K_{10}/K_{10})\%$ is equal to -3.25. This indicates that the stress intensity factor at the main crack tip is reduced due to the presence of the defect. In other words, for this case, the presence of the defect produces a "shielding" effect on the main crack. However, when the value of d is increased from 0 mm. to 3 mm., the value of $(K_1-K_{10}/K_{10})\%$ is increased from -3.25 to 4.46. This result for $h=3$ mm. is different from that obtained for the $h=1$ mm. case. It is interesting to note that when $d=3$ mm. the values of $(K_1-K_{10}/K_{10})\%$ for $h=3$ mm. and for $h=1$ mm. are close to each other.

The effect of the vertical distance h on the stress intensity factor at the main crack tip is also shown in Fig. 5. According to Fig. 5 we note that, for a given value of d, the stress intensity factor increases with decreasing vertical distance between the crack and the defect. Since the crack growth behavior is controlled by the stress intensity factor, it is believed that the interaction between the crack and the defect is a contributing factor to the fluctuation in crack growth rate as shown in Fig. 4.

It is interesting to note that if the vertical distance h is small enough and the crack growth rates at the tips of the main crack and the secondary crack are slow, the high interaction of the cracks may cause the two cracks to propagate toward each other.
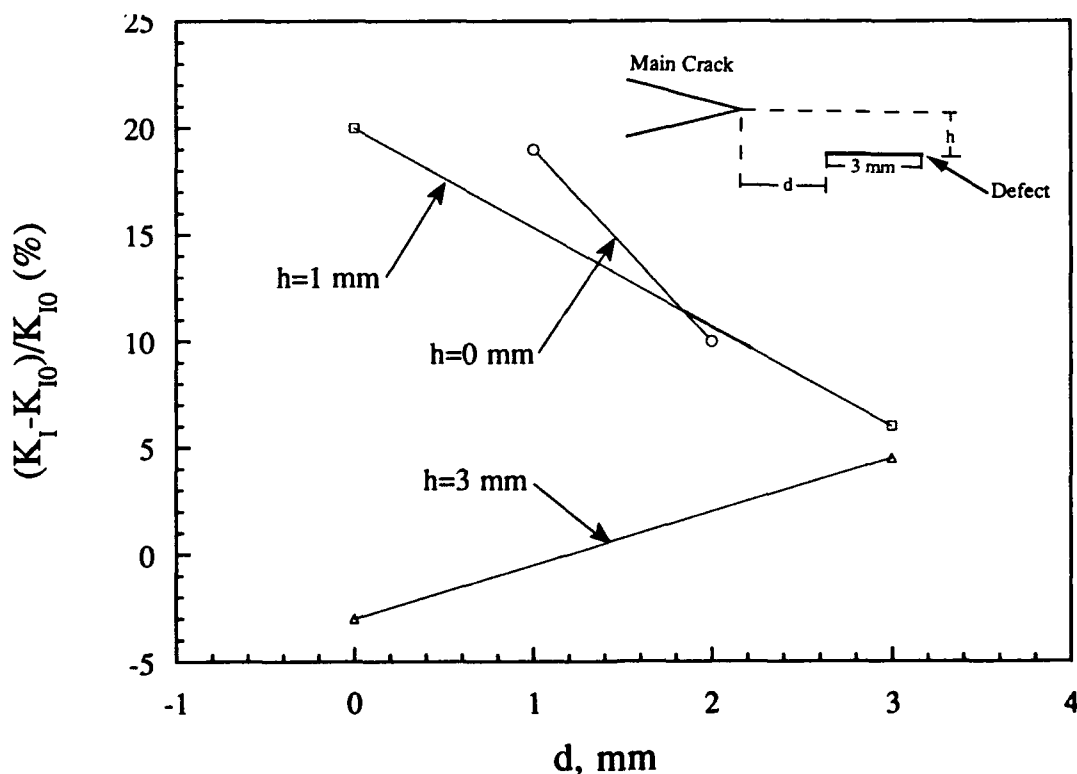
FIGURE 5.   Finite Element Estimate of Effect of Crack–Defect
                    interaction on Main Crack K

Under this condition, the two cracks will not propagate along their own planes or will not propagate in a self—similar manner, resulting in a rough fracture surface. On the other hand, if the vertical distance h is relatively large and the crack growth rates at the interacting tips of the two cracks are relatively far apart, the two cracks may propagate independently. Under this condition, the two cracks are overlapped and the two tips of the two cracks will grow into two low stress regions or grow into "a shielded" region as mentioned earlier. Consequently, the value of K_I at the main crack tip is decreased. Since the crack growth rate is controlled by the local stress near the crack tip, the interaction between the main and the secondary cracks may increase or decrease the crack growth velocity of the main crack or even lead to the arrest of the main crack and to propagation of the secondary crack at the non—interacting tip. Based on these discussions it is believed that the interaction between the main and the secondary cracks is a contributing factor the fluctuation in crack growth rate as shown in Fig. 4.

The above discussions were centered on damage mechanisms and fracture and crack growth behavior near the crack tip. In the following paragraph we will discuss the effect of the applied strain level on the strain distributions near the crack tip region.

Plots of the distributions of vertical displacement, u_y, normal strain ϵ_y, and shear strain ϵ_{xy} are shown in Figs. 6 and 7. These figures show that the contour lines are not smooth but are irregular. It is believed that a portion of the irregularities stems from experimental error but that the irregularities are mainly due to the nonhomogenity of the material. The experimental data indicate that the normal strain ϵ_y is significantly higher than that of the shear strain ϵ_{xy}. It also indicates that the shear strains are significant near the crack tip, and insignificant elsewhere. In addition, the large normal strain occurs in a small zone, or the intense strain zone, which is immediately ahead of the crack tip. These characteristics of the strain fields were found in the specimens subjected to the two different applied strain levels. From Figs. 6 and 7, it can be seen that the increase of the applied strain level from 6.6% to 11.6% alters the strain fields but the iso—strain contours are of the same general form.

(1) Limit of data without extrapolation.
(2) Crack profile according to extrapolated Uy contours.

(a) Vertical displacement Uy. (mm)
$\bar{\epsilon}_y$= 6.6%.

(b) Normal strain ϵ_y.
$\bar{\epsilon}_y$= 6.6%

(c) Shear strain ϵ_{xy}.
$\bar{\epsilon}_y$= 6.6%.
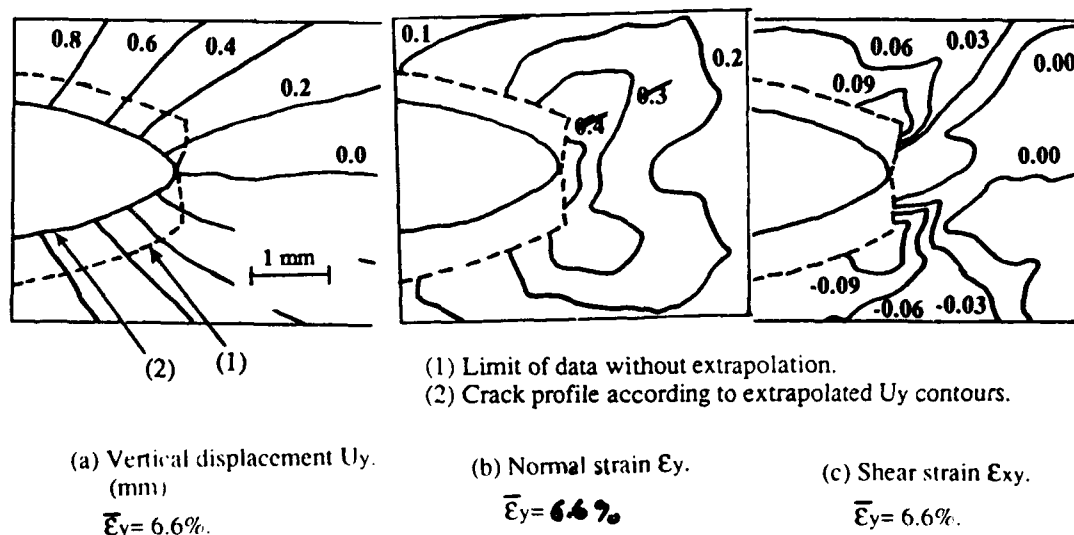
FIGURE 6. Crack Tip Displacement and Strain Fields for Moderate Global Strain Level

(1) Limit of data without extrapolation.
(2) Crack profile according to extrapolated Uy contours.

(a) Vertical displacement Uy.
   (mm)
$\overline{\varepsilon}y$= 11.6%.

(b) Normal strain εy.
$\overline{\varepsilon}y$= 11.6%.

(c) Shear strain εxy.
$\overline{\varepsilon}y$= 11.6%.
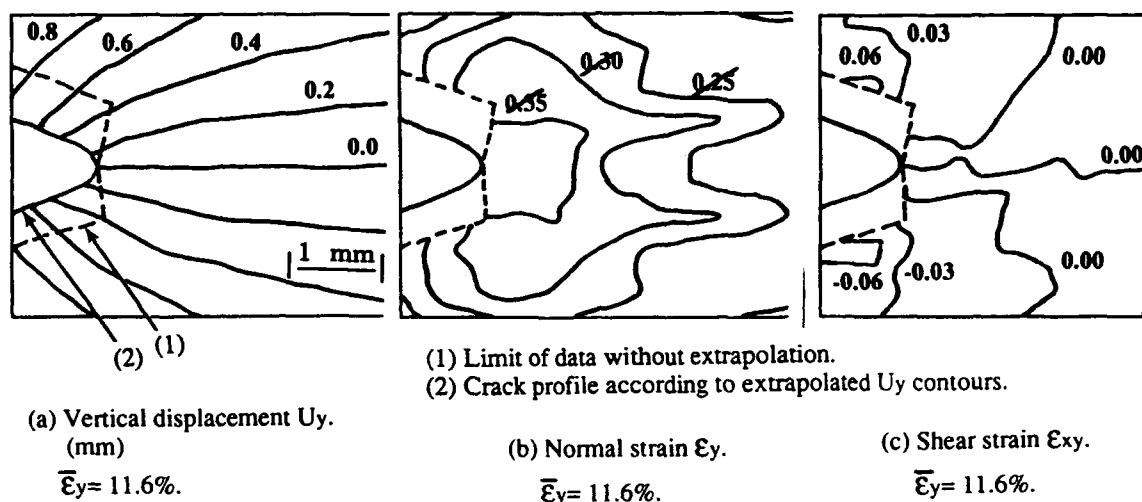
FIGURE 7.   Crack Tip Displacement and Strain Fields for
High Global Strain Level

It is interesting to note that, by comparing Fig. 6 with Fig. 7, the shear strain ϵ_{xy} decreases as the applied strain is increased. A careful review of the deformed grid near the crack tip region reveals that this phenomenon is closely related to the crack tip radius during crack growth. When the crack tip is blunted, the relatively large rotation of the initially horizontal sides of the grid causes a relatively larger shear strain. When the crack tip becomes sharp during crack growth this rotation is much smaller, resulting in a smaller shear strain near the crack tip. It's known that, dependent upon the level of interest, micro, or macro, the material's microstructure can have a significant effect on the strain fields. On the macro level, if the magnitude of the strain is relatively large, the effect of the material's inhomogeneity on the magnitude of the strain is relatively small. For example, due to relatively large magnitudes of the strain levels, the normal strain and the shear strain shown in Fig.7 are less affected by the material's microstructure than those in Fig. 6. On the other hand, due to relatively small magnitude of the strain level, the material's microstructure may have a relatively large effect on the strain.

CONCLUSIONS

The local fracture and strain fields near the crack tip in a highly filled polymeric material were investigated. Experimental results indicate that the time–dependent damage process is a contributing factor to the time–dependent fracture behavior near the crack tip, and the crack–damage interaction is a contributing factor to the fluctuation of the crack growth behavior. They also indicate that, prior to crack growth, a large crack tip blunting occurs during the process of loading and the crack growth consists of a blunt–growth–blunt phenomenon which appears to be highly nonlinearly. In addition, experimental results reveal that the increase of the applied strain alters the strain fields but the iso–strain contours are of the same general form.

ACKNOWLEDGEMENTS

REFERENCES

1. Liu, C. T., "Crack Growth Behavior in a Composite Solid Propellant with Strain Gradients — Part I," AIAA Paper No. 84–1294, AIAA/ASME/SAE 20th Joint Propulsion Conference, p.641–648, June 1984.

2. Liu, C. T., "Crack Growth Behavior in a Composite Solid Propellant with Strain Gradients — Part II," J. of Spacecraft and Rockets, V27, n6, p.614–620, Nov.–Dec., 1990, pp. April 1985.

3. Liu, C. T., "Crack Propagation in a Composite Solid Propellant," Society of Experimental Mechanics 1990 Spring Conference, p. 614–620, June 4–7, 1990.

4. Smith, C. W., Chang, C. W. and Liu, C. T., "Measurement of Crack Induced Damage in Particulate Composites," (Invited Paper), Proc. of 1990 Annual Society for Experimental Mechanics, pp. 241–246, June, 1990.

5. Liu, C. T. and Smith, C. W., "Near Tip Behavior in a Particulate Composite Material — An Experimental and Analytical Investigation," (In Press)Proc. of 2nd International Conf. on Computational Engineering Science, Aug. 1991.

6. Post, D. and Smith, C. W. "Crack Opening and Extension in Inert Solid Propellant" AFAL TR–87–043, 113 pages, Sept. 1987.

7. Schapery, R. A., On a Theory of Crack Growth in Viscoelastic Media, Report MM 2765–73–1, Texas A&M University, March 1973.

8. Knauss, W. G., "Delayed Failure — The Griffith Problem for Linearly Viscoelastic Materials," International Journal of Fracture Mechanics, Vol. 6., pp. 7–20 March 1970.

Fatigue Properties of Carbon/PEEK [±30] Tubes under Multiaxial Cyclic Loading

TOSHIO TANIMOTO, TOHRU MORII, HAJIME SATOH AND HIROSHI HARAKAWA

ABSTRACT

Multiaxial fatigue behavior of carbon/PEEK tubes is discussed in this paper. Carbon/PEEK tubular specimens were fabricated from UD prepreg (APC-2/AS4 : ICI Fiberite Co., Ltd.) with a lamination of [±30] by a newly developed fabrication method. Repeated loadings of tension and compression combined with torsion were applied on the samples with an electro-hydraulic fatigue testing machine at a frequency of 10Hz. Multiaxial fatigue tests were actually performed under combined tension-compression-torsion cycles for the different ratio of axial stress and shear stress.

Methodology of fatigue strength estimation was discussed for the different biaxial stress ratio, σ/τ. Proposed method was confirmed to be useful for estimation of fatigue strength at the given lives for the various combinations of axial stress and shear stress, if the fatigue life data is available for the respective condition of cyclic axial loading and torsion. Discussion is also made on the fatigue failure mode of the tubular specimens under the different combinations of axial stress and shear stress.

INTRODUCTION

Poly-ether-ether-keton (PEEK) resin is extensively used as a matrix of composites. That is because of its superior heat resistance, high fracture toughness and high fatigue properties as well. In carbon/PEEK

Toshio Tanimoto and Tohru Morii, Department of Materials Science and Ceramic Technology, Shonan Institute of Technology, Tsujido-Nishikaigan, Fujisawa, Kanagawa 251, Japan
Hajime Satoh and Hiroshi Hirakawa, MB Technical Development Center, The Yokohama Rubber Co.,Ltd., Oiwake, Hiratsuka, Kanagawa 254, Japan

composites with continuous fiber, development of efficient fabrication method is fundamentally needed to utilize for wide application.   In addition, a good understanding of the fatigue properties of the material is essentially of vital importance for the successful application as a structural material.   Because, the majority of engineering structures are generally subjected to cyclic loading, either constant amplitude, or random spectrum[1].   For producing a hollow shape product of fiber reinforced plastics in thermoset matrices, method used an expansible core which induces radial forces by thermal expansion of polymeric materials, are useful as well as a filament winding method.   The application of such an idea to thermoplastic composite, carbon/PEEK composite, was attempted to produce tubular specimen by The Yokohama Rubber Co., Ltd.

In the present work, multiaxial fatigue tests were first conducted on the carbon/PEEK [±30] tubes produced by a newly developed fabrication method.   Then methodology of fatigue strength estimation is discussed for the different biaxial stress ratio, σ/τ.

SPECIMEN PREPARATION AND EXPERIMENTAL METHOD

The tubes were fabricated from unidirectional carbon/PEEK prepreg sheet(APC-2/AS4, ICI-Fiberite Co., Ltd.).   A new method was developed in the fabrication of pipes, where a thermally expansible mandrel made of PTFE is used to produce radial forces pressing tubes against the wall of outer mold.   PTFE is thermally stable and keep rubber-like stiffness at the temperature of 360-400°C.   The pressure of 0.3MPa observed was found to be enough to make an excellent pipe with good surface finish and good consolidation.

The tubular specimens have a lamination sequence of [±30].   The dimensions of the specimen are shown in Figure 1.   The volume content of the fiber is approximately 61%.   Test pieces were kept for two days or more prior to testing under constant conditions of 296K in
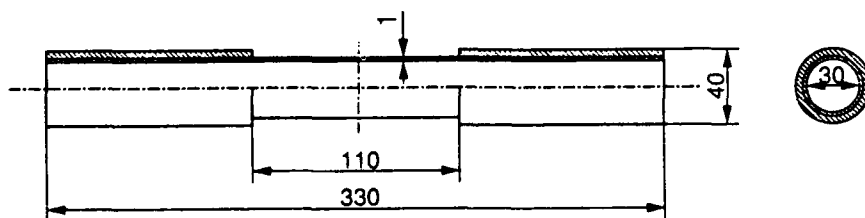
Figure 1   Dimensions of the specimen.

temperature and 65% in humidity.

Fatigue tests were conducted by an electro-hydraulic fatigue testing machine (Servopulser EHF-E, Shimadzu Co., Ltd.) at the frequency of 10Hz. Multiaxial fatigue tests were performed under combined tension-compression and torsion for the different stress ratios, σ/τ. Biaxial stress ratio, σ/τ, was changed in the five different ways of 1/0, 5/1, 1/1, 1/5 and 0/1. Stress ratios of 1/0 and 0/1 signify tension-compression fatigue and torsion fatigue, respectively.

EXPERIMENTAL RESULTS AND DISCUSSIONS

ESTIMATION OF FATIGUE LIFE FOR VARIOUS BIAXIAL STRESS RATIOS

Biaxial stress ratio σ/τ is varied in each fatigue test as mentioned above. In producing S-N diagram which is a relation between cyclic stress and number of fatigue cycles, resultant stress representation was adopted in the ordinate, as provided in the following equations.

$$\sigma_1 = \frac{\sigma_x}{2} + \sqrt{\frac{\sigma_x^2}{4} + \tau_{xy}^2}$$

(1)

$$\tau_1 = \sqrt{\frac{\sigma_x^2}{4} + \tau_{xy}^2}$$

(2)

Figure 2 shows the maximum principal stress [Equation (1)] plotted as a function of number of the cycles to fatigue failure. The linear
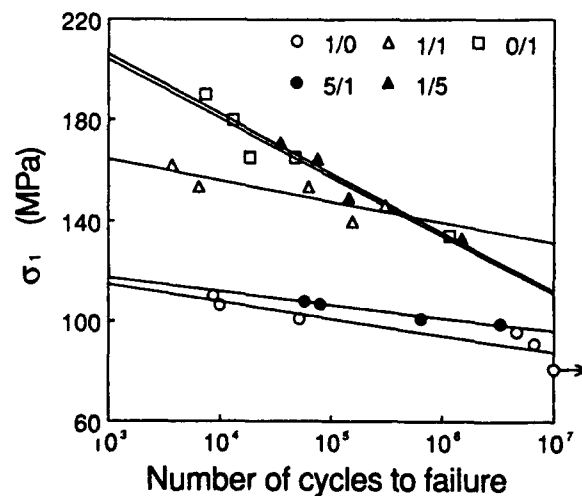
Figure 2   Maximum principal stress vs. number of cycles to failure.
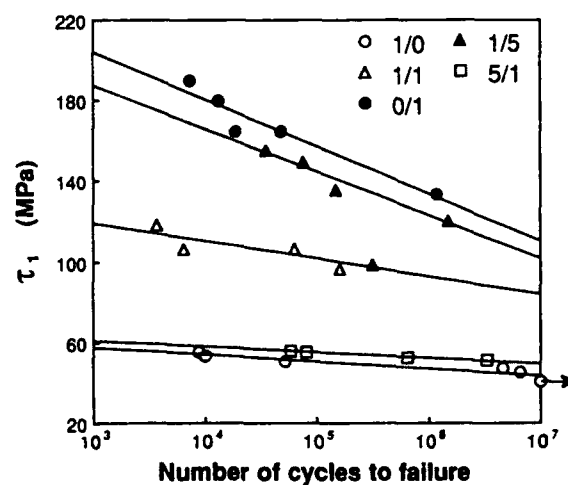
Figure 3   Maximum shear stress vs. number of cycles to failure.

approximation between the maximum principal stress and fatigue life in semi-log scale is drawn by a solid line.

Figure 3 is the maximum shear stress [Equation (2)] plotted against fatigue cycles. The resultant shear stress representation seems to be reasonable in understanding fatigue test results for the various biaxial stress ratios σ/τ. It is clearly observed from Figure 3 that the fatigue strength is the highest in repeated torsion and the lowest in repeated tension and compression in axial direction, in case of the present fiber orientation angle.

Figure 4   Variation of Young's Modulus E and torsion rigidity G.

For reference, the variation of Young's modulus E and torsion rigidity G with fiber orientation angle in tubular specimen are shown in Figure 4. In fiber orientation angle of 30° torsion rigidity is highest and Young's modulus is lowest in the present study. Fatigue S-N curve for biaxial stress ratio of 1/5 is very close to that of repeated torsion test, while fatigue S-N curve for biaxial stress ratio of 5/1 is almost the same as that of repeated tension and compression test.

Estimation of fatigue strength at the given lives for the various values of biaxial stress ratio can practically be performed by an elliptical failure stress criterion which is represented by:

$$a \left(\frac{\sigma_x}{\sigma_0}\right)^2 + b \left(\frac{\tau_{xy}}{\sigma_0}\right)^2 = 1 \qquad (3)$$

Where σ_0 is the fracture strength in static tension and constants, a and b, are determined from respective result for tension-compression fatigue and torsion fatigue.

The comparison between test data and theoretical prediction shown in Figure 5 suggests that the elliptical

Figure 5   Comparison between test data and theoretical prediction.
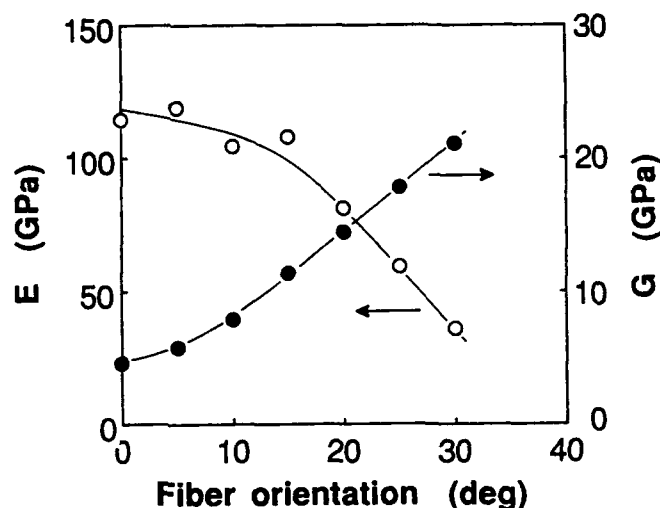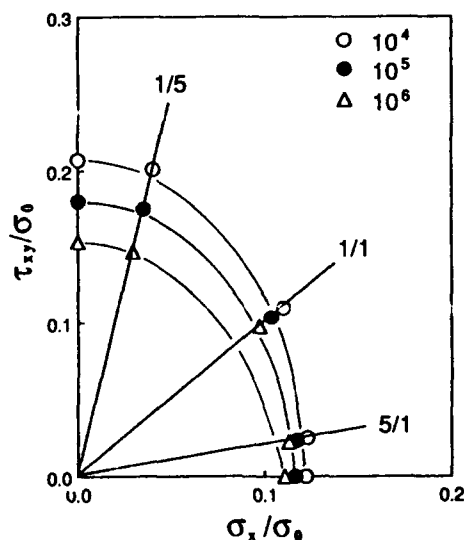
criterion is favorable in estimating fatigue lives for the various combinations of axial stress and shear stress, if we have only obtained the fatigue S-N data for the respective of cyclic axial loading and cyclic torsion.

FATIGUE FAILURE MODE AND SURFACE TEMPERATURE RISE

Fatigue failure mode of the tubular specimens will now be discussed for the different combinations of cyclic axial stress and cyclic shear stress. Figure 6 shows the appearance of the failed specimen after subjected to repeated tension and compression loading. Two typical fracture mode were observed in this loading condition. First type is shear fracture along fiber direction. Second type is localized buckling

<div align="center">

Shear Fracture   Localized Buckling Failure

Figure 6   Fracture appearance of failed specimen $(\sigma/\tau = 1/0)$.

</div>

<div align="center">

Carbon/Epoxy Laminate   Carbon/PEEK Laminate

Figure 7   Fracture appearance of quasi-isotropic laminates.

</div>

failure which is observed particularly at the higher stress levels. According to our previous study [2],[3] on fatigue failure mode in quasi-isotropic carbon/epoxy laminate, the main fatigue failure mode has been observed to be progressive delamination between plies. It has been observed in the side view of the laminate during fatigue testing that the delamination grows between plies especially free edges in early stage of fatigue. Such a delamination extends the amount of interface damage gradually with increasing the fatigue cycles. On the other hand, delamination damage between plies is much less observed in case of quasi-isotropic carbon/PEEK laminate. This probably be due to the use of PEEK as matrix, which is generally believed to possess higher fracture toughness. The fracture appearance of carbon/epoxy laminate is compared with that of carbon/PEEK in Figure 7. Figure 8 shows the

appearance of the failed tubular specimen after subjected to repeated torsion loading. In this case, multiple shear fracture were observed, in which shear crack propagates zigzagging. Fatigue failure mode in biaxial stress ratio of 5/1 was shear fracture along fiber direction similar to the first failure mode in repeated tension and compression fatigue test, as mentioned above (Figure 9). Fracture appearance in biaxial stress ratio of 1/5 is almost the same as that in the case of repeated torsion test (Figure 10).

Figure 8   Fracture appearance of failed specimen ($\sigma/\tau = 0/1$).

Figure 9   Fracture appearance of failed specimen ($\sigma/\tau = 5/1$).

Surface temperature of the tubular specimen was measured during fatigue testing. Figure 11 shows the temperature change and stroke increase with increasing fatigue cycling in repeated tension and compression

Figure 10   Fracture appearance of failed specimen ($\sigma/\tau = 1/5$).

test. Similarity is observed in the failed specimen ($\sigma/\tau = 1/5$). tendency of the changes in temperature and stroke with number of fatigue cycles. In other words, modulus reduction is reflected in the change of surface temperature of the specimen. In repeated torsion test, similarity is found between temperature change and twisting angle increase as shown in Figure 12, indicating that the change of torsion rigidity is well reflected in the change of surface temperature. In case

Figure 11   Temperature change and stroke increase with fatigue cycling ($\sigma/\tau = 1/0$).
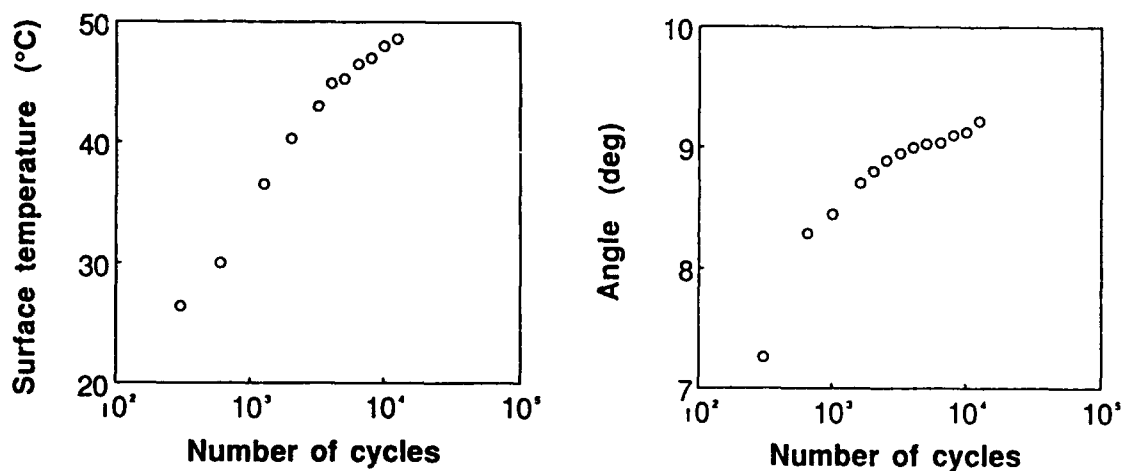
Figure 12   Temperature change and twisting angle
increase with fatigue cycling (σ/τ = 0/1).
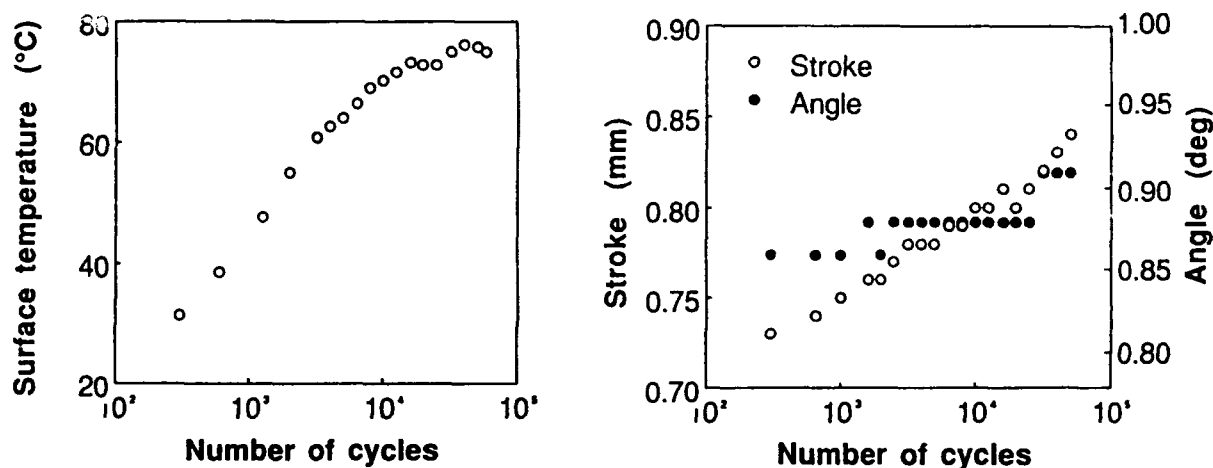
Figure 13   Temperature change, stroke increase and
twisting angle increase with fatigue cycling (σ/τ = 5/1).
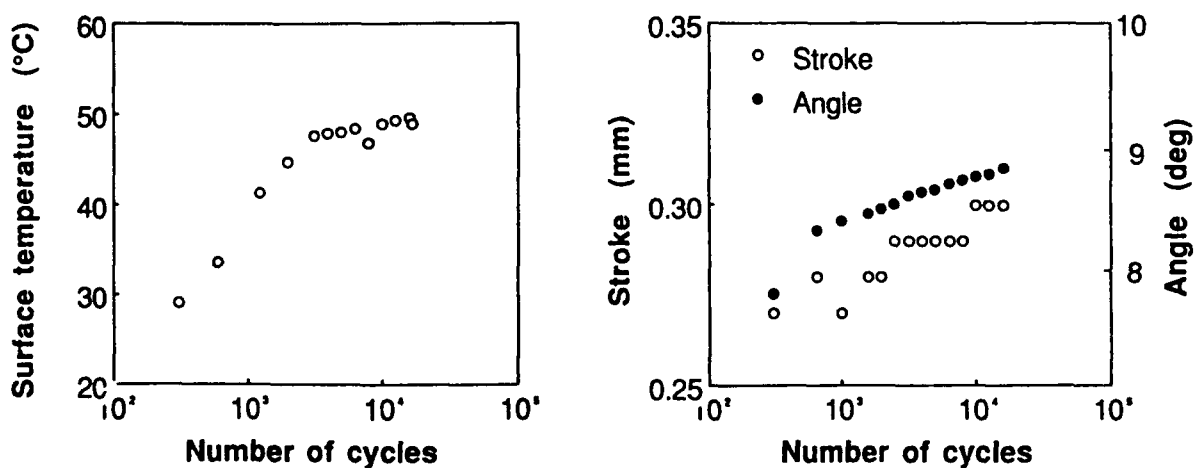
Figure 14   Temperature change, stroke increase and
twisting angle increase with fatigue cycling (σ/τ = 1/5).

394

of axial stress ratio of 5/1, it is found in Figure 13 that the stroke change is well corresponded to the surface temperature. On the other hand, it is clear from Figure 14 that the angle change is well corresponded to that in the case of biaxial stress ratio of 1/5.

CONCLUDING REMARKS

The present investigation on the multiaxial fatigue properties of carbon/PEEK tubular specimen led to the following conclusions:

1. The newly developed fabrication method of carbon/PEEK pipes seems to have excellent qualities, judging from the shape with very smooth surface, accurate dimension and reasonable mechanical performance.

2. An elliptical failure stress criterion represented Equation(3) is concluded to be reasonable in estimating the fatigue lives for the various combinations of axial stress and shear stress, if we have only obtained the fatigue S-N data for the respective condition of cyclic axial loading and cyclic torsion.

3. Discussion was made on the fatigue failure mode of the tubular specimens under the different combinations of axial stress and shear stress. As a result of measurement of surface temperature of the specimen during fatigue testing, the modulus reduction was well reflected in the change of surface temperature in cyclic axial loading. On the other hand, torsion rigidity change was found to be related to the change of surface temperature in repeated torsion fatigue.

REFERENCES

1.   Tanimoto, T., S. Amijima and T. Matsuoka, 1985, "Fatigue Life Estimation of Laminated GRP Materials under Various Random Load Patterns" Proc. of the 5th International Conference on Composite Materials, 199-210.

2. Tanimoto, T., H. Ishikawa and Z. Maekawa, 1988, "Fatigue Behavior and Reliability of Quasi-Isotropic Carbon/Epoxy Laminates" Proc. of the 4th Japan-U.S. Conference on Composite Materials, 416-425.

3. Tanimoto, T. and T. Morii, 1991, "Influence of Thermal Cycling on Compressive Fatigue Properties of Quasi-Isotropic Carbon/Epoxy Laminates" Proc. of the 8th international Conference on Composite Materials, 38H1-9.

Effects of Layer Waviness on the Compression Fatigue Behavior of Thermoplastic Composite Laminates

D. O. ADAMS AND **M. W. HYER**

ABSTRACT

The influence of layer waviness on the compression fatigue response of carbon/polysulfone composite laminates was studied. Isolated layer waves were fabricated into the central $0°$ layer of $[90_2/0_2/90_2/0_2/90_2/\overline{0_{2w}}]_S$ laminates. Specimens with a moderate level of layer waviness as well as wave-free control specimens were cycled to failure at a variety of maximum stress levels to establish S-N curves. A one and a half decade loss of compression fatigue life was obtained for wavy layer specimens as compared to the control specimens. The stress level corresponding to the 10^6 cycle run-out for these layer waves specimens was reduced to approximately 45% of the static compression strength of the wave-free laminate.

INTRODUCTION

Layer waviness is a manufacturing imperfection most commonly observed in thick-section composite laminates. This imperfection is characterized by the out-of-plane undulation of a layer or a group of layers within a multidirectional laminate. While most commonly observed in cylindrical structures, layer waviness has also been found in thick, flat laminates. The causes of layer waviness have in some cases been identified, and the degree of waviness reduced by altering the manufacturing process. However, in many applications, some degree of layer waviness remains and must be tolerated within the composite structure.

Daniel O'Hare Adams, Iowa State University, Aerospace Engineering and Engineering Mechanics Department, 2019 Black Engineering Bldg., Ames, IA, 50011

M. W. Hyer, Virginia Polytechnic Institute and State University, Engineering Science and Mechanics Department, Norris Hall, Blacksburg, VA, 24061

With the increased usage of thick-section composite laminates for compressively loaded applications, layer waviness has recently become an issue. To date, however, no studies have been performed to investigate the effects of layer waviness on the compression fatigue performance of composite laminates. In fact, only recently have the effects of layer waviness on the static compression strength of composite laminates received attention. Testing of 15 mm (0.6 in.) thick carbon/epoxy cylinders under external hydrostatic pressure loading has been conducted [1,2]. Failures well below the design pressure were in some cases believed to be due to layer waviness, but these assessments could not be confirmed. Analysis of layer waviness in composite cylinders under such loading indicates regions of high interlaminar shear stress and the possibility of tensile interlaminar normal stress [3,4]. These stresses have been shown to be of sufficient magnitude to produce failure below the design pressure of a perfect cylinder [5].

In this study, isolated layer waves were intentionally fabricated into otherwise wave-free composite laminates. Specimens were cycled to failure at a variety of maximum stress levels to establish an S-N curve for a particular level of layer waviness. In addition, wave-free control specimens were tested to develop an S-N curve for the case of no layer waviness. Thus, the reduction in compression fatigue life associated with a specific layer wave geometry was established.

LAMINATE FABRICATION

Laminates were fabricated from T300/P1700 carbon/polysulfone prepreg tape. A 22 ply $[90_2/0_2/90_2/0_2/90_2/\overline{0_{2w}}]_S$ cross-ply laminate was selected for investigation. The two-ply wavy $0°$ layer (designated as 0_{2w}, the overbar indicating this layer is not repeated in the symmetric stacking sequence) was placed at the laminate centerplane. This location reduced any localized nonsymmetry of the laminate and best simulated a layer wave in the interior of a thicker laminate. A three-step fabrication method was established for fabricating the isolated layer wave into the thermoplastic composite laminate [6]. The first step consisted of preforming the wave shape into a two-ply $0°$ layer using a matched mold. In the second step, a "sublaminate" with the built-in wavy layer was fabricated. Thin strips from a unidirectional laminate were placed in the three troughs of the wavy layer. Two $90°$ plies were placed on either side of the wavy $0°$ layer and the assembly was placed in the steel mold and consolidated. The third step consisted of adding the remaining eight prepreg plies on each side of the wavy sublaminate to obtain the final stacking sequence. The assembly was again placed in the steel mold and consolidated. Variations in layer wave geometries were obtainable by changing the cross-sectional dimensions of the three unidirectional strips used in producing the wavy sublaminate. A representative layer wave geometry fabricated using this procedure is shown in Figure 1.

Figure 1. Moderate Layer Wave Geometry Fabricated in
$[90_2/0_2/90_2/0_2/90_2/\overline{0_{2w}}]_S$ Laminate Using the Three Step Fabrication Method.

COMPRESSION FATIGUE TESTING

Compression fatigue testing was performed to determine the influence of layer waviness on compression fatigue life. A group of specimens with similar layer wave geometries as well as "control" specimens without layer waviness were tested. Thus, reductions in compression fatigue life were assessed and attributed to a specific layer wave geometry.

TEST SETUP

Compression fatigue testing was performed using a test fixture designed and manufactured at NASA Langley Research Center [7]. This fixture, shown in Figure 2, consists of two massive steel blocks aligned by four rods and linear bearings. The compression fatigue specimen is placed between end plates within the cavity of each block. The thickness of the end plates are machined to be slightly less than the specimen thickness. Four bolts are used to secure each cover plate. Thus, the specimens are supported along a portion of their length and end-loaded through the end plates. The dimensions of the specimens were 102 mm (4.0 in.) in length and 25 mm (1.0 in.) in width. The layer wave was centered within the 25 mm (1.0 in.) long gage section.

A total of eight 152 mm (6 in.) square T300/P1700 laminates were fabricated for this investigation. Five laminates with layer waviness were fabricated using the three-step fabrication method. The remaining three laminates were fabricated using single-step processing without layer waviness. All laminates were ultrasonically C-scanned to ensure laminate quality prior to cutting into test specimens using a water-cooled diamond saw.

The layer wave geometry was characterized separately for each specimen. At each cut within a laminate, the layer wave region was photographed under a microscope at low magnification. From photographic enlargements, the wavelength, λ, and wave amplitude, δ, were measured as shown in Figure 3. In

this figure, t denotes the thickness of the two-ply wavy layer (ca. 0.4 mm, 0.016 in.). The values of λ and δ for each specimen were taken as the average of the measurements from the two edges. A layer wave "severity" parameter δ/λ was calculated for each specimen. Intuitively, a more "severe" wave implies a shorter wavelength, λ, coupled with a larger wave amplitude, δ, and thus a larger value of δ/λ. Although a variety of layer wave geometries were produced [6], the five laminates used in this investigation produced specimens with values of δ/λ ranging from 0.05 to 0.06. This level of layer waviness, shown in Figure 1, was classified as a moderate layer wave.

Testing was performed under load control using an Instron servo-hydraulic load frame. All fatigue testing was performed with a stress ratio, R, of 10. Thus, the maximum compression stress during each loading cycle was 10 times the minimum compressive stress. Specimens were cycled at a frequency of 5 Hz using a sinusoidal waveform. All specimens were cycled either to failure or to 10^6 cycles, considered a run-out in this study.

TEST RESULTS

A total of 38 specimens were cycled; 14 control specimens and 24 specimens with layer waviness. The 14 control specimens were tested at maximum stress levels ranging from -586 MPa (-85 ksi) to -414 MPa (-60 ksi). Results are presented as an S-N diagram in Figure 4. The laminate number for each specimen is indicated in the figure. The average strength from monotonic compression testing of nine control specimens [6] are also shown on the diagram at N=1 along with the spread in the data. The 10^6 cycle strength is approximately 75 percent of the average static compression strength, 608 MPa (88.2 ksi). Failure within the loading grip occurred in all but one of the control specimens cycled to failure.

The 24 specimens with layer waviness were cycled at maximum stress levels ranging from -552 MPa (-80 ksi) to -276 MPa (-40 ksi). Results are presented as an S-N diagram in Figure 5. The average strength from monotonic compression testing of two layer wave specimens (0.05 < δ/λ < 0.06) [6] as well as control specimen results are also shown on the diagram. Results clearly show a reduction in the compression fatigue life due to layer waviness. With layer waviness in the range 0.05 < δ/λ < 0.06, approximately one and a half decade loss of fatigue life results relative to the control specimens. The 10^6 cycle strength of the specimens with layer waviness is reduced to approximately 45% of the static compressive strength of the control specimens. A considerable amount of scatter is seen in the data, due in part to laminate-to-laminate variations. All but one specimen failed at the location of the layer wave. The remaining specimen (from laminate 2) failed within the grip and is not represented in Figure 5.
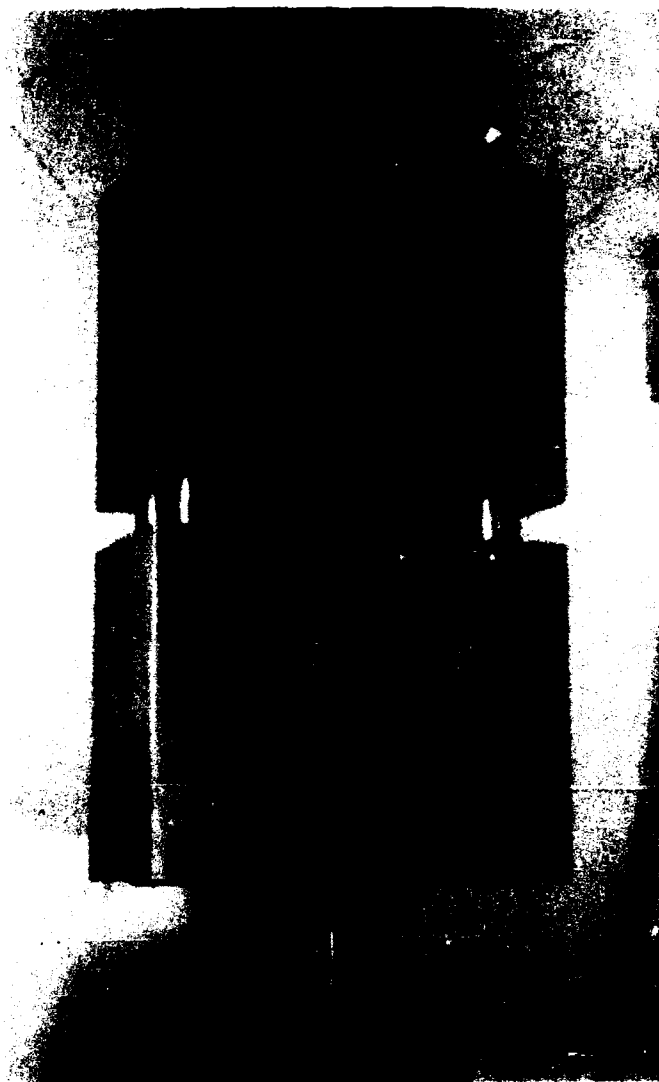
Figure 2. Compression Fatigue Test Fixture.
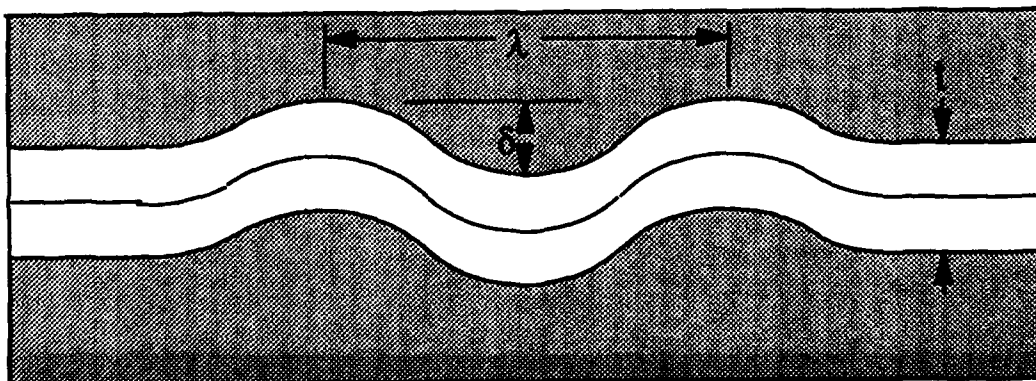
Figure 3. Definition of Layer Wave Geometry Parameters.
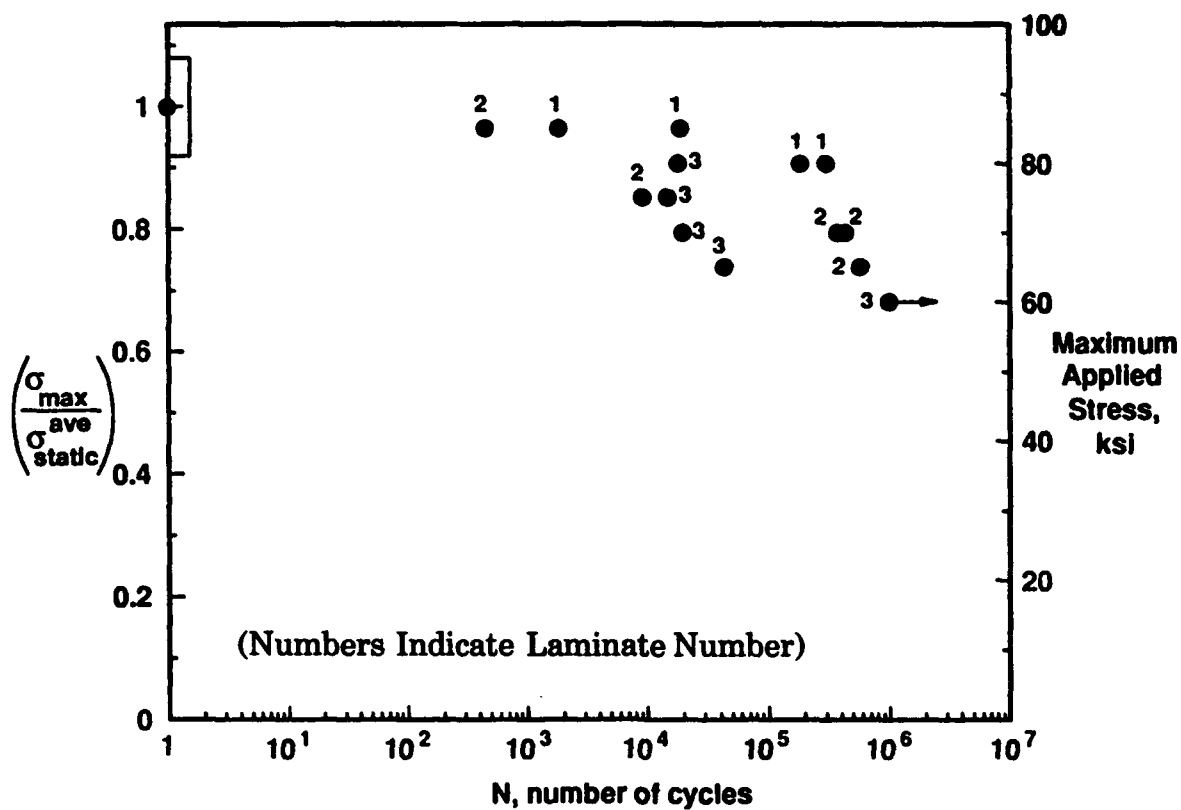
Figure 4. Compression Fatigue Results of Control Specimens.
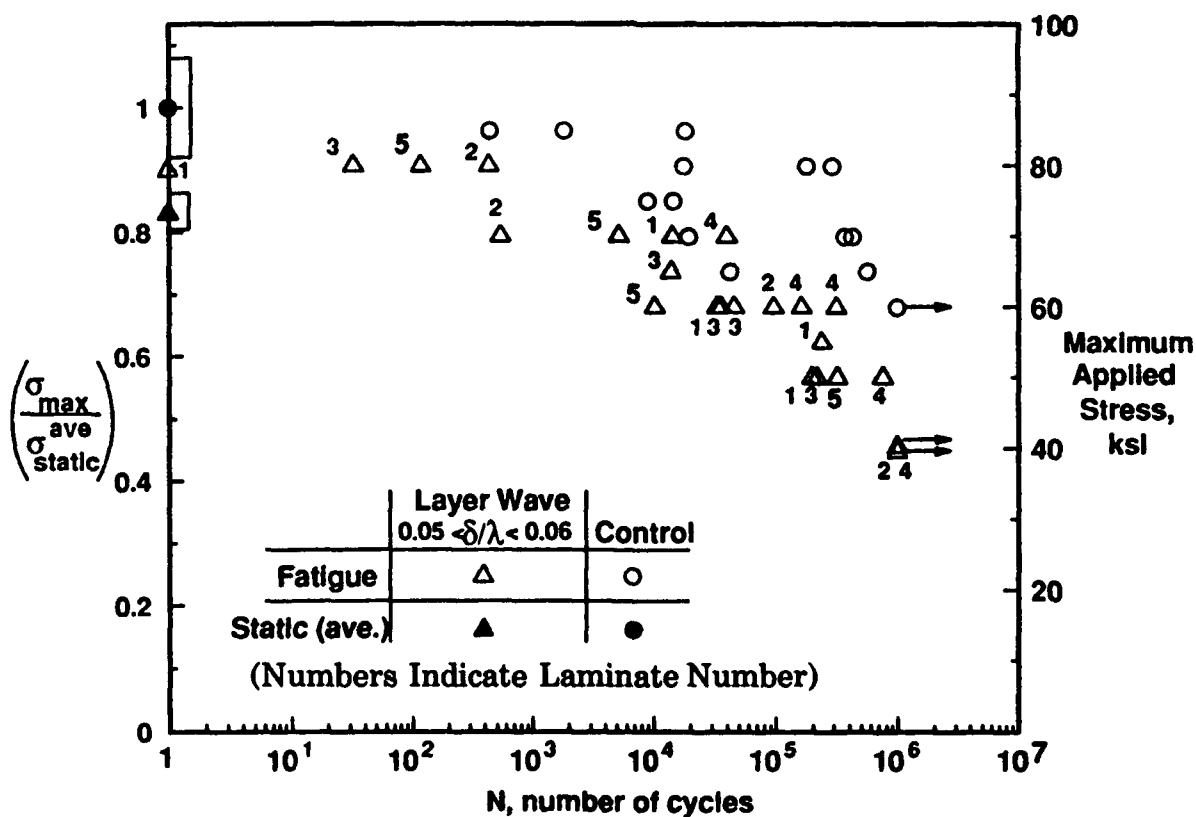
Figure 5. Compression Fatigue Results of Layer Wave Specimens.

OBSERVATIONS FROM FAILED SPECIMENS

Brooming was observed in the post-test evaluation of failed wavy layer specimens. As shown in Figure 6, the post-test condition of these specimens was characterized by through the thickness splaying of the layers and by numerous delaminations. Angled fracture surfaces through the thickness were commonly observed, resulting in a single fracture of each $0°$ layer. The degree of actual out-of-plane brooming varied greatly, and was believed to be dependent on the amount of post-failure actuator motion of the load frame and subsequent crushing prior to stoppage.

In no instance was the initiation of failure detectible audibly, visually, or by actuator stroke or load limits such that the test could be stopped and the specimen examined for failure initiation. Thus, the determination of the failure sequence could only be based on inferences made from post-failure observations. Inferences based on the absence of damage were believed to be most significant, since damage could have resulted from post-failure crushing rather than initial failure. Unfortunately, no consistent inferences could be made based on the post-failure condition of the specimens. Thus the post-failure damage present in the specimens was of little use in determining the probable cause of failure or dominant failure modes.

Two layer wave specimens and one control specimen completing 10^6 cycles without failing were subsequently X-rayed to investigate the extent of damage. Specimens were treated with a zinc iodide penetrant prior to X-ray to enhance damage detection. Results from the two layer wave specimens show no evidence of delamination or localized damage associated with the layer wave within the specimen gage section.

Figure 6. Post-Failure Condition of Layer Wave Specimen.

CONCLUSIONS

Compression fatigue specimens with moderate layer waves ($0.05 < \delta/\lambda < 0.06$) exhibited a one and a half decade loss of compression fatigue life as compared to specimens without layer waviness. The stress level corresponding to the 10^6 cycle run-out for these layer wave specimens was reduced to approximately 45% of the static compressive strength of the wave-free laminate. Specimens with layer waves failed at the location of the layer wave in a sudden, undetected manner. Brooming failure, characterized by through-the thickness splaying of the layers and numerous delaminations was the common failure mode. Layer wave specimens cycled to the 10^6 cycle run-out showed no evidence of delamination in the vicinity of the layer wave.

ACKNOWLEDGEMENT

REFERENCES

1.   Garala, H. J., "Experimental Evaluation of Graphite-Epoxy Composite Cylinders Subjected to Hydrostatic Compressive Loading," Proceedings of the 1987 SEM Spring Conference on Experimental Mechanics, Society for Experimental Mechanics, Houston, TX, June 1987, pp. 948-951.

2.   Garala, H. J. "Structural Evaluation of 8-inch Diameter Graphite-Epoxy Composite Cylinders Subjected to External Hydrostatic Compressive Loading," David Taylor Research Center Report DTRC-89/016, Bethesda, MD, 1989.

3.   Hyer, M. W., Maahs, L. C., and Fuchs, H. P., "The Influence of Layer Waviness on the Stress State in Hydrostatically Loaded Cylinders," Journal of Reinforced Plastics and Composites, Vol. 7, No. 11, 1988, pp. 601-613.

4.   Telegadas, H. K. and Hyer, M. W., "The Influence of Layer Waviness on the Stress State in Hydrostatically Loaded Cylinders: Further Results," Journal of Reinforced Plastics and Composites, Vol. 9, No. 5, 1990, pp. 503-518.

5.   Telegadas, H. K. and Hyer, M. W., "The Influence of Layer Waviness on the Stress State in Hydrostatically Loaded Cylinders: Failure Predictions", Journal of Reinforced Plastics and Composites, Vol. 11, No. 2, 1992, pp. 127-145.

6.	Adams, D. O. and Hyer, M. W., "Effects of Layer Waviness on Compression-Loaded Thermoplastic Composite Laminates," Virginia Tech Center for Composite Materials and Structures Report CCMS-92-06, 1992. (Ph.D. thesis in Engineering Mechanics of 1ˢᵗ author).

7.	Gardner, M. R., "Continuous Linear Alignment Testing Grips," NASA TM LAR-13493, National Aeronautics and Space Administration, Washington, D. C., May, 1980.

Evaluation of Time-Dependent Thermal Deformation of Epoxy Resin and CFRP Laminated Composites

SHIRO TAKADA, KEITARO TSUKUI AND SUMIO YOSHIOKA

ABSTRACT

Time-dependent mechanical properties of epoxy resin and CFRP laminated composites have been studied by time-dependent thermal deformation tests and computational analyses. Time-dependent thermal deformation of epoxy resin was measured at several temperatures(T=333K-373K); then, the master curve of compliance modulus S_{epoxy} and time-temperature shift factor a_T was obtained by a time-temperature superposition method. Furthermore, time-dependent compliance moduli S_{22} and S_{66} of CFRP were also measured by the time-dependent deformation tests of CFRP[90]$_8$ and [±45]$_S$ specimens respectively; then, the master curves of S_{22} and S_{66} were obtained and discussed in comparison with that of S_{epoxy}. The analysis program for time-dependent thermal deformation was developed on the basis of these time-dependent properties; this program utilizes a finite element method and can predict the in-plane time-dependent thermal deformation of symmetrically laminated CFRP structures with any laminate constitution. Then, time-dependent thermal deformation of [±45/90]$_S$ and [±30]$_S$ CFRP laminated composites was discussed on the basis of both the results of 5 hours of time-dependent deformation tests and the predictions calculated by the analysis program for time-dependent deformation. The predictions about the CFRP laminated composites are in good agreement with the experimental results demonstrating that this analytical method is effective for the prediction of the time-dependent thermal deformation of CFRP laminated composites.

INTRODUCTION

CFRP is one of the most favorable materials for space structures because of its advantageous properties, for example, lightweight, high modulus and low thermal expansion; therefore, it has been applied to many space satellites. These space structures, however, are exposed to thermal cycles in space; thus, the time-dependent deformation of CFRP in such a thermal environment is a legitimate concern. In particular, for space antennas, the time-dependent behavior should be accurately predictable, since they are required to maintain their initial shape for a long period.

It is well-known that composite materials, such as CFRP, show time-dependent behavior, in particular, at high temperatures. This time-dependent behavior of CFRP has been studied in several investigations [1-4]; some of them proposed prediction methods of time-dependent thermal deformation of CFRP, but in most cases the predictions do not show quite good agreement with the experimental results.

In the present paper, time-dependent mechanical properties of epoxy resin and high modulus

Shiro Takada, Central Research Laboratory, Mitsubishi Electric Corporation, 1-1, Tsukaguchi-honmachi 8-chome, Hyogo, Amagasaki, 661 Japan
Keitaro Tsukui, 1-1, Tsukaguchi-honmachi 8-chome, Hyogo, Amagasaki, 661 Japan
Sumio Yoshioka, 1-1, Tsukaguchi-honmachi 8-chome, Hyogo, Amagasaki, 661 Japan

CFRP are discussed on the basis of the results of time-dependent thermal deformation tests and the predictions by the analysis program for time-dependent thermal deformation.

EVALUATION OF TIME-DEPENDENT MECHANICAL PROPERTIES OF EPOXY RESIN AND UNIDIRECTIONAL CFRP

TIME-DEPENDENT THERMAL DEFORMATION TESTS

Time-dependent thermal deformation tests of epoxy resin(MS-1) and high modulus CFRP (M40/MS-1) were carried out to obtain the time-dependent material properties of epoxy and CFRP in a thermal environment. The dimensions of test specimens are shown in Fig. 1. CFRP [90]$_8$ laminated specimen (CT90) was used to obtain transverse properties and [±45]$_S$ laminated specimen (CT45) was used to obtain shear properties. The test conditions are shown in Table 1. The load was applied for 5 hours(1.8×10^{4}s) in each test and the deformation was measured by strain gages.
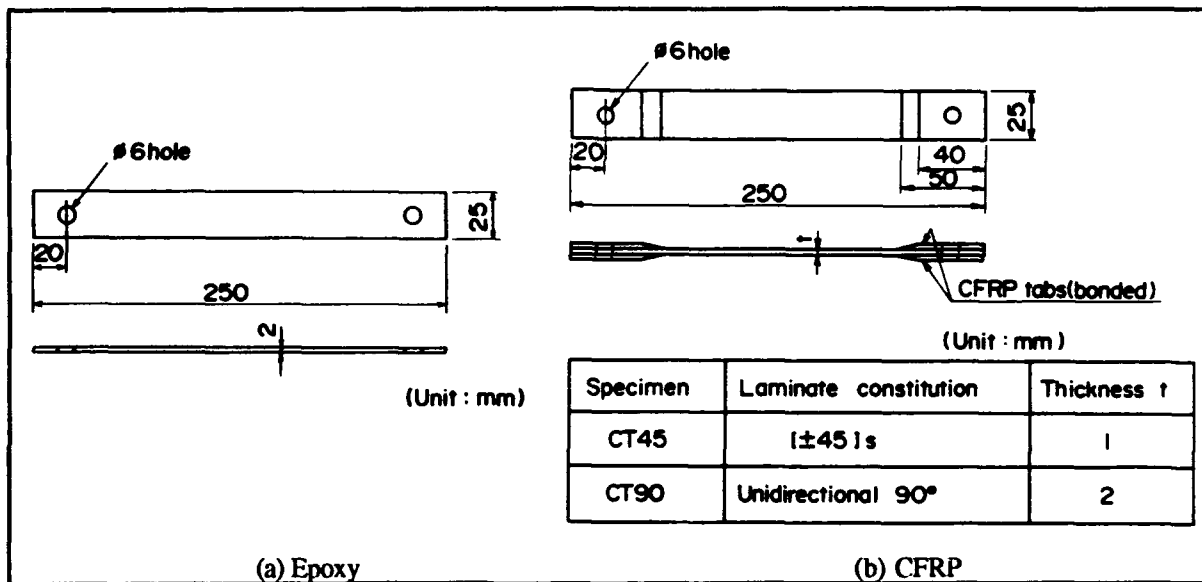
Figure 1 Dimensions of the specimen

Table I Test conditions

	Stress(MPa)	333K	343K	353K	363K	373K
Epoxy	2.94	O	O	O	O	O
CT90	2.45	—	—	—	—	O
	4.9	O	—	O	O	O
	6.86	—	—	—	—	O
CT45	2.45	—	—	—	—	O
	4.9	O	—	O	O	O
	5.88	—	—	—	—	O

RESULTS AND DISCUSSION

The change of compliance modulus $S_{epoxy}(=\varepsilon/\sigma)$ with time is shown in Fig. 2, which is given by the relation between applied stress and measured strain in the time-dependent test of epoxy. The master curve of S_{epoxy} obtained by considering the time-temperature shift factor a_T is shown in Fig. 3. From these figures, it was found that time-dependent deformation was observed in each test and a time-temperature superposition method was applicable to the deformation of epoxy.
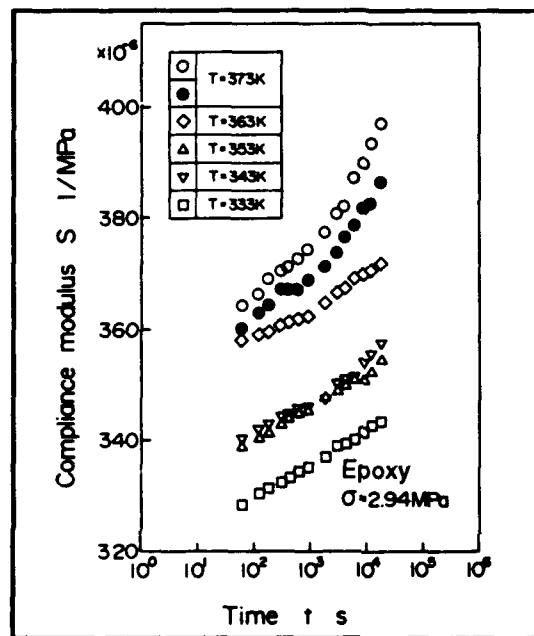
Figure 2 Change of compliance modulus
S_{epoxy} with time
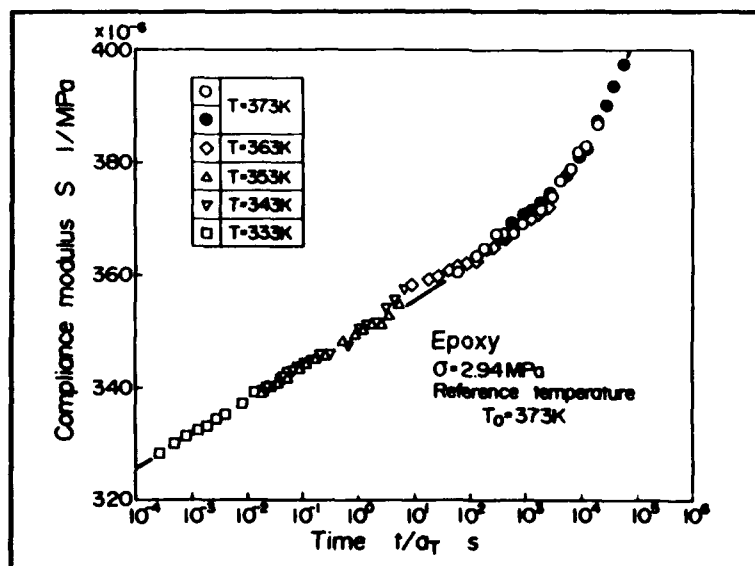
Figure 3 Master curve of compliance modulus S_{epoxy}

The change of compliance moduli $S_{22}(=\varepsilon_T/\sigma_T)$ and $S_{66}(=\gamma_{LT}/\tau_{LT})$ with time was given by the relation between applied stress and measured strain in the time-dependent deformation tests of CT90 and CT45. Then, the master curves of S_{22} and S_{66}, obtained by considering the time-temperature shift factor a_T, are shown in Fig. 4 and Fig. 5, respectively. In these figures, the compliance modulus increases with time, which is also shown in Fig. 3; moreover, the time-temperature superposition method was found to be also applicable to time-dependent thermal deformation of CFRP in the temperature range 333-373K.

Figure 6 shows the relation between the time-temperature shift factor a_T and temperature.
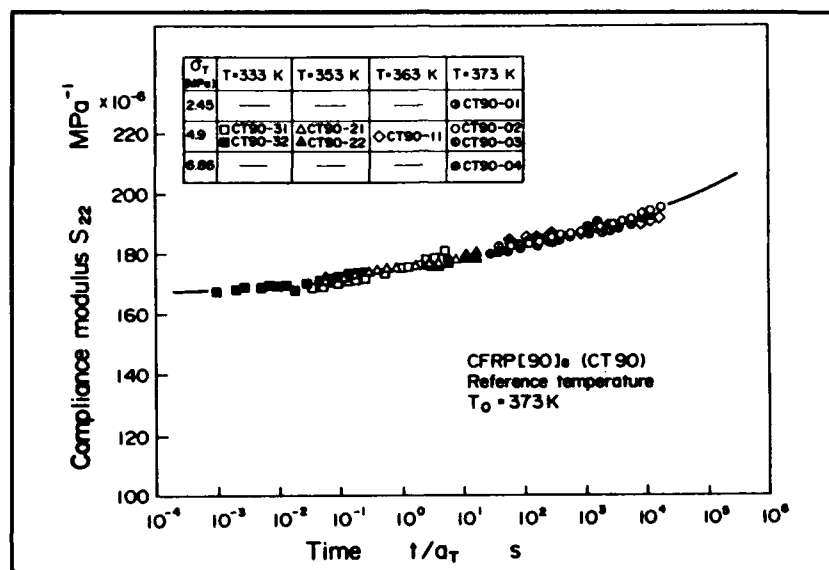
Figure 4 Master curve of transverse compliance modulus S_{22}
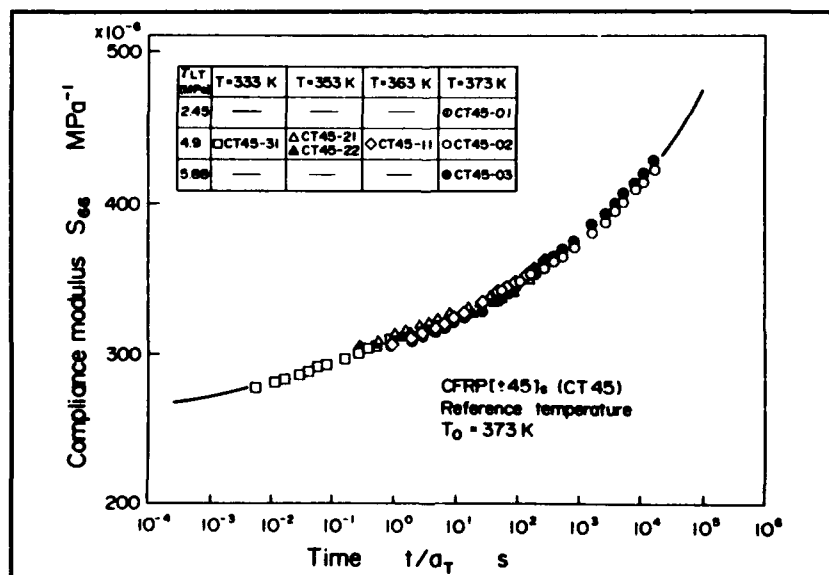
Figure 5 Master curve of transverse compliance modulus S_{66}

Time-temperature shift factors for S_{epoxy}, S_{22} and S_{66} are almost on the same line, that is, the same time-temperature superposition method is applicable to both epoxy and CFRP.

The measured master curve of S_{22} is shown in Fig. 7, where the calculated master curve of S_{22} is also shown for comparison. The calculated master curve was obtained by a rule of mixtures on the basis of the master curve of S_{epoxy} and fiber properties which were obtained by back calculation[5] from the additional tensile test results. From this figure, it was found that a simple rule of mixtures is applicable to the predictions of time-dependent properties of CFRP.
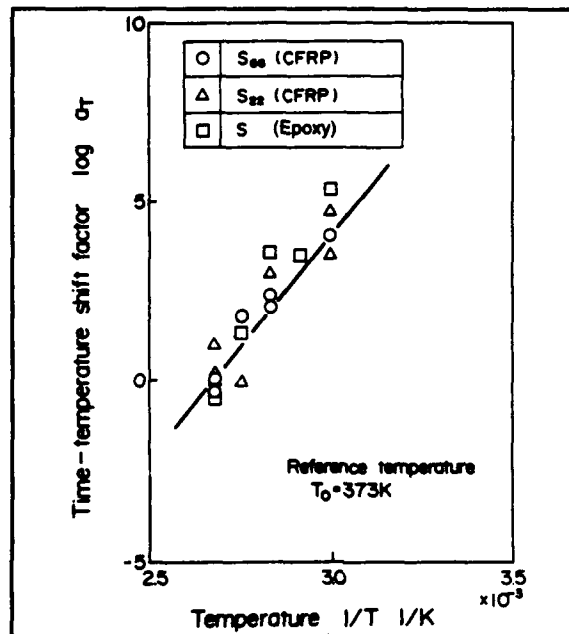
Figure 6 Relation between time-temperature shift
factor a_T and temperature
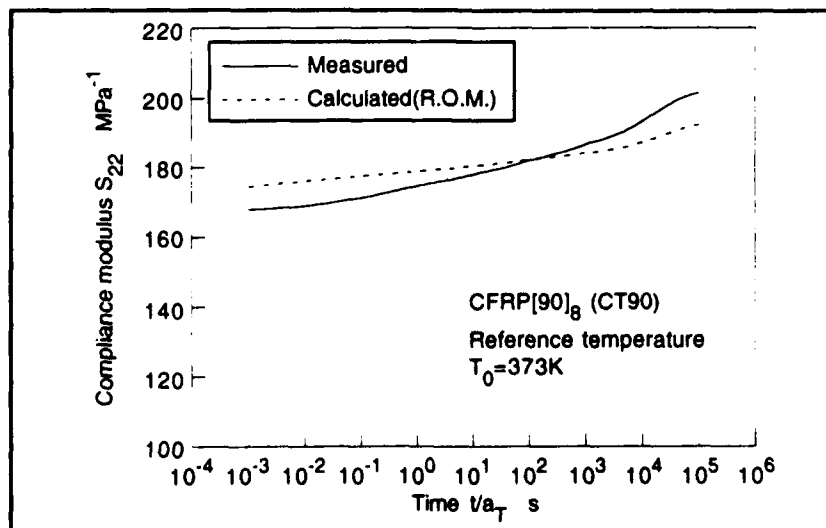
Figure 7 Comparison of measured master curve and
calculated master curve of S_{22}

ANALYSIS PROGRAM FOR TIME-DEPENDENT THERMAL DEFORMATION

The analysis program for time-dependent thermal deformation has been developed to predict time-dependent thermal deformation of CFRP laminated composites on the basis of the fundamental properties obtained above, that is, the master curves of S_{22} and S_{66} and a_T. Figure 8 shows the flowchart of the program; a finite element method (2-dimensional quadrilateral iso-parametric element) is applied with an incremental time control method. In this program, the time and temperature dependent material properties and stress redistribution at every time step in each element are taken into account. This program predicts inplane time-dependent thermal deformation of symmetrically laminated CFRP structures at constant temperature. Furthermore, the following equation is assumed;

$$\begin{Bmatrix} \varepsilon_L \\ \varepsilon_T(t,T) \\ \gamma_{LT}(t,T) \end{Bmatrix} = \begin{bmatrix} S_{11} & S_{12} & 0 \\ S_{12} & S_{22}(t,T) & 0 \\ 0 & 0 & S_{66}(t,T) \end{bmatrix} \begin{Bmatrix} \sigma_L \\ \sigma_T \\ \tau_{LT} \end{Bmatrix}$$

where, compliance moduli S_{11} and S_{12} are treated as time and temperature independent properties and S_{22} and S_{66} are treated as time and temperature dependent properties.
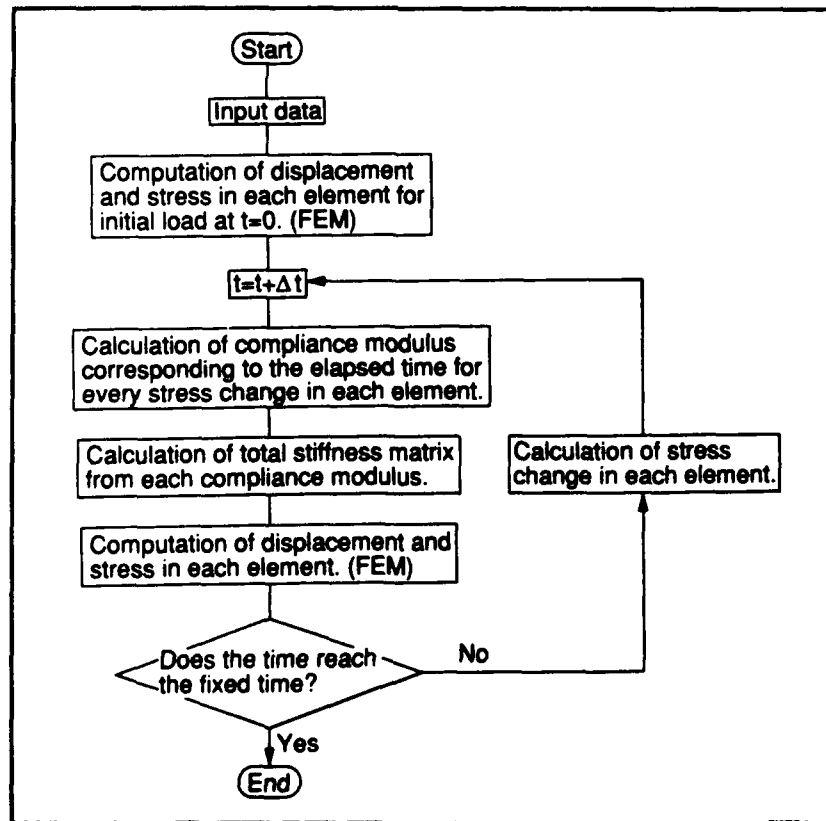
Figure 8 Flowchart of the analysis program for time-dependent
thermal deformation

EVALUATION OF TIME-DEPENDENT MECHANICAL PROPERTIES OF CFRP LAMINATED COMPOSITES

TIME-DEPENDENT THERMAL DEFORMATION TESTS OF CFRP LAMINATED PLATES

First, time-dependent thermal deformation of CFRP under a changing stress condition is discussed, since element stress changes with time in CFRP laminated composites. Thermal deformation tests of CFRP[±45]s laminated plates were carried out at 373K, where the stress was changed in every 5 minutes: σ_T=1.62MPa→3.24MPa→4.85MPa→3.24MPa→1.62MPa →0MPa.

Second, time-dependent thermal deformation tests of CFRP laminated plates with different laminate constitutions were carried out. The tested CFRP specimens were [±45/90]s and [±30]s laminates. The tests were carried out at 333K and 373K, where the applied stress was 29.4MPa. The load was applied for 5 hours(1.8×10^4s) and then removed.

RESULTS AND DISCUSSION

Figure 9 shows the change of shear strain with time obtained from the time-dependent deformation test of CFRP[±45]s, where the analytical values by the program are also shown. The experimental results are in good agreement with the analytical results. Therefore, the time-dependent thermal deformation of CFRP under a changing stress condition is accurately predictable from the fundamental time-dependent mechanical properties of unidirectional CFRP by this program.

Figure 10 and Figure 11 show the change of longitudinal strain with time for a [±45/90]s and a [±30]s laminated specimen, respectively, where both experimental results and analytical results are shown in the same figures. Experimental results are in good agreement with analytical results on both CFRP laminates demonstrating that time-dependent thermal deformation of CFRP laminated plates can be accurately predicted from the mechanical properties of unidirectional CFRP by this program.
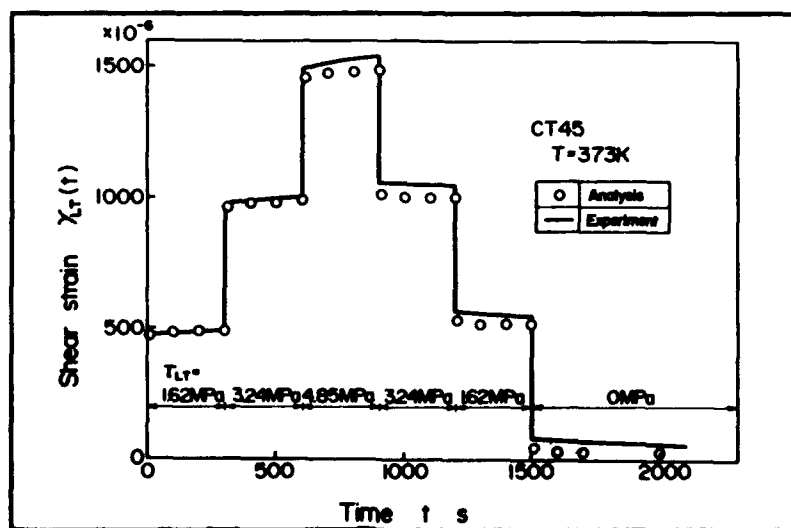
Figure 9　Change of shear strain with time on CFRP[±45]s under the changing stress condition
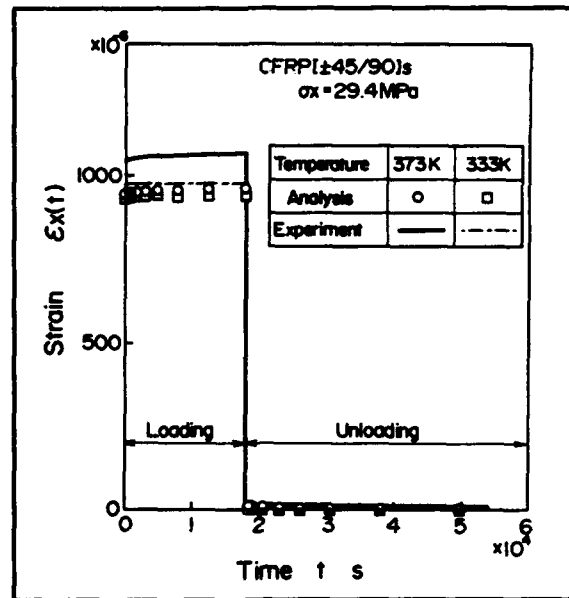
Figure 10 Change of longitudinal strain with time
on CFRP[±45/90]s
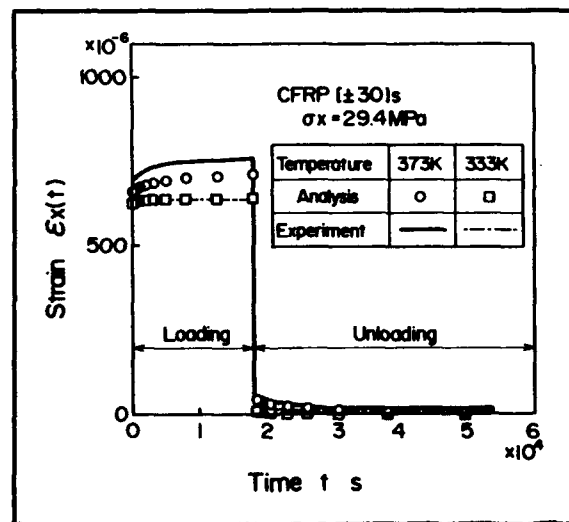
Figure 11 Change of longitudinal strain with time
on CFRP[±30]s

CONCLUSIONS

Time-dependent thermal deformation of epoxy resin and CFRP laminated composites has been
evaluated on the basis of time-dependent thermal deformation tests and the analysis program
for time-dependent thermal deformation. The results are summarized as follows:

(1) The same time-temperature superposition method is applicable to the time-dependent mechanical properties of epoxy resin and CFRP.

(2) The analysis program for time-dependent thermal deformation of CFRP laminated composites has been developed on the basis of a finite element method; this program takes into account the time and temperature dependent material properties and stress redistribution.

(3) The analysis program developed here was found to be effective for the prediction of time-dependent thermal deformation of CFRP laminated composites.

REFERENCES

1. Tuttle, M. E. and H. F. Brinson. 1986. "Prediction of the Long-Term Creep Compliance of General Composite Laminates." Experimental Mechanics, 26: 89-102.

2. Yeow, Y. T., D. H. Morris and H. F. Brinson. 1979. "Time-Temperature Behavior of a Unidirectional Graphite/Epoxy Composite." ASTM STP, 674: 263-281.

3. Kibler, K. G.. 1980. "Effects of Temperature and Moisture on the Creep Compliance of Graphite-Epoxy Composites." Agard Conf. Proc., 288: 8.1-8.8.

4. Dillard, D. A., D. H. Morris and H. F. Brinson. 1982. "Predicting Viscoelastic Response and Delayed Failures in General Laminated Composites." ASTM STP, 787: 357-370.

5. Tsai, S. W.. 1988. Composites Design, 4th edition, Dayton, OH: Think Composites, pp. 10.1-10.14.

Metal Matrix Composites I

Fabrication and Mechanical Properties of Cf/NiAl and SiCw/NiAl Composites

K. NISHIYAMA, M. MOHRI AND S. UMEKAWA

Abstract

Fabrication condition and mechanical properties of NiAl matrix composites reinforced with discontinuous carbon fiber(C_f) as well as silicon carbide whisker(SiC_w) were investigated. The intermetallic compound NiAl powder at the composition of Ni-49.4at%Al prepared by a self-propagating high-temperature synthesis(SHS) method were used in this study. The C_f/NiAl and SiC_w/NiAl composites with the reinforcement content up to 40 volume percent were fabricated by hot-pressing in the temperature range of 900°C and 1400°C and the pressure range 20MPa and 60MPa in vacuum. The bending strength of the C_f/NiAl composite slightly decreased with increasing fiber content. On the other hand, the strength of the SiC_w/NiAl increased to a maximum value of 1150MPa at 2vol%SiCw content, then decreased with increasing the whisker content. The increase of strength was presumably be contributed by solid-solution strengthening mechanism in the matrix. The fracture toughness of both composites increased with increasing the reinforcement content. Other mechanical properties of the composites, such as high temperature hardness, were also examined, and discussed the interfacial phenomena in the composites.

Introduction

Intermetallic compounds in the Ni-Al system have long been recognized as candidates for high temperature applications because thermally activated process such as diffusion are inhibited by the ordered crystal structure[1,2]. There are five intermetallic compounds in the Ni-Al system, $NiAl_3$(854°C), Ni_2Al_3(1,133°C), NiAl(1,638°C), Ni_5Al_3(700°C) and Ni_3Al(1,395°C). The NiAl has a wide solubility range from 42.5 to 69.5at% nickel. The NiAl is especially attractive since this compound offers oxidation and corrosion resistance, and the

Katsuhiro Nishiyama, Masashi Mohri and Sokichi Umekawa, Science University of Tokyo, 2641 Yamazaki, Noda, 278, Japan

structure is stable up to just below the melting point of 1,638°C. Previous works have shown that the high temperature creep resistance of NiAl can be improved to a comparable level of some conventional superalloys[1,2]. Nevertheless the attractive characteristics of NiAl for a matrix of metal matrix composite(MMC), few results of the system has been reported.

In this paper, the fabrication condition of hot-pressing and the mechanical properties of NiAl based composites with short carbon fiber and silicon carbide whisker were described.

Experimental procedure

The NiAl powder with a composition of Ni-49.4at%Al prepared by a self-propagating high-temperature synthesis(SHS) method[3] were used in this study. Table 1 shows the chemical composition of NiAl powder with an average particle size of <45μm. The mechanical properties of NiAl hot-pressed at 1200°C under a pressure of 60MPa in vacuum are given in Table 2. Pan based carbon fiber with an average diameter of 7μm was a commercial grade product supplied by Nippon Carbon Co., Ltd. β-type silicon carbide whisker supplied by Tokai Carbon Co., Ltd. has an average diameter of 0.5μm and an aspect ratio of 130. The characteristics of Cf and SiCw are summarized in Table 3 and Table 4. The constituent materials were wet-mixed with toluene in a polyethylene lined container for 24h, then dried in air at about 40°C. The Cf/NiAl and SiCw/NiAl composites were hot-pressed at temperatures range from 900°C to 1400°C and the pressure range 20MPa and 60MPa in vacuum. Fracture strength was measured by a four-point bending test. The dimensions of the bending tested specimen were 3mm x 4mm X 30mm. High temperature hardness of the composites were carried out by a micro-Vickers tester using the indentor of sapphire. Fracture toughness was measured by single edged pre-cracked beam(SEPB) technique. Microstructure investigations were accomplished by optical microscope, scanning electron microscope(SEM), electron micro-prove analyzer (EPMA) and transmission microscope(TEM).

Result and Discussion

Wettability and contact interaction

Sessile drop experiments were performed in graphite furnace. Wetting of a liquid on a solid is defined by contact angle θ that a drop of the liquid form at the point of contact with solid. A non-wetting configuration is one where the contact angle is θ>90. Full wetting is achieved when θ=0. When θ -0 but <90 partial wetting occurs.

Fig. 1 shows the microstructure in the vicinity of the interface between silicon carbide and NiAl. The contact angle of NiAl on SiC

Table 1 Chemical analysis of NiAl powder (wt%)

Ni	Al	O	N	Others
68.7	30.8	0.26	0.018	Bal.

Table 2 Mechanical properties of NiAl hot-pressed at 1200°C under a condition 60MPa for 0.5h

Density (g/cm)	5.93
Porosity (%)	3
Bending strength(MPa)	1028
Vickers hardness (GPa)	3.7
Young's modulus (GPa)	165.5
Shear modulus (GPa)	64.4
Bulk modulus (GPa)	128.3
Poisson's ratio	0.285
Compressional velocity (km/sec)	6.01
Shear velocity (km/sec)	3.30

Table 3 Mechanical properties of SiC whisker

Crystal type	β type
Average diameter (mm)	0.5
Average length (mm)	125
Density (g/cm^3)	3.19
Bulk density (g/cm^3)	0.1
Average aspect ratio (L/D)	130
Heat resistance (in air)	up to 1600°C
SiC particulate content	less than 1wt%

Table 4 Mechanical properties of PAN based carbon fiber

Diameter (μm)	7
Density (g/cm^3)	1.78
Tensile strength (MPa)	3300
Tensile modulus (MPa)	235
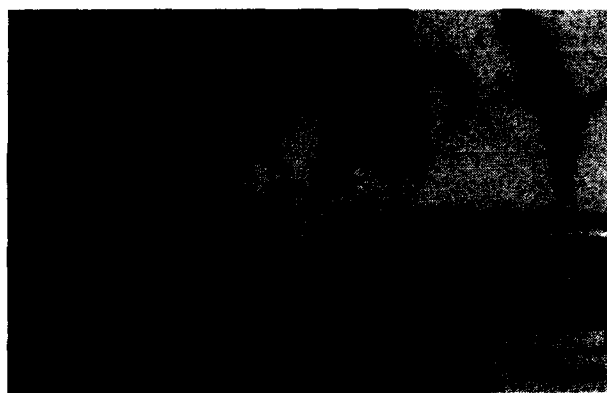
Fig.1 Optical micrograph that shows the reaction zone produced by liquid NiAl on sintered SiC.

Fig.2 Optical microgrph showing the reaction zone produced by liquid NiAl on carbon.
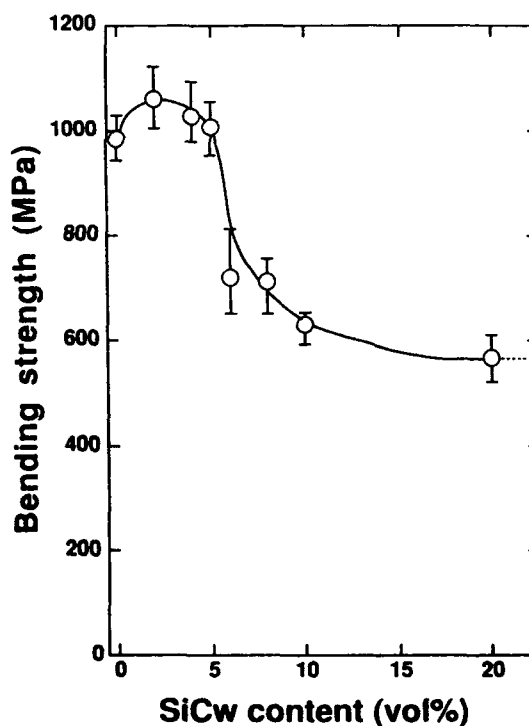
Fig.3 Effect of SiCw content on bending strength of SiCw/NiAl composites hot-pressed at 1300℃ under a pressure of 60 MPa for 30 min.
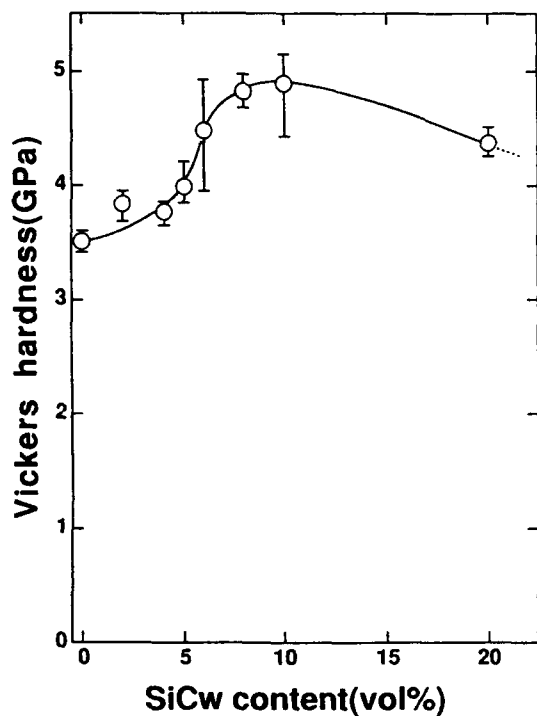
Fig.4 Effect of SiCw content on Vickers hardness of SiCw/NiAl composites hot-pressed at 1300℃ under a pressure of 60 MPa for 30 min .
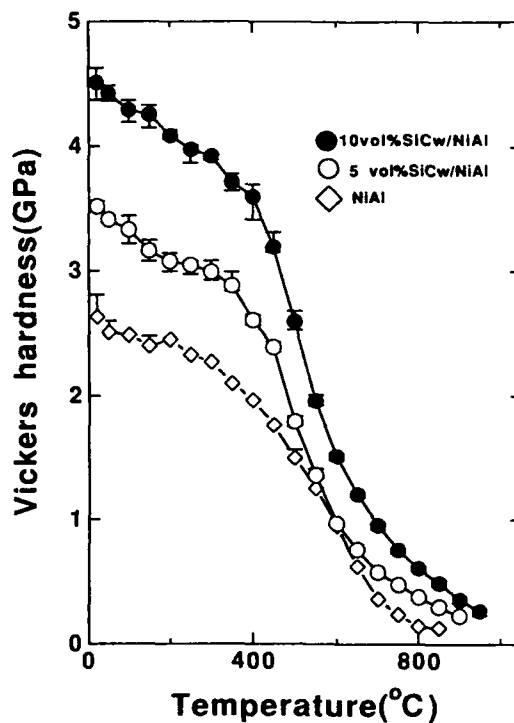
Fig.5 Effect of temperature on Vickers hardness of NiAl, 5vol%SiCw/NiAl and 10vol%SiCw/NiAl composite hot-pressd at 1300℃ under a pressure of 60 MPa for 30 min
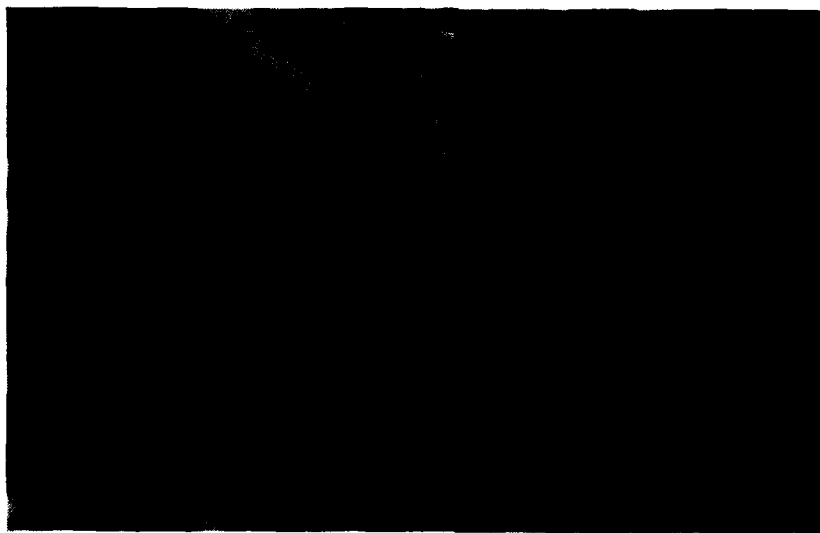
Fig.6 SEM micrograph of fracture sureface of 20vol%SiCw/NiAl composite hot-pressed at 1300℃ under a pressure of 60 MPa for 30 min.

was 50° after heated at 1700°C for 0.5h. and a large reaction layers was observed. The phase of reaction layer was detected by EPMA analysis, which could be estimated as (Al, Si)$_7$Ni$_3$. Many pores were observed in NiAl, which would be built up by a diffusion-controlled process known as Kirkendal effect.

Fig. 2 shows the optical microstructure in the vicinity of the interface between carbon and NiAl after heated at 1700°C for 0.5h. The contact angle of NiAl on carbon was 86° and a little reaction was observed.

SiCw/NiAl composite

Fig. 3 shows the effect of the SiCw content on the 4-point bending strength of SiCw/NiAl composite hot-pressed at 1300°C for 0.5h under a pressure of 60MPa in vacuum. The strength of the composite increases to a maximum value of approximately 1150MPa at 2vol%SiCw and then decrease with increasing SiCw content. At the 20vol%SiCw content the bending strength was obtained 600MPa. The increase of strength was presumable be contributed by a solid-solution strengthening mechanism of the matrix.

Fig. 4 shows the micro-Vickers hardness of the SiCw/NiAl composite hot-pressed at 1300°C for 0.5h under a pressure of 60MPa. The hardness of the composite increases with increase of the silicon carbide whisker content and reaches 5GPa at 10vol%SiCw.

Fig. 5 shows the temperature-dependent hardness of NiAl matrix, and of 5vol%SiCw/NiAl and 10vol%SiCw/NiAl composite hot-pressed at 1300°C for 0.5h under a pressure of 60MPa. The hardness of the matrix and the composites decrease slightly with a temperature rise. The high-temperature hardness of the composites increased with increasing silicon carbide whisker content.

Fig. 6 shows the SEM photograph of fracture surface of 20vol%SiCw/NiAl composite hot-pressed at 1300°C for 0.5h under a pressure of 60MPa. The round-shaped circles observed in Fig. 6 are silicon carbide whisker.

Fig. 7 shows the TEM photograph of 5vol%SiCw/NiAl composite hot-pressed at 1300°C for 0.5h under a pressure of 60MPa. A low density of dislocation in undeformed NiAl matrix is observed.

Cf/NiAl composite

Fig. 8 shows the carbon fiber content on the bending strength of Cf/NiAl composite hot-pressed at 1200°C for 0.5h under a pressure of 60MPa. The bending strength of the composites decrease slightly with increase of the carbon fiber content.
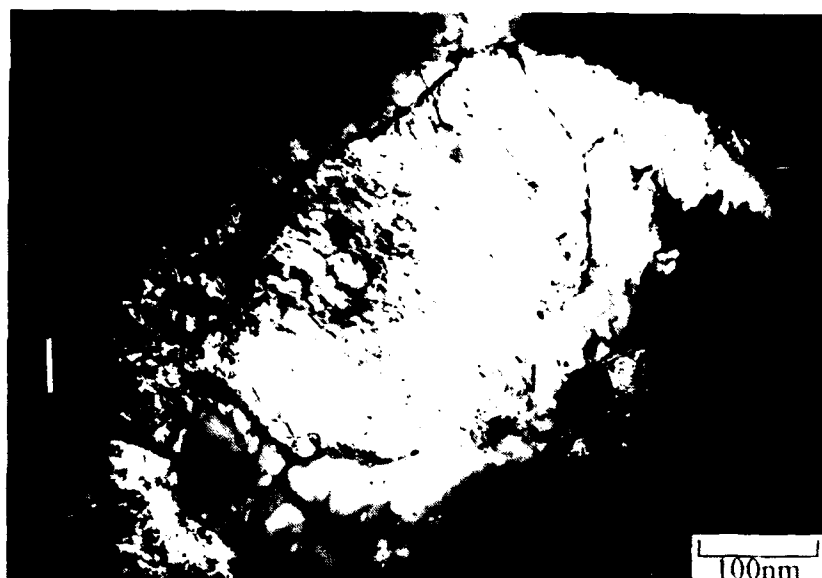
Fig.7 TEM micrograph of 5vol% SiCw/NiAl composite hot-pressed at 1300°C under a pressure of 60 MPa for 30 min.
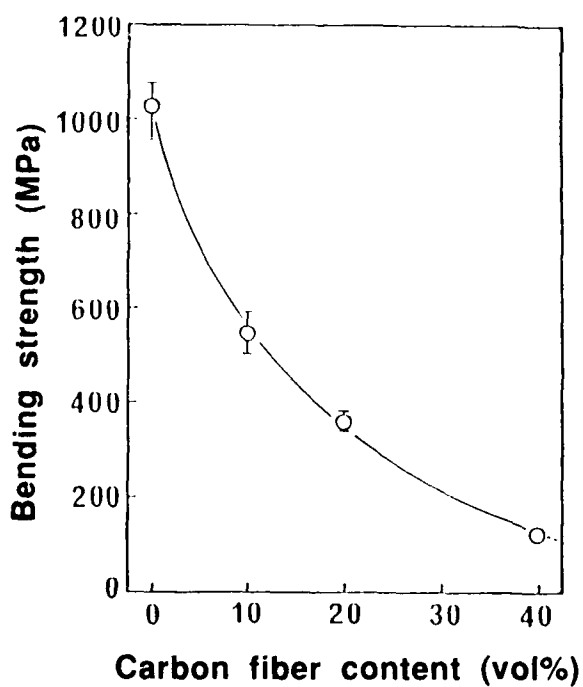
Fig.8 Effect of Cf content on bending strength of Cf/NiAl composites hot-pressed at 1200°C under a pressure of 60 MPa for 30min.
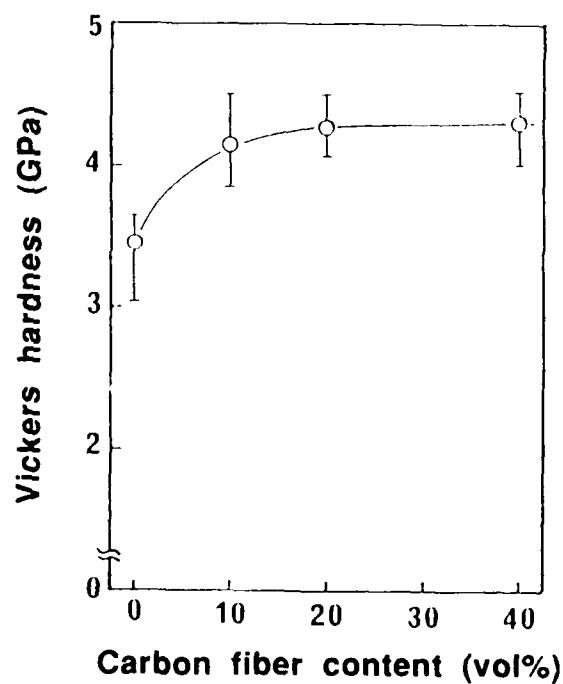
Fig.9 Effect of Cf content on Vickers hardness of Cf/NiAl composites hot-pressed at 1200°C under a pressure of 60 MPa for 30 min.
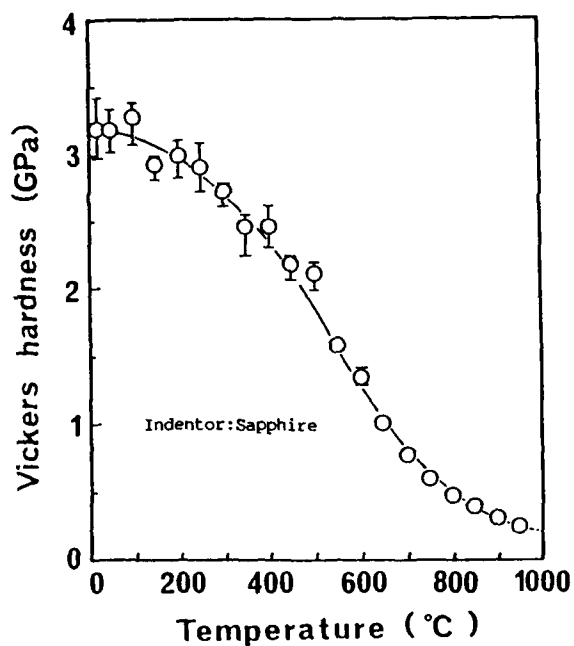
Fig.10 Effect of temperature on Vickers hardness of 10vol%Cf/NiAl composites hot-pressed at 1200°C under a pressure of 60 MPa for 30 min.

Fig.11 Optical micrographs of 10vol%Cf/NiAl composites hot-pressed at 1200℃ under a pressure of 60 MPa for 30 min.
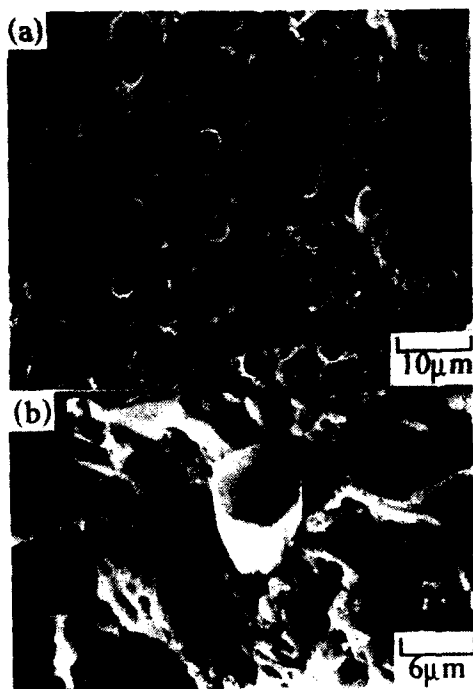
Fig.12 SEM photograhs of fracture of 10vol%Cf/NiAl composites hot-pressed at 1200°C under a pressure of 60 MPa for 30 min.

Fig.13 SEM photographs of Cf/NiAl composites hot-pressed at :(a) 1200°C and (b) 1400°C.

Fig. 9 shows the micro-Vickers hardness of Cf/NiAl composites at room temperature as a function of the carbon fiber content. The hardness of the composite increases with increase of the carbon fiber content and reaches 4 5GPa at 10vol%SiCw.

Fig. 10 shows the temperature-dependent hardness of 10vol%Cf/ NiAl composite hot-pressed at 1200°C for 0.5h under a pressure of 60MPa. The hardness of the composites decrease slightly with temperature rise. The high-temperature hardness of the composites increased with increasing carbon fiber content.

Fig. 11 and Fig. 12 shows the optical and SEM photographs of 10vol%Cf/NiAl composite hot-pressed at 1200°C for 0.5h under a pressure of 60MPa. In Fig. 12, a large amount of carbon fiber pullout on the fracture surface was observed.

Fig. 13 shows the SEM photograph of the fracture surfaces in the vicinity of the interface between carbon fiber and NiAl. The interfacial reaction between fiber and matrix was observed. The reaction layer of the interface between carbon fiber and NiAl grew thicker with an increase of hot-pressing temperature and holding time.

Fracture toughness of SiCw/NiAl and Cf/NiAl composites increase with increase of the reinforcement. The K_{IC} value for the NiAl matrix obtained by SEPB method was approximately $4MPa \cdot m^{-1/2}$. The 30vol%Cf/NiAl composite and 20vol%SiCw composite exhibit K_{IC} values of $12MPa \cdot m^{-1/2}$ and $7.8MPa \cdot m^{-1/2}$ at room temperature, respectively.

Conclusion

Fabrication condition and mechanical properties of NiAl based composites with discontinuous carbon fiber and silicon carbide whisker were examined. Results are summarized as follows:

(1) The bending strength of the SiC_w/NiAl increased to a maximum value of 1150MPa at 2vol%SiCw content, then decreased with increasing whisker content. The increase of strength was presumably be contributed by a solid-solution strengthening mechanism in the matrix.

(2) The bending strength of the Cf/NiAl composite slightly decreased with increasing fiber content.

(3) The fracture toughness of both composites increased with increasing the reinforcement content.

References

1. M. Sherman and K. Vedula, Journal of Materials Science, 21(1986) 1974.
2. E. M. Grala, "Investigation of NiAl and Ni₃Al," in Mechanical Properties of Intermetallic Compounds, J.H.Westbrook: Wiley, New York, 1960, 358.
3. A. G. Merzhanov, V. M. Shkiro and I. P. Borovinskaya, U.S. Patent No.3,726,643(1973), Japan Patent No.108,839(1982).

Preparation of SiC Whisker Reinforced Al Alloy Composites by Compocasting Process

KENJI MIWA, TAKASHI IKEDA, KOUJI MIZUNO AND TERUO OHASHI

ABSTRACT

Incorporation of SiC whisker into Al-Cu alloy slurry by compocasting process has been tried to get good mixing. Then, progress conditions of the reaction between aluminum alloy and SiC whisker have been made clarified by the heating experiments of pellets compacted with aluminum powder and SiC whisker. To get good mixing of SiC whisker into the alloy slurry by compocasting process, the size of primary solid crystals in the alloy slurry should be controlled so adequately as to incorporate easily the balls of whisker into the alloy slurry. The reason is that each whisker do not exist independently, but it forms balls prior to addition. Aluminum and SiC whisker do not react during fabrication of composites by compocasting process, for the reaction temperature of both materials is higher than the fabrication temperature and the reaction start time of them is later than the fabrication time.

INTRODUCTION

Compocasting process [1,2] is a very useful method of producing nonmetallic particulate or fiber reinforced metal matrix composites because it allows uniform distribution of reinforcement in the metal matrix. In compocasting process, the reinforcement is entrapped by the primary solid crystals in the semi-solid slurry and it is prevented from settling, floating, or agglomeration [2]. Entrapment of the non-metallic reinforcement materials into an alloy slurry allows the fabrication of metal matrix composites regardless of the lack of wettability of the reinforcement with matrix metals [3]. However, it is very difficult that very fine non-metallic materials powder are nicely wetted and dispersed in metal also by compocasting process, for they are stuck together in clumps. So very few works [4-7] have been reported for incorporating of whisker by compocasting process.

In our previous studies [8,9], preparation of fine SiC particulate, $5\mu m$ and less in size, reinforced aluminum alloy matrix composites by compocasting process was tried. In order to get good incorporation, the addition rate of SiC needed making slow with decrease in the size of SiC. Most of gas absorbed on the surface of SiC which was prepared in air was H_2O and it liberated by heating to 873K. SiC particles incorporated and dispersed well as a single particle in the alloy slurry by the preheating treatment at 873K for 1 hour.

In this study, to get good mixing of SiC whisker with Al-Cu alloy slurry and a better understanding of mechanism to produce whisker reinforced Al-Cu alloy composites by compocasting process, the effects of the volume fraction and the size of primary crystals on incorporating of whisker into the slurry is discussed. Furthermore, the reaction between Al-Cu alloy and SiC whisker by mixing has been investigated. Progress conditions of the reaction have been made clarified by the heating experiments of pellets compacted with aluminum powder and SiC whisker.

Kenji Miwa, Government Industrial Research Institute, Nagoya, 1-1 Hirate-cho, Kita-ku, Nagoya, 462, Japan
Takashi Ikeda, Matsushita Electronic Components Co., LTD., 1006, Kadoma, Osaka, 571, Japan
Kouji Mizuno, Mitsubishi Motor Corporation, 1 Nakasinkiri, Hashime-cho, Okazaki, 444, Japan
Teruo Ohashi, Nagoya Institute of Technology, Gokiso-cho, Showa-ku, Nagoya, 466, Japan

EXPERIMENTAL PROCEDURE

The alloys used mainly Al-5mass%Cu, in addition Al-5mass%Cu-0.3mass%TiB as fine grain ones and Al-3mass%Cu as coarse grain ones. Alloy melt was poured into the crucible which was preheated at about 50K above its liquidus temperature. The melt temperature was constantly dropped at the rate of 5K/min under the liquid state and held at the fixed semi-solid temperature isothermally. The melt was stirred at the rate of 250rpm from just after pouring to the end of SiC whisker addition. Whisker was added to the slurry during stirring through a glass funnel with heating element for preheating run at the constant rate of 0.12mass%/min. The amount of whisker added was constantly 5mass%. Whisker was no treated on the surface before addition but heated at 873K for 1 hour inside the glass funnel for only preheating run. Composite slurry finished addition of whisker were stirred continuously for 50 minutes and were rapidly quenched by dropping with the crucible into a water bath placed just under a furnace to examine by metallographic techniques. This experiment was progressed under sealed system to prevent from scattering of SiC whisker in the atmosphere.

Preparation of composite pellets mixed SiC whisker and pure aluminum powder (under 100 mesh) was as follows. Both materials were mixed in isopropyl alcohol solution and were stirred by ultrasonic generator. Then they were filtrated, dried in air and mixed again homogeneously. These materials were hot pressed with the load of 3 ton at 723K in vacuum. Composite pellets were heated at 973K to 1273K within 60 minutes. The amounts of reaction products in these pellets were measured by X-ray diffraction test and observed microscopically.

RESULTS AND DISCUSSION

Representative microstructures of Al-5mass%Cu alloys compocast with SiC whisker are shown in Fig.1 [10]. They are divided into four classes according to mixed grade, that is, the extent of incorporation of SiC whisker into Al-Cu alloy matrix. The mixed grade 1 shows no mixing of whisker. The grade 2 indicates partially mixing into a liquid part. Whisker was incorporated like an aggregate and existed mainly around primary dendrites, as if it was entrapped by a dendrite arm. The grade 3 denotes much mixed whisker. In this grade, the content of incorporated whisker was much, so the viscosity of composite increased strongly. Ambient atmosphere was caught up into a composite slurry during stirring and blow hole defects formed after solidification. The grade 4 shows very high condensed mixing. So, amounts of mixed whisker increase according as the class number increases.

Based on the mixed grades described above, effects of volume fraction solid of primary crystals on mixed grade of SiC whisker in Al-5mass%Cu alloy slurry is shown in Fig.2. In this alloy, the size of primary solid was about 500µm in diameter in the range of volume fraction solid of 0.4 or so. The extent of incorporation of whisker became good gradually with increase in the volume fraction solid of primary crystals from 0.3 to 0.5 as shown in Fig.2. Especially good mixing of whisker was attained almost all for the volume fraction solid more over 0.45. As the apparent viscosity of composite slurry increased with increase in the volume fraction solid of primary crystals, whisker could be incorporated in the slurry.

Our previous study [8] for incorporation of fine SiC particulates into Al-Cu alloy slurry showed that finer SiC particle could be incorporated easily by means of refinement of the size of primary solid crystals. So, the same technique as applied for mixing of SiC particulate into the alloy slurry has been tried for the incorporation of SiC whisker. TiB is the most popular refining element for aluminum alloys and was added 0.3mass% in Al-5mass%Cu alloy. The primary crystal size decreased about half of it, about 250µm in diameter, in comparison with that of no addition alloys. SiC whisker could not be incorporated into matrix in the all range of the volume fraction solid of primary crystals [10].

Then, the average size of primary solid crystals was inversely increased about three times of that

Mixed grade   Mag. x40   Mag. x750

1

2

3

4
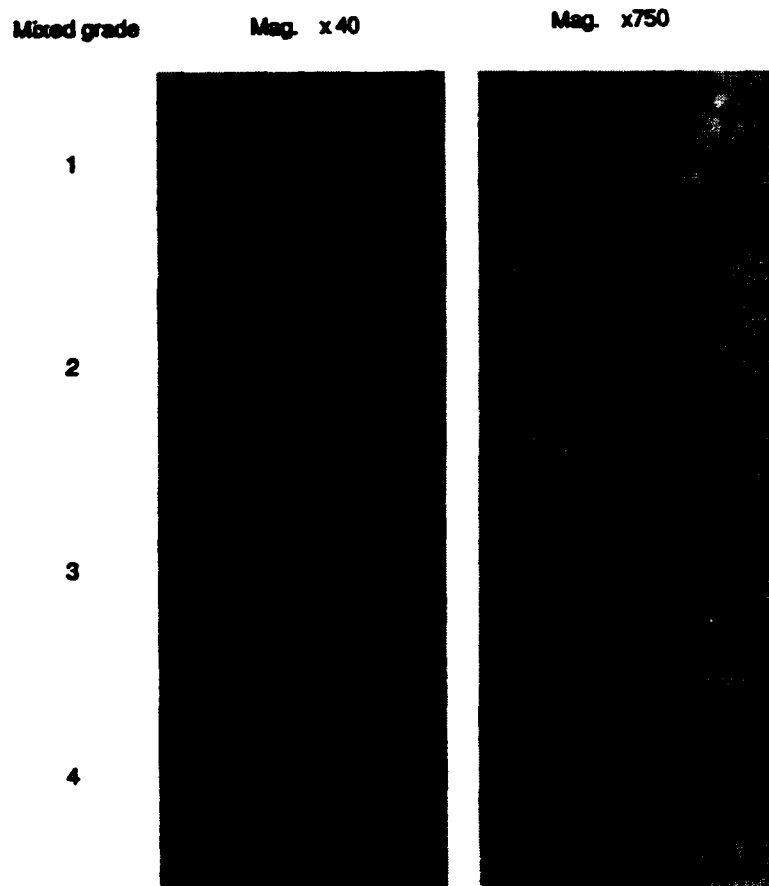
Fig. 1 Microstructures of compocast materials.
mixed grade 1:no incorporated, mixed grade 2:partially incorporated.
mixed grade 3:much incorporated, mixed grade 4:richly incorporated.

Al-5%Cu
(average size : 500μm)
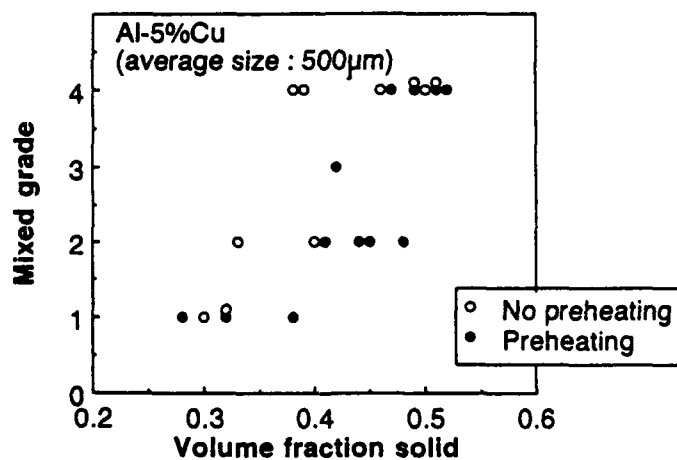
Fig. 2 Effects of volume fraction solid of primary crystals
on mixed grade of SiC whisker in Al-5%Cu alloy slurry.

427

of Al-5mass%Cu alloy, that is, 1700μm in diameter by means of decrease in Cu content till 3mass%. Incorporation of the whisker was tried for Al-3mass%Cu alloy slurry. The extent of incorporation of whisker became good gradually with increase in the volume fraction solid of primary crystals and mixed grade decreased somewhat in comparison with that in Al-5mass%Cu alloy slurry [10].

As mentioned above, incorporation of SiC whisker into Al-Cu alloy slurry by compocasting process was different from the case of incorporation of SiC particle. Mixing of whisker with Al-Cu alloy slurry became difficult by decrease in the size of primary solid crystals. It is presumed that the shape of whisker which added into the alloy slurry may have not been appropriate for incorporation. Usually, ceramic whisker has a tendency to have a shape of ball as-received state. So, the shape of SiC whisker just before mixing with alloy slurry was observed by Scanning Electron Microscopy (SEM) and the result is shown in Fig.3. Whisker was not separately each other but formed aggregates and they had clearly a shape of ball. The size distribution of these whisker balls was measured on the basis of SEM micrographs. The average size of whisker balls was about 95μm. Therefore, to incorporate whisker into alloy slurry by compocasting process, whisker balls with much space inside it and about 95μm in average diameter should be introduced into alloy slurry.

Fig. 3 Scanning electron micrograph of SiC whisker just before mixing with alloy slurry.

Figure 4 shows the model of incorporation of SiC whisker into Al-Cu alloy slurry by compocasting process. When the average size of primary solid crystals was about 500μm, good incorporation of whisker was achieved with increase in the volume fraction solid as shown in Fig.2. This reason is explained by the fact that the apparent viscosity of slurry was enough high and the shape of free surface of slurry was easy to introduce whisker balls into a slurry as shown in Fig.4(b). When, however, the average size of primary solid crystals was too small, that is, about 250μm, the apparent viscosity increased, but thixotropy effect due to stirring revealed remarkably and the shape of free surface of slurry was too smooth to introduce whisker balls into slurry as shown in Fig.4(a). When the average size of primary solid crystals was so large as about 1700μm, a small number of primary crystals suspended in the liquid part during stirring. So, apparent viscosity of slurry was low level and the shape of free surface of it presented a smooth pattern as shown in Fig.4(c). Consequently, whisker could not be introduced into slurry. However, in this case, thixotropy effect is small, so the shape of free surface of slurry changed roughly with increase in the volume fraction solid of primary crystals. As a result, slurry turned to be able to introduce whisker easily. The incorporated balls into the slurry were broken down each whisker and dispersed homogeneously in the residual liquid part. Each shape of free surface of slurry described above was confirmed by visual observation. It has been clear that the size of primary solid crystals
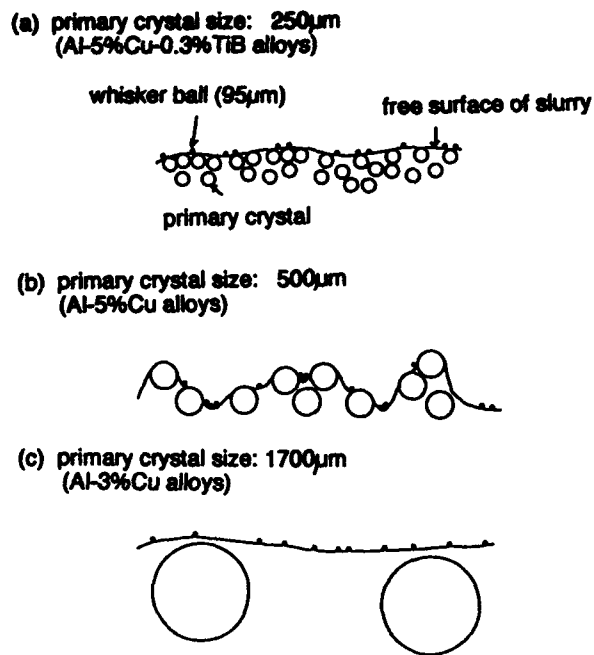
(a) primary crystal size: 250μm
    (Al-5%Cu-0.3%TiB alloys)

whisker ball (95μm)   free surface of slurry

primary crystal

(b) primary crystal size: 500μm
    (Al-5%Cu alloys)

(c) primary crystal size: 1700μm
    (Al-3%Cu alloys)

Fig. 4 Model of incorporation of SiC whisker into Al-Cu alloy slurry by compocasting process.

Al - 3%Cu

● Al
▲ SiC
■ Al₂Cu
▲ Al₄C₃
○ Si

Al - 5%Cu

Intensity

20   30   40   50
              2θ
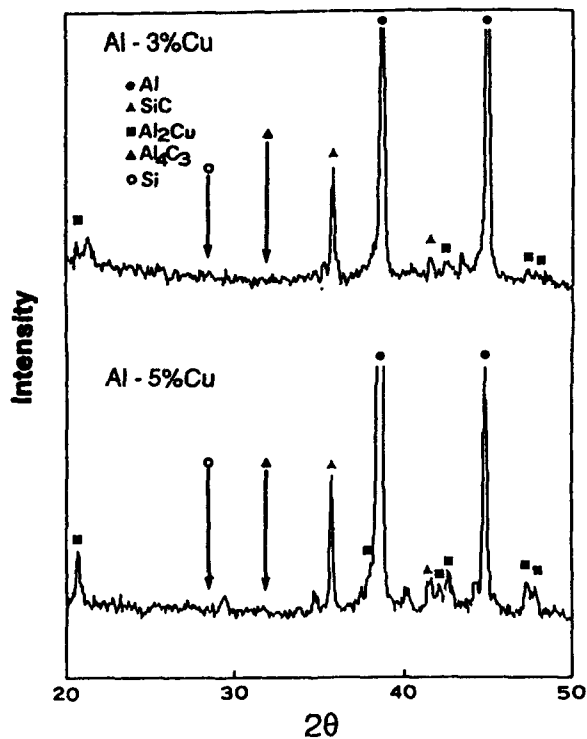
Fig. 5 X-ray diffraction patterns of good mixed alloy composites.

429

in a slurry should be controlled appropriately for the purpose of easy incorporation of whisker into a slurry by compocasting process.

As described above, we could well incorporate SiC whisker into Al-Cu alloy slurry by compocasting process on the basis of controlling the size of primary solid crystals in the slurry. Usually good incorporation brings good bonding between reinforcement and metal matrix. Good bonding is attended with the reaction of both materials more or less. On incorporation of whiskers, it is easy for whiskers to disappear by the reaction of both materials, because of their small size. Therefore, it is important for incorporation of whisker to suppress the reaction of them as little as possible. So, the reaction between Al-Cu alloy and SiC whisker by mixing was measured by means of X-ray diffraction test. If the reaction occurs, reaction products such as free silicon (Si) and aluminum carbide (Al4C3) must be detected. The results for good mixed alloy composites are shown in Fig.5. No reaction products were observed as shown in this figure.

Furthermore, these composites were remelted and stirred again at 973K, that is about 50K higher than the liquidus temperature. No changes in microstructures and in X-ray diffraction patterns were detected as such tendency as shown in Fig.5. So, for the composites prepared by compocasting process, good incorporation and good bonding of whisker were obtained.

Then, to clarify the progress conditions of the reaction between aluminum and SiC whisker, they were examined by heating pellets which were compacted with aluminum powder and SiC whisker as described in the section of experimental procedure. X-ray diffraction patterns of composite pellets heated at different temperatures for 60 minutes are shown in Fig.6. At 973K, only both materials, aluminum and SiC, were detected, but at higher temperature than this, silicon and aluminum carbide were also found out. These intensity increased with heating temperature.
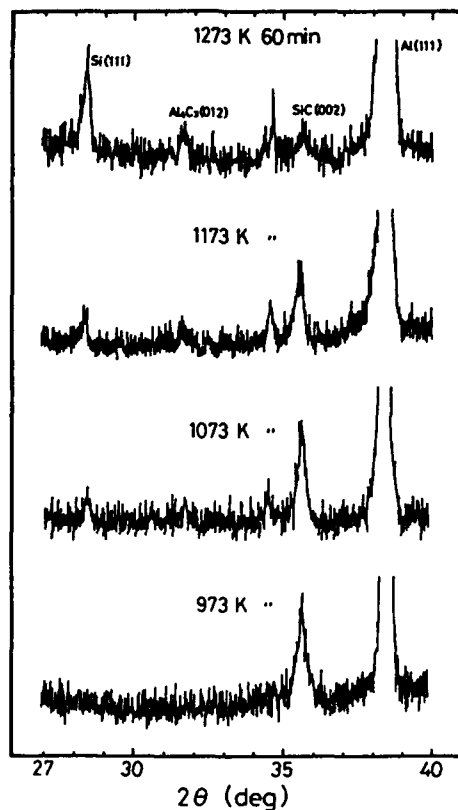
Fig. 6 X-ray diffraction patterns of composite pellets heated at different temperatures for 60minutes.

The microstructures of SiC whisker/aluminum composite pellets are shown in Fig. 7. Massive structures as shown in Fig.7(a) are aluminum powders and other fine fibrous structures are SiC whisker. The reaction products were not observed as hot pressed state. But, as shown in Fig.7(b), the morphology of whisker changed remarkably after heating at 1273K for 60 minutes.
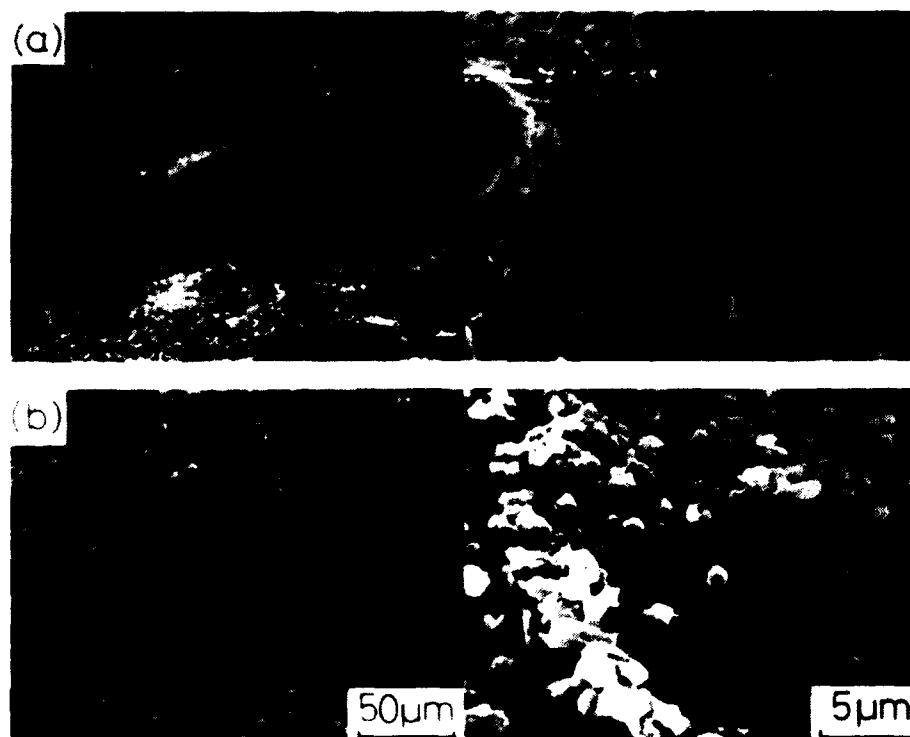
**Fig. 7 Microstructures of SiCw/Al pellets.   (a) as hot pressed.
(b) heated at 1273K for 60 minutes.**

Effects of heating temperature and heating time on the progress conditions of the reaction are denoted in Fig. 8. At 973K, no reaction occurred after 60 minutes, but, at 1073K, it started after 6 minutes and progressed with the heating time. The amounts of reaction products increased within a short time with increase in the heating temperature.

The microstructures of composite pellets heated at different temperatures are shown in Fig.9. Reaction products, silicon, formed in aluminum matrices at each temperature. These above-mentioned results suggest that the reaction between aluminum and SiC whisker starts above 973K within 60 minutes and progresses fast with increase in the heating temperature. This means that silicon decomposed from SiC by the reaction between SiC whisker and aluminum powder penetrated into aluminum melt and insoluble silicon crystallized as a free silicon. Consequently, these microstructures are similar to them of Al-Si eutectic.

CONCLUSIONS

In this paper, incorporation of SiC whisker into Al-Cu alloy slurry by compocasting process is carried out. Progress conditions of the reaction between aluminum alloy and SiC whisker are made clarified by the heating of pellets compacted with aluminum powder and SiC whisker.

To get good mixing of SiC whisker into Al-Cu alloy slurry, the size of primary solid crystals in the alloy slurry should be controlled so adequately as to incorporate easily the balls of whisker into

the alloy slurry, because the whisker forms balls before mixing with alloy slurry. Aluminum and SiC whisker do not react during fabrication of composites by compocasting process, for the reaction temperature and the reaction start time of both materials are higher and later than the fabrication temperature and its time.
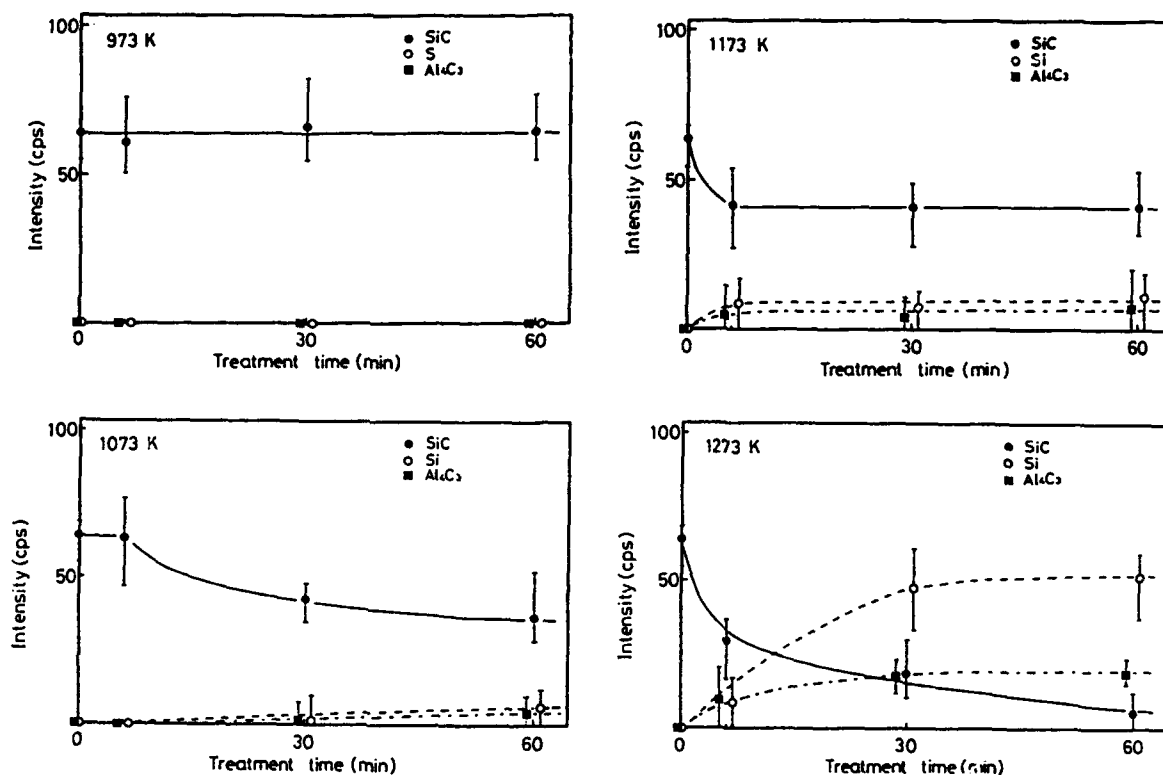
Fig. 8 Effects of heat treatment time on X-ray diffraction intensity of products formed by the reaction between aluminum and SiC whisker.
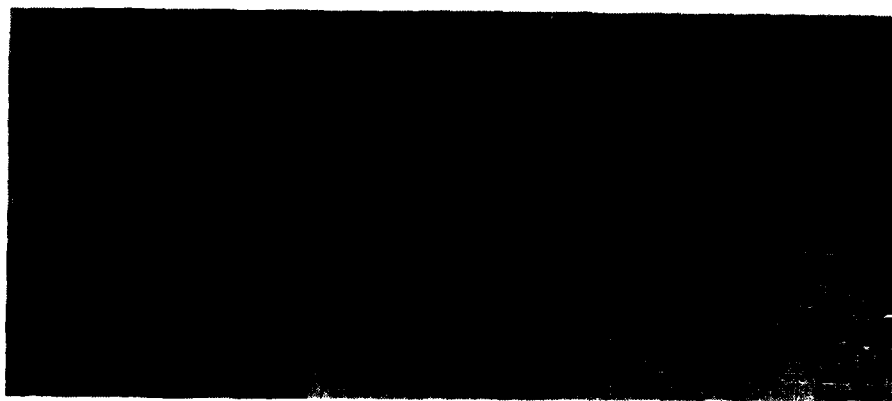
Fig. 9 Microstructures of SiCw/Al pellet heated at different temperatures for 60minutes. (a) 1273K, (b) 1173K, (c) 1073K.

REFERENCES

1. Spencer, D.B., Mehrabian, R., and Flemings, M.C., 1972."Rheological Behavior of Sn-15%Pb in the Crystallization Range." Metallurgical Transactions, 3:1925-1932.

2. Flemings, M.C. and Mehrabian, R, 1973. "Casting Semi-Solid Metals. " Transactions of the American Foundry Society, 81:81-88.

3. Mehrabian, R., Reik, R.G.,and Flemings, M.C.,1974."Preparation and Casting of Metal-Particulate Non-Metal Composites." Metallurgical Transactions, 5:1899-1905.

4. Mehrabian, R., and Sato, A., and Flemings, M.C.,1975. "Cast Composites of Aluminum Alloys."Light Metals, II: 177-193.

5. Sato, A., and Mehrabian, R.,1976."Aluminum Matrix Composites: Fabrication and Properties." Metallurgical Transactions, 7B:443-451.

6. Girot, F.A., Albingre, L., Quenisset, J.M., and Naslain, R.,1987."Rheocasting Al Matrix Composites." Journal of Metals, 39:18-21.

7. Girot, F.A., L., Quenisset, J.M., Naslain, R., Coutand, B., and Macke, T.,1987."Mechanical Behavior of Aluminum matrix Composites Reinforced by Short Fibers and Processed by Compocasting." ICCM VI & ECCM 2, 2:2.330-2.339.

8. Miwa, K.,1990."Fabrication of SiCp Reinforced Aluminum Matrix Composites by Compocasting Process."the Journal of the Japan Foundrymen's Society,62:423-428.

9. Miwa, K. and Ohashi, T.,1990. "Preparation of Fine SiC Particle Reinforced Al Alloy Composites by Compocasting Process." Proceedings of the Fifth Japan-U.S. Conference on Composite Materials,pp.355-362.

10. Miwa, K. and Ikeda, T., and Ohashi, T,1992."Fabrication of SiC Whisker Reinforced Aluminum Alloy Matrix Composites by Compocasting Process." Proceedings of the Second International Conference on the Processing of Semi-Solid Alloys and Composites,pp.398-405.

The Concept and Fabrication of Secondarily Formable Continuous Fiber Reinforced Metals

HIROSHI ASANUMA, MITSUJI HIROHASHI, TAKASHI KIKUCHI AND HIDEYA KITAGAWA

ABSTRACT

As an example of the secondarily formable continuous fiber reinforced metals, stainless steel fiber reinforced aluminum composites with several types of fiber-matrix interfacial layers are fabricated with using zinc, copper and Al-12mass%Si alloy inserts. The best hot pressing conditions for them were common in the sense that temperature is just above the eutectic temperature, pressure is as low as 5 to 11MPa and time is as short as 30 to 60s. The fiber-matrix interfacial shear strength of each type of the composites remarkably reduces with increasing test temperature above the each eutectic temperature. Secondary forming (bending) of the composite without fiber breakage becomes possible by taking advantage of the loose state of the interfacial layer. The once remarkably decreased interfacial shear strength or the composite tensile strength can be increased by the mutual diffusion between the interfacial layer and the matrix and the composite becomes sufficiently strengthened even at high temperatures.

INTRODUCTION

Lots of advanced materials have been developed. But most of them have such problems as hard workability and high cost. Continuous fiber reinforced metal is also regarded as one of them. Under the situation, one of the authors proposed the concept of secondarily formable continuous fiber reinforced metals [1].

The concept can be briefly explained using Figure 1. The composite has fiber-matrix interfacial layer, which becomes very loose at a temperature far below melting point of the matrix. Taking advantage of the loose state, secondary forming of the composite becomes possible without fiber breakage. After forming, the composite can be strengthened by mutual diffusion between the interfacial layer and the matrix.

In the studies concerning secondary forming of continuous fiber reinforced metals, the matrices were wholly softened [2,3], and such a composite as shown above could not be found.

In the previous study, the composite fabrication method to efficiently introduce the interfacial layer was developed, where stainless steel fiber reinforced aluminum and Zn-Al alloy interfacial layer were selected as an example, as shown in Figure 2. In this study, several types of the interfacial layers are produced and properties of the composites are

Hiroshi Asanuma, Mitsuji Hirohashi, Takashi Kikuchi and Hideya Kitagawa, Dept. of Mechanical Engineering, Faculty of Engineering, Chiba University, 1-33, Yayoi-cho, Inage-ku, Chiba City 263, Japan
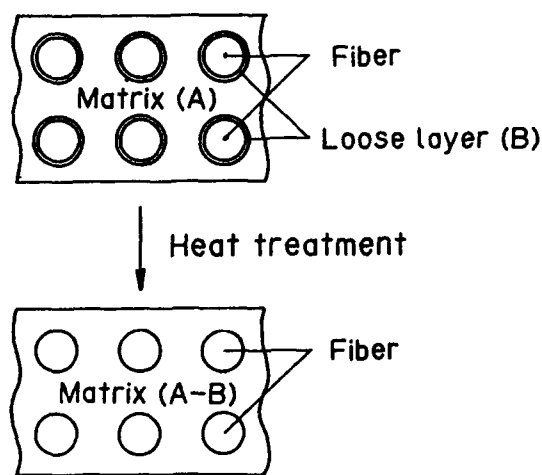
Figure 1. The concept of secondarily formable continuous fiber reinforced metals.
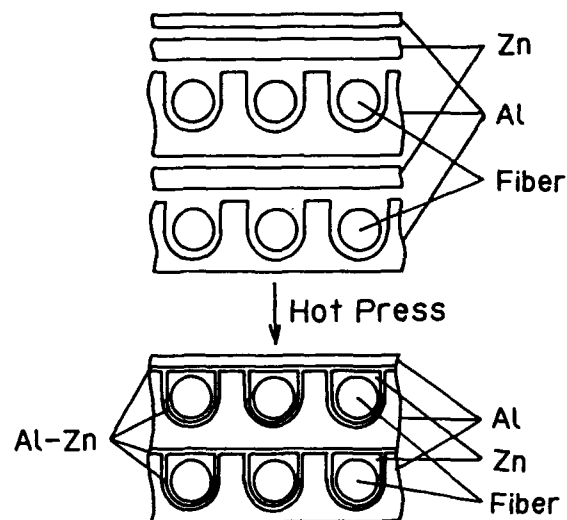
Figure 2. A brief fabrication method of the type of composite.

Table 1. Materials to form the interfacial layer and their supplied forms.

Type of composite	Candidate for fiber-matrix interfacial layer		
	Material	Supplied form	Thickness/μm
①	Zinc	Foil	50
②	Zinc	Arc-sprayed with N_2	~50
③	Zinc	Arc-sprayed with air	~50
④	Copper	Foil	20
⑤	Al-12mass%Si	Plasma sprayed with Ar+He	~50

investigated for the same composite system to increase the reality of the concept.

EXPERIMENTAL

MATERIALS

Stainless steel fiber of which average diameter and tensile strength were 0.095mm and 2.8GPa, respectively, and pure aluminum plates (A1050) of 0.2-2.0mm thickness were used. Materials to form the interfacial layer and their supplied forms are summarized in Table 1.

FABRICATION OF COMPOSITES

First of all, the aluminum plates were cut into piece (30mm×60mm), annealed at 623K for 1.8ks in vacuum, and then, the surfaces for bonding were roughened with abrasive paper. Next, U-type grooves of which diameter (0.14mm) was larger than that of the fiber (0.095mm) were made on the pieces of the plates. Then, the foils were inserted between the bonding surfaces or the metals were sprayed onto the bonding surfaces and inside the grooves as shown in Figure 3. The piles were hot pressed in the air. Actually, four types of composites as shown in Figure 4 were fabricated.
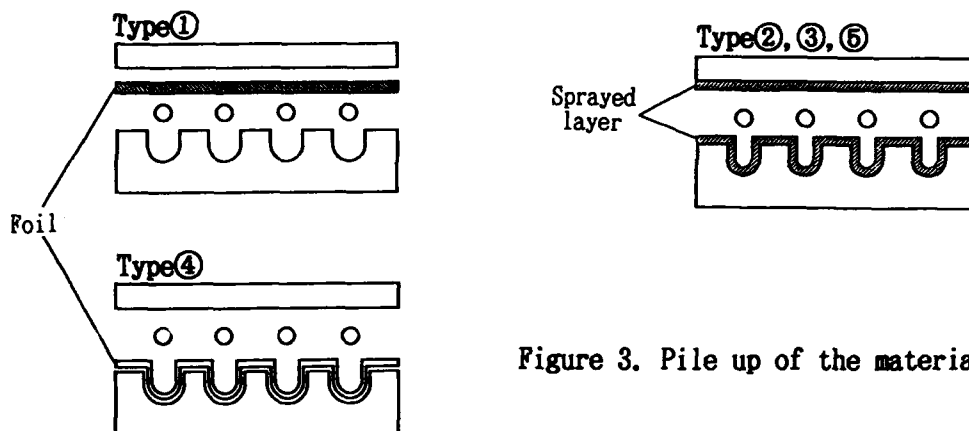
Figure 3. Pile up of the materials.
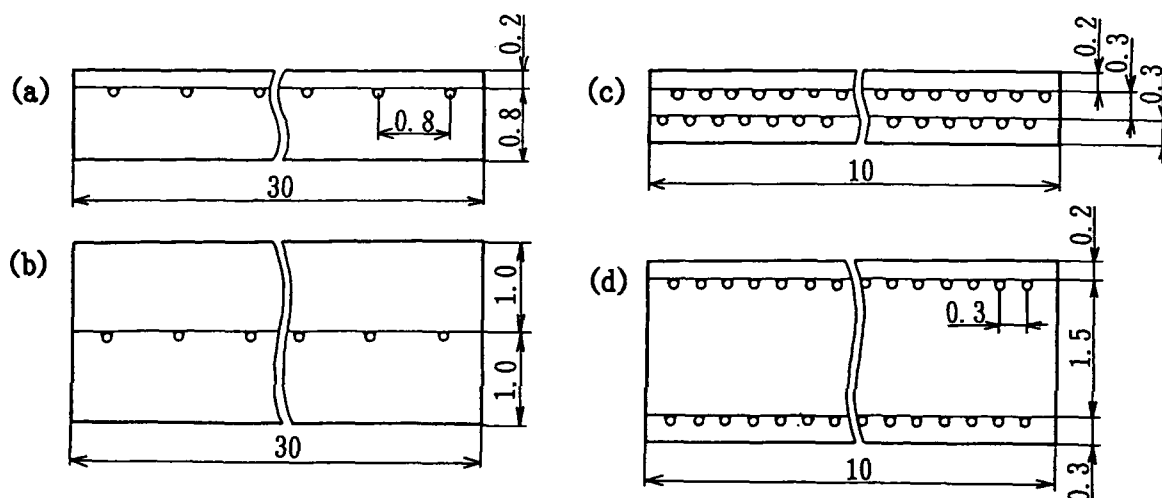
Figure 4. Cross sections of composites used for (a)fiber pull-out test, (b)interlaminar shear test, (c)tensile test and (d)bending test.

FIBER PULL-OUT TEST

The specimen shown in Figure 5 was taken form the type of composite shown in Fig.4(a). The embedded end of the mostly bared out fiber was pulled out at elevated temperatures under constant crosshead speed (0.017mm/s). The fiber-matrix interfacial shear stress, i.e., the maximum pulling out load just when the fiber sliding against the matrix began divided by the sheared fiber surface area of the embedded portion, was calculated.

INTERLAMINAR SHEAR TEST

The specimen shown in Figure 6 was cut from the type of composite shown in Fig.4(b). The specimen ends were pulled and the adhered portion between the notches were sheared apart at room temperature under constant velocity (0.017mm/s), of which maximum load was divided by the sheared area to obtain interlaminar shear strength.

COMPOSITE TENSILE TEST

The specimen shown in Figure 7 was taken from the type of composite shown in Fig.4(c) and was tensile tested at elevated temperatures under constant crosshead speed (0.017mm/s).
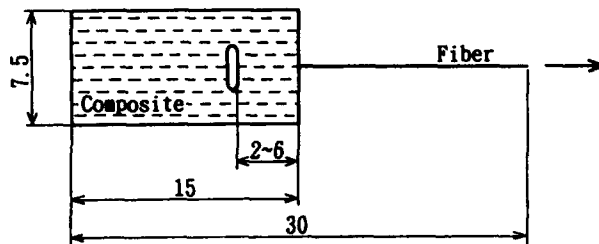
Figure 5. The specimen used for
fiber pull-out test.
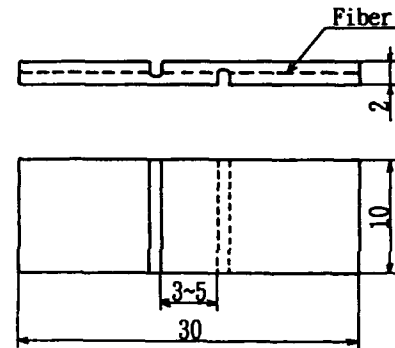
Figure 6. The specimen used for
interlaminar shear test.
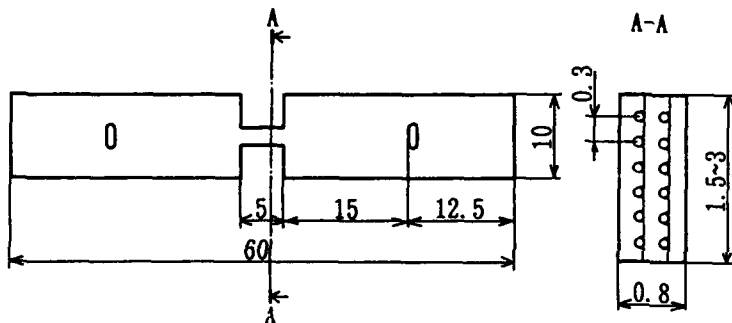
Figure 7. The specimen used for tensile test.
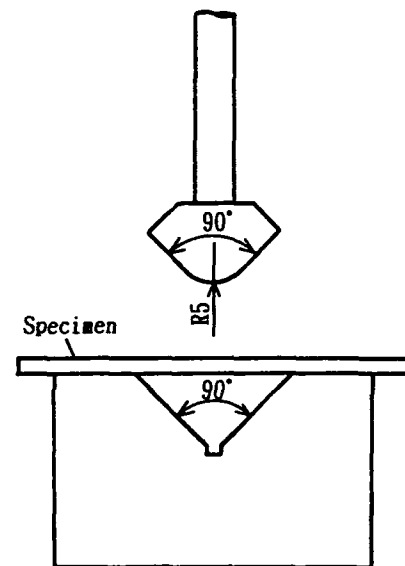
Figure 8. Bending set-up.

BENDING TEST

The composite shown in Fig.4(d) was cut into pieces (5mmx50mm) to be bent with the apparatus shown in Figure 8. The specimen was put on the V-block, heated up to test temperature, and then, it was bent with the punch moving down at constant velocity (0.083mm/s).

RESULTS AND DISCUSSION

HOT PRESSING CONDITION

When the composites, type 1 to 5 shown in Table 1 and Fig.3, were hot pressed under the conditions given in Table 2, formation of interface layers became possible as shown in Fig.9. The hot pressing temperature is 18K above the eutectic temperature of Zn-Al alloy (655K) in the case of type 1 to 3, 7K above that of Al-Cu alloy (821K) in the case of type 4 and 3K above that of Al-Si alloy (850K) in the case of type 5. The conditions are common in the sense that temperature is just above the eutectic temperature, pressure is as low as 5 to 11MPa and time is as short as 30 to 60s.

Type② Type④ Type⑤

50μm 50μm 50μm
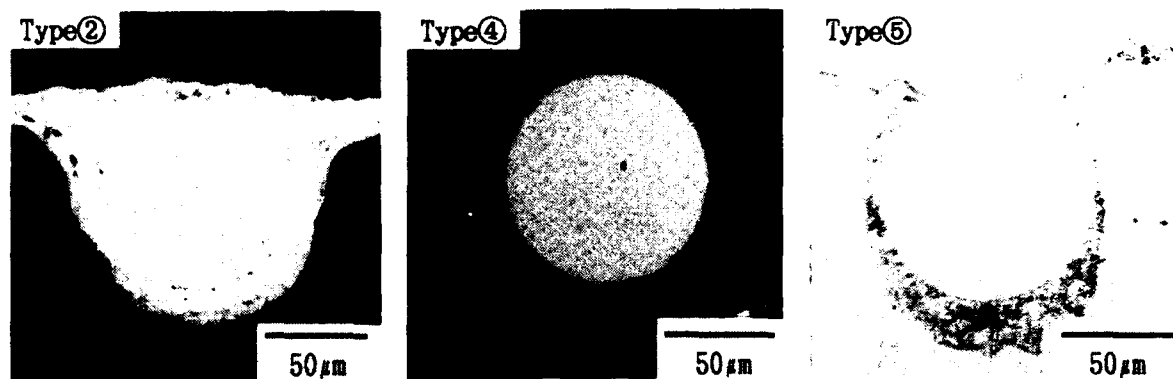
Figure 9. Cross sections of the composites.
Type 2 and 4: SEM micrographs(composition images).
Type 5: Optical micrograph.

Table 2. Successful hot pressing condition for each type of the composites.

Type of	Hot pressing condition		
composite	Temp./K	Pressure/MPa	Time/s
①	673	11	60
②	673	11	60
③	673	11	60
④	828	5	30
⑤	853	11	30

Table 3. Interlaminar shear strength of the composites as hot pressed and after heat treatment are summarized.

Type of	Interlaminar shear strength/MPa	
composite	As hot pressed	After heat treatment
①	3.5	4.6 (673K×3.3ks)
②	6.6	7.9 (703K×3.3ks)
③	8.8	9.4 (753K×3.3ks)
④	13.0	—
⑤	17.8	20.2 (863K×1.2ks)

In Table 3, interlaminar shear strength of the composites are summarized. In the case of zinc (type 1 to 3), interlaminar shear strengths are lower than those of copper and silicon mostly because hot pressing temperature is much lower . As shown in the same table, the interlaminar shear strength can be improved by heat treatment even in the case of zinc (type 1 to 3), which is supposed to be still increased by further investigation of conditions.

FIBER-MATRIX INTERFACIAL SHEAR STRESS

In Figure 10, temperature dependence of the fiber-matrix interfacial shear stress is shown for each type of the composites. In every case, with increasing test temperature, the interfacial shear stress remarkably reduces and approaches zero above each eutectic temperature.

The difference of the temperature dependence among the type 1,2 and 3 is considered to attribute to the degree of oxidation of zinc layer as shown in Table 4. In the case of type 5, interfacial shear strength reduces not straight down to zero but stepwise, of which reason is the severe reaction between fiber and matrix.

The temperatures where the fiber-matrix interfacial shear strength suddenly reduces are summarized as fiber-matrix interfacial loosing temperatures in Table 5, which are preferable for secondary forming of the composites.
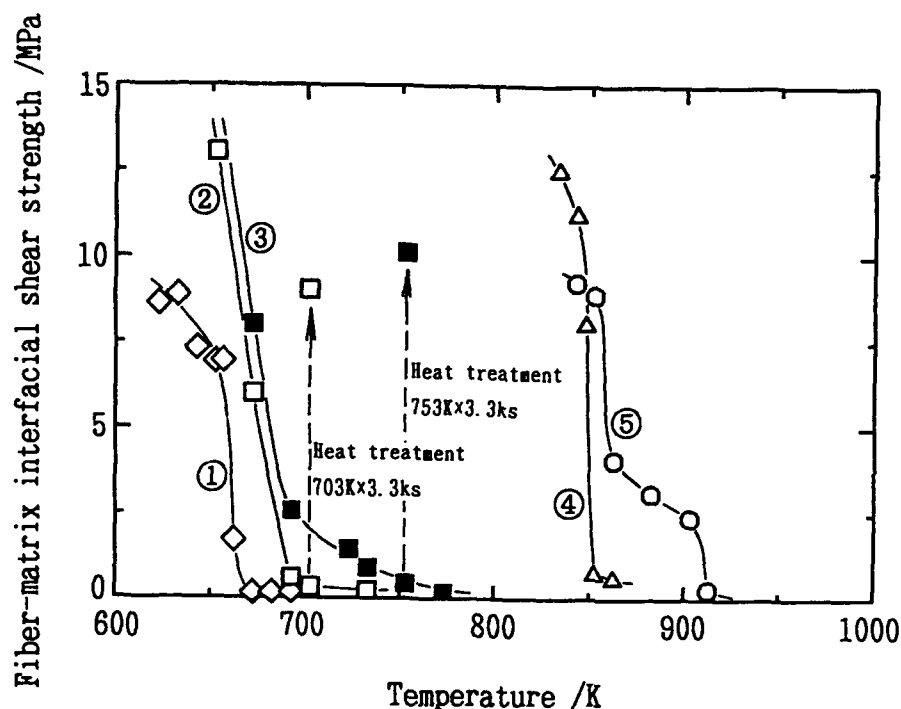
Figure 10. Temperature dependence of the fiber-matrix interfacial
shear strength for each type of the composites.

Table 4. Oxygen content for various
forms of zinc.

Form of zinc	Oxygen content/mass%
Foil	0.015
Wire for arc-spray	0.001
Arc-sprayed with N₂	0.121
Arc-sprayed with air	0.301

Table 5. Fiber-matrix interfacial loosen-
ing temperature for each type of
the composites.

Type of composite	Fiber-matrix interfacial loosening temperature/K
①	673
②	703
③	753
④	853
⑤	863

The other important results are also given for type 2 and 3 in the
same figure, that is, even at the temperatures where the interfacial
shear stresses become almost zero, the stresses can be remarkably in-
creased by heat treatment. This improvement leads to the strengthening
of the composites after secondary forming.

In the case of copper (type 4) and silicon (type 5), adhesion of
matrix plates is stronger than those of zinc (type 1 to 3). But, unfor-
tunately, severe reactions between fiber and matrix are caused. The
stainless steel fiber must be replaced by more stable one such as
SiC(CVD) fiber. So, in this study, composites of the type 2 are used for
further investigations.
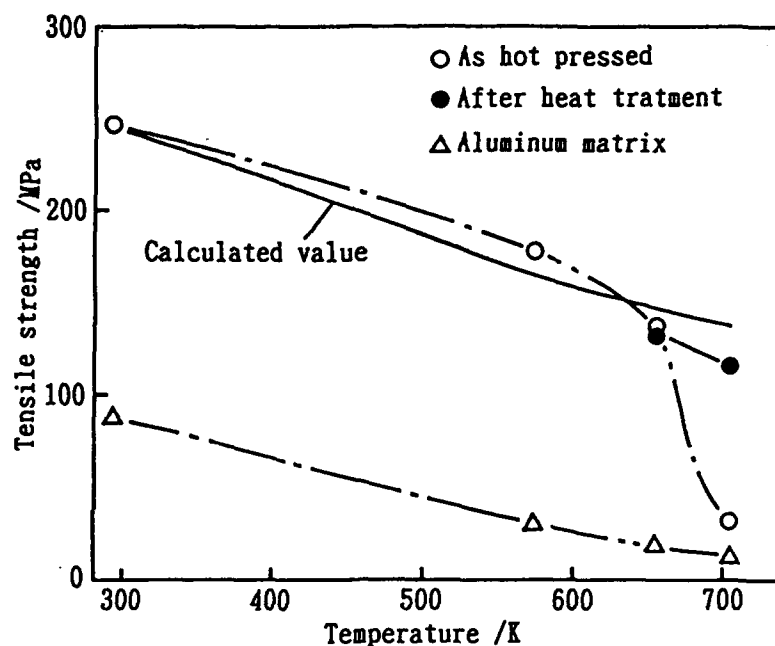
Figure 11. Temperature dependence of the composite
and the matrix tensile strength.

COMPOSITE TENSILE STRENGTH AT ELEVATED TEMPERATURES

Temperature dependence of the type 2 composite and the matrix tensile
strength are given in Figure 11. The composite strength is almost the
same as that of the calculated rule of mixture value up to 653K, but it
remarkably decreases above 653K down close to that of the matrix at
703K. On the other hand, tensile strength of the heat treated composite
at 703K is as high as just below the calculated value. Fiber pull-out is
not observed at 653K. But the fibers are completely pulled out at 703K.
And even at this temperature, the fiber pull-out again disappears after
heat treatment.

SECONDARY FORMING

In Figure 12, the punch load-stroke diagrams during the composite
bending at high temperatures are shown. In Fig.12(a) and (b), results of
the as hot pressed composites bent at 653K and 703K, respectively, are
shown. And in Fig.12(c) and (d), results of the composite after heat
treatment and the matrix pure aluminum plate for comparison, both bent
at 703K, are shown, respectively. The sudden reductions of the punch
load observed on the diagrams proved to correspond with the fiber break-
age and buckling by observing the composite longitudinal sections, i.e.,
the fibers of the outer(tensile) side of bending were fractured apart
and those of inner(compressive) side were buckled. In Figure 13, gener-
al appearances of those bent composites are shown.

According to Fig. 12(a), the punch load increased at the beginning of
bending is remarkably reduced by fiber breakage and buckling, where the
radius of the inner curvature of the bent composite is far smaller than
that of the punch and the bent composite is cracked as shown in
Fig.13(a). Contrary to this, according to Fig.12(b), the punch load
constantly remains at a low level and fiber breakage is not observed.

Fig.13(b) shows that the composite can be successfully bent at 703K along the curvature of the punch. These results mean that the composite is sufficiently strengthened at 653K but is remarkably weakened at higher temperatures such as 703K. At the ends of the successfully bent composite, fibers of the outer sides of bending are withdrawn and those of the inner sides are projected out, which stands for the evidence of fiber sliding against matrix during bending.

In the case of the heat treated composite as shown in Fig.12(c), fiber breakage again appears, which means that the loose fiber-matrix interface at 703K was strengthened by heat treatment at 703K.
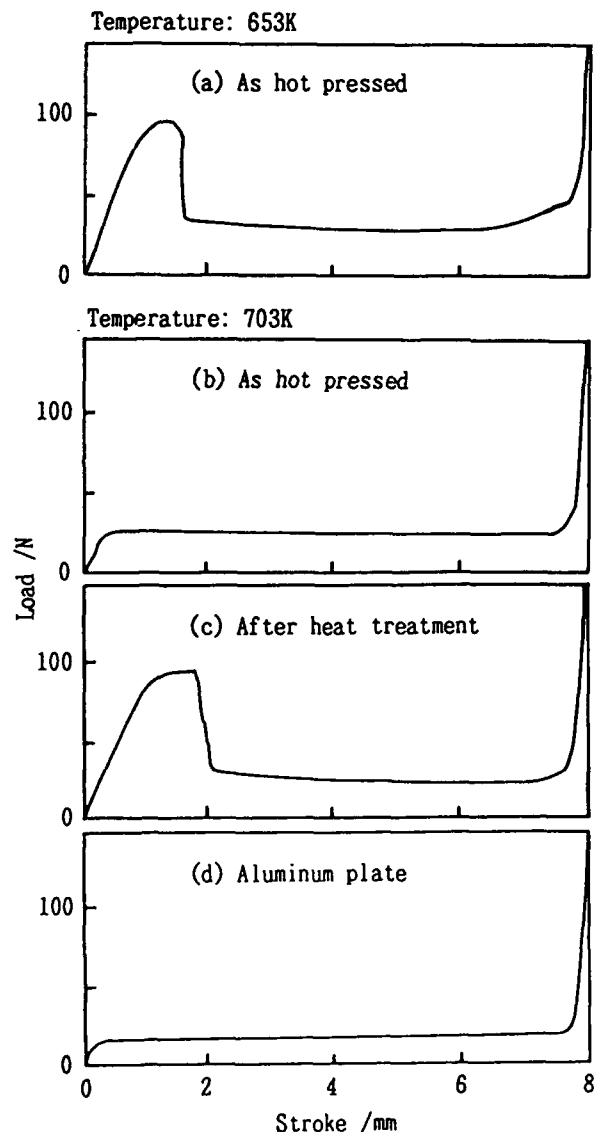
Figure 12. The punch load-stroke diagrams of the composite bending.

Figure 13. General appearances of the bent composites. Tested at (a)653K, (b)703K and (c)heat treated and tested at 703K.

CONCLUSIONS

As an example of the secondarily formable continuous fiber reinforced metals, stainless steel fiber reinforced aluminum composites with several types of fiber-matrix interfacial layers were fabricated. The important conclusions obtained are as follows.

(1)Methods to easily fabricate the type of aluminum matrix composite were developed with using zinc, copper or Al-12mass%Si alloy inserts. The best hot pressing conditions for them were common in the sense that temperature was just above the eutectic temperature, pressure was as low as 5 to 11MPa and time was as short as 30 to 60s.

(2)In the case of using zinc insert, adhesion strength of matrix plates were not so high as those in the case of using copper or Al-12mass%Si alloy insert mostly because the hot pressing temperature was much lower. But the adhesion strength was supposed to be increased by further investigation of heat treatment condition.

(3)The fiber-matrix interfacial shear strength of each type of the composites remarkably reduced and approached zero with increasing test temperature above the each eutectic temperature. The fiber-matrix interfacial loosening temperatures are preferable for secondary forming of the composites.

(4)Further investigation, that is, heat treatment, tensile test and secondary forming were undertaken only for the composite with zinc interfacial layer because severe reaction between fiber and matrix was caused in the case of copper and Al-12mass%Si alloy. As the result, secondary forming (bending) of the composite without fiber breakage became possible by taking advantage of the loose state of the interfacial layer at 703K.

(5)The once remarkably decreased interfacial shear stress or the composite tensile strength could be increased by the mutual diffusion between the interfacial layer and the matrix caused at 703K and the composite became sufficiently strengthened even at high temperatures such as 703K.

ACKNOWLEDGEMENT

REFERENCES

1. H.Asanuma, M.Hirohashi, M.Kase and T.Kikuchi: Bending of stainless steel fiber/aluminum composite plate by softening Zn-Al alloy phase formed around fibers and its strengthening, Journal of Japan Institute of Light Metals, 40, 7(1991), 527.
2. J.L.Christian: Fabrication - Methods and Evaluation - of Boron/Aluminum Composites, Proceedings of the 1st International Conference on Composite Materials, 2(1975), 706.
3. H.Nishimura, T.Itoh, H.Yamamoto and S.Wakayama: Bending of multiple layers Fiber Reinforced Metal, Journal of Japan Institute of Light Metals, 39, 11(1989), 843.

Influence of the Thermally Induced Plasticity and Residual Stresses on the Deformation of SiC/Al Composites

N. SHI AND R. J. ARSENAULT

ABSTRACT

The Finite Element Method (FEM) was employed to investigate the matrix plastic flow in a whisker reinforced SiC/Al composite under external tensile load. It was found that the plastic zone induced by the plastic relaxation of thermal stresses expands under the external tensile load. The overall matrix plastic flow was characterized by the expansion and interconnection of the plastic zones around whiskers. This process can be divided into several characteristic stages, and related to the global stress-strain relationship. It was also found that composite asymmetric constitutive response to external tensile and compressive loads as well as the composite asymmetric Bauschinger behavior was due to the thermally induced plasticity and residual stresses.

1 INTRODUCTION

Arsenault *et al.* proposed that a high dislocation density due to the difference in coefficients of thermal expansion (ΔCTE) should account for the strengthening of composites [1]. Miller *et al.* suggested that the strengthening of SiC/Al composites may result from the Orowan mechanism [2]. However, it is still unclear as how the thermally induced plasticity affects the evolution of the matrix plastic flow which is important to the understanding of the composite strengthening.

When SiC/Al composites are subjected to either a tensile or compressive load, their constitutive behavior is distinctly different. It was generally found that the compressive yield strength of these composites was larger than that of the tensile yield strength, while the apparent Young's modulus for compression was smaller than that for tension [3]. If a material is initially plastically deformed in tension, then reverse deformed in compression, a difference in stress is required to initiate plastic deformation in the reverse cycle. Usually, the magnitude of the yield stress in the reverse cycle is less than the flow stress in the forward cycle. This reduction in stress (or the strain necessary to reach the previous level of flow stress) is defined as the Bauschinger Effect. In the case of monolithic Al, the direction of initial deformation (*i.e.*, tensile or compressive) does not have any influence on the Bauschinger Effect. The SiC/Al composites, however, exhibit a remarkable characteristic, *i.e.*, the flow stress drop (or alternatively, the Bauschinger strain) is larger when the composite deforms in a compression-tension sequence than vise versa [3].

In this investigation, FEM modeling was performed on the evolution of matrix plastic flow of a SiC whisker (SiC$_W$) reinforced annealed 6061 Al by monitoring the load-induced

N. Shi and R. J. Arsenault, graduate student and professor, respectively, Metallurgical Materials Laboratory, Department of Materials and Nuclear Engineering, University of Maryland, College Park, MD 20742-2115.

changes of the plastic zone generated by ΔCTE, and then a correlation was determined between the matrix microplastic flow and the global composite tensile stress-strain curve. Based on the knowledge of the evolution of the matrix plasticity, a fundamental quest leading to an understanding of the asymmetric composite constitutive behavior was initiated, especially the asymmetric apparent Young's modulus and the Bauschinger Effect.

2 FEM ANALYSIS

In this investigation, a 2-D plane strain FEM thermo-elasto-plastic analysis was performed, in which the Von Mises yield criteria and the incremental flow rule were employed [4]. The composite was assumed to be a 2-D infinite periodic array of hexagonally distributed SiC whiskers of 20V% embedded in the matrix (or the staggered array), as shown in Fig. 1. An aspect ratio of four was selected. This value is a typical average from experimental observations [5, 6]. Due to symmetry conditions, a unit cell, as shown in Fig. 1, may be selected. The details of the boundary conditions along the unit cell boundary were published elsewhere [7].

To account for the thermally generated plasticity due to cooling from the annealing temperature, a temperature change, ΔT, was applied to the FEM unit cell. The materials properties were obtained from Ref. [8, 9]. During modeling, neither thermal gradient nor matrix creep was considered. Due to a large ΔCTE, thermally induced matrix plastic flow from $\Delta T = 480°C$ is likely to spread over the entire matrix. To better understand the evolution of the matrix plasticity, two temperature changes of $\Delta T = 30$ and $480°C$ were employed, respectively.

It has been reported previously that the matrix longitudinal thermal residual stress is compressive at the tip of the whisker, and tensile in the rest of the matrix [10]. Therefore, in the current analysis, the matrix is categorized into two different zones: the initial compressive and tensile zones at the tip of and along the longitudinal sides of the whiskers, respectively. The schematics of this partition is shown in Fig. 1.

3 RESULTS AND DISCUSSIONS

3.1 THE BEHAVIOR OF THE PLASTIC ZONE

Following the temperature change of $\Delta T = 30°C$, longitudinal loading is applied to $\overline{AB}$ (in Fig. 1) incrementally. Fig. 2 shows the behavior of the thermally induced matrix plastic zone in a 20V% composite under external tensile loading. In this diagram, the locations of plastic zone boundary are plotted at different load levels, the label on each line represents the level of the applied traction in MPa, The hatched side of the line represents matrix that is *currently plastically deforming*, and we refer this enclosure as the *plastic zone*. Prior to external loading, the matrix has partially plastically deformed around the whisker due to plastic relaxation of the thermal stresses. When a tensile load is imposed, the shape of the plastic zone changes. It expands along the longitudinal whisker-matrix interface, while unloading from the initial residual compression occurs at the tip of the whisker.

As the applied load increases, plastic zones around two adjacent whiskers attract each other. This is characterized by the bowing-out of the plastic zone boundary shown in Fig. 2 when applied stress reaches 35.5 MPa.

When the external load reaches about 36 MPa, the plastic zone boundaries interconnect along $\overline{BC}$. Upon further load increases (*e.g.* to 44 MPa in Fig. 2), the only part of the matrix behaving elastically is at the tip of the whisker where it is still going through unloading and loading in reverse direction with respect to the compressive longitudinal thermal residual stress. When the internal stresses gradually reach the matrix flow stress,
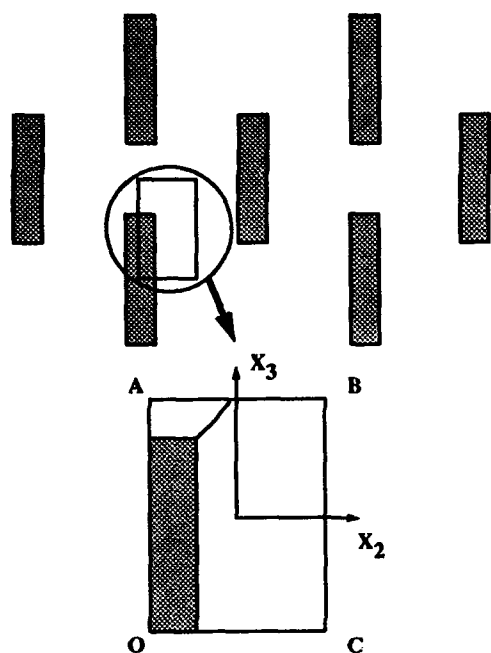
Figure 1. Schematics of an unit cell taken from an infinite hexagonally distributed array. In this unit cell, the boundary between the initial compressive and tensile zones is shown.
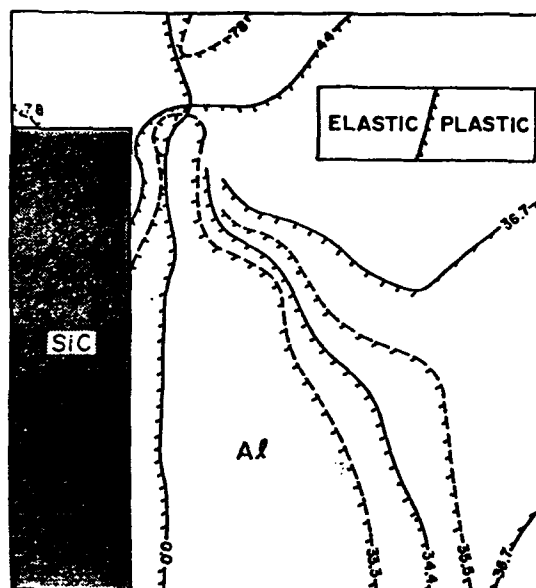
Figure 2. Sequence of the plastic zone expansion in the matrix of a 20V% whisker reinforced SiC-6061 Al composite with a thermal history of $\Delta T = 30°C$. An external load in MPa is applied incrementally.

the plastic zone starts to propagate into the initial compressive zone. The emergence of the load-induced plastic flow in the initial compressive zone then breaks the remaining elastic region into two "elastic pockets" — one immediately next to the matrix-whisker interface at the tip of the whisker, the other some distance away from the corner of the whisker.

To summarize, the entire process of plastic zone expansion can be divided into four stages: (1) plastic zone expansion in the initial tensile zone; (2) plastic zone interconnection along the cell boundary $\overline{BC}$; (3) overcoming the compressive thermal residual stresses at the tip of the whisker; (4) fragmentation of the elastic matrix to form remnant elastic pockets at SiC_W tip surrounded by the matrix plastic flow.

The matrix microplasticity is also correlated to the composite mechanical properties. Fig. 3 shows the initial portion of the stress-strain curve produced by FEM, and how it is related to the plastic zone expansion process. At the start, the stress-strain relationship is approximately linear. However, because of the thermally induced plasticity in the matrix, the thermally induced plastic zone expands even within this approximately linear region as shown in Fig. 2. As the plastic zones attract to each other and interconnect, the stress-strain curve goes quickly out of the approximate linearity. Once the entire initial tensile zone is plastically deforming, the slope of the stress-strain curve approaches a constant again (Fig. 3). This is due to the fact that the rate of propagation of the plastic zone boundary is greatly reduced because of the ongoing process of overcoming the compressive residual stress in the initial compressive zone.

As the load further increases, onset of the composite global yielding is characterized by the formation of the remnant elastic pockets. At .2% yield stress, the entire matrix is plastically deforming except within the elastic pocket away from the corner of the whisker.
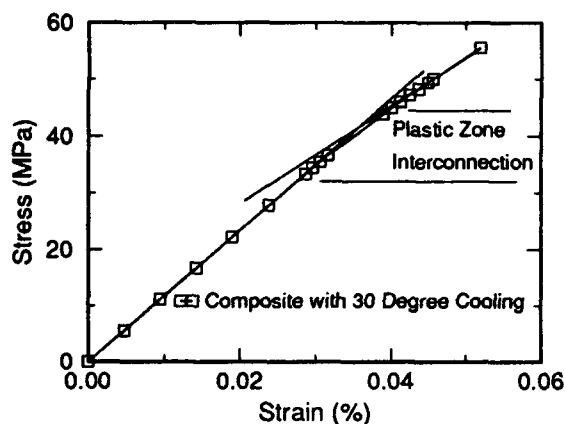
Figure 3. Initial response of a 20V% composite with $\Delta T = 30°$C, where the deviation from the approximate linearity is characterized by the plastic zone interconnection in the initial tensile zone.
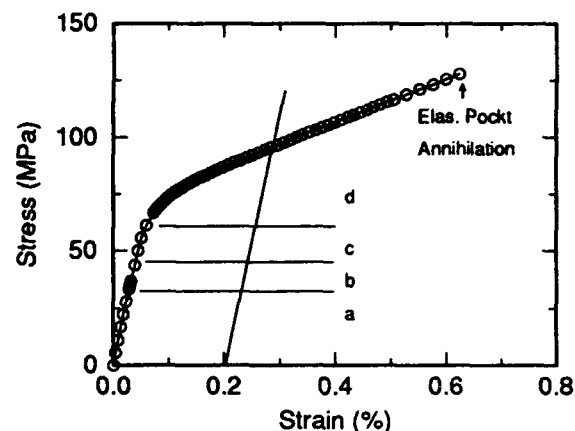
Figure 4. Four stages of the plastic zone expansion and their chara cteristics reflected on the tensile behavior of a 20V% SiC_w/Al composites with a thermal history of $\Delta T = 30°$C, a: expansion of the initial tensile plastic zone; b: interconnection of the initial tensile plastic zones; c: deformation-induced plastic flow in the initial compressive plastic zone; d: fragmentation of the the remnant elastic matrix.
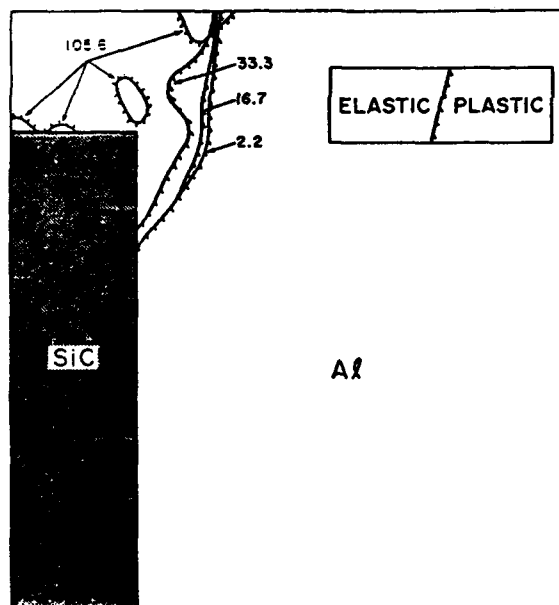
Figure 5. Process of the plastic zone expansion and interconnection in the matrix of a 20V% SiC_w/Al composites with a thermal history of $\Delta T = 480°$C. The applied stress(MPa) is applied incrementally.
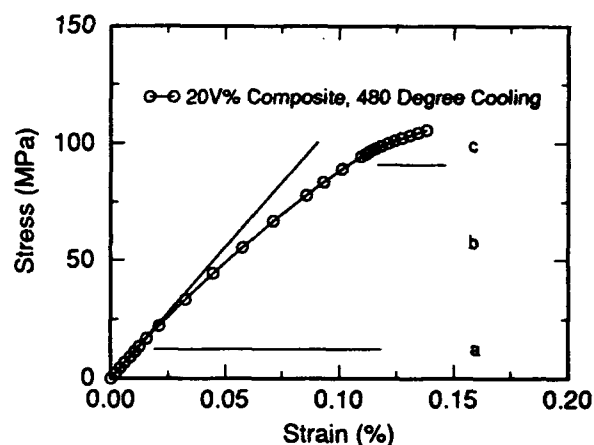
Figure 6. Different stages of plastic deformation and the tensile behavior of a 20V% SiC_w/Al composites with a thermal history of $\Delta T = 480°$C, a: steady plastic zone size; b: consumption of elastic matrix at the tip of the whisker by incremental plastic flow; c: fragmentation of the remnant elastic matrix.

446
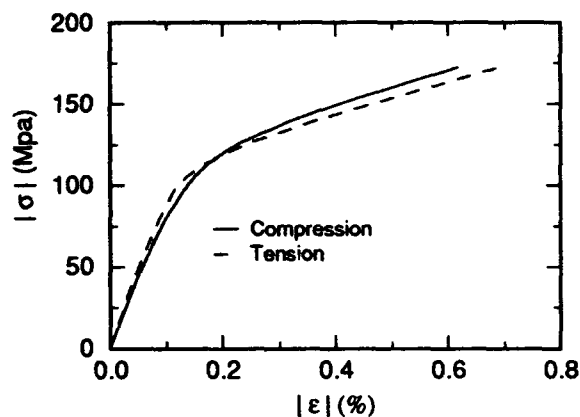
Figure 7. Stress-strain curves under tension and compression predicted by the FEM, where the apparent young's modulus of the composite is higher when it is uder tension, whereas the yield strength is greater when it is under compression.
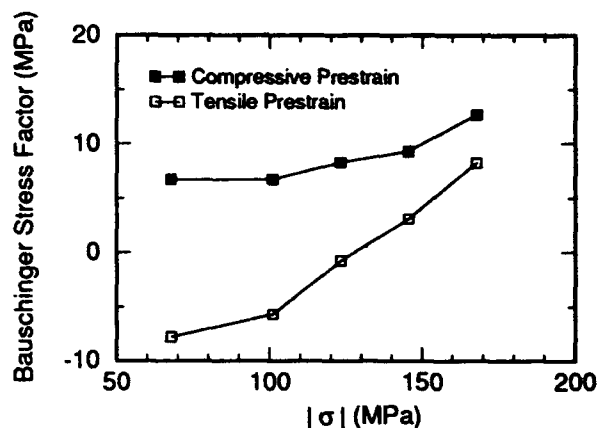
Figure 8.   FEM prediction of the Bauschinger stress factor, σ_b, as a function of the applied forward strain, where σ_b is larger if the forward load is in compression, and the initial value of σ_b is negative.

As will be seen during the remainder of this study, the final location of the remaining elastic zone is a strong function of reinforcement concentration. The correlation of each stage of the plastic zone expansion with the stress-strain relationship is shown in Fig. 4.

For $\Delta T = 480°C$, which is a more realistic temperature change when cooling from the annealing temperature, the evolution of the matrix plasticity is shown in Fig. 5, where the same convention, as employed in Fig. 2, is used. Due to a larger ΔT, the thermally induced plastic flow has spread over the entire matrix prior to any external loading. As compared with the cooling of $\Delta T = 30°C$, the development of matrix plasticity due to a tensile load is the same in characteristics except that the first two stages of the plastic zone expansion occur during "thermal loading", which leads to that the changes of the matrix plasticity is concentrated at the tip of the whiskers.

Fig. 6 shows the predicted stress-strain curve of the composite along with the corresponding characteristics of the plastic zone. Comparing with Fig. 3, the "proportional limit" is considerably smaller, the difference comes from the fact that, for $\Delta T = 480°C$, the matrix is experiencing a different stage of plastic zone expansion. When the initial loading is applied within the approximate proportional limit, the matrix is unloading in the initial compressive zone, where the boundary of the plastic zone is insensitive to the external deformation. However, it takes significantly more additional work to spread the deformation-induced plasticity to reach the stage of fragmentation of remnant elastic matrix. This is due to the increase of compressive residual stress and the amount of thermally induced work hardening when ΔT is larger, *i.e.*, the thermally induced dislocations due to ΔCTE.

3.2 COMPOSITE ASYMMETRIC CONSTITUTIVE BEHAVIOR AND THE THERMALLY INDUCED PLASTIC FLOW

Fig. 7 displays the uniaxial stress-strain curves generated by FEM when a 20V% composite is under tensile and compressive loads, respectively. Fig. 8 shows the Bauschinger stress factor, σ_b, as a function of the applied forward strain. Here, the Bauschinger stress factor is defined as $\sigma_b = \sigma^F - \sigma^R$, where σ^F and σ^R represent the forward and reverse flow stresses, respectively. In this figure, σ_b is consistently larger when forward applied stress is in compression. These results match the observations by Arsenault *et al.* [3].
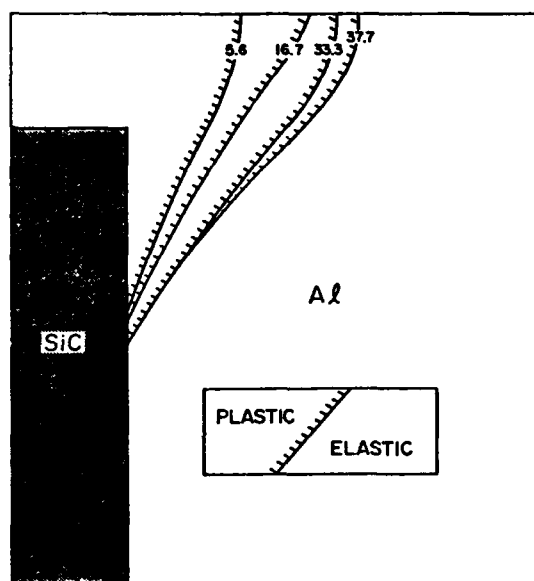
Figure 9.   Matrix plastic zone expansion process of a 20V% SiC$_w$/Al composite under compressive loading condition with a thermal history of $\Delta T = 480°$C.
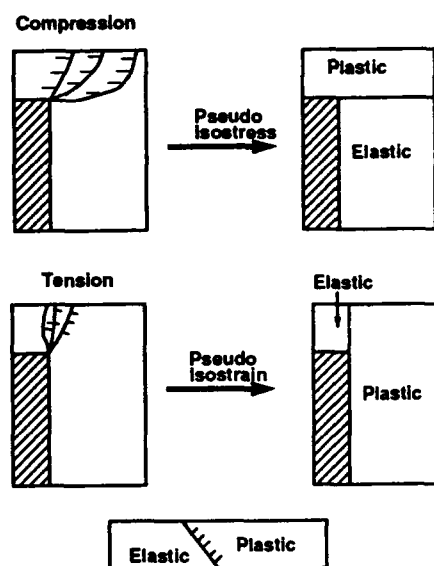
Figure 10.   Schematics of the morphologies of the plastic zone under different loading conditions, where tensile loading will produce a pseudo-isostrain condition and compressive loading will produce a pseudo-isostress condition.

In addition, FEM analysis also predicts that the Bauschinger stress factor is initially negative ($\sigma_b < 0$), which means that there is an initial reverse strain hardening rather than normally observed reverse strain softening.

3.2.1 Asymmetric Apparent Young's Modulus

It is commonly believed that the asymmetric composite apparent Young's modulus is related to the asymmetric development of the shear stresses at the interface near the tip of the whisker [11, 12]. From FEM modeling, Levy et al. found that the interfacial thermal residual shear stress near the end of the whisker increases with compressive loading, and decreases with tensile loading [12]. Therefore, they argued that micro-plastic flow induced by the asymmetric development of the shear stress near the longitudinal interface produces early micro-yielding during compressive loading, so that the apparent Young's modulus is lower. However, this theory cannot explain how the asymmetric development of matrix shear stress leads to a higher compressive composite yield strength as shown in Fig. 7.

On initial tensile deformation, the development of the interfacial shear stresses induces unloading in the matrix. However, from the evolution of the matrix plastic flow shown in Fig. 5, the effect of such unloading is restricted to the immediate proximity along the longitudinal interface near the tip of the whisker, and its influence remains at small applied load, e.g., at a load as small as 2.2 MPa, the plastic zone starts to expand toward the tip of the whisker.

Fig. 9 shows the characteristics of the plastic zone under a compressive load. Comparing the morphologies of the plastic zone under tensile and compressive loading, respectively, as shown in Figs. 5 and 10, the unit cell may be divided into three distinct regions:

elastic, plastic deforming regions and the whisker. Fig. 10 display an idealization based on this partition. If we consider the two stiffer regions to be an imaginary phase, we may define the morphology of the initial development of matrix plastic zone under tension and compression as pseudo-isostrain and pseudo-isostress conditions, respectively, in reference to the isostrain and isostress loading.

For isostrain condition:

$$E_c = E_1(1 - V_2) + E_2 V_2. \tag{1}$$

For isostress condition:

$$E_c = \frac{E_1 E_2}{(1 - V_2)E_2 + E_1 V_2}. \tag{2}$$

where E_i ($i = 1, 2$) and E_c are the Young's moduli of constituent phase i and the composite, respectively. V_i is the volume fraction of constituent phase i.

For the pseudo-isostrain model (Fig. 10), the stiffness can be evaluated by substituting Eq. 1 with the equations shown below:

$$E_1 = \frac{E_w E_m}{V_p^\sigma E_w + (1 - V_p^\sigma)E_m}; \tag{3}$$

$$E_2 = E_{mp}, \tag{4}$$

where V_p^σ corresponds to the volume fraction of the plastic zone in the pseudo-isostress model; E_m and E_w are the Young's moduli of the matrix and whisker, respectively; E_{mp} is the matrix work hardening rate. Substitute Eqs. 3 and 4 into Eq. 1 and consider $V_2 = V_p^\epsilon$ where V_p^ϵ corresponds to the volume fraction of the plastic zone in the pseudo-isostrain model, the modulus, E_c^ϵ, of the pseudo-isostrain model can be obtained:

$$E_c^\epsilon = \frac{(1 - V_p^\epsilon)E_w E_m}{V_p^\sigma E_w + (1 - V_p^\sigma)E_m} + E_{mp}V_p^\epsilon \tag{5}$$

For the pseudo-isostress model (Fig. 10), $E_1 = (1 - V_p^\epsilon)E_w + V_p^\epsilon E_m$, $E_2 = E_{mp}$, and $V_2 = V_p^\sigma$. Substitute E_1 and E_2 into Eq. 2, we obtain:

$$E_c^\sigma = \frac{(1 - V_p^\epsilon)E_w E_{mp} + V_p^\epsilon E_m E_{mp}}{(1 - V_p^\sigma)E_{mp} + (1 - V_p^\epsilon)V_p^\sigma E_w + V_p^\epsilon V_p^\sigma E_m} \tag{6}$$

where E_c^σ is the modulus for the pseudo-isostress condition. Considering material properties: $E_m = 68.3$ GPa; $E_{mp} = 2.08$ GPa; $E_w = 483$ GPa [9], and for a unit cell shown in Fig. 1 which corresponds to a 20V% composite, we obtain $E_c^\sigma = 9.887$ GPa; $E_c^\epsilon = 50.09$ GPa, i.e., $E_c^\epsilon > E_c^\sigma$. The magnitude of the asymmetry of the Young's modulus is exaggerated because, as compared with that of the actual plastic zone shown in Fig. 9, the morphology of the plastic zone shown in Fig. 10 during compression leads to a lower bound for the composite stiffness.

From this result, it can be seen that the asymmetric apparent composite Young's modulus is due to an asymmetric plastic zone expansion which induces isostress or isostrain type of loading. This process continues until the morphology of the plastic zone can no longer be represented by the idealization shown in Fig. 10, that is, when the applied stress is approaching the composite yield stress.

3.2.2 Asymmetric Bauschinger Effect

In explaining the phenomenon of asymmetric Bauschinger stress factor, the "back

stress" model can be modified [13], in which the forward (σ_f^F) and reverse (σ_f^R) flow stresses can be expressed as:

$$|\sigma_f^F| = \sigma_y + \Delta\sigma_b^F + |\Delta\sigma_{fh}| \tag{7}$$

$$|\sigma_f^R| = \sigma_y - \Delta\sigma_b^R + |\Delta\sigma_{fh}| \tag{8}$$

where σ_y is the yield strength; $\Delta\sigma_b^F$ and $\Delta\sigma_b^R$ are the contributions of the back stress during forward and reverse cycle, respectively; $\Delta\sigma_{fh}$ is the plastic friction.

From Eq. 7 and 8, the Bauschinger stress factor can be expressed as: $\sigma_b = |\sigma_f^F| - |\sigma_f^R| = \Delta\sigma_b^F + \Delta\sigma_b^R$. Approximating the back stress as the matrix residual stress, we obtain the following equations:

$$\Delta\sigma_b^F \approx -\frac{\varepsilon^F}{|\varepsilon^F|}\langle\sigma_m^r\rangle; \tag{9}$$

$$\Delta\sigma_b^R \approx -\langle\sigma_m^{ru}\rangle = -C(\varepsilon^F)\frac{\varepsilon^F}{|\varepsilon^F|}\langle\sigma_m^r\rangle, \tag{10}$$

where $\langle\sigma_m^r\rangle$ is the thermal residual stress; $C(\varepsilon^F)$ is a function of forward applied strain, ε^F. $\langle\sigma_m^{ru}\rangle$ represents the changes of residual stress induced by the external deformation. Then the Bauschinger stress factor is

$$\sigma_b \approx -\left[1 + C(\varepsilon^F)\right]\frac{\varepsilon^F}{|\varepsilon^F|}\langle\sigma_m^r\rangle \tag{11}$$

Considering $C(\varepsilon^F) = 1 - k\varepsilon^F + O(\varepsilon^F)$, where $k > 0$, and $O(\varepsilon^F)$ represents the terms with higher order than ε^F. For the first order approximation, $O(\varepsilon^F)$ may be neglected, that is, $C(\varepsilon^F) = 1 - k\varepsilon^F$. Substituting C into Eq. 11, we obtain:

$$\sigma_b \approx (k\varepsilon^F - 2)\frac{\varepsilon^F}{|\varepsilon^F|}\langle\sigma_m^r\rangle \tag{12}$$

Eq. 12 reflects the general trend of the changes predicted by the FEM shown in Fig. 8. For tension-compression loading scheme $(\varepsilon^F > 0)$,

$$\sigma_b \begin{cases} < 0 & \varepsilon^F < \frac{2}{k}; \\ \geq 0 & \varepsilon^F \geq \frac{2}{k}. \end{cases} \tag{13}$$

For compression-tension loading scheme $(\varepsilon^F < 0)$, $\sigma_b > 0$. In both cases, $\frac{d\sigma_b}{d|\varepsilon^F|} = k > 0$.

4 CONCLUSIONS

From the above analysis, the following conclusions can be reached:

(1) The evolution of the matrix plasticity in a whisker reinforced SiC/Al composite is characterized by the expansion and interconnection of the thermally induced plastic zones.

(2) The process of plastic zone expansion can be divided into four different stages. Plastic zone expansion in the initial tensile zone; plastic zone interconnection in the initial compressive zone; overcoming the longitudinal compressive matrix thermal residual stress at the tip of the whisker; and the fragmentation of the remnant elastic matrix into pockets.

(3) The onset of global yielding is characterized by the fragmentation of the remnant elastic matrix at the tip of the whisker, where isolated remnant elastic pockets remain.

(4) The composite asymmetric constitutive behavior, the asymmetric Bauschinger effect and the apparent Young's modulus, can be related to the asymmetric matrix plastic flow due to the thermally induced plasticity and residual stresses.

5 ACKNOWLEDGEMENTS

REFERENCES

1. Arsenault, R. J., and R. M. Fisher, 1983. "Microstructure of Fiber and Particulate SiC in 6061 Al Composites." Scripta metall., 17:67-68.

2. Miller, W. S., and F. J. Humphreys, 1991. "Strengthening Mechanisms in Particulate Metal Matrix Composites." Scripta metall., 25:33-38.

3. Arsenault, R. J., and S. B. Wu, 1987. "The Strength Differential and Bauschinger Effects in SiC-Al Composites." Mater. Sci. Engng., 96:77-88.

4. Snyder, M. D. and K. -J. Bathe, 1981. "A Solution Procedure for Thermo-Elastic-Plastic and Creep Problem." Nucl. Engng. Design, 64:49-80.

5. Arsenault, R. J., 1984. "The Strengthening of Aluminum Alloy 6061 by Fiber and Platelet Silicon Carbide." Mater. Sci. Engng., 64:171-181.

6. Papazian, J. M., and P. N. Adler, 1990. "Tensile Properties of Short Fiber-Reinforced SiC/Al Composites: Part I. Effects of Matrix Precipitates." Metall. Trans., 21A:401-410.

7. Shi, N., B. Wilner, and R. J. Arsenault. "A FEM Study of the Plastic Deformation Process of Whisker Reinforced SiC/Al Composites." Accepted for publication in Acta metall. mater.

8. Mahan, R. L., and J. A. Herzog, 1970. Whisker Technology, New York, NY: J. Wiley-Interscience.

9. ALCOA (Aluminum Company of America), 1967. Aluminum Handbook.

10. Arsenault, R. J., N. Shi, C. R. Feng, and L. Wang, 1991. "Localized Deformation of SiC-Al Composites." Mater. Sci. Engng., A131:55-68.

11. Hamann, R., P. F. Gobin, and R. Fougeres, 1990. "A Study of the Microplasticity of Some Discontinuously Reinforced Metal Matrix Composites." Scripta metall. mater., 24:1789-1794.

12. Levy, A., and J. M. Papazian, 1991. "Elastoplastic Finite Element Analysis of Short-Fiber-Reinforced SiC/Al Composites: Effects of Thermal Treatment." Acta metall. mater., 39(10):2255-2266.

13. Taya, M., K. E. Lulay, K. Wakashima, and D. J. Lloyd, 1990. "Baucshinger Effects in Particulate SiC-6061 Aluminum Composites." Mater. Sci. Engng., A124:103-111.

SESSION 6B

Micromechanics I

A Plasticity Model for the Bond between Matrix and Reinforcement

JAMES V. COX[1] AND LEONARD R. HERRMANN[2]

ABSTRACT

Micromechanical models of reinforced composite systems require constitutive models for the constituent materials and their interaction. Material constitutive models have been the subject of extensive research, however, bond models have been the subject of far less. The type of composite systems of interest in this study are those where the reinforcement is in the form of long filaments, wires or rods.

We initially propose a six degree of freedom plasticity model for describing the interaction between reinforcement and the matrix material. We then make simplifying assumptions to reduce the number of degrees of freedom to three, retaining only the stress components needed to define the interface traction. The corresponding deformation variables are the radial dilation and the two components of shear that occur at the interface. The model uses a yield function *that hardens and softens as a function of a bond "damage measure."* Because friction is an important component of bond behavior, a nonassociative flow rule is used.

Assuming axismmetry near the bar, we further simplify and develop the model retaining only the dilation and relative axial movement (slip) as deformations. These restrictive conditions probably capture the dominant features of bond behavior for many configurations.

The simplified model is rather general and should be of value in the construction of micromechanical models for many reinforced materials and systems. In this paper the model has been calibrated for the particular application of bond between reinforcing steel and concrete. The resulting model requires only knowledge of two fundamental mechanical properties of the matrix material (tensile strength and elastic modulus) and two geometric properties of the reinforcement (diameter and rib spacing).

The application of the model to bond between concrete and steel reinforcement presents a significant challenge since the presence of the ribs on the bars produces a complex mechanical interaction over a relatively thick bond layer; this interaction results in a bond failure that is characterized by local crushing and fracture which occur at much higher stresses than the early breakdown of adhesion. The mechanism that dominates the failure is dependent upon the stress history in the bond layer.

We have used the calibrated model to analyze a variety of different tests. These tests (reported by researchers from Europe, Japan, and the United States) differ significantly in specimen geometry, material properties, and stress histories. In terms of elastic-plastic response, the model successfully explains what had appeared to be widely divergent experimental results. In this paper, we compare the model to a series of tests from Japan and find good agreement. Additional comparisons can be found in [1].

---

[1] Research Structural Engineer, Structures Division – Code L51, Naval Civil Engineering Laboratory, Port Hueneme, CA 93043.

[2] Prof. of Civil Engineering, Department of Civil Engineering, University of California, Davis CA 95616

a) Member-Scale Example: piece of a plane stress beam model with embedded reinforcement.

b) Bar-Scale Example: small cylindrical bond specimen model with bar modeled as a cylinder.

c) Rib-Scale Example: piece of a model where the geometry of the ribs is explicitly modeled.
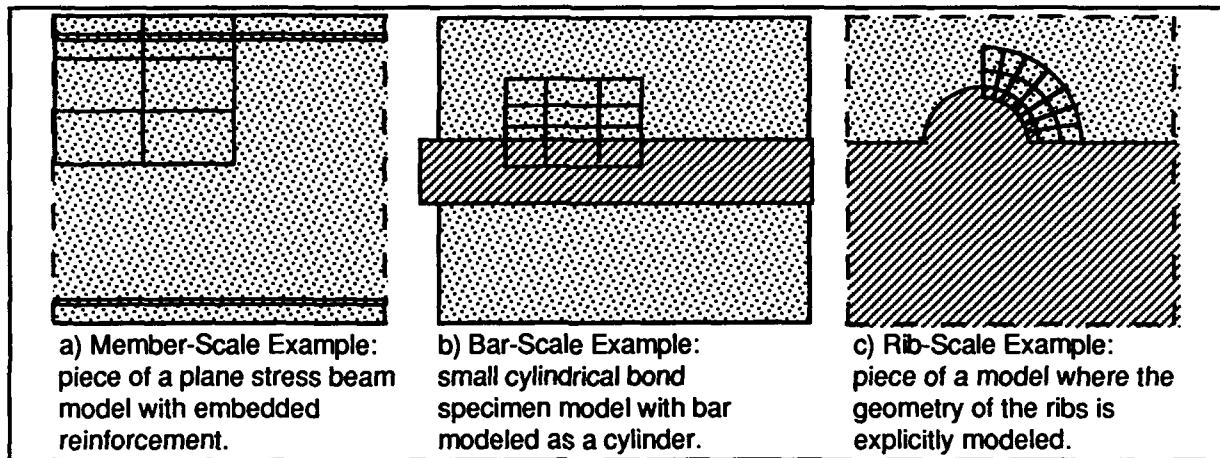
Figure 1.   Examples of scales used in modeling reinforced concrete. Representative sizes of quadrilateral elements used in numerical approximations are shown.

INTRODUCTION

The objective of this research project is to study and model bond phenomena for a wide range of reinforced composite materials. With this broad range of applications in mind the proposed model is cast in a very general elastoplastic framework. The initial application to reinforced concrete was selected for the following reasons: 1) reinforced concrete is the most commonly used composite material in the world; 2) due to the brittle nature of concrete and the presence of ribs on the reinforcing bars, its bond behavior is exceptionally complicated and, thus its description should severely tax the proposed model; 3) a wealth of experimental data exists for use in calibrating and verifying the model for reinforced concrete; and 4) we have proposed a future study to investigate the feasibility of using various types of composite reinforcing rods in reinforced concrete applications.

In the context of bond modeling between reinforcement and concrete, analysts have described bond at three distinct scales (figure 1): 1) at a *member-scale* where the tensile strength of the matrix material is viewed as supplementing the greater tensile strength of the reinforcement, 2) at the *bar-scale* where a phenomenological description attempts to capture the various bond mechanisms, and 3) at the *rib-scale* where the actual "micromechanics" of the problem is considered to occur. While the rib-scale analyses have provided insight to the bond phenomena, they have failed to produce a predictive capability that can be extended to the member-scale. At the other extreme, member-scale analyses allow entire structural systems to be analyzed but fail to incorporate the effects of bond-slip in an accurate manner. The goal of this work is to "bridge the gap" by developing a bar-scale model that captures the phenomena that occur at the rib-scale in a form that has potential to be used at the member-scale.

For applications where the reinforcement has significant *local surface structure* the bond is clearly not a "pure interface phenomenon" [2]. In reinforced concrete, bars are fabricated with ribs to obtain a greater bond strength from the mechanical interaction. Analogous to a boundary layer in fluid mechanics, a region near the bar is defined that will be referred to as the *process-zone*. In an average sense, the bond model provides a continuum mechanics description of the process-zone.

Our choice of using elastoplasticity to model bond phenomena is based upon: 1) experimental results that exhibit classical elastoplastic behavior, 2) extendibility of a "monotonic model" to a "cyclic model" by using a multiple branch yield surface and 3) the potential of extracting the characterization from a database of existing bond tests. Elastoplasticity is a natural framework in which to develop a constitutive model for bond; Coulomb's equation has been used to describe the behavior of many interfaces. For reinforcement with significant local surface structure a more complicated model is required to

obtain accurate predictions. Many experimental studies on ribbed steel bars in a concrete matrix (see *e.g.* Eligehausen *et al.* [3]) reflect classical elastoplastic response for both cyclic and monotonic loadings. Cyclic bond behavior is currently being characterized by a multiple branch plasticity model. Because of space restrictions the scope of this paper only covers the monotonic loading.

ELASTOPLASTIC BOND MODEL

In this section we present the elastoplastic framework and some of the simplifying assumptions used in our bond model development. From the more general framework, we then make additional assumptions and present a bond model for reinforced concrete applicable to axisymmetric or *near-axisymmetric* stress states.

OVERVIEW OF GENERAL FRAMEWORK

In classical elastoplasticity it is assumed that for some set of stress states a material behaves in an elastic manner such that stress and strain are uniquely related. Let's define a set of *generalized* stresses and strains that will be represented in vector form as Q and q respectively. We define a local cylindrical coordinate system where the z-axis corresponds to the axis of the reinforcement. The generalized stresses and strains are then defined as:

$$Q^T = (\tau_{rz} \quad \sigma_r \quad \tau_{r\theta}; \quad \sigma_z \quad \sigma_\theta \quad \tau_{\theta z}) \text{ and } q^T = \left(\frac{\delta_z}{D_b} \quad \frac{\delta_r}{D_b} \quad \frac{\delta_\theta}{D_b}; \quad \varepsilon_z \quad \varepsilon_\theta \quad \gamma_{\theta z} \right). \quad (1a,b)$$

where the δ's denotes relative displacements, in the designated local coordinate direction, of a point on the outside of the process zone relative to a point on the inside of the process zone differing only in their r coordinate (*i.e.* along a radial line in the undeformed state), and D_b denotes the diameter of the reinforcement. Though these are not a unique measure of strain, the particular form of the first three generalized strains has been effective in the simplified law presented in the next subsection. The stresses and strains are partitioned to separate the typical interface components from the additional components necessary to define the state of stress and deformation in a solid. The stresses and strains are to be interpreted as average values over a unit cell that includes a "single rib."

The first component of the model description is a quantitative definition of the stress states for which elasticity alone governs the behavior – the *yield criterion*. There exist stress increments which will result in permanent deformation when $\phi(Q,h)=0$ where ϕ denotes the *yield function* and h denotes a set of internal variables which quantify the internal structure of the material. The surface in stress space defined by $\phi(Q,h)=0$ is known as the *yield surface*.

By definition all valid stress states must lie on or within the yield surface. Except for the case of perfect plasticity where plastic deformations occur without a change in the stress state, the *consistency condition* requires a change in the internal variables to accommodate changes in stress during yielding. Assume that the rate constitutive equations for the internal variables, or evolution laws, are of the form $\dot{h}_i = \langle \lambda \rangle \bar{h}_i$ where λ is the *loading index* which will be a natural result of the consistency condition. The loading index is only positive for plastic loading, and thus the Macaulay bracket notation denotes that the internal variables only evolve when plasticity occurs. Each evolution law, $\bar{h}_i$, is a function of the state variables. The enforcement of consistency during loading (*i.e.* $\dot{\phi}(Q,h) = 0$) implies that the loading index is defined as: $\lambda = (\partial\phi/\partial Q_i)(\dot{Q}_i/K^P)$ where $K^P = - (\partial\phi/\partial h_i)\bar{h}_i$ denotes the *plastic modulus*.

We assume the strain rates can be decomposed in an additive form as $\dot{q} = \dot{q}^e + \dot{q}^P$. The plastic strain rate relationship should be written in a form similar to the evolution law for the internal variables since the plastic strains are associated with their evolution. Thus the plastic strain rates are given by $\dot{q}^P = \langle \lambda \rangle R^P$. The vector R^P, the *flow rule*, depends upon the state

variables and defines the direction of plastic deformation. Though the assumption of an associative flow rule is quite common in many material models, we will see in the next section that the generalization to a nonassociative flow rule is regretfully necessary in the modeling of bond. This is not surprising since friction is nonassociative and is a component mechanism of bond.

Now only the elastic relations remain to be defined. For some materials plastic deformation directly affects the elastic behavior. This *elastoplastic coupling* has been observed by numerous researchers working on bond of reinforcement in concrete (see *e.g.* [3]). However for simplicity, at this stage of the model development, we omit the coupling and assume a simple linear elastic relationship as

$$\underline{Q} = \mathbf{D}^e \underline{q}^e \tag{2}$$

A minor change in the equation reflecting the underlying contact problem will be made in the next section.

The next section addresses individual components (*e.g.* flow rule) of the elastoplastic model developed specifically for steel reinforcement in concrete. For each model component the micro-mechanics of the bond phenomena will be related to the component's phenomenological form.

DEVELOPMENT FOR REINFORCED CONCRETE

Now we reduce the stresses, and associated strain components, to those necessary to define a traction on the surface of an axisymmetric solid; that is, we retain only the first two components in equations (1a) and (1b). Dropping the two normal stress components may limit the scope of application of the bond model to problems where the reinforcement fails by pulling out of the concrete matrix under relatively small strains and where prestresses in the matrix material are small. This is an area of continuing research. For clarity we will now refer to the components of the generalized stress and strain vectors as:

$$\underline{Q}^T = (\ \tau\ \ \sigma\ ) \text{ and } \underline{q}^T = \frac{1}{D_b}(\ \delta_t\ \ \delta_n\ ). \tag{3a,b}$$

Even when assuming linear elasticity, the elastic properties can be allusive. Interpretation of experimental data [4] has led to the relationship

$$\mathbf{D}^e = E_c \begin{bmatrix} 0.1 & -0.0012\ \text{sgn}(\delta_t)\ \text{H}(|\delta_t|-\varepsilon) \\ -0.0012\ \text{sgn}(\delta_t)\ \text{H}(|\delta_t|-\varepsilon) & 0.04 \end{bmatrix} \tag{4}$$

where ε denotes "numerical zero," E_c is the elastic modulus of concrete, and H is the Heaviside function. These elastic moduli must be used incrementally and only apply to monotonic loading.

Note that the relatively small off-diagonal terms imply that there is little normal bond stress developed due to shear deformation until plastic deformation occurs (with an analogous interpretation for the upper off-diagonal term). This is qualitatively consistent with rib-scale analyses and experimental investigations that suggest that the ribs produce a significant wedging action against the concrete only after local concrete crushing has occurred in front of them. For a cementitious matrix material like concrete, the chemical adhesion can break down at a relatively low stress with negligible plastic deformation and thus the contact problem can occur for stress states that can be interpreted as elastic states. The $\text{sgn}(\delta_t)$ $\text{H}(|\delta_t|-\varepsilon)$ factor reflects this contact character of the interface between the inclined rib surface and the adjacent
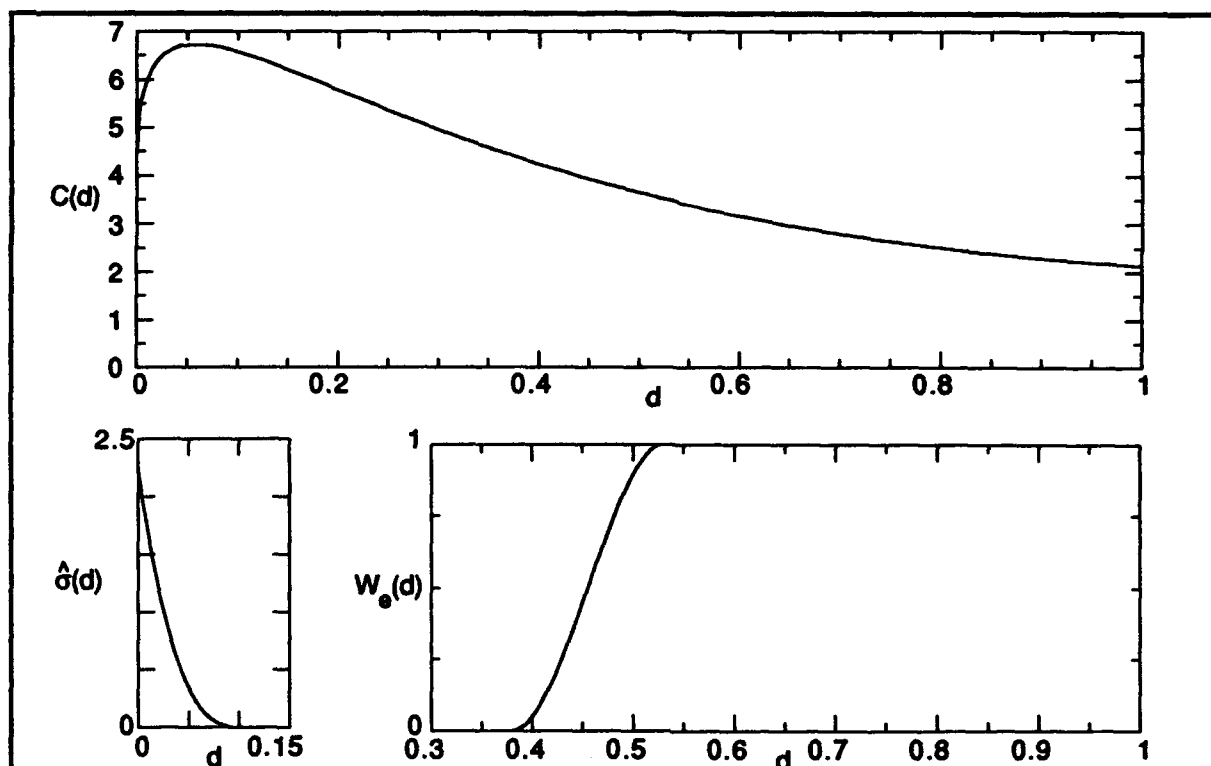
Figure 2. Hardening and weight function evolutions.

concrete. The Heaviside function sets the terms to zero for "zero slip" since in this case a radial contraction of the process zone, by symmetry, causes no tangent resultant force.

Except for the underlying "contact problem" the elastic moduli have been expressed in a simple form, proportional to E_c. Though one might expect a form including the shear modulus of the matrix material, rib-scale analyses have shown that after the break-down of adhesion, the elastic response is rather localized to the contact regions in front of the ribs; thus the stiffness of the material in compression would be very important suggesting the above form.

The complication of multiple mechanisms (fracture, crushing, shearing, and friction) appear to require corresponding complicated relations for the yield surface and flow rule. The form of the yield function is given as follows:

$$\left|\frac{\tau}{f_t}\right| = C(d)\left\{W_e(d)[1 - e^{-\alpha(-\sigma/f_t + \hat{\sigma}(d))}] + M(1 - W_e(d))\left|\frac{-\sigma}{f_t} + \hat{\sigma}(d)\right|^{\alpha_p} \text{sgn}\left(\frac{-\sigma}{f_t} + \hat{\sigma}(d)\right)\right\} \quad (5)$$

where f_t denotes the tensile strength of the concrete matrix.

Various evolution laws have been considered for C, W_e, and $\hat{\sigma}$. In this study we have used relatively simple nonincremental forms for these three functions in terms of a "damage measure," d. For brevity the details on the forms of these functions have been omitted, see reference [1] for details. The graphs of these functions are shown in figure 2.

Because of the forms of C, W_e, and $\hat{\sigma}$, d can be regarded as the only internal variable. This measure of "damage" in the bond is defined in terms of the plastic slip as: $d = \min(\delta_t^{sp}/s_r, 1)$ where s_r is the spacing of the ribs along the bar. Eligehausen et al. [3] suggested that when the slip equals the rib spacing the bond is completely failed and only frictional resistance remains.

The yield function weights the contribution of an exponential function and a power function via the weighting function, W_e. Initially the yield surface is a power function and then with increasing damage transitions to an exponential function. The exponential form of the yield
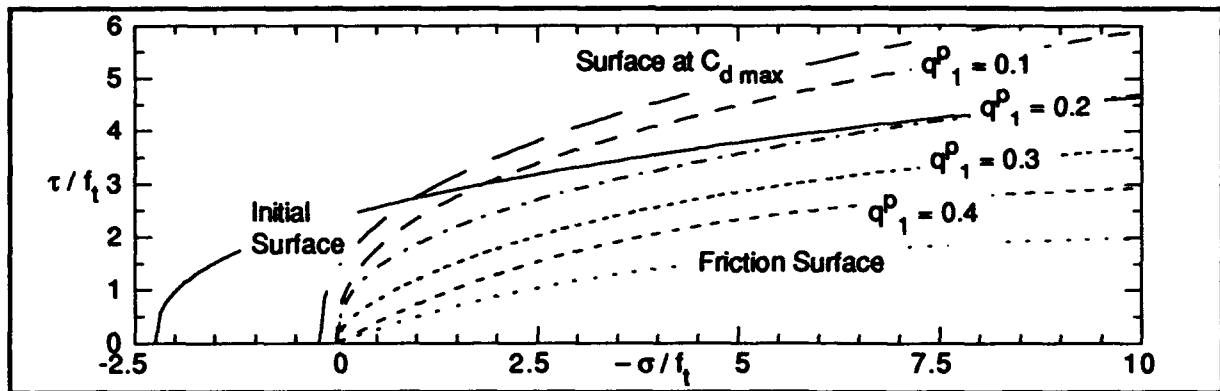
Figure 3. Yield surface evolution.

surface reflects the dominance of the friction mechanism. One might expect the surface to reduce to the more common Coulomb surface usually used to characterize frictional behavior. Certainly for small confinement stresses, a Coulomb surface would provide a good approximation to the exponential surface – in a Taylor series sense. Thus the effective coefficients of friction for the high confinement stresses seem relatively small. This behavior will be considered further in the flow rule discussion below.

The functions C and $\hat{\partial}$ are essentially the isotropic and kinematic hardening functions, respectively. The initial isotropic hardening might be attributed to a compaction of a rather porous matrix material in front of the rib which reduces the contact stresses and increases the force required to produce additional damage. The subsequent isotropic softening can be attributed to the extension of transverse cracks and the reduction in undamaged material between ribs. The value of C(d) changes very little after d reaches a value of 0.7; experimental data suggest that friction is the dominant mechanism at this point and that the interface is smoothing thus reducing the effective coefficient of friction. The kinematic hardening function could be attributed to the propagation of splitting cracks and/or the geometric effect of the rib wedging under the concrete and reducing the effective angle at the interface.

The combined effect of the two types of hardening is shown by the evolution of the yield surface in figure 3. At relatively small values of $-\sigma$ the bond failure has a more brittle nature than at relatively large values of $-\sigma$ where the isotropic hardening is dominant. This agrees with both experimental results and rib-scale analyses which indicate that fracture mechanisms dominate at low confinement stresses and crushing and shearing mechanisms dominate at high confinement stresses.

For reinforcement that has a measure of local surface structure but does not produce a mechanical interaction to the extent found in this application, the given bond law can be calibrated to yield a form close to a classical Coulomb surface while retaining some of the behavior not typical of "true interface phenomena."

Various forms have also been considered for the flow rule. The version used in this study was derived from the experimental data of Malvar [4]. When the flow rule is expressed as:

$$\left\{ \dot{q}^P \right\} = \langle \lambda \rangle \left\{ \begin{array}{c} sgn(\tau) \\ g \end{array} \right\}$$

$$(17)$$

the function g is obtained from the experimental data by using a 3-point, unevenly spaced, finite difference approximation to obtain the derivative [1]. Figure 4 qualitatively shows the nature of the flow rule for three values of $-\sigma$. Comparisons with figure 3 illustrate the need for a nonassociative flow rule. The area under the positive portion of g is proportional to the radial dilation of the process zone. Except for very special test specimens (e.g. Malvar [4]), the normal stress would vary during the course of the test. For small values of $-\sigma$ where the failure appears to be dominated by longitudinal and transverse cracking, the rib is able to slide
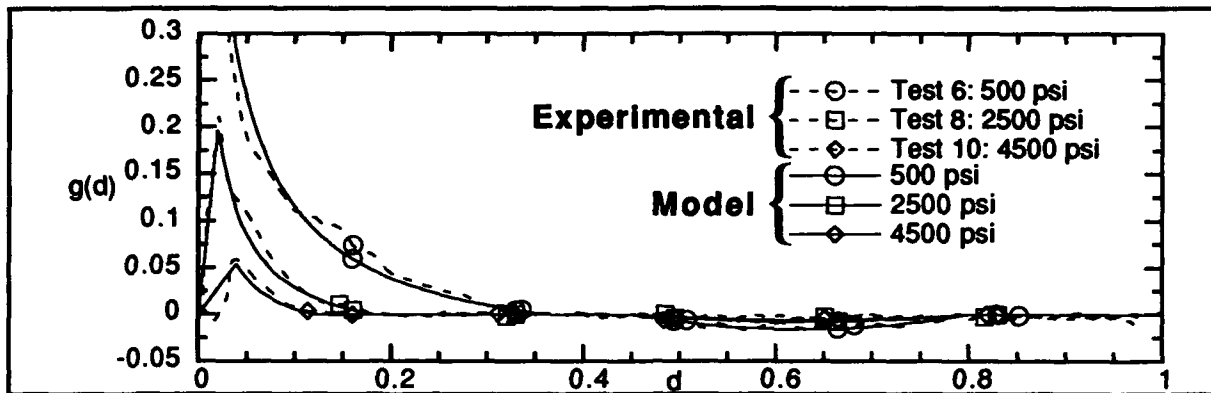
Figure 4. Model's flow rule function, g, compared to experimental data.

along the interface surface with limited crushing. Thus the dilation is relatively large. For large values of $-\sigma$ the failure is dominated by local crushing and shearing of the concrete between the ribs, and thus the dilation is less. These modes of failure are well documented in the literature and are consistent with the post-testing condition of Malvar's specimens.

The two flat regions of g indicate the presence of slip without radial dilation or contraction. For the first flat region it appears the ribs are punching thru the concrete matrix. The last flat region represents a pure frictional behavior. Between these two regions the process zone radially contracts. This is interpreted as a "propagation of the failure" from the rib face to the cavity in the matrix left by the adjacent rib. The area of the negative region of g is proportional to the radial contraction. For all values of $-\sigma$ the radial contraction is less than the original dilation; the difference increases with smaller $-\sigma$ values All of the specimens considered in the Malvar experiments [4] have longitudinal cracks. The behavior seen here is related to the shape of the yield surface during the frictional behavior. Apparently the debris created during the early plastic slip not only accumulates on the rib face but also enters the open longitudinal cracks. This prevents the process zone from fully contracting and thus allows the process zone to act as a "thick-walled cylinder." So the normal stress actually reaching the interface is reduced, and thus the effective coefficient of friction is smaller. Compared to the exponential yield surface, the Coulomb surface is only applicable for relatively small confinement pressures where the opening of the longitudinal cracks is relatively large and thus the bar is not effectively isolated from the confinement pressures. This mechanism again indicates the need to consider the bond phenomena as occurring within a process zone rather than as occurring on an interface.

Though the forms of the constitutive relations may appear to be complex, there is a single internal variable for monotonic loading. In addition, after an initial calibration only four physical parameters (f_t, E_c, D_b, s_r) are needed to reproduce results from a variety of experimental tests. For other applications additional parameters may be necessary to quantify both the behavior of the matrix material and the local structure of the surface.

COMPARISONS TO EXPERIMENTAL RESULTS

In this section we compare finite element (FE) analysis results using the proposed bond model to experimental results from a series of bond tests by Shima, Chou and Okamura [5]. All of the specimens used by these researchers are pull-out type specimens with a diameter of 50 cm and bar diameters ranging from 25.4 to 30.7 mm. Figure 5 shows the relative size of specimen 4 (having a bonded length of 20 cm) to the calibration specimens of Malvar [4].

The bond law is implemented in a research FE code. The use of a nonassociative flow rule implies the Jacobian for the Newton-Raphson method is unsymmetric. For ease of implementation, the constitutive equations are currently integrated using the cutting-plane algorithm. While finite thickness interface elements are used to model the process zone, the
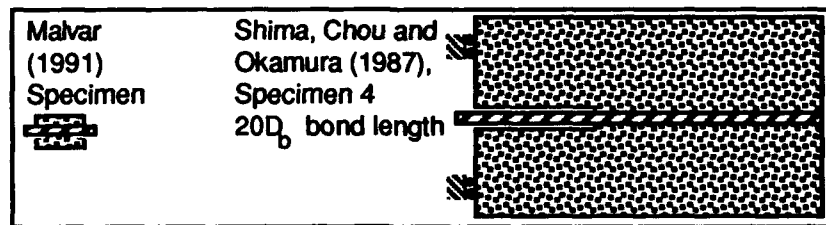
Figure 5. Reinforced concrete pull-out bond specimens.

integration points are on the surface of the bar; thus the only size effect is the variation in response due to replacing matrix material with the process zone model [1]. For example, in this study we assumed that most of the inelastic behavior would be captured by the bond model and treated the remaining concrete as an elastic-brittle material that could only crack longitudinally (splitting). We used a process zone size of 3.3 mm in the following analyses.

Figure 6 shows two comparisons of the model to experimental results. The first plot compares the force in the loaded end of several bars to the relative end displacement at the free ends of the bars. The displacements are measured relative to the outer edge of the specimen, specifically where the displacement transducer is mounted, and the bars differ in embedment length as designated. Note that the results are generally very good with differences between experimental and model responses, near ultimate, of less than 20%. The increase of difference with embedment length could be suggesting the need for including the additional normal stress in the constitutive relationship. There is also uncertainty in the properties of the bars since the original yield strength was 217 N but is not given after heat treatment.

The second plot compares a more local response for three specimens with embedment lengths of $6D_b$. The three experiments differ in their unbonded length at the free end of the bar. The relative displacement represents the displacement of a point on the bar $2D_b$ from the free end relative to the displacement transducer mounting point. Experimentally this displacement is obtained from the integration of the strain along the bar and the relative end displacement. The experimental bond stress results require the strain in the bar to be differentiated and thus are difficult to obtain accurately. Not all the local responses of the model have compared this favorably with the results of Shima, Chou and Okamura [5]. This comparison only demonstrates the model's agreement up to the maximum bond stress. For comparisons with other experimental data, which include a larger range of slip, see [1].

Another important result is the state of the specimen at the end of the test. As observed in the experiment, numerically a longitudinal crack was produced by the mechanical interaction but it remained internal and did not fail the specimen.
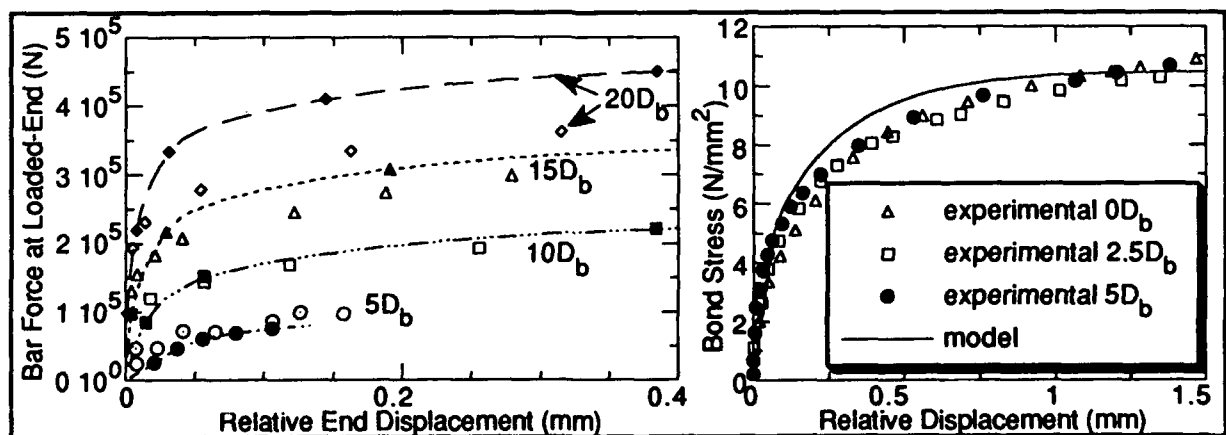
Figure 6.   Comparison of model predictions to experimental results of Shima, Chou and Okamura [5].

CONCLUSIONS

The somewhat complicated form of the proposed plasticity law reflects the difficulty in representing bond phenomena that involve many mechanisms, typical of reinforcement with local surface structure. The phenomena are clearly not limited to the interface yet we would like to limit our constitutive law to the corresponding components of the interface traction so that the model might be suitable for large scale calculations. The complete limitations on this simplification must still be determined.

In developing the model for monotonic loading of reinforced concrete, relatively simple evolution laws are proposed that ease the numeric burden. After an initial calibration, only four physical material parameters have been required to reproduce many experimental results [1]. Two of the parameters describe the strength and stiffness of the concrete matrix and two describe the geometry of the reinforcement and its surface structure.

Since the specimens of Shima *et al.* [5] were designed to avoid failures by cracking the simplified model for concrete was adequate, giving good predictions of the response over a range of embedment lengths. Including the normal stress and corresponding radial dilation in the model allows it to initiate cracking and "sense" the effects of variations in the thickness in the matrix material.

ACKNOWLEDGEMENTS

REFERENCES

1. Cox, J. V. 1992. "A Plasticity Model for Bond between Steel Reinforcement and Concrete," Ph.D. dissertation, Civil Engineering Department, University of California, Davis (in publication).

2. Gerstle, Walter H. and Anthony R. Ingraffea, June 1990. "Does Bond-Slip Exist?" in Micromechanics of Failure of Quasi-Brittle Materials, Proceedings of the International Conference, Albuquerque, NM, S.P. Shah, S.E. Swartz, and M.L. Wang eds.

3. Eligehausen, R., E.P. Popov, and V.V. Bertero, October 1983. "Local bond stress-slip relations of deformed bars under generalized excitations," Report UCB/EERC-83/23, University of California, Berkeley, CA.

4. Malvar, L.J. June 1991. "Bond of Reinforcement under Controlled Confinement," Technical Note 1833, Naval Civil Engineering Laboratory, Port Hueneme, CA 93043 (also accepted for publication in ACI Materials Journal).

5. Shima, H., L. Chou and H. Okamura, 1987. "Micro and Macro Models for bond in reinforced Concrete," Journal of the Faculty of Engineering, The University of Tokyo (B), 39(2): 133-194.

Fabric Nesting and Some Effects on Constitutive Behavior of Plain-Weave Cloth-Reinforced Laminates

JULIUS JORTNER

ABSTRACT

For composites reinforced with plain-woven cloth laid up in warp-aligned laminates, a simplified 2D numerical model shows that the elastic constants may be significantly affected by variations in the nesting of fabric layers. Illustrative results, representing one type of carbon-carbon laminate, show potential effects of nesting are greater for shear moduli than Young's moduli, increase with increasing yarn crimp angle, and increase with increasing anisotropy of the fiber bundles. The work suggests nesting variations may contribute to the scatter in mechanical-property data for such laminates.

INTRODUCTION

Considerable scatter in measured mechanical-property data is observed for plain-weave-reinforced carbon-carbon laminates like those studied in [1-3]. Coefficients of variation sometimes exceed 15 percent. Variations in average crimp angle of the load-directed yarns seem to explain much of the variation of on-axis in-plane tensile strength [3,4]. Here, we focus on variations in the nesting of cloth layers and some potential effects on elastic constants.

The material of immediate concern is a carbon-carbon composite ("Material A") made from a plain-weave carbon fabric prepregged with phenolic resin. After compaction, cure, and carbonization of the prepreg laminate, several cycles of

Julius Jortner, Jortner Research & Engineering, Inc., P O Box 2825, Costa Mesa, CA 92628-2825.

impregnation and carbonization add more carbon matrix. The
layups are warp-aligned; that is, the warp-yarn direction is
the same in each cloth layer. The "unit cell" of the cloth,
outlined with straight lines in the upper half of Fig. 1,
contains excess space that becomes occupied by portions of
neighboring cloth layers when the laminate is compacted. This
intrusion of one cloth layer into the space of the next (Fig.
1, lower) is called nesting. In a well compacted laminate of
this type, very little space is occupied by matrix outside
fiber bundles [5].
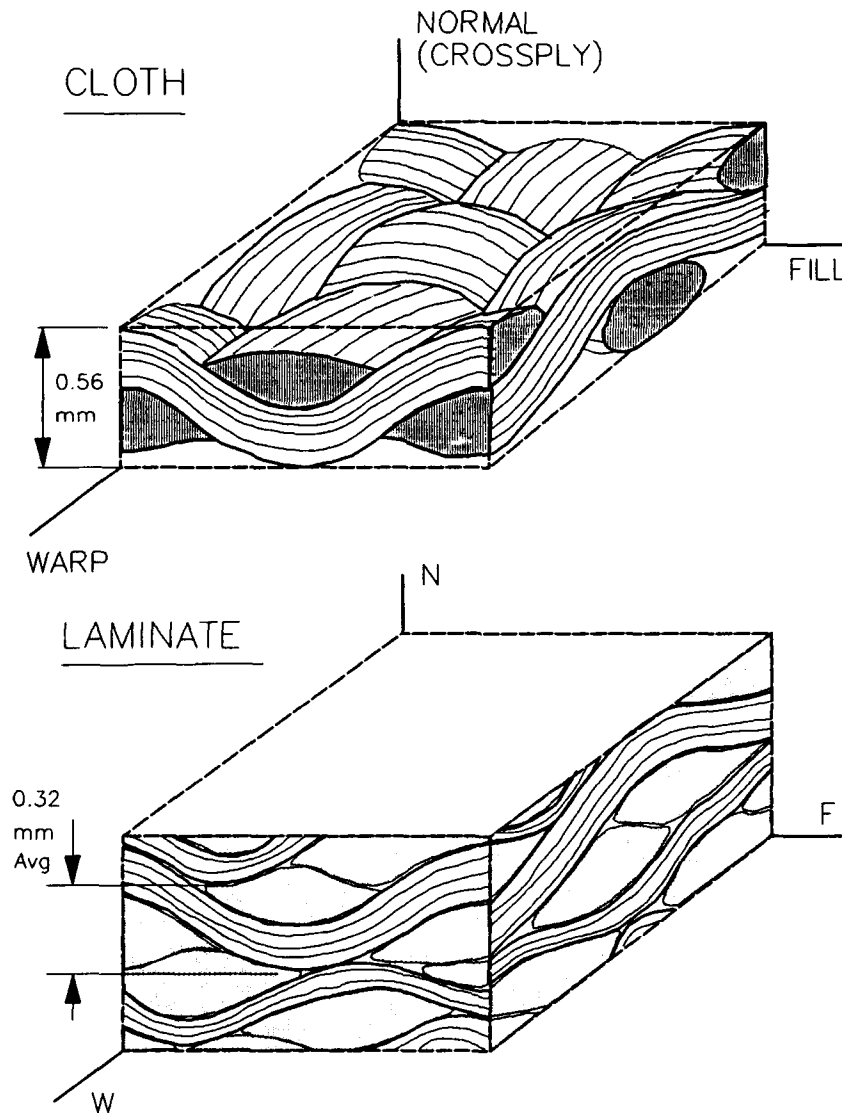
Fig. 1. Structure of Material A. Upper sketch is a unit cell
of the plain-weave cloth. Lower sketch shows a region of the
carbon-carbon laminate. Adapted from [5].

The nesting favored theoretically, because it would require
the least relative movements of fibers during compaction,
would have the peaks on one cloth layer fit easily into the
valleys of the neighboring layer. For a balanced square
weave, this favored displacement of one layer over the one
below is indicated in Fig. 2. From symmetry, we see this
shift to be one-quarter wavelength of the yarn waveform in
each direction. For the real Material A, which is made from
slightly unbalanced fabric (the warp yarn count is about 11
per cm and the fill yarn count about 8.5 per cm, the average
amplitude of the warp waveform is less than the fill-waveform
amplitude, and the fill yarns are able to move laterally more
easily than warp yarns [5]), the favored shift is not as
readily defined. Also, in real laminates, departures from
"preferred" nesting would be forced by any external
constraints on relative lateral movement of layers, by
friction between cloth layers, by local departures from
fill-warp perpendicularity, by deviations from true
warp-alignment, and by the usual variations in yarn count from
place to place in a cloth (Fig. 3).

It seems probable, especially in thin laminates of few
layers, that there will be substantially different stacking
patterns in various samples. Four elementary stacking
patterns are illustrated (in two-dimensional simplifications)
in Fig. 4. These elementary arrays are analyzed, in this
paper, to show how much the elastic constants of the laminate
may differ for nested and collimated stackings.

Not much analytical attention has been paid to the effects
various nesting patterns might have on mechanical behavior.
Most analyses (eg, [6,7]) treat one layer of cloth as a unit
cell, thereby ignoring various stacking possibilities. In a
finite-element analysis that requires explicit information on
stacking to define boundary conditions, Whitcomb [8] treats
only a collimated stacking (as in Fig. 4D). Whether there is
explicit mention or not, some information on stacking/nesting
usually is implied in analytical models; for example,
uniform-microstrain analyses probably apply best to random
stacking. Maurer [9] attempts a model to relate stacking
displacements in satin-weave laminates to interlaminar
strength. To help quantify nesting in a real composite,
Yurgartis et al [10] give statistics for layer-to-layer
differences in yarn-inclination angles for samples of Material
A. Perhaps the results provided here will motivate additional
measurements and modelings.

PLAN VIEW OF LOWER LAYER
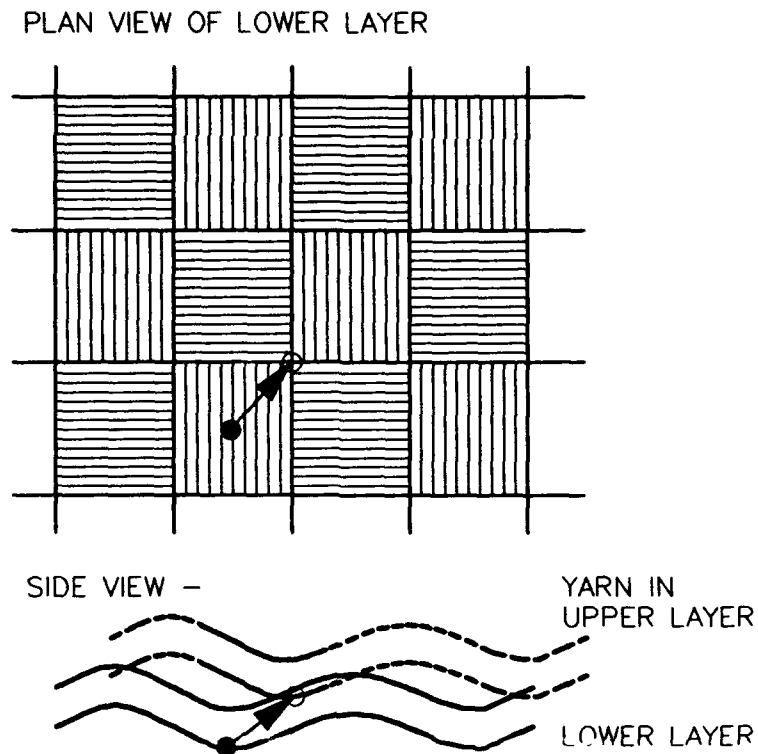
Fig. 2. Arrow shows displacement of one cloth layer over another for optimal nesting.

UPPER LAYER OF YARNS

LOWER LAYER

NESTED   COLLIMATED   NESTED
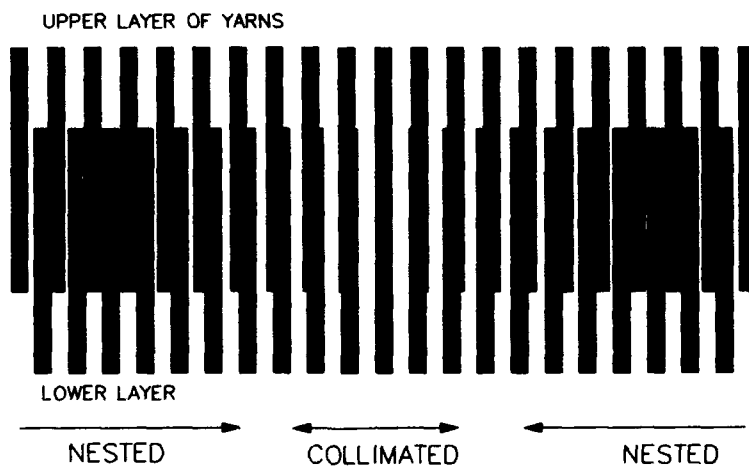
Fig. 3. Small differences in yarn count can produce alternations of nested and collimated stacking.
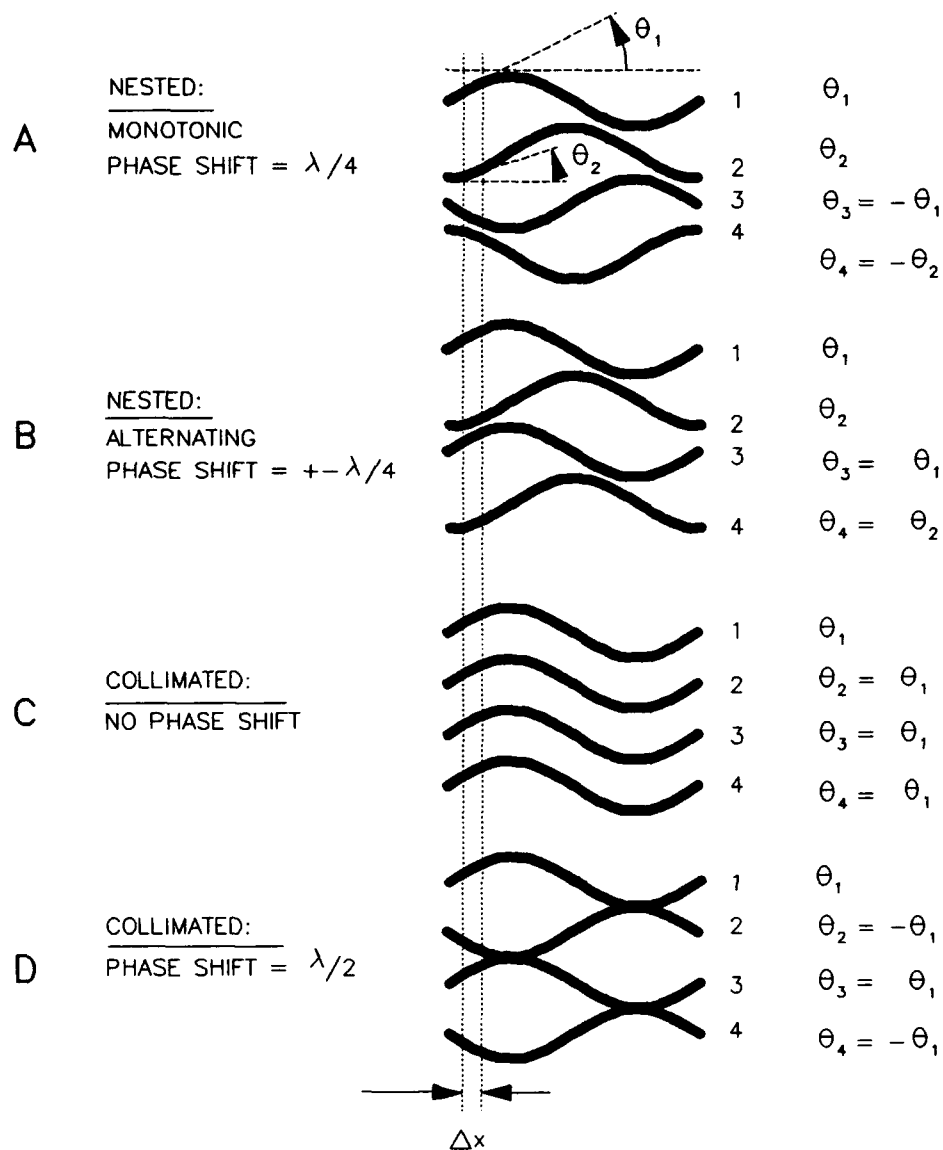
Fig. 4. Several elementary stackings for four cloth layers.
Each slice, $\Delta(x)$, contains yarns of orientations $\pm\Theta_i$ for
$i = 1,2,3,4.$

NUMERICAL MODEL

For each of the idealized four-layer stackings of Fig. 4,
we do a calculation of the laminate's elastic constants, in
two dimensions. We assume loadings such that each slice of
the laminate, Δx, is subjected to the same tractions. To
estimate the effective stiffnesses of a slice, we view it as
an assembly of variously oriented yarn-bundle elements

(representing the undulating yarns in the plane of analysis) and a transverse phase to represent the crossing yarn bundles. In a major simplification consistent with a 2D model, the transverse phase is taken as orthotropic in the principal laminate coordinates. The fill yarns of each cloth layer are represented by two yarn elements of angles $\pm\Theta$. Then, as implied in Fig. 4, the four stackings may be represented by two cases: a <u>nested</u> stacking for which each slice contains yarn elements of $\pm\Theta_1$ and $\pm\Theta_2$, and a <u>collimated</u> stacking for which each slice contains yarn elements of $\pm\Theta_1$ only. Θ_1 varies with x as if the yarn undulation were a sinusoid. Θ_2 is obtained from the same sinusoid displaced laterally one-quarter wavelength. The crimp angle (the maximum value of Θ) is assumed the same for each sinusoidal yarn. The volume fraction of each yarn element depends on Θ, assuming the yarn-bundle cross-sectional area is constant, consistent with the assumed overall yarn-volume fraction.

The stiffnesses of each yarn element are calculated from the input orthotropic stiffnesses for the yarn bundle, expressed in yarn-bundle coordinates (L = longitudinal, T = transverse), and the angular transformation from LT-coordinates to laminate coordinates (1 = in-plane, 2 = cross-ply). In this context, Θ is the angle between the L and 1 axes. The effective stiffnesses of the slice are obtained as the volume-weighted average of the constituent stiffnesses. In other words, the slice's elastic constants are estimated as the uniform-strain (upper) bound for stiffness of the assembly of constituents.

To estimate the elastic constants for the laminate, the effective constants for each slice are combined assuming the stress is uniform from slice to slice. That is, the effective stiffness matrix for each slice is inverted to obtain the effective compliances for that slice. The slice compliances then are averaged over all the slices in a wavelength to obtain the effective compliance of the laminate. For the cases at hand, we may represent the entire wavelength by one-quarter wavelength; the results reported are based on 20 slices to one-quarter wavelength. Individual compliance components are inverted to obtain the respective engineering moduli.

The needed angular transformations and the relationships among engineering, stiffness, and compliance constants are well known (eg, [11]).

The general approach is similar to other two-dimensional treatments (eg, [6,7]), except more than one cloth layer is considered. Also, we differ from the "crimp model" of [6] by including both positive and negative Θ within each slice; and we differ from [7] by adopting a uniform-stress summation of slices.

To provide an upper bound to laminate stiffness, thought to correspond to random stacking, calculations also were made using uniform-strain summation of slices.

ILLUSTRATIVE RESULTS

For Material A, the following properties were used to represent the wavy phase: $E_L = 35$ GPa, $E_T = 3.5$ GPa, $G_{LT} = 1.4$ GPa, $v_L = .2$. The transverse phase was represented by $E_1 = 1.7$ GPa, $E_2 = 3.5$ GPa, $G_{12} = 1.4$ GPa, $v_2 = .1$. Here, E, G, and v, respectively represent Young's modulus, shear modulus, and Poisson's ratio. The in-plane stiffness of the transverse phase was assumed lower than its cross-ply stiffness because of the periodic cracking typical of carbon-carbon laminates [5]. Calculations were done for crimp angles up to 43°, near the high end of the range observed [3,5,10]. The volume fraction of the wavy yarns was taken as 0.44, corresponding approximately to the fill-yarn volume fraction in Material A.

Over the range of crimp angles, Fig. 5 shows the percentage by which the major elastic stiffnesses for a collimated stack are less than the stiffnesses of a nested stack. The differences increase with crimp angle. The shear modulus is the most affected by the postulated stacking difference. For crimp angles less than about 25°, the effect of stacking on the extensional moduli appears negligible, according to this model.

Fig. 6 shows results of additional calculations to explore the effects of yarn-bundle anisotropy. A low crimp angle was selected for these calculations because higher-modulus yarns tend to weave with lower crimps. We see shear modulus is affected by nesting, to a degree that increases with increasing longitudinal stiffness of the fibers.

Predictions of elastic constants for the nested stacking of Fig. 4 are negligibly different (<2%) from predictions for random stacking over the entire range of variables studied.
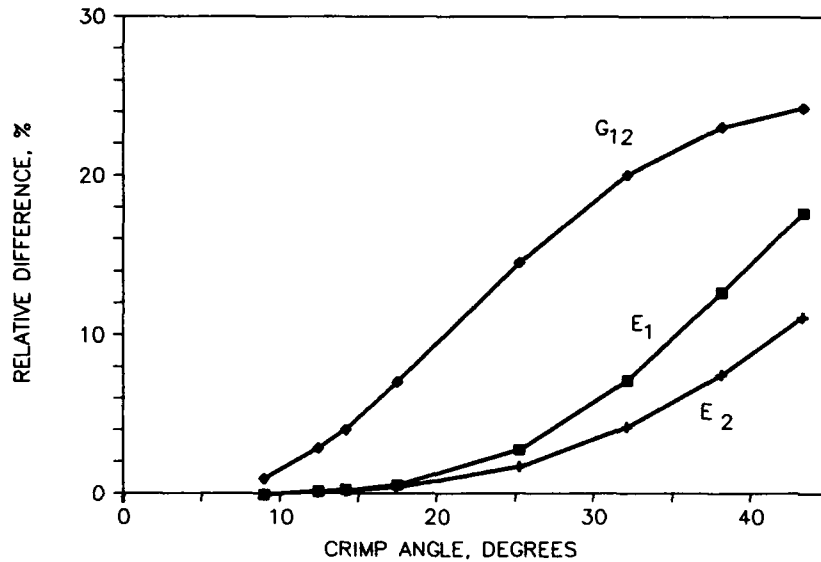
Fig. 5. Calculated percentage by which elastic constants for collimated stacking are less than for nested stacking, for various crimp angles, a wavy-yarn volume fraction of 0.44, and the input constituent properties given in text for Material A.
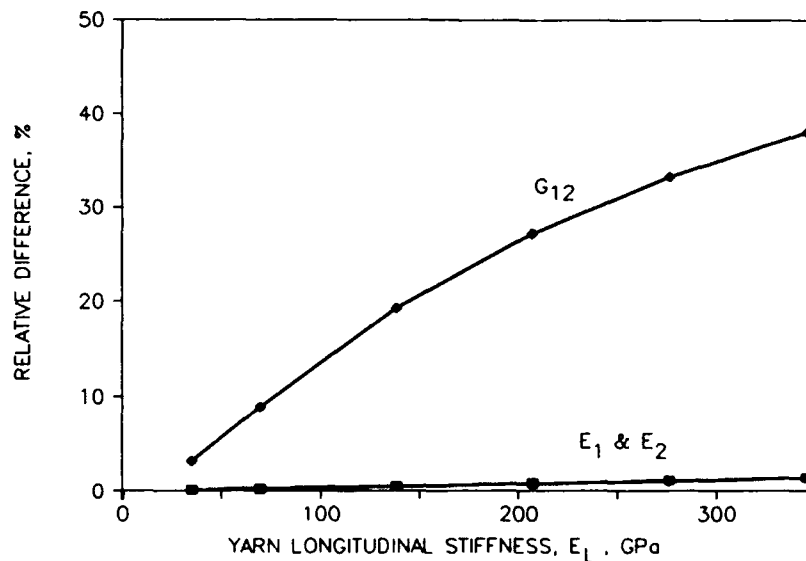
Fig. 6. Calculated effect of longitudinal stiffness of yarns on difference between elastic constants for collimated and nested stackings. For a yarn crimp angle of 12.4° and a wavy-yarn volume fraction of 0.5. Except for yarn longitudinal stiffness, constituent properties are as for Material A.

CONCLUDING REMARKS

These numerical exercises show nesting can affect the
elastic response of warp-aligned laminates reinforced with
plain-weave fabric. For inputs that loosely represent one
low-modulus carbon-carbon laminate, regions of collimated
stacking are shown to be significantly more compliant than
regions of nested stacking. The transverse shear modulus
appears to be the elastic constant most affected by stacking
variations. Increases in longitudinal stiffness of the yarns,
without proportionate increases in transverse and shear
stiffnesses, are found to increase the differences in elastic
behavior between the two stacking extremes. It is likely, and
is the subject of some continuing study, that the effects of
nesting variations on the nonlinear stress-strain behaviors
(where nonlinearity is induced by microdamage [7]) will prove
larger than the effects on elastic behaviors.

To the extent that nesting details cannot be controlled
fully during manufacture, and because a range of stacking
geometries is observed in warp-aligned plain-weave laminates
(see photos in [3,4,5,10]), there seems in such laminates an
inherent potential for significant variability of elastic
properties.

ACKNOWLEDGMENTS

REFERENCES

1.   Davis, H. O., and D. F. Vronay, 1979. "Structural
Assessment of Involutes." Report AFML-TR-79-4068, Air Force
Materials Lab, Wright-Patterson AFB, Ohio.

2.   Stanton, E. L. and T. E. Kipp, 1985. "Nonlinear Mechanics
of Two-Dimensional Carbon-Carbon Composite Structures and
Materials". AIAA Journal, 23(8):1278-1284.

3. Jortner, Julius, 1989. "Effects of Crimp Angle on the Tensile Strength of a Carbon-Carbon Laminate." in <u>Symposium on High Temperature Composites</u>, Proceedings of Amer. Soc. Comp., Technomic Publishing Co, pp. 243-251.

4. Pollock, P. B., 1990. "Tensile Failure in 2-D Carbon-Carbon Composites." <u>Carbon</u>, 28(5):717-732.

5. Jortner, Julius, 1992. "Microstructure of Cloth-Reinforced Carbon-Carbon Laminates." <u>Carbon</u>, 30(2):153-163.

6. Chou, Tsu-Wei, and Takashi Ishikawa, 1989. "Analysis and Modeling of Two-Dimensional Fabric Composites." in <u>Textile Structural Composites</u>, Tsu-Wei Chou and Frank K. Ko, ed., Elsevier, chapter 7, pp.219ff.

7. Jortner, J., 1986. "A Model for Nonlinear Stress-Strain Behavior of 2D Composites with Brittle Matrices and Wavy Yarns." in <u>Advances in Composite Materials and Structures</u>, S. S. Wang and Y. D. S. Rajapakse, ed. American Society of Mechanical Engineers, AMD-Vol.82, pp. 135-146.

8. Whitcomb, John D., 1989. "Three Dimensional Stress Analysis of Plain Weave Composites." Report NASA TM-101672, NASA Langley Research Center.

9. Maurer, John P., 1992. "Characterizing Weave Geometry and its Effects on Mechanical Properties in 2D Reinforced Carbon-Carbon Composites." MS Thesis, Dept of Mechanical and Aeronautical Engineering, Clarkson University, Potsdam, NY.

10. Yurgartis, S. W., K. Morey, and J. Jortner, 1992. "Measurement of Yarn Shape and Nesting in Plain-Weave Composites." <u>Composites Sci. & Techn.</u>, in press.

11. Tsai, Stephen W., and H. Thomas Hahn, 1980. <u>Introduction to Composite Materials</u>, Technomic Publishing Co.

On Mechanics of Periodic Matrix Cracks in Brittle Matrix Fiber Reinforced Composites

AUTAR K. KAW AND GLEN H. BESTERFIELD

ABSTRACT

A fracture model based on two dimensional plane stress/strain elasticity theory is developed for the problem of periodic, interacting and regularly spaced matrix cracks in a unidirectional fiber reinforced brittle matrix composite. The solution is obtained in terms of a hypersingular integral equation. The effect of the fiber reinforcement; and spacing, location and length of cracks on the stress intensity factors at the crack tips in the composite is studied.

INTRODUCTION

Ceramic materials, such as glass ceramic and silicon carbide, are being used for high temperature applications in many engineering components. The advantages in their use are their strength, low density, excellent corrosion and oxidation resistance, and low cost. Their main drawback, however, is that they are brittle in nature and therefore have a tendency to fail catastrophically. This has limited their use in relatively low stress applications, or where catastrophic failure is not a critical issue.

One of the most promising methods to increase the toughness of ceramics is by reinforcing them by continuous fibers such as silicon carbide and carbon. However, fiber reinforced ceramic matrix composites are highly anisotropic and exhibit complex fracture behavior. Consequently, a full understanding of this complex behavior is essential.

Consider a unidirectional ceramic matrix composite under a tensile load applied in the direction of the fibers. If no cracking has taken place, the loading results in equal axial strains in the matrix and the fiber. In some ceramic matrix composites, the fracture strain of the fiber is much higher than that of the matrix. Hence, prefailure damage under a tensile load may involve extensive cracks in the matrix which are oriented in the matrix perpendicular to the loading. A few examples of materials that exhibit such a behavior include glass ceramics reinforced by carbon [1] and silicon carbide fibers [2]. In many cases where the fiber is strong and the interfaces are weak, these cracks are more or less of equal length and are equally spaced in the matrix [3]. These cracks are of major concern as it signifies the onset of permanent damage and / or

Autar K. Kaw and Glen H. Besterfield, ENG 118, Mechanical Engineering Department, University of South Florida, Tampa, FL 33620-5350.

catastrophic failure. Also, since many practical applications involve a corrosive atmosphere, the protection provided by the matrix to the fibers against corrosion can also be lost. These concerns make understanding the mechanics of matrix fracture in ceramic matrix composites important.

The pioneering work on matrix cracking in brittle matrix fiber reinforced composites has been done by Aveston, et. al [4], commonly called the ACK theory. The ACK theory has also been extended and improved upon by Aveston and Kelly [5], Marshall and Evans [2], Budiansky, et. al [6], and McCartney [7]. These theories have given a better understanding of the strength and toughness of ceramic matrix composites.

Elasticity solutions to a few fracture problems with parallel periodic cracks have been reported in the literature. The problem of a half-plane with an infinite row of periodic cracks was solved by Benthem and Koiter [8] using an asymptotic expansion to solve the problem. Bowie [9] used conformal mapping to solve the same problem. The first solution in Cauchy singular integral equation form for interacting arrays of parallel edge cracks was given by Nemat-Nasser, et. al [10]. Nied [11] found an elasticity solution of interacting embedded or edge cracks in a half-plane under uniaxial tension. The solution is given in a strongly singular integral equation form. It should be noted that the results of a single crack or periodic noninteracting cracks are not appropriate to understand the problem of interacting periodic cracks. This is because the stress intensity factors at the crack tips and the crack opening displacements are found to decrease as the spacing between the cracks is reduced.

In this paper, the problem of a fiber embedded in a matrix with parallel periodically spaced cracks is solved (Figure 1). An arbitrary normal load is applied perpendicular to the cracks. An elasticity solution is found in terms of a hypersingular integral equation. The stress *intensity factors at* the crack tips and the maximum crack opening displacements are found numerically and evaluated as a function of fiber and matrix moduli; and length, spacing and location of cracks in the matrix.

FORMULATION

The geometry of the problem, shown in Figure 1, consists of a fiber approximated by an infinite, isotropic, linearly elastic strip with shear modulus, μ_1, Poisson's ratio, ν_1 and width, 2h. The fiber is perfectly bonded to a matrix approximated by two isotropic, linearly elastic half-planes with shear modulus, μ_2 and Poisson's ratio, ν_2. The matrix is assumed having a large number of small cracks of equal length, 'b-a', spaced equally and periodically at a distance of 'c' from each other. The crack starts at a distance of 'a-h' from the fiber-matrix interface.

The following are the continuity, symmetry and boundary conditions for the perturbation problem.

$$\sigma^1_{xx}(h,y) - \sigma^2_{xx}(h,y), \quad 0 \leq |y| < \infty, \tag{1.a}$$

$$\sigma^1_{xy}(h,y) - \sigma^2_{xy}(h,y), \quad 0 \leq |y| < \infty, \tag{1.b}$$

$$v_1(h,y) - v_2(h,y), \quad 0 \leq |y| < \infty, \tag{1.c}$$

$$u_1(h,y) - u_2(h,y), \quad 0 \leq |y| < \infty, \tag{1.d}$$

$$\sigma^1_{xy}(x,nc) - 0, \quad |x| < h, \quad n = -\infty, \ldots, \infty, \tag{1.e}$$
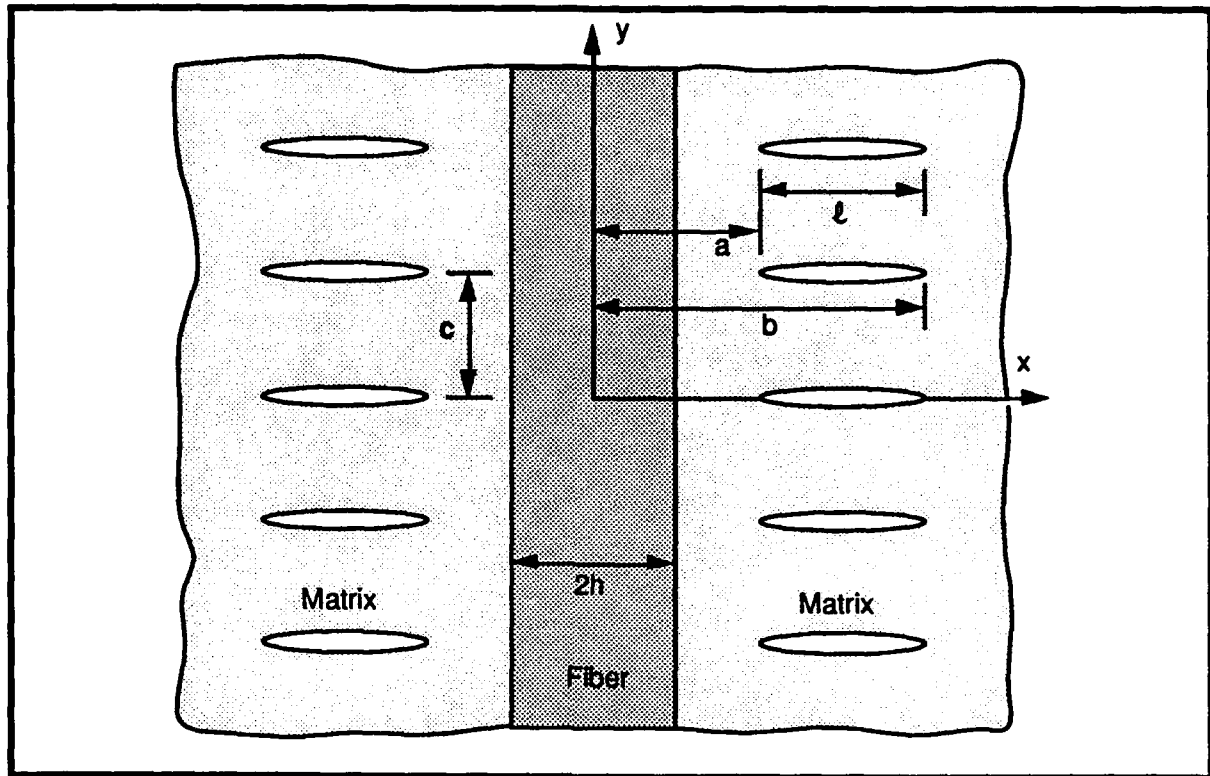
FIGURE 1. SCHEMATIC OF A PARALLEL PERIODIC ARRAY OF MATRIX CRACKS IN FIBER-REINFORCED COMPOSITES.

$$\sigma^2_{xy}(x,nc) = 0, \quad h<|x|<\infty, \quad n=-\infty,\dots,\infty, \tag{1.f}$$

$$v_1(x,nc) = 0, \quad 0<|x|<h, \quad n=-\infty,\dots,\infty, \tag{1.g}$$

$$v_2(x,nc) = 0, \quad h<|x|<a, \quad b<|x|<\infty, \quad n=-\infty,\dots,\infty, \tag{1.h}$$

$$\sigma^2_{yy}(x,nc) = -p(x), \quad a<|x|<b, \quad n=-\infty,\dots,\infty. \tag{1.i}$$

Equations (1.a-d) are the stress and displacement continuity conditions at the fiber-matrix interface, x-h. Equations (1.e-f) are the symmetry conditions. Equations (1.g-i) are the mixed boundary conditions on the line of the crack. The pressure p(x) is the arbitrary traction on each of the cracks and is same for all the infinite cracks.

The problem of periodic cracks is solved by first finding the normal stress in the y-direction at any x,y location for the problem of a single pressurized crack at y=0 (or n=0). The results from this problem are then superimposed by shifting the x-axis to all the infinite crack locations in the solution of the single crack. This gives the solution to the crack problem of the infinite periodic cracks of Figure 1.

The normal stress σ_{yy} in the matrix due to a single crack at y=0 is given by

$$\frac{\pi(1+\kappa_2)\ \sigma^2_{yy}(x,y)}{4\mu_2} = \int_a^b v(t)\ \left[\ \frac{3\ y^4 - 6(t-x)^2\ y^2 - (t-x)^4}{[y^2+(t-x)^2]^3}\right.$$
$$\left. + \sum_{i=1}^{2M+3}\sum_{j=1}^{M+5} C_{ij}\ (-1)^{j-1}\ \frac{d^{j-1}}{dx^{j-1}}\ \left(\frac{2h(i-1)+(x+t-2h)}{[2h(i-1)+(x+t-2h)]^2 + y^2}\right)\right]\ dt. \tag{2}$$

where C_{ij}'s are given in [12].

Now one can find the expression for the matrix normal stress at $y=0$ for the infinite periodic cracks by superposition [11]. The change in the normal stress in the y-direction in the matrix along $y=0$ due to the infinite periodic cracks is the infinite sum of contributions from equation (2) for values of $y = nc$, $n = -\infty,..,\infty$. Putting $y = nc$ in equation (2) and conducting the summation on n from $-\infty$ to ∞, one obtains the singular integral equation for the problem of an infinite array of periodic cracks as

$$-\frac{\pi(1+\kappa_2)\ p(x)}{4\mu_2} = \int_a^b \frac{v(t)}{(t-x)^2}\ dt + \int_a^b v(t)\ [K_a^s(x,t)+K_b^s(x,t)]\ dt, a<x<b, \quad (3)$$

where

$$K_a^s(x,t) = -6/c^2\ \iota_1\{(t-x)/c\} - 12\ (t-x)^2/c^6\ h_2\{(t-x)/c\}-(t-x)^4/c^6$$
$$h_3\{(t-x)/c\}, \qquad (4.a)$$

$$K_b^s(x,t) = \sum_{i=1}^{2M+3} \sum_{j=1}^{M+5} C_{ij}(-1)^{j-1}\ \frac{\pi}{c}\ \frac{d^{j-1}}{dx^{j-1}}\ \{Coth[\frac{\pi\ \{2h(i-1)+(x+t-2h)\}}{c}\ ]\},(4.b)$$

$$h_1(x) = \frac{1}{16}\ [x\ w_2'(x) + 3x^2 w_1''(x)]-w_2(x), \qquad (4.c)$$

$$h_2(x) = \frac{1}{16}\ [\ w_1''(x) + 3\ \frac{w_2'(x)}{x}\ ], \qquad (4.d)$$

$$h_3(x) = \frac{1}{16}\ [\ \frac{w_2'(x)}{x^3} + 3\ \frac{w_1''(x)}{x^2}\ ], \qquad (4.e)$$

$$w_1(x) = \sum_{n=1}^{\infty} \frac{1}{x^2 + n^2} - \frac{1}{2\ x^2}\ [\ \pi x\ Coth(\pi x) - 1], \qquad (4.f)$$

$$w_2(x) = \sum_{n=1}^{\infty} \frac{x^2 - n^2}{(x^2 + n^2)^2} - \frac{\pi^2}{2}\ Cosech^2(\pi x) - \frac{1}{2x^2}, \qquad (4.g)$$

$$w_3(x) = \sum_{n=-\infty}^{\infty} \frac{x}{x^2 + n^2} = \pi\ Coth(\pi x). \qquad (4.h)$$

Equation (3) has $\frac{1}{(t-x)^2}$ integrands and are called strong singularities. Such singularities are classically non-integrable and cannot be defined even in the Cauchy principal value sense. However, such problems can be solved provided the integral is interpreted in the Hadamard [13] sense by retaining the finite part only. This concept was used by Kaya and Erodgan [14] to develop formulas for strong singular integrals as found in this problem. The derivatives of the Coth function in eqn (4.b) were found by using the MACSYMA [15] symbolic manipulator.

The stress intensity factor at $x=b$ for uniform pressure $p(x)=p_0$ at the crack tip away from the interface is

$$K_1(b) = \lim_{x \to b+} \sqrt{2(b-x)} \ \sigma_{yy}^2(x,0) = \lim_{x \to b-} - \frac{4 \ \mu_2}{(\kappa_2 + 1)} \sqrt{2(b-x)} \ \frac{dv(x)}{dx}, \quad (5)$$

The stress intensity factor at x=a for uniform pressure $p(x)=p_0$ at the crack tip close to the interface is

$$K_1(a) = \lim_{x \to a-} \sqrt{2(x-a)} \ \sigma_{yy}^2(x,0) = 2 \ \mu^* \ \sqrt{2(x-a)} \ \lim_{x \to a+} \frac{dv(x)}{dx}, \quad a > h,$$

$$= \lim_{x \to a-} \sqrt{2}(x-a)^{1-\gamma} \ \sigma_{yy}^1(x,0) = 2 \ \mu^* \ \sqrt{2}(x-a)^{1-\gamma} \lim_{x \to a+} \frac{dv(x)}{dx}, \quad a = h, \quad (6)$$

where
　　γ is given by the root of the characteristic equation

$$2 \cos \pi(1-\gamma) + 4 \ q_2 \ \gamma^2 - (q_1 + q_2) = 0, \quad (7)$$

$$\mu^* = \frac{2 \ \mu_2}{(\kappa_2 + 1)} \quad \text{and} \quad \gamma = 1/2, \ \text{if } a > h,$$

$$\mu^* = \frac{\mu_1 \mu_2}{\sin \pi(1-\gamma)} \ [\ \frac{1 + 2q_1\gamma}{\mu_2 + \kappa_2\mu_1} + \frac{1 - 2q_2\gamma}{\mu_1 + \kappa_1\mu_2} \ ], \ \text{if } a = h. \quad (8)$$

RESULTS AND DISCUSSION

The normalized stress intensity factors at the crack tips are studied as function of fiber-matrix moduli ratio, and length, location and spacing of cracks. The results are presented for plane strain with constant pressure on the crack surfaces.

The stress intensity factors at the crack tips for the periodic cracking problem solved here are normalized by the stress intensity factor for the problem of periodic cracking in a homogeneous infinite plane (a→∞). The normalized stress intensity factors are then a direct measure of the degree of fracture toughening of the composite due to reinforcement. Values of the normalized stress intensity factor close to one show the insensitivity to the fiber reinforcement, while values away from one show the dominance of the fiber reinforcement over crack spacing.

Figures 2 and 3 show the normalized stress intensity factor at x=a and x=b, respectively, as a function of the normalized spacing parameter $(\ell/(\ell+c))$ for constant location of the crack to the interface. The value of the stress intensity factor for the case of periodic cracking in a homogeneous infinite plane (a→∞) $(K_{A\infty} = K_1(a)/(p_0\sqrt{(\ell/2)}))$ is also plotted,

if one is interested in the actual value of the stress intensity factors. The case of $[\ell/(2(a-h))=1]$ is close to the values obtained for the limiting case of a→∞. This implies that the fiber reinforcement has no effect on the stress intensity factors when the crack lengths are of the same order or less of the distance from the interface. The same conclusions were drawn in [11] for the problem of a half-plane with periodic cracks and traction free surface $(\mu_1=0)$. It is also seen that the stress inten-

sity factors away from the interface are insensitive to the fiber reinforcement for all crack spacings and crack locations. The stress intensity factor at x=a decreases as the location of the crack becomes
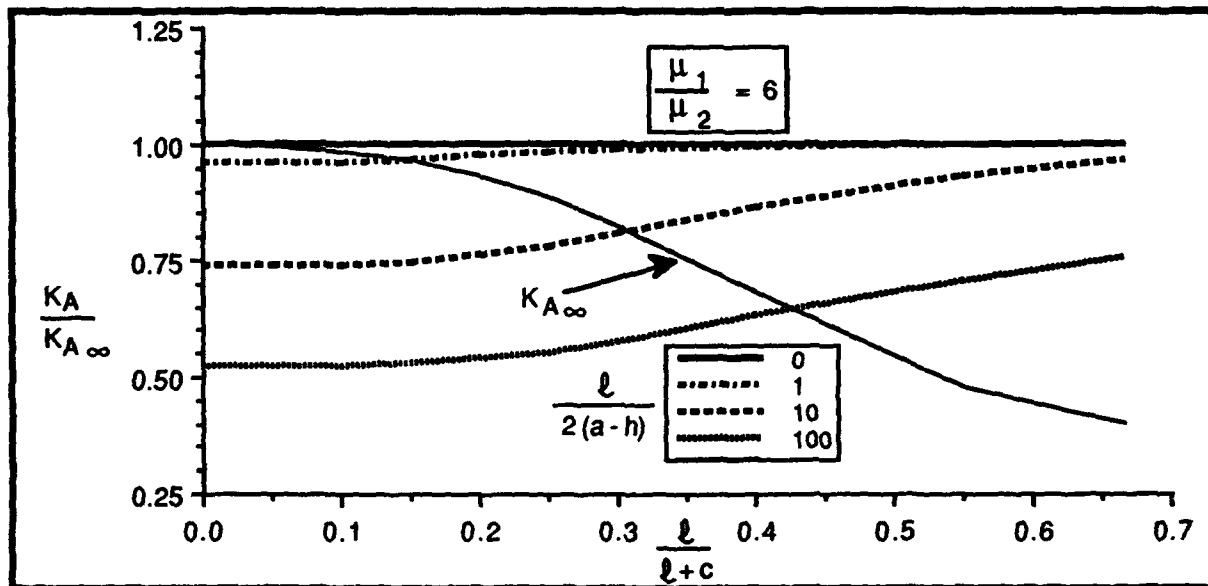
FIGURE 2. NORMALIZED STRESS INTENSITY FACTOR AT THE CRACK TIP NEAR THE INTERFACE AS A FUNCTION OF THE NORMALIZED CRACK LENGTH FOR CONSTANT CRACK LOCATION.
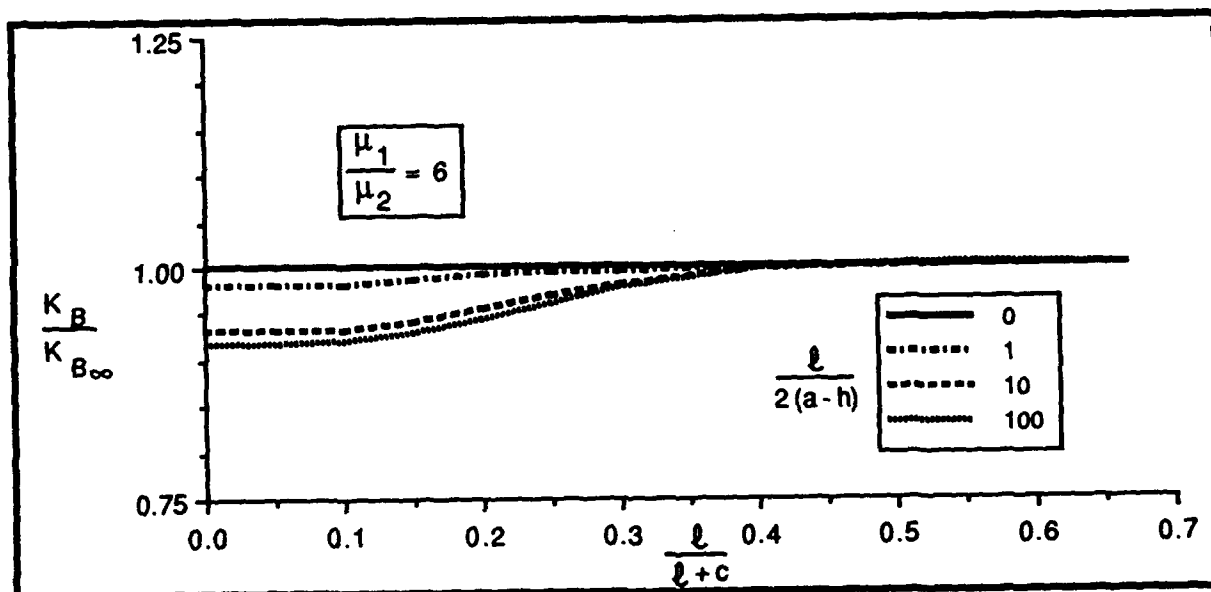
FIGURE 3. NORMALIZED STRESS INTENSITY FACTOR AT THE CRACK TIP AWAY FROM THE INTERFACE AS A FUNCTION OF THE NORMALIZED CRACK LENGTH FOR CONSTANT CRACK LOCATION.

closer to the interface. This shows that the crack growth towards the interface is stable if the fiber is stiffer than the matrix.

Figures 4 and 5 show the stress intensity factors at x=a and x=b, respectively, as a function of the crack spacing for constant fiber-matrix moduli ratio. The stress intensity factor at x=a is shown to decrease as a function of fiber-matrix moduli ratio. Also, the effect of the spacing of the cracks predominates the effect of the fiber-matrix moduli ratio as the crack spacing decreases to the order of the crack length. The stress intensity factor at x=b shows the same effect but not to such a large extent. The effect of the crack spacing in that case predominates that of the moduli ratio at crack spacings as high as one order higher than the crack length.

The results for the limiting case of the crack touching the interface are shown in Figure 6. The stress intensity factor at x=a (Eqn (6)) cannot be normalized as done for the previous results (Figures 2-5) because the stress at x=a does not have a square root type singularity. In this case, the stress singularity is given by the root of the characteristic eqn (7), while the intensity of the stress singularity is given by eqns (5) and (6). The stress intensity factors in this case are normalized with respect to the corresponding stress intensity factor for a single crack touching the interface (a=h, c=∞). From Figure 6, the stress intensity factor decreases as a function of the crack spacing, but has a more predominant effect when the fiber is stiffer than the matrix.

ACKNOWLEDGEMENTS
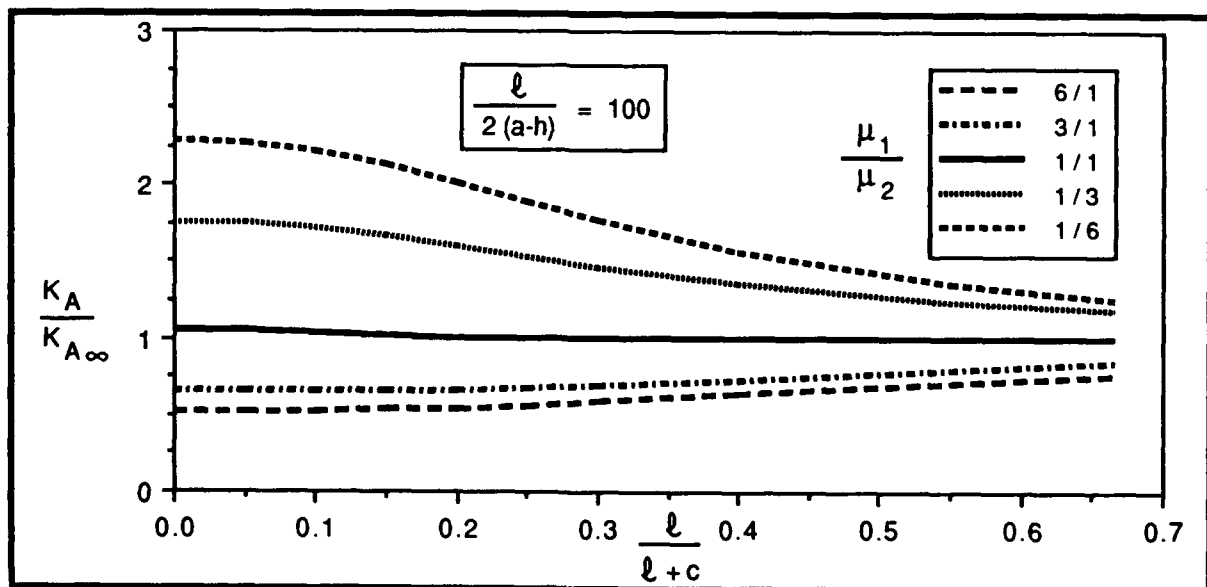
FIGURE 4. NORMALIZED STRESS INTENSITY FACTOR AT THE CRACK TIP NEAR THE INTERFACE AS A FUNCTION OF THE NORMALIZED CRACK LENGTH FOR CONSTANT FIBER-MATRIX MODULI RATIO.
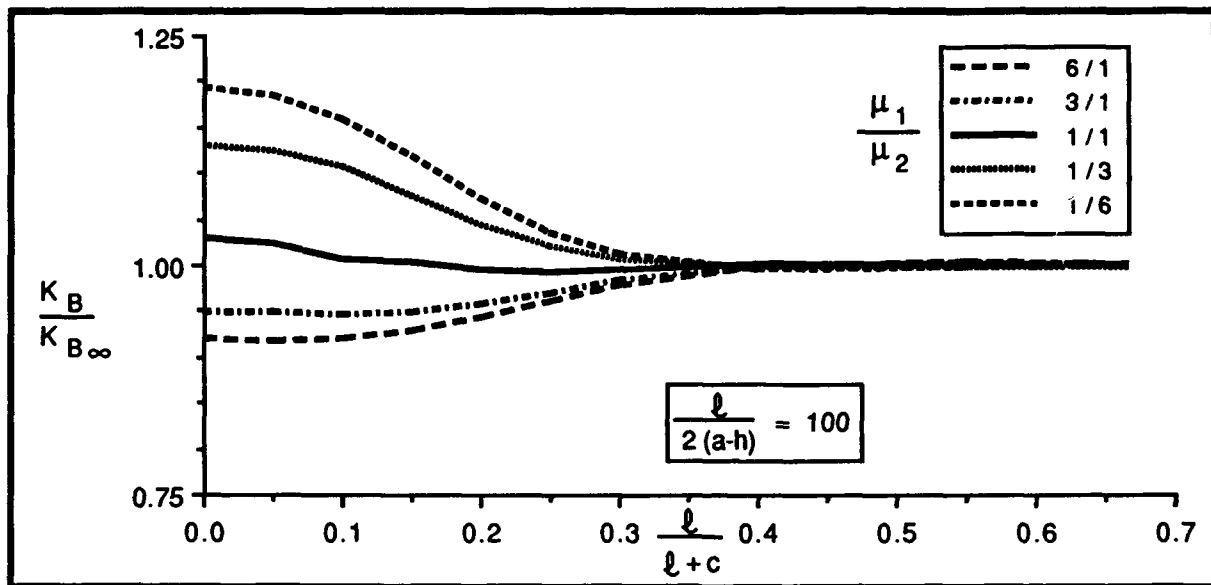
FIGURE 5. NORMALIZED STRESS INTENSITY FACTOR AT THE CRACK TIP AWAY THE INTERFACE AS A FUNCTION OF THE NORMALIZED CRACK LENGTH FOR CONSTANT FIBER-MATRIX MODULI RATIO.
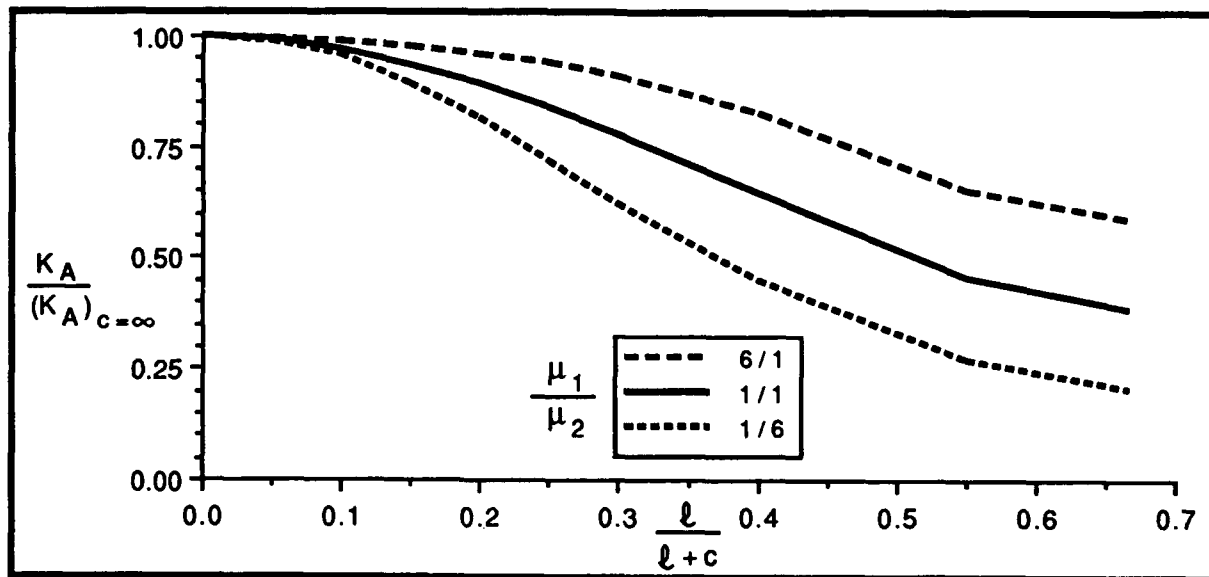
FIGURE 6. NORMALIZED STRESS INTENSITY FACTOR AT THE CRACK TIP AT THE INTERFACE AS A FUNCTION OF THE NORMALIZED CRACK LENGTH FOR CONSTANT FIBER-MATRIX MODULI RATIO.

REFERENCES

1. Brennan, J.J., and K.M. Prewo, 1982. "Silicon Carbide Fibre Reinforced Glass-Ceramic Matrix Composites Exhibiting High Strength and Toughness." Journal of Materials Science, 17:2371-2383.

2. Marshall, D.B., and A.G. Evans, 1985. "Failure Mechanisms in Ceramic-Fiber /Ceramic-Matrix Composites." Journal of the American Ceramic Society, 68:225-231.

3. Marshall, D.B., B.N. Cox, and A.G. Evans, 1985. "The Mechanics of Matrix Cracking in Brittle-Matrix Fiber Composites." Acta Metallurgica, 33:2013-2021.

4. Aveston, J., G.A. Cooper, and A. Kelly, 1971. "The Properties of Fiber Composites," in Proceedings of National Physical Laboratory, IPC Science and Technology Press, Surrey, England, 15-26.

5. Aveston, J., and A. Kelly, 1973. "Theory of Multiple Fracture of Fibrous Composites." Journal of Materials Science, 8:352-362.

6. Budiansky, B., J.W. Hutchinson, and A.G. Evans, 1986. "Matrix Fracture in Fiber-Reinforced Ceramics." Journal of Mechanics of Physics and Solids, 34:167-189.

7. McCartney, L.N., 1987. "Mechanics of Matrix Cracking in Brittle-Matrix Fiber-Reinforced Composites." Proceedings of the Royal Society of London, Series A, 409:329-350.

8. Bentham, J.P., and W.T. Koiter, 1973. "Asymptotic Approximations to Crack Problems," in Methods of Analysis and Solutions to Crack Problems, G.C. Sih, ed, Noordhoff, Netherlands, pp. 131-178.

9. Bowie, O.L., 1973. "Solution of Plane Crack Problems by Mapping Technique," in Methods of Analysis and Solutions to Crack Problems, G.C. Sih, ed. Noordhoff, Netherlands, pp. 179-191.

10. Nemat-Naseer, S., L.M. Keer, and K.S. Parihar, 1978. "Unstable Growth of Thermally Induced Interacting Cracks in Brittle Solids." International Journal of Solids and Structures, 14:409-430.

11. Nied, H.F. 1987. "Periodic Array of Cracks in a Half-Plane Subjected to Arbitrary Loading." ASME Journal of Applied Mechanics, 54:642-648.

12. Kaw, A.K., and G.H. Besterfield, 1992, "Mechanics of Multiple Periodic Matrix Cracks in Unidirectional Fiber-Reinforced Composites." International Journal of Solids and Structures, 29:1193-1207.

13. Hadamard, J. 1923. Lectures on Cauchy's Problems in Linear Partial Differential Equations, Yale University Press, New Haven, CT.

14. Kaya, A.C., and F. Erdogan, 1987. "On the Solution of Integral Equations with Strong Singular Kernels." Quarterly of Applied Mathematics, 45:105-122.

15. MACSYMA Reference Manual, 1985. Version 11, Symbolics Incorporated, Boston.

Application of In-Situ Scanning Acoustic Microscopy to Microfracture Characterization of Fiber Reinforced Composites

NOBUO TAKEDA, DONG YEUL SONG AND AKIRA KOBAYASHI

ABSTRACT

Scanning acoustic microscopy (SAM) has proven to be an excellent technique to study the fundamental roles of constituent materials including fibers, matrix and fiber/matrix interfaces in the microfracture process of composites, because the excellent contrast between fibers and matrix can be accomplished due to the large acoustic impedance mismatch. In the present study, in-situ SAM observation technique was developed to characterize the microscopic damage progress under tensile loading in injection-molded nylon 6 matrix composites reinforced with randomly-oriented short glass fibers. Three different kinds of fiber surface treatments were used to obtain composites with different static in-plane fracture toughness and drop-weight impact fracture resistance. Difference in microscopic damage progress of these three materials was investigated by the in-situ SAM technique, which revealed micro-deformation and fracture mechanisms such as, matrix plastic deformation and/or matrix microcracking, and fiber/matrix debonding and pull-out during the loading and unloading. These quantitative microscopic characteristics were, then, successfully correlated with the macroscopic fracture properties.

INTRODUCTION

Injection-molded fiber reinforced thermoplastic (FRTP) composites are being more extensively used in many load-bearing applications. Such interests have accelerated the recent studies on static and impact fracture properties of FRTP. The authors showed that fracture properties and damage developments are strongly influenced by fiber surface treatments in both static and impact loading conditions [1]. The detailed micromechanical characteristics, however, should be investigated to understand the fundamental roles of constituent materials including fibers, matrix and fiber/matrix interfaces in the microfracture process. Scanning acoustic microscopy (SAM) [2] has proven to be an excellent technique for detecting matrix plastic deformation and/or matrix microcracking, fiber/matrix debonding and pull-out [3, 4], because the excellent contrast between fibers and matrix can be accomplished due to the large acoustic impedance mismatch.

Nobuo Takeda, Dong Yeul Song, Research Center for Advanced Science and Technology, The University of Tokyo, 4-6-1 Komaba, Megoro-ku, Tokyo 153, Japan
Akira Kobayashi, Department of Mechanical Engineering, Faculty of Science and Engineering, Science University of Tokyo, 2641 Yamazaki, Noda-shi, Chiba 278, Japan

In the present study, in-situ SAM observation technique is developed to characterize the microscopic damage progress in FRTP compact-tension (CT) specimens. Three different kinds of fiber surface treatments are used to obtain composites with different static in-plane fracture toughness and drop-weight impact fracture resistance, and the difference in microscopic damage progress of these three materials is investigated. These quantitative microscopic features are, then, correlated with the macroscopic fracture properties.

EXPERIMENTAL PROCEDURE

TESTED MATERIALS

Injection-molded short glass fiber/nylon 6 plates (60 x 60 x 3 mm³, V_f = 30 %) were prepared with three different kinds of fiber surface treatments (denoted by materials D, E and F, Nippon Glass Fiber Co., Ltd.). Average fiber length and diameter were 300 μm and 13 μm, respectively. There exists some anisotropy in mechanical properties because of fiber orientation effects [1]. The molded specimens were kept at about 20 % humidity until testing (water weight content: approximately 2 %). Several mechanical properties are summarized in Table I.

TABLE I - SUMMARY OF MECHANICAL PROPERTIES OF TESTED FRTP COMPOSITES

Material	Tensile Strength [MPa]	E_{IZOD} [kJ/m²] (with notch)	E_{IZOD} [kJ/m²] (without notch)	H_{50} [cm]	E_{50} [J]	P_1 [kN]	E_1 [J]	E_t [J]	J_c [kJ/m²]
D	163.2	8.1	73.8	29.5	0.87	1.40	0.66	3.46	7.8
E	162.3	8.4	77.9	37.5	1.10	1.48	0.72	3.70	10.3
F	157.2	7.3	63.8	27.0	0.79	1.28	0.53	2.95	7.3

DROP-WEIGHT IMPACT TESTS

Two types of drop-weight impact tests were conducted. The first test was a simple drop-weight test. A 300-gram weight was fallen from prescribed heights on a cylinder, whose head was of hemispherical shape with 12.7 mm in diameter and contacted with the specimen plate. The height where 50 % of tested specimens had an initial detected crack (denoted by H_{50}) and the corresponding absorbed energy (E_{50}) were calculated. The second test was an instrumented drop-weight test, where the shape of the impactor was similar to that of the first test. The impactor energy of 10 J (2 kg, 3.2 m/s) was well above the perforation energy, and the dynamic load (or energy)-time diagrams were recorded. A strain gage was adhered on the specimen surface to monitor the crack initiation upon impact.

STATIC IN-PLANE FRACTURE TOUGHNESS TESTS

In-plane crack growth behavior was monitored using CT specimens with two acoustic emission (AE) sensors on surfaces. The crack growth direction was chosen to correspond to the injection-mold direction. The J-integral approach was used to consider stable crack

growth and nonlinear load *P*-COD δ curves. The *J*-values were calculated at different loading stages, and then, the critical *J*-value (J_c) was determined at the point where the critical increase in the cumulative AE energy occurred. This critical point corresponded well with the optically-detected unstable crack growth [1].

IN-SITU SAM OBSERVATIONS

Surface and subsurface images were obtained with a SAM (Olympus UH-3). Input r. f. pulses are supplied to the piezoelectric transducer through a circulator and a matching-box unit, and then a planar longitudinal wave is introduced into a sapphire rod. Water is used as a couplant, and the sapphire/water interface acts as an acoustic lens. The wave is focused on the specimen surface or subsurface. The reflected acoustic wave is then amplified for signal processing to obtain the acoustic image of the specimen, which depends on the elastic modulus, density and viscosity of the specimen [3]. The 200 or 400 MHz burst signals were used in the present study. A loading apparatus, as shown in Fig. 1, was developed for in-situ observations of microscopic damage progress near the crack tip under tensile loading in CT specimens.
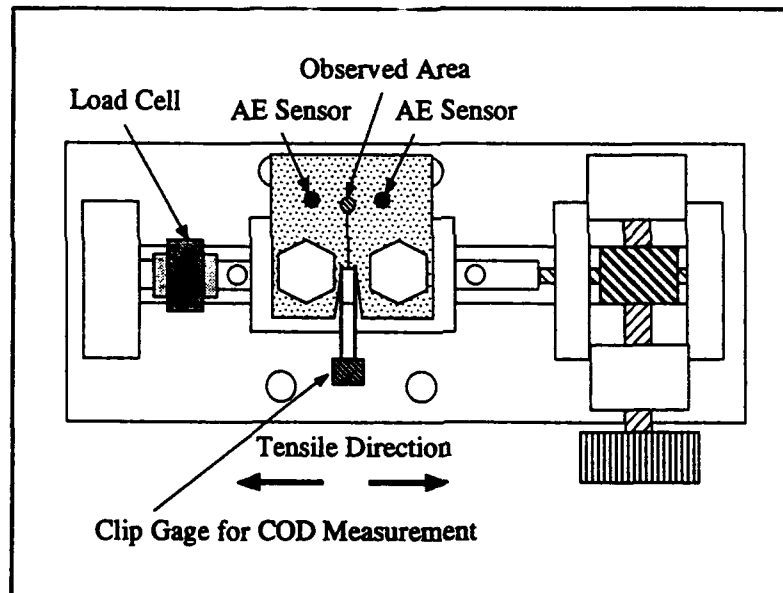
Figure 1. Loading Apparatus for In-Situ SAM Observations in Static In-Plane Fracture Toughness Tests.

RESULTS

Drop-weight impact test results are summarized in Table I. The H_{50} or E_{50} values increase in the order of materials F, D and E. The initial crack always extends in the mold fill direction just beneath the impact point at the back surface, which is due to the fiber orientation effects. In the load(or energy)-time diagrams of instrumented drop-weight tests, the crack initiation on the tensile surface could be detected by a sudden change in the strain-gage output, and corresponded well with the first peak load (P_1) or the corresponding energy (E_1) in the dynamic load diagram. The total absorbed energy, E_t, indicates the overall energy absorbing capability.
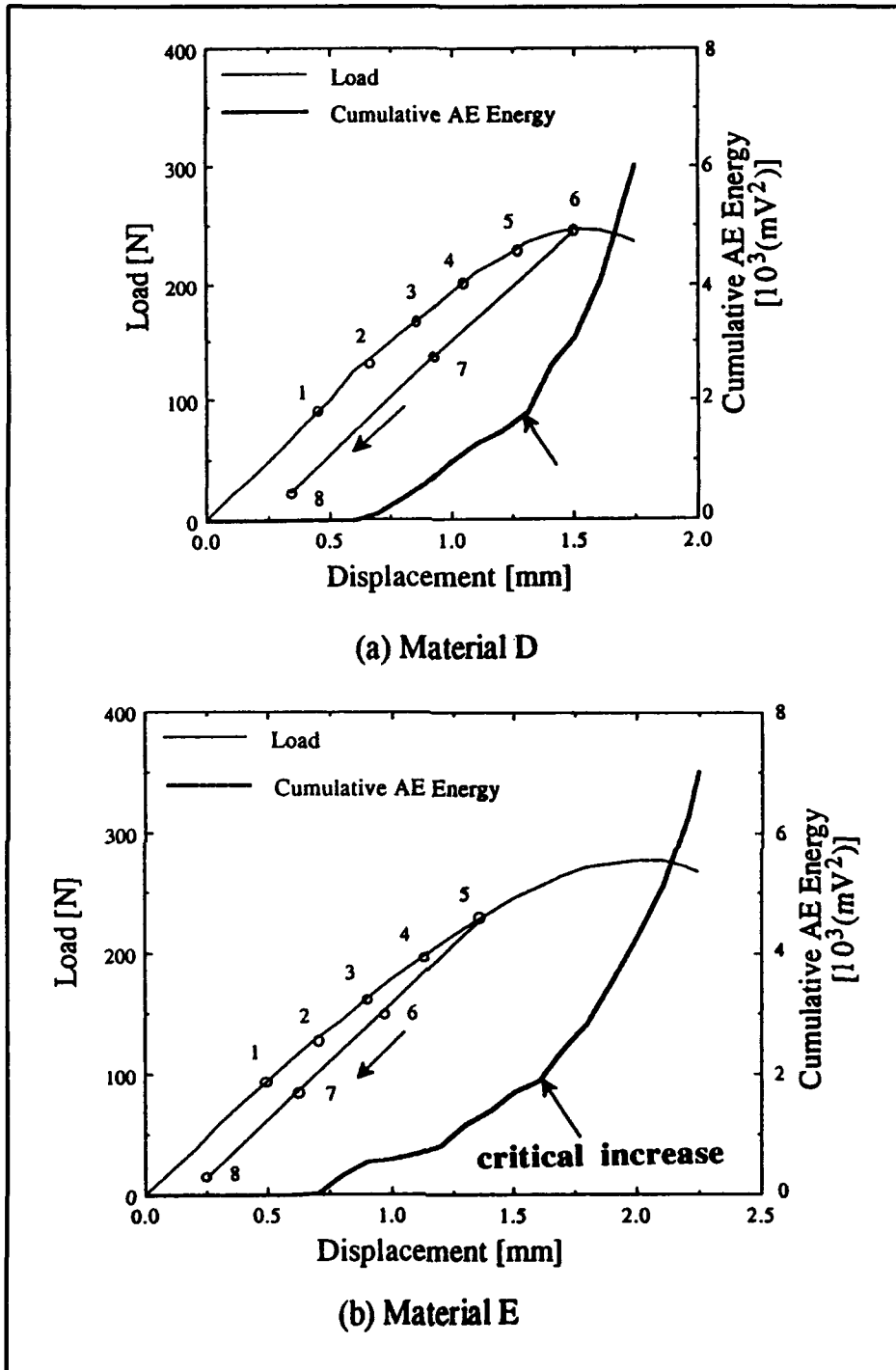
Figure 2. Load P-COD δ Diagrams and Cumulative AE Energy in Static In-Plane Fracture
Toughness Tests.   An arrow indicates a critical increase in the cumulative AE energy.
(a) Material D, (b) Material E

Typical P-δ curves with cumulative AE energies are shown in Fig. 2.   The J-δ diagrams
are then obtained using these data.   The critical displacement for unstable crack growth, δ_c,
can be determined by the point where the increasing rate of the cumulative AE energy becomes
large.   Comparison of J_c values is also summarized in Table 1.
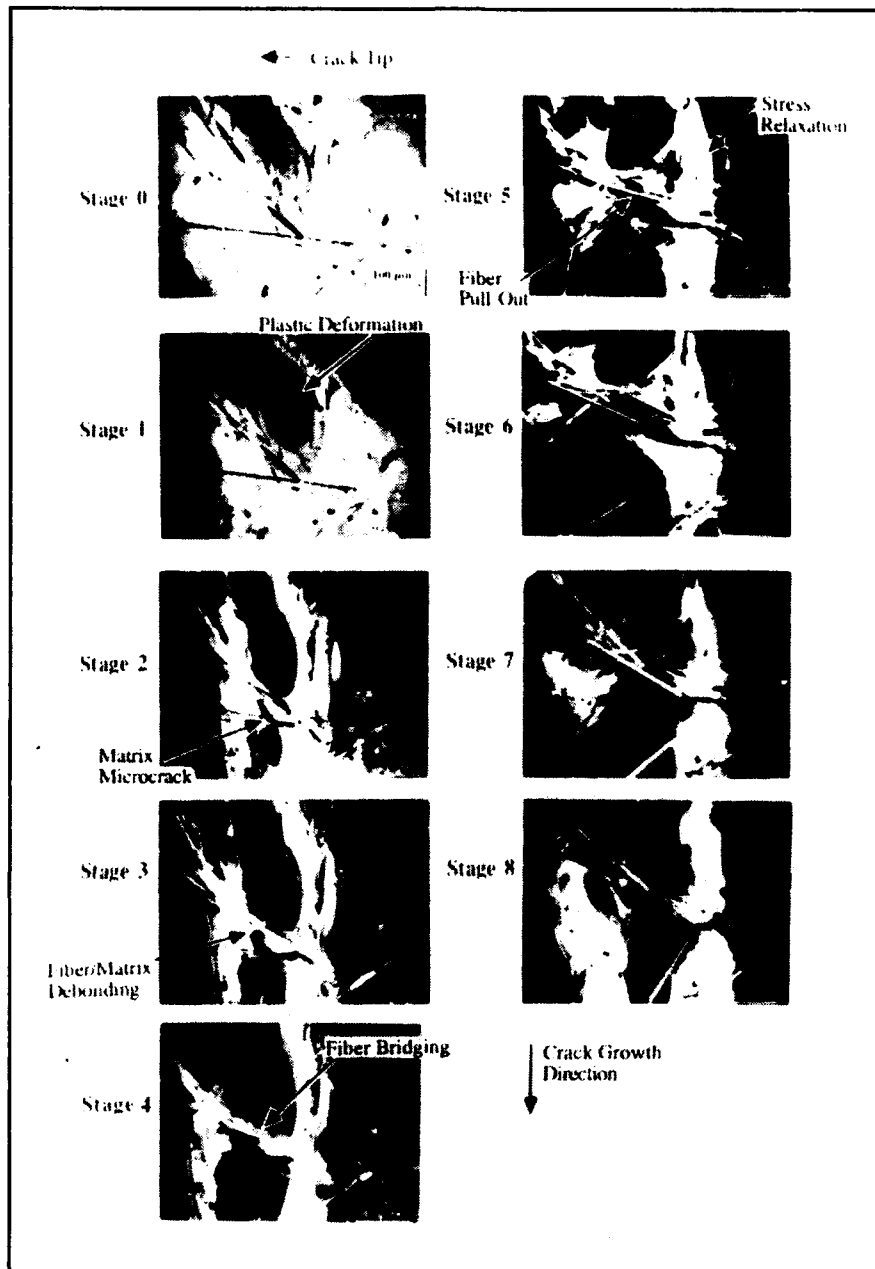
Figure 3. In-Situ SAM Surface Images of Damage Progress near Crack Tip for Material D.
Stage numbers correspond to those in Fig. 2(a).   Quantitative load levels can be
determined for local matrix plastic deformation, matrix microcracking, fiber/matrix
debonding and fiber pull-out.

In-situ SAM surface images of damage progress near a crack tip are shown for material D
in Fig. 3, where the loading stage numbers correspond to those in Fig. 2 (a).   Materials D
and F are similar in SAM surface images, which reflects similar fiber/matrix interfacial
properties as well as macroscopic static and impact properties.   SAM photos along crack
paths are shown for material F in Fig. 4.   Figure 5 shows in-situ SAM surface images of
damage progress near a crack tip for material E, where the loading stage numbers correspond
to those in Fig. 2 (b).   Fiber/matrix interfacial strength is expected to be higher for material E
than materials D and F.   Damage zone near a crack tip is shown for material E in Fig. 6.
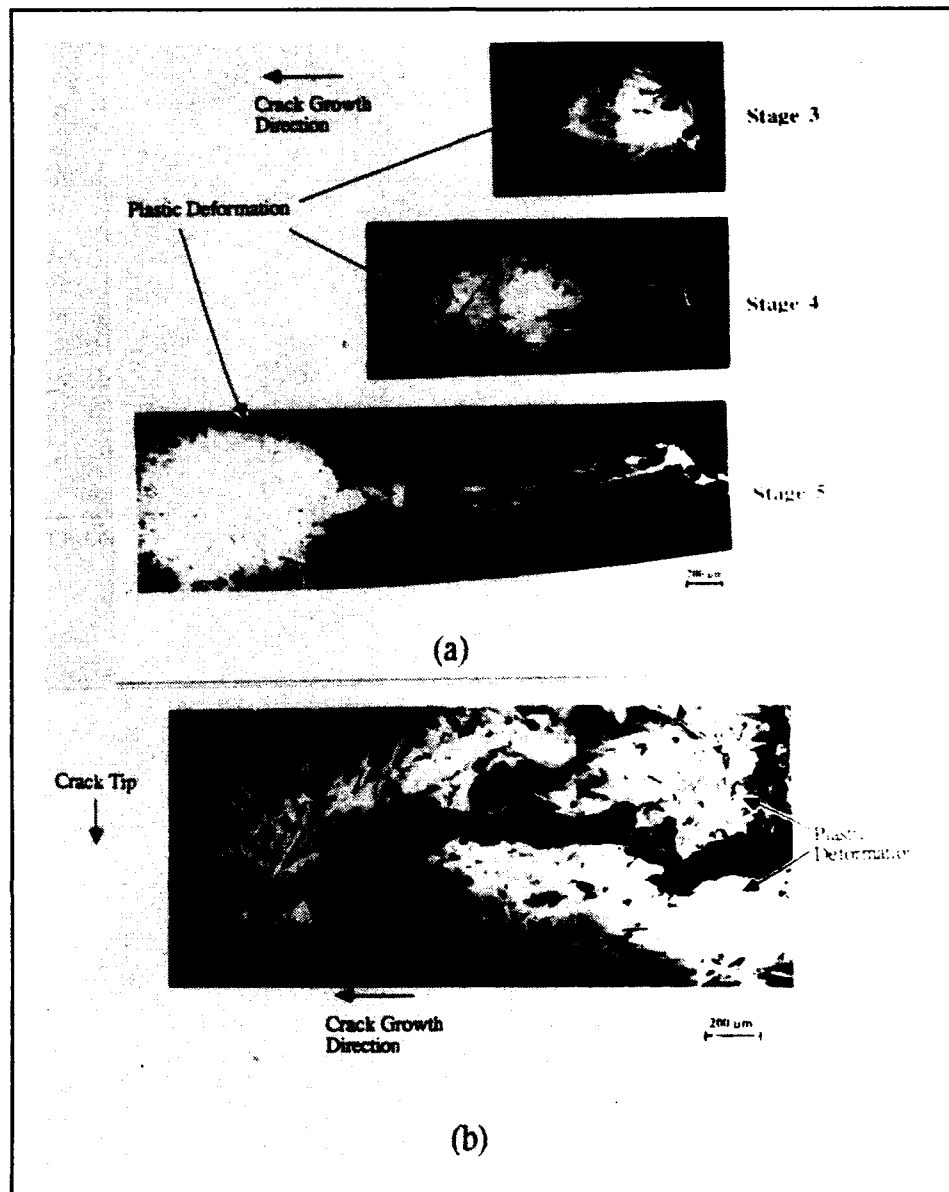
Figure 4. In-Situ SAM Surface Images along Crack Paths for Material F.
(a) Crack Growth and Damage Development.   The load level at each stage number is
similar to the one at the same stage number in Fig. 2 (a) for material D.
(b) Residual Plastic Deformation along Crack Path behind Crack Tip after Unloading.

DISCUSSION

All the drop-weight impact characteristic values of H_{50}, E_{50}, P_1, E_1 and E_t increase in the order of materials F, D and E, as listed in Table I.   Among all, both P_1 (or the corresponding energy E_1) and E_{50} provide most useful parameters which correspond to the first cracking on the tensile surface and which demonstrate well the impact fracture performance of materials. However, the P_1 or E_1 value is more reliable than the E_{50} value, because the instrumented drop-weight test is much more well documented.   The static fracture resistance parameter J_c also increases in the order of materials F, D and E, which agrees well with the order in impact fracture parameters.   Thus, the correlation between static in-plane fracture toughness and drop-weight impact properties is found noticeable in this composite system, which is expected
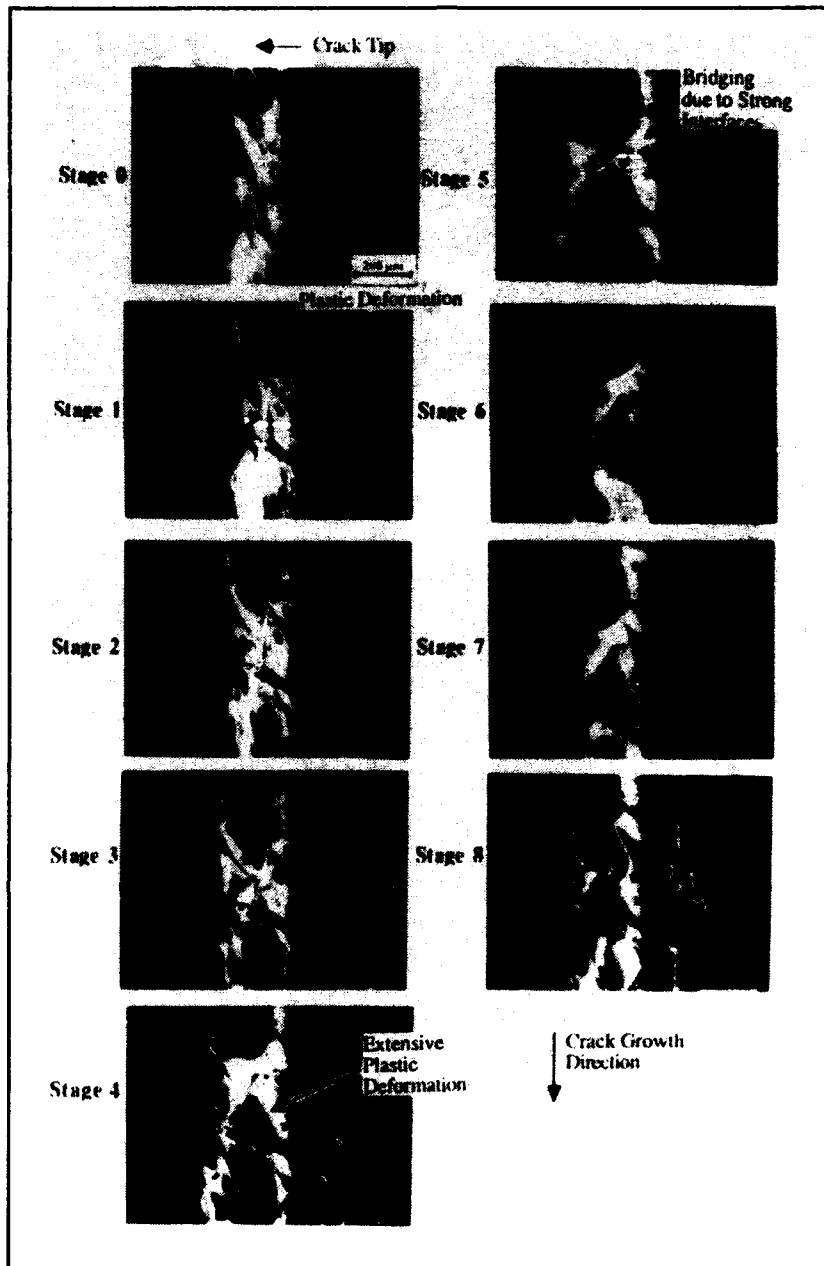
Figure 5. In-Situ SAM Surface Images of Damage Progress near Crack Tip for Material E.
Stage numbers correspond to those in Fig. 2(b).

to hold true in general thermoplastic composites. This indicates that one property can be predicted by the other one.

In general, black and white contrast in acoustic images of FRTP specimens is determined from the following acoustic factors:

(a) Difference in reflection indexes of fibers and resin,
(b) Difference in surface wave speeds,
(c) Difference in attenuation coefficients, and
(d) Surface curvatures.

Since the observed specimen surfaces are almost flat, the factor (d) can be neglected in the present study. Factors (a), (b) and (c) are discussed in the following.
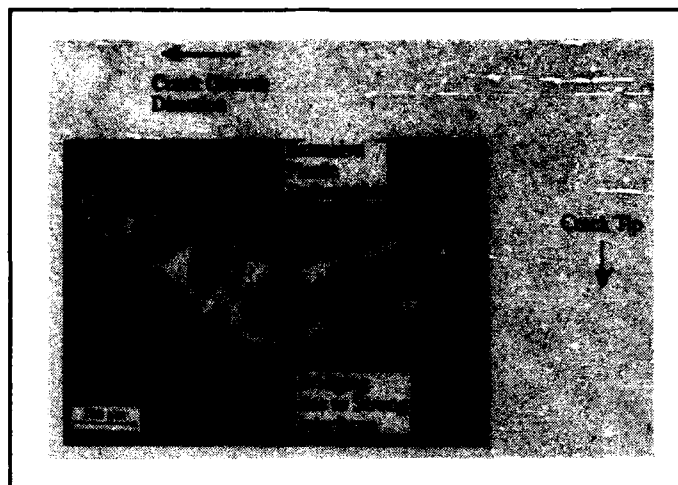
Figure 6. SAM Surface Image along Damage Zone near Crack Tip for Material E.
Strong fiber/matrix interfaces introduced much plastic deformation in matrix.

Difference in reflection indexes of fibers and resin corresponds to the difference in acoustic impedances Z of constituent materials. The reflection ratio R is calculated from the following equation: $R = (Z_1 - Z_2)^2 / (Z_1 + Z_2)^2$, where subscripts 1 and 2 denote fibers and resin, respectively. Fibers and resin can be more clearly distinguished in SAM photos than in optical micrographs. Moreover, SAM reveals various features on flat specimen surfaces, which cannot be clearly observed by scanning electron microscopy (SEM). Large acoustic impedance mismatch is expected for fiber/resin debonding, where the brightness at the debonded region becomes large (for example, see Stages 3 and 4 in Fig. 3).

Let us consider the acoustic contrast at crack-tip regions of specimen surfaces, as shown in Fig. 4 (a). This contrast at specimen subsurfaces clearly changes if the focal depth is deeper [4]. The above contrast at the crack-tip region is believed to correspond to the highly plastically-deformed region, which appears due to the difference in surface wave speeds.

Surface SAM images after unloading in Fig.4 (b) show clear acoustic contrast along the crack path. Acoustic impedance mismatch is small between water and the present specimen itself, and the reflection ratio is small at the specimen surface. Attenuation of surface waves was measured to be 3-9 dB close to the crack path. This high attenuation along the crack path, which corresponds to residual crazing or plastic deformation, gives strong contrast even in surface images.

As shown in Figs. 3-5, quantitative load levels can be determined for micromechanical fracture events such as, local matrix plastic deformation, matrix microcracking, fiber/matrix debonding and fiber pull-out. No other experimental techniques could not accomplish such quantitative analysis of microfracture events directly related to individual fibers, matrix and fiber/matrix interfaces. First, let us discuss the damage progress for material D in Fig. 3. Plastic deformation near a crack tip begins to grow at Stage 1. Matrix microcracking also begins to open at Stage 2. In addition, fiber/matrix debonding occurs at Stage 3 from the matrix microcrack connected with the fiber/matrix interface. It should be noted that the debonded fiber surface becomes highly bright due to the wave reflection. Moreover, fiber bridging can be clearly distinguished at Stage 4. Then, fiber pull-out occurs at Stage 5, where the stress relaxation in matrix around the pull-out fiber is observed. Fiber pull-out is completed at Stage 6, which corresponds to the maximum load in the present specimen. Stages 7 and 8 during unloading demonstrate that the permanent damages have occurred and cannot be recovered.

Fiber/matrix interfacial strength in material E is expected to be superior to those in materials D and F, since all the macroscopic mechanical properties are better. Damage progress sequences in material E are quite different from those in materials D and F, as shown

in Fig. 5. Strong interfaces introduce much more crazing or plastic deformation in the matrix region, and few matrix microcracks and fiber debondings can be observed up to Stage 5. Fibers bridge highly-deformed craze regions. SAM observations under further loading were difficult due to the highly-deformed crazing. An attempt is being made for in-situ SAM observations under further loading. Thus, difference in micro-deformation and micro-fracture process due to different fiber surface treatments was well demonstrated in Figs. 3 and 5.

CONCLUSIONS

The in-situ SAM observation technique was developed to characterize the microscopic damage progress under tensile loading in injection-molded nylon 6 matrix composites reinforced with randomly-oriented short glass fibers. Three different kinds of fiber surface treatments were used to obtain composites with different static in-plane fracture toughness and drop-weight impact fracture resistance. Difference in microscopic damage progress of these three materials was investigated by the in-situ SAM technique, which revealed micro-deformation and fracture mechanisms such as, matrix plastic deformation and/or matrix microcracking, and fiber/matrix debonding and pull-out during the loading and unloading stages. These quantitative microscopic characteristics were, then, successfully correlated with the macroscopic fracture properties.

The present in-situ SAM technique is also quite effective to characterize other types of composites such as CFRP, metal matrix composites and ceramic matrix composites. The study is in progress for these composites.

ACKNOWLEDGEMENTS

REFERENCES

1. Takeda, N. and K. Nakata. 1989. "Effects of Fiber Surface Treatments on Static and Impact Fracture Toughness of Injection-Molded GFRTP Plates," in Proc. 1st Japan SAMPE Symp. (Chiba, Japan, Sept. 1989), N. Igata et al. ed., Tokyo: Nikkan Kogyo Shinbun, Ltd., pp. 1350-1355.

2. Lemons, R. A. and C. F. Quate. 1979. "Acoustic Microscopy," in Physical Acoustics, Vol. XIV, W. P. Mason and R. N. Thurston, ed., New York: Academic Press, Inc., Chapter 1.

3. Hollis, R. L., R. Hammer, and M. Y. Al-Jaroudi. 1984. "Subsurface Imaging of Glass Fibers in a Polycarbonate Composite by Acoustic Microscopy," J. Materials Science, 19: 1897-1903.

4. Takeda, N., C. Miyasaka and K. Nakata. 1991. "Microfracture Process Characterization of Short Glass Fiber Reinforced Thermoplastic Composites by Scanning Acoustic Microscopy," in Proc. 8th Int. Conf. Comp. Mater. (Hawaii, July 1991), S. W. Tsai and G. S. Springer, ed., Covina, CA: SAMPE Int., Section 27-J.

Microstructural Design of C/C Composite

SHIUSHICHI KIMURA, EIICHI YASUDA, YASUHIRO TANABE, HIDEKI HORIZONO AND SEI-MIN PARK

ABSTRACT

Since the graphitic crystal shows strong anisotropy, the key technology in the development of carbon-carbon (C/C) composite into a tailored material is the control of anisotropy by changing the microstructure of fiber and matrix carbons, and fiber arrangement.

Microstructure of glassy carbon and pitch derived carbon could be changed by addition of fine graphite powder and/or metal compound powder less than 5%. In carbonized composite, the fracture pattern changed by the addition of graphite powder from catastrophic tensile failure to fiber-pull out failure.

Fiber orientation and fiber arrangement are also important factors. In a UD composite off-axis test cleared that the strength followed well the maximum stress theory, and inter laminar shear strength play an important role to the fracture of C/C composite. ILSS of glassy carbon matrix composite was low as 20MPa, but it increased to 40 MPa by heat treatment at 2600°C. Addition of TiO_2, SiC change not only the microstructure, but also the oxidation performance of the carbon materials.

1. INTRODUCTION

Carbon/Carbon (C/C) composite is an excellent material, not only for aerospace applications but also for structural ones at high temperatures, e.g., gas-turbine components, because it has a specific light weight, a low thermal expansion coefficient and a high strength at elevated temperatures. However, the graphitic crystal possesses strong anisotropy, so that one key technology in the development of C/C composites is the control of anisotropy by purposefully arranging the microstructure of both fibers and matrix carbons. The Young's modulus of graphitic crystal in an off-axis can be expressed as a function of Ψ ($\Psi = \cos\Phi$) as follows[B.K 86];

Shiushichi KIMURA: Facul. of Engig, Tokyo Institute of Technology, 2-12-1 Ookayama, Meguro-ku, Tokyo, 152 JAPAN
Eiichi YASUDA, Yasuhiro TANABE, Hideki HORIZONO and Sei-Min PARK: R.L.E.M., Tokyo Institute of Technology,
4259 Nagatsuta, Midoriku, Yokohama, 227 JAPAN.

$$1/E = S_{11}(1-\Psi^2)^2 + S_{33}\Psi^4 + (2S_{13}+S_{44})\Psi^2(1-\Psi^2) \tag{1}$$

Therefore the deformation of graphite crystal in off-axis from 20° to 87° against c-axis is mainly governed by the shear modulus. Young's modulus of polycrystalline material is also able to express as summation of each crystallite component.

The carbon/carbon composite which is composed of controlled types and shapes of graphitic crystal will also show strong anisotropy. In short we judge that, control of microstructure is the key technology for the successful development of the tailored C/C composites.

This paper deals with one possible way to control the microstructure including a metal compounds addition and therefore the relation between microstructure and mechanical properties of the C/C composites. In addition, oxidation behavior of metal compounds addition are discussed.

2.EXPERIMENTAL

Furfuryl alcohol condensate (Hitafuran 302) was used as a starting material of the matrix in the C/C composite. UD composite was prepared by a filament winding technique after impregnating the resin into fiber tows. After curing at 100°C for few days it was carbonized at 1000°C for 2 hours and graphitized at 2600-3000°C for 30 minutes in flowing Ar gas[S.K.75]. To better control the microstructure, two different kinds of powders were used. The first employed is fine graphite powders of ca. 1 μm in diameter. The other utilized are metal compounds such as HfC, HfO$_2$, Si, SiC, SiO$_2$, Ti, TiC, TiO$_2$, ZrC and ZrO$_2$. In both cases 1 w/o graphite powder or 5 w/o metal compound powder was added into the furfuryl alcohol condensate directly.

XRD analysis using Ni-filtered Cu-Kα was carried out to examine the graphitization. (002) profiles were used both for measuring the interlayer spacing $d_{(002)}$ and the crystallite size (Lc). Si metal powders were used as an internal standard. (002) XRD profiles were separated into three assumed components: graphitic(G), turbostratic(T), and broad(B) components. The deconvolution calculation was based upon a Damped Least-Square method. Each component was separated into a Kα_1 component and a Kα_2 component. Only the Kα_1 component was used for calculation of $d_{(002)}$ based on JSPS method[JSPS78]. Quantitative analysis was carried out by calculations of the products of intensity and width at half maximum(°) of separated peaks. Microstructure of the specimens after heat-treatments was further investigated through optical microscope under polarized light (Nikon HFX-II, Japan).

Flexural test was carried out for the specimens of 50 mm long, 10mm wide and 1-2 mm thick. Span/depth ratio was selected to be 20-40 depending on the fracture pattern. Shear test was carried out by double notched specimen of 50x11x2 mm following the test method of ASTM D-3846. Oxidation behavior was measured by thermo-gravimetric analysis in a flowing air with a heating rate of 5°C/min up to 950°C using specimen of 10mmx10mmx2mm.

3. RESULTS AND DISCUSSION
3-1: MICROSTRUCTURAL CHANGE OF MATRIX

3-1-a: Powder additions to thermosetting resin derived char

Thermosetting resin generally yields glassy carbon even if it is heat
treated at above 3000° C.   However, when it is combined with carbon fiber, the
shrinkage of the resin during carbonization (ca. 30%) assists the internal
shear strain of the matrix during carbonization which causes the preferred
orientation of the graphite layer, surrounding the fiber[E.Y.87].
Microstructural change of the furan resin derived carbon matrix composite is
shown in **Fig.1**.   At above 2200° C the graphitic component can be detected by
both X-ray and optical microscopy.   At above 2600° C all the matrix carbon
change into the graphitic component.
     Figure 2 represents the optical microscopic observation of the addition
of graphite powder and metal compounds added specimens after heat-treatment at
2600° C.   As can be seen in **Fig.2**, even though mixed resins with additives
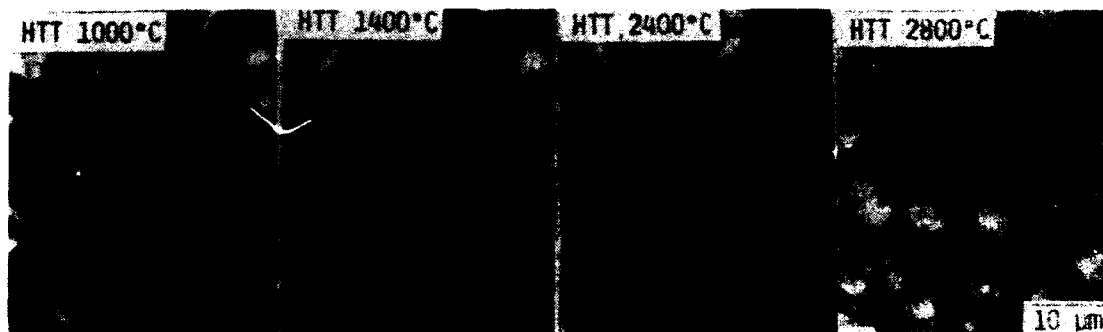
Fig.1. Microstructural change of furan resin matrix composite with heat
        treatment temperature. (Optical micrograph under closed Nichols).
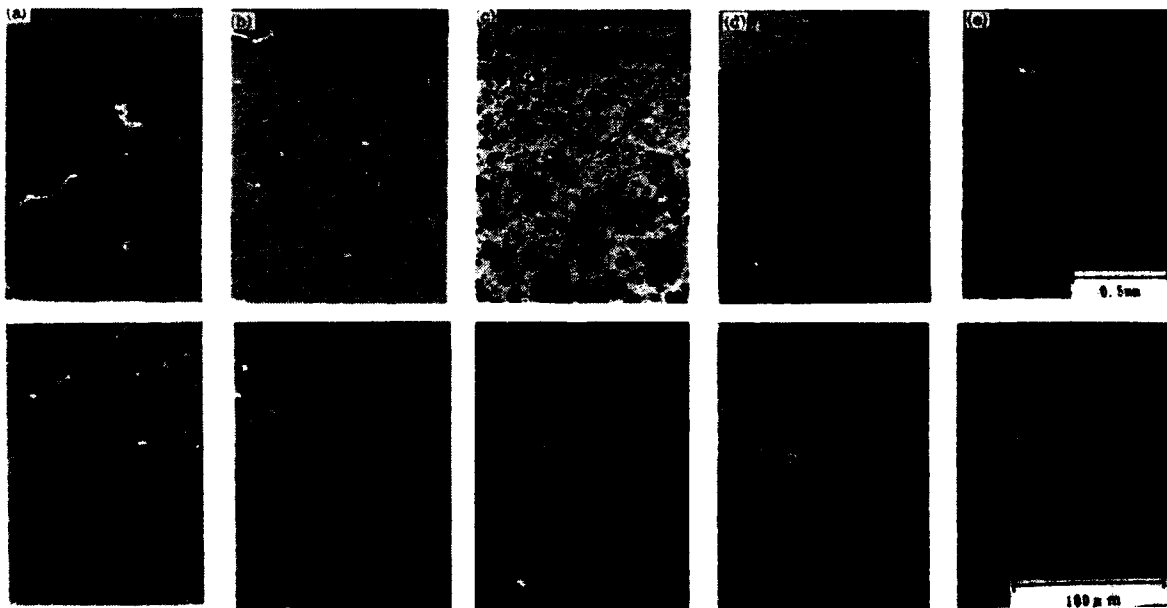
Fig.2. Change of microstructure of furan resin derived carbon heat treated
        at 2600° C with the addition of metal compounds.
        (a): TiO_2, (b): ZrO_2, (c):Si (d): SiC and (e):graphite.
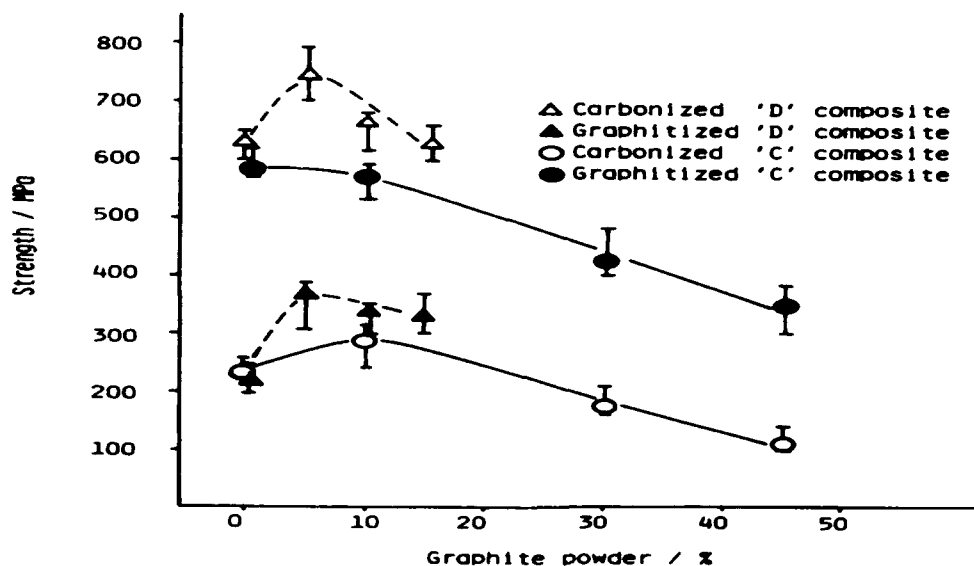
Fig.3. Effect of graphite powder addition on flexural strength of furan
        resin derived matrix C/C composites.

C:Surface treated fiber,   D: Non-Surface treated fiber

Flexural strength of graphite powder added composite is shown in **Fig.3**.
Too much addition decrease the strength, but few percent addition is effective
for the increase of the strength in both case of carbonized and graphitized
composite[E.Y.88].

3-1-b: Addition of graphite powder to the pitch derived matrix

When the pitch contains a benzene soluble component and does not contain a
pyridine insoluble component, the pitch provides a flow texture carbon.
During carbonization Brooks-Taylor type mesophase spherules grow and develop.
Wettability of the mesophase is very good to the carbon materials, so that the
mesophase spherules grown in the matrix pitch attach to the fiber and sur-
round all the carbon fibers, aligning the c-plane parallel to the fiber direc-
tion[J.W.89].

Graphite powder addition to the pitch was also shown to be effective for
changing the microstructure.   We observed that the flow type texture of the
matrix changes into uniform fine mosaic microstructure with the addition of
graphite powder less than 1 w/o.   The flexural strength of the carbonized
composite also increased by 50% with the addition of graphite powder as shown
in **Fig.4** [E.Y.89].   Both carbonized composites and graphitized composite
showed the increase of the flexural strength.   The increased tensile strength
will depend on the strengthening of the brittle matrix by the addition of the
graphite powder.

Table 1: Effect of metal compounds addition on the X-ray parameters, the
contents graphitic component and weight loss after TG measurement.
HTT: heat treatment tempcrature.   *: Sedimentation occurred.

Additive	G-component after 2600°C		Weight loss after TG analysis	
	d(002) (A)	content(%)	HTT:1000°C	HTT:2600°C
Reference	3.361	1	90	34
C/C compo.	3.371	17	89	36
Graphite	3.359	26	-	34
HfC	3.367	2	69	16
HfO2 *	3.369	6	61	9
Si *	3.369	20	-	61
SiC	3.399	56	57	38
SiO2	-	-	63	-
Ti	3.363	9	66	18
TiC	3.364	9	67	31
TiO2	3.365	47	54	81
ZrC	3.368	10	83	20
ZrO2 *	3.371	10	-	22

were ball-milled for 24h, ZrO_2 HfO_2 and Si powders   gave sedimentation after
pouring into a polystyrene container.   All the metal added carbons
contained large pores. The reason is not clear yet, but we believe it arises
from the reaction of metal with hardener of paratoluensulfonic acid.

On the other hand, all the specimens heat-treated at 2600°C represented
typical multi-phase graphitization.   The oxidized additives from carbides or
metals changed into carbides again after heat treatment at 2600°C.   Interlay-
er spacing $d_{(002)}$ and Lc heat-treated at 2600°C are summarized in Table 1.
The graphitic components of the neat resin (reference) and the C/C composite
were 1% and 17% respectively.   Additions of TiO_2 and SiC promoted superior
graphitizability of carbon matrices.   The contents of the G-component in the
TiO_2 and SiC were 47% and 56% respectively.

These graphitization behaviors of metal compounds added carbons are con-
sidered to be due to the catalytic graphitization, and stress-induced graphi-
tization.   The catalytic graphitization mechanism[M.I.72] in G-effect has
been explained through the mechanism of solution-reprecipitation of carbon.
In the binary system of Si and C, the incongruent melting   temperature of
SiC/C system is 2545°C and the decomposition temperature is 2840°C.   The
eutectic temperatures of HfC, ZrC, and TiC with carbon system are 3150, 2876
and 2776°C respectively[T.M.86]. Considering above, reprecipitation from
liquid would be difficult to occur except for SiC.

TiO_2 added carbon displayed strong graphitization, however, Ti metal added
or TiC added carbon did not yield strong graphitization.   Considering from
the eutectic temperature of Ti-C system, the graphitization by TiO_2 addition
is not due to the solution-reprecipitation mechanism, but rather stress
graphitization mechanism should be considered.   The thermal expansion
coefficients of TiC and glassy carbon are 7.61×10^{-6} and $2.0-3.0 \times 10^{-6}$
respectively, hence, the thermal mismatch of TiC/C is the largest among the
prepared carbides.   The graphitization mechanism of TiO_2 added carbon is not
unambiguous, but it may be partially explained by thermal mismatch between
carbon matrix and prepared TiC.
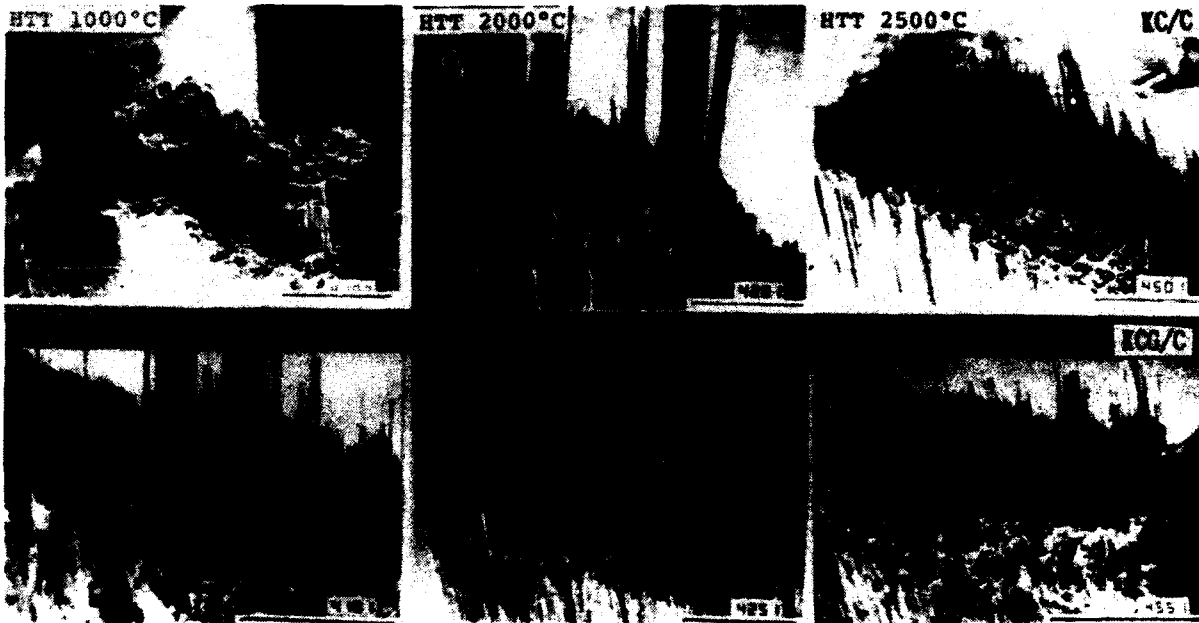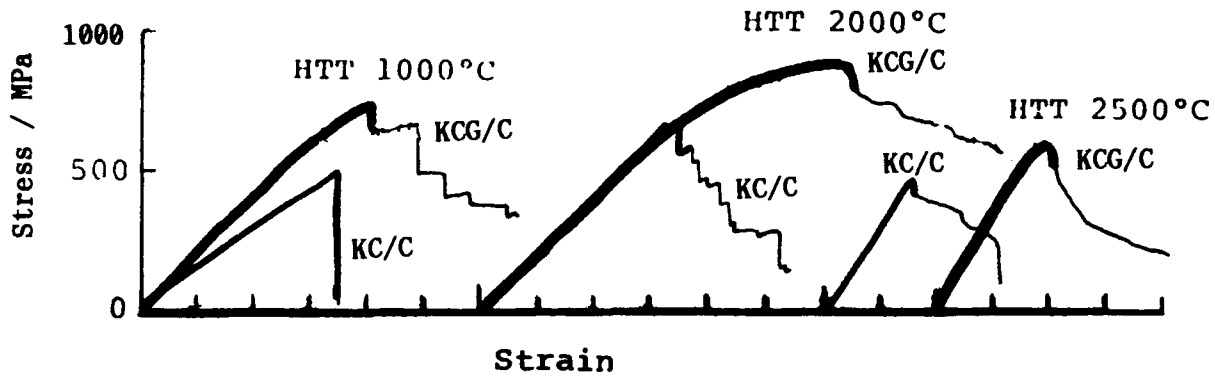
Fig.4. Stress-strain diagrams and fractured surface of pitch based C/C
       composite with various heat-treatment temperatures. (bar:1mm)
       upper: pitch matrix (KC/C), lower: matrix with graphite powder(KCG/C).

3-2: EFFECT OF FIBER ORIENTATION ON THE MECHANICAL PROPERTIES OF C/C COMPOSITE

The flexural strength of unidirectionally aligned C/C composites with furan resin derived matrix was shown in **Fig.5**.   The strength decreased steeply with increase of off-axis angle and reached the transverse strength.   The dotted lines in Fig.5 indicate the calculated strength of fiber fracture and transverse fracture, and real line indicates the shear fracture, based on the maximum stress theory.   The calculated shear fracture stress always exceeds the measured value.   The shear strength measured by double notched specimen were 44 MPa for 1000°C treated composite, and 46MPa for 2600°C treated composite respectively.   These values are extremely higher than that for pitch derived matrix composite (14-25MPa).   The fractured surfaces of the
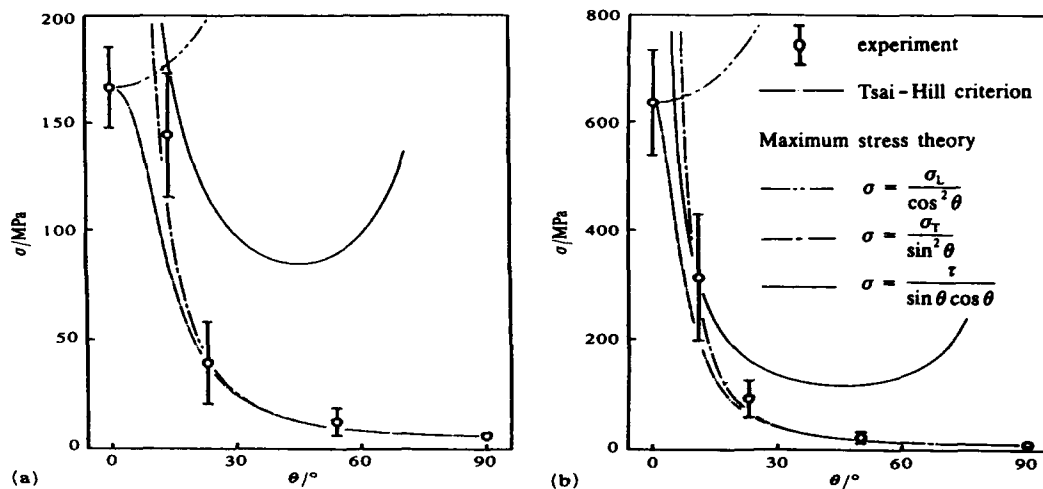
Fig.5. Flexural strength of UD C/C composite of carbonized and graphitized.
(σ_L: longitudinal stress, σ_T: transverse stress, τ: shear stress)
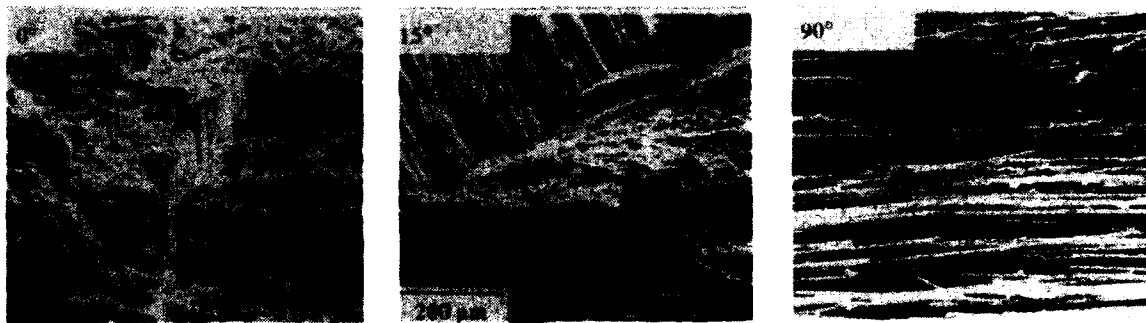
Fig.6. Fractured surfaces of UD C/C composite tested at different off-axis
angle.

composite are shown in **Fig.6** with a different off axis test for carbonized
specimen.   The fractured surfaces were generally flat in longitudinal and
transverse tests.   However, many steps were observed in the fractured surface
of the off-axis between 8° and 50°.   The step indicates a mixed modes of
longitudinal and transverse tensile fractures and shear fracture[E.Y.90].

3-3: OXIDATION OF METAL COMPOUNDS ADDED CARBON.

Many efforts are now being done to the coating process.   Since thermal
mismatch between coating material and C/C is large, self protection of fiber,
interface and matrix becomes important.   Addition of oxidation protective
substance into the fiber and matrix must be best way, then Hf, Si, Ti and Zr
compounds powder were added into the starting material, and then carbonized or
graphitized.   Oxidation of metal compounds added carbon was tested by

thermal gravimetric analysis. The weight loss of carbonized material and graphitized material after TG measurement was listed in **Table 1**. All of the carbonized materials oxidized more than 50%. Generally oxidation rate of graphitized material is lower than the carbonized material[E.Y.80]. As can be seen in Table 1, all of the graphitized materials showed oxidation resistance than the carbonized material. Especially Hf and Zr compounds added materials showed excellent oxidation resistance and remained more than 80%. Although TiO_2 added and SiC added materials graphitized well, SiC added material did not change the oxidation behavior, and TiO_2 added material showed higher oxidation than without addition. For precise discussion, isothermal measurement and surface area measurement are necessary, but for the qualitative discussion this results suggest that the addition of Hf and Zr compounds showed excellent oxidation protection behavior than Si and Ti compounds.

4: Conclusions

Microstructure of a C/C composite depends primarily on the initial raw material of the matrix. Secondary, it depends on the heat treatment temperature employed. The crystallite of the matrix is generally preferentially oriented aligning the c-plane surrounding the carbon fiber. Young's modulus, strength, and thermal conductivity also strongly depend on the microstructure of the composite. Since too strong preferred orientation makes the shear strength and tensile strength of C/C composite weak, then control of microstructure becomes important. Preferred orientation of the matrix can be suppressed by the addition of graphite powder to act as a nucleus for the matrix crystallization, or by the addition of metal compound as a catalytic reagent for graphitization. On the other hand flexural strength strongly depend on the fiber orientation. To make a tailored C/C composite, the precise crystallite orientation and fiber orientation control must be done depending on the desired properties. For resolving the oxidation problem of C/C composite, addition of oxidation protective powder into fiber, interface and matrix must be the best way. Hf and Zr compounds addition showed excellent oxidation protection behavior.

References

[B.K.86]: B.T.Kelly, 1986. Physic of Graphite, Appl.Sci.Pub., London.

[S.K.75]: S.Kimura et al., 1975. Yogyo-Kyokai-Shi, **83** 122-127.

[JSPS78]: Edt. by Japan Society of Carbon, 1978. Introduction to Carbon Materials, pp.184.

[E.Y.87]: E.Yasuda et al., 1987. Tanso, No. **128**, 7-11.

[I.M.72]: M. Inagaki et.al., 1972. Tanso, 71 135.

[T.M.86]: Edt.by T.B.Massalski, 1986. Binary Alloy Phase Diagrams, Amer.Soc.Metals.

[E.Y.88]: E.Yasuda et al., 1988. Carbon, **26** 225-227.

[J.W.89]: J.White & P.Sheaffer, 1989. Carbon **27** 697-707.

[E.Y.90]: E.Yasuda et al., 1990. High Temp. and high Press., **22** 329-337.

[E.Y.80]: E.Yasuda et al., 1980. Trans. Jap.Soc.Compo.Mater., **6** vol.1 14-23.

Approximate Stress Analysis of a Unidirectional Composite Containing a Broken Fiber

JAMES M. WHITNEY AND HOWARD W. BROWN, III

ABSTRACT

A self-consistent model is considered in which a broken cylindrical fiber surrounded by a matrix cylinder is embedded in a homogeneous media of infinite radial extent. The homogeneous media is assumed to have the same properties as the effective properties of the concentric composite cylinder. Axisymmetric deformation is assumed in the model and an approximate solution based on classical theory of elasticity is obtained. Stresses in the vicinity of the broken fiber are approximated by a decaying exponential function multiplied by a polynomial. An exact solution is obtained for the far field stresses at a distance away from the end of the broken fiber. Transversely isotropic properties are assumed for the fiber, while the matrix is assumed to be isotropic. The model also includes the effect of thermal residual stresses. Numerical results are presented for a graphite fiber embedded in an epoxy matrix. Comparison is made to classical shear lag analysis.

INTRODUCTION

Stress distributions around discontinuous fibers have been studied by a number of researchers. Analysis of the "shear lag" class have been performed by Cox [1], Rosen [2], and Kelly and Tyson [3]. In such an approach only the fiber axial stress distribution and the fiber matrix interfacial shear stress distribution are determined. Amirbayat and Hearle [4] included the distribution of fiber matrix interfacial pressure in their model.

An approximate closed form solution has been developed by Whitney and Drzal [5] which predicts the axisymmetric stress distribution in a system consisting of a single broken fiber surrounded by an unbounded matrix. In this approximate model the equilibrium equations and the boundary conditions of classical theory of elasticity are exactly satisfied throughout the fiber and matrix, while compatibility is only approximately satisfied. The far field solution away from the end of the broken fiber exactly satisfies all of the equations of elasticity. In addition to allowing for orthotropic fiber properties this model also includes the effect of expansional strains as a result of moisture and temperature. A recent paper by Nairn [6] addresses the single fiber problem with an approximate analysis based on complementary energy. An approximate model for the stress analysis of a broken fiber in a unidirectional composite has been developed by McCartney [7]. However, his analysis only considers isotropic fibers. Pagano and Brown [8] recently developed a more complex micromechanics

James M. Whitney, Professor of Graduate Materials Engineering, University of Dayton, 300 College Park, Dayton, OH 45469-0240, USA.
Howard W. Brown, III, Materials Research Engineer, Materials Directorate, Air Force Wright Laboratory, Wright-Patterson Air Force Base, OH 45433-6533, USA.

damage model based on concentric cylinders in which the r-dependence is assumed with the axial field equations being developed from Reissner's variational theorem. Accuracy of this model has been ascertained by comparison to an exact elasticity solution for the fiber pullout problem. In

In the present paper the model developed in Ref. [5] will be extended to the case of a single broken fiber in a unidirectional composite (bounded matrix). Numerical results will be compared to classical shear lag analysis [2].

FAR FIELD SOLUTION

Models for both the single fiber problem and the unidirectional composite are shown in Fig. 1. The far field solution, which represents the stress distribution away from the end of
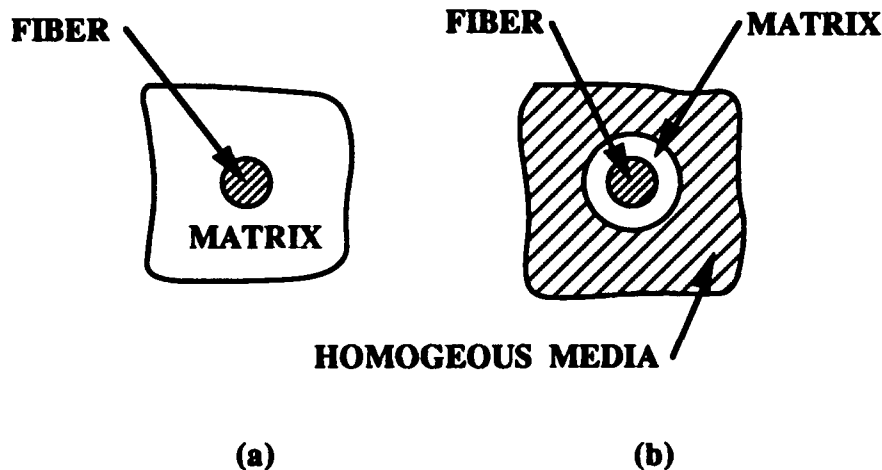
Fig. 1   Axisymmetric model: (a) single fiber; (b) unidirectional composite

the broken fiber, is axisymmetric. In Fig. 1a we see a circular fiber surrounded by a matrix of infinite extent. This represents the model developed in Ref. [5]. In the present paper we will focus on Fig. 1b in which a cylindrical fiber surrounded by a matrix cylinder is embedded in a homogeneous media of infinite extent. The homogeneous media is assumed to have the same properties as the effective properties of the concentric composite cylinder. A uniform axial strain, $\varepsilon_z = \varepsilon_0$, is assumed to be applied. Fiber radius is denoted by R_f, and the radius of the matrix cylinder in Fig. 1b is denoted by R_m. The solution for both of these models is exact within the framework of classical theory of elasticity.

Consider a coordinate system with the origin at the center of the fiber. The z-axis is oriented along the centerline of the fiber. The displacement field is assumed to be of the form

$$u_r = F(r), \quad u_\theta = 0, \quad w = z\varepsilon_0 \tag{1}$$

where u_r, u_θ, and w represent the radial, tangential, and axial displacements, respectively. The stress-strain relations for a transversely isotropic material (including thermal strains) in cylindrical coordinates are of the form

$$\sigma_r = 2Kv_{zr}(\varepsilon_z - \alpha_z\Delta T) + (K + G_{r\theta})\frac{dF}{dr} + (K - G_{r\theta})\frac{F}{r} - 2K\alpha_r\Delta T$$

$$\sigma_\theta = 2Kv_{zr}(\varepsilon_z - \alpha_z\Delta T) + (K - G_{r\theta})\frac{dF}{dr} + (K + G_{r\theta})\frac{F}{r} - 2K\alpha_r\Delta T$$

$$\sigma_z = (E_z + 4Kv_{zr}^2)(\varepsilon_z - \alpha_z\Delta T) + 2Kv_{z\theta}(\frac{dF}{dr} + \frac{F}{r} - 2\alpha_r\Delta T)$$ (2)

$$\tau_{r\theta} = \tau_{rz} = \tau_{\theta z} = 0$$

where σ_r, σ_θ, and σ_z denote normal stresses in the radial, hoop, and axial directions, respectively, while $\tau_{r\theta}$, τ_{rz}, and $\tau_{\theta z}$ are the shear stresses relative to the r-θ, r-z, and θ-z planes, respectively. In addition, E_z, K, $G_{r\theta}$, α_r, and α_z, are the axial modulus, plane strain bulk modulus, shear modulus relative to the r-θ plane, radial thermal expansion coefficient, and axial thermal expansion coefficient, respectively. The Poisson's ratio v_{zr} is determined from a tensile test in the z direction while measuring contraction in the radial direction. Temperature change is denoted by ΔT.

Using the equilibrium equations of classical theory of elasticity for axisymmetric deformation in conjunction with eqs. (3), we obtain the second order differential equation

$$\frac{d^2F}{dr^2} + \frac{1}{r}\frac{dF}{dr} - \frac{F}{r^2} = 0$$ (3)

The solution to eq. (3) is of the form

$$F = a_0 r + \frac{a_1}{r}$$ (4)

where a_0, a_1 are undetermined coefficients. To avoid a singularity at r = 0,

$$a_{1f} = 0$$ (5)

where the subscript f refers to the fiber, that is, $0 \le r \le R_f$. Continuity at the fiber/matrix interface requires that

$$u_{rf}(R_f) = u_{rm}(R_f), \quad \sigma_{rf}(R_f) = \sigma_{rm}(R_f)$$ (6)

Here the subscript m denotes the matrix, that is, $R_f \le r$ for the single fiber model and $R_f \le r \le R_m$ for the self-consistent composite model. In the single fiber model [5] the radial and hoop stresses dissipate in the matrix. In the self-consistent composite model, however, we have the condition that

$$\sigma_{rm}(R_m) = 0$$ (7)

In the homogeneous media the stress is reduced to σ_z = constant.

TRANSIENT SOLUTION

The transient solution describes stress distributions near the fiber break and is based on the model illustrated in Fig. 2. We take the origin of the axis system at the free end of the broken fiber. In this model we assume that

$$\tau_{r\theta} = \tau_{\theta z} = 0$$ (8)
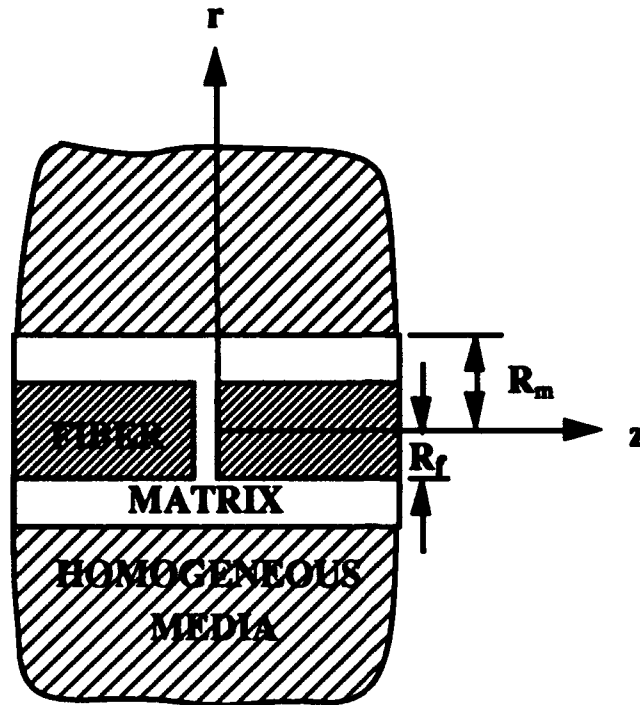
Fig. 2   Cross-section of model for transient solution

For this case the equilibrium equations of classical theory of elasticity reduce to

$$\frac{\partial \sigma_z}{\partial z} + \frac{\partial \tau_{rz}}{\partial r} + \frac{\tau_{rz}}{r} = 0$$

$$\frac{\partial \tau_{rz}}{\partial z} + \frac{\partial \sigma_r}{\partial r} + \frac{\sigma_r - \sigma_\theta}{r} = 0$$

$$(9)$$

These equations can be exactly satisfied by defining a stress function Φ such that

$$\sigma_z = \frac{\partial^2 \Phi}{\partial r^2} + \frac{1}{r}\frac{\partial \Phi}{\partial r}, \quad \tau_{rz} = -\frac{\partial^2 \Phi}{\partial r \partial z}$$

$$\sigma_r = \frac{\partial^2 \Phi}{\partial z^2} + \frac{1}{r}\frac{\partial \Phi}{\partial r}, \quad \sigma_\theta = \frac{\partial^2 \Phi}{\partial z^2} + \frac{\partial^2 \Phi}{\partial r^2}$$

$$(10)$$

For the model developed in Ref. [5] it was assumed that $\sigma_r = \sigma_\theta$ in the region near the fiber break. Thus, eq. (10) represents a more general application of the stress function. Guided by a knowledge of the general nature of the stress distribution in the vicinity of a broken fiber, we assume that

$$\underline{0 \leq r \leq R_f}$$

$$\Phi_f = [B_0 + B_1 r^2 (1 + \lambda \frac{z}{R_f})] e^{-\lambda z/R_f} \tag{11}$$

$$\underline{R_f \leq r \leq R_m}$$

$$\Phi_m = \frac{B_2}{r^2} (1 + \lambda \frac{z}{R_f}) e^{-\lambda z/R_f} \tag{12}$$

$$\underline{R_m \leq r}$$

$$\Phi_c = \Phi_m \tag{13}$$

where B_i and λ are constants. Because the broken end of the fiber must be free

$$\sigma_{zf}(r, z) = - A_1 \varepsilon_0, \quad \tau_{rz}(r, 0) = 0 \tag{14}$$

The first of eqs. (14) assures that the total solution for the axial stress vanishes at the broken end of the fiber. Other conditions to be satisfied involve continuity at the fiber/matrix interface. In particular,

$$\tau_{rzf}(R_f, z) = \tau_{rzm}(R_f, z), \quad \sigma_{rf}(R_f, z) = \sigma_{rm}(R_f, z) \tag{15}$$

Continuity of these same stresses at the interface between the matrix cylinder and the homogeneous media is assured by eq. (13).

TOTAL SOLUTION

Combining the results from the transient and far field solutions, we obtain the following total stress field

$$\underline{0 \leq r \leq R_f}$$

$$\sigma_{zf} = [1 - (1 + \lambda \frac{z}{R_f}) e^{-\lambda z/R_f}] A_1 \varepsilon_0$$

$$\tau_{rzf} = - \lambda^2 r(\frac{z}{R_f}) e^{-\lambda z/R_f} \frac{A_1 \varepsilon_0}{4} \tag{16}$$

$$\sigma_{rf} = \{4\frac{A_2}{A_1} - [2(1 + \lambda \frac{z}{R_f}) + \lambda^2 r^2 (2\frac{R_f^2}{r^2} - 1)(1 - \lambda \frac{z}{R_f})] e^{-\lambda z/R_f}\} \frac{A_1 \varepsilon_0}{4}$$

$$\underline{R_f \leq r \leq R_m}$$

$$\sigma_{zm} = [\frac{E_m}{A_1}(1 - \alpha_m \Delta T) + (\frac{R_f}{r})^4 (1 + \lambda \frac{z}{R_f}) e^{-\lambda z/R_f}] A_1 \varepsilon_0$$

$$\tau_{rzm} = - \lambda^2 R_f (\frac{R_f}{r})^3 \frac{z}{R_f} e^{-\lambda z/R_f} \frac{A_1 \varepsilon_0}{4} \tag{17}$$

$$\sigma_{rm} = \{\frac{4}{A_1}(A_4 - 2G_m \frac{A_5}{r^2}) - (\frac{R_f}{r})^4 [2(1 + \lambda \frac{z}{R_f}) + \lambda^2 r^2 (1 - \lambda \frac{z}{R_f})] e^{-\lambda z/R_f}\} \frac{A_1 \varepsilon_0}{4}$$

$$\underline{R_m \le r}$$

$$\sigma_{zc} = [\frac{E_{zc}}{A_1}(1 - \alpha_{zc}\Delta T) + (\frac{R_f}{r})^4(1 + \lambda\frac{z}{R_f})e^{-\lambda z/R_f}]A_1\varepsilon_0$$

$$\tau_{rzc} = - \lambda^2 R_f(\frac{R_f}{r})^3\frac{z}{R_f}e^{-\lambda z/R_f}\frac{A_1\varepsilon_0}{4} \tag{18}$$

$$\sigma_{rc} = - (\frac{R_f}{r})^4[2(1 + \lambda\frac{z}{R_f}) + \lambda^2 r^2(1 - \lambda\frac{z}{R_f})]e^{-\lambda z/R_f}\}\frac{A_1\varepsilon_0}{4}$$

where the subscript c denotes composite properties. In addition, the constants A_i are a function of material properties and volume fraction of fiber as determined from the conditions prescribed by eqs. (6) and (7). For efficiency they will not be displayed in detail in the present paper. The hoop stress, σ_θ, is of little interest and is not displayed in eqs. (16) - (18). In Ref. [5], λ was determined from a shear lag type analysis in conjunction with assumed displacements in conjunction with the transient solution. However, recent analysis [6-8] has suggested that the transient solution dissipates much faster than predicted by a shear lag type argument. In the present work λ is chosen as unity. This maximizes the value of τ_{rz} at one fiber radius away from the broken fiber.

NUMERICAL RESULTS

Fiber/matrix interface stresses are shown in Figs. 3 and 4 for a self-consistent model with an applied strain $\varepsilon_0 = 0.015$ and $\Delta T = - 156°C$ (-280°F) which is the difference between cure temperature and room temperature for a state-of-the-art advanced composite. The following constituent materials properties are assumed

Fiber

$$E_{zf} = 241 \text{ GPa (35 MSI)}, \quad K_f = 23.5 \text{ GPa (3.4 MSI)}, \quad \nu_{zrf} = 0.25$$

$$G_{r\theta f} = 34.5 \text{ GPa (5 MSI)}, \quad \alpha_{zf} = 0, \quad \alpha_{rf} = 4.25 \times 10^{-6}/°C \ (2 \times 10^{-6}/°F)$$

Matrix

$$E_m = 3.4 \text{ GPa (0.5 MSI)}, \quad K_m = 4.25 \text{ GPa (0.62 MSI)}, \quad \nu_m = 0.35$$

$$G_m = 1.4 \text{ GPa (0.2 MSI)}, \quad \alpha_m = 68 \times 10^{-6}/°C \ (32 \times 10^{-6}/°F)$$

Homogeneous Media

$$E_{zc} = 146 \text{ GPa (21.2 MSI)}, \quad \alpha_{zc} = 6.4 \times 10^{-6}/°C \ (3 \times 10^{-6}/°F)$$

These properties are typical of state-of-the-art graphite fibers embedded in an epoxy matrix. Stresses are normalized by the far field fiber axial stress. Comparison is made to classical shear lag theory [2] in Figs 3 and 4. For a fiber of infinite length, shear lag analysis reduces to the following stresses [2]

$$\sigma_{zf} = E_{zf}(1 - e^{-\beta z/R_f})\varepsilon_0$$

$$\tau_{rz}(R_f, z) = \frac{G_m\sqrt{V_f}}{\beta(1 - \sqrt{V_f})}e^{-\beta z/R_f}\varepsilon_0 \tag{19}$$
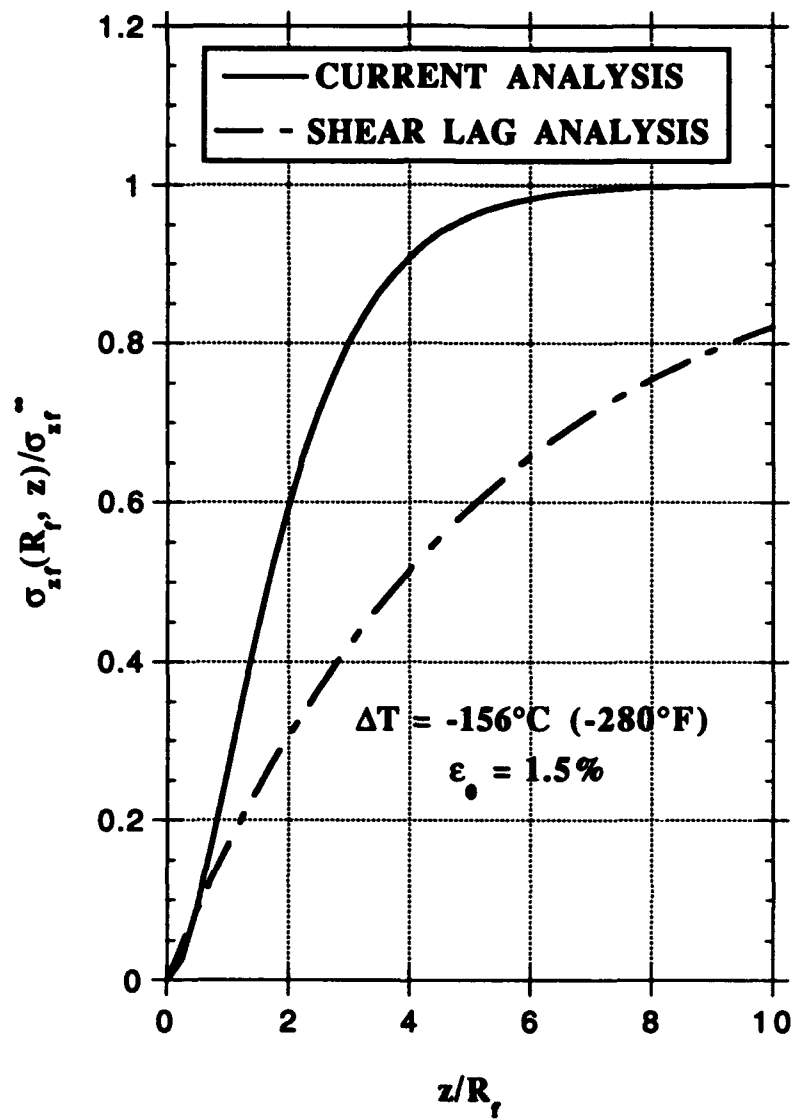
Fig. 3 Axial stress distribution in fiber at fiber/matrix interface

where V_f denotes volume fraction of fiber and

$$\beta^2 = \frac{2G_m \sqrt{V_f}}{E_{zf}(1 - \sqrt{V_f})}$$

As previously pointed out, shear lag analysis only produces the fiber axial stress and the shear stress at the fiber/matrix interface.
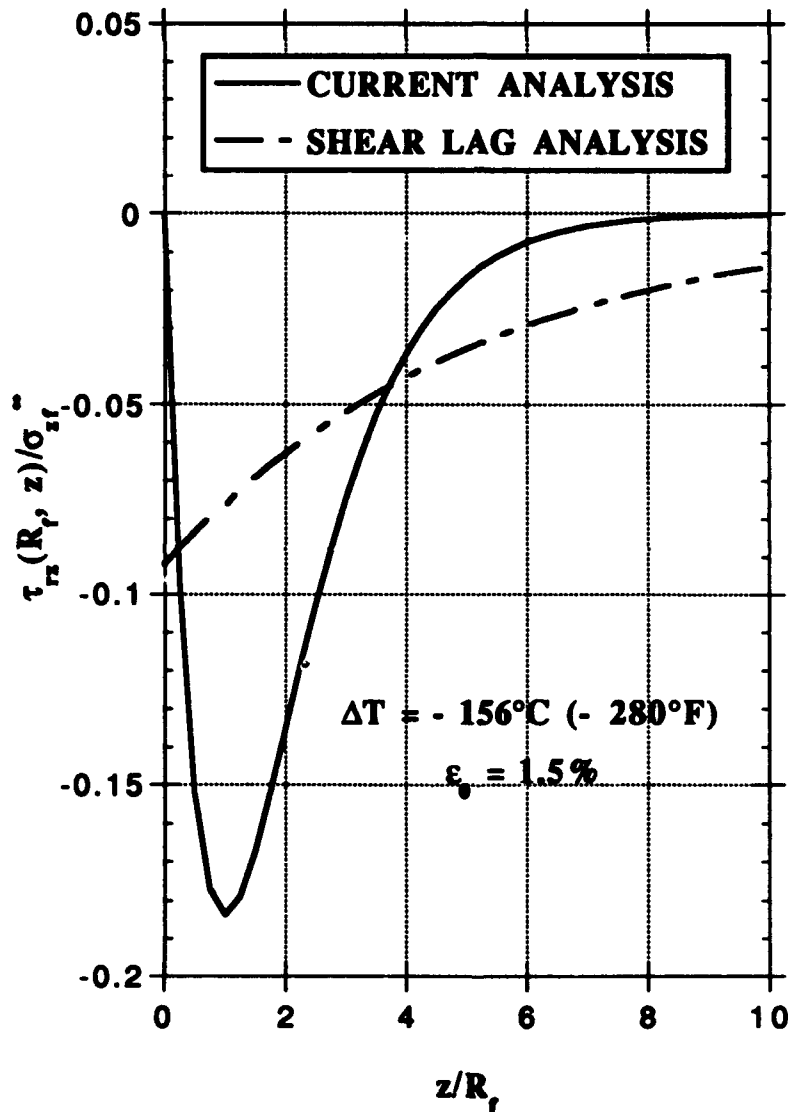
Fig. 4   Shear stress at fiber/matrix interface

DISCUSSION

In Figs. 3 and 4 we see how slow shear lag analysis dissipates the effect of the fiber break. In the case of axial stress, as shown in Fig. 3, the initial slope at the fiber break is zero. This

is due to the vanishing of τ_{rz} at the free end of the fiber. As shown in eq. (21), and illustrated in Fig. 4, the maximum value of τ_{rz} in shear lag theory occurs at the free end of the fiber, and as a result does not satisfy the free surface boundary condition. In addition, symmetry requires that τ_{rz} vanish along the plane $z = 0$. However, at the corner of the fiber break, $r = R_f$, $z = 0$, a singularity will occur. Thus, neither the present theory or shear lag analysis produce the correct result at this point. The present analysis does satisfy the correct condition at all other points on the plane $z = 0$.

The present analysis has obvious advantages over shear lag analysis by producing a complete stress distribution within the framework of a self-consistent model, including effects of thermal residual stresses. It is also less complex than other current approaches such as those presented in Refs. [6] and [7].

Future work will address a more formal procedure for determining the exponent λ, such as minimizing potential energy relative to this parameter.

ACKNOWLEDGEMENTS

REFERENCES

1. Cox, H. L., "The Elasticity and Strength of Paper and Other Fibrous Materials," *British Journal of Applied Physics*, Vol. 3, No. 1, 1952, pp. 72-79.

2. Rosen, B. W., "Mechanics of Composite Strengthening", Chapter 3, *Fiber Composite Materials*, ASM International, pp. 37-75.

3. Kelly, A. and Tyson, W. R., "Fibre Strengthened Materials," *Journal of Mechanics and Physics of Solids*, Vol. 10, No. 2, 1963, pp.199-208.

4. Amirbayat, J. and Hearle, W. S., "Properties of Unit Composites as Determined by the Properties of the Interface, Part I: Mechanism of Matrix-Fibre Load Transfer", *Fiber Science and Technology*, Vol. 2, No. 2, 1969, pp. 123-141.

5. Whitney, J. M. and Drzal, L. T., "Axisymmetric Stress Distribution Around an Isolated Fiber Fragment," *Toughened Composites, ASTM STP 937*, Norman J. Johnston, Editor, American Society for Testing and Materials, Philadelphia, 1987, pp. 179-196.

6. Nairn, J. A., "A Variational Mechanics Analysis of the Stresses Around Breaks in Single-Fiber Composites," *Mechanics of Materials*, to be published.

7. McCartney, L. N., "New Theoretical Model of Stress Transfer Between Fib.e and Matrix in a Uniaxially Fibre-Reinforced Composite," *Proceedings of the Royal Society of London*, A25, 1990, pp. 215-244.

8. Pagano, N. J. and Brown H. W., "Axisymmetric Micromechanical Stress Fields in Composites," *Proceeding of the IUTAM Conference*, to be published.

SESSION 7A

Metal Matrix Composites II

Corrosion of Magnesium-Matrix Composites

L. H. HIHARA AND P. K. KONDEPUDI

ABSTRACT

An experimental SiC monofilament/ZE41 Mg metal-matrix composite was found to corrode at higher rates in oxygenated compared to deaerated 0.5 M NaNO$_3$ at 30°C. The higher corrosion rates in oxygenated solutions were caused by galvanic corrosion between Mg and the SiC monofilaments, which were effective O$_2$-reduction sites. In deaerated solutions, galvanic corrosion was driven by proton reduction. The alloying elements in ZE41A Mg should not have significant effects on galvanic-corrosion rates since anodic polarization curves of ZE41A Mg and pure Mg were very similar. The carbon core and carbon-rich surface of the SiC monofilaments apparently caused cathodic polarization behavior of the monofilaments to be more like that of graphite than that of hot-pressed SiC.

INTRODUCTION

Magnesium metal-matrix composites (MMCs) are structural materials that are strong, stiff and light weight, and therefore, have potential application in the aerospace [1] and automotive industries [2]. Magnesium, however, is the most active structural metal in the electromotive force series [3], and has a strong tendency to corrode. Dissolved oxygen in solution does not significantly affect the corrosion of Mg [3]. Corrosion rates are highly dependent on metallic purity [3]. Noble impurity elements that have low hydrogen overvoltages (e.g., Fe, Ni, Co, and Cu) [4] serve as efficient cathodic sites, which accelerate the corrosion rate of Mg. In seawater, distilled Mg corrodes at the rate of 0.25 mm/y, but commercial Mg corrodes at about 100 to 500 times faster due to impurities [3]. Since the corrosion rate of Mg is highly dependent on the presence of cathodic sites, the incorporation of noble fibers and particles into Mg MMCs can result in severe galvanic corrosion.

Czyrklis [5] and Trzaskoma [6] have shown that galvanic corrosion is significant in graphite/Mg (Gr/Mg) MMCs. In deaerated 50 ppm chloride-containing solutions at 25°C, Gr/Mg MMCs corrode about 40 times faster than the matrix alloy [5]. Timonova, et al. [7] have shown that the galvanic-corrosion rate also depends on the type of reinforcement constituent. They reported that an Mg alloy could corrode about 1000 times faster when coupled to carbon filaments than when coupled to as-manufactured, tungsten-core, boron filaments in 0.005 N NaCl (it was not specified if the solution was deaerated or aerated).

In this study, the corrosion behavior of an experimental SiC monofilament/ZE41 Mg MMC was investigated using potentiodynamic polarization and the zero-resistance ammeter (ZRA) techniques. The SiC was in the form of a monofilament (MF) having a carbon core and carbon-rich surface. The MMC and the SiC MFs were produced by Textron Specialty Materials, Lowell, MA. The objectives of the study were to determine the role of each MMC

Department of Mechanical Engineering
University of Hawaii at Manoa
Honolulu, HI 96822

constituent and dissolved oxygen on MMC corrosion behavior. Experiments were conducted in deaerated and oxygenated 0.5 M NaNO$_3$ at 30 °C. Sodium nitrate is a non-oxidizing salt and was used to increase solution conductivity to perform the experiments. Monolithic ZE41A Mg, pure (99.95%) Mg, SiC MF, hot-pressed SiC, pitch-based graphite fiber, and the SiC MF/ZE41 Mg MMC were examined. The corrosion behavior of ZE41A Mg was compared to that of pure Mg to determine if the alloying elements significantly affect corrosion behavior. Hot-pressed SiC and graphite fibers were also studied to determine if the SiC MFs (which are actually carbon/SiC composites) are electrochemically similar to SiC, graphite or neither.

MATERIALS
SILICON CARBIDE MF/ZE41 Mg MMC ELECTRODES

The SiC MF/ZE41 Mg MMCs were produced by Textron Specialty Materials for experimental purposes. The MMCs were in rod form having diameters equal to about 0.43 cm. The SiC MFs were aligned uniaxially along the length of the rod with a volume fraction of about 0.49. The MMCs were aged at 329 °C for 2 h to achieve the T5 temper. To make planar electrodes, the MMC rod was sectioned into disks. One surface of the disks was coated with silver paint to make electrical contact with a copper wire lead. The sides and silver-coated surface of the disks were then sealed with an epoxy adhesive (EPOXY-PATCH of Dexter Corp., Seabrook, NH). The front planar surface was left bare and served as the electrode surface. The SiC MFs were oriented perpendicularly to the electrode surface.

PURE Mg and ZE41A Mg ELECTRODES

Planar pure Mg (i.e., 99.95% metallic purity) and ZE41A Mg electrodes were fabricated from rods using the same method described above for the MMC. The nominal composition of the ZE41A Mg alloy is 4.2 wt% Zn, 0.7 wt% Zr, 1.2 wt% rare-earth elements, and a balance of Mg. The alloy was heat treated under identical conditions to the MMC.

GRAPHITE ELECTRODES

Planar graphite electrodes were fabricated from Thornel P-100 graphite fibers (Union Carbide Co., Danbury, CT), which are unidirectional, continuous, about 10 μm in diameter, and pitch-based with an elastic modulus equal to 690 GPa. Fifteen tows of the fiber (about 2000 fibers/tow) were aligned unidirectionally and infiltrated with an epoxy resin (EPON 828 RESIN of Miller-Stephenson Chemical Co. Inc., Danbury, CT). The resulting product, a graphite/epoxy composite rod, was cut into disks by sectioning the rod perpendicularly to the axis of the fibers. The disks were then made into electrodes by silver painting the back side to make electrical contact with a copper-wire lead. The silver paint and copper wire were then coated with EPOXY-PATCH. The total cross-sectional surface area of the graphite fibers was about 0.024 cm^2.

SILICON CARBIDE MF ELECTRODES

Planar SiC MF electrodes were fabricated from Textron SiC MF, which are unidirectional, continuous, and about 140 μm in diameter. A total of 147 SiC MFs were bundled and then processed in an identical manner to the graphite-fiber planar electrodes described above. The total cross-sectional surface area of the SiC MFs was about 0.023 cm^2. Note that in these planar electrodes, only the cross-sectional filament surface is exposed.

To study the electrochemical properties of the carbon-rich surface of the SiC MFs, electrodes baring only the carbon-rich circumferential surface were prepared. Silicon carbide MFs were cut into lengths of about 3 cm. Only the circumferential surface near each end of the MFs was silver painted onto a copper-wire lead to make electrical contact. The electrical-contact area and the copper-wire lead were then sealed in EPOXY-PATCH so that only the circumferential surface of the MF was exposed. A sufficient number of SiC MFs was used so that the total circumferential surface area was about 0.79 cm^2.

HOT-PRESSED SILICON CARBIDE ELECTRODES

Planar electrodes were fabricated from bars of SiC that were produced by Ceradyne, Inc., Costa Mesa, CA. The SiC was hot-pressed to near theoretical densities (>98%) without sintering aids or binders. The SiC bars were cut into 9 x 9 mm-square wafers about 1 mm thick. The entire back side of the SiC wafers was silver painted to make electrical contact with a copper-wire lead. This procedure was followed to ensure that the ohmic drop through the SiC wafer would be uniform over the electrode face during polarization experiments. The resistance through the thickness of the SiC wafers was about 1 KΩ, and thus, ohmic losses were calculated to be less than about 0.1 V for current densities (CDs) less than 10^{-4} A/cm^2. The sides and silver-coated surface of the wafers were then sealed with EPOXY-PATCH. The front planar surface was left bare and served as the electrode surface.

AQUEOUS SOLUTIONS

Near neutral 0.5 M NaNO$_3$ solutions were prepared from 18 MΩ•cm water and analytical grade NaNO$_3$. The solutions were kept at 30 ± 0.1°C, and deaerated with high-purity nitrogen (99.9%) or oxygenated with high-purity oxygen (99.6%). Gas pressure was 1 atm.

INSTRUMENTATION AND PROCEDURES

The surface of all planar electrodes was polished to a 0.05 μm finish with gamma alumina powder, kept wet, and rinsed with 18 MΩ•cm water prior to immersion in the aqueous solutions.

Potentiodynamic polarization experiments were conducted with a Model 273 PAR potentiostat/galvanostat (EG&G, Princeton, NJ). The electrodes were stabilized at their corrosion potential (E$_{CORR}$) prior to polarization. Potentials were measured against a saturated calomel electrode. All electrodes were polarized at a rate of 0.1 mV/s except the SiC MF/ZE41 Mg MMC electrodes, which were polarized at a rate of 1 mV/s. Each polarization experiment was performed three times. To generate polarization diagrams, the logarithm of the CD was averaged over three trials and plotted as a function of potential.

The galvanic current (I$_{GALV}$) was measured with a ZA 100 zero shunt ammeter (Intertech Systems, Inc., San Jose, CA).

RESULTS

The anodic and cathodic polarization diagrams of pure Mg and ZE41A Mg are plotted together in Figure 1 for both deaerated and oxygenated 0.5 M NaNO$_3$ at 30°C. Data from Figure 1 was used to obtain the normal corrosion CD (i$_{CORR}$) for pure Mg and ZE41A Mg by Tafel extrapolation.

In Figure 2, the anodic polarization diagrams of pure Mg and ZE41A Mg are plotted with the cathodic polarization diagrams of SiC MF (cross section exposed and fiber surface exposed), hot-pressed SiC, and P-100 graphite fiber (cross section exposed) for deaerated 0.5 M NaNO$_3$ at 30°C. Figure 3 corresponds to oxygenated solutions, but is otherwise similar to Figure 2. The data from Figures 2 and 3 was used to predict values of i$_{GALV}$ for Mg coupled to the various materials.

In Figure 4, anodic and cathodic polarization diagrams of the SiC MF/ZE41 Mg MMC are plotted for both deaerated and oxygenated 0.5 M NaNO$_3$ at 30°C. Data from Figure 4 was used to estimate the galvanic-corrosion CD (i$_{GALV}$) (normalized with respect to the matrix area) of the MMC.

Figure 5 shows actual values of i$_{GALV}$ measured as a function of time using the ZRA technique for pure Mg coupled to SiC MF (cross section exposed and fiber surface exposed), hot-pressed SiC, and P-100 graphite fiber (cross section exposed) for deaerated 0.5 M NaNO$_3$ at 30°C. Figure 6 shows values of i$_{GALV}$ for oxygenated solutions.

DISCUSSION

The effects of MMC constituents and dissolved oxygen on corrosion behavior of SiC MF/ZE41 Mg MMC were deduced from polarization and ZRA data. The corrosion and elec-

trochemical properties of the MMC constituents are discussed first to understand how these materials behave individually; then, the corrosion behavior of the MMC is discussed.

ELECTROCHEMICAL PROPERTIES OF THE CONSTITUENTS

The corrosion of Mg is not affected significantly by the presence of oxygen [3]. That is exemplified by the polarization diagrams of pure Mg and ZE41A Mg immersed in 0.5 M NaNO$_3$ (see Figure 1), which are virtually unaffected by solution oxygenation. For pure Mg immersed in either deaerated or oxygenated 0.5 M NaNO$_3$, i$_{CORR}$ obtained by Tafel extrapolation was about 3×10^{-4} A/cm^2. The value of i$_{CORR}$ for ZE41A Mg immersed in the oxygenated solution was about 3×10^{-4} A/cm^2 and ranged from about to 3×10^{-4} A/cm^2 to 6×10^{-4} A/cm^2 in the deaerated solution. The slightly higher values corresponding to the deaerated solution was attributed to normal variation in data and not to a different corrosion mechanism since the shape of the polarization curves in the deaerated and oxygenated solutions was very similar. The alloying elements in ZE41A Mg had the effect of increasing cathodic CDs (in comparison to pure Mg). The alloying elements did not have significant effects on anodic polarization behavior, and thus, pure Mg and ZE41A Mg will have very similar galvanic-corrosion rates when coupled to cathodic reinforcements (see Figures 2 and 3).

The SiC MF is comprised of a carbon-filament core surrounded by chemical-vapor-deposited SiC with an outer, carbon-rich surface. Since the SiC MF is actually a composite comprised of SiC and carbon, it was of particular interest to determine if the SiC MFs are electrochemically similar to SiC, graphite, or neither. The SiC MFs were compared to hot-pressed SiC and P-100 graphite fiber (cross section exposed). The cross-sectional surface baring the carbon core of the SiC MFs and the carbon-rich outer surface were examined independently. In deaerated 0.5 M NaNO$_3$ (see Figure 2), the cathodic polarization curve of the cross-sectional SiC-MF surface was very similar in shape and in CD to that of P-100 graphite fiber, indicating that both materials have similar proton reduction kinetics. The cathodic polarization curve of the carbon-rich SiC-MF surface was also similar in shape to that of P-100 graphite, but CDs were about 1 to 2 decades less at a given potential. The cathodic curve of hot-pressed SiC was different in shape from the other materials, and had lowest CDs when potentials were less than about -1.2 V$_{SCE}$. In oxygenated 0.5 M NaNO$_3$ (see Figure 3), the reduction of oxygen caused cathodic CDs of all materials to increase. The polarization curves show an initial Tafel regime followed by a diffusion-limited, oxygen-reduction regime. The highest cathodic CDs were observed for the P-100 graphite fibers. In descending order of cathodic CDs, P-100 graphite was followed by the cross-sectional surface of the SiC MFs, the carbon-rich surface of the SiC MFs, and hot-pressed SiC. The CDs for P-100 graphite and the cross-sectional and carbon-rich surfaces of the SiC MFs were greater than 10^{-3} A/cm^2 in the diffusion-limited, oxygen-reduction regime; however, that of hot-pressed SiC was about a decade less. In both deaerated and oxygenated solutions, the carbon core and carbon-rich surface of the SiC MFs apparently caused the cathodic curves of the SiC MFs to show stronger resemblance to that of P-100 graphite than that of hot-pressed SiC.

MMC CORROSION

As determined by Tafel extrapolation, the SiC MF/ZE41 Mg MMC corroded at slightly higher rates in oxygenated solutions (see Figure 4). The corrosion CD of the matrix (i$_{CORR,MATRIX}$) in oxygenated 0.5 M NaNO$_3$ was about 2×10^{-3} A/cm^2, which was approximately three times the value for the deaerated solution. The value of i$_{CORR,MATRIX}$ is twice the corrosion CD of the MMC since i$_{CORR,MATRIX}$ is normalized with respect to the matrix area, which is one-half the MMC area due to the 50 vol.% content of SiC MFs. Unlike the corrosion of monolithic ZE41A Mg which was not affected by oxygen, corrosion of the MMC increased in the presence of oxygen due to galvanic corrosion with the SiC MFs. The total corrosion of an anode in a galvanic couple results from galvanic corrosion between the anode and cathode plus additional simultaneous corrosion of the anode, which is called local corrosion, caused by cathodic reactions that occur on the anode. Thus, to obtain i$_{GALV}$ between the matrix and the SiC MFs, the local-corrosion component (i$_{LOCAL}$) must be subtracted from i$_{CORR,MATRIX}$,

which represents the total corrosion of the matrix. We have assumed that there is no difference effect [8]; that is, i_{LOCAL} is equal to the normal i_{CORR} of uncoupled, monolithic ZE41A Mg. The assumption was made because the open-circuit potential of ZE41A Mg should shift only slightly if the alloy is galvanically coupled to SiC MF (see Figure 3). A very small shift in potential should not significantly affect cathodic-reaction kinetics of ZE41A Mg, indicating that i_{LOCAL} should be about equal to i_{CORR}. Hence, i_{GALV} for the oxygenated solution was determined to be about 2×10^{-3} A/cm^2, which was the difference between $i_{CORR,MATRIX}$ (equal to 2×10^{-3} A/cm^2) and i_{LOCAL} (equal to 3×10^{-4} A/cm^2). It was not possible to get a reasonable value of i_{GALV} for the deaerated solution since the values of $i_{CORR,MATRIX}$ and i_{LOCAL} were of the same magnitude.

Values of i_{GALV} can also be obtained from Figures 2 and 3 by using the mixed-potential theory or from the ZRA technique (Figures 5 and 6). In Figures 2 and 3, the anodic polarization diagrams of pure Mg and ZE41A Mg are plotted with the cathodic polarization diagram of SiC MF (cross section exposed). The CD at the intersection of the anodic and cathodic curves is the value of i_{GALV} for a galvanic couple having equal anode and cathode areas. The value of i_{GALV} obtained using this procedure corresponds to an MMC having a 50% content of SiC MFs with their cross sections exposed. For oxygenated 0.5 M NaNO$_3$ (Figure 3), the mixed-potential theory predicts that i_{GALV} for ZE41A Mg coupled to SiC MF (cross section exposed) will be equal to about 3×10^{-3} A/cm^2, which is in fairly good agreement to the steady-state value of 1×10^{-3} A/cm^2 obtained from the ZRA experiment for pure Mg coupled to SiC MF (cross section exposed). Both of those values are in good agreement to the value obtained in the preceding paragraph (i.e., 2×10^{-3} A/cm^2), which was obtained using the polarization diagrams of the MMC. For deaerated 0.5 M NaNO$_3$, the mixed-potential theory predicts that i_{GALV} will be equal to about 8×10^{-4} A/cm^2, which is closely bracketed by two steady-state values obtained from the ZRA experiments (see Figure 5).

Galvanic corrosion can be mitigated by thoughtful materials selection. Galvanic corrosion in Mg MMCs are cathodically controlled, and thus, galvanic-corrosion rates can be reduced by selecting reinforcement constituents that sustain low cathodic CDs. However, it is not likely that significant reduction in galvanic corrosion can be achieved by small variations in matrix composition since the anodic curves of ZE41A Mg and pure Mg were almost identical.

In deaerated 0.5 M NaNO$_3$, i_{GALV} could be limited to about 10^{-5} A/cm^2 (a fraction of the normal i_{CORR} of Mg) by using hot-pressed SiC (see Figure 2). Galvanic-corrosion CDs could be about 100 times higher if P100 graphite or SiC MFs were used. In oxygenated solutions, i_{GALV} could be limited to about 10^{-4} A/cm^2 using hot-pressed SiC, but could be as high as 3×10^{-3} A/cm^2 using P100 graphite or SiC MFs (see Figure 3). These i_{GALV} values were in relatively good agreement with those measured from actual galvanic couples using the ZRA technique (see Figures 5 and 6). Thus, fabricating Mg MMCs with SiC of electrochemical properties similar to that of hot-pressed SiC could result in SiC/Mg MMCs that possess corrosion resistance approaching that of the matrix alloy. Ideally, reinforcement materials should impart beneficial properties such as strength and stiffness to the composite without sacrificing corrosion resistance. The techniques discussed here can be used to screen potential candidate reinforcement materials for compatibility with metal matrices regarding corrosion resistance.

CONCLUSIONS

In 0.5 M NaNO$_3$, SiC MF/ZE41 Mg MMCs corroded at higher rates in oxygenated than in deaerated solutions. That is uncharacteristic of the corrosion behavior of Mg and its alloys which is normally unaffected by the presence of dissolved oxygen. The SiC MFs, which are inert electrodes upon which proton and oxygen reduction may occur, induced galvanic corrosion in the MMC. The reduction of oxygen on SiC MFs caused MMC corrosion rates to be higher in oxygenated solutions compared to deaerated solutions, where galvanic corrosion was driven by proton reduction. The cathodic CDs of the SiC MFs were generally much greater than that of hot-pressed SiC and closer to that of P-100 graphite fiber. The carbon core and carbon-rich surface of the SiC MFs apparently caused the MFs to behave more

like graphite than SiC. Since hot-pressed SiC sustained significantly lower cathodic CDs than the SiC MFs, the fabrication of Mg MMCs from SiC that is electrochemically similar to hot-pressed SiC could significantly reduce galvanic-corrosion rates in these materials.

ACKNOWLEDGEMENTS

REFERENCES

1)   Harrigan, Jr., W.C., 1991. "Metal Matrix Composites," in Metal Matrix Composites: Processing and Interfaces, R.K. Everett and R.J. Arsenault, ed., Academic Press, pp. 1 - 16.

2)   Lampman, S.R., May 1991. "Tuning Up the Metals in Auto Engines," Advanced Materials and Processes, pp. 17 - 22.

3)   Uhlig, H.H., and R.W. Revie, 1985. Corrosion and Corrosion Control, third edition, John Wiley and Sons.

4)   Butler, G., and H.C.K. Ison, 1978. Corrosion and its Prevention in Waters, Robert E. Krieger Publishing Company, p. 91.

5)   Czyrklis, W.F., 1985. "Corrosion Evaluation of Graphite-Aluminum and Graphite-Magnesium Metal Matrix Composites," in Proc. Conf. 'Corrosion 85', Boston MA, National Association of Corrosion Engineers, Paper Number 196.

6)   Trzaskoma, P.P., 1986. "Corrosion Behavior of a Graphite Fiber/Magnesium Metal Matrix Composite in Aqueous Chloride Solution," Corrosion, 42, pp. 609 - 613.

7)   Timonova, M.A., et al., 1980. "Corrosion Resistance and Electrochemical Characteristics of a Composite Material with a Magnesium Matrix," Metallovedenie i Termicheskaya Obrabotka Metallov, 11, pp. 33 - 35.

8)   Wesley, W.A. and R.H. Brown, 1948. "Fundamental Behavior of Galvanic Couples," in Corrosion Handbook, H.H. Uhlig, ed., John Wiley and Sons, pp. 481 - 496.
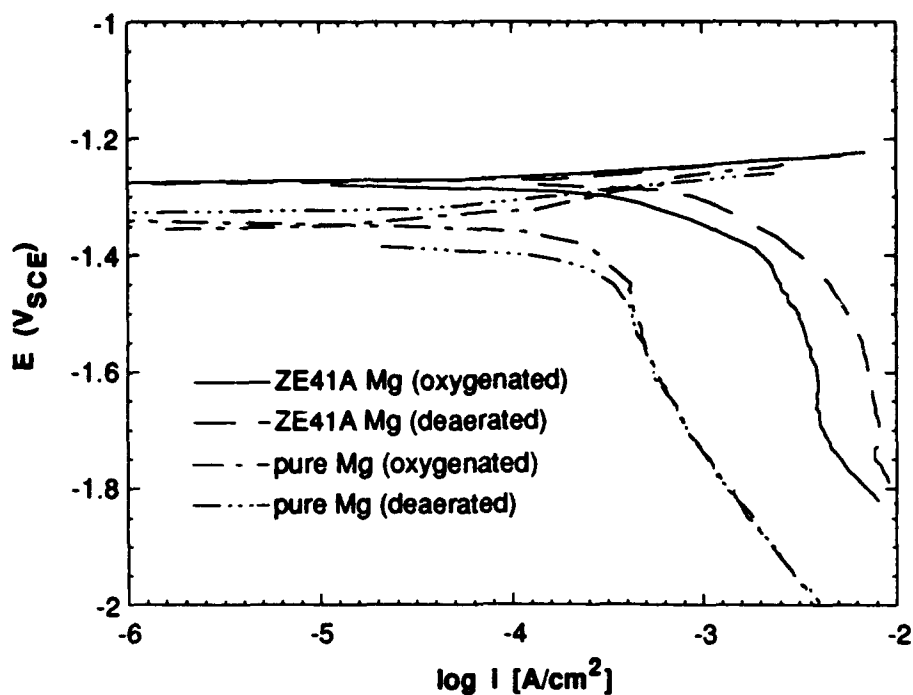
Figure 1: Polarization diagrams of pure Mg and ZE41A Mg exposed to deaerated and oxygenated 0.5 M NaNO$_3$ at 30°C. Scan rate = 0.1 mV/s.
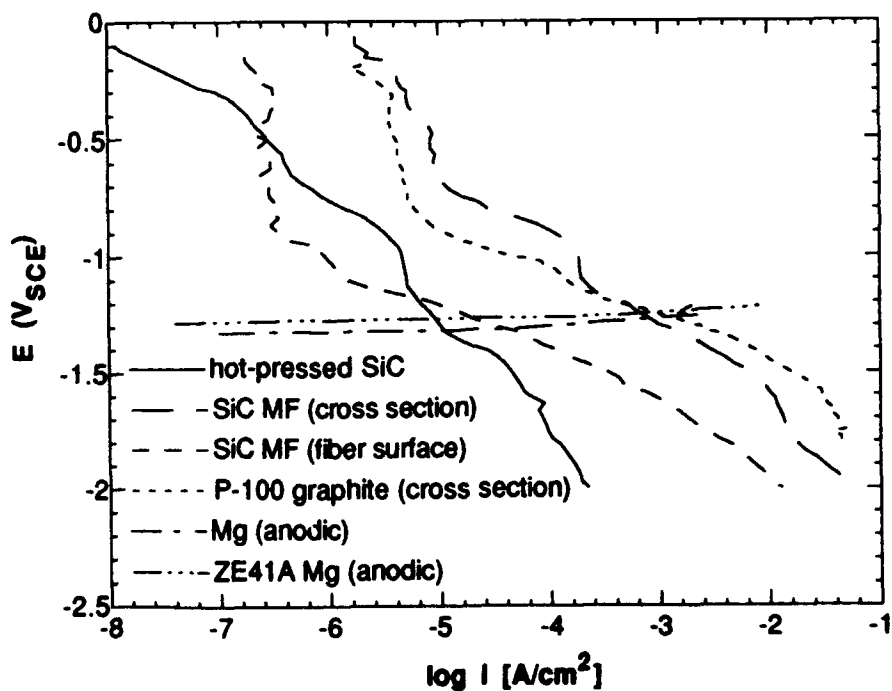
Figure 2: Anodic polarization diagrams of pure Mg and ZE41A Mg plotted with the cathodic polarization diagrams of hot-pressed SiC, SiC MF, and P-100 graphite exposed to deaerated 0.5 M NaNO$_3$ at 30°C. Scan rate = 0.1 mV/s.
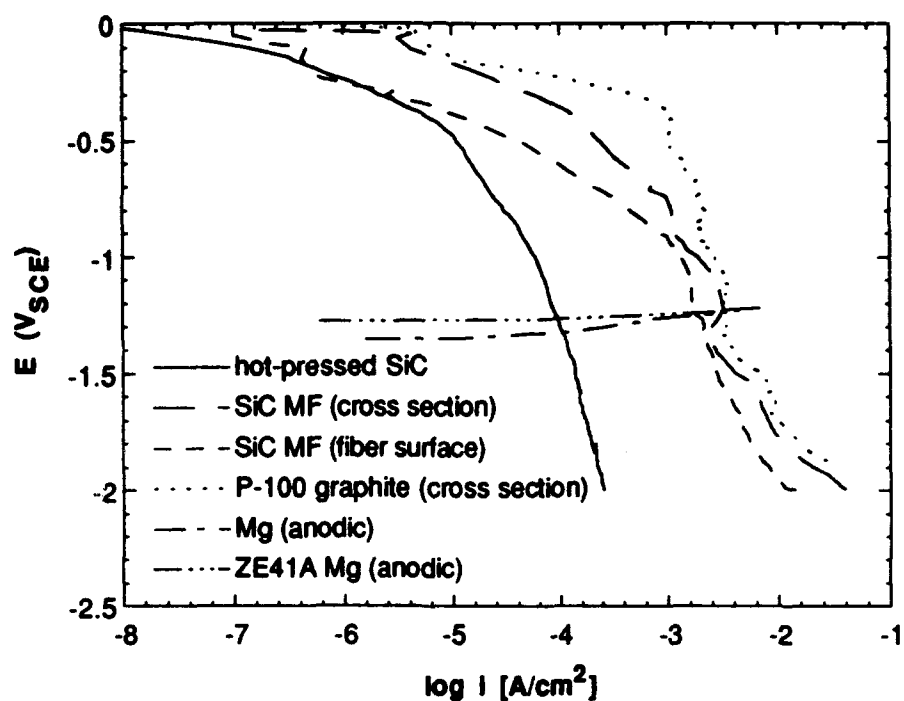
Figure 3: Anodic polarization diagrams of pure Mg and ZE41A Mg plotted with the cathodic polarization diagrams of hot-pressed SiC, SiC MF, and P-100 graphite exposed to oxygenated 0.5 M $NaNO_3$ at 30°C. Scan rate = 0.1 mV/s.
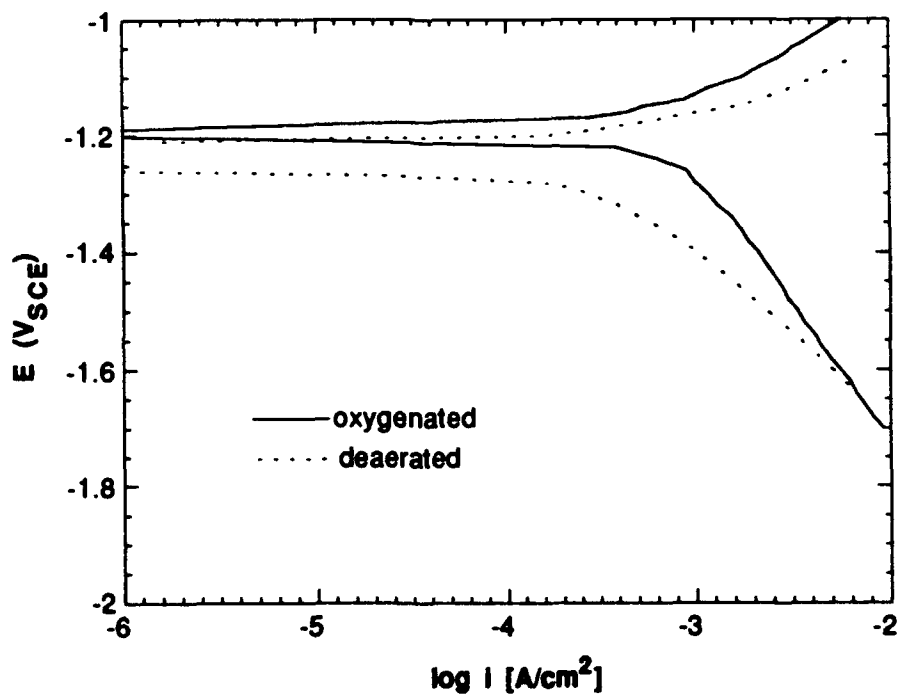
Figure 4: Polarization diagrams of SiC MF/ZE41 Mg MMC exposed to 0.5 M $NaNO_3$ at 30°C. Scan rate = 1 mV/s.
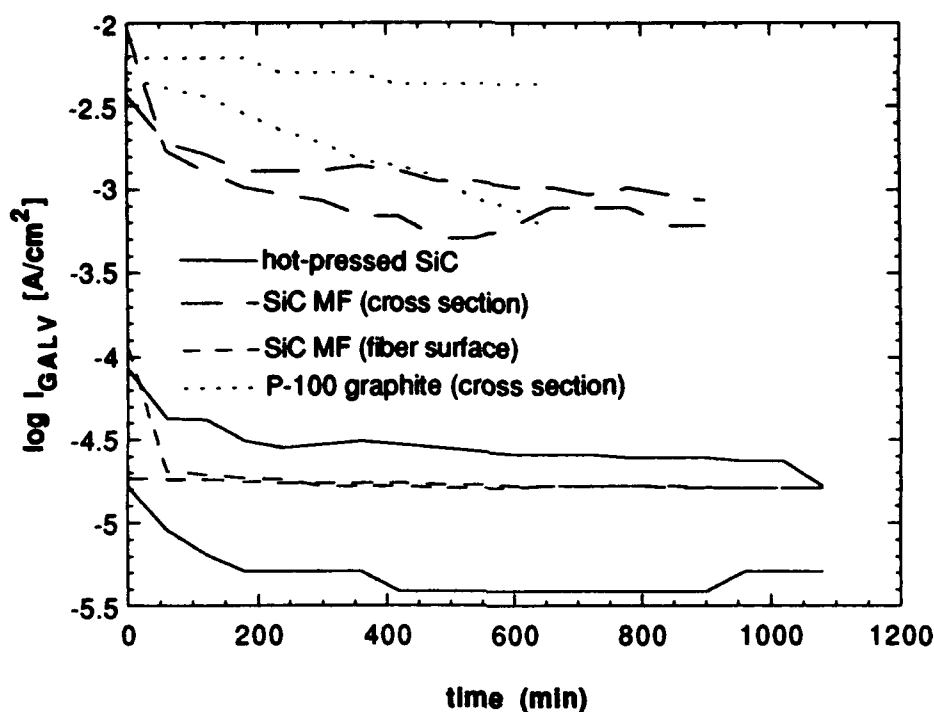
Figure 5: Galvanic-corrosion CD vs. time for pure Mg coupled to hot-pressed SiC, SiC MF, and P-100 graphite exposed to deaerated 0.5 M NaNO$_3$ at 30°C.
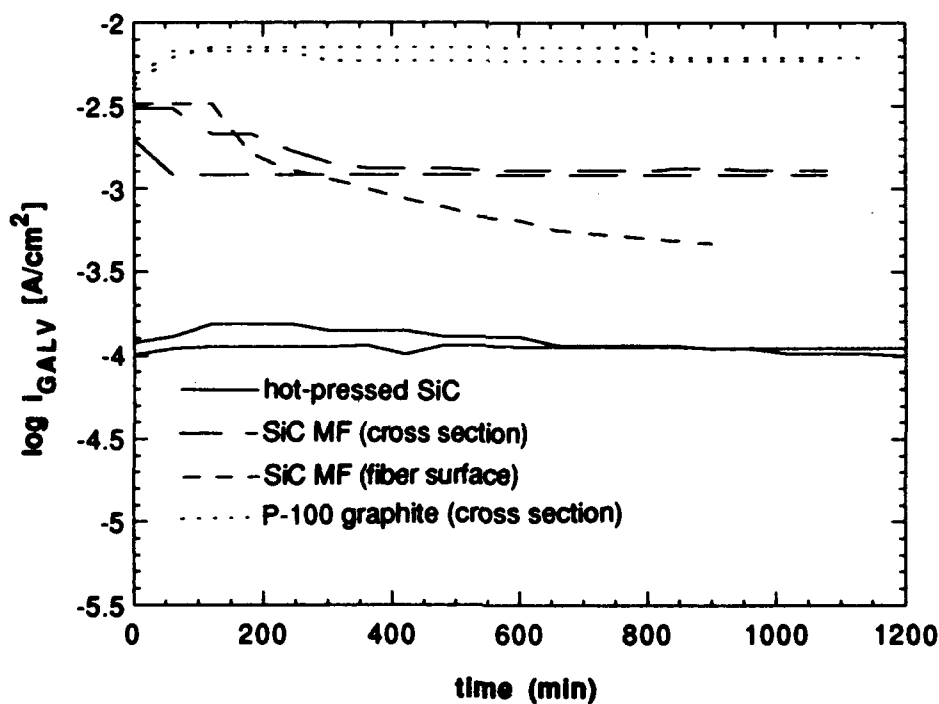
Figure 6: Galvanic-corrosion CD vs. time for pure Mg coupled to hot-pressed SiC, SiC MF, and P-100 graphite exposed to oxygenated 0.5 M NaNO$_3$ at 30°C.

Microstructure-Property Relations in Discontinuous SiC Aluminum Composites

JIALIANG QIN AND DAVID G. TAGGART

ABSTRACT

In this study the microstructural characteristics of SiC_p (particulate) and SiC_w (whisker) reinforced 2009 aluminum composites are evaluated and correlated with the macroscopic composite behavior. The composite specimens were sectioned from a 6"x1/2" extruded bar supplied by the Advanced Composite Materials Corporation. Microstructural features of the virgin materials were evaluated using optical and scanning electron microscopy. Features such as reinforcement distributions (clustering), particle size distributions, whisker aspect ratio distributions, and whisker orientation are presented. The uniaxial tensile response of these materials was characterized both parallel and transverse to the extrusion direction. Correlation of the macroscopic response with the microstructural features indicates a strong whisker orientation effect. The plastic response is also demonstrated to be dependent on the heat treatment of the composite. Examination of the microstructure of specimens after mechanical loading reveals evidence of particle and whisker cracking, whisker pullout, inclusion/matrix interfacial failure and ductile failure of the matrix. Finally, the observed macroscopic composite elastic-plastic response is correlated with existing micromechanical models.

INTRODUCTION

Metal matrix composites are currently being developed for numerous structural applications. These advanced composite materials may contain either continuous fiber reinforcements or discontinuous particle or whisker reinforcements. Discontinuously reinforced metal matrix composites are particularly attractive since they can be manufactured using conventional metal-working techniques [1]. Both discontinuously particle- and whisker-reinforced metal matrix composites provide high stiffness, superior yield strength and dimensional stability as compared to the unreinforced metals. Unfortunately, these enhancements in stiffness and strength are accompanied by a low ductility and fracture toughness [2]. This disadvantage is the primary obstacle preventing their introduction into many applications. In order to improve the

Jialiang Qin and David G. Taggart, Department of Mechanical Engineering and Applied Mechanics, University of Rhode Island, Kingston, RI 02881

mechanical properties of a discontinuously reinforced metal matrix composites, it is very important to understand the strengthening and failure mechanisms. A thorough examination of the effects of microstructural evolution on the macroscopic composite behavior is critical to a more complete understanding of composite constitutive response and to evaluation of composite strengthening properties.

The present work focuses on experimental observations of the mechanical response and microstructural characterization of both discontinuous particle reinforced (SiC_p) and whisker reinforced (SiC_w) 2009 aluminum metal matrix composites in an attempt to better understand the strengthening behavior and failure mechanisms. The results of mechanical testing provide the effects of reinforcement geometry, extrusion direction and heat treatment on the macroscopic composite response. Detailed metallography was carried out for both deformed and undeformed microstructures using optical microscopy and scanning electron microscopy. Quantitative metallographic techniques are utilized to characterize the materials with respect to reinforcement geometry, volume fraction, aspect ratio, orientation and distributions. Additional microstructural characterization consist of the examination of fracture surfaces and internal damage associated with mechanical loading. Finally, the elastic-plastic response of these composites are correlated with the analytical predictions.

EXPERIMENTAL PROCEDURES

The materials considered in this study are commercial metal matrix composites SXA 2009 (S-silicon carbide, X-reinforced, A-aluminum) supplied by the Advanced Composite Material Corporation (ACMC). Two types of silicon carbide (SiC) reinforced aluminum metal matrix composites were investigated. One composite is a commercial 2009 aluminum alloy reinforced by about 15 v/o SiC particles. And the second material is the same alloy containing approximately 15 v/o whiskers. Both composite materials were fabricated by an extrusion process and supplied as sections of a 6" wide and 1/2" thick extruded plate. Details of the experimental procedures are given in ref. [3].

MECHANICAL TESTING

Mechanical tests were performed on both SiC_p and SiC_w reinforced aluminum matrix specimens sectioned such that the tensile specimen axes were taken both parallel and normal to the extrusion direction. The specimens were machined to rectangular cross-section dog-bone tensile specimens (as specified in ASTM test method B557 sub-size specimen) with a 1 inch gage length and 0.025 in^2 cross sectional area. The uniaxial tension specimens were tested on an INSTRON Model 1125 Universal Testing Machine at strain rates of 0.02 in/min. Strain and load data were recorded using LABTECH software and OMEGA Series 900 data acquisition system interfaced with a personal computer.

Composites were tested in both the as-received, under-aged condition and in the peak-aged condition. As recommended by the material supplier [4], the peak-aged condition is achieved by heat treatment at 493°C (920°F) for 1 hour, water quench, and

subsequent aging at 160°C (320°F) for 24 hours.

MICROSTRUCTURAL CHARACTERIZATIONS

Detailed metallography was performed for both deformed and undeformed microstructures of particle and whisker-reinforced composites with a Nikon optical microscope and a SX-40A scanning electron microscope (SEM). Both undeformed and fractured specimens were sectioned along the tensile axis, polished and coated with gold sputtering for metallographic observation. In particular, the particle size distribution and whisker aspect ratios were examined on undeformed specimens. Quantitative metallographic techniques were utilized to characterize the size distribution of the particle and whisker reinforcements. Evidence of particle or whisker debonding and cracking were evaluated by examining the microstructure of specimens after mechanical loading. The fracture surfaces were examined without further preparation on the SEM.

EXPERIMENTAL RESULTS

UNDEFORMED MICROSTRUCTURES

Microstructural characterizations were performed on the undeformed microstructures for both particle and whisker reinforced 2009 aluminum metal matrix composites in the plane containing the tensile axis. Typical undeformed microstructures of both particle and whisker reinforced composites at low magnification (480X) are shown in Fig. 1. A highly non-uniform reinforcement distribution with alternating layers of matrix rich regions and inclusion clustering regions are observed. This non-uniform reinforcement distribution is expected to influence both the mechanical properties and fracture behavior of the composite.
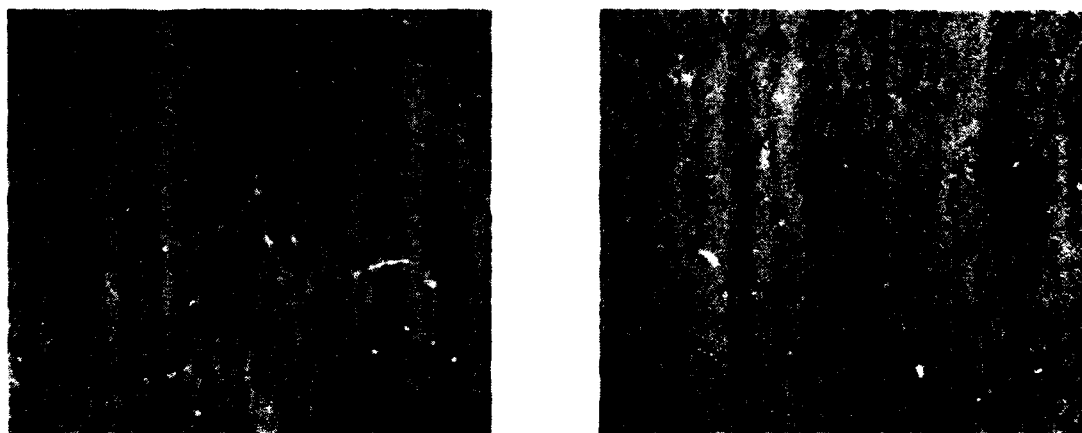
Figure 1. Undeformed microstructure of a) particle and b) whisker reinforced composites (480X).

The undetormed microstructures were also studied at high magnification using scanning electron microscopy. Typical SEM micrographs for SiC_p and SiC_w reinforced composites are shown in Fig. 2. Statistical analysis of 200 particles in the SiC_p composite and 300 whiskers in the SiC_w composite revealed particle sizes of 0.5-4.0 μm and whisker diameters of 0.5 μm and lengths of 0.5-15.0 μm. The average particle size was found to be 1.83 μm and the average whisker length was 3.45 μm which yields an average whisker aspect ratio of 6.9. Note that the extrusion process induces a high degree of whisker alignment parallel to the extrusion direction.

Figure 2. Scanning electron micrographs of undeformed a) SiC_p/Al and b) SiC_w/Al composites.

UNIAXIAL COMPOSITE RESPONSE

Fig. 3 shows the observed composite stress-strain responses for under-aged (Fig. 3a) and for peak-aged (Fig. 3b) SXA 2009 composites. Curves 1 and 2 correspond to SiC_w/Al specimens sectioned parallel and normal to the extrusion direction, respectively. Curves 3 and 4 are similar curves for the SiC_p/Al specimens. Note that the SiC_p composites are nearly isotropic while the SiC_w composites are anisotropic due to the high degree of whisker alignment parallel to the extrusion direction. All results demonstrate that the addition of the reinforcing phase results in an increase in the elastic modulus, yield strength and ultimate strength, and a decrease in the strain to failure as compared to the nominal unreinforced matrix properties.

Analysis of the stress-strain curves provide the elastic modulus, 0.2% offset yield stress, and ultimate stress. These results are summarized in Table I for under-aged and Table II for peak-aged composites. Note that these properties are slightly lower (5-15%) than those reported in ACMC literature.
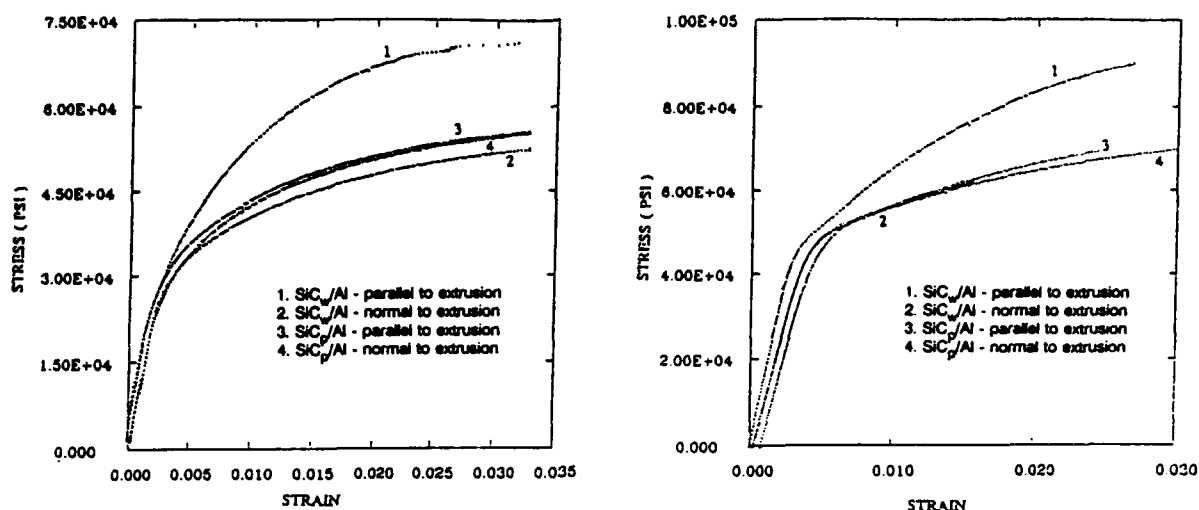
Figure 3. Uniaxial stress-strain response of a) under-aged and b) peak-aged SiC/Al composites.

TABLE I. Mechanical Properties of SXA 2009 (under-aged condition)

Material	Youngs Modulus GPa (Msi)	Yield Stress MPa (ksi)	Ultimate Stress MPa (ksi)
SiC$_w$/Al ‖*	104 (15.1)	255 (37)	498 (72.2)
SiC$_w$/Al ⊥	85.6 (12.4)	235 (34)	389 (56.4)
SiC$_p$/Al ‖	93.2 (13.5)	228 (33)	410 (59.4)
SiC$_p$/Al ⊥	84.9 (12.3)	228 (33)	399 (57.8)

TABLE II. Mechanical Properties of SXA 2009 (peak-aged condition)

Material	Youngs Modulus GPa (Msi)	Yield Stress MPa (ksi)	Ultimate Stress MPa (ksi)
SiC$_w$/Al ‖*	110 (15.9)	366 (53)	664 (96.2)
SiC$_w$/Al ⊥	90.4 (13.1)	359 (52)	566 (82.0)
SiC$_p$/Al ‖	86.3 (12.5)	359 (52)	538 (77.9)
SiC$_p$/Al ⊥	89.0 (12.9)	352 (51)	545 (79.0)

* ‖ - parallel to extrusion direction
⊥ - normal to extrusion direction

* ‖ - parallel to extrusion direction
⊥ - normal to extrusion direction

DEFORMED / FRACTURED SPECIMEN MICROSTRUCTURE

The microstructure of the composites after mechanical loading was also evaluated. Microscopic examination of the fracture surfaces revealed a dimpled microstructure characteristic of ductile fracture (see Fig. 4). To better understand the failure mechanisms of these composites, detailed metallography was performed both on fracture surfaces and on longitudinal sections taken through fractured specimens.

For the case of particle reinforced composites, there is evidence of particle/matrix interfacial failure, ductile failure of the matrix and some particle cracking. Examination of the SiC$_p$ composite fracture surface (Fig. 4a) reveals fractured SiC particles on the fracture surface. Therefore, the observed dimples are attributed to either particle fracture or particle/matrix decohesion. The fractured specimens were also sectioned and polished for metallographic evaluation of deformed microstructures in the SEM. The

Figure 4. Scanning electron micrograph of fracture surface in a) SiC_p/Al and b) SiC_w/Al composites.

results also indicate a number of fractured particles just below the fracture surface (Fig 5a). Particle fracture is often associated with the more elongated particles aligned parallel to the tensile direction. This observation has also been reported previously [5]. It is concluded that fracture initiation in the SiC_p/Al composites appears to be due to particle cracking, followed by void growth and coalescence rapidly leading to macroscopic failure.

In the case of SiC_w/Al composites, the failure mechanism associated with the dimpled microstructure was determined by examining details of fracture surface. As shown in Fig. 4b, failure involves the whisker-matrix decohesion and pull-out of whiskers from the matrix. In addition, longitudinal sections along tensile axis of the failed specimens revealed evidence of whisker fracture below the fracture surface as shown in Fig. 5b. Whisker fracture was often associated with the longer aspect ratio whiskers. Thus, the failure process in whisker-reinforced composites involves whisker fracture, whisker-matrix decohesion and pull-out of the whiskers from the matrix.
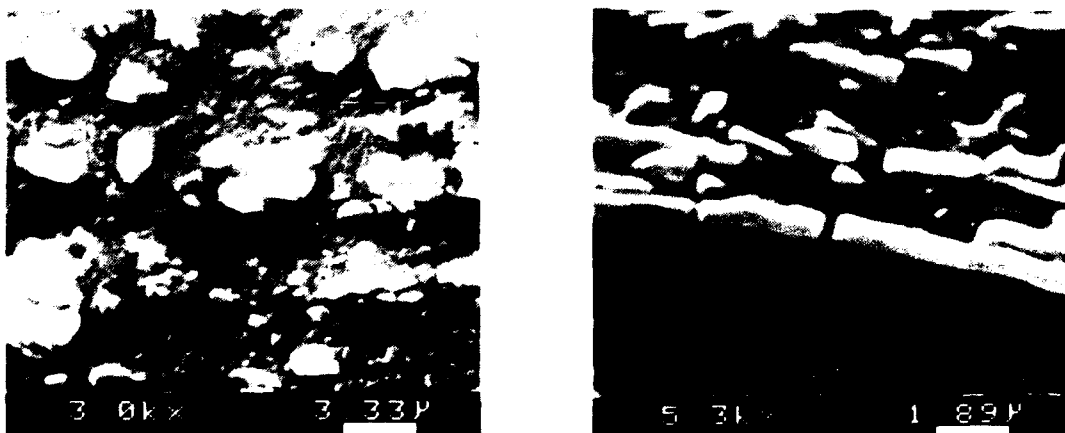
Figure 5. Polished section showing deformed microstructure of a) SiC_p/Al and b) SiC_w/Al composites.

CORRELATION OF ANALYTICAL AND EXPERIMENTAL RESULTS

The stress-strain data for unreinforced 2009 aluminum matrix in the peak-aged condition were provided by ACMC. To correlate the observed composite response with analytical predictions, the experimental matrix stress-strain curve was fit by a piecewise power law relation of the form

$$\sigma = \begin{cases} \sigma_o\left(\dfrac{\epsilon}{\epsilon_o}\right), & \epsilon \leq \epsilon_o \\[2ex] \sigma_o\left(\dfrac{\epsilon}{\epsilon_o}\right)^{1/N}, & \epsilon > \epsilon_o \end{cases} \tag{1}$$

The parameters $E_m = \sigma_o/\epsilon_o = 74.5$ GPa (10.81×10^6 psi), $\sigma_o = 279$ MPa (4.04×10^4 psi) and the hardening exponent $N = 7.5$ provide a close fit to the experimental data. The matrix Poisson's ratio, v_m, was assumed to be 0.3. The inclusion was assumed to be elastic with a Young's modulus $E_i = 483$ GPa (70.0×10^6 psi) and Poisson's ratio $v_i = 0.3$. The inclusion volume fraction of both SiC_p and SiC_w reinforced composites are 15%.

The experimental results of uniaxial stress-strain relations were compared with the existing micromechanics modeling predictions. The models considered include a dilute approximation which neglects interactions between inclusions and a generalized self-consistent (or three-phase) model (GSCM) which approximates inclusion interactions by introducing an effective material phase. Details of these model formulations are given in ref. [6].

The stress-strain response of a peak-aged SiC_p/Al composite was compared to the dilute and GSCM model predictions. It can be seen (Fig. 6a) that the three phase and dilute model predictions are nearly identical and both models provide good estimates of the elastic modulus and post-yield strain hardening behavior of composites. However, the models underestimate the flow stress. The reason for this discrepancy is not clear. One possible explanation is that the particles are not exactly spheroidal and uniformly distributed. Another factor neglected by the theoretical models is the residual stress state induced during cooling from processing temperatures which have been shown to stiffen the composite response [7].

Similar comparisons are made for the whisker reinforced composites (see Fig. 6b). The theoretical results given by the three phase and dilute models were obtained using an aspect ratio of 6. The results reveal that both models provide good estimates of the elastic modulus of composites. The dilute model underestimates the post yield strain hardening while the three phase model provides a good prediction of the hardening behavior. Both models, however, overestimate the yield stress. A potential explanation for this discrepancy is that the whisker lengths are not uniform and the longer whiskers fail at low macroscopic load levels, resulting in a reduced yield strength. Current analysis models do not consider this effect. An analytical investigation into this effect is required in future work.

The GSCM model also provides detailed microstructure level stress fields which aid in the understanding of the critical deformation and failure mechanisms. Fig. 7
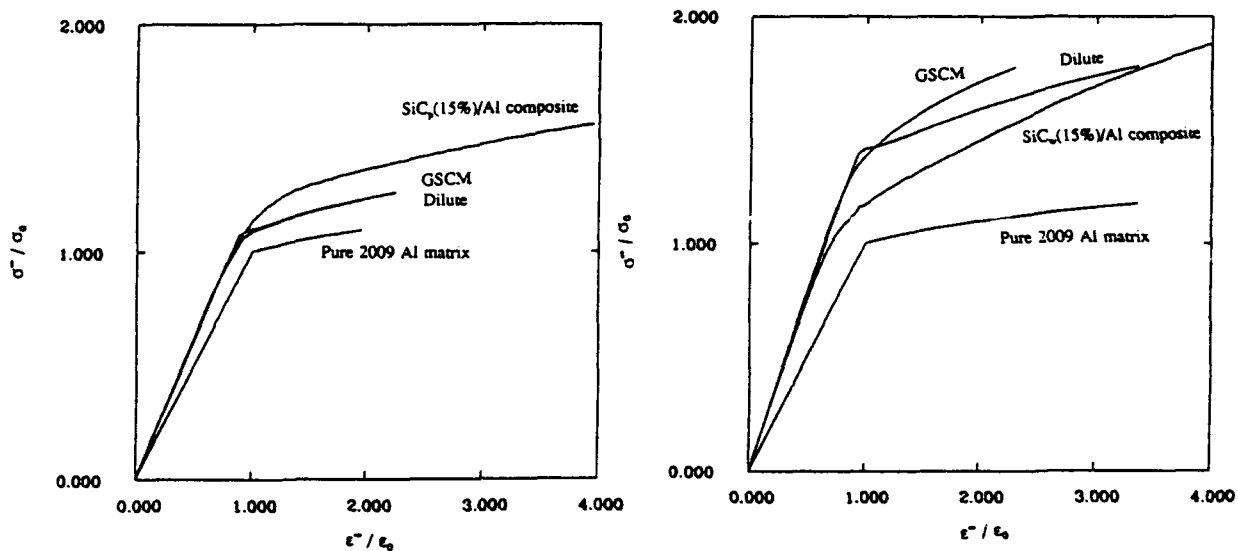
Figure 6. Comparison of experimental and analytical uniaxial composite responses.

shows the inclusion and matrix von Mises effective stress distributions when the macroscopic stress equals the matrix yield stress. Note that at this stress level, plastic deformation is induced near the poles of the inclusions. Also note that the inclusion stresses are far lower than published SiC strength properties [8]. The observation of cracked particles and whiskers, therefore, implies that the in-situ inclusion strength is much lower than the intrinsic material strength.

1. 24.2 ksi (167 MPa)	1. 20.2 ksi (139 MPa)
2. 32.3 ksi (233 MPa)	2. 32.3 ksi (223 MPa)
3. 40.4 ksi (279 MPa)	3. 40.4 ksi (279 MPa)
4. 42.4 ksi (293 MPa)	4. 101 ksi (697 MPa)
5. 44.4 ksi (307 MPa)	5. 109 ksi (753 MPa)
6. 60.0 ksi (418 MPa)	6. 117 ksi (808 MPa)
7. 64.6 ksi (446 MPa)	7. 119 ksi (822 MPa)
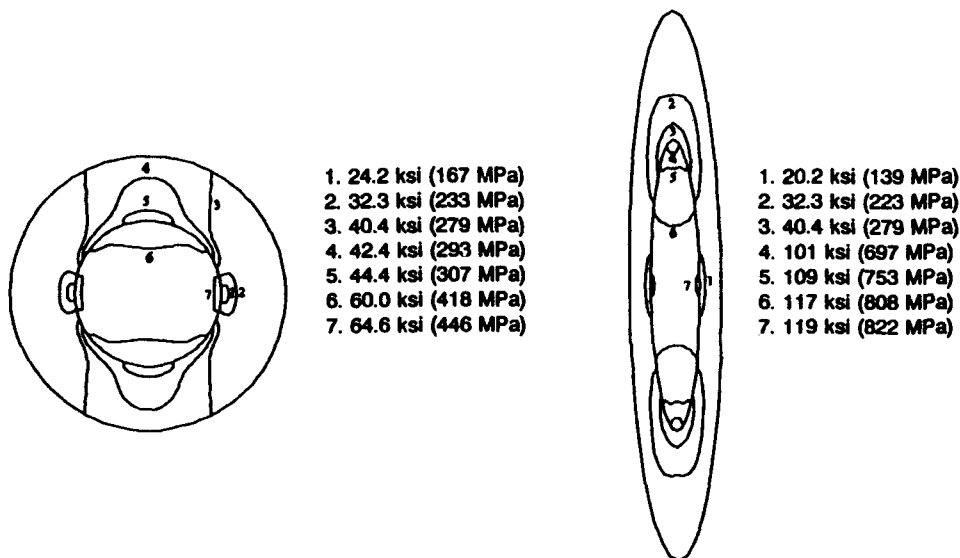
Figure 7. Predicted effective stress distributions at $\sigma^{\infty}=\sigma_0$ in SiC_p/Al and b) SiC_w/Al composites.

CONCLUSIONS

In this study, the uniaxial tensile stress-strain response and microstructural characterizations of both SiC_p and SiC_w reinforced 2009 aluminum metal matrix composites were investigated. The microstructural characterization of undeformed

samples provides the reinforcement geometry, volume fraction, aspect ratio, orientation and distributions. Examination of the fracture surface and the internal microstructure of specimens after mechanical loading reveals evidence of reinforcement failure, ductile matrix failure and reinforcement/matrix debonding. The uniaxial mechanical tests provide quantitative measurements of the effect of reinforcement geometry on the composite response. It is shown that the reinforcements (particles or whiskers) provide an increase in the elastic modulus, yield strength and ultimate strength, but a decrease in the strain to failure for the composite materials.

The failure micromechanisms in these materials were also investigated. For the case of SiC_p/Al composites, it is shown that brittle fracture of the reinforcing particles initiates failure in these composites. Particle fracture is then followed by rapid void growth and coalescence. For the case of whisker-reinforced SXA 2009 composites, the results indicate a more complex fracture process involving whisker fracture, whisker-matrix decohesion and pull-out of whisker from the matrix.

Finally, comparisons are made between the experimental uniaxial stress-strain response and the theoretical model predictions. The results show that the GSCM model provides good estimates of the elastic modulus and post-yield strain hardening for both particulate and whisker reinforced composites. The correlation between experimental and theoretical yield stress, however, is not as good and requires future study of the evolution of microstructural damage.

ACKNOWLEDGEMENTS

REFERENCES

1. Rack, H. J. and Ratnaparkhi, P. L., "Powder Metal Composites," in Encyclopedia of Composites, VCH, New York.
2. Logsdon, W. A. and Liaw, P. K., 1986, "Tensile Fracture Toughness and Fatigue Crack Growth Rate Properties of Silicon Carbide Whisker and Particulate Reinforced Aluminum Metal-Matrix Composites,", Eng. Fract. Mech., 24, pp. 737-751.
3. Qin, J., 1991, "Elastic-Plastic Micromechanics Modeling of Metal Matrix Composites and Porous Materials." M.S. Thesis, University of Rhode Island, pp. 51-54.
4. Walker, A., Advanced Composite Materials Corporation, private communication.
5. Lewandowski, J. J., Liu, C. and Hunt, W. H., 1989, "Effects of Matrix Microstructure and Particle on Fracture of an Aluminum Metal Matrix Composite," Mat. Sci. and Eng., A107, pp. 241-255.
6. Taggart, D. G., Qin, J, and Adley, M. D., 1992,"Evaluation of Analytical and Numerical Models for the Elastic-Plastic Response of Particulate Composites," to appear Proceedings of ASME Winter Annual Meeting.
7. Taggart, D. G. and Bassani, J. L., 1991, "Elastic-Plastic Behavior of Particle Reinforced Composites - Influence of Residual Stress," Mech. of Mat., 12, pp. 63-80.
8. DeBolt, H. E., 1982, "Boron and Other Reinforcing Agents," in Handbook of Composites, G. Lubin, ed., Van Nostrand Reinhold, New York, pp. 179-183.

Optimization of the Fabrication Process to Improve the In-Service Loading Capacity of Metal Matrix Composites

M. R. MOREL, D. A. SARAVANOS AND C. C. CHAMIS

ABSTRACT

A methodology is presented to tailor the fabrication process of metal matrix laminates for improved load carrying capacity. A unique feature is the concurrent inclusion of effects from fabrication, residual stresses, material nonlinearity, and thermo-mechanical loading on the response of the post-fabricated laminate. The effectiveness of the method is demonstrated on a [0/90]s and a [±45]s Gr/Cu laminates. Additional strong beneficial coupling was observed between the fabrication process, laminate characteristics, and thermo-mechanical loading.

OVERVIEW

A growing demand for lightweight, high-temperature materials for structural applications in which thermo-mechanical loading is a primary consideration has led to a focus on metal matrix composites (MMCs). Yet, the combination of inhomogeneous constituents with widely differing mechanical properties and high thermal stability is not free of problems, and considerable attention is required before MMCs may be successfully used in aerospace applications. Perhaps the most acknowledged problem is the presence of residual stresses as a result of the mismatch in the coefficients of thermal expansion (CTE) between the fibers and matrix. The development of residual stresses during the fabrication adversely affects many thermomechanical properties and the performance of the composite. Typically, the property reduction is induced by either: cracks in the matrix, as has been observed experimentally [1] after processing; or by interactions between the residual stresses, the inelastic behavior of the metallic matrix, and the post-fabrication thermomechanical load cycles. Nevertheless, strong coupling exists between processing and the thermomechanical performance of MMCs and metal-matrix laminates (MMLs) which needs to be addressed, quantified, and possibly explored to improve the composite properties. Some work in this direction is reviewed and extended in this paper.

M. R. Morel, Sverdrup Technology, Inc., 2001 Aerospace Parkway, Brookpark, Ohio, 44142

D. A. Saravanos, Ohio Aerospace Institute, 2001 Aerospace Parkway, Brookpark, Ohio, 44142

C. C. Chamis, NASA Lewis Research Center, 20001 Brookpark Rd., M.S. 49-8, Cleveland, Ohio, 44135

Research has shown that it is possible to individually or concurrently tailor the fabrication process and interphase (fiber coating) layer for unidirectional MMCs to minimize the residual stresses [2]. A significant conclusion from reference [2] was the potential to "control" the microstresses during fabrication by altering the temperature and pressure histories and introducing a tailored interphase layer. Yet minimization of the residual stresses alone, does not ensure the optimal performance of the composite laminate in aggressive thermomechanical environments. However, with the ability to control thermal stresses during fabrication a metal matrix laminate can be "engineered" with improved strength, stiffness, and other characteristics by tailoring critical fabrication and laminate parameters [3]. This suggests that to successfully tailor MMLs the effects of residual stresses, fabrication dependence, material nonlinearity, and operation at elevated temperatures should be included in the design procedures.

Hence, a methodology is developed that takes into account all these effects in the concurrent fabrication-laminate tailoring of MMLs. The method is reviewed in the present paper. The objectives of the design are to improve the in-service load carrying capacity. The possibility to improve the isothermal fatigue life is also currently investigated. The candidate design variables are the temperature and pressure histories of the fabrication process. Demonstrations of the method on ultra-high modulus graphite (Gr)/copper (Cu) composite are included. Additional investigations of the optimum stress state quantify the coupling between the design variables and applied thermo-mechanical loads.

FABRICATION AND LOADING CYCLE

A typical TM life cycle of a MMC laminate from fabrication to failure at operational conditions (e.g. engine components) is schematically shown in Figure 1. MMCs are most often fabricated by hot-pressing the matrix onto the fibers at elevated temperatures. Temperature and pressure are controlled to ensure adequate consolidation between constituents as the composite is cooled to room conditions (21°C and 0 MPa). The post-fabrication TM loading consists of a combination of increased temperature and mechanical loads, which can be static or dynamic.

As previously mentioned, residual stresses are developed during the cool-down, and directly affect the performance of MMCs during its service life. The residual stresses may again be reduced due to the differential between fabrication and the in-service temperature. Additional mechanical stresses are imposed on the composite, in addition the mechanical properties change due to the elevated temperature and cumulative stresses. Nevertheless, the development of residual stresses will affects the TM performance of the laminate which implies that its response will depend on the fabrication and loading parameters, as a result, strong coupling may exist.

COMPOSITE MECHANICS

Nonlinear micromechanics are used to capture the temperature effects, the non-
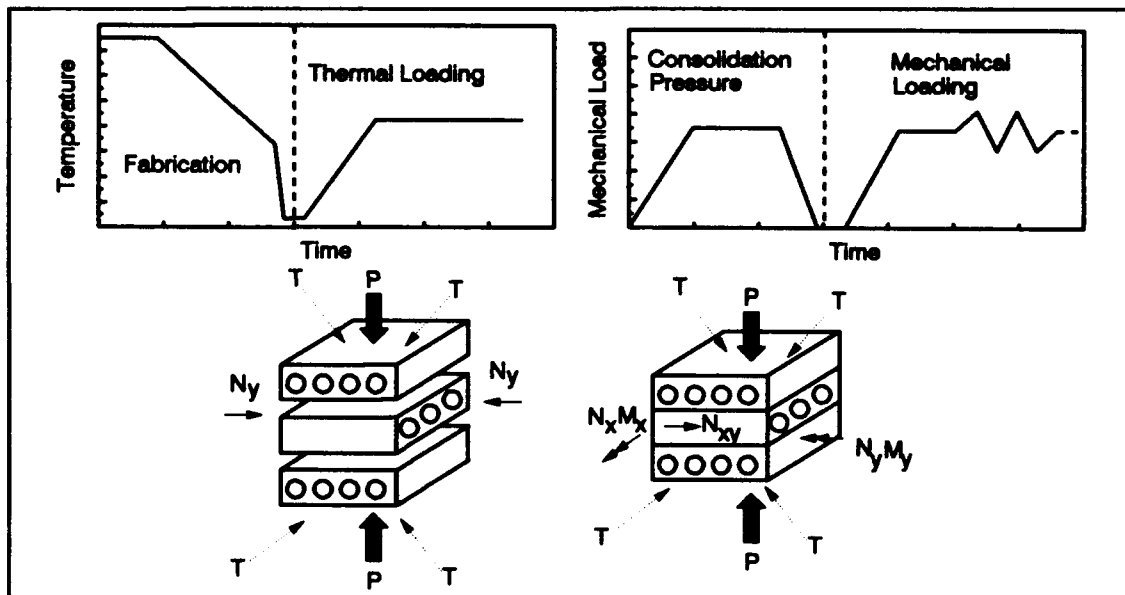
Figure 1:   Typical fabrication and thermo-mechanical loading phases of metal matrix laminates.

linear response of the constituent materials, the interaction among plies, and the residual stress build-up. The theory was developed on the assumptions of constant average stresses, principles of displacement compatibility, and force equilibrium. The composite mechanics have been implemented into an in-house research code, METCAN [4], which has been shown to sufficiently predict the nonlinear response of the MMC and its constituents. Fig. 2 shows the representation of inelastic effects in a copper matrix.

This incremental procedure is used to simulate the nonlinear composite response, assuming that the homogenized composite and the individual constituent materials behave elastically during each load increment. The mechanical laminate loads, temperature, and resultant stresses at any increment are the cumulative quantities at the respective increment.

TAILORING METHODOLOGY

The proposed method aims to optimally control the development of residual microstresses by tailoring the fabrication process in order to maximize the load carrying capacity. Considering the design criteria and the complexity of the simulation, this may be best accomplished with non-linear mathematical programming (NLP) [5]. It is recalled that a standard constrained NLP problem involves the maximization of an objective function, $F(z)$, subject to constraints of the following form:
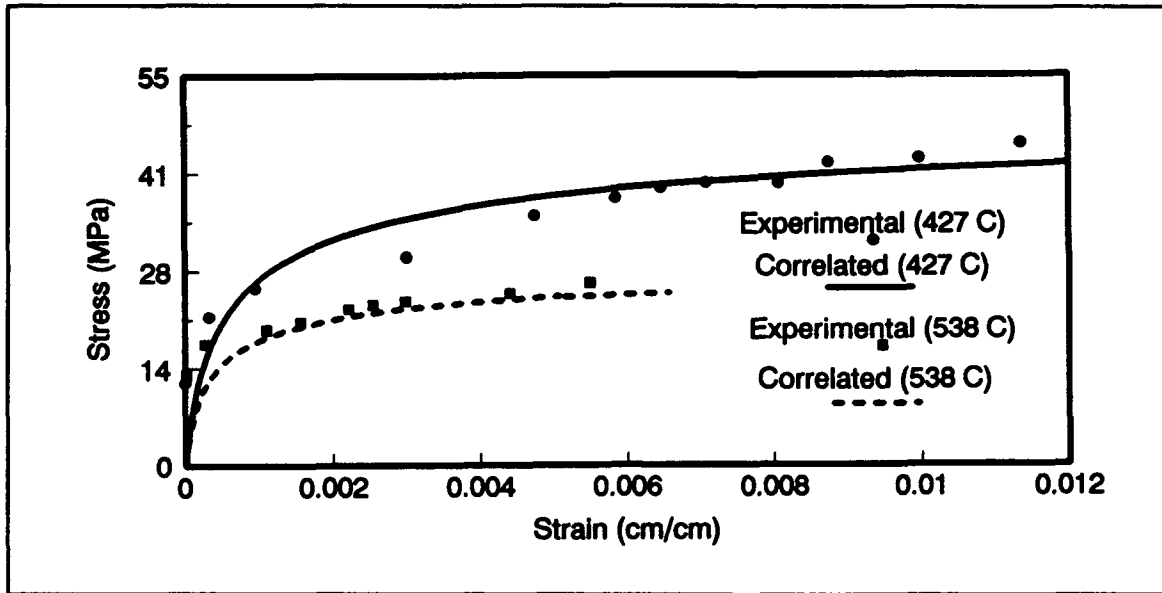
Figure 2: Typical matrix inelastic response for a copper matrix alloy, correlated and measured results.

$$z^L \le z \le z^U \tag{1}$$

$$Q(z) \le 0 \tag{2}$$

The design variables are represented by the vector z with U and L indicating upper and lower bounds. Also, $Q(z)$ are the inequality performance constraints. Eqs. 1 and 2 define the feasible region for the design variables. In the present paper the design vector includes the temperatures and consolidation pressures histories with the objective function being formulated by maximizing the in-plane forces $\{N\} = \{N_x, N_y, N_{xy}\}$ and moments $\{M\} = \{M_x, M_y, M_{xy}\}$.

Constraints are imposed in the form of the maximum stress criterion on the fiber (f) and matrix (m) microstresses at various time steps t during the processing and TM loading

$$S_{Cm}^t \le \sigma_m^t \le S_{Tm}^t \tag{3}$$

$$S_{Cf}^t \le \sigma_f^t \le S_{Tf}^t \tag{4}$$

The subscripts C and T identify compressive and tensile material strengths (S) at the corresponding thermo-mechanical state. The significance of these constraints is stressed, as they ensure the elimination of damage in the fibers and matrix during fabrication. Additional stress-range constrains are imposed on the cyclic stresses when isothermal fatigue is considered.

The tailoring problem described above is highly nonlinear, because the nonlinearity in the performance criteria is coupled with the nonlinear thermo-

mechanical response of the material. The method of feasible directions [6] was used for its ability to handle the complex nature of the tailoring procedure, confine the search within the feasible domain, and its computational efficiency.

RESULTS AND ANALYSIS

Two different laminate lay-ups, $[0/90]_S$ and $[\pm 45]_S$, were selected to demonstrate the method. This basic composite system, Gr/Cu, was chosen because of its acceptance as a potential candidate material for aerospace applications and the availability of experimental data [7-8]. Also, due to the properties of the graphite fibers, the high anisotropy, and the ductility of the copper matrix makes this composite system a prime candidate for fabrication tailoring. The initial FVR was 36% and the thickness of each ply was assumed to be 0.01 in.

The consolidation temperature and pressure histories of the fabrication process were tailored for two biaxial loading cases: (1) an in-plane compressive load ($N_x = N_y$, $N_{xy} = 0$); and (2) an out-of-plane bending moment ($M_x = M_y$, $M_{xy} = 0$).

The post processing loading cycle consisted of a linear temperature increase to 316°C followed by application of the previously mentioned biaxial load cases. In both cases the tailoring involved two objective functions. Case 1 required maximization of the in-plane compressive load ($F_1 = N_x$) and case 2 required maximization of the out-of-plane bending moment ($F_1 = M_x$) at the end of TM loading. All fabrication processes are presented as normalized values due to proprietary information.

IN-PLANE COMPRESSIVE LOADING CASE

In TABLE I are the resultant values of the maximum compressive load carrying capacity for the current and tailored fabrication processes. The maximum loading was determined when either the fiber or matrix stress reached failure their current ultimate strength. A higher compressive load was achieved when the fabrication process was tailored for both laminate lay-ups. These results demonstrate the effectiveness of the tailoring methodology.

The increase in load carrying capacity for both laminate lay-ups can be attributed to the changes in the fabrication processes (Fig. 3). Consolidation pressure proved to be a critical parameter in the tailoring procedure. By increasing the consolidation pressure, thereby keeping the matrix in a "flow" state, as the temperature was decreased to room condition, the tensile residual matrix microstresses are reduced and lower compressive fiber microstresses are required to balance them. Also very similar trends in the tailored fabrication process were achieved for the different laminate lay-ups.

The critical stresses in both laminates are the longitudinal fiber stresses in each ply, as seen in Figs. 4-5, which show the stress distribution at the corresponding maximum loads. This state of residual stress, lower residual compressive fiber and tensile matrix stresses, is favorable to the laminate compressive loading. This, also, explains the observed insensitivity for the tensile loading case to fabrication tailoring. Due to the redistribution of stresses in the tailored laminates, the matrix does carry more of the load, but the stresses are still well below their failure threshold.

TABLE I: MAXIMUM LOAD CARRYING CAPACITY

Loading/Lay-up	Current Process Maximum Load	Tailored Process Maximum Load	% Increase in Load Carrying Capacity
compressive (lb/in) [0/90]$_S$	1010.0	1335.0	32
compressive (lb/in) [± 45]$_S$	1025.0	1375.0	25
bending moment (lb/in^2) [0/90]$_S$	14.0	17.8	27
bending moment (lb/in^2) [± 45]$_S$	13.2	15.8	20

Although the fabrication process and loading have only a slight effect on the fiber *in situ* properties, both affected the matrix *in situ* properties. This effect was beneficial as it enabled the control of residual stresses, but also induced a dependence of the extensional laminate stiffness to the applied load. One example of this interdependence was the observed decrease in laminate stiffness because the matrix was strained by the higher biaxial compressive load.
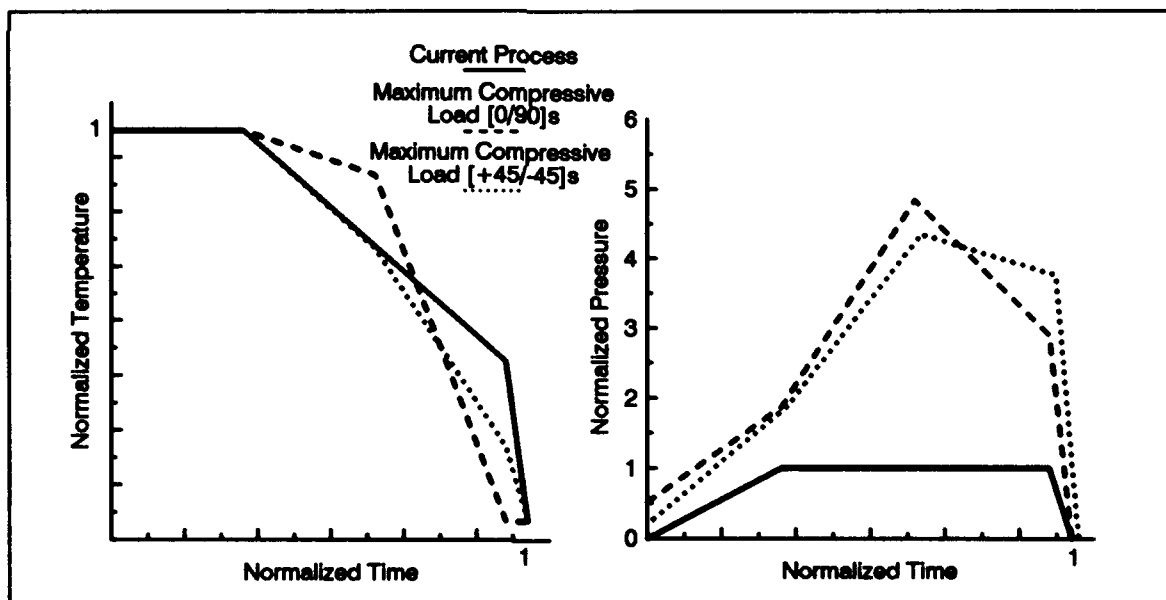
Figure 3:   Current and tailored fabrication processes for [0/90]$_S$ and [±45]$_S$ laminates under a thermal compressive load.

BENDING LOAD CASE

The values for maximum biaxial bending load at a constant elevated temperature
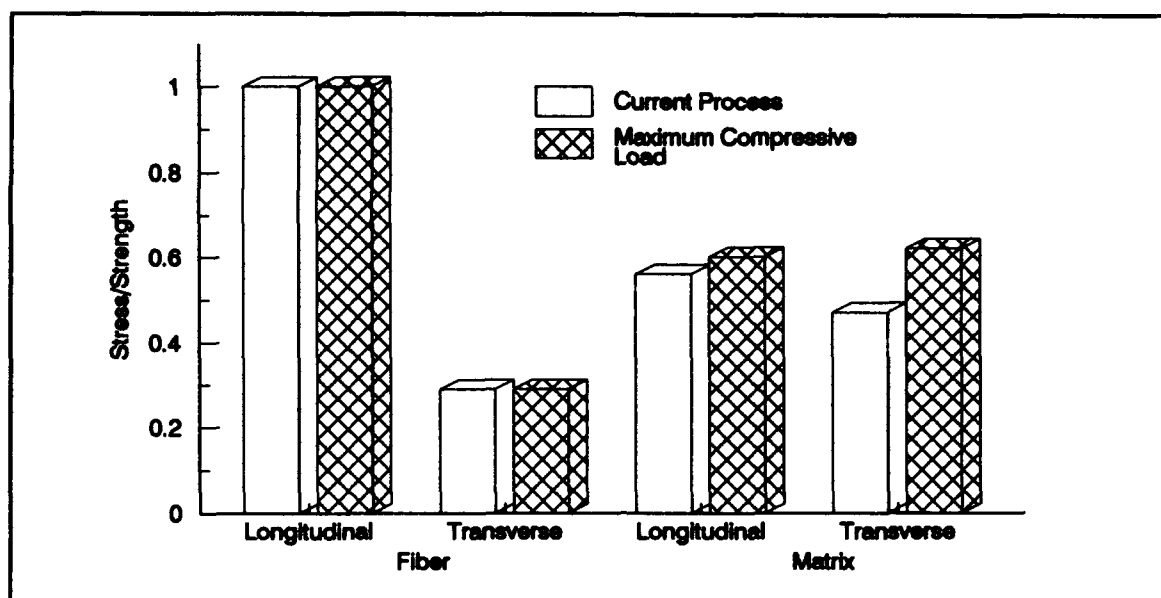
Figure 4:   Final normalized microstresses at the end of thermal compressive loading for $[0/90]_S$ Gr/Cu. The $0°$ and $90°$ plies are equivalent.
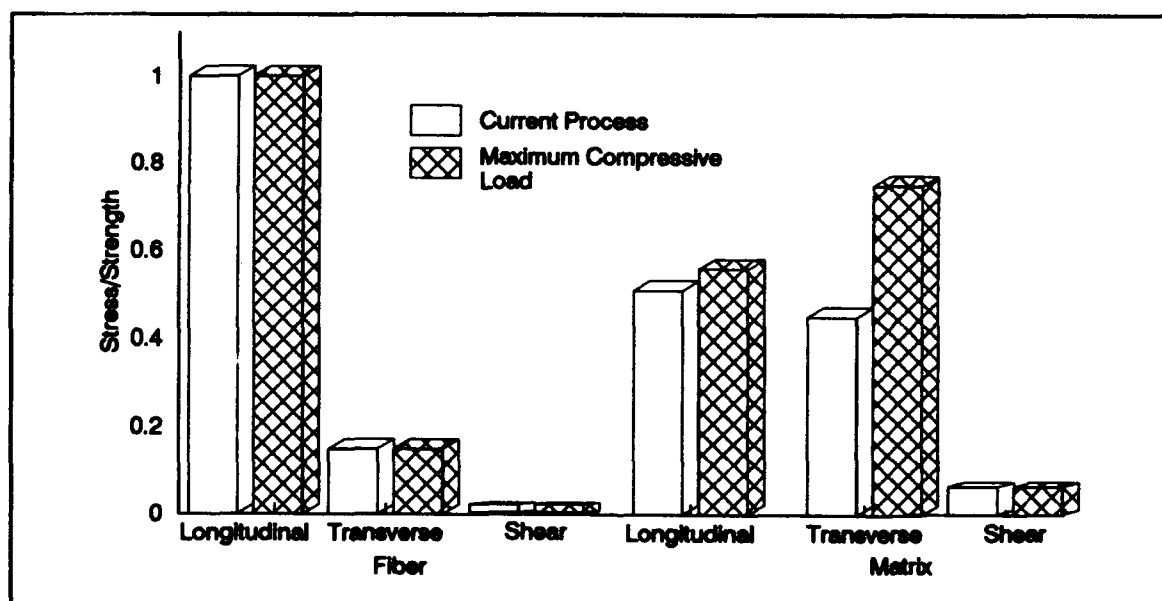
Figure 5:   Final normalized microstresses at the end of thermal compressive loading for $[\pm 45]_S$ Gr/Cu. The $+45°$ and $-45°$ plies are equivalent.

for the two different lay-ups are shown in TABLE I. For the current process, the maximum biaxial moment was determined and used as the reference value. Similar trends to the previous case of compressive loading were attained, whereby tailoring the fabrication process improved the load carrying capacity significantly.

The increases in bending load capacity for the fabrication tailoring can again be attributed to changes in the fabrication process (Fig. 6). The tailored fabrication process led to a more favorable residual stress state when compared to the current process, as both the fiber and matrix residual stresses decreased.

Shown in Figs. 7-8 are the final normalized microstresses which indicated the

failure mechanism to be the *longitudinal stress in the matrix* of the compressed ply (C) for the current process. The tailored process redistributed the stresses such that the fibers now carry more bending load. As previously explained, the resultant high consolidation pressure (see Fig. 6) decreased both the matrix stresses and the precompression in the fibers. Most important was the ability to control the stress build-up during fabrication and TM loading, demonstrated by the final longitudinal stress in the compressed ply (C) of the matrix which were reduced to a more favorable state due to fabrication tailoring. In contrast, the final matrix transverse stress increased when compared to the current process but has little effect on the load carrying capacity of the laminate. Finally shear stresses in the [±45]s are negligible.

Due to the bending load, different states of final stress exist in each ply, e.g. the top ply is in tension and the bottom ply is in compression. Even though the top ply is in tension, the reduction in compressive residual stress does not seem to affect the laminate load carrying capacity because the tensile strength of the fibers is much greater than its compressive strength. Also in this case there is a higher dependency on the matrix to carry the biaxial moment and provide some flexural rigidity when compared to the compressive loading case.

Finally, some dependence of processing to the laminate configuration and type of loading is also illustrated in the previous examples (see Figs. 3 and 6). This suggests of the possibility of coupling between laminate and fabrication tailoring.
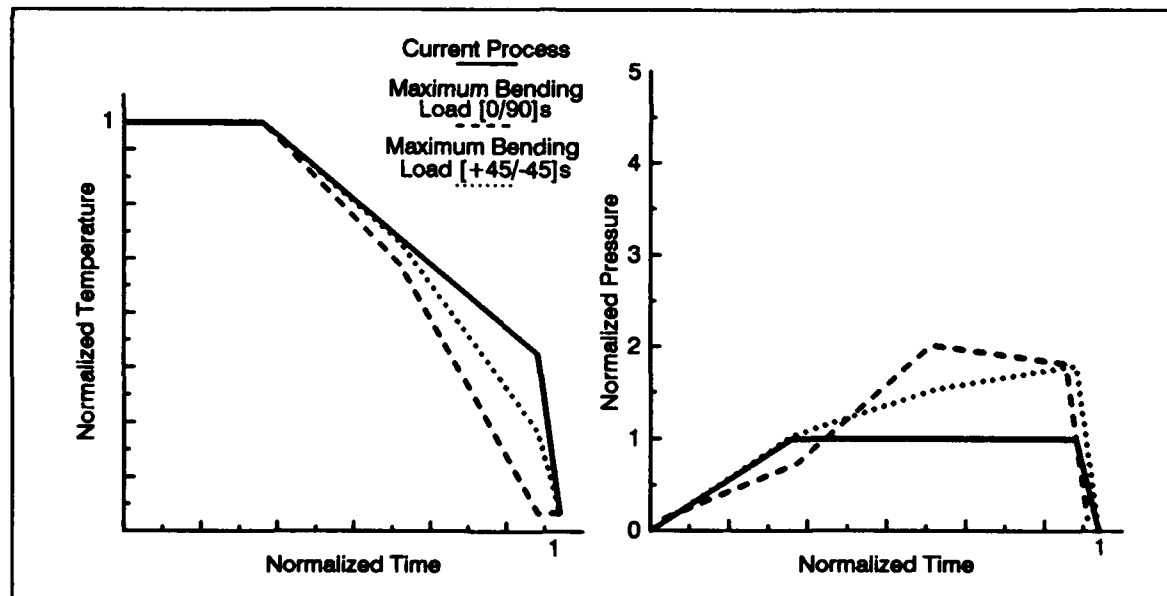
Figure 6:   Current and tailored fabrication processes for $[0/90]_S$ and $[\pm 45]_S$ laminates under a thermal bending load.
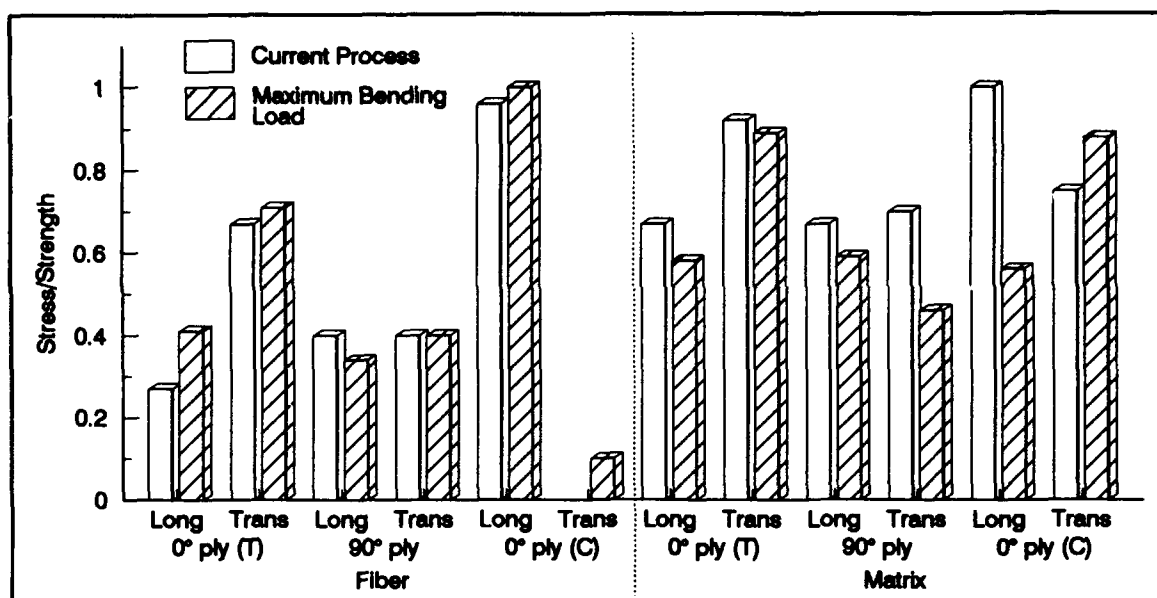
Figure 7:   Final normalized microstresses at the end of a thermal bending load for
$[0/90]_S$ Gr/Cu, T = tensile ply and C = compressive ply.
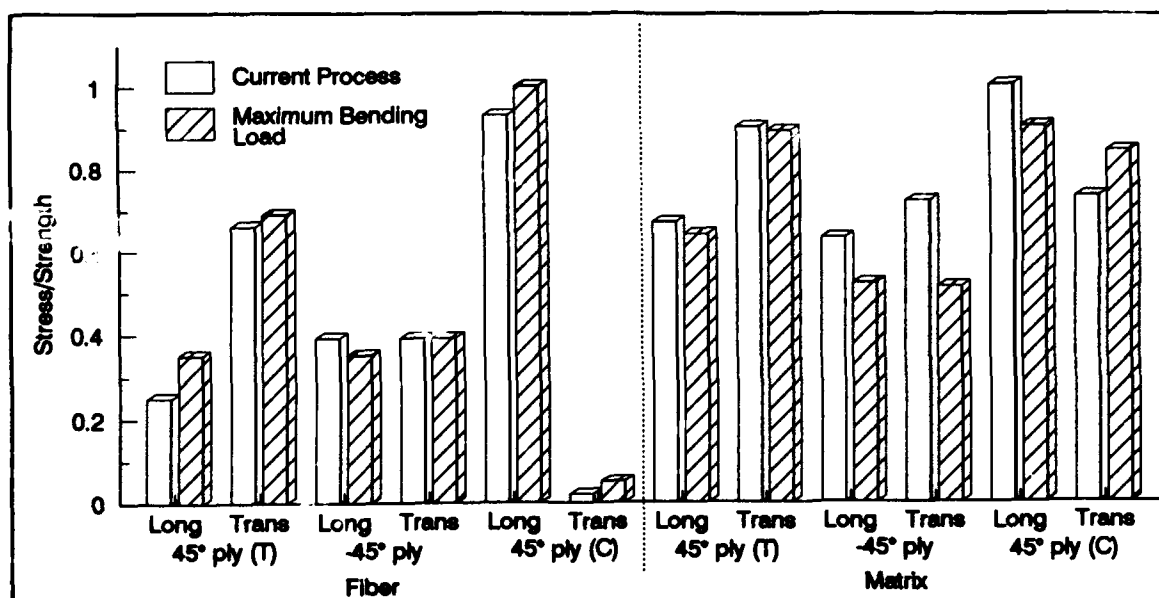
Figure 8:   Final normalized microstresses at the end of a thermal bending load for
$[\pm 45]_S$ Gr/Cu, T = tensile ply and C = compressive ply.

SUMMARY AND CONCLUSIONS

A computational methodology to tailor the fabrication process of inelastic composite laminates was developed. The performance of the laminate in the post-fabrication phase included the coupled effects of processing, residual stress build-up, and material inelasticity. An in-house research code has been developed incorporating this method.

Evaluations of the method for the maximization of the post-fabrication load carrying capacity at elevated temperatures were reported on $[0/90]_S$ and $[\pm45]_S$ Gr/Cu composite laminates. The tailoring of fabrication parameters significantly increased the strength of the composite. The results also illustrated the significance of process tailoring for these MMLs. The coupling between fabrication and material inelasticity was vital to achieving the final tailored designs. In conclusion, the results demonstrated the ability of the method and the potential of controlling the fabrication to produce "engineered" materials with improved mechanical properties.

REFERENCES

1. Gabb T. P., Gayda J., and MacKay R. A., "Isothermal and Nonisothermal Fatigue Behavior of Metal Matrix Composites," *Journal of Composite Materials*, Vol. 24, June 1990, pp. 667-686.

2. Saravanos D. A.,Morel M. R., and Chamis C. C., "Concurrent Tailoring of Fabrication Process and Interphase Layer to Reduce Residual Stresses in Metal Matrix Composites," *SAMPE Quarterly*, Vol. 22, No. 4, July, 1991.

3. Morel M. R., Saravanos D. A., and Chamis C. C., "Tailoring of Inelastic Metal Matrix Laminates with Simultaneous Processing Consideration," to appear in *Composite Science and Technology*, 1992.

4. Murthy P. L. N., Hopkins D. A., and Chamis C. C., "Metal Matrix Composite Micromechanics: In-Situ Behavior Influence on Composite Properties," *NASA TM 102302*, 1989.

5. G. N. Vanderplaats, *Numerical Optimization Techniques for Engineering Design: With Application*, McGraw-Hill Book Company, New York, 1984.

6. G. N. Vanderplaats, "ADS - A Fortran Program for Automated Design Synthesis," *NASA CR 177985*, 1985.

7. D. L. McDanels and J. O. Diaz, "Exploratory Feasibility Studies of Graphite Fiber Reinforced Copper Matrix Composites for Space Power Radiator Panels," *DOE/NASA/16310-12*, September, 1989.

8. R. H. Titran, T. L. Grobstein, and D. L. Ellis, "Advanced Materials for Space Nuclear Power Systems," *DOE/NASA/16310-16*, September, 1991.

SESSION 7B

Micromechanics II

Macro Finite Element for Analysis of Textile Composites

JOHN WHITCOMB, KYEONGSIK WOO AND SITARAM GUNDAPANENI

ABSTRACT

The analysis of textile composites is complicated by the complex microstructure. It is not practical to account for this microstructure directly using traditional finite elements. A new type of finite element was developed to efficiently account for microstructure within a single element. These new elements, which are referred to herein as macro elements, performed well in initial tests.

INTRODUCTION

Traditionally, advanced composite structures have been fabricated from tape prepreg, which was stacked to form a laminate. This type of construction tends to give optimal in-plane stiffness and strength. Since the primary loads usually are in-plane, this fabrication procedure appears logical. However, there are at least two reasons why the usual laminated construction may not be optimal. First, secondary loads due to load path eccentricities, impact, or local buckling can sometimes dominate the failure initiation because of the low through-thickness strength of traditional laminates. Second, for thick laminates there are many opportunities for mistakes in orienting the laminae.

Several alternatives which are receiving attention are weaving, braiding, stitching, knitting, and combinations of these. These various forms are referred to as textile composites. Approximate analyses have been developed for predicting moduli, but these analyses are far too crude to predict details of the local stress field (Refs. 1-3). Very little detailed three-dimensional analysis has been performed. These studies, which used 3-D finite elements (Refs. 4, 5), required tedious modeling, many simplifying assumptions about the material microstructure, and only considered very simple loading. The computational challenge is obvious when one examines the schematic of a simple plain weave in Fig. 1.

John Whitcomb, Associate Professor, Texas A&M University, Aerospace Engineering Department, College Station, TX 77843-3141

Kyeongsik Woo, Graduate Student, Texas A&M University, Aerospace Engineering Department, College Station, TX 77843-3141

Sitaram Gundapaneni,Graduate Student, Texas A&M University, Aerospace Engineering Department, College Station, TX 77843-3141

The resin pockets are removed to show the fiber tow architecture. This tiny piece of material, which is only about .28mm thick and about 1.4mm wide, is in fact, a fairly complicated structure. If four mats are stacked to obtain a thicker composite (still only about 1.1mm thick), it is obvious that the number of elements required becomes intolerable very quickly even for a coarse mesh. (See Fig. 2) A variationally consistent and organizationally (and computationally) tolerable procedure is needed for analyzing textile composites.

The objective of this paper is to describe a displacement based finite element which accounts for the spatial variation of material properties within a single element. This is in contrast to the usual choices of either adding more elements to account for microstructure or using averaged material properties within each element. The formulation of this new element will be discussed first. Then several configurations will be analyzed to evaluate the performance. For simplicity in the discussion, only two-dimensional configurations will be considered. However, the approach is general and can be extended easily to three dimensions.

THEORY

To simplify the discussion, a rectangular element with multiple layers of materials will be discussed first. Such an element might be used where the tows are straight or for ordinary laminated composites when there are too many lamina to model each individually. Then microstructure of arbitrary shape will be considered.

Consider the four node rectangular element in Figure 3 which contains three lamina of composite material. To facilitate the following discussion, the element will be referred to as a macro element and the subregions (lamina) will be referred to as subelements. The displacement field within the macro element is assumed to take the form

$$u(x,y) = N_i(x,y) u_i$$
$$v(x,y) = N_i(x,y) v_i \tag{1}$$

where $N_i(x,y)$ are interpolation functions and u_i and v_i are macro element nodal displacements. In equation (1) and subsequent equations cartesian index notation is used. In particular, a repeated subscript indicates summation. In equation (1) the summation is for the range $i=1$ to 4 since there are four interpolation functions for a four node element. The assumed displacement field is referred to herein as single field because a single approximation is used through the entire macro element. In contrast, a multi-field approximation would use approximations which are defined within a single subelement. The stiffness matrix can be calculated using the familiar formula

$$K_{ij} = \iint B_{mi} D_{mn} B_{nj} \, dx \, dy \tag{2}$$

where B_{nj} and D_{mn} are the strain-displacement and constitutive matrices, respectively. They are defined by the following equations

$$\varepsilon_n = B_{nj} q_j$$

$$\sigma_m = D_{mn} \varepsilon_n \tag{3}$$

where q_j = list of the element nodal displacements.

The complication that we have is that the constitutive matrix D_{mn} is now a discontinuous function of position. However, because of the simple geometry, one can perform the required integrations in closed form for each subelement and add the contributions. The details were described in Ref. 6 for a four node element. It was shown in Ref. 6 that the closed form expressions for the K_{ij} are quite simple for a four node element.

Rectangular macro elements with rectangular subelements cannot accurately model wavy regions like that shown in Figure 4. For such microstructure one needs to use distorted subelements. In the more general case, such as when the interface between woven mats is not straight, the macro element will also be distorted. Figure 5 shows a distorted quadrilateral macro element with distorted subelements. The large numbers (1-4) are the macro element node numbers. The smaller numbers are the subelement node and element numbers. For simplicity the resin pockets are not modeled.

To obtain a single field approximation, the subelement degrees of freedom (dof) must be expressed in terms of the macro element dof. There are several ways in which we can proceed. Two procedures will be discussed herein. Before proceeding it should be pointed out that in general the single field character is only exactly satisfied at the subelement nodes. The first procedure is to consider the subelement mesh to be an ordinary finite element mesh. The only difference is that after the subelement stiffness matrix and equivalent nodal load vector are determined, they are not immediately assembled, but are first transformed. This transformation can be expressed in matrix notation as

$$K_{ij} = T_{mi} K_{mn}^s T_{nj}$$

$$F_i = T_{mi} F_m^s \tag{4}$$

where T_{im} is defined by $q_i^s = T_{im} q_m$ and

$$
\begin{array}{lll}
q_i^s & = & \text{nodal displacements for subelement} \\
q_m & = & \text{nodal displacements for macro element} \\
K_{mn}^s & = & \text{stiffness matrix for subelement} \\
K_{ij} & = & \text{subelement contribution to stiffness matrix for macro element}
\end{array}
$$

The transformation matrix T_{im} is calculated using the macro element interpolation functions (which are defined in terms of local coordinates ζ and η) evaluated at the subelement nodes. For example, for a four-node macro element and a three-node subelement the transformation is

$$
\begin{bmatrix} u_1^s \\ v_1^s \\ \vdots \\ u_3^s \\ v_3^s \end{bmatrix} = \begin{bmatrix} t_{11} & t_{12} & t_{13} & t_{14} \\ t_{21} & t_{22} & t_{23} & t_{24} \\ t_{31} & t_{32} & t_{33} & t_{34} \end{bmatrix} \begin{bmatrix} u_1 \\ v_1 \\ \vdots \\ u_4 \\ v_4 \end{bmatrix} \qquad (5)
$$

where $\quad t_{ij} = \begin{bmatrix} N_j(\zeta_i, n_i) & 0 \\ 0 & N_j(\zeta_i, n_i) \end{bmatrix}$

Another possibility involves transforming the interpolation functions. This alternative is much more efficient unless there are a very large number of integration points. This procedure will be illustrated by considering the interpolation for the displacement in the x-direction, "u". A few more definitions are required before proceeding.

u $\quad=\quad$ macro element displacement in x-direction

u_i $\quad=\quad$ macro element nodal displacements in x-direction

u^s $\quad=\quad$ subelement displacement in x-direction

u_i^s $\quad=\quad$ subelement nodal displacements in x-direction

N_i $\quad=\quad$ interpolation functions for macro element

N_i^s $\quad=\quad$ interpolation functions for subelement

Within a subelement the x-displacement is approximated as

$$
u^s = N_i^s u_i^s \qquad (6)
$$

But the subelement nodal displacements are slaves to the macro element nodal displacements, as described earlier. This can be expressed as

$$
u_i^s = N_j(\zeta_i, \eta_i) u_j \qquad (7)
$$

where ζ_i, η_i = coordinates of subelement node i.

Combining equations 6 and 7 gives

$$u^s = N_i^s N_j(\zeta_i, \eta_i) u_j \qquad (8)$$

or

$$u^s = N_i^s T_{ij} u_j \qquad (9)$$

where $T_{ij} = N_j(\zeta_i, \eta_i)$. Note that this transformation matrix T_{ij} is similar to that in equation 4. The approximation for u can also be expressed in terms of modified interpolation functions,

$$u^s = \bar{N}_j u_j \qquad (10)$$

where $\bar{N}_j = N_i^s T_{ij}$.

Since the range of "i" in eqn. 10 is 1 → (number of nodes in the subelement) and the range of *j* is 1 → (number of nodes in the macro element), the "modified" interpolation functions can be different in number than the original functions. These modified interpolation functions are used when calculating the subelement stiffness matrices. Recall that the B matrix contains derivatives of the interpolation functions N_j. This presents no problem since the T_{ij} contains only constants. For example,

$$\frac{\partial \bar{N}_j}{\partial x} = \frac{\partial N_i^s}{\partial x} T_{ij} \qquad (11)$$

These modified interpolation functions are used in evaluating the terms related to the displacement interpolation. The unmodified interpolation functions are used to determine the determinant of the Jacobian for use in mapping the differential area dζdn from the subelement local coordinate system to a global coordinate system. Since the subelement displacements are slaved to the macro element displacements, there is considerable freedom in defining the subelements. For example, there is no need to prevent "dangling" nodes like that shown in Figure 5. In fact, one can even define the stiffness matrix for a macro element to be a summation of some very unlikely looking subelements. This is shown schematically in Fig. 6. This is probably of little practical utility for two-dimensional models, but for three-dimensional models this represents a major simplification.

The single field approximation gives very poor results for some configurations. For example, if the lamina in Figure 3 have large differences in E_Y, it is very difficult to approximate the stiffness in the y-direction using a single field approximation. This is because the single field assumption results in continuity of strains, which causes a discontinuity of stresses which should be continuous at the lamina interfaces. A numerical example of this poor performance will be given in the Results and Discussion section. However, as will be illustrated later, there are realistic configurations with significant inhomogeneity for which a single field approximation performs well. Also, the macro elements described herein cannot be evaluated using the usual mesh refinement convergence

methods. As the mesh becomes more refined, the inhomogeneity within an element disappears and the macro element becomes an ordinary element.

RESULTS AND DISCUSSION

Results for two basic configurations will be presented. The first is a one-dimensional bimaterial rod and the second is a 2D idealization of a woven textile. The material properties for the woven textile were assumed to be

$$E_{11} = 100 \text{ GPa} \qquad E_{22} = 10 \text{ GPa} \qquad E_{33} = 10 \text{ GPa}$$
$$\nu_{12} = 0.35 \qquad \nu_{13} = 0.35 \qquad \nu_{23} = 0.3$$
$$G_{12} = 5 \text{ GPa} \qquad G_{13} = 5 \text{ GPa} \qquad G_{23} = 3.845 \text{ GPa}$$

Two dimensional material properties were obtained by imposing plane strain conditions. The material properties were transformed to account for the inclination of the fiber bundle.

The bimaterial rod (shown schematically in figure 7) was used to evaluate the accuracy of a single field approximation when two materials are loaded in series. The axial displacement was assumed to vary as $\sum_{i=1}^{n} a_i x^i$, where n equals the order of the polynomial. Figure 7 shows the error in predicted stiffness versus the ratio E_b/E_a. As expected, the error increases with the ratio E_b/E_a. Perhaps surprising is the inability of an eighth order polynomial to adequately predict the response when E_b/E_a is larger than about 2. Obviously, the single field approximation is not very useful when two very different materials are loaded in series. However, most realistic configurations involving dissimilar materials have load paths which are a combination of series and parallel. The example of primary concern in this paper is a textile composite, which will be discussed next.

Two dimensional idealizations of textile composites were analyzed using single field macro elements. Waviness ratios b/a (see sketch in figure 8) were varied from .083 to .333. It should be noted that a woven composite is inherently three-dimensional. There is no typical cross-section. Concomitantly, results from any two-dimensional textile model must be used with caution. Consequently, the results presented should only be interpreted as an evaluation of the effectiveness of the macro elements for handling microstructure. Figure 8 shows the variation of extensional stiffness with waviness. Two symmetrically stacked mats were considered. Results were obtained using 120 eight-node traditional finite elements (reference solution) and 4 eight-node macro elements. The macro elements predict the stiffness variation quite well, except for very large waviness ratios.

Figure 9 shows undeformed and deformed finite element meshes for a single textile mat using 8-node traditional and 12-node macro elements. The absence of symmetry constraints results in large bending deformation. The deformed meshes are also shown overlaid to compare the predicted shapes. The macro elements predict the deformed shape very well.

CONCLUSIONS

A new type of finite element was developed for analysis of textile composites. This new element (referred to herein as a macro element) accounts for the spatial variation of material properties within a single element. Although only two-dimensional elements were evaluated, the formulation is valid for three-dimensions. Tests of the macro elements showed good performance for modeling the deformation behavior of textile composites.

ACKNOWLEDGEMENTS

REFERENCES

[1]   Halpin, J. C., Jerine, K., and Whitney, J. M., "The Laminate Analogy for 2 and 3 Dimensional Composite Materials," *Journal of Composite Materials*, Vol. 5, Jan. 1971, pp. 36-49.

[2]   Ishikawa, T., "Anti-Symmetric Elastic Properties of Composite Plates of Satin Weave Cloth," *Fibre Science and Technology*, Vol. 15, 1981, pp. 127-145.

[3]   Ishikawa, T. and Chou, T. W., "Stiffness and Strength Behavior of Woven Fabric Composites," *Journal of Material Science*, Vol. 17, 1982, pp. 3211-3220.

[4]   Whitcomb, J. D., "Three-Dimensional Stress Analysis of Plain Weave Composites," *Composite Materials: Fatigue and Fracture*, Volume 3, ASTM STP 1110, T. K. O'Brien, Ed., American Society for Testing and Materials, Philadelphia, 1991, pp. 417-438.

[5]   Blackketter, D. M.; Walrath, D. E.; and Hansen, A. C., "The Study of Woven Fabric Reinforced Composite Materials," University of Wyoming Composite Materials Research Group Report LIW-CMRG-R-89-102, April, 1989.

[6]   Whitcomb, J.D., "A Simple Rectangular Element for Two-Dimensional Analysis of Laminated Composites." Computer and Structures, vol. 22, no. 3, 1986, pp. 387-393.
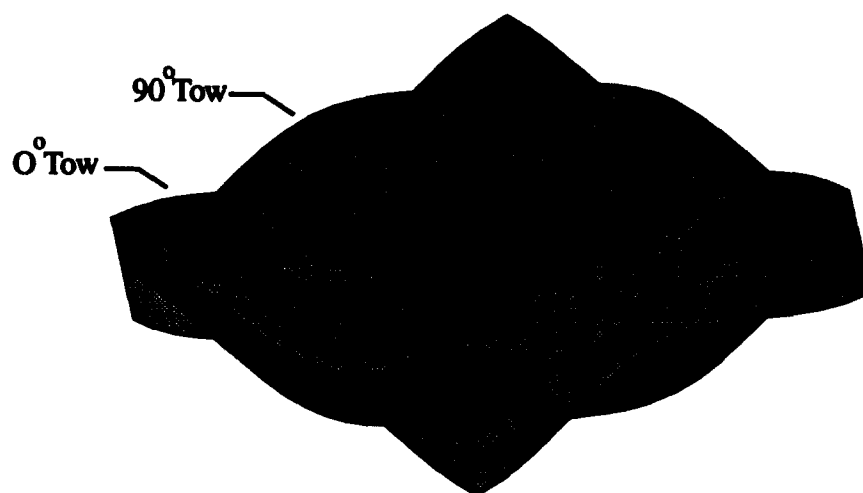
Figure 1 Schematic of plain weave composite.
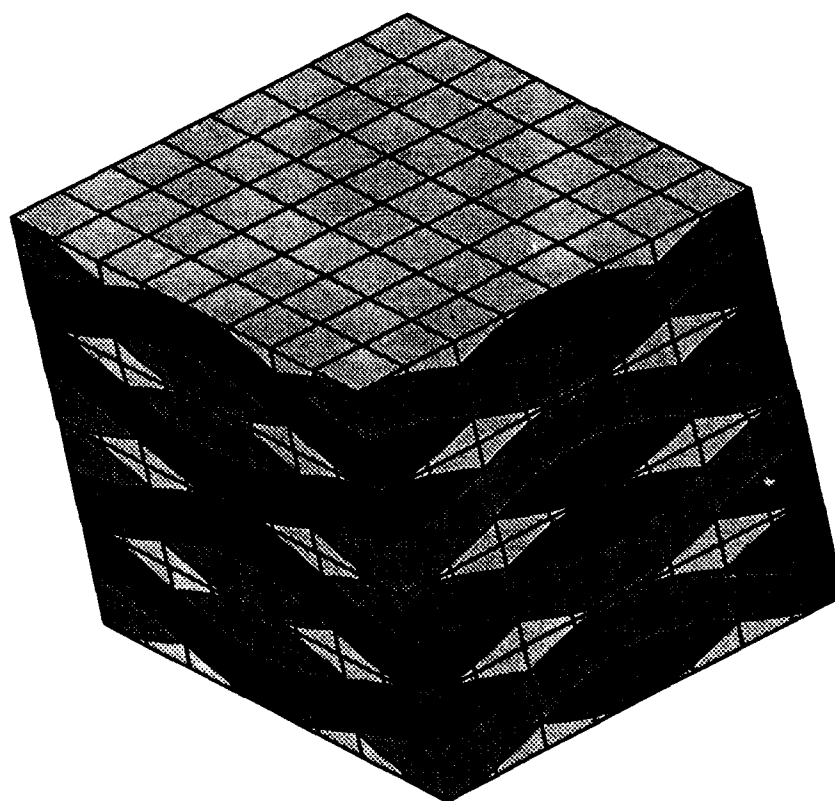
Figure 2 Schematic of symmetrically stacked plain weave composite.
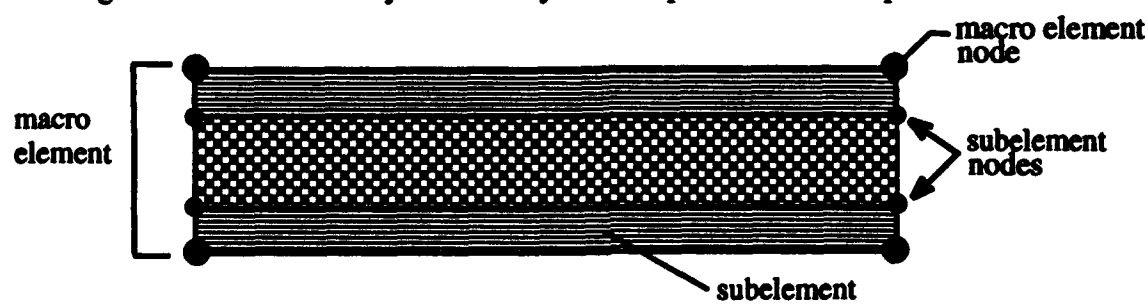
Figure 3 Macro element with layered microstructure.
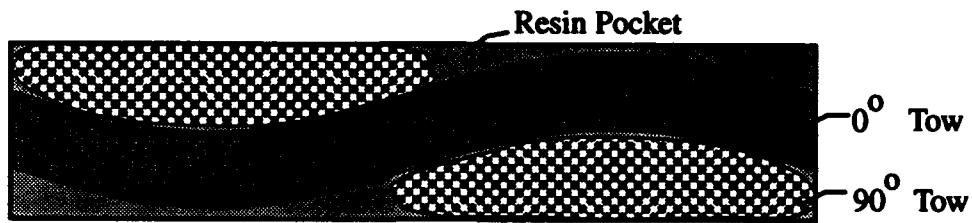
Figure 4   Schematic of plain weave cross-section
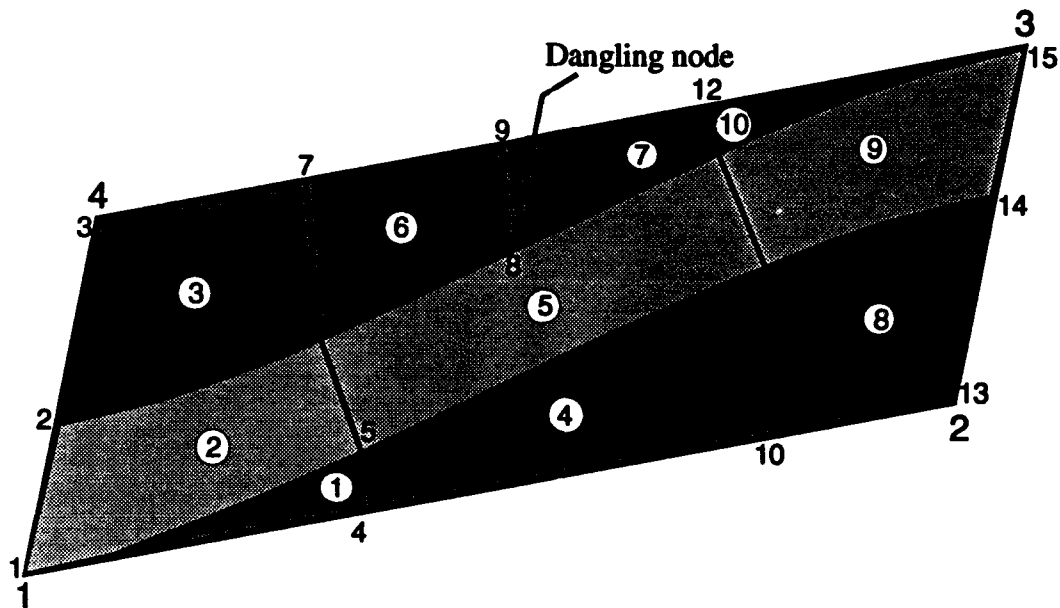
Figure 5 Distorted quadrilateral macro element with
distorted subelements

$$K^A = K^B + K^C$$
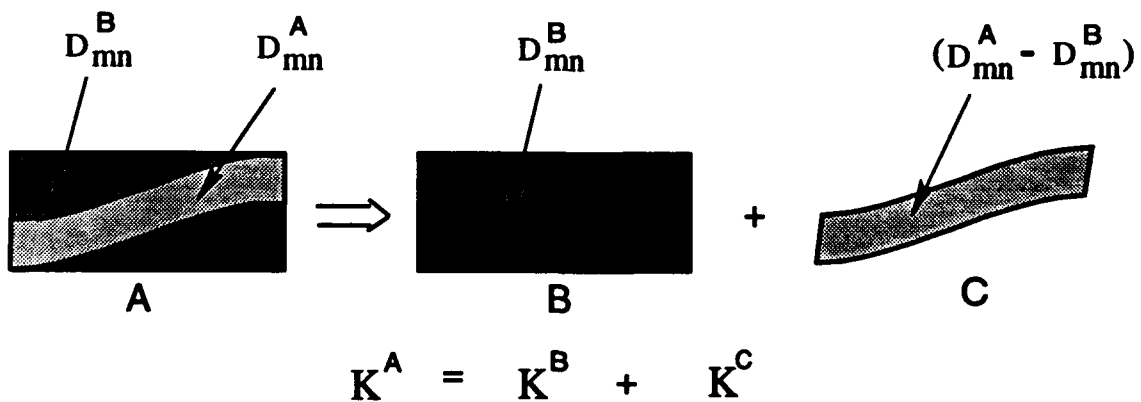
Figure 6 Alternate calculation of macro element stiffness matrix
for two dimensional configuration . (D_{mn} = Constitutive coefficients)
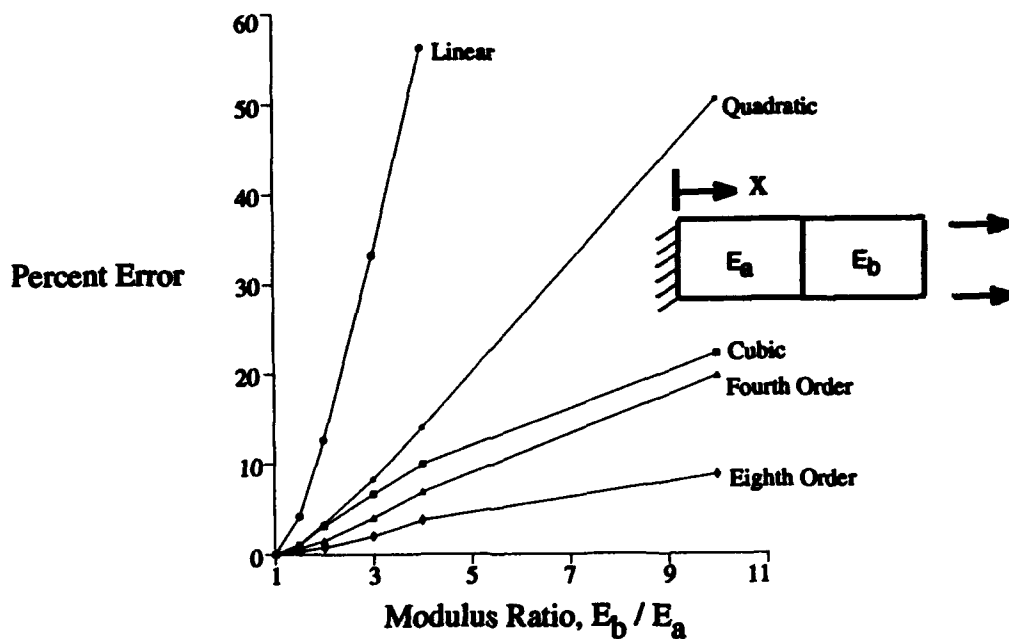
Figure 7 Error in calculated stiffness using single field approximation.
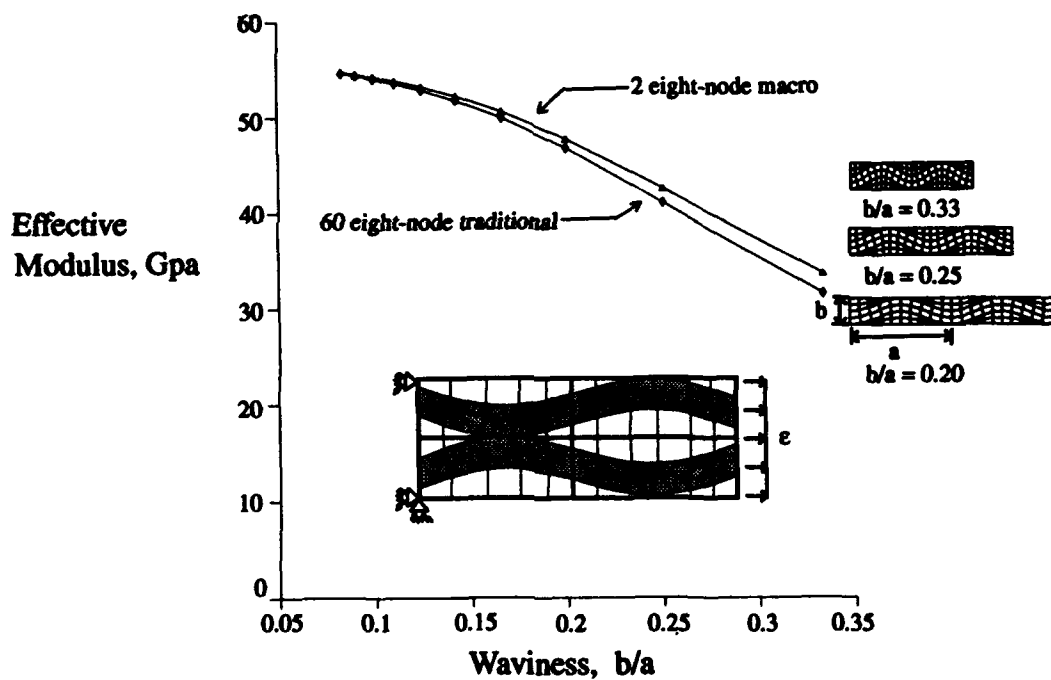
Figure 8 Extensional modulus versus waviness.
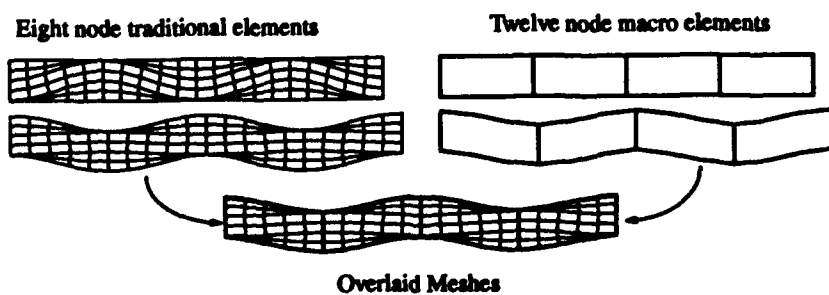
Figure 9 Comparison of deformed traditional and macro element meshes.

Simulation and Visualization of Stress Wave Propagation in a Composite with Interphase Layer and a Small Defect

TOSHIYUKI OSHIMA, RONALD D. KRIZ, YOSHIHIRO TAKAHASHI, SUMIO G. NOMACHI AND SHUICHI MIKAMI

ABSTRACT

In order to obtain a physical interpretation of a experimental data of ultrasonic-acoustic measurements, we simulate the experiment by numerical calculation on a supercomputer. The composite we discuss here is a two dimensional rectangular beam which has one reinforcement layer located at middepth. The Finite Strip Method (FSM) is used to formulate the composite and modal analysis and Duhamel integral equation are also used to obtain its dynamic response for the impulsive incident wave. And a ultrasonic wave diffraction by a small defect the data of which are given by FET, is also discussed by using a 3D scientific visual analysis (SVA). Making use of the Visualization Technique of Stress Wave Propagation (VTSWP) we obtain the animated simulation of stress wave propagation in a composite.

INTRODUCTION

In acoustic-ultrasonic measurement for NDE, much data on wave scattering is available. However, as long as we cannot visualize the dynamics of the scattering, we need to have the additional information of wave propagation and scattering from the physics to interpret the wave scattering at the boundary of the inclusion [1-6]. The Visualization Technique of Stress Wave Propagation (VTSWP) is a Numerical Visualization Method (NVM) using workstation-oriented graphic software by which we could analyze the above physical phenomena of stress wave scattering problem.

We recently have used an advanced graphic visualization software to investigate physical phenomena through a visualized simulation of stress wave propagation for which the data are given by a supercomputer calculation.

Toshiyuki Oshima, Kitami Institute of Technology, Kitami-city, #090, Japan
Ronald D. Kriz, Department of Engineering Science and Mechanics, Virginia Polytechnic Institute and State University, Blacksburg, VA 24061, U.S.A.
Yoshihiro Takahashi, Hokkaigakuen University, Sapporo-city, Hokkaido, #064, Japan.
Sumio G. Nomachi, College of Industrial Science, Nihon University, Narashino-city, Chiba #275, Japan.
Shuichi Mikami, Kitami Institute of Technology, Kitami-city, #090, Japan

In this paper we also discuss the effect of interphase layer [7] (rather than interface) between fiber and matrix of composite on the stress wave propagation by using VTSWP. As in composite the interphase region has some gradient distributions of the stiffness, and we need to clarify how these different types of gradient distribution contribute on the wave energy transmission from matrix to fiber during stress wave propagation.

The numerical model to formulate this composite is a Finite Strip Method (FSM)[8] and the modal analysis and Duhamel integral equation are used to obtain the simulation data of stress wave propagation [9]. The equation also contains the internal damping effect of the composite in the calculation.

The wave diffraction which is caused by a small defect like crack is also analyzed by using a scientific visual analysis. The wave diffraction of a two dimensional rectangular beam with a small defect is simulated by using a finite element method of a rectangular element. The results are shown by a 3D animation of CG procedure.

ANALYSIS OF TWO DIMENSIONAL RECTANGULAR COMPOSITE WITH INTERPHASE LAYER

EQUATION OF FINITE STRIP METHOD

A two dimensional rectangular beam subjected to a impulsive incident load is shown in Figure 1. The composite has one reinforcement layer together with the interphase layer located at middepth and its interphase layer has a gradient distribution of the stiffness from the matrix to the fiber. Finite Strip Method (FSM)[8] is used to formulate this two dimensional composite beam. FSM equation for two dimensional rectangular element is obtained by means of Galarkin's method, employing Fourier series in the longitudinal direction and linear variation in the transverse direction of the displacement field.
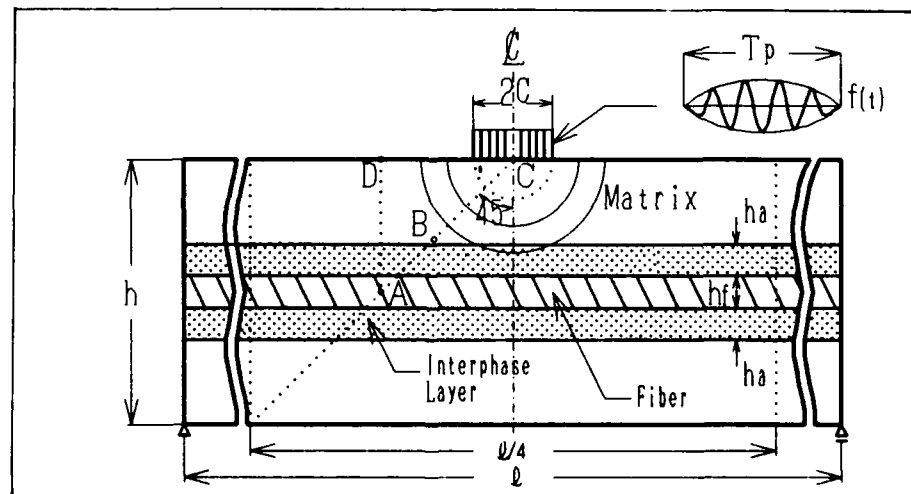
Figure 1. A composite laminate model with interphase layer.

We have the following equations relating to nodal displacements and nodal forces of a finite strip element

$$[K^m] \{ \delta_m \} + [C^m] \{ \delta_m' \} + [M] \{ \delta_m'' \} = \{ F_m \} \tag{1}$$

where

$$\{ \delta_m \} = \{ U^m_i, V^m_i, U^m_{i+1}, V^m_{i+1} \}^T \tag{2}$$

$$\{ F_m \} = \{ T^m_{i, i+1}, S^m_{i, i+1}, T^m_{i+1, i}, S^m_{i+1, i} \}^T \tag{3}$$

and prime ′ means the differentiation with respect to time t.

Superposing Eq.(1) for all elements of a whole composite beam, we obtain the following equation for the impulse response of a composite rectangular beam as follows;

$$[K] \{ \delta_{st} \} + [C] \{ \delta_{st}' \} + [M] \{ \delta_{st}'' \} = \{ F_{st} \} \tag{4}$$

where $[K]$ = stiffness matrix, $[C]$ = damping matrix, $[M]$ = mass matrix, $\{ \delta_{st} \}$ = displacement vector, and $\{ F_{st} \}$ = external force vector for the whole system of the beam shown in Fig. 1, respectively.

Making use of modal analysis and Duhamel integral equation for Eq.(4), the impulse response of composite rectangular beam is obtained.
In this paper it is assumed that both the coupling effect between different modes of the eigen-frequencies and the damping effect in the calculation of eigenvalues are negligible small. Thus we finally have a set of 1-DOF equations from which the impulse response of composite beam is obtained.

In this paper the damping coefficient h_r is taken to be frequency dependent and its value is given by the equation;

$$h_r = \frac{b \omega_r}{\omega_r^2 + a} \tag{5}$$

where a and b are given by the experiment [9,10].

VISUALIZATION OF STRESS WAVE PROPAGATION UNDER AN IMPULSIVE INCIDENT WAVE

To make the problem simple we deal with the composite rectangular beam which has one reinforcement layer at the middepth of the beam and simply supported at the ends. A impulsive incident load is applied at the centerspan of the beam with a finite aperture and its time history is taken as a actual impulse wave of acoustic-ultrasonic experiment.
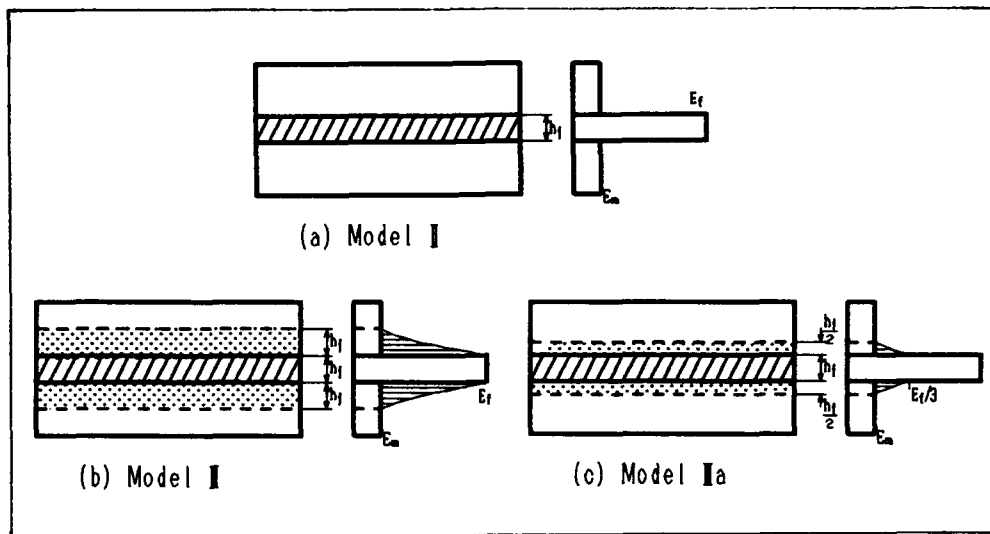
Figure 2. Three different models of interphase region.
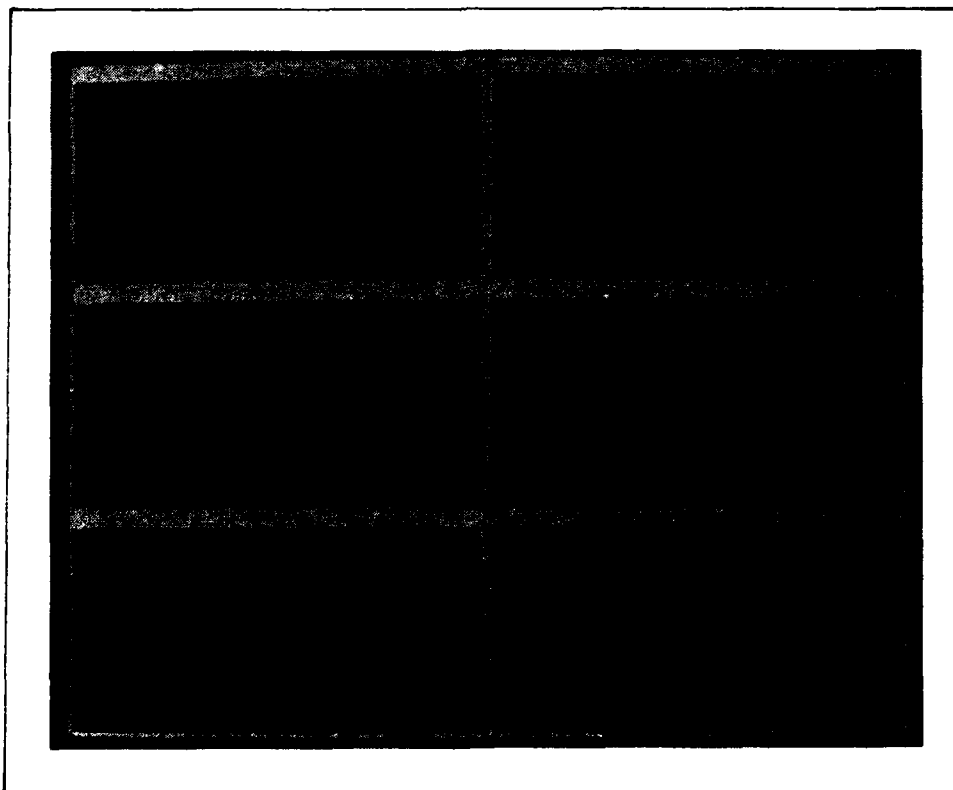
Figure 3. Animated stress waves of σ_x, σ_y and τ_{xy} from top to bottom, respectively, and left row is for a uniform beam without fiber and right row is for a composite model Ⅲ in Figure 2.

554

$$f(t)= \begin{cases} F_0 \sin 2\pi f_a t \sin 2\pi f_o t & \text{for } 0 \leq t \leq Tp \\ 0 & \text{elsewhere} \end{cases} \tag{6}$$

The numerical input data are;

E_m= 30GPa, E_T = 210GPa, ν =0.17, ν_T=0.30, ρ = 0.2347 g/cm^3, ρ_T= 0.801 g/cm^3,
ℓ = 320 cm, h= 40 cm, h_T= 4 cm, 2c= 6 cm,
M= 80 (summed-up terms for Fourier series),
n= 100 (number of finite strip elements),
Tp= 50 μs (duration time of impulsive incident load),
f_a= 10 KHz, f_o= 80 KHz (frequency of incident load),
$\triangle$t= 2 μs (time pitch of numerical calculation),
F_0= 1 (amplitude of incident load),
and a= 13935, b= 15.52 (coefficient of Equation (5) for damping effect).

Since we want to obtain the effect of interphase layer on the transmission of stress wave energy, we took the numerical models of the composite in three cases called Model II, Model III and Model IIIa as shown in Figure 2. Model I corresponds to a uniform beam without any fiber in it.
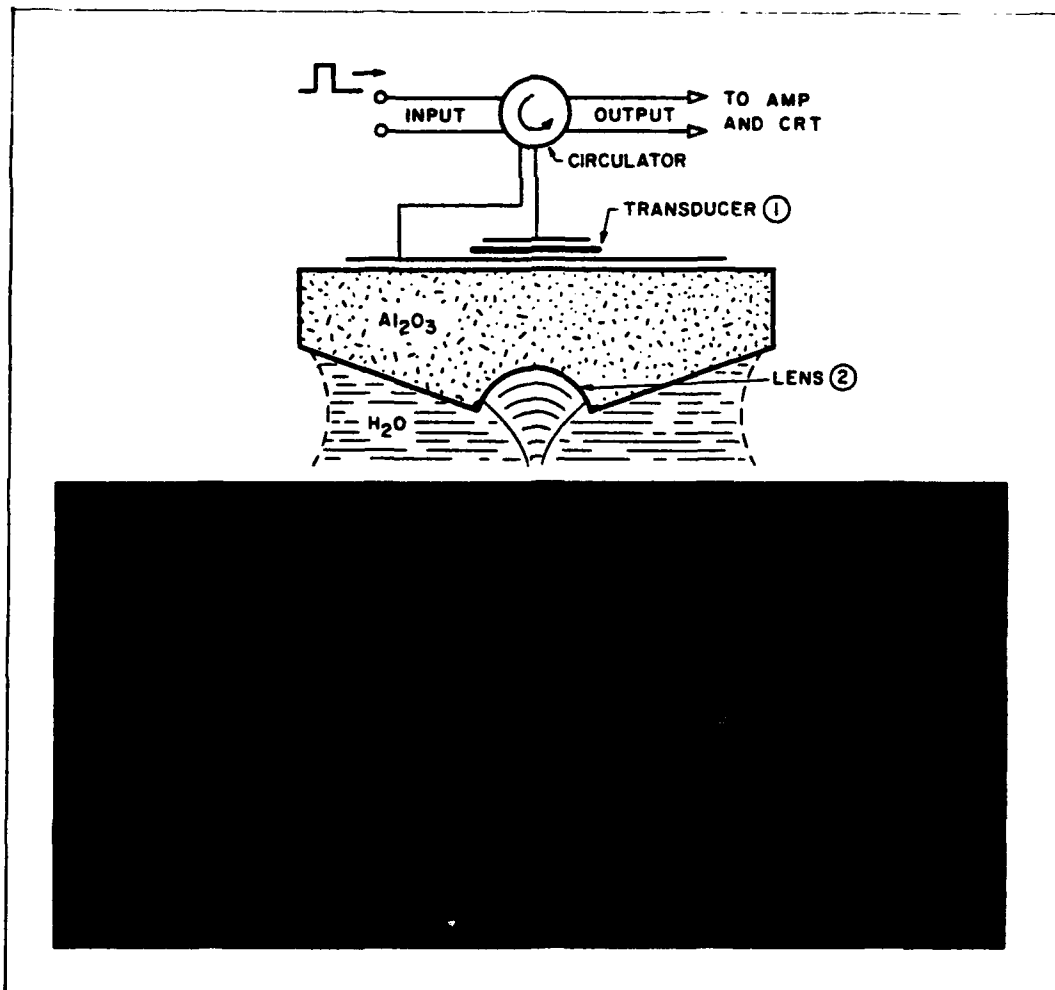
Figure 4. Lamb wave mode travelling along a fiber.

Model II has no interphase region. Model III has a full-range gradient of stiffness distribution from matrix to fiber and the thickness of this interphase layer is as same as the fiber layer and this region is divided to ten finite strip elements of equal size, changing its stiffness smoothly. The numerical calculations were done for 151 time steps up to 300μ s from initial impulse and a 200×100 equi-distantly located point grid of the beam was used to make a movie of the data. The size of this grid is 80cm$\times$40cm and located at midspan.

As a result of a two dimensional wave propagation in composite, the several kinds of wave modes such as longitudinal wave, shear wave, surface wave and Lamb wave (Fig.4) are involved in our data. So our attention is focused on these different types of wave modes to find out how mode transition occurs and how the wave energy changes its type of wave mode during the propagation and scattering. We can see in a visualized simulation each types of wave modes in the series of a movie. The individual stress responses of normal stress, shearing stress and principal stresses give us a slightly different aspects of mode transitions.

3D ANALYSIS OF ULTRASONIC WAVE DIFFRACTION BY A SMALL DEFECT

It is important for NDE of composite to find how ultrasonic wave is affected by a small defect embedded in a composite material. Ultrasonic wave which is applied on the surface of a specimen is reflected and diffracted at the boundary of a defect during its propagation. Then the received wave has to be analyzed its phase delay and amplitude change by the waveform analysis in the experiment. By this purpose we simulate a two dimensional wave propagation and represent its response of displacement by a 3D display procedure of computer Graphics(CG) and thus we obtain a comprehensive interpretation to understand how diffraction occurs within a composite.

NUMERICAL MODEL AND CALCULATION

A uniform deep beam with 30cm depth and 70cm length is divided into 30×70 elements of FEM and a small defect is located upper side of the beam as shown in Fig.5. Incident wave is applied at the span center of upper side of the beam and its time history is shown in Fig.6. Calculation was carried out in the case of uniform beam with and without a small slit.

Elastic constants and damping coefficient are as follows;

$$E=3\times10^5 kgf/cm^2 , \quad \nu =0.17 ,$$
$$h=\alpha + \beta \omega_r^2 , \quad \alpha =591 , \quad \beta = 8.52\times10^{-8}.$$

(a) without slit   (b) with slit
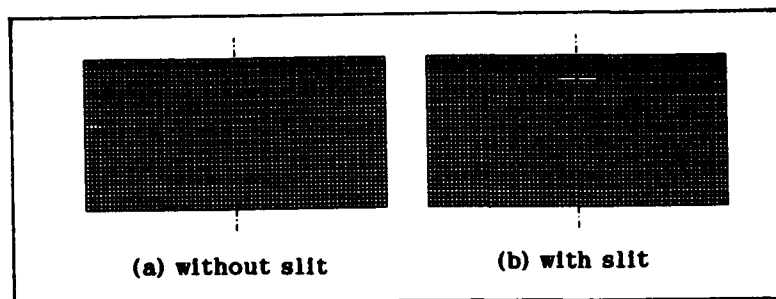
Figure 5. A uniform deep beam.
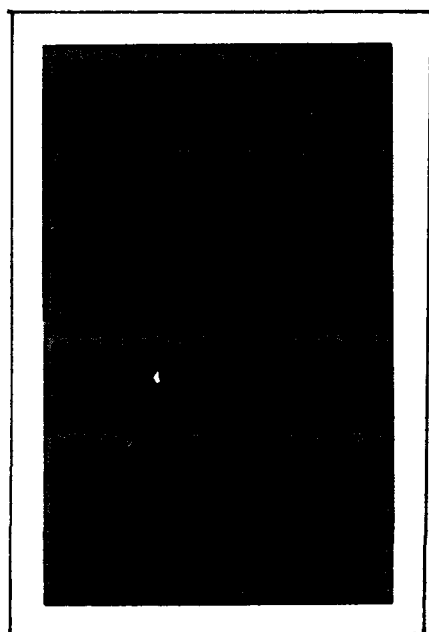
Figure 7. Dynamic displacement in the cases of with and without a slit.
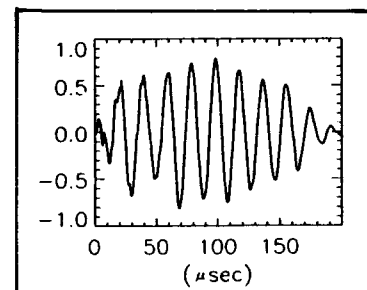
Figure 6. Incident wave.
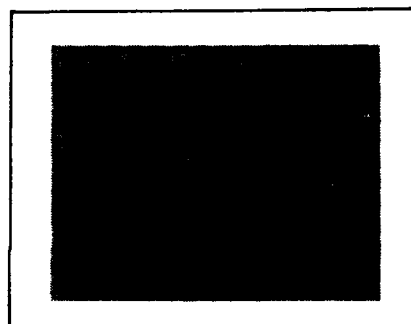
Figure 8. The results of subtraction without defect from that with defect.
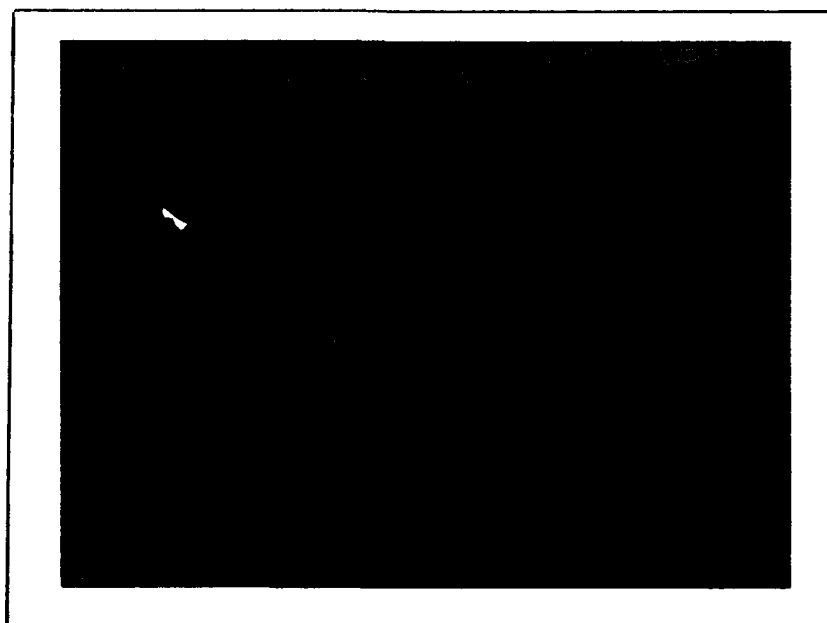
Figure 9. 3D displays of displacement in the cases with and without a defect.

557

RESULTS

Dynamic displacements are shown in Fig.7 by a monochrome display in the
cases of with and without a slit. By the comparison between two results we
can see how the wave diffract at the edge of a slit. And in Fig.8 the
results which is given by the subtraction of the results without defect
from that with defect. From these results we find the effect of only the
defect. In Fig.9 3D displays of displacement in the cases with and without a
defect are shown by using CG software. The amplitude of the dynamic
displacement is expressed in the perpendicular direction to the original
plane of propagation and we find how the incident wave diffract the small
defect.

CONCLUSIONS

   Summarizing the above on the stress wave propagation in a composite
rectangular beam, we have come to the conclusions as follows;

(1) In a animated simulation longitudinal wave, shear wave and their
reflected waves, surface wave and Lamb wave, are shown. The visualization
technique of stress wave propagation (VTSWP) by using the
workstation-oriented graphic software is helpful to represent the
results of supercomputer calculation. By this VTSWP we can perform the
numerical experiment on the workstation.

(2) By the comparison of simulated experimental data of a received
signal with the animated movies, the arrival of each wave modes can be
identically determined in the time history.

(3) The effect of a small defect on the wave diffraction are obtained by an
animated simulation. We see how ultrasonic wave diffract through a small
defect.

REFERENCES

 1. A. Briggs, 1985. An Introduction to Scanning Acoustic Microscopy,
Oxford University Press.
 2. K. Harumi, M. Uchida, 1990. "Computer Simulation of Ultrasonics and Its
Applications.", Journal of Nondestractive Evaluation, Vol. 9, pp.81-99.
 3. R.D. Kriz, P.R. Heyliger, 1989. "Finite Element Model of Stress Wave

Topology in Unidirectional Graphite/Epoxy: Wave Velocity and Flux Deviations.", Review of Progress in Quantitative Nondestructive Evaluation, Vol.8A, Edited by D.O. Thompson and D.E. Chimenti, Plenum Press, pp.141-148.
4. Z. You, W. Lord, 1989. "Finite Element Study of Elastic Wave Interaction with Cracks." Review of Progress in Quantitative Nondestructive Evaluation, Vol.8A, Edited by D.O. Thompson and D.E. Chimenti, pp.109-116.
5. R.D. Kriz, J.M. Gray, 1990. "Numerical Simulation and Visualization Models of Stress Wave Propagation in Graphite/Epoxy Composites." Review of Progress in Quantitative Nondestructive Evaluation, Vol.9, Edited by R.O. Thompson and D.E. Chimenti, Plenum Press, pp.125-132.
6. F. Fellinger, K.J. Langenberg, 1990. Numerical Techniques for Elastic Wave Propagation, Elastic Waves and Ultrasonic Nondestructive Evaluation, Elsevier Science Publishers.
7. L.H. Sharpe, 1974. "Some Thoughts about the Mechanical Response of Composites." Journal of Adhesion, Vol.6, pp.15-21.
8. Y.K. Cheung, 1976. Finite Strip Method in Structural Analysis, Pergamon Press.
9. T. Oshima, S.Mikami, S.G. Nomachi. 1990. "Analysis of Stress Wave Propagation in Composite Rectangular Beam in the Case of Ultrasonic Pulse Method." Proc. of Japan Society of Civil Engineers, No.416/I-13, pp.89-99.
10. H. Kolsky, 1963. Stress Waves in Solids, Dover Publications.

Banquet Speech

Carbon-Carbon: Bringing It to the Market Place

E. F. SCHAUB

(Figure 1) Thank you, Ken, and thank you ladies and gentlemen. It is indeed a pleasure for me to be here tonight and speak to you about some of the trials and tribulations we at BFGoodrich have experienced in bringing carbon-carbon products to the market place.

As Ken has mentioned, I have been with BFGoodrich for over 20 years working in a variety (Figure 2) of positions and in several different businesses. One of the most exciting businesses that I have worked with during my tenure with Goodrich has been our carbon products business. It is dynamic, technically demanding and has great growth potential.

(Figure 3) Tonight, I hope to give you a flavor of that growth while relating, somewhat tongue-in-cheek, some of our experiences in bringing carbon-carbon products to the market place.

Before I start, however, let me first make sure that we all are in agreement of what a carbon-carbon composite is and what it is not.

A few of you may think of carbon-carbon composites as a kind of fiberglass such as the type used in making boat hulls or automobile bodies. Or, if you are like me, you might think of it as graphite of the type that golf clubs or tennis rackets are made (Figure 4). However, most of you probably think of carbon-carbon as a composite of the type used in aircraft structures, like the wings or tails of airplanes.

Actually, none of those is a carbon-carbon composite, although many of them contain some form of carbon or graphite. A true carbon-carbon composite has carbon fibers or carbon cloth embedded within a carbon matrix. Under a microscope it would look like this (Figure 5), with the carbon fibers looking like they are surrounded by rings of carbon.

There are three things that differentiate carbon-carbon from other types of composites. One is that it requires temperatures above $1000°c$ in order to create the composite. The second is that it has a co-efficient of expansion almost equal to zero (Figure 6). This is significant, because it means that even with dramatic changes in temperature, the composite will not change in size.

Group Vice-President, BF Goodrich Aerospace & Defense Division, Akron, OH 44313-0501

The third differentiating feature is that carbon-carbon is a light weight material that retainsits strength at high temperatures (Figure 7). The later two properties lend carbon-carbon to be suitable in a variety of environmentally unique applications.

I should note that in addition to these three unique properties, carbon-carbon has other properties that many other composites or non-metallic materials have. It is lighter than aluminum, it has a high specific heat, it accepts additives or property enhancers, and it can be tailored to work in high temperatures either as a conductor or as an insulator -- whichever is required.

(Figure 8) With all of these fine attributes, two questions come to mind -- "Why doesn't this material have more uses?", and, "Why is it considered to be a relatively new material?"

I'll tackle the second question first. In the early 1960's, a forerunner of carbon-carbon, which many of us know as graphite, was a familiar material in the aerospace industry. Graphite is a form of carbon material that does not have any type of fiber embedded in the carbon matrix and is therefore structurally weaker than carbon-carbon. By adding fibers to graphite, aerospace engineers improved the strength of graphites and thereby led to the early development of carbon-carbon composites.

These newer composites provided the thermal characteristics of graphite, however, because they had reinforcing fibers, they had higher mechanical strength than just plain graphite.

In the mid 1960's (Figure 9), rocket nozzles were developed using both graphite and carbon-carbon materials. So although the nature of the material is over thirty years old, the use of carbon-carbon composites is relatively recent.

Today, carbon-carbon composites are made by taking a specific quantity of carbon fibers or cloth and holding them together (Figure 10) by molds, fixtures, or resins in order to form a preform. The preform is then carbonized by one of two processes.

In one process, the preform is converted to a carbon-carbon composite by placing it in a very high (Figure 11) temperature vacuum furnace. The preform is then infiltrated with carbon by flowing natural gas through the heated furnace and thereby "cracking" the hydrogen from the gas. The second method of creating a carbon-carbon composite is by soaking (Figure 12) the preform in a liquid coal tar, petroleum pitch or other resin and then heating it in a furnace to drive off the volatiles, thus leaving a carbon matrix.

In either process, the infiltration cycle is repeated over and over again in order to obtain the desired composite of a carbon fiber contained within the carbon matrix. Hence, the name carbon-carbon.

That brings us back to the first question, why aren't there more uses for carbon-carbon? By virtue of its light weight, strength at high temperatures and excellent thermal-conductivity properties, the aerospace industry is best suited for, and makes up the majority of the applications for this material today. For example, carbon-carbon is being used to make components of jet engines or on the leading edges of very high speed vehicles such as the black tiles that you see on the space shuttle. At BFGoodrich, however, the primary use of

carbon-carbon is in aircraft brakes. In fact, although carbon-carbon is also used in train and racing car braking applications (Figure 13), worldwide, the greatest use of carbon-carbon composites today is in aircraft braking applications.

The main reason carbon-carbon is not used in other applications that it is well suited for is because of its high cost. Expensive raw materials, high utility processing costs and the high engineering content contribute to the costs (Figure 14). For that reason, carbon-carbon composites are usually used only in those applications in which component life or weight are critical.

Even with the burden of having a very high unit cost, carbon-carbon has moved from being used strictly as an aerospace material to one with many industrial applications. These include uses in the glass forming industry, the electronics industry and in the insulation business. As you can imagine, the surface has only been scratched in discovering uses for carbon-carbon composites.

I told you earlier that aircraft brakes are the largest user of carbon-carbon materials worldwide. What I should have added is that BFGoodrich produces the greatest amount of carbon used for aircraft brakes in the world. We are not only recognized as a leader in aircraft brakes, but also in the development and manufacturer of carbon-carbon for the types of applications that I mentioned earlier. Although today we lead all of our competitors in the volume of carbon brakes produced worldwide, it is has been a long and expensive journey for us to get there -- and we didn't get there overnight. It has taken us, and our predecessor company, Super-Temp, many, many years to achieve a position of leadership in the manufacture of carbon-carbon.

The story begins more than thirty years ago. In the early 1960's, as an independent company in the Los Angeles area (Figure 15), Super-Temp used four small furnaces to become a pioneer in the development of carbon-carbon materials. Their involvement with the design, development and the use of high-temperature electric induction vacuum furnaces, gained Super-Temp the reputation of being a leader in carbon-carbon composites.

At about the same time, makers and users of military aircraft were encouraging brake manufacturers to provide lighter weight, more effective friction materials. When the carbon brake development efforts eventually proved to be successful, Super-Temp was awarded a contract to produce the first commercial aircraft carbon-carbon brakes. Those being for the Anglo-French supersonic aircraft, the Concorde. In the late 1970's, BFGoodrich acquired Super-Temp and used it to expand BFG's own knowledge of carbon and to develop brakes for a variety of aircraft applications.

Talking about Super-Temp reminds me of a story that I should tell you about the company. As I mentioned, Super-Temp is located just outside of los angeles, in the city of Santa Fe Springs, California. The business is physically located about a half mile north of a hospital for those who have mental illness.

One day a man came to our reception desk and asked for a job application (Figure 16). It was summer time and the man was not wearing a shirt. The receptionist, who was sitting behind a high reception desk, took an application out of the drawer and stood up to hand it

to the man. It was only then that she noticed that the man was completely nude. Instead of calling the hospital and having the man taken back, the receptionist probably should have hired the guy. He showed us a lot of initiative and creativity - among other things!

In our fourteen years owning Super-Temp, we have extended a significant effort to perfect the operating parameters of the unique furnaces so that we can obtain production efficiencies and the proper product microstructure. Today, this experimental and development experience enables Super-Temp to operate furnaces at very high temperatures -- and when I say high temperatures, I mean very hot! (Figure 17) Today our water cooled electric induction furnaces can operate at temperatures up to 3700°c. Getting to these operating temperatures was a continual learning experience for Super-Temp. As with many things of this nature, improvements came in incremental steps. Sometimes, however, it seemed as if each two steps forward resulted in one step backward.

For example, something we learned early on was the consequences of having a furnace overheat. Usually this causes one of the copper cooling coils within the furnace to burst and leak water into the furnace. As you might expect, steam is quickly generated causing what we term as a "furnace eruption" to occur. A furnace eruption is a nice way of saying that the carbon dust, which is used to insulate the furnace, is blown all over the place -- (Figure 18) causing power outages and days worth of cleanup.

In an experiment to learn about processing carbon in other than natural gas environments, we once accepted an order to clean some electrodes for a utility company. We planned on cleaning the electrodes by chemically etching during a bake-out in a furnace that was flowing chlorine gas, rather than the natural gas we usually used in carbonization cycles. The procedure worked well. In fact, we did such a fine job cleaning these electrodes they are still in service after 12 years. Unfortunately, I can not say the same for the furnace. (Figure 19) The hydrochloric acid that we created when we cleaned the electrodes severely corroded the graphite interior of the furnace causing us to scrap portions of it. Needless to say, we haven't taken any repeat orders to do that job again!

Throughout the years we have learned that as furnaces are operated at higher and higher temperatures, furnace components will melt if they are not adequately protected - as in the case of the copper cooling coils I mentioned earlier. In order to overcome these problems we simply had to learn about furnace cooling and insulating.

It didn't take a genius to figure out that if we wanted to add more insulation, we would have to enlarge the furnace. Beside providing better protection for furnace components, the added insulation enabled us to reach higher operating temperatures; get to these temperatures faster, and maintain them more efficiently. This resulted in substantial savings in electricity costs.

During the early check-out runs of the improved furnace, we were all very pleased with the initial results. We were proud as we increased operating temperatures because we did not have any damage to the furnace or components. Unfortunately, we lost many of these gains we made when we found it took days and days before we could open the furnace to remove parts. In fact, in this "improved" furnace (Figure 20), we found it took as long for the furnace to cool down as it did to process parts.

We finally recognized that if we did not have enough insulation, the furnaces got too hot and we ended up with overheating which led to furnace eruptions. However,if we had too much insulation, the production cycle was too long and resulted in great inefficiencies. In another learning experience, we saw that we had to balance (Figure 21) the amount of insulation and any gain in operating efficiencies.

One of the most unusual requests we had came about because of an incident that occurred when we processed a rocket nozzle in our furnaces.

It happened several years ago when a furnace overheated in the middle of a processing cycle. At the time, we had limited expertise in handling over-heated furnace problems, so we tried to cool the furnace down by flooding it with water. Once we over-came the steam problem, we checked to see if we still had a nozzle left (Figure 22). We contacted the customer and the U.S. Air Force and both of them asked us to try and salvage the nozzle. We then dried the nozzle in another furnace, and completed the furnace processing. After completing the part, and passing all of the quality and engineering criteria, the rocket was fired successfully. Wouldn't you know it - the customer and the U.S. Air Force came back to us and asked us if we could repeat our flooding technique because that was one of their most successful rocket launches up until that time!

(Figure 23) As you can see, operating vacuum furnaces at very high temperatures and using different gases for infiltration have been on-going learning experiences for us as we moved towards producing large volumes of carbon-carbon composites.

Unfortunately, our learning experiences were not limited only to furnaces. We also learned a few things about which materials can and can not be carbonized. Remember I told you that carbon-carbon is a composite of carbon fibers and carbon gas. In developing new materials over the years, we have carbonized many strange materials. Rice and wheat are among many of the fibers that we have carbonized in an attempt to find the ideal composite.

There's one story that goes around Super-Temp about a young engineer who, early in our product development years, had a very heated disagreement with his boss over the range of products that could be carbonized in a furnace. The boss, after one such argument, told the employee that he wanted to hear no more about it -- the employee should go back to his work and do his job. That evening, the young engineer went to a local dairy farm and picked up some cow manure, or cow chips as we call them. During the next few days at work, he processed them in a furnace until they were fully carbonized. He then placed the carbonized cow chips on his bosses desk along with his resignation paper and said to his boss "I told you so" (Figure 24). Now there is another item that can be added to the list of materials that can be processed and carbonized in a furnace -- although I am not sure we have a business use for this one!

I mentioned to you that Super-Temp, in its very early years, worked with all the major aircraft brake manufacturers in the world, and that one such development effort led to a production contract for carbon brakes on the Concorde. In fact, Super-Temp taught both Dunlop in England and SEP in France, the carbon-carbon process and eventually licensed them to produce it by the Super-Temp method. However, as you would expect, when BFGoodrich acquired Super-Temp in 1978, all brake development activities for competitors came to an

abrupt stop. As the new owners of Super-Temp, BFGoodrich increased its development efforts multi-fold.

All the research, development and the extended brake testing we did eventually led to our first major carbon brake contract -- brakes for the Lockheed C5B (Figure 25). Since the early 1970's, BFGoodrich had been supplying brakes for what was then the world's largest aircraft, the U.S. Air Force Lockheed C5A. Over the years, we developed a successful relationship with the Air Force and Lockheed as we supplied both the original equipment and the replacement parts for a brake whose heat sink material was beryllium rather than steel. In the early 1980's, the U.S. Government decided to build more C-5's, incorporating improved wings among several other modifications, to make up a "B" model.

In 1983, Lockheed and BFGoodrich offered the U.S. Air Force a substantial cost and weight saving if they would switch from BFG supplied beryllium brakes to brakes with carbon-carbon heat sink material supplied by Super-Temp. Although we expected a slight reduction in revenue and income in the conversion from beryllium to carbon brakes, we anticipated that we would gain a great deal of valuable carbon braking experience (Figure 26). We also expected to gain invaluable manufacturing experience in producing over 60,000 pounds of carbon as was required for the 24 carbon brakes on each of the 50 new aircraft.

In addition to offering a lower weight brake, part of our enticement to the U.S. Air Force and lockheed for making the change from beryllium to carbon brakes, was that we offered the carbon brakes at a price lower than we were charging for the beryllium. This turned out to be the first of a series of reductions in revenue for BFGoodrich on this, our first carbon brake, program.

Our second revenue reduction occurred through lower spare part sales because we were replacing beryllium brakes that were lasting less than 1000 landings, with a carbon brake that would last about 1500 landings or about 50% more.

Although each of these revenue reductions were anticipated to some degree, we were about to get an education in the differences between carbon and other brake programs. What really happened is that the carbon brakes have lasted even longer than we expected (Figure 27). In many cases, they are lasting four to five times longer than the beryllium brakes. As a result, our first carbon braking experience resulted in BFGoodrich generating reductions in revenue three ways -- first with lower prices for carbon brakes, second with carbon brakes having a longer life and third with the carbon lasting longer than we anticipated! In spite of this, the total C-5 experience has been a very positive one for all parties concerned because the Air Force and Lockheed obtained a great performing and low cost product, while BFGoodrich obtained some valuable product and production experience along with a good, although expensive, sales reference point.

We point with pride when we say that the carbon that we designed on that aircraft in the early 1980 's, is still flying without design or process changes on that aircraft today. In fact, many of the original C-5B's still are flying and stopping with the same brakes that they came with from the factory.

If we had more time, I could talk for the next several hours about the series of aircraft carbon brake successes, and the problems that often come with handling success, that we have had since the C5. Suffice it to say (Figure 28), that from our positive experience with the C5 we went on to provide carbon brakes for the Boeing 757, 747-400, the airbus A-320, A-330 and A-340, the U.S. Air Force General Dynamics F-16, and soon, Boeing's newest aircraft, the 777. Being awarded these new carbon brake programs led us to build a new carbon brake manufacturing facility in Pueblo, Colorado as we went from a position of having one under-utilized production facility at Super-Temp to two facilities working hard to keep up with our production requirements. For five solid years we expanded (Figure 29) our fabrication capability, furnace capacity, machining shop, and added new people in a series of continual, ongoing expansions. We have now exhausted the capability to expand at this site, and in july of 1992, we will finally have completed the last expansion phase. Because we have been so fortunate, in 1993, we will have to start looking for a new site, and begin another new start-up operation.

Our largest carbon braking program, the 747-400 has been in service for over three years now and there are virtually no product or performance problems with carbon brakes. Although the manufacturing facilities have been expanded continuously since start-up, productivity and quality continue to improve as new efforts are directed toward cost improvement and newer brake materials.

The more we continue to work on carbon brake and carbon brake applications for a variety of new aircraft, the more we recognize that the product has some unique capabilities and that the material has many applications (Figure 30). Carbon brakes are like any other product -- once you know you can make good product you move on to making it less expensively, work towards making improved derivatives of the product, and finding new applications for the material. Some of our early efforts at making lower cost carbon have proven to be expensive development programs. When I say expensive, I don't mean expensive only in the terms of the labor and materials that we have expended, but in variety of other things.

(Figure 31) For example destructive testing of prototype carbon brakes has caused us to damage our test dynamometer on many occasions. Besides equipment damage, I couldn't give you any count of the number of prototype brakes that we have completely destroyed or the fires we started due to brakes over-heating. Besides these things, I am very sure we could fill up this room with the tires that have blown up over the years during brake testing and development. One more thing we destroyed was the ego of several engineers -- each of whom believed that he had the right solution for a carbon brake problem. These things have happened numerous times, over many years, during the development and testing of carbon brakes.

Today we are extending the range of applications for carbon-carbon and have developed a ceramic process to encapsulate the carbon fibers. We are finding that there are appropriate applications for both ceramic carbon and carbon-carbon materials and technologies. As an example, we have recently developed and tested a carbon brake (Figure 32) for the high speed mag-lev train which is being proposed for the Osaka to Tokyo route. We have also been as`ed by the Japanese team members to assist in the development of a carbon brake for the next generation Shinkensan bullet train. As you can see, carbon brakes have not gone out of

our mind completely, they have just shifted applications to other vehicles which will benefit from the heat absorption capability and the light weight of this material.

As I mentioned earlier, carbon-carbon has great potential as a leading edge on very high speed aircraft. In this area, we have participated in the development of carbon structural material for the orient express or the high speed civil transport and the NASP program. In addition, we are looking at carbon-carbon and ceramic carbon for the high performance engines that will permit these aircraft to obtain the higher speeds available from hotter engine operating temperatures. We can take advantage of carbon's high specific heat in certain applications and are testing materials that could reduce the heat build-up and the size of critical printed wiring boards by replacing the current materials used in thermal planes within avionics packages for jet fighter aircraft. These thermal planes will permit us to take heat and weight out of a fighter aircraft cockpit and therefore allow them to be smaller and lighter and give us a technology edge. Finally, we are looking at carbon-carbon in satellite arrays or radiators in space. Because of its light weight and its heat absorption capabilities, carbon-carbon can be used in a variety of space satellite applications by providing strong light weight structural material that will serve multiple purposes.

(Figure 33) Whether we use carbon composites in satellites, electronics, or industrial applications here on earth, there are a variety of application potentials and lessons that we can learn as we continue to develop this unique material. As with the introduction of carbon brakes, I am sure that as we get there we will have another set of challenges waiting for us in bringing this material to production levels. For us at BFGoodrich, however we have a real advantage. We have already been through it once. Perhaps now you have gained a little bit of insight into some of the issues that you would face in bringing this great material to the world's doorstep.

Thank you and good night!!
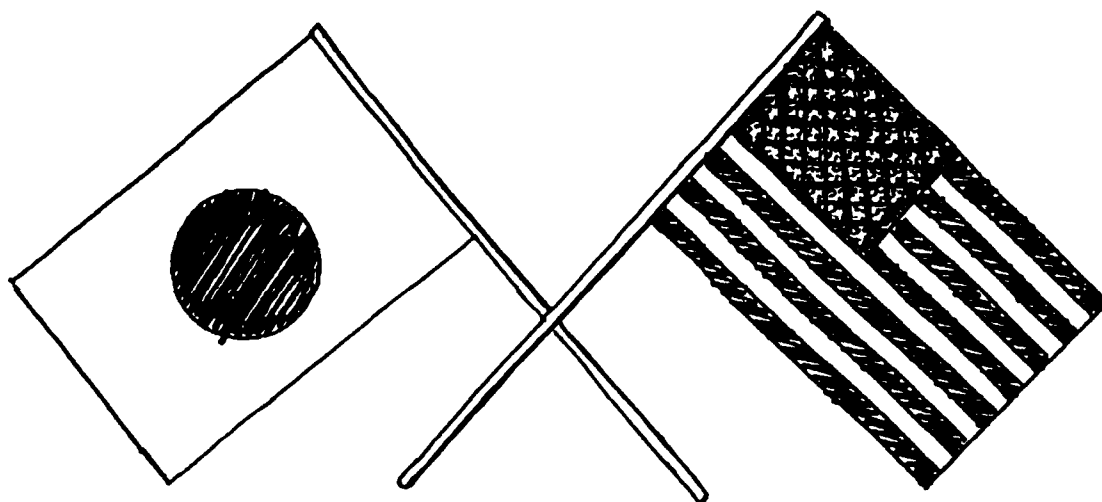
6TH JAPAN-U.S. COMPOSITES CONFERENCE
CONFERENCE
ORLANDO, FLORIDA
JUNE 23, 1992

Figure 1

Figure 2

B.F. GOODRICH CARBON BUSINESS!

Figure 3

Figure 4

CARBON MATRIX

CARBON FIBER
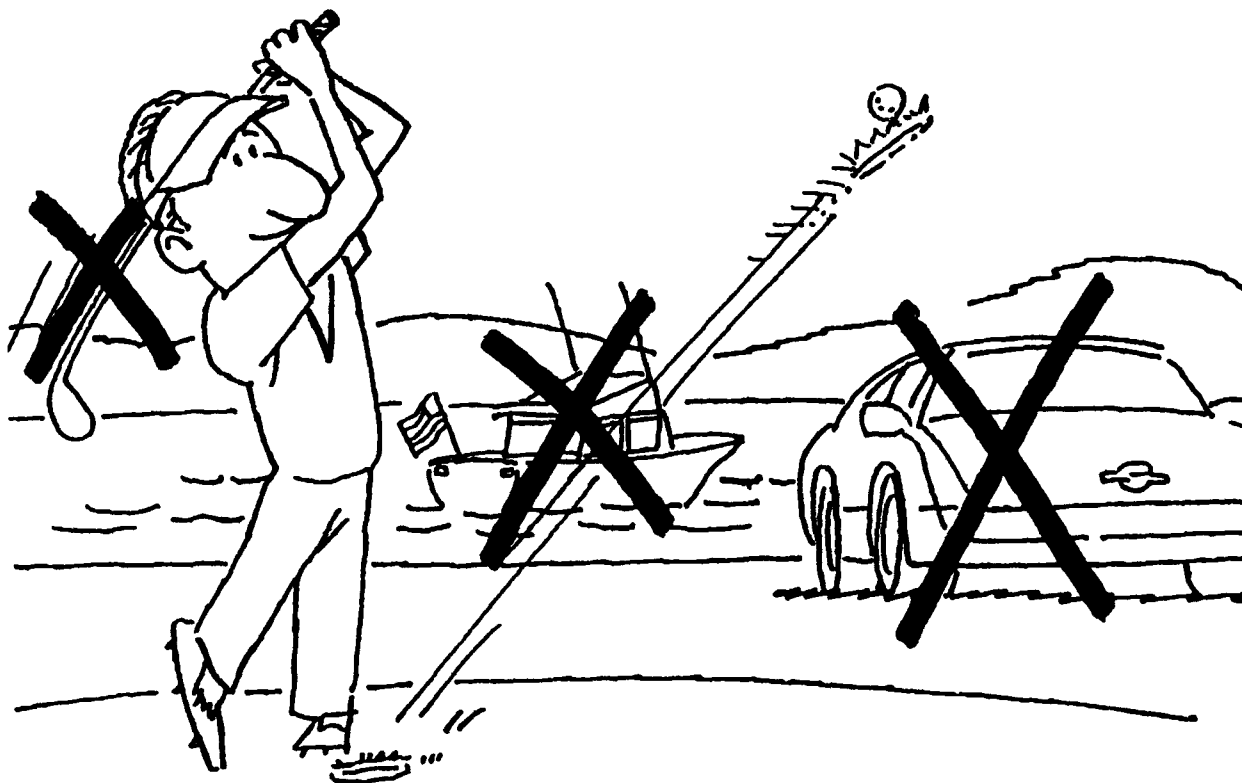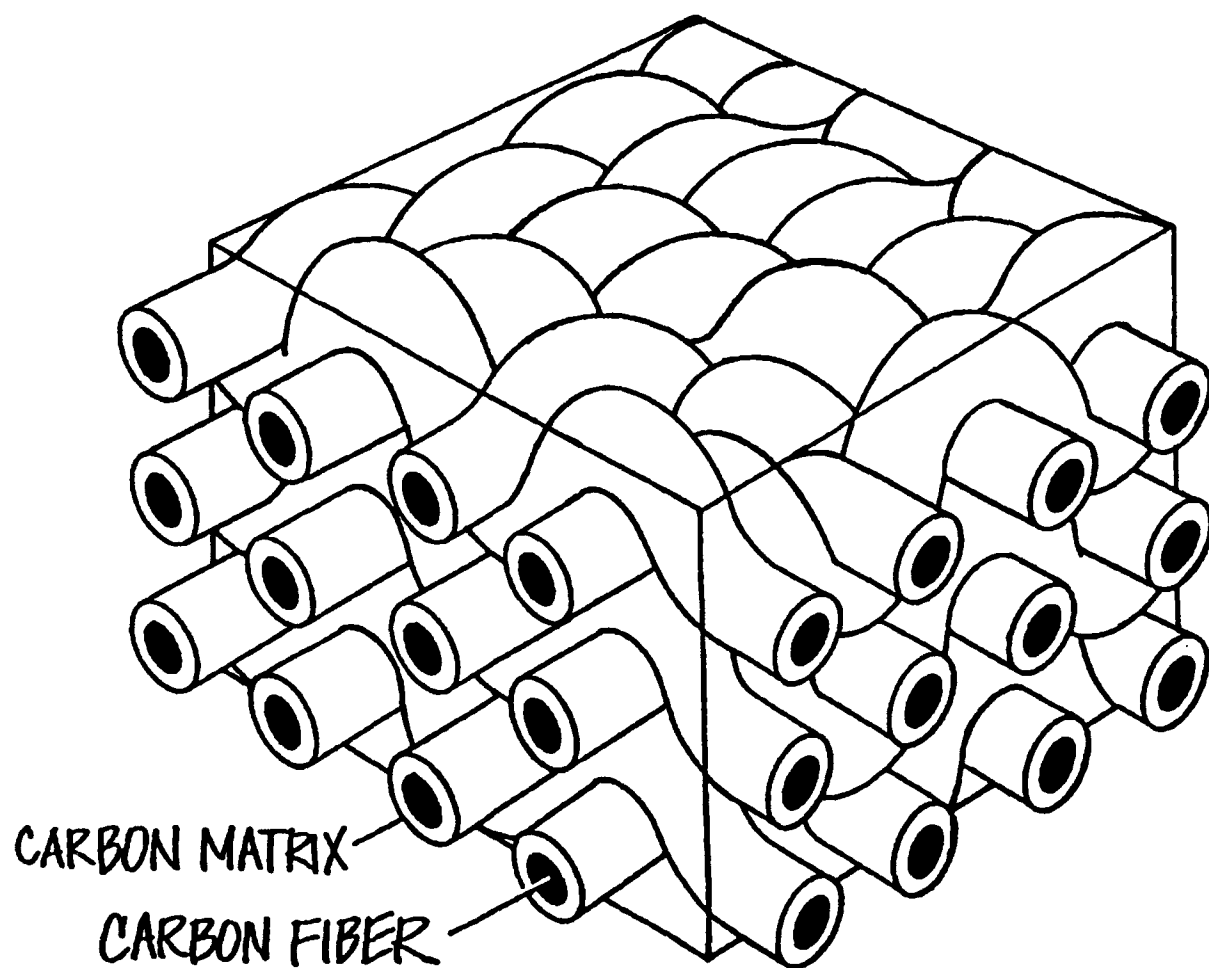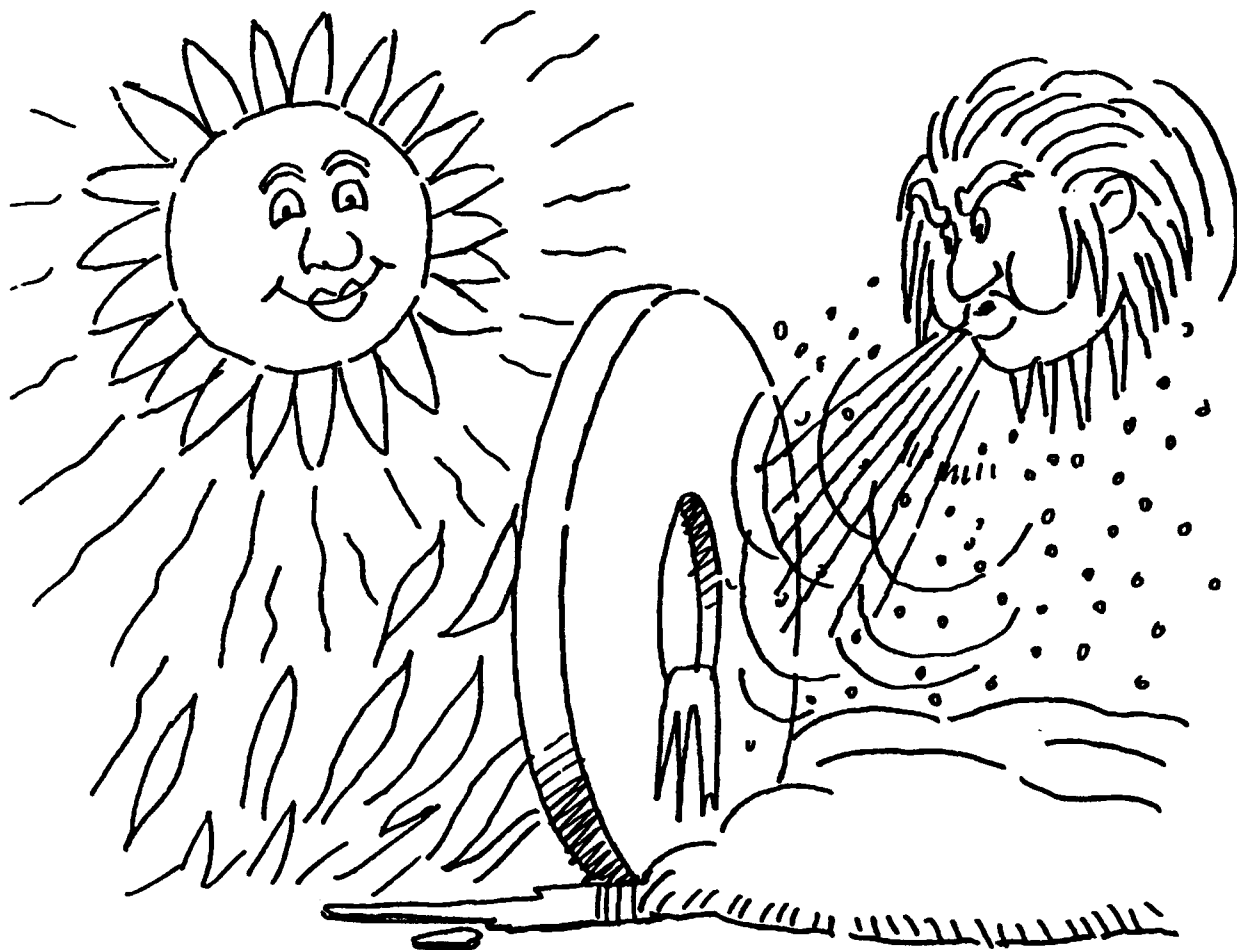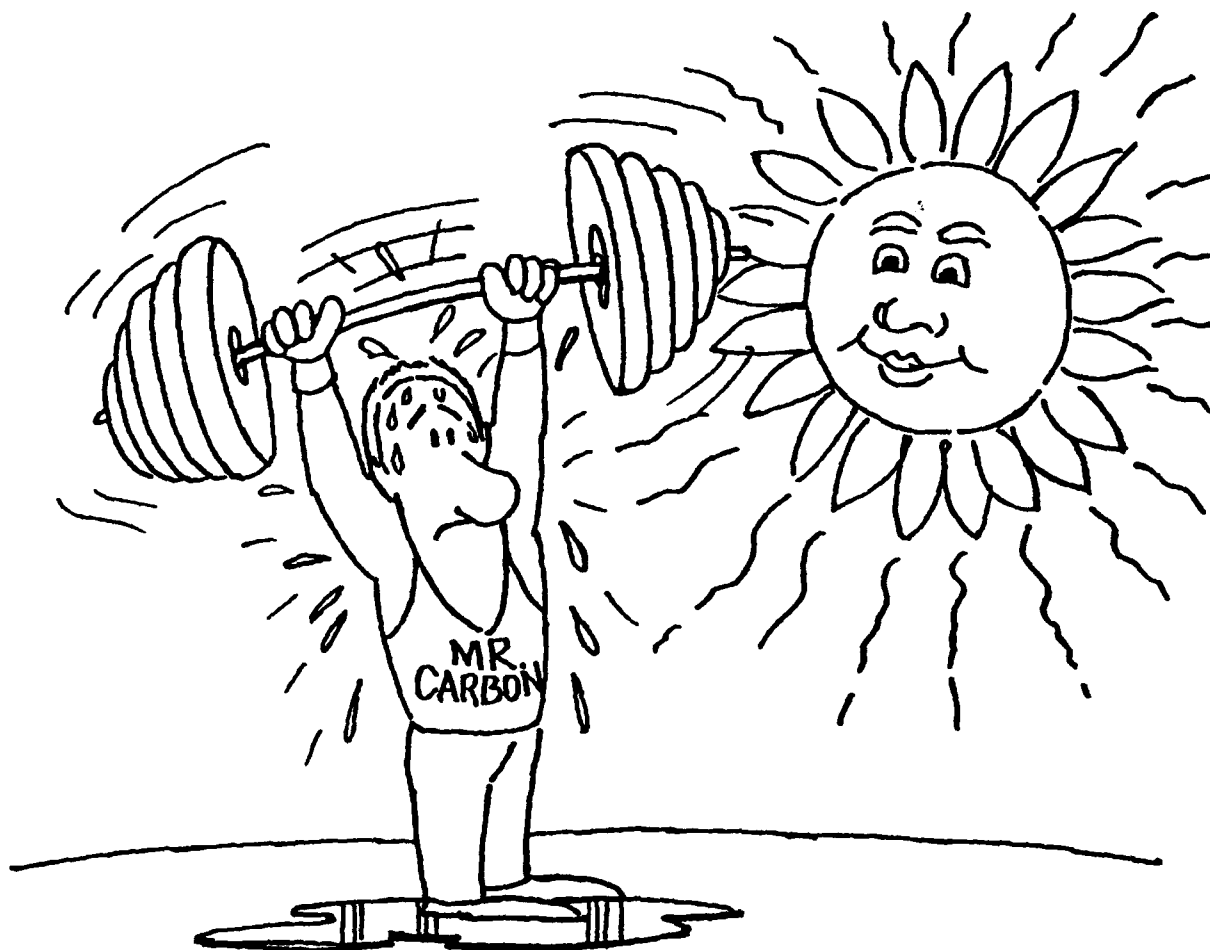
Figure 5

Figure 6

Figure 7

- LIGHTWEIGHT
- HIGH SPECIFIC HEAT
- INSULATOR OR CONDUCTOR
- CAN BE "TAILORED"

Figure 8
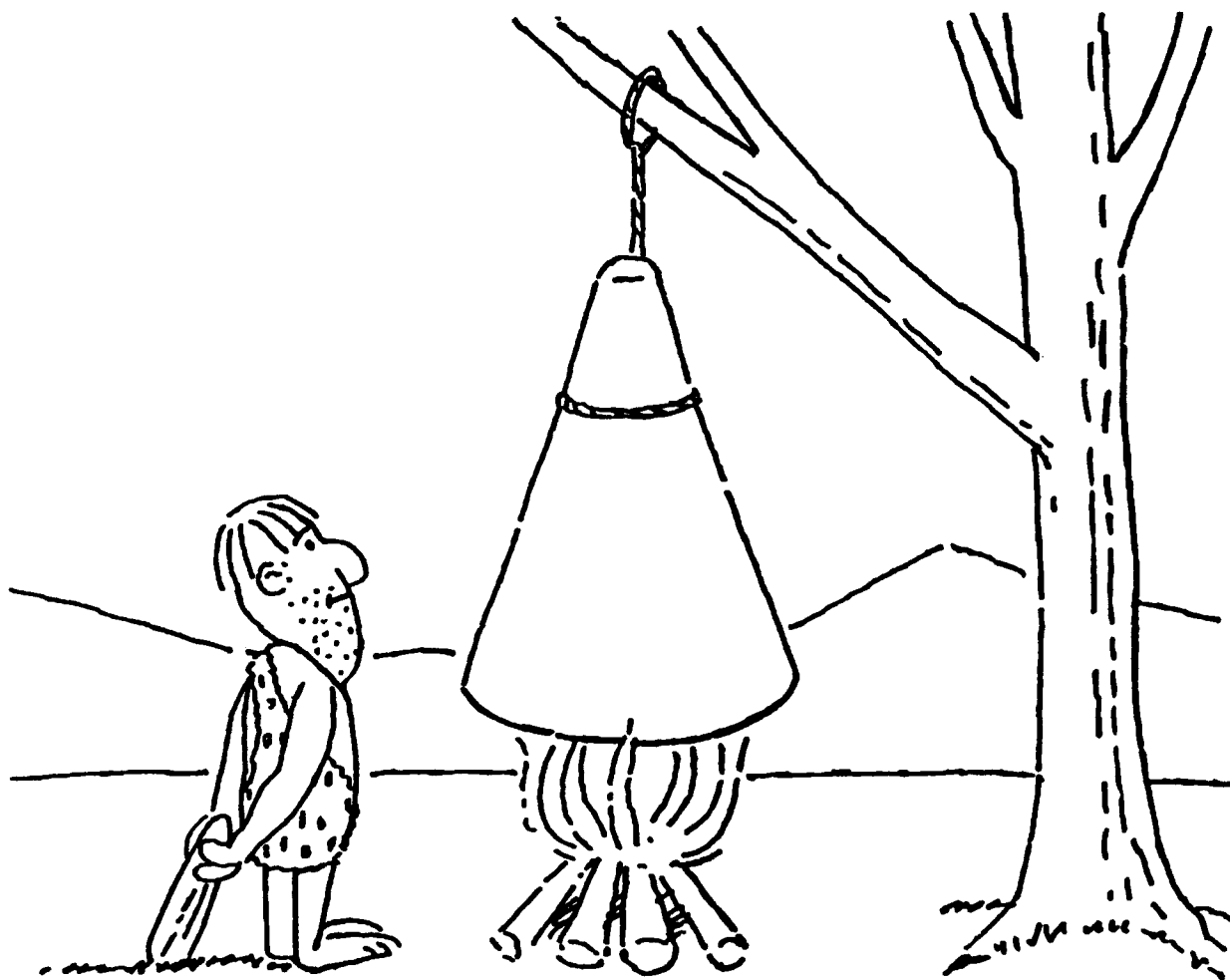
Figure 9
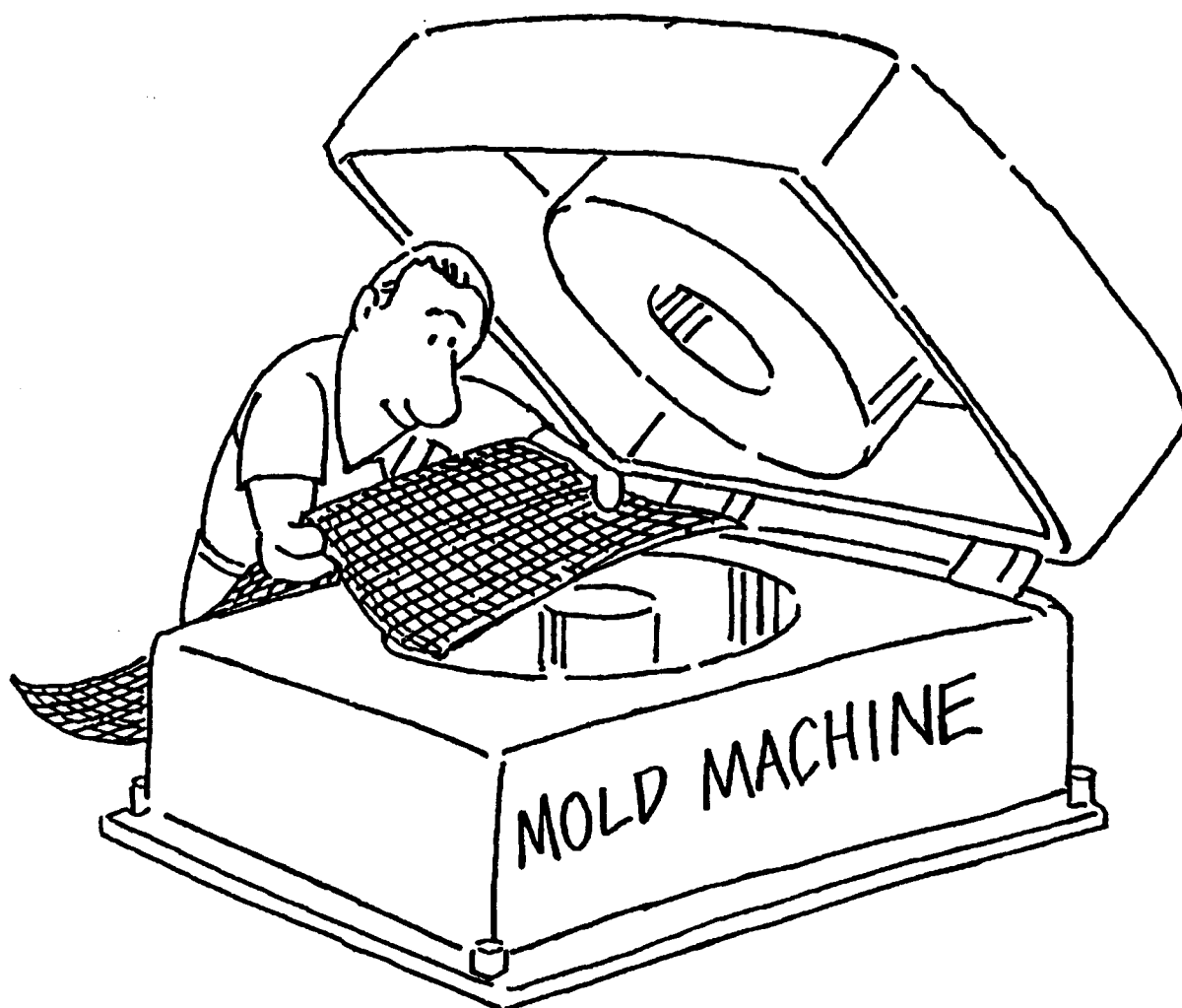
Figure 10
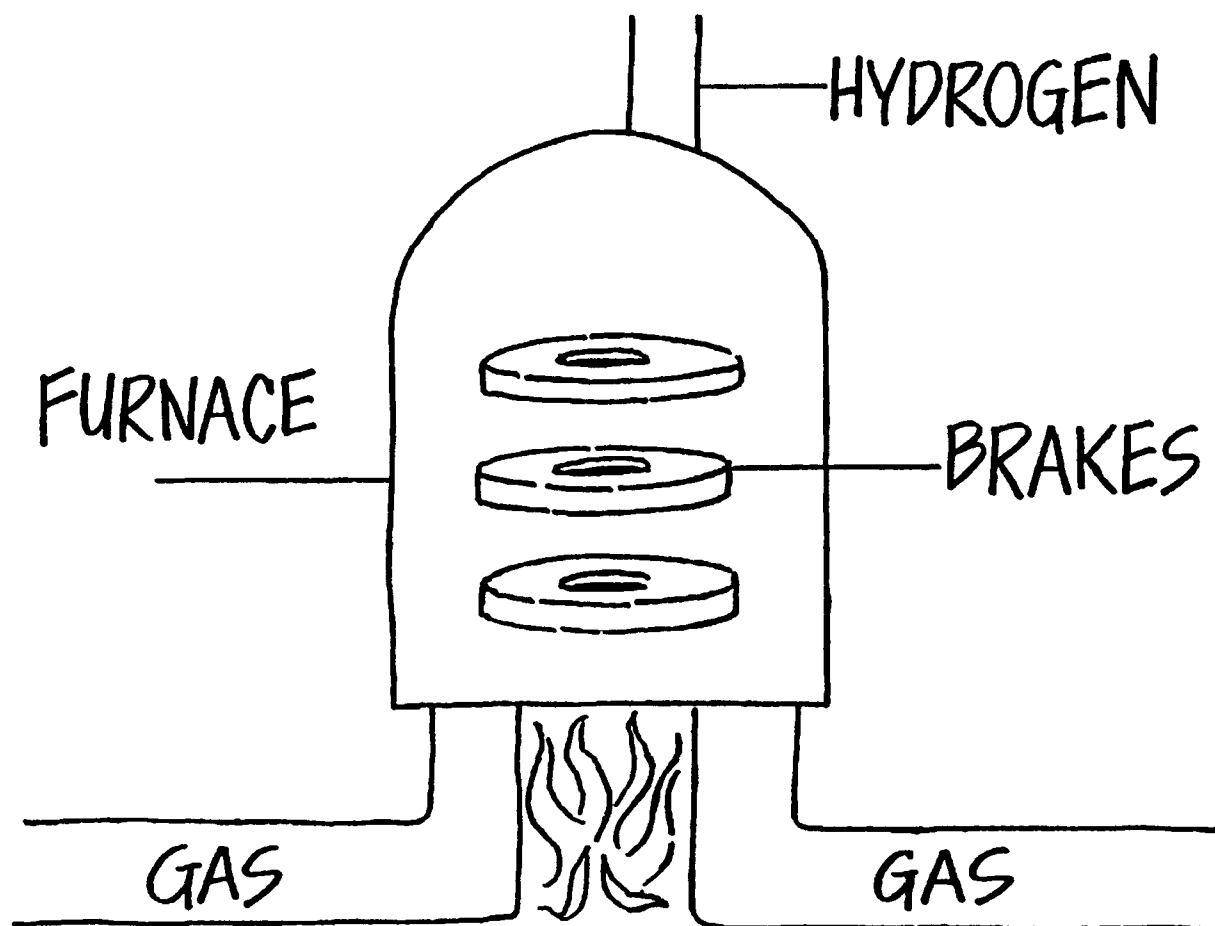
Figure 11

Figure 12

Figure 13

WEIGHT

COST
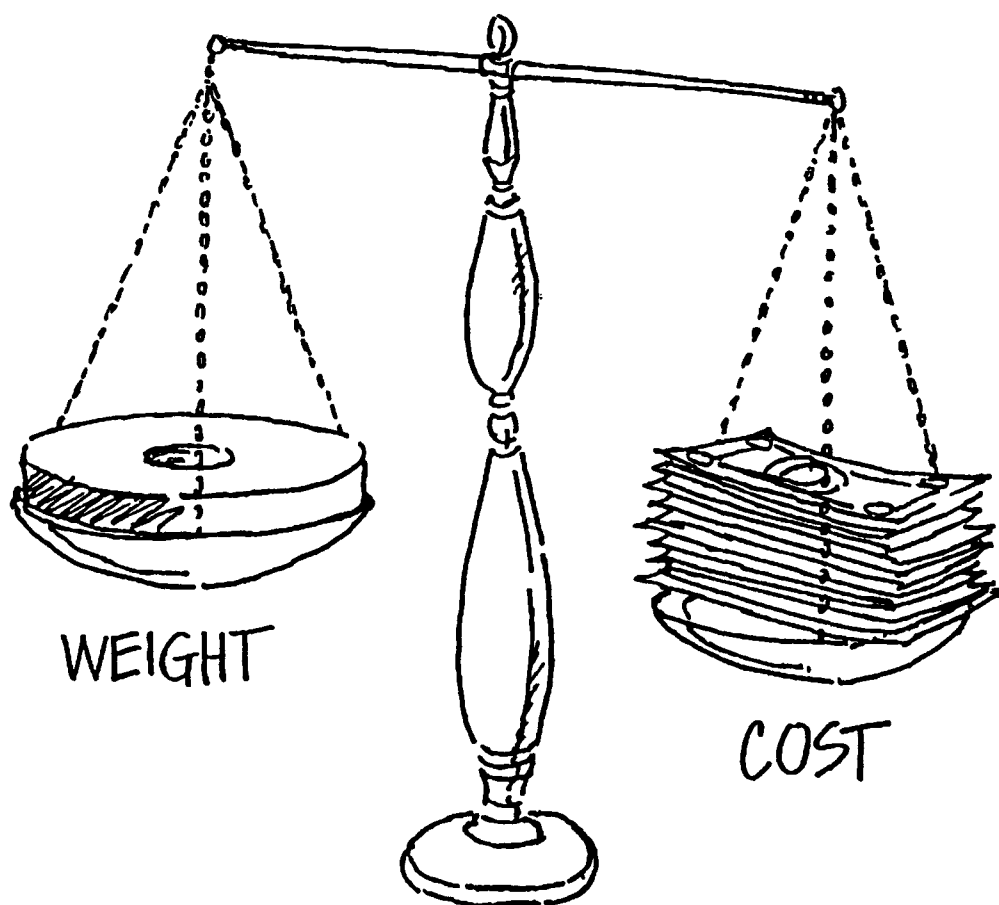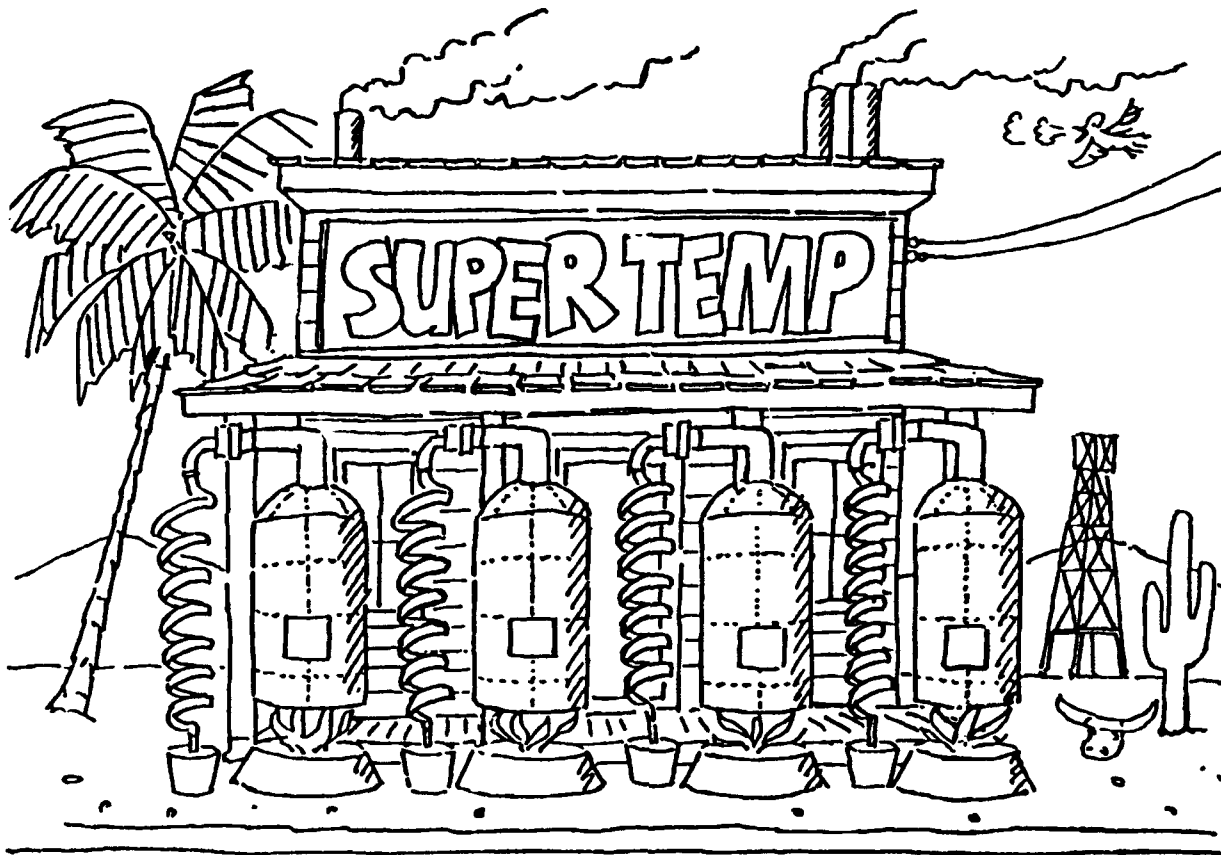
Figure 14

Figure 15

585

NEED ANY HELP!

Figure 16
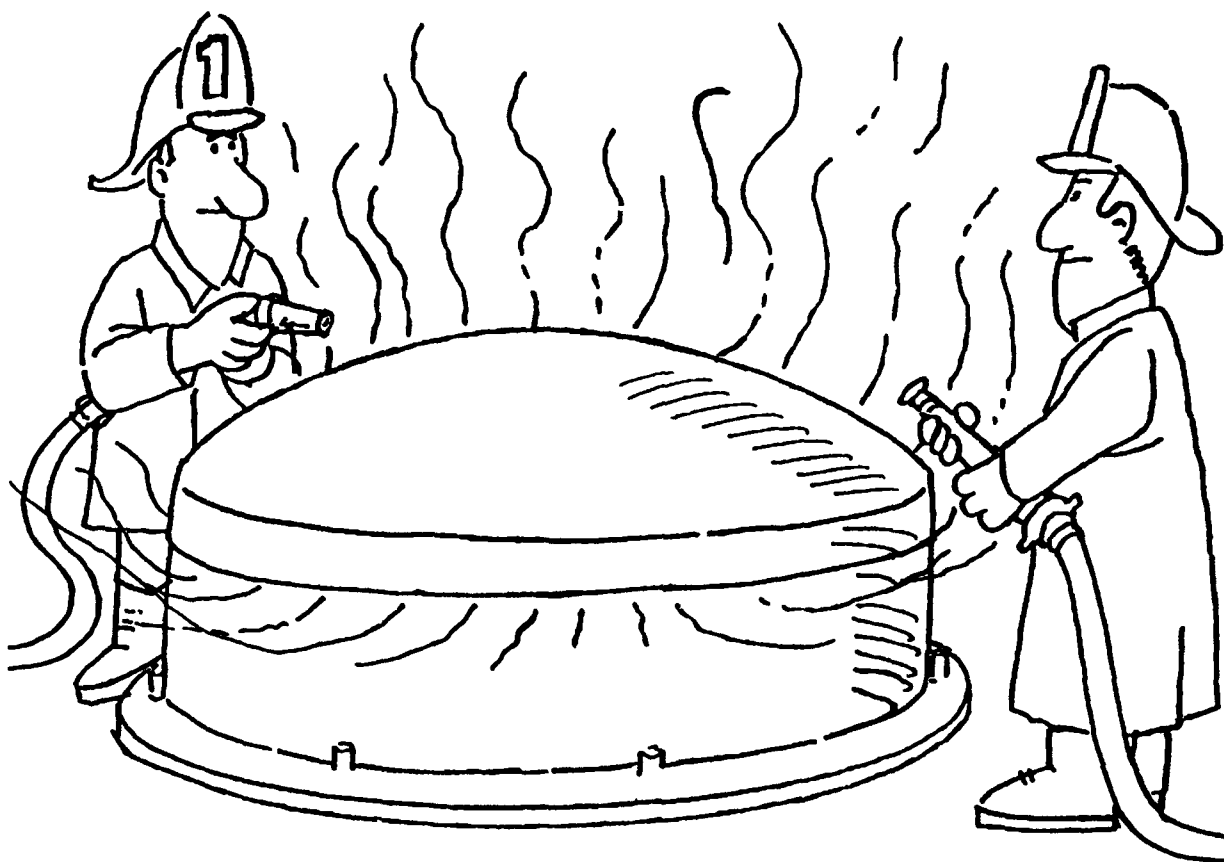
Figure 17

Figure 18
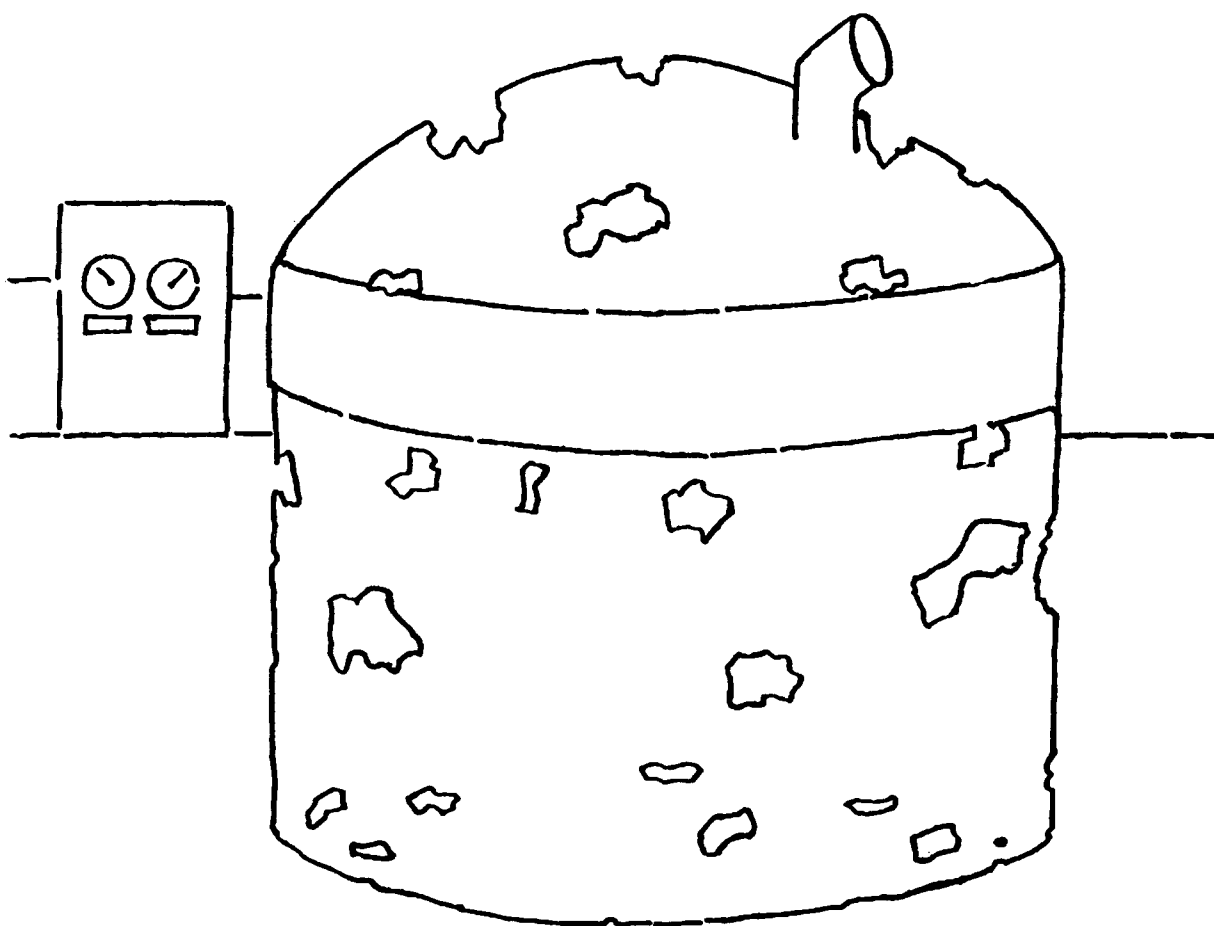
Figure 19
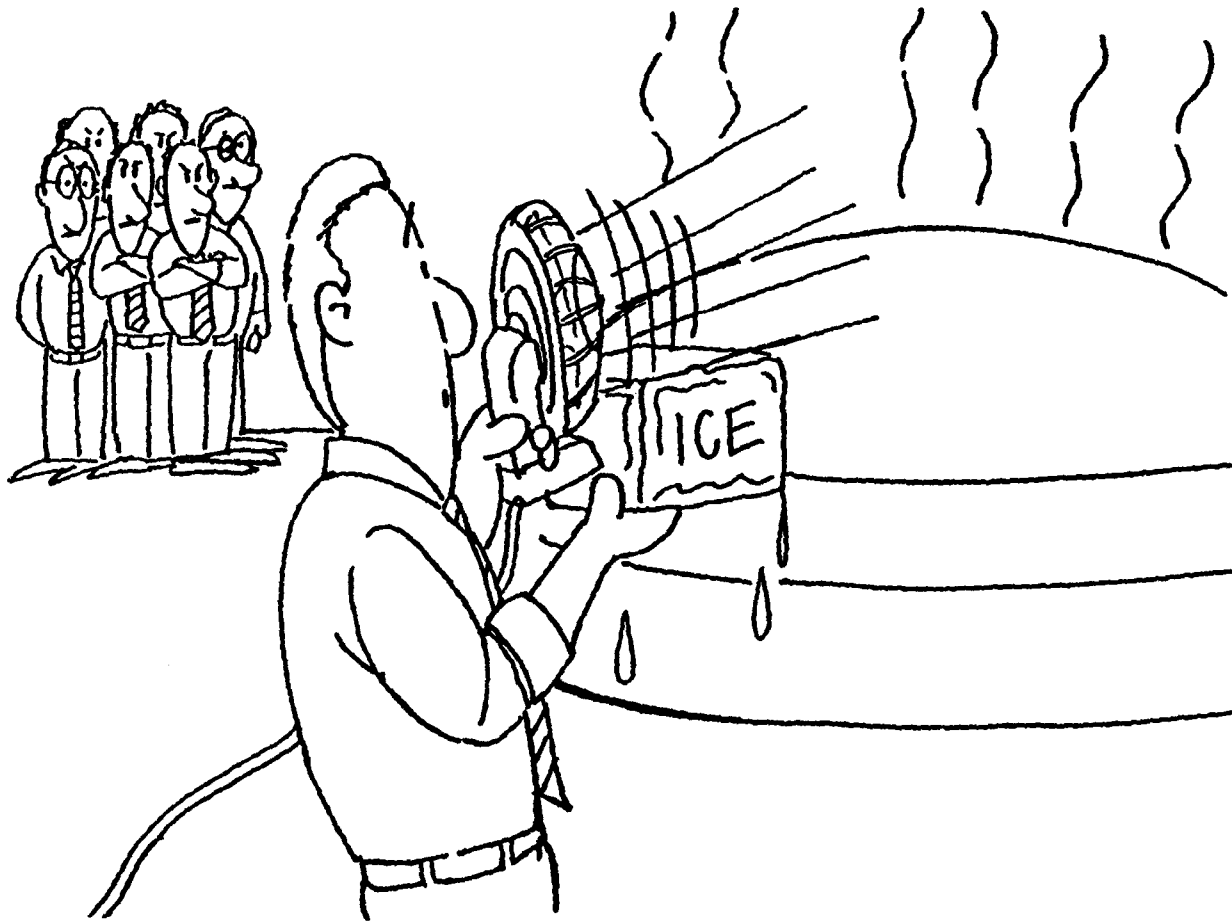
Figure 20

INSULATION

OPERATING EFFICIENCIES

Figure 21

"IS THE NOZZLE OKAY?"
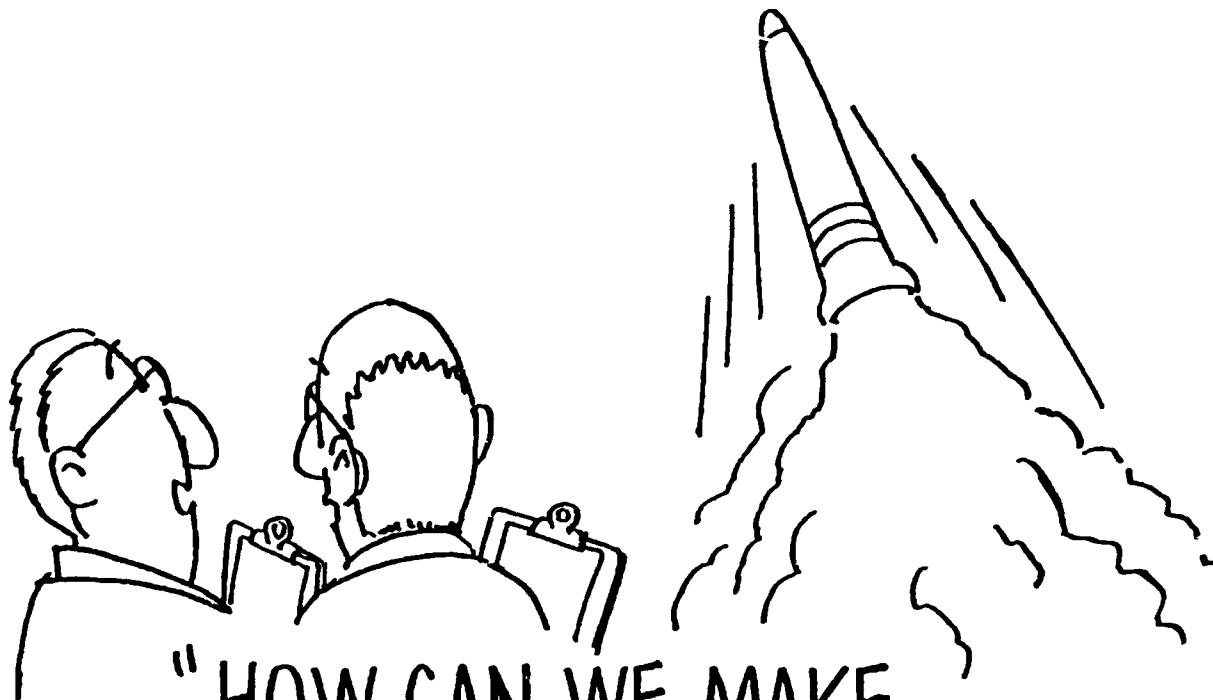
Figure 22

Figure 23

"THERE'S PLENTY MORE WHERE THIS CAME FROM!"

Figure 24

Figure 25

"THAT'S CONFIDENCE!"

Figure 26

"DON'T THEY EVER WEAR OUT?"
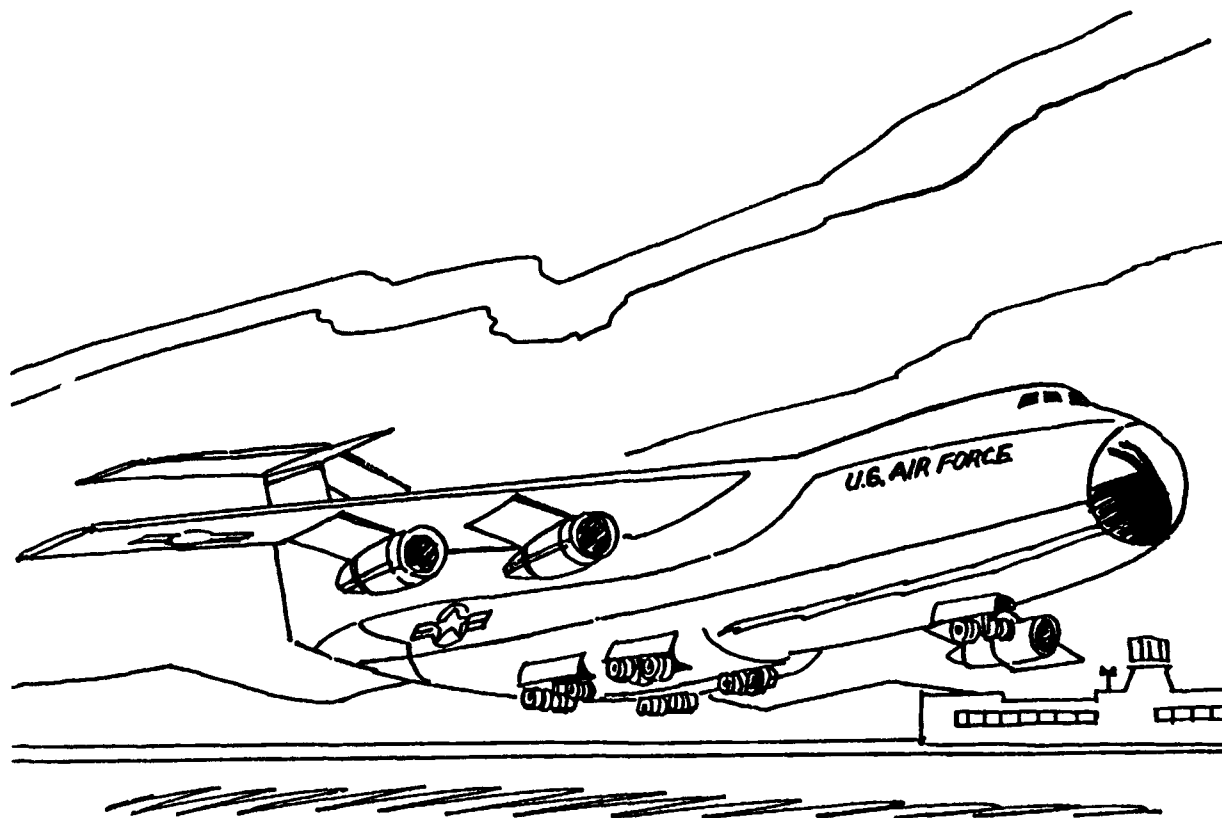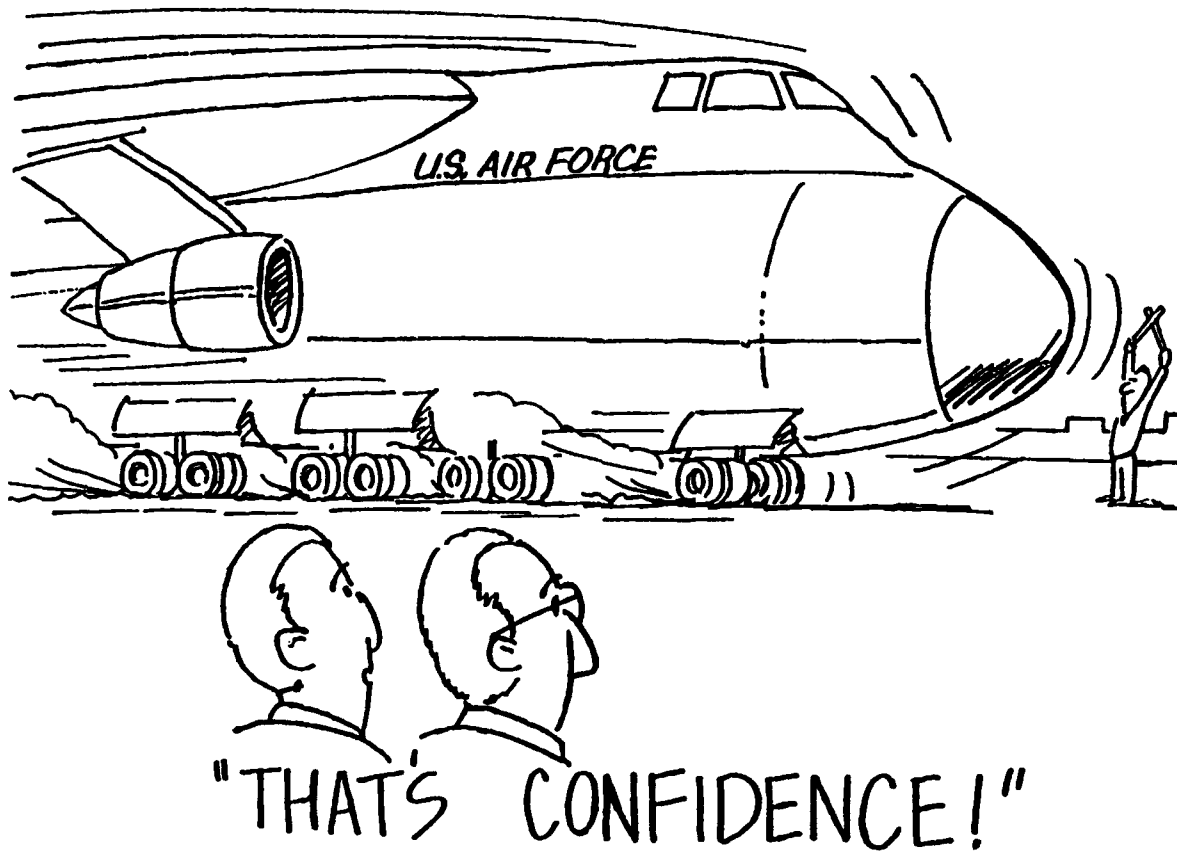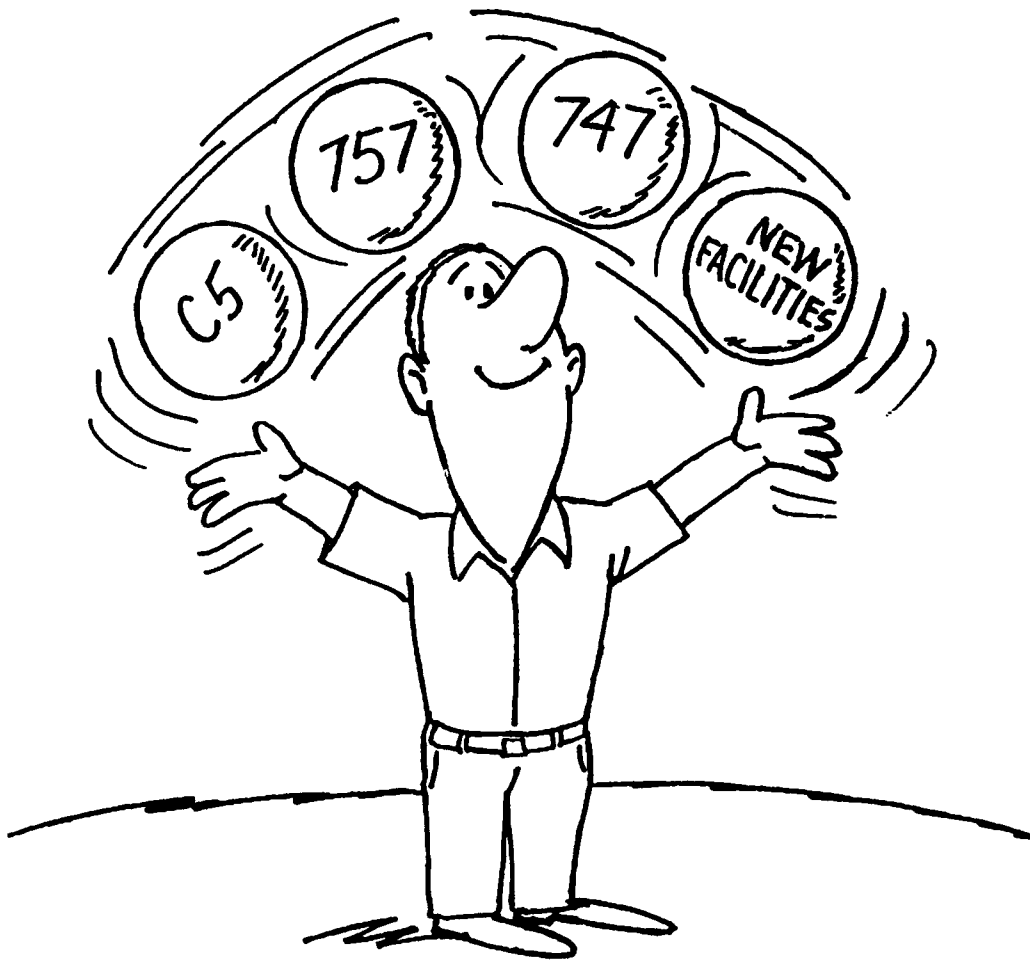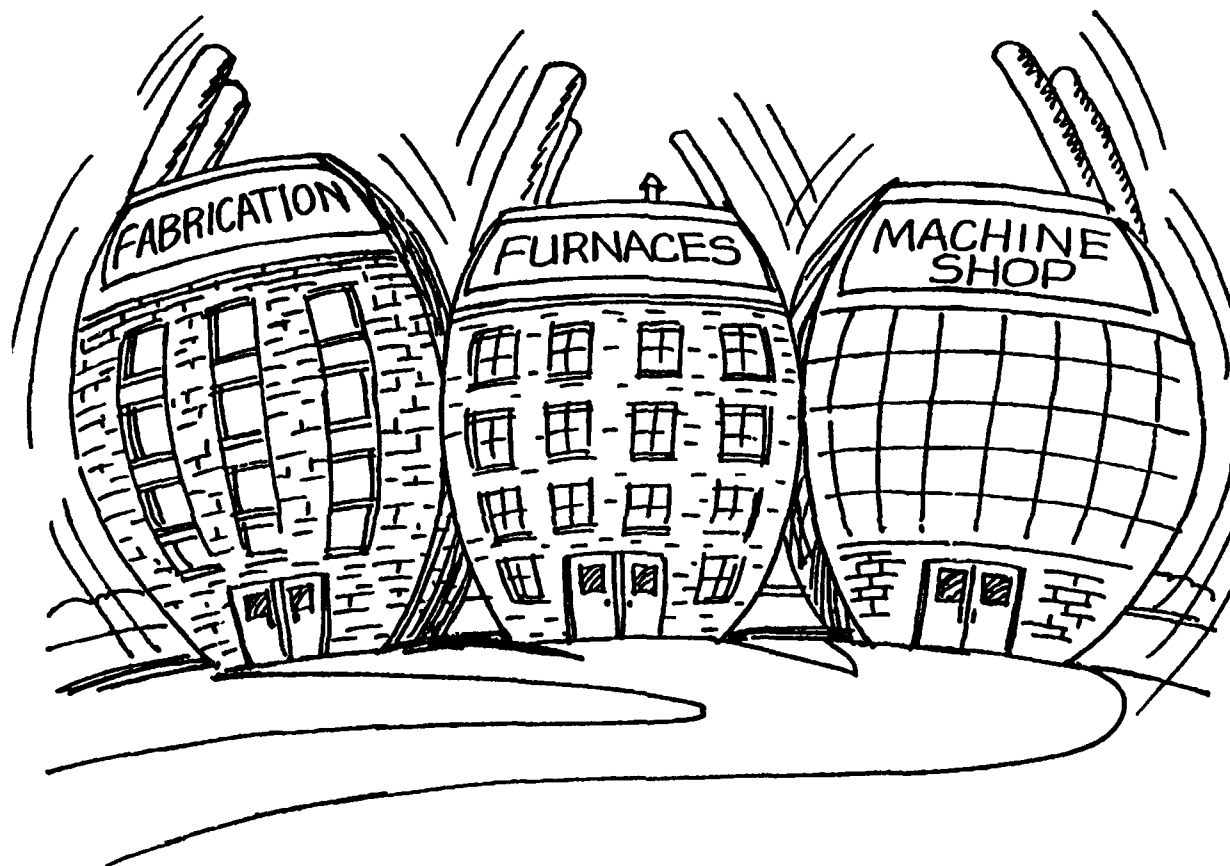
Figure 27

Figure 28

Figure 29
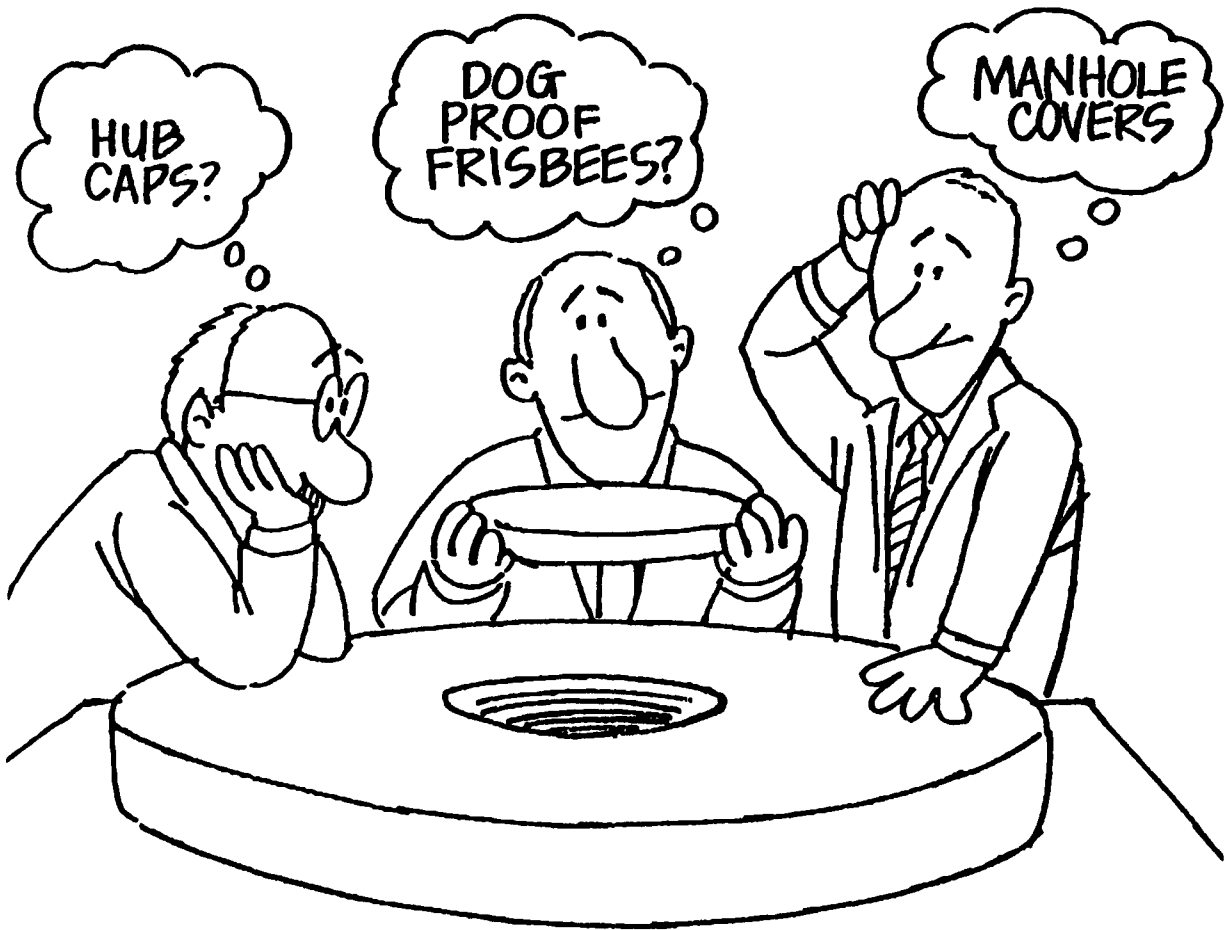
Figure 30

"BACK TO THE DRAWING BOARD"
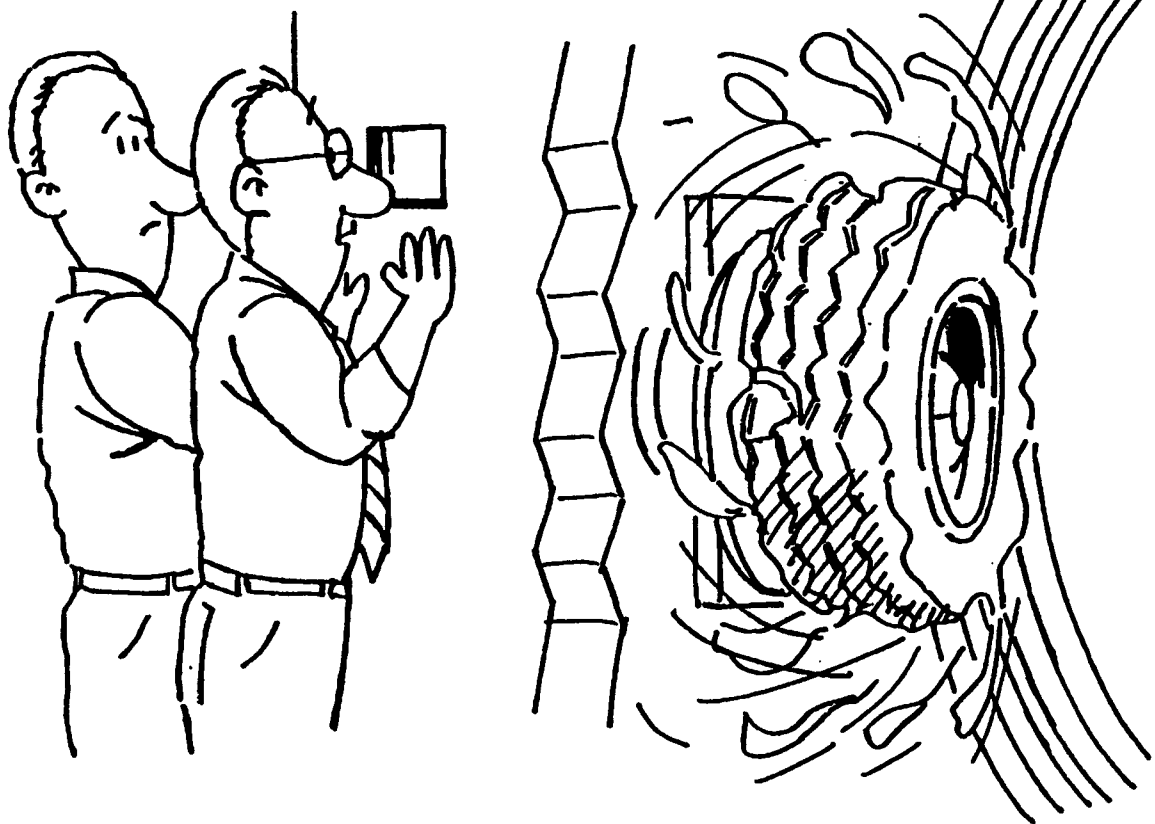
Figure 31
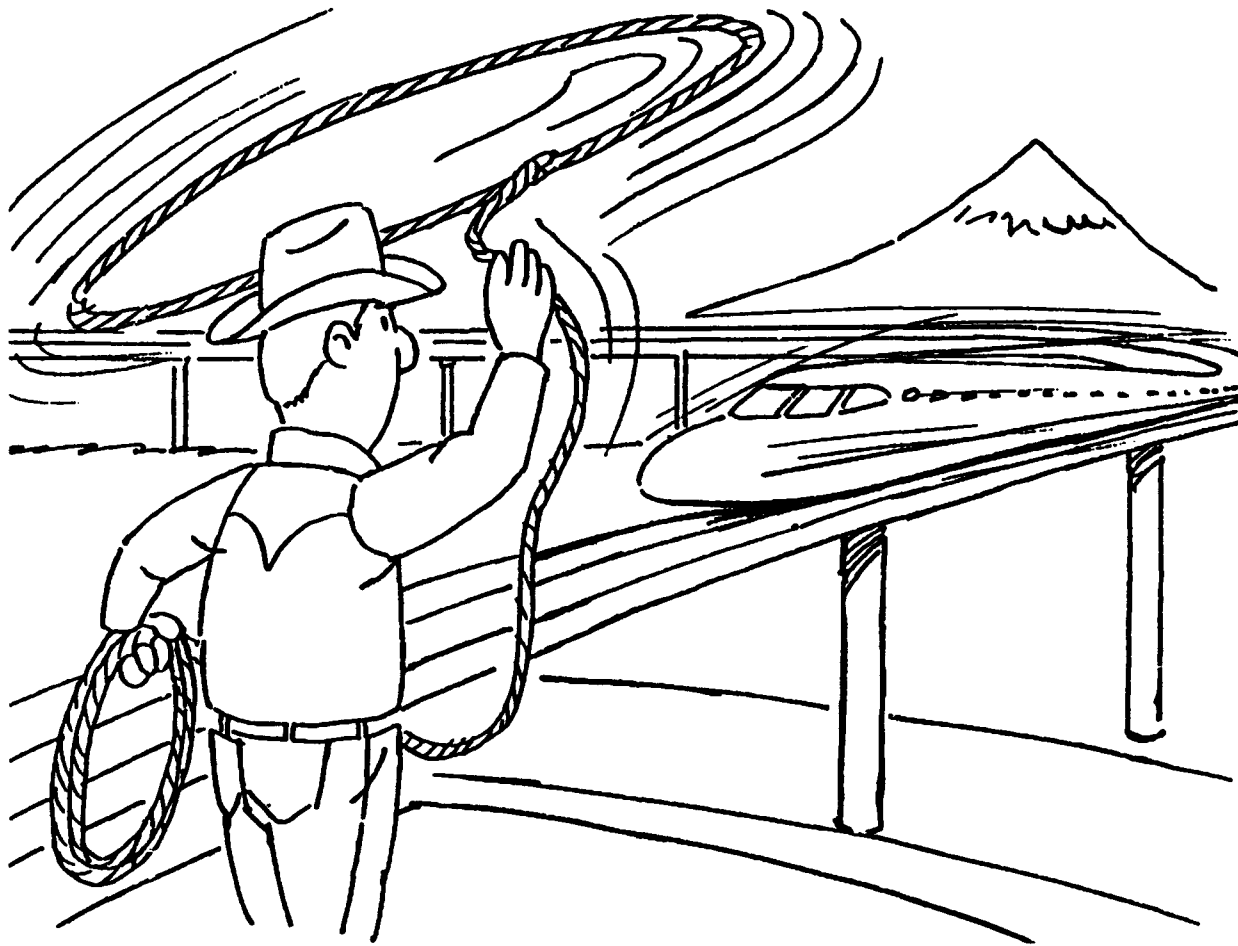
Figure 32

Figure 33

603
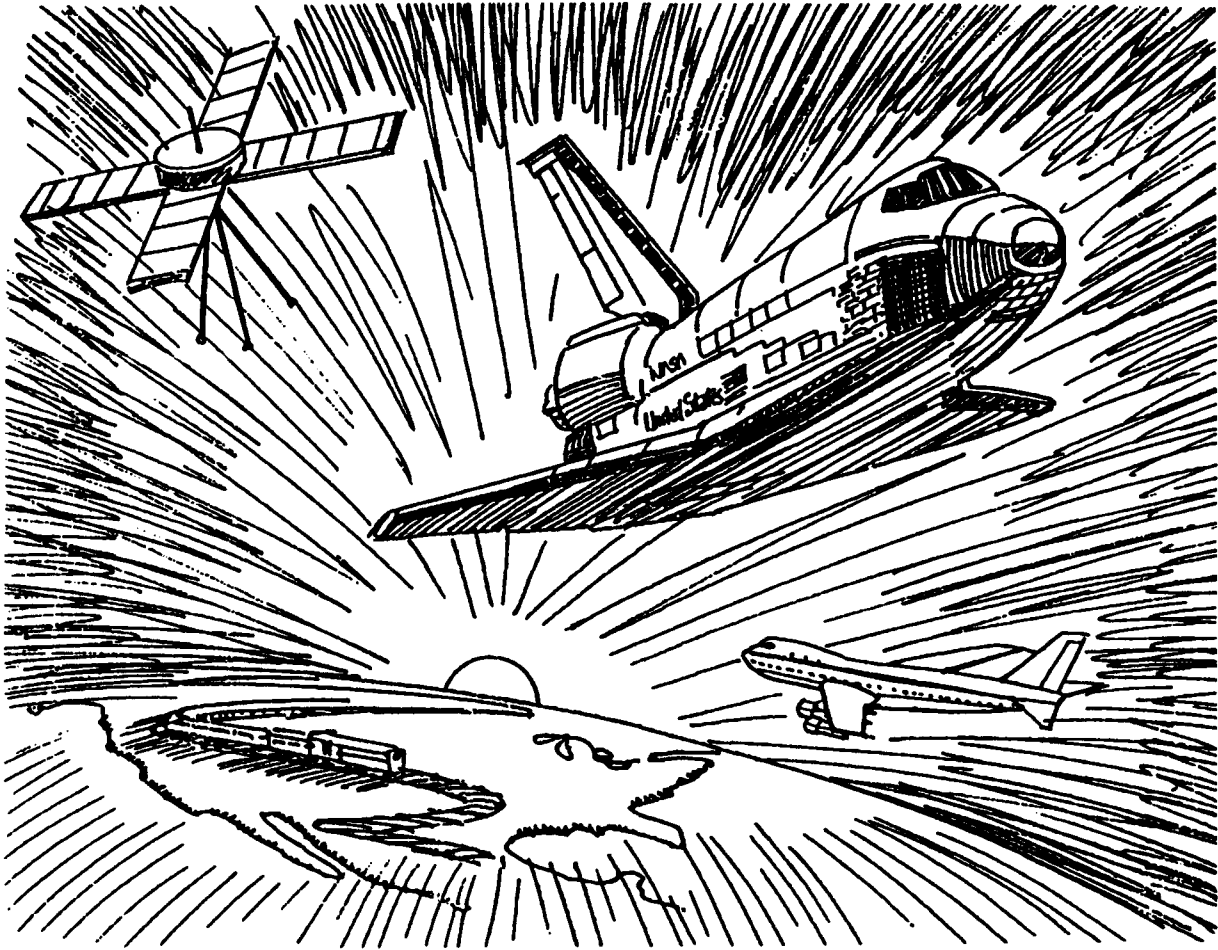
Structural Analysis, Design, and Optimization I

Load Transfer from a Multiply-Connected Anisotropic Plane Structure to an Edge Stringer

E. C. KLANG AND E. J. LEE

ABSTRACT

The stress concentrations in an edge-stiffened, fully anisotropic, semi-infinite plate with a circular cutout are investigated to address the role of the edge-stringer in regards to load transfer. A new combined formulation of the boundary element method (BEM) and the finite difference method (FDM) is presented. The necessity of such a combined formulation arises from the fact that Melan's stringer equation is governed by a second order differential equation of the displacement of the stringer and can be discretized utilizing the finite difference scheme. An effective algorithm using isoparametric quadratic elements is developed to combine the existing standard BEM algorithm with the FDM. The problem of multiply connected, edge-stiffened composite laminates subjected to uniform tensile loading is numerically investigated. The effect of the load transfer from an edge-stringer to the stress concentration around the cutout is analyzed.

1 INTRODUCTION

Load transfer from one elastic medium to another is a fundamental phenomenon. Examples include the micromechanics behavior of composite materials or a stringer bonded to a plate. By stiffening structures with reinforcing fibers or stringers, structural performances can be increased in areas such as mechanical strength, buckling resistance, stress concentrations, weight, and so on. Though the importance of this subject has been recognized for years, progress in understanding the fundamental nature of load transfer in multiply-connected plane structures has been impeded to date, and few useful formulation or solutions have been achieved.

In a recent paper by Lee and Klang [1], an idealized structural model of an edge-stiffened, isotropic, semi-infinite plate with a circular cutout subjected to uniform tensile loading was investigated using an elasticity approach. The solution was sought in series form in bipolar coordinates. A corresponding anisotropic model using an elasticity approach has not been found yet. As mentioned by Lehknitskii [2], multiply connected anisotropic plane structures are much more difficult to solve than their isotropic counterparts. Mathematical difficulties due to the affine transformation still remain unsolved, and intensive research for practical methods of solution is needed.

The research effort here is directed toward establishing the role of the stringer in regards to the load transfer from an edge-stringer to a multiply connected anisotropic plate using the

E. C. Klang, Assistant Professor, North Carolina State University, Raleigh, NC 27695-7921

E. J. Lee, Senior Researcher, SAMSUNG Aerospace R&D Center, 42 Sungju-dong, Changwon, Kyungham 641-120, Republic of Korea

boundary element method (BEM) formulation. As stated by Brebbia [3], the BEM offers not only several benefits to reduce computational effort, but also gives improved accuracy when high stress concentrations occur around cutouts. The boundary integral equation (BIE) for anisotropic materials was initially formulated by Rizzo and Shippy [4], and Cruise [5]. The fundamental solution for orthotropic materials derived by Green and Taylor [6] was used and extended to cover the general anisotropy by Rizzo and Shippy [4]. However, an exhaustive consideration for composite laminates appears not to have been fully made yet, particularly lacking is the fundamental solution for angle-ply laminates. In a recent formulation by Lee [7], the existing fundamental solutions for two-dimensional, fully anisotropic materials were examined and updated with a general formulation to cover all the constitutive models for composite laminates.

In this paper, anisotropic constitutive models of composite laminates are taken into account to investigate the hoop stress distribution around a circular cutout. Anisotropic composite laminates stiffened with an edge-stringer also receive further attention in conjunction with a new combined formulation of the BEM and the finite difference method (FDM). The necessity of such a formulation arises from the fact that the boundary edge-stringer model used in this paper is based on Melan's stringer [8,9] and is governed by a second order ordinary differential equation of the boundary displacement. The stringer condition is formulated as a boundary partially enclosing the elastic body compatible with the boundary integral equation. The resulting BIE is numerically implemented using isoparametric quadratic elements. Utilizing the finite difference scheme, the stringer boundary condition is reduced to a linear combination of element nodal displacements and is decomposed into the system equation matrices.

The combined formulation of BEM/FDM is examined through a comparison study with the analytical solution for the isotropic example given by Lee and Klang [1]. Constitutive effects of composite laminates in the load transfer due to the presence of the edge-stringer are investigated as the stringer stiffness parameter varies. The patterns of hoop stress distributions for the composite laminates are plotted.

2 BOUNDARY INTEGRAL EQUATIONS

A plane elastic body in a state of equilibrium which occupies a multiply connected domain Ω enclosed by the boundary Γ in Cartesian coordinates is considered under prescribed boundary conditions in terms of tractions and displacements. The elastic state under consideration is referred to as the stress σ_{ij}, the strain ε_{ij}, the displacement u_i, the traction p_i and the body force b_i, and is assumed to be coincident with the another elastic body in equilibrium denoted by a domain Ω^* in which all quantities are referred to as starred terms such as σ^*_{ij}, ε^*_{ij}, u^*_i, p^*_{ij} and b^*_i. In the following BIE formulation, the starred quantities are used as the fundamental field of stresses and single-valued displacements due to a concentrated in-plane loading. In particular, terms u^*_{ji} and p^*_{ji} represent the resulting displacement and traction at a point (x,y) due to a concentrated unit force in the j-direction at point (p,q) along the boundary Γ.

Using the equilibrium equations, the strain-displacement relation and the divergence theorem, the Somigliana's identity can be derived from the Betty's reciprocal work theorem. When the body force is negligible, Somigliana's identity contains only boundary integrals as follows:

$$C_{ji}\, u_i(p,\, q) + \int_\Gamma p^*_{ji}\, u_i\, d\Gamma = \int_\Gamma p_i\, u^*_{ji}\, d\Gamma, \tag{1}$$

where C_{ji} equals δ_{ji} within the domain Ω and it equals $\delta_{ji}/2$ on a smooth boundary. Other cases such as the non-smooth cusps along the boundary must be interpreted in the sense of Cauchy's principal value.

3 STRINGER PARAMETER

For a comparison with the analytical solution, a dimensionless stringer parameter is defined in the same way given by Lee and Klang [1] as:

$$\kappa = \frac{AE_s}{atE} \, , \tag{2}$$

where "a" represents a positive real measure of a bipolar pole, t the thickness of the plate and A the area of stringer cross-section. The subscript s represents the stringer related quantity, thus E_s and E being the Young's modulus of the stringer and multiply connected isotropic plate, respectively. For an anisotropic plate, the compliance S_{11} is taken instead of the inverse of E in the isotropic case as a reference material property of stiffened plate where the tensile loading is applied in x_1-direction. Thus, one has

$$\kappa = \frac{AE_s S_{11}}{at} \, . \tag{3}$$

The stringer is assumed to be a uniaxial bar where the transverse components of stresses are negligible compared with the axial stress. The axial displacement can then be described in terms of the coordinate along the bar: that is, cross sections along the bar remain plane and normal to the centroidal axis after the deformation. It is noted that the uniaxial bar is distinguished from the simple beam in that it does not carry the bending stiffness effect.

4 MELAN'S STRINGER MODEL

The edge-stiffened, semi-infinite, multiply connected elastic plate is subjected to uniform tensile loading as shown in Fig. 1a). The Cartesian coordinate system is taken with its origin at the center of the circular hole. The normal stress along the straight edge of plate is assumed to be negligible when compared with other stresses such as shear or axial stress along the stringer.

Referring to Fig. 1b), the stringer condition as in Melan's problem [8,9] is described by:

$$\frac{dp(x)}{dx} = tq(x) \, , \tag{4}$$

where p(x) is the longitudinal force in the edge-stiffener, t the thickness of the plate, and q(x) the shearing stress between the plate and the stiffener. The axial strain along the stiffener is represented as:

$$\varepsilon_s(x) = \frac{p(x)}{AE_s} \, , \tag{5}$$

where the subscript s means the stringer and A represents its area of cross-section.

Along the interface between the plate and the stringer, the displacement of the plate and that of the stringer must be the same and joined together to transmit the shear stress. This condition can be stated by strain terms such that

$$\varepsilon_s(x) = \varepsilon_{xx}(x, -d),$$

(6)

where d is the distance between the center of the circle and the straight edge. The axial force distribution p(x) may be expressed in terms of the displacement u(x,–d) given by

$$p(x) = AE_s\varepsilon_s(x) = AE_s\varepsilon_{xx}(x, -d) = AE_s\frac{du(x, -d)}{dx}.$$

(7)

From now on, the distance –d frequently encountered along the straight edge is omitted for convenience. Substitution of (7) into the stringer condition (4) leads to a new expression:

$$\frac{AE_s}{t}\frac{d^2u(x)}{dx^2} = q(x).$$

(8)

Now, we consider the traction (p_x, p_y) on the straight boundary as follows:

$$p_x = \sigma_{xx}(x)n_x + \sigma_{xy}(x)n_y, \quad p_y = \sigma_{yx}(x)n_x + \sigma_{yy}(x)n_y$$

(9)

where $(n_x, n_y) = (0, -1)$ is the unit normal vector on the straight boundary. Recalling that the normal stress component $\sigma_{yy}(x,-d)$ was assumed to be negligible, the traction conditions are written as:

$$p_x = -\sigma_{xy}(x) = q(x), \quad p_y = -\sigma_{yy}(x) \approx 0.$$

(10)

The second traction condition $p_y=0$ will be utilized as a direct boundary condition. However, since the traction p_x is given in a form of the ordinary differential equation, it is used to change the traction quantities appearing in the boundary integral equation.
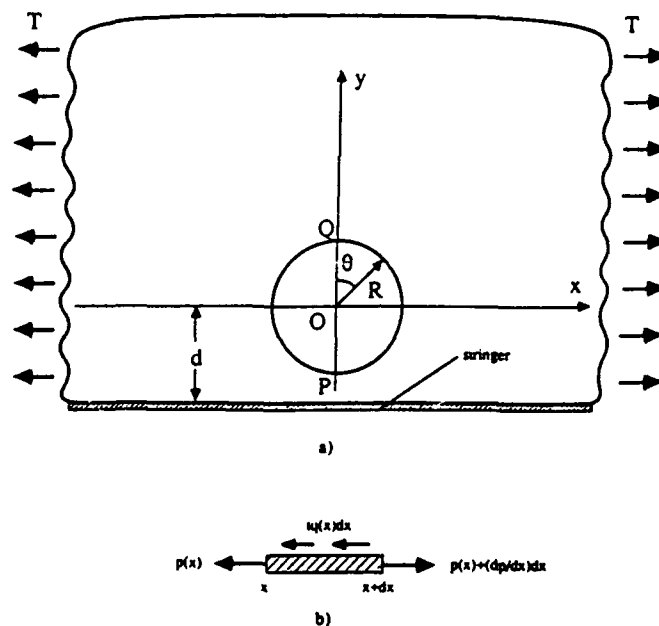
Figure 1 Edge-Stiffened Semi-Infinite Plate with a Circular Cutout

5 THE BIE WITH STRINGER BOUNDARY

The contour Γ along the boundary of an elastic body is assumed to be made of two parts $\Gamma-\Gamma_s$ and Γ_s. Referring to Fig. 1a), the contour Γ_s corresponds to the straight stringer boundary. For an isotropic plate stiffened with the stringer, the BIE (1) can be reduced to the following form as:

$$C_{ji} u_i(p, q) + \int_{\Gamma} p^*_{ji} u_i d\Gamma = \int_{\Gamma-\Gamma_s} u^*_{ji} p_i d\Gamma + \int_s \delta_{i1} u^*_{j1} \kappa E a \frac{d^2 u(x)}{dx^2} d\Gamma,$$ (11)

where the stringer boundary conditions (10) were used on the contour Γ_s. In a similar manner, for an anisotropic plate or composite laminate, the corresponding BIE takes the following form:

$$C_{ji} u_i(p, q) + \int_{\Gamma} p^*_{ji} u_i d\Gamma = \int_{\Gamma-\Gamma_s} u^*_{ji} p_i d\Gamma + \int_s \delta_{i1} u^*_{j1} \kappa \frac{a}{S_{11}} \frac{d^2 u(x)}{dx^2} d\Gamma,$$ (12)

where the starred field refers to the fundamental solution in anisotropic plates as developed by Lee (1991). In order to numerically implement the integral equalities (11) and (12), an algorithm based on the BEM/FDM is developed to seek the solution.·

6 NUMERICAL IMPLEMENTATION

The boundary of a plane elastic body is discretized with quadratic elements. Each element is assumed to have an inter-node at the center of the element. The quadratic shape functions used are referred to as:

$$\phi_1(\eta) = -\frac{1}{2}\eta(1-\eta),$$

$$\phi_2(\eta) = (1-\eta^2), \qquad \text{for } -1<\eta<+1,$$ (13)

$$\phi_3(\eta) = \frac{1}{2}\eta(1+\eta),$$

The boundary shape, the displacement and the traction are isoparametrically interpolated as:

$$x_i^{(e)} = \sum_{k=1}^{3} \phi_k(\eta) x_i^{(e), k},$$

$$u_i^{(e)} = \sum_{k=1}^{3} \phi_k(\eta) u_i^{(e), k},$$ (14)

$$p_i^{(e)} = \sum_{k=1}^{3} \phi_k(\eta) p_i^{(e), k},$$

where (e), k means a kth local node in an element numbered (e), and the index i represents a component of position, displacement or traction in Cartesian coordinates. Then, equation (1), when discretized, results in the standard boundary integral system of equations:

$$\mathbf{Hu=Gp}$$ (15)

where u and p are displacements and tractions, respectively, on the boundary, and H and G are associated matrices. It is noted that in obtaining this matrix system, a rigid body motion of the elastic body may be used to determine the matrix H.

The stringer boundary condition given in a second order differential form on the boundary Γ_s in the BIE (11) and (12) can also be obtained from the isoparametrically interpolated displacement. The second order derivative of the displacement in (14) is discretized using chain rule as follows:

$$\frac{d^2 u_i^{(e)}}{dx^2} = \frac{1}{J^2} \sum_{k=1}^{3} \phi''_k(\eta) u_i^{(e),k} = \frac{1}{J^2}(u_i^{(e),1} - 2u_i^{(e),2} + u_i^{(e),3}),$$
(16)

where the Jacobian J is assumed constant for the present analysis for each element. This assumption is exact only whenever the inter node is located at the center of quadratic element.

The substitution of (16) into the vector p in (15) forms a matrix mixed with traction terms and linear combinations of displacements. To make the matrix system manageable for the numerical solution, the column vector p needs to be split into two column vectors p_s and

$P \equiv p - p_s$, respectively. The subscript s represent the stringer boundary. In the latter vector P, the nodal traction terms along the stringer are filled with zeros. Conversely, the former p_s contains the expression (16) at the positions corresponding to the stringer node and everywhere all terms are filled with zero. Immediately, one obtains the following system equation of matrices:

$$Hu - Gp_s = GP.$$
(17)

Note that the second term in the left hand side of (17) can be decomposed in terms of the column vector u as follows:

$$Gp_s = -G'u.$$
(18)

Thus, one has the final system equation of matrices:

$$[H + G']u = GP.$$
(19)

In conclusion, if well-posed boundary conditions are prescribed along the boundary regardless of type such as the displacement, the traction, or mixed, a global system of linear equations is set up as:

$$AX = f,$$
(20)

where the coefficient matrix A is fully populated. The solution vector X can be obtained by using a solver such as the Gaussian elimination method.

7 MODEL DESCRIPTION

A computational model with an angle resolution of 3 degrees around the hole was used. To approximate the effect of the semi-infinite plate, the width and height of a rectangular plate were taken to be sufficiently large when compared with the radius R and the distance d. By adjusting the parameter value (d/R) from a large value of 40.0 to a low value of 1.185, the influence between the cutout and the straight edge with regards to stress concentration can be closely examined.

The entire boundary was modeled to exclude corners at $\theta = 0$ and $\theta = \pi$ as opposed to modeling half of the domain. This was done because the highest stress concentrations were expected to occur in the neighborhood of $\theta = 0$ and $\theta = \pi$. Double nodes at the four corner points on the square boundary were established to maintain displacement continuity. Since these points are far from the region of interest, their influence on the edge of the cutout region is negligible. The direction of the boundary contour for the numerical integration should be specified consistent with the boundary integral equations (BIE) such that the counterclockwise

direction is taken as positive for the outer square and clockwise for the circle. Four point Gaussian quadrature was employed to compute influence coefficients.

The orthotropic material properties of unidirectional graphite epoxy ply used by Andrew and Hong (1981) are listed as: E_L=21.3 x10^6 psi, E_T=1.58 x10^6 psi, v_{LT}=0.38, G=0.930 x10^6 psi. The averaged properties for unidirectional, cross- and angle-ply laminates were calculated using the above data.

8 NUMERICAL RESULTS AND DISCUSSION

First, the results for the isotropic problems were obtained using a mesh of 4 degrees resolution around the circular cutout, and compared with the analytical solutions. Fig. 3 presents variations of hoop stresses as the parameter κ varies for a fixed value of (d/R). Conversely, Fig. 4 presents variations of hoop stresses as the parameter (d/R) varies for a fixed value of κ. The comparison illustrates that the BEM/FDM solution deviated from the analytical solution by less than 1 % .

The hoop stress profiles for unstiffened anisotropic plates with various values of the parameter (d/R) are given in Fig. 2, 4, 6, and 8. In particular, when the parameter (d/R) takes a large value, (i.e., 40.0), it can be easily verified that the BEM/FDM solution approaches the analytical solution for the infinite anisotropic plate given by Lehknitskii (1963). The stiffened cases are presented and illustrate the effect of the stringer parameter κ in Fig. 3, 5, 7 and 9.

The $[0_n]_s$ laminate shows typical hoop stress patterns locally concentrating around θ=0 and θ=π as shown Fig. 2. The stress concentration factor ranges between 6.0 and 10.0. Weak compressive zones appear along the circumference of the circle. When stiffened, a strong effect of load transfer as κ varies is observed as shown Fig. 3, and the stress concentrations locally concentrating around θ=0 and θ=π are significantly reduced due to the strong load transfer effect.

The $[90_n]_s$ laminate reveals a characteristic distribution with strong compressive stress concentration around θ=π/2 as shown in Fig. 4. In this case, the proximity effect due to the presence of the adjacent straight boundary is seen to be more dominant than for any other laminate. The results even for (d/R)=1.811 present a widely varying stress distribution over the circular boundary. The solutions for (d/R)=1.337 and 1.185 may need to employ more finely meshed models due to the severe stress concentrations. The effect of load transfer is seen to be weaker than for the three other composite laminates (Fig. 5), thus showing little reduction of the stress concentrations at θ= π/2 as κ varies.

The cross-ply laminate of $[0/90]_{2s}$ illustrated in Fig. 6 shows similar patterns to the $[0_n]_s$ laminate of Fig. 2, but the stress concentrations around θ=0 and θ=π are more moderate when compared with the $[0_n]_s$ laminate and range from 4.0 to 8.0. The effect of load transfer for varying κ is illustrated in Fig. 7.

The hoop stress profiles for an $[\pm 45]_{2s}$ angle-ply laminate are presented in Fig. 8. It is seen that maximum hoop stress occurs at some angle off of θ=0 or π/2. This is because the modulus E_θ takes maximum values at angles off of the symmetry axis. In addition, the hoop stress profiles are seen to be lower than all the other laminates, being bounded under 6.0 for all ranges of (d/R). For (d/R)= 1.811 or above, the stress concentration takes place between θ=0 and θ=π/2, approximately at π/5 , but as d/R decreases, the point at which the stress concentration occurs moves to θ=π. For the stiffened case, the effect of load transfer occurs around θ=π/5 and θ=π as illustrated in Fig. 9.
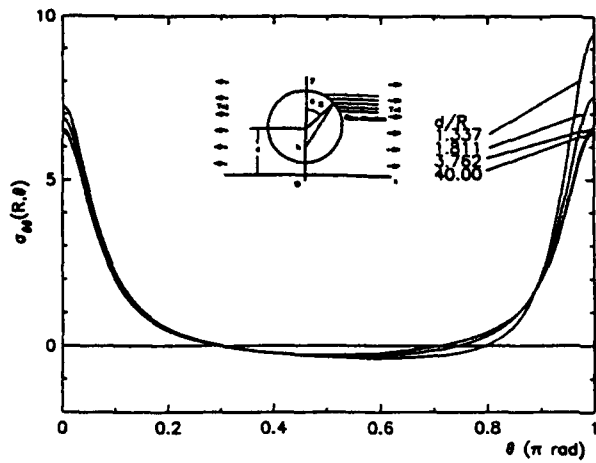
Figure 2 $[0_n]_s$ unstiffened panel
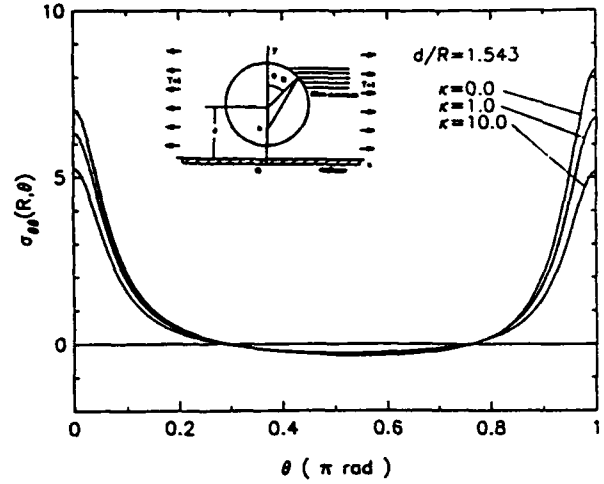
Figure 3 $[0_n]_s$ stiffened panel
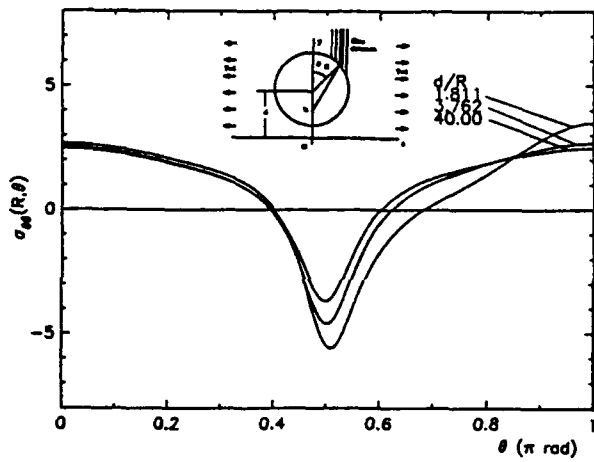
Figure 4 $[90_n]_s$ unstiffened panel
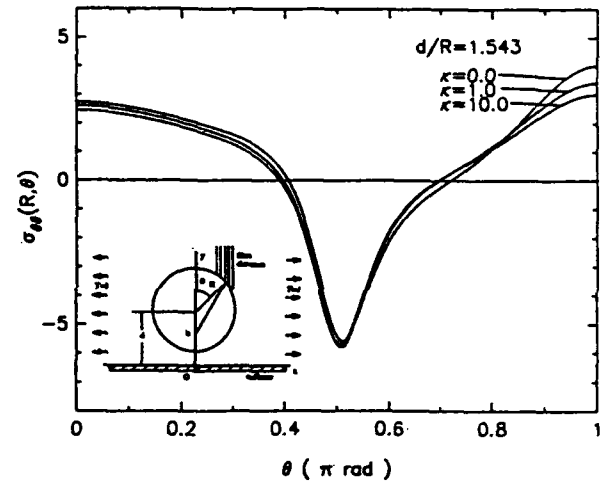
Figure 5 $[90_n]_s$ stiffened panel
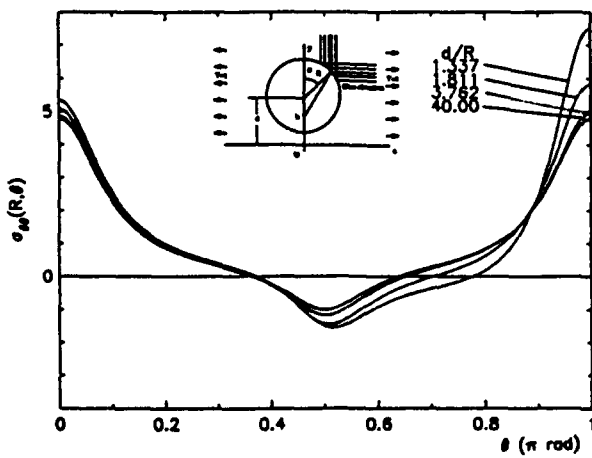
Figure 6 $[0/90]_{2s}$ unstiffened panel
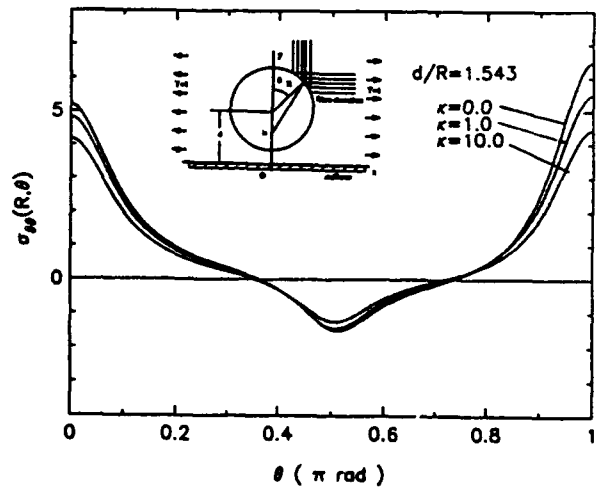
Figure 7 $[0/90]_{2s}$ stiffened panel
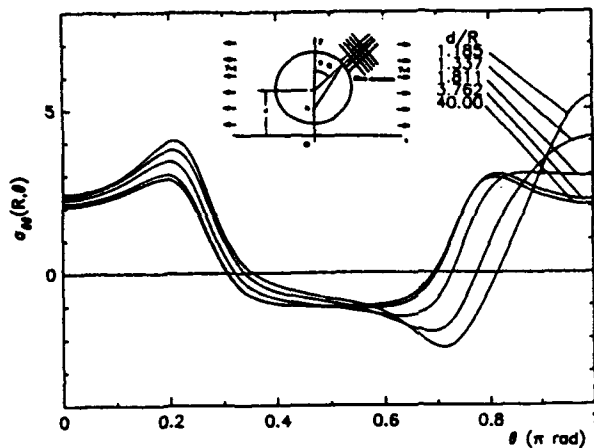
Figure 8 [±45]$_{2s}$ unstiffened panel
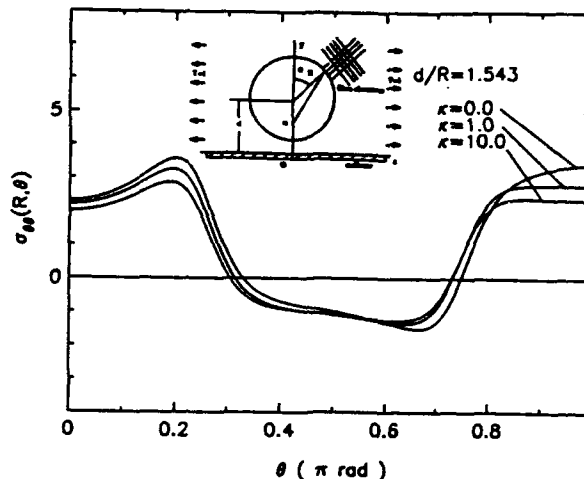
Figure 9 [±45]$_{2s}$ stiffened panel

10 CONCLUDING REMARKS

To investigate the effect of load transfer to the hoop stress around the circular cutout under the influence of an edge-stringer in the semi-infinite anisotropic plate, a new combined formulation of BEM/FDM was developed and numerically implemented using quadratic elements. The effect of load transfer for the composites strongly depends upon the fiber direction of the laminate, and is stronger than isotropic plates or quasi-isotropic laminates.

REFERENCES

1. Lee, E.J. and Klang, E.C., 1992, "Stress Distribution in an Edge-Stiffened Semi-Infinite Elastic Plate Containing a Circular Hole", *Journal of Applied Mechanics*

2. Lehknitskii, S.G. , 1963, Theory of Elasticity of an Anisotropic Elastic Body, Holden-Day Inc.

3. Brebbia, C.A., 1980, The Boundary Element Method for Engineers, 2nd ed., Pentech Press Limited Inc., London.

4. Rizzo, F.J. and Shippy, D.J., 1970,"A Method for Stress Determination in Plane Anisotropic Elastic Plate", *Journal of Composite Materials*, Vol. 4, p.36.

5. Cruse, T., U.S.A. Air Force Report, No. AFML-TR-71-268.

6. Green, A.E. and Taylor, G.I., 1939, "Stress Systems in Aeolotropic Plates. I", *Proc. Roy. Soc.* A, 173,p.162.

7. Lee, E.J., 1991, "Load Transfer From Multiply Connected Plane Anisotropic Structure to an Edge-Stringer," North Carolina State University, Ph.D. thesis.

8. Melan E., 1932a, "Der Spannungszustand Der Durch Eine Einzelkraft Im Innern Beanspurchten Halscheibe," *Zeitschrift fuer angewandte Mathematik und Mechanik*, Vol.12, pp. 343-346.

9. Melan E., 1932b, "Ein Beitrag zur Theori geschweisster Verbindungen," *Ingenier - archiv*, Vol.3, pp.123-129.

Neutral Holes in Laminated Plates

EROL SENOCAK AND ANTHONY M. WAAS

Abstract

In [1], the concept of a neutral hole, where certain reinforced holes do not alter the stress state in the cut structure (isotropic plane sheets) is introduced. This approach is extended to laminated anisotropic plates. The case of symmetrically laminated plates is examined in [2]. In the present work, unsymmetrically laminated plates are considered. In-plane and out-of-plane responses are coupled through unsymmetric lamination of the plate material, and this effect is considered. The reinforcement is modeled as a one-dimensional beam type structural element.

1. Introduction

The efficiency (advantages such as high strength to weight ratio) of laminated composite plates forces us to replace many current engineering structures with composite plates. Especially, in the aerospace industry the advantages of such structures are tremendous. The desire to use laminated plates is growing rapidly in other areas of industry (automative, ship) as well.

Plates with cutouts are widely used structural elements in many engineering applications (a common occurence in the aircraft industry), hence the analysis of such structures is crucial. For this reason the corresponding boundary-value problems of plane elasticity have received special consideration throughout many years. The concept of a "Neutral hole" was first introduced by Mansfield [1]. Mansfield's contention was to design a reinforced cutout in a plane sheet such that the stress state in the cut structure remains unchanged to that of the corresponding uncut structure.

The problem of planar and out-of-plane responses for symmetrically laminated plates is examined in [2]. Since these two responses are uncoupled for symmetric lamination, their solutions are investigated separatly. These two responses are coupled in the case of unsymmetrically laminated plates. In the present paper, this coupling effect is examined.

The bending-stretching coupling in the case of unsymmetric lamination leads us to consider the effect of the planar forces on the bending of the plate and these effects must be included in deriving the corresponding differential equation of the deflection

surface. The planar forces not only creates middle plane strain, but also curvatures due to material coupling. In-plane equations are entirely independent from the out-of-plane equations, and they are treated separatly. (This is the same approach as in the derivation of von Kármán's plate equations.)

The reinforcement is assumed to be made of the ply material that is used to construct the laminate. In addition, the fiber direction in the reinforcement is required to be tangential to the edge of the cutout. Since the sectional areas of the reinforcing member are small compared to the other dimensions of the plate, they are treated within the framework of one dimensional technical beam theories.

2. Formulation

2.1. Shape of a neutral hole

Consider the equlibrium of an element (see Figs.1,3 and 4) adjacent to the cutout and including a part of the reinforcement. Let a set of cartesian coordinates be located in the mid-plane of the laminate (symmetrically laminated about mid-plane) such that the xy plane coincides with the lamination plane. The reinforcing member is treated as a one dimensional beam element. Then, the force and moment equilibrium equations are as follows.

$$
\begin{aligned}
d(P\sin\alpha) &= N_y dx - N_{xy} dy \\
d(P\cos\alpha) &= N_{xy} dx - N_x dy \\
dQ &= -P\left(\cos\alpha\, w_{,xs} + \sin\alpha\, w_{,ys}\right) ds \\
d(M\sin\alpha + T\cos\alpha) &= Q dy \\
d(M\cos\alpha - T\sin\alpha) &= Q dx
\end{aligned}
\tag{1}
$$

where P is tension, Q is shear, M and T are bending and twisting moments in the reinforcement respectively, and $w(x,y)$ is the out of plane deflection. Also, $w_{,xs} = \frac{\partial^2 w}{\partial x \partial s}$, $w_{,ys} = \frac{\partial^2 w}{\partial y \partial s}$. Now introduce a stress function ϕ defined as below.

$$
\begin{aligned}
N_x &= \frac{\partial^2 \phi}{\partial y^2} \\
N_y &= \frac{\partial^2 \phi}{\partial x^2} \\
N_{xy} &= -\frac{\partial^2 \phi}{\partial x \partial y}
\end{aligned}
\tag{2}
$$

Then, substituting (2) into the first two equations of (1) and integrating, yields,

$$
\phi + \acute{a}x + \acute{b}y + \acute{c} = 0
\tag{3}
$$

where $\acute{a}$, $\acute{b}$ and $\acute{c}$ are constants.

Terms of the type $(\acute{a}x + \acute{b}y + \acute{c})$ do not alter the stresses, so without loss of generality (3) can be written as

$$\phi = 0. \tag{4}$$

Equation (4) gives the condition to determine the shape of the hole.

2.2. Sectional area of the reinforcement

The total force in the reinforcing member is determined from equations (1) and (2), by eliminating α.

$$P = \left[\left(\frac{\partial\phi}{\partial x}\right)^2 + \left(\frac{\partial\phi}{\partial y}\right)^2\right]^{\frac{1}{2}} \tag{5}$$

The next step is to determine the distribution of Q (out-of-plane shear force) from the third equation of (1). Here, it should be noted that, the positive s coordinate is measured counterclockwise and tangent to the cutout, and its crossing point with the positive x axis is its origin. Then, with reference to Fig.3,

$$\frac{\partial()}{\partial s} = \cos\alpha\frac{\partial()}{\partial x} + \sin\alpha\frac{\partial()}{\partial y}. \tag{6}$$

From (1), (5) and (6), the following is derived.

$$Q = \int P\left(\cos^2\alpha\frac{\partial^2 w}{\partial x^2} + 2\sin\alpha\cos\alpha\frac{\partial^2 w}{\partial x\partial y} + \sin^2\alpha\frac{\partial^2 w}{\partial y^2}\right)ds + C_1, \tag{7}$$

where C_1 is a constant of integration. The plate curvatures are related to the deflection $w(x, y)$, in the following manner.

$$
\begin{aligned}
\kappa_x &= -\frac{\partial^2 w}{\partial x^2} \\
\kappa_y &= -\frac{\partial^2 w}{\partial y^2} \\
\kappa_{xy} &= -\frac{\partial^2 w}{\partial x\partial y}
\end{aligned}
\tag{8}
$$

Combining (7) and (8) yields,

$$Q = \int P\kappa_s + C_1 \tag{9}$$

where κ_s is defined later in (13).

The constitutive relation, derived on the basis of classical lamination plate theory (CLT) is [3],

$$N = A\epsilon + B\kappa$$
$$M = B\epsilon + D\kappa. \tag{10}$$

Solving for ϵ and κ from (10), yields,

$$\epsilon = (A - BD^{-1}B)^{-1}(N - BD^{-1}M)$$
$$\kappa = (D - BA^{-1}B)^{-1}(M - BA^{-1}N). \tag{11}$$

First, consider the plate under planar loading only ([M]=[0]). Then the strains and plate curvatures are given by,

$$\epsilon = E^{-1}N = E^*N$$
$$\kappa = F^{-1}N = F^*N \tag{12}$$

where $E = (A - BD^{-1}B)$ and $F = (D - BA^{-1}B)$.

The strains and curvatures in the plate are continuous and therefore the strains and curvatures along the reinforcement are found via the transformation law,

$$\epsilon_s = \epsilon_x \cos^2\alpha + \epsilon_y \sin^2\alpha + \epsilon_{xy} \sin\alpha \cos\alpha$$
$$\kappa_s = \kappa_x \cos^2\alpha + \kappa_y \sin^2\alpha + 2\kappa_{xy} \sin\alpha \cos\alpha \tag{13}$$
$$\kappa_{sn} = (\kappa_y - \kappa_x) \sin\alpha\cos\alpha + \kappa_{xy}(\cos^2\alpha - \sin^2\alpha).$$

¿From (1), the last two equations are to be integrated along the cutout to find the moment and torque distribution as,

$$M\sin\alpha + T\cos\alpha = \int Q dy + C_2$$
$$M\cos\alpha - T\sin\alpha = \int Q dx + C_3 \tag{14}$$

where C_2 and C_3 are constants of integration. Thus, at this stage all forces and moments in the reinforcement are determined in terms of plate quantities (see (5), (9) and (14)).

In addition we know that the axial force P, moment M and torque T in the reinforcing member can be written as,

$$P = E_s A\epsilon_s$$
$$M = E_s I(s)\kappa_s \tag{15}$$
$$T = G_{nx} J(s)\kappa_{sn}.$$

Here, $E_s A$, $E_s I$ and $G_{nx} J$ are the axial, bending and twisting rigitidies of the reinforcement. Thus, from (5), (9), (14) and (15), the cross-section shape of the reinforcement can be determined.

3. Example

For a plate under biaxial planar loading, the stress function is,

$$\phi = \frac{1}{2}(P_1 y^2 + P_2 x^2) - C \tag{16}$$

where P_1 and P_2 are the tension forces per unit length in the x and y directions respectively (in the principal axes). Under the loading, as defined above, the plate resultants are $N_x = P_1$, $N_y = P_2$. An ellipse, with lengths of major axes in the ratio $\sqrt{P_1/P_2}$ is obtained for the hole shape from (4). Here the constant C defines the size of the hole.

Next, Q is determined from (9) as;

$$Q = A_1 x\sqrt{a^2 - x^2} + A_2 x^2 + A_3 \sin^{-1}(\frac{x}{a}) + C_1 \tag{17}$$

where, $A_1 = \frac{\kappa_y P_2^2 - \kappa_x P_1 P_2}{2\sqrt{P_1 P_2}}$, $A_2 = \kappa_{xy} P_2$, $A_3 = -\frac{\kappa_y P_2^2 a^2 + \kappa_x P_1 P_2 a^2}{2\sqrt{P_1 P_2}}$, $a = \sqrt{\frac{2C}{P_2}}$.

Now define $G(x)$ and $H(x)$ as the following,

$$
\begin{aligned}
G(x) &= M\sin\alpha + T\cos\alpha \\
H(x) &= M\cos\alpha - T\sin\alpha.
\end{aligned}
\tag{18}
$$

From (14) and using (17), the following is derived.

$$G(x) = B_1 x^3 + B_2\sqrt{a^2 - x^2}(x^2 + 2a^2) + B_3(x - \sqrt{a^2 - x^2}\sin^{-1}(\frac{x}{a})) + B_4\sqrt{a^2 - x^2} + C_2$$

$$H(x) = -\frac{A_1}{3}(a^2 - x^2)^{\frac{3}{2}} + \frac{A_2}{3}x^3 + A_3(\sqrt{a^2 - x^2} + x\sin^{-1}(\frac{x}{a})) + C_1 x + C_3 \tag{19}$$

where, $B_1 = -\frac{A_1 k}{3}$, $B_2 = \frac{A_2 k}{3}$, $B_3 = -A_3 k$, $B_4 = C_1 k$, $k = \sqrt{\frac{P_2}{P_1}}$.

From (18), the bending moment and twisting moment distribution is solved as;

$$
\begin{aligned}
M &= G(x)\sin\alpha + H(x)\cos\alpha \\
T &= G(x)\cos\alpha - H(x)\sin\alpha.
\end{aligned}
\tag{20}
$$

Finally, from (15) and (20) the reinforcement cross-section properties A, I and J are determined.

$$
\begin{aligned}
A &= \frac{P}{E_s \epsilon_s} \\
I &= \frac{M}{E_s \kappa_s} \\
J &= \frac{T}{G_{ns} \kappa_{sn}}.
\end{aligned}
\tag{21}
$$

In general, these three quantities define the cross-section uniquely. In practice, the twisting moment compared to the bending moment in the reinforcement is small. Therefore, if the shape of the cross-section is prescribed, say, rectangular (Fig.2), with h being the height and d, the width, then the first two equations give the distribution of h and d (see Figs.5 and 6). Without loss of generality, the constants C_1, C_2 and C_3 can be chosen to be zero.

A typical numerical example is given below.

Example: Lay-up: $[+40/-40]_4$

Ply Properties: E_1=133 GPa, E_2=9 GPa, G_{12}=3 GPa, ν_{12}=0.26.

Ply Thickness: 1 mm.

Loading: $P_1 = 200$ N/mm, $P_2 = 150$ N/mm.

Shape of Hole (from above solution): Ellipse, $200y^2 + 150x^2 - 15.10^5 = 0$

Reinforcement thickness (h):

$$h = \left(\frac{2.84\ 10^9 + 2.20\ 10^4 x^2 - 1.57x^4}{3\ 10^6 - 75x^2}\right)^{1/2} \tag{22}$$

Reinforcement width (d):

$$d = \frac{(3\ 10^8 - 7500x^2)^2}{(5.59\ 10^7 + 1554.87x^2)^{1/2}(8.98\ 10^7 - 1796.51x^2)^{3/2}} \tag{23}$$

4. Conclusions

In this paper we have presented a method to design the shape of a cutout and the cutout edge reinforcement distribution for an unsymmetrically laminated plate, when it is remotely loaded by uniform planar loads. The in-plane and out-of-plane plate equations are coupled through material behavior ([B] matrix is present). The governing equations are derived within the class of intermediate plate deformations (von Kármán [4], [5]). The effect of the planar forces on the bending of the plate is examined. When the [B] matrix is set to zero (symmetric lamination), this case reduces to the symmetrically laminated plate, and solutions given in [2] are recovered.

References

[1] Mansfield, E.H.,"Neutral Holes in Plane Sheet-Reinforced Holes Which are Elastically Equivalent to the Uncut Sheet," *Quarterly Journal of Mechanics and Applied Mathematics,* London, England, Vol.VI, Part 3, 1953, pp. 370-378.

[2] Senocak, E.,Waas, A.M.,"Design Considerations for Symmetrically Laminated Plates With Cutouts,"*33. AIAA, SDM Congress*, Texas, April,1992.

[3] Whitney, J.M.,"Structural Analysis of Laminated Anisotropic Plates", Technomic Publishing Co., Inc., Penn.,1987.

[4] Timoshenko, S., Woinowsky-Krieger, S., "Theory of Plates and Shells", McGraw-Hill, New York, 1959.

[5] Brush, D.O., Almroth, B.O., "Buckling of Bars, Plates and Shells", McGraw-Hill, New York, 1975.
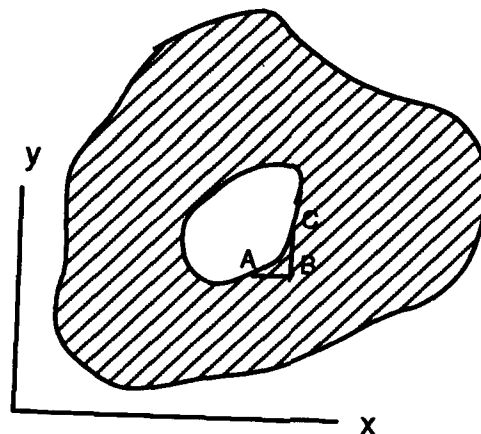
Fig.1 Plate with a cutout.
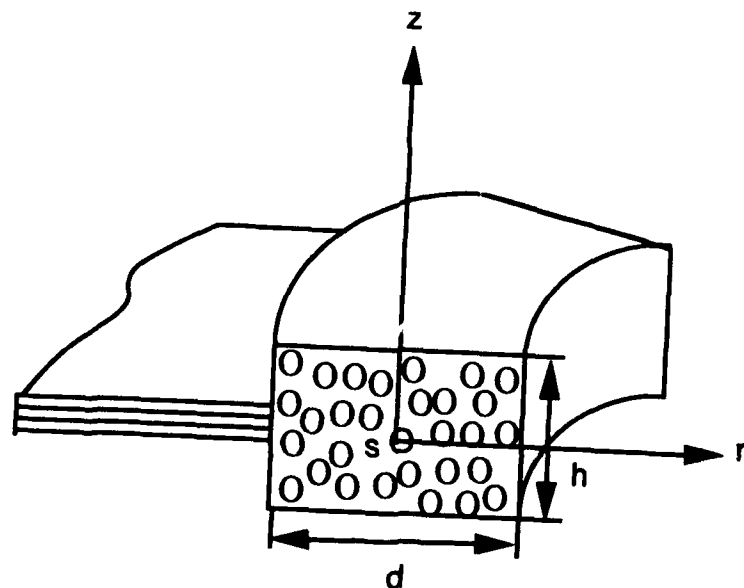
Fig.2 Coordinates used to define the reinforcement.
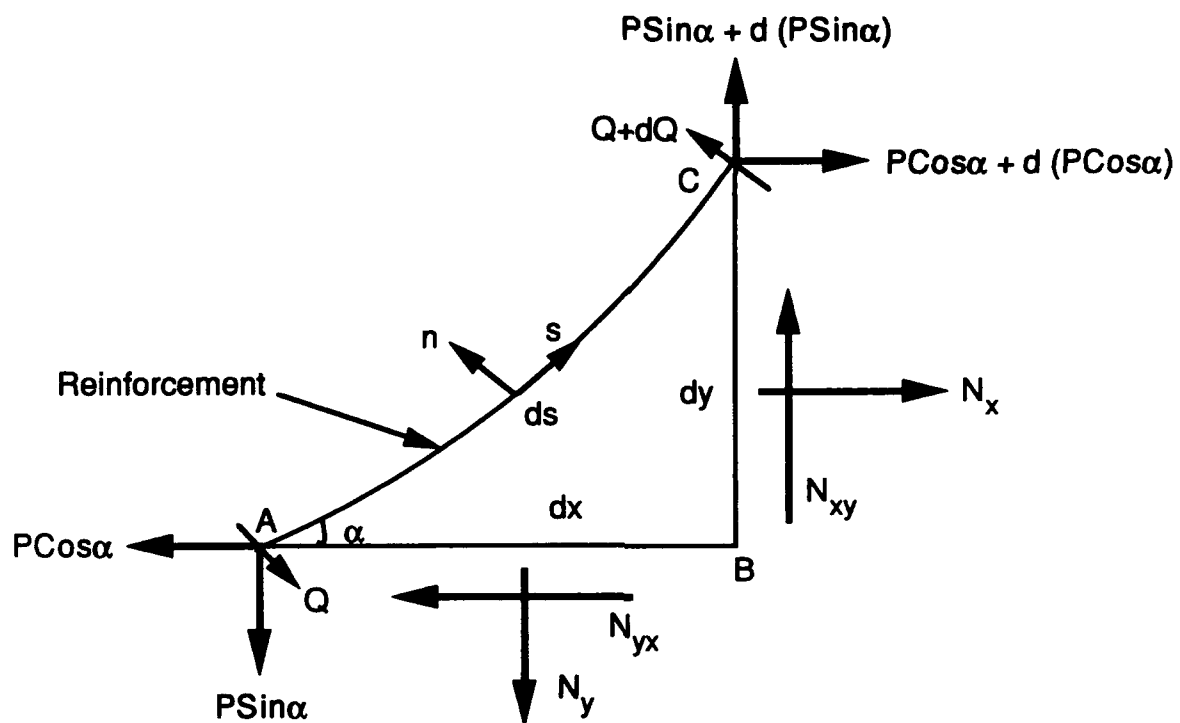
Fig.3 Forces on the small element 'ABC' indicated in Fig.1.
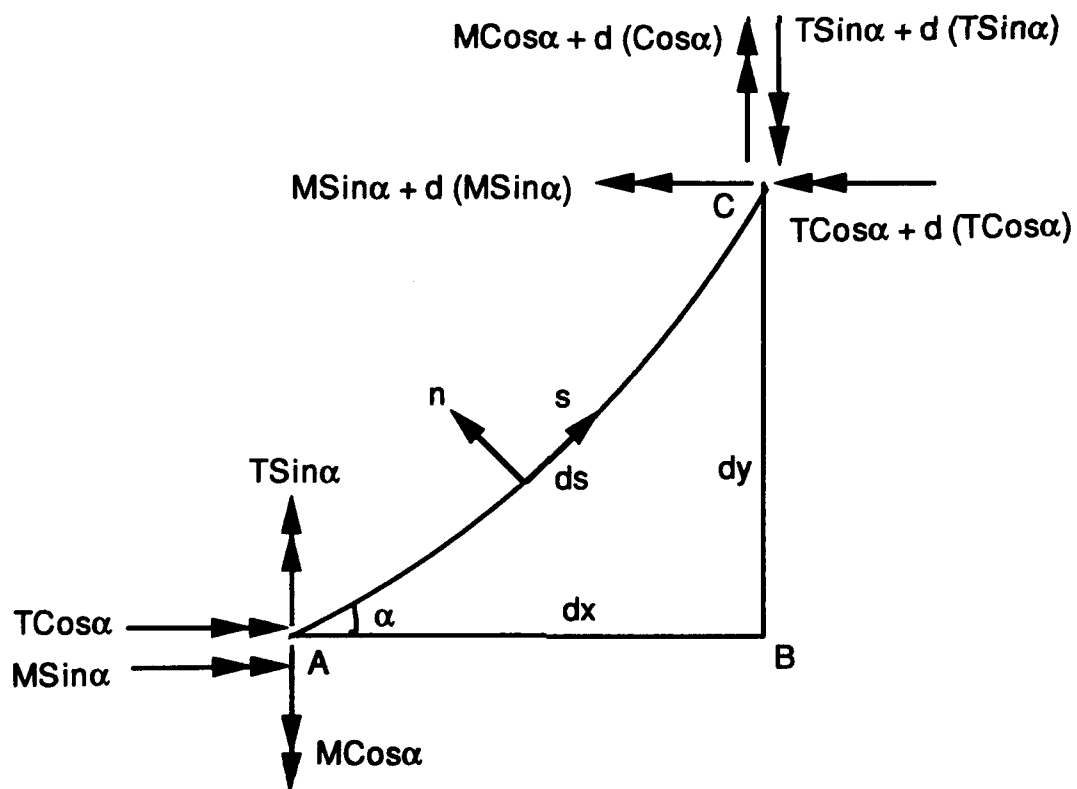
Fig.4 Moments on the element 'ABC'.
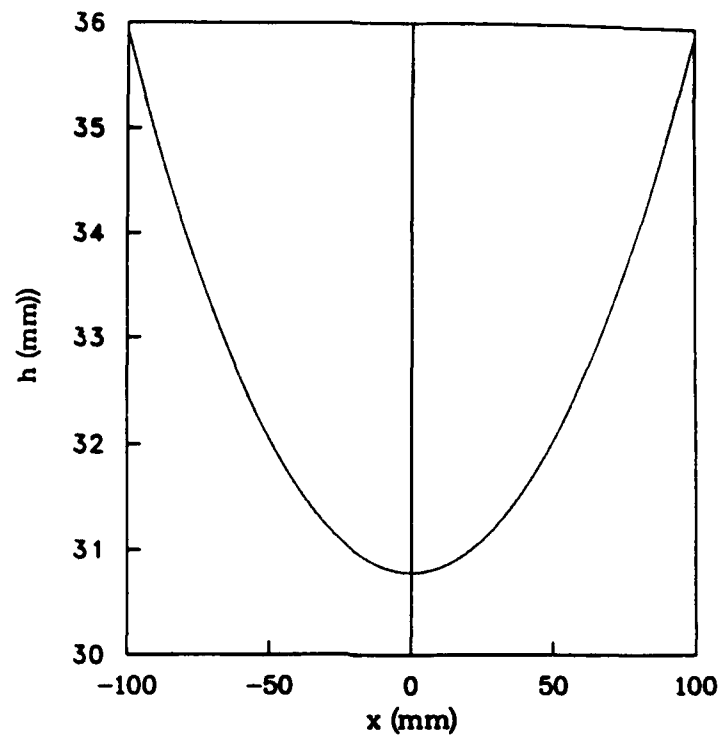
Fig.5 Reinforcement height (h) distribution.
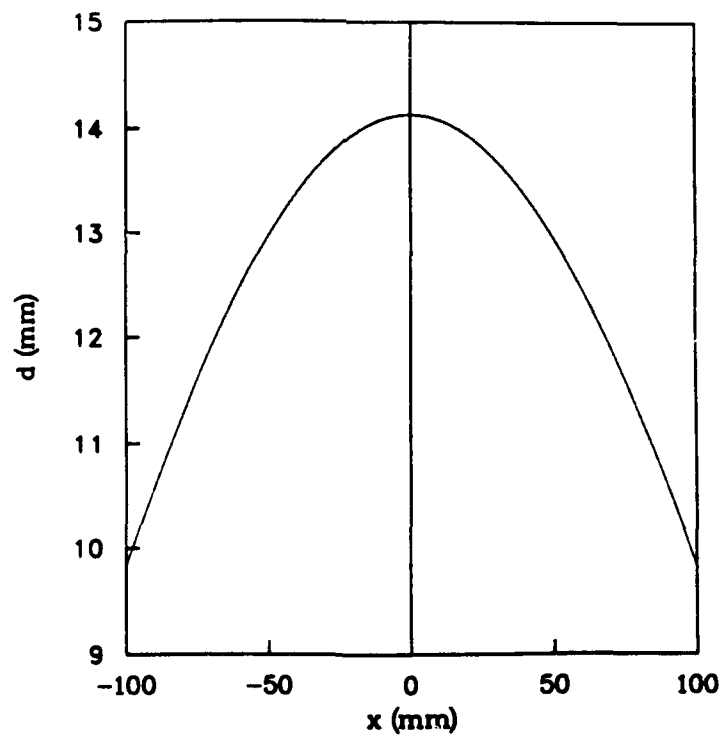
Fig.6 Reinforcement width (d) distribution.

624

Stiffness Design of Symmetric Laminates with Coupling

HISAO FUKUNAGA AND HIDEKI SEKINE

ABSTRACT

The present paper shows a stiffness design method of symmetric laminates with extension-shear or bending-twisting coupling. Lamination parameters are introduced for a full utilization of design freedom in symmetric laminates. Feasible regions are obtained for a general symmetric laminate and for a conventional symmetric laminate such as 0/±45/90 laminates. A method is also shown for determining laminate configurations from lamination parameters. Based on the fundamental relations of lamination parameters, in-plane elastic properties are examined as well as buckling characteristics of symmetric laminated plates. The effect of extension-shear coupling or bending-twisting coupling on the stiffness characteristics of symmetric laminates is clarified.

INTRODUCTION

The stiffness characteristics of laminated composites depend strongly on layer angles and layer thicknesses. Therefore, it is important to tailor laminate configurations of laminated composites.

In the classical lamination theory, the stiffness components of laminated composites are expressed by twelve lamination parameters and four independent stiffness invariants [1]. Introduction of lamination parameters is useful for a full utilization of design freedom in a stiffness design of laminated composites. To use the lamination parameters in the stiffness design, we need know the feasible region of lamination parameters and also the determining method for laminate configurations corresponding to the lamination parameters. The previous papers [2]-[4] have shown those fundamental relations for orthotropic laminates without coupling.

In the symmetric laminate, there occurs extension-shear coupling or bending-twisting coupling. The effect of the coupling on the stiffness characteristics has been examined in the aeroelastic tailoring of composite wings [5], in the buckling of laminated plates [6], and in the intelligent composites with induced strain actuators [7].

The in-plane and out-of-plane stiffness characteristics are governed by four in-plane and four out-of-plane lamination parameters, respectively. The feasible region of those lamination parameters has been examined in Refs.[8]-[10]. Reference [10] has derived an explicit relation of four in-

---

H. Fukunaga, Associate Professor, and H. Sekine, Professor, Department of Aeronautics and Space Engineering, Tohoku University, Sendai 980 Japan

plane or four out-of-plane lamination parameters in general symmetric laminates. A method for determining laminate configurations was also shown in Ref.[10].

The present paper examines the stiffness characteristics of general symmetric laminates and of conventional symmetric laminates such as 0/±45/90 laminates. We discuss the effect of extension-shear coupling on the in-plane elastic properties, and also the effect of bending-twisting coupling on the buckling characteristics of symmetric laminated plates.

STIFFNESS CHARACTERISTICS OF SYMMETRIC LAMINATES

Characteristics of Lamination Parameters

Based on the classical lamination theory, the constitutive equation of symmetric laminates is expressed as follows:

$$\left\{ \begin{array}{c} N \\ M \end{array} \right\} = \left[\begin{array}{cc} A & 0 \\ 0 & D \end{array} \right] \left\{ \begin{array}{c} \varepsilon \\ \kappa \end{array} \right\} \tag{1}$$

where N and M, respectively, denote the stress and moment resultants; ε and κ, respectively, denote the strains and the curvature changes at the midplane; A_{ij} and D_{ij}, respectively, represent the in-plane stiffnesses and the out-of-plane stiffnesses.

Introducing the stiffness invariants and the lamination parameters, A_{ij} and D_{ij} can be expressed as follows;

$$(A_{11}, A_{22}, A_{12}, A_{66}, A_{16}, A_{26}) = h[(U_1, U_1, U_4, U_5, 0, 0)$$
$$+ (\xi_1, -\xi_1, 0, 0, \xi_3/2, \xi_3/2)U_2 + (\xi_2, \xi_2, -\xi_2, -\xi_2, \xi_4, -\xi_4)U_3] \tag{2}$$

$$(D_{11}, D_{22}, D_{12}, D_{66}, D_{16}, D_{26}) = h^3/12[(U_1, U_1, U_4, U_5, 0, 0)$$
$$+ (\xi_9, -\xi_9, 0, 0, \xi_{11}/2, \xi_{11}/2)U_2 + (\xi_{10}, \xi_{10}, -\xi_{10}, -\xi_{10}, \xi_{12}, -\xi_{12})U_3] \tag{3}$$

where h is the thickness of the plate. The stiffness invariants U_i (i=1-5) are defined in Ref.[1], and the lamination parameters are written by using the symmetric condition at the midplane as follows.

$$(\xi_1, \xi_2, \xi_3, \xi_4) = \int_0^1 (\cos 2\theta, \cos 4\theta, \sin 2\theta, \sin 4\theta)du \tag{4}$$

$$(\xi_9, \xi_{10}, \xi_{11}, \xi_{12}) = 3 \int_0^1 (\cos 2\theta, \cos 4\theta, \sin 2\theta, \sin 4\theta)u^2 du \tag{5}$$

where $\theta(u)$ is a distribution function of the fiber angles through the thickness, and $(\xi_1, \xi_2, \xi_3, \xi_4)$ and $(\xi_9, \xi_{10}, \xi_{11}, \xi_{12})$ represent the in-plane and out-of-plane lamination parameters, respectively. The lamination parameters not only characterize the laminate configurations but also govern the stiffness characteristics of symmetric laminates. It is important to note that the stiffness components are expressed by a linear function with respect to the lamination parameters in Eqs.(2) and (3). Thus the stiffness design of symmetric laminates is an easy task when the lamination parameters are used as design variables.

The lamination parameters depend on each other. The relation between the four in-plane or out-of-plane lamination parameters has been shown in
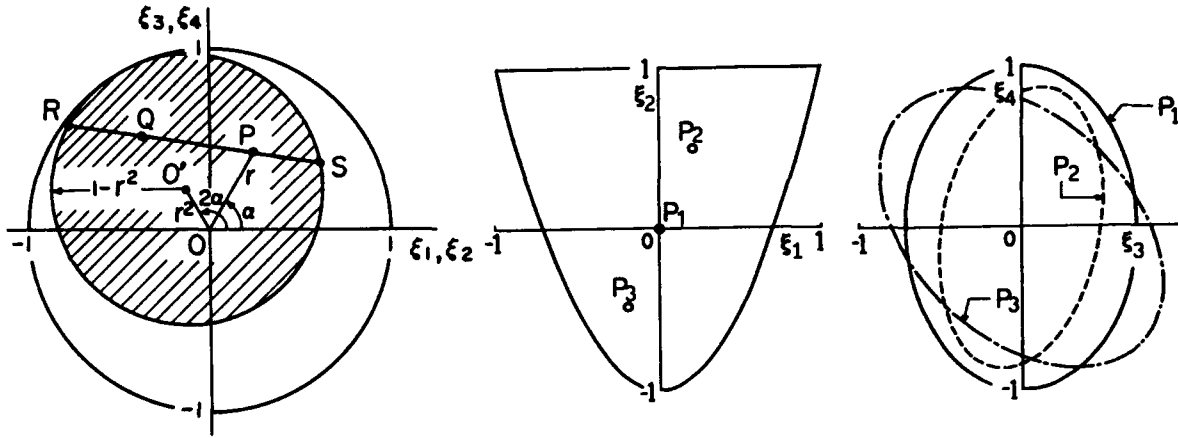
Fig.1 Feasible region of
Q(ξ_2,ξ_4) for P(ξ_1,ξ_3).

(a) ξ_1-ξ_2 plane   (b) ξ_3-ξ_4 plane
Fig.2 Feasible region of (ξ_3,ξ_4) for
P(ξ_1,ξ_2) = P$_1$(0,0), P$_2$(0.2,0.5) and
P$_3$(-0.2,-0.5).

Ref.[10]. For the in-plane lamination parameters, we can obtain the following relations:

$$\xi_1^2 + \xi_3^2 \leq 1 \tag{6}$$

$$(\xi_2 - \xi_1^2 + \xi_3^2)^2 + (\xi_4 - 2\xi_1\xi_3)^2 \leq (1 - \xi_1^2 - \xi_3^2)^2 \tag{7}$$

or equivalently,

$$2\xi_1^2 - 1 \leq \xi_2 \leq 1 \tag{8}$$

$$2(1 + \xi_2)\xi_3^2 - 4\xi_1\xi_3\xi_4 + \xi_4^2 \leq (\xi_2 - 2\xi_1^2 + 1)(1 - \xi_2) \tag{9}$$

Equation (7) shows the feasible region of Q(ξ_2,ξ_4) for the fixed values of P(ξ_1,ξ_3) within the region of Eq.(6). The feasible region is within a circle as shown in Fig.1. On the contrary, Equation (9) shows the feasible region of (ξ_3,ξ_4) for the fixed values of (ξ_1,ξ_2) within the region of Eq.(8). The feasible region of (ξ_3,ξ_4) is represented as the region within an ellipse. Figure 2 shows the feasible regions of (ξ_3,ξ_4) for P(ξ_1,ξ_2)= P$_1$(0,0), P$_2$(0.2,0.5) and P$_3$(-0.2,-0.5).   When the lamination parameters (ξ_1,ξ_2) are specified, the in-plane stiffness components, A$_{11}$, A$_{12}$, A$_{22}$ and A$_{66}$, are determined uniquely.   On the other hand, the extension-shear coupling terms, A$_{16}$ and A$_{26}$, are determined by specifying the coupling lamination parameters (ξ_3,ξ_4). Those in-plane stiffness components are the linear function of the in-plane lamination parameters as shown in Eq.(2).

The relation between the out-of-plane lamination parameters is obtained in the same manner when replacing (ξ_1,ξ_2,ξ_3,ξ_4) with (ξ_9,ξ_{10},ξ_{11},ξ_{12}) in Eqs.(6)-(9).

Feasible Region of Lamination Parameters in Conventional Laminates

We will examine the feasible region of lamination parameters when the layer angles are preassigned. For [0/±45/90]$_s$ laminates, the relation between the lamination parameters (ξ_1,ξ_2,ξ_3,ξ_4) and the layer thickness components is expressed as follows.
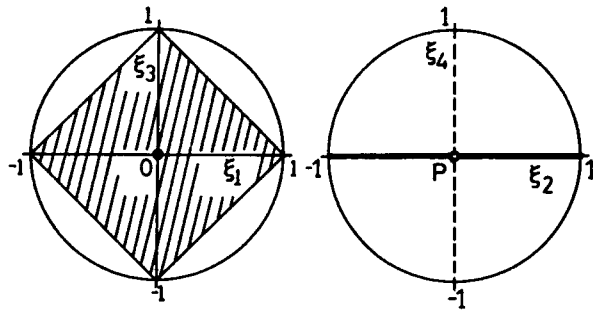
(a) (ξ_1,ξ_3) (b) (ξ_2,ξ_4)
Fig.3 Feasible region of lamination parameters for $[0/\pm45/90]_s$ laminates.
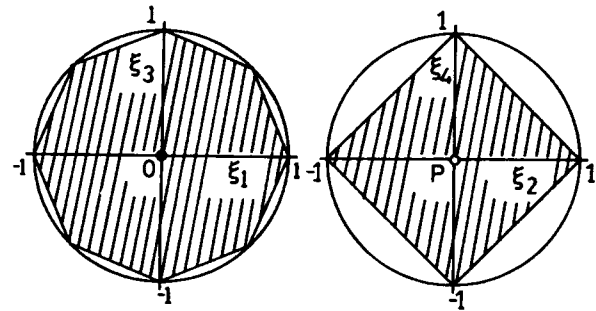
(a) (ξ_1,ξ_3) (b) (ξ_2,ξ_4)
Fig.4 Feasible region of lamination parameters for $[0/\pm22.5/\pm45/\pm67.5/90]_s$ laminates.
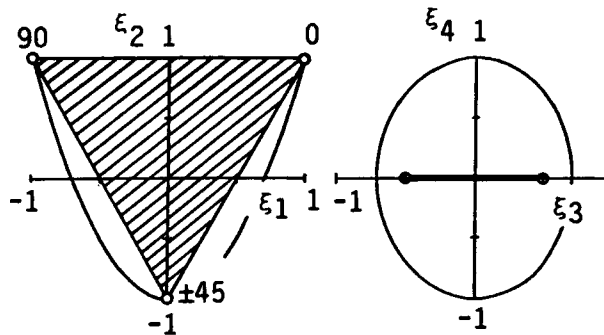
(a) (ξ_1,ξ_2) (b) (ξ_3,ξ_4)
Fig.5 Feasible region of lamination parameters for $[0/\pm45/90]_s$ laminates.
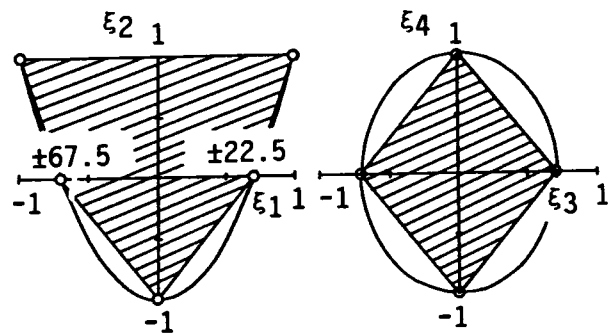
(a) (ξ_1,ξ_2) (b) (ξ_3,ξ_4)
Fig.6 Feasible region of lamination parameters for $[0/\pm22.5/\pm45/\pm67.5/90]_s$ laminates.

$$\xi_1 = h_0 - h_{90} \ , \quad \xi_2 = h_0 + h_{90} - h_{45} - h_{-45}$$
$$\xi_3 = h_{45} - h_{-45} \ , \quad \xi_4 = 0$$
$$h_0 + h_{90} + h_{45} + h_{-45} = 1 \ , \quad h_i \geq 0$$

(10)

where h_i denotes the layer thickness and h_i is taken as a continuous variable.

Figure 3(a) shows the feasible region of (ξ_1,ξ_3) for $0/\pm45/90$ laminates. The region is a little smaller than that represented in Eq.(6). Figure 3(b) shows the feasible region of (ξ_2,ξ_4) for $(\xi_1,\xi_3)=(0,0)$ in $0/\pm45/90$ laminates. Substituting $\xi_1=\xi_3=0$ into Eq.(7), the maximum feasible region is given by $\xi_2{}^2+\xi_4{}^2\leq1$. For $0/\pm45/90$ laminates, the region is only on the straight line $\xi_4=0$ ($-1\leq\xi_2\leq1$). When more kinds of layer angles are used, for example, $[0/\pm22.5/\pm45/\pm67.5/90]_s$ laminates, the feasible regions are greater than those for $0/\pm45/90$ laminates as shown in Fig.4.

We examined the feasible regions of (ξ_1,ξ_3) and (ξ_2,ξ_4). Now we consider the feasible regions of (ξ_1,ξ_2) and (ξ_3,ξ_4). Figure 5(a) shows the feasible region of (ξ_1,ξ_2) for $[0/\pm45/90]_s$ laminates while the maximum feasible region is given by Eq.(8). Figure 5(b) shows the feasible region

of (ξ_3,ξ_4) for the fixed values of $(\xi_1,\xi_2)=(0,0)$. From Eq.(9), the maximum feasible region is given by $2\xi_3^2+\xi_4^2 \leq 1$ when $(\xi_1,\xi_2)=(0,0)$. The feasible region for 0/±45/90 laminates is on the straight line of $\xi_4=0(-1/2\leq\xi_3\leq1/2)$. Figure 6 shows the corresponding feasible regions for the case of $[0/\pm22.5/\pm45/\pm67.5/90]_s$ laminates. The feasible regions for 0/±22.5/±45/±67.5/90 laminates are greater than those for 0/±45/90 laminates, but they are still restricted to smaller regions as compared with the maximum feasible regions.

Method for Determining Laminate Configurations

We consider a method for determining laminate configurations corresponding to the in-plane lamination parameters within the feasible region. One of the laminate configurations consisting of four fiber angles is given as follows [10]:

$$[(\theta_1)_{h_1}/(\theta_2)_{h_2}/(\theta_3)_{h_3}/(\theta_4)_{h_4}]_S \quad laminate$$

(11)

$$\theta_{1,2} = (\pi + \beta_R \mp 2\gamma_R)/4 \quad , \quad \theta_{3,4} = (\pi + \beta_S \mp 2\gamma_S)/4$$

where

$$\cos\beta_R = \frac{x_R - r^2\cos 2\alpha}{1 - r^2} \quad , \quad \sin\beta_R = \frac{y_R - r^2\sin 2\alpha}{1 - r^2} \quad , \quad \cos\gamma_R = -r\sin\frac{\beta_R - 2\alpha}{2} \quad ,$$

$$\cos\beta_S = \frac{x_S - r^2\cos 2\alpha}{1 - r^2} \quad , \quad \sin\beta_S = \frac{y_S - r^2\sin 2\alpha}{1 - r^2} \quad , \quad \cos\gamma_S = -r\sin\frac{\beta_S - 2\alpha}{2} \quad (12)$$

$$r\cos\alpha = \xi_1 \quad , \quad r\sin\alpha = \xi_3$$

and

$$h_1 = \frac{PA_2}{A_1A_2}\frac{QS}{RS} \quad , \quad h_2 = \frac{PA_1}{A_1A_2}\frac{QS}{RS} \quad , \quad h_3 = \frac{PA_4}{A_3A_4}\frac{RQ}{RS} \quad , \quad h_4 = \frac{PA_3}{A_3A_4}\frac{RQ}{RS} \quad (13)$$

where R and S denote two points shown in Fig.1 where the points are the intersection of the straight line PQ and the small circle representing the equality relation of Eq.(7). In Eq.(13), $A_i=(\cos 2\theta_i, \sin 2\theta_i)$ (i=1,2,3,4). Table I shows examples of laminate configurations corresponding to some sets of in-plane lamination parameters $(\xi_1,\xi_2,\xi_3,\xi_4)$.

The method of determining the laminate configurations corresponding to the out-of-plane lamination parameters $(\xi_9,\xi_{10},\xi_{11},\xi_{12})$ is similar. The layer angles are obtained using Eq.(12). The layer thicknesses of the $[(\theta_1)_{\bar{h}_1}/(\theta_2)_{\bar{h}_2}/(\theta_3)_{\bar{h}_3}/(\theta_4)_{\bar{h}_4}]_S$ laminate are determined from the following relations:

$$\bar{h}_j = \sqrt[3]{h_j + h_{j+1} + \cdots + h_4} - \sqrt[3]{h_{j+1} + \cdots + h_4} \quad (j = 1,2,3,4)$$

(14)

where h_j is the thickness component shown in Eq.(13). Table II shows the laminate configurations for some sets of $(\xi_9,\xi_{10},\xi_{11},\xi_{12})$.

TABLE I Laminate configurations of $[(\theta_1)_{h_1}/(\theta_2)_{h_2}/(\theta_3)_{h_3}/(\theta_4)_{h_4}]_s$ corresponding to in-plane lamination parameters.

$(\xi_1,\xi_2,\xi_3,\xi_4)$	θ_1	θ_2	θ_3	θ_4	h_1	h_2	h_3	h_4
(0.1,-0.2,0.4,0.6)	32.8	-64.3	10.8	77.0	0.51	0.22	0.15	0.12
(0.5,0.5,0,-0.2)	-9.2	64.0	9.2	-64.0	0.46	0.18	0.26	0.10
(0.3,0.4,0.4,0)	22.2	-76.2	3.5	64.6	0.17	0.06	0.44	0.33

TABLE II Laminate configurations of $[(\theta_1)_{\bar{h}_1}/(\theta_2)_{\bar{h}_2}/(\theta_3)_{\bar{h}_3}/(\theta_4)_{\bar{h}_4}]_s$ corresponding to out-of-plane lamination parameters.

$(\xi_9,\xi_{10},\xi_{11},\xi_{12})$	θ_1	θ_2	θ_3	θ_4	$\bar{h}_1$	$\bar{h}_2$	$\bar{h}_3$	$\bar{h}_4$
(0.1,-0.2,0.4,0.6)	32.8	-64.3	10.8	77.0	0.21	0.14	0.15	0.50
(0.5,0.5,0,-0.2)	-9.2	64.0	9.2	-64.0	0.18	0.11	0.24	0.47
(0.3,0.4,0.4,0)	22.2	-76.2	3.5	64.6	0.06	0.02	0.23	0.69

TABLE III Material properties of carbon/epoxy unidirectional composites.

$$E_L = 142 \text{ GPa}, \quad E_T = 10.8 \text{ GPa}, \quad G_{LT} = 5.49 \text{ GPa}, \quad \nu_L = 0.3$$

STIFFNESS DESIGN OF SYMMETRIC LAMINATES

We consider a stiffness design of symmetric laminates using lamination parameters. First, in-plane elastic properties are represented on the lamination parameter plane. Next the buckling characteristics of symmetric laminated plates are discussed. The effect of bending-twisting coupling on the buckling is clarified. As numerical examples, carbon/epoxy composites are adopted where the elastic properties are shown in Table III.

In-Plane Elastic Properties of Symmetric Laminates
From Eq.(2), the in-plane elastic properties are expressed as follows:

$$\begin{bmatrix} 1/E_x & -\nu_x/E_x & \nu_{xs}/E_x \\ -\nu_x/E_x & 1/E_y & \nu_{ys}/E_y \\ \nu_{xs}/E_x & \nu_{ys}/E_y & 1/G_{xy} \end{bmatrix} = h \begin{bmatrix} A_{11} & A_{12} & A_{16} \\ A_{12} & A_{22} & A_{26} \\ A_{16} & A_{26} & A_{66} \end{bmatrix}^{-1} \tag{15}$$

where E_x, E_y, G_{xy} and ν_x denote Young's moduli in the x and y directions, the shear modulus and Poisson's ratio in the x-direction; ν_{xs} and ν_{ys} represent the extension-shear coupling in the x and y directions, respectively. The out-of-plane elastic properties are given when replacing A and h with D and $h^3/12$ in Eq.(15), respectively.

When the coupling lamination parameters, ξ_3 and ξ_4, vanish, the elastic properties of symmetric laminates are governed by two lamination parameters (ξ_1,ξ_2). Figure 7 shows the contours of elastic properties on the lamination parameter plane ξ_1-ξ_2. Figure 8 shows the contours of elastic properties on the lamination parameter plane ξ_3-ξ_4 for $(\xi_1,\xi_2)=(0,0)$ where Young's modulus E_y is symmetrical with E_x with respect to the ξ_4 axis. As

(a) E_x, E_y (b) G_{xy}, ν_x
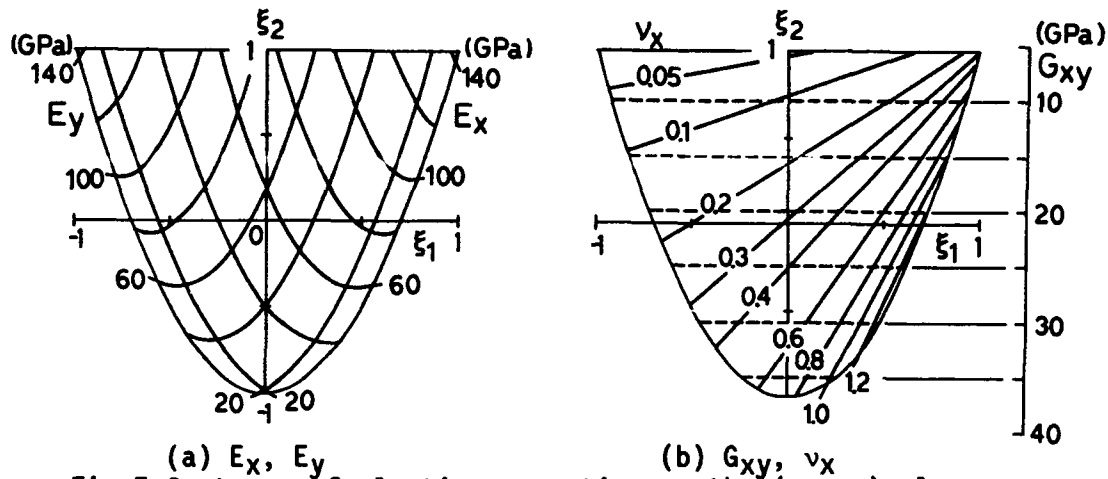
Fig.7 Contours of elastic properties on the (ξ_1,ξ_2) plane.

(a) E_x (GPa)   (b) G_{xy} (GPa)   (c) ν_x
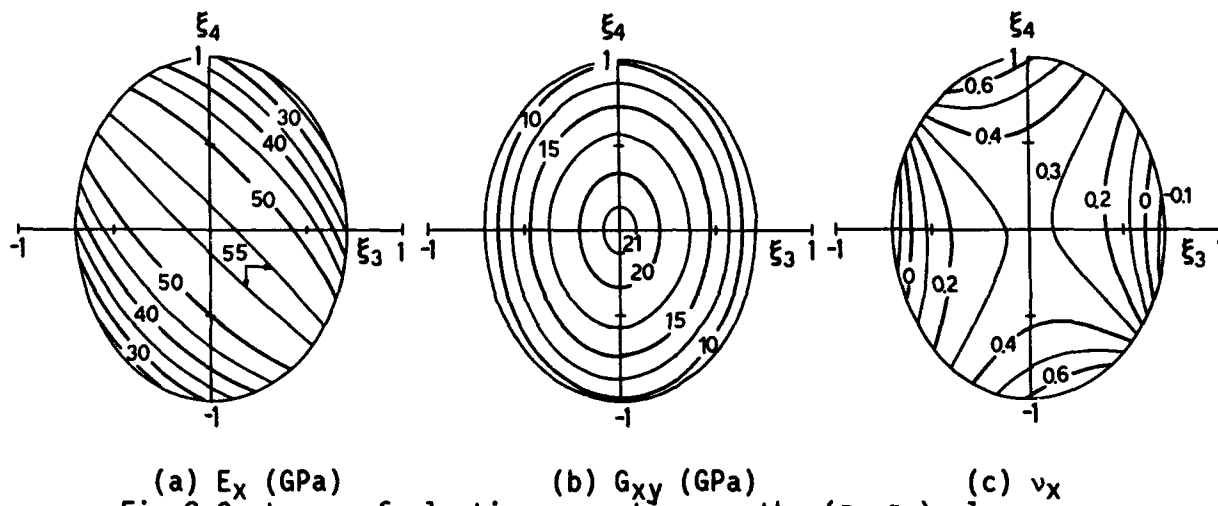
Fig.8 Contours of elastic properties on the (ξ_3,ξ_4) plane.

shown in Fig.8, Young's moduli and the shear modulus have the maximum values at $(\xi_3,\xi_4)=(0,0)$. On the other hand, Poisson's ratio seems to have a saddle point at $(\xi_3,\xi_4)=(0,0)$.

When the required elastic properties involving the coupling properties are specified, we can obtain the corresponding lamination parameters easily. Then the laminate configurations can be determined from the lamination parameters.

Buckling Characteristics

We consider the buckling characteristics of symmetric laminated plates with the simply-supported boundary conditions. The governing equation is given as follows:

$$D_{11}w_{,xxxx} + 4D_{16}w_{,xxxy} + 2(D_{12} + 2D_{66})w_{,xxyy} + 4D_{26}w_{,xyyy} + D_{22}w_{,yyyy}$$
$$= -N_x w_{,xx} + 2N_{xy}w_{,xy}$$

(16)

$$x = 0, a \quad ; \quad w = D_{11}w_{,xx} + D_{12}w_{,yy} + 2D_{16}w_{,xy} = 0$$
$$y = 0, b \quad ; \quad w = D_{12}w_{,xx} + D_{22}w_{,yy} + 2D_{26}w_{,xy} = 0$$

(17)

where N_x and N_{xy}, respectively, denote the axial compressive load and the shear load; h is the thickness of the plate. In Eq.(16), D_{16} and D_{26} represent the bending-twisting coupling.

We assume the following deflection function.

$$w(x,y) = \sum_{m=1}^{M} \sum_{n=1}^{N} A_{mn} \sin \frac{m\pi x}{a} \sin \frac{n\pi y}{b}$$

(18)

In the simply-supported case, the assumed deflection function does not satisfy the mechanical boundary condition, and Rayleigh-Ritz method is adopted. Then we can get an eigenvalue equation. The buckling load is normalized as follows.

$$N^* = \frac{12b^2}{\pi^2 Q_{22} h^3} N$$

(19)

where Q_{22} is the reduced stiffness transverse to the fiber.

The effect of bending-twisting coupling on the buckling characteristics of symmetric laminated plates has been examined using the nondimensional anisotropic parameter in Ref.[6]. When we examine the buckling characteristics using the lamination parameters, more general examination is possible than that in Ref.[6] since the four out-of-plane lamination parameters can express the laminate configurations of all kinds of symmetric laminates.

Figure 9(a) shows the contours of the normalized compressive buckling load on the ξ_9-ξ_{10} plane when the coupling lamination parameters (ξ_{11}, ξ_{12}) vanish. The aspect ratio of the plate used is a/b=1. Figure 9(b) shows the contours of the buckling load on the ξ_{11}-ξ_{12} plane for (ξ_9, ξ_{10})=(0,0). It can be seen that the bending-twisting coupling reduces the buckling load as compared with that of the laminate without the coupling.

Figure 10(a) shows the contours of the normalized shear buckling load on the ξ_9-ξ_{10} plane for (ξ_{11}, ξ_{12})=(0,0) while Fig.10(b) shows those on the ξ_{11}-ξ_{12} plane for (ξ_9, ξ_{10})=(0,0). It is seen from Fig.10(b) that the lamination parameters to maximize the shear buckling load are given by a point on the boundary of the coupling lamination parameter plane.
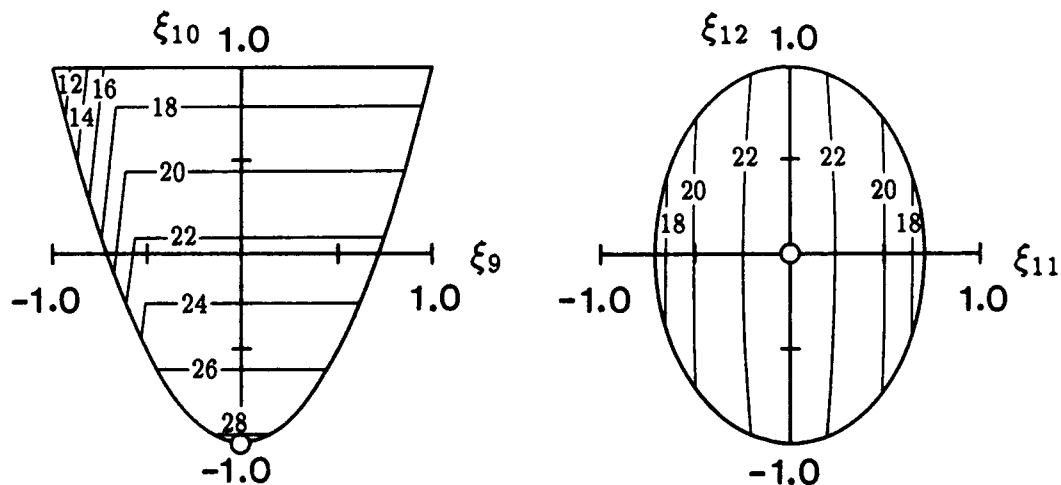
(a) ξ_9-ξ_{10} plane (ξ_{11}=ξ_{12}=0)   (b) ξ_{11}-ξ_{12} plane (ξ_9=ξ_{10}=0)
Fig.9 Contours of the normalized compressive buckling load (a/b=1).
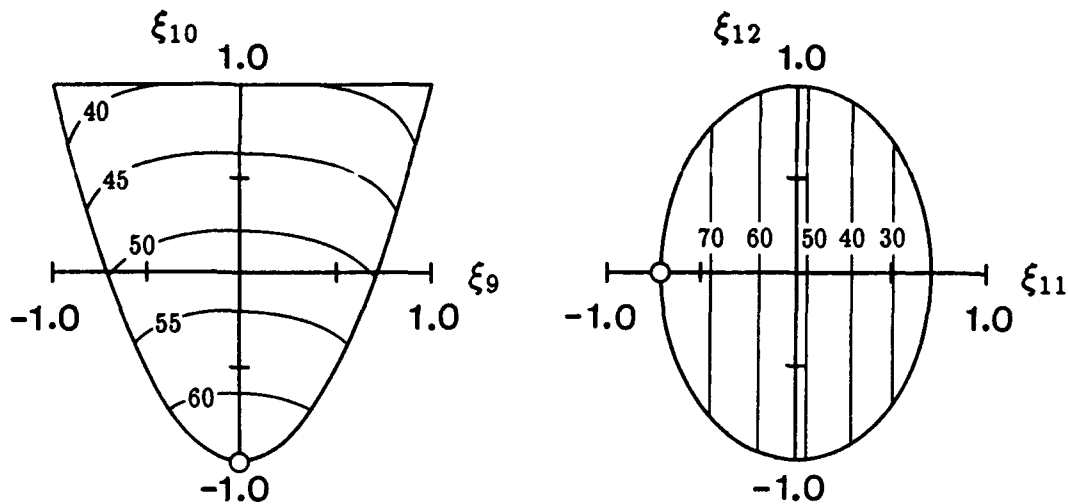
(a) ξ_9-ξ_{10} plane (ξ_{11}=ξ_{12}=0) (b) ξ_{11}-ξ_{12} plane (ξ_9=ξ_{10}=0)
Fig.10 Contours of the normalized shear buckling load (a/b=1).

CONCLUSIONS

The present paper has shown the stiffness design method of symmetric laminates using lamination parameters. The effect of extension-shear or bending-twisting coupling on the stiffness characteristics was clarified. The limitation of conventional laminates such as 0/±45/90 laminates has also been discussed from the design viewpoint. When the lamination parameters have been obtained in a laminate design, the corresponding laminate configurations can be determined easily.

REFERENCES

1 Tsai, S. W. and H. T. Hahn, 1980. <u>Introduction to Composite Materials</u>, Lancaster, PA: Technomic Publishing Company, Inc..

2 Fukunaga, H. and Y. Hirano, 1982. "Stability Optimization of Laminated Composite Plates under In-Plane Loading." <u>Proc. 4th ICCM</u>, pp.565-572.

3 Miki, M. 1982. "Material Design of Composite Laminates with required In-Plane Elastic Properties." <u>Proc. 4th ICCM</u>, pp.1725-1731.

4 Fukunaga, H. 1990. "On Isotropic Laminate Configurations." <u>J. Composite Materials</u>, 24:519-535.

5 Shirk, M. H., T. J. Hertz and T. A. Weisshaar, 1986. "Aeroelastic Tailoring Theory, Practice, and Promise." <u>J. Aircraft</u>, 23:6-18.

6 Nemeth, M. P., 1986."Importance of Anisotropy on Buckling of Compression-Loaded Symmetric Composite Plates." <u>AIAA J.</u>, 24:1831-1835.

7 Crawley, E. F. and K. B. Lazarus, 1991. "Induced Strain Actuation of Isotropic and Anisotropic Plates." <u>AIAA J.</u>, 29:944-951.

8 Miki, M. and T. Fujii, 1985. "Material Design of Laminated Fibrous Composites with Required Bending-Twisting Coupling." <u>Materials System</u>, 4: 61-65 (in Japanese).

9 Grenestedt, J. L. 1991. "Layup Optimization Against Buckling of Shear Panels." <u>Structural Optimization</u>, 3:115-120.

10 Fukunaga, H. and H. Sekine, 1992. "Stiffness Design Method of Symmetric Laminates Using Lamination Parameters." <u>AIAA J.</u>, to appear.

Minimum Weight Foam Core Composite Sandwich Shells under Axial Compression

JACK R. VINSON AND ANDREW J. LOVEJOY

ABSTRACT

Foam core sandwich cylindrical shells with specially orthotropic composite face materials are treated herein. Methods by which to analyze and design these shells are presented to prevent overstressing, overall buckling, core shear instability and face wrinkling. In addition, analytic methods to determine the configuration and materials to achieve absolute minimum weight are developed and presented herein. These procedures provide the means to select the face thickness (t_f), the core depth (h_c) and the optimum foam core shear modulus (G_c) to attain minimum weight for a given face material. Moreover, a factor of merit is developed for selecting the composite face material to attain a minimum weight sandwich. In addition, the methods clearly define the maximum loads the sandwich shell can withstand without buckling or the faces becoming overstressed.

INTRODUCTION

Sandwich construction plays an increasingly important role in various structures because of its exceptionally high flexural stiffness compared to monocoque and various reinforced thin wall architectures. Because of this favorable flexural stiffness, the use of sandwich construction results in lower lateral deformations, higher buckling loads, and higher natural frequencies than do other types of structures.

For instance, it was once again shown recently (Reference 1) that in comparing a foam core or honeycomb core sandwich construction in which each of the two faces is of thickness t_f, to an analogous monocoque structure of thickness $2t_f$, see Figure 1, the ratio of the flexural stiffnesses D is

$$\frac{D_{sand.}}{D_{mon.}} = \frac{3}{4}\left(\frac{h_c}{t_f}\right)^2 \tag{1}$$

where h_c is the core depth of the sandwich construction, and $t_f \ll h_c$. For example if $t_f/h_c = 1/20$, the flexural stiffness of the sandwich construction is 300 times greater than the flexural stiffness of the monocoque construction. Similarly the ratio of the face stress in a sandwich

Jack R. Vinson, H. Fletcher Brown Professor of Mechanical and Aerospace Engineering and the Center for Composite Materials
Andrew J. Lovejoy, Currently, Graduate Student, Virginia Polytechnic Institute and State University

(a) Sandwich Construction

(b) Monocoque
Construction
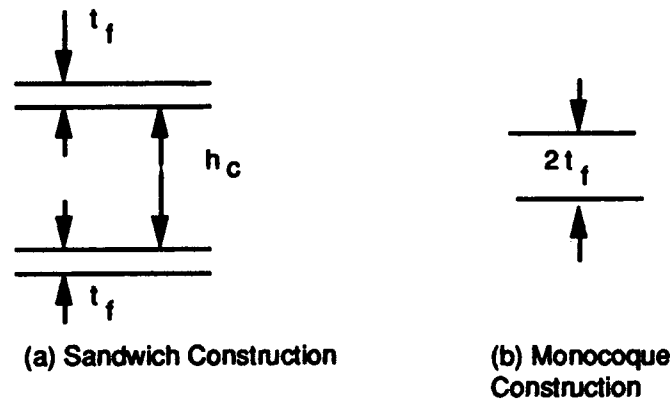
Figure 1. Cross-section of Sandwich and Monocoque Construction

construction compared to that in a monocoque structure when both an subjected to the same bending moment M is

$$\frac{\sigma_{sand.}}{\sigma_{mon.}} = \frac{2}{3}\left(\frac{t_f}{h_c}\right)$$

(2)

Once more if $t_f/h_c = 1/20$, the maximum bending stress in the face of the sandwich is 1/30 that of the maximum bending stress in a monocoque construction, thus the sandwich may be able to withstand higher applied loads.

Even with these advantages, it is very important and desirable to develop methods by which to structurally optimize sandwich constructions to:

1. determine the absolute minimum weight for a given type of sandwich, loading and material system,
2. rationally select the best face and core material to minimize structural weight,
3. rationally compare the use of one type of sandwich construction with other types of sandwich constructions,
4. rationally compare the best of sandwich construction with alternative configurations (monocoque, rib-reinforced, etc.),
5. select the best stacking sequences for faces composed of laminated composite materials,
6. suggest to materials scientists and suppliers how to develop improved materials for use in sandwich construction,
7. to rationally compare the optimum weight to weights of non-optimum construction where restruction such as cost suggest other solutions, hence a dollars per pound penalty function can be easily found and used.

METHODS OF ANALYSIS FOR THIS SANDWICH SHELLS SUBJECTED TO AXIAL COMPRESSIVE LOADS

For a foam core sandwich shell subjected to an axially symmetric compressive load (Figure 2) it is generally assumed that all of the in-plane and bending loads are resisted by the faces only, and that these loads are not introduced appreciably into the foam core material. Therefore for an in-plane axial load per unit of circumference, N_x, the face stress in the axial direction σ_{fx} is given as follows:

$$\sigma_{xf} = N_x/2t_f \tag{3}$$

In the above it is assumed that the sandwich faces are of the same thickness and material; otherwise Equation (3) would be modified. Thus, the face stresses are calculated
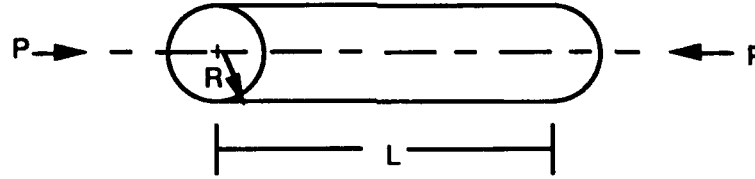
Figure 2. Circular Cylindrical Shell

straightforwardly for an applied axially symmetric compressive load P, which in turn is related to N_x by

$$N_x = P/2\pi R, \tag{4}$$

where R is the radius of the shell to the midsurface of the sandwich construction.

Along with the face stress in the axial direction σ_{fx}, due to an applied axial loading P, there is also a circumferential face stress $\sigma_{f\theta}$ in the shell, which is a Poisson ratio effect, given by Reference 2:

$$\sigma_{f\theta} = -v_{\theta x}\, \sigma_{fx} \tag{5}$$

where $v_{\theta x}$ is a Poisson ratio of the specially orthotropic face material, defined in Reference 2, and which follows the orthotropic relationship

$$\frac{v_{x\theta}}{E_x} \approx \frac{v_{\theta x}}{E_\theta} \tag{6}$$

where x and θ are the axial and circumferential directions respectively.

The reason that Equation (5) is introduced here is because in some unidirectional composites, although the material can withstand a very high axial loading P, because the compressive failure stress in the axial direction is so large, the load carrying capability of the shell is limited by the low circumferential tensile strength of the material, since circumferential tensile stresses depicted by (5) cannot be avoided.

Equations for the overall buckling of a specially orthotropic shell subjected to axial compression are given in References 4 and 5. These equations are complicated, and extensive computation is needed to determine the axial and circumferential wave numbers m and n that result in a minimum critical load. However Bert [Reference 6] provided a simple but accurate equation for overall buckling that is straightforward and amenable to easy computation while retaining accuracy.

$$\left(\sigma_{fx}\right)_{cr} = \frac{\phi h_c}{R}\left(\frac{E_x E_\theta}{1-v_{x\theta}v_{\theta x}}\right)^{1/2}\left\{1-1/2\left[\phi\left(\frac{E_x E_\theta}{1-v_{x\theta}v_{\theta x}}\right)^{1/2}\frac{t_f}{RG_{xzc}}\right]\right\} \tag{7}$$

$$\text{where } \phi = \quad 1 \text{ or} \left[\frac{2G_{x\theta}\left[1 + (v_{x\theta}v_{\theta x})^{1/2}\right]}{(E_x E_\theta)^{1/2}}\right]^{1/2} \quad (8)$$

whichever is less.

In (7), G_{xzc} is the core material shear modulus in the xz plane, where z is the radial coordinate. Equation (7) differs from the expression in Reference 6 only in that for this study $t_f \ll h_c$, which is the usual case in sandwich structures.

A second mode of failure that can occur is core shear instability, given by:

$$(\sigma_{fx})_{cr} = \frac{G_{xzc} h_c}{2t_f} \quad (9)$$

This is the same equation used by Bert [6] (for a cylindrical shell), and used in numerous papers by Vinson [2, 3] for sandwich plates. Since it is a local instability, Equation (9) applies for beams, plates and shells.

Likewise, another local buckling can occur - face wrinkling. The most accurate equation for this is developed by Heath [7]

$$(\sigma_{fx})_{cr} = \left[\frac{2}{3} \frac{t_f}{h_c} \frac{E_c(E_x E_\theta)^{1/2}}{1 - v_{x\theta}v_{\theta x}}\right]^{1/2} \quad (10)$$

where E_c is the modulus of elasticity of the foam core in the radial or thickness direction.

From the above it is seen that for design and analysis, one can proceed to determine the applied face stresses in the axial direction, and the critical face stresses for overall buckling, core shear instability and face wrinkling. In a shell of given radius R, length L, core depth h_c, face thickness t_f, and specified core and face materials, one can calculate to determine if the faces are overstressed and if any of the three buckling modes occurs. For the design of a shell of given radius R, length L, and face and core materials, the designer can select h_c and t_f to insure no failure occurs for a given compressive load P.

However, it would be beneficial to have an analytical procedure which would select h_c and t_f to insure minimum weight for the shell to aid in shell design.

To optimize the shell it is seen that there are three failure modes of buckling, i.e. overall buckling, core shear instability and face wrinkling, each of which is synonymous with structural failure. Also there are two geometric variables: the core depth (h_c) and the face thickness (t_f). However it can be seen that the foam core shear modulus may also be used as a third continuous dependent variable, as discussed below.

CORE MATERIAL PROPERTIES

In looking at various foam core materials used in sandwich construction it is noticed that the core shear modulus (G_c) varies almost linearly with the foam density (ρ_c). Not only does it vary but within a sizeable range of densities there is a continuous spectrum of shear moduli commercially available. Thus for foam core sandwich construction G_c can be a continuous variable, not limited to discrete values for a given material. For example consider closed cell PVC foams (References 8 and 9). One can plot the properties as in Figure 3. For these materials the relationship between G_c and ρ_c is almost linear, but whatever the
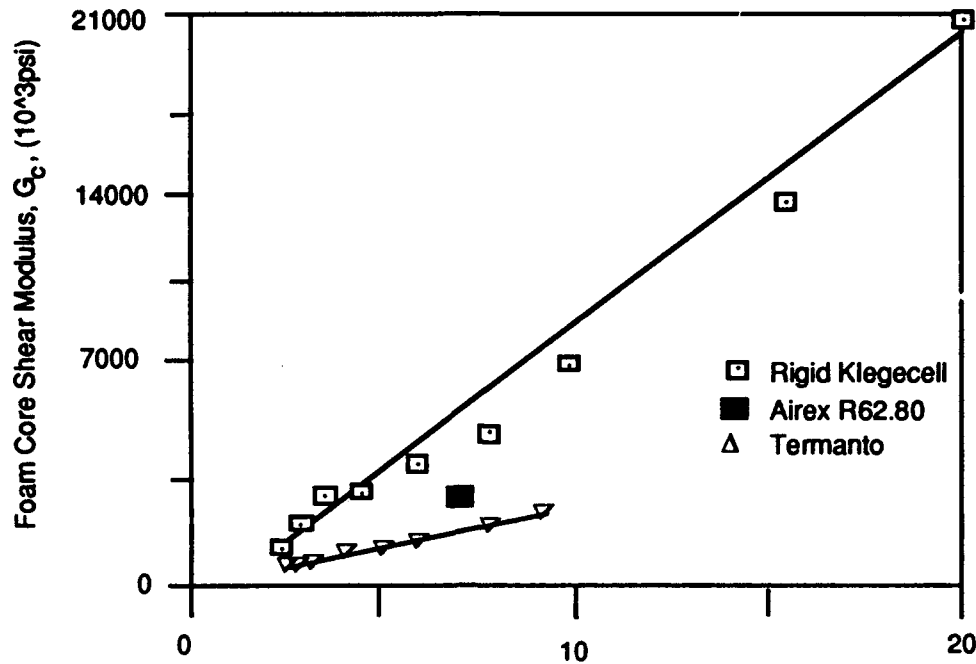
Figure 3. Foam Core Density, ρ_c, (lbs./ft^3)

relationship the important thing is that one can select any value of G_c, just as t_f and h_c, as a variable in a foam core sandwich construction. This has been utilized by Vinson (Reference 10 though 13) previously in the optimization of foam core sandwich panels subjected to in-plane loads.

For the calculations performed subsequently herein, from the Figure the following linear equation is used:

$$G_c = A\rho_c \qquad (11)$$

where G_c is in lbs/in.^{2}, ρ_c is in lb/in^3 and $A = 1.728 \times 10^6$.

WEIGHT EQUATION

The equation to determine the sandwich shell weight per unit midsurface area, W, is straightforwardly given by

$$W = 2\rho_f t_f + \rho_c h_c + W_{ad}$$

where ρ_f and ρ_c are the weight densities of the face material and the foam or solid core respectively, and W_{ad} is the weight per unit area of the bonding or adhesive material to connect core and face materials. It is non-analytic, and is a function of the material used, the core and experience of the worker and various other factors. Therefore in what follows, the equation above shall be written as

$$(W - W_{ad}) = 2t_f\rho_f + \rho_c h_c \qquad (12)$$

OPTIMIZATION TO ATTAIN MINIMUM WEIGHT

In the previous Section, three critical stresses are given pertaining to overall instability, face wrinkling and core shear instability, each of which would cause structural demise. For a given set of materials, there are three variables, namely face thickness t_f, core depth h_c and core shear modulus G_c. Thus, there are three equations and three unknowns. This suggests a unique solution may be available for these dependent variables.

Since any one of the instabilities causes structural failure, it follows that the most efficient structure occurs when all three buckling stresses are equal. This follows the philosophy of the weak link in the chain. Otherwise material is being inefficiently used and can be shifted or eliminated to reduce weight and/or increase load carrying ability. Vinson (and others) have used this technique, and have optimized honeycomb core, foam core, truss core and web core sandwich panels subjected to in-plane compressive and shear loads.

In carrying out the optimization one can employ the following elasticity relationship for the isotropic foam core:

$$G_c = E_c/2(1 + \upsilon_c) \tag{13}$$

Also because all three buckling stresses are equated in the optimized construction, these critical face stresses shall simply be labeled σ_o, and it must be remembered that the optimized face stress σ_o must not exceed some allowable stress based upon static strength, factors of safety, fatigue limits, etc.

Therefore in this process of optimization wherein all three buckling face stresses are equated, the optimum face stress σ_{fx} is denoted σ_o. Of course the upper bound on this face stress is an allowable material strength, either in the axial or the circumferential direction.

From equating (9) and (10)

$$G_c = \frac{6^{1/2}}{2} \frac{(1-\nu_{x\theta}\nu_{\theta x})^{1/2} \sigma_o^{3/2}}{(1+\nu_c)^{1/2} (E_x E_\theta)^{1/4}} \tag{14}$$

Utilizing (9), (10) and (14), (7) can be written in the form of a perfect square in (h_c/R), with the result that for the optimum construction,

$$\left(\frac{h_c}{R}\right) = \frac{2(1-\nu_{x\theta}\nu_{\theta x})^{1/2} \sigma_o}{\phi (E_x E_\theta)^{1/2}} \tag{15}$$

Proper substitution into one of several equations, results in

$$\frac{t_f}{R} = \frac{3^{1/2}}{2^{1/2}} \frac{(1-\nu_{x\theta}\nu_{\theta x}) \sigma_o^{3/2}}{\phi (1 + \nu_c)^{1/2} (E_x E_y)^{3/4}} \tag{16}$$

Substitution of (16) into (3) provides the load index-optimum face stress relationship, referred to by previous authors as the "universal relationship":

$$\left(\frac{N_x}{R}\right) = \frac{6^{1/2}\,(1-v_{x\theta}v_{\theta x})\,\sigma_o^{5/2}}{\phi\,(1+v_c)^{1/2}\,(E_x E_\theta)^{3/4}} \tag{17}$$

This equation is very important because in (17) whenever σ_o is an allowable stress of the face material, then that is the upper limit of the applied load that the optimized structure can withstand. To attempt to apply a significantly larger load for this structure results in a prohibitive weight penalty.

Finally, the weight relationship (12) is written in terms of the applied load index for the optimized construction:

$$\left(\frac{W-W_{ad}}{R}\right) = \frac{6^{1/5}\,\rho_f\,(1-v_{x\theta}v_{\theta x})^{2/5}\,(N_x/R)^{3/5}}{\phi^{2/5}\,(1+v_c)^{1/5}\,(E_x E_\theta)^{3/10}}$$

$$+ \frac{2\,\rho_c\,(1-v_{x\theta}v_{\theta x})^{1/10}\,(1+v_c)^{1/5}\,(N_x/R)^{2/5}}{6^{1/5}\,\phi^{3/5}\,(E_x\,E_y)^{1/5}} \tag{18}$$

In this equation, the weight per unit area of the two faces is determined from the first term on the right hand side, and the core weight per unit area is determined by the second term. It is remembered that in the second term ρ_c, the core density is uniquely related linearly to the core shear modulus by some equation like (11), which is used herein, because the optimum shear modulus is given by (13) for the foam core material.

Looking at (18) it is obvious that as far as face material selection, the lowest weight foam core sandwich face material is indicated by a factor of merit (F.M.) defined by

$$F.M. = (E_x E_\theta)^{3/10}/\rho_f \tag{19}$$

where the moduli of elasticity are compressive moduli.

The structural optimization of the foam core composite faced circular cylindrical sandwich shell subjected to axially compressive loads is now completed.

COMPARISON OF VARIOUS FACE MATERIALS

Comparisons of forty-one various composite materials were made for which the density and the compressive moduli were available. In addition, to perform the structural optimization, both the compressive strength of the material in the 1-direction, and the tensile strength in the 2-direction must be known. In Table I, material for several materials studied herein are listed.

In Table I are representative examples of each of the major fiber and matrix systems of interest. All quantities have been defined previously except V_f, which is the fiber volume fraction. It is interesting to note how often it occurs that one or more properties of a material are lacking which prevents an optimization, design or analysis from being complete. The value of ϕ, see (8), and the factor of merit (F.M.), see (19), for these materials are given in Table II.

Table I - MATERIAL PROPERTIES FOR VARIOUS MATERIALS.

MATL	CONF	V_f (%)	E_1 (MSI)	E_2 (MSI)	G_{12} (MSI)	v_{12}	ρ (lb/in^3)	$\sigma_1{}^a$ (KSI)	$\sigma_2{}^b$ (KSI)
Boron/6061 Al	UNI	50	32	20	6	.3	.09145	250	20
T300 GR/934EP	UNI	60	23.69	1.7	0.94	.3	.0555	105	?
Boron/Epoxy	UNI	?	30	3	1	.3	.074	400	12
Hi St. Gr/Ep	UNI	60	21	1.5	0.7	.25	.057	180	6
Glass/Epoxy	UNI	?	7.8	2.6	1.3	.25	.0555	150	4
7075-T6Al	150	-	10.4	10.4	3.92	.3	.101	73.0^c	73.0

a. Compressive Strength, b. Tensile Strength, c. Compressive Yield Stress

TABLE II - FACTOR OF MERIT OF FACE MATERIALS OF TABLE I

MATERIAL	ϕ	F.M.
Boron/6061 Al	0.766	75.97
T300 Gr//934 Ep	0.5657	54.60
Boron/Epoxy	0.4806	52.12
Hi St. Gr./Ep	0.5159	49.39
Glass/Epoxy	0.8127	44.45
7075-T6Al	1.0	40.36

It is seen from Table II that the boron-aluminum metal matrix composite has the highest factor of merit of the representative face material systems. In fact, using this boron-aluminum metal matrix composite results in faces that are (52.12/75.92) 31.4% lighter then using faces of a boron-epoxy composite. In fact, fourteen metal matrix composites (including continuous fiber, short fiber and 3D braided) had factors of merit higher than the best polymer matrix composite (a T300-934 epoxy unidirectional composite). Of course, the factor of merit does not identify how much load the shell can withstand before failure.

The upper limit of load carrying capability is determined by the universal relationship (17). Here σ_o is the optimum load, where in this construction it is an allowable compressive stress in the axial direction, or an allowable tensile stress in the circumferential directions. In the former equations (3) and (4) determine the compressive axial stress, bounded by the allowable compressive stress in the material; in the latter (5), (3) and (4) determine the circumferential tensile stress, bounded by the allowable tensile stress. It is obvious that in using a specially orthotropic material like most composites, the 1 - direction should be the axial direction and the 2-direction is the circumferential direction, since in (5) it is seen the circumferential stress is a Poisson's ration effect - but is significant. In fact, looking at Table I it is seen that the circumferential tensile stress is the limit on both the unidirectional boron/aluminum MMC, and the unidirectional glass/epoxy composite. Therefore, it is seen that in unidirectional composites used in this application, in some cases the 90° properties limit

the usefulness.

In fact from (19) and the research of Vinson and Handel [12], for a given fiber-matrix composite lamina system, the best stacking sequence to attain minimum weight is a cross-ply laminate. However, it would probably be limited to lower maximum loads, because the cross-ply compressive strength would be less than that of the unidirectional composite of the same material.

EXAMPLE OPTIMIZATION STUDIES

Utilizing the materials of Table I, the optimized construction given by Equations (13) - (18), the values of ϕ in (8), and the foam core relationship given by (11), several optimizations are provided as examples. The results are presented in Table III.

Table III - OPTIMIZED CONSTRUCTIONS FOR TABLE I MATERIALS

FACE MATL	σ_0 $(10^3$ psi)	Nx/R (psi)	$\frac{W-Wad}{R}$ $(10^{-5}$ lb/in$^3)$	h_c/R (10^{-2})	(t_f/R) (10^{-4})	t_f/h_c	G_c (psi)	ρ_c $(10^{-3}$ psi)
B/6061 Al	50	11.21	2.695	.5015	1.121	.0224	2235	1.293
B/6061 Al	75	31.57	5.617	.7523	2.060	.0274	4106	2.376
B/6061 Al	100	63.4	9.468	1.003	3.171	.0316	6321	3.658
B/6061 Al	106.7	74.5	10.70	1.070	3.494	.0327	6964	4.030
Boron/Ep.	100	462	60.86	4.367	23.10	.0529	10580	6.123
Boron/Ep.	200	2614	248.0	8.734	65.35	.0748	29930	17.32
Boron/Ep.	300	7203	594.4	13.10	120.1	.0917	59980	31.81
Boron/Ep.	400	14790	1129.9	17.47	184.9	.1058	84660	49.0
Hi St. G/Ep	50	167.9	31.41	3.446	16.79	.0487	4873	2.820
Hi St. G/Ep	100	949.9	116.3	6.892	47.49	.0689	13780	7.976
Hi St. G/Ep	150	2617.7	264.1	10.34	87.25	.0844	25320	14.65
Hi St. G/Ep	180	4131	387.2	12.41	114.7	.0924	33290	19.27
Glass/Ep	20	14.76	4.948	1.082	3.691	.0341	1365	0.789
Glass/Ep	30	40.69	9.878	1.622	6.781	.0418	2508	1.451
Glass/Ep	40	83.52	16.43	2.163	10.44	.0483	3862	2.235
Glass/Ep	48	131.8	22.86	2.596	13.73	.0529	5078	2.939
7075-T6	25	5.551	2.542	.4585	1.110	.0242	1210	.7002
7075-T6	50	31.40	8.039	.9170	3.140	.0342	3422	1.980
7075-T6	73	80.88	15.55	1.339	5.539	.0414	6036	3.493

From the Tables above, for representative materials involving popular fibers and matrix materials, it is interesting to note that the weight parameter - load index relationships are such that the materials fall naturally into two load categories - small loads and large loads. Even though the Factor of Merit values clearly show the relative merits of the materials, three of these fall into a range of load index values below 135 psi, while the other two materials are capable of load indices nearly one hundred times greater than this. Thus to resist high load values for a given cylinder radius, of these materials one would select the unidirectional boron/epoxy or the unidirectional High Strength graphite/epoxy over the other materials. In fact for lowest weight one would always select the boron/epoxy over the high strength graphite/epoxy composite. This is shown graphically in Figures 4 and 5.
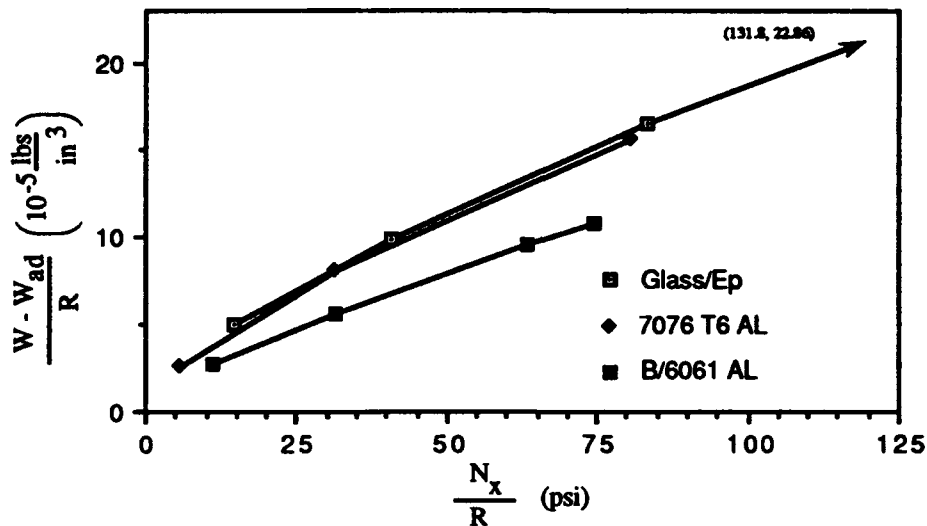
Figure 4. Weight Parameter for Various Materials for Optimized Construction as a Function of Load Index (Low Load Range)
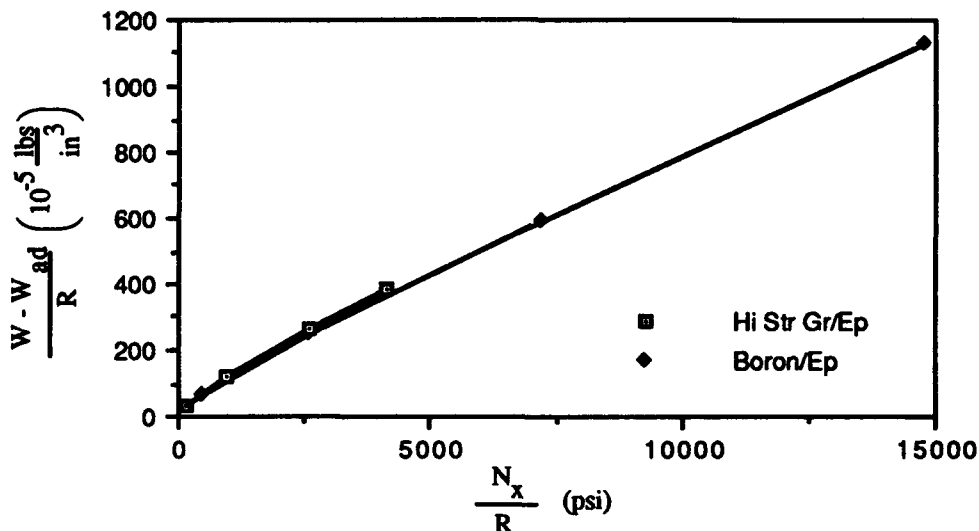
Figure 5 Weight Parameter for Various Materials for Optimized Construction as a Function of Load Index (High Load Range)

CONCLUSIONS

Analytical methods to use in analyzing designing and optimizing foam core (or solid core) sandwich circular cylindrical shells subjected to an axially-symmetric compressive load are presented and discussed.

When using a specially orthotropic composite material the 1-direction should always be in the axial direction.

To analyze or design the shell one straightforwardly uses equations (3) through (12). The face stress in the axial direction cannot exceed the value of any of Equations (7), (9), or (10), while not exceeding the allowable stress of the face material in the 1-direction as denoted

by Equation (3) and (4). Also, the circumferential tensile stress denoted through Equations (3) - (5), cannot exceed the allowable strength of the composite material in the 2-direction.

For the optimized (minimum weight) construction Equations (3) - (5), and (14) - (18) are used. It has been shown in great detail [1] that any deviation from the optimized construction results in significant weight penalties.

In selection of face materials to result in a minimum weight construction, Equation (19) is useful.

For core materials, the core with the highest ratio of G_c/ρ_c is the best.

ACKNOWLEDGMENTS

REFERENCES

1. Vinson, J. R., "Analysis and Optimization of Composite and Metallic Sandwich Cylindrical Shells", Transactions of the Second International Conference on Sandwich Constructions", Gainesville, March 9-12, 1992.
2. Vinson, J. R. and R. L. Sierakowski, "The Behavior of Structures Composed of Composite Materials", Martinus-Nijhoff Publishers (now Kluwer Academic Publishers), Dordrecht, The Netherlands, 1986.
3. Vinson, J. R., "On the Analysis and Optimization of Sandwich Structures", Proceedings of the Workshop on Advanced Materials Sandwich Structures (Professor Roberto Teti, Editor), Capri, October 20-23, 1991.
4. Anon., "Buckling of Thin Walled Circular Cylinders", NASA SP-8007, Revised, 1968 (N69-23320).
5. Bert, C. W., W. C. Crisman and G. M. Nordby, "Buckling of Cylindrical and Conical Sandwich Shells with Orthotropic Facings", AIAA Journal, Vol. 7, No. 2, February, 1969, pp. 250-257.
6. Reese, C. D. and C. W. Bert, "Simplified Design Equations for Buckling of Axially Compressed Sandwich Cylinders with Orthotropic Facings and Core", AIAA Journal of Aircraft, November - December 1969, pp. 515-519.
7. Heath, W. G., "Sandwich Construction, Pt. 1, The Strength of Flat Sandwich Panels", Aircraft Engineering, Vol. 32, July 1960, pp. 186-191.
8. Technical Data Sheet, "Klegecell in Buoyancy", Klegecell Division of Hutchinson Corporation, Grapevine, TX, USA.
9. "Termanto Rigid PVC Foam for Insulation, Buoyancy and Sandwich Core Construction," Torin, Inc., Ridgewood, NJ, USA.
10. Vinson, J. R., "Minimum Weight Solid Core Composite Sandwich Panels Subjected to In-Plane Compressive Loads", Transactions of the International Conference on Composite Materials and Structures, Madras, Jan. 6-9, 1988.
11. Vinson, J. R., "Minimum Weight Solid Core Composite Sandwich Panels Subjected to In-Plane Shear Loads", American Society for Composites/UD CCM Joint Symposium on Composite Materials Science and Engineering, September 23-25, 1987.
12. Vinson, J. R. and P. I. Handel, "Optimal Stacking Sequences of Composite Faces for Various Sandwich Panels and Loads to Attain Minimum Weight", Transactions of the 29th Annual AIAA/ASME/ASCE/AHS/ASC Structures, Structural Dynamics and Materials Conference, Williamsburg, April 18-20, 1988.
13. Vinson, J. R., "Comparison of Optimized Sandwich Panels of Various Constructions Subjected to In-Plane Loads", Sandwich Constructions I, Engineering Materials Advisory Services, Ltd., 1989, pp. 23-49.

Optimizing the Bi-Axial Buckling Load of a Laminated Plate by Restacking the Laminate or Adding Plies

MICHAEL C. SCIASCIA, CHARLENE R. PLUMB AND MICHAEL F. GASICK

ABSTRACT

A buckling optimization method is described for simply supported symmetric laminates. The method considers the effect of adding a ply to either side of an existing laminate in order to increase the critical buckling load. Simple constraints are applied to keep the optimum ply angle within predetermined values. The result is an equation based on plate aspect ratio and material properties that will help the designer maximize the buckling load. Design guidelines are proposed for simply supported symmetric laminated plates under bi-axial loading and includes consideration of the mode shape.

INTRODUCTION

Much of the work investigating the optimum laminate configuration for the highest buckling load has been limited to angle-ply laminates. For this reason these investigations have had little utility to common industrial laminates.

Muc [1] investigated simply supported angle-ply laminates and showed that the maximum buckling load occurs when the ply orientation of each layer is the same. Hirano [2] used a numerical method to determine the optimum ply angles and reported that a uniform ply angle is best. Hirano's results are essentially the same as Muc's, although it is not clear from Hirano's examples if his algorithm permits an angle-ply laminate to be the optimum solution. Both studies allow complete freedom in optimizing the ply angles of the laminate. It is this lack of constraint that permits the angle-ply laminate to be the optimum for buckling. Unfortunately, most designers are not able to construct their laminates with the same freedom.

Typically, laminate designers must consider factors other than buckling when designing a laminate. Some of these factors are inplane and bending stiffnesses, producibility, manufacturing expense, availability of test data and service experience. Any of these factors or constraints can preclude the use of angle-ply laminates.

This paper adds some simple constraints to the optimization problem by limiting the choice of ply angle to $0°$, $±45°$, and $90°$. This set of ply angles represents a significant portion of the laminates in service. The approach taken is to consider the effect of adding a ply to the top and bottom of a laminate. The buckling optimization is performed within the constraint on the allowed ply angles. The basic assumption is that the percentage of ($0°$, $±45°$, $90°$) plies has been pre-determined by requirements other than buckling. The goal is to determine the optimum angle for the added plies only. No attempt is made to optimize any other plies in the laminate. However, these results are extended to the entire laminate in the form of laminate
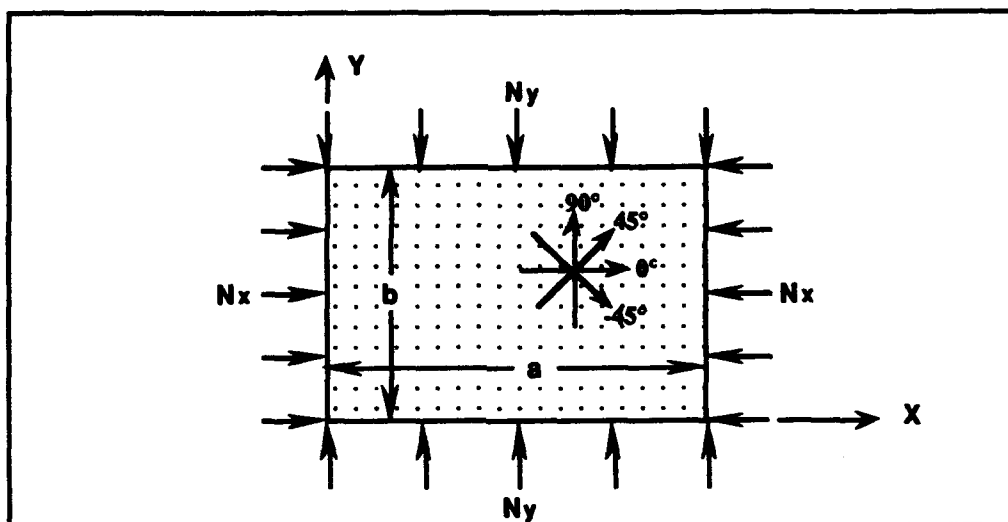
Figure 1 - The Laminate Coordinates, Loading and Sign Convention.

stacking sequence design guidelines.

The method will also be useful to the designer or analyst when it becomes necessary to increase the buckling load of an existing laminate. This can be a common occurrence in the early design phases of an aircraft. If the required increase in buckling load is small, a typical approach is to add a ply to each side of the laminate and recalculate the buckling load to see if it is sufficient. This is a satisfactory approach if the number of additional plies is small.

NOTATION AND SIGN CONVENTION

The notation used is given here and the sign conventions are shown in Figure 1.

a, b	The panel lengths in the x and y coordinates respectively.
m, n	The number of half waves in the x and y coordinates respectively.
N	The total number of plies in the laminate.
N_x, N_y	Applied compressive load per unit width.
ΔN_x	$N_x^{total} - N_x^{basic}$, Increase in the buckling load due to the added plies.
ρ	N_y / N_x,

$$U_1 \qquad \frac{1}{8}\left(3Q_{11} + 3Q_{22} + 2Q_{12} + 4Q_{66}\right), \qquad \text{Orthotropic material invariant.}$$

$$U_2 \qquad \frac{1}{2}\left(Q_{11} - Q_{22}\right), \qquad \text{Orthotropic material invariant.}$$

$$U_3 \qquad \frac{1}{8}\left(Q_{11} + Q_{22} - 2Q_{12} - 4Q_{66}\right), \qquad \text{Orthotropic material invariant.}$$

$$U_4 \qquad \frac{1}{8}\left(Q_{11} + Q_{22} + 6Q_{12} - 4Q_{66}\right), \qquad \text{Orthotropic material invariant.}$$

$$U_5 \qquad \frac{1}{8}\left(Q_{11} + Q_{22} - 2Q_{12} + 4Q_{66}\right). \qquad \text{Orthotropic material invariant.}$$

$$C_1 \qquad [(\tfrac{m}{a})^4 + (\tfrac{n}{b})^4] U_1 + 2[U_4 + 2U_5] (\tfrac{mn}{ab})^2,$$

$$C_2 \qquad [(\tfrac{m}{a})^4 - (\tfrac{n}{b})^4] U_2,$$

$$C_3 \qquad [(\tfrac{m}{a})^4 + (\tfrac{n}{b})^4 - 6(\tfrac{mn}{ab})^2] U_3,$$

z_k The distance from the midplane of the laminate to the kth ply.

$\bar{Z}_k$ $\frac{1}{3}(z_k^3 - z_{k-1}^3)$.

θ Angle between x-axis and the ply fiber orientation.

α The intersection of the $\theta=0°$ and the $\theta=45°$ ΔN_x curves.

β The intersection of the $\theta=45°$ and the $\theta=90°$ ΔN_x curves.

γ The intersection of the $\theta=0°$ and the $\theta=90°$ ΔN_x curves.

ξ U_3/U_2

η The intersection point of the buckling curves for two adjacent modes.

BASIC EQUATIONS

The bi-axial buckling load for a simply supported specially orthotropic laminated plate is,

$$N_x = \pi^2 \left[\left(\frac{m}{a}\right)^2 + \rho \left(\frac{n}{b}\right)^2 \right]^{-1} \left[D_{11}\left(\frac{m}{a}\right)^4 + 2\left[D_{12} + 2D_{66} \right]\left(\frac{mn}{ab}\right)^2 + D_{22}\left(\frac{n}{b}\right)^4 \right]. \quad (1)$$

The assumptions made in the development of this equation are; the panel is simply supported, the laminate is symmetric (which gives $[B_{ij}] = 0$), and the laminate is specially orthotropic so that D_{16} and D_{26} are identically zero. The derivation of equation (1) and a discussion of the assumptions is given in references [3] and [4]. Whitney and Leissa [5] give an alternate and more complete derivation of the buckling problem and is the starting point for both Muc's and Hirano's work. Their equation will be useful for laminates and boundary conditions other than those considered here, and will reduce to equation (1) when the above assumptions are imposed.

An equation for the increase in buckling load due to additional outer plies is obtained by subtracting the contribution of the inner plies from equation (1). A convenient form is obtained by first substituting the definition of D_{ij},

$$D_{ij} = \sum_{k=1}^{N} \bar{Q}_{ij}^{\,k} \, \bar{Z}_k, \quad (2)$$

into equation (1) to yield,

$$N_x = \pi^2 \left[\left(\frac{m}{a}\right)^2 + \rho \left(\frac{n}{b}\right)^2 \right]^{-1} \sum_{k=1}^{N} \left[\bar{Q}_{11}^{\,k} \left(\frac{m}{a}\right)^4 + 2\left[\bar{Q}_{12}^{\,k} + 2\bar{Q}_{66}^{\,k} \right]\left(\frac{mn}{ab}\right)^2 + \bar{Q}_{22}^{\,k} \left(\frac{n}{b}\right)^4 \right] \bar{Z}_k. \quad (3)$$

Substituting for $\bar{Q}_{ij}$ in terms of the orthotropic material invariants and simplifying gives,

$$N_x = \pi^2 \left[\left(\frac{m}{a}\right)^2 + \rho \left(\frac{n}{b}\right)^2 \right]^{-1} \sum_{k=1}^{N} \left[\left(C_1 + C_2 \cos 2\theta_k + C_3 \cos 4\theta_k \right) \bar{Z}_k \right], \quad (4)$$

The contribution of the added (outer) plies can be separated from that of the original (inner) laminate by bringing the terms for k = 1 and k = N out of the summation:

$$N_x = \pi^2 \left[\left(\frac{m}{a}\right)^2 + \rho \left(\frac{n}{b}\right)^2 \right]^{-1} \sum_{k=2}^{N-1} \left[\left(C_1 + C_2 \cos2\theta_k + C_3 \cos4\theta_k\right) \overline{Z}_k \right]$$

$$+ \pi^2 \left[\left(\frac{m}{a}\right)^2 + \rho \left(\frac{n}{b}\right)^2 \right]^{-1} \left[\left(C_1 + C_2 \cos2\theta_1 + C_3 \cos4\theta_1\right) \overline{Z}_1 \right]$$

$$+ \pi^2 \left[\left(\frac{m}{a}\right)^2 + \rho \left(\frac{n}{b}\right)^2 \right]^{-1} \left[\left(C_1 + C_2 \cos2\theta_N + C_3 \cos4\theta_N\right) \overline{Z}_N \right]. \qquad (5)$$

The change in buckling load due to the added plies is obtained by subtracting the terms in the summation from k = 2 to k = N-1 (the basic laminate buckling load), from both sides of equation (5). Applying the symmetric laminate assumptions and simplifying yields

$$\Delta N_x = 2\pi^2 \left[\left(\frac{m}{a}\right)^2 + \rho \left(\frac{n}{b}\right)^2 \right]^{-1} \left[C_1 + C_2 \cos2\theta_N + C_3 \cos4\theta_N\right] \overline{Z}_N. \qquad (6)$$

As cosine is an even function, it is observed that the increase in buckling load is a function of the absolute value of the ply angle. Thus a positive 45° ply or a negative 45° ply increase the buckling load by the same amount. Note that if $N_y = 0$, equation (6) is independent of the number of half waves in the transverse direction.

INITIAL RESULTS

Equation (6) is plotted in Figure 2 for θ = 0°, 45° or 90° plies added to an 8-ply AS/3501-6 basic laminate as a function of aspect ratio. The plot is limited to the first buckled mode shape (m=1, n=1) and uni-axial loading. The b dimension is held constant at 20 inches.
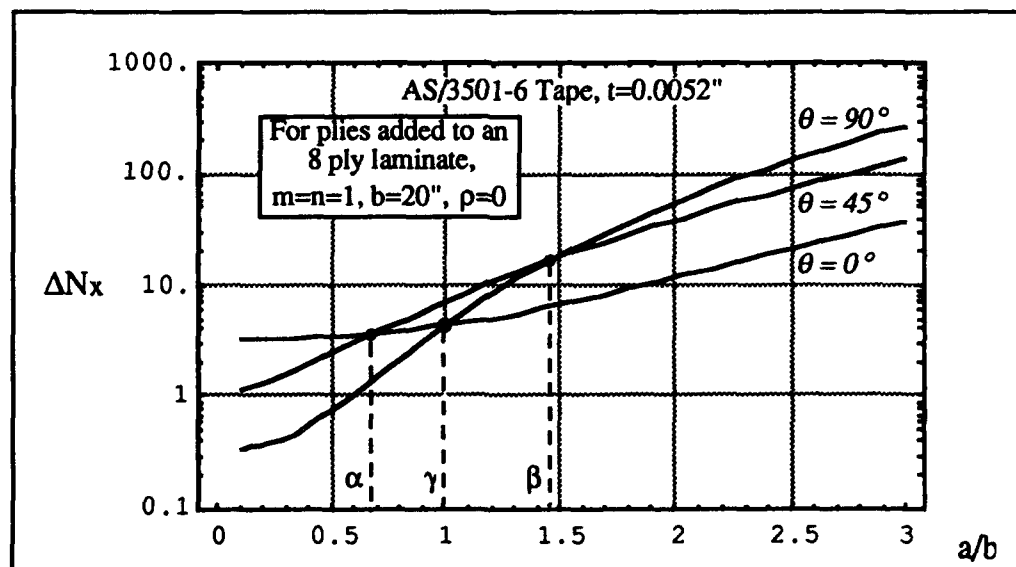
Figure 2 - Mode 1 Added Buckling Capability.
ΔN_x for one ply added top and bottom to a laminate for the first buckled mode shape.

Observe that optimum orientation of the added plies depends on the aspect ratio of the panel. In this example, 0° plies increase the buckling capability the most for aspect ratios less than 0.69; 90° plies are best for aspect ratios greater than 1.45; and a 45° orientation is best for the range of aspect ratios 0.69 < a/b < 1.45. The limits described are the intersection of the 0° and 45° curves, and the intersection of the 45° and 90° curves. The intersection of the 0° and 90° curves is also of interest.

These intersections, defined as α, β and γ respectively, are located by equating the curves in question and solving for the intersection aspect ratio in terms of the invariants. These results are given as the positive real solutions of equations (7). Note that the equations are independent of the bi-axial load ratio ρ, and that γ is dependent only on the mode shape.

$$
\alpha = \frac{m}{n} \sqrt{\frac{6\,\xi \pm (32\,\xi^2 + 1)^{1/2}}{(2\,\xi - 1)}} \quad , \quad \beta = \frac{m}{n} \sqrt{\frac{6\,\xi \pm (32\,\xi^2 + 1)^{1/2}}{(2\,\xi + 1)}} \quad , \quad \gamma = \frac{m}{n} . \quad (7)
$$

Typical values of α, β and the invariant ratio ξ = U_3/U_2 for several material systems are listed in Table I. The data is based on compressive material properties [6].

Further inspection of Figure 2 reveals that it also identifies the stacking sequence with the greatest buckling load for any panel aspect ratio. For example, at an aspect ratio of 0.9 the added ply angles are ranked 45°, 0° and 90° in order of greatest to least potential increase in the buckling load. Because the outer plies contribute the most to a laminate's buckling capability this ranking is also the optimum stacking sequence: in this example (±45°, 0°, 90°)sym. This result is of course limited to the first mode shape and uni-axial loading. Figure 2 is summarized in Table II in the form of design guidelines. The optimum laminate stacking sequence for buckling is also listed in Table II as a function of the plate aspect ratio.

Finally a normalized plot of equation (6) is presented in Figure 3, The plot is valid for all simply supported specially orthotropic AS/3501-6 laminates. The plot is limited to uni-axial loading solely for clarity in presentation. A more complete figure including a bi-axial load ratio axis would require several three dimensional surfaces and would likely be confusing.

TABLE I - CONSTANTS FOR TYPICAL MATERIAL SYSTEMS.

Material System	α	β	U3/U2
AS/3501-6 Tape	.688 m/n	1.45 m/n	.239
IM7/8551-7A Tape	.692 m/n	1.45 m/n	.234
HMF 133/3501-6 Fabric	.427 m/n	2.34 m/n	8.13

Based on compressive material properties. m and n are mode shape indices.

TABLE II - GUIDELINES FOR ADDING PLIES TO INCREASE BUCKLING LOAD.

Aspect Ratio a/b	Optimum Outer Fiber Angle†	Optimum Stacking Sequence†
a/b < α	Add 0 degree plies.	(0,45,-45,90)sym
α < a/b < γ	Add 45 degree plies.	(45,-45,0,90)sym
γ < a/b < β	Add 45 degree plies.	(45,-45,90,0)sym
β < a/b	Add 90 degree plies.	(90,45,-45,0)sym

The optimum orientation of the added plies is a function of the plate aspect ratio, mode shape and material properties. † +45° and -45 plies are interchangeable
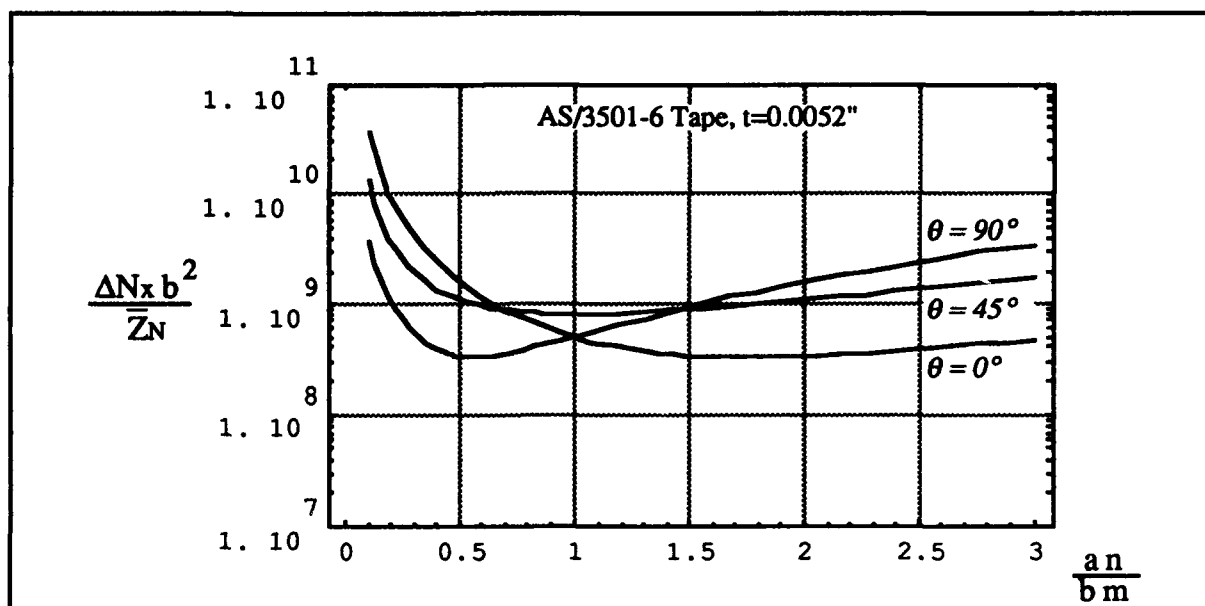
Figure 3 - Normalized Added Buckling Capability for Uni-Axial Loading.
$\Delta Nx\, b^2 \,/\, \overline{Z}_N$ for one ply added top and bottom to a AS/3501-6 laminate for all mode
shapes and baseline thicknesses, (see text).

MODE SHAPE CONSIDERATIONS

The previous discussion outlining the optimization approach assumed that the buckled
mode shape was known. The analyst must accurately predict the mode shape before the
optimization can be performed. As will be demonstrated, it is quite possible that adding plies
or restacking a laminate will change the mode shape. It is important that the optimized
laminate's final mode shape be checked against the predicted mode shape.

A simple test to determine the correct mode shape can be derived by evaluating
equation (1) for two different mode shapes (say for example (m, n) and (m+1,n)), and
solving for the aspect ratio η that equates the two. Performing this manipulation and
simplifying yields

$$\eta^2 = \frac{-B \pm \sqrt{B^2 - 4AC}}{2n^2 A} \, , \tag{8}$$

where

$$A = 2\rho\,(D_{12} + 2D_{66}) - D_{22} \, , \qquad B = \rho\,(1 + 2m + 2m^2)\,D_{11} \, , \qquad C = m^2\,(1 + 2m + m^2)\,D_{11} \, .$$

For uni-axial loading equation (8) reduces to,

$$\eta^2 = m\,(1+m)\,\sqrt{\frac{D_{11}}{D_{22}}} \, . \tag{9}$$

To apply these results, compare the laminate's aspect ratio to η. If $a/b > \eta$ then the mode will be greater than m. If $a/b < \eta$ then the mode will be m or less. The correct buckled mode shape for uni-axial loading will satisfy

$$(m - 1) m \ < \ \left(\frac{a}{b}\right)^2 \sqrt{\frac{D_{22}}{D_{11}}} \ < \ m (m + 1) . \tag{10}$$

Note there is a positive value of load ratio ρ that (if exceeded) alters the characteristics of the problem so that the critical buckling curves do not intersect and equation (8) becomes invalid. A trial and error scan through the mode shapes will often be a fast and appropriate approach for bi-axial loading.

EXAMPLES AND DISCUSSION

The derivations and discussion presented have been limited to simply supported, specially orthotropic, symmetric laminates under bi-axial loading. In the examples that follow the laminates violate the specially orthotropic laminate assumptions. Specifically, the D_{16} and D_{26} bending-twisting coupling terms are non-zero. The effect of these terms is neglected on the basis that they are small and will not introduce a large error. This is a generally accepted practice and is valid except for laminates that are very thin relative to their panel dimensions. Sawyer [7] found that if the number of layers in the plate is sufficiently large ($N \geq 6$), then the D_{16} and D_{26} terms become insignificant and can be neglected with little error. For these examples, mode 1 will be defined by $m = 1$, $n = 1$ and mode 2 by $m = 2$, $n = 1$.

In Table III, an 18" by 20" simply supported, 8-ply, AS/3501-6, $(45°,-45°,0°,90°)_{sym}$ laminate loaded in uni-axial compression is used as a baseline for improvement in buckling load. First, the mode shape for each case is determined by using Tables I and II and equation (10). The buckling load is then calculated and tabulated. The baseline laminate is given as Case 1, and the 0°, 45° and 90° added ply solutions are listed as Cases 2, 3 and 4. In this example the stacking sequence for the baseline laminate has been optimized. Note the large variation in buckling load with added ply angle. The greatest improvement is obtained in Case 3 by adding 45° plies. This is also the recommendation of Table II. The table values can be generated directly from Figure 2.

In Table IV, the baseline is a 36" by 20" simply supported, 8-ply, AS/3501-6, $(0°,45°,-45°,90°)_{sym}$ laminate loaded in uni-axial compression. In this example, adding a 45° or a 90° ply to the baseline changes the mode shape from 1 to 2 (adding a 0° ply does not change the mode shape). This is significant because the buckling load would be overestimated if the change in mode shape was not recognized. In this example the stacking sequence selected for the baseline laminate is not optimum for either mode 1 or mode 2. Case 5 not

TABLE III - COMPARISON OF OPTIONS TO IMPROVE BUCKLING LOAD.

Case	Laminate Description	Layup	a/b	Mode	N_x lb/in (% Baseline)
1	Baseline	(45,-45,0,90)$_{sym}$	0.9	1	5.95 (100%)
2	Baseline / added 0°	(0,45,-45,0,90)$_{sym}$	0.9	1	10.1 (170%)
3	Baseline / added 45°	(45,45,-45,0,90)$_{sym}$	0.9	1	11.9 (199%)
4	Baseline / added 90°	(90,45,-45,0,90)$_{sym}$	0.9	1	9.08 (153%)

An 18" by 20" AS/3501-6 (45°,-45°,0°,90°)sym laminate loaded in uni-axial compression with plies added top and bottom.

TABLE IV - COMPARISON OF OPTIONS TO IMPROVE BUCKLING LOAD

Case	Laminate Description	Layup	a/b	Mode	N_x lb/in (% Baseline)
1	Baseline	$(0,45,-45,90)_{sym}$	1.8	1	4.66 (100%)
2	Baseline / added 0°	$(0,0,45,-45,90)_{sym}$	1.8	1	7.00 (150%)
3	Baseline / added 45°	$(45,0,45,-45,90)_{sym}$	1.8	2	11.0 (236%)
4	Baseline / added 90°	$(90,0,45,-45,90)_{sym}$	1.8	2	8.22 (176%)
5	Baseline / Restack	$(45,-45,0,90)_{sym}$	1.8	2	5.95 (128%)
6	Baseline / Cross Stiffener	$(0,45,-45,90)_{sym}$	0.9	1	5.08 (109%)
7	Baseline / Crosswise Stiffener / Restack	$(45,-45,0,90)_{sym}$	0.9	1	5.95 (128%)
8	Baseline / Lengthwise Stiffener	$(0,45,-45,90)_{sym}$	3.6	3	17.5 (375%)

A 36" by 20" AS/3501-6 $(0°,45°,-45°,90°)_{sym}$ laminate loaded in uni-axial compression with plies added top and bottom, adding stiffeners and restacking.

only demonstrates that a substantial increase in buckling load can be obtained by simply restacking the laminate, it also shows that restacking can change the mode shape. The stacking sequence in case 5 is the optimum for mode 2.

The last 3 cases in Table IV list the improvement obtained by adding a stiffener to the original panel. Cases 6 and 7 demonstrate the effect of halving the panel aspect ratio by dividing it with a cross stiffener, with and without restacking the laminate. Note that the improvement in buckling load is marginal when compared to other available options. Comparing cases 5 and 7 reveals that restacking the laminate eliminates the need for the cross stiffener in case 7. Case 8 adds a lengthwise stiffener to double the panel aspect ratio and greatly improves the buckling load as is expected.

Some care should be exercised when interpreting the results in Table IV. Adding a lengthwise stiffener to double the aspect ratio of the baseline gives the greatest potential improvement in buckling load; however, it may not be the ideal solution that the simple interpretation suggests. Mechanical factors such as interference with adjacent substructure or equipment, or the extra weight could preclude the addition a lengthwise stiffener. The buckling load improvement options should be weighed against all design requirements to determine an appropriate solution. It should be clear from Table IV that simply restacking the original laminate is the most weight efficient way to increase the buckling load.

To keep this paper at a reasonable length an example of the method applied to a bi-axially loaded laminate is not included. The procedure is much the same as that presented for the uni-axial cases.

CONCLUDING REMARKS

An analytical laminate buckling optimization method has been derived for symmetric, simply supported, specially orthotropic laminates under bi-axial compression and can be applied to symmetric orthotropic laminates provided that the bending-twisting coupling is small. The method acknowledges the existence of design constraints other than buckling and optima other than angle-ply laminates are permitted. Design guidelines have been proposed and includes consideration of the buckled mode shape. To expand the method's applicability to industry needs, the permissible ply angles are constrained to 0°, ±45°, and 90°.

The equations developed in the preceding discussion are in a simple and explicit form because the buckled mode shapes for simply supported, bi-axially loaded, specially orthotropic laminates are accurately described by the shape function $\text{Sin}(m\pi x/a)\text{Sin}(n\pi y/b)$. The Rayleigh-Ritz formulation of this buckling problem is straightforward and yields a form independent of the mode shape functions. For shear loading, combined loading, and boundary conditions other than simply supported, the buckled mode shape must be represented by a series approximation. As a result, the Rayleigh-Ritz formulation yields a matrix eigenvalue problem. A simple equation or design guideline cannot be derived for these cases because any given series cannot represent a solution for a family of load cases or boundary conditions. Computer trade studies will need to be performed in these situations.

REFERENCES

1   Muc, A., 1988. "Optimal Fibre Orientation for Simply-Supported, Angle-Ply Plates Under Biaxial Compression." Composite Structures, **9**, pp. 161-172.
2   Hirano, Y., 1979. "Optimum Design of Laminated Plates under Axial Compression." AIAA J., **17**, pp. 1017-1019.
3   Whitney, J. M., 1987. Structural Analysis of Laminated Anisotropic Plates, Lancaster, PA: Technomic Publishing Company, Inc.
4   Jones, R. M., 1975. Mechanics of Composite Materials, New York, NY: McGraw-Hill Co.
5   Whitney, J. M., and Leissa, A. W., 1969. "Analysis of Heterogeneous Anisotropic Plates." J. Appl. Mech., **36**, pp. 261-266.
6   Plumb, C., 1991. Composites Manual, McDonnell Aircraft Company, McDonnell Douglas Corporation, St. Louis, MO.
7   Sawyer, J. W., 1977, "Flutter and buckling of general laminated plates." J. Aircraft, **14**, pp. 387-91.

ACKNOWLEDGMENT

SESSION 8B

Test Methods II

Flatwise Tension Strength of Damaged Composite Laminates

J. M. PEREIRA AND C. C. CHAMIS

ABSTRACT

A flatwise tension test was evaluated as a tool for measuring the reduction in the out-of-plane strength of composite laminates due to in-service loading. A finite element analysis was performed to determine the stress distribution in samples modeled using various layups. Experiments were performed to measure the out-of-plane strength of samples removed from tensile coupons that had been subjected to either monotonic loads or tension-tension cyclic loading. The finite element analysis indicated that the out-of-plane stress in the sample is uniform and close to the nominal applied stress. In-plane normal, and shear stresses are generally small compared to the out-of-plane stress. Experimental results indicated that there is no significant reduction in the out-of-plane strength due to monotonic loading. However, initial results indicate that cyclic loading produces a decrease in the out-of-plane strength. The technique appears to be a promising method of detecting damage.

INTRODUCTION

Failure mechanisms in multidirectional polymer composite laminates include matrix cracking, delamination, fiber/matrix debonding, and fiber fracture. However, under in-plane monotonic loading the ultimate failure in these types of laminates is generally governed by the ultimate tensile strain in the fibers [1]. Damage in the matrix or fiber/matrix interface regions usually occurs prior to any damage in the fibers themselves [2]. Damage caused by fatigue loading in composite laminates is usually widespread, unlike the situation in monolithic materials where fatigue often results in the nucleation and growth of a single crack. Significant damage may exist in the laminate before it is reflected in a reduction of the in-plane strength. A practical method, other than the in-plane strength test, can be useful in detecting

J.M. Pereira, Aerospace Engineer, NASA Lewis Research Center, Cleveland, Ohio 44135
C.C. Chamis, Senior Research Scientist, NASA Lewis Research Center, Cleveland, Ohio 44135

early indications of damage in a composite laminate.

One such method proposed here is the flatwise tension (FWT) test. This test has been used in the characterization of composite laminates [3] and several different configurations and sample geometries have been proposed [4, 5]. Typically, in this test, a solid tab is bonded to each face of a flat sample from a composite laminate and the sample is loaded in a direction normal to the plane of a laminate. In some cases, a thick specimen is manufactured and machined so as to produce a tapered section [6]. Other methods of measuring the strength normal to the direction of the ply layup include specially designed semi-circular and elliptical specimens [7]. Because the loading direction is normal to the direction of the fibers, it is expected that the strength of the laminate will be much more sensitive to damage-induced degradation in matrix properties, the existence of delaminations and fiber/matrix debonding.

In this study a particular FWT test system was developed and used to measure the strength of two different graphite/epoxy laminates that had been subjected to monotonic and cyclic in-plane loading of varying levels. The aim of the study was to evaluate the experiment as a tool for detecting damage in in-service structures and laboratory samples.

METHODS

The flatwise tension test apparatus used in this study consisted of two rectangular aluminum blocks with a 3 cm by 3 cm cross section, between which a flat specimen was bonded (Figure 1). The specimens measured 3.5 cm by 3.5 cm, which produced an overhang of .25 cm around the perimeter of the aluminum tabs. During the course of the study several different adhesives for bonding the samples to the tabs were evaluated. The adhesive which proved to be the most successful was AF-163-2K-06 Structural Adhesive Film (3M Corp., St. Paul, Minnesota). Careful surface preparation of the sample and the tabs was necessary to avoid failure at the interface. Specimens were prepared by placing the samples, adhesive film and aluminum blocks in a spring loaded fixture designed to provide pressure and maintain alignment of the tabs during the adhesive cure. The adhesive was cured at 250°F for one hour.

The flatwise tension test was conducted by applying a load in a displacement controlled mode at a rate of 0.1 mm/min until failure occurred. The test was considered satisfactory if the composite specimen split in two through a plane roughly parallel to the plane of the laminate, with part of the specimen completely covering each of the faces of the tabs.
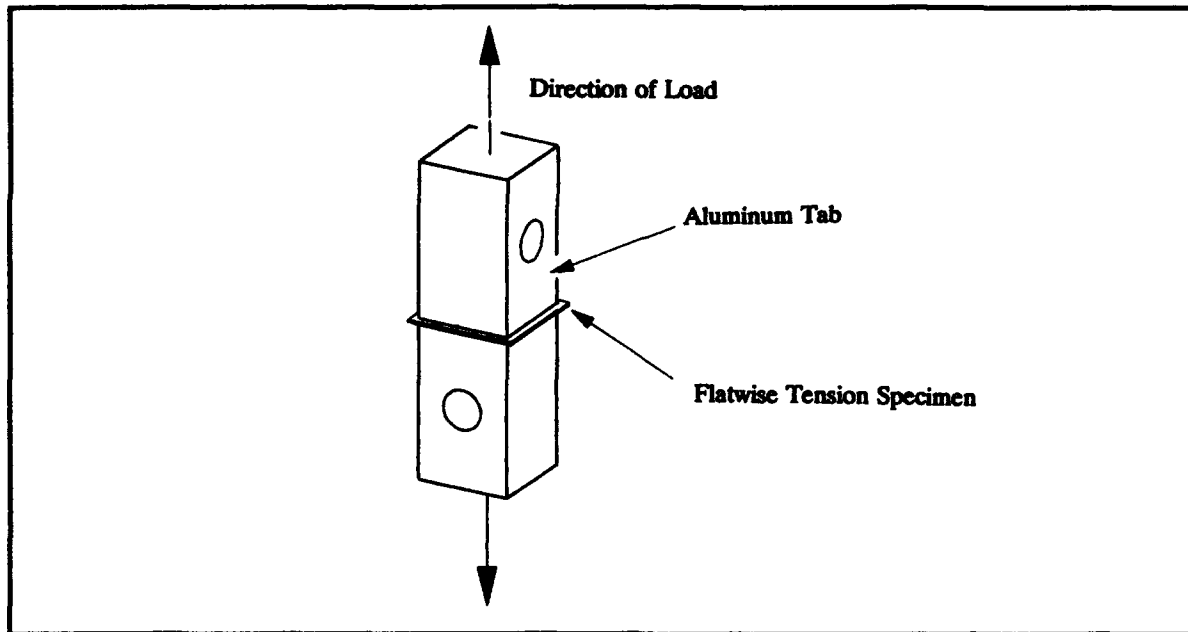
Figure 1. Schematic of the Flatwise Tension Test Apparatus

FINITE ELEMENT ANALYSIS

A finite element analysis was conducted to determine the distribution of the out-of-plane component of stress in the sample, as well as the relative magnitudes of in-plane normal and shear stress. In the analysis, both the specimen and a portion of the tab were modeled, taking advantage of symmetry through the mid-plane of the sample (Figure 2). The tabs were modeled using linear elastic hexagonal elements with the mechanical properties of aluminum while the specimen was modeled using orthotropic linear elastic finite elements with the mechanical properties representing T300/934 graphite/epoxy with three different configurations: a $[(45/-45)_2]_{sym}$ layup, a $[0/(45/-45)_2]_{sym}$ layup and a $[0]_8$ layup. In the analysis, specimens were modeled with and without the overhang. A tensile pressure load of 35 MPa was applied in the z direction (Figure 2) to the top surface of the tab while the nodes at the bottom of the specimen were constrained in the z direction.

APPLICATION TO LOADED SPECIMENS

The FWT test was used to measure the out-of-plane strength of samples taken from coupons that were subjected to in-plane monotonic loads, and a limited number of samples that had been subjected to cyclic loading. Two different graphite/epoxy composite laminates were fabricated for this study: a $[0/(45/-45)_2]_{sym}$ laminate and a
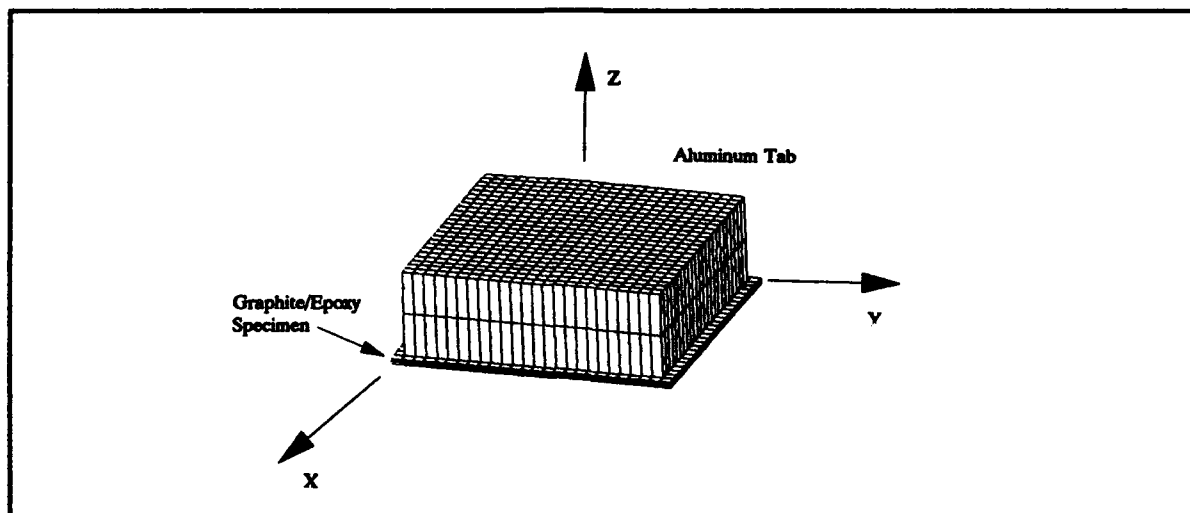
Figure 2. Finite Element Model of the Specimen and Tab

$[(45/-45)_2]_{sym}$ laminate. Both were manufactured from the same batch of 0.6 FVR T300/934 unidirectional graphite/epoxy pre-preg tape. For the monotonic loading program, tensile coupons 3.5 cm wide and 23 cm long were cut from the laminates and fitted with glass/epoxy tabs. The specimens used for the cyclic loading program were 3.5 cm wide and 12 cm long, with a length of 4 cm between the tabs.

Monotonically Loaded Specimens

As a baseline, the in-plane longitudinal tensile strength of the coupons was measured by loading a number of coupons from each of the two laminates in longitudinal tension in a displacement controlled mode at a rate of 1 mm/min. Two $[0/(45/-45)_2]_{sym}$ coupons and three $[(45/-45)_2]_{sym}$ coupons were loaded to failure, and the computed average failure stress of each of the sets was taken to be the tensile strength for the corresponding layup.

Other coupons were subjected to in-plane, monotonic tensile loads of varying magnitude, ranging from 20% to 90% of the measured failure load. After application of the longitudinal load, specimens were cut from the coupons and tested in FWT. Several samples from loaded and unloaded coupons were examined microscopically to determine whether the monotonic loading produced any visible damage in the matrix prior to failure. Small specimens were cut at 90 degrees and 45 degrees from the longitudinal axis, polished and examined at magnifications of 50x and 100x.

Cyclic Loaded Specimens

A limited number of coupons from the $[(45/-45)_2]_{sym}$ laminate were subjected to tension-tension cyclic loading of varying magnitude. Two different loading ratios were used based on fatigue data obtained from similar specimens [8]. Five coupons

were tested at stresses of 100 MPa ± 50 MPa at a rate of 1 cycle/sec. One of these was removed after 5000 cycles, while the others were removed after 10000 cycles. Another coupon was tested at a stress of 100 MPa ± 40 MPa at the same frequency and removed after 328000 cycles. After cyclic loading, square test specimens were cut from the coupons and tested in flatwise tension.

RESULTS

FINITE ELEMENT ANALYSIS

The predicted normal stress in the z direction, σ_{zz}, was relatively uniform throughout the specimen, with no stress concentrations (Figure 3). The presence of an overhang had little effect on the stress distribution. At the mid-plane of the
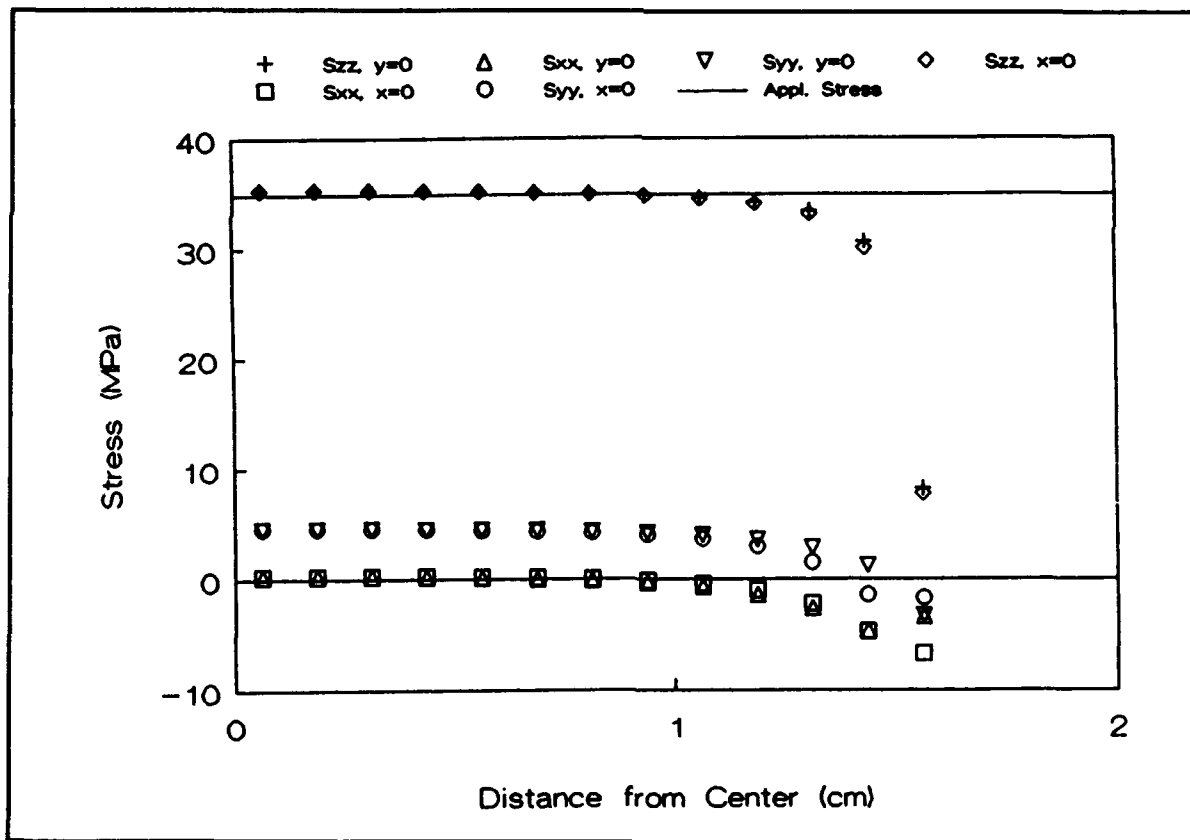
Figure 3.   Predicted normal and in-plane stress at the mid-plane of the [0/(45/-45)$_2$]$_{sym}$ sample with the overhang, compared with the nominal applied stress.
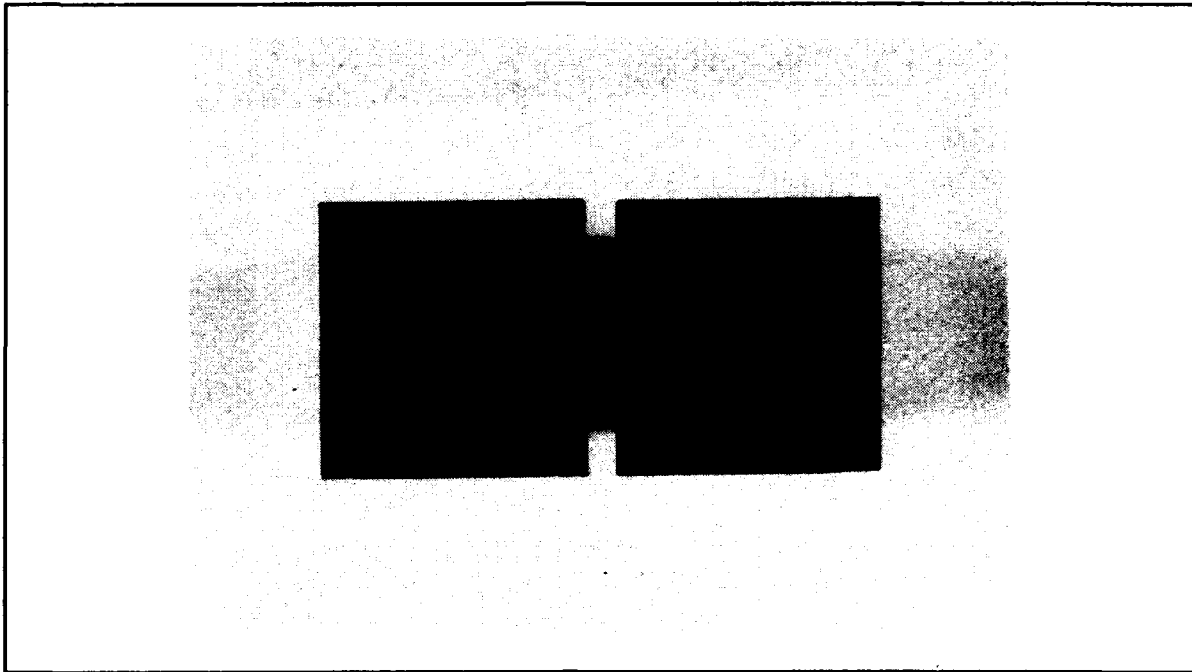
Figure 4. Surfaces of the FWT specimen after failure.

specimen, between the tabs, this component was very close to the applied stress. In most cases components of stress in other directions were relatively small compared with σ_{zz}. However, in the most anisotropic case, the case with the $[0]_8$ layup, the normal stress in the fiber direction, σ_{xx}, was almost 40% of the value of the normal stress.

EXPERIMENTAL RESULTS

With proper surface treatment and a good adhesive, the FWT test generally produced failure completely through the specimen. In most cases the failure surface exposed more than one ply near the mid-plane of the sample (Figure 4).

In-plane tensile testing of the $[(45/-45)_2]_{sym}$ laminate produced a nonlinear stress-strain curve that is typical for this layup, while the stress-strain curve of the $[0/(45/-45)_2]_{sym}$ laminate was linear to failure. Microscopic examination of coupons that had been loaded to 90% of the failure load, however, showed no indication of damage in either coupon. Flatwise tension tests on samples removed from both types of coupons showed no degradation in strength as a result of the in-plane monotonic loading (Figure 5). The average out-of-plane failure stress was 38.8 MPa for the $[0/(45/-45)_2]_{sym}$ layup and 39.1 MPa for the $[(45/-45)_2]_{sym}$ layup.

The cyclically loaded coupons exhibited some reduction in the out-of-plane
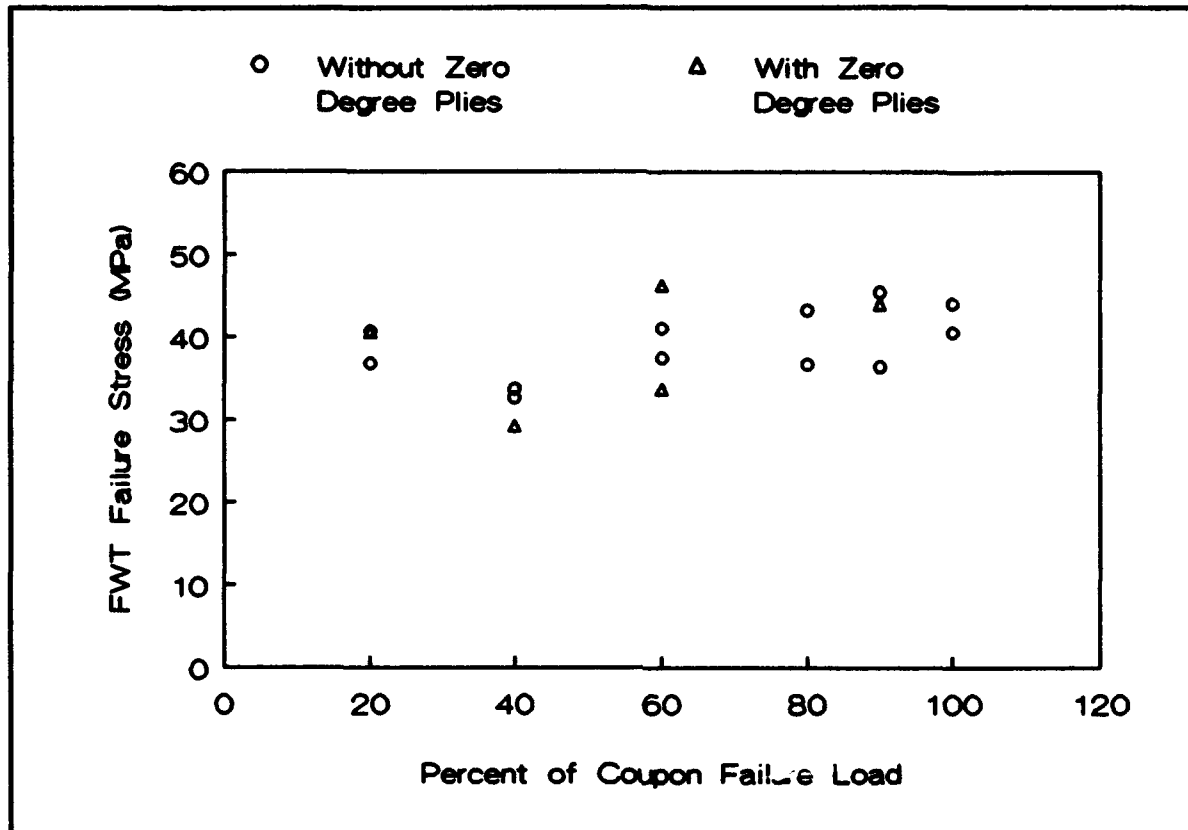
Figure 5. Measured out-of-plane strength of $[0/(45/-45)_2]_{sym}$ and $[(45/-45)_2]_{sym}$ samples as a function of in-plane monotonic load, expressed as a percentage of the measured failure load.

strength (Figure 6). In the figure the FWT strength of coupons subjected to tension-tension cyclic loads of different levels are compared with the results from the monotonic loading case.

DISCUSSION

In the development of the FWT test that was used, a number of issues needed to be addressed. The most important issue was the ability to produce an adhesive bond which was stronger than the composite itself. Proper surface preparation and a device for aligning the tab/specimen system during the adhesive cure were critical in obtaining a strong adhesive bond. At the present time, this issue appears to be the main limitation of the technique. However, as was shown here, for many composites the proposed flatwise tension test can be used.

The finite element analysis indicated that the nominal applied stress is a good measure of the normal stress at failure. The presence of an overhang in the sample
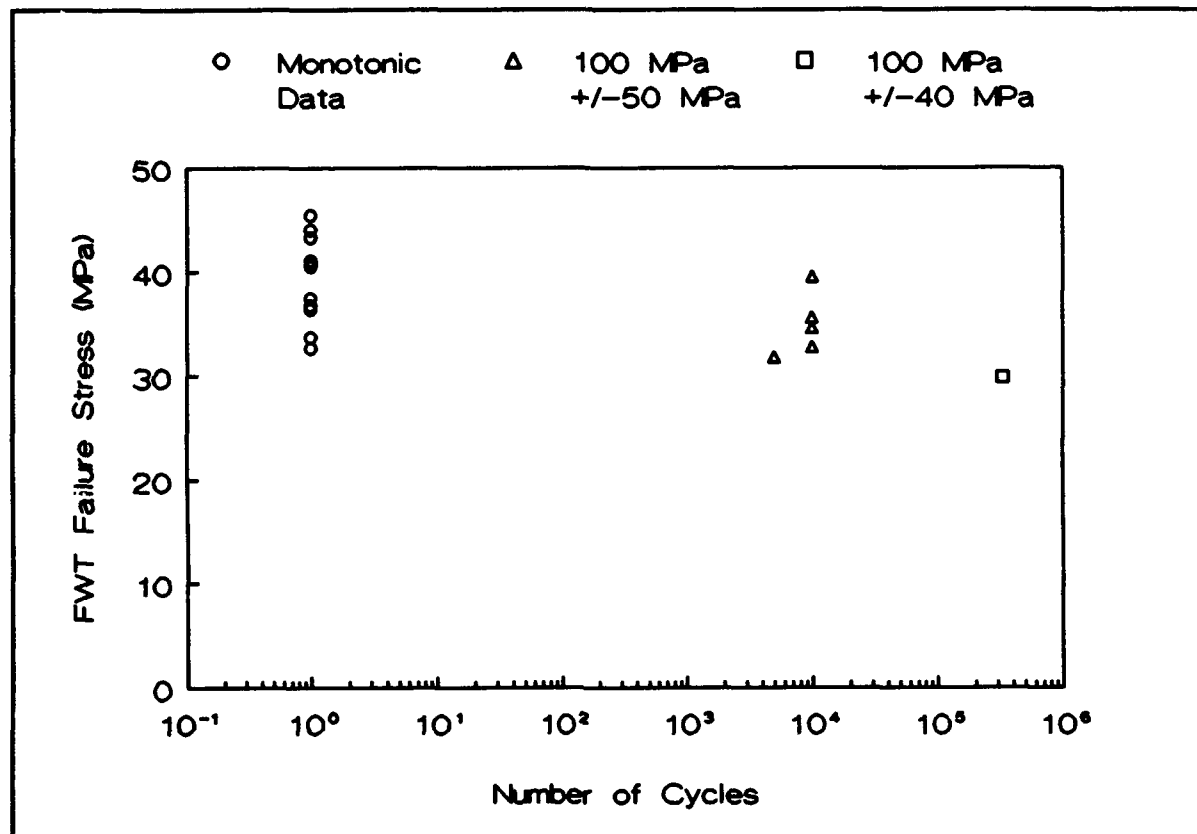
Figure 6.   Measured out-of-plane strength of $[(45/-45)_2]_{sym}$ samples as a function of the number of loading cycles. Data at 1 cycle corresponds to the monotonic data shown in Figure 5.

had little effect on the stress. The main advantage of the overhang was that it simplified specimen preparation, and reduced the possibility of machining damage occurring in the stressed region. In most cases, the in-plane stresses and shear stresses were low compared to the normal stress. However, for certain layups, particularly in the case of unidirectional composites, the in-plane normal stresses may be a significant fraction of the out-of-plane stress. The effect of this must be considered when analyzing results.

The average failure stress for the monotonically loaded samples was 39 MPa. This compares well with the value of 43 MPa, reported by Lagace and Weems [6], who used thick, tapered samples manufactured from AS4/3501-6 graphite/epoxy. The different ply layups had no effect on the out-of-plane strength, also agreeing with the results in [6].

The monotonic loading applied to the coupons had no effect on the measured out-of-plane strength. However, initial results indicated that cyclic loading did cause a reduction in out-of-plane strength. This should be studied further with more

samples, particularly for samples subjected to high cycle fatigue where matrix damage is more important.

Although the technique may have some limitations due to the problem of obtaining a strong adhesive bond between the specimen and tabs, it has the advantage that specimens are simple to prepare and may be obtained either from in-service structures or laboratory coupon samples.

REFERENCES

1. Daniel, I.M. and J.-W. Lee, 1990. "Damage Development in Composite Laminates Under Monotonic Loading." Journal of Composites Technology and Research, 12(2):98-102.

2. Stinchcomb, W.W. and K.L. Reifsnider, 1983. "Damage Accumulation Concepts for Fatigue Loaded Composite Laminates." in Proceedings of the A.S.M.E. Symposium on Mechanics of Composite Materials, pp. 143-148.

3. Cushman, J.B. and S.F. McCleskey, 1982. "Design Allowables Test Program, Celion 3000/PMR-15 and Celion 6000/PMR-15, Graphite/Polyimide Composites." Contractor Report 165840, NASA.

4. Hercules Incorporated, 1987. "Radial tensile final report for filament wound case." Contract No. 114010. Hercules Incorporated, Magna, Utah, 1987.

5. Munjal, A.K., 1989. "Test Methods for Determining Design Allowables for Fiber Reinforced Composites." in Test Methods and Design Allowables for Fibrous Composites: 2nd Volume, ASTM STP 1003, C.C. Chamis, ed., American Society for Testing and Materials, Philadelphia, pp. 93-110.

6. Lagace, P.A. and D.B. Weems, 1989. "A Through-the-Thickness Strength Specimen for Composites." in Test Methods and Design Allowables for Fibrous Composites: 2nd Volume, ASTM STP 1003, C.C. Chamis, ed., American Society for Testing and Materials, Philadelphia, pp. 197-207.

7. Hiel,C.C., M.Sumich, and D.P.Chappell, 1991. "A Curved Beam Test Specimen for Determining the Interlaminar Tensile Strength of a Laminated Composite."Journal of Composite Materials, (25):854-868.

8. Rotem, A. and H.G. Nelson, 1989. "Failure of a Laminated Composite under Tension-Compression Fatigue Loading." Composites Science and Technology, (36): 45-62.

Ultrasonic Determination of Anisotropic Elastic Constants and Flaw Sizes in Thick Composite Laminates

DAVID K. HSU, ALI MINACHI AND FRANK J. MARGETAN

ABSTRACT

This paper deals with two nondestructive evaluation methods for thick composites. The first method is for the in situ determination of elastic constants with one-sided access. The method utilizes the acousto-ultrasonic technique and deduces the elastic constants from the time of flight of obliquely reflected echoes in a thick composite plate of known thickness. The second method uses the elastic anisotropy information to improve the accuracy of flaw sizing in thick composites by immersion pulse-echo line scans. The Gauss-Hermite beam model is used in the computation of the scanned flaw signal amplitude while taking into account effects of elastic anisotropy, frequency, flaw depth, and transducer size. The flaw size is determined iteratively by minimizing the difference between the computed and measured results.

INTRODUCTION

In the design and manufacture of large scale thick-walled composite structures, especially structures designed to withstand compressive loads, the need arises for nondestructively characterizing the macroscopic properties and for evaluating defect sizes in the composite. Estimates of the elastic constants are needed in the prediction of structural response to external loads. When ultrasonic methods are used for flaw detection and characterization in anisotropic composite structures, one needs the elastic constants in order to know the wave field in the composite and to interpret and size the defects. In-situ measurement of the anisotropic elastic constants would be desirable for manufacture quality assurance and for in-service monitoring of damages and possible property degradation. Since the backside of large structures is rarely available for testing, one-sided access is often a necessary capability of the testing method.

D. K. Hsu, A. Minachi, and F. J. Margetan are respectively senior scientist, graduate student, and associate engineer of Center for NDE, Iowa State University, Ames, IA 50011.

In laminated or filament-wound composite structures, delaminations remain the primary concern for internal flaws or defects. The sizing of delaminations in anisotropic composites also requires a knowledge of the elastic constants. In this work, quantitative ultrasonic methods requiring only one side access are developed for the nondestructive determination of the elastic constants and for estimating the delamination sizes [1,2]. In both cases, the methods make use of the "slowness surfaces" of the composite and the techniques are verified in unidirectional thick composite laminates, where the degree of anisotropy is the highest [3,4].

ACOUSTO-ULTRASONICS IN THICK COMPOSITES

The single-sided measurement of elastic constants in this work makes use of the acousto-ultrasonic (AU) technique, a method often used for the nondestructive evaluation of composites [5-7]. In this configuration, two contact transducers are coupled to the same surface of the structure, one serving as transmitter and the other as the receiver. In thin composite plates, the AU signals are a mixture of numerous modes and multiple echoes, and are therefore extremely complex to analyze. In thick section composites, however, echoes of the different modes are temporally separated due to the large acoustic paths. The AU signals in thick composites are amenable to quantitative analysis and identification. Hsu and Margetan [4] found that AU signals in thick composites consisted of many types of waves, including obliquely reflected quasi-longitudinal and quasi-transverse bulk waves, mode converted waves upon reflection, and surface waves. The measurement results were successfully interpreted using the slowness surfaces.

Figure 1 shows the measured and computed time-of-flight (TOF) of the various modes in a thick unidirectional graphite-epoxy laminate. The plane of propagation is the "meridian" plane of the transversely isotropic solid, containing the fibers. In the figure QL and QSV are quasi-longitudinal and quasi-shear vertical waves, respectively, and SH is the (pure) shear horizontal wave. The first-arrival signal (lowest branch in Fig. 1) is usually the one-bounce QL-to-QL echo. Since the composite is anisotropic, the energy vector of the quasi-modes deviate from the phase velocity direction. The model used in analyzing the various modes in the AU signal is based on the slowness surfaces of the composite under study. In the "forward" problem, the elastic constants are used in the computation of the slowness surfaces, which in turn are used for the calculation of the time of flight of the various modes. This calculation uses the fact that the group velocity direction (i.e., the direction along which the energy propagates) is always perpendicular to the local curvature of the slowness surface [3]. For the "inverse problem", a subject

of this paper, the times-of-flight of the AU signals are used
for the extraction of the elastic constants of the composite.
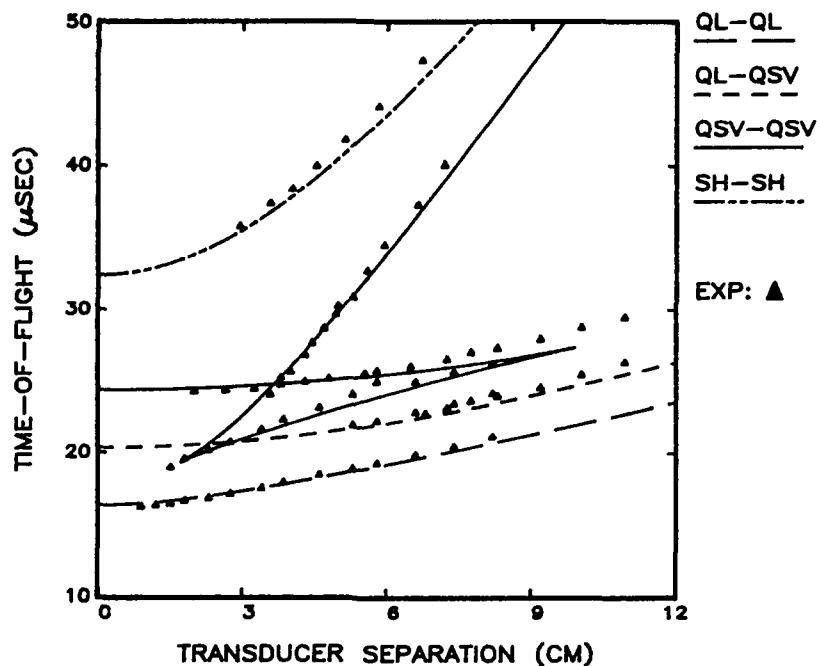
Fig. 1 Time of flight of AU signals in 2.51" GR/EP.

EXTRACTION OF ELASTIC CONSTANTS FROM AU DATA

For a given composite plate of known thickness, three
elastic constants can be determined immediately using one
normal incident longitudinal wave and two normal incident shear
waves with mutually perpendicular polarizations. (It is
assumed that the direction perpendicular to the plate is one of
the principal axes of the elastic solid, as is usually the
case.) The remaining elastic constants may be determined from
the times-of-flight of the AU signals in an iterative manner.
The exact iteration procedures depend on the symmetry of the
composite, but the approach may be illustrated in the
unidirectional case, as follows.

A unidirectional composite has hexagonal symmetry and five
independent elastic stiffness constants. Assuming that the
fibers are oriented parallel to the x-direction, the five
constants are then C_{11}, C_{22}, C_{44}, C_{55}, and C_{12}. For a plate of
unidirectional composite with fibers lying in the plane, the
three constants C_{22}, C_{44} and C_{55} can be determined using normal
incidence contact mode ultrasonic velocity measurements. The
determination of the two remaining constants in an in-situ,
one-sided manner is achieved using the TOF of the QL -> QL echo
in the AU signal in an iterative procedure. The QL -> QL echo
was easily identified because it has the smallest time-of-

flight, except the surface echoes. The surface echoes were identified because their times-of-flight extrapolated through zero at zero separation of the transducers.

The iteration process began by making initial guesses for the values of C_{11} and C_{12}; these guesses need not be of the correct order of magnitude as the actual values. Together with the three constants C_{22}, C_{44}, and C_{55} obtained earlier using normal incidence, the slowness surfaces of the composite were computed. Based on the slowness surfaces, the QL -> QL times-of-flight were calculated as a function of transducer separation distance. The values of C_{11} and C_{12} were varied to minimize the sum of the squares of the TOF differences (between the measured and computed values.) This sum is written as follows:

$$Q = \sum_{i=1}^{n} d_i^2 \qquad (1)$$

where $d_i = t_i - t_{ic}$, t_i is the measured TOF and t_{ic} is the computed TOF for the ith separation distance, and n is the total number of data points (separation distances) in the experiment. When Q was minimized, its value was called the "residual".

It was found that the C_{11} and C_{12} values that gave the best fit to the experimental data were often significantly different from the correct answers obtained by ultrasonic measurements after cutting the sample. This was believed to be caused by errors in the measured time-of-flight data; a study of the sensitivity of the "inverse process" to random and systematic errors in TOF ensued. Computer simulations were performed for both random errors commensurate with the experimental apparatus accuracy and constant systematic errors such as those caused by an error in the trigger zero of time. It was found that, for the random errors tested, the accuracy for extracting the elastic constants (C_{11} and C_{12}) was quite good when there was a sufficient number of data points, e.g., n was 10 or greater. However, systematic errors in TOF were found to have a large effect on the extraction accuracy. Based on the assumption that the systematic error was an additive constant, the simulated TOF data were varied by adding or subtracting a small constant, called the "time shift", while C_{11} and C_{12} were determined at each step using the minimization procedure described above. After each time shift, the "residual" was computed. It was found in the computer simulation that the "residual" showed a minimum and the values of C_{11} and C_{12} corresponding to this minimum were closest to the true values. (In the simulated data the correct time shift is of course automatically zero.) The computer simulation results for systematic error is shown in Fig. 2(a). This method was applied to the AU data obtained on three unidirectional composites.

(a)   (b)
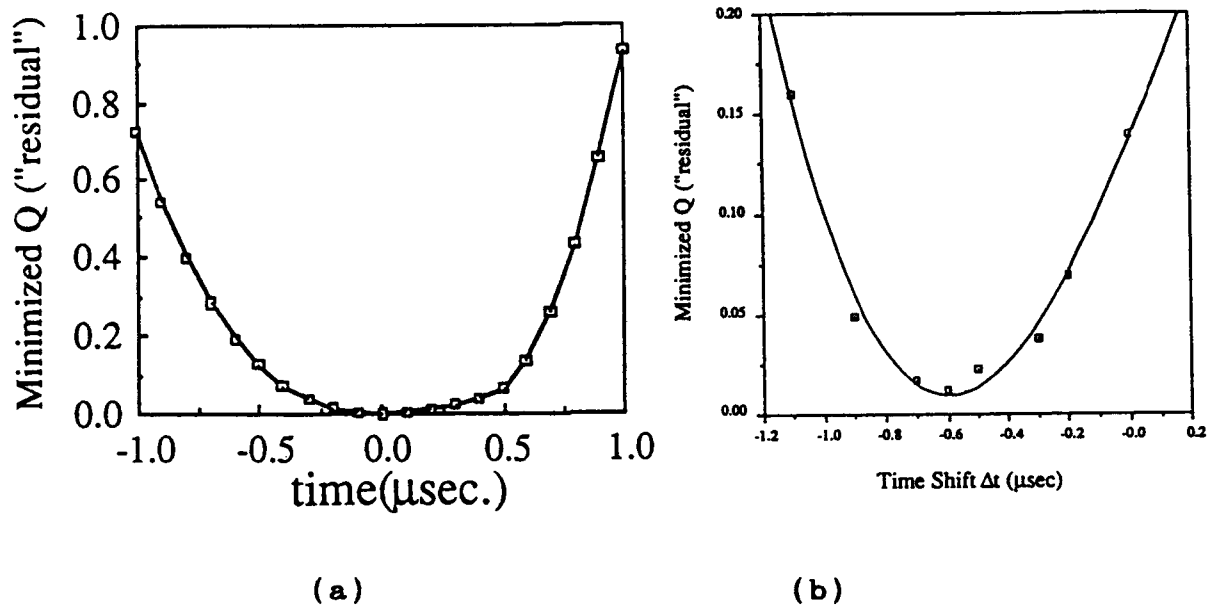
Fig. 2   Effect of systematic error on the extraction of
elastic constants. (a) Computer simulation, (b)
Experimental results in unidirectional graphite/epoxy.

RESULTS OF ELASTIC CONSTANTS EXTRACTION

Three 1" thick unidirectional graphite/epoxy laminates,
made by LTV Aerospace and Hercules Aerospace, were used as
samples.   The transducers used in the AU configuration were 1
MHz, 0.5" diameter longitudinal wave transducers.   The
experimental data were taken at various transducer separation
distances.   The measured QL -> QL mode TOF data versus the
separation distance for one of the samples are shown as the
lowest branch in Fig. 1.   This curve was then shifted up and
down by a small correction time and, after each shift, the
values of C_{11} and C_{12} were varied until Q was minimized.   The
minimized Q was plotted versus the time shift; much like the
computer simulation, the "residual" showed a minimum.   The C_{11}
and C_{12} values corresponding to this minimum, at a time shift
of 0.6 microseconds, were taken to be the final answers.   The
experiments were performed twice on each of the three one-inch
thick samples and the results are summarized in Table 1.   The
nominal correct values of C_{11} and C_{12} for these samples were,
respectively, 128 GPa and 6.9 GPa.   As can be seen, the results
extracted from the AU data were reasonably accurate.

Table 1. Elastic constants extraction from AU data
for unidirectional graphite epoxy composites

	Sample	LTV No. 1	LTV No. 2	Hercules
Trial 1	C_{11}	127 GPa	142 GPa	126 GPa
	C_{12}	7.8	8.3	6.4
Trial 2	C_{11}	121	141	122
	C_{12}	7.6	8.8	7.4

DELAMINATION SIZING IN THICK COMPOSITES

In anisotropic composites, the nonuniform beam spreading in different directions lead to distortion of the flaw size and shape. For example, a pulse-echo C-scan of a circular delamination in a unidirectional graphite epoxy laminate would appear as elliptical with its long axis along the fiber direction. In this paper the problem of flaw sizing in the presence of material anisotropy is addressed. Attention is given to the case where the ultrasonic beam is of the same order as the flaw size and the measurement mode is a pulse-echo immersion test. In this regime a line scan over a delamination will generally produce a bell-shaped curve of flaw signal amplitude versus scan distance. However, the "apparent size" using the full width at the half maximum (FWHM) usually does not relate to the flaw size in a simple manner because the width of the curve depends on a large number of parameters, including transducer frequency and size, flaw depth, water path, attenuation, elastic anisotropy of composite, and, of course, flaw size.

In this work, while making a linear scan through the center of a circular delamination, the flaw echo waveform was digitized and Fourier transformed at each position along the scan. The amplitude of several frequency components within the signal bandwidth were stored for subsequent analysis. Each frequency component will produce a bell-shaped curve when plotted against scan coordinate. To extract size information from these curves, theoretical curves were produced for each frequency based on the transducer size, flaw depth, water path, elastic anisotropy of the host, and an initial guess of the flaw size. The size of the flaw was iterated while the computed and experimental bell-shaped curves were compared and their difference minimized in the least squares sense. The size that produced the best agreement between the computed and measured curves was taken to be the answer.

The theoretical computation of the flaw response curve was achieved using Auld's reciprocity relationship [8] and the Gauss-Hermite model of Newberry and Thompson [9]. The anisotropy of the composite enters into the calculation via the slowness surfaces. The details of the calculation were given elsewhere [2]. The steps of the iterative flaw sizing procedure are shown in Fig. 3.
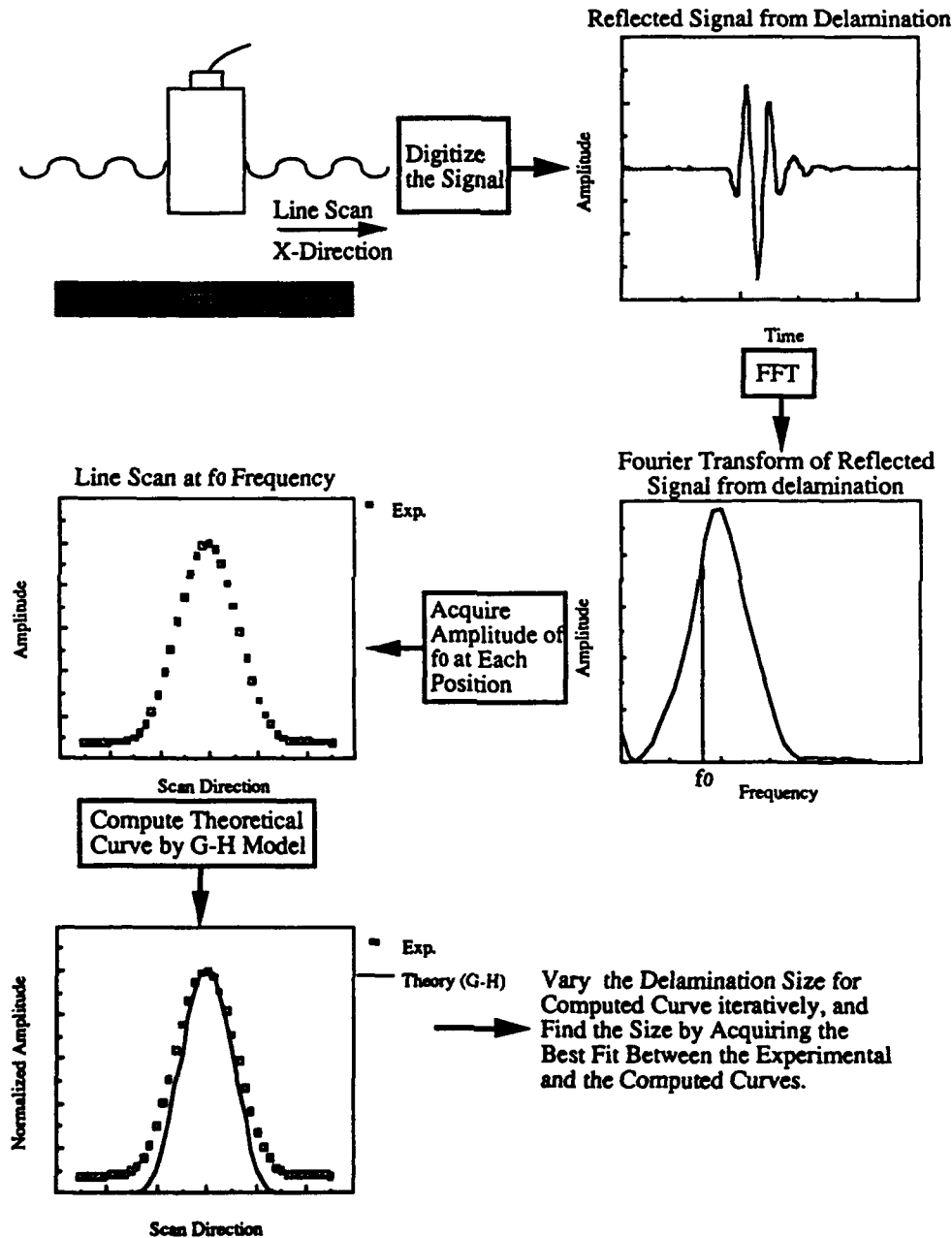
Fig. 8   Procedure for iterative flaw sizing using the Gauss-Hermite beam model.

The experiments were performed on a nominal 0.25" (6.4 mm) diameter circular delamination in a 7 mm thick unidirectional graphite epoxy laminate [2,10]. Thicker pieces of unidirectional composites were added on top of the 7 mm sample to simulate a thicker composite and to allow flaw sizing at different depth. A number of transducer of different frequency, size and focal length were used. Table 2 lists some of the experimental flaw sizing results, and their comparison to the apparent sizes.

Table 2. Apparent size and computed size using the Gauss-Hermite beam model for a 0.25" flaw at three different depths in graphite epoxy. The 2 MHz component of a 2.25 MHz, 0.5" diameter transducer was used.

Flaw depth	Size method	Scan along to fiber	Scan normal to fibers	% diff.
1.07 cm	Apparent	0.303"	0.272"	11
	Computed	0.289	0.278	4
1.92 cm	Apparent	0.325	0.270	18
	Computed	0.274	0.272	1
2.72 cm	Apparent	0.382	0.285	30
	Computed	0.272	0.253	1

In Table 2 the "% difference" is between the scan direction along fibers and the scan direction normal to fibers. This difference was found to increase with the depth of the flaw for results based on the apparent (FWHM) sizing method. The apparent sizes for scans along the fibers were overestimated considerably. The computed sizes after the Gauss-Hermite beam model correction for material anisotropy were much closer to the nominal size and also showed less of a difference between the two scan directions.

CONCLUSION

We have developed two ultrasonic methods for (1) determining the elastic constants of composite laminates by conducting single-sided time of flight measurements of the acousto-ultrasonic signal, and (2) for improving the flaw sizing procedure in thick composites by reducing the distortion effects due to material anisotropy. Both methods have been validated experimentally on unidirectional composites.

REFERENCES

1. A. Minachi, D. K. Hsu and R. B. Thompson, "Single-Sided
Determination of Elastic Constants of Thick Composites Using
Acousto-Ultrasonic Technique", to be published.

2. A. Minachi, F. J. Margetan and D. K. Hsu, "Delamination
Sizing in Composite Materials Using Gauss-Hermite Beam Model",
to be published.

3. B. A. Auld, Acoustic Fields and Waves in Solids, John Wiley
and Sons, New York, 1973.   Appendix 3.

4. D. K. Hsu and F. J. Margetan, "Quantitative Analysis of
Oblique Echoes in Thick Composites Using the Slowness Surface",
Proceedings of American Society for Composites, Fifth Technical
Conference, East Lansing, MI., June 12-14 (1990).   pp.945-954.

5. A. Vary and K. J. Bowles, "Ultrasonic Evaluation of the
Strength of Unidirectional Graphite-Polyimide Composites", NASA
TM-X-73646 (1977).

6. A. Vary, "Acousto-Ultrasonic Characterization of Fiber
Reinforced Composites", Materials Evaluation, 40, 650 (1982).

7. A. Vary, "The Acousto-Ultrasonic Approach", in Acousto-
Ultrasonics:Theory and Application, edited by J. C. Duke, Jr.,
Plenum Press, 1988.

8. B. A. Auld, "General Electromechanical Reciprocity Applied
to Calculation of Elastic Wave Scattering Coefficients", Wave
Motion, 1, 3-10 (179).

9. B. P. Newberry and R. B. Thompson, "A Paraxial Theory for
the Propagation of Ultrasonic Beam in Anisotropic Solids", J.
Acoust. Soc. Amer., 85, 2290-2300 1989).

10. D. K. Hsu and A. Minachi, "Defect Characterization in Thick
Composites by Ultrasound", Review of Quantitative NDE, Vol. 9,
edited by D. O. Thompson and D. E. Chimenti, Plenum Press,
1990.   pp. 1481 - 1488.

Application of Neutron Diffraction in Measuring Residual Strains in High-Temperature Composites

A. SAIGAL AND D. S. KUPPERMAN

ABSTRACT

An experimental neutron diffraction technique was used to measure residual thermal strains developed in high–temperature composites during postfabrication cooling. Silicon carbide–fiber–reinforced titanium aluminide (over the temperature range 20–950°C) and tungsten and Saphikon–fiber–reinforced nickel aluminide composites (at room temperature) were investigated. As a result of thermal expansion mismatch, compressive residual strains and stresses were generated in the silicon carbide fibers during cooldown. The axial residual strains were tensile in the matrix and were lower in the nickel aluminide matrix than in the titanium aluminide matrix. The average transverse residual strains in the matrix were compressive. Liquid–nitrogen dipping and thermal cycling tend to reduce the fabrication–induced residual strains in silicon carbide–fiber–reinforced titanium aluminide matrix composite. However, matrix cracking can occur as a result of these processes.

INTRODUCTION

Silicon carbide–fiber–reinforced titanium matrix composites are currently being evaluated for structural applications in jet engines because of their low weight, high strength, and high stiffness potential at high temperatures. In addition, tungsten and Saphikon–fiber–reinforced nickel aluminide matrix composites are also being investigated.

High–temperature composites are usually fabricated at temperatures above 900°C and, because there is usually a significant mismatch between

A. Saigal, Department of Mechanical Engineering, Tufts University, Medford, MA 02155

D. S. Kupperman, Materials and Components Technology Division, Argonne National Laboratory, Argonne, IL 60439

the coefficients of thermal expansion of the fibers and the matrix, the thermally induced residual strains and stresses can be significant. In many engineering composites, frictional forces at the interfaces often provide the necessary link between the reinforcements and the matrix because chemical bonding is either weak or nonexistent (1,2). Because frictional forces and subsequent behavior of the composites depend on the residual stresses that develop during cooldown after fabrication, it is important to have an idea of the residual strains and stresses that exist in the composites.

For all composites with crystalline constituents, neutron diffraction is a powerful tool for measuring bulk elastic residual strains from which residual stresses can be calculated in much the same way as done with X-ray diffraction (3, 4). Allen et al. used a neutron diffraction method to measure residual stresses and load-induced bulk stresses in a metal matrix composite (5). Kupperman et al. used a neutron diffraction technique to study the variation of residual strains and stresses in a silicon carbide–whisker–reinforced alumina matrix composite with temperature and volume fraction of whiskers (6). The results agreed reasonably well with calculated values (7). Krawitz et al. measured residual stress as a function of temperature in a high volume fraction tungsten carbide–nickel cemented carbide composite (8). In addition, Majumdar et al. used the Intense Pulsed Neutron Source (IPNS) and the General Purpose Powder Diffractometer (GPPD) at Argonne National Laboratory to measure residual strains in a number of engineering composite materials (9).

In the present study, the neutron diffraction technique was used to measure residual thermal strains, developed during cooling, in silicon carbide–fiber–reinforced titanium aluminide and tungsten and Saphikon–fiber–reinforced nickel aluminide high–temperature composites. The effects of fabrication procedures and thermal processing, such as liquid–nitrogen dipping and thermal–cycling, on residual strains were also studied.

NEUTRON DIFFRACTION MEASUREMENTS

Thermal neutrons with wavelengths on the order of the lattice spacings are used in the experiments. Bragg's law of diffraction can be applied to neutrons as follows:

$$2\ d_{hkl}\ \sin\theta\ =\ \lambda\ hkl \qquad (1)$$

where d_{hkl} is the lattice spacing, 2θ is the angle between the incident and the scattered neutron beams when a Bragg peak is detected, λ is the

de Broglie wavelength of the neutron, and *hkl* are the Miller indices of the diffracting planes. The data were collected in the GPPD. The GPPD is a time–of–flight instrument. The spectrum is measured at a fixed Bragg angle 2θ of $\pm 90°$. The main advantage of a pulsed neutron source over a steady neutron source is that it uses a "white" spectrum of neutron energies. Therefore, during a single measurement at IPNS, many diffraction peaks, i.e., crystallographic directions, of each phase are recorded simultaneously in various spatial directions.

In neutron diffraction, the lattice spacings in various crystallographic directions of stress–free powders and/or fibers (which are used to fabricate the composite) are determined first. The shifts in the Bragg peaks of the stresses constituents of the composite are then determined. For any {*hkl*} diffraction peak, the lattice strain is given by

$$\varepsilon_{hkl} = \frac{d_{hkl} - d_0}{d_0} \tag{2}$$

where d_{hkl} and d_0 represent the average interplanar spacings in the stressed and unstressed lattice, respectively. With a pulsed source, changes in lattice spacing are related to time–of–flight shifts in the Bragg peaks. The relationship of time–of–flight to neutron wavelength is described by

$$\lambda = ht/mL \tag{3}$$

where h is the Planck's constant, t is the time of flight for a neutron to reach a detector after leaving its source, L is the flight path of the neutron from its source to the detector, and m is the neutron mass. Bragg's law can then be written as

$$t = (2dmL/h) \sin\theta \tag{4}$$

and $$\varepsilon_{hkl} = \Delta t/t \tag{5}$$

Residual strains in the fibers and the matrix, parallel and perpendicular to the fibers, are measured simultaneously by aligning the fibers at an angle of $45°$ to the neutron beam and analyzing neutron diffraction data with detectors $\pm 90°$ from the neutron beam direction, as shown in Fig. 1.

The composite systems under investigation consist of:

1. 35 volume percent silicon carbide (SCS–6) fibers in a Ti–14Al–21Nb
    (Ti3Al) matrix. Titanium aluminides (Ti3Al) offer significant
    advantages in operating temperature and weight as compared to the
    traditional Ti–6Al–4V matrix. Columnar grains of the 140 μm
    diameter fibers were oriented normal to the fiber axis. The samples
    were 35 x 35 x 2 mm in size.

2. 35 volume percent tungsten and 30 volume percent Saphikon fibers
    in nickel aluminide matrix. The samples were 150 x 150 x 1.25 mm
    in size. The tungsten fibers and saphikon fibers were 150 μm and
    200 μm in diameter, respectively.

RESULTS AND DISCUSSIONS

A temperature–dependent experiment was carried out on the as–
fabricated silicon carbide–fiber–reinforced titanium aluminide sample.
Lattice parameters for various crystallographic directions were measured
parallel and perpendicular to the fiber axis. The diffraction peak that
provided the most useful data for silicon carbide fibers was that for the
{220} plane. For the matrix, the 1.75 Å line provides the average residual
strains in the matrix. Figure 2 shows the measured average residual
strains in the silicon carbide (SCS–6) fibers and the titanium aluminide
(Ti–14Al–21Nb) matrix, parallel to the fiber axis, as a function of
temperature. At room temperature, the strain in the fiber is compressive
(–0.0019) and that in the matrix is tensile (+0.0042). As expected, the
residual strains decreased as the temperature was increased from room
temperature to the processing temperature, approaching a value of zero
and a strain–free state near 806°C. This indicates that during the early
cool down period following fabrication at 950°C, the thermal stresses
generated in the composite may be quickly relaxed by creep. At room
temperature, the transverse strains in the fiber and matrix are both
compressive (–0.0005 and –0.0007, respectively) and, as in the axial
strains, decrease as the temperature is increased from room temperature
to processing temperature.

The relative increases in the fiber and matrix lattice spacings with
increasing temperature, relative to the room–temperature value, for
directions parallel and perpendicular to the fiber axis, are shown in Figs.
3 and 4. The similarity in expansion curves (parallel to fiber) for various
crystallographic planes of the matrix indicates a state of plane strain in
the sample. In addition, the anisotropy of the matrix can be clearly seen
in Fig. 4, where the expansion curves for different crystallographic

directions vary significantly for the matrix. This is most likely because the sample is very thin perpendicular to the fiber axis.

To reduce residual strains and stresses, the fabrication procedures and the thermal history of the composites can be altered. Two commonly used procedures are liquid–nitrogen dipping (LND) and thermal cycling. Figure 5 compares the measured residual strains in as–fabricated, liquid–nitrogen–dipped, and thermally cycled specimens. It can be seen that tensile strains in the matrix and compressive strains in the fibers (parallel to the fiber axis) are lower in the LND and thermally cycled specimens than in the as–fabricated sample. Thermal cycling appears to reduce the residual strains more than LND. It was also found that the matrix and fiber strains perpendicular to the fibers did not change significantly with processing.

Using Hooke's law, the residual stresses in the fibers can be calculated from the residual strains. Based on Table 1, there is no doubt that the axial stresses (parallel to fibers) in the fibers, and to a certain extent the stresses perpendicular to fibers, are reduced by the processing methods discussed. The limited plastic deformation of the matrix is not sufficient to produce the observed reductions in residual strains and stresses. It is possible that matrix cracking occurs because of thermal processing; this is further suggested by elastic moduli measured by the velocity of ultrasound propagating perpendicularly to the fibers. Decreases in Young's modulus for liquid–nitrogen–dipped (134 GPa) and thermally cycled (131 GPa) samples were measured as compared to the as–fabricated (137 GPa) sample.

Table 2 shows the measured strains in the matrix in various composites. The axial residual strains are tensile in the matrix and are lower in the nickel aluminide matrix than in the titanium aluminide matrix. It also shows that the strains in the nickel aluminide matrix due to 35 vol.% tungsten fibers and 30 vol.% Saphikon fibers are similar.

CONCLUSIONS

Neutron diffraction was used to measure, as a function of temperature, residual thermal strains in a 35 vol.% silicon carbide (SCS–6) fiber–reinforced titanium alloy (Ti–14Al–21Nb) matrix, high–temperature composite. Residual strains (parallel to fiber axis) decreased as the temperature rose from room temperature to the processing temperature, approaching a value of zero and a strain–free state near 806°C. This indicates that during the early cooldown period following fabrication at 950°C, the thermal stresses generated in the composite may be quickly relaxed by creep.

The similarity in expansion curves (parallel to fiber axis) for various crystallographic planes of the titanium aluminide matrix indicates a state of plane strain in the sample.

It has been shown that significant residual strains and stresses develop in these composites during cooldown from the processing temperature to room temperature. The silicon carbide fibers are under compressive residual strains and stresses. Strains in the matrix (parallel to fiber axis) are tensile and are lower in the nickel aluminide matrix than in the titanium aluminide matrix. The average transverse strains in the matrix are compressive.

Liquid–nitrogen–dipping and thermal cycling tend to reduce the fabrication–induced residual strains in the silicon carbide–fiber–reinforced titanium aluminide matrix composite. However, matrix cracking can occur as a result of these processes.

ACKNOWLEDGMENTS

REFERENCES

1. Phillips, D. C., 1974. "Interfacial Bonding and Toughness of Carbon Whisker Reinforced Glass and Glass–Ceramics." Journal of Materials Science, 9(11):1847–54.

2. Prewo, K. M. and J. B. Brennan, 1980. "High–Strength Silicon Carbide Fiber–Reinforced Glass–Matrix Composites," Journal of Materials Science, 15(2):463–68.

3. Hutchings, M. T. and C. G. Windsor, 1986. "Industrial Application of Neutron Scattering," in Neutron Scattering, K. Skold and D.L. Price, ed. Academic Press, New York.

4. Noyan, I. C. and J. B. Cohen, 1987. Residual Stress, Springer–Verlag, New York.

5. Allen, A. J., M. Bourke, M. T. Hutchings, A. D. Krawitz, and C. G. Windsor, 1987. "Neutron Diffraction Measurements of Internal Stress in Bulk Materials:–Metal Matrix Composites," in Residual Stresses in Science and Technology, E. Macherauch and V. Hauk, ed. DGM Informations–gelsellschaft Verlag, Oberursel, 1:151–57.

6. Kupperman, D. S., S. Majumdar, S. R. MacEwen, R. L. Hitterman, J. P. Singh, R. A. Roberts, and J. L. Routbort, 1988. "Nondestructive Characterization of Ceramic Composite Whiskers with Neutron Diffraction and Ultrasonic Techniques," in Review of Progress in Quantitative Nondestructive Evaluation, D.O. Thompson and D.E. Chimenti, ed. Plenum Publishing Corp., 7B:961–69.

7. Majumdar, S., D. S. Kupperman, and J. P. Singh, 1988. "Determination of Residual Thermal Stresses in a SiC–Al2O3 Composite Using Neutron Diffraction," Journal of American Ceramic Society, 71(10):858–63.

8. Krawitz, A. D., D. G. Reichel, and R. L. Hitterman, 1989. "Residual Stress and Stress Distribution in a WC–Ni Composite," Journal of Materials Science and Engineering, A119:127–34.

9. Majumdar, S., J. P. Singh, D. S. Kupperman, and A. D. Krawitz, 1991. "Application of Neutron Diffraction to Measure Residual Strains in Various Engineering Composite Materials," Journal of Engineering Materials and Technology, 113:51–59.

Table I - Residual strains and stresses in fibers in as-fabricated, liquid–nitrogen–dipped (LND), and thermally cycled (TC) Ti aluminide matrix/SiC fiber composites

	Parallel to Fiber		Perpendicular to Fiber	
Processing	Strain	Stress (MPa)	Strain	Stress (MPa)
As–fabricated	-0.0019	-970	-0.0005	-483
LND	-0.0012	-652	-0.0005	-408
TC	-0.0008	-470	-0.0005	-366

Table II -   Residual Strains in Matrix

Matrix	Parallel to Fiber	Perpendicular to Fiber
Titanium Aluminide (35 vol.% SiC fibers)	0.0042	−0.0007
Nickel Aluminide (35 vol % W fibers)	0.0013	−0.0005
Nickel Aluminide (30 vol%. Saphikon fibers)	0.0014	−0.0004
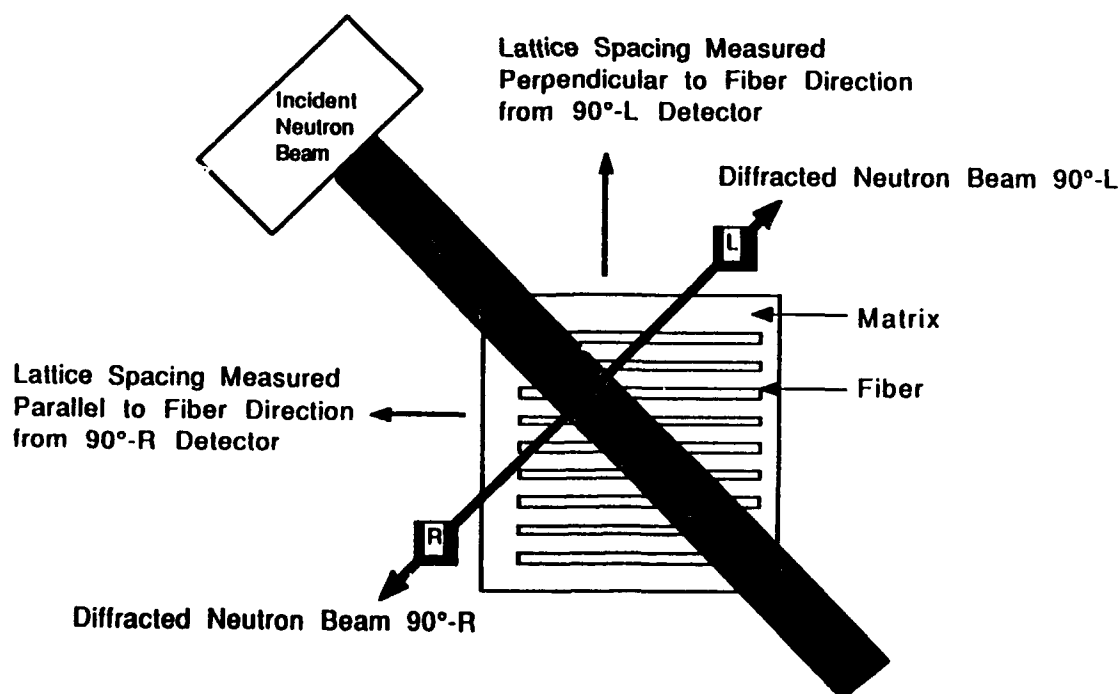
Figure 1.   Schematic representation of experimental set-up.
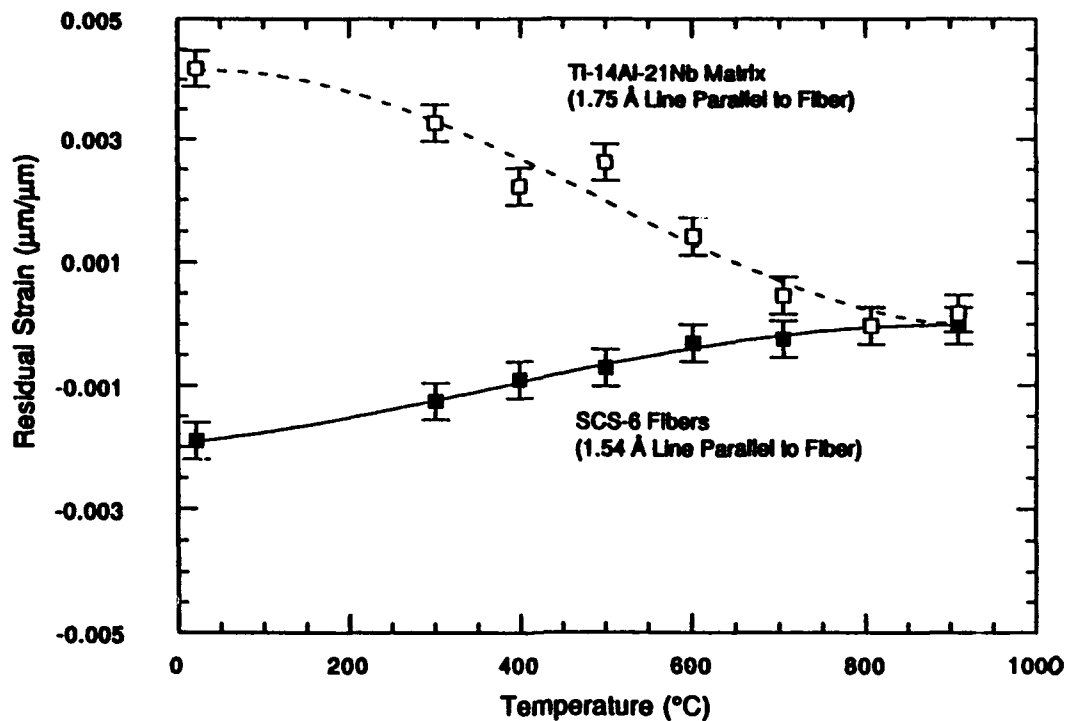
Figure 2.   Residual strains in silicon carbide (SCS–6) fibers and
titanium aluminide (Ti–14Al–21Nb) matrix, parallel
to fiber axis, as a function of temperature.
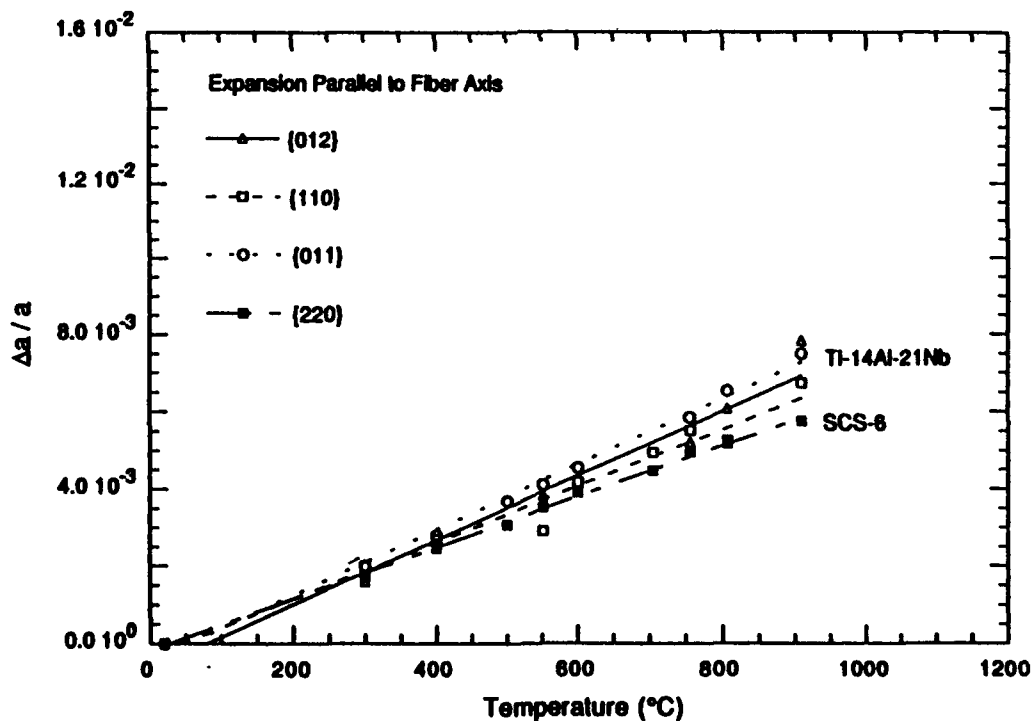
Figure 3.   Increases in lattice spacing, relative to room
temperature and parallel to fiber axis, as a function
of temperature for SiC fiber (220) plane and several
Ti alloy matrix crystallographic directions.
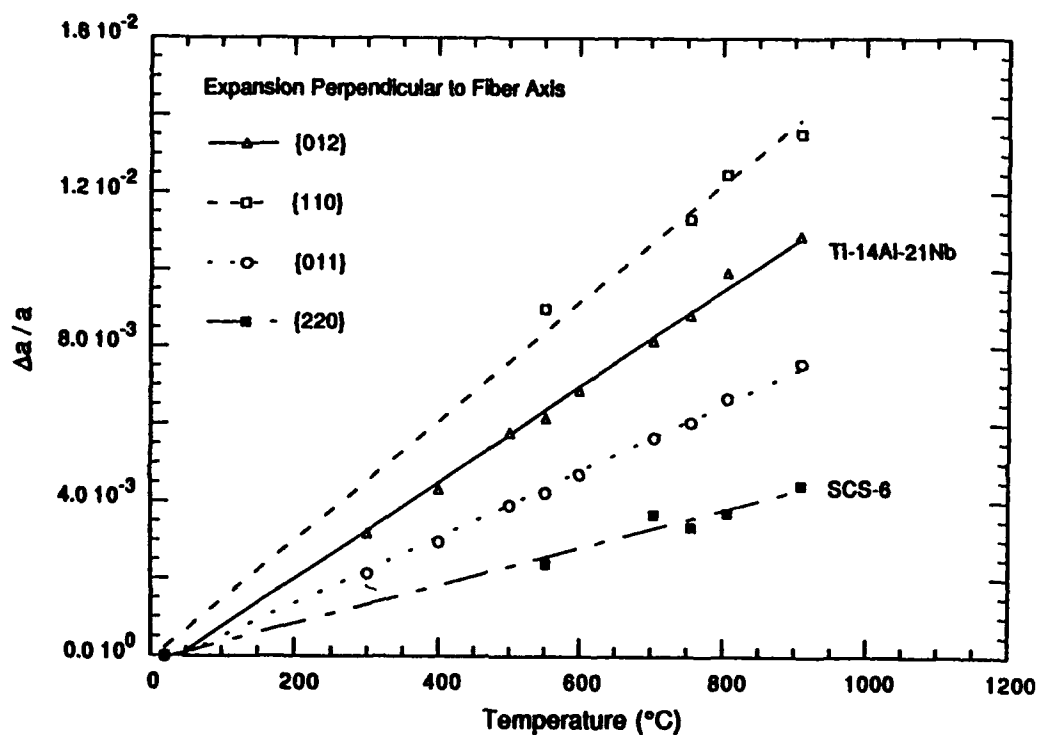
Figure 4. Increases in lattice spacing, relative to room temperature and perpendicular to fiber axis, as a function of temperature for SiC fiber {220} plane and several Ti alloy matrix crystallographic directions.
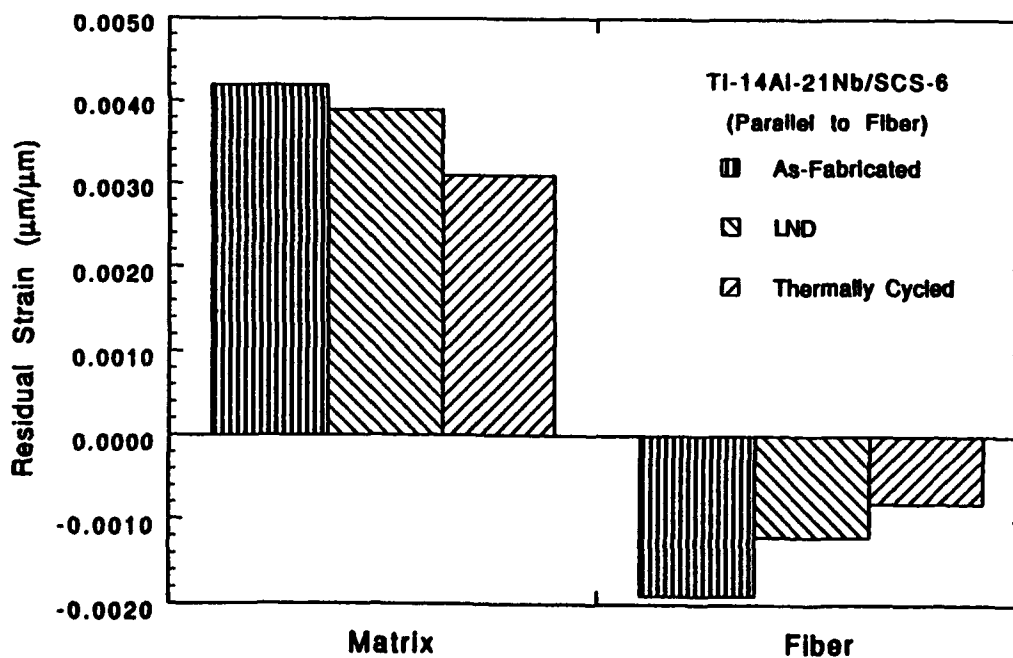
Figure 5. Residual strains in silicon carbide (SCS–6) fibers and titanium aluminide (Ti–14Al–21Nb) matrix, parallel to fiber axis, in as–fabricated, liquid–nitrogen–dipped, and thermally cycled specimens.

Stabilization of Mode II Interlaminar Fracture Toughness Test by Means of Coordinate Conversion Control Method

KIYOSHI TANAKA

ABSTRACT

Application of the Coordinate Conversion Control method to End Notched Flexure (ENF) tests on unidirectional carbon fiber reinforced plastics made it possible to stabilize the fracture propagation and to obtain a continuous R-curve for Mode II interlaminar fracture toughness.

By means of this method, fracture propagation behavior of various CFRPs as well as the effects of the thickness and the material of the fracture starter film were investigated.

It was found that the Polyimide film with 7.5 micro-millimeter thickness was suitable to obtain a low fracture initiation toughness enough to lead to stable fracture propagation even in very brittle epoxy matrix CFRPs. It is also notable that the APC-2 and the toughened epoxy matrix CFRP showed increasing R-curves reaching a plateau after 15 to 25 mm long propagation, whereas the conventional epoxy matrix CFRPs showed flat R-curves from the start of the fracture.

Furthermore comparison was made between this Mode II propagation toughness and Mode I fracture propagation toughness obtained by means of DCB tests on these materials.

INTRODUCTION

In the case of advanced fiber reinforced plastics for aeronautics and space application, the Mode II interlaminar fracture toughness, GIIc, is considered to have close relationship with the compression after impact (CAI) strength, one of the most important characteristics to evaluate advanced FRP. In order to investigate GIIc of unidirectional advanced fiber reinforced plastics the end notched flexure (ENF) test is widely used because it requires only ordinary bending test apparatus. Although the fracture toughness at initiation or at the maximum load can be calculated from the ENF test result, fracture propagation toughness can not be studied because an unstable fracture takes place after the maximum load is reached.

Stabilization of the fracture propagation in ENF test was achieved by Kageyama et al.(1) by means of the COD controlled ENF test method, in which the sliding between upper and lower surfaces of the crack of the

Kiyoshi Tanaka, Chemicals Res. Lab., Advanced Materials & Technology Research Labs., Nippon Steel Corpora-
tion, 1618 Ida, Nakaharaku, Kawasaki 242, Japan

test specimen is measured by a well designed displacement gage mounted on the specimen and the servo hydraulic test machine controls the loading head position so that the sliding amount increases slowly and monotonously, hence preventing fast crack propagation. The fact that this control method was successful to stabilize the Mode II crack propagation suggested that the reason of occurrence of unstable fracture propagation was not a result that a materials critical toughness was reached as in the case of the cleavage fracture in steel materials, but a result of breakage of energy balance between the driving force and the material fracture resistance curve, R curve, in terms of crack extension. Furthermore this indicates that the fracture toughness at the maximum load is not the material constant and it is necessary to obtain the whole figure of the R curve for correct evaluation of the Mode II interlaminar fracture characteristics.

After the report by Kageyama et al. the present author considered that it should be possible to stabilize the ENF test if the test machine is properly controlled so that the actuator retreats as soon as crack propagation takes place, and decrease the driving force.

In the present paper results of experiments conducted with this consideration and discussions on the results are reported.

EXPERIMENTAL PROCEDURE

One of the methods that has possibility to stabilize the unstable fracture in fracture test is the Coordinate Conversion Control method. In this method, the movement of actuator to load the specimen is controlled so that the amount F shown by Eq.(1) increases monotonously.

$$F = D - k \cdot P \tag{1}$$

where D : Actuator stroke output (i.e. output of amplifier to measure the actuator stroke)

P : Load out put

k : a constant

The basic idea is simple as shown in Fig. 1. The curve 0-a-b-c-0 is an illustration of the relationship between the load and the deflection in the ENF test. In an ordinary test method, the curve between a and c can not be observed and an unstable fracture takes place leaving a direct line from a to c. The reason for the unstable fracture is that just the deflection is controlled in the ordinary method and test machine can not follow the curve from a to c through b. However, when the coordinate is changed as shown by Y2-0-X2 , the whole curve will become as illustrated in Fig. 1.b, and the reason for the unstableness between a and c disappears.

In other words, if P drops at some moment in an actual test because of small amount of fracture, the test machine moves so as to keep the amount F unchanged when the Coordinate Conversion Control method is applied. This control induces decrease in D, i.e. retreat of the loading head, resulting in unloading of the specimen and prevention of further propagation of the fracture. Further fracture propagation is possible if F is increased. Thus the fracture propagates stably when slow increase of F is set in the test machine program.

In the actual test process, the load and displacement outputs from the test machine is input into a conditioner consisting of two amplifiers as shown in Fig. 1.c. Here amplifiers are used just for separation purpose. Another type of conditioner consisting of just electric resistances are

also possible if the potential drop caused by the internal resistance is taken into account. The difference between the two amplifiers as shown in the figure gives F and is used as the feed back signal to the test machine. The test machine is set to control this feed back signal just the same way as in the strain control method in a fatigue test. Because F is similar to the deflection, in the meaning and in the size as well, the program for the machine is same as deflection speed control, i.e. 0.5 mm/min for example.

The constant, k, decides the degree of response of machine to the drop in the load, which is the result of the crack propagation, and shall be a proper number determined after consideration on the relationship between the load and the actuator stroke before and after the maximum load and also on the condition of amplifiers. The constant, k, can be obtained by calculation as follows.

$$k = 0.6 \sim 0.8 \cdot Co \cdot Sp / Sd \qquad\qquad (2)$$

where Co : Compliance of specimen (deflection / load) at the initial
           linear portion of loading
      Sp : load vs load output ratio (N / volt)
      Sd : Deflection vs. deflection output ratio (mm / volt)

An arbitrary number of 0.6 to 0.8 shown in Eq.(2) corresponds to the slope of Y2-O in Fig. 1.a. When k = 1, Y2 axis becomes parallel to the first linear portion of the record, whereas it becomes parallel to the Y axis when k = 0. The value k shall be decided such that the Y2 axis is steeper than the initial portion of the record(O to a) but not steep as the line from a to b. The value k can be calculated using fracture mechanics because the curve a to c can be calculated assuming a constant fracture propagation toughness.

For this control method, a test machine with quick response capability may be required. Although it is not clear what level of quickness is required, an electro-servo-hydraulic controlled test machine made by Shimadzu, as shown in Fig. 2 was used during the present investigation and was satisfactory in the stabilization. This machine is a fatigue test machine with a capacity of 10 kN for cyclic loading. Though two amplifiers were used at the initial stage of study, a controlling board as shown in the figure has been prepared and used eventually. This control board facilitates the same circuit as Fig. 1.c and simplifies the setting of the constant, k, which can be set by the vernier dial on its panel surface.

Using the new method, fracture propagation behavior of various PAN-CF/epoxy, Pitch-CF/epoxy, APC-2 and toughened epoxy unidirectional CFRPs was studied. The characteristics of those materials are show in Table 1. Effects of the thickness and material difference of the fracture starter film placed during CFRP lay-up process were also investigated.

RESULTS OF EXPERIMENTS

Figures 3 shows the typical examples of the test results. Figure 3.a is the result of the test on the material 1 of PAN/250°F-epoxy under the stroke control method whereas Fig. 3.b under the Coordinate Conversion Control method on the same material. Although an unstable fracture took place in Fig. 3.a, a stable fracture propagation became possible, as shown in Fig. 3.b, by the Coordinate Conversion Control method. The unloading curves shown in the Fig. 3.b were used to calculate the crack length during propagation. (The unloading is not the necessary sequence

for the stabilization of the crack propagation.)

For the stabilization of the fracture propagation a careful setting of the test machine was necessary. Even though the settings for the test machine are adequate the unstable fracture tends to take place when any of the following conditions is satisfied.

1) Fracture initiation toughness is high compared to the fracture propagation toughness, because of the dullness of the initial notch tip.
2) The R curve is flat or decreasing.
3) The R curve is zigzag like saw blades showing up and down changes.
4) The crack length is large.
5) The test speed is high.

The basic reason for the unstable fracture found in the cases shown above is thought to be just one and is the lack of the capacity (sensitivity, speed and accuracy).

Figure 4 shows test results on the effects of the conditions of the starter film preparation for the ENF test specimens. Here four different conditions were applied. One is the precrack method by means of mode I opening fracture from a film starter. Others are film starter without a precrack. Three different materials were employed. For polyimide films of 13 micro-m and 7 micro-m thickness, a spray type release agent was applied. A 13 micro-m PTFE film without any release agent was also used.

It was found from this investigation that the unstable fracture propagation could not be prevented even in the Coordinate Conversion Control method when the film was thick. Polyimide film with 7 micro-mm thickness was suitable to obtain a stable fracture indicating that a low initiation toughness is necessary for the stable fracture propagation as stated above. It is thought that the test machine can not respond the quick change of the toughness in the case of high initiation fracture toughness.

It was also found in the tests that the control was easy for the materials with tough matrices such as the toughened epoxy and PEEK. The reason for this is the rising R curve for these materials. Figure 5 shows the R curves for 3 kind of materials. The fracture toughness values for continuous curves in the figures are calculated continuously by a computer using all data during loading. The kinked lines show toughness values calculated using the actual unloading compliance from the unloading records. For materials with the increasing R curve as shown in Fig. 5b and 5c, no serious problem was found in controlling the fracture propagation when the Coordinate Conversion Control method was employed.

For the materials used in the present study, the Mode I fracture toughness by means of the double cantilever beam (DCB) test has been obtained. In Table 2 the fracture propagation toughness of all materials are summarized. The pitch based CF showed comparatively high Mode II fracture toughness. The reason for this may be napping caused by fiber breakage, which was found in DCB tests on this material.

Figure 6 illustrate the comparison between Mode I and Mode II fracture propagation toughness values. Although the correlation seems to be better when compared to the reported data in references, one data locates far from the correlation curve. This data is for the CFRP with toughened epoxy matrix, and tells that it may be difficult to obtain universal relationship between the two kind of fracture toughness values.

CONCLUSIONS

1) The coordinate conversion control method is effective for the stabilization of the Mode II fracture propagation in the end notched flexure

test.
2) Test condition and material characteristics affect the stability of test. Some qualitative information has been obtained.
3) Conventional epoxy matrix materials showed flat R-curves from the start of the fracture, whereas the APC-2 and toughened epoxy matrix CFRPs showed increasing R-curves reaching a plateau after 15 to 25 mm long propagation.

REFERENCES

1. Kageyama, K., Kikuchi, M., and Yanagisawa, N., " Stabilized End Notched Flexure Test: Characterization of Mode II Interlaminar Crack Growth", Composite Materials: Fatigue and Fracture (Third Volume), ASTM STP 1110, American Society for Testing and Materials, 1991, pp.210-225.

Table 1   Materials used

	Carbon fiber			Matrix
	Type	Y.P. MPa	Mod. GPa	
1	PAN	4000	250	250°F Epoxy
2	PAN	4300	239	250°F Epoxy
3	PAN	4300	239	Bismaleimide
4	PAN	5700	290	350°F Tough Epoxy
5	Pitch Hi.Mod.	3600	514	250°F Epoxy
6	PAN AS4	3400	220	PEEK

Table 2   Fracture Propagation tohghness obtained

	Material	G_{IR} kJ/m²	G_{IIC} kJ/m²
1	PAN	0.12	0.50
2	PAN	0.12	0.80
3	PAN	0.19	0.74
4	PAN/Tough Ep	0.46	2.45
5	Pitch Hi.Mod.	0.15	0.85
6	PAN AS4	1.60	2.30
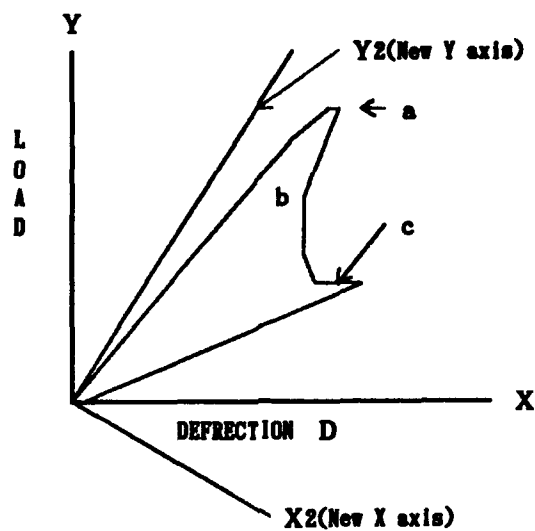
a. Load vs. deflection diagram for stroke controlled (ordinary) method
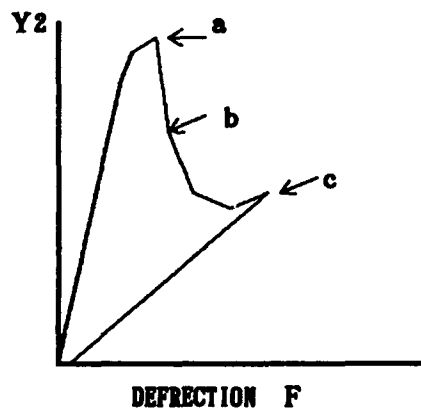
b. Load vs. deflection diagram for the coordinate conversion controlled method
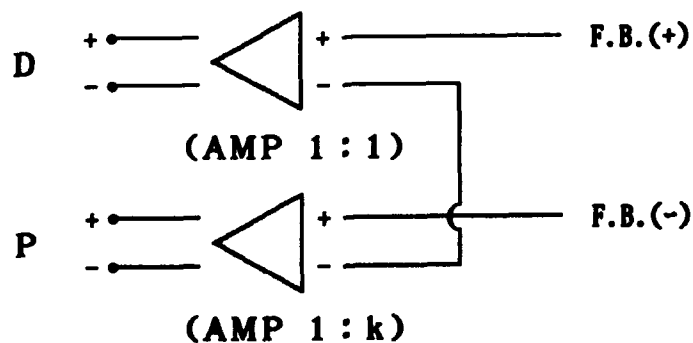
c. Connection of load and deflection output for feed back to test machine

Fig. 1 Stabilization of ENF test by means of coordinate conversion control method.
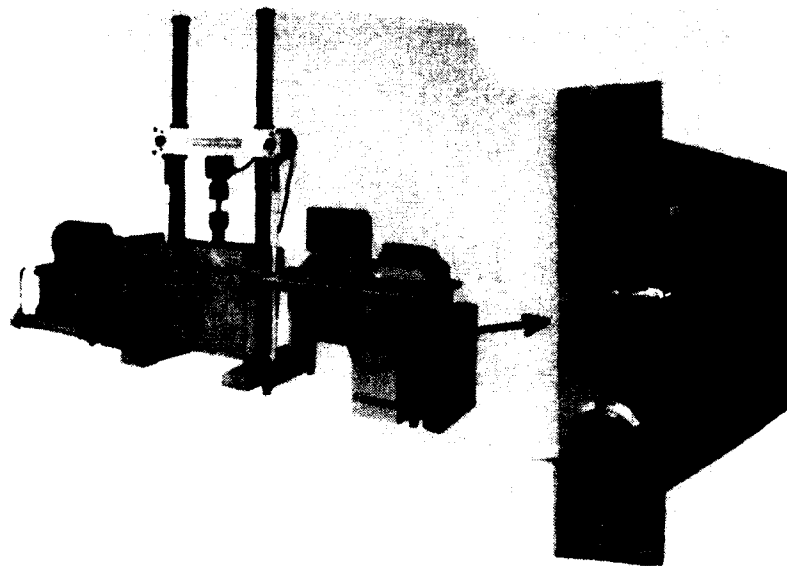
Fig. 2 Test machine used and the control board for the
Coordinate Conversion Control method
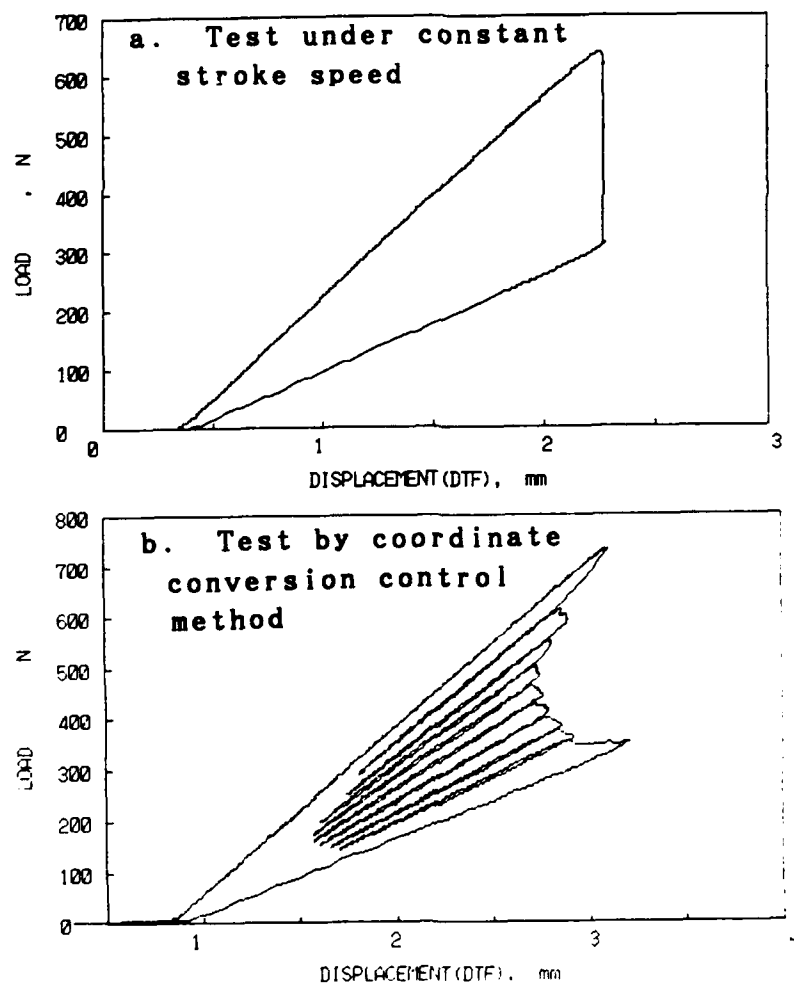
Fig. 3 Comparison of load vs. deflection diagrams.
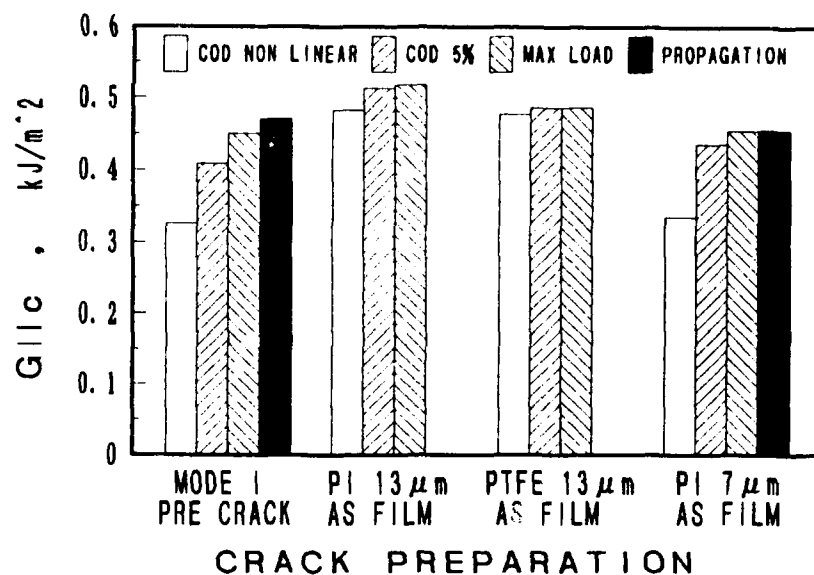
Fig. 4 Effect of crack preparation on the toughness obtained
and the stability of the test under the coordinate
conversion control method.
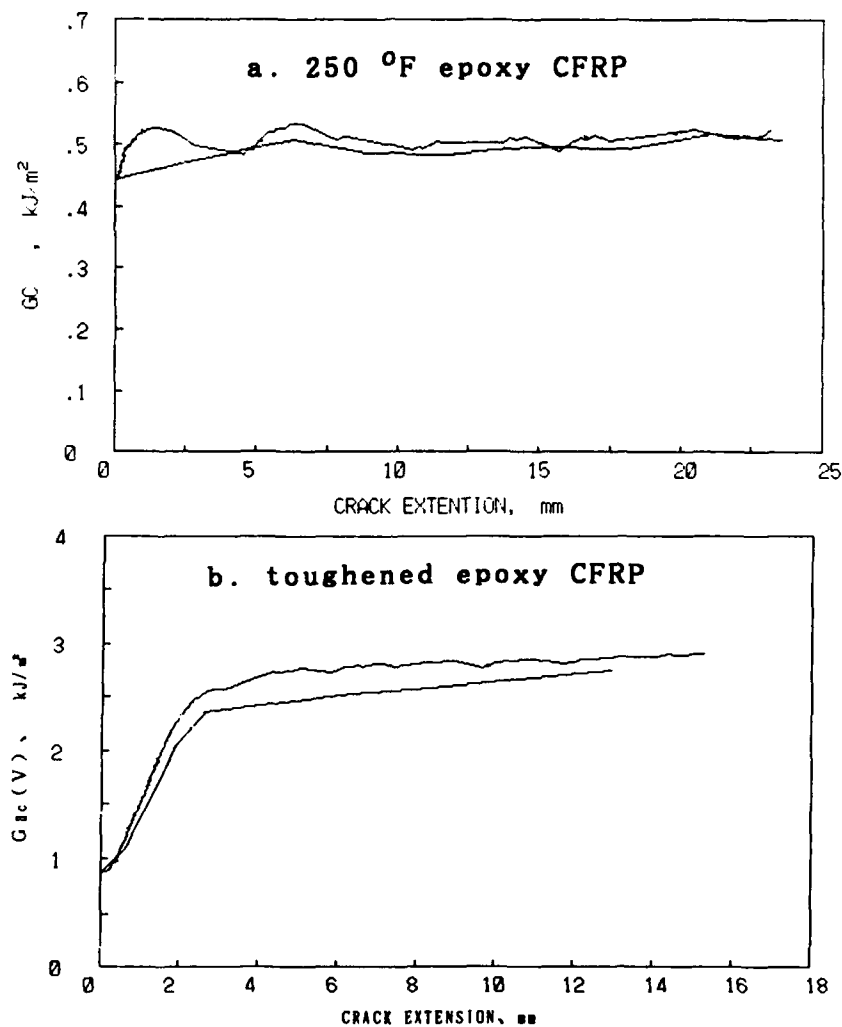
Fig. 5 Fracture propagation, R, curves for CFRPs.
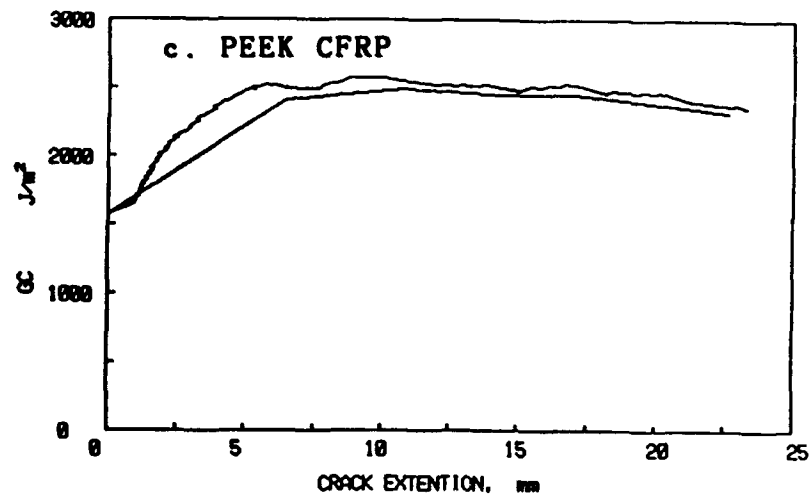
Fig. 5   Fracture propagation, R, curves for CFRPs.
         (continued)
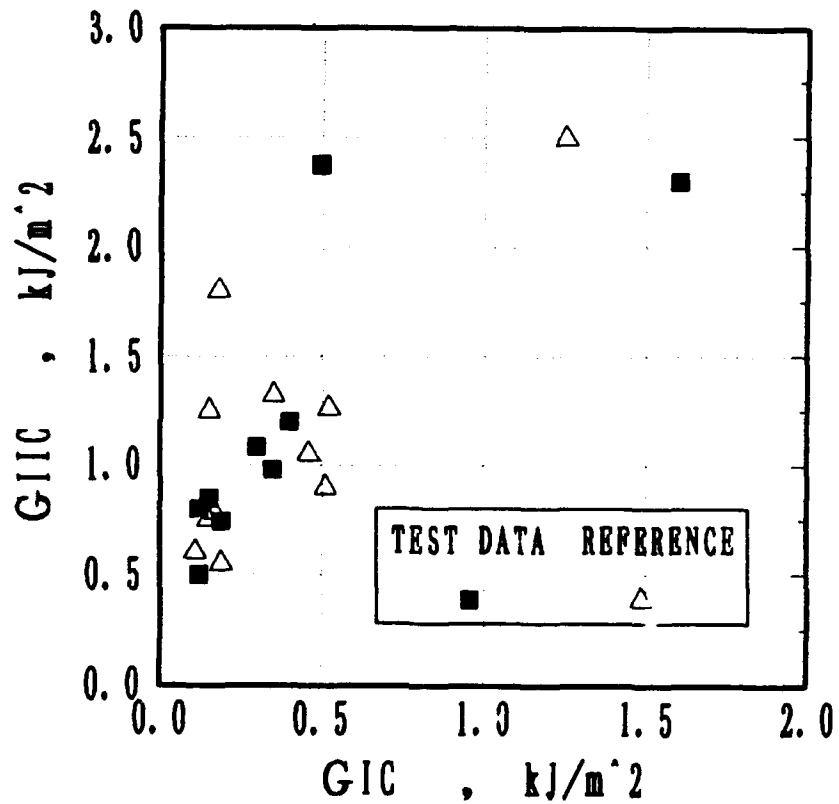
Fig. 6   Comparison between Mode I and Mode II fracture
toughness.

Dynamic Interlaminar Fracture Toughness of Composite Laminates: A Review

MITSUGU TOHDOH, SHIVE K. CHATURVEDI AND ROBERT L. SIERAKOWSKI

ABSTRACT

A review of rate effects on the interlaminar fracture toughness of polymer composite laminates is presented. In addition, the effect of impact loading on interlaminar fracture toughhness is also discussed.

INTRODUCTION

Delamination is recognized as a dominant failure mode in composite laminates leading to substantial reductions in both stiffness and strength and leading eventually to failure. This has focused attention on delamination control from the viewpoint of durability and damage tolerance design. Delamination can be produced in composite material structures by both static and dynamic loading. Once a composite material structure has initiated a delamination, repeated static or dynamic loading can lead to the propagation of an interlaminar crack and subsequent failure of the laminate.

A number of attempts have been made to characterize the interlaminar crack problem of composite laminates using linear elastic fracture mechanics [1]. One approach to quantifying the resistance of a laminated composite to interlaminar crack growth is by the fracture toughness parameter G_C. A number of investigators have given attention to characterization of the static fracture toughness in either a Mode I, II, III or mixed-mode state [2], with less attention forcused in the dynamic characterization [3-6]. For the case of dynamic loading, it has been observed that matrix failure/fracture differs from that of static loading [5]. For example, the static interlaminar fracture surface of graphite/PEEK laminates

M. Tohdoh, S. K. Chaturvedi, and R. L. Sierakowski
Department of Civil Engineering, The Ohio State University, 470 Hitchcock Hall
2070 Neil Avenue, Columbus, OH, 43210-1275

exhibited a large scale plastic deformation; on the other hand, the dynamic fracture surface exhibited significantly less plastic deformation [5]. To examine the development of damage under two distinct ranges of dynamic loading Cantwell and Morton [7] studied graphite/epoxy laminates. It was found that the impact response of the material under low velocity impact was different from that under high velocity impact. Thus the particular loading condition may affect the delamination mechanisms resulting in a need to determine the interlaminar fracture toughness over a range of loading rates.

Loading rate effects on Mode I, II, and III interlaminar fracture toughness of composite laminates have been studied by several researchers [8-18]; however the experimental results do not exhibit a definitive trend as to a correlation between the material strain rate and interlaminar fracture toughness. Furthermore the tests performed have been in the range of strain rates (less than 10 per sec), while to the best of the authors knowledge, no one has attempted to measure dynamic interlaminar fracture toughness at high strain rates (greater than 10^2 per sec).

This has forcused attention on the need to examine the research issues associated with rate effects and interlaminar fracture toughness of polymer matrix composites. Each of these issues is discussed with respect to the reported mode of testing. In addition, the associated issue of interlaminar fracture toughness as related to impact loading is also discussed.

RATE EFFECTS ON THE INTERLAMINAR FRACTURE TOUGHNESS OF COMPOSITE LAMINATES

MODE I The rate effect on the Mode I interlaminar fracture toughness, G_{IC}, of composites has been studied by several investigators [8-14] using double cantilever beam (DCB) specimens. Since electrohydraulic testing machines are widely available, most interlaminar fracture tests have been conducted using such test equipment in the range of strain rates up to 10^{-1} per sec. Table 1 shows some results obtained from studies of rate effect on G_{IC} for graphite/epoxy and graphite/PEEK laminates.

Aliyu and Daniel [9] obtained G_{IC} for unidirectional graphite/epoxy laminates as a function of deflection rate and crack velocity. It was shown that there was a definite increase in G_{IC} with crack velocity of up to 28% for the range of loading rates considered.

Gillespie et al. [10] studied the rate-dependence of G_{Ic} for unidirectional graphite/epoxy and graphite/PEEK composite

laminates.   For graphite/epoxy, G_{IC} was not found to be rate-sensitive in the range of loading rates tested. For graphite/PEEK, a subcritical crack growth prior to critical crack growth was observed; therefore, the Mode I fracture toughness was characterized by the strain energy release rates, G_{ISC} and G_{IC}, respectively. It was observed that G_{IC} and G_{ISC} coincided at low and high crack tip opening displacement rates. A critical value of G_{IC} existed in the range of strain rates tested. It was considered that the critical value could be attributed to a ductile to brittle transition of the matrix material (PEEK) in the process zone around the crack tip.

Smiley and Pipes [11] investigated rate effects on G_{IC} in unidirectional graphite/epoxy and graphite/PEEK laminates. Their results indicated that the toughness of both material systems was rate sensitive (Fig.1). The G_{IC} of APC-2 decreased significantly over 5 decades of crack tip opening rates. It was noted that the decrease observed was related to the transition from ductile to brittle behavior observed in the load-displacement response of APC-2.

Daniel et al. [12] studied the rate effect on G_{IC} of T300/F-185 graphite/epoxy composites, using an elastomer-modified epoxy resin matrix. A width-tapered double cantilever beam (WTDCB) specimen was used to eliminate the dependence of test results on crack length. Experimental results showed that G_{IC} decreased by up to 20% for the range of loading rates considered.

Mall et al. [13] suggested that the observed rate dependence of G_{IC} could be characterized by an expression between G_{IC} and the nominal strain rate in the DCB specimen, that is,

$$\dot{\varepsilon} = 3h\dot{\delta} / 4a^2$$

where h is the thickness on each side of the DCB specimen, $\dot{\delta}$ is the crosshead speed of the testing machine and a is the crack length. Figure 2   shows the effect of loading rate on Mode I interlaminar fracture toughness of three composite systems in addition to those of Mall [13]. It should be noted that Mall [13] tested plane weave graphite cloth reinforced PEEK; on the other hand,   other investigators   tested   unidirectional   composite   systems.   This comparison shows that an observed loading rate dependence of G_{IC} for AS4/3501-6 graphite/epoxy is not clear at present.

Yaniv and Daniel [14] employed a height-tapered double cantilever beam (HTDCB) specimen to produce a stable and smooth crack propagation. They conducted Mode I interlaminar fracture tests of unidirectional graphite/epoxy using HTDCB specimen over a range of crack extension rates of up to 26 m/sec. This represents a 500-fold increase in crack velocity over that studied in their

previous work [9]. It was found that G_{IC} increased with crack velocity up to a value of approximately 1 m/sec; thereafter it decreased with increasing crack velocity.

MODE II   Carlsson et al. [16] investigated loading rate effects on the Mode II interlaminar fracture toughness of unidirectional AS4/3501-6 graphite/epoxy and APC-2 graphite/PEEK over a range of loading rates from 4.17×10^{-3} to 4.17 mm/sec. The toughness was measured using end notched flexure (ENF) specimens. The elastic strain energy release rate, G_{IIC}, and the nonlinear fracture energy, G_{IICNL}, were obtained as functions of the crack tip velocity. It was found that G_{IIC} and G_{IICNL} decreased as the crack tip velocity increased for both materials.

Smiley and Pipes [17] studied the effect of rate on G_{IIC} in unidirectional AS4/3501-6 graphite/epoxy and APC-2 graphite/PEEK laminates in a range of loading rates from 4.2×10^{-3} to 92 mm/sec. The toughness was obtained as a function of the shear displacement rate, this is practically the same as the crack tip velocity measurements reported on Ref.17 (Fig.3). Their results indicated that both material systems were rate-sensitive in Mode II. Although G_{IIC} remained fairly constant for several rate decades, the toughness began to decrease with rate at the relatively high rates.

MODE III   Lingg et al. [18] investigated the loading rate effect on Mode III interlaminar fracture toughness, G_{IIIC}, of unidirectional AS4/3502 graphite/epoxy laminates using a split cantilever beam (SCB) specimen in a range of crosshead speeds from 5.0×10^{-3} to 500 mm/sec. The rate dependence of G_{IIIC} was expressed in terms of a nominal strain rate in a manner similar to that reported in Ref.14. Figure 4 shows that there is a definite decrease in G_{IIIC} with increased loading rate.

RATE EFFECTS MECHANISMS ON THE INTERLAMINAR FRACTURE TOUGHNESS OF COMPOSITE LAMINATES

Because an interlaminar crack propagates in the resin-rich region between plies, the energy absorption during interlaminar fracture is mainly related to the work of deformation of the polymer matrix. Fracture studies of polymers have shown that the fracture toughness is rate-sensitive [19]. The relationship between matrix toughness and composite interlaminar fracture toughness over a range of loading rates was investigated by Friedrich et al. [15]. Results obtained for graphite/PEEK composites are shown in Fig.5. In the low velocity

range the PEEK matrix toughness and the composite toughness are rate insensitive. As the crack velocity increases, the PEEK toughness and the composite toughness decrease significantly.

Smiley and Pipes [11] proposed a mechanism for explaining rate effect on the interlaminar fracture toughness of ductile matrix composites as shown in Fig.1. Although the yield stress increases with loading rate, the composite plastic zone size, r_{pc}, remains constant at approximately the composite fiber spacing, r_f, for all rates up to some critical deformation rate, δ_{cr}. The critical deformation rate ie defined as the rate at which the composite plastic zone size is no longer constrained by the fibers and r_{pc} is just less than r_f. Thus any further increase in rate above the critical rate will decrease r_{pc} and subsequently decrease G_{IC}.

INTERLAMINAR FRACTURE TOUGHNESS
UNDER IMPACT LOADING

Few attempts have been made to measure the dynamic interlaminar fracture toughness of composites under impact loading [3-6]. Among the reported studies is that of Grady and Sun [3,4] who have estimated dynamic delamination fracture toughness of $[90/0]_{5 S}$ T300/934 graphite/epoxy laminates. A beam specimen with embedded delamination crack in the mid-plane of the laminate was tested at an impact velocity of approximately 150 m/sec. The dynamic fracture toughness which was basically a Mode II fracture toughness in their study was much higher than the static value.

Maikuma et al. [5] investigated the Mode II interlaminar fracture of unidirectional AS4/2220-3 graphite/epoxy and APC-2 graphite/PEEK composite laminates subjected to impact loading using a center notch flexural (CNF) specimen. CNF specimens were tested using an instrumented falling weight impact tester at impact velocities ranging between 1.25-1.50 m/sec for AS4/2220-3 and 2.50-3.00 m/sec for APC-2, respectively. The dynamic Mode II interlaminar fracture toughness decreased under impact loading. These results were in agreement with the trends reported in Ref.17; however, the dynamic toughness exhibited a gradual decrease compared to the rapid decline of the data in Ref. 17.

Kageyama et al. [6] have measured Mode II interlaminar fracture toughness of unidirectional T300/2500 carbon/epoxy laminates under impact loading. A CNF specimen has been used to estimate dynamic Mode II toughness with an instrumented impact test system. G_{IIC} was found to increase as the impact velocity increased. Interestingly, this result is opposite to the results reported in Refs.5

and 7 which showed that Mode II interlaminar fracture toughness decreased at high loading rates.

CONCLUSION

Several attempts have been made to investigate rate effect on Mode I interlaminar fracture toughness using DCB specimen; however, the experimental results do not exhibit a definite trend about correlations between strain rates and interlaminar fracture toughness. For Mode II and Mode III interlaminar fracture, only a few experimental results have been reported. These results show that Mode II and Mode III interlaminar fracture toughness decreased as loading rate increased.

Only a few attempts have been made to measure interlaminar fracture toughness under impact loading. One study has shown that the dynamic interlaminar fracture toughness is smaller than the static one; however other experimental results exhibited that the interlaminar fracture toughness increased as the impact velocity increased. Further investigation would be required in this area.

In order to understand what the effects of loading rate are on the interlaminar fracture toughness and to characterize dynamic interlaminar fracture of composite laminates more precisely, we need to perform experimental studies at higher strain rates (greater than 10^2 per sec). The split Hopkinson pressure bar represents one of the devices which can be used to evaluate the effects of high strain rates on interlaminar fracture toughness. This apparatus has, been modified to measure dynamic fracture toughness using a three point bending type specimen [20, 21] and appears to be a useful method to evaluate the Mode II interlaminar fracture toughness of composite laminates using a CNF specimen.

REFERENCES
1. For example, WANG, S. S., "Fracture mechanics for delamination problems in composite materials," J. Comp. Mater., 17(1983), pp.210-223.
2. SELA, N., and ISHAI, O., "Interlaminar fracture toughness and toughnening of laminated composite materials: a review," Composites, 20(1989), pp.423-435.
3. GRADY, J. E., and SUN, C. T., "Dynamic delamination crack propagation in a graphite/epoxy laminate," Composite Materials: Fatigue and Fracture, ASTM STP 907, 1986, pp.5-31.
4. SUN, C. T., and GRADY, J. E., "Dynamic delamination fracture toughness of a graphite/epoxy laminate under impact," Comp. Sci. Tech., 31(1988), pp.55-72.

5. MAIKUMA, H., GILLESPIE, J. W., Jr, and WILKINS, D. J., "Mode II interlaminar fracture of the center notch flexural specimen under impact loading," J. Comp. Mater., 24(1990), pp.124-149.

6. KAGEYAMA, K., KIMPARA, I., and SUZUKI, T., "Mode II interlaminar fracture toughness under impact loading," Proceedings of "Benibana" International Symposium on How to Improve the Toughness of Polymers and Composites, Yamagata, 1990, pp.190-194.

7. CANTWELL, W. J., and MORTON, J., "Comparison of the low and high velocity impact response of CFRP," Composites, 20(1989), pp.545-551.

8. MILLER, A. G., HERTZBERG, P. E., and RANTALA, V. W., "Toughness testing of composite materials," Proceedings of the 12th National SAMPE Technical Conference, 1980, pp.279-293.

9. ALIYU, A. A., and DANIEL, I. M., "Effects of strain rate on delamination fracture toughness of graphite/epoxy," Delamination and Debonding of Materials, ASTM STP 876, 1985, pp.336-348.

10. GILLESPIE, J. W., Jr, CARLSSON, L. A., and SMILEY, A. J., "Rate-dependent Mode I interlaminar crack growth mechanisms in graphite/epoxy and graphite/PEEK," Comp. Sci. Tech., 28(1987), pp.1-15.

11. SMILEY, A. J., and PIPES, R. B., "Rate effects on Mode I interlaminar fracture toughness in composite materials," J. Comp. Mater., 21(1987), pp.670-687.

12. DANIEL, I. M., SHAREEF, I., and ALIYU, A. A., "Rate effects on delamination fracture toughness of a toughened graphite/epoxy," Toughened Composites, ASTM STP 937, 1987, pp.260-274.

13. MALL, S., LAW, G. E., and KATOUZIAN, M., "Loading rate effect on interlaminar fracture toughness of a thermoplastic composite," J. Comp. Mater., 21(1987), pp.569-579.

14. YANIV, G., and DANIEL, I. M., "Height-tapered double cantilever beam specimen for study of rate effects on fracture toughness of composites," Composite Materials: Testing and Design (Eighth Conference), ASTM STP 972, 1988, pp. 241-258.

15. FRIEDRICH, K., WALTER, R., CARLSSON, L. A., SMILEY, A. J., and GILLESPIE, J. W., Jr, "Mechanisms for rate effects on interlaminar fracture toughness of carbon/epoxy and carbon/PEEK composites," J. Mater. Sci., 24(1989), pp.3387-3398.

16. CARLSSON, L. A., GILLESPIE, J. W., Jr, and TRETHEWEY, B. R., "Mode II interlaminar fracture of graphite/epoxy and graphite/PEEK," J. Rein. Plas. Comp., 5(1986), pp.170-187.

17. SMILEY, A. J., and PIPES, R. B., "Rate sensitivity of Mode II interlaminar fracture toughness in graphite/epoxy and

graphite/PEEK composite materials," Comp. Sci. Tech., **29**(1987), pp.1-15.

18. LINGG, C. L., MALL, S., and DONALDSON, S. L., "Loading rate effect on Mode III delamination fracture toughness of graphite/epoxy," Proceedings of the American Society for Composites, Fourth Technical Conference, 1989, pp.267-276.

19. For example, KINLOCH, A. J., SHAW, S. J., TOD, D. A., and HUNSTON, D. L., "Deformation and fracture behavior of a rubber-toughened epoxy: 1. Microstructure and fracture studies," Polymer, **24**(1983), pp.1341-1354.

20. RUIZ, C., and MINES, R. A. W., "The Hopkinson pressure bar: an alternative to the instrumented pendulum for Charpy tests," Inter. J. Frac., **29**(1985), pp.101-109.

21. YOKOYAMA, T., and KISHIDA, K., "A novel impact three-point bend test method for determining dynamic fracture-initiation toughness," Exper. Mech., **29**(1989), pp.188-194.

Table 1. Rate effect on Mode I interlaminar fracture toughness
of graphite/epoxy and graphite/PEEK

Material	Specimen	Loading rate (mm/sec)	GIC (J/m²)	Rate effect	Ref.
AS4/3501-6	DCB	.0085 - 8.5	198 - 254	Increase	9
AS4/3501-6	DCB	.0042 - 4.2	190	Constant	10
AS4/3501-6	DCB	.0042 - 670	140-170	Decrease	11
AS4/3501-6	HTDCB	.0075 - 460	185 - 276	Decrease	14
T300/F-185	WTDCB	.0085 - 8.5	1500 - 1880	Decrease	12
APC-2	DCB	.0042 - 4.17	1560 - 1980	Max. at the mid-rate	10
APC-2	DCB	.0042 - 670	350 - 1700	Decrease	11
Graphite/PEEK	DCB	.0083 - 16.7	1600 - 4700	Decrease	13
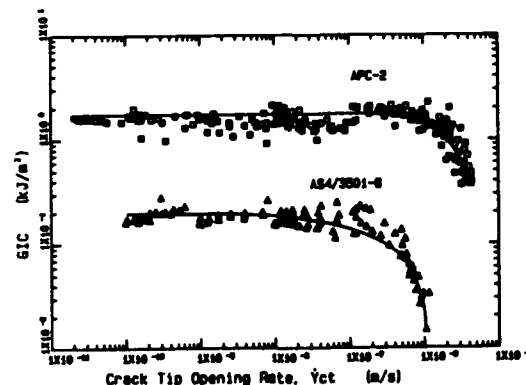
Fig. 1   Rate sensitivity of Mode I interlaminar fracture toughness [11]
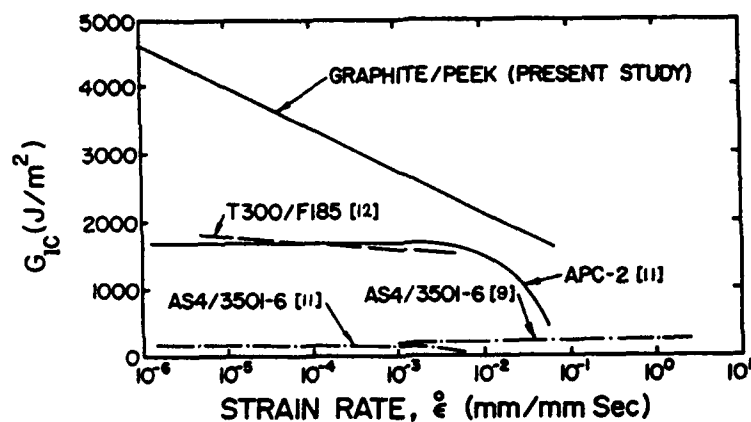
Fig. 2 Strain rate effect on Mode I interlaminar fracture toughness [13]
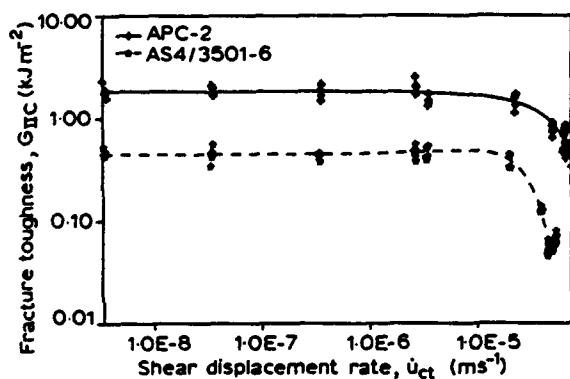
Fig. 3 Rate sensitivity of
Mode II interlaminar
fracture toughness [17]
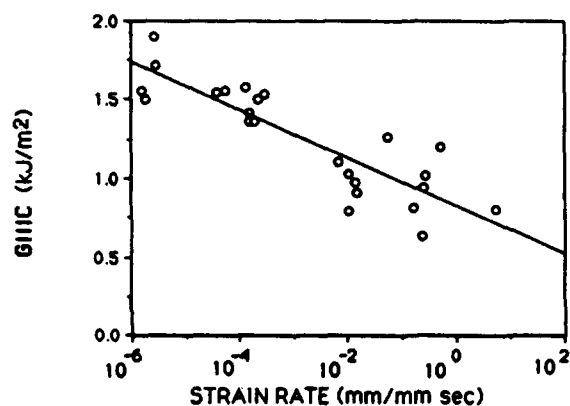
Fig. 4 Rate sensitivity of
Mode III interlaminar
fracture toughness [18]
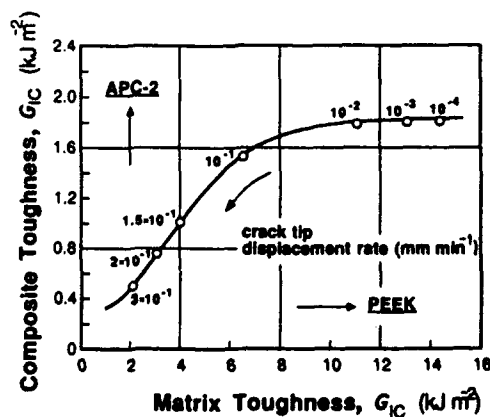
Fig. 5 Composite toughness versus matrix toughness [15]

Measurement of Strain Field around Microdamages in Composite Materials

M. J. SUNDARESAN AND T. M. SRINIVASAN

ABSTRACT

The present paper is concerned with the experimental determination of the strain field around damages such as fiber breaks in composite materials. This is accomplished using digital image processing technique and scanning electron microscopy. Glass/epoxy specimens are loaded inside the chamber of a scanning electron microscope. Digital correlation technique is used for mapping the deformed image of the region containing damage on to the corresponding undeformed image and from such a mapping process, the strain field is calculated. The strain distribution along the width of the first neighbor is calculated using this experimental technique. The results are compared with those obtained through finite element analysis.

INTRODUCTION

The stress distribution around broken fiber and matrix in unidirectional composites is of considerable interest. The rate of damage growth in composites is determined by the stress distribution and in particular by the stress concentration factor in the neighborhood of internal damages such as isolated fiber breaks. When a unidirectional composite material is subjected to a gradually increasing load, a distribution of fiber fractures occur due to the statistical variations in the strength of the fibers. Such a distribution happens well before the ultimate strength of the material. In the presence of such fiber fractures, the ultimate strength of the material is determined by the efficiency with which the load from the broken fibers are distributed among the neighboring undamaged fibers.

Extensive literature exists on the theoretical analysis of stress distribution around microdamages in composites. Available solutions use drastic simplifications to render the

M.J. Sundaresan, Assistant Professor, Mechanical Engineering
T.M. Srinivasan, Graduate Student, Mechanical Engineering
University of Miami, Coral Gables, FL 33124

problem tractable. As a consequence of such simplifications, some of the physical phenomenon are not well represented in these models. Further, traditional experimental techniques are not capable of measuring deformation around broken fibers, whose diameters are in the range of a few hundredths of a millimeter.

The measurement of strain at microscopic level has been attempted by many researchers in the recent time. Davidson and Lankford [1] used stereo-imaging technique for the measurement of strain field around fatigue crack tip. James et. al [2] used image processing technique to measure crack tip plastic strains. Chu et. al [3] used a completely automated technique for measuring strains and displacements from digitized images. Kortschot [4] used direct measurement of the displacement in the scanning electron microscope for determining the strain between two markers on the specimen surface. Lhotellier and Brinson [5] used polarized light on single fiber samples and calculated ineffective length, the length of the rupture zone near the fiber tip and the length of the strained zone and compared the results with analytical predictions. Hedgepeth and Van Dyke [6] used a shearlag analysis to determine the local stress concentration in the presence of a fiber break. Reedy [7-9] used finite element method to calculate the stress concentration in Boron/Aluminum and Kevlar/Epoxy composites. He found out that for a linear matrix, the maximum stresses occur in the region of the first neighbor closest to the crack tip and the fiber stresses become more uniform at farther regions.

FINITE ELEMENT RESULTS

A detailed finite element analysis was done for various fiber volume fractions and different material combinations. Separate investigation has been carried out for 2-D and 3-D elastic finite element models. In the 3-D model the fibers were arranged in a square array. Fig 1. shows the strain distribution in the first neighbor for a monolayer with elastic matrix. The variation of strain concentration factor (SCF) with fiber volume fractions is given in fig 2. The SCF obtained through 2-D and 3-D elastic finite element analysis for the Glass/Epoxy material used in the experiment were found to be 1.48 and 1.14 respectively. In the 3-D case, the corresponding valu: of SCF when the matrix behavior is elastoplastic is expected to be even lesser, probably in the range of 1.05 to 1.10.

EXPERIMENTAL PROCEDURE AND RESULTS

A schematic of the experimental setup is shown in fig 3. It consists of an ISI DS 130 scanning electron microscope (SEM) interfaced to a digital image processor and a microcomputer. Glass/Epoxy specimens (5209 E-Glass from BASF Structural Materials, approximately 65 % fiber volume fraction) cut from a 10 layered laminate were used in this study. The specimen was 2.50" long, 0.25" wide and 0.06" thick. The specimen was polished using standard metallographic techniques and a speckle pattern was created by depositing dilute suspension of microspheres on its surface. Then the specimen was coated with palladium. A typical speckle pattern on the surface of the fiber is shown in
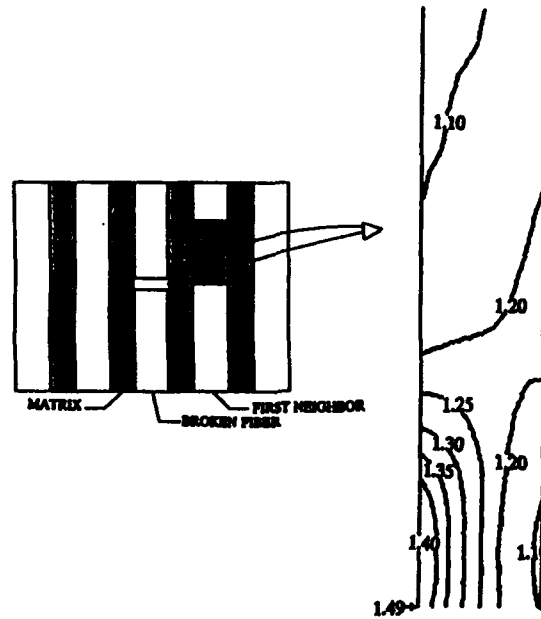
Fig 1. Contours of constant strain lines on the nearest neighbor
2-D case, Volume fraction = 0.65
Fiber/Matrix stiffness ratio = 80
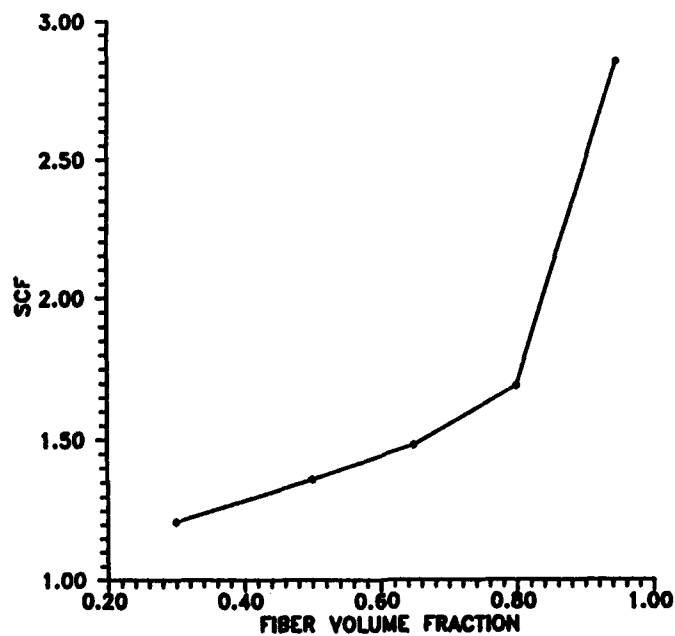
Fig 2. Variation of strain concentration factor (SCF) with fiber volume fraction
Fiber/Matrix stiffness ratio = 30
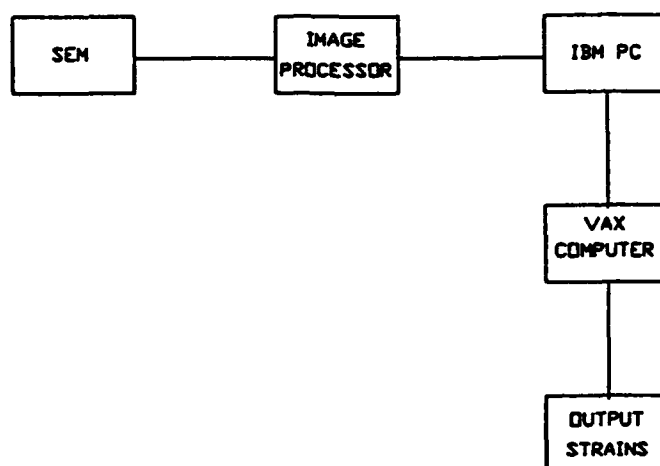
Fig 3. Experimental set up used for digitizing the images from scanning electron microscope

fig 4. The specimens were subjected to four point bending inside the SEM chamber. The central displacement of this four point bending specimen was gradually increased until fiber breaks were observed. The Glass/Epoxy specimens were subjected to approximately 1 % strain. The image of the region containing the fiber break was digitized and recorded at a magnification of 5000x. These images were compared with the corresponding images under no load conditions to extract information about displacements and strains.

The digital correlation technique developed by Chu et. al [3] was used for determining strains and displacements. The images were digitized into 256 discrete levels of light intensity. In order to reduce the effects of noise on the quality of the digitized image, averaging upto 10 images were performed. The digital correlation was performed on the VAX 8650 computer.

In fig 5., the variation of strain along the width of the first neighbor is shown. The square symbols indicate experimentally determined strains. A straight line which is a least square fit through the data points is also shown in this figure. While the errors of the order of $\pm$ 500 microstrains are apparent from the scatter in the data points, the trend in the strain distribution across the fiber width, as indicated by the least square fit does agree with the expected strain concentration, as discussed in the earlier section. In particular the values of strain at the edge of the fiber nearest to the broken fiber is 1.07 times the strain at the edge farthest from the fiber break.
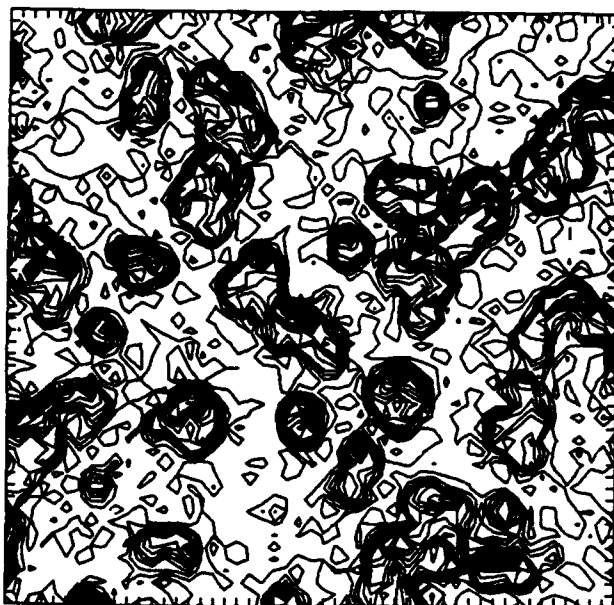
Fig 4. Typical speckle pattern created on the fiber surface
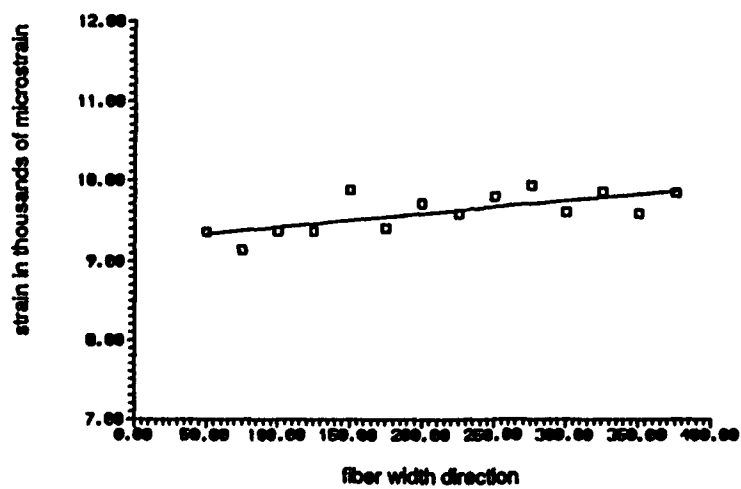
Fig 5. Strain measured across the width of the nearest neighbor

CONCLUSIONS

An experimental technique suitable for measuring strains around microscopically small regions has been developed. Current limit of strain accuracy (including the errors added in the SEM) is $\pm$ 500 microstrains for the case studied. The technique is being refined and with improvements in the accuracy of strain measurement, it is expected that this procedure will be useful in a wide class of micromechanical problems.

ACKNOWLEDGEMENT

We would like to thank BASF for providing composite prepreg materials, Prof. Ed Henneke and Chuck Chandler of Virginia Tech for their help in the fabrication of composite specimens and Mr. G. Shankar for help in some of the finite element work.

REFERENCES

[1]   D.L. Davidson and J. Lankford, "Fatigue Crack Tip Strains in 7075-T6 by Stereo-imaging and their Uses in Crack Growth Models", ASTM STP 811, pp. 371-391, Am. Soc. Test. Mat., Philadelphia, 1983.

[2]   M.R. James, W.L. Morris, B.N. Cox and M.S. Dadkhah, "Description and Application of Displacement Measurements Based on Digital Image Processing", ASME AMD, Vol. 102, pp. 89-99, 1989.

[3]   T.C. Chu, W.F. Ranson, M.A. Sutton and W.F. Peters, "Application of Digital Image Correlation Technique to Experimental Mechanics", Experimental Mechanics, Vol. 25, pp. 232-244, 1985.

[4]   M.T. Kortschot, "High Resolution Strain Measurement by Direct Observation in SEM", J. Material Science, Vol. 23, pp. 3970-72, 1988.

[5]   F.C. Lhotellier and H.F. Brinson, "Matrix-Fiber Stress Transfer in Composite Materials: Elasto-Plastic Model with an Interphase Layer", Composite Structures, 10, pp. 281-301, 1988.

[6]   J.M. Hedgepeth and P. Van Dyke, "Local Stress Concentrations in Imperfect Filamentary Composite Materials", J. of Composite Materials, Vol. 1, pp. 294-309, 1967.

[7]   E.D. Reedy, "Analysis of Center-Notched Monolayers with Application to Boron/Aluminum Composites", Journal Mech. Phys. Solids, Vol. 28, pp. 265-286, 1980.

[8]   E.D. Reedy, "Fiber Stresses in a Cracked Monolayer: Comparison of Shear-lag and 3-D finite Element Predictions", Journal of Composite

Materials, Vol. 18, pp. 595-607, Nov 1984.

[9]   E.S. Reedy, "Fiber Stress Concentrations in Kevlar/Epoxy Monolayers", Journal of Composite Materials, Vol. 19, pp. 533-542, Nov 1985.

SESSION 9A

Structural Analysis, Design, and Optimization II

Static and Dynamic Behavior of Adaptive Aircraft Wing Structures Modelled as Composite Thin-Walled Beams

L. LIBRESCU,† C. A. ROGERS* AND O. SONG†

ABSTRACT

Several results concerning the static and dynamic behavior of aircraft wing structures incorporating adaptive control capabilities are presented. These problems involve the free vibration, the static aeroelastic response as well as the bending response of cantilevered wing structures carrying heavy weights.

The control capability is achieved through the integration in the structure of a system of piezo—actuator devices whose action is considered in conjunction with a control law. The pertinent equations of adaptive thin—walled beams are established via a Hamilton variational principle extended to the case of a linear 3—D piezoelectric medium. The results obtained reveal the great potentialities of applying adaptive technology to the control of static and dynamic behavior of cantilevered structures, in general, and of aircraft wings, in particular.

INTRODUCTION

The successful development of smart material systems technology is likely to generate new avenues and concepts toward the design of the next generation of aeronautical and aerospace vehicles. In spite of the complexity and severity of environmental conditions to which these vehicles are likely to be exposed, they must be designed as to be capable to operate safely within their flight envelope, at higher angles of attack, at superior speeds, and without weight penalties. The implementation in these structures of piezoelectric devices could play an important role in the design of future advanced space vehicles.

Based on the direct and converse effects, the piezoceramic layers sandwiched between conductive surfaces (electrodes) and polarized in a convenient direction can be used as both distributed sensors and actuators. In spite of the great amount of interest in the field of adaptive structures, only an incipient work has been done in the field of aeroelasticity of aeronautical structures exhibiting such adaptive properties. An exhaustive list of references is presented in [1].

On the other hand, it is well known that in the determination of both the dynamic response to time—dependent excitations, of resonant conditions as well as of the flutter instability, the natural frequencies are an important physical parameter that intervenes in an explicit way. For this reason, the ability to conveniently control the eigenfrequencies of the structure should constitute a basic feature of the adaptive

†Engineering Science and Mechanics Department, Virginia Polytechnic Institute and State University, Blacksburg, Virginia, USA 24061
*Center for Intelligent Materials Systems and Structures, Virginia Polytechnic Institute and State University, Blacksburg, Virginia, USA 24061

structural technology applied to aeronautical structures. Associated with this topic, a comprehensive list of references could be found in [2].

The adaptive response control of wing structures carrying heavy weights constitutes another problem deserving special attention. During their complex missions and escape maneuvers, high load factors are experienced. At high load factors (which could be equal to the limit load factors), excessive deflections of the wing tip as well as large bending moments at the wing root may arise. In order to avoid the shortcomings arising from the reinforcement of the structure (accompanied by an unaffordable increase of the weight), more refined techniques have to be implemented. One of such techniques is based on smart material system technology [3].

In the following, several results which concern the static and vibrational behavior of adaptive wing structures will be presented.

BASIC ASSUMPTIONS

In order to obtain more realistic results when dealing with the type of advanced constructions mentioned above, the concept of solid beam will be discarded in the favor of the one corresponding to a thin—walled beam model. The theory of thin—walled cross—section beams considered herein is based on the following assumptions [4,5]:

a)   The original shape of the cross—sections of the beam is preserved,
b)   The transverse shear effects are incorporated. As a result, the considered beam model is capable to provide results also for thick walled beams and/or when the constituent materials exhibit low rigidities in transverse shear,
c)   The warping effects (primary and secondary) are incorporated [4,5],
d)   The hoop stress resultant N_{ss} is considered negligibly smll when compared to the remaining ones,
e)   Associated with the problem of wing carrying concentrated weights, it is assumed that the stores located at $z=z_i$ are of mass M_j and mass moment of inertia I_{0j} $(j=\overline{1,N})$ while the one located at the wing tip is of characteristics M and I_M. It is further assumed that the stores are located along the wing centroidal axis.

KINEMATIC EQUATIONS

Based on the above assumptions, the displacement field can be expressed as:

$$u(x,y,z,t) = u_0(z,t) - y\Theta(z,t), \quad v(x,y,z,t) = v_0(z,t) + x\Theta(z,t), \qquad (1a,b)$$

$$w(n,s,z,t) = w_0(z,t) + x(s)\theta_y(z,t) + y(s)\theta_x(z,t) - F_\omega(s)\Theta'(z,t)$$

$$+ n\left[\frac{dy}{ds}\theta_y(z,t) - \frac{dx}{ds}\theta_x(z,t) - a(s)\Theta'(z,t)\right], \qquad (2)$$

where

$$\theta_x(z,t) = \gamma_{yz}(z,t) - v_0'(z,t), \quad \theta_y(z,t) = \gamma_{xz}(z,t) - u_0'(z,t), \qquad (3a,b)$$

$$a(s) = -y(s)\frac{dy}{ds} - x(s)\frac{dx}{ds}. \qquad (4)$$

The warping function F_ω is expressed as:

$$F_\omega(s) = \int_0^s [r_n(s) - \psi]ds \, , \tag{5}$$

where the torsional function ψ is given by:

$$\psi = \frac{\oint_C r_n(s) \, ds}{\oint_C ds} \left[\equiv \frac{2A_C}{\beta} \right] , \tag{6}$$

and

$$r_n(s) = x(s) \frac{dy}{ds} - y(s) \frac{dx}{ds} . \tag{7}$$

As a result, six kinematic variables $u_0(z,t)$, $v_0(z,t)$, $w_0(z,t)$, $\theta_y(z,t)$, $\theta_x(z,t)$, and $\Theta(z,t)$ representing three translations in the x, y, z directions and three rotations about the y, x, z axes, respectively, are used to define the displacement vector (i.e., the displacement components u, v and w in the x, y and z directions, respectively). Here (s,z,n) and (x,y,z) denote the surface and cross–section reference coordinate systems, respectively (see Fig. 1a). A_C denotes the cross–sectional area bounded by the mid–line; β denotes the total length of the contour mid–line, $\oint_C (\cdot)ds$ denotes the integral around the entire periphery C of the mid–line cross–section of the beam while; variable $\int_0^s r_n(s)ds[\equiv \Omega(s)]$ is referred to as the sectorial area while t denotes the time.

Based on the kinematic representations, Eqs. (1)–(3), the strain measures assume the form:

Axial Strain:

$$S_{zz}(n,s,z,t) = \bar{S}_{zz}(s,z,t) + n \overline{\overline{S}}_{zz}(s,z,t) , \tag{8}$$

where

$$\bar{S}_{zz}(s,z,t) = w_0'(z,t) + \theta_y'(z,t)x(s) + \theta_x'(z,t)y(s) - \Theta''(z,t)F_\omega(s) ,$$

and

$$\tag{9a,b}$$

$$\overline{\overline{S}}_{zz}(s,z,t) = \theta_y'(z,t) \frac{dy}{ds} - \theta_x'(z,t) \frac{dx}{ds} - \Theta''(z,t)a(s) ,$$

are the axial strains associated with the primary and secondary warping, respectively.

Membrane Shear Strain:

$$S_{sz}(s,z,t) = [\theta_y(z,t) + u_0'(z,t)] \frac{dx}{ds}$$

$$+ [\theta_x(z,t) + v_0'(z,t)] \frac{dy}{ds} + 2 \frac{A_C}{\beta} \Theta'(z,t) . \tag{10}$$

Transverse Shear Strain:

$$S_{nz}(s,z,t) = [\theta_y(z,t) + u_0'(z,t)] \frac{dy}{ds} - [\theta_x(z,t) + v_0'(z,t)] \frac{dx}{ds}. \tag{11}$$

Within the present theory the warping measure is expressible as

$$W_M = \Theta'(z,t) . \tag{12}$$

Here, and in the following developments $(\cdot)' \ \partial(\cdot)/\partial z$.

LOCAL CONSTITUTIVE EQUATIONS

It is assumed that the master structure is composed of m elastic layers exhibiting transversely–isotropic symmetry properties, while the actuator (superposed on the master structure) is composed of ℓ piezoelectric layers.

It is also stipulated that the actuators are distributed over the entire span of the wing, while along the circumferential s– and transversal n–directions they are distributed according to the law (see Fig. 2):

$$R_{(k)}(n) = H(n - n_{(k^-)}) - H(n - n_{(k^+)}) \, ,$$

$$R_{(k)}(s) = H(s - s_{(k^-)}) - H(s - s_{(k^+)}) \, , \tag{13}$$

where H denotes Heaviside's distribution and R is a spatial function. In terms of the coordinates (s,z,n), related to the beam, the constitutive equations are expressed as:

$$\begin{Bmatrix} \sigma_{ss} \\ \sigma_{zz} \\ \sigma_{sz} \end{Bmatrix}_{(k)} = \begin{bmatrix} C_{11} & C_{12} & 0 \\ C_{12} & C_{11} & 0 \\ 0 & 0 & \dfrac{C_{11}-C_{12}}{2} \end{bmatrix}_{(k)} \begin{Bmatrix} S_{ss} \\ S_{zz} \\ S_{sz} \end{Bmatrix}_{(k)} - \begin{Bmatrix} e_{31}^{(k)} \mathcal{E}_3^{(k)} R_{(k)}(n) R_{(k)}(s) \\ \\ e_{31}^{(k)} \mathcal{E}_3^{(k)} R_{(k)}(n) R_{(k)}(s) \\ \\ 0 \end{Bmatrix}$$

and

$$\sigma_{nz} = C_{44} S_{nz} \tag{14a,b}$$

where σ_{ij} and S_{ij} denote the components of the stress and strain tensors, respectively, c_{ij} and e_{ri} are the elastic (measured for conditions of constant electric field) and piezoelectric constants, respectively, and $\mathcal{E}_3$ denotes the transversal electric field. The **local constitutive equations** could be obtained through integration across the thickness of Eqs. (14). These equations were displayed in [1,2].

THE EQUATIONS OF MOTION AND BOUNDARY CONDITIONS
OF ADAPTIVE THIN–WALLED BEAMS

In order to obtain the equations of motion of the adaptive thin–walled beam and the associated boundary conditions, Hamilton's variational principle extended to the case of a 3–D piezoelectric continuum is used. Use of this principle enables one to derive the equations of motion of adaptive TWBs expressed in terms of 1–D stress–resultants and stress–couples.

They are:

$$\delta u_o: \qquad Q_x' - I_1 + p_x = 0 \, , \tag{15a}$$

$$\delta v_o: \qquad Q_y' - I_2 - \sum_{j=1}^{N} m_j \ddot{v}_o \delta(z{-}z_j) + \sum_{j=1}^{N} m_j g \delta(z{-}z_j) + p_y = 0, \tag{15b}$$

$$\delta w_o: \qquad T_z' - I_3 + p_z = 0 \, , \tag{15c}$$

$$\delta\theta: \qquad B''_\omega + M'_z - (I_4 - I'_8) + \textbf{m}_z + b'_\omega = 0 \ , \tag{15d}$$

$$\delta\theta_x: \qquad M'_x - Q_y - I_5 - \sum_{j=1}^{N} I_j \ddot{\theta}_x \delta(z-z_j) + \textbf{m}_x = 0 \ , \tag{15e}$$

$$\delta\theta_y: \qquad M'_y - Q_x - I_7 + m_y = 0 \ . \tag{15f}$$

Here T_z, Q_x, Q_y; M_x, M_y, M_z and B_ω denote the axial and shear forces (in the x and y directions); the moments (in the x,y and z directions) and the bimoment global quantities depending on z and t, only; p_x, p_y, p_z and m_x, m_y and m_z denote the distributed loads and moments in the x, y, and z–directions, respectively, b_ω is the bimoment of the external loads, $I_i (i=1,8)$ are the inertia terms not displayed in the paper, while $\delta(\ )$ denotes Dirac's distribution. It could easily be seen that the stress resultant T_z, the stress couples M_x and M_y as well as the bimoment B_ω could be recast in a form in which the actuator effect appears in a separated form, namely

$$T_z = \hat{T}_z - \tilde{T}_z \ ; \quad M_x = \hat{M}_x - \tilde{M}_x \ ,$$

$$M_y = \hat{M}_y - \tilde{M}_y \ ; \quad B_\omega = \hat{B}_\omega - \tilde{B}_\omega \ , \tag{16a-d}$$

where the quantities affected by an overhat (^) and an overtilde (~) identify the pure mechanical and piezoelectric contributions to the indicated quantities, respectively.

From the Hamilton's principle, in addition to the equations of motion (Eqs. 15), the boundary conditions (BCs) are also obtained. For the case of the beam clamped at z=0 and free at z=L, the BCs are:

At the clamping edge (z = 0):

$$u_0 = \underset{\sim}{u}_0 \ ; \ v_0 = \underset{\sim}{v}_0 \ ; \ w_0 = \underset{\sim}{w}_0 \ ; \ \theta_x = \underset{\sim}{\theta}_x \ ; \ \theta_y = \underset{\sim}{\theta}_y \ ; \ \Theta = \underset{\sim}{\Theta} \ ; \ \Theta' = \underset{\sim}{\Theta}' \ , \tag{17a-g}$$

and at the free edge (z = L):

$$Q_x = \underset{\sim}{Q}_x \ ; \ Q_y = \underset{\sim}{Q}_y \ ; \ T_z = \underset{\sim}{T}_z \ ; \ M_x = \underset{\sim}{M}_x \ ; \ M_y = \underset{\sim}{M}_y \ ,$$

$$M_z + B'_\omega = \underset{\sim}{M}_z \ ; \ B_\omega = \underset{\sim}{B}_\omega \ , \tag{18a-g}$$

where the undertilde sign affects the prescribed quantities and where L denotes the length of the beam. It could be verified that consistent with seven boundary conditions at each edge, a fourteenth order governing equation system is obtained.

In the case of the general anisotropy of the layer materials (i.e., of the master structure, of the actuator patches or of both of them), the system of governing equations results in a complete coupled form. However, in the present case of anisotropy, and for the problems which are studied herein, a decoupling of the equations of motion is obtained.

In the case of swept wings, the loads of aerodynamic nature expressed within the strip–theory aerodynamics are:

$$p_y = q_n c a_0 (\Theta_0 + \Theta - v_0' \tan \Lambda) - NW/2L,$$

$$(19a,b)$$

$$m_z = q_n c a_0 e (\Theta_0 + \Theta - v_0' \tan \Lambda) + q_n c^2 C_{MAC} - NWd/2L$$

In Eqs. (19), $q_n (\equiv (\rho/2)U_n^2)$ denotes the dynamic pressure normal to the leading edge of the swept wing; c denotes the chord of the wing; a_0 denotes the "corrected lift" curve slope coefficient; Λ denotes the angle of sweep (considered positive for swept–back wings); e denotes the offset between the aerodynamic center line and reference axis; Θ_0 denotes the rigid angle of attack (measured in planes normal to the leading edge); and C_{MAC} is the wing section pitching moment coefficient. W/2L is the airplane weight per unit length of wing span, N denotes the load factor normal to the wing surface, while d denotes the distance between the lines of centers of mass and the reference axis.

Having in mind the kind of anisotropy considered in this paper, the governing equations derived from the equations of motion (Eqs. (15b,d,e)) result decoupled from the remaining ones (Eqs. (15a,c,f)). The same is valid for the boundary conditions when the decoupling of BCs (Eqs. (17b,d,f,g) and Eqs. (18b,d,f,g) from the (Eqs. (17a,c,e) and (Eqs. (18a,c,e)) is obtained. For this problem, only the system of equations and the associated boundary conditions expressed in terms of the unknown functions v_0, θ_x and Θ are relevant. Considering the boundary conditions as homogeneous (i.e., dropping the undertilded terms in the underlined boundary conditions) and realizing that the stress resultants and moments as they occur in homogeneous BCs also contain the piezoelectric effects, it could be shown that the BCs at z = L expressed in terms of displacement quantities are:

$$a_{33} \theta_x'(L) - Mgr_M = \hat{M}_x ,$$

$$(20a)$$

$$a_{55}(v_0' + \theta_x) + Mg = 0 ,$$

$$(20b)$$

$$a_{66} \Theta''' + a_{77} \Theta' = 0 ,$$

$$(20c)$$

$$a_{66} \Theta'' = \hat{B}_\omega ,$$

$$(20d)$$

whereas at z = 0, the BCs are:

$$v_0 = \theta_x = \Theta = \Theta' = 0$$

$$(21a-d)$$

In Eqs. (20) the coefficients a_{33}, a_{55}, a_{66} and a_{77} are rigidity quantities (see [1,2]), while $\hat{M}_x$ and $\hat{B}_\omega$ are the piezoelectrically induced moment and bimoment quantities whose expressions were displayed in [1,2].

In light of the assumed distribution of the actuator layer, (i.e., along the entire span of the wing), it may be inferred that the expressions of $\hat{M}_x$ and $\hat{B}_\omega$ are independent on the z–coordinate. As a result, their contribution in the governing equations is immaterial, while in the BCs they intervene as nonhomogeneous terms.

Their effects on the mentioned problems will be investigated.

THE CONTROL LAW

The adaptive nature of the wing (or rotor blade) structure is a result of the direct and converse piezoelectric effects and is controlled by requiring the applied electric field, $\mathcal{E}_3$, to be dependent on one of the mechanical quantities of the structure in motion. In the case of the static aeroelasticity problem, the external electric field, $\mathcal{E}_3$, is required to be proportional to the bending moment at the wing root, $\hat{M}_x(0)$, which yields:

$$\mathcal{E}_3 = c_1 \hat{M}_x(0), \tag{22}$$

or in terms of displacement quantities:

$$\mathcal{E}_3 = c_1 a_{33} \theta'_x(0)$$

On the other hand, the piezoelectrically induced moment, $\hat{M}_x$, is given by:

$$\hat{M}_x = c_2 \mathcal{E}_3, \tag{23}$$

which, by virtue of Eq. (22), yields:

$$\hat{M}_x = c_1 c_2 a_{33} \theta'_x(0) \tag{24}$$

which in conjunction with one of the boundary conditions at $z=L$ yields:

$$\theta'_x(L) = K_p \theta'_x(0) \quad \text{or} \quad K_p = \frac{\theta'_x(L)}{\theta'_x(0)}, \tag{25}$$

where K_p is the feedback gain. This control law, Eq. (25), expresses the fact that the control bending moment at the wing tip (induced piezoelectrically) is proportional to the mechanical one at the wing root (which increases with the increase of the aircraft speed). Equations (15b,d,e), expressed in terms of displacements coupled with the control law (Eq. (25)), were solved in conjunction with BCs in Eqs. (17b,d,f,g) and Eqs. (20) to determine either the eigenvalue (i.e., the divergence speed) or the static response characteristics (i.e., to deterine Θ and v'_0), on which basis the distributions of the effective angle of attack α_{eff} and of the lift coefficient C_L:

$$\alpha_{eff} = \Theta_0 + \Theta - v'_0 \tan \Lambda, \quad C_L = dC_L/d\alpha \, \alpha_{eff}, \tag{26}$$

along the wing span can be determined. Needless to say, the goal of the control is to maximize the divergence speed and to attenuate the lift distribution, especially when a swept–forward wing (SFW), $(\Lambda < 0)$, aircraft is involved.

In the case of a free bending vibration problem, two independent control laws are implemented. The laws require that: i) the applied electric field $\mathcal{E}_3$ be proportional to the vertical or lateral bending moments at the wing root, $\hat{M}_x(0)$ or $\hat{M}_y(0)$, (depending on whether the control of the natural frequencies is associated with vertical or lateral motion, respectively) and ii) the applied electric field $\mathcal{E}_3$ is proportional to the vertical($v_0(L)$) or lateral ($u_0(L)$) deflections of the beam tip (depending on the two directions of vibrations whose frequencies are to be controlled). In light of these control approaches, by also involving the boundary condition given in Eq. (20a) we may formulate the following control laws (labelled as CL1 and CL2). A similar control law enabling one to control the bending moment $\hat{M}_x$ at the wing root produced by the concentrated masses, will be used.

CL1)   Associated with vertical and lateral bending:

$$\theta'_x(L) = K_p \theta'_x(0), \quad \theta'_y(L) = K_p \theta'_x(0). \tag{26a,b}$$

CL2)   Associated with vertical and lateral bending:

$$\theta'_x(L) = \bar{K}_p v_0(L), \quad \theta'_y(L) = \bar{K}_p u_0(L). \tag{27a,b}$$

The feedback gains $\bar{K}_p$ and K_p are dimensional and nondimensional, respectively. The nondimensional counterpart of $\bar{K}_p$ is $\check{K}_p = \bar{K}_p L^2$.

NUMERICAL ILLUSTRATIONS

The adaptive wing is modelled as a symmetric composite box–beam (Fig. 1b). The piezoceramic (PZT–4) with aactuator layers are located on the top and bottom surfaces of the master structure. The geometrical characteristics of a beam with attached weights are displayed in Figs. 1b and 1c.

In Fig. 3, the variation of $\tilde{q}_D (\equiv (q_D)_A/(q_D)_{NA})$ vs. the feedback gain for two sweep angle configuration wings is depicted, where $(q_D)_A$ and $(q_D)_{NA}$ denote the divergence speed of the adaptive and its non–adaptive counterpart, respectively. However, in the remainder, the analysis is confined only to the case of $\Lambda = -30°$. The similarity of the trend of variation of $\tilde{q}_D$ vs. K_p as resulting from this figure to the one obtained within the solid beam model [6] is noteworthy.

In Figs. 4 and 5, the variations of $\tilde{\alpha}_{eff} \big[\equiv (\alpha_{eff})_A/(\alpha_{eff})_{NA} \big]$ for $N = 0$ and $N \neq 0$ vs. η are depicted. Here $q_n = 0.5(q_n)_D$.

For the eigenvibration problem, the variation of the eigenfrequencies ω vs. the feedback gains K_p and $\check{K}_p$ are depicted (Figs. 6–9).

In Figs. 6 and 7, by using the control law CL1, the variation of the first four eigenfrequencies associated with the vertical and lateral bending vs. the associated feedback gain was diagramatically represented, while in Figs. 8 and 9, by using the control law CL2, the variation of the vertical (plunging) and lateral bending fundamental frequencies ω vs. the feedback gain $\check{K}_p$ was obtained. Figures 6 and 7 reveal that within control law CL1, the increase of the odd eigenfrequencies occurs for negative feedback gains while the increase of the even eigenfrequencies reqires implementation of positive feedback gains. Figures 8 and 9 (as well as the results obtained but not displayed in the paper) reveal that within control law CL2 the increase of the eigenfrequencies occurs generally for positive feedback gains.

Figures 10 and 11 reveal that by applying an electric field, whose intensity is proportional to the feedback gain, alleviation and even suppression of transverse deflections and rotations of the beam can be achieved. In addition, Fig. 12 reveals the effect of the electric field on the bending moment and its significant decrease at the root section.

It should be mentioned in passing that in order to derive the equations associated with the free vibration problem, the assumption of harmonic time–dependent motion, entailing the representation $f(z,t) = \bar{f}(z) \exp(i\omega t)$ for all the field variables, was used. It is also mentioned that the eigenvalue problems (which concern the divergence instability and free vibration) and the response problems (which concern the subcritical aeroelastic response and static response of beams with

attached stores), were solved by using unified exact approach based on Laplace transform technique, devised in [7].

DISCUSSION AND CONCLUSIONS

The results diagrammatically displayed reveal the great potentialities offered by such an adaptive wing to control the divergence instability and the aeroelastic lift distribution on a forward swept wing by jugulating the wash—in effect which is characteristic to such wings. While Fig. 3 reveals that such an adaptive wing could experience an important increase of the divergence speed (namely four times or more the one corresponding to its non—adaptive counterpart), the remaining figures reveal the power of the adaptive control technique also in the sub—critical speed range. It should also be noted that the attenuation of elastic deformations become more prominent and consequently, the wing adaptiveness becomes more efficient as the speed increases up to the divergence speed.

Regarding the control of eigenfrequencies, it is important to realize that, roughly speaking, $\omega \sim D^{1/2} \sim h^{3/2}$, where D and h are the associated bending rigidity and thickness of the beam. It could be then inferred that the linear increase of eigenfrequencies would have been accomplished, without the help of this adaptive technology, through an unaffordable weight penalty.

Finally, the results concerning the adaptive control applied to the statics of cantilevered thin—walled beams carrying heavy concentrated masses reveals once more the great power of this technology.

REFERENCES

1. Song, O., Librescu, L. and Rogers, C.A.,"Static Aeroelastic Behavior of Adaptive Aircraft Wing Structures Modelled as Thin—Walled Beams," DGLR Bericht 91—144, pp. 46—55, Aachen, Germany, 1991 (an amended version is under print in *AIAA Journal.*

2. Song, O., Librescu, L. and Rogers, C.A.,"Vibrational Behavior of Adaptive Aircraft Wing Structures Modelled as Composite Thin—Walled Beams," Ninth DoD/NASA/FAA Conference on Fibrous Composites in Structural Design, Nov. 1991, Lake Tahoe, NV (an amended version of the paper is under print in *International Journal of Engineering Science*).

3. Librescu, L., Song, O. and Rogers, C.A.,"Adaptive Response Control of Cantilevered Thin—Walled Beams Carrying Heavy Concentrated Masses," *AIAA Paper*, AIAA—92—2527CP.

4. Rehfield, L.W.,"Design Analysis methodology for Composite Rotor Blades," Proceedings of the Seventh DoD/NASA Conference on Fibrous Composites in Structural Design, AFWAL—TR—85—3094, June 1985, pp. v(a)—1—v(a)—15.

5. Librescu, L. and Song, O.,"Behavior of Thin—Walled Beams Made of Advanced Composite Materials and Incorporating Non—Classical Effects," *Mechanics Pan—America, Applied Mechanics Review*, Vol. 44, No. 11, Part 2, R.A. Kittle and D.T. Mook (eds.), pp. 174—180, 1992.

6. Ehlers, S.M. and Weisshaar, T.A.,"Static Aeroelastic Behavior of an Adaptive Laminated Piezoelectric Composite Wing," Proceedings of the 31st SDM Conference, Long Beach, California, April 2—4, 1990.

7. Librescu, L. and Thangjitham, S.,"Analytical Studies on Static Aeroelastic Behavior of Forward—Swept Composite Wing Structures," *Journal of Aircraft*, Vol. 28, 2, pp. 151—157, 1991.
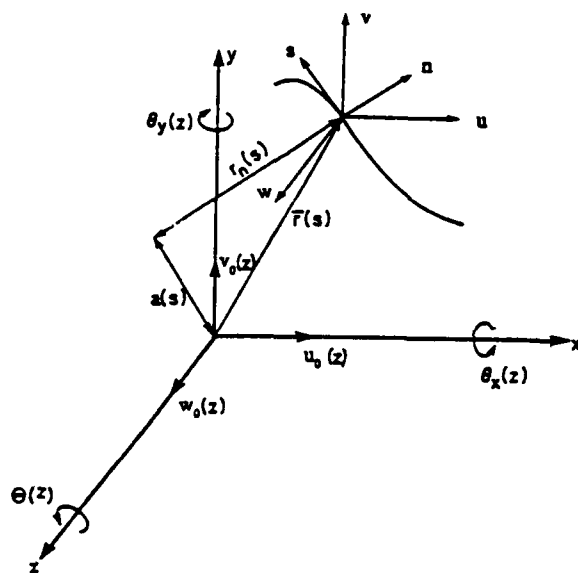
Fig.1a Coordinate systems and kinematic variables.
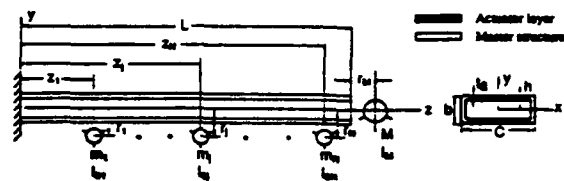
Fig. 1c Configuration of cantilevered beam carrying concentrated masses. (Continuous Actuator Patch)
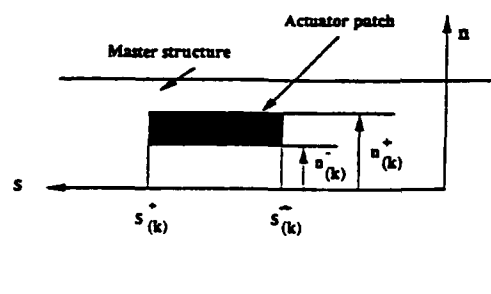
Fig.2 Actuator patch.
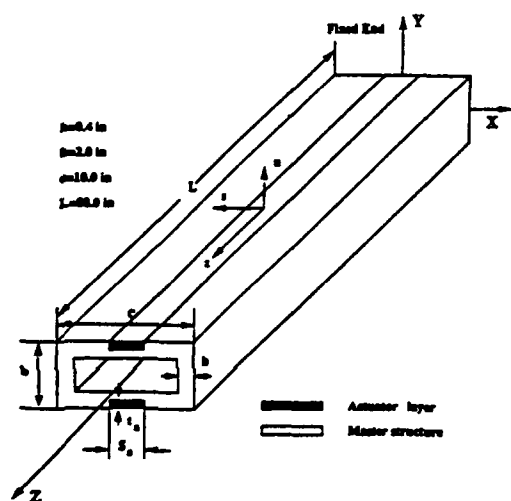
Fig.1b Geometry of a cantilevered box beam (not scaled).
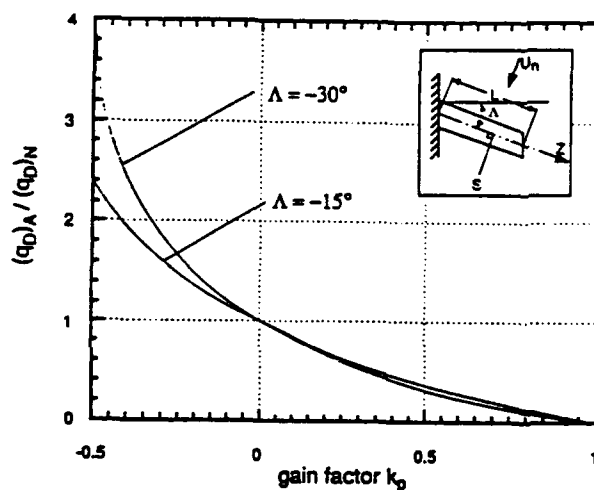
Fig. 3 Variation of $(q_D)_A/(q_D)_N$ vs. Feedback Gain for Two Sweep Angle Configuration Wings.

722
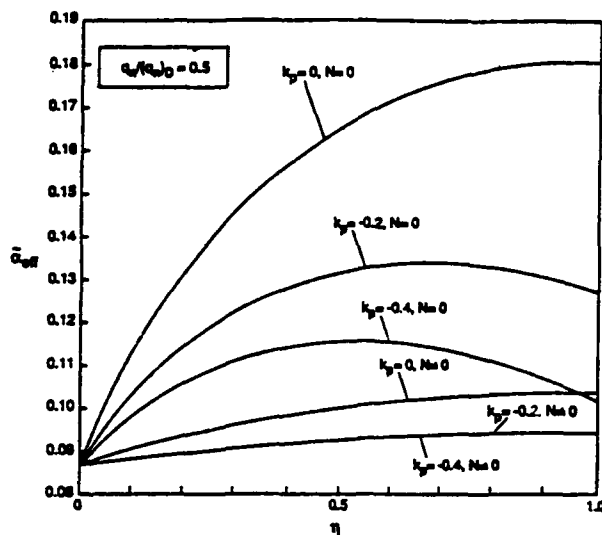
Fig.4 Variation of $\bar{\alpha}_{eff}$ vs. η for Various K_p. Here $q_n/(q_n)_D = 0.5$, $N = 0$, $N \neq 0$.

Fig.6 Variation of Eigenfrequency vs. Gain Factor (Vertical Vibration Mode).
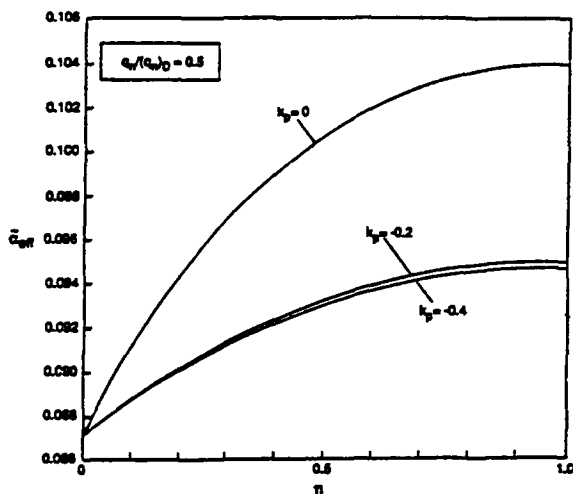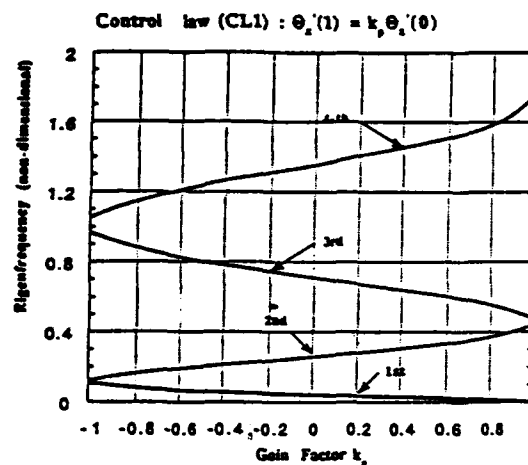
Fig.5 Variation of $\bar{\alpha}_{eff}$ vs. η for Various K_p. Here $q_n/(q_n)_D = 0.5$, $N \neq 0$.
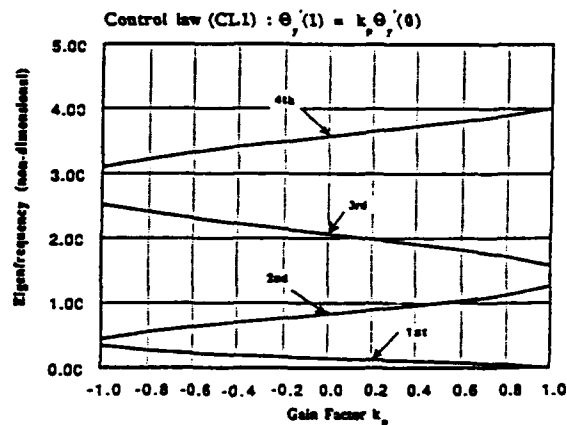
Fig.7 Variation of Eigenfrequency vs. Gain Factor (Lateral Vibration Mode).
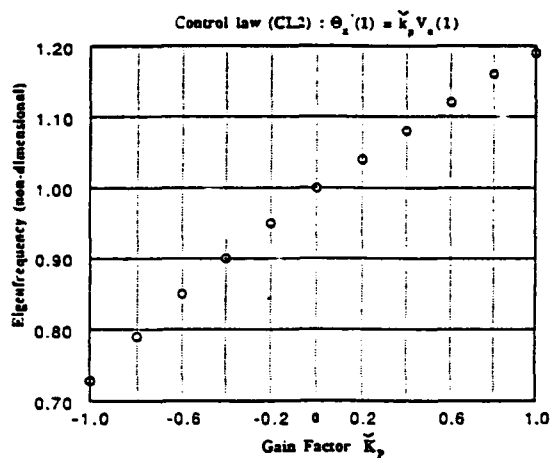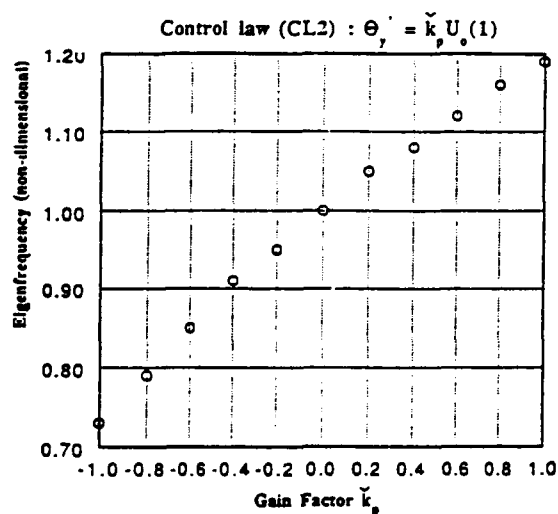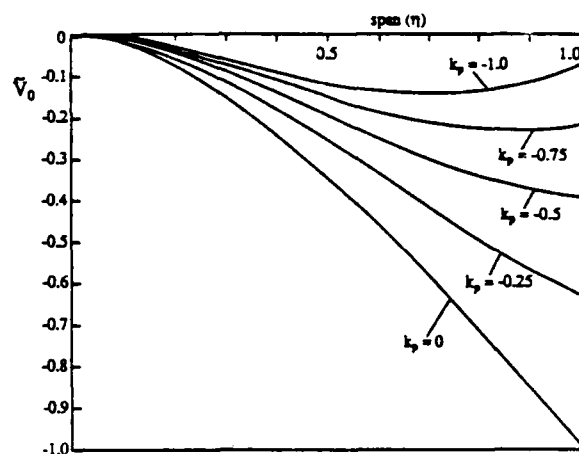
Fig. 10 Distribution of the deflection along the span η ($\equiv z/L$) for the controlled and uncontrolled beams.

Fig.8 Variation of Fundamental Eigenfrequency vs. Gain Factor (Vertical Vibration Mode).
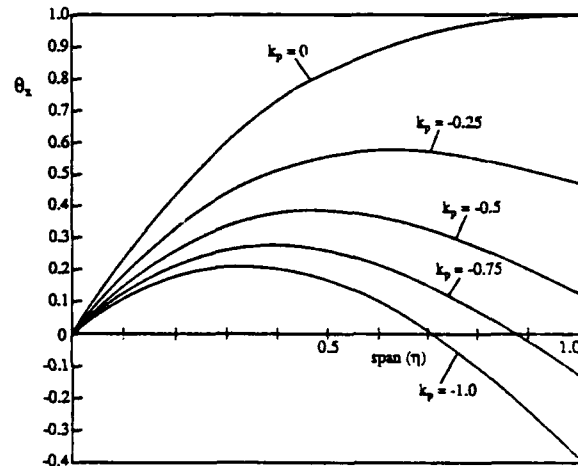
Fig. 11 Distribution of the rotation along the span η ($\equiv z/L$) for the controlled and uncontrolled beams.

Fig.9 Variation of Fundamental Eigenfrequency vs Gain Factor (Lateral Vibration Mode).
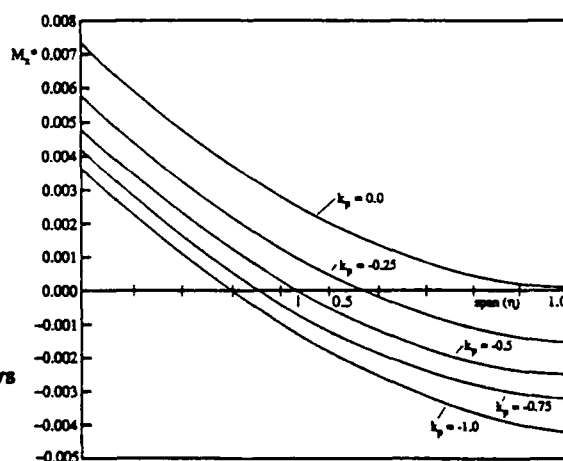
Fig.12 Bending moment distribution along beam span ($\eta = \frac{z}{L}$) for various K_p (where $M^* =$ non—dimensional bending moment).

724

Development of Carbon Fiber Reinforced Epoxy (CFRE) Rod for Small External Fracture Fixation Frames

JOHN A. DISEGI AND LYLE D. ZARDIACKAS

ABSTRACT

The AO/ASIF Small External Fixator is primarily used to stabilize a) open and/or comminuted fractures of the hand, wrist, and forearm; b) unstable distal radius fractures; c) wrist/hand/foot dislocations; d) open Grade III pediatric fractures with bone loss; e) pediatric osteotomies. This type of fracture management provides good stability at the fracture site and permits unrestricted access to soft tissue injury that may include vascular and/or neural involvement.

Cold worked stainless steel connecting rods have typically been used in conjunction with metallic clamps and implant quality 316L stainless Schanz screws to provide fracture stabilization. The purpose of this work was to develop and evaluate a carbon fiber reinforced epoxy (CFRE) rod that could replace the stainless connecting rod and provide an enhanced combination of properties.

Composite formulation and four point bending data are presented for the CFRE rod. Axial sliding tests indicated that improved frictional properties were obtained when a thermally cured coating was applied to the pultruded rod.

CFRE bending strength was satisfactory while the 75% reduction in weight and X-Ray radiolucency were considered major advantages compared to stainless steel.

INTRODUCTION

The AO/ASIF Small External Fixator (Ex Fix) has been designed for fracture management of the hand, wrist, and forearm [1]. This fracture treatment concept may also be used to correct secondary deformities such as shortening or angulation that result from failure of casting treatment to achieve closed reduction. Upper extremity fractures in conjunction with soft tissue damage and/or bone loss, represent major trauma applications for the small external fixation systems.

John Disegi, Synthes (USA), 1690 Russell Road, Paoli, PA, 19301
Lyle D. Zardiackas, Division of Biomaterials, University of Mississippi Medical Center, Jackson, MS 39216
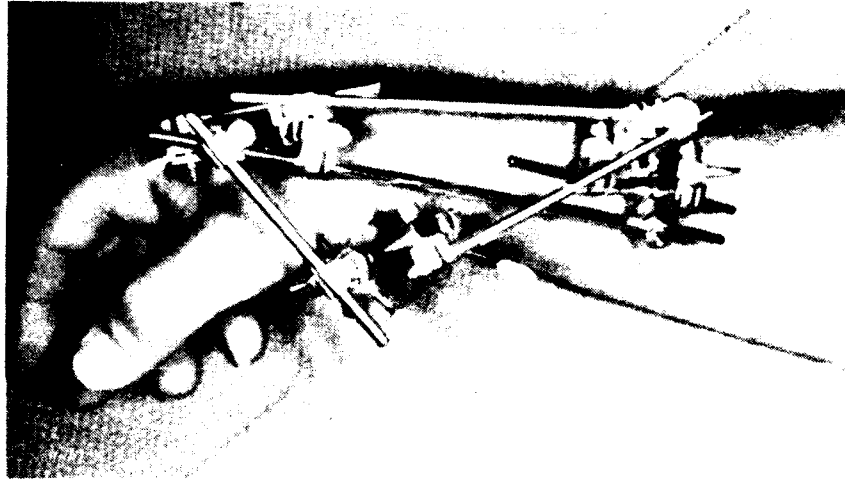
Figure 1. Stainless Ex Fix Triangular Frame for Wrist Fracture Stabilization

The standard AO/ASIF system is composed of four major stainless steel components to provide fracture stabilization: a) 4.0/2.5 mm pin-to-bar clamps; b) 4.0/4.0 mm bar-to-bar clamps; c) 4.0 mm connecting rod; d) implant quality 316L Schanz screws. Double stacked, triangulated, and special frame configurations can be utilized to increase the rigidity of the system. Figure 1 depicts a standard Small Ex Fix triangular frame with multiple pin placement for stabilization of a wrist fracture.

Complex or highly comminuted fractures may require the use of multiplanar frame assemblies which span the fracture site. The frame configurations can interfere with complete X-Ray visualization of various fracture patterns. A project was undertaken to develop and evaluate a radiolucent composite material to replace the stainless steel connecting rod.

PROCEDURE

Carbon fiber reinforced epoxy (CFRE) was selected as a possible replacement for the stainless connecting rod because of successful use of this composite material for applications involving the AO/ASIF Large External Fixation System [2]. CFRE rod had demonstrated good bending strength, stiffness, weight, and radiolucency. Attributes that were evaluated in the present study included four point bending properties, axial friction characteristics, component weight, and radiolucency.

TABLE I - CFRE COMPOSITE FORMULATION DATA

Epoxy Resin:	165°C Heat Deflection Temperature
	1.2 gm/cc Cured Density
Carbon Fiber:	207-228 GPa Modulus of Elasticity
	Epoxy Compatible Finish
Pultruded Rod:	57-60 Volume % Carbon Fiber
	Two Part Thermally Cured Coating

The CFRE composite formulation was identical to the composition previously utilized for the Large External Fixation System. Advanced composite manufacturing methods were closely controlled to ensure that uniform mechanical properties would be achieved. Table I lists some of the composite formulation properties that were controlled to provide the required level of CFRE product uniformity.

Four point bending tests were performed with an MTS servo-hydraulic testing machine to compare the bending properties of the solid 4.0 mm round CFRE rod with the standard 4.0 mm round 300 series stainless steel rod. The load fixture rollers were 25 mm diameter and the distance between the two bottom support rollers was 114 mm. The load was applied from the top at the mid-span location. Three specimens each of CFRE and stainless were tested in ambient air environment at a stroke rate of 1.0 mm/minute.

Each sample was preloaded to approximately 1.0 kg. Values of load and stroke were continuously recorded. Bending strength and bending rigidity values were calculated according to the method outlined in ASTM F 383 specification [3].

Surface modification to increase the frictional properties of the CFRE rod was evaluated since the pultruded rod surface was very smooth. A thermally cured two part coating system was selected. Axial slippage tests were performed by inserting a metallic clamp on uncoated and coated 4.0 mm round CFRE rods. The clamp nuts were pretorqued to 2.5 Nm, the clamps were held firmly in place, and a vertical axial load was applied to the rod at a rate of 5 mm/minute. The test measured the minimum axial force necessary to initiate sliding of the CFRE rod through the clamp.

TABLE II - FOUR POINT BEND TEST RESULTS
IN AIR AT AMBIENT TEMPERATURE

4.0 mm CFRE

Sample	Max. Load (N)	Max. Deflection (mm)	Bending Strength[1] (Nm)	Bending Rigidity[2] (N)
1	45.4	8.0	8.4	1211
2	44.1	7.5	8.2	1093
3	44.9	6.9	8.4	1063
x	44.8	7.5	8.3	1123
s.d.	±0.6	±0.5	±0.1	±79

4.0 mm Stainless

1	79.5	11.7	9.7	1587
2	77.5	11.7	10.1	1598
3	76.5	15.0	9.7	1613
x	77.8	12.8	9.8	1600
s.d.	±1.5	±1.9	±0.2	±13

1
Bending Strength per ASTM F 383: The bending moment required to produce a permanent deflection of 0.13 mm (offset method).

2
Bending Rigidity per ASTM F 383: The maximum slope of the bending moment-deflection curve.

RESULTS

All of the CFRE rods fractured while the stainless rods were permanently deformed. The mean bending strength for CFRE was calculated as the bending moment at fracture because the load versus deflection curve was linear. The mean bending strength of stainless steel was calculated as the bending moment at 0.13 mm offset deflection per ASTM F 383.

Four point bend test results are compiled in Table II. The maximum bending load was significantly higher for the stainless steel rod when compared to the CFRE rod. This result was not alarming, since the 300 series stainless connecting rod is fabricated from highly cold worked raw material that meets an ultimate tensile strength in excess of

1400 MPa. The reduced maximum deflection of the CFRE reflected the relatively low ductility of the composite material when compared to the stainless steel.

The mean bending strength of the CFRE was about 15% less than the stainless rod. The CFRE demonstrated a mean bending rigidity that was 30% less than the stainless rod.

The Student's (t) Test for unknown population variance at the 95% confidence interval was applied to the bending strength and bending rigidity data. Calculations confirmed that the stainless and CFRE exhibited statistically significant differences in bending strength and rigidity.

A scanning electron micrograph of the fractured CFRE surface at 15X magnification is shown in Figure 2. The fracture pattern was characterized by longitudinal cracking and transverse separation of the fibers from the epoxy matrix. There was some evidence of matrix delamination at the center of the rod.
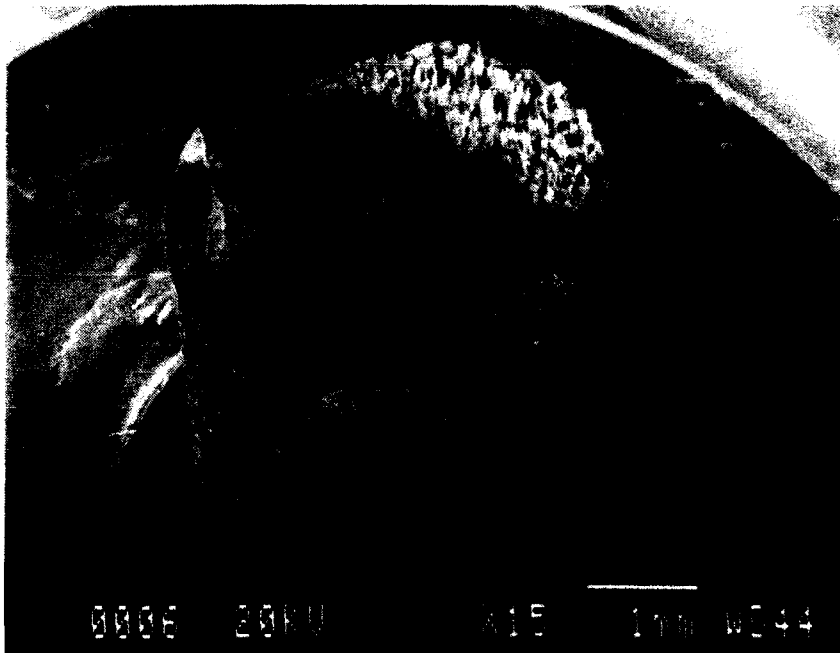
Figure 2. Scanning Electron Micrograph of Fractured CFRE Surface (15X)

Higher SEM magnification at the one o'clock position is shown in Figure 3. Continuous fiber bundles were present in the vicinity of the CFRE fracture region. Carbon fibers with intermittent areas of well bonded epoxy were also observed at 750X magnification.
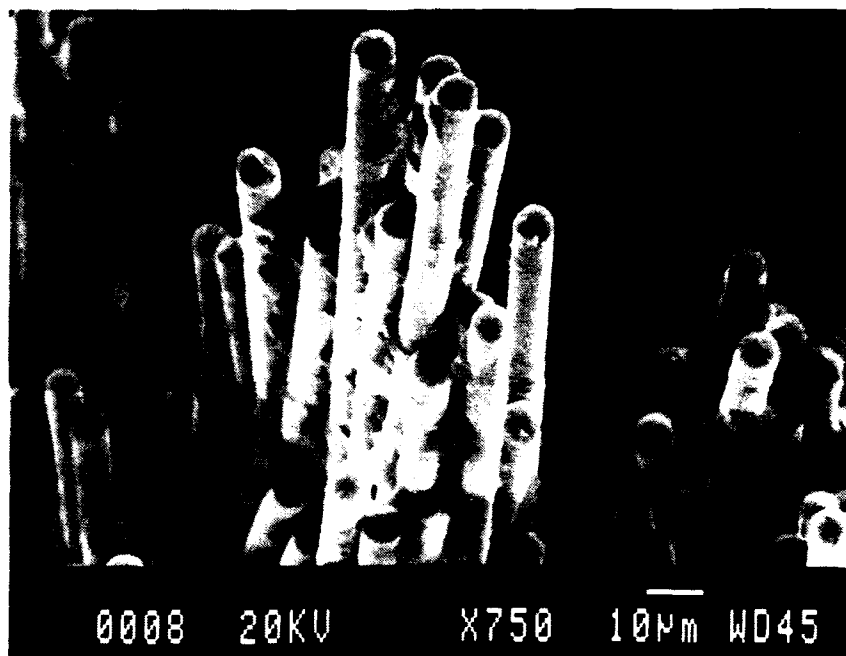
Figure 3. High Magnification Scanning Electron Micrograph of CFRE Fracture Area (750X)

TABLE III - AXIAL SLIPPAGE RESULTS FOR COATED AND UNCOATED 4.0 mm CFRE RODS

Clamps Pretorqued to 2.5 Nm;		Load rate = 5mm/minute:
Condition	Number of Tests	Load to Initiate Axial Sliding of Stainless Clamp (N)
Uncoated	5	88.3 ± 7.6
Coated	5	131.6 ± 16

Axial slippage test results are shown in Table III. Coated CFRE rod demonstrated a significantly higher load to initiate sliding of the metallic clamp when compared to uncoated rod. The thermally cured coated improved the frictional characterisitcs of the CFRE rod. The special coating was also expected to provide increased protection against fiber damage when the clamps were tightened and to minimize moisture penetration during steam autoclaving.
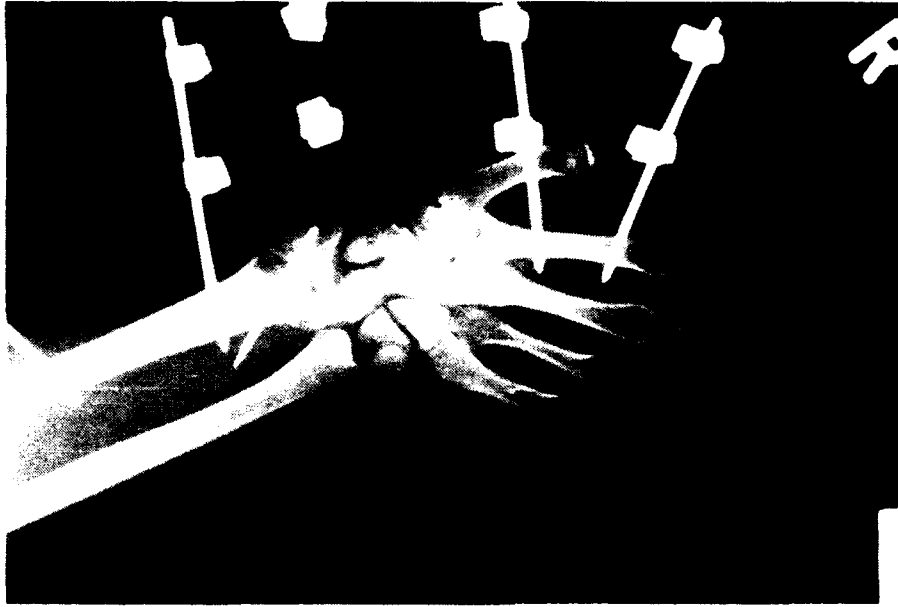
Figure 4. X-Ray of Distal Radius Fracture Treated With CFRE Ex Fix Frame

The excellent X-Ray transparency of the CFRE rod is verified in Figure 4 which shows a radiograph of a Colles fracture of the distal radius. The CFRE rod permits unobstructed X-Ray visualization of complex fracture patterns when simple or multiplanar Ex Fix frames are constructed for fracture stabilization.

The low density of the 4.0 mm round solid CFRE rod yielded a 75% reduction in weight when compared to the solid 4.0 mm round solid stainless rod of equivalent length. The large weight reduction represents a patient comfort factor and has a favorable influence on postoperative patient recovery in the home or work environment.

CONCLUSIONS

1. The 4.0 mm round CFRE Ex Fix connecting rod exhibited satisfactory bending strength which was 15% less than a high tensile stainless steel connecting rod.

2. CFRE bending rigidity was 30% less than a 300 series stainless steel.

3. A thermally cured coating improved the axial friction characteristics of CFRE rod in contact with a stainless steel clamp.

4. Major clinical advantages for CFRE material included a 75% weight reduction and X-Ray radiolucency.

ACKNOWLEDGEMENT

REFERENCES

1. Jakob, R.P. May 1983. "The Small External Fixator," AO Bulletin No. 2660, Department of Orthopaedic Surgery, University of Berne, Switzerland.

2. Disegi, J. and M. Sherman, November 1988. "Carbon Fiber Reinforced Epoxy Rod for External Fracture Fixation Frames," ASTM F4 Medical Composites Workshop, Atlanta, GA.

3. ASTM F 383 "Standard Practice for Static Bend and Torsion Testing of Intramedullary Rods," in 1991 Annual Book of ASTM Standards Section 13 Medical Devices and Services, American Society for Testing and Materials, pp. 93-94.

Repair of Damaged Composite Materials

KRISTIN B. ZIMMERMAN AND DAHSIN LIU

ABSTRACT

The techniques for repairing glass/epoxy thermoset composites and restoring their flexural strength are being developed. The repair techniques involve: (1) determining the damage mode, (2) selecting the joining technique and geometry, (3) choosing an adhesive that is compatible with the matrix material, (4) applying reinforcement patches to both sides of the damaged zone, and (5) assessing the strength of the repaired composites. The patch material must be the same type as the fibers in the composites and, if possible, aligned with the specimen's fiber direction. And the adhesive should be compatible with the epoxy of the composites. Due to ease of operation and simplicity in specimen preparation, a three-point bending test is used to evaluate the repaired strength. Testing results have shown that by using fillers and reinforcing materials in the damaged zone, accompanied by two reinforcing patches on each surface, at least 90% of the flexural strength can be restored. It should also be noted that restoring strength greater than 100% of the original strength of the composites is not realistic since it can initiate failure in regions other than the repaired zone.

INTRODUCTION

With the introduction of composite materials to today's industries, questions regarding the repair of such materials arise. Many techniques have already been developed to investigate this problem [1-3]. However, new composite materials are being developed and employed in new territories at a steady pace. This rapid development creates the necessity for a systematic study to design a more feasible technique for restoring the strength of damaged composites. The present study is an extension from previous research on the composite repair [4]. It is especially focused on scarf joining.

Many articles [5,6] describing composite repair on glass/epoxy composites agree on the fact that if the bondable surface area around the damaged zone is increased, then there will be greater contact surface area for the reinforcing repair patch to not only mechanically, but also chemically bond to the specimen. The larger bonding area therefore reduces the risk of debonding between the reinforcement patch and the damaged composite. The technique

Kristin B. Zimmerman and Professor Dahsin Liu, Michigan State University, Material Science and Mechanics Department, East Lansing, MI, 48824

being used to increase this bonding surface is called scarfing.

In scarf joining, a bonding area is created that bevels away from the damaged zone at a very shallow angle and radially encompasses the area outward from the damaged zone. Beveling or scarfing the surrounding area of the damaged zone also reduces the stress concentration in this area. The research being presented illustrates the effects of: (1) scarfing the damaged area, (2) using multiple reinforcing patches in the repair, and (3) using various fillers in the damaged zone. The reproducibility of repair procedure is also of concern.

ARTIFICIAL DAMAGE MODES

Tests were conducted to demonstrate the significance of scarf joining in composite repair. Both a straight line-crack and a circular cut-out were investigated. The line-scarf joints were prepared by cutting a 51mm x 152mm specimen into two 51mm x 76mm halves. The particular scarfing angles of interest were 5, 10, 15, and 90 degrees with respect to the specimen surface. Therefore, the 90 degree scarf or so-called butt joint did not require any scarfing. For scarf angles other than 90-degrees, each of the halves were sanded with a pneumatically controlled die-grinder.

The circular-scarf joints were prepared by drilling a designated diameter hole through a 102mm x 152mm composite specimen. This hole was to simulate the damaged zone in composite materials. The scarfing regions were then prepared radially outward from the hole.

REPAIR TECHNIQUES

For most automotive applications, a room temperature adhesive can be used to produce both mechanical and chemical bonding at the reinforcing patch/specimen interface. It is very important to note the chemical compatibility between the specimen's matrix and the repair adhesive since this will help to prevent debonding of the reinforcing patch.

Once the damage mode has been determined, a desirable repair procedure can be established. In the present study, only line crack and circular cut-out are of concern.

A. OVERALL PROCEDURES

The procedure for repairing the glass/epoxy specimen can be expressed as follows:

(1) Abrading a 51mm x 152mm area surrounding the damaged zone (cut/drilled) on both top and bottom surfaces of the composite.

(2) Cleaning the bonding area with isopropyl alcohol.

(3) Mixing the resin and curing agent in a pot with appropriate proportion as suggested by the manufacturer. The low viscosity of the epoxy is critical for proper wetting of the scarfing surface and reinforcing patch. Epoxy must permeate through the woven glass patch to avoid the formation of a void. The pot life of epoxy should be long enough for application.

(4) Applying the epoxy to the specimen. The epoxy should be poured and spread evenly to fully wet the repair zone. Gloves are required, as well as, good ventilation. The hole (damage zone) fillers, i.e. resin, plug, and fibers, are then put into place.

(5) Placing the reinforcing patch on top of the fillers. Each patch is positioned over the repair zone and additional epoxy is massaged into the patches until they are evenly saturated. Once repair is performed on the scarfing side, the specimen must be flipped over

for installing the reinforcing patch on the other side. After the application of the reinforcing patches on both sides, it is important to make sure that the respective fillers are still intact. (6) Curing the repaired composites is the last step of the repair procedure. With all of the repair work complete, two sheets of release film, one per side, are placed on the wet specimen. Then the repaired specimen are placed between two aluminum plates. The stacked aluminum plates containing the repaired specimen are placed into a vertical press and a compressive load of approximately 1000 lbs is applied. This compressive load squeezes much of the excess epoxy out and away from the repair joint and initiates a uniform bond line and bonding pressure at the patch/specimen interface. The curing process takes a couple of hours.·

Once the specimen are cured, they are removed from the press, trimmed, and prepared for the three-point bending evaluation.

B. SCARF JOINING

For both the scarf and butt joints, various techniques for repair were used. Both the scarf angle and filler for the scarfing area were being evaluated in the composite repair. Various fillers, such as a rolled glass patch, chopped glass fibers, pure resin, and a deliberate gap at the joining area were used to determine the effect of bonding surface between the glass reinforcing patch and the specimen on the strength of the joint. The butt joint was repaired using the same filler and gap variables as the scarf joint, and was also used exclusively to determine the influence of the glass reinforcing patch on the repair strength of the joint.

For the circular cut-out specimen, tests were conducted to determine the effect of a circular cut-out or damaged zone in the specimen. In this test, three different hole sizes (6.35mm, 12.7mm, 15.88mm) were cut into the 51mm x 152mm specimen. A representative amount of specimen out of each set were tested after being repaired by (1) injecting pure epoxy into the cut-out zone, (2) filling the cut-out zone with a plug. (The plug was cut out of a scrap of the same material with a commercial plug cutter and was dimensioned to create a press-fit with the hole.) and (3) filling the cut-out zone with chopped glass fibers. Two woven glass reinforcing patches measuring 51mm x 102mm were applied per side.

EVALUATION OF COMPOSITE REPAIR

The evaluation procedure to determine the damaged composite's restored strength is being addressed. The testing procedure used to evaluate the particular repair technique utilizes the three-point bending apparatus on the Instron machine. Each 51mm x 152mm specimen is placed in the three-point fixture and loaded compressively until failure occurs. The maximum strength is recorded for each particular specimen and it is compared to the various repair techniques and configurations.

The influence of a scarfing angle on the ultimate strength of the joint is illustrated in Figure 1. The illustration also compares the butt joint since again this is simply a 90 degree scarf. All of these specimen were repaired using 2 glass reinforcing patches per side. To summarize Figure 1 note the following...

(1) Both the 5 and 10 degree scarf are superior to the 15 degree scarf, and (2)
using chopped glass fibers and the rolled glass patch at the joint reduces the very brittle resin content at the bond line.

The influence of each glass reinforcing patch on the ultimate strength of the repair is illustrated in Figure 2. In each case there were two glass patches on the top (compressive)

side and one to four layers on the bottom (tension) side of the butt joint specimen. Note that the average undamaged specimen strength is 290 MPa. Also note that, (1) two and three layers of glass patch are very close to reaching 100% of the original strength, and (2) four layers far exceeds the 100% of original strength and could cause failure in an undamaged portion of the specimen.

The effect of the circular cut-out and the influence of using fillers in the damage zone is illustrated in Figure 3. Note the following: (1) The circular cut-outs illustrate the effect of a void induced into the specimen. By increasing the hole size or damage size the integrity or strength of the specimen is reduced. In this figure, the illustrated hole size is of the nondimensional parameter 2R/W. (2) The trend that is illustrated by the different fillers shows that regardless of the damage size, a filler/patch combination can be added to restore the specimen's original strength.

To evaluate the influence of damage zone versus repair zone, a series of tests were conducted by first impacting, to the point of perforation, approximately ten 102mm x 152mm glass/epoxy panels. The Dynatup impactor utilized a Tup which measured 12.7mm in diameter. The motivation of this study was to create a 12.7mm impacted hole (void) in the specimen and then test the impacted specimen for flexural strength integrity. The flexural strength was then compared with the drilled hole or cut-out zone specimen data to determine the equivalent hole size (damage zone) created by the impactor upon perforation of the specimen. Two different materials were tested. One was a combination of bi-ply and random fiber glass in a polyester resin and has a code number 2415 and the other was a combination of random glass and continuous fiber swirl mat in a polyester resin designated by 8610. The results for the 2415 specimen illustrated equivalent hole sizes between 6.35mm and 12.7mm, while the equivalent hole sizes for the 8610 specimen were approximately 12.7mm. This would imply that the 8610 panels are absorbing more energy than the 2415 panels. Figures 4-6 illustrate the progression of the strength evaluation by first drilling a known hole size, superimposing a plot of total impact energy vs strength after creating perforated damage, and finally deducing the equivalent damage hole size for material 2415. Figures 7-8 illustrate the same progression for material 8610.

CONCLUSIONS

In this study, the repair technique that is being developed has proven to be an efficient technique to repair damaged glass/epoxy thermoset composites. It has also been shown that the combination of fillers and reinforcing patches is capable of restoring the original flexural strength.

Depending on the particular thermoset composite that is being repaired, the selection of reinforcing material is critical. If a woven glass reinforcement patch is used to repair a randomly oriented glass fiber specimen, then there is somewhat of a mismatch between the orientations of the glass fibers. The woven fabric has higher strength in the fiber direction than the random one. Therefore, the number of layers of reinforcing materials used in the repair zone is critical in order to avoid exceeding the original flexural strength of the composite specimen.

REFERENCES

1. Baker, A.A. and Jones, R., Bonded Repair of Aircraft Structures, Martinus Nijhoff Publishers, 1988.

2. Composite Repairs, ed. Henry Brown, SAMPE Monograph, No. 1, 1985.

3. Bonding and Repair of Composites, ed. John Herriot, Butterworths, 1989.

4. Dahsin Liu, C.Y. Lee, X. Lu, "Repairability of Damaged Structural Composites," an annual report submitted to Michigan Materials Processing Institute, 1991.

5. "Field-Level Repair Materials and Processes," Stone, Robert H., 28th Nat. SAMPE Symp., 1983.

6. "Composite Repair Concepts For Depot Level Use," Labor, James D., 26th Nat. SAMPE Symp., 1981.

ACKNOWLEDGEMENTS
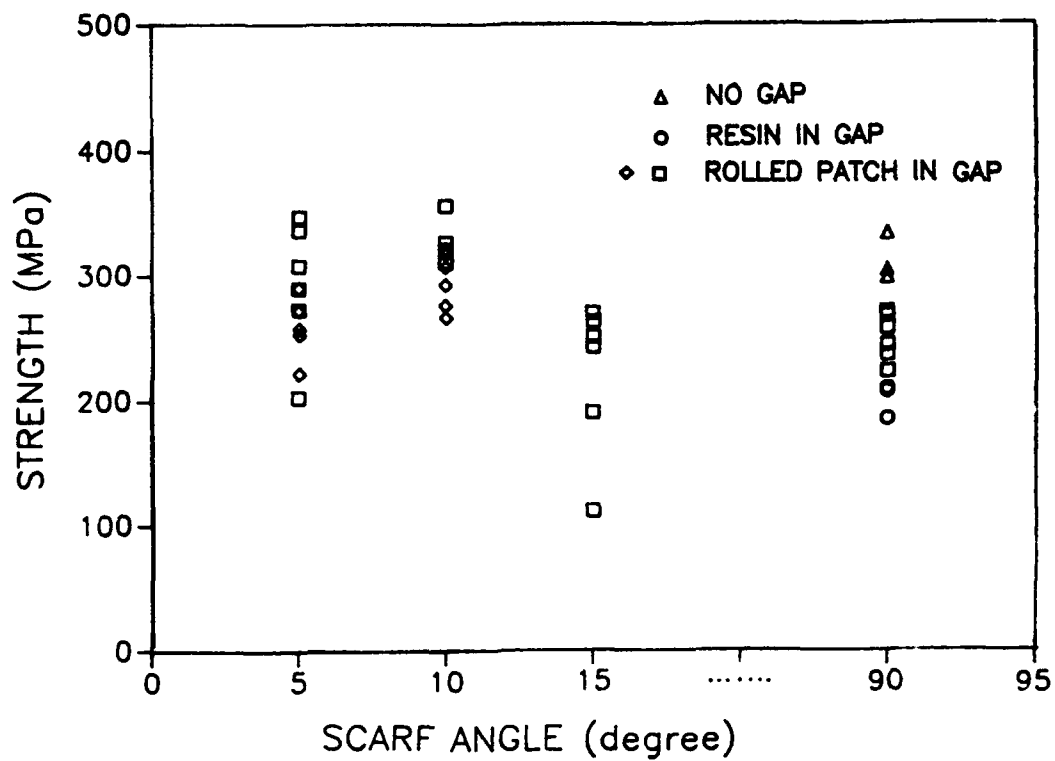
Figure 1. Owens Corning Fiberglas panels in a line-scarf study.
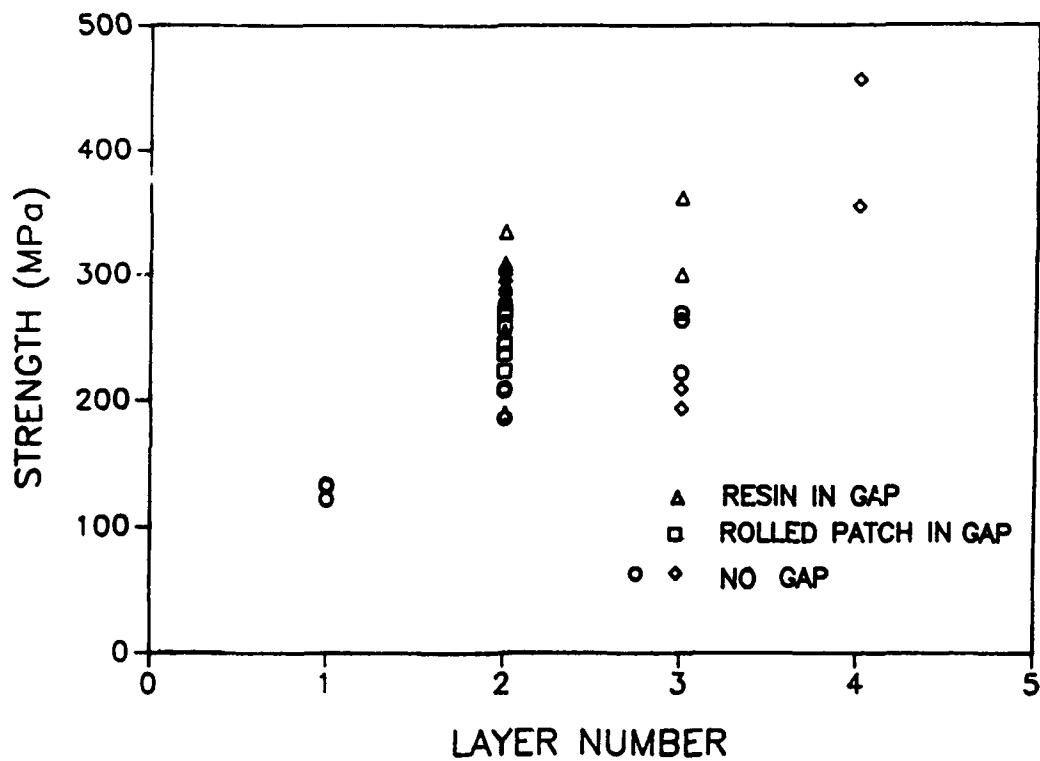
Figure 2. Owens Corning Fiberglas panels in a butt-joint patch layer study.
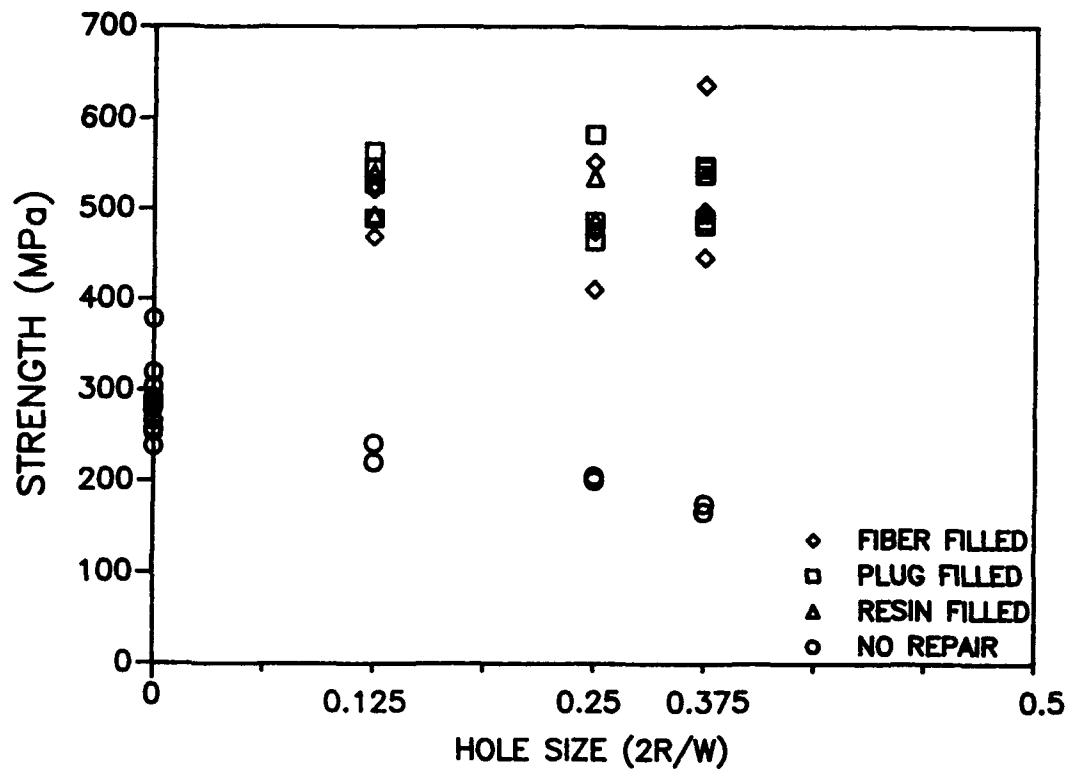
Figure 3. Owens Corning Fiberglas panels in a drilled hole study.
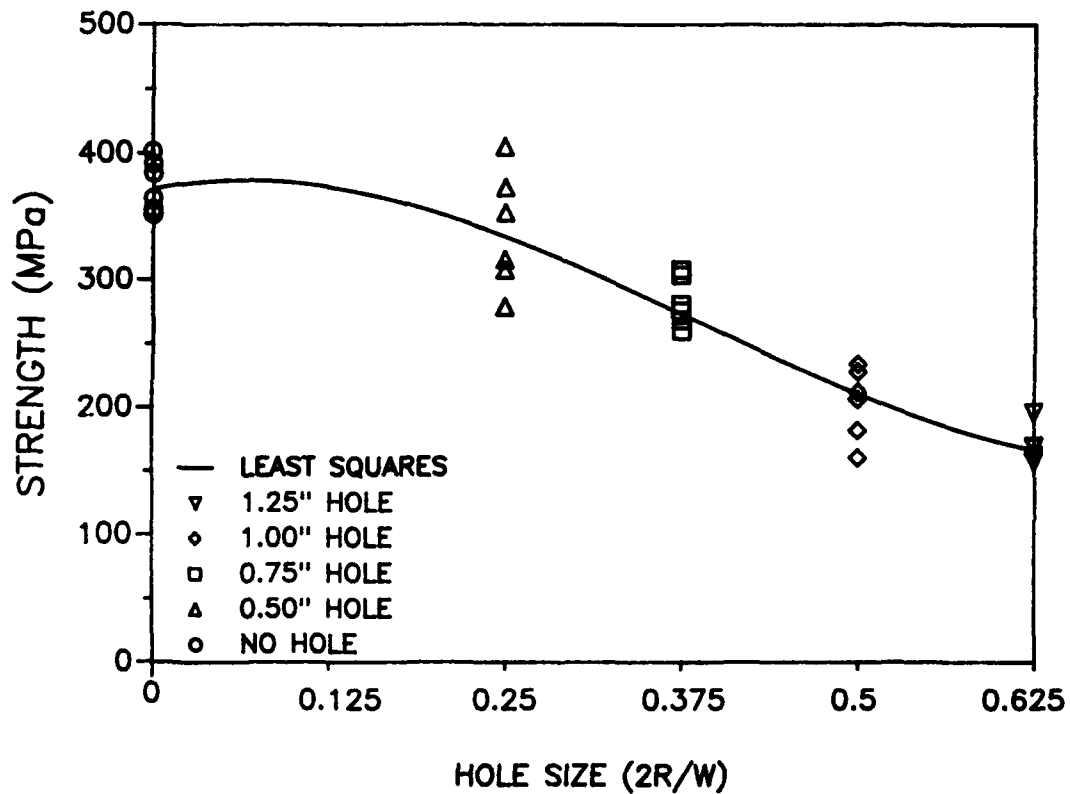
Figure 4. Excel 2415 panels illustrating the effects of drilled holes.
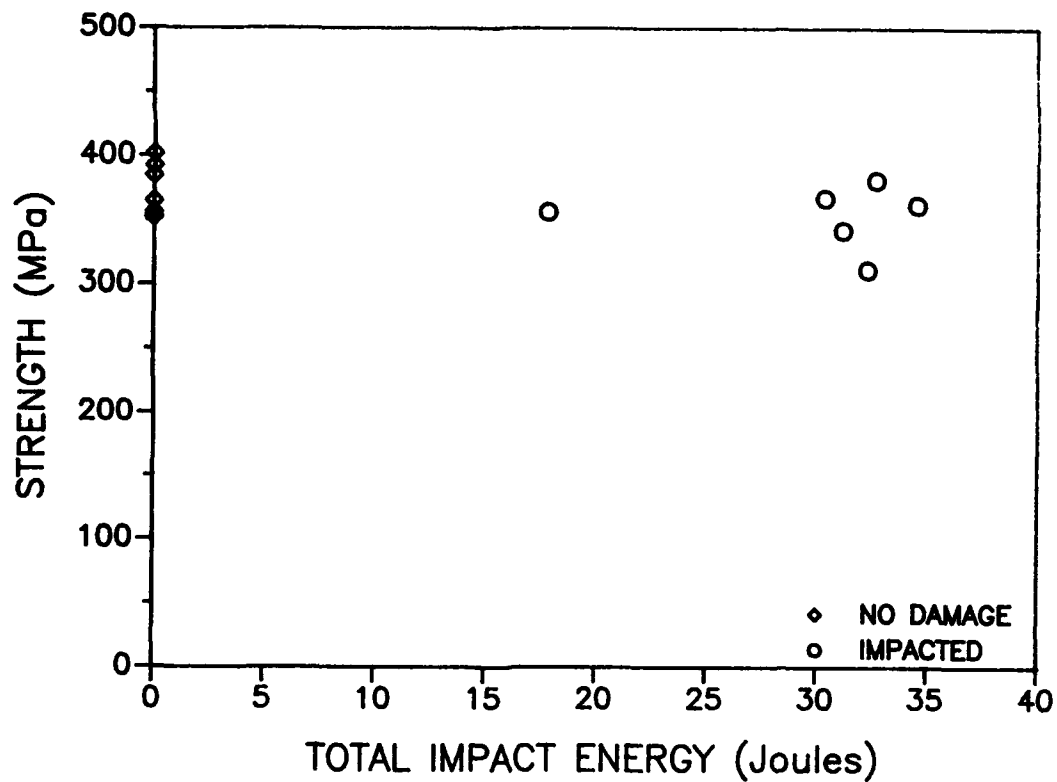
Figure 5. Excel 2415 panels illustrating total impact energy after perforated damage.
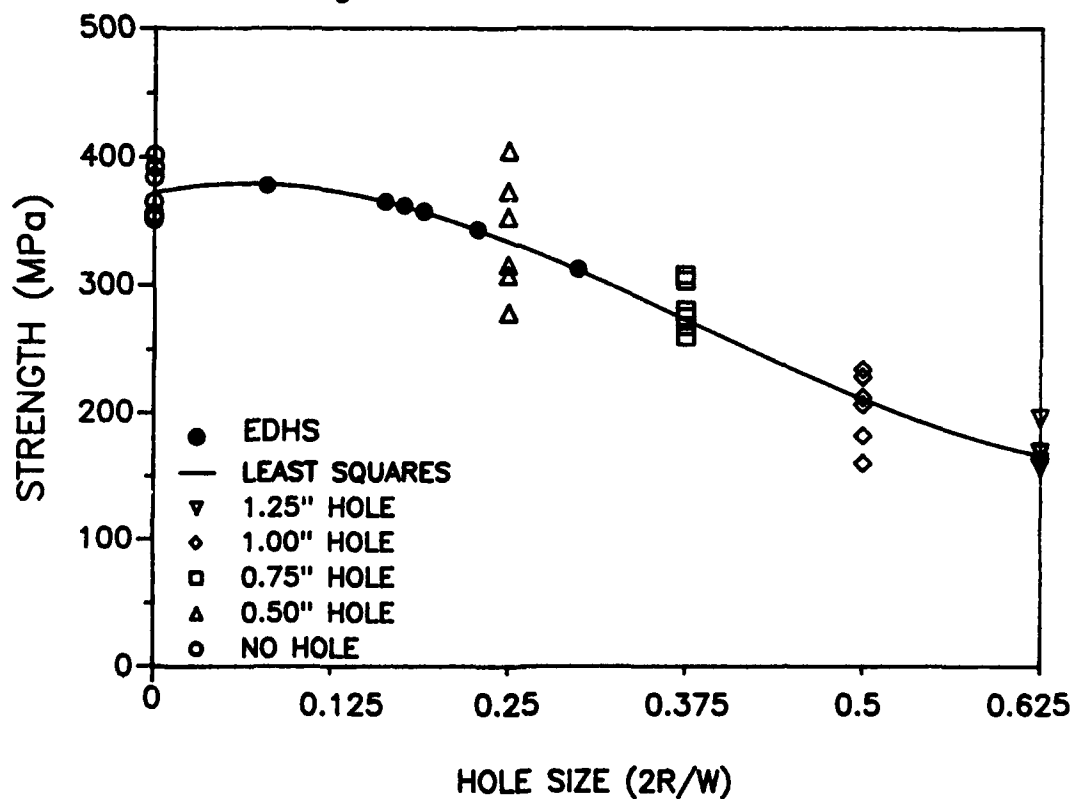
Figure 6. Excel 2415 panels illustrating the equivalent damage hole size.
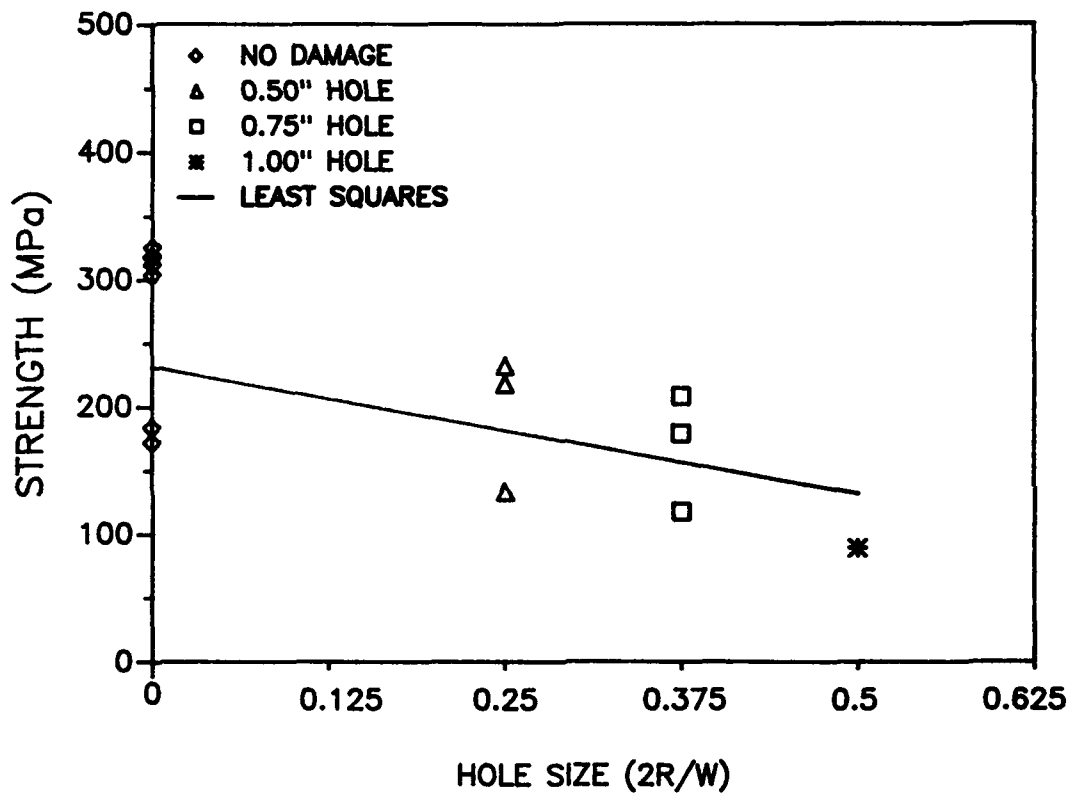
Figure 7. Excel 8610 panels illustrating the effects of drilled holes.
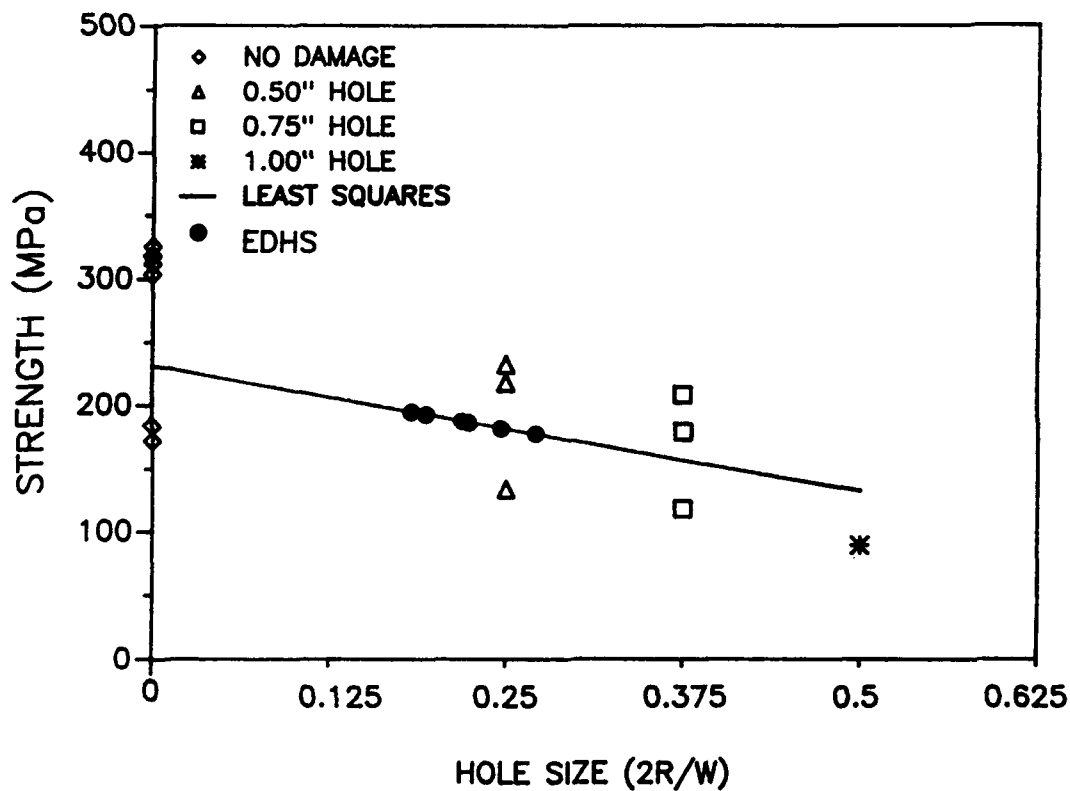
Figure 8. Excel 8610 panels illustrating the equivalent damage hole size.

On Use of Joule Effects for Curing/Joining/Patching of CFRP Composites

KAZUMASA MORIYA

ABSTRACT

A curing method for CFRP/CFRTP composite laminates using their electrical conductivity in the direction transverse to fiber axes is presented. Experimental verifications have been carried out to demonstrate the feasibility of the present method. The application to the joining of CFRP/CFRTP composite parts and to the patch repair of defective composite components has also been demonstrated.

INTRODUCTION

In CFRP composites, the matrix resin is generally an electrical insulator but the carbon fiber is a conductor. Due to the presence of touching fibers, CFRP composites and their prepregs exhibit electrical conductivity in the direction transverse to fiber axes as well as in the fiber direction. Even in the plane normal to fiber axes they can be considered as electrically homogeneous on a gross scale, i.e., on a scale of dimensions dozens of times as large as a fiber diameter[1]. Therefore, passing an electrical current through a laid-up prepreg in through-the-thickness direction, heat is generated inside as a result of Joule effect and it raises the prepreg temperature[2,3].

The amount of Joule heat generated is proportional to the square of current and the inverse of electrical conductivity. The electrical conductivity of CFRP composites is highly anisotropic. It is on the order from 10^{-3} to 10^{-1} S/m in the direction perpendicular to the fibers at room temperature, while it is on the order of 10^4 S/m parallel to the fibers. Therefore, the electrical conductivity in the direction transverse to fiber axes is several orders of magnitude lower than that in the fiber direction. Owing to the low electrical conductivity in the transverse direction, the present method requires far less amount of current to heat the prepreg stack to the cure temperature in comparison with the method which utilizes the electrical conductivity in the fiber direction[4-6].

Since the processing techniques for thermoplastic matrix composites are essentially the same as those of thermosetting matrix composites as far as we start with the prepreg material, the present method can easily be applied to process CFRTP composites.

It can be performed wherever a current source and a temperature monitor are available.

Kazumasa Moriya, Dept. of Aerospace Engineering, National Defense Academy, 1-10-20 Hashirimizu, Yokosuka, 239, JAPAN
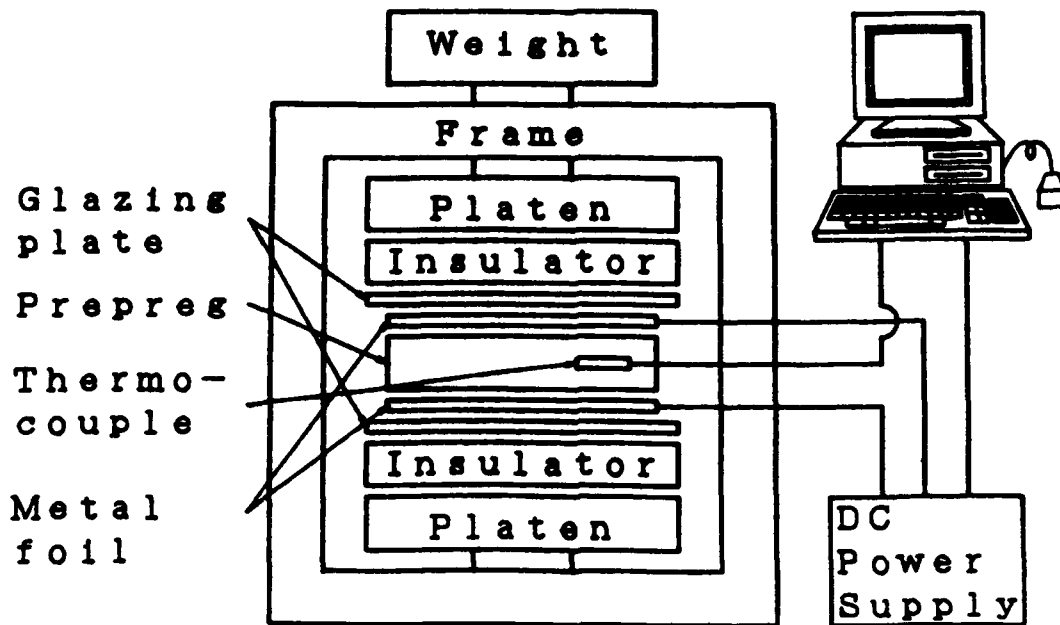
Figure 1. Schematic of experimental setup used in the present study.

The heated area is confined to the current path and it does not require the removal of the parts to be processed. Therefore, the present method can suitably be applied to the repair of damaged composite structures in the field.

METHODS

A schematic of the experimental set-up used in the present study is shown in Figure 1. First, the layers of CFRP prepreg are placed on top of each other in the prescribed stacking sequence and to the prescribed thickness, after which a thin metallic foil, which serves as a release film as well as an electrode, is applied on top and bottom surfaces of the prepreg stack. A glazing plate is placed over each metallic foil to obtain a smooth surface finish. Then, they are sandwiched by the insulator plate which provides insulation against electricity as well as against heat. The whole assembly is mounted on upper and lower platens of a press. It is noted that unlike the external heating system, the insulator is located between the press–platen and the prepreg stack. A dc current, which is supplied by a computer controlled power supply, passes across the top and bottom foil through the prepreg stack in the through–thickness direction. Thermocouples are inserted into the prepreg stack at the midpoint near the corner to monitor the internal temperature. Since the electrical conductivity in through–the–thickness direction of a prepreg stack depends upon the temperature, the applied pressure and the degree of cure, it changes with time during the curing process and the curing current needs to be adjusted continuously in response to the change of the material conductivity. The current density is controlled in real time by a computer so that the prepreg temperature follows the predetermined cure cycle. The cure pressure is applied by a known weight. The applied pressure not only compacts the prepreg stack to squeeze out the excess resin and to remove volatiles but also keeps good electrical contact between the metallic foil electrode and the prepreg.
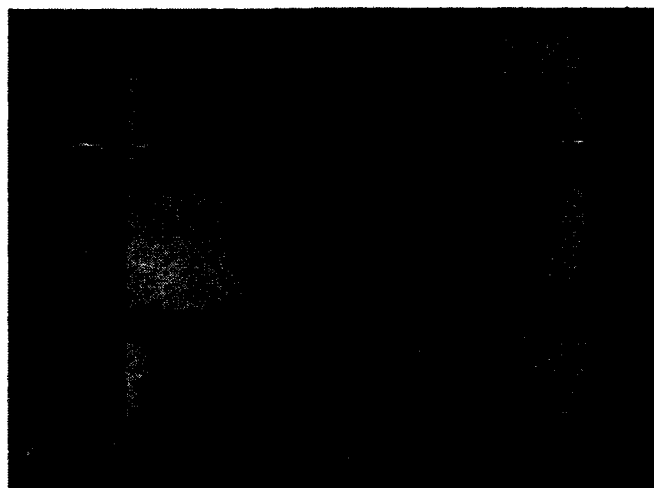
Figure 2. Cured laminates with copper foil on top and bottom surfaces.

CURING OF CFRP LAMINATES

Four types of graphite/epoxy laminates are cured by the present method: 8 ply unidirectional, cross–ply $(0_2/90_2)_s$ and 8 and 16 ply woven fabrics. The fiber volume fraction of these laminates is nominally around 60%. The prepreg is cut into a rectangular shape with dimensions 90 mm wide and 100 mm long and laid up in the specified stacking sequence. A thin copper foil which serves as a release film as well as an electrode is applied on the top and bottom surfaces of the prepreg stack (Figure 2). A type K thermocouple is inserted at the midpoint near the corner of the prepreg stack. If the thermocouple wire contacts the prepreg directly, the curing current which passes through the prepreg stack may flow into the thermocouple causing malfunction of the temperature measurement system. Therefore, precaution must be taken to electrically insulate the thermocouple wire from the prepreg.

At the first stage, the prepreg is heated up to 130°C at a rate of 3°C per min., while the curing current is adjusted to maintain this prescribed heat–up rate. In the second stage the temperature is held at 130°C for 60 minutes. At the last stage the prepreg is cooled down at a cooling rate of 3°C per min. The pressure is kept constant until the end of the cooling stage.

For an 8–ply unidirectional specimen, the specified cure cycle and the variation of the applied voltage during cure are shown in Figure 3. In Figure 4 the variation of the prepreg temperature, the input current and the resistance across the upper and lower electrodes are plotted against time. It is seen that the prepreg temperature plotted in Figure 4 follows closely the prescribed temperature profile shown in Figure 3 even at the break point turning from the heat up stage to the hold period in the cure cycle. For the cross–ply and woven fabric laminates, the prepreg temperature, the curing current and the resistance are plotted in Figures 5–7. Although the resistance is initially very high upto several tens of ohms, it drops rapidly to a fraction of one ohm at the start up of the cure and it further decreases as the cure proceeds. Then, it approaches a constant value towards the end of the cure. This indicates that the change in the resistance between the upper and lower electrodes provides some indication on the extent of the cure.
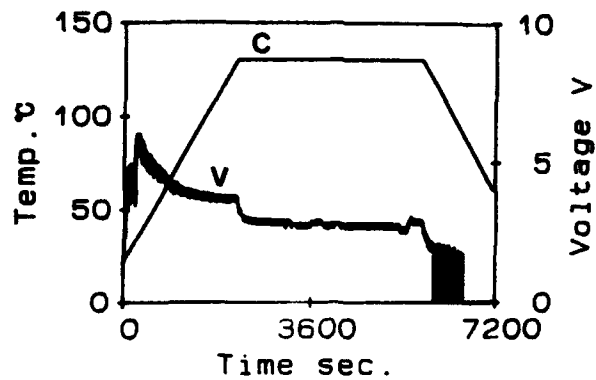
Figure 3. Cure cycle and voltage variation (8–ply unidirectional laminate): C, cure cycle; V, voltage.
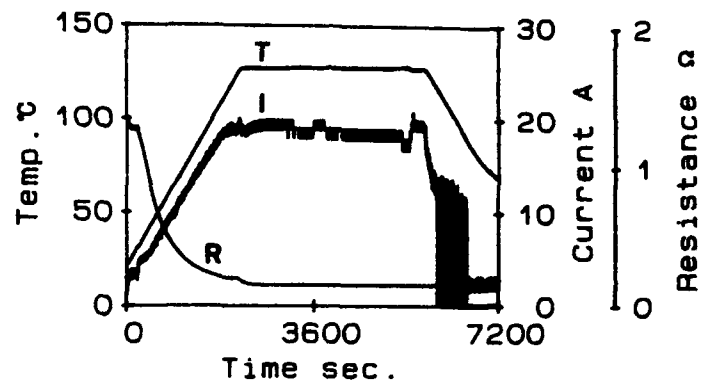
Figure 4. Variation of prepreg temperature, current and resistance (8–ply unidirectional laminate): T, temperature; I, current; R, resistance.
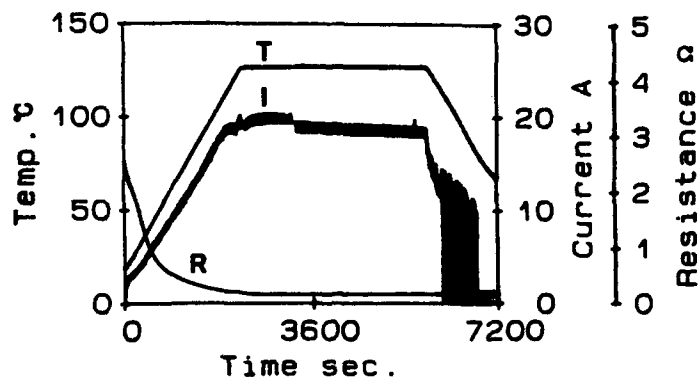
Figure 5. Variation of prepreg temperature, current and resistance ($[0_2/90_2]_s$): T, temperature; I, current; R, resistance.
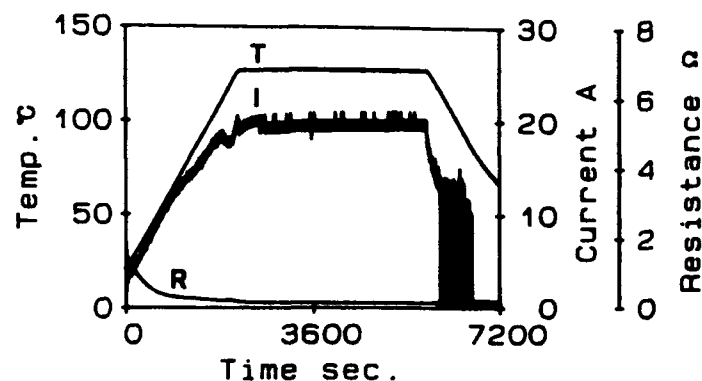
Figure 6. Variation of prepreg temperature, current and resistance (8-ply woven fabric): T, temperature; I, current; R, resistance.
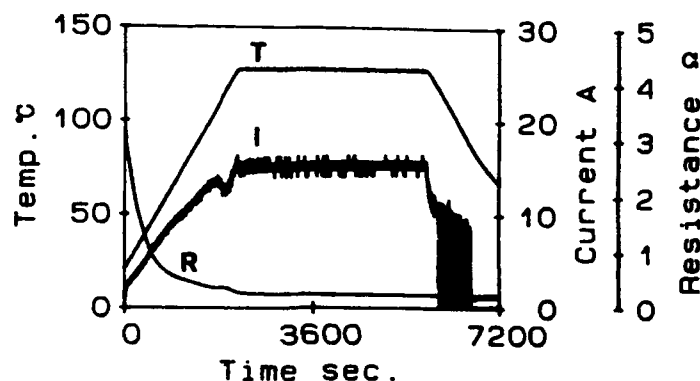
Figure 7. Variation of prepreg temperature, current and resistance (16-ply woven fabric): T, temperature; I, current; R, resistance.

JOINING AND REPAIR OF CFRP COMPOSITES

The present method does not require the use of expensive curing equipments with large heat capacity such as a hot press or an autoclave. It can be performed wherever a current source and a temperature monitor are available. Heat efficiency is very high and the heated area is confined to the current path. Therefore, it is suitably applied to the joining of composite parts and to the repair of damaged composite structures, especially in the field.

Two pieces of unidirectional CFRP coupon specimen with length L and thickness t_1 are joined together by applying a prepreg patch with length 2a and thickness t_2 as shown in Figure 8. The two coupons are joined apart from each other at distance d. This can be regarded as the case where the through-thickness damage of width d in a CFRP panel is repaired by applying an external patch on each surface of the panel. The x-axis corresponds to the fiber direction, while y is transverse to the laminate plane. The unidirectional prepreg patch is laminated directly onto each surface of the specimen to make a double strap joint. A thin metallic foil whose length is 2b is applied on top of each patch to serve as a release film as well as an electrode. Passing a dc current between the upper and lower metallic foil
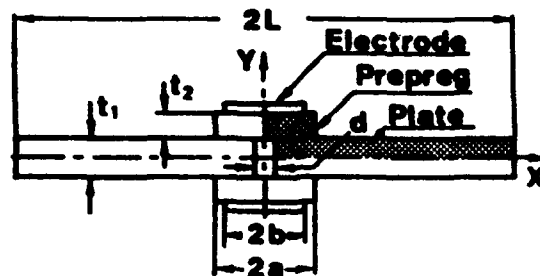
Figure 8. Joining of coupon specimens of composite laminate.
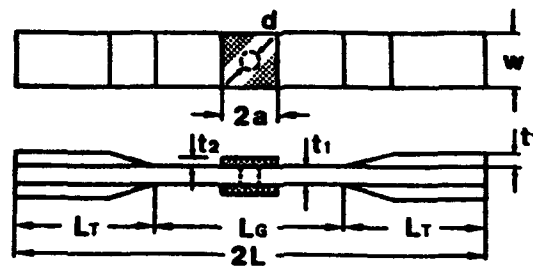
Figure 9. Patch repair of coupon specimen with a circular hole.

and pressing the whole assembly together, Joule heat is generated in the patch. Due to the double symmetry of the geometry, the temperature distribution within a quarter of the assembly is analyzed by FEM. The geometries are L=100 mm, d=4 mm, $t_1=t_2=1$ mm and a=10 mm. The length of the electrode is varied from b/a=1/4 to 1. For b/a=1, 3/4,1/2 and 1/4, the temperature deviation ΔT in the prepreg patch, which is defined by $\Delta T=(T_{max}-T_{min})/T_{max}$, is 1.86%, 1.87%, 1.94% and 2.14%, respectively. Corresponding to these, the required voltage to maintain the cure temperature 130°C is 0.483 V, 0.484 V, 0.490 V and 0.503 V, respectively. As the contact area of the metallic foil electrode is reduced, both the temperature deviation and the required voltage tend to increase.

Next, the present method is applied to the repair of damaged composite parts. An unidirectional coupon specimen with a circular hole, which is intended to simulate a damage, is prepared. The specimen geometry is 20 mm in width, 200 mm in length and 6 plies in thickness. A circular hole 4 mm in diameter is drilled at the center of the specimen. The beveled aluminum tabs of 2 mm thick are adhesively bonded to the end of the specimen where they are clamped for load introduction in the tensile test. The unidirectional prepreg patch which is 20 mm square and 6 plies in thickness is laminated directly onto each surface of the specimen to cover the hole as shown in Figure 9. The procedure of curing the repair patch is the same as that of curing laminates.

In order to evaluate the quality of the repair, tensile tests have been conducted on both the specimens with and without a patch. The tensile strength of the unidirectional laminate is nominally 1500 MPa. The specimens with a drilled hole but without a patch have the average tensile strength of 1470 MPa. The specimens having a drilled hole over which a
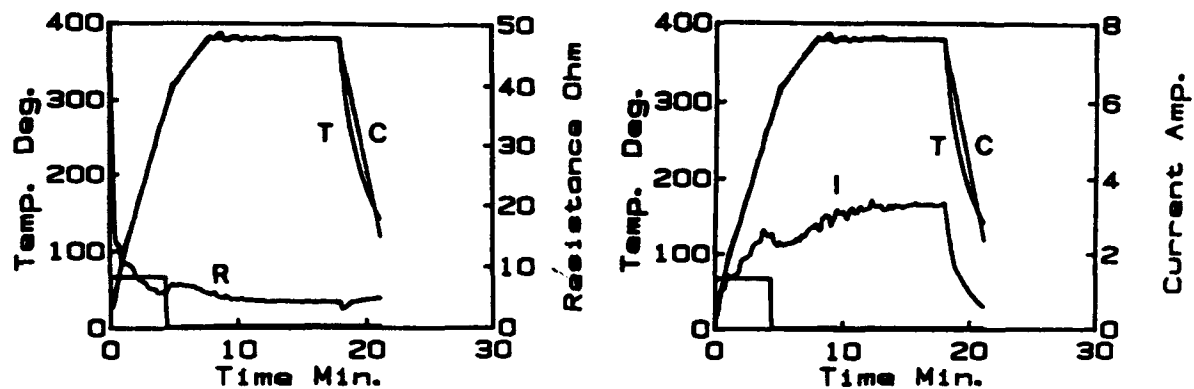
Figure 10. Cure cycle and variation of temperature, resistance and current during consolidation of CFRTP composite laminate: T, temperature; I, current; R, resistance.

patch is applied by the present method exhibit the average tensile strength of 1730 MPa.

CURING AND JOINING OF CFRTP COMPOSITES

The processing techniques for thermoplastic matrix composites are essentially the same as those for thermosetting matrix composites as far as we start with the prepreg material. The main differences are associated with higher temperature and pressure requirements and lesser cycle time. Therefore, the extension of the present method to process CFRTP composites is straightforward.

First, a commingled yarn prepreg in which PEEK filaments are intermingled with AS4 filaments is consolidated by the present method. The specimen is 20 mm square and 6 plies in thickness. In this experiment, although the current, voltage, temperature and pressure data are processed in real time by a microcomputer, an off-line power supply is used and hence, the curing current is adjusted manually to the appropriate value. Therefore, the heat up rate is decreased from 70°C/min to 20°C/min towards the end of the heat up stage to avoid overshooting. In Figure 10, the specified cure cycle, the variation of the prepreg temperature, the resistance across the upper and lower electrodes and the curing current are plotted against time. It is seen that the high heat up rate of 70°C/min is accomplished and that the prepreg temperature closely follows the specified cure cycle even at the break point turning from the heat up stage into the hold period. It is also noted that very high cooling rate of 80°C/min is obtained simply by turning off the power supply without using any special cooling devices.

Next, two piece of unidirectional CFRTP coupon specimen are joined together by attaching a prepreg patch of the same material as shown in Figure 8. The distribution of the electrical potential during consolidation calculated by FEM is plotted in Figure 11, where the y coordinate is scaled up ten times. It is seen that the steep gradient of the electrical potential appears inside the patch, while the potential variation is small in the coupons. It means that the Joule heat is generated mainly within the patch being cured. The temperature distribution is plotted in Figure 12. It is seen that the temperature in the coupons decreases rapidly as far away from the patch. The heated area is confined to the inside of the patch
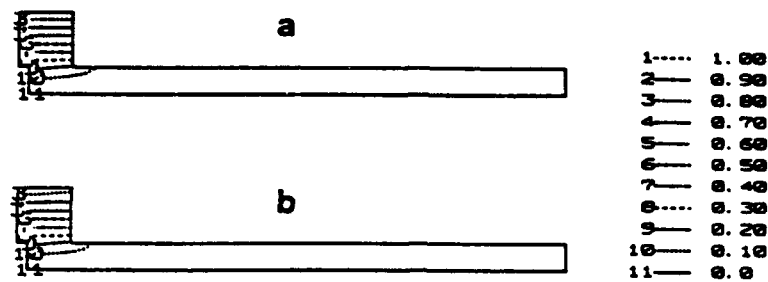
Figure 11. Electrical potential in CFRTP coupon specimen during joining: (a) b/a=1, (b) b/a=1/2, where a and b represent the length of patch and electrode, respectively.
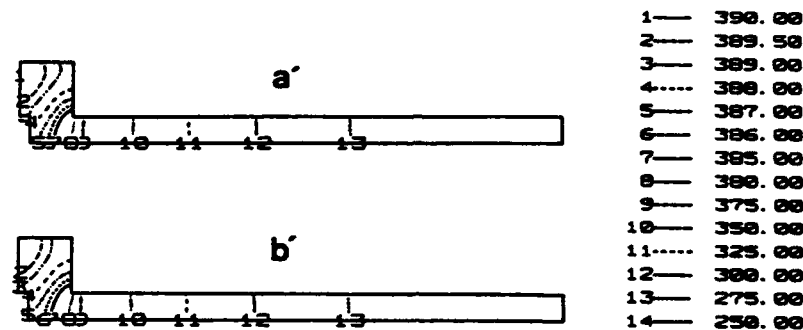
Figure 12. Temperature distribution in CFRTP coupon specimen during joining: (a) b/a=1, (b)b/a=1/2, where a and b represent the length of patch and electrode, respectively.

and its neighborhood.

In the experiment, two pieces of unidirectional CFRTP coupon specimen made of a commingled yarn prepreg are joined together by attaching a prepreg patch of the same material. Each coupon is 20 mm in width, 100 mm in length and 6 plies in thickness and the patch is 20 mm square and 6 plies in thickness. The average tensile strength of the joined specimens is 18 kN which corresponds to the lap shear strength of 45 MPa.

CONCLUSIONS

A curing method of CFRP/CFRTP composites which utilizes Joule heat generated by passing an electrical current through a laid-up prepreg in the through-thickness direction has been presented. The application to the joining of composite parts and to the patch repair of defective composite components has also been demonstrated. The present method can be performed wherever a current source and a temperature monitor are available. The heated area is confined to the current path and it does not require the removal of the parts to be cured. Therefore, the present method becomes especially convenient when we are required to join composite parts or to repair damaged composite structures in the field.

REFERENCES

1. K. Moriya and T. Endo, 1988."A Study on Flaw Detection Method for CFRP Composite Laminates (1st Report) The Measurement of Crack Extension in CFRP Composites by Electrical Potential Method", J. Japan Soc. for Aero. and Space Sci., 36(410): 139–146 (in Japanese).

2. K. Moriya, 1989."A Study on Flaw Detection Method for CFRP Composite Laminates (2nd Report) Use of Joule Effect for Detecting Flaws and Local Fiber Concentrations in CFRP composites", J. Japan Soc. for Aero. and Space Sci., 37(424): 238–246 (in Japanese).

3. K. Moriya, 1990."Study on Fabrication Methods of Composite Structures", J. Japan Soc. for Aero. and Space Sci., 38(438): 371–378 (in Japanese).

4. D.M. Maguire, 1989."Joining Thermoplastic Composite", SAMPE J., 25(1): 11–14.

5. A.M. Maffezzoli, J.M. Kenny and L. Nicolais, 1989."Welding of PEEK/Carbon Fiber Composite Laminates", SAMPE J., 25(1): 35–39.

6. Roderic C. Don et.al., 1990."Fusion Bonding of Thermoplastic Composite by Resistance Heating", SAMPE J., 26(1): 59–66.

SESSION 9B

Strength Analysis I

Analysis and Testing of S2/SP250 Glass/Epoxy Laminates under Torsion Loading

ERIAN A. ARMANIOS,* JIAN LI** AND DAVID HOOKE**

ABSTRACT

A shear deformation theory and a sublaminate approach is used to analyze S2/SP250 Glass/Epoxy laminates under torsion loading. Two lay-ups are considered, namely $[\pm 45/0_{12}/\pm 45_2/0_6/\pm 45]_s$ and $[(\pm 45/0_6)_3/\pm 45]_s$. A fixture is designed in order to test the laminates under torsion using a uniaxial loading platform. Comparison between the experimental torsional stiffness and the analytical predictions is performed. Potential critical interfaces are identified through the interlaminar peel stress distribution.

INTRODUCTION

Torsion is a prevalent loading condition in a number of composite components such as flex beams, rotor hubs, and faces of sandwich constructions. Delamination caused by interlaminar stresses can initiate at the free edges and ply terminations in this structures. The interlaminar stress analysis of laminates under torsion loading has received considerable attention. A number of analytical technique has been used for symmetric laminates under torsion. Those include finite element method[1-2], closed form solution[3-4].

The objective of this work is to analyze and test two laminate configurations with $[\pm 45/0_{12}/\pm 45_2/0_6/\pm 45]_s$ and $[(\pm 45/0_6)_3/\pm 45]_s$ lay-ups made of S2/SP250 Glass/Epoxy laminates under torsion loading. This material system is used in composite rotor hub designs due to its high strain to failure. The analysis is based on a shear deformation theory that allow for the interlaminar stresses to be determined in closed form. Delamination sites are predicted based on the interlaminar peel stress distribution. Tests are conducted in order to measure the torsional stiffness and comparison with the analytical prediction is performed.

---

*Associate Professor and ** Graduate Research Assistant, respectively. School of Aerospace Engineering, Georgia Institute of Technology, Atlanta, Georgia 30332-0150

GOVERNING EQUATIONS

The laminate is treated as made of sublaminates, or groups of plies treated as single laminated unit. Each sublaminate can be treated as a homogeneous anisotropic elastic body bounded by a cylindrical surface. A schematical representation of a generic sublaminate appears in Fig. 1 along with its coordinate system. A generalized plane deformation [5] exists in a laminate when it is subjected to a remote twist moment such that the stress tensor is independent of the x-coordinate. The displacement field within each sublaminate may be written as

$$u(x,y,z) = \varepsilon_0 x + \kappa x(z+\delta) + U(y) + z\beta_x(y)$$
$$v(x,y,z) = V(y) + z\beta_y(y) + Cx(z+\delta)$$
$$w(x,y,z) = -\tfrac{1}{2}\kappa x^2 - Cx(y+\rho) + W(y) \tag{1}$$

where u, v, and w denote displacements relative to the x, y, and z axes, respectively. The extension strain is ε_0. The arbitrary constants δ and ρ associated with each sublaminate are to be determined from continuity of displacements between sublaminates and from overall boundary conditions. The relative angle of rotation and bending curvature are denoted by C and κ, respectively. These result from the coupling effects associated with unsymmetrical lay-ups. Shear deformation is recognized through the rotations β_x and β_y. The bending about the y-axis is neglected since the sublaminate thickness is small compared to its width.

The strains corresponding to the displacement field in Eq. (1) are defined as

$$\varepsilon_{xx} = \varepsilon_{xx}^0 + z\kappa_x \qquad \varepsilon_{yy} = \varepsilon_{yy}^0 + z\kappa_y \qquad \varepsilon_{zz} = 0$$
$$\gamma_{xy} = \gamma_{xy}^0 + z\kappa_{xy} \qquad \gamma_{yz} = \gamma_{yz}^0 \qquad \gamma_{xz} = \gamma_{xz}^0 \tag{2}$$

The strain components associated with the reference surface are denoted by superscript ^{0}. These and the associated curvatures are defined as

$$\varepsilon_{xx}^0 = \varepsilon_0 + \kappa\delta \qquad \varepsilon_{yy}^0 = V_{,y} \qquad \gamma_{xy}^0 = U_{,y} + C\delta$$
$$\kappa_x = \kappa \qquad \kappa_y = \beta_{y,y} \qquad \kappa_{xy} = \beta_{x,y} + C$$
$$\gamma_{yz}^0 = \beta_y + W_{,y} \qquad \gamma_{zx}^0 = \beta_x - C(y+\rho) \tag{3}$$

where partial differentiation is denoted by a comma. The constitutive relationship is written in terms of the resultant forces and moments, shown in Fig. 1, and associated strains and curvatures as follows

$$
\begin{Bmatrix} N_x \\ N_y \\ N_{xy} \\ M_x \\ M_y \\ M_{xy} \end{Bmatrix} = \begin{bmatrix} A_{11} & A_{12} & A_{16} & B_{11} & B_{12} & B_{16} \\ A_{12} & A_{22} & A_{26} & B_{12} & B_{22} & B_{26} \\ A_{16} & A_{26} & A_{66} & B_{16} & B_{26} & B_{66} \\ B_{11} & B_{12} & B_{16} & D_{11} & D_{12} & D_{16} \\ B_{12} & B_{22} & B_{26} & D_{12} & D_{22} & D_{26} \\ B_{16} & B_{26} & B_{66} & D_{16} & D_{26} & D_{66} \end{bmatrix} \begin{Bmatrix} \varepsilon_{xx}^o \\ \varepsilon_{yy}^o \\ \gamma_{xy}^o \\ \kappa_x \\ \kappa_y \\ \kappa_{xy} \end{Bmatrix}
$$

(4)

$$
\begin{Bmatrix} Q_y \\ Q_x \end{Bmatrix} = \begin{bmatrix} A_{44} & A_{45} \\ A_{45} & A_{55} \end{bmatrix} \begin{Bmatrix} \gamma_{yz}^o \\ \gamma_{xz}^o \end{Bmatrix}
$$

(5)

For a sublaminate of thickness h, the stiffness coefficients are defined as

$$
\left(A_{ij}, B_{ij}, D_{ij}\right) = \int_{-\frac{h}{2}}^{\frac{h}{2}} \overline{Q}_{ij}\left(1, z, z^2\right) dz
$$

(6)

where $\overline{Q}_{ij}$ are the transformed reduced stiffnesses as defined in Ref. 6.

The equilibrium equations can be written as

$$
N_{xy,y} + t_{ux} - t_{lx} = 0
$$

$$
N_{y,y} + t_{uy} - t_{ly} = 0
$$

$$
Q_{y,y} + p_u - p_l = 0
$$

$$
M_{xy,y} - Q_x + \tfrac{h}{2} \cdot (t_{ux} + t_{lx}) = 0
$$

$$
M_{y,y} - Q_y + \tfrac{h}{2} \cdot (t_{uy} + t_{ly}) = 0
$$

(7)

where the interlaminar shear and peel stresses at the sublaminate upper and lower surfaces are denoted by t_{ux}, t_{uy}, p_u and t_{lx}, t_{ly}, p_l, respectively, as shown in Fig. 1.

SUMMARY OF SOLUTIONS

Two level of modeling are used in the analysis. In the first, or Model I, the entire cross section is modeled using one sublaminate as shown in Fig. 2. This model is used to

capture global parameters such as torsional stiffness, twisting curvature and the induced bending curvature. The second model, or Model II, is used to predict interlaminar stresses. In this model, the upper half of the laminate cross section is modeled using two sublaminates as shown in Fig. 3.
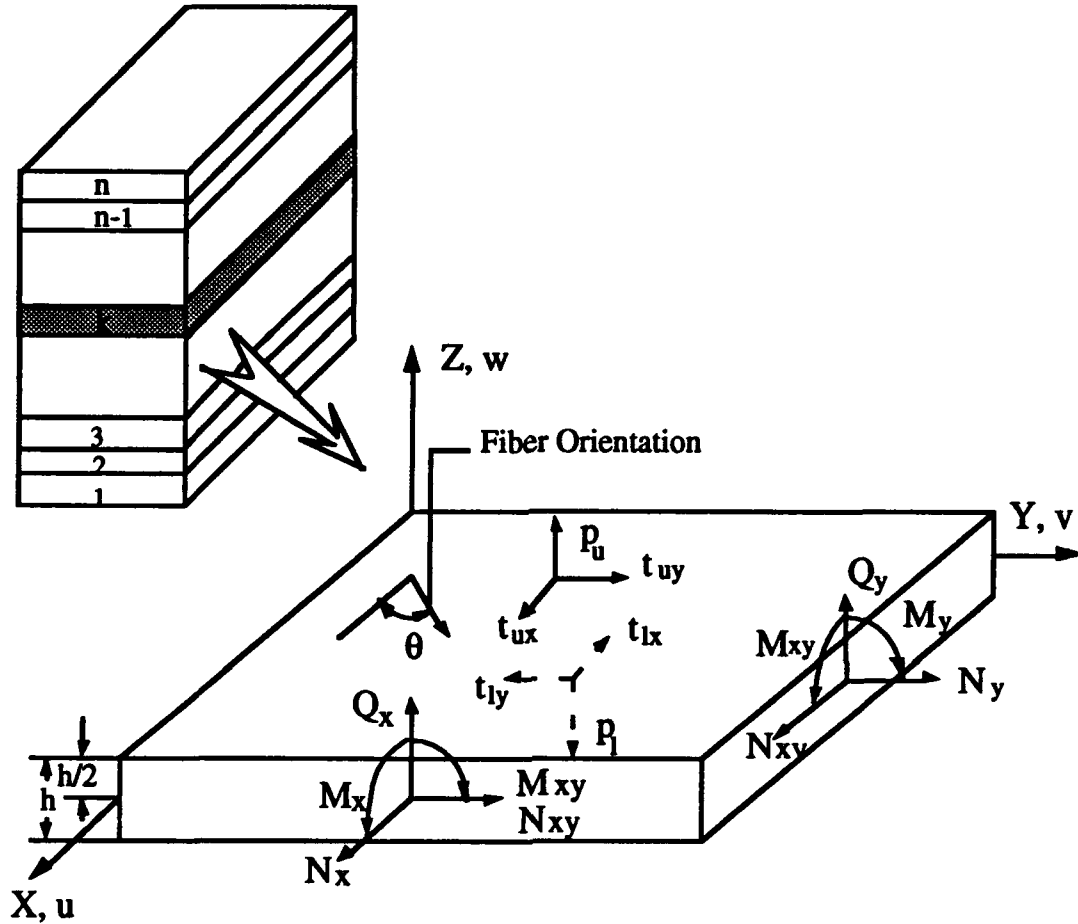
Fig.1 Sublaminate Notation and Sign Convention

TORSIONAL STIFFNESS AND CURVATURES

From Model I, the torsional stiffness and the twisting curvature are given by

$$\frac{T}{2C} = 2b\left(\lambda_{31}\frac{\varepsilon_0}{2C} + \lambda_{32}\frac{\kappa}{2C} + \lambda_{33}\right) + \frac{2I}{C}\lambda_{33}\sinh(sb) \tag{8}$$

$$\kappa_{xy} = 2C + I s\cosh(sy) \tag{9}$$

where T is the applied torsional moment. The parameters λ_{ij}, s, I and the induced extension strain and bending curvature are defined in Ref. 3.
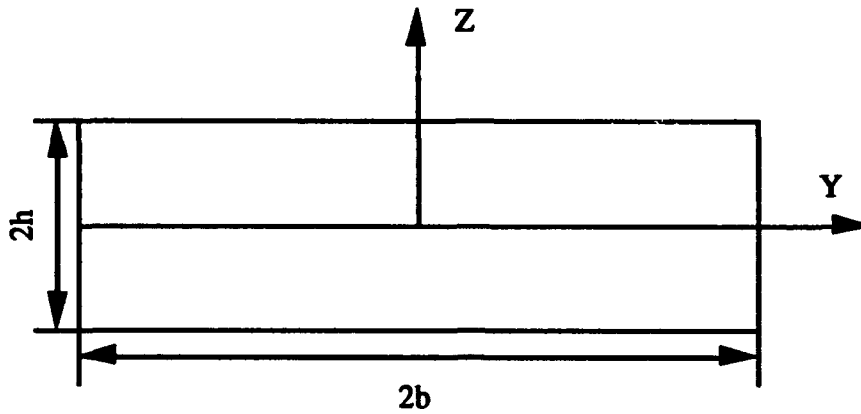
Fig. 2. Global Analysis Model: Model I
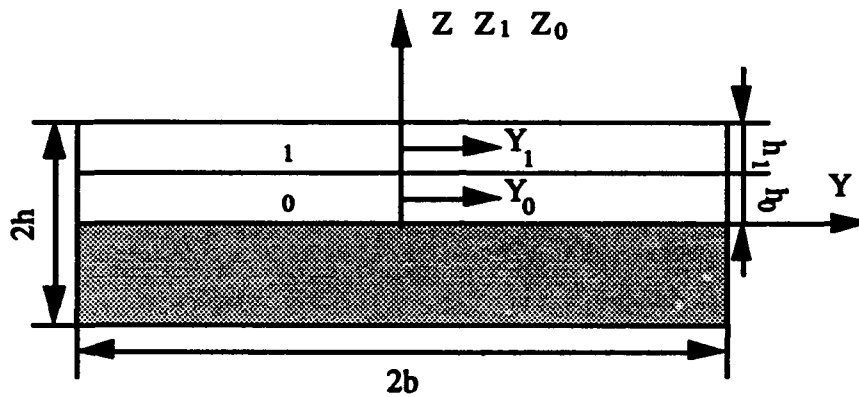
Fig. 3. Interlaminar Stress Analysis Model: Model II

INTERLAMINAR STRESSES

The interlaminar stresses at the interface between sublaminates 0 and 1 in Model II are given by

$$\tau_{xz} = \alpha_1 s_2^2 \text{shin}(s_2 y) + \alpha_2 s_3^2 \text{shin}(s_3 y) + \alpha_3 s_4^2 \text{shin}(s_4 y) \tag{10}$$

$$\sigma_z = \alpha_0 C + \alpha_4 s_2 \cosh(s_2 y) + \alpha_5 s_3 \cosh(s_3 y) + \alpha_6 s_4 \cosh(s_4 y) \tag{11}$$

where the parameters α_0 through α_6 and s_2 through s_4 are defined in Ref. 3.

TESTING METHOD

The test apparatus consists of a rigid aluminum frame with an adjustable fixed clamp at one end and a bearing supported swivel clamp at the other. The specimen is clamped

between these supports with the long axis of the specimen oriented horizontally. The swivel clamp is equipped with a loading arm which is offset from the axis of rotation. Load applied at the tip of this arm, therefore, applies a resultant torque to the specimen. A representative view of the apparatus is displayed in Fig. 4.

After the specimens were clamped in the apparatus and all initial offsets removed, various increasing loads were applied to the tip of the loading arm. The data collected consists of the displacement of the loading tip in the vertical direction and the resultant load for each of the displacements. This procedure was repeated for each of the specimens in the set.
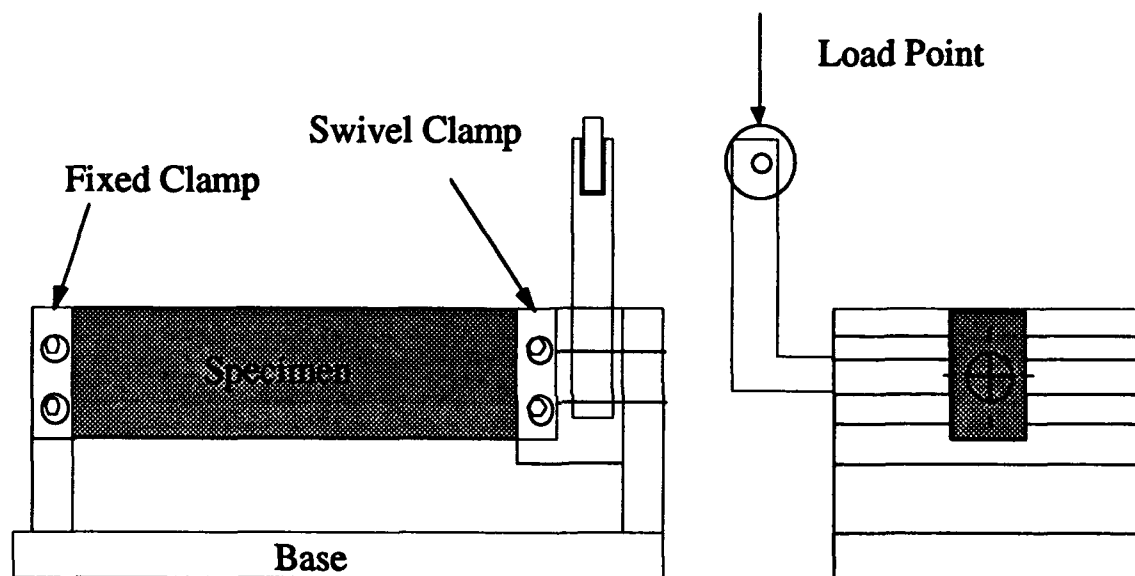
Fig. 4 Testing Apparatus

The specimens are made of S2/SP250 Glass/Epoxy materials. Two types of laminates are considered, namely type A with $[\pm45/0_{12}/\pm45_2/0_6/\pm45]_s$ lay-up and type B with $[(\pm45/0_6)_3/\pm45]_s$ lay-up. The material properties and geometry are given in Table I.

TORSIONAL STIFFNESS

The specimen is fixed at one end and a twisting moment is applied at the other end. Both the applied twisting moment and the rotation of the specimen are measured to determine the torsional stiffness experimentally. A comparison of torsional stiffness is given in Table II. The analytical results are obtained from Eq. (8). The analytical solution and the elasticity solution [5] for a unidirectional laminate are given in Table II as a reference.

Table I Material Properties and Geometry for S2/SP250 Glass/Epoxy

E_{11}=7.29 Msi (50.3 GPa)
E_{22}=E_{33}=2.1 Msi (14.5 GPa)
G_{12}=G_{13}=0.88 Msi (6.1 GPa)
G_{23}=0.49 Msi (3.4 GPa)
υ_{12}=υ_{13}=0.275
υ_{23}=0.46
Ply thickness H=0.008 in (0.203 mm)
Semi-width b=125H
Total Length=8 in (203 mm)
Effective Length=6 in (152.4 mm)

The differences between analytical and experimental results are about 22% and 24% for type A and type B specimens, respectively. This is due to the boundary effects at the laminate ends since the specimens are relatively thick and short.

Table II Comparison of Torsional Stiffness

Specimen	Analytical	Experimental	Elasticity
Type A	$5.024\ 10^4$	$3.93\ 10^4$	-
Type B	$5.318\ 10^4$	$4.06\ 10^4$	-
Unidirectional	$3.716\ 10^4$	-	$3.687\ 10^4$

INTERLAMINAR STRESSES PREDICTIONS

The interlaminar peel stress σ_z and shear stress τ_{xz} distributions through the thickness at the free edge are shown in Fig. 5 and Fig. 6, respectively. The twist angle per unit length C is taken as 0.5 rad/in (0.02 rad/mm). The interlaminar peel stress increases at the 45/-45 interfaces with the largest value occurring at the first 45/-45 interface from the top. For the Glass/Epoxy material system considered, free edge delamination may develop at this interface. The interlaminar shear and peel stress distributions are similar for both lay-ups.
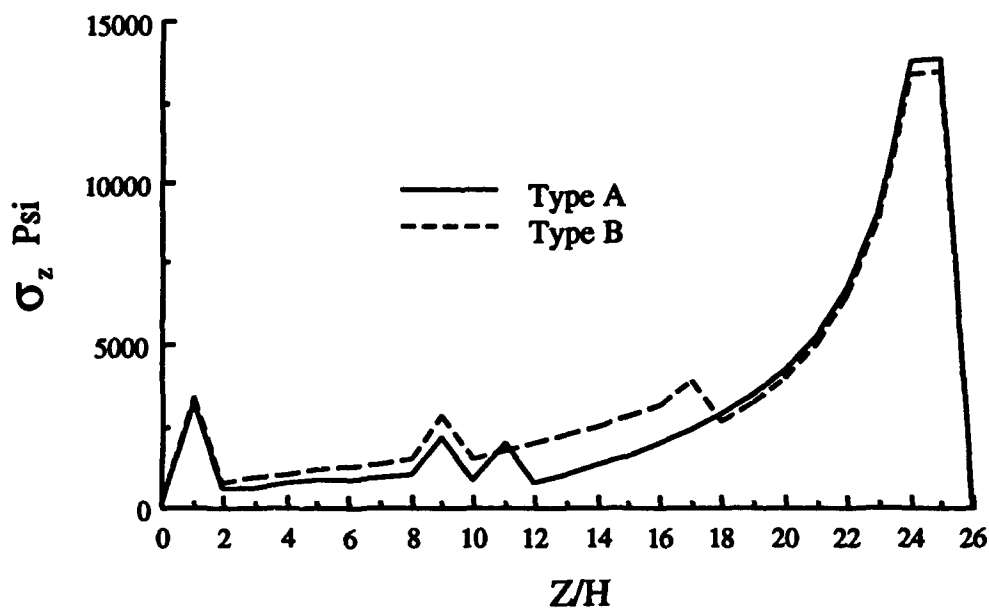
Fig. 5. Interlaminar Peel Stress Distributions
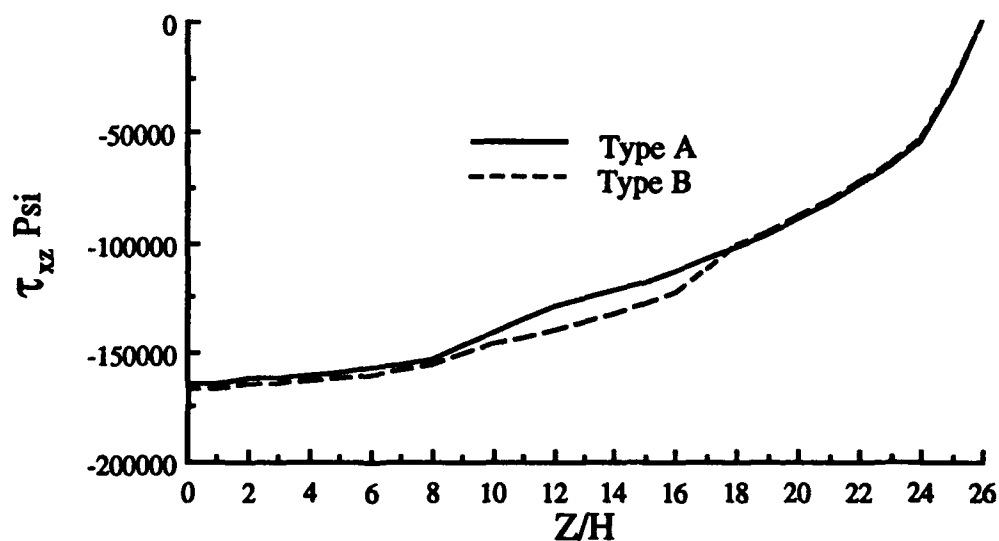
Fig. 6.Interlaminar Shear Stress Distributions

CONCLUSION

A shear deformation model is used to analyze the behavior of $[\pm45/0_{12}/\pm45_2/0_6/\pm45]_s$ and $[(\pm45/0_6)_3/\pm45]_s$ laminates made of Glass/Epoxy under torsion loading. Both lay-ups show similar interlaminar stress distributions. Potential delamination sites are determined based on the maximum interlaminar peel stress.

ACKNOWLEDGMENT

REFERENCES

1. Chan, W. S. and Ochoa, O. O. 1987. "Assessment of Free-Edge Delamination Due to Torsion," Proceedings of the Second Technical Conference, American Society for Composites, Lancaster, pp. 469-478.

2. Murthy, P. L. N. and Chamis, C. C., "Free-Edge Delamination: Laminate Width and Loading Conditions Effects," Journal of Composites Technology & Research, JCTRER, Vol. 11, No. 1, Spring 1989, pp. 15-22.

3. Armanios, E. A. and Li, J. 1991. "Interlaminar Stress Predictions for Laminated Composites Under Bending, Torsion and Their Combined Effect," Composite Engineering, Vol. 1, No. 5, pp. 277-291.

4. Yin, W. -L. 1991. "Free-Edge Effects in Laminates Under Extension, Bending and Twisting, Part I: A Stress Function Approach," Proceedings of the 32th Structures, Structural Dynamics, and Material(SDM) Conference, Part 2, pp. 985-995.

5. Lekhitskii, S. G., 1963. Theory of elasticity of an anisotropic elastic body, Holden-Day, San Francisco, pp. 107-108.

6. Vinson, J. R. and Sierakowski, R. L., 1986. The behavior of structures composed of composite materials, Martinus Nijhoff Publishers, p. 47.

Failure Criterion for Thick Multi-Fastener Graphite/Epoxy Composite Joint

D. COHEN,[1] M. W. HYER,[2] M. J. SHUART,[3] O. H. GRIFFIN,[2] C. PRASAD,[4] L. Q. DO[1] AND S. R. YALAMANCHILI[2]

ABSTRACT

A method for accurately predicting multi-fastener, thick composite joint strength is discussed. The method is based on the average stress criterion applied around the hole circumference. Basic laminate strength variation data are obtained from single-hole and reduced-section notched specimens. Using ABAQUS finite element analyses, the stress field distribution around the pin-loaded hole in both the single-hole and the multi-fastener joints is determined. Using the basic strength data and the finite element analyses, multi-fastener joint strength of three different laminate layups are predicted and compared with experimental results.

INTRODUCTION

The increased application of composite materials in multi-segment thick structures, such as solid rocket boosters and deep submergence pressure hulls, has resulted in an increased need to understand and predict mechanical joint strength. In the type of structures mentioned, the joints are heavily loaded. These joints may be the limiting factor in overall structural capacity. Therefore, the benefit from an optimal joint may be substantial. To achieve an optimum design, it is important that the failure modes and failure loads can be accurately predicted for any multi-fastener geometry or material layup.

The literature documents both experimental and analytical studies that address failure load and failure mode predictions for bolted joints using thin laminates [e.g., Refs. 1 and 2]. Typically, these studies concentrate on a single-hole geometry in which failure exhibits three modes: shearout, bearing, or net tension. Some studies [3,4] has focused on multiple-hole joint configurations but typically addresses thin quasi-isotropic laminates and may not be totally applicable to thick fiber-dominated composite joints. For the type of structures discussed above failure may occur away from the net-section area at some other location around the hole circumference, as shown in the X-ray of Figure 1. In this figure it is seen that failure appears to occur 20° to 30° away from the net-section.

[1] Hercules Aerospace Company, Magna, UT 84108-0098.
[2] Professor, Associate Professor, and Graduate Research Assistant, respectively, Dept. of Engineering Science & Mechanics, Virginia Polytechnic & State University, Blacksburg, VA 24061.
[3] Assistant Branch Head, Aircraft Structures Branch, NASA Langley Research Center, Hampton, VA 23665-5225.
[4] Research Engineer, Analytical Services and Materials, Inc., Hampton, VA 23665-5225.

This paper discusses a failure criterion that addresses the observed failure mechanism in thick fiber-dominated composite joints. The criterion is based on the average stress failure criterion [5,6,7] applied around the hole boundary and uses laminate tensile strength variation around the hole. The strength variation is determined using single-hole pin loaded specimens and notched specimens. The failure criterion is validated using test data

Figure 1. Post-Failure Dye Penetrant Photo of 5-Hole T45 Laminate

from thick multi-fastener composite specimens where the number of loaded holes varied from 3 to 9. The stress distribution around each hole is determined from a nonlinear finite element analysis, which accounts for the pin-to-hole contact condition. Three different laminates (designated as T45, T30, and T60), which lead to different failure modes and failure loads, were tested. In this paper only the results for the T45 laminate are discussed.

Figure 2. Pin-Loaded Hole Coordinate System Nomenclature

FAILURE CRITERION

The failure criterion applies the average stress concept around the hole circumference. This failure criterion assumes that only the tangential tensile stress and the inplane shear stress components are significant in the joint failure process. As shown in Figure 2, the tensile tangential component will be designated by subscript tt and the shear component by subscript rt, indicating their dependence on the local r-t hole (radial-tangential) coordinate system. In this nomenclature, the load is directed in the y direction, the z direction is out of the plane of the laminate, and the net-section plane is the x-z plane, as also shown in Figure 2. The proposed average stress failure criterion for the present study is,

$$\left[\frac{1}{d_o} \int_R^{R+d_o} \left(\left\{ \frac{\sigma_{tt}(r,\phi)}{\sigma_{tt}^o(\phi)} \right\}^2 + \left\{ \frac{\tau_{rt}(r,\phi)}{\tau_{rt}^o(\phi)} \right\}^2 \right) dr \right]_{\phi=0^\circ \to 90^\circ} = \kappa^2 \tag{1}$$

$$\kappa^2 \geq 1 \text{ failure,}$$
$$\kappa^2 < 1 \text{ no failure}$$

where $\sigma_{tt}^o(\phi)$ and $\tau_{rt}^o(\phi)$ are the unnotched laminate tensile and shear strengths that are dependent on the hole circumferential coordinate, ϕ, and d_o is the laminate characteristic distance which can be a function of ϕ, i.e., $d_o(\phi)$. As shown in Figure 2, ϕ is measured from the net-section.

The proposed failure criterion is semi-empirical: σ_{tt}^o and τ_{tt}^o are determined from test; and d_o is selected to obtain the best correlation between predicted and experimental results. Initially, only the tangential tensile component is considered and Eq. 1 is simplified to:

$$\left[\frac{1}{d_o} \int_R^{R+d_o} \sigma_{tt}(r,\phi) \, dr \right]_{\phi=0^\circ \to 90^\circ} = \sigma_{tt}^o(\phi) \tag{2}$$

The criterion states that failure will occur when the average tangential stress for the interval $R \leq r \leq R+d_o$ (left-hand side of Eq. 2) is equal to the laminate unnotched strength, $\sigma_{tt}^o(\phi)$. To calculate the left-hand side of Eq. 2, the stresses $\sigma_{tt}(r,\phi)$ calculated by the finite element analysis are expressed as an analytical function using an nth order polynomial and a least-squares technique,

$$\sigma_{tt}(r) = b_1 + b_2 r + b_3 r^2 + \ldots + b_n r^{n-1} + \varepsilon \tag{3}$$

For convenience Eq. 3 is independent of ϕ to indicate that the data reduction is conducted for a unique orientation ϕ. The coefficients $b_1 \ldots b_n$ are determined by a least-squares regression method in which the error ε is minimized. Using the following substitution,

$$z = \frac{r}{R}$$
$$dr = R dz \tag{4}$$

Equation 3 becomes,

$$\frac{R}{d_o} \int_1^{\frac{R+d_o}{R}} (b_1 + b_2 z + b_3 z^2 + \ldots + b_n z^{n-1}) dz = \sigma_{tt}^o \tag{5}$$

or

$$\frac{R}{d_o} \sum_{i=1}^n \frac{b_i}{i}(\xi^i - 1) = \sigma_{tt}^o \tag{6}$$

where

$$\xi = \frac{R + d_o}{R}$$
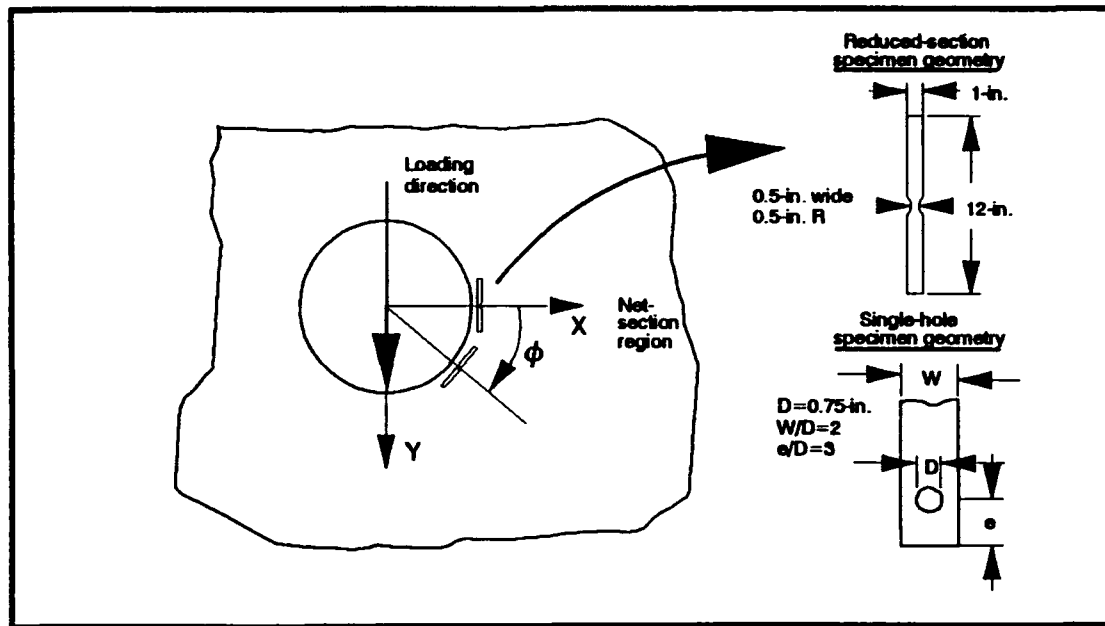
Figure 3. Net-Tension Notch-Strength Variation Coupon Orientation and Geometry

The degree of the polynomial is chosen such that convergence in the regression variance is achieved to within a given tolerance. Typically, the degree of the polynomial was between 3rd and 4th order. Once the degree of the polynomial is selected and the coefficients are evaluated, the average stress is calculated according to Eq. 6.

BASIC LAMINATE STRENGTH TEST PROGRAM

Analyses and tests were conducted to verify the proposed failure criterion. The determination of the tensile strength variation, $\sigma_u^o(\phi)$, consists of testing tensile coupons cut at orientation ϕ from the laminate, ϕ varying from 0° to 50° in 10° increments. Typical specimens are depicted in Figure 3. Both reduced-section notched specimens (shown in Figure 3) and pin-loaded single-hole specimens were used. The pin-loaded single-hole specimen was designed to fail by tension in the net-section region by proper selection of the specimen width-to-diameter (W/D) and edge-distance-to-diameter (e/D) ratios. The test laminate for the reduced-section and single-hole specimens (thin laminate) was approximately 3/8 the thickness of the laminate for the multi-fastener test specimens (thick laminate). This subscale thickness appeared sufficient to characterize the strength of the full laminate thickness and was less costly. The thin laminate has a similar stacking sequence to the thick, Both the thin and the thick laminates use repeating groups of plies. The thin laminate has two groups, and the thick laminate has six groups. Both the thin laminate and the thick laminate were fabricated using Hercules IM7G/3501-6 graphite/epoxy preimpregnated tapes and cured in an autoclave according to the manufacturer's recommended procedures. Strength data as a function of ϕ for the T45 laminate reduced-section notched and single-hole specimens are summarized in Table 1.

Both the reduced-section notched specimen and the single-hole pin-loaded specimen were analyzed using the general-purpose ABAQUS finite element program [8]. In the analysis the force used corresponded to the failure load listed in Table 1. The

single-hole pin-loaded specimen was analyzed using the nonlinear contact analysis procedure in ABAQUS.

MULTI-FASTENER JOINT TEST PROGRAM

Multiple-fastener thick composite joints with 3, 5, 7, and 9 staggered pin-loaded holes, as shown in Figure 1, were tested. The laminate layup sequences are:

$$\left\{ \left[(\pm 15)_3/90_2/0/\pm 45/0/\pm 45/0/\pm 45/0/\pm 45/0/\pm 45/0/90_3 \right]_{R6}/(\pm 15)_3 \right\} \qquad (7)$$

This laminate (referred to as T45 laminate) layup sequence represents a typical layup used in a multi-segment composite space booster. In the laminate nomenclature, the $\pm 15°$ plies represent the helical layers and the $90°$ plies represent the hoop layers. The $0°/\pm 45°$ represent the broadgood layers used to reinforce the pressure vessel membrane laminate in the joint region.

The average failure loads for the T45 laminate multi-fastener specimens are summarized in Table 2. The last column in the table lists the laminate gross-section average strength as calculated by dividing the failure load by the specimen cross-sectional area, i.e., width x thickness. The data in Table 2 show a slight increase in gross joint strength with increases in specimen width (i.e., the number of holes per specimen) indicating finite width effects. The strength of the 3-hole specimen will yield the most conservative joint strength allowable.

The multi-fastener test specimens were analyzed using a plane stress finite element analysis procedure. The analysis again used the general-purpose ABAQUS finite element code [8]. The model consisted of two separate finite element models: one for the steel laps and the other for the composite specimen. The two separate models interacted through rigid cylindrical surfaces, representing the pins used in the experiment, passing through the holes common to both the steel laps and composite specimen. A detailed discussion of the analysis procedure is given in Ref. 9.

Table 1. T45 Laminate Reduced-Section and Single-Hole Test Results (Failure Loads in lbs)		
Specimen Orientation,	Reduced-Section	Single-Hole
0°	16,180	17,590
10°	17,206	16,364
20°	16,466	15,182
30°	14,876	13,759
40°	13,287	12,618
50°	12,838	12,469

Table 2. Summary of T45 Laminate Multi-Fastener Joint Strength Tests		
Number of Holes	Average Failure Load (kips)	Gross-Section Average Strength (ksi)
3	147	39.2
5	222	39.5
7	305	40.6
9	372	40.8

ANALYSIS RESULTS

The unnotched laminate strength, $\sigma_u^0(\phi)$, at various characteristic lengths, $d_o(\phi)$, can be calculated using the reduced-section notched and single-hole specimens, test data in conjunction with finite element analysis, and the average stress criterion (Eqs. 2

through 6). A summary of such calculations for , d_o=0, 0.1, and 0.15 in., for the T45 laminate are given in Table 3. In this table, the unnotched laminate strength is also calculated based on classical lamination theory assuming fiber-dominated failure at a maximum fiber strain of 1.2% and 1.4% strain.

Table 3 shows some significant points related to the average stress criterion predictive strength in a single-hole and/or reduced-section notched thick composite specimen. The data indicate that the predicted unnotched laminate strength at d_o=0 in. is close to the strength predicted by classical lamination theory based on 1.2% fiber strain to failure. The predicted strengths at larger d_o are much lower than the strength predicted by laminated plate theory. For the type of graphite fiber used in this investigation, the reported fiber ultimate strain to failure is approximately 1.7% strain [10]. These results indicate that either the failure is not dominated by fiber failure, or other failure mechanisms contribute to the low observed unnotched laminate strength.

Table 3. T45 Unnotched Laminate Strength Analysis Results (in ksi)					
	Based on Laminate Analysis		Based on Average Stress Criterion & Reduced-Section Specimen Data		
Specimen Orientation	for 1.2% fiber strain	for 1.4% fiber strain	for d_o=0 in.	for d_c=0.10 in.	for d_o=0.15 in.
0°	158	186	142	107	100
10°	142	168	149	114	106
20°	124	145	137	107	102
30°	103	121	118	97	91
40°	97	114	101	86	81
50°	97	114	96	82	78

Another observation is that the unnotched laminate strength calculation based on the average stress criterion is relatively insensitive to the characteristic length beyond 0.1 in. This finding is consistent with data reported in the literature [6] that used 0.15 in. for the characteristic length. Finally, a comparison between the unnotched laminate strength calculations based on a reduced-section notched specimen and a single-hole pin-loaded net-tension specimen is given in Table 4. The table shows that at d_o=0, i.e., at the hole boundary, for a small angle, ϕ, the single-hole specimens give a higher unnotched laminate strength than the reduced-section specimen. However, at larger angles, ϕ, the two specimen types give an identical strength. On the other hand, at larger values of d_o, the opposite is observed. That is, at small angles, ϕ, the two specimen types predict approximately the same unnotched laminate strength. However, at larger angles, analysis based on the reduced-section notched specimen predicts as much as 10 to 15% higher strength.

The multi-fastener specimens were analyzed using the method outlined in [9]. In each case, the specimen model was loaded to 75% of the average failure load summarized in Table 2. The failure analysis to be discussed in the following sections was conducted at discrete circumferential locations around the hole, along radial rays. These discrete locations followed the finite element grid lines. These radial lines were aligned with

ϕ=0°, 11°, 22°, 32°, and 42° which did not correspond exactly to the laminate strength variation test angles. However, this discrepancy was deemed insignificant. The cylindrical tangential stress component, $\sigma_{tt}(r,\phi)$ (in Eq. 2 through 6), was calculated using the cartesian stress components from the finite element analysis along these radial lines.

Table 4. T45 Unnotched Laminate Strength Analysis Results: Single-Hole Pin-Loaded Specimen Versus Reduced-Section Notched Specimen (in ksi)						
	d_o=0 in.		d_o=0.15 in.		d_o=0.15 in.	
Specimen Orientation	Single-Hole	Reduced-Section	Single-Hole	Reduced-Section	Single-Hole	Reduced-Section
0°	163	142	106	107	94	100
10°	151	149	99	114	89	106
20°	133	137	91	107	82	102
30°	115	118	81	97	74	91
40°	101	101	74	86	67	81
50°	97	96	72	82	66	78

Using the finite element data in conjunction with the average stress criterion procedure discussed previously, the left-hand side of Eq. 6 can be determined as a function of d_o. The calculated values are then normalized by the values of σ_{tt}^o based on the single-hole and reduced-section notched specimens (Table 4). The results of such an analysis are summarized in Tables 5 and 6 for the T45 laminate with 3-hole and 5-hole specimens, respectively. The tables include normalized strength ratios at characteristic lengths d_o=0, d_o=0.1, and d_o=0.15 in. Because, in the analysis, the specimen is loaded to 75% of the failure load, a normalized strength ratio equal to or greater than 0.75 will indicate failure.

The following observations are made from the data in the tables:

1. For d_o=0.1 and/or d_o=0.15 in. the maximum normalized strength ratio is at or near the net-section region ($\phi \cong 0°$). However, X-ray data (Figure 1) indicates that failure does not occur at the net-section and therefore the validity of this predicted failure location is questionable.

2. In general, for the same characteristic distance the normalized strength ratios calculated based on a single-hole specimen data is higher than that determined by a reduced-section notched specimen data.

3. The calculated strength ratios appear to be insensitive to the characteristic length larger than d_o=0.1 in.

From the above discussion the average stress criterion presented herein cannot predict the location of failure. The location of failure may be determined using destructive and/or nondestructive evaluation methods such as; X-ray, deplying, and/or edge replicate of pre- and/or post-failure specimens.

An X-ray observation of the T45 laminate (Figure 1) indicates the failure location to be at approximately $\phi \cong 30°$. Using this X-ray information in conjunction with the average stress calculations of Tables 5 and 6, the most probable average strength ratios for the T45 3-hole and 5-hole specimens were highlighted in those tables. Considering

that the load level used in the analysis was 75% of the failure load level, the results show excellent agreement for strength ratios calculated based on the single-hole specimen data. These results indicate that the characteristic length is around 0.125 in., at which point the average strength factor is 0.76. In this case, the average strength ratio based on the reduced-section notched specimen is about 18% lower. Also, it should be noted that the predicted strength based on the strength ratios at the net-section (i.e., $\phi = 0°$) is 13% and 17% lower than the actual average strength of the 3-hole and 5-hole joint coupons, respectively.

Table 5. Summary of Normalized Average Stress Calculation for T45 Laminate 3-Hole Specimen

Specimen Orientation	$d_o = 0$ in.		$d_o = 0.10$ in.		$d_o = 0.15$ in.	
	Single-Hole	Reduced-Section	Single-Hole	Reduced-Section	Single-Hole	Reduced-Section
0°	0.89	1.03	0.9	0.89	0.9	0.85
11°	0.81	0.83	0.92	0.8	0.93	0.78
22°	0.62	0.61	0.83	0.71	0.88	0.71
32°	0.47	0.46	░░	0.6	░░	0.64
42°	0.32	0.32	0.52	0.45	0.62	0.51

Table 6. Summary of Normalized Average Stress Calculation for T45 Laminate 5-Hole Specimen

Specimen Orientation	$d_o = 0$ in.		$d_o = 0.10$ in.		$d_o = 0.15$ in.	
	Single-Hole	Reduced-Section	Single-Hole	Reduced-Section	Single-Hole	Reduced-Section
0°	0.85	0.97	0.87	0.86	0.86	0.81
11°	0.75	0.76	0.86	0.76	0.88	0.73
22°	0.61	0.6	0.79	0.67	0.84	0.68
32°	0.52	0.5	░░	0.61	░░	0.63
42°	0.45	0.45	0.63	0.55	0.69	0.57

CONCLUSIONS

A method by which multi-fastener thick composite joint strength can be predicted has been developed. The method is based on the average stress criterion applied around the hole circumference. Basic laminate strength data, used in the failure criterion, were obtained from single-hole net-tension specimens. Using ABAQUS finite element analyses, the stress field distributions around a pin-loaded hole in single-hole and multi-fastener joints were determined. The single-hole test data in conjunction with this finite element analysis and the average stress criterion were used to predict the multi-fastener joint strength. The joint strength of a selected laminate was predicted to within 1% accuracy. However, the average stress criterion presented herein does not predict the location of failure initiation around the hole accurately. Hence, this criterion must be used in conjunction with other analytical and/or experimental methods that pinpoint the location

of failure around the hole. In the current investigation X-ray photos were used to locate possible sites of failure initiation. When this information is used in conjunction with the average stress criterion, the predicted multi-fastener joint strength based on single-hole net-tension data can be accurate. It is recognized that additional investigation is needed to better understand the failure mechanism in multi-fastener thick composite joint. The understanding of that mechanism together with an analytical method which can be used to accurately determine the location of failure initiation around the hole can be used to improve on the proposed failure criterion in the future.

REFERENCES

1. Joining Fiber-Reinforced Plastics, Edt. F. L. Matthews, Elsevier Applied Science, New York, 1987.
2. Tsiang, T-H., "Survey of Bolted-Joint Technology in Composite Laminates," Composite Technology Review, Vol. 6, Sept. 1984, pp. 74-77.
3. Ramkumar, R. L. and Tossavainen, E., "Bolted Joint in Composite Structures: Design, Analysis and Fabrication, Task II Test Results--Multifastener Joints," AFWAL-TR-85-3065, August, 1985.
4. Cloud, G., Sikarskie, D., Vadle, M., Franco, P. H., and Bayer, M., "Experimental and Theoretical Investigation of Mechanically Fastened Composites," Technical Report No. 12844, Feb. 1987, U.S. Army Research , Development & Engineering Center, Warren, MI.
5. Whitney, J. M. and Nuismer, R. J., "Stress Fracture Criteria for Laminated Composites Containing Stress Concentrations," J. of Composite Materials, Vol. 8, 1974, pp. 253-275.
6. Nuismer, R. J. and Whitney, J. M., "Uniaxial Failure of Composite Laminate Containing Stress Concentrations," Fracture Mechanics of Composites, ASTM STP 593, American Society for Testing and Materials, Philadelphia, 1975, pp. 117-142.
7. El-Zein, M. S. and Reifsnider, K. L., "The Strength Prediction of Composite Laminates Containing a Circular Hole," J. Composite Tech. & Research, Vol. 12, No. 1, 1990, pp. 24-30.rt II, NASA Langley Research Center, NASA TM X-337, 1976, pp. 536-602.
8. ABAQUS Finite Element Computer Program, Hibbitt, Karlsson, and Sorensen, Inc., Providence, RI.
9. Griffin, Jr., O. H., Hyer, M. W., Yalamanchili, S. R., Shuart, M. J., Prasad, C. B., and Cohen, D., "Analysis of Multifastener Composite Joints," Proceedings of the 33rd AIAA/ASME/ASCE/AHS/ASC, SDM Conference, Paper No. , 1992, pp.
10. Graphite Fiber Products Handbook, Hercules Advanced Materials & Systems Co., Hercules Incorporated, Magna, UT.

Mechanical Characterization and High Velocity Ductility of HTPB Propellant Binder

KOZO KAWATA,[1] HSING-LIAO CHUNG[2] AND MASAAKI ITABASHI[1]

ABSTRACT

The mechanical properties of an amorphous rubbery HTPB solid composite propellant binder are evaluated by consideration of stress-strain curves up to rupture measured at various strain rates and temperatures. The high velocity ductility behaviour is found. Test results at strain rate range from $10^{-3}s^{-1}$ to $10^{0}s^{-1}$ show that the tensile breaking strain increases with increasing strain rate. That is, the HTPB propellant binder shows a high velocity ductility behaviour quite different from polymers such as epoxy resins, etc., glassy in room temperature.

INTRODUCTION

Hydroxyl Terminated Polybutadiene (HTPB) is a widely used binder in solid composite propellant. Because of the viscoelastic nature of the binder, the modulus and ultimate mechanical properties (the tensile strength and ultimate elongation) of propellants depend markedly on temperature and strain rate [1 − 3], and a good tensile breaking elongation is the prime mechanical property required for propellant grains of case bonding [4 − 5]. Studies were made previously on the dependence of the stress at break (tensile strength) and ultimate elongation of some elastomers on temperature and strain rate [6 − 9]. The tensile strength was found to increase as the temperature is decreased or the strain rate is increased. However, the ultimate elongation may either increase or decrease with increasing strain rate, depending on the temperature and the range of strain rate covered.

As the matter of fact, the stress analysis for pressurized solid composite propellants bonded to an elastic motor case indicates that a tensile hoop strain may cause the failure of solid propellants through crack formation under the high strain rate produced

---

[1]Professor and research associate, respectively, Department of Materials Science and Technology, Science University of Tokyo, 2641, Yamazaki, Noda, Chiba 278, Japan.

[2]Graduate student, Department of Mechanical Engineering, Science University of Tokyo, 2641, Yamazaki, Noda, Chiba 278, Japan.

by motor ignition [5]. The effect of temperature and strain rate on the mechanical behaviour in high strain rate ($\sim 10^3 s^{-1}$) tensile impact of rubber-like materials has not been investigated. In this study, a dynamic tensile stress-strain measuring system designated KHKK one bar method [10-11], was used for determining the impact response of rubbery HTPB solid composite propellant binder in high strain rate up to $10^3 s^{-1}$. The formulae to give dynamic stress $\sigma(t)$ and strain $\varepsilon(t)$ as functions of time t from the data obtained by this system, were established based upon stress wave propagation theory.

The present investigation was conducted to evaluate the effect of strain rate and temperature on stress-strain relations up to breaking, especially breaking stress, breaking strain and absorbing energy, for an amorphous rubbery HTPB solid composite propellant binder in the strain rate range from $10^{-3} s^{-1}$ to $10^3 s^{-1}$.

KHKK ONE BAR METHOD FOR OBTAINING DYNAMIC TENSILE STRESS-STRAIN RELATIONS

The one bar method of block-to-bar type has been adopted because of its accuracy and simplicity in measuring dynamic tensile mechanical properties up to breaking [10-11]. Figure 1 depicts the high velocity tensile loading system for the method. The system used in the present study is a horizontal type impact tester to transmit an impact force to the test specimen via a hammer, which moves on two parallel rail. The hammer is connected with rubber ropes, fixed to a rod connected with worm wheel. An impact block is attached to one end of the specimen while the other end of the specimen is attached to an output bar. When the impact block is given an impact by the hammer accelerated by the elasticity of rubber ropes, the specimen is deformed and the strain $\varepsilon_g(t)$ and velocity $V(t)$ are recorded simultaneously, where $\varepsilon_g(t)$ is the strain of the output bar that is measured to evaluate the dynamic stress at a distance "a" from the end of the output bar and $V(t)$ is the velocity of the impact block measured by Zimmer OIIG electro-optical displacement transducer (Figure 2).
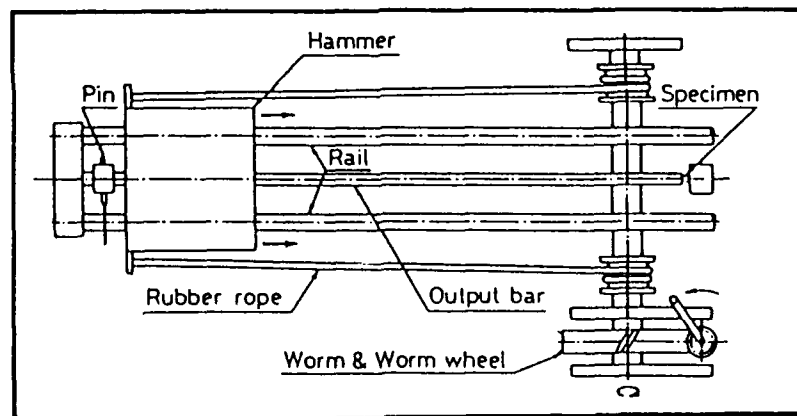
Figure 1. High Velocity Tensile Loading System for KHKK One Bar Method.
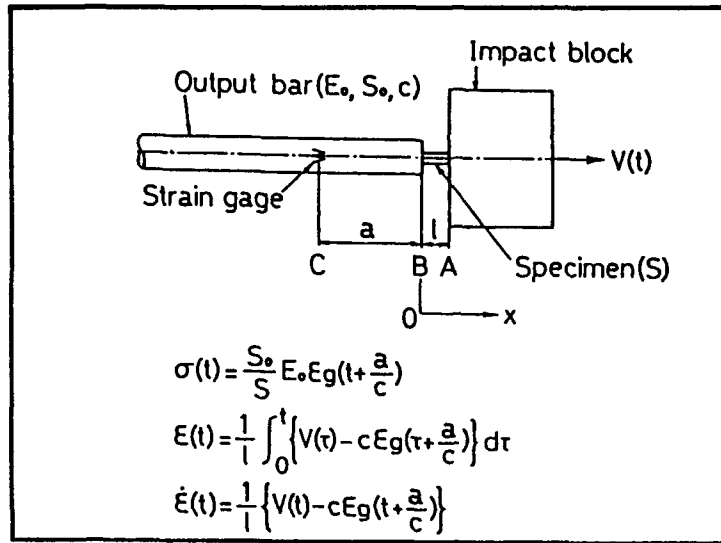
Figure 2. Principle of One Bar Method.
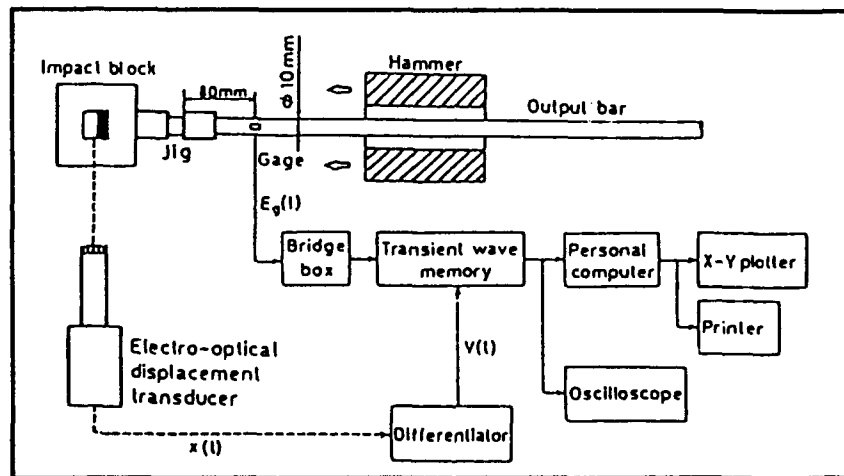
Figure 3. Block Diagram for Data Acquisition of Dynamic Properties.

The fundamental system of one bar method is shown in Figure 2. The dynamic tensile stress $\sigma(t)$, strain $\varepsilon(t)$ and strain rate $\dot{\varepsilon}(t)$ in the specimen are calculated based upon the measured strain $\varepsilon_g(t)$ and velocity $V(t)$. The formulae for calculating dynamic stress, strain and strain rate derived using one-dimensional elastic wave propagation theory, are as follows [10-11]:

$$\sigma(t) = (\frac{S_\circ}{S})E_\bullet\varepsilon_g(t + \frac{a}{c}) \tag{1}$$

$$\varepsilon(t) = \frac{1}{\ell}\int_\circ^t [V(\tau) - c\varepsilon_g(\tau + \frac{a}{c})]d\tau \tag{2}$$

$$\dot{\varepsilon}(t) = \frac{1}{\ell}[V(t) - c\varepsilon_g(t + \frac{a}{c})] \tag{3}$$

Where ℓ and S are the length and cross-sectional area of the specimen, and S_o, E_o and c are the cross-sectional area, Young's modulus and longitudinal wave velocity of the output bar, respectively, $V(t)$ is the velocity of the impact block. The block diagram for data acquisition of dynamic properties is shown in Figure 3. The strain $\varepsilon_g(t)$ and velocity $V(t)$ are recorded in two transient wave memories respectively, then the dynamic stress $\sigma(t)$, strain $\varepsilon(t)$ and strain rate $\dot{\varepsilon}(t)$ are calculated using a personal computer using Eqs.(1) $\sim$ (3). The major feature of this testing system is that dynamic tensile stress-strain relations can be obtained up to the breaking strain.

TEST SPECIMEN

A typical amorphous rubbery HTPB solid propellant binder was adopted. The molecular formula is $HO - [-CH_2 - CH = CH - CH_2-]_n - OH$. It consists of 88.2 wt% of HTPB and 11.8 wt% of Sumidur N-3200 curing agent produced by Nippon Oil & Fats Co. Ltd. All test specimens were prepared by die-cutting from the same batch of HTPB binder sheets with dimensions of 10mm in gauge length, 16mm in width and 16mm in thickness. To secure enough shearing strength of adhesion between specimen and jig of A2017 aluminium alloy, an adhesive epoxy resin (CEMEDINE EP001) was adopted to be a bonding agent. The specimen configuration and an assembly drawing is shown schematically in Figure 4.

EXPERIMENTAL PROCEDURE

In order to obtain the characteristic curves, a series of uniaxial tensile tests were conducted at various strain rates and temperatures. Quasi-static and intermediate speed tests, at crosshead speeds of 0.5, 5, 50, 500 mm/min. at a temperature of $22°C$, were performed on a universal material testing machine (SHIMADZU, Autograph AGS-500A, loading capacity 0.5ton.) using the same design of test specimen as in dynamic tests. Samples were also tested at constant crosshead speeds of 50, 500 mm/min. at temperatures of 40 and $60°C$. According to these constant crosshead speeds, the stress-strain behaviour of HTPB propellant binder up to rupture were measured at strain rate range from 10^{-3} to $10^0 s^{-1}$.
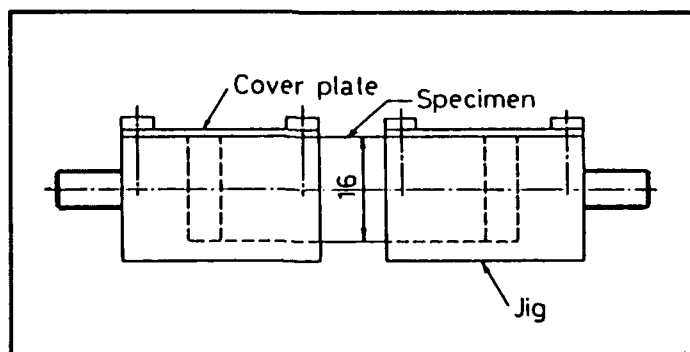
Figure 4. Dimensions of Specimen and an Assembly Drawing (Dimensions in mm).

For high strain rate tests, the one bar method was used. The hammer impacting the impact block at a velocity of 7 ~ 11 m/s yields a strain rate of about $10^3 s^{-1}$ on the gauge section of the specimen. Using Eqs.(1) ~ (3), the dynamic tensile stress $\sigma(t)$, strain $\varepsilon(t)$ and strain rate $\dot\varepsilon(t)$ in the specimen are calculated based upon the measured strain $\varepsilon_g(t)$ and the impact block velocity $V(t)$.

RESULTS AND DISCUSSION

EFFECT OF TENSILE STRAIN RATE ON FAILURE PROPERTIES

Typical tensile stress-strain behaviour of the HTPB binder at four different strain rates ranging to $0.58 \times 10^0 s^{-1}$ in $22°C$, is shown in Figure 5. The curves in Figure 5 show that tensile strength σ_p (maximum stress supported by the specimen), strain at tensile strength ε_p, and total strain ε_T (breaking strain) increase with increasing strain rate. The initial slope of the curves also increases slightly with increasing strain rate, and the tangent gradient of the curves becomes smaller smoothly as the strain level is increased gradually. For all of the curves, yield point does not exist. It is quite different from glassy polymer such as epoxy resins in room temperature [12].

The dynamic stress-strain response in $10^3 s^{-1}$ up to 80% strain of HTPB binder at the same temperature, $22°C$, is shown in comparison with the corresponding static ones in Figure 6. The dynamic response shows that the initial slope of the curve rises drastically, and tensile stress also rises significantly.

In these curves it is noted that there is a S-like dip or stress reduction in the initial part of the curve. It was repeated on different days, different temperature conditions and even in dynamic tensile test. It is accepted as real behaviour based on entropy elasticity.
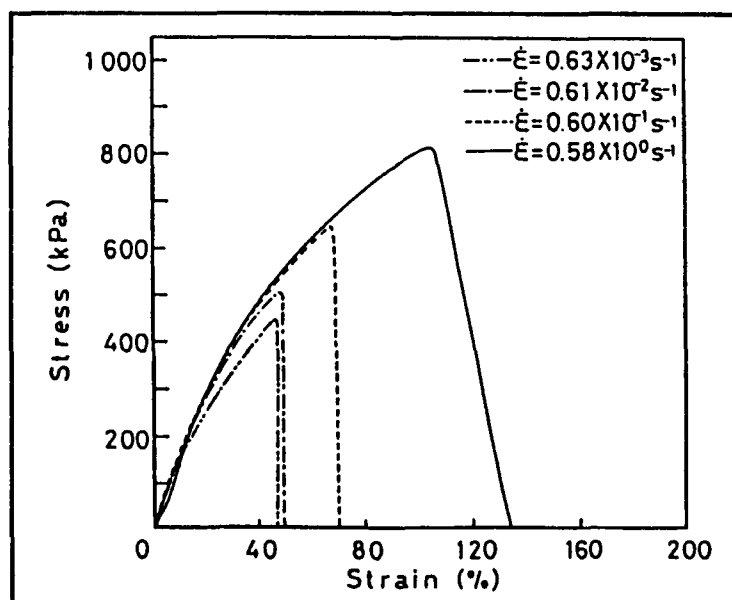
Figure 5. Typical Stress-Strain Curves for HTPB Binder at Various Tensile Strain Rates.
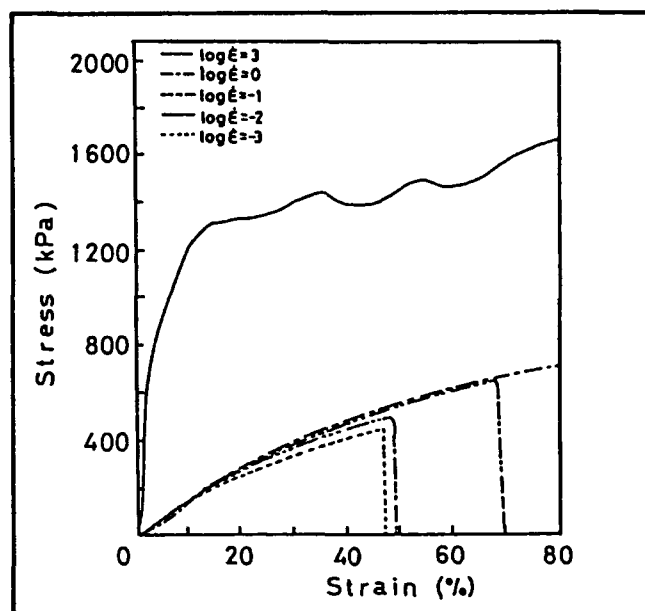
Figure 6. Comparison of Dynamic and Static Stress-Strain Curves up to 80% Strain for HTPB Binder.

TABLE I - SUMMARY OF EXPERIMENTAL RESULTS ON HTPB BINDER AT VARIOUS STRAIN RATES.

Strain Rate $\dot{\varepsilon}$ (s^{-1})	Number of Specimen N	Tensile Strength σ_P(kPa)		Strain at Tensile Strength ε_P(%)		Total Strain ε_T(%)		Absorbed Energy per Unit Volume Eab(kJ/m^3)	
		M[a]	SD[b]	M[a]	SD[b]	M[a]	SD[b]	M[a]	SD[b]
0.63×10^{-3}	3	412	27.6	40.5	3.86	44.0	1.88	111	9.13
0.61×10^{-2}	3	480	15.6	47.5	0.53	49.7	1.04	147	6.56
0.60×10^{-1}	4	621	40.7	67.0	2.18	71.8	3.12	281	18.0
0.58×10^{0}	3	751	39.2	96.1	6.21	124	7.38	566	69.0

[a] M = Mean

[b] SD = Standard deviation

Figure 7. Effect of Strain Rate on HTPB Binder Mechanical Properties
(a) Tensile Strength σ_p; (b) Total Strain ε_T; (c) Absorbed Energy per Unit Volume E_{ab}.
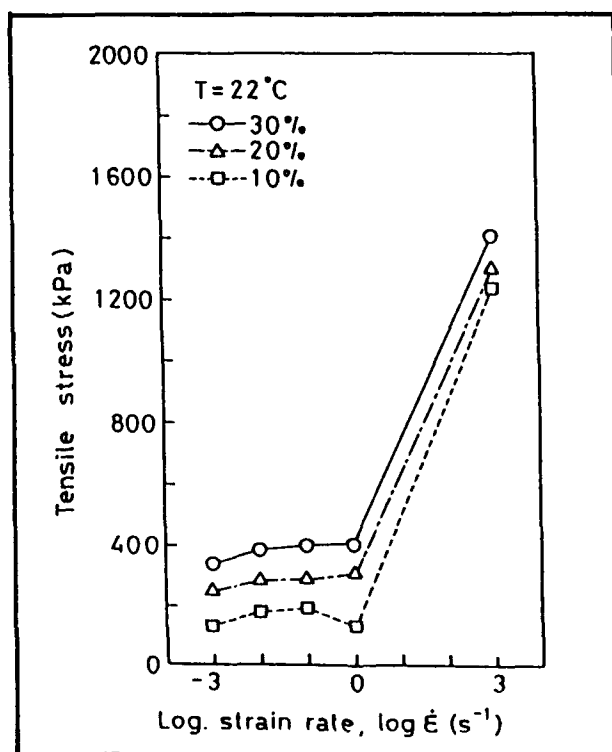
Figure 8. Effect of Strain Rate on Tensile Stress at Different Strain Levels.

Measured data of mechanical characteristic values for HTPB binder are summarized in Table I, The effects of tensile strain rate on σ_p, ϵ_p, ϵ_T and E_{ab} are clear as shown in Figure 7. For HTPB binder, all σ_p, ϵ_p, ϵ_T and E_{ab} increase remarkably with increasing strain rate. Especially for strain rate up to $10^0 s^{-1}$, obviously the behaviour of high velocity ductility is exhibited. Furthermore, the effect of strain rate up to $10^3 s^{-1}$ on tensile stress for different strain levels is shown in Figure 8. From these results, HTPB propellant binder is considered to have a suitable impact-absorbing ability and relatively large ultimate elongation capability at high strain rates. These are the most important mechanical properties required for propellant binder of case-bonded grains.

EFFECT OF TEMPERATURE ON FAILURE PROPERTIES

The effect of test temperature on the stress-strain behaviour of the HTPB propellant binder is shown typically in Figure 9 for three temperatures and one crosshead speed, 500 mm/min. As one would expect, decreasing test temperature has similar effect on the stress-strain behaviour with increasing tensile strain rate. The strain at rupture shows significant low values for the tests conducted at higher temperature condition. The results are consistent with the ultimate properties of unfilled vulcanizates rubber at the same temperature region that has been investigated previously [6-9].

Test results for mechanical characteristic values are summarized in Table II for three temperatures and two strain rates. From the measured data, all σ_p, ϵ_p, ϵ_T and E_{ab} increase with decreasing test temperature. Figure 10 also illustrates this relationship between temperature and mechanical properties. The curves in Figure 10(b) show that as the test temperature is increased from 22 to $40°C$, the total strain decreases by about 34% and 43% at strain rate of 10^{-1} and $10^0 s^{-1}$ respectively. HTPB propellant binder is highly sensitive to ambient temperature.
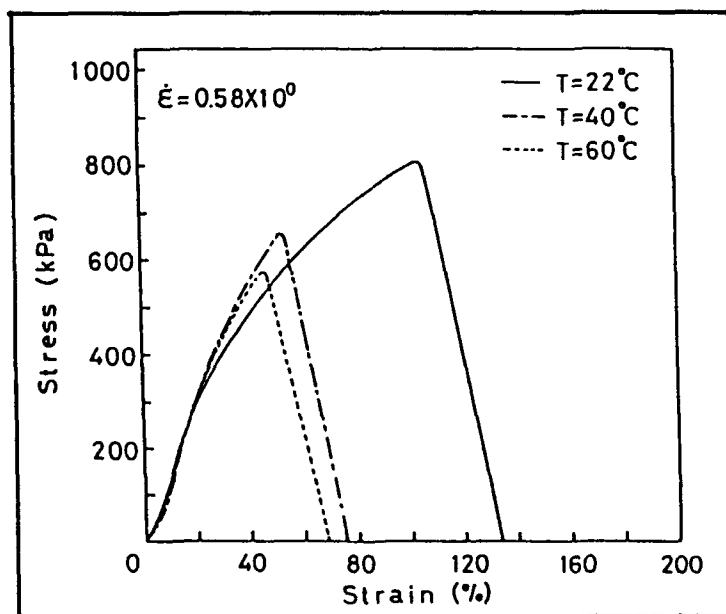
Figure 9. Typical Stress-Strain Curves for HTPB Binder at Various Ambient Test Temperatures.

TABLE II - SUMMARY OF EXPERIMENTAL RESULTS ON HTPB BINDER AT VARIOUS TEST TEMPERATURES.

Strain Rate $\dot{\varepsilon}$ (s^{-1})	Temperature T(°C)	Tensile Strength σ_P(kPa)		Strain at Tensile Strength ε_P(%)		Total Strain ε_T(%)		Absorbed Energy per Unit Volume Eab(kJ/m^3)	
		M[a]	SD[b]	M[a]	SD[b]	M[a]	SD[b]	M[a]	SD[b]
0.62×10^{-1}	22	621	40.7	67.0	2.18	71.8	3.12	281	18.0
	40	547	13.2	45.1	1.33	47.4	1.65	151	2.32
	60	546	47.4	39.9	4.54	421	4.81	134	29.5
0.58×10^{0}	22	751	39.2	96.1	6.21	124	7.38	566	69.0
	40	636	20.6	49.2	2.83	70.8	4.83	245	24.7
	60	565	12.0	45.1	0.89	67.2	1.67	201	12.9

[a] M = Mean

[b] SD = Standard deviation
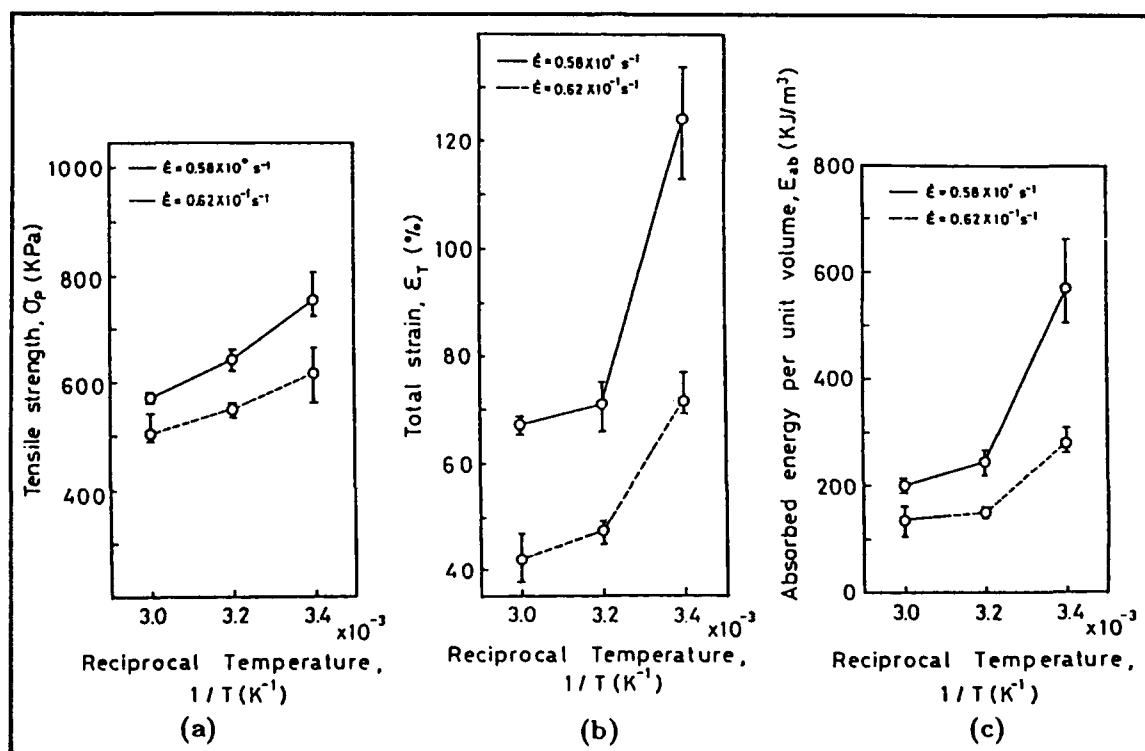
Figure 10. Effect of Temperature on HTPB Binder Mechanical Properties
(a) Tensile Strength σ_p; (b) Total Strain ε_T; (c) Absorbed Energy per Unit Volume E_{ab}.

CONCLUSIONS

1. For HTPB propellant binder, the mechanical properties (σ_p, ϵ_p, ϵ_T and E_{ab}) increase noticeably with increasing strain rate. The behaviour of high velocity ductility is exhibited.

2. The mechanical behaviour of HTPB binder is contrary to glassy polymers which shows high velocity brittleness. Tht is, high strain rates showed the effect to improve in tensile strength and breaking strain.

3. The HTPB propellant binder has an excellent impact-absorbing ability and relatively large breaking elongation capability at high strain rates. It means to be a suitable propellant binder for case-bonded grains.

4. The temperature dependence of HTPB binder is summarized as follows: decreasing test temperature has similar effect on the mechanical properties with increasing tensile strain rate. The breaking elongation shows lower values at higher test temperature.

ACKNOWLEDGEMENT

REFERENCES

1. Landel, R. F. and T. L. Smith, 1961. "Viscoelastic Properties of Rubberlike Composite Propellants and Filled Elastomers," Journal of the American Rocket Society, 31:599-608.

2. Bills Jr., K. W. and J. H. Wiegand, 1963. "Relation of Mechanical Properties to Solid Rocket Motor Failure," AIAA Journal, 1:2116-2123.

3. Rajan, M. and C. V. Mohandas, September 29-October 1, 1975. "Mechanical Characterization and Failure Behavior of PBAN Propellant," AIAA Journal, NO. 75-1344, AIAA/SAE 11th Propulsion Conference, California.

4. Smith, T. L., 1960 "Elastomeric-Binder and Mechanical-Property Requirements for Solid Propellants," Industrial and Engineering Chemistry, 52:776-780.

5. Lee, T. Y. and H. L. Chung, 1979. "Stress Analysis for A Case-Bonded Viscoelastic Cylinder," Proceedings of the 3rd Conference on Theoretical and Applied Mechanics, The Republic Of China, PP. 55-65.

6. Smith, T. L. and P. J. Stedry, 1960. "Time and Temperature Dependence of the Ultimate Properties of an SBR Rubber at Constant Elongations," Journal of Applied Physics, 31:1892-1898.

7. Smith, T. L., 1958. "Dependence of the Ultimate Properties of a GR-S Rubber on Strain Rate and Temperature," Journal of Polymer Science, 32:99-113.

8. Smith, T. L., 1963. "Ultimate Tensile Properties of Elastomers, I. Characterization by a Time and Temperature Independent Failure Envelope," Journal of Polymer Science, Part A, 1:3597-3615.

9. Smith, T. L., 1964. "Ultimate Tensile Properties of Elastomers, II. Comparison of Failure Envelopes for Unfilled Vulcanizates," Journal of Applied Physics, 35:27-36.

10. Kawata, K., S. Hashimoto, K. Kurokawa, and N. Kanayama, 1979. "A New Testing Method for the Characterization of Materials in High-Velocity Tension," Mechanical Properties at High Rates of Stain 1979 (Conf. Ser. No.47), Harding, J. ed., Inst. of Phys., Bristol and London, pp. 71-80.

11. Kawata, K., 1980. "Micromechanical Study of High Velocity Deformation of Solids," Proceedings of the 15th International Congress of Theoretical and Applied Mechanics (Toronto, August 1980), Rimrott, F.P.J. and Tabarrok, B. eds., North Holland Publ. Co., pp. 307-317.

12. Kawata, K., S. Ninomiya, and S. Fujitsuka, March 13, 1989. Proceedings of 19th Aircraft/Aerospace Materials Symposium, University of Tokyo, pp. 51-56 (in Japanese).

Tensile Strength of Unidirectional Fiber Composites at Low Temperatures

PIYUSH K. DUTTA

ABSTRACT

Results of a number of tests by others and the author show that the longitudinal tensile strength of the unidirectional-fiber-reinforced polymer composites degrades at low temperatures. An explanation of this behavior is not obvious. Assuming that, to begin with, the fibers are curved, and when embedded in the resin they continue to maintain the curvature to a certain degree, an examination of the problem at low temperatures is presented. The critical fiber stress of such curved fibers is shown to be temperature dependent. Higher critical stress at lower temperatures is thought to be the possible reason of the strength degradation.

INTRODUCTION

Some new longitudinal tensile strength results for unidirectional-fiber-reinforced polymer composites were obtained recently by Springer [1], Mazzio and Huber [2], DFVLR [3], Dutta et al. [4], and MIL-HDBK-17 [22]. These results show that, on cooling, the tensile strength of the unidirectional-long-fiber composites degrades, which, in fact, contradicts the common perception of materials becoming stronger at low temperatures. Possible causes of this apparently anomalous result were first examined by Gadke in 1985 [6] and later by Dutta [4]. This paper will analyze the problem further in the light of the experimental results obtained at the U.S. Army Cold Regions Research and Engineering Laboratory (CRREL) from the low temperature testing of three composites—glass fiber-epoxy, graphite-epoxy, and kevlar-epoxy—and put forward a hypothesis to explain that the reason for the strength degradation can be traced to the fiber curvature (buckling) or waviness, which produces greater stress concentration at low temperatures when the matrix becomes stiffer.

Most authors adopt the micromechanics approach to describe the longitudinal stress distribution along the fiber/matrix interface, and for design purposes, the modes of failure in tension and compression. Based on this approach, Rosen [8], Cox [9], and Dow [10] produced a number of theories on the load sharing mechanism between the fibers and matrix. These theories were further extended by Wadsworth and Spilling [11] to analyze the failure modes of composites,

Piyush K. Dutta, U.S. Army Cold Regions Research and Engineering Laboratory, 72 Lyme Road, Hanover, NH 03755
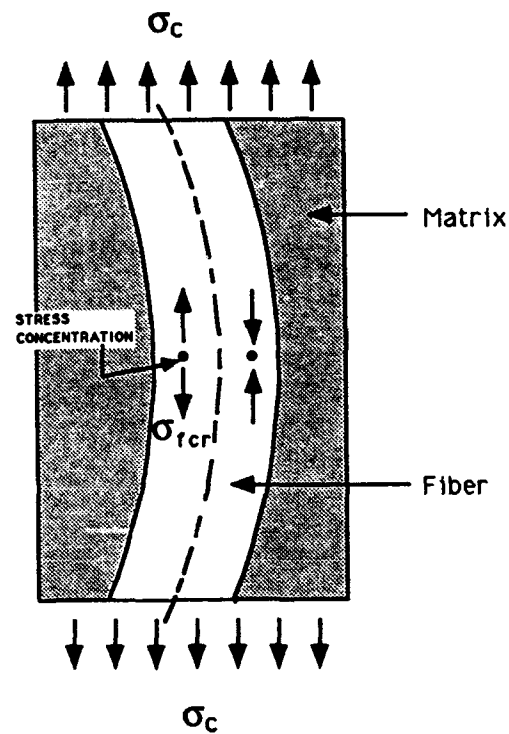
Figure 1. Stresses in the buckled fiber-
embedded polymer matrix.
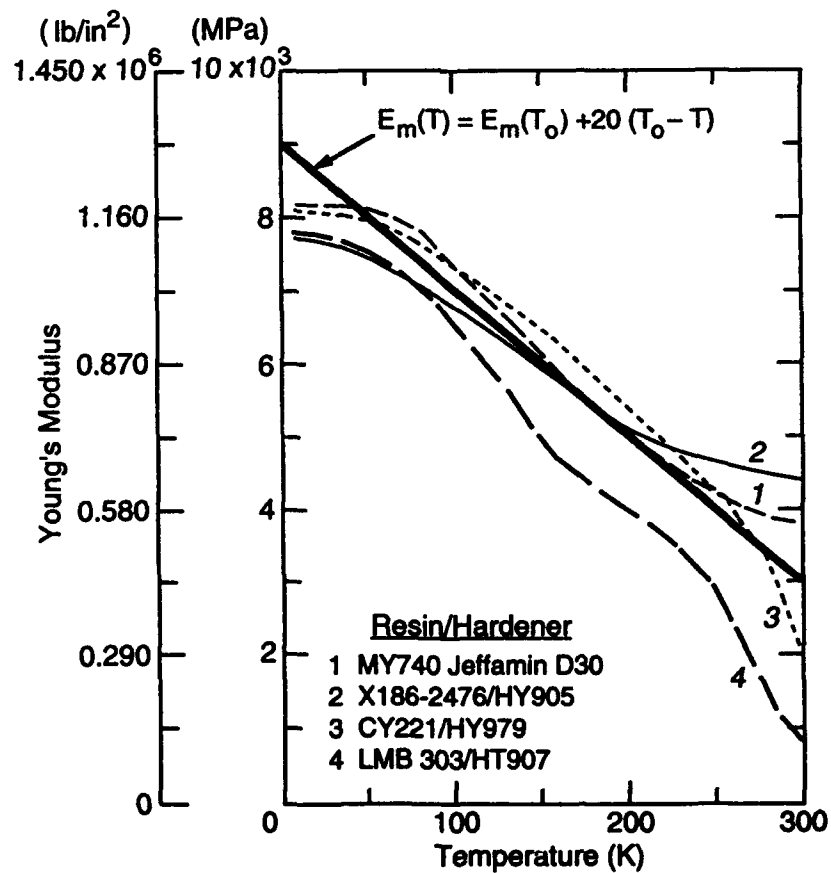
Figure 2. Change of Young's modulus with temperature (after [19]).

and in 1974 Chamis [12] predicted the existence of at least three modes of failure under longitudinal tensile load: 1) brittle, 2) brittle with fiber pullout, and 3) brittle with fiber pullout, interface-matrix shear failure and constituent debonding. However, none of the above modes takes into consideration of any microbuckling or waviness of fibers due to shrinkage from curing. While the influence of microbuckling or fiber waviness has been commonly accepted for describing the failure of unidirectional composites under longitudinal compressive loads (Rosen [8], Budiansky [13], Kuo et al. [14], Fleck and Budiansky [15]), no such consideration is evident in literature on the influence of microbuckling in tensile failures under longitudinal loads. The suspected reason for this is that the modulus of elasticity of the matrix is much less than the modulus of elasticity of the fiber, so that under uniaxial tension in the fiber direction the fibers will generally align with very little shear load transfer to the matrix. However, at low temperatures, the matrix modulus can increase significantly and can influence the stress distribution along the fiber, requiring a modification of the theory of stress transfer.

STRESS TRANSFER IN WAVY FIBERS

It has long been recognized that during the manufacturing of composites the cooling produces a shrinkage of the matrix. Photoelastic studies have shown repetitious stress patterns along the length of the fiber, indicating that the fibers have buckled. Holister and Thomas, [16], Comninou and Yannas [17], Bert [18] and more recently Kuo et al. [14], all commonly employed the micromechanical analysis to study the effect of fiber waviness (curvature) on the stress strain response.

In the analysis of compressive failure modes of fibers, the phenomenon of elastic buckling or waviness was considered critical by Rosen [8] and Holister and Thomas [16]. Using the strain energy method of computation and assuming that the buckling pattern of the fiber is sinusoidal (Figure 1), they analyzed the stresses developed in the fibers. Their results have been quoted profusely in literature for predicting the ultimate compressive failure strength of unidirectional composites. However, we find that there is no reason why their arguments on stress concentrations induced in the wavy fiber cannot be considered for tensile loading as well. The critical stress in the fiber developed in this case will only change from compression to tension or vice versa, depending on the location of the point on the cross section of the fiber in consideration (Figure 1). Under the applied tension load, the wavy fibers will simply tend to straighten up.

In opposition to the extensional mode of deformation of the matrix, as predicted by Rosen [8], here the applied tensile load will cause a contraction mode of deformation and possible failure of the matrix. But, as the final failure of the composite will not happen without the fiber failure, it is necessary to consider the maximum stresses induced in the wavy fiber. The maximum critical fiber stress σ_{fcr} in this mode as shown by Rosen [8] is

$$\sigma_{fcr} = 2[(V_f E_m E_f)/(3(1-V_f))]^{0.5} \tag{1}$$

where V_f is the volume fraction of the fiber, E_f is the elastic modulus of the fiber and E_m is that of the matrix. Failure of the composite will be initiated when the fiber stress σ_{fcr} is larger than or equal to the failure strength of the fiber σ_{fu}. Equation (1) shows that σ_{fcr} is a function of the elastic modulus of the matrix, E_m which, as we know, varies with temperature. Figure 2, taken from Hartwig [19], shows that as the temperature decreases, E_m, in a very general way, can be approximated as a linear function of temperature. Empirically, this function can be expressed as
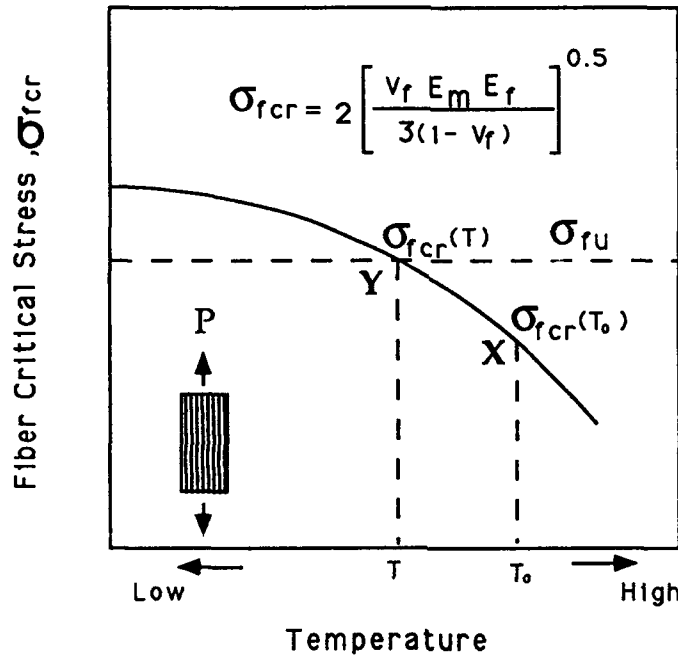
Figure 3. Schematic showing low-temperature induced increase of fiber critical stress.

$$E_m(T) = E_m(T_0) + K(T_0 - T) \tag{2}$$

where temperature $T_0 > T$ in °C, $E_m(T_0)$=longitudinal elastic modulus (MPa) of the resin at temperature T_0, $E_m(T)$=longitudinal elastic modulus (MPa) of the resin at low temperature, T, and K= empirical constant; for most resins the value of K is of the order of 20 MPa °C^{-1} as shown in Figure 2. It is reasonable to assume that the variation of fiber modulus with temperature is negligible compared to that of the polymeric matrix. The relationship between σ_{fcr} and temperature can now be established by substituting eq (2) into eq (1); thus

$$\sigma_{fcr}(T) = 2\left[\frac{V_f E_f (E_m(T_0) + K(T_0 - T))}{3(1 - V_f)}\right]^{0.5} \tag{3}$$

Figure 3 is a schematic that illustrates how the critical stress σ_{fcr} in fiber increases with the reduction of temperature as per eq (3). The curve shows that as the temperature is reduced, a given applied load of P, which is safe at temperature T_0 (point X on the curve, $\sigma_{fcr}(T_0) < \sigma_{fu}$) may cause the fiber to break or fail if the temperature is reduced to T (point Y, where $\sigma_{fcr} = \sigma_{fu}$). As stated before, in tensile loading it is the fiber failure that initiates the final failure of the composite. Thus, a unidirectional composite that does not fail at higher temperatures may fail at lower temperatures. It is interesting to note that the greater the induced fiber critcal stress from buckling and matrix stiffening is, the less would be the failure stress (σ_c) of the composite. The tensile strength of the composite in the fiber direction σ_c can be related to the fiber failure stress σ_{fcr} as

$$\sigma_c = CV_f[\sigma_{fcr}]^{-n} \tag{4}$$

where the constant C is the stress transfer function coefficient controlled by the fiber waviness and the bond strength of the fiber to matrix. The constant C would be an independent constant for a given batch of composites. The exponent n represents the empirical relationship of σ_{fcr} to σ_c, and would possibly be closer to unity. The negative sign indicates the inverse relationship of the strength to the induced fiber stress.

Therefore, for a given batch of composite laminae using eq (3) and (4) we have

$$\frac{\sigma_c(T)}{\sigma_c(T_0)} = \left[\frac{\sigma_{fcr}(T_0)}{\sigma_{fcr}(T)}\right]^n \tag{5}$$

Rewriting eq (5) with eq (3)

$$\frac{\sigma_c(T)}{\sigma_c(T_0)} = \left[\frac{E_m(T_0) + K(T_0 - T)}{E_m(T_0)}\right]^{-0.5\,n} \tag{6}$$

Equation (6) allows us to predict the failure strength of a unidirectional composite at a lower temperature (T) if the failure strength of the composite is known at higher or room temperature (T_0). Obviously, the value of n has to be reasonably assessed. We will estimate the value of n from the analysis of the experimental results presented later.

Rosen's prediction of failure strength of the unidirectional composites usually overestimates the compressive strength by an order of magnitude [15] but his analysis clearly demonstrates a quantitative dependence of the composite's strength on the matrix stiffness, which is useful for assessing the influence of temperature on the strength.

EXPERIMENTAL RESULTS

The fiber resin systems used for the test specimens are identified in Table 1. These include glass fiber-epoxy, graphite-epoxy, and DuPont Kevlar-J2 resin systems. Besides unidirectional laminae, the fiber glass epoxy test specimen batch also included laminates with several different ply orientations and stacking sequences. The dimensions, ply number and orientations, and the stacking sequence of the laminates used for tensile testing are also identified in Table 1. The glass and graphite epoxy material samples were procured from the U.S. Army Materials Technology Laboratory (MTL), Watertown, MA. The Kevlar-J2 coupons were supplied by DuPont. Dogbone-shaped specimens were prepared for the first four glass epoxy materials tested. Straight-sided specimens were manufactured from the graphite-epoxy laminates and Kevlar-J2 laminates using aluminum end-tabs as specified in the ASTM 3039 procedures.

All specimens were statically tested under tension at room temperature and at low temperatures. Some glass fiber laminates were tested at two or three different low temperatures. All low temperature tests were performed inside a special low temperature environmental chamber built around a servohydraulic testing machine. The majority of the specimens were strain gauged to monitor the stress/strain relationship during tensile tests.

The effects of low temperature on tensile strengths of glass fiber-epoxy laminates are shown in Figure 4. In this figure the strength data are shown as function of temperature with lines drawn

TABLE 1–TEST SPECIMENS.

Material Designation	Batch No.	Type of Resin Fiber	No. of Plies	Stacking Sequence
Fiberglass-Epoxy Laminates	SS10–A	SP250 S2 Glass	6	$[0_6]$
	099–T	SP250 S2 Glass	8	$[90_2 0_2]_s$
	SS17–T	SP250 S2 Glass	6	$[90_2 0]_s$
	099–X	SP250 S2 Glass	6	$[+45_2/-45]_s$
	273–T	SP250 S2 Glass	6	$[90_2 0]_s$
Graphite Epoxy Laminate	Hercules	3501 AS4	7	$[0_7]$
	Fiberite	934 T–300	7	$[0_7]$
Kevlar	DuPont	J2		Unidirectional

through the mean values of the ultimate tensile strengths of the four glass fiber-epoxy laminates tested. There is no significant change in strength values of the various cross- and angle-ply glass-epoxy laminates tested. However, the unidirectional glass-epoxy shows a reduction in longitudinal strength with a reduction in temperature. Test results of unidirectional laminates of fiberglass-epoxy, graphite-epoxy, and Kevlar-J2 laminates are summarized in bar charts of Figure 5. These data show a reduction in strength for all specimens at low temperatures. In Figure 4 it will be seen that the $[45/-45]_6$ glass fiber-epoxy laminates do not show much change in strength with lowering of temperatures, but as the proportion of fibers (in plies) in the loading direction ($0°$ orientation) increases, say from 0 to 100%, the strength reduction becomes more pronounced.

DISCUSSION OF THE RESULTS

The tensile test data obtained from this series of tests is given in Part 1 of Table 2. All three diverse varieties of unidirectional fiber composites show that the ultimate tensile strength degrades when the temperature is reduced. Part 2 of Table 2 gives the experimental data obtained by other researchers. Here also the tensile strengths at low temperatures are lower than those at room temperatures. The strength reduction factor (SRF) is defined as the ratio of the low temperature strength to the room temperature strength:
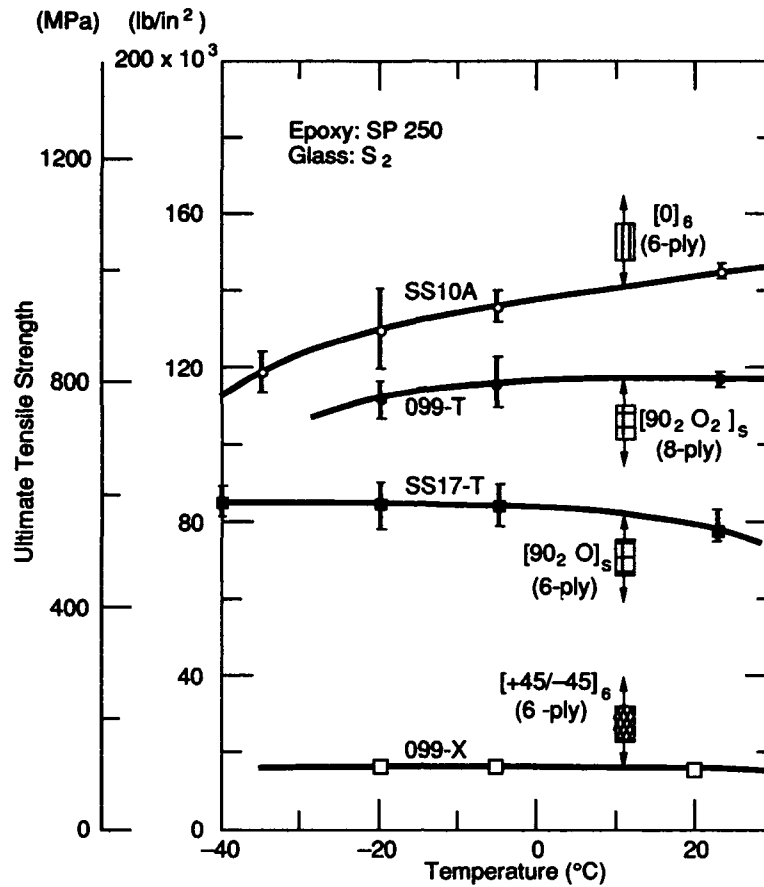
Figure 4. Low-temperature effects on the strength of fiberglass epoxy laminate.
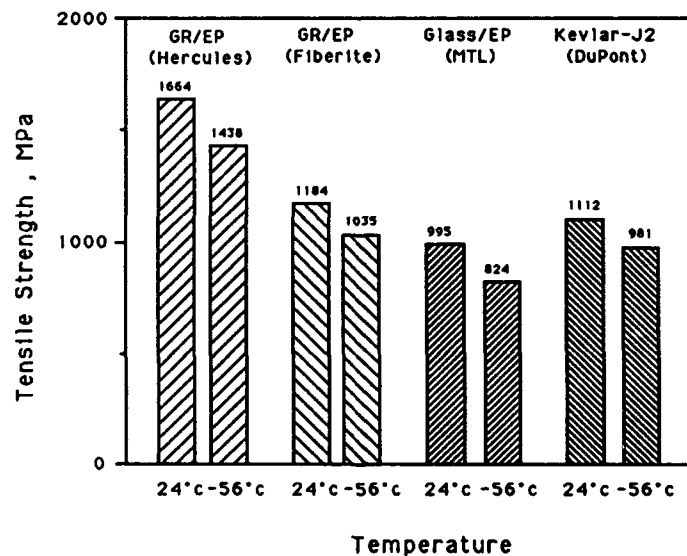
Figure 5. Tensile test data for unidirectional composites showing degradation of the strength at lower temperatures.

TABLE 2–ROOM AND LOW TEMPERATURE TENSILE TEST DATA

Laminate	Room Temperature (°C) (GPa)		Low Temperature (°C) (GPa)		Strength Reduction Factor (SRF)	Reference
Part 1. Author's experimental data:						
A. Glass fiber-epoxy						
$\quad$ S2/SP250 $[0]_6$	24	0.993	-35	0.827	0.83	Dutta et al. [4]
B. Graphite-epoxy						
$\quad$ T40/974 $[0]_7$	24	1.186	-56	1.034	0.87	Dutta et al. [4]
$\quad$ AS4/3501 $[0]_7$	24	1.662	-56	1.441	0.87	Dutta et al. [4]
C. Kevlar-J2	24	1.103	-50	0.972	0.88	Dutta et al. [19]
Part 2. Other published data:						
D Graphite Epoxy						
$\quad$ T300/5208 Dry	24	1.358	-54	1.193	0.88	Springer [1]
$\quad$ $[0]_6$ wet	24	1.641	-54	1.510	0.92	
$\quad$ P75-S/CE3	24	0.793	-129	0.414	0.52	Mazzio and
$\quad$ $[0]_5$						Huber [2]
$\quad$ T300/934*	24	1.600	-129	1.276	0.80	Mazzio and
	24	1.600	-184	1.103	0.69	Huber [2]
$\quad$ PRD49/FRLB4617*	24	2.206	-196	1.655	0.75	Hanson [20]
	24	2.206	-253	1.793	0.81	
$\quad$ 2002/HMS GR.	24	0.896	-162	0.551	0.61	Philpot and
$\quad$ and 2002/S901						Randolph [21]
$\quad$ glass hybrid						
$\quad$ T300/914C	24	1.772	-60	1.627	0.91	DFVLR [3]
$\quad$ $[0]_{16}$						
$\quad$ T300/Code 69	24	1.496	-60	1.269	0.84	DFVLR [3]
$\quad$ $[0]_{16}$						
$\quad$ T300/F550	24	1.593	-60	1.351	0.85	DFVLR [3]
$\quad$ $[0]_{16}$						
E. Boron Epoxy						
$\quad$ NARMCO 5505	24	1.434	-55	1.386	0.96	MIL-HDBK-17A [5]
$\quad$ Boron/Epoxy						
$\quad$ SP272	24	1.296	-55	1.268	0.98	MIL-HDBK-17a [5]
$\quad$ Boron/Epoxy						
F. Graphite-epoxy						
$\quad$ G30-500 3k						
$\quad$ /E7K8 PW	24	0.883	-54	0.731	0.83	MIL-HDBK-17 [22]
$\quad$ $[0]_{10}$						
$\quad$ $[0]_{12}$	24	0.841	-54	0.793	0.94	MIL-HDBK-17 [22]

* The number of plies were not reported
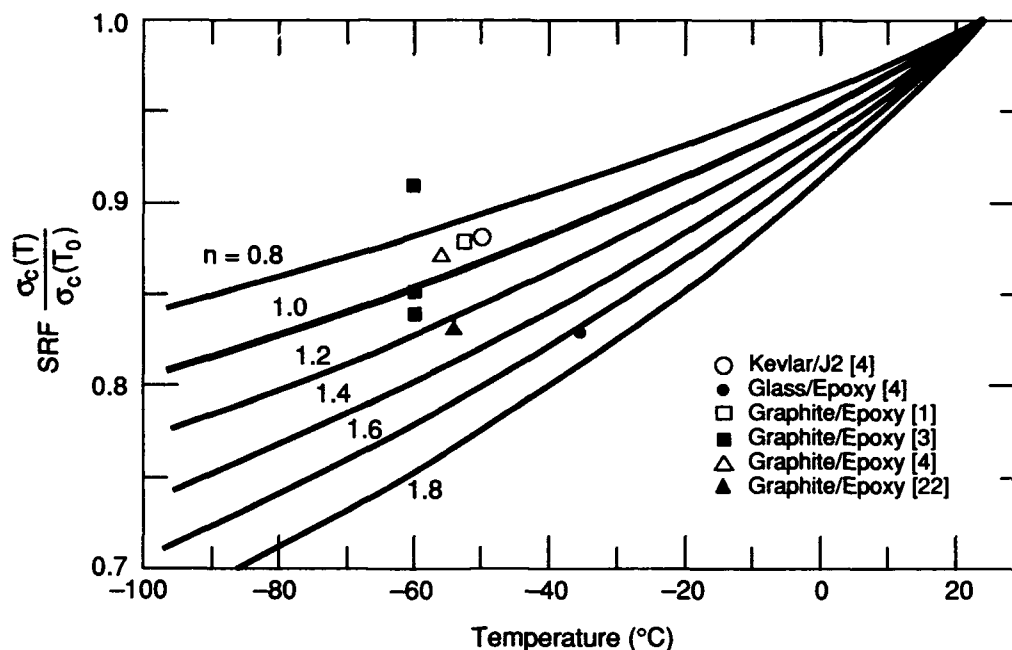
Figure 6. Prediction of low-temperature strength from SRF.

$$SRF = \frac{\sigma_c(T)}{\sigma_c(T_0)}$$

(7)

Values of SRF are also shown in Table 2.

Figure 6 is a plot of SRF's for a number of values of n with the initial temperature considered as 24°C. The experimental values from Table 2 are also plotted in Figure 6. Most data cluster around n = 0.8 to 1.2. These data, taken from widely scattered sources of literature, and the experiments performed at CRREL, suggest that the reason for strength degradation is the development of stress concentration in the curved fibers that may exist in the unidirectional lamina. Implicit in this conclusion is that the degree of curvature (waviness) is the same for any given batch of composite lamina. The waviness may be different between batches, and the stress transfer coefficient, C, and therefore the ultimate strength, too, may differ from batch to batch. Although this is an interesting problem to study, the influence of curvature radius has not been considered in this paper.

By naked eyes it is difficult to observe any fiber curvature in lamina. But it is a common experience that an unconstrained (unstretched) fiber is always curved under the influence of its own internal stresses. When these fibers are impregnated with resin to make lamina and subsequently cured, the residual curvature will be somewhere between a constraint-free curvature (maximum) and a stretched and constrained straight line (minimum). If the manufacturing process does not allow for stretching and straightening of the fibers, it is reasonable to assume that a good percentage of fibers will have curvature (waviness), and critical fiber stresses will develop in them first, making them prone to fail under an applied tensile load.

CONCLUDING REMARKS

A basis for the reduction of strength of unidirectional fiber composites when loaded parallel to fiber direction at low temperatures has been developed. The approach is based on the assumption

of the existence of curvature (waviness) in the cured composite. It has been shown that the elastic modulus of the matrix controls the stresses induced in the curved fibers for a given load. Because of increase of the modulus with reduction of temperature, the stresses in the wavy fibers also increase. Thus, a given load that can be supported at relatively higher temperature (room temperature) can cause fiber failure at lower temperatures.

REFERENCES

1. Springer, G.S., 1984. "Moisture and Temperature Induced Degradation of Graphite Epoxy Composites," in Environmental Effects on Composite Materials, G.S. Springs, Technomic Publishing, Vol. 2, p. 10.

2. Mazzio, V.F. and G. Huber, 1984. "Effect of Temperature, Moisture and Radiation Exposures on Composite Mechanical Properties," SAMPE Journal, 20: 18 and 20.

3. DFVLR Institute for Structural Mechanics, 1985. ETEC Contract No. 4825/81/NL/AK(SC) Final report: "Development of Fracture Mechanics Maps for Composite Materials." H.W. Bergmann, ed. Braunschweig, W. Germany, p. 6–3.

4. Dutta, P.K., J. Kalafut and H. Lord, 1988. "Influence of Low Temperature Thermal Cycling on Tensile Strength of Fiber Composites," in Advances in Macro-Mechanics of Composite Material Vessels and Components – ASME.PVP. D. Hui and T.J. Kozik, ed. p. 141–147.

5. Military Handbook, 1971. MIL–HDBK–174 Part–1 Reinforced Plastics, Washington, D.C.: Department of Defense, p. 4–129.

6. Gadke, M., 1985. "Response of Statically Tested Unnotched Specimens, Mechanical Properties and Damage Mechanisms of Carbon." Fiber-Reinforced Composites. Tension Loading. H.W. Bergmann, ed. West Germany: Institute of Structural Mechanics, Braunschweig, DFLVR Report No. DFLVR–FB 85–45.

7. Garber, D.P., D.N. Morris and R.A. Everett, Jr., 1980. "Elastic Properties and Fracture Behavior of Graphite/Polimide Composites at Extreme Environments." N.R. Adsit, ed. ASTM STP 768. p. 75.

8. Rosin, B.W., 1964. "Mechanics of Composite Strengthening," in Fiber Composite Materials, American Society of Metals.

9. Cox, H.L., 1952. "The Elasticity and Strength of Paper and Other Fibrous Materials," British J. App. Phys., 72.

10. Dow, N.F., 1963. GEC Missile and Space Division, Report No. R63SD61.

11. Wadsworth, N.J. and I. Spilling, 1968. British J. App. Phys., Ser. 2, Vol. 1: 1048.

12. Chamis, C.C., 1974. "Mechanics of Load Transfer at the Interface," in Composite Materials, vol. 6, Edwin P. Plueddemann, ed. Academic Press, pp. 31–73.

13. Budiansky, B., 1983. "Micromechanics," Computers and Structures, 16: 3–12.

14. Luo Chen-Ming, K. Takahashi and T.W. Chou, 1988. "Effect of fiber waviness on the nonlinear elastic behavior of flexible composites," Journal of Composite Materials, 22: 1004–1025.

15. Fleck, N.A. and B. Budiansky, 1990. "Compressive Failure of Fibre Composites Due to Microbuckling." IUTAM Symposium on Inelastic Deformation of Composite Materials, Rensselaer Polytechnic Institute, Troy, New York (May 29–June 1).

16. Holister, G.S. and C. Thomas 1966. "Fiber Reinforced Materials," Elsevier, p. 108.

17. Comninou, M. and I.V. Yannas, 1976. "Dependence of stress-strain nonlinearity of connective tissues on the geometry of collagin fibers." J. Biomechanics, 9: 427–433.

18. Bert, C.W., 1979. "Micromechamics of the Different Elastic Behavior of Filamentary Composites in Tension and Compression," Mechanics of Bimodulus Materials, 33: 17–28.

19. Hartwig, G., 1979. "Mechanical and Electrical Low Temperature Properties of High Polymers," in Nonmetallic Materials and Composites at Low Temperatures, A.F. Clark, R.P. Reed and G. Hartwig, ed. New York: Plenum Press, pp. 33–50.

20. Hansen, M.P., 1972. "Effect of Temperature on the Tensile and Creep Characteristics of PRD49 Fiber/Epoxy Composites," in Composite Materials in Engineering Design, B.R. Noton, ed. American Society for Metals, Technical Division and Activities, pp. 717–724.

21. Philpot, K.A. and R.E. Randolph, 1982. "The Use of Graphite/Epoxy Composites in Aerospace Structures Subject to Low Temperatures," in Non-Metallic Materials and Composites at Low Tempertures, vol. 2, G. Hartwig and D. Evans, ed. Plenum Press.

22. MIL–HDBK–17, 1991. Coordination Group Meeting, Santa Barbara, April 2–4.

23. Dutta, P.K., 1989. "Low Temperature Tensile Strength of Kevlar/J–2 Composite," U.S. Army Cold Regions Research and Engineering Laboratory. Unpublished technical note.

SESSION 10A

Data Bases

Standards for Computerization of Composite Material Data

CRYSTAL H. NEWTON

ABSTRACT

Material property data for composites are most often difficult and expensive to obtain. Consequently, it is very important that the maximum use be obtained from the data that are available. To maximize the use of composite material property data, standard test methods, material specifications, and processing specifications are required. Computerized data bases for materials properties are needed for increased availability of data which can be compared to similar data directly. In order to have independent databases of comparable materials data, common test methods and documentation are necessary. In this article, progress on the development of data documentation recommendations and requirements from these activities is reported. The information required to adequately identify the material and the test method based on each system is compared.

STANDARD TEST METHODS

One of the difficulties with composite materials is the lack of standard test methods. In some cases, there is no consensus standard test method for a given property and material. More commonly, there are too many test methods which means there is no one single standard. Examples of this situation are ASTM D 3410[1] for composite properties and the collection of ASTM shear test methods. ASTM D 3410 contains methods for wedge-loaded, end-loaded, and sandwich beam specimens. ASTM Committee D-30 on High Modulus Fibers and Their Composites is incorporating these test methods into separate documents. However, there will continue to exist different test methods for the same properties, which produce results that do not agree. Similarly, several different methods for obtaining shear properties are defined in standard test methods. Since a single standard test method is not used consistently for testing composite materials, documentation requirements are used to provide information to the engineer. It is hoped that, with enough information combined with engineering judgment, data from different materials can be compared.

Crystal H. Newton, Materials Sciences Corporation, 930 Harvest Drive, Blue Bell, PA, USA, 19422

DATA DOCUMENTATION

Requirements for data documentation are being approached in three different ways. From the computerized database viewpoint, ASTM Committee E-49 on Computerization of Material and Chemical Data in conjunction with ASTM Committee D-30 and other groups is developing a series of guides for identifying materials and recording test results. One use of these guides is as recommendations for data documentation. American Society for Testing and Materials (ASTM) Committee D-30 on High Modulus Fibers and Their Composites is updating and revising many test methods for composite material properties. As part of these revisions, the data reporting requirements are generally being expanded. Military Handbook 17, Polymer Matrix Composites, contains requirements for data documentation for submission of data for the handbook [2]. These requirements are also recommendations for data generation for all other purposes. These three approaches to data documentation are discussed and compared.

DATA COMPUTERIZATION GUIDES

In order to compare properties for composite materials, it is essential to be able to identify both the material and how it is tested. Guides for standard data records for composite materials are being developed by ASTM Committees E-49 on the Computerization of Material and Chemical Databases and D-30 on High-Modulus Fibers and Their Composites. Separate guides concentrate on the identification of the material and the documentation of the test procedure. These guides apply to all types of composite materials. Based on a categorization of composite materials by matrix, the scope of the guides includes polymer matrix, metal matrix, ceramic matrix, and carbon-carbon matrix materials. Examples for polymer matrix composites are currently included in the composite material identification guide and the mechanical test data recording guide. Examples for metal matrix, ceramic matrix, and carbon-carbon composite materials are planned or under development. Four guides are planned for the identification of composite materials and their constituents as shown in Figure 1. Two of theses are completed - the composite material identification guide (ASTM E 1308 [3]) and the guide for the identification of fibers, fillers, and core materials (ASTM E 1471 [4]). Two additional guides for the identification of preimpregnated materials and fiber assemblies. Fiber assemblies include woven, braided, and knitted materials. Primarily composed of fibers, matrix material may be included in a commingled fiber form. Preimpregnated material may include fibers, fiber assemblies, or both with the addition of matrix material in a partially cured state. The completion of the four guides will cover composite materials and their constituents at all stages of processing. In addition to guides developed for identifying the composite materials, guides for the identification of polymers, metals, and ceramics are referenced to document the constituent materials. These guides have been developed by ASTM Committee E-49 with the cooperation of other committees related to the materials. As an example, full identification of a glass/epoxy composite made from a woven prepreg may include information from the guides shown in Table I. This approach may seem rather complex, however it is much more practical than developing a guide for each possible combination of composite material level and reinforcement and matrix chemical families.

FIBER

FIBER ASSEMBLY	↔	**FIBER(S)** alone or with commingled **MATRIX MATERIAL(S)**
PREIMPREGNATED **MATERIAL**	↔	**FIBER(S)** and/or **FIBER ASSEMBLY(S)** with **MATRIX MATERIAL(S)**
COMPOSITE **MATERIAL**	↔	**FIBER(S)** and/or **FIBER ASSEMBLY(S)** with **MATRIX MATERIAL(S)** or/and **PREIMPREGNATED MATERIALS** and possibly **CORE MATERIALS**
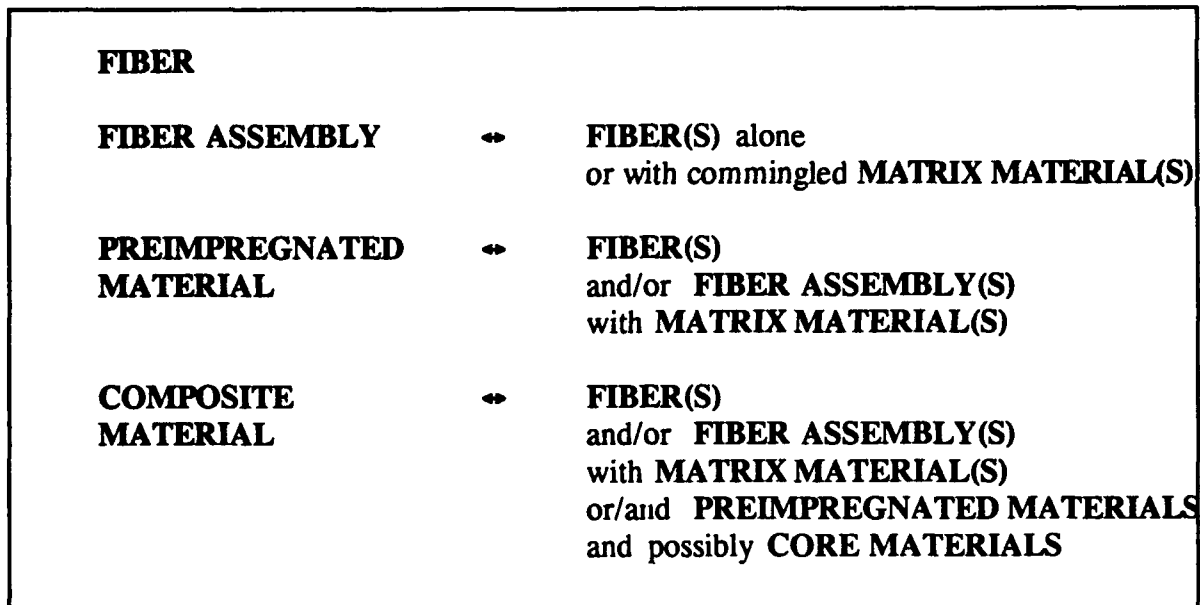
Figure 1. Levels of Composite Material Identification.

The second requirement for data comparisons is identification of the how the material was tested. In the area of advanced composite materials, one guide has been developed for mechanical properties testing [5]. This guide was developed in ASTM Committee E49 with the cooperation of ASTM Committee D30 and then transferred to the latter committee. This guide applies to a variety of ASTM test methods for tensile, compressive, and shear testing of polymer-matrix and metal-matrix composite materials. In addition, the guide is relevant to other test methods.

The concept of an *essential field* is important in understanding the material identification and test reporting guides. ASTM Committee E49 has defined an essential field as:

TABLE I - EXAMPLE OF THE USE OF COMPUTERIZATION GUIDES

	Guide	Example Information
1	ceramics identification guide	glass composition
2	fibers, fillers, and core material guide	fiber diameter
3	polymers identification guide	epoxy composition
4	fiber assembly guide	weave description
5	preimpregnated materials guide	areal weight
6	composite material identification guide	fiber volume

essential field, n - a field in a record which must be completed in order to make the record meaningful in accordance with the pertinent guidelines or standard [6].

Some of the fields in the data computerization guides are identified as essential fields. It is recommended that these fields be included in any database. It is also recommended that the datum that goes into the field is essential. Consequently, these essential fields define a set of data documentation requirements. It is left to the database designer for the definition of the fields such that

1) essential fields are included in the database design,
2) these fields must be filled for valid records, and
3) provision is made for null, not applicable, or unknown   responses.

The difference between essential fields and essential data will be considered below.

ASTM COMMITTEE D-30 TEST METHOD DATA REPORTING

ASTM Committee D30 on High Modulus Fibers and Their Composites has developed a number of test methods for properties of polymer-matrix composite materials and two for metal matrix composite materials. These standard test methods each contain a section on data reporting requirements. ASTM Committee D30 is in the process of reviewing and revising all test methods under its jurisdiction. As part of this revision, the data reporting requirements are generally being expanded to more precisely reflect the test method. While the data reporting sections were used as input in the development of the computerization guides, there are significant differences between the computerization guides and the data reporting sections. An effort is underway to compare the data reporting requirements with the computerization guides. Two approaches are being considered. The first is an incorporation of the computerization guides in the test methods by reference. The second approach is to differentiate between essential data and essential fields. The computerization guides, particularly ASTM E 1434, would be used to identify recommended and essential fields for a database record. Each data reporting section would list the information which is recommended and essential for a testing facility and a material supplier to report. This also addresses a concern from organizations which frequently test material without necessarily knowing what it is. Strictly speaking, if the computerization guides in their present form would be referenced by a test method, a testing house could not meet all requirements, including material identification, of that test method. If this second approach is followed, all data essential to material supplier and testing house would correspond to essential fields in the computerization guide. With this information, the computerization guide could also be used as a planning document to ensure consistency in the test method data reporting sections.

MILITARY HANDBOOK 17 DATA DOCUMENTATION REQUIREMENTS

Military Handbook 17 on polymer matrix composites is a handbook supported by the Department of Defense and the Federal Aviation Administration and developed by

a Coordination Group representing industry and government. The handbook consists of three volumes. The first volume includes guidelines for the development of material property data, the second volume contains the data, and the third volume offers information on how the data can be used. Figure 2 shows the scope of the handbook. First released in 1959, the handbook has undergone an almost complete revision with the most recent release dated 28 February 1992.

In addition to the ASTM data record guides, data documentation requirements are included in Military Handbook 17. These documentation requirements were developed at the same time as the ASTM composites guides. However, as the ASTM and Military Handbook 17 documents have developed there has been significant divergence. The ASTM data records are much more specific in the development of records field by field. The Military Handbook 17 requirements are directed toward a more limited range of application and data fields are not identified. While the handbook data documentation requirements and the computerization guide have noticeable differences, a recent revision and ongoing work may bring the handbook requirements closer to the computerization guides and test method reporting section. A comparison of the information needed for each is worthwhile at this time.
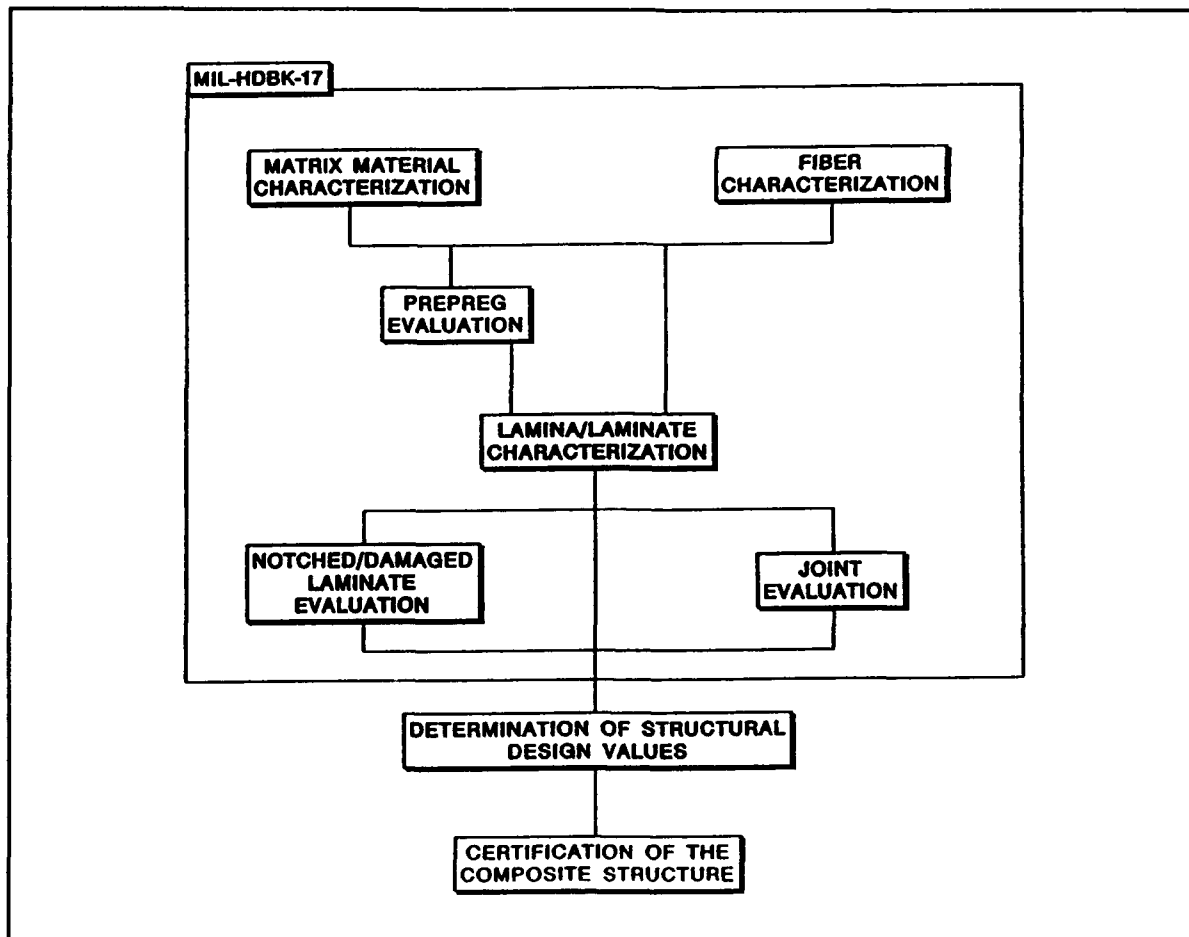

Figure 2. Scope of Military Handbook 17, *Polymer Matrix Composites.*

COMPARISON OF REQUIREMENTS

A comparison of requirements and recommendations for data documentation may show areas for further coordination and mutual improvement. Overall, the handbook data documentation requirements are presented in the most general terms. The computerization guide is the most specific with individual fields defined, while the data reporting requirements generally fall between the other two. In some areas, the data reporting requirements are the most specific. The differences between the handbook data documentation requirements and the test method data reporting requirements are minimized in the recent revision which directs that any deviations from a test method "including data reporting requirements" must be noted. The handbook also differentiates between data documentation required for fully approved data and less stringent requirements for screening data. Table II shows the information required or recommended for the identification of the prepreg material. Note that the impregnation method is recommended in the handbook data documentation requirements, required in the computerization guide, and not mentioned in the data reporting requirements. These are relatively small changes but a detailed comparison shows the need for additional coordination among these requirements and recommendations.

This coordination is, in fact, underway with significant efforts in all three areas within the last year. Since the revision of the handbook requirements refers to the test methods and the test methods and computerization guides will be related, all three types of data documentation will be similar or equivalent. It is hoped that full coordination of these data documentation requirements will alleviate differences that prevent a direct comparison of the data.

DATA EXCHANGE

Data exchange is an issue which must be considered when developing a database. The most noteworthy activity in the area of data exchange is the ongoing development of the STEP (Standard for the Exchange of Product Model Data) system [7]. STEP is intended to provide a common protocol or format for the exchange of data. The materials model has been developed as far as identifying the material and characterizing finite element material property information. Much of this effort has been based on the ASTM data record guides, but again changes have resulted during development. The most recent development is the separation of the composite material model from the material model [8]. While STEP serves a different purpose from the other guides and requirements noted above, coordination of the STEP composite material model with these guides and requirements should continue.

OTHER DATA COMPUTERIZATION ISSUES

Other data computerization issues which are applicable to composite material information are needs for adequate database management, concerns with evaluating quality and accuracy of information, and the evaluation of data. ASTM Committee E49 has developed guidelines for database management [9], and for assessing the quality of data and databases [10]. The evaluation of composites materials data is discussed

TABLE II - PREPREG IDENTIFICATION

	Military Handbook 17 Data Documentation Requirements	Test Method Reporting Requirements	Computerization Guide
Ply Manufacturer	•	•	•
Date of Manufacturer	•	•	è
Material Lot Number	•	•	è
Commercial Designation	•	•	•
Material Form	•	•	
Precursor Reinforcement Orientation			è
Reinforcement Areal Weight	•	•	è
Resin Content	F	•	
Precursor Reinforcement Content			è
Impregnation Method	è		•
• Essential è Recommended but not essential F Required for fully-approved data			

in Reference [11]. The evaluation and computer representation of data accuracy are still to be addressed.

SUMMARY

The requirements for computerization of data so that the data can be compared to data from other sources have been discussed. The development of a single standard test method for a given property would alleviate many of these concerns. In the meantime, requirements and recommendations for adequate documentation of the data have been made. With adequate documentation and engineering judgment, it is hoped that useful data comparison can be made.

ACKNOWLEDGEMENTS

REFERENCES

1. ASTM D 3410-87, 1990. "Compressive Properties of Unidirectional of Crossply Fiber-Resin Composites," *1990 Annual Book of ASTM Standards*, 15.03, Philadelphia: American Society for Testing and Materials.

2. MIL-HDBK-17-1C, 28 February 1992. *Polymer Matrix Composites*, Volume 1, Guidelines, Philadelphia: Naval Publications and Forms Center, pp. 8-5 - 8-7.

3. ASTM E1309, 1992. "Standard Guide for the Identification of Composite Materials in Computerized Material Property Databases, Philadelphia: American Society for Testing and Materials.

4. ASTM E 1471, 1992. "Standard Guide for the Identification of Fibers, Fillers, and Core Materials in Computerized Material Property Databases," Philadelphia: American Society for Testing and Materials.

5. ASTM E1434, 1991. "Standard Guide for the Development of Standard Data Records for Computerization of Mechanical Test Data for High-Modulus Fiber-Reinforced Composite Materials," Philadelphia: American Society for Testing and Materials.

6. ASTM E 1443, 1992. "Terminology of Computerized Material and Chemical Property Databases," Philadelphia: American Society for Testing and Materials.

7. J. R. Rumble, Jr., 1992. "The STEP Model of Materials Information," in *Computerization and Networking of Materials Databases: Third Volume, ASTM STP 1140*, T.I. Barry and K.W. Reynard, ed. Philadelphia: American Society for Testing and Materials.

8. John Rumble, Jr., 1992. "Step Materials Team Newsletter 5,"Gaithersburg: National Institute for Standards and Technology.

9. ASTM E1407, 1990. "Standard Guide for Materials Database Management," Philadelphia: American Society for Testing and Materials.

10. ASTM E 1511, 1992. "Guide for Formatting and Use of Material and Chemical Property Data and Database Quality Indicators," Philadelphia: American Society for Testing and Materials.

11. C. H. Newton, P. M. Brady, and D. L. Volk, 1992. "Analysis and Evaluation of Data for Advanced Composite Materials," in *Computerization and Networking of Materials Databases: Third Volume, ASTM STP 1140*, T.I. Barry and K.W. Reynard, ed. Philadelphia: American Society for Testing and Materials.

Constructing Material Databases for CAE Systems

EDWARD L. STANTON AND STEVEN E. RAHMANN

ABSTRACT

The computerization of materials information for CAE systems
has lagged that of geometry information for CAD systems. Here
we illustrate the progress made by the ASTM and others using a
model database from the Automotive Composites Consortium with an
architecture based on the EXPRESS language. Differences between
CAD and CAE application data environments and the mechanics of
actually constructing a material database are described.
Finally a PDES/STEP physical file for exchange of the model
material database is constructed.

INTRODUCTION

ASTM Committee E49 is developing standards [1] for
computerizing materials information to clearly identify a
material, its state, its test condition and other property
metadata necessary to define both the material and the
conditions under which the property data from a test are valid.
This is the traditional approach to materials information,
defining the right property test for a specific material type
and specimen form relevant to a specific design application.
The standards allow us to compare materials and their properties
using databases without getting apples and oranges confused.
This traditional view leads to handbook like databases
useful in design allowable applications usually focused on final
mechanical properties with perhaps their temperature dependence.
The Automotive Composite Consortium (ACC) has expanded this view
to include process critical properties of raw materials and
collections of specimens that come close to defining all the
properties required by linear mechanical CAE applications.
When the CAE application includes nonlinear response
simulation of even the most elementary kind we must rely on
mathematical models to leverage the limited test data available.
Since these models can range from entirely empirical to ones
based on fundamental laws of material science we clearly require
metadata that identify model type in some way. As low cost
computer simulations displace expensive prototype testing the

Edward Stanton and Steven Rahmann, PDA Engineering, 2975 Redhill Avenue,
Costa Mesa, CA 92626

quality of both the material data and material model must be
considered in developing material databases for CAE
applications. Continuing this reasoning standards for models
are needed to ensure that process model data, for example, are
not used for performance analyses.

CONSTRUCTING A MATERIAL DATABASE

An ASTM publication scheduled for release soon has an
EXPRESS based schema for an ACC model database that is too long
to repeat here. The organization of that data is illustrated in
Figure 1 showing the process, performance and product data sets.
These data were collected using a PC program available from the
ACC and then transformed by the authors into a load file for a
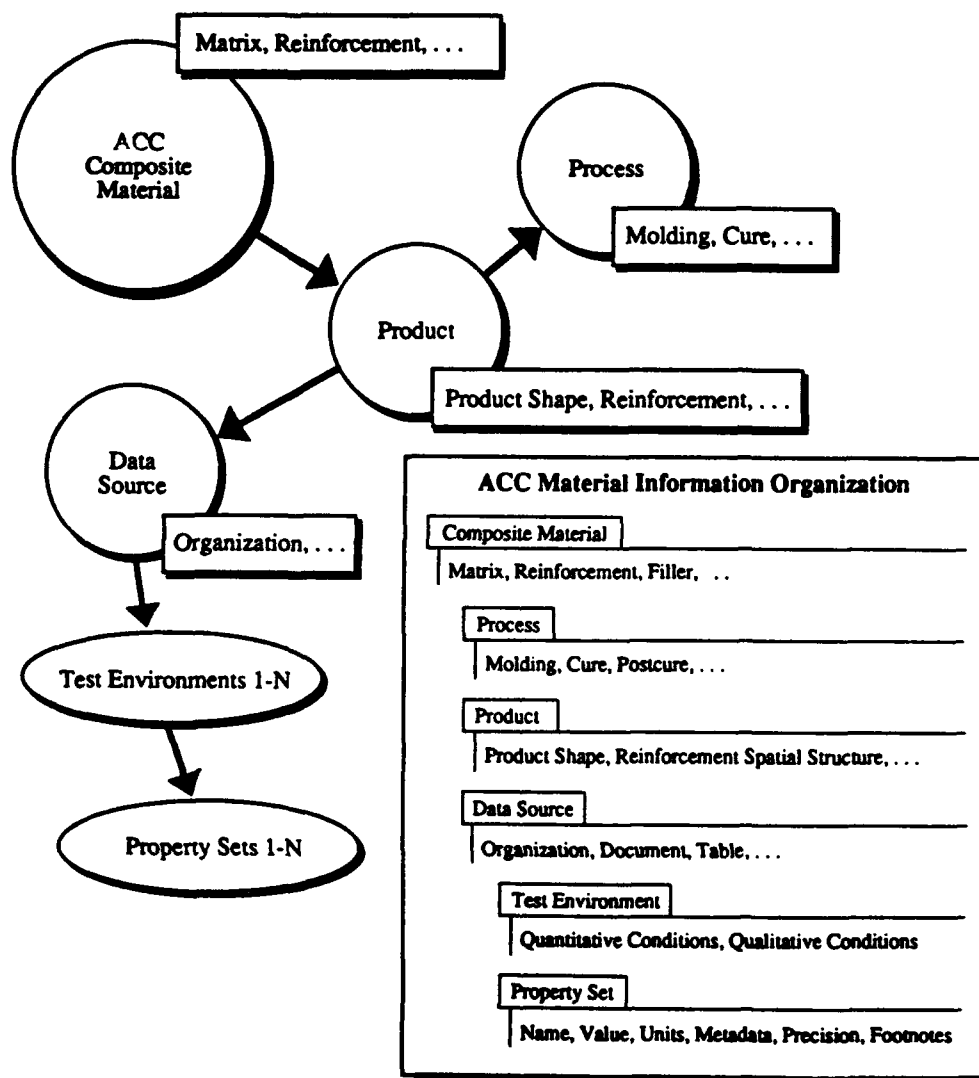commercial material database system, M/VISION. A brief summary

Figure 1. ACC Material Information Organization

of the material and process information are shown in Table 1 where over thirty data and metadata items designate this information before any mechanical property test data are presented. The steps in moving data in electronic format from raw test data to various material databases is shown in Figure 2 where for space reasons we cannot repeat all the steps in detail. It is important to note in passing that integrity constraints modeled as Where Rules in EXPRESS are important to this process.

The mechanical properties for three test temperatures are in Reference [2] and in abbreviated form are in the Appendix to this paper as an EXPRESS physical file. In both instances the 'PDA' rule was used to provide a mnemonic for each property based on Property_Direction_Attribute convention shown here

Property Description

E	Extensional Modulus
NU	Poisson Ratio
G	Shear Modulus
CTE	Coefficient of Thermal Expansion
US	Ultimate Strength
UE	Ultimate Elongation
ER	Modulus of Rupture

Direction Measured

11	Uniaxial Property in Material Direction 1
22	Uniaxial Property in Material Direction 2
33	Uniaxial Property in Material Direction 3
12	Biaxial Property in Material Plane 12
13	Biaxial Property in Material Plane 13
23	Biaxial Property in Material Plane 23

Attribute

T	Tension
C	Compression
SA	Shear (ACC Direct Shear Test)

for this particular database. Note the convention is extensible and we often have multiple shear property test attributes for larger databases. It is also possible to add thermal, electronic or other property types to the convention which plays the role of a database specific dictionary.

After all the steps shown in Figure 2, we have a database useful for design applications but less useful for linear FEA stress analysis applications. The situation with computerized materials information is like that for geometry information in that the CAD data files contain reams of data the analyst cannot use in a CAE application code like NASTRAN or ABAQUS. Today we must provide special translators for this job. The material information modeling community is at the calculator stage in many respects with no truly CAE oriented databases commercially available.
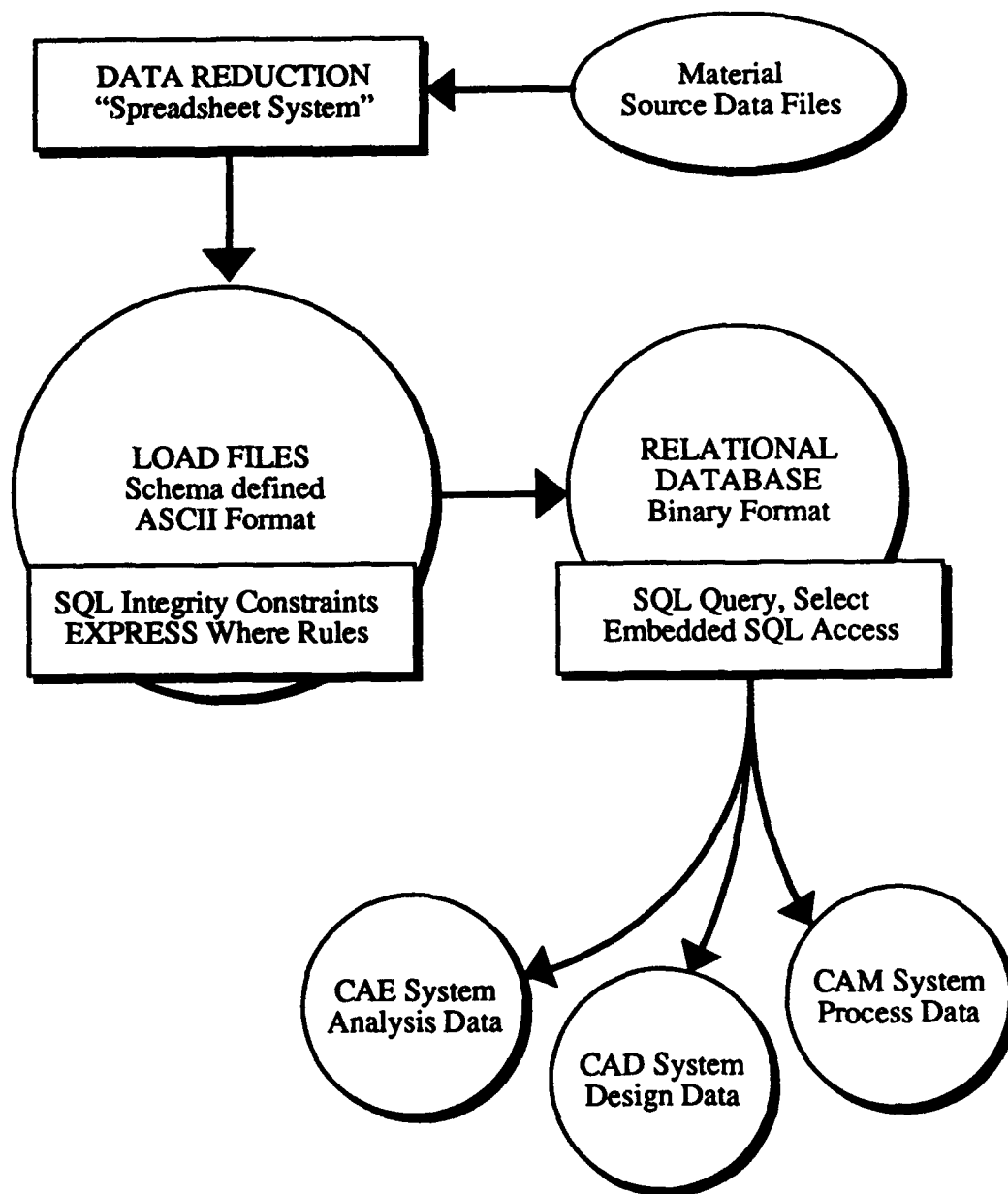
Figure 2. Database Development Steps and Application Interfaces

CAD/CAE ACCESS TO MATERIAL DATABASES

The investment in developing quality materials data in electronic formats benefits the design process most when it is used in CAD/CAE applications. This integration function needs the PDES/STEP standards for product data exchange which are just now emerging for materials information. The IGES standard has very limited FEA materials data, namely basic linear coefficient data like initial elastic modulus and coefficients of linear thermal expansion. The system used to load our ACC model database has an export feature to PATRAN and to IGES neutral files. Access to various application codes for process simulation or structural performance analyses is then possible from these neutral files for linear property data.

The problems with CAE use of a CAD database include missing properties required for a specific analysis and differences between the available test property parameters and the related analysis property parameters. An example of missing data might be a transverse modulus, $E22$, in a unidirectional ply material and the CAE application requires the missing property to function. An example of property parameter differences actually occurs in our model databases; the Elastic Modulus in tension and compression are unequal while linear finite element models require a single value. In both instances an engineering judgement is required to complete the data exchange as far as the CAE application is concerned.

TABLE I - ACC COMPOSITE MATERIAL AND PROCESS DATA SHEET[a]

Database Name	Value	Units	ACC Name
ACC_DESIG	Dow 411-C50/CT U750	-0-	Composite Designation
M-CLASS	Polymer	-0-	-0-
R_CLASS	Fiber	-0-	-0-
Ply_Type	Dry Mat	-0-	-0-
Ply_Name	U750	-0-	Product Code
Ply_Manuf	Certainteed	-0-	Manufacturer
M_COMP	Vinyl Ester	-0-	Resin Composition
M_CODE	DOW 411-C50	-0-	Manufacturer
M_SG	1.12	g/cc	Specific Gravity (cured)
M_TG	121	Deg C	Glass Transition Temperature
M_VISC	100	cp	Viscosity
M_UST	79.2	MPa	Neat Resin Tensile Strength
M_ET	3.30	GPa	Neat Resin Tensile Modulus
M_UET	1.00	%	Neat Resin Elongation
R_TYPE	E_Glass	-0-	Fiber Material Type
R_COMP	Borosilicate Glass	-0-	-0-
R_FORM	1.50	oz.CSM	Fiber Product Form
R_SG	2.60	g/cc	Specific Gravity
R_MANF	Certainteed	-0-	Manufacturer
R_LENG	Continuous	mm	Fiber Length
R_YLD	6633	g/km	Roving/Yarn Yield
R_SZS	2500	-0-	Bundle Size/Splits
R_FDIA	16.0	micro m	Filament Diameter
R_CHSZ	Siline_KE6N850501	-0-	Chemical Size Description
R_BIND	Polyester	-0-	Binder Description
PRC_TYPE	RTM	-0-	Molding Process
PRC_DATE	90/02/10	YYMMDD	Molding Date
MOL_COMP	Epoxy	-0-	Mold Composition
INJ_RATE	2.1	kg/min	Resin Injection Rate
INJ_PRES	275	MPa	Resin Injection Pressure
MOL_TEMP	20.	Deg C	Mold Temperature
MOL_PRES	689.	MPa	Mold Pressure
FILLTIME	90.	sec	Fill Time
CURETIME	1200.	sec	Cure Time
POS_TEMP	123.	Deg C	Postcure Temperature
POS_TIME	3.	hrs	Postcure Time

[a] The symbol -0- indicates a null value in this paper.
Additional data are in the source ACC file not shown here.

PDES/STEP MATERIAL DATABASE EXCHANGE

We have described the general difficulty today in making
material database information available for CAE. The older IGES
fixed template exchange of material data is limited both by the
template and the method. PDES/STEP standards offer object
oriented models that can be tailored using the EXPRESS language
to specific applications. The PDES Application Protocol Suite
for Composites (PAS-C) is defining information needs for
analysis, design and manufacturing of aircraft composite
structures. When databases are developed using such PDES/STEP
models the databases can be exchanged in clear text using the
EXPRESS physical file standard [4]. As in any new technology
there is confusion early on when concepts are first applied to
actual problems and we offer in the Appendix the results of our
work in applying the standard to the ACC model database which
contains only one material and three test conditions. The
EXPRESS schema is much too long for a paper but the Entities are
in general of the form

```
ENTITY M_TG_property SUBTYPE OF mvision_real_property;
DERIVE
    description : STRING := 'Resin Glass Transition Temperature';
    units : STRING := 'deg C';
END_ENTITY;
```

and certain Entities like ACC_Product have many attributes.
This is an appropriate place to close the paper and caution the
reader that these results are work-in-progress using the
emerging PDES/STEP standards efforts of many people and are
subject to chagne as these standards move thorugh the ballot
process.

CONCLUSIONS

There are two main points to be made; first, the early material
database work is CAD in focus and retains the traditional view
of material data, and second, the use of ASTM and PDES/STEP
standards are essential to clearly designating a material and
exchanging relevant property data. As CAE application protocols
are defined using the EXPRESS language and other PDES/STEP
infrastructure are developed the difficult problem of modeling
composites for analysis and obtaining reliable ASTM quality data
for the models will greatly improve.

APPENDIX

```
STEP;

HEADER;

FILE_name( 'acc.pf', '1992-06-19T16:04:26' ( 'E. L. Stanton' ), ( 'PDA Engineering' ),
'STEP version 1.0', 'MV_STEP 1.0', 'SGI Indigo', 'S. E. Rahmann' );

FILE_DESCRIPTION( ( 'A STEP physical file of the contents of the M/VISION ',
                    'databank acc.DES.  Produced using the translation ',
                    'program MV_STEP 1.0.'
                  ),
                  'STEP version 1.0' );

FILE_SCHEMA( ( 'acc,DES' ) );

ENDSEC;

DATA;

#1      =    m/vision_metadata( ' ASTM D3039' );
.........................................................
#28     =    mvision_metadata( ' ASTM D638' );
#29     =    &SCOPE
#30     =    ACC_DESIG_property( 'Dow 411-C50/CT U750', $);
#31     =    CMP_NAME_property( 'Fiberglass/Vinyl Ester', $);
#32     =    PMC_property( 'M22GL100UP0320', $);
.........................................................
.........................................................
#57     =    M_VISC_property( 100.000000, $, $);
#58     =    M_UST_property( 79.199997, #26, $);
#59     =    M_ET_property( 3.300000, #27, $);
#60     =    M_UET_property( 1.000000, #28, $);
ENSCOPE ACC_Material ( $, #30, #31, #32, #33, #34, #35, #35, #37, #38, #39, #40, #41,
#42, #43, #44, #45, #46, #47, #48, #49, #50, #51, #52, #52, #53, #54, #55, #56, #57, #58,
#59, #60, $, $, $, $, $, $, $);

#61     -    &SCOPE
#62     =    INI_CON_property( 2.000000, $, $);
#63     =    INI_TYPE_property( 'MEKP', $);
#64     =    PRC_TYPE_property( 'RTM', $);
.........................................................
.........................................................
#80     =    FILLTIME_property( 90.000000, $, $);
#81     =    CURETIME_property( 1200.000000, $, $);
#82     =    POS_TEMP_property( 123.000000, $, $);
#83     =    POS_TIME_property( 3.000000, $, $);
ENDSCOPE ACC_Process( $, #62, #63, #64, #65, #66, #67, #68, $, $, #69, #70, $, $, #71,
#72, #73, #74, $, #75, #76, #77, #78, #79, #80, #81, #82, #83);

#84     =    &SCOPE
#85     =    PRD_SG_property( 1.500000, $, $);
#86     =    PRD_SG_SD_property( 0.000000, $, $);
.........................................................
.........................................................
#91     -    PRD_M_WPCT_property( 60.099998, $, $);
#92     =    PRD_M_WPCT_SD_property( 2.000000, $, $);
#93     =    PRD_TH_property( 3.000000, $, $);
#94     -    PRD_TH_SD_property( 0.100000, $, $);
ENDSCOPE ACC_Product( $, $, $, $, #85, #86, #87, #88, $, #89, #90, #91, #92, $, $, #93,
#94);
#95     -    &SCOPE
#96     -    TEMP_property( -40.000000, $, $);
#97     -    &SCOPE
#98     -    TEMP_property( 23.000000, $, $);
```

```
ENDSCOPE Test_Environment( $, #98, $);


#99   =   &SCOPE
#100  =   TEMP_property( 121.000000, $, $);
ENDSCOPE Test_Environment( $, #100, $);


#101  =   &SCOPE
#102  =   TABLE_NAME_property( 'Sample Test Data Summary', $);
#103  =   TEST_ENGR_property( 'Peterson, Johnson, Hagerman', $);
#104  =   TEST_ORGN_property( 'Automotive Composites Consortium', $);
#105  =   DATA_USE_property( 'Structural Design (ACC Model Database Testing)', $);
ENDSCOPE Source ( $, #102, $, #103, #104, #105);


#106  =   &SCOPE
#107  =   CTE11_property( 27.900000, #23, $);
#108  =   CTE11_SD_property(1.600000, $, $);
#109  =   US11T_property( 152.800000, #5, $);
..............................................
..............................................
#149  =   ER22C_property( 4.800000, #18, $);
#150  =   ER22C_SD_property( 0.920000, $, $);
ENDSCOPE property_set( $, #107, #108, #109, #110, #111, #112, #113, #114, #115, #116,
#117, #118, #119, #120, #121, #122, #123, #124, #125, #126, #127, #128, #129, #130, $, $,
#131, #132, #133, #134, #135, #136, #137, #138, #139, #140, #141, #142, #143, #144, #145,
#146, #147, #148, #149, #150, #151, $, #152, $, $, $, $, $, $, $, $, $);


#153  =   &SCOPE
#154  =   CTE11_property( 22.400000, #23, $);
#155  =   CTE11_SD_property( 1.900000, $, $)'
#156  =   US11T_property( 132.800000, #5, $);
..............................................
..............................................
ENDSCOPE property_set( $, #154, #155, #156, #157, #158, #159, #160, #161, #162, #163,
#164, #165, #166, #167, #168, #169, #170, #171, #172, #173, #174, #175, #176, #177, #178,
#179, #180, #181, #182, #183, #184, #185, #186, #187, #188, #189, #200, #201, $, $, $, $,
$, $, $, $, $);


#202  =   &SCOPE
#203  =   CTE11_property( 17.600000, #23, $);
#204  =   CTE11_SD_property( 2.700000, $, $);
#205  =   US11T_property( 112.300000, #5, $);
..............................................
..............................................
#243  =   ER22C_property( 1.020000, #18, $);
#244  =   ER22C_SD_property( 0.150000, $, $);
ENDSCOPE property_set( $, #203, #204, #205, #206, #207, #208, #209, #210, #211, #212,
#213, #314, #215, #216, #217, #218, #219, #220, #221, #222, #223, $, #224, $, $, $, #225,
#226, #227, #228, #229, #230, #231, #232, #233, #234, #235, #236, #237, #238, #239, #240,
#241, #242, #243, #244, #245, $, #246, $, $, $, $, $, $, $);


#247  =   mvision_record( #29, #61, #84, #95, #106, #101);


#248  =   mvision_record( #29, #61, #84, #97, #153, #101);


#249  =   mvision_record( #29, #61, #84, #99, #202, #101);
```

REFERENCES

1. ASTM Annual Book of Standards, Section 14, Volume 14.01 Analytical Methods-Spectroscopy; Chromatography; Computerized Systems, June 1991.

2. M/VISION User Manual, Chapter 12, pp. 12-11 to 12-15, 1991.

3. ISO CD 10303-32, Product Data Representation and Exchange — Part 21: Clear Text Encoding of the Exchange Structure.

Databases in Materials Science and Engineering: An International Approach

W. A. WEIDA AND J. G. KAUFMAN

ABSTRACT

Worldwide sources of information for engineering materials are now available from many database services. One unique service for actual mechanical and physical property data is the Materials Property Data (MPD) Network. The result of a cooperative venture between the National Materials Property Data Network, Inc. and The American Chemical Society (ACS), MPD Network is now available on STN International, the online scientific and technical information service, operated jointly by ACS and the Japanese Information Center for Scientific and Technical Data (JICST) and the Fachinformationszentrum (FIZ-K) in Karlsruhe Germany. The MPD Network, which was released on the STN International host system in April 1991, is designed to allow materials scientists and engineers to successfully locate materials property data with little or no prior training. By means of a menu-guided search software and an online materials thesaurus, inexperienced researchers can retrieve property data from a number of networked materials databases produced by experts in the field.

In addition to a description of the textual databases that provide access to the research literature for materials science and engineering information, the breadth and depth of content of the MPD Network numeric property databases are described to illustrate the capabilities of the user interface and the kinds of property data that can be located.

TEXTUAL DATABASES IN MATERIALS SCIENCE AND ENGINEERING

The fields of materials science and engineering have benefited greatly from the information explosion that has occurred over the last two decades. There are literally millions of research papers that have been published during this time, covering all aspects of the science and technology of engineering materials. This vast array of information is, in itself, a problem for the materials community of today. Sorting through the millions of technical papers that have been published to find only those that will advance a specific area of research is now a major, initial step in any major research project.

J. G. Kaufman, W. A. Weida, National Materials Property Data Network, Inc., (MPD Network), 2540 Olentangy River Road, P.O. Box 02224, Columbus, Ohio 43202

The most effective tools for searching through this massive amount of information are the computerized database services that provide centralized access to many databases in one place. The major database services include STN International, the Dialog Information Service, and the Maxwell Online Orbit Search Service, along with other large systems, such as the European Space Agency's IRS service in Italy and Questel in France, all of which serve an international audience.

One of these database services, STN International, is dedicated entirely to scientific and technological information and will be used here to illustrate how computerized databases can be used to access the current research literature for engineering materials.

STN International is a collection of over 120 databases that cover the full spectrum of science and technology, from chemistry and physics through engineering and materials science. In addition to databases covering the entire scope of a discipline such as engineering, many of these files concentrate on highly specific areas such as plastics, crystal structure, or the fracture toughness of aluminum alloys.

STN is also a very successful example of international cooperation—a cooperative effort that embodies a spirit consistent with this sixth Japan-U.S. Conference on Composite Materials. For nearly ten years now, three technical organizations from three continents have shared their resources to provide worldwide access to scientific and technological research. In 1983, the Fachinformationszentrum (FIZ-K) in Karlsruhe, Germany and the Chemical Abstracts Service of the American Chemical Society (ACS) in Columbus Ohio joined forces to initiate the STN International system. They were soon joined in 1986 by the Japan Information Center for Science and Technology (JICST) in Tokyo. Since that time, the number of databases on STN has grown to over 100 and more new files are added each year.

These databases can be accessed from any personal computer or terminal that can be connected by modem to a telephone line; the databases are available twenty-four hours a day during the week and for most of the week-end. From anywhere in the world, a researcher can connect a computer to a phone line and can access the STN databases.

There are many databases on STN International that contain information on composite materials. Following is a partial list of these databases, along with the number of bibliographic citations in each which contain information on composite materials.

| STN Bibliographic Databases Containing Information on Composites | | No. of Records on |
Database		Composite Materials
CERAB	-Ceramic Abstracts	4,500
COMPENDEX	-Engineering Index	22,000
EMA	-Engineered Materials Abstracts	22,000
JICST-E	-Japan Information Center for Science and Technology	18,000
METArEX	-Metals Abstracts	23,000
NTIS	-National Technical Information Service	10,000

Most of the listed databases cover all types of composite materials. The editorial scope of some databases, however, will limit coverage to specific types of materials, e.g., the Ceramic Abstracts file that contains over 4,000 records on ceramic composites or the Metals Abstracts database that covers metal matrix composites research from 1968 to date.

The number of bibliographic records for composites shown here are only a small part of each database. These databases contain over five million records to covering all aspects of materials science and engineering. The important point is that a search through millions of research articles can be accomplished in minutes, focusing on a specific area of research.

These databases are one major type of database that can be searched on STN. The answers retrieved from these databases are bibliographic references to a published research article. Another type, numeric property databases, provides actual property values for a broad range of engineering materials. If the researcher needs an immediate answer, such as an actual tensile or impact strength or some other actual mechanical or physical property for an engineering material, these numeric databases may well provide a fast and efficient method of locating the desired property data.

For these types of property-related research questions, the Materials Property Data Network, also a service of STN International, has been developed.

THE MATERIALS PROPERTY DATA NETWORK

The National Materials Property Data Network, Inc., (MPD Network), began development operations in 1985 in response to increased recognition of the importance of improving computerized access to reliable numeric materials performance data. (1) Initiation of this action was spearheaded on an international scale by several groups including CODATA (2), NIST (3), and the Materials Properties Council (MPC, then called Metals Properties Council) (4).

An agenda for action was initiated following the Fairfield Glade Conference in 1982 (5), sponsored by the above groups, and a study by the National Materials Advisory Board in 1983. (6) Both groups concluded independently that there was a critical need for a broad cooperative approach to easier access to high-quality data. They recommended a cooperative approach including industry, government agencies, and universities. In late 1984, MPC undertook the formation of a new, independent not-for-profit organization to respond to that need, the MPD Network.

The means selected to fulfill the MPD Network mission was a an online network of well-documented databases, each focused in a specific area and managed by experts in that area. The system was intended to be easy to use, even for the occasional, non-professional searcher, and permitted the use of a single, logical search and retrieval language for all databases involved. (7)

As an added service, the MPD Network would help users locate needed data. Rather than compete with other suppliers of materials information, MPD Network would provide users with knowledge about all available sources as part of its online service. This information would include publicizing sources of and, to the extent practical, aiding in the distribution of data of interest to personnel involved in materials research, material selection, design, quality assurance, and failure analysis for all types of applications.

CLOSE COOPERATION WITH INTERNATIONAL STANDARDIZATION ACTIVITIES

In developing the worldwide materials database network, MPD Network today not only works closely and cooperatively with many technical societies, government agencies (notably the Standard Reference Data group at the National Institute for Standards and Technology), and private industry but also many international organizations concerned with standards and issues of quality and reliability. These include:

ASTM Committee E-49 on the Computerization of Material Property Data, which is developing standard formats for recording, storing, and exchanging materials data (8);

CODATA, the international Committee on Scientific and Technical Data, of the International Council of Scientific Unions, through its Task Group on Materials Database Management (9), and the Referral Database Task Group (10);

VAMAS, the Versailles Advanced Materials and Standards group, through its fact-finding studies and developmental workshops (11); and

ICSTI, the International Council for Scientific and Technical Information, in its directory of worldwide databases. (12)

MPD Network is also in regular communication with other major scientific information organizations that are current producers of materials property data.

IMPLEMENTATION OF THE MPD NETWORK

In 1987, MPD Network and the American Chemical Society initiated a joint development program, which has led to the availability of MPD Network services on STN International. The production version of MPD Network became available to sponsors and financial associates on January 7, 1991, and began full commercial operations worldwide on April 4, 1991. The individual files have been loaded over the period from April 1990 to the present and continue to be available to users of STN International who prefer the standard command language rather than the menu-driven MPD Network interface, which is of most value to end-users of the information.

Production software enhancements have been made to the underlying STN MESSENGER software to optimize searchers' ability to handle numeric data. All of the features of the pilot system interface have been retained, while many new capabilities have also been added.

A broad range of numeric information is already available on the MPD Network and much more is scheduled for addition in coming years as described further below. The intended scope of the MPD Network databases includes not only mechanical, physical, and other performance data for all structural materials, including metals, polymers, ceramics, and composites, but also the properties of connections and joints in these materials.

Among the specific databases currently available through the MPD Network are:

AAASD, from the Aluminum Association--typical and minimum tensile properties, typical mechanical and physical properties, and fabricating and application information on more than 150 commercial aluminum alloys;

ALFRAC, from NIST/SRD, Materials Properties Council and the Aluminum Association--plane strain fracture toughness data for about 25 high strength aluminum alloys, with validity documentation;

COPPERDATA, from the Copper Development Association-- properties of all commercial copper-base alloys;

IPS (International Plastic Selector), from D.A.T.A. Business Communications, a Division of IHS--mechanical and physical properties of commercially available plastics;

MIL-HDBK-5 (MH5)--design tables from the MIL-HDBK-5 Coordination Committee publication, covering the design mechanical and physical properties of ferrous and non-ferrous alloys;

MARTUF, from Materials Property Council--about 10,000 individual toughness test results for steels for marine applications;

METALS DATAFILE (MDF), from Materials Information (ASM International and the Institute of Metals)--data from more than 40,000 literature citations from technical journals, handbooks, and other data compilations;

NISTCERAM--properties of silicon carbide and silicon nitride structural ceramics from NIST;

PDLCOM, from the Plastics Design Library--covers the chemical, environmental and radiation effects on commercially available plastics;

PLASPEC, from D&S Data Resources--typical properties from manufacturers on about 12,000 plastics; includes applications and price information;

STEELTUF, from the Electric Power Research Institute and Materials Properties Council--the results of more than 20,000 individual tests of steels for the power and petroleum industries.

Also available are two support textual files on materials:

MPDSEARCH--directory of electronic materials and chemical substance properties databases worldwide

PLASNEWS--daily news updates, with a historical database, on developments, prices, and production information on plastics

Programs are in place to continue adding three or four databases to the MPD Network each year. Among the subject areas in development to address limitations in current coverage are

- J-integral values for high-temperature structural steels

- Creep and stress-rupture properties of metals

- Fatigue properties of metals and alloys

- Optical properties of glasses

- Properties of timber and other wood products

Specific database names will be announced as distribution arrangements are completed.

In December, 1991, the Chemical Property Data (CPD) Network, composed of a new menu-driven, thesaurus-supported network of six numeric property databases for organic and inorganic chemical substances, also became available on STN International.

THE KEY FEATURES OF AN INTEGRATED ONLINE SYSTEM FOR NUMERIC PROPERTY DATA

Among the many features being included in the MPD Network to address previous limitations of online search and retrieval systems are a) software

features for searching numeric data, b) an easy-to-use interface for the new
or occasional searcher, c) search options, and d) distributed geographic
sources. Each of these will also be examined in the context of the MPD
Network.

NUMERIC SOFTWARE FEATURES

Among the special features required in dealing with numeric databases are
the following, all provided for within the MPD Network on STN International:

- Range searching—the ability to search for materials
  with combinations of properties in specific ranges
  or above or below certain limiting values;

- Units conversion—the ability to convert to any of
  the worldwide standard systems of units:
  International Standard, (SI), meter-kilogram-second
  (MKS), centimeter-gram-second, (CGS), engineering, (ENG),
  and the STN user-friendly SI system;

- Tolerance setting—the ability to define ranges of
  search values by the tolerance on the search value
  (e.g., 50,000 +/- 1000 psi);

- Table display—the ability to obtain tabular display
  of data that match your specific query and
  pre-define certain types of tabular displays;

- Calculation packages—the capability for interpolation
  and estimation of additional information or the
  application of parametric analysis of multi-variant
  properties is valuable in providing specific answers
  to some complex materials questions.

A number of other capabilities are also present that enhance numeric
searching; others, such as multi-level sorting, are still in development.

USER INTERFACE

Users of the MPD Network will include not only information specialists
trained in the use of online command-driven systems but also a broad new
audience of engineers and scientists who are the so-called end-user audience.
In the case of numeric or factual data, searches are often so specific that
relying upon intermediate searchers, however knowledgeable, may require many
iterations and still be largely unsatisfactory. It is often more efficient
for the user of the information to perform the search.

This end-user audience includes staff in small engineering design
companies, individual consultants as well as employees in larger
organizations. Such users are busy with many other activities and so will be
occasional users in contrast to the information specialists, who can search
online every day. These end-users will not have the time to read ponderous
manuals, learn complex command languages, and deal with cryptic response
messages, all of which require a re-learning process each time the system is
used. Thus a logical, easy-to-use interface is a critical element of
providing data for this large new audience.

The MPD Network deals with this situation by providing:

a. Logical, easy-to-use, menu-driven search paths;

b. A variety of search paths, recognizing that different
    types of users and different applications will require
    different queries;

c. A "metadata" system in the form of an interactive
    thesaurus that both deals with user queries, translating
    them to all other acceptable nomenclature and
    terminology, and responds quickly to clarify the meaning
    of names, terms, and abbreviations; and

d. A directory of data sources, including those outside the
    MPD Network.

SEARCH OPTIONS

     Depending upon the nature of a query, users may approach the MPD Network
with different pieces of information at the heart of their query:

a. A specific database with a certain type of data, e.g.,
    design values,

b. A specific material for which a variety of types of data
    are sought, or

c. A specific property or properties for which a comparison
    of materials is required perhaps in regard to a
    specific range of values, notably those equaling or
    exceeding certain limiting values.

     In addition, because an experienced user will not need the depth of
guidance offered by menu-driven screens that is required by a first-time or
relatively inexperienced user, an "expert" mode of searching is provided.
This option circumvents the many menus and permit the searcher to go directly
to the information of interest.
     Finally, the experienced professional searcher knowledgeable in STN
International command language has the option of searching in the familiar STN
command mode.

DISTRIBUTED SOURCES

     A key element of a true network of interactive data bases is the ability
to provide access to various geographic locations without interfering with the
efficiency and ease of the search. Ideally, such a network would have nodes
in many locations and be able to deal with a variety of database management
systems and languages. Realistically, those requirements impose a level of
complexity for which we are not yet prepared.
     The MPD Network approach takes full advantage of the three nodes or
service centers on STN International and is working toward linking European
and Japanese-based databases on materials with those in the USA. Thus,

materials databases loaded by JICST in Tokyo and FIZ-K in Karlsruhe will be available to users under the MPD Network "umbrella" and with all of the MPD Network interface capabilities in a manner transparent to users. To accomplish this network, all such databases will be loaded in STN files accessible via MESSENGER software. Databases not loaded at one of the STN service centers will not be accessible directly via the MPD Network, though information on their availability will be provided in a separate online directory file called MPDSEARCH.

SUMMARY

Database services available today allow materials scientists and engineers to focus easily on their area of specialization. In addition to searching databases containing references to published research, other types of databases containing actual numeric property data can now also be searched to obtain immediate access to actual physical and mechanical property values for engineering materials.

The MPD Network is a unique not-for-profit service for the material science and engineering communities that provides easy, single-point access to worldwide sources of materials data. Provision has been made to assure that the MPD Network handles the variety of types of users and queries and minimizes the confusion of multiple names, terms, and abbreviations.

The MPD Network began production operations on STN International on January 7, 1991. Eleven different materials databases covering the properties of steel, aluminum, titanium, magnesium alloys, structural ceramics, and a wide range of plastics are part of the current system. New databases on metals, plastics, optical materials, and polymer-matrix composites will be added shortly. Searchers of MPD Network also have the advantage of easy access to about 100 other information sources on STN International, including a number of textual databases on engineering and materials, along with the the Chemical Property Data Network cluster of numeric databases for chemicals.

REFERENCES

1. Kaufman, J. G., "The National Materials Property Data Network: A Cooperative National Approach to Reliable Performance Data," Proceedings of the First International Symposium on Computerization and Networking of Materials Data Bases, J. S. Glazman and J. R. Rumble, Editors, ASTM STP 1017, Philadelphia, April, 1989, pp 7-22.

2. Materials Data for Engineering, Proceedings of a CODATA Workshop, Schluchsee, FRG, J. H. Westbrook et al., Editors, FIZ-Karlsruhe, September, 1985.

3. Ambler, E., "Engineering Property Data-A National Priority," Standardization News, pp 46-50, ASTM, Philadelphia, August, 1985.

4. "An Online Materials Property Database," Presented at the Winter Annual Meeting of ASME, MPC-20, J. A. Graham, Editor, ASME, New York, 1983.

5. Computerized Materials Data Systems, Proceedings of the Fairfield Glade Conference, J. H. Westbrook and J. R. Rumble, Editors, National Bureau of Standards, Gaithersburg, MD, 1983.

6. <u>Materials Data Management - Approaches to a Critical National Need,</u> National Materials Advisory Board (NMAB) Report No. 405, September, National Research Council, National Academy Press, Washington, September, 1983.

7. Kaufman, J. G., "Increasing Data System Responsiveness to User Expectations," <u>Computerizations and Networking of Materials Databases,</u> Volume 2, J. G. Kaufman and J. S. Glazman, Editors, ASTM STP 1106, ASTM, Philadelphia, May, 1991, pp 103-113.

8. Rumble, J. R., "Standards for Materials Databases: ASTM Committee E49," <u>Computerizations and Networking of Materials Databases,</u> Volume 2, J. G. Kaufman and J. S. Glazman, Editors, ASTM STP 1106, ASTM, Philadelphia, May, 1991, pp 73-83.

9. CODATA Bulletin No. 69, <u>Guidelines For Materials Database Management,</u> November, 1988, Hemisphere Press.

10. "CODATA Referral Database," available in diskette only; CODATA, 51 Boulevard de Montmorency, 75016 Paris, France.

11. "Factual Materials Databanks - The Need for Standards," Report of VAMAS Technical Working Area 10, Editors: H. Kroeckel, K. Reynard, and J. Rumble, June, 1987.

12. "Numeric Databases - A Directory," ICSTI, May, 1991, ISBN 929027 011X, 51 Boulevard de Montmorency, 75016 Paris, France.

SESSION 10B

Strength Analysis II

Tension-Softening Relation and Fracture Energy of Short-Fiber Reinforced Composites

HIROSHI SUZUKI† AND HIDEKI SEKINE†

ABSTRACT

By use of a probabilistic model, the tension-softening relation for short-fiber-re-inforced composites is determined. The cohesive stress on the fictitious crack surface is evaluated from the loads acting on the bridging fibers, and the crack opening displacement is estimated from the elongation of the bridging fibers in debonded region. The area enclosed with the tension-softening curve, and the horizontal and vertical axes gives the fracture energy of the composites. In this paper, the influences of fiber orientation, fiber geometry and fiber-matrix interfacial conditions on the fracture energy are examined in detail. The results are presented on charts showing the influences of these parameters on the fracture energy. The influences of these parameters on the pull-out length are also considered.

INTRODUCTION

Many models to predict the fracture energy of fiber-reinforced composites have been proposed [1-5]. In most of the models, the fracture energy of the composites is expressed as the sum of the energy consumed by the individual micromehanisms of toughening, i.e., interfacial debonding, post-debonding friction, fiber pull-out, etc. On the basis of this idea, Wells and Beaumont [6,7] have related the fracture energy of unidirectional fiber-reinforced composites to the properties of the continuous fiber, matrix and fiber-matrix interface on a chart. The chart indicates the key variables which control the fracture energy. However, no similar chart for short-fiber-reinforced composites has been reported.

Recently, the authors [8,9] have proposed a probabilistic model to predict the tension-softening relation for short-fiber-reinforced composites. The fracture energy of the composites can be obtained by the area enclosed with the tension-softening curve, and the horizontal and vertical axes. In this paper, the influences of fiber orientation, fiber geometry and fiber-matrix interfacial conditions on the fracture energy are clarified in detail. The results are presented on charts.

---

† Hiroshi Suzuki and Hideki Sekine, Department of Aeronautics and Space Engineering, Tohoku University, Aramaki Aza Aoba, Aoba-ku, Sendai 980, Japan

THEORY

TENSILE STRESS IN FIBERS IN DEBONDING PROCESS AND PULL-OUT PROCESS

In debonding and pull-out processes of fibers, frictional forces act on the debonding interfaces of the fibers. It is well known that the coefficient of friction increases with the relative displacement between the fiber and matrix on contact surfaces for the relative displacement to be small, and it becomes constant for the large relative displacement [10]. On the debonding interfaces in debonding process, the relative displacement is so small, that the coefficient of friction μ is assumed to increase proportionally with the relative displacement η for $\eta < \eta_c$ and to be a constant μ_c for $\eta \geq \eta_c$. Here η_c is a critical relative displacement. The relative displacement is replaced, as the first approximation, by the elongation of the fiber measured from the tip of debonding. Therefore, the coefficient of friction μ at a distance ξ from the tip of debonding is expressed by

$$\mu = \begin{cases} \dfrac{\mu_c}{\eta_c}\eta & (\eta < \eta_c) \\ \mu_c & (\eta \geq \eta_c) \end{cases} \tag{1}$$

where

$$\eta = \int_0^\xi \frac{\sigma_s(\xi')}{E} d\xi' \tag{2}$$

Here, σ_s is the tensile stress in the fiber in the debonding process and E is Young's modulus of the fiber. On the other hand, in the pull-out process the coefficient of friction μ is assumed to be μ_c.

The tensile stresses σ_s and σ_f in the fibers in the debonding process and the pull-out process can be obtained by solving the equilibrium equation of the tensile stresses and frictional forces. Then, the boundary condition is the following: in the debonding process the tensile stress at the position of the tip of debonding is the debond stress σ_d and in the pull-out process no tensile stress acts on the broken location.

TENSION-SOFTENING RELATION

Consider a fiber of length l_f, which is embedded in an infinite isotropic matrix. The strength distribution of the fiber is assumed to be uniform in the longitudinal direction. When the uniform tensile stress is applied to the matrix at infinity parallel to the fiber and a matrix crack extends perpendicular to the load direction across the fibers, the fiber bridging occurs, as shown in Figure 1. Then, the probabilistic expectation of tensile stress in the bridging fiber at the position of the matrix crack σ_h is the sum of the probabilistic expectation of the tensile stress in a surviving fiber σ_{s0} and that in a pull-out fiber σ_{f0}, i.e.,

$$\sigma_h = \sigma_{s0} + \sigma_{f0} \tag{3}$$

When the debonding extends to a certain length l, the probabilistic expectation of tensile stress in a surviving fiber σ_{s0} is the product of the tensile stress in the surviving
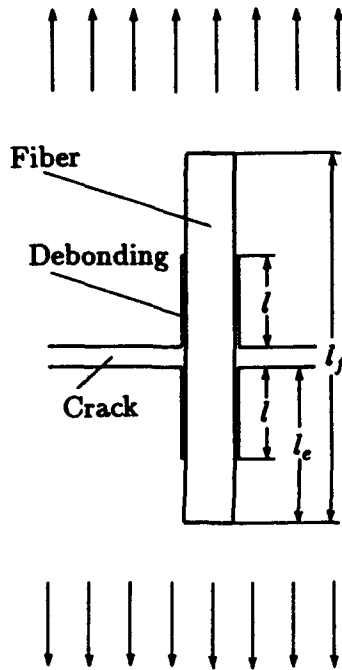
Figure 1. Bridging fiber.
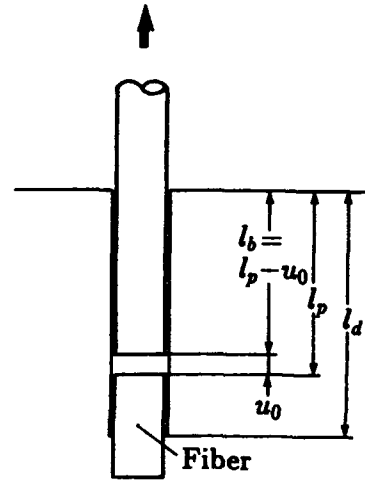
Figure 2. Pull-out fiber.

fiber at the position the matrix crack $\sigma_s(l)$ and the survival probability of the fiber $S(l)$, i.e.,

$$\sigma_{s0} = \sigma_s(l)S(l) \tag{4}$$

If we define the pull-out displacement u_0 by the elongation of the fiber in the debonding region, u_0 is estimated by using the tensile stress $\sigma_s(\xi)$ as follows:

$$u_0 = 2 \int_0^l \frac{\sigma_s(\xi)}{E} d\xi \tag{5}$$

The difference between the pull-out length l_p and the pull-out displacement u_0 of the fiber is named as the embedded length l_b, i.e., $l_b = l_p - u_0$ (Figure 2). The probabilistic expectation of the tensile stress in a pull-out fiber at the position of the matrix crack σ_{f0} given by

$$\sigma_{f0}(l) = \int_0^{l-u_0} \sigma_f(l_b) f_{pd}(l_p, l) dl_b \tag{6}$$

where $f_{pd}(l_p, l)$ is the probability density for the pull-out length l_p in the case of the debonding length l of the surviving fiber.

The survival probability of the fiber $S(l)$ and the probability density $f_{pd}(l_p, l)$ are given on the basis of the Weibull weakest link theory in reference [8].

Let us consider the opening of a matrix crack extending perpendicular to load direction across the fibers. When the crack opening displacement is u_c, the pull-out

displacement of the fiber which makes an angle θ with the load direction, u_0 is approximately given by

$$u_0 = \frac{u_c}{\cos \theta} \tag{7}$$

Since the debonding length l is prescribed by u_c, the probabilistic expectations of the tensile stress in the surviving fiber and in the pull-out fiber can be evaluated for the fiber which makes an angle θ with the load direction. The cohesive stress acting on the crack surface is the sum of the probabilistic expectations of the component of the tensile load on the fibers in the applied load direction per unit area. Therefore, the cohesive stress acting on the crack surface σ_c is expressed as

$$\sigma_c = nA_f \int_{-\frac{\pi}{2}}^{\frac{\pi}{2}} f_\theta(\theta)\sigma_h \cos \theta d\theta \tag{8}$$

where n is the average number of the bridging fibers per unit area of crack surface, A_f the cross sectional area of the fiber and $f_\theta(\theta)$ is the probability density of the number of bridging fibers for the angle θ. Equation (8) provides the relationship between cohesive stress and crack opening displacement, namely tension-softening relation.

When the fibers in a composite are aligned in the applied load direction, n and $f_\theta(\theta)$ can be expressed by

$$n = \frac{v_f}{A_f}, \quad f_\theta = \delta(\theta) \tag{9}$$

where v_f is the fiber volume fraction and δ is the Dirac delta function. If the fibers are distributed at two-dimensional random in the plane, n and $f_\theta(\theta)$ can be described as

$$n = \frac{2v_f}{\pi A_f}, \quad f_\theta = \frac{1}{2}\cos\theta \tag{10}$$

By using σ_c and u_c, fracture energy of the composites W can be given by

$$W = \int_0^\infty \sigma_c du_c \tag{11}$$

Finally, note that the cohesive stress increases linearly with the fiber volume fraction, because the average number of the bridging fibers per unit area n is proportional to the fiber volume fraction.

NUMERICAL RESULTS AND DISCUSSION

TENSION-SOFTENING RELATIONS FOR UNIDIRECTIONAL AND TWO-DIMENSIONAL RANDOM FIBER-REINFORCED COMPOSITES

The tension-softening relations for unidirectional and two-dimensional random fiber-reinforced composites have been determined numerically by using Equation (8). On the numerical calculations, the debond stress σ_d, the coefficient of friction μ_c, the fiber diameter d, the critical relative displacement η_c and the fiber volume fraction v_f have been taken as σ_d=0.44 GPa, μ_c=0.25, d=14 μm, $\eta_c = 3.4\times10^{-2}$ mm and v_f=0.2. The

TABLE I-MECHANICAL PROPERTIES CONSTANTS OF FIBER AND MATRIX

		fiber	matrix
Young's modulus	GPa	72.5	3.3
Poisson's ratio		0.22	0.39
Weibull modulus			
Scale parameter	GPa	0.536	—
Shape parameter		6.4	—
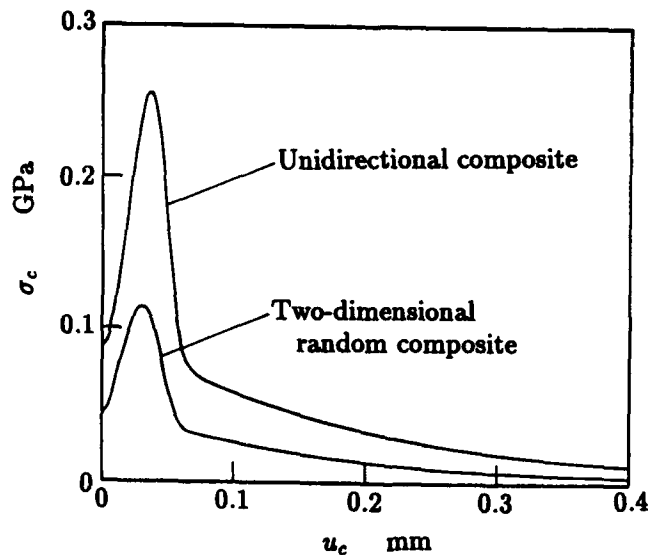
Figure 3. Tension-softening relations for the unidirectional and two-dimensional random fiber-reinforced composites.

mechanical properties of the fiber and the matrix are listed in TABLE I. In this section, continuous fibers are considered. The result is shown in Figure 3. The cohesive stress σ_c increases with the crack opening displacement u_c at the early stage of crack opening. This is attributed to the fact that few fibers break until the debonding region grows to a certain extent. After the cohesive stress becomes the maximum value, the cohesive stress decreases abruptly. When the crack opening displacement becomes 0.07 mm, almost all of the bridging fibers break and only frictional forces in the pull-out process cause the cohesive stress. The ratio of the maximum value of the cohesive stress in the unidirectional fiber-reinforced composite to that in the two-dimensional random fiber-reinforced composite is about 2.22, and manipulation of Equation (11) gives that the fracture energy of the unidirectional fiber-reinforced composite is $3\pi/4$ times as large as that of the two-dimensional random fiber reinforced composite.
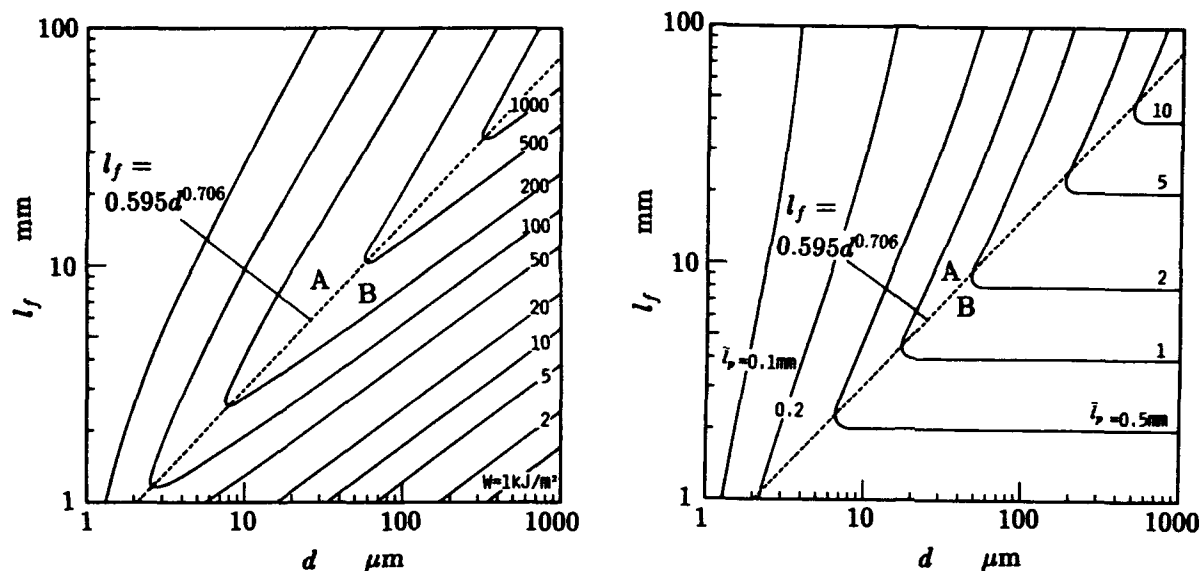
(a) Influences of l_f and d on
the farcture energy W

(b) Influences of l_f and d on the average
value of the pull-out length $\bar{l}_p$

Figure 4. Influences of the fiber geometry on the fracture energy and
pull-out length.

INFLUENCES OF THE FIBER GEOMETRY ON THE FRACTURE ENERGY AND PULL-OUT LENGTH

We examined the influences of the fiber length l_f and diameter d on the fracture energy W and the average value of the pull-out length $\bar{l}_p$ of the unidirectional fiber-reinforced composite. It is well known that the debond stress decreases with the increasing fiber diameter. In this study, the debond stress σ_d is assumed to be inversely proportional to $\sqrt{d}$ [11]. Other values used in the calculations are the same as in the previous section. The results are presented on charts as shown in Figure 4. Let the region above the line of $l_f = 0.595d^{0.706}$ in Figure 4 name as Region A and below the line as Region B.

Since the debond stress and tensile stress in the fibers induced by the frictional forces acting on the debonding interfaces decrease with the increasing fiber diameter, the debonding tends to extend farther with the increasing fiber diameter. In Region A, some fibers break in the debonding region and the number of the broken fibers increases with the increasing fiber length. Therefore, the average value of the pull-out length decreases with the increasing fiber length and then the fracture energy also decreases. In Region B, the debonding easily extends and the tip of the debonding reaches the fiber end before fiber breakage. Then, the fiber is pulled out. Therefore, the average value of the pull-out length $\bar{l}_p$ is nearly quarter of the fiber length l_f. As a consequence, the fracture energy increases with the increasing fiber length.

These charts show that there appears to be high correlation between the fracture energy and the pull-out length. Furthermore, the suitable aspect ratio for getting the expected fracture energy can be obtained on the chart.

(a) $l_f=1$ mm

(b) $l_f=5$ mm

(c) $l_f=20$ mm

(d) Continuous fiber
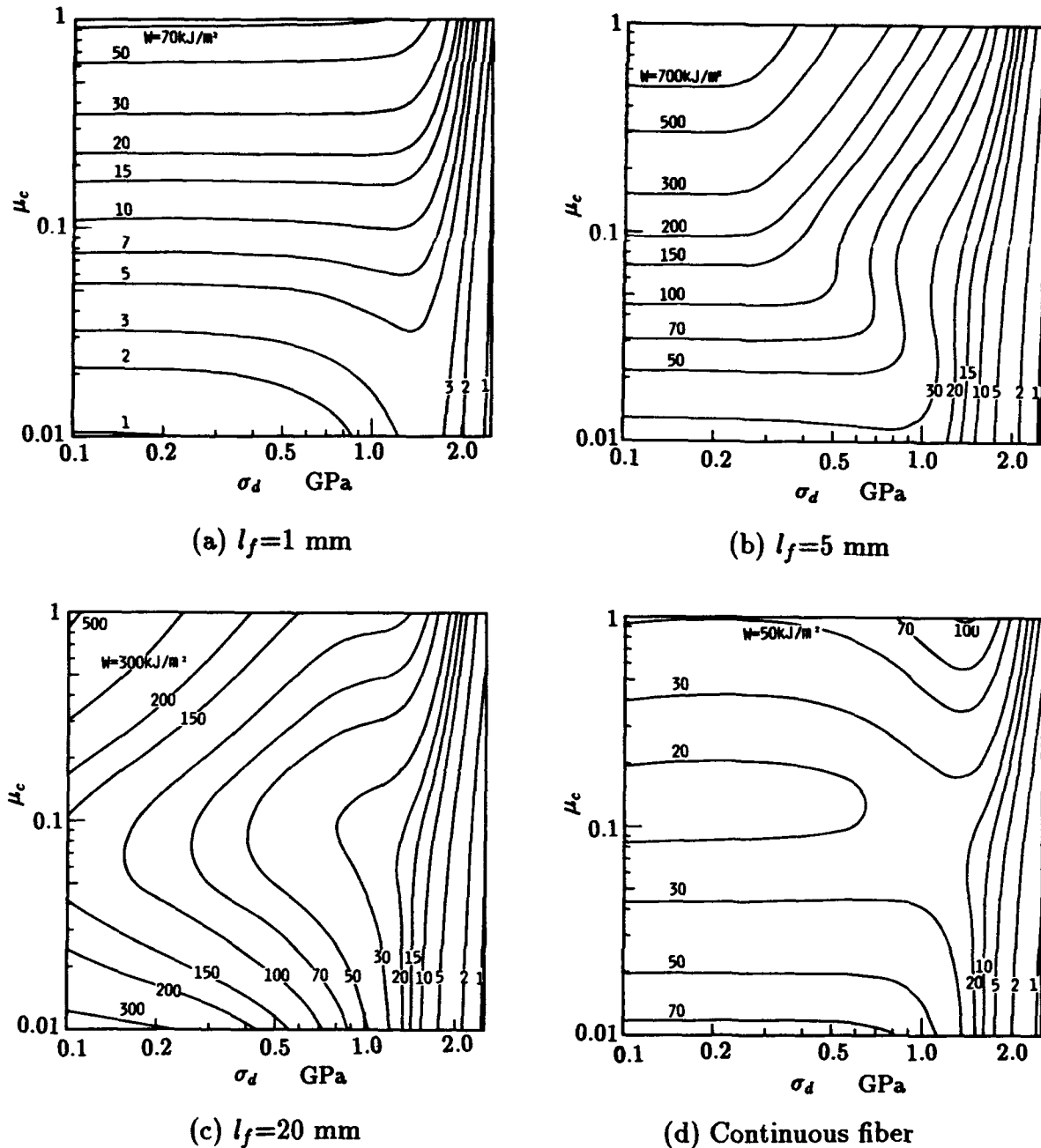
Figure 5. Influences of the debond stress and coefficient of friction on the fracture energy.

INFLUENCES OF FIBER-MATRIX INTERFACIAL CONDITIONS ON THE FRACTURE ENERGY

Finally, we examine the influences of the fiber-matrix interfacial conditions, i.e., the debond stress σ_d and the coefficient of friction μ_c on the fracture energy of the unidirectional fiber-reinforced composite. The results are presented for the fiber length $l_f=1$, 5, 20 mm and ∞(a continuous fiber) in Figure 5.

In Figure 5(a) for l_f=1 mm, when σ_d >1.5 GPa, the fracture energy W increases with the decreasing debond stress σ_d and is less sensitive to the coefficient of friction μ_c. Higher debond stress causes higher tensile stress in the fiber and fiber breakage occurs before the debonding grows to a certain extent. This is the reason that the coefficient of friction less affects the fracture energy. On the other hand, for σ_d ≤1.5 GPa the fracture energy increases with the increasing μ_c and is less sensitive to σ_d. In this case, fiber breakage scarcely occurs. Higher coefficient of friction causes higher tensile stress in the fiber in the pull-out process. Therefore, the energy consumed in the pull-out process is more and then the fracture energy increases.

In Figure 5(b) for l_f=5 mm, the same tendency as Figure 5(a) is observed except for the region of 0.5 GPa< σ_d <1.5 GPa and μ_c >0.05. In this region, the fracture energy increases with the decreasing σ_d and increasing μ_c.

In Figure 5(c) for l_f=20 mm, when σ_d >1.2 GPa, the fracture energy increases with the decreasing σ_d and is less sensitive to μ_c. For σ_d ≤1.2 GPa and μ_c >0.08, the fracture energy increases with the decreasing σ_d and increasing μ_c, whereas, for μ_c ≤0.08, the fracture energy increases with the decreasing σ_d and μ_c.

In Figure 5(d) for $l_f = \infty$, when σ_d ≤1.2 GPa, the fracture energy is less sensitive to σ_d and it increases with the increasing μ_c for μ_c >0.1 and the decreasing μ_c for μ_c ≤0.1.

The charts show that suitable fracture energy may be obtained by controlling the fiber-matrix interfacial conditions.

ACKNOWLEDGEMENT

REFERENCES

1.Aveston, J., G. A. Cooper and A. Kelly,1972."Single and Multiple Fracture," in the Properties of Fiber Composites, National Physical Laboratory, Surrey:IPC Science and Technology Press Ltd., pp. 15-26.

2.Beaumont, P. W. R.,1979,"Fracture Mechanics in Fibrous Composites," in Fracture Mechanics Current Status, Future Prospects, R. A. Smith ed. Oxford:Pergamon Press,pp.211-233.

3.Budiansky, B., J. W. Hutchinson and A. G. Evans,1986."Matrix Fracture in Fiber-Reinforced Ceramics." Journal of Mechanics and Physics of Solids, 34(2):167-189.

4.Lauke, B. and W. Pompe, 1988."Relation between Work of Fracture and Fracture Toughness of Short-Fiber Reinforced Polymers." Composites Science and Technology, 31(1):25-33.

5.Sutcu, M., 1988."Statistical Fiber Failure and Single Crack Behavior in Uniaxially Reinforced Ceramic Composites." Journal of Materials Science, 23(3):928-933.

6.Wells J. K. and P. W. R. Beaumont,1982."Fracture Energy Maps for Fiber Composites." Journal of Materials Science,17(2):397-405.

7.Wells J. K. and P. W. R. Beaumont,1985."Crack-Tip Energy Absorption Processes in Fiber Composites." Journal of Materials Science, 20(8):2735- 2749.

8.Sekine, H. and H. Suzuki,1991,"Prediction of the Tension-Softening Relation for Short-Fiber-Reinforced SMC Composites by a Probabilistic Model." JSME International Journal, Series I, 34(2):228-233.

9.Sekine, H. and H. Suzuki,1991,"Tension-Softening Relation for Short-Fiber-Reinforced Composites," in International Conference on Materials Engineering for Resources, '91 Akita, pp.242-249.

10.Rabinowicz, E., 1965. Friction and Wear of Materials, New York:John Wiley and Sons, Inc.

11.Outwater, J. O. and M. C. Murphy, 1970."Fracture Energy of Unidirectional laminates." Modern Plastics,47(9):160-169.

Fiber Strength Reduction Due to Band Weaving in Filament Wound Composites

KURT GRAMOLL, SRINIVASAN RAMAPRASAD AND FUMIHARU NAMIKI

ABSTRACT

Filament winding of composite structures inherently causes fiber bands to weave or undulate throughout the structure in a non-periodic fashion. This causes the filament wound fiber bands, made from multiple groups of filaments called tows, to fail below the fiber strength for straight fibers. This fiber failure strength reduction is investigated by performing a finite element stress analysis and developing a strength of material type closed form solution for curved fibers. The stress analysis results from both methods are compared to actual test results conducted on a single and double type weave patterns. The predicted failure stress from the analysis match closely with the experimental results. Application of this work to filament wound composite pressure vessels is discussed.

INTRODUCTION

In the filament winding process, multiple bundles of small continuous fibers, called a tow, are grouped together to form a continuous band that is wound on a rotating mandrel. Except for very simple winding patterns, such as hoop winding on a cylinder, the band must cross over other previously wound bands in a non-uniform manner. This band weaving is particularly troublesome problem for pressure vessels, such as rocket motor cases, that have dome closures at each end of the vessel. The length and amplitude of this weaving will vary with the size and shape of the vessel, location on the vessel, and the width and thickness of the band. In addition to the shape of the vessel and the winding pattern, it has been found that the manufacturing process also affects the weaving size. For example, the use of an autoclave will increase the amount and size of weaving due to the high pressures needed to consolidate the fibers during cure. The weaving, or fiber undulation, directly affects the strength of the fiber band which is investigated in this paper.

The strength of fiber reinforced composites is maximized when the fibers are straight and in line with the applied load. If the fibers are kinked, such as an undulating fiber, the load will not be uniformly distributed across the fiber and bending stresses will develop causing failure at a lower stress. Strength reduction due to weaving can be readily seen in the lower failure strength of fabric materials over similar unidirectional composite materials. Previously research has been done by Ishikawa and Chou [1,2] and Zhang and Harding [3]

Kurt Gramoll, Assistant Professor, Aerospace Engineering,
   Georgia Institute of Technology, Atlanta, Georgia, USA 30332-0150
Srinivasan Ramaprasad, Graduate Research Assistant, Aerospace Engineering,
   Georgia Institute of Technology, Atlanta, Georgia, USA 30332-0150
Fumiharu Namiki, Research Engineer, Aerospace Division,
   Nissan Motors Co., Ltd., 3-5-1 Momoi, Suginami, Tokyo, Japan 167

on the strength reduction of fabric materials but their results are generally for material properties reduction and can not be applied directly to filament winding for two reasons. First, unlike a uniform woven fabric, the weaving effects in a filament wound vessel are not constant and a single structure will have various shapes and sizes of undulation. Secondly, fabrics are easily tested for actual ultimate strength with a high degree of reliability because of the uniformity of the material. Again, band undulation will vary in a filament wound vessel making it difficult to reproduce equivalent test specimens. Furthermore, a large number of test specimens would be required due to the large number of possible shapes and sizes of undulation. Bogetti, et al [4,5] at the University of Delaware examined strength reduction in undulating fibers and they concluded that the axial stress in the fiber is significantly reduced but the transverse and interlaminar stresses increase, causing failure.
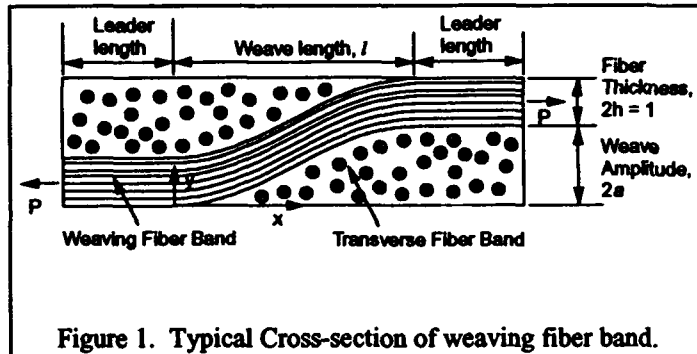
Figure 1. Typical Cross-section of weaving fiber band.

Stress analyses and experimental results done in this study on single fiber weave show that axial stress actually increase due to micro-bending and is the main cause of failure. Transverse and interlaminar stresses are present, but are secondary to the large axial stresses.

This paper will primarily investigate a both single and double fiber weave patterns over a flat surface. The strength loss due to undulation is determined using strength of materials approach and finite elements. The stress and failure load obtained by these methods are then compared to actual test results.

The undulating model for fiber band weaving is assumed to be a basic cosine wave as shown in Fig. 1 and is described by

$$y = a(1 - \cos\frac{\pi x}{l}) \qquad 0 \le x \le l \tag{1}$$

Equation 1 describes only the bottom edge of the fiber band. The top edge is obtained by adding the fiber thickness, $2h$, to Eq. 1. This equation not only allows easy derivation of the strength of materials stress analysis but also accurately represents the actual undulating fiber (see Fig. 11). Previously, a circular arc type of weaving pattern was investigated, but was found inappropriate to model the bending stresses and gave poor results.

SINGLE UNDULATING FIBER BANDS WITHOUT TRANSVERSE FIBERS

As a first step in understanding the reduction in fiber strength of an undulating fiber a simple single fiber band is investigated. This model is the same as shown in Fig. 1. but the transverse fibers and the two leader lengths are deleted. The two end boundary conditions remain vertical during loading as if the fiber band was mounted between two walls and the walls were pulled apart. Eliminating the transverse fibers and leader lengths allows a simple closed form solution for the stress using strength of materials (SOM) principles which is then compared with finite element (FE) results. In the last section of this paper actual test results are presented for the single weave pattern

The strength of material solution assumes that the walls do not rotate and can sustain end moments due to an axial load in the horizontal direction. In actuality, the fiber continues indefinitely, but to allow for a closed form solution a non-rotating boundary condition is specified. The solution method uses Castigliano's principle to calculate the end rotations, θ_A,

in terms of M_1 and R and then θ_A is set to zero to find M_1. The curvature of the beam is also taken into account in the derivation of the bending moment. The bending moment is then used to calculate the bending stress for curved beam structures.

Figure 2. a) Single weave model and b) free body diagram.
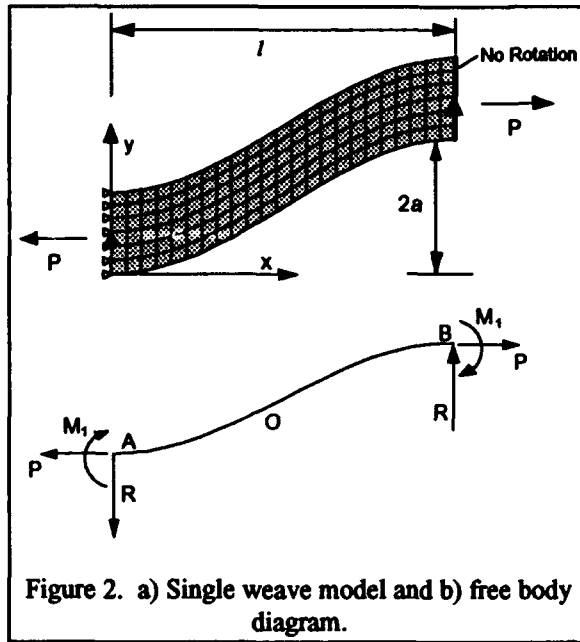
The statically indeterminate curved beam under consideration shown in Fig. 2. shows the fixed end moments applied to the ends A and B of the beam to enforce the condition of zero slope. The strain energy due to bending is given by

$$U_b = \int_0^l \frac{M^2}{2EI}\,ds \tag{2}$$

Referring to Fig. 2b, the moment equilibrium equation about the point A gives

$$R = \frac{2}{l}\{M_1 + Pa\} \tag{3}$$

where M_1 is the moment applied at the ends A and B, and R is the vertical reaction. The bending moment at any section x in the beam obtained from moment equilibrium, is given by

$$M_x = -Rx + Py + M_1 \tag{4}$$

Substituting Eqs. 3 and 4 into Eq. 1 gives

$$M_x = Pa\left\{1 - \cos\frac{\pi x}{l} - \frac{2x}{l}\right\} + M_1\left\{1 - \frac{2x}{l}\right\} \tag{5}$$

Using Castigliano's principle the end rotations are

$$\frac{\partial U_b}{\partial M_1} = \theta_A = \int_0^l \frac{\left[Pa\left\{1 - \cos\frac{\pi x}{l} - \frac{2x}{l}\right\} + M_1\left\{1 - \frac{2x}{l}\right\}\right]\left\{1 - \frac{2x}{l}\right\}}{EI}\,ds \tag{6}$$

To satisfy the boundary conditions, the rotation at each wall will be zero. Also, the curvature of the beam should be taken into account by writing the distance ds as

$$ds = \sqrt{1 + \frac{a^2\pi^2}{l^2}\sin^2\frac{\pi x}{l}}\,dx \cong \left\{1 + \frac{a^2\pi^2}{2l^2}\sin^2\frac{\pi x}{l}\right\}dx \tag{7}$$

giving

$$\theta_A = 0 = \int_0^l \left[Pa\left\{1 - \cos\frac{\pi x}{l} - \frac{2x}{l}\right\} + M_1\left\{1 - \frac{2x}{l}\right\}\right]\left\{1 - \frac{2x}{l}\right\}\left\{1 + \frac{a^2\pi^2}{2l^2}\sin^2\frac{\pi x}{l}\right\}dx \tag{8}$$

Completing the integration and solving for the end moments gives

$$M_1 = Pa \frac{0.1220a^2 + 0.07195l^2}{0.3225a^2 + 0.3333l^2} \tag{9}$$

This can be substituted back into Eq. 5 to give the actual moment at any location along the curved beam. For the case where the amplitude and weave length are $a = 0.5$ and $l = 10.0$, respectively, the bending moment M_x becomes

$$M_x = \left\{1 - \frac{2x}{l}\right\} 0.6081 \, P - \frac{P}{2} \cos \frac{\pi x}{l} \tag{10}$$

which is graphed in Fig. 3.

The actual bending stress in the fiber band can be calculated using curved beam theory. The curvature of the fiber band is taken into consideration by applying the Winkler-Bach curved beam bending theory [6]. The circumferential stresses due to pure bending in a curved flexural member is given by

$$\sigma_b = \frac{M(y - e)}{Ae(r - y)} \tag{11}$$

where

e = Distance between the centroid and the neutral surface
A = Area of the cross section
r = Radius of curvature
2h = Thickness of the curved beam

The e term is defined as
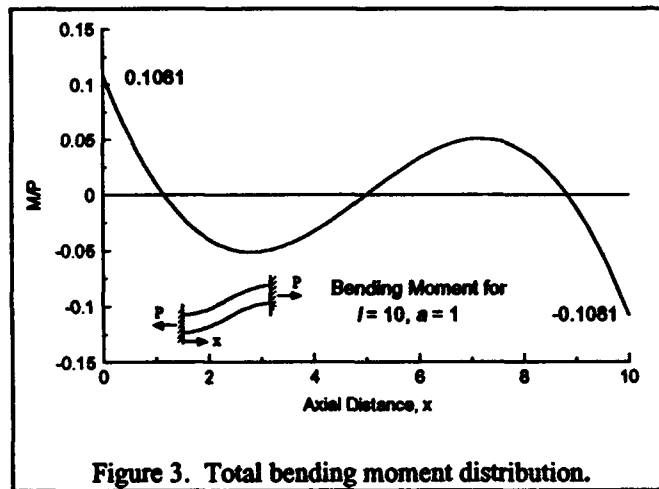
$$e = \frac{rm}{m + 1} \tag{12}$$

Figure 3. Total bending moment distribution.

where

$$m = \frac{1}{A} \int_{-h}^{h} \frac{y}{r - y} dA \tag{13}$$

For an arbitrary curved beam, the radius of curvature changes at every point affecting e, r, and m. For the curve given in Eq. 1 the radius of curvature at any axial distance x can be computed as

$$r_x = \frac{(1 + a^2 \frac{\pi^2}{l^2} \sin^2 \frac{\pi x}{l})^{\frac{3}{2}}}{a \frac{\pi^2}{l^2} \cos \frac{\pi x}{l}} \tag{14}$$
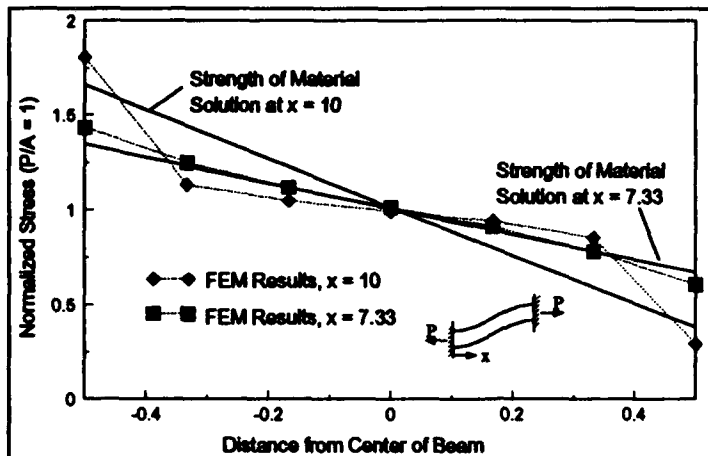
Figure 4. Comparison of FE and SOM results at two locations.

Table 1. Material Properties.

E_x	160 GPa (23.2 MSI)
E_y	9.06 GPa (1.31 MSI)
E_z	9.06 GPa (1.31 MSI)
v_{xy}	0.28
v_{xz}	0.28
v_{zy}	0.318
G_{xy}	11.1 GPa (1.61 MSI)
G_{xz}	11.1 GPa (1.61 MSI)
G_{zy}	6.0 GPa (0.87 MSI)
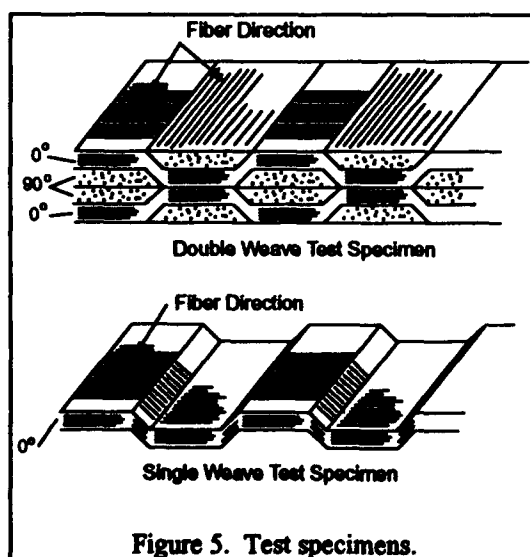
Figure 5. Test specimens.

For a rectangular cross section, Eq. 13 can be simplified to yield

$$m_x = \frac{r_x}{2h} \ln \left\{ \frac{r_x + h}{r_x - h} \right\} - 1 \qquad (15)$$

The total circumferential stress is a combination of axial stress and bending stress as

$$\sigma_t = \frac{P}{A} + \frac{M(y-e)}{Ae(r_x - y)} \qquad (16)$$

Substituting Eq. 10 into 16 gives the axial stress distribution for any point x along the fiber. For the case where $a = 0.5$ and $l = 10$, the bending stress is plotted in Fig. 4.

In addition to the strength of material analysis, a finite element analysis was performed to determine the axial stress. The FE model is shown in Fig. 2a and is based on the single weave test specimen shown in Fig. 5. The material properties used in the model were based on the actual material used in experimental tests. These material properties are shown in Table 1 and were supplied by Nissan Motors Co., Ltd. The model did not include transverse fibers since neither the actual test specimens nor the SOM analysis include them. The FE results matched the SOM results at the local bending maximum near $x = 2.6667$ and $x = 7.3333$ as shown in Fig.4. However at the fixed ends, the FE analysis predicts stresses that are different than the SOM results. This can be primarily attributed to the boundary conditions and that the SOM approach did not account for the thickness in the curved beam which will have the largest error at the fixed boundary. Away from the boundaries, the FE gave good results and confirmed the assumption that the curved beam with non-rotating boundary conditions can be analyzed with finite elements.

STRESS ANALYSIS OF DOUBLE WEAVE FIBER PATTERN

The second model of fiber band weaving is based on the double weave test specimens as shown in Fig. 5. These test specimens consisted of two symmetric undulating fiber bands about

the mid-plane surface. A strength of material solution was not possible for this model, so only a FE analysis was done. The basic model used in the analysis is shown in Fig. 6. The fiber was assumed to make a sinusoidal path, as described by Eq. 1, which closely matches the actual path as determined by inspection of cut specimens. This choice of path also allowed the model to be easily modified by simply changing the weave length, *l*, and weave amplitude, *a*. The mid-surface was restricted to horizontal motion only.
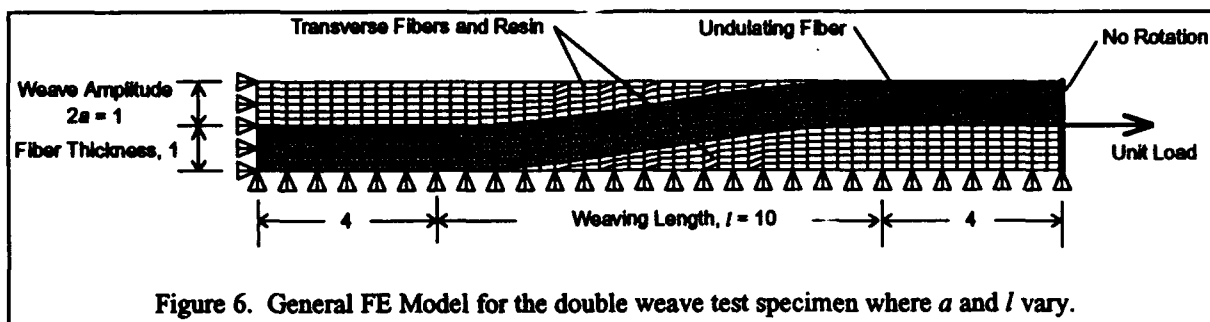
Figure 6. General FE Model for the double weave test specimen where *a* and *l* vary.

The FE model consisted of a single undulating fiber group with the bottom surface fixed in the vertical direction since the actual test specimen is symmetrical about the mid-plane. To simulate the non-periodic nature of the undulating fiber band, a leading and trailing fiber segment were included. Cross fibers, perpendicular to the paper, were also included in the model. The cross fibers were considered to be perpendicular to the fiber band path at all times, i.e. there were no angle rotation in the surface of the laminate. The model was assumed to have infinite depth which required using the plane strain condition. Also, both ends of the FE model were prevented from rotationg or warping to model the continuation of the fibers in both directions.

To understand the effect of fiber weaving, the amplitude, *a* and cycle length, *l* of the fiber band were varied to simulate different weave shapes. One critical aspect of the undulating band is the maximum slope of the fiber with respect to the horizontal which is dependent on *a* and *l*. This slope is obtained by taking the first derivative of Eq. 1, giving

$$\tan\theta = \frac{dy}{dx} \quad \Rightarrow \quad \theta_{max} = \tan^{-1}(a\frac{\pi}{l}) \tag{17}$$

The variation of angles verses weave lengths and amplitudes are given in Table 2 to compare the effect of *a* and *l* on the slope. This slope is the critical factor in determining the fiber axial stress and the failure load. The shaded portions of the table indicate those fiber conditions that most closely match actual conditions in test specimens.

Figures 7-9 show the axial fiber stress (fiber coordinate system) for three different cases. The vertical direction has been expanded and thus the models are not to scale. As the weave length, *l* increases, the bending stress decreases for a specified amplitude. The maximum bending stress is at the inside surface, near the top of the weave path. The stress in the transverse fiber bands are not included in the contour plot.

Table 2. Maximum Rotation Angle of Fiber.					
Amplitude,	Weave Length, *l*				
2*a*	4	6	8	10	12
0.5	11.11°	7.46°	5.61°	4.49°	3.75°
1	21.44°	14.67°	11.11°	8.93°	7.46°
1.5	30.50°	21.44°	16.41°	13.26°	11.11°
2	38.15°	27.64°	21.44°	17.44°	14.67°

EDGE
A = 0.690
B = 0.750
C = 0.810
D = 0.870
E = 0.930
F = 0.991
G = 1.051
H = 1.111
I = 1.171

Min = 0.635

Max = 1.22

Figure 7. Axial stress in fiber, $l = 6$, $a = 0.5$. (vertical direction not to scale)

EDGE
A = 0.799
B = 0.834
C = 0.869
D = 0.905
E = 0.940
F = 0.976
G = 1.011
H = 1.047
I = 1.082

Min = 0.768

Max = 1.106

Figure 8. Axial stress in fiber, $l = 8$, $a = 0.5$. (vertical direction not to scale)

Min = 0.836

EDGE
A = 0.859
B = 0.893
C = 0.927
D = 0.961
E = 0.995
F = 1.028

Max = 1.048

Figure 9. Axial stress in fiber, $l = 10$, $a = 0.5$. (vertical direction not to scale)

VERTICAL DIRECTION COMPARISON OF TEST RESULTS AND FE ANALYSIS

Three different types of experimental tests were performed in order to compare the analytical results to actual failure strength of undulating fiber bands. The first set of tests were baseline tests on non-weaving fiber bands to determine the actual strength of the fibers bands. The second set of tests were performed to determine the strength of single weave fiber bands without any transverse fibers. The last set of tests were done to find the failure strength of the double weave fiber configuration. The last set of specimens had two symmetric layers of undulating fiber bands (Fig. 5).

All three specimen types were fabricated from prepreg graphite/epoxy (Hercules IM7/2020) tow bands of 12,000 filaments. This material was used for both the load and transverse directions. The specimens were hand laid up by placing the fiber bands into special specimen forms. The unidirectional specimens consisted of 4 plys and were made using a hotpress. The overall thickness of these specimens were approximately 0.5 mm. The fiber volume ratio for all specimens ranged from 0.58 to 0.62. The average fiber stress (10 specimens) at failure for the unidirectional (0°) specimens was 4.0 GPa (582 ksi) which was 25% lower than the manufacture reported strength of 5.31 GPa (770 ksi). This strength reduction can be attributed to non-ideal test conditions and specimen fabrication. All specimens were tested according to ASTM D-3039 procedures.

The single weave specimens were constructed using metal filler plates as the transverse fibers. After curing the specimens in an autoclave, these plates were removed. The average thickness of the remaining 0° fiber material was 0.3 mm. The average failure stress for 10 specimens was 1.51 GPa (219 ksi) or 62% of the baseline test. The SOM analysis predicted the maximum stress to be 1.68 times the applied stress or 59% of the unidirectional specimens failure load. The FE results predicted failure at 55% of the baseline load, which is lower than both the SOM and the actual tests. One reason for this lower FE prediction is the boundary conditions at the fixed ends. This boundary condition should be

moved further down the fiber by using a leader length as was done with the double weave stress analysis. However, this would have prevented a strength of material solution derivation. Overall, the results were in good agreement with the analytical results.

Test	Stress in 0° Ply (Avg.) at Failure	Standard Deviation	% of 0° Specimen	SOM Predicted	FEM Predicted
0° Specimen	2.41 GPa (349 ksi)	.17 7 (2 6)	100%	--	--
Single Weave	1.51 GPa (219 ksi)	.13 6 (2 0)	62%	59%	55%
Double Weave	1.95 GPa (277 ksi)	.8 7 (1 3)	81%	--	85%

Table 3.   Test Results and Comparison to Stress Analysis.

The double weave specimens were fabricated using the same prepreg fiber material (IM7/2020) in both directions. The specimens were cured in an autoclave to assure consolidation of fibers in both direction. Again, a total of 10 samples were tested. The failures accured primarily in the center gage section. The average failure occurred at 2.91 GPa (277 ksi) which is 81% of the baseline failure specimens. The FE results ranged from 82% to 95% depending on the amplitude, a, and weave length, l, of the model. To accurately predict the failure strength it is important to know both a and l. These parameters were determined from cutting the failed test specimens and making an edge replica. Figure 11 shows two such edge replicas taken from a photograph. As expected, the amplitude is the same thickness as the fiber thickness, $2a = 1.0$. To determine the weave length, the maximum weave angle was estimated by visually drawing the maximum slope of the fiber in the weave section. These angle are shown in Fig. 11. These angles correspond to weave lengths (see table 2) of between 6 and 10 fiber thicknesses. The maximum angle of 13.0° would require a weave length of 6.80. Interpolating between Figs. 7 and 8 will give a maximum normalized stress of 1.19. This will cause failure at 85% of the baseline strength of the unidirectional specimens. The actual strength (ave-raged over 10 specimens) of the double weave specimens was 1.95 GPa (277 ksi) or 81% of the baseline strength.

Both the single and double weave tests verify that the finite element stress analysis and strength of material analysis correctly predicts the failure of undulating fiber bands in a composite laminate. The key to using this information is knowing the amplitude and weave length. Both these parameters could be estimated from the initial conditions and sample specimens examined during the manufacturing process.
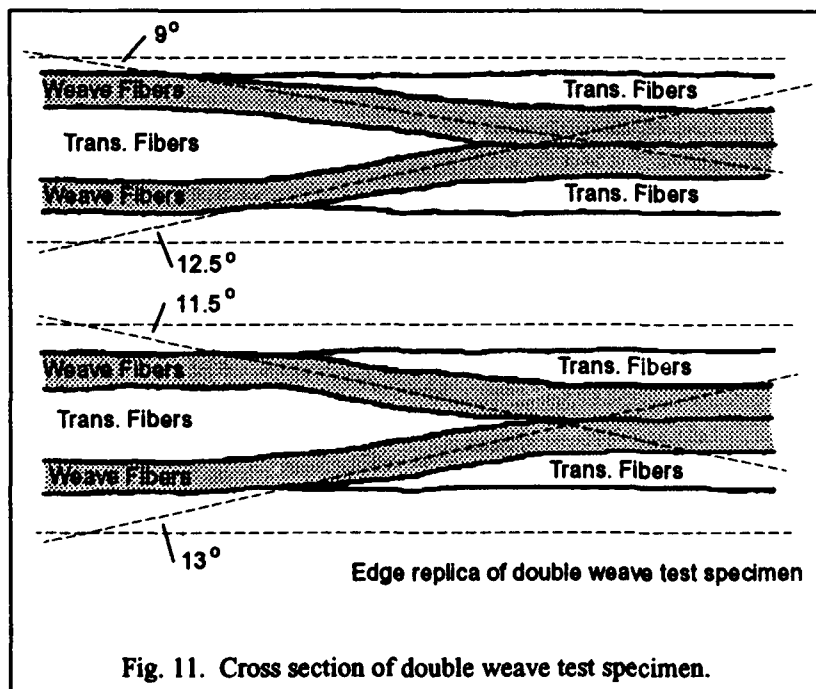
Fig. 11. Cross section of double weave test specimen.

CONCLUSIONS AND SUMMARY

Fiber weaving between plys is a main problem in filament wound structures because of the decrease in ultimate failure strength. The undulating fiber bands generally follow a sinusoidal weave pattern as they progress from layer to layer . This paper examined non-periodic weaving of fiber bands that are made up of several fiber tows commonly used in filament winding. The fibers were assumed to stay in the plane of weave without changing direction.

A stress analysis was performed on two different types of undulating fibers, a single weave fiber without transverse fibers, and a double weave fiber with transverse fibers. The strength of material analysis and finite element analysis of the single weave fiber with an amplitude equal to the fiber band thickness correlated well with one another and with actual test results. Likewise, the finite element analysis of the double weave model matched the experimental test results.

It was found that the amplitude and weave cycle length are both critical parameters in determining the actual fiber strength reduction. The failure is caused primarily by a induced bending moment in the fiber, causing the inside surface to experience a increase of 5 to 40% stress above the average P/A stress load.

ACKNOWLEDGMENTS

REFERENCES

1. Ishikawa, T. and T.W. Chou (1983), *One-Dimensional Micromechanical Analysis of Woven Fabric Composites*, AIAA Vol. 21, No. 12, pp. 1714-1721.

2. Ishikawa, T. and T.W. Chou (1985), *On Stiffness and Strength Behavior of Woven Fabric Composites*, J. Mater. Sci., Vol. 18, pp. 3211-3220.

3. Zhang, Y.C. and J. Harding (1990), *A Numerical Micromechanics Analysis of the Mechanical Properties of a Plain Weave Composite*, Computers & Structures, Vol. 36, No. 5, pp. 839-844.

4. Bogetti, T., J.W. Gillespie, and M. Lamontia (1991), *Influence of Ply Waviness on Stiffness and Strength Reduction of Composite Laminates*, University of Delaware, Center for Composite Materials, Report CCM-91-27, June 1991.

5. Bogetti, T., J.W. Gillespie, and M. Lamontia (1991), *Influence of Ply Waviness on Stiffness and Strength Reduction in Filament Wound Composite Cylinders*, The 45th meeting of the Mechanical Failures Prevention Group, ONR, DTRC, Naval Civil Engineering Lab, and The Vibration Institute.

6. Timoshenko, S.P., Strength of Materials, 3rd Ed., Von Nastrand, 1962.

Poster Papers

Stress Wave Propagation through the Thickness of Graphite/Epoxy Laminated Plates Using PVDF Sensors

DAVID HUI AND PIYUSH K. DUTTA

ABSTRACT

The object of this study was to determine the stress wave (or pulse) propagation through the thickness of a graphite-epoxy laminated plate. This was part of an overall study to understand the damage of these plates under normal projectile impact. Upon a sharp impact by a tiny spherical steel ball, the stress wave propagated from the impact point into the rest of the material. It was found that the embedded polyvinylidene fluoride (PVDF) sensors enabled prediction of the wave velocities and wave attenuation.

INTRODUCTION

The impact behavior of laminated plates is an important topic because composite plates are known to respond to impact loading and energy dissipation in a very different way than metallic plates. In fact, impact resistance is one of the most serious weaknesses of composite material plates. Excellent recent survey articles on this topic was reported by [1] and [2]. The impact of metallic plates by spherical balls was reported by [3], [4] and more recently by [5].

The concept of embedded strain gages was employed by [6, 7] to study the deformation and damage of composite laminates under impact loading. The characteristic features of the strain records are associated with specific failure modes of the laminates. The load history, imparted energy and transient strains at various locations through the thickness were obtained. Wave propagation in transversely impacted composite laminates was obtained by [8] and [9].

The objective of this work is to examine the wave velocities and wave attenuation in the thickness direction using the PVDF sensors that are embedded in the interior of the laminate. Upon a sharp impact, the stress wave propagates from the impact point into the rest of the material. Immediately below the impact point over a small area, the stress wave can be assumed to propagate with a plane front in the thickness direction. A plane pressure sensor of relatively small dimension

Dr. David Hui, University of New Orleans, Dept. of Mechanical Engineering, New Orleans, LA 70148

Dr. Piyush K. Dutta, U.S. Army Cold Regions Research, and Engineering Laboratory, 72 Lyme Road, Hanover, NH 03755

will respond to this propagating stress wave front. A series of such sensors embedded in various depths in the interfaces of the laminate will respond to this incoming stress pulse in the sequence at which the sensors meet the pulse. A measurement of the time difference between the start of successive pulses, divided by the distance between the sensors, would give the velocity of the stress wave between sensors.

The present impact problem is concerned with an extremely short duration pulse so that the wavelength is short relative to the thickness of the individual lamina. Such short-wave length pulse is especially needed in laminates that contain relatively few layers, because one needs to examine the reflection, transmission and superposition of wave through a laminated plate.

The present work is concerned with the impact of tiny spheres on laminated plates. Such impact does not cause damage of the composite plates. The validity of the techniques of using embedded sensors is demonstrated. Further, knowing the velocity of the stress wave will enable one to measure the Young's modulus in the thickness direction, which is known to be hard to measure. The drop test enables one to determine the compressive stresses of a particular lamina as the wave propagates toward the free back surface and the superposition of the tensile stresses as the wave is reflected from free back surface.

The use of piezoelectric polymer as a material that transforms an electric field to a small mechanical deformation directly through a readjustment of internal polarization is well known [10]. The polyvinylidene fluoride (PVDF) piezoelectric sensors are embedded in the interior of the laminated plate. The purpose of these sensors is to enable one to "look" inside the composite specimens and to determine the sequence and propagation of the stress waves. Of particular concern is the duration of the stress wave as it crosses a lamina due to impact and the reflection of waves from the back free surface. It appears that the data collection instruments (CREATEC and NICOLET) were sensitive enough to measure the stress pulse through the charge in the PVDF and hence the force applied to the sensor within the laminate.

The wavelength of the pulse is assumed to be short relative to the lamina thickness but long relative to the diameter of the individual fiber. Thus, the material is governed by the effective properties of the equivalent homogeneous material. The "interface" effects are neglected and the analysis is thus identical to that of the homogeneous material.

The laminated plate consists of four sets of layers (each set consists of seven layers). The plate dimensions are 4 in. by 4 in. The plate is clamped in a fixture so as to become a circular plate with a diameter of 3 in. The fixture was used in previous experiments involving Hopkinson bar tests [11].

WAVE SPEED AND ATTENUATION

As a first approximation, the "interface" effects are neglected and the composite plates can be modeled as transversely isotropic materials. The wave speed in the thickness direction [9] is

$$v = \left[\left(c_{13t}^2 + c_{23t}^2 \right) / 2 \right]^{1/2} \tag{1}$$

where $c_{13t} = \left(G_{13/\rho} \right)^{1/2} \approx \left(G_{12/\rho} \right)^{1/2}$ \hfill (2)

and $c_{23t} = \left(G_{23/\rho}\right)^{1/2} \approx \left(\dfrac{E_{22}}{2\rho(1 + v_{23})}\right)^{1/2}$ (3)

In the above, E_{22} is Young's modulus in the direction perpendicular to the fiber, G_{12}, G_{13} and G_{23} are the shear moduli, v_{23} is Poisson's ratio and ρ is the density of the material. Further subscripts, 1, 2, 3, refer to the fiber direction, in-plane perpendicular to the fiber and out-of-plane perpendicular to the fiber, respectively. Note that the above velocities are independent of the frequency so that for plane waves, a pulse shape composed of a spectrum of frequencies can propagate without distortion of its shape. The laminae are manufactured with a 28-layer stacking sequence $(0_7, 45_7, 90_7, 0_7)$.

The experimental wave speed was measured by any two of the three embedded sensors. The wave speed, measured by the two sensors that are seven plies apart and with the pulse duration of 0.5 ms (that is, 500 ns) can be found from

> v = lamina thickness/propagation time
>   = $(0.041/12)/(500\times10^{-9})$
>   = 6833 ft/sec

For an eight-layer stacking sequence of $(0_2/\pm45)_s$ graphite epoxy specimens, the wave speed in the thickness direction was calculated by [9] to be 6525 ft/sec. This value agrees well with the present experimental result. The wave propagation is accompanied by attenuation of its amplitude for three major effects: (1) geometric attenuation, (2) interfacial friction between fibers and matrix and (3) the interlaminar friction between adjacent plies. Geometric attenuation is due to the spreading out of the wave in a spherical direction starting from the point of impact. Normally, the geometric attenuation is predominant over the remaining effects. However, since the distance of wave propagation in the thickness direction is so small compared to the planar direction, it is not necessarily the dominant factor.

The dispersion effects are expected to be small because all layers (with different stacking orientation) are identical in the thickness direction. Careful calibration of the PVDF sensor is needed. Since the forces on the PVDF sensors are proportional to the charge, proportional constants are determined that are a function of the applied force.

The analysis is confined to the transient stage since one wishes to determine the process of damage in the first crucial nanoseconds. The subsequent vibration problem in the transition from a transient to steady-state stage may also be important. Since one is interested in the initial process of damage, particular emphasis is placed on the wave velocities and attenuation in the transient stage. The subsequent steady-state vibration problem is also of interest as it gives the complete damping process involving wave attenuation; this will be investigated in the future.

EXPERIMENTAL WORK

The experimental setup for the drop test is shown in Figure 1. The sample square plate is clamped in a fixture to produce a circular plate with diameter being 3 in. A schematic diagram for the impactor and the clamped circular plate is shown in Figure 2.

The PVDF sensors of 28 μm (1 μm = 10^{-6} m) thickness are embedded at every seven-ply interval where adjacent plies change the orientation. Two thin lead wires of diameter 41 standard gauge are soldered onto each PVDF sensor and extended out to the edge of the plate and are
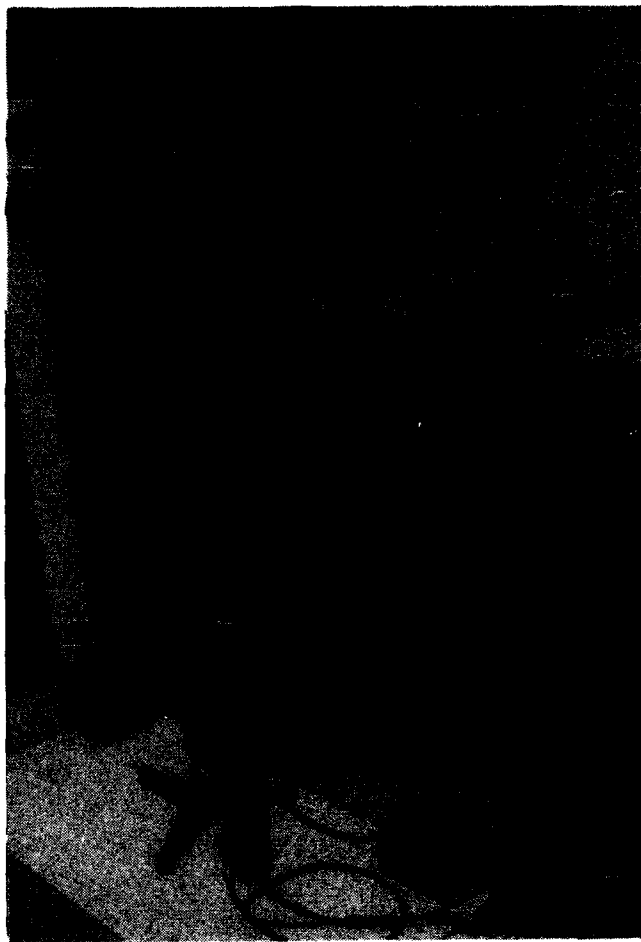
Figure 1. Experimental setup for drop ball stress
waves measurement.
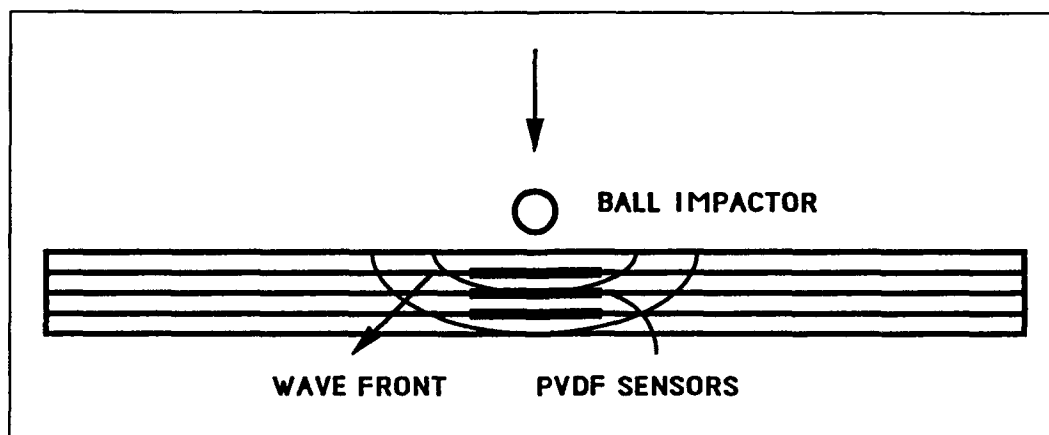
Figure 2. Schematic diagram of the embedded sensors and the clamped circular
plates and typical stress versus time as sensed by each of the embedded sensors.
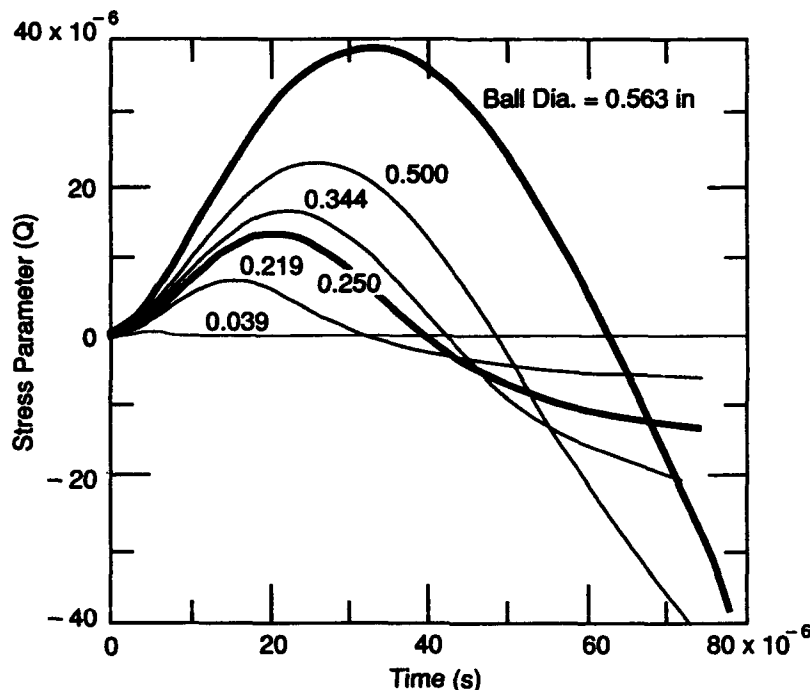
Figure 3. Stress parameter vs. time for different ball diameters.

connected to the digital oscilloscope. The velocity measurements are made by monitoring the pressure sensed by two consecutive sensors with a high resolution digital oscilloscope capable of sampling at 50-ns intervals. Attenuation and energy of the stress pulses are monitored with a four-channel oscilloscope having a sampling rate of 500 ns.

The stress waves are generated by dropping spherical steel balls of six different sizes (0.038-in., 0.219-in., 0.250-in., 0.344-in., 0.500-in., and 0.563-in. diameters). The resulting stress vs. time curves for each of these balls are presented in Figure 3. The wave forms are recorded on the high speed digital oscilloscope. The repeatability of the wave forms from the PVDF sensors from eight consecutive drop ball impacts is demonstrated in Figure 4.

RESULTS

Figure 5 shows the front part of the plot of two waves generated by the drop of a 0.038-in.-diam. steel ball. The time difference between the start of the two stress waves shown in Figure 5 is the time that the wave has taken to propagate from the first sensor to the next sensor through a thickness of seven plies (0.041 in.). The velocity is computed by dividing this distance by the time interval.

Figure 6 shows the amplitude decay of the stress wave as it propagates through the three consecutive sensors located at seven-ply intervals. It can be seen that as the wave propagates, the peak amplitude decays. These tests are repeated with six different sizes of steel balls. For each ball, five measurements of the wave form decay are made. This figure depicts the wave form recorded from the drop of a single size ball (0.039 in.). One vertical division represents 0.292×10^{-3} psi and a horizontal division represents 1.953 μs.
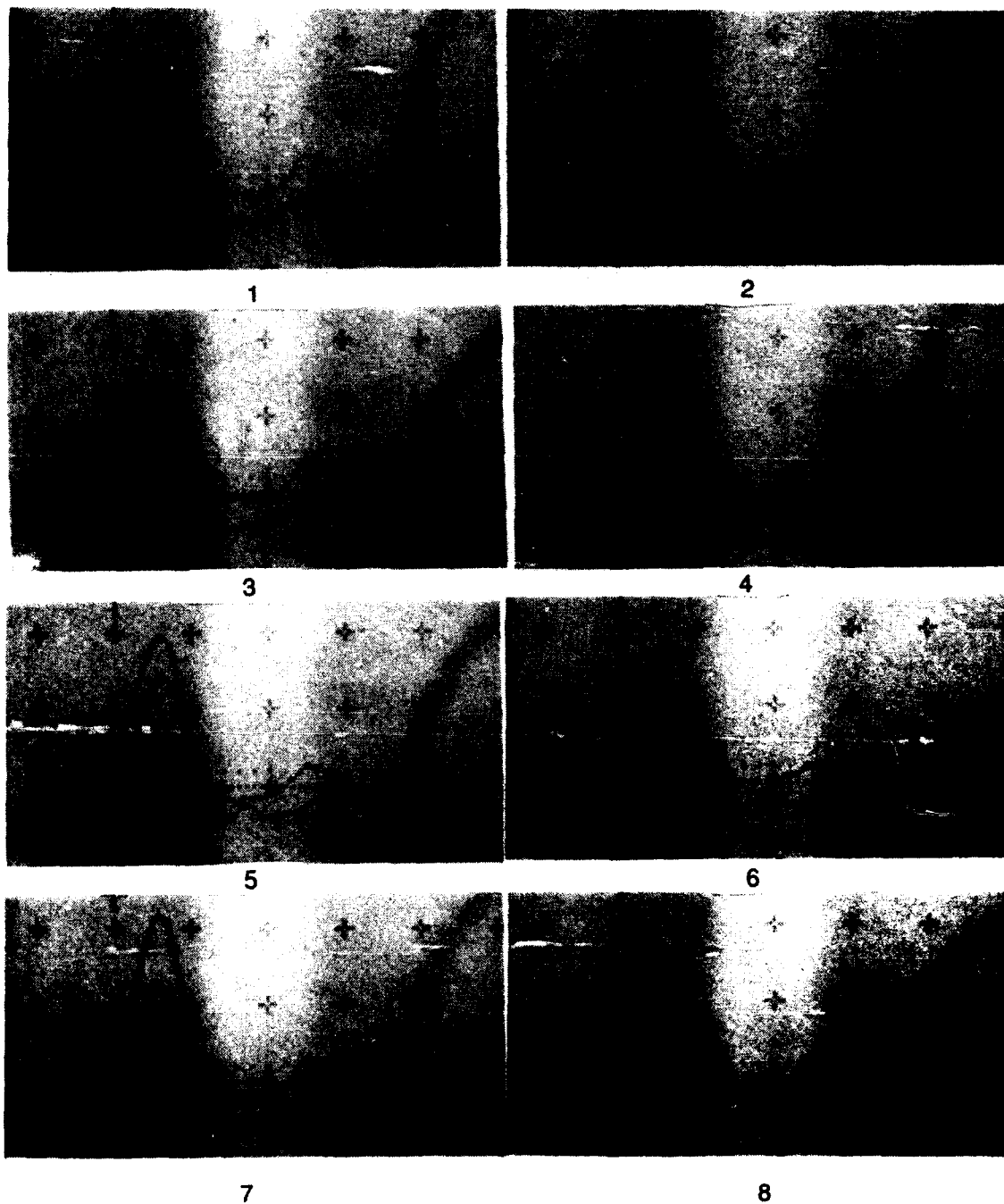
Figure 4. Wave forms from the PVDF sensors show repeatability of the test in eight consecutive drop ball impacts.
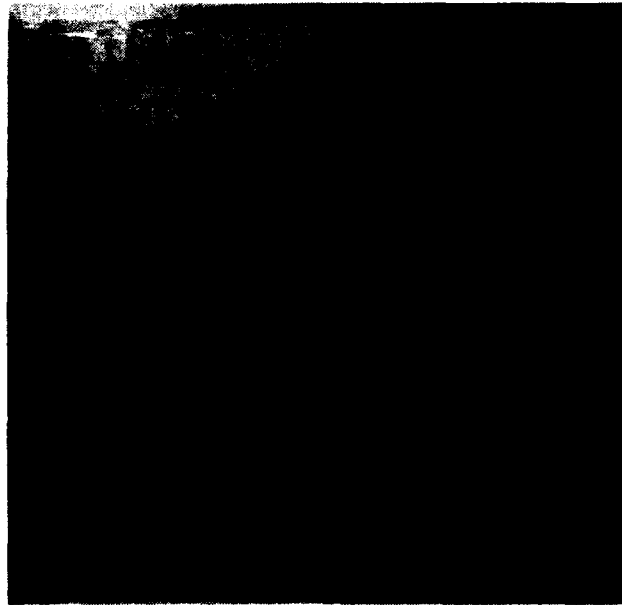
Figure 5. An enlarged photograph from the oscilloscope showing the delay in the starting times from the two sensors.
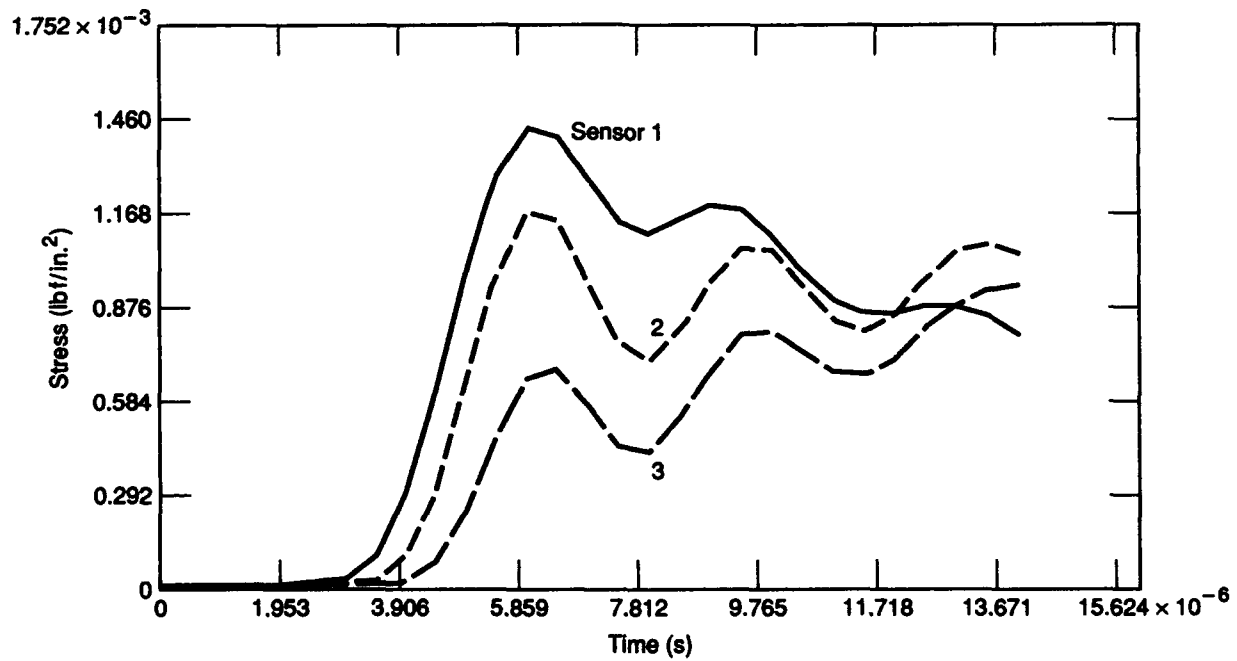
Figure 6. Amplitude decay of the stress wave as it propagates through the three consecutive sensors located at seven ply intervals.

CONCLUSIONS

The embedded PVDF sensors were found to be effective for studying the wave propagation in the thickness direction of the laminated plates. The interference from reflected waves can be minimized or even eliminated by reducing the size of the impactor balls. The method provides a way to determine Young's modulus in the thickness direction from the measured wave speed. This method also allows an estimation of the wave attenuation in the thickness direction.

ACKNOWLEDGMENTS

REFERENCES

1. Abrate, S. 1991. "Impact on Laminated Composite Materials," ASME Applied Mechanics Review, Volume 44, No. 4, April, pp. 155-190.

2. Cantwell, W.J. and J. Morton. 1991. "The Impact Resistance of Composite Materials - A Review," Composites, Vol. 22, No. 5, September, pp. 347-362.

3. Goldsmith, W. 1960. "Impact: The Theory and Physical Behavior of Colliding Solids," Edward Renold, London.

4. Goldsmith, W. and P.T. Lyman. 1960. "The Penetration of Hard-Steel Spheres into Plane Metal Surfaces," ASME J. of Applied Mechanics, December, pp. 717-725.

5. Sondergaard, R., K. Chaney, and C.E. Brennan. 1990. "Measurements of Solid Spheres Bouncing Off Flat Plates," ASME J. of Applied Mechanics, Vol. 57, September, pp. 694-699.

6. Daniel, I.M. and S.C.Wooh. 1985. "Embedded Gages for Study of Transient Deformation and Dynamic Fracture in Composites," Proc. of Fall Meeting of SEM, Grenelefe, FL, November, pp. 62-68.

7. Daniel, I.M. and S.C.Wooh. 1990. "Deformation and Damage of Composite Laminates under Impact Loading," Impact Response and Elastodynamics of Composites, edited by A.K. Mal and Y.D.S. Rajapakse, AMD-Volume 116, Winter Annual Meeting, Nov. 25-30, pp. 11-26.

8. Kim, B.S. and, F.C. Moon. 1979. "Impact Induced Stress Waves in an Anisotropic Plate," AIAA Journal, Vol. 17, pp. 1126-1133.

9. Daniel, I.M., T. Liber and R.H. LeBedz. 1979. "Wave Propagation in Transversely Impacted Composite Laminates," Experimental Mechanics, Vol. 19, No. 1, pp. 9-16.

10. Cundari, M. and B. Abedian. 1991. "The Dynamic Behavior of a Polyvinylidene Fluoride Piezoelectric Motional Device," Smart Structures and Materials, G.K. Haritos and A.V. Srinivasan, ed. ASME Ad-volume 24, AMD-Volume 123, Winter Annual Meeting, Atlanta, Dec 1-6, 1991, pp. 25–31.

11. Altamirano, M. 1991. "Experimental Investigation of High and Low Impact Energy Absorption of AS4/3502 Graphite/Epoxy Panels." MS thesis, University of New Orleans, May.

APPENDIX A1. THE PVDF SENSORS

The PVDF sensor being used has the following properties:

Thickness   = 28×10^{-6} m = 1.102×10^{-3} in.)
Lead wires = 41 swg
Readout   = digital oscilloscope
Speed   = 50×10^{-9} sec/div

Number of channels = 2 (for velocity study)
                      = 4 (for attenuation study)

Lamina thickness (seven plies) = 1.04×10^{-3} m = 0.041 in.
Sensor to lamina thickness   = 1/37.2

A schematic diagram of the PVDF film is shown in Figure A1. The PVDF sensor measurement principle is shown in Figure A2. The applied stress σ can be found from

$$\sigma = Q/(Ad)$$

where Q is the charge, A is the sensor area and d is the charge sensitivity. Further,

$$d\sigma/dt = (1/(Ad)) \, dQ/dt$$

and the current I can be found from

$$dQ/dt = I = V/R$$

where V is voltage and R is resistance. Finally,

$$d\sigma/dt = V/(RAd).$$

Integrating, one obtains,

$$\sigma(t) = \left(1/(RAd)\right) \int_{0}^{t} v \, dt.$$

For application purposes,

$R = 10^6$ ohms

$d = 33 \times 10^{-12}$ (C/m^2)/(N/m^2)

$A = 1.88 \times 10^{-4}$ m^2

Thus, one obtains

$$\sigma(t) = 6.119 \times 10^8 \left(1/(RAd)\right) \int_0^t v \, dt \text{ (Pa)}$$
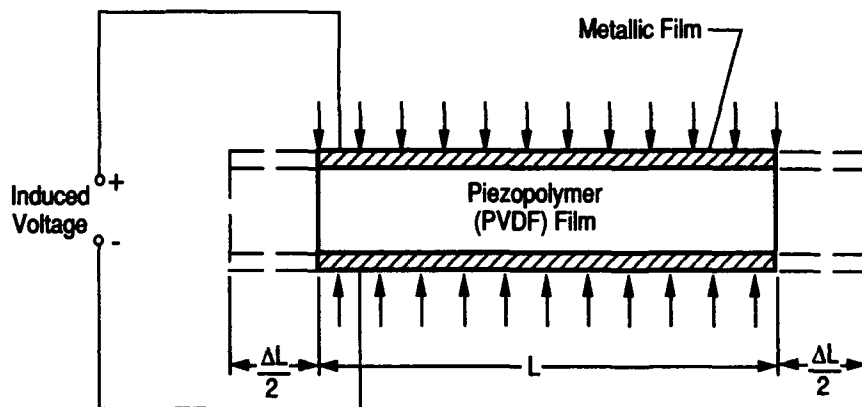
Figure A1. Schematic of the PVDF film inducing electric charge from an applied mechanical stress.
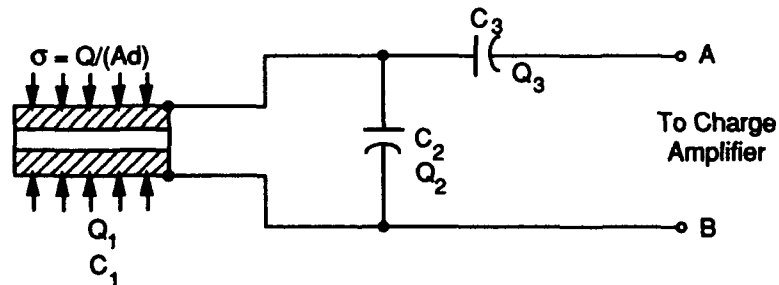
Figure A2. Principle of measurement of stress from PVDF sensors.

Compact Plain Weave Fabric Laminates

N. K. NAIK AND V. K. GANESH

ABSTRACT

A method for increasing the overall fiber volume fraction of the plain weave fabric laminates is presented. Such laminates with the maximum possible overall fiber volume fraction are termed as compact laminates. The thermo-elastic properties of the compact laminates are compared with those of the other typical plain weave fabric laminates for different weave geometries. It is shown here that there is a considerable improvement in the thermo-elastic properties of the plain weave fabric laminates with compaction.

INTRODUCTION

Woven fabric (WF) composites are gaining technological importance and substantial attention has been directed towards the investigations on the thermo-elastic behavior [1-6]. The attractive reasons for their acceptability are the high toughness and thermal stability, better drape and efficient manufacturability. In-plane elastic and strength properties of WF composites having small crimps are comparable to those of corresponding unidirectional (UD) tape crossply laminates for the same overall fiber volume fraction (V_f^o) [1-3]. But, because of the inherent nature of the woven fabrics, the practically achievable V_f^o of WF composites is much lower than those of UD composites. Hence, in absolute terms, UD composites would give higher in-plane elastic and strength properties as compared to the equivalent WF composites. WF composite overall in-plane properties can be considerably enhanced by increasing its V_f^o for the weave geometry considered within the practical limitations. The increase in V_f^o can be achieved either by reducing the number of pure resin pockets or reducing the size of the pure resin pockets.

The reduction in the number of pure resin pockets can be achieved by modifying the weave of the fabric, i. e. using satin weave fabric as reinforcement. Here, the strands are

N. K. Naik, Professor; Ganesh, V. K., Project Engineer.

Aerospace Engg. Dept., IIT, Powai, Bombay - 400 076, India.

straight for a larger portion of its length and therefore would reduce the number of crimps and hence the number of pure resin pockets. Higher the harness of fabric higher would be the V_f^o. But, with higher weave harness satin fabric composite would tend to UD composite and the advantages of woven fabric composites would be lost. Therefore, it is necessary to increase the V_f^o keeping the interwoven nature of the fabric intact to reap the benefits of WF composites and the higher fiber volume fraction of UD composites.

COMPACT FABRIC LAMINATES

Figure 1 shows the cross section of two types of 2D orthogonal plain weave fabric composite layers at fill strand mid-section. In Figure 1a, it is seen that the strand is straight for a part of its length and then undulated, whereas in Figure 1b, the strand is undulated throughout its length. The laminates having strands with certain straight portion would have slightly higher V_f^o compared to those of with completely undulated strands for a given strand fiber volume fraction (V_f^s). Partially straight shape of the strand can be achieved in fabrics with low strand thickness to strand width (h/a) ratio under normal processing conditions. But, fabrics with higher strand thickness to strand width ratio may require higher cure pressure to achieve this shape. Higher cure pressure can lead to resin starved strands and therefore would effect the quality of the composite.

Fabric composites used in actual structures are mostly in the form of laminates made up of a large number of layers. While stacking the layers to form a laminate, the strands of one layer may not be in exact alignment with that of the corresponding strand in the adjacent layer. The shift of the layer with respect to the adjacent layer can be along the fill direction (x-direction), warp direction (y-direction) or/and the thickness direction (z-direction). A variety of laminate configurations are possible depending upon the number of layers in the laminate and the number of shifts involved. In actual laminates, the shifts can be random. The goal of the present work is to show that, if the layers of the laminate are shifted in a controlled manner, a laminate with maximum possible V_f^o can be achieved without compromising on the quality of the laminate.

Figure 2 presents the stacking of four WF layers in the idealized laminate configurations. In configuration-1 (C1), there is no relative shift between the adjacent layers. In configuration-2 (C2), the layers are shifted by a distance (a+g)/2 both in the x- and y-directions with respect to the adjacent layers. Here, `a' is the strand width and `g' is the gap between the two adjacent strands. In this configuration it is seen that pure resin pockets are bridged by the warp strands of the adjacent WF layers and there is an increase in stiffness compared to laminate C1 [5,6]. But, as the pure resin pockets are still present, the V_f^o remains unchanged. In laminate C2, if the layers are given an appropriate shift in the z-direction such that the warp strand of one layer occupies the resin pocket created by the fill strand of the adjacent layer and vice versa as shown in Figure 2c, the laminate V_f^o can be substantially increased. This laminate con-

figuration is termed as compact laminate. Here, it is to be noted that higher V_f^o is achieved for the same given V_f^* and puts no constrains in the processing conditions and hence the quality of laminate is not compromised. Such compaction is possible only with plain weave fabric as reinforcement.

2D WOVEN FABRIC COMPOSITE MODELS

A representative unit cell was considered to analyze the plain weave fabric laminate. The strand cross sectional geometry and the undulation geometry of the strands were defined using the 2D shape functions [2]. These shape functions consider the presence of the gap between the adjacent strands. The V_f^* was evaluated using the geometry defined and the fabric composite V_f^o [2]. The elastic constants of the equivalent UD strand was determined using the CCA model [7] with the elastic constants of the fiber and matrix and V_f^* as input. The overall stiffness of the WF laminate was determined using the 2D WF models presented in Refs. 2-4 and the laminate analysis methodology presented in Ref. 5. The effect of the weave parameters such as strand thickness to strand width ratio (h/a) and gap width to strand width ratio (g/a) on the thermo-elastic properties of all the three idealized laminate configurations are studied.

RESULTS, DISCUSSION AND CONCLUSIONS

The maximum z-shift possible between two layers is a function of the strand thickness and the amount of gap between the adjacent strands. Figure 3 shows the plot of maximum z-shift versus h/a ratio for different g/a ratios. It is seen that the maximum z-shift increases linearly with the increase in h/a and the rate of increase is higher for larger gaps. Here, V_f^o remains constant for all the h/a ratios for a given g/a ratio and V_f^* [2]. The variation of V_f^o for a constant V_f^* as a function of number of layers is shown in Figure 4. The V_f^o for C1 and C2 are same irrespective of the number of layers in the laminate, whereas V_f^o for C3 increases with the increase in the number of layers in the laminate. The increase is very steep initially upto 10 layers for the weave geometry considered and later stabilizes at about 25 layers. The V_f^o of laminate C3 tends towards V_f^*, but cannot be equal to V_f^* as some amount of pure resin is present even after the maximum possible z-shift.

Figure 5 presents the variation of Young's modulus with respect to h/a ratio for different g/a ratios for three idealized laminate configurations. It is seen that the Young's modulus decreases with the increase in h/a for all the three laminate configurations. As expected, the Young's modulus is the highest for C3. The Young's modulus of C2 is almost same as that of C1 at smaller h/a ratios, whereas it shows a gain at higher h/a ratios. At smaller h/a ratios, the gain in stiffness due to compaction is higher than at higher h/a ratios. This is because at smaller h/a, the V_f^o of WF laminates is

the primary parameter which reduces the stiffness, whereas at higher h/a, it is the undulation of the strand which reduces the stiffness. By compacting the laminate, only V_f^o is increased without changing the undulation and therefore higher gain in stiffness is obtained at lower h/a. The effect of g/a on Young's modulus at a constant V_f^s is relatively less for the range of g/a considered as seen from Figure 6. The g/a has a greater effect at smaller h/a on Young's modulus as seen in Figure 6. At h/a=0.2, the Young's modulus is seen to increase for C3 with the increase in g/a for the range of parameters considered, whereas it is almost constant for C1 and C2. It can be noted that there is reduction in undulation with the increase in the gap. Incase of C1 and C2, the increase in the gap reduces V_f^o substantially, but its effect on C3 is not critical. At higher g/a, Young's modulus is expected to decrease even for C3.

The effect of h/a ratio is negligible on modulus of rigidity for all the laminate configurations and g/a ratios as shown by Figure 7. The laminate C1 has the least modulus of rigidity whereas C3 has the highest and C2 falls inbetween. The effect of increase in g/a is to reduce the modulus of rigidity for all the laminate configurations. This is because of the reason that with the increase in the gap for a given V_f^s, the V_f^o reduces and therefore modulus of rigidity also decreases. The drop in V_f^o for a constant V_f^s is less for laminate C3 and therefore the rate of reduction in modulus of rigidity with increasing gap is also less for C3.

The variation of thermal expansion coefficient (TEC) with respect to h/a ratio for different g/a ratios is shown in Figure 8. Here, the value of TEC is same for both C2 and C3. This is because TEC is the ratio of two elements of stiffness matrix and the reduction in thickness in the case of C3 affects all the elements of the stiffness matrix equally. The effect of increase in h/a is to increase the value of TEC for all the laminate configurations. For smaller h/a, C1 gives lower TEC, but at higher h/a, C2 and C3 give lower TEC. This is because the effect of strand undulation is significant in the case of C1 as compared to that of C2 and C3. At smaller crimps, the strands tend to be straight and therefore lower TEC is obtained. But as the crimp increases, TEC increases and the rate of increase is more for C1 than for C2 and C3. The crossover of the curves is at lower h/a for smaller gaps and at higher h/a for larger gaps. This behavior can be seen in Figure 8. The variation of TEC with gap is similar for all h/a ratios, but the absolute value of TEC is higher for higher h/a ratios in the case of C2 and C3. For C1, the increase in TEC is less steep at higher h/a ratios than at lower h/a ratios.

KEYWORDS :

Plain weave fabric laminate, 2D woven fabric composite models, shift of layers with respect to each other, Compact laminates.

ACKNOWLEDGEMENT

REFERENCES

1. Chou, T. W. and T. Ishikawa. 1989. "Analysis and Modeling of Two-Dimensional Fabric Composites," in Textile Structural Composites, T. W. Chou and F. K. Ko, ed. Amsterdam: Elsevier Science Publishers B. V., pp. 209-264.
2. Naik, N. K. and V. K. Ganesh. "Prediction of On-Axes Elastic Properties of Plain Weave Fabric Composites," To appear in Composites Science and Technology.
3. Naik, N. K. and P. S. Shembekar. October 1991. "Elastic Analysis of Woven Fabric Composites," Technical Report No. IITB/AE/ARDB/STR/659/01, Aerospace Engineering Department, IIT, Bombay.
4. Naik, N. K. and P. S. Shembekar. "Elastic Behavior of Woven Fabric Composites: I - Lamina Analysis," To appear in Journal of Composite Materials.
5. Shembekar, P. S. and N. K. Naik. "Elastic Behavior of Woven Fabric Composites: II - Laminate Analysis," To appear in Journal of Composite Materials.
6. Naik, N. K. and P. S. Shembekar. "Elastic Behavior of Woven Fabric Composites: III - Laminate Design," To appear in Journal of Composite Materials.
7. Hashin, Z.. 1972. "Theory of Fiber Reinforced Materials," NASA-CR-1974.
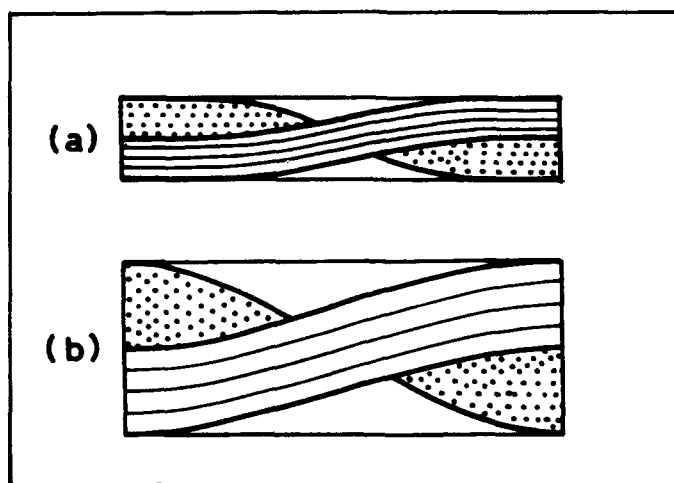
Figure 1. Cross - sections of typical plain weave fabric laminae.
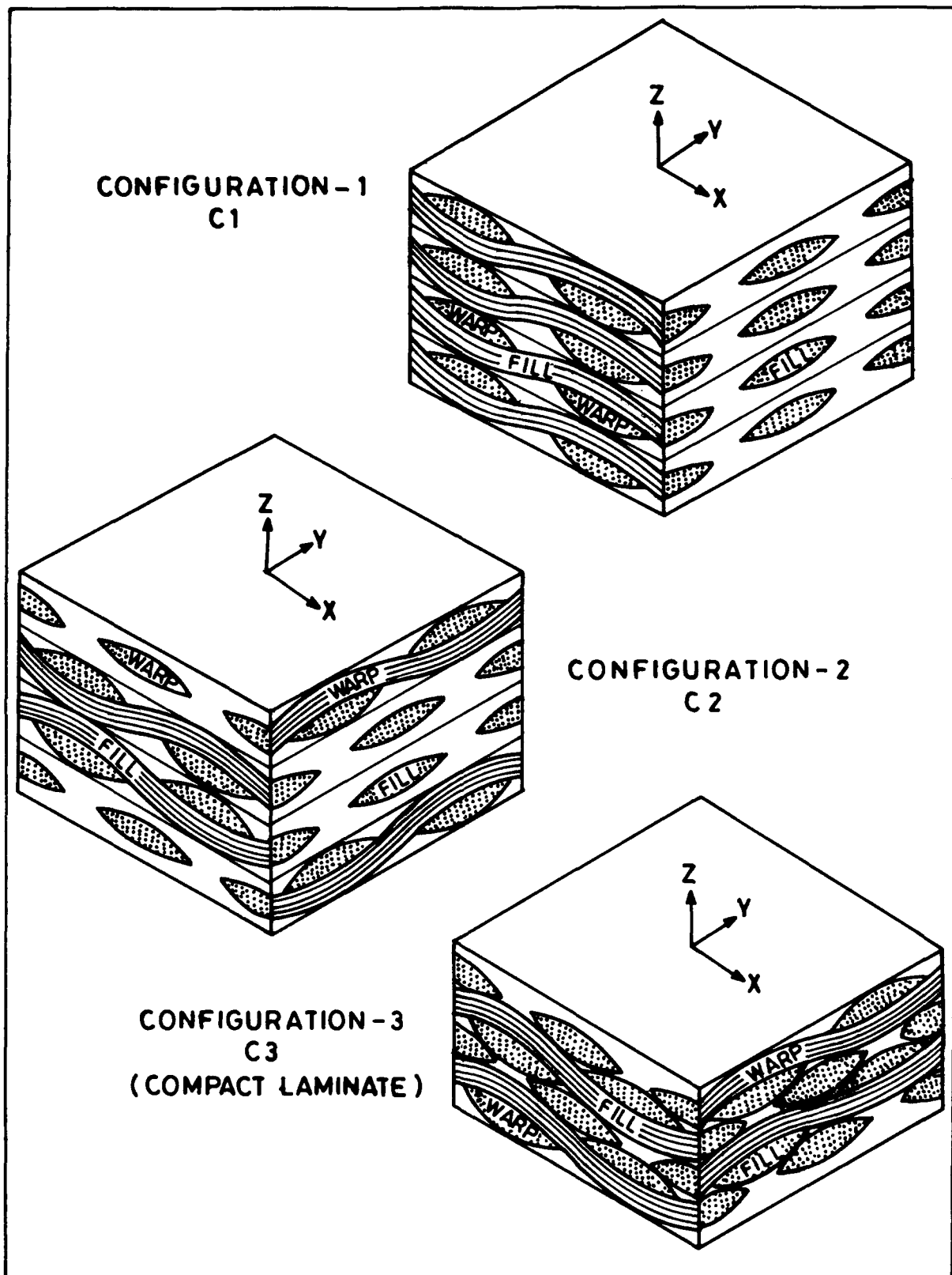
Figure 2. Stacking of layers in different idealized laminate configurations.
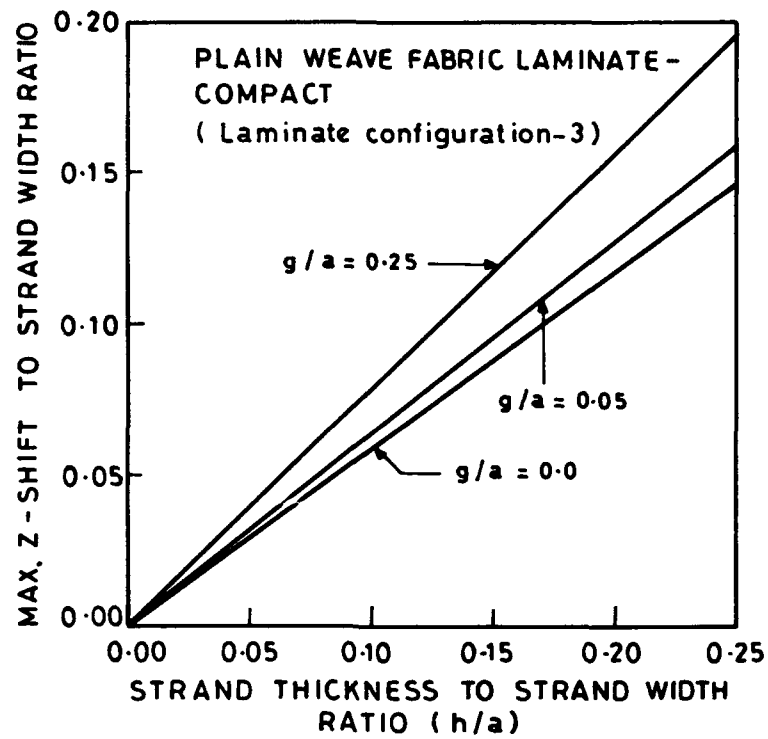
Figure 3. Effect of h/a on compaction.
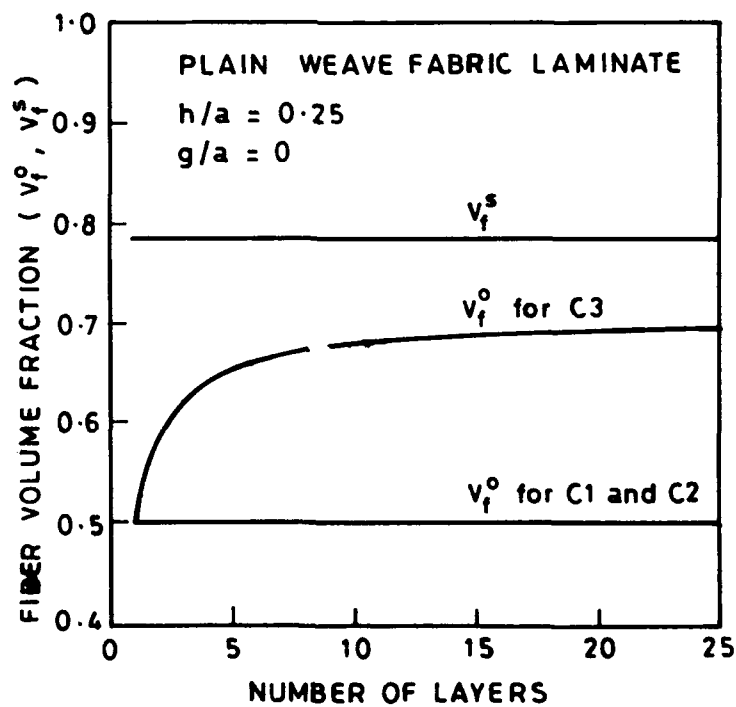
Figure 4. Effect of number of layers on overall fiber volume fraction for compact laminates.
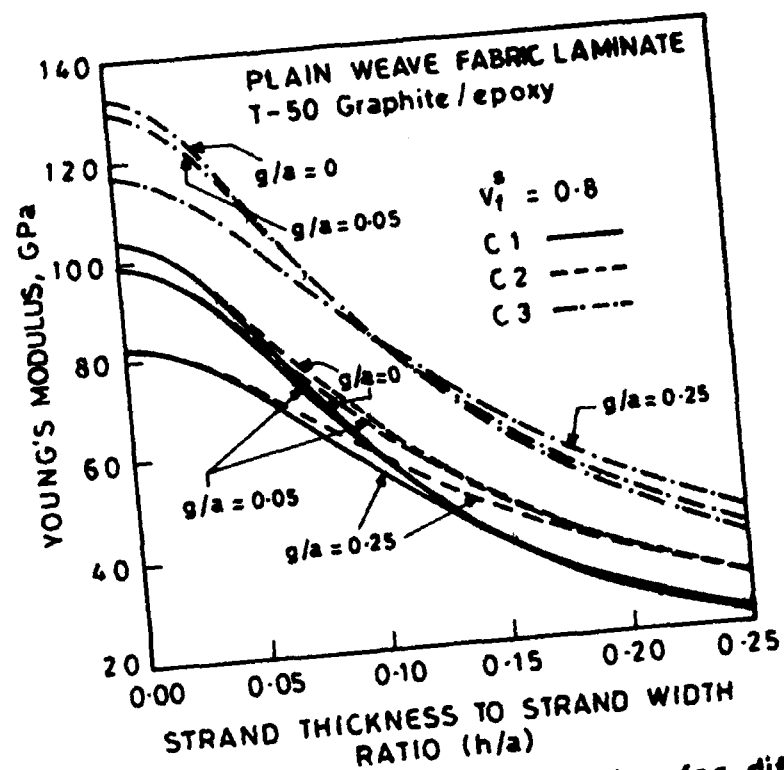
Figure 5. Effect of h/a on Young's modulus for different laminate configurations.
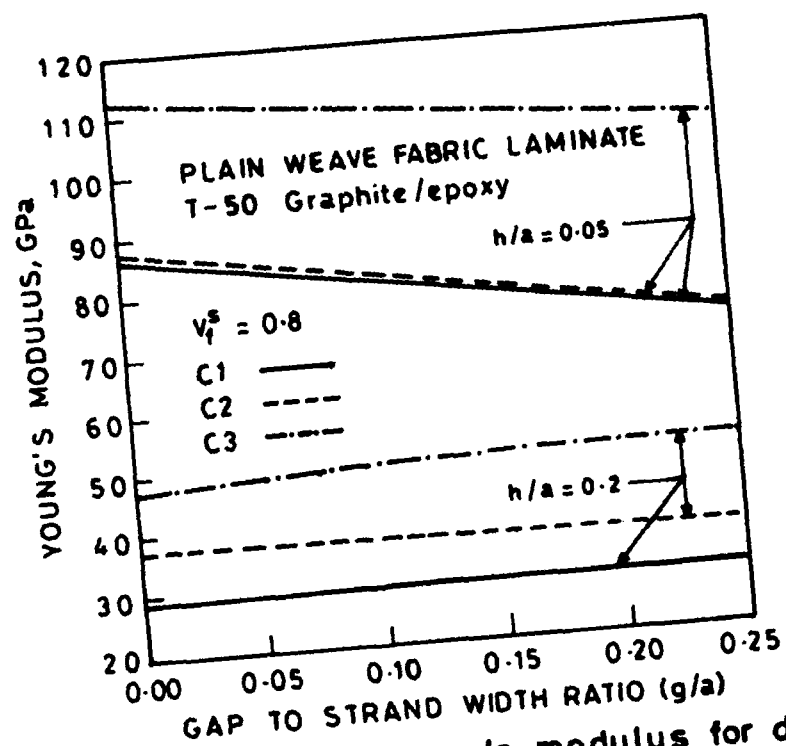
Figure 6. Effect of g/a on Young's modulus for different laminate configurations.
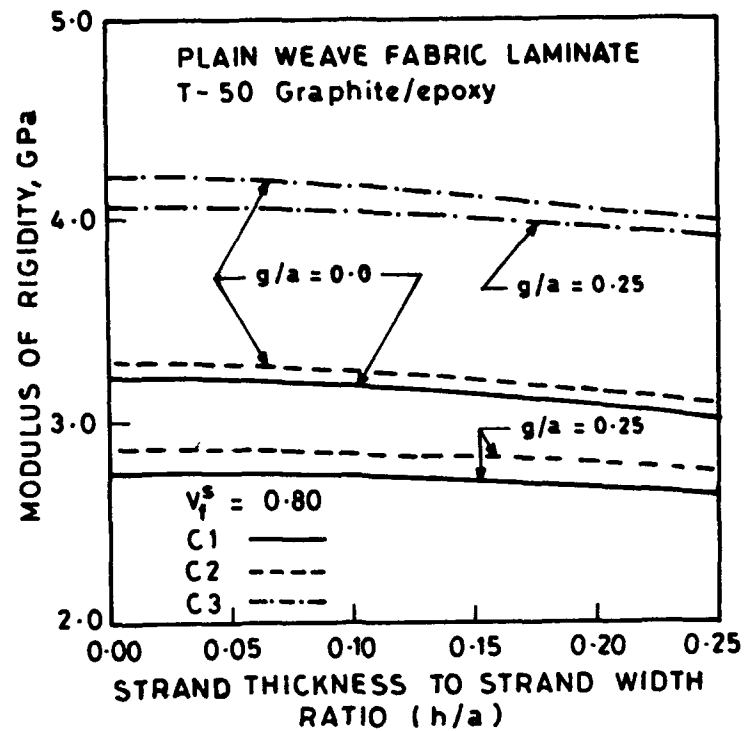
Figure 7. Effect of h/a on modulus of rigidity for different laminate configurations.
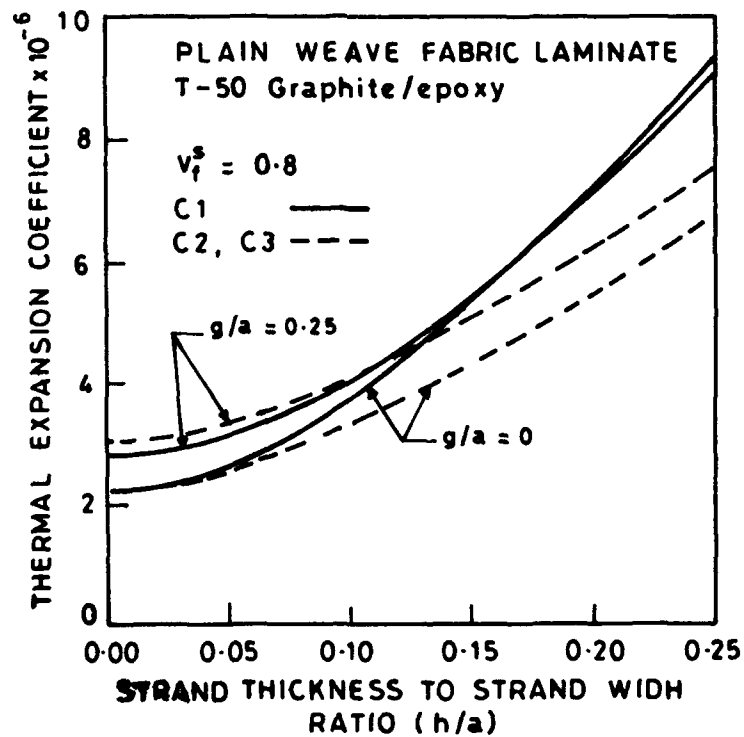
Figure 8. Effect of h/a on thermal expansion coefficient for different laminate configurations.

Author Index